

**Evaluation of Fire
Models for Nuclear
Power Plant
Applications:**

**Fuel Pool Fire Inside
A Compartment**

International Panel
Report

Compiled by
W. Klein-Heßling (GRS),
M. Röwekamp (GRS),
O. Riese (iBMB)

November, 2006

Final Version



Gesellschaft für Anlagen-
und Reaktorsicherheit
(GRS) mbH

Evaluation of Fire Models
for Nuclear Power Plant
Applications:
Fuel Pool Fire Inside A
Compartment

- International Panel Report -

Compiled by
W. Klein-Heßling (GRS),
M. Röwekamp (GRS),
O. Riese (iBMB)

November 2006

Final Version

Vorhaben: SR 2491

Anmerkung:

Das diesem Bericht zugrunde liegende Vorhaben "Übergreifende Bewertung des Brandschutzes bei Kernkraftwerken - Auswertung von spezifischen Brandereignissen, Mitarbeit in internationalen Gremien, Entscheidungshilfe bei der Verwendung von Brand-simulationsprogrammen" wurde im Auftrag des Bundesministeriums für Umwelt, Naturschutz und Reaktor-sicherheit (BMU) durchgeführt.

Die Verantwortung für den Inhalt dieser Veröffentlichung liegt beim Auftragnehmer.

Abstract

Fire simulations as well as their analytical validation procedures have gained more and more significance, particularly in the context of the fire safety analysis for operating nuclear power plants. Meanwhile, fire simulation models have been adapted as analytical tools for a risk oriented fire safety assessment.

Calculated predictions can be used, on the one hand, for the improvements and upgrades of fire protection in nuclear power plants by the licensees and, on the other hand, as a tool for reproducible and clearly understandable estimations in assessing the available and/or foreseen fire protection measures by the authorities and their experts. For consideration of such aspects in the context of implementing new nuclear fire protection standards or of updating existing ones, an "International Collaborative Project to Evaluate Fire Models for Nuclear Power Plant Applications" also known as the "International Collaborative Fire Model Project" (ICFMP) was started in 1999. It has made use of the experience and knowledge of a variety of worldwide expert institutions in this field to assess and improve, if necessary, the state-of-the-art with respect to modeling fires in nuclear power plants and other nuclear installations.

This document contains the results of the ICFMP Benchmark Exercise No. 4, where two fuel pool fire experiments in an enclosure with two different natural vent sizes have been considered. Analyzing the results of different fire simulation codes and code types provides some indications with respect to the uncertainty of the results. This information is especially important in setting uncertainty parameters in probabilistic risk studies and to provide general insights concerning the applicability and limitations in the application of different types of fire simulation codes for this type of fire scenario and boundary conditions.

During the benchmark procedure the participants performed different types of calculations. These included totally blind simulations without knowledge of the pyrolysis rate, semi-blind calculations with knowledge of this rate only, and completely open post-calculations with knowledge of all experimental measurements. It has been demonstrated, as expected, that the pyrolysis rate has a strong influence on the calculation results. This could be derived from the large differences in the quality of results between the few blind and 'semi-blind' or open calculations. The range of the results is much larger for the blind simulations compared to the semi-blind ones. This reduces

the reliability of the results in the event of fire simulation codes being applied e.g. in the frame of probabilistic risk analyses.

The Benchmark Exercise has furthermore shown that the simulation of under-ventilated fires is more difficult for the fire simulation codes and that a highly transient fire behavior leads to a wider range of the code simulation results. Compared to typical fire scenarios analyzed in the fire PSA the considered Benchmark Exercise is extreme in terms of thermal loads. This has to be considered for the assessment of the deviations between the simulation results and the experimental data.

Kurzfassung

Brandsimulationen sowie deren analytische Validierung erhalten mehr und mehr Bedeutung im Rahmen von Brandsicherheitsanalysen in Betrieb befindlicher Kernkraftwerke. Mittlerweile sind Brandsimulationsmodelle als analytische Werkzeuge, welche sich insbesondere für risikoorientierte Brandsicherheitsbewertungen eignen, anerkannt.

Die Verwendung rechnerischer Vorhersagen kann zum einen die Verbesserungen und Nachrüstungen des Brandschutzes durch die Betreiber aufzeigen, zum anderen aber auch als ein Hilfsmittel für reproduzierbare und klar verständliche Abschätzungen im Rahmen der Bewertung vorhandener bzw. geplanter Brandschutzmaßnahmen seitens der Genehmigungs- und Aufsichtsbehörden und deren Gutachter genutzt werden. Zur Berücksichtigung derartiger Aspekte auch bei der Umsetzung neuer oder der Erweiterung kerntechnischer Brandschutzregelwerke wurde ein so genanntes 'International Collaborative Project to Evaluate Fire Models for Nuclear Power Plant Applications' auch bekannt unter 'International Collaborative Fire Model Project (ICFMP)' im Jahr 1999 initiiert, in welchem Erfahrungen und Kenntnisse einer Vielzahl von Experteninstitutionen auf diesem Fachgebiet dazu genutzt werden sollen, den Stand von Wissenschaft und Technik auf dem Gebiet der Modellierung von Bränden für Anwendungen in Kernkraftwerken und anderen kerntechnischen Einrichtungen zu bewerten und, falls erforderlich, zu verbessern.

Der nachfolgende Bericht beinhaltet die Ergebnisse des ICFMP Benchmark Exercise Nr. 4, bei welchem zwei Versuche zum Treibstoffflächenbrand in einem Brandraum mit unterschiedlicher natürlicher Ventilation betrachtet werden. Die Analyse der Ergebnisse von Simulationsrechnungen mit unterschiedlichen Brandsimulationscodes und -codearten gibt Hinweise in Bezug auf die Unsicherheiten der Resultate. Dies ist zum einen von Bedeutung für die Auswahl von Unsicherheitsparametern in probabilistischen Sicherheitsanalysen. Zum anderen ergeben sich daraus Erkenntnisse hinsichtlich der Anwendbarkeit und Anwendungsgrenzen verschiedener Arten von Brandsimulationscodes für solche Brandszenarien und die entsprechenden Randbedingungen.

Im Verlauf des Benchmarks werden von den Teilnehmern unterschiedliche Arten von Simulationsrechnungen durchgeführt. Dabei handelt es sich um so genannte 'blinde' Vorausrechnungen ohne Kenntnis der Pyrolyserate, um 'semi-blinde' Rechnungen, bei welchen nur die Pyrolyserate bekannt ist, und um vollständig offene Nachrechnungen unter Kenntnis der Versuchsdaten. Wie erwartet, zeigte sich, dass die Pyrolyserate

einen erheblichen Einfluss auf die rechnerischen Ergebnisse hat. Dies zeigte sich insbesondere an den doch erheblichen Qualitätsunterschieden der Rechenergebnisse von den wenigen blinden im Vergleich zu den ‚semi-blinden‘ bzw. offenen Rechnungen. Die Bandbreite der Ergebnisse ist bei den blinden Vorausrechnungen erheblich größer als bei den semi-blinden, was zu höheren Ergebnisunsicherheiten bei Nutzung von Brandsimulationsrechnungen bei z.B. probabilistischen Analysen führt. Es zeigt sich weiterhin, dass die Simulation unterventilierter Brände für die Brandsimulationscodes erheblich schwieriger ist. Ein sehr instationäres Brandverhalten führt zu einer größeren Bandbreite der Ergebnisse. Die betrachtete Benchmarkaufgabe ist in Bezug auf die thermischen Belastungen extrem im Vergleich zu den in Rahmen von Brand PSA betrachteten Szenarien. Dies ist bei der Betrachtung der Abweichungen der Simulationsergebnisse von den experimentellen Werten zu berücksichtigen.

Table of Contents

	Abstract	I
	Kurzfassung	III
1	Introduction	1
2	Specification of Benchmark Exercise No. 4	3
2.1	Review of Previous Related Work within the ICFMP Project	3
2.2	Specification of the Experiments	5
2.2.1	Description of the Test Facility	5
2.2.2	Measurements Performed.....	15
2.2.3	Experimental Procedure.....	21
3	Experimental Results	29
3.1	Summary of Test 1	30
3.2	Summary of Test 3.....	34
3.3	Conclusions.....	37
4	Input Parameters and Assumptions	39
5	Comparison of Code Simulations and Experimental Results	43
5.1	Blind Calculations.....	44
5.1.1	FDS (CFD Code) Applied by K. McGrattan (NIST, USA).....	44
5.1.2	JASMINE (CFD Code) Applied by S. Miles (BRE, UK)	47
5.2	Semi-blind Calculations.....	52
5.2.1	FDS (CFD Code) Applied by K. McGrattan (NIST, USA).....	52
5.2.2	FDS (CFD Code) and CFST (Zone Model) Applied by M. Dey (USNRC, USA).....	55
5.2.3	CFAST (Zone Model) and JASMINE (CFD CODE) Applied by S. Miles (BRE, UK)	61
5.3	Open Calculations.....	70
5.3.1	FATE (Zone Model) Applied by T. Elicson (Fauske & Associates LLC, USA).....	70
5.3.2	FLAMME-S (Zone Model) Applied by L. Rigollet (IRSN, France)	75

5.3.3	CFX (CFD Code) Applied by M. Heitsch (GRS, Germany)	78
5.3.4	FDS (CFD Code) Applied by W. Brücher (GRS, Germany)	81
5.3.5	COCOSYS (Lumped Parameter Code) Applied by B. Schramm (GRS, Germany)	87
5.3.6	VULCAN (CFD Code) Applied by V.F. Nicolette (SNL, USA)	91
5.3.7	MAGIC (zone code) Applied by B. Gautier (EDF, France).....	95
6	Code to Code Comparison	97
6.1	Test 1	97
6.1.1	Plume Temperatures (M1 to M6)	97
6.1.2	Temperatures inside the Fire Compartment	99
6.1.3	Layer Height and Upper Layer Temperature	106
6.1.4	Gas Concentration inside the Fire Compartment	108
6.1.5	Probe Temperatures	113
6.2	Test 3	116
6.2.1	Plume Temperatures (M1 to M6)	116
6.2.2	Temperatures inside the Fire Compartment	119
6.2.3	Layer Height and Upper Layer Temperature	126
6.2.4	Gas Concentrations inside the Fire Compartment	129
6.2.5	Probe Temperatures	134
7	General Conclusions and Recommendations	137
7.1	General Conclusions	137
7.2	Recommendations	138
8	Summary	139
9	References	141
	List of Figures	143
	List of Tables	147
	List of Appendices	149
	Appendices A – J on CD	
	Acknowledgements	151

1 Introduction

Fire simulations as well as analytical validation procedures have gained more and more significance, particularly in the context of fire safety analysis for operating nuclear power plants (NPPs). Fire simulation models have been developed as analytical tools for a risk oriented fire safety assessment.

The use of calculated predictions could be considered, on the one hand, for improvements and upgrades of the fire protection by the licensees and, on the other hand as a tool for reproducible and clearly understandable estimations in assessing the available and/or foreseen fire protection measures by the authorities and their experts. For consideration of such aspects even in the frame of implementing new nuclear fire protection standards or upgrading existing ones, an “International Collaborative Project to Evaluate Fire Models for Nuclear Power Plant Applications” also known as the “International Collaborative Fire Model Project” (ICFMP)” was started in 1999, to make use of the experience and knowledge of a variety of expert institutions in this field worldwide to assess and improve, where necessary, the state-of-the-art with respect to modeling fires for application to nuclear installations/plants.

Within the ICFMP project the following Benchmark Exercises have been performed:

- Benchmark Exercise No. 1: Cable fire and thermal load on cables in a cable spreading room (theoretical) /DEY 02/;
- Benchmark Exercise No. 2: Heptane pool fire in a large hall (experiment) and large oil fire in a turbine hall with 2 floor levels and horizontal openings /MIL 04/;
- Benchmark Exercise No. 3: Heptane spray fire in a cable room to investigate thermal loads on cables and cable trays (experiments) /MCG 06/;
- Benchmark Exercise No. 4: Relatively large fuel pool fire with two variations of the door cross section area (experiments);
- Benchmark Exercise No. 5: Fire spreading on vertical cable trays with variations on the pre-heating and cable material (experiments) /RIE 06/.

In this Panel Report, Benchmark Exercise No. 4 will be discussed and the results of the different participants will be evaluated. The individual reports of the participants are presented as attachments.

The main objective of the experiments for Benchmark Exercise No. 4 was to analyze the thermal load on the structures surrounding a fire relatively large compared to the floor area and volume of the fire compartment. In several experiments the natural and forced ventilation has been changed to investigate the influence of oxygen depleted conditions on the fire. Both the thermal loads and the oxygen depleted conditions are somewhat difficult aspects to calculate. Therefore these experiments can contribute to the further improvement of fire codes. Additionally, the results give some insight concerning the uncertainties of fire simulations of pool fires in an enclosure under the given boundary conditions. This information is important for the definition of uncertainty input parameters for PSA studies.

2 Specification of Benchmark Exercise No. 4

At iBMB (Institut für Baustoffe, Massivbau und Brandschutz) of Braunschweig University of Technology, a set of nine real scale fuel pool fire experiments has been performed. The objective of these experiments was to systematically vary the major influencing parameters on the burning behavior to derive standard fire curves (time dependence of temperatures and heat flow densities at different distances from the fire source, burning rates, energy release rates and temperature loads) and to examine the dependence on the pool surface area, the fuel filling level and the ventilation conditions.

The fire compartment OSKAR of iBMB, an enclosure with a compartment floor size of 3.6 m x 3.6 m = 12.96 m² and a height of 5.7 m, was used for the pool fire test series. This facility has 3 possible openings for the natural ventilation of the fire compartment. At the ceiling, the hot gases and smoke can be extracted and cleaned by a fan system with filters. During the experiments gas and surface temperatures, gas composition, velocities and heat flux densities were measured.

2.1 Review of Previous Related Work within the ICFMP Project

In this section, the relation of Benchmark Exercise No. 4 to the previous Benchmark Exercises is discussed.

Looking to Benchmark Exercise No. 1, one result was the strong influence of the assumed lower oxygen limit (LOL) on the calculated results /DEY 02/. Fig. 2-1 presents the calculated oxygen concentrations for the Benchmark Exercise No. 1, Part II base case. The results depend on the assumed parameter of LOL. The range of this parameter varied between 0 and 10 Vol.-%. The difference between calculations with the zone model MAGIC by different users, MAGIC-EDF (with 10 Vol.-%) and MAGIC-CTICM (with 0 Vol.-%) are of special interest. The consequences of this parameter on the hot gas layer temperature (HGL) are shown in Fig. 2-2. In particular, the fire duration is predicted quite differently.

The main difference between Test 1 and Test 3 in Benchmark Exercise No. 4 is the ventilation opening at the front wall, leading to oxygen depleted conditions in Test 3.

Therefore, this Benchmark Exercise gives some indications for the appropriate estimation of the LOL value as well as for the simulation of oxygen depleted conditions.

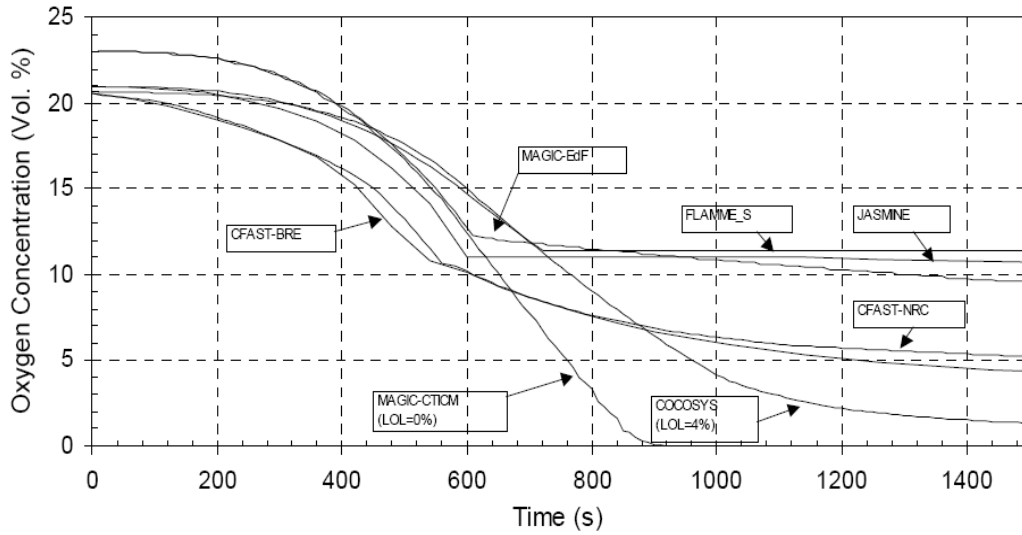


Fig. 2-1 Benchmark Exercise No.1, Part II base case - calculated oxygen concentrations

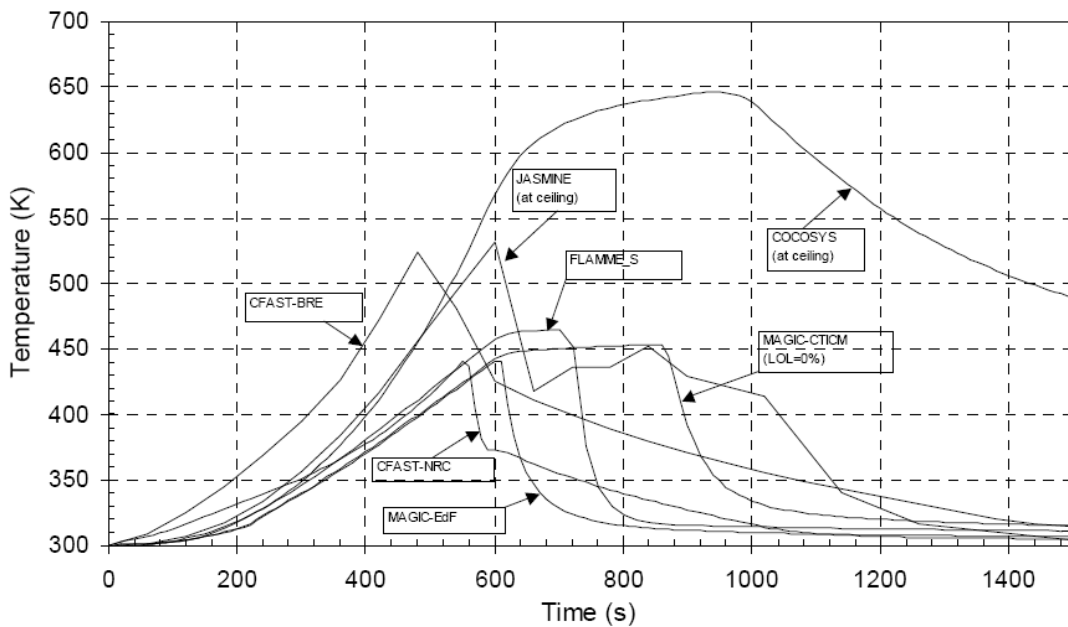


Fig. 2-2 Benchmark Exercise No. 1, Part II base case - calculated HGL temperatures

One of the main tasks of fire simulation codes applied within the ICFMP is the calculation of thermal loads to safety significant targets. These include electrical components, cable trays and wall structures. Benchmark Exercise No. 3 shows, that this topic should be further improved /MCG 06/.

In Benchmark Exercise No. 4 the relation between fire load and compartment floor area (267 MJ/m^2) is quite high. This leads to some extent to a rather high thermal load on the wall structures. Different material types (concrete, aerated concrete and steel) have been investigated in these experiments. In addition, a barrel type waste container with a rather complex material composition has been positioned close to the fire source. Therefore, the Benchmark Exercise No. 4 results can be used to evaluate the simulation of the target by the fire codes.

2.2 Specification of the Experiments

This section contains the specification of the experiments delivered to the participants.

2.2.1 Description of the Test Facility

In the following, the OSKAR test facility of iBMB is described in detail.

Geometry

Fig. 2-3 to Fig. 2-6 show the test facility. It has a floor area of $3.6 \text{ m} \times 3.6 \text{ m} = 12.96 \text{ m}^2$ and a height of 5.7 m. At the ceiling, there are two ventilation ducts with a width of 0.42 m and a height of 1.03 m. The length of both ducts is approximately 3.625 m and leads to the fan system.

In the center of the floor area a steel pan with a size of 4 m^2 has been installed on a weight scale. The lower level of this pan has an elevation of about 0.36 m. The side walls are approx. 0.3 m high (Fig. 2-7). The weight loss of the liquid fuel was measured by the scale. To protect this measurement aerated concrete had been added to the fire compartment around this pan on the complete floor area up to an elevation of 0.6 m. The inner side of the large pan had been covered by a 0.05 m thick light concrete plate for protection. In the center of the large pan, a smaller pan of 1 m^2 was placed. The bottom of this pan has an elevation of approx. 0.51 m. The height of the side walls is

Ventilation

In the experiments considered only the front vent (door) was opened. The door is located at the center of the front wall ($x = 1.8$; $y = 0.$). In Test 1, the door was completely open with a free cross section of 0.7 m x 3.0 m. The lower edge of the door is just above the aerated concrete at $z = 0.6$ m. In the Test 3, the opening was partly restricted. The open (free) cross section was reduced to 0.7 m x 1.0 m and the opening started at an elevation of 1.6 m (1 m above the aerated concrete bottom surface).

Although the FUCHS fan system extracting air from the top of the fire compartment was not in use, some velocity flow (measurements V11 and V12) could be measured, because the valves were not leak-tight. The values are specified below (Table 2-7 and Table 2-8).

A hood had been installed above the open front door (Fig. 2-10). Using the oxygen consumption method the energy release could be estimated. The volume flow rates are given in Table 2-9 and Table 2-10.

Infiltration

All other vents were closed. However, some leakage area can be assumed in the lower part of the fire compartment. Due to the construction kit technique used, it is difficult to measure the leakage. A rough estimation of the leakage is about 0.05 m² in the lower region of the facility.

Wall Structures and Properties

The following Table 2-1 gives information on the composition of the fire compartment wall structures.

Table 2-1 Composition of the wall structures

Position	Material	Thickness [m]
Floor	Concrete	0.30
	Aerated concrete	0.60 (see Fig. 2-5)
Side walls	Light concrete	0.25
	Insulation	0.05
Ceiling	Concrete	0.25
	Insulation	0.05
Side walls channel	Light concrete	0.125
	Insulation	0.06
Ceiling channel	Concrete	0.13
	Insulation	0.07

The properties of the different materials are:

Table 2-2 Properties of the fire compartment materials

Material	Heat conductivity λ [W/mK]	Heat capacity c_p [kJ/kgK]	Density ρ [kg/m ³]
Concrete	2.10	880	2400
Light concrete	0.75	840	1500
Aerated concrete (bottom)	0.11	1350	420
Insulation	0.05	1500	100

Targets

Behind the large pan, a barrel type waste container typically used in nuclear facilities was installed. The center of the bottom of the barrel was located at ($x = 1.8\text{m}$, $y = 3.2\text{m}$, $z = 0.6\text{m}$). This container had a diameter of 0.64 m and a height of 0.96 m. It was a double vessel container. The diameter of the inner barrel is 0.515 m (Fig. 2-12, Fig. 2-13) consisting of tinsplate and is filled with styrene divinylbenzene copolymer with sul-

Three different types of material probes were positioned on the right side of the fire compartment ($x = 0$ m). The materials are "aerated concrete", concrete and steel. The size of these elements is 0.3 m x 0.3 m (Fig. 2-11). For the concrete probes, the thickness is 0.1 m, for the steel plate it is 0.02 m. The properties of the materials used are given in Table 2-3. The location of the center surface is given in Table 2-4.

Table 2-3 Properties of the target materials

Material	Heat conductivity λ [W/mK]	Heat capacity c_p [J/kgK]	Density ρ [kg/m ³]
Granulate (styrene)	0.233	1600	1000
Tin plate	63	230	7280
Concrete (between barrels)	2.1	880	2400
Steel	44.5	480	7743
Concrete (probe)	2.1	880	2400
Aerated concrete	0.11	1350	420

Table 2-4 Location of the material probes

Material probe	x [cm]	y [cm]	z [cm]
Aerated concrete	8	65	170
Concrete	8	190	170
Steel	2	280	170

Hood

To measure the oxygen consumption of the fire, a hood in front of the front door was installed. The cross section of the hood is 2.9 m x 2.9 m = 8.41 m² and the hood was positioned at the center of the front door just at the upper edge (at $z = 3.6$ m). A flexible soot apron of 1 m height was fixed at the hood inlet. Therefore, the lower edge of the hood apron is at $z = 2.6$ m. The scheme of the hood is shown in Fig. 2-9.

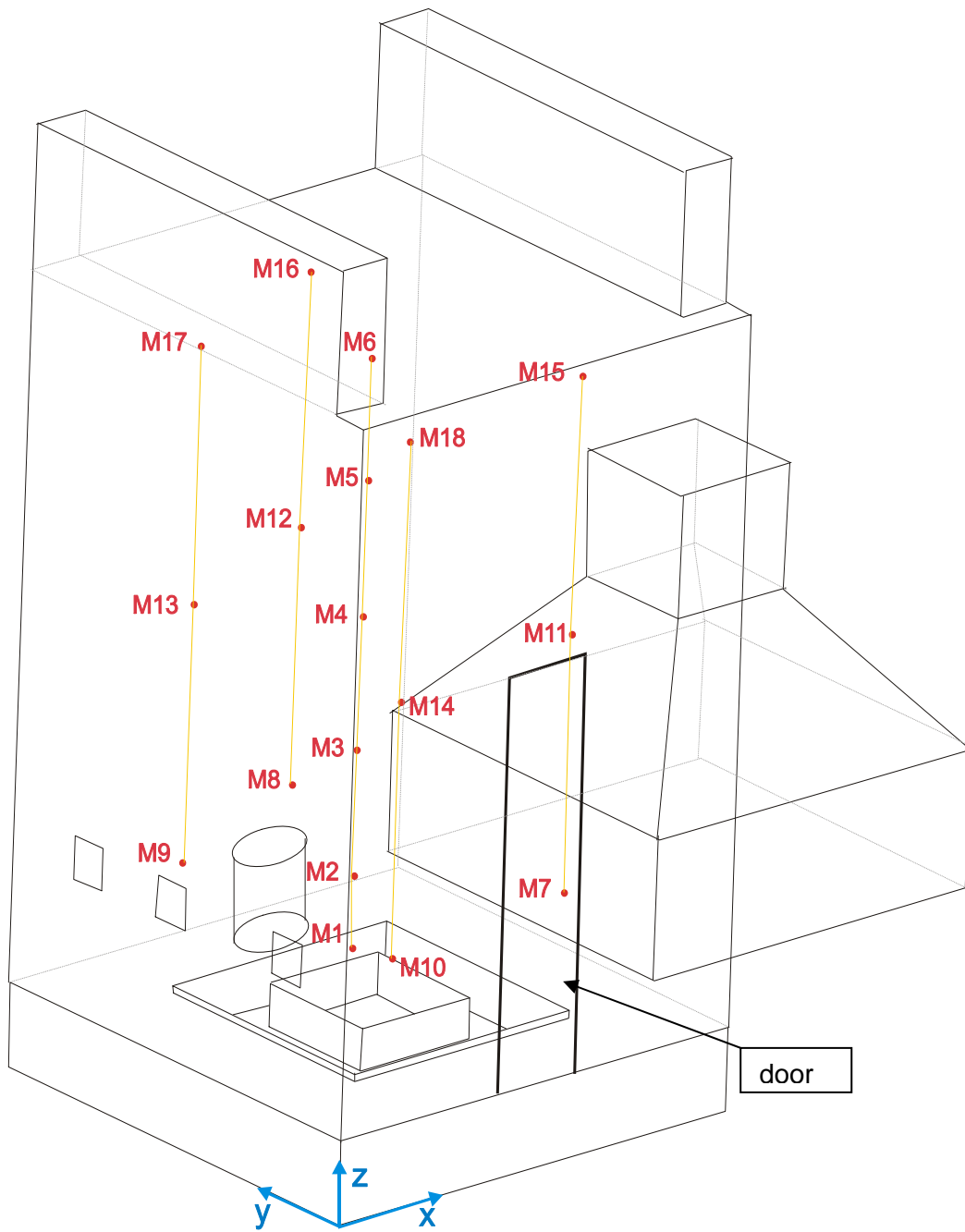


Fig. 2-3 3D view of the OSKAR fire compartment

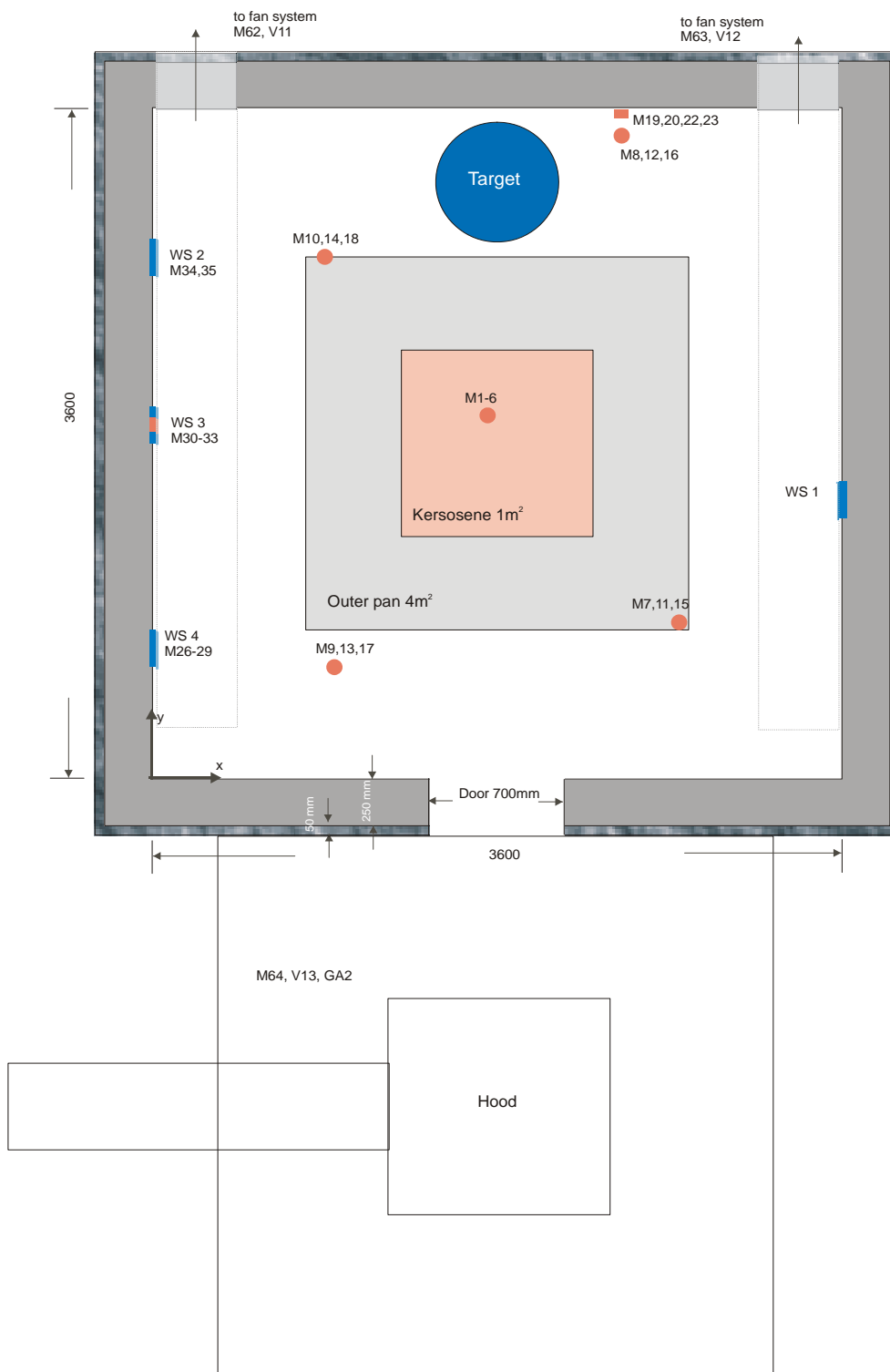


Fig. 2-4 Top view of the OSKAR fire compartment

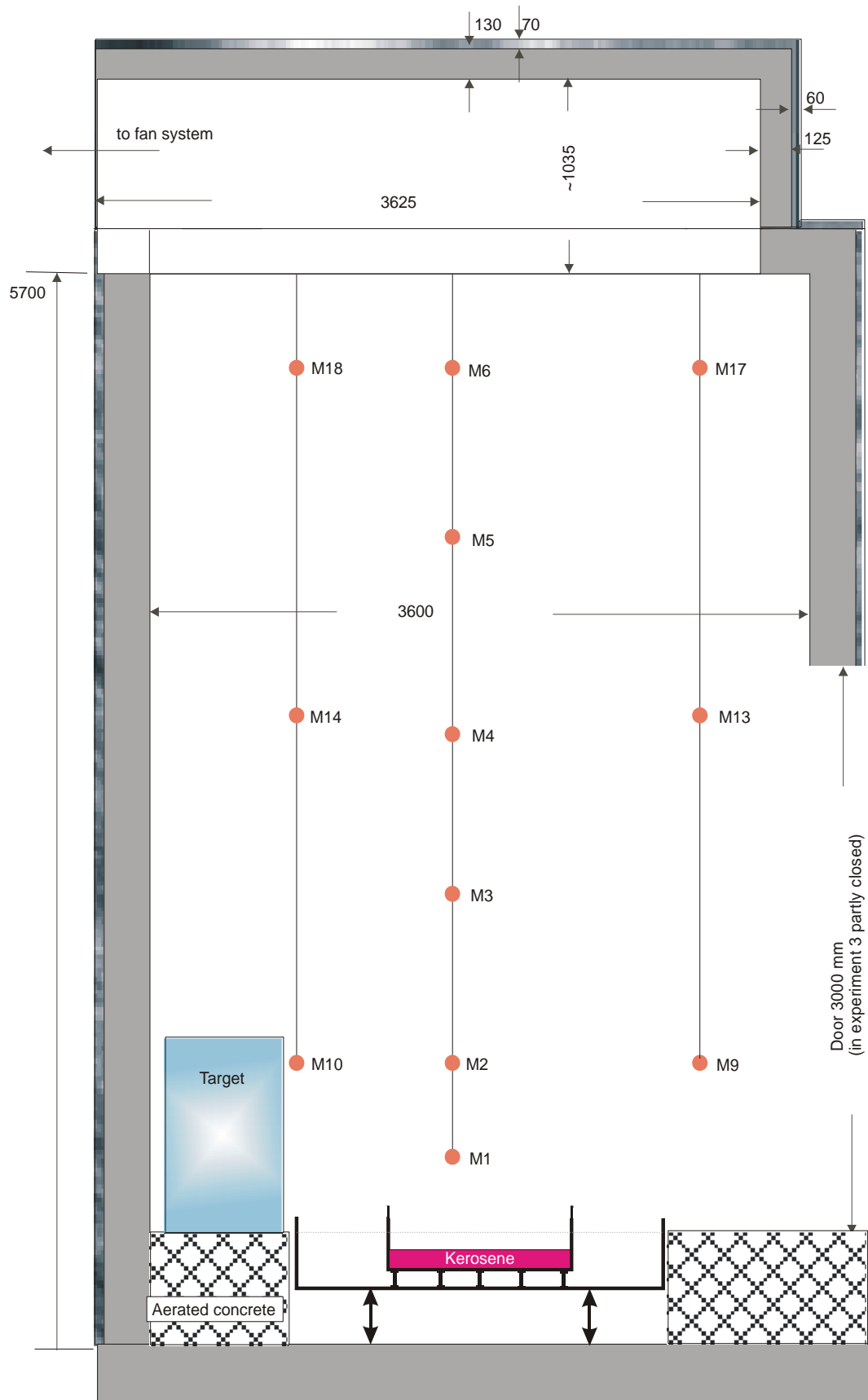


Fig. 2-5 Side view of the OSKAR fire compartment (in + y direction)

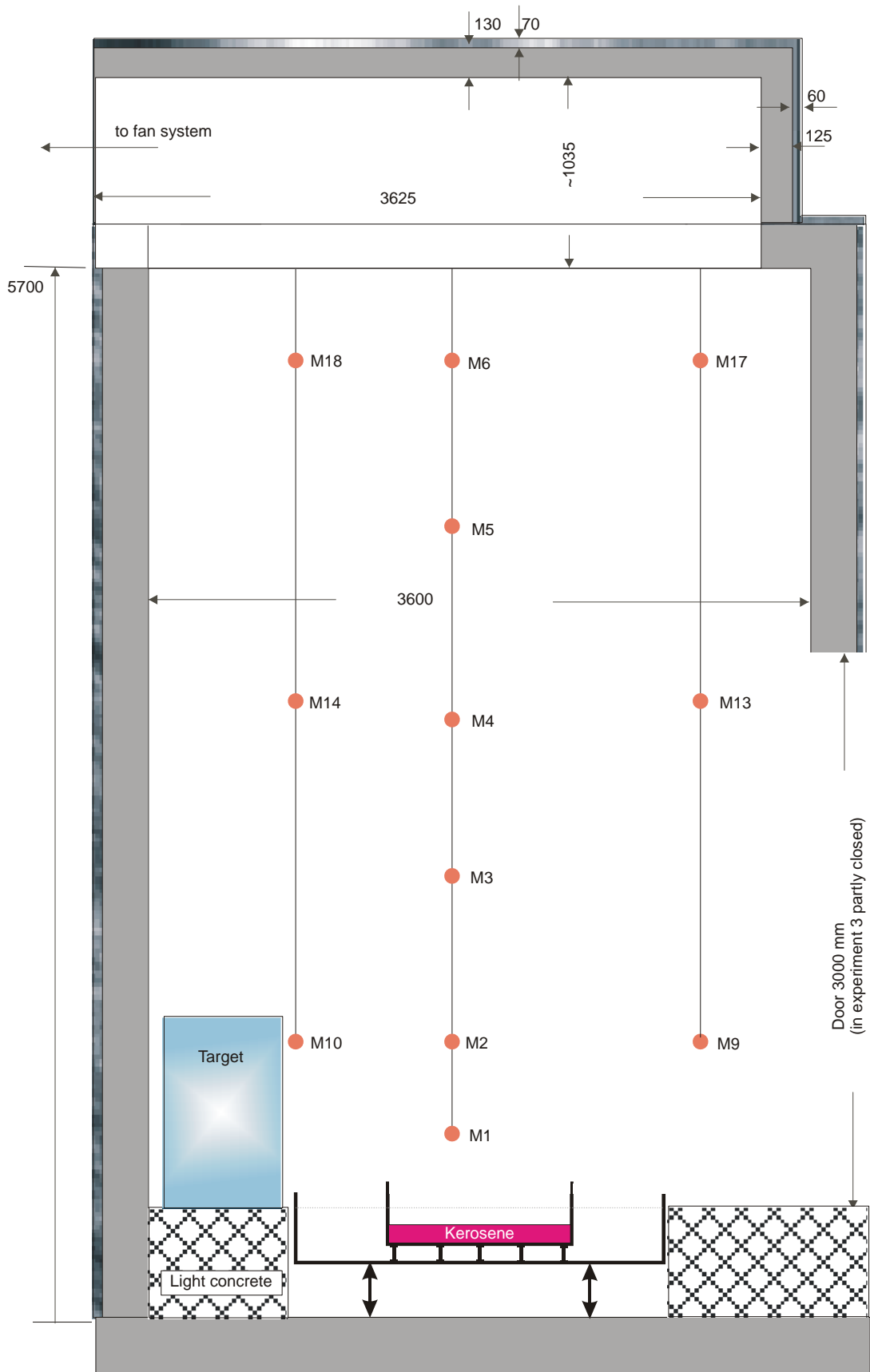


Fig. 2-6 Side view of the OSKAR fire compartment (in + x direction)

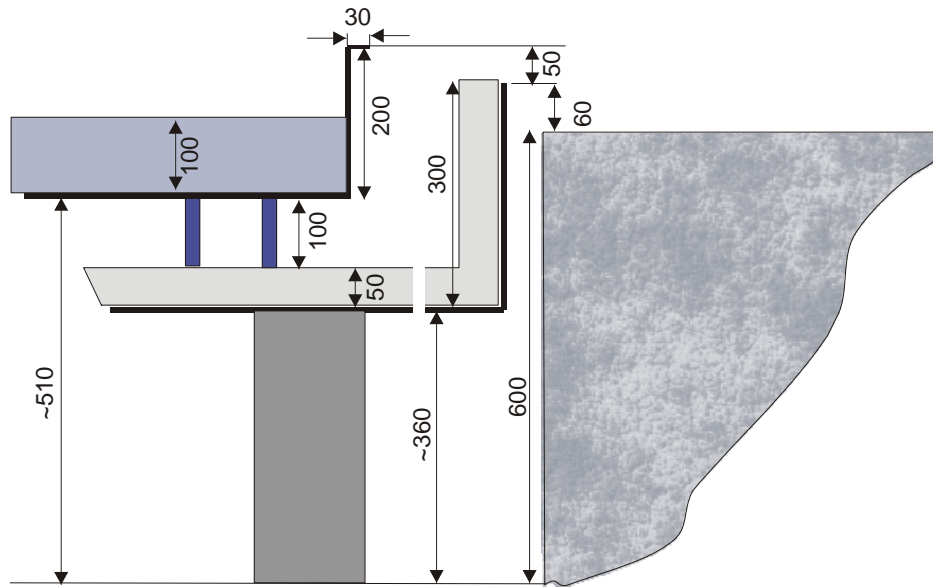


Fig. 2-7 Height of the fuel pan side walls and its elevations



Fig. 2-8 View of the fire compartment through the front door

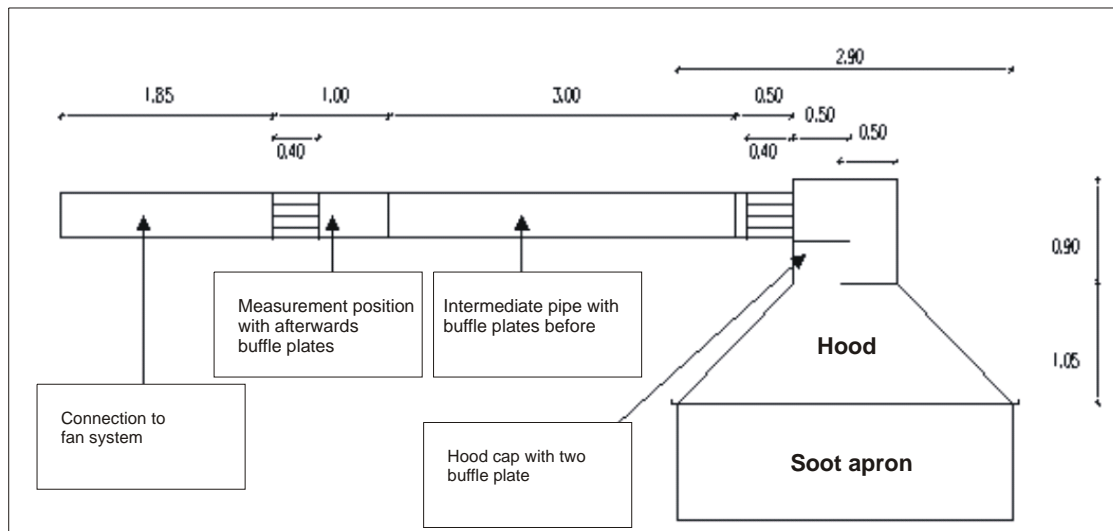


Fig. 2-9 Scheme of the hood above the front door



Fig. 2-10 View onto the hood installed above the front door

2.2.2 Measurements Performed

For measuring the temperatures inside the fire compartment, 3 mm-thick thermocouples were used. These were not protected against flame radiation. The position of the thermocouples was fixed on a grid.

To measure the surface temperatures, the measuring point was fixed with a 5 mm thick thermo-wire. In parallel, “coated thermocouples” with a diameter of 3 mm were used.

To measure the temperatures of typical materials used at NPPs, three different types of material probes (concrete, aerated concrete, steel) were inserted into the fire compartment (Fig. 2-11). The convective and radiative heat flow into the material probes were measured by water cooled heat transfer blocks. The coolant temperature was approximately 10 °C.

Along three lines, the temperatures inside the barrel container were measured (M36 to M53). The location of these measurements is shown in Fig. 2-13.

The velocity inside the plume, at the door and inside the fan systems were measured using bi-directional probes. The cross section area at the measurement positions V11 and V12 is 0.4 m x 0.8 m, and at the velocity measurement position V13 inside the hood the diameter of the pipe was 0.4 m.

To measure the gas concentrations and pressure, open pipes were routed to the outside of the fire compartment and connected to the measurement systems. The positions and nomenclature of the different measurements are shown in Fig. 2-3 to Fig. 2-6 and in Table 2-5.

Table 2-5 List of measurements performed

Nomenclature		
WS = Heat flow density measurement		
M = Temperature measurement		
GA = Measurement of gas composition		
V = Gas velocity measurement		
P = Measurement of total pressure		
GV = Measurement of weight loss		
Measurement position	Comment for Test 1	Comment for Test 3
<u>Plume-temperature</u> (x = 175, y = 195):		
M 1 (z = 100 cm)		
M 2 (z = 150 cm)		
M 3 (z = 240 cm)		
M 4 (z = 335 cm)		
M 5 (z = 430 cm)		
M 6 (z = 520 cm)		
<u>Temperature inside fire compartment:</u>		
Level 1: (z = 150 cm)		
M 7 (x = 275; y = 85)		
M 8 (x = 245; y = 345)		
M 9 (x = 95; y = 60)		
M 10 (x = 90; y = 280)		
Level 2: (z = 335 cm)		
M 11 (x = 275; y = 85)		
M 12 (x = 245; y = 345)		
M 13 (x = 95; y = 60)		
M 14 (x = 90; y = 280)		
Level 3: (z = 520 cm)		
M 15 (x = 275; y = 85)		
M 16 (x = 245; y = 345)		
M 17 (x = 95; y = 60)		
M 18 (x = 90; y = 280)		
<u>Surface temperature</u>		
Plates on the surface		
M 19 (x = 245; y = 360; z = 150)		
M 20 (x = 245; y = 360; z = 335)		

M 21 (x = 0; y = 190; z = 170)		
<u>"Coated thermocouples" on the surface:</u>		
M 22 (x = 245; y = 360; z = 150)		
M 23 (x = 245; y = 360; z = 335)		
M 24 (x = 0; y = 190; z = 170)		
<u>Fuel temperature:</u>		
M25 (x = 175; y = 195; z = 33)		
<u>Material probes:</u>		
"Aerated concrete" (plate 10 cm thickness)		
M26 (x = 2; y = 65; z = 170) *)		
M27 (x = 5; y = 65; z = 170)		
M28 (x = 8; y = 65; z = 170) *)		
M29 (x = 10; y = 65; z = 170)		
Concrete (plate 10 cm thickness)		
M30 (x = 2; y = 190; z = 170) *)		
M31 (x = 5; y = 190; z = 170)		
M32 (x = 8; y = 190; z = 170) *)		
M33 (x = 10; y = 190; z = 170)		
Steel (plate 2 cm thickness)		
M34 (x = 2; y = 280; z = 170)		
M35 (x = 0; y = 280; z = 170)		
<u>Barrel type target (waste package):</u>		
Upper level (z = 140)		
M36 (x = 180; y = 288; z = 140)		
M37 (x = 180; y = 292; z = 140)		
M38 (x = 180; y = 294.5; z = 140)		
M39 (x = 180; y = 299; z = 140)		
M40 (x = 180; y = 310; z = 140)		
M41 (x = 180; y = 320; z = 140)		
Center level (z = 110)		
M42 (x = 180; y = 288; z = 110)		
M43 (x = 180; y = 292; z = 110)		
M44 (x = 180; y = 294.5; z = 110)		
M45 (x = 180; y = 299; z = 110)		

M46 (x = 180; y = 310; z = 110)		
M47 (x = 180; y = 320; z = 110)		
Lower level (z = 85)		
M48 (x = 180; y = 288; z = 85)		
M49 (x = 180; y = 292; z = 85)		
M50 (x = 180; y = 294.5; z = 85)		
M51 (x = 180; y = 299; z = 85)		
M52 (x = 180; y = 310; z = 85)		
M53 (x = 180; y = 320; z = 85)		
<u>Temperature measurement at velocity probe positions:</u>		
Front door		
M54 (x = 180; y = 0; z = 80)		not used
M55 (x = 180; y = 0; z = 140)		not used
M56 (x = 180; y = 0; z = 180)		
M57 (x = 180; y = 0; z = 240)		
M58 (x = 180; y = 0; z = 280)		not used
M59 (x = 180; y = 0; z = 340)		not used
Door, right side	not used	
M60 (x = 360; y = 210; z = 100)		
Door, left side	not used	
M61 (x = 0; y = 335; z = 140)		
Fan system FUCHS (at ceiling)	although valves are closed some flow has occurred	
M62 (outside fire compartment)		
M63 (outside fire compartment)		
Hood above open front door		
M64 (outside fire compartment)		
<u>Heat flow density:</u>		
WS 1 (x = 360; y = 150; z = 180)		
WS 2 (x = 0; y = 280; z = 170)		
WS 3 (x = 0; y = 190; z = 170)		
WS 4 (x = 0; y = 70; z = 170)		
<u>Weight loss of kerosene:</u>		
GV 1 (x = 180; y = 180; z = 0)		
<u>Gas velocities:</u>		
Centerline Plume		
V1 (x = 175; y = 195; z = 150)		

V2 (x = 175; y = 195; z = 335)		
Door		
V3 (x = 180; y = 0; z = 80)		
V4 (x = 180; y = 0; z = 140)		
V5 (x = 180; y = 0; z = 180)		
V6 (x = 180; y = 0; z = 240)		
V7 (x = 180; y = 0; z = 280)		
V8 (x = 180; y = 0; z = 340)		
Door, right side	not used, door closed	
V9 (x = 360; y = 210; z = 100)		
Door, left side	not used, door closed	
V10 (x = 0; y = 335; z = 140)		
Fan system FUCHS		
V11 (outside fire compartment)		
V12 (outside fire compartment)		
Hood above open front door		
V13 (outside fire compartment)		
<u>Gas composition:</u>		
Fire compartment		
GA1 (x = 10; y = 190; z = 380)		
Hood above front door		
GA2 (outside fire compartment)		
Fan system FUCHS	not used	
GA3 (outside fire compartment)		
<u>Pressure:</u>		
P1 (x = 110; y = 240; z = 540)		
P2 (x = 30; y = 200; z = 280)		

^{*)} corrected after performance of calculations and documentation



Fig. 2-11 View of the three material probes



Fig. 2-12 View from top into the open barrel container

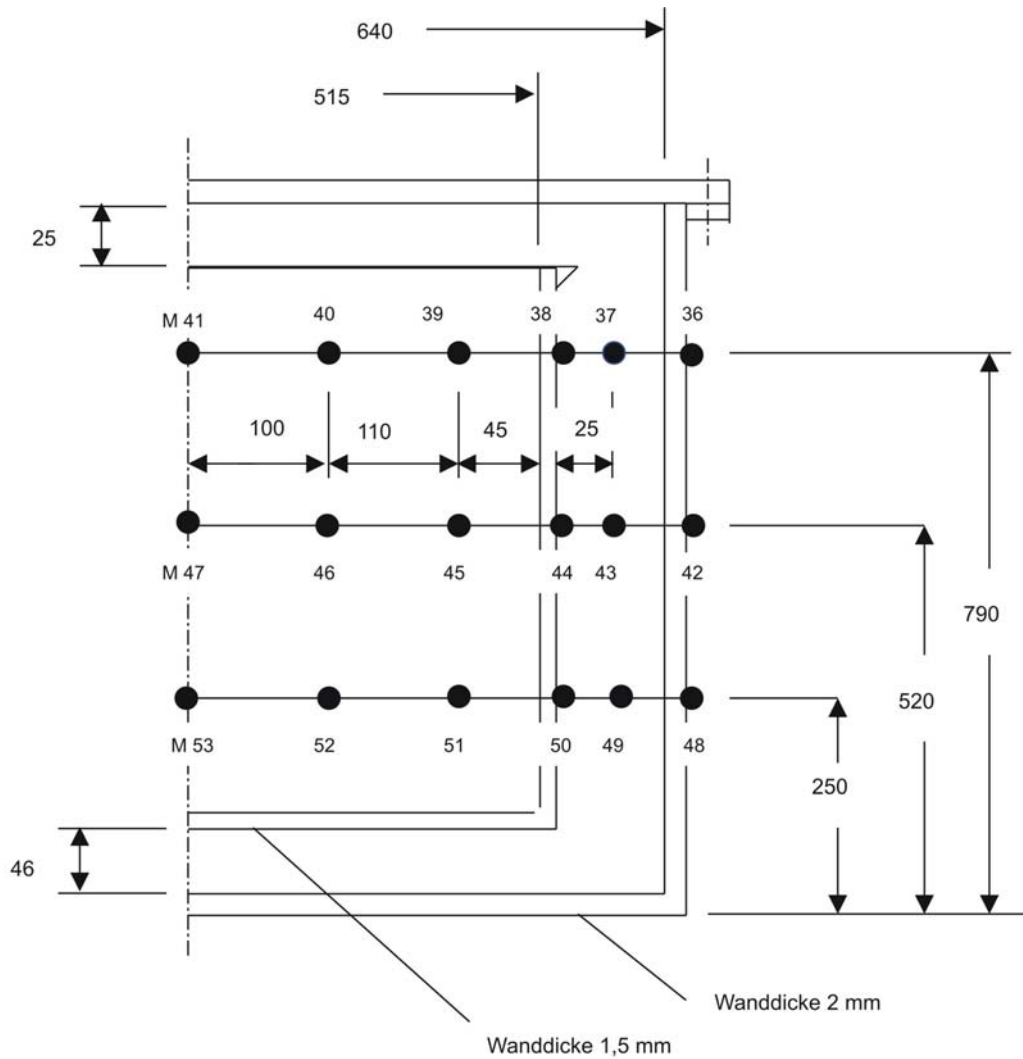


Fig. 2-13 Measurement positions inside barrel

2.2.3 Experimental Procedure

Procedure

At the beginning of the experiments the pan was filled with fuel. In all experiments the fuel level was 0.1 m. Fig. 2-14 shows a typical composition of the fuel used with the chemical summary formula $C_{11.64}H_{25.29}$. Other fuel characteristics are outlined in Table 2-6.

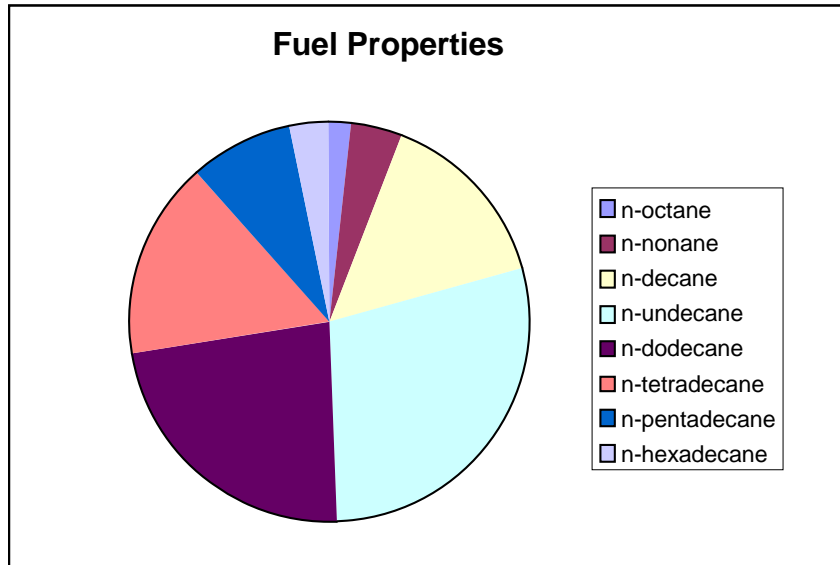


Fig. 2-14 Typical chemical composition of fuel

Table 2-6 Fuel material properties

Density [kg/m ³]	810
Heat capacity [J/kgK]	2400 ^{*)}
Heat conductivity [W/mK]	0.109 ^{*)}
Heat release [MJ/kg]	42.8

^{*)}: values for dodecane taken

To ignite the fuel pool, a cleaning rag soaked with liquid fuel was put at the corner of the pan. Then the outer end was ignited, so that the pool was then ignited. The duration of this process was approx. 30 to 60 s. The experiments ran until the fuel was burned down. In the Test 3, the cool-down behavior was measured for a time period of approx. 16 h.

Ventilation

In those tests considered for Benchmark exercise No. 4 the fan system was running. Although the valves on the top of the fire compartment should have been closed, some velocity (measurements V11 and V12) was measured. Due to these measurements some leakages from the ceiling of the fire compartment have to be assumed. Because

negative values were measured part of the time, the resulting volume flow through fan system is assumed to be

$$\dot{V} = 0.4 \cdot 0.8 \cdot \max[0., (v_{V11} + v_{V12})]. \quad (3-1)$$

Table 2-7 and Table 2-8 contain the smoothed volume flow and velocity values for each experiment.

Table 2-7 Smoothed values for the total volume flow and velocity through the FUCHS fan system (measurements V11 and V12) for Test 1

Test 1 (V11 and V12)		
Time [s]	Velocity v [m/s]	Volume flow \dot{V} [m ³ /s]
0.00	0.00	0.00
150.00	0.00	0.00
165.00	0.26	0.08
180.00	1.38	0.44
195.00	2.59	0.83
210.00	4.12	1.32
225.00	4.41	1.41
551.00	6.82	2.18
615.00	6.78	2.17
666.00	6.64	2.13
720.00	7.03	2.25
859.00	6.01	1.92
1011.00	4.92	1.57
1245.00	3.41	1.09
1405.00	1.36	0.43
1650.00	0.45	0.14
1800.00	0.19	0.06

Table 2-8 Smoothed values for the total volume flow and velocity through the FUCHS fan system (measurements V11 and V12) for Test 3

Test 3 (V11 and V12)		
Time [s]	Velocity v [m/s]	Volume flow \dot{V} [m ³ /s]
0.00	1.22	0.39
37.00	1.22	0.39
61.00	2.21	0.71
88.00	2.33	0.74
120.00	4.65	1.49
195.00	5.06	1.62
255.00	5.75	1.84
1324.00	6.43	2.06
1400.00	5.52	1.77
1500.00	3.93	1.26
1714.00	3.20	1.02

To calculate the gas concentrations inside the hood above the open door, one has to know the velocity. Table 2-9 and Table 2-10 show the smoothed table values for the volume flow rate and the velocity (measurement V13).

Table 2-9 Smoothed values for the total volume flow and velocity through the hood
(measurement V13) for Test 1

Test 1 (V13)		
Time [s]	Velocity v [m/s]	Volume flow \dot{V} [m ³ /s]
0.00	0.37	2.12
15.00	0.39	2.24
30.00	0.42	2.41
45.00	0.39	2.26
195.00	0.44	2.55
210.00	0.55	3.20
225.00	0.53	3.08
240.00	0.55	3.20
255.00	0.56	3.26
405.00	0.57	3.30
886.00	0.61	3.51
1449.00	0.63	3.66
1711.00	0.46	2.65
1755.00	0.52	3.03
1770.00	0.46	2.68
1785.00	0.49	2.86
1800.00	0.49	2.82

Table 2-10 Smoothed table values for the total volume flow and velocity through the hood (measurement V13) for Test 3

Test 3 (V13)		
Time [s]	Velocity v [m/s]	Volume flow \dot{V} [m ³ /s]
0.00	0.50	2.90
37.00	0.52	3.00
61.00	0.52	3.00
211.00	0.53	3.06
504.00	0.52	2.99
1102.00	0.56	3.22
1177.00	0.62	3.60
1280.00	0.65	3.77
1400.00	0.56	3.25
1591.00	0.56	3.22
1748.00	0.58	3.37

Initial and Ambient Conditions

The initial and ambient conditions are given in Table 2-11.

Table 2-11 Initial and ambient conditions

Description	Name(s)	Unit	Test 1	Test 3
Temperature in fire compartment	M1 - M24	°C	18.9	24.7
Temperature outside fire compartment		°C	18.9	18.9
Fuel temperature	M25	°C	18.3	19.0
Material probe: gas-concrete	M26 - M29	°C	17.2	25.6
Material probe: concrete	M30 - M33	°C	18.8	26.3
Material probe: steel	M34 - M35	°C	19.5	24.1

Description	Name(s)	Unit	Test 1	Test 3
Barrel Target	M36, M42, M48	°C	18.8	32.3
	M37, M43, M49	°C	18.8	30.2
	M38, M44, M50	°C	18.8	31.1
	M39, M45, M51	°C	18.8	36.4
	M40, M46, M52	°C	18.8	43.3
	M41, M47, M53	°C	18.8	45.0
Time of ignition		S	165	15

Experiment 1 - velocity - hood and fan system (FUCHS) (V 11-13)

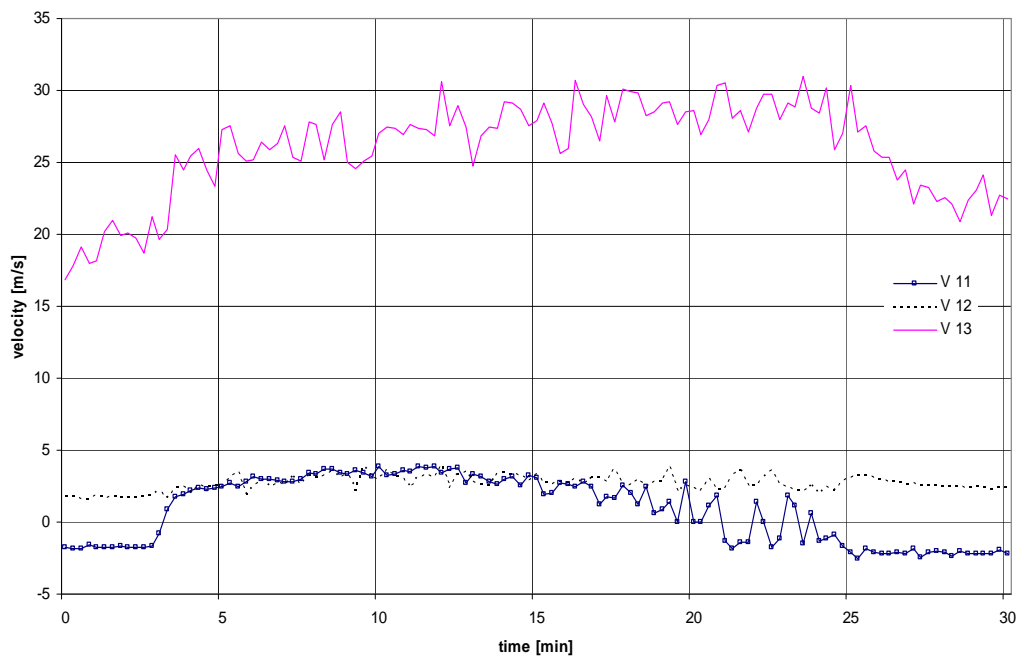


Fig. 2-15 Test 1 - Measured velocities (V11 - V13)

Experiment 3 - velocity - hood and fan system FUCHS (V 11-13)

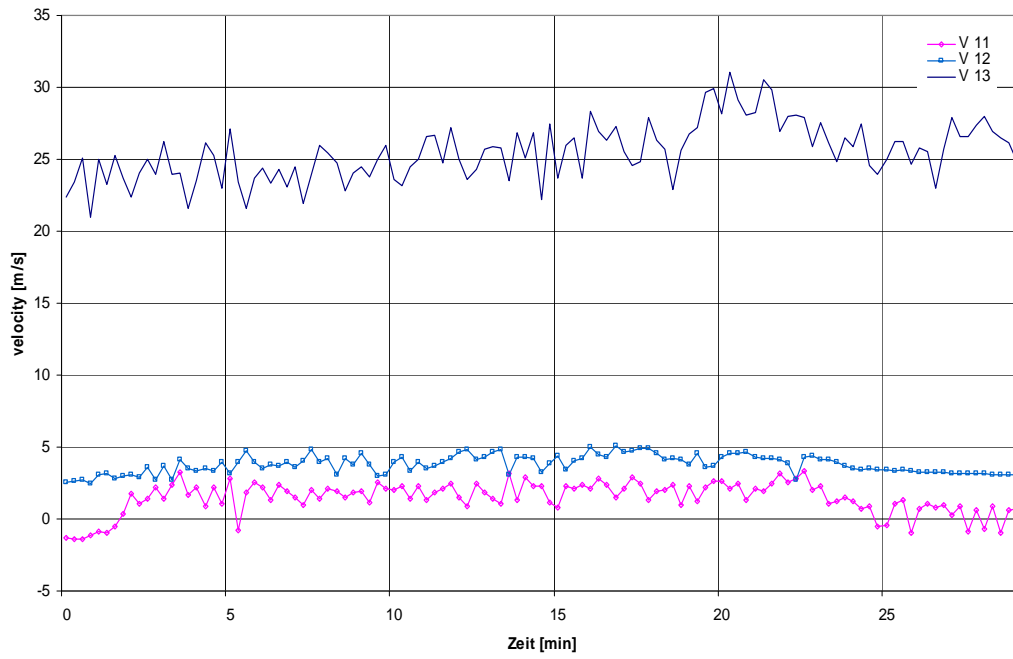


Fig. 2-16 Test 3 - Measured velocities (V11 - V13)

3 Experimental Results

The following section provides data and results from both experiments of the ICFMP Benchmark Exercise No. 4. The results have been made available to the participants of ICFMP in two steps. In April 2004, the pyrolysis rates of the fuel pool fires were released. Most of the results were delivered in May 2004. These results were presented during the 8th ICFMP Meeting at VTT in Finland /KLE 04/.

The tests 1 and 3 are part of a total of 9 fuel pool fire tests at iBMB. Table 3-1 shows the test matrix. In the frame of these tests, the influence of openings as well as of the forced ventilation and the pool size on the thermal load has been investigated. In some tests large pool sizes compared to the fire compartment volume were used, leading to rather high temperature loads.

Table 3-1 Test matrix of the iBMB fuel pool fire tests

Test	Pool area [m ²]	Openings [m ²]	Ventilation
1	1	door: 3 x 0.7	no
2	1	door: 2 x 0.7	no
3	1	door: 1 x 0.7 (1 m above floor)	no
4	1	door: 1 x 0.7 (2 m above floor)	no
5	1	door: 2 x 0.7 (1 m above floor) sides: 0.6 x 0.7 and 0.6 x 1.2	yes
6	1	door: 2 x 0.3 (1 m above floor) sides: 0.3 x 0.7 and 0.4 x 1.2	yes
7	2	door: 3 x 0.7 sides: 0.6* x 0.7 and 0.6 x 1.2	yes
8	2	door: 2 x 0.7 (1 m above floor)	yes
9	4	door: 2 x 0.7 (1 m above floor)	yes

3.1 Summary of Test 1

The fire compartment had a 3 m high opening at the front wall. The smoke was extracted via the ventilation in a natural way. The pool size was 1 m² filled with 100 litres of fuel. To ignite the fuel pool, a cleaning rag steeped with fuel was placed on the edge of the pan. It took approx. 15 s until the whole surface area was burning. The duration of the fire was about 20 min. Fig. 3-1 shows the fully developed fire phase during the experiment.

In Fig. 3-2, a thermo-graphic view of the temperature distribution inside the fire is presented. This has been recorded via the infrared camera at a 10 m distance from the front door.

The measurements of the weight loss show a continuous decrease (Fig. 3-3). At about half-way through the test the measurement was defective. Until this time, the measured data may be used. From the pyrolysis rate, the energy release was estimated. The temperature distribution inside the fire compartment was relatively constant. The maximum temperature was about 800 °C (Fig. 3-4). The temperatures increased due to the heating of the compartment structure. The measurements of the heat flux into the walls are rather unsteady. But according to the temperature the heat flux increased with time. The evaluated heat flux is approx. 10 to 30 kW/m² (Fig. 3-5). Heat fluxes in this range may lead to an ignition of cellulose products and PVC insulated cables. The temperatures inside the fuel are presented in Fig. 3-6. The measuring point was located approx. 3 cm above the bottom of the pan.



Fig. 3-1 Fire development inside the fire compartment - Test 1, view through front door

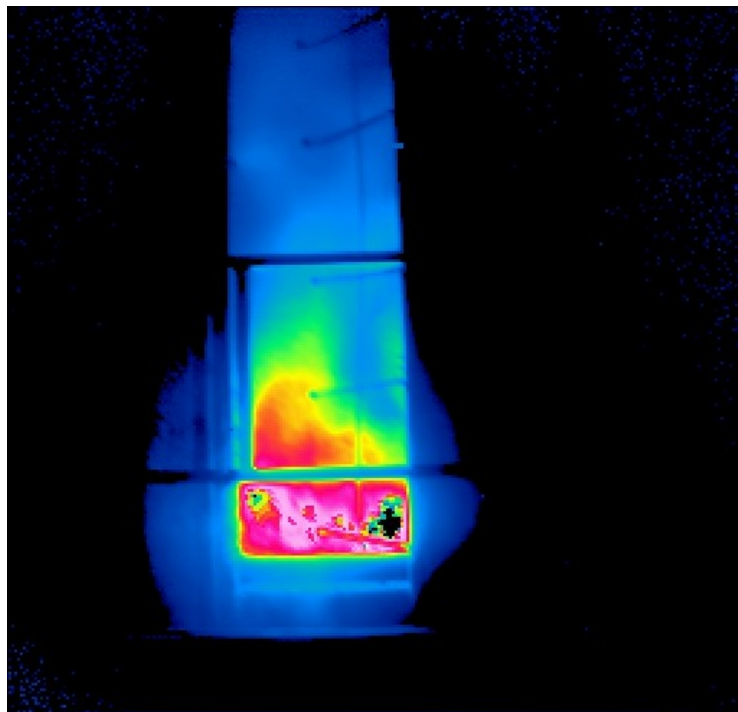


Fig. 3-2 Temperature distribution during the fully developed fire phase - Test 1, view through front door

Versuch 1 - Gewichtsverlust Abbrandwaage (GV 1)

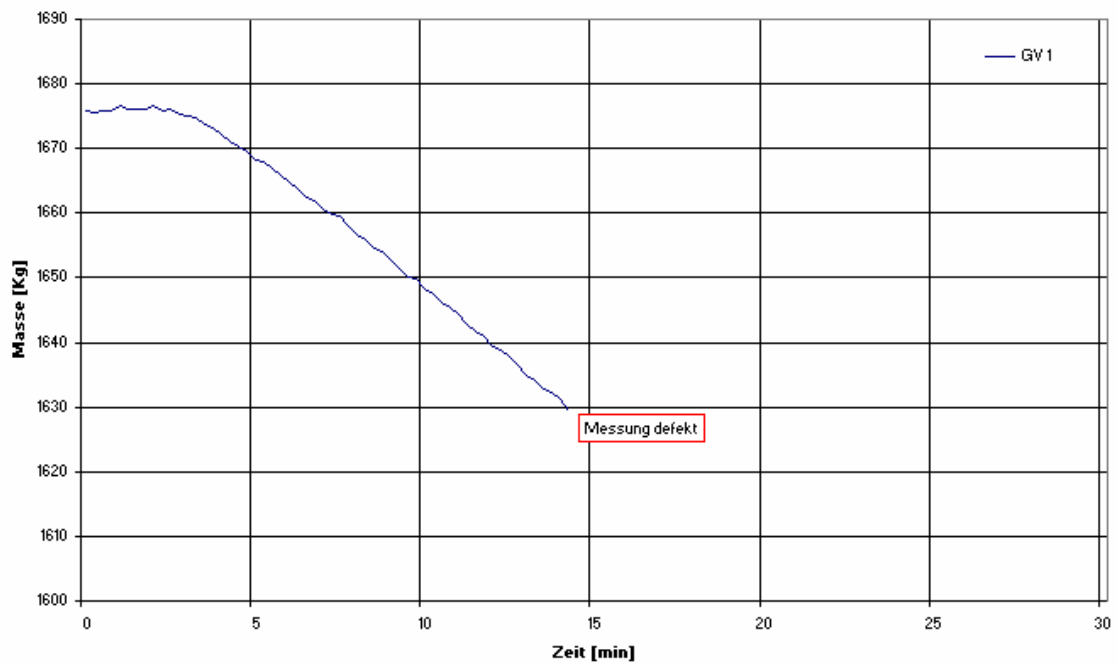


Fig. 3-3 Weight loss - Test 1

Versuch 1 (innen) - Messebene 2 (M 11-14)

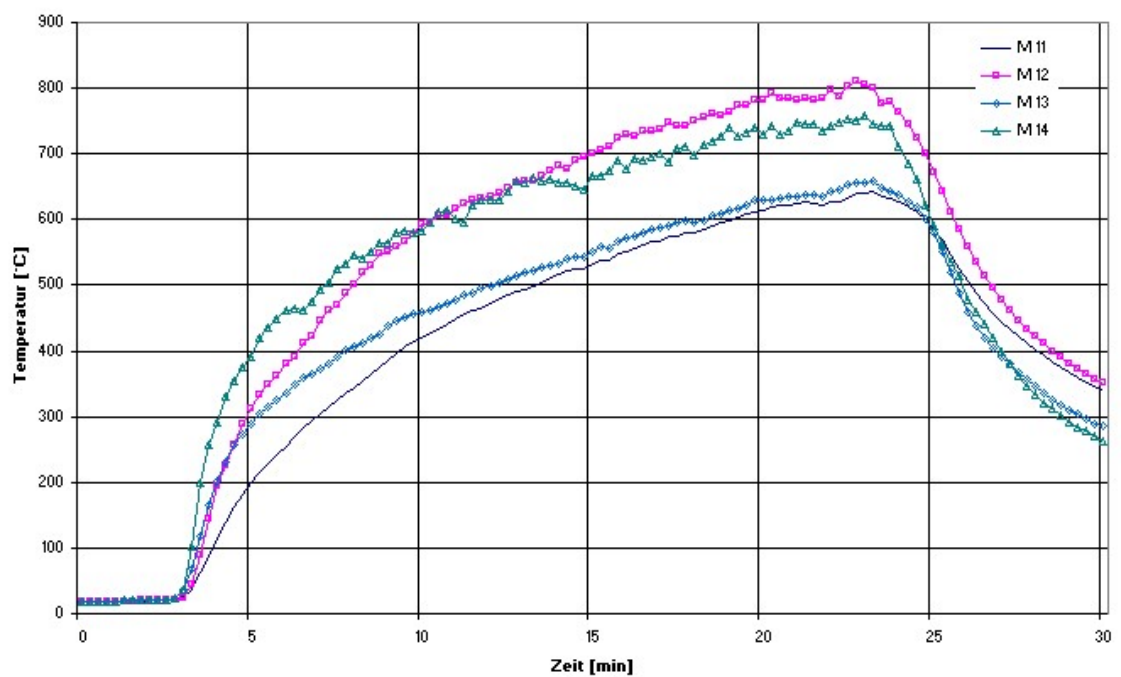


Fig. 3-4 Temperature distribution in measurement level 1 - Test 1

Versuch 1 (innen) - Wärmestromdichte (WS 1-4)

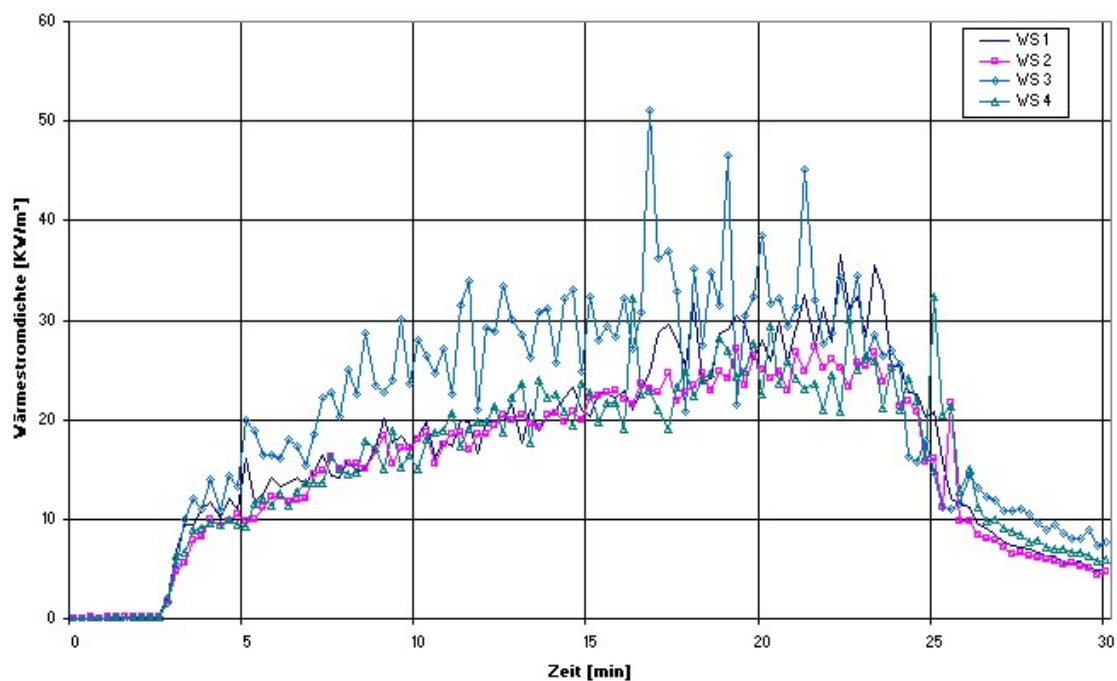


Fig. 3-5 Heat flux into material probes - Test 1

Versuch 1 (innen) - Kerosintemperatur (M 25)

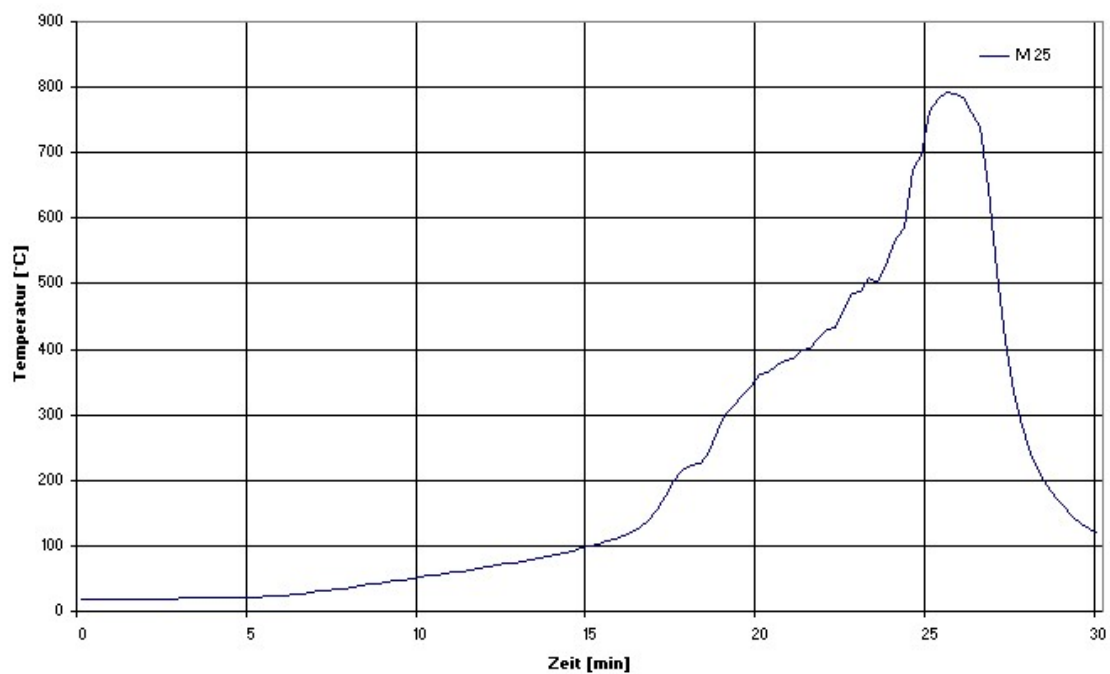


Fig. 3-6 Measured fuel temperature 3 cm above pan bottom - Test 1

3.2 Summary of Test 3

In comparison to Test 1, the opening at the front wall of the compartment was only one third of the size and started at 1 m above the floor of the fire compartment. All other conditions were quite similar to those of Test 1.

The duration of the fire was about 22 min. Fig. 3-7 shows the temperature distribution inside the fire plume during the fully developed fire phase. The measurement of the weight loss shows a constant decrease in the initial phase (Fig. 3-8). During the last third of the test the fire changed from a fuel controlled state to a ventilation controlled one (Fig. 3-9), due to the increased pyrolysis rate and complete consumption of the oxygen available. In this phase of the test some erratic weight loss measurements occurred with deviations of more than 80 kg. After the test, the measurement device was checked and found to work properly. Maximum temperatures of approx. 1000 °C were reached during ventilation controlled conditions (Fig. 3-10). The measured heat fluxes were between 10 and 60 kW/m² with peaks up to 100 kW/m² (see Fig. 3-11).

The heating curves inside the inner barrel of the barrel type target are comparable for all tests. Fig. 3-12 illustrates the temperature progression at the medium level of the target. The temperature decrease over several hours is presented in Fig. 3-13.

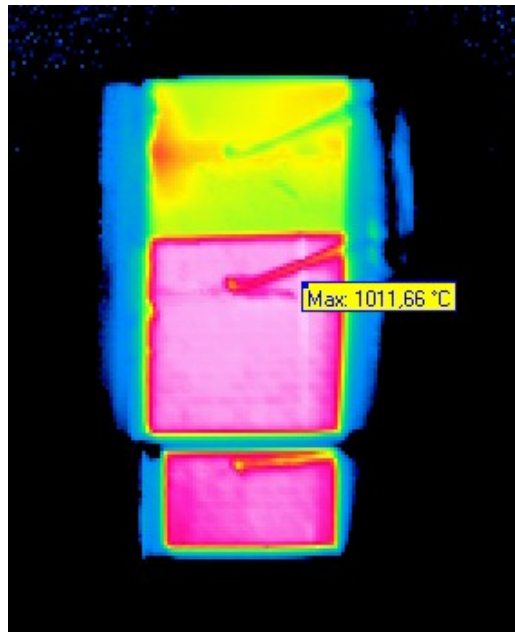


Fig. 3-7 Temperature distribution inside the fire - Test 3

Versuch 3 (innen) - Gewichtsverlust Abbrandwaage (GV 1)

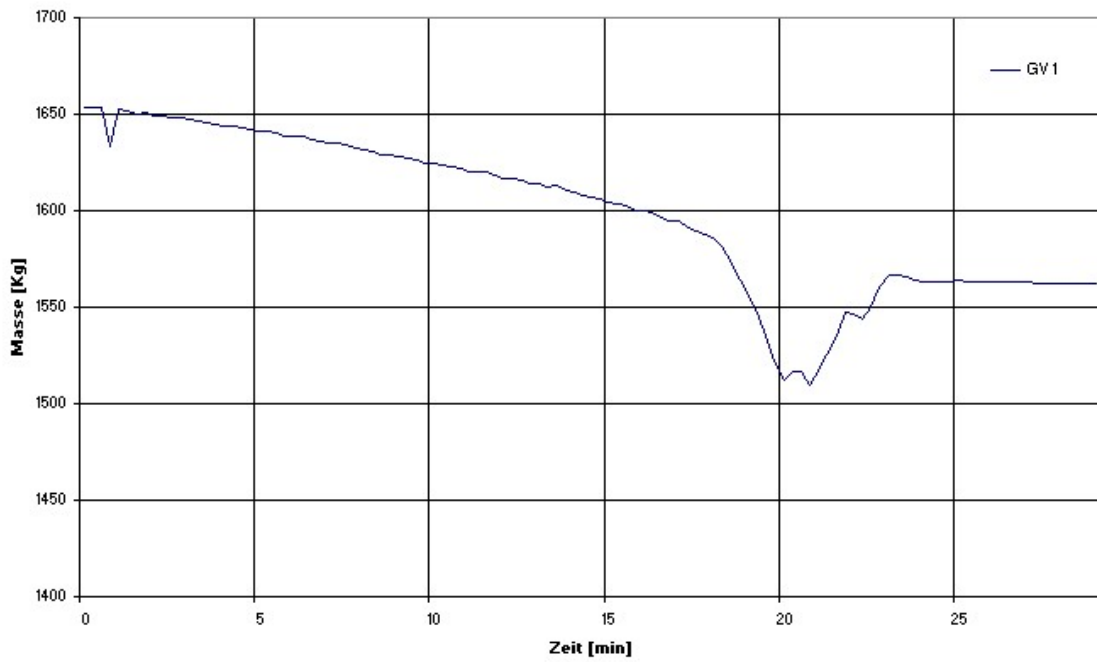


Fig. 3-8 Weight loss - Test 3

Versuch 3 (innen) - Gasanalyse (GA 1) - Brandraum

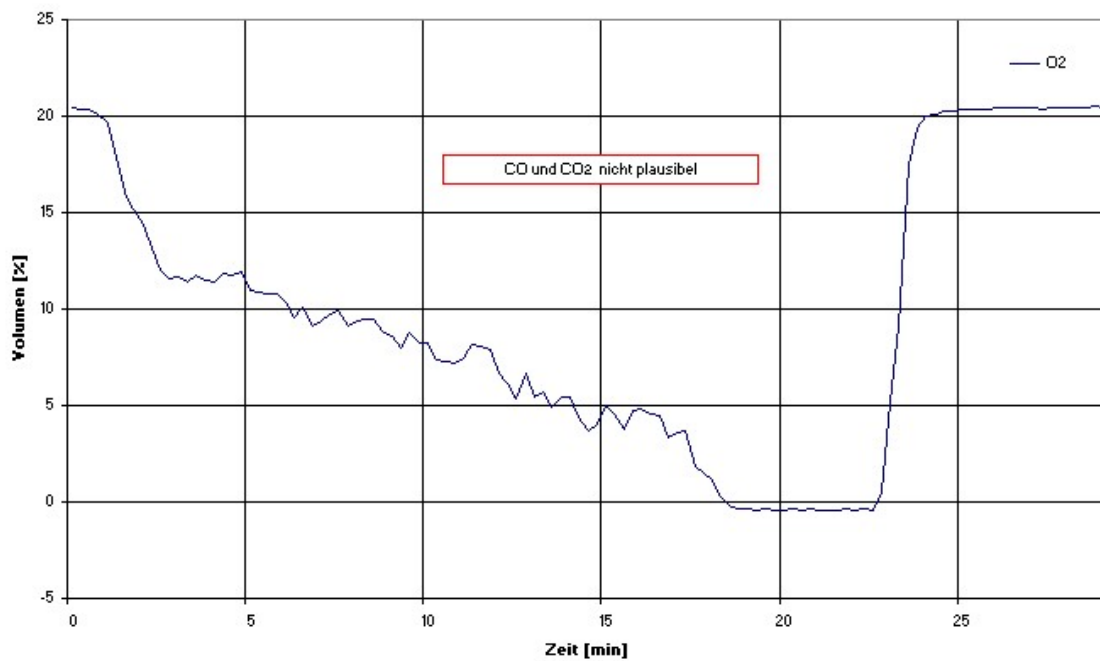


Fig. 3-9 Oxygen concentration in the fire compartment - Test 3

Versuch 3 (innen) - Plumetemperatur (M 1-6)

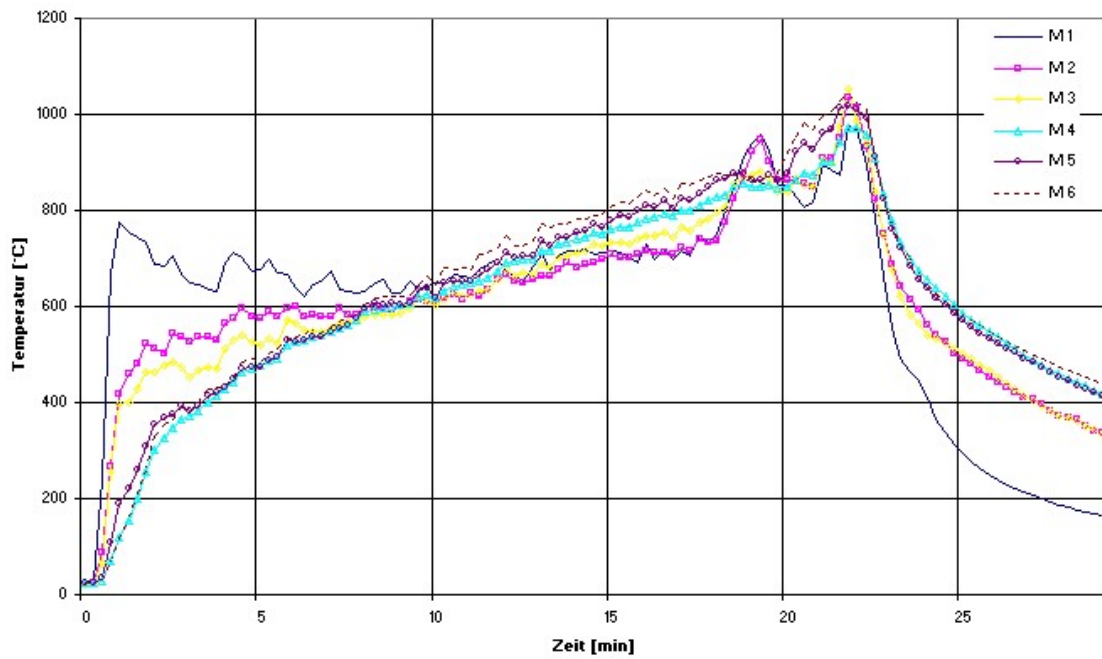


Fig. 3-10 Plume temperatures - Test 3

Versuch 3 (innen) - Wärmestromdichte (WS 1-4)

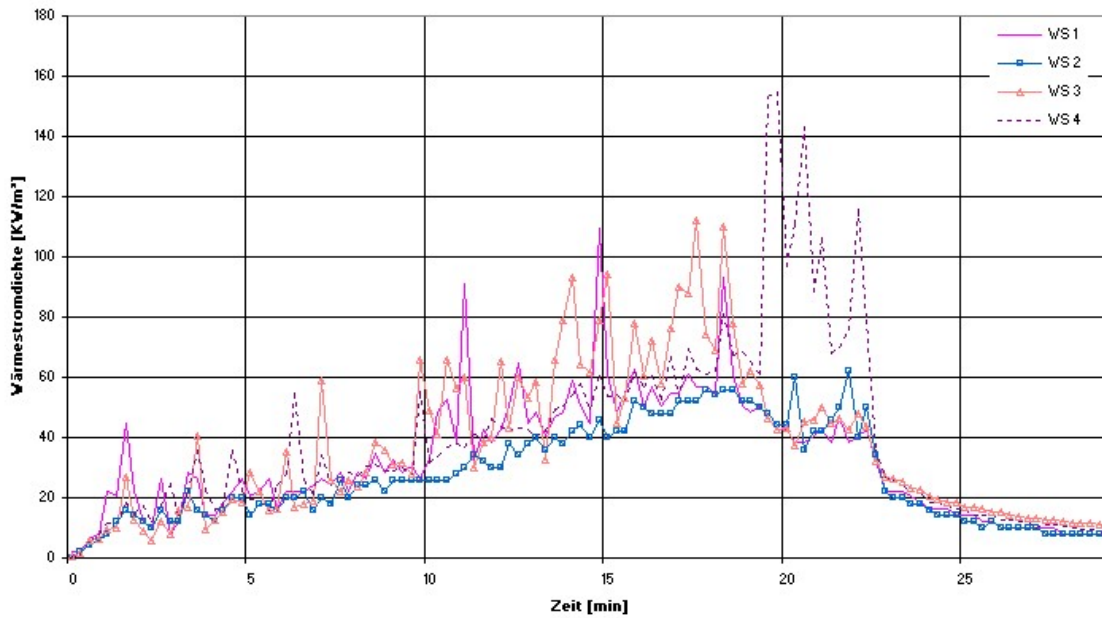


Fig. 3-11 Heat flux into the test probe structures - Test 3

Versuch 3 (innen) - Wärmesenke (Fass) - mittlere Ebene (M 42-47)

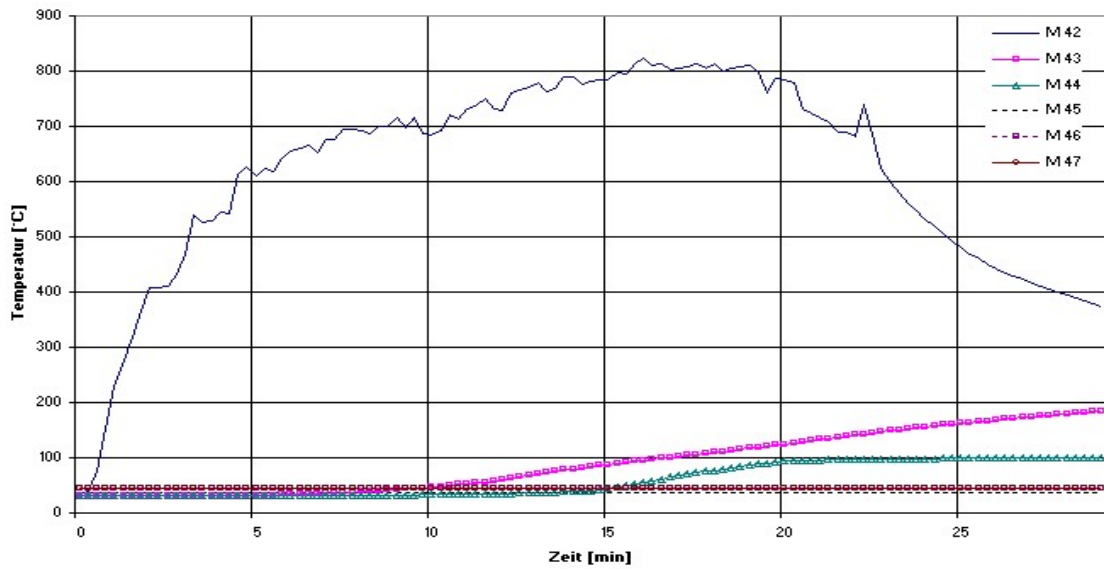


Fig. 3-12 Temperature distribution inside the barrel during Test 3

Versuch 3 (innen) - Fassabkühlung - mittlere Ebene (M 42-47)

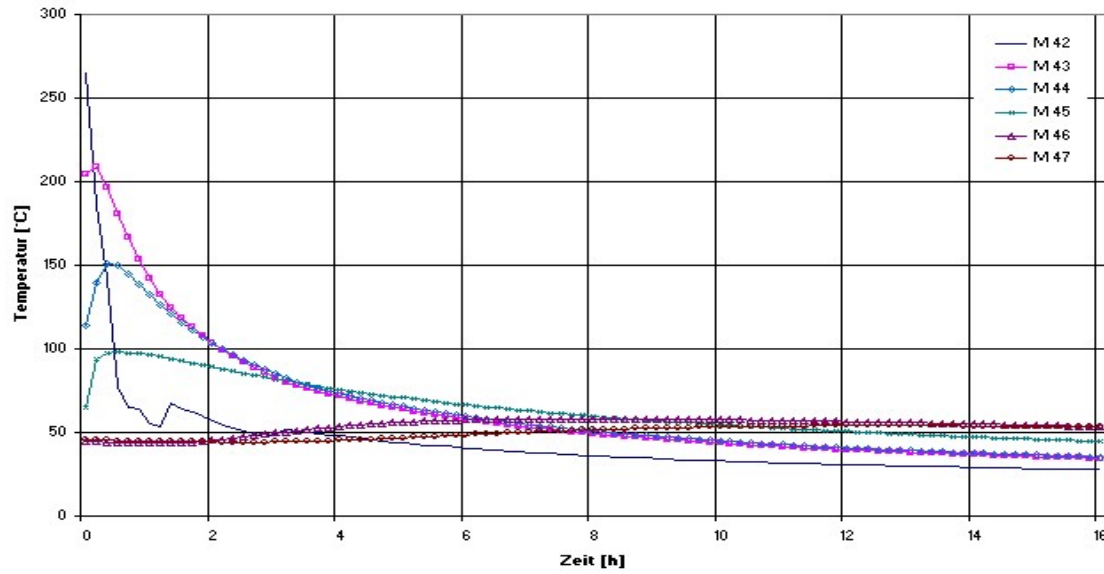


Fig. 3-13 Temperature decrease after Test 3

3.3 Conclusions

In this section, some conclusions are drawn, partly regarding the results from the other tests listed in Table 3-1.

Ventilation

In both tests, the smoke was extracted through the door vent. But as the measurements show, some flow occurs also through the FUCHS fan system installed on top of the fire compartment. This volume flow has to be considered in the evaluation of energy balance. In the case of the natural (door) ventilation, the velocity through the door is between 2 and 6 m/s. This flow leads to some leaning of the plume towards the rear of the fire compartment. Larger openings lead to a higher convection heat loss through the openings. Regarding all experiments of this series, the largest temperatures occur in case of an optimum size of openings with minimum heat loss and enough oxygen being available, just before changing to ventilation controlled phases.

Temperatures

A pool fire with an area of 1 m² did not completely fill the fire compartment which had a floor area of approx. 13 m² and a volume of 76 m³ and an opening to the environment of area of 2.1 m². Therefore, in Test 1 temperature variation with height could be observed. In case of the smaller opening (Test 3) the temperature inside the fire compartment was much more homogenous.

Heat Flux Density

Four heat flux measurements were implemented at a height of about 1.7 m on opposite walls. They measured the total heat flux including convection and radiation. In all tests, the heat flux density increased due to the heating of the surrounding compartment structures leading to a higher reflection of heat. Due to the intensity of the pool fires a strong pulsation occurred in temperature of the burned gases. In addition, this was influenced by the entrance of fresh air leading to a relatively high oscillation in the measured heat flux densities.

Oxygen Concentration

The oxygen concentration inside the fire compartment was measured at an elevation of 3 m above the floor. In the tests the concentration decreased to practically zero, indicating the presence of ventilation controlled conditions.

4 Input Parameters and Assumptions

For the Benchmark Exercise No. 4, it was intended to perform blind calculations without knowing the pyrolysis rate or the other experimental results, semi-blind calculations (knowing only the pyrolysis rate) and open calculations with all data being available to the modelers. From the beginning, it was clear that performing blind calculations is a challenging task. But, on the other hand, this is a typical situation for real applications in nuclear power plants and installations. The deviations of the calculated results from the measured data provides some insights into the uncertainties of the results for such (somewhat extreme) situations, particularly due to the high heat release rate compared to the volume of the fire compartment.

In the following section the major assumptions employed in performing the calculations are listed and discussed:

Heat Release Rate

The specified pyrolysis rate (used in the semi-blind and open calculations) is based on the measurement of the weight loss, which had some problems for Test 1 (weight loss data available until 850 s only) and Test 3 (containing positive gradients leading to negative pyrolysis rates). Therefore, some approximations and assumptions have been made influencing the results to some extent. Fig. 4-1 and Fig. 4-2 show the proposed smoothed pyrolysis rates compared to the raw measured data.

LOL Value

Main difference between the two tests is the cross section of the door opening. This leads to under-ventilated conditions in Test 3. Some codes have to specify the LOL value or it is fixed inside the program. A too high value for LOL reduces the accuracy of the predictions for Test 3. In case of high temperatures the entrained oxygen seems to be completely consumed by the combustion process.

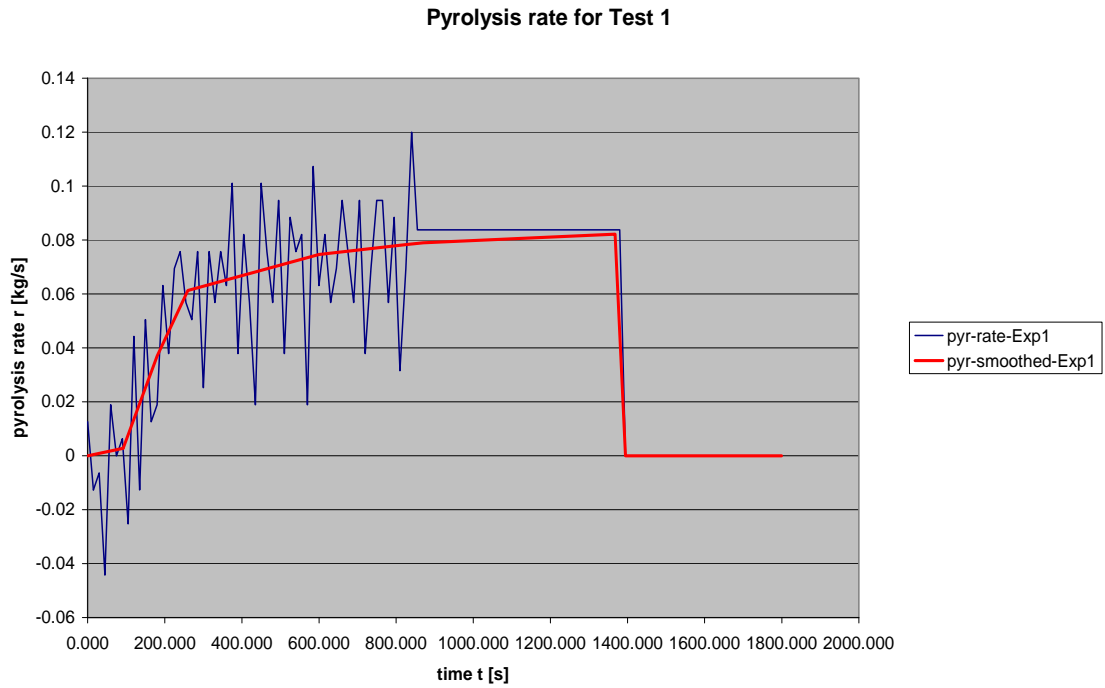


Fig. 4-1 Smoothed pyrolysis rate for Test 1

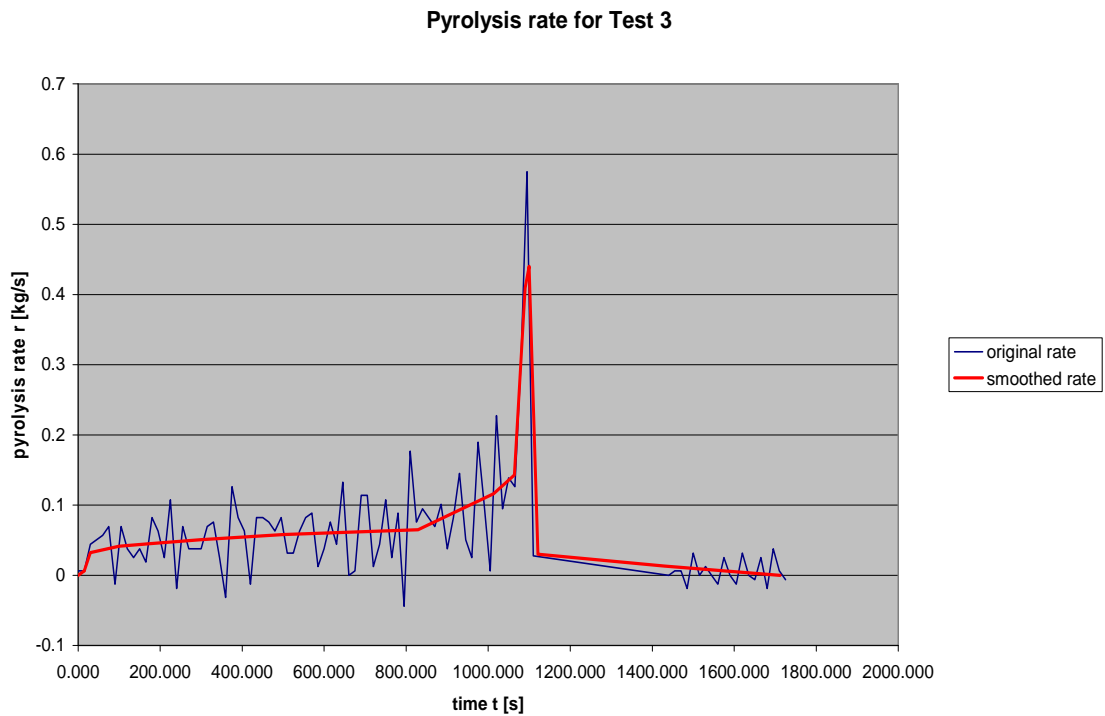


Fig. 4-2 Smoothed pyrolysis rate for Test 3

Ventilation

In most cases, the ventilation was defined as it was described in the specification. Some participants decided not to simulate the ventilation system and the hood.

Radiation Fraction

The radiation fraction has to be defined by the user. Values about 40% have been used. In some calculations the radiation fraction is assumed to be released from the pan, possibly leading to different temperature loads on the targets.

Targets

The targets (three material probes) and the barrel type container are not always considered in the calculations. For the material probes (particularly for steel) one problem was the thickness. Furthermore, a backward heating was possible, which was not (and could not be) considered in any of the calculations. With respect to the barrel, the cylindrical shape could not be modeled with some of the codes. In addition, the multi-layer material composition could not be considered in all codes.

Combustion Scheme and Yields

The composition of the fuel was specified, but not the chemical reaction itself. Therefore, the user had to specify the yields and to decide if the combustion is complete or not. In particular for Test 3, the input may have an impact on the results, due to the under-ventilated condition and production of CO and soot.

Grid Size

For CFD (computational fluid dynamics) codes the user has to specify the grid size. The cell size used in FDS /MCG 04/ with a width of approx. 10 cm is somewhat larger than the cell size used in CFX-5.7 /CFX 04/. The choice of suitable grid size will depend on the type of CFD model (e.g. RANS or LES) and the numerical schemes employed.

Air Entrainment

For zone models, the simulation of the air entrainment (the plume mode) seems to be a key parameter, as this affects the available oxygen for the combustion.

5 Comparison of Code Simulations and Experimental Results

For Benchmark Exercise No. 4 full blind calculations (without knowing the pyrolysis rate), semi-blind calculations (knowing pyrolysis rate) and full open calculations have been performed. Table 5-1 lists the participants for this Benchmark Exercise, the fire codes used, type of analysis and the reference to the Appendix provided by the participant. A summary of the performed calculations is provided below.

Table 5-1 List of fire simulations performed within Benchmark Exercise No. 4

Participant	Fire Code	Code Type	Tests	Type of Analysis	Appendix
K. McGrattan, NIST	FDS	zone	1 & 3	blind, semi-blind	A
S. Miles, BRE	JASMINE	CFD	1 & 3	blind, semi-blind, open (3 only)	B
	CFAST	zone	1 & 3	semi-blind	B
M. Dey, USNRC	FDS	CFD	1 & 3	semi-blind	C
	CFAST	zone	1 & 3	semi-blind	C
T. Elicson (Fauske)	FATE	zone	1 & 3	open	D
L. Rigollet (IRSN)	FLAMME-S	zone	1 & 3	open	E
M. Heitsch (GRS)	CFX	CFD	1 & 3	open	F
W. Brücher (GRS)	FDS	CFD	3	open	G
B. Schramm (GRS)	COCOSYS	LP	1 & 3	open	H
V. Nicolette (SNL)	VULCAN	CFD	3	open	I
B. Gautier (EdF)	MAGIC	zone	1 & 3	open	J

5.1 Blind Calculations

5.1.1 FDS (CFD Code) Applied by K. McGrattan (NIST, USA)

FDS Code Description and Input

In cooperation with the fire protection engineering community, a computational fire model, Fire Dynamics Simulator (FDS) /MCG 04/, has been developed at the National Institute of Standards and Technology (NIST) in the USA to study fire behavior and to evaluate the performance of fire protection systems in buildings. The software was released into the public domain in 2000, and since then has been used for a wide variety of analyses by fire protection engineers. Briefly, FDS is a computational fluid dynamics code that solves the Navier-Stokes equations in low Mach number, or thermally expandable, form. The transport algorithm is based on large eddy simulation techniques, radiation is modeled using a gray gas approximation and a finite-volume method is used to solve the radiation transport equation. Combustion is modeled using a mixture fraction approach, in which a single transport equation is solved for a scalar variable representing the fraction of gas originating in the fuel stream.

The dimensions of the grid were 36 by 72 by 56, and the cells were exactly 10 cm in size throughout. All objects within the computational domain were approximated to the nearest 10 cm. The decision to use a 10 cm grid was based on the observation that the ratio of the fire's characteristic diameter D^* to the size of the grid cell dx is an indicator of the degree of resolution achieved by the simulation. D^* is given by the expression $(\dot{Q} / \rho_{\infty} c_p T_{\infty} \sqrt{g})^{2/5}$, and was about 1 m for this series of fires. Past experience has shown that a ratio of 10 produces favorable results at a moderate computational cost.

FDS performs a one-dimensional heat transfer calculation into an assumed homogeneous material of given thickness and (temperature-dependent) thermal properties. The compartment walls and ceiling were made of various types of concrete, the thermal properties of which were input directly into the model. It was assumed that the target slabs of concrete, aerated concrete, and steel were only exposed at the front surface, although the internal temperature measurements suggested otherwise. No attempt was made to model the barrel container at the rear of the compartment, due to its cylinder geometry and composition of different materials.

Some of the properties of the liquid fuel used in the tests were provided. For kerosene, the fuel properties of “dodecane” ($C_{11.64}H_{25.29}$) were input into the model with assumed soot and CO yields of 0.042 and 0.012, respectively. The current version of FDS did not adjust the soot or CO yield as a consequence of reduced compartment ventilation or combustion efficiency. The assumed heat of vaporization and boiling temperature: 256 kJ/kg and 216 °C, respectively, were important input values for the simulation. For the blind calculations the fire was simulated by including in the simulation a small, hot block that heated up the surface of the pool until the fire was self-sustaining, after which the block literally disappeared from the calculation. FDS predicted the radiative and convective heat flux from the fire to the fuel surface, and the evaporation of the fuel according to the Clausius-Clapeyron equilibrium pressure of the fuel vapors above the pan.

FDS uses a finite volume method to solve the radiation transport equation in the gray gas limit. By default, the radiation from the fire and hot gases is tracked in 100 directions, which is adequate to predict the radiation heat flux to nearby targets.

The ventilation rates for all the compartment fans and hood were input directly into the model.

Code Results

For blind calculations only the heat release has been discussed. For Test 1, the predicted heat release rate (HRR) rose very quickly to about 3 MW following ignition, followed by a gradual rise over 15 min as the compartment heated up and the increased thermal radiation from the hot upper layer led to an increased burning rate (Fig. 5-1). The measured HRR did not exhibit the rapid rise, taking several minutes to grow to 3 MW and then gradually increasing at a rate comparable to the prediction. The reason for the discrepancy is that FDS uses a mixture fraction model of combustion. Briefly, the evaporated fuel burns readily with oxygen when mixed to the appropriate ratio, regardless of temperature. Thus, FDS did not simulate properly the spreading of the fire across the pan; rather it predicted an almost instantaneous involvement of the entire fuel surface.

In Test 3, FDS over-emphasized the effect of the small compartment opening (Fig. 5-1). Initially, it predicted the same rapid growth as it had in Test 1, but then the fire consumed the available oxygen, and the fire died down, decreasing the burning rate.

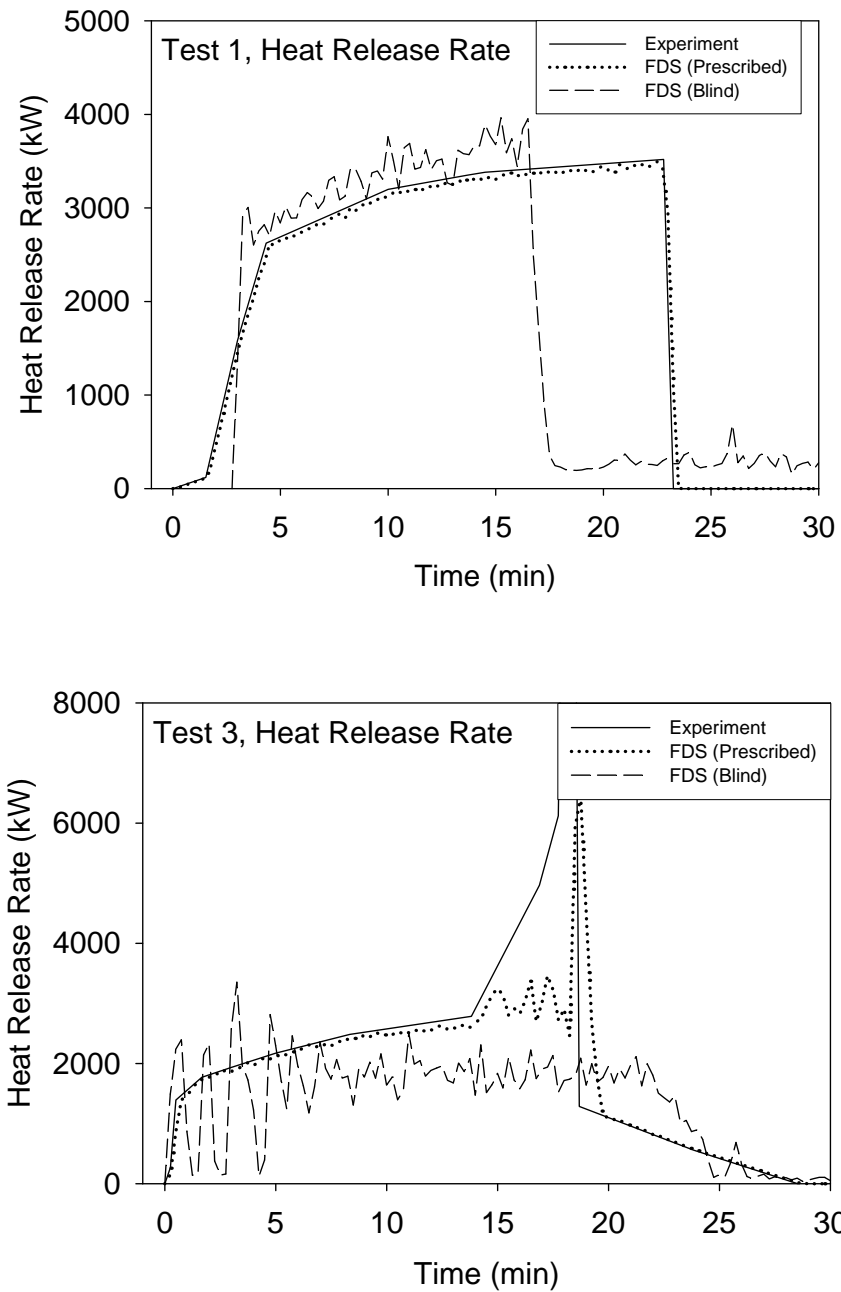


Fig. 5-1 Measured and predicted (blind) heat release rates for Tests 1 and 3 (from Appendix A)

5.1.2 JASMINE (CFD Code) Applied by S. Miles (BRE, UK)

Blind calculations (prior to the dissemination of the experimentally measured fuel mass release rate) were conducted for Tests 1 and 3 with JASMINE Version 3.2.3 /COX 87/. One important purpose of these blind simulations was to examine how realistic predictions could be made for gas temperatures, fluxes etc using a simple, empirical expression for fuel pyrolysis rate.

JASMINE Code Description and Input Assumptions

JASMINE solves the Reynolds-Averaged Navier Stokes (RANS) equations of fluid flow on a single-block Cartesian grid. The coupled set of equations for each of the three Cartesian velocity components, enthalpy (heat) and other scalars required by the various sub-models (e.g. fuel mass and mixture fractions for combustion) is approximated as a system of algebraic equations that are solved numerically on a discrete grid. This generates a solution value for each variable at each grid location. JASMINE uses the finite volume method, where the differential equations are first transformed into an integral form and then discretized on the control volumes (or cells) defined by the numerical grid. This solution procedure is coupled with a variant of the SIMPLE pressure-correction scheme. Transient solutions are generated by a first-order, fully-implicit scheme. A standard κ - ϵ turbulence model with additional buoyancy source terms was used. Standard wall functions for enthalpy and momentum describe the turbulent boundary layer adjacent to solid surfaces.

In the benchmark exercise combustion was modeled using the eddy break-up sub-model in which the fuel pyrolysis rate is specified as an input boundary condition. Reaction (oxidation) is calculated at all control volumes as a function of fuel concentration, oxygen concentration and the local turbulent time-scale. A simple one-step, infinitely fast chemical reaction is assumed. Complete oxidation of the fuel is assumed where sufficient oxygen is available. The effect of oxygen concentration on the local rate of burning may be incorporated by setting oxygen and temperature limits which define 'burn' and 'no burn' regions. For the blind simulations no oxygen concentration limit was specified, i.e. there was only a 'burn' region.

A fuel source area of 1 m^2 and a heat of combustion of $4.28 \times 10^7 \text{ J kg}^{-1}$ were used in all calculations. For the blind calculations a fixed fuel pyrolysis rate was assumed from 60 s after ignition (increasing linearly to this value over the first 60 s). A value of

0.039 kg s⁻¹ was chosen, based upon published engineering information. The sensitivity to reducing this value to 0.0234 kg s⁻¹ was investigated.

Radiant heat transfer is modeled with either the six-flux model, which assumes that radiant transfer is normal to the co-ordinate directions, or the potentially more accurate discrete transfer method. All blind calculations were performed using the six-flux radiation model. Local absorption-emission properties are computed using a mixed grey-gas model, which calculates the local absorption coefficient as a function of temperature and gas species concentrations. As soot was not modeled in this benchmark exercise, only CO₂ and H₂O acted as participating media in the radiation calculations.

Where soot is not explicitly modeled, its influence on the overall energy budget may be incorporated, somewhat crudely, by reducing the heat release rate of the fire, i.e. either the pyrolysis rate or the effective heat of combustion, by a fixed fraction. This is akin to the radiative fraction employed in zone models such as CFAST. The amount of heat then removed represents what could be expected to be 'lost' by radiation from the sooty flame region above the fuel source. The remainder of this heat is assumed to be convected into the rest of the compartment or, as a relatively small fraction, by radiation from the plume region due to CO₂ and H₂O. Note also that of the heat convected into the compartment (from the fire source), some of this is subsequently radiated from the 'smoke gases' (due to CO₂ and H₂O).

Thermal conduction into solid boundaries may be included by means of a quasi-steady, semi-infinite, one-dimensional assumption, which is appropriate for many smoke movement applications. Alternatively, the solution of the one-dimensional heat conduction equation into the solid is also available. The quasi-steady, one-dimensional assumption was employed in the blind calculations. The thermal properties of the concrete walls, floor and ceiling were included as specified.

The dimensions of the compartment, doorway opening and exhaust ventilation duct were modeled exactly as in the problem specification. Only half the compartment was modeled, imposing symmetry at the $x = 1.8$ m plane, and using a numerical mesh of approximately 80,000 cells. A fixed numerical time-step of 2.5 s was employed in all simulations.

Ventilation through the fan system was modeled as a time-dependent mass sink, set to a value corresponding to the experimentally measured volumetric flow rate.

The thermal response of the material probe targets and the heat flow densities (WS2, WS3 & WS4) was included in the JASMINE calculations. Furthermore, the wall surface temperatures at the locations of the plates/thermocouples (M19 etc) were calculated. While the blockage due to the barrel target was included, its thermal response was not modeled and so no comparisons were made with the barrel temperature measurements.

Further general information on JASMINE is provided in the Appendix B to this report.

JASMINE Code Results

Two sets of blind predictions were made for each of Test 1 and Test 3, one using a fixed fuel pyrolysis rate of 0.039 kg s^{-1} and the other a rate of 0.0234 kg s^{-1} . These calculations were performed only for the first ten minutes of the experiments.

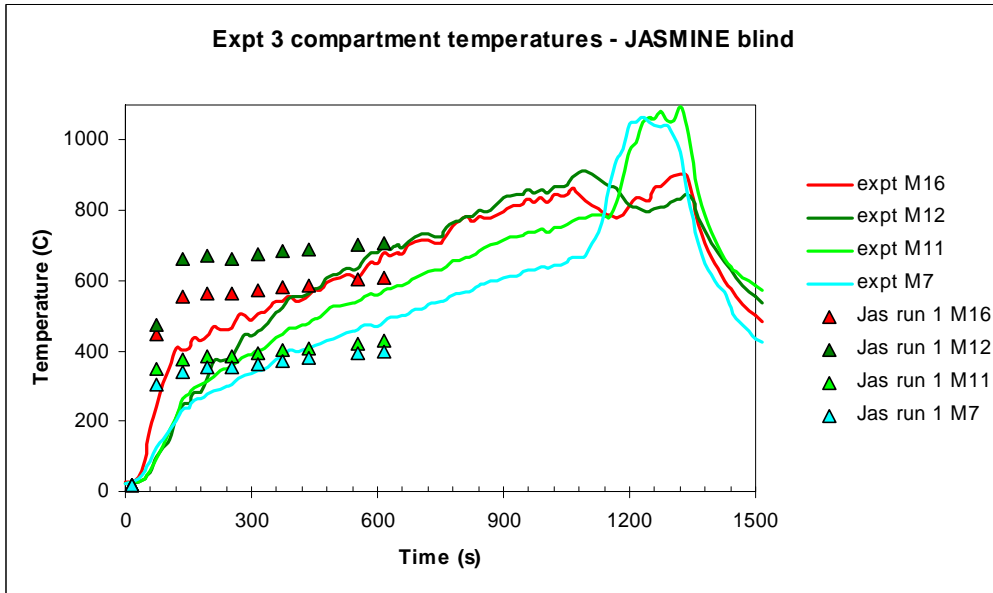
Comparisons between prediction and measurement were made for gas temperatures, oxygen concentration, door/wall vent velocities and compartment surface temperatures. The blind predictions made with the higher value of the pyrolysis rate were closer to the experimental measurements than those made with the lower pyrolysis rate.

Fig. 5-2 and Fig. 5-3 (from the Appendix B) show the gas phase and wall surface temperature calculations for Test 3 using the two fuel pyrolysis specifications.

The blind calculations using the higher fuel pyrolysis rate of 0.039 kg s^{-1} were quite encouraging considering the complexity of the physics involved. A simple engineering estimate of the pyrolysis rate was in this case sufficient to capture the main gas phase properties of the experiments. It was noted, however, that the transient effects due to changes in the pyrolysis rate due to the development of conditions inside the enclosure were not captured. Effects due to the feedback of radiation from soot particulates and the compartment walls are likely to be highly transient.

A main discrepancy between the blind calculations and the measurements was in the doorway vent flow in Test 3, where in contrast to the flow being predominantly into the compartment as indicated in the predictions, the measurements suggest a more distinct two-way flow at the wall vent. This discrepancy may be due, in part at least, to the imposed exhaust flow at the mechanical ventilation duct in the JASMINE calculations forcing a significant amount of air into the compartment through the wall vent.

Pyrolysis rate = 0.039 kg s^{-1}



Pyrolysis rate = 0.0234 kg s^{-1}

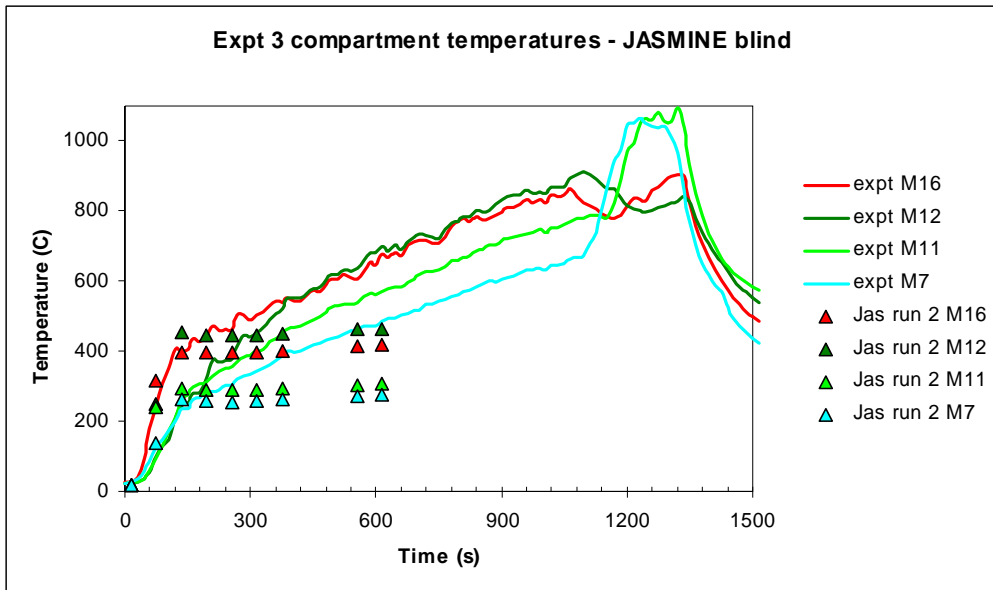
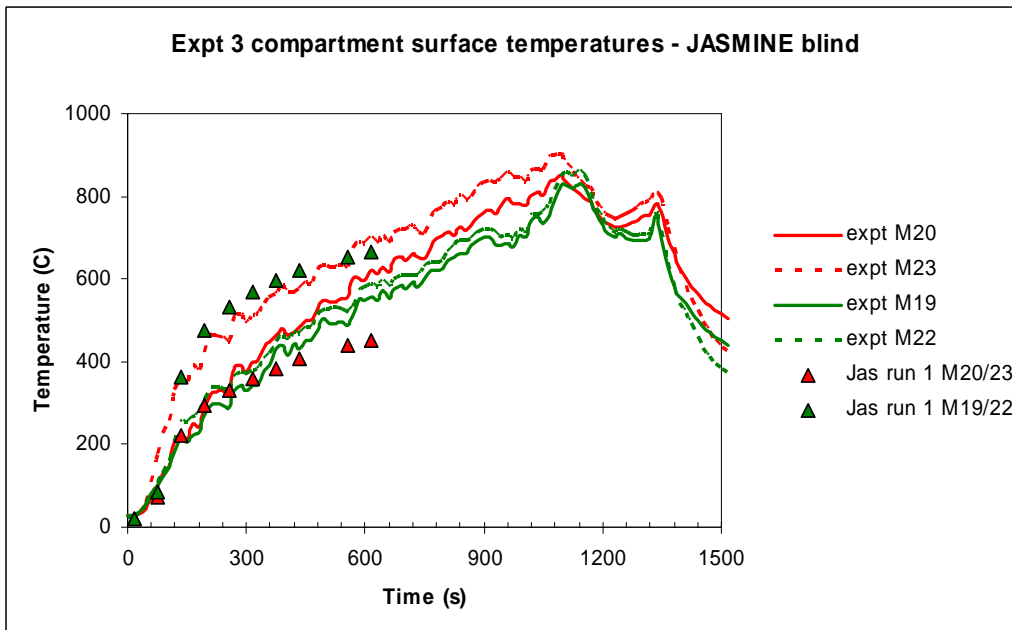


Fig. 5-2 Measured and predicted (blind) gas temperatures for Test 3 (from Appendix B)

Pyrolysis rate = 0.039 kg s⁻¹



Pyrolysis rate = 0.0234 kg s⁻¹

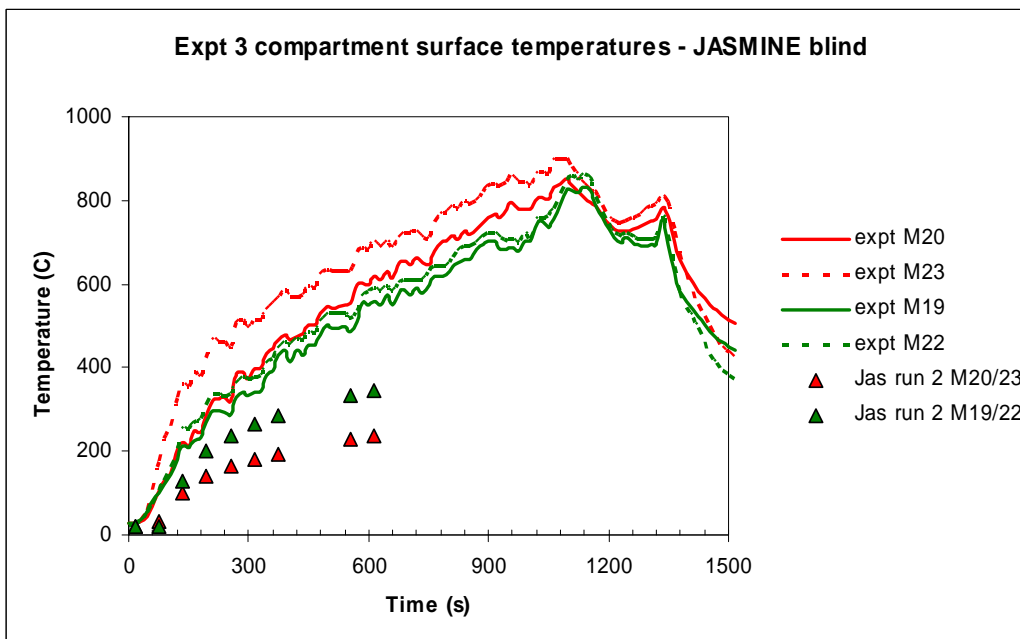


Fig. 5-3 Measured and predicted (blind) wall surface temperatures for Test 3 (from Appendix B)

5.2 Semi-blind Calculations

5.2.1 FDS (CFD Code) Applied by K. McGrattan (NIST, USA)

FDS Code Description and Input

(See paragraph 5.1.1)

Code Results

Assuming an uncertainty of 15 % for the heat release rate (HRR) an uncertainty of temperatures about 10 % can be concluded. In general, the difference between measured and predicted compartment temperatures in Tests 1 and 3 was within the uncertainty bounds established by the prescribed HRR, but there were some exceptions, especially in Test 3. In making comparisons between model and experiment, the temperatures were compared from 10 min onwards. Earlier in the tests, the measured temperatures exhibited a delay relative to the predictions, probably due to the thermal inertia of the thermocouples.

Three plates were positioned on the side wall of the compartment, about 1.7 m above the floor. FDS did compute the inner temperatures of the slabs, and the temperatures decreased monotonically with depth since FDS considered the slab to back up to an ambient temperature environment. However, the measured temperatures did not decrease monotonically, either because of a measurement error or the slab might have been heated from behind. Sometimes the comparison of surface temperatures and heat flux with the experimental data was somewhat inconsistent. In some situations, the predicted surface temperature was more accurate than the predicted heat flux, suggesting either that the heat flux measurement was inaccurate, or that the model benefited from “two wrongs making a right”; that is, an under- or over-prediction in the heat flux was compensated by a comparable error in the surface properties or solid phase heat transfer calculation.

FDS uses a mixture fraction combustion model, meaning that all gas species within the compartment are assumed to be functions of a single scalar variable. For the major species, like carbon dioxide and oxygen, the predictions are essentially an indicator of how well FDS is predicting the bulk transport of combustion products throughout the

space. For minor species, like carbon monoxide, FDS at the present time did not account for changes in combustion efficiency, relying only on a fixed yield of CO from the combustion product. In reality, the generation rate of CO changes depending on the ventilation conditions in the compartment.

The quality of the calculated velocity depends strongly on the grid resolution at the door opening. The model used 10 cm grid cells, fine enough to compute the bulk temperatures and flows within the compartment, but not fine enough to capture the steep gradient in horizontal velocity over the height of the doorway, especially in Test 3 where the door was resolved by just a few cells spanning the vertical dimension.

Sensitivity studies have been performed using a double grid size. In general, there were no significant degradations of the results using the 20 cm grid. Indeed, it appeared that the heat fluxes and surfaces temperatures were predicted more accurately with the coarse grid. The coarse grid tends to “smooth out” the temperature and heat flux fields, sometimes resulting in lower predicted values that are closer to the measured values. However, this “smoothing” of the temperature field more often leads to less accurate predictions. For example, consider the plume temperature predictions. The upper layer temperature predictions (M-3 and M-6) were not degraded on the 20 cm grid, but the lower level prediction (M-1) was significantly degraded due to the “smoothing” of high temperatures near the base of the fire.

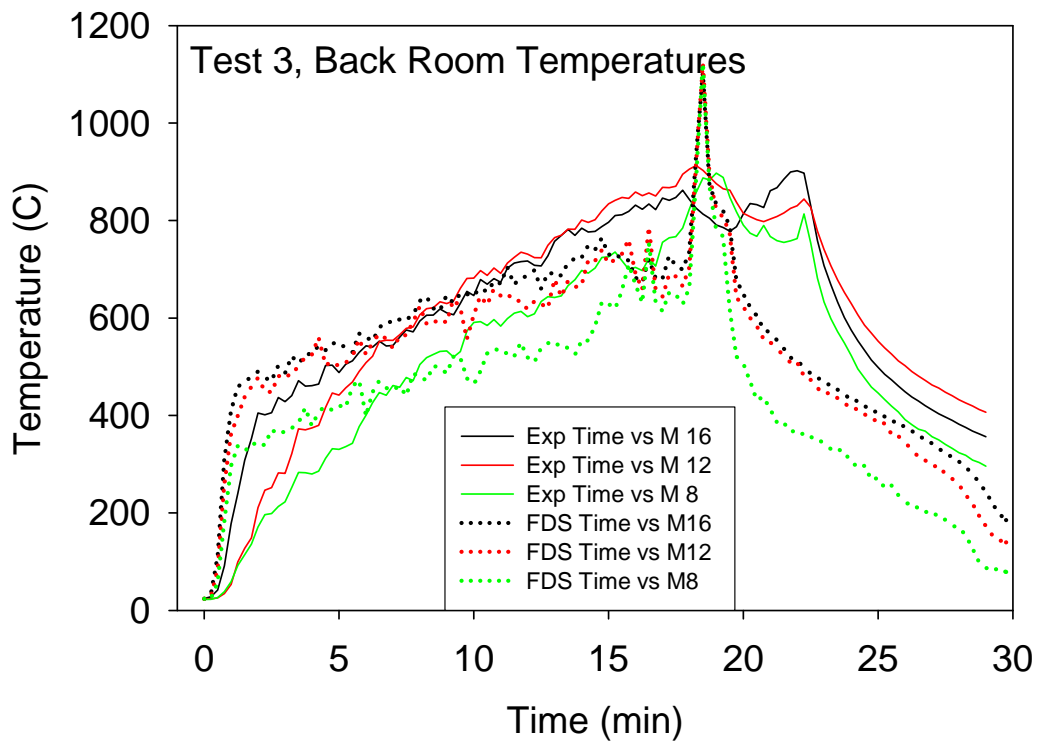
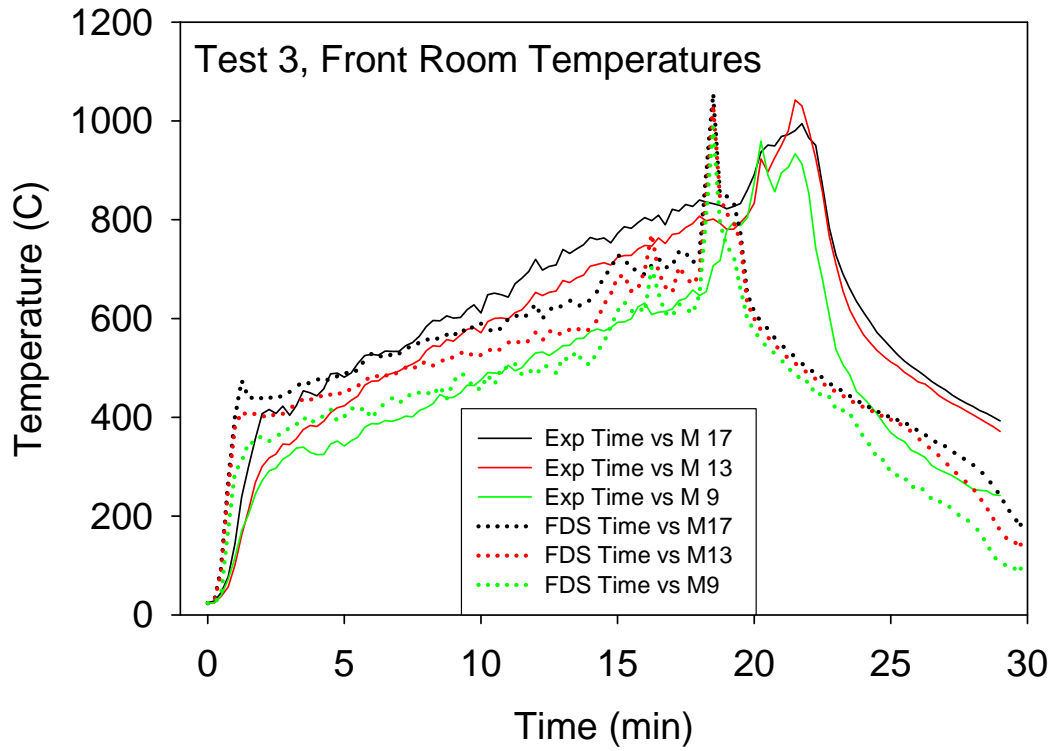


Fig. 5-4 Gas temperature comparisons for Test 3 (from Appendix A)

5.2.2 FDS (CFD Code) and CFST (Zone Model) Applied by M. Dey (USNRC, USA)

The following paragraph provides a comparison of semi-blind predictions by CFAST and FDS for the tests conducted for ICFMP Benchmark Exercise No. 4. CFAST Version 3.1.7 and FDS Version 3.1.5 were used for the computations.

The FDS code simulated Tests 1 and 3 successfully. The CFAST code simulated Test 1 to the end of the specified transient, however, instabilities were noted. There were convergence issues in the CFAST simulation of Test 3. The simulation halted at about 14 % to completion. CFAST is sensitive in cases with a high heat flux. The penetration of the thermal wave in the compartment floor and in less dense materials with low thermal conductivity poses numerical challenges for the CFAST code.

CFAST Code Description

CFAST is a widely used zone model, available from the National Institute of Standards and Technology (NIST), USA. It is a multi -room zone model, with the capability to model multiple fires and targets /JON 04/. Fuel pyrolysis rate is a pre-defined input, and the burning in the compartment is then modeled to generate heat release and allow species concentrations to be calculated. CFAST was used as a conventional two-zone model, whereby each compartment is divided into a hot gas upper layer and a cold lower layer. In the presence of fire, a plume sub-model (zone) transports heat and mass from the lower to upper layer making use of an empirical correlation. Flows through vents and doorways are determined from correlations derived from the Bernoulli equation. Radiation heat transfer between the fire plume, upper and lower layers and the compartment boundaries is included using an algorithm derived from other published work. Other features of CFAST relevant to the benchmark exercise include a one-dimensional solid phase heat conduction algorithm employed at compartment walls and targets and a network flow model for mechanical ventilation.

FDS Code Description

(See paragraph 5.1.1)

Input Assumptions for FDS and CFAST

For both codes the pre-defined heat release rate was used. The use of prescribed heat release rates neglects the feedback effect between the fire and the compartment conditions. Therefore, the use of prescribed HRRs will include some uncertainty due to the lack of complete simulation of the fire phenomena in the compartment. The given peak in the heat release rate for Test 3 and the assumptions made for Test 1 may lead to a larger source of uncertainty in the predicted results.

The lower oxygen limit needs to be input to the CFAST code for the simplistic sub-model for predicting the extinction of the fire. There was no value for LOL included in the specifications, allowing judgment from users to define the most appropriate value for the experiments. The specification of this parameter has a large effect on the prediction of extinction and could be a large source of user effects, especially for under-ventilated conditions. In FDS internal values are used, generally eliminating the need for user intervention.

The barrel was not simulated in FDS or CFAST, due to its cylindrical geometry and multi-material configuration which cannot be modeled in the codes. Standard material properties have been used elsewhere.

The radiative fraction of the fuel was not specified. The value of the radiative fraction available in the literature for n-dodecane was assumed for the analysis. This parameter was identified as a key parameter effecting fire compartment conditions in ICFMP Benchmark Exercise No. 2.

The FUCHS fan system was simply modeled in CFAST and FDS with prescribed flow rates, without accounting for any feedback effects between the ventilation system and the compartment. Furthermore, the flow through the FUCHS system was assumed to be constant for the CFAST calculations as there is no direct means for providing input for varying ventilation flow rates in the code. The exhaust hood was not simulated in CFAST.

Code Results of FDS and CFAST for Test 1

The initial development of the HGL based on measured data seems erratic and may be due to discrepancies in the offset in the initiation of the transient. The measured data

shows the hot gas layer (HGL) interface reaches approx. 1.5 m at about 600 s. Both CFAST and FDS under-predict the steady state HGL interface height by 19 %.

Both CFAST and FDS predictions follow the same trend of temperature increase of HGL as the experimental data, but with CFAST over-predicting the increase by a larger amount. Once reaching the end of the rapid increase at approx. 360 s, the increase in temperature is greater in the experiment than that predicted by both CFAST and FDS. This discrepancy may be due to smaller heat loss in the experiments due to the presence of insulation that was ignored in the code calculations.

The O₂ level at GA1-O2, located at 3.8 m above the floor in the HGL (top of door is at 3.0 m), predicted by CFAST and FDS at the end of the transient phase is 8.9 % and 5.7 %, respectively. The measured O₂ level at the end of the transient is 13.5 %. Since the measured O₂ level does not decrease much after approx. 465 s, there is potentially an error in the measured O₂ level.

FDS predicts peaks in the plume temperature at approx. 50 s. These peaks are explained by the plume development predicted by FDS. Observations of the plume predicted by FDS indicate a steady vertical plume until approx. 50 s when the plume is pushed to the rear wall by flow into the compartment through the door. This causes peaks in the thermocouples, M2, M4, and M6 which are located directly above the fuel pan. The experimental measurements do not indicate this extensive movement of the fire plume. The measured temperatures M7 to M10 of measurement level 1 show a rapid increase in temperature followed by a more gradual increase until the end of the transient. The temperature measured at M10 is much higher than that measured at M7, M8, and M9. This is due to the tilting of the fire plume toward M10. FDS also shows a rapid increase in temperature followed by large oscillations and unexpected trends. These oscillations may be caused by oscillations in the flow through the door predicted by FDS. The temperature predicted at M8 by FDS is highest since the code predicts the fire plume to be pushed more toward the rear wall. For higher levels the effect of plume tilt is not evident.

The comparison of heat flux prediction with measured data poses several challenges. It is important that equivalent measures of flux are used in the comparison. The flux gauges in the experiments were cooled and maintained at a constant temperature (10 °C). The CFAST and FDS codes normally output the net heat flux on targets based on the target temperature. These fluxes were reformulated to give to the incident radiative

heat flux and the convective heat flux to a block with a constant temperature of 10 °C. Even with this reformulation, an exact comparison is not possible due to the inability to exactly measure the calculated values from the models. CFAST significantly over-predicts the heat flux with an uncertainty up to +215 %, whereas the uncertainties of the FDS predictions lie between 14 and 59 %. It should be noted that FDS predicts an increase in the heat flux toward the end of the transient phase, possibly due to the heat flux from the boundaries (walls etc) to the targets. This increase in heat flux toward the end of the transient phase is not observed in the measurements.

Corresponding to the overestimation of the heat flux in CFAST the calculated surface temperatures are also too high. The uncertainties in FDS are between 7 and 28 %.

The uncertainty of heat flux into the walls (WS3 and WS1) in the FDS calculation is about -45 %. The results for WS1 and WS3 are rather different, not observed in the experiment. The uncertainty of the surface temperature is about 26 %.

Code Results of FDS and CFAST for Test 3

The CFAST calculation crashed, so the results are not discussed here.

The measured HRR increases rapidly to 1500 kW in approx. 50 s, and then increases more gradually reaching 2700 kW at 850 s. The HRR increases rapidly from this point to 6000 kW at approx. 1050 s before being extinguished. Although the measured HRR has been input to the FDS code the FDS internal calculation of the HRR decreases after the initial rise at approx. 50 s. Although the HRR calculated by FDS starts to increase at about 200 s, it is less than the measured HRR. This may be due to the internal algorithm in FDS that inadvertently decreases the HRR for under-ventilated conditions.

FDS predicts the hot gas layer to develop and descend to about 0.6 m above the floor in approx. 90 s. The measured data shows the HGL interface starts to level to approx. 1.6 m (bottom of vent) at about 95 s. FDS predicts that a steady state level is reached more quickly after the initial drop compared to experiment. FDS under-predicts the steady state HGL interface height by 24 %.

The FDS prediction is similar to experimental observation until 840 s at which point FDS predicts a rapid reduction in O₂ level to 0 %, while experimental observation indicates the O₂ level reaches 0 % more gradually at approx. 1095 s.

FDS predicts again that the flame is pushed significantly towards the rear wall by the flow of ambient air into the compartment through the door. Observations of the temperature fields show that FDS predicts that the flow through the door pulsates with a period of approx. 2 s. This pulsating behavior was noted during the experiments. The pulsating flow through the door provides sufficient oxygen to the fire and prevents it from being under-ventilated.

The plume temperature behavior is similar to Test 1 with an intermediate peak at about 50 s. These peaks are explained by plume development predicted by FDS. But the experimental measurements do not indicate this extensive movement of the fire plume. The measured data shows the plume to be fully developed at approx. 180 s after which the plume temperatures increase to approx. 1000 °C without any intermediate peaks.

The measured temperatures in the compartment at Level 1 for M7, M8, M9, and M10 show a rapid increase followed by a more gradual increase until the end of the transient phase. The temperature measured at M10 and M8 is higher than that measured at M7 and M9. This is due to the tilting of the fire plume toward the back wall. The plume temperature at M10 is higher than at M8 indicating that the tilt is more toward M10, but not as far as M8. FDS also shows a rapid increase in temperature followed by oscillations and a gradual increase in plume temperature, caused by flow oscillations at door opening.

The temperatures at higher levels (elevations) show a notable peak due to increased HRR at about 800 s. This was not simulated in the FDS calculations. The uncertainty was about 24 % to 33 %.

The uncertainty and the problem in comparing the heat flux and surface temperature for the material blocks are similar to those reported for Test 1. The uncertainty values are about 70 % for the heat flux and 35 % for the temperatures.

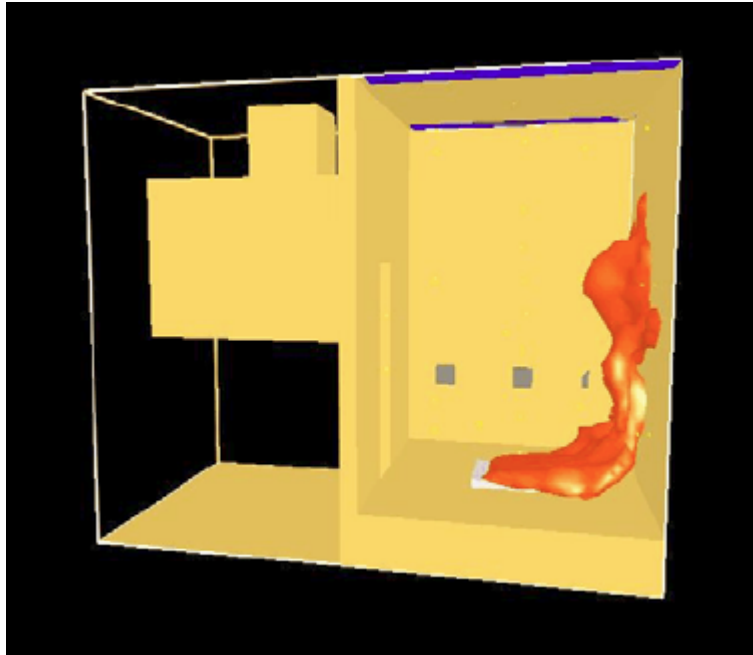


Fig. 5-5 View of flame sheet output from FDS - Test 1 (from Appendix C)

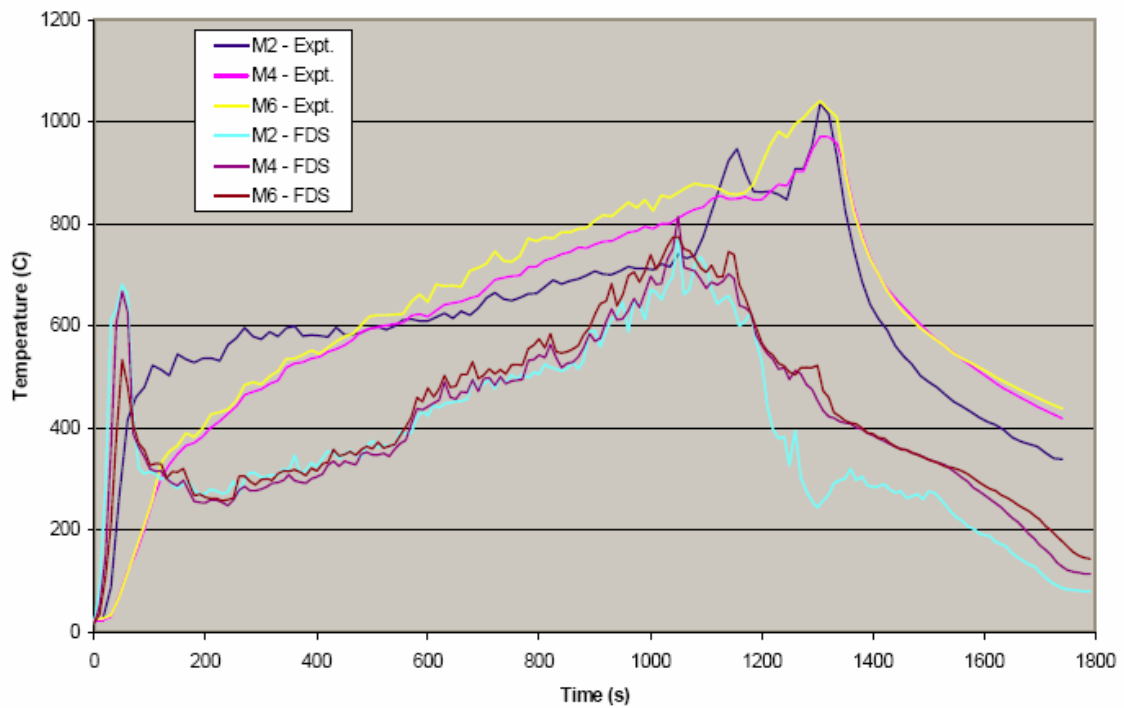


Fig. 5-6 Plume temperature (from Appendix C)

5.2.3 CFAST (Zone Model) and JASMINE (CFD CODE) Applied by S. Miles (BRE, UK)

Semi-blind calculations were made for Tests 1 and 3 with CFAST Version 3.1.6 and JASMINE Version 3.2.3. The main difference with the blind calculations was that the fuel mass loss measurement data were available, from which the fuel pyrolysis rates had been derived, allowing a more accurate fuel source term to be specified in the calculations. While most calculations had been conducted prior to the release of the other experimental measurements, some further calculations had then been conducted to explore various issues. The results of all these calculations are presented in detail in the Appendix B, and summarized below.

CFAST Code Description and Input Assumptions

CFAST is described above in paragraph 5.2.2. Version 3.1.6, without the FAST graphical user interface, was employed in all calculations. Additional information relevant to the application of CFAST to this Benchmark Exercise No. 4 is given below.

The dimensions of the OSKAR fire compartment and the doorway ventilation openings were modeled as in the problem specification. The thermal properties of the walls, floor and ceiling were included by creating new user defined materials with the required (concrete) properties. Conduction losses to the room walls, ceiling and floor were included, using the one-dimensional heat conduction sub-model.

The ventilation through the fan system was modeled using a mechanical exhaust vent. A limitation was that a fixed value for the volume flow rate was required, i.e. the time-dependent measured profile was not followed.

The fire was treated as a constrained fire (i.e. oxygen controlled) with an area 1 m^2 , located at the center of the compartment at floor level. The fuel was modeled as kerosene, using a heat of combustion of $4.28 \times 10^7 \text{ J kg}^{-1}$. The time-dependent pyrolysis rate was set to that measured experimentally for the initial calculations, and was then adjusted in subsequent parametric calculations. For Test 1 two calculations were conducted using a fixed fuel pyrolysis rate of 0.039 kg s^{-1} , based upon published engineering information. This provided a comparison with the blind JASMINE calculations where the same pyrolysis specification had been used.

In all calculations a two-layer gas assumption was assumed inside the room, but the 'ceiling jet' option was inactive. The radiative fraction was set to 0.3 in most calculations (0.6 was also investigated). While in most calculations the lower oxygen limit (LOL) was set to 0 %, it was adjusted to 10 % in some parametric calculations.

A required approximation in CFAST is that targets are treated as rectangular slabs. Furthermore, heat conduction is modeled in one-dimension, i.e. in the direction of the surface normal. The surface temperature of the three material probes was calculated, with the target surface normal directed into the compartment (x-direction). The response of the barrel target was not included in the CFAST calculations.

JASMINE Code Description and Input Assumptions

JASMINE is described above in 5.1.2. It was applied as described for the blind calculations with the main exception that the measured, transient fuel pyrolysis (or a fixed fraction thereof) was used to specify the fuel source term. In addition the effect of employing the discrete transfer radiation model was investigated. The influence of applying an oxygen concentration limiter on the combustion process was also investigated for Test 3. Furthermore, for Test 3 the consequence of reducing the imposed exhaust flow rate at the mechanical (FUCHS) duct by 50 % was explored.

CFAST Code Results

Appendix B presents details of the scenarios, for which converged CFAST simulations were achieved. Other parametric combinations were attempted for which a converged solution was not achieved, which is perhaps a consequence of the complex physics of the two experiments. The main observations and findings are summarized below:

For Test 1, the choice of a radiative fraction of 0.6, coupled to the measured fuel pyrolysis rate, resulted in an upper gas layer temperature reasonably close to that measured. The layer height predictions, with the layer dropping to approximately 1 m, were perhaps less representative of the actual experiment. For Test 3, the upper gas layer temperature predictions were less encouraging, with an over-prediction in all parametric calculations undertaken. This was observed, in particular, in the earlier stage of the experiment. It should be noted that radiative fractions higher than 0.3, and up to 0.6, were attempted but that converged solutions were not then obtained. Fig. 5-7 (from

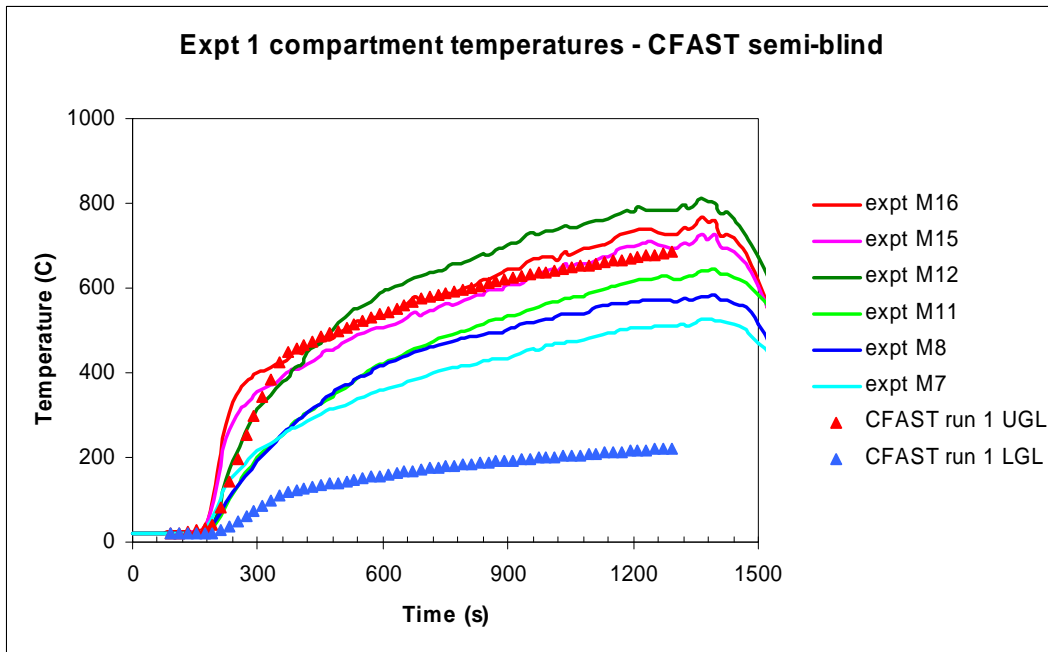
For Test 1, the calculated oxygen concentration appears reasonable. For Test 3, the calculated oxygen concentration, while dropping to zero, does so much more quickly than suggested by the experimental measurement. This is most likely coupled to the fact that too much burning, and associated gas temperature rise, was predicted in the calculation compared to the actual experiment. For Test 3, where the oxygen concentration dropped to zero, whether the lower oxygen limit was set to 10 % or zero had very little influence on the calculated values.

Surface temperatures and incident fluxes for Test 1 were reasonable for the two calculations using a fixed fuel pyrolysis rate of 0.039 kg s^{-1} , but for the calculation using the measured pyrolysis rate they were notable higher than the measured values. Fig. 5-8 (from Appendix B) illustrates wall surface temperature calculations for Test 1 using the measured and fixed (0.039 kg s^{-1}) fuel pyrolysis specifications.

Test 3 calculations for wall surface temperature were reasonably close to the experimental measurements for all the parametric runs. Material probe surface temperatures and the heat flux densities were, however, over-predicted compared to measurement in all parametric runs. This may be due, in part at least, to three-dimensional geometry effects that cannot be captured using a zone model such as CFAST.

The limitation that the flow rate through the mechanical exhaust was fixed in value, and did not vary according to the measurement data, probably had only a small consequence.

Measured pyrolysis rate



Pyrolysis rate = 0.039 kg s^{-1}

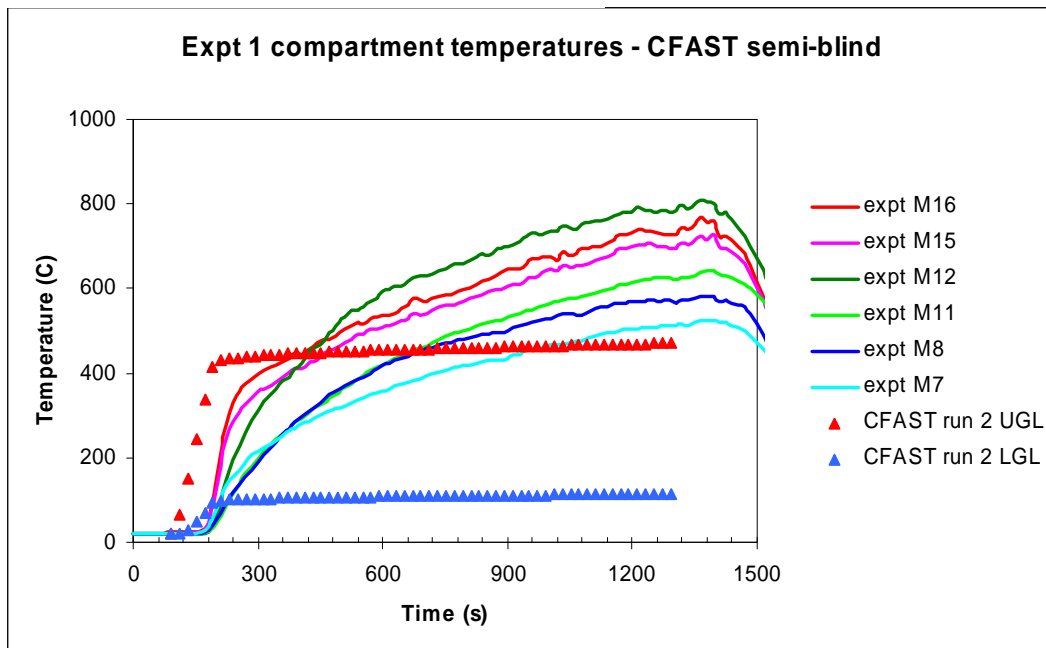
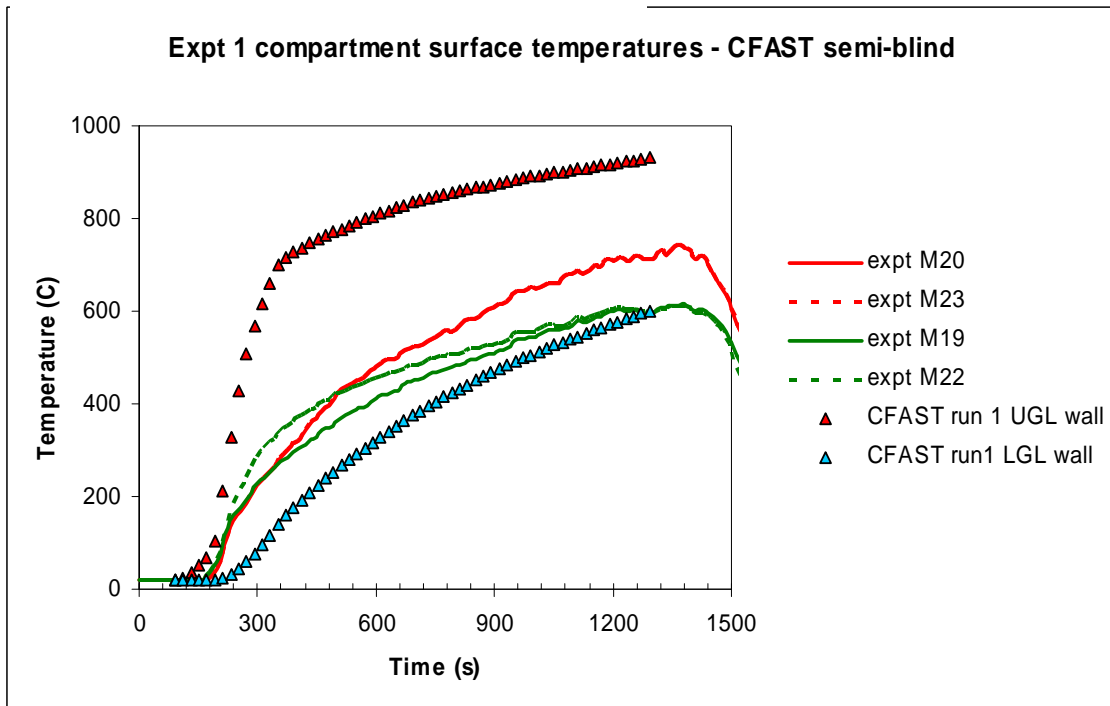


Fig. 5-7 Measured and predicted (open) gas temperatures for Test 1 (from Appendix B)

Measured pyrolysis rate



Pyrolysis rate = 0.039 kg s^{-1}

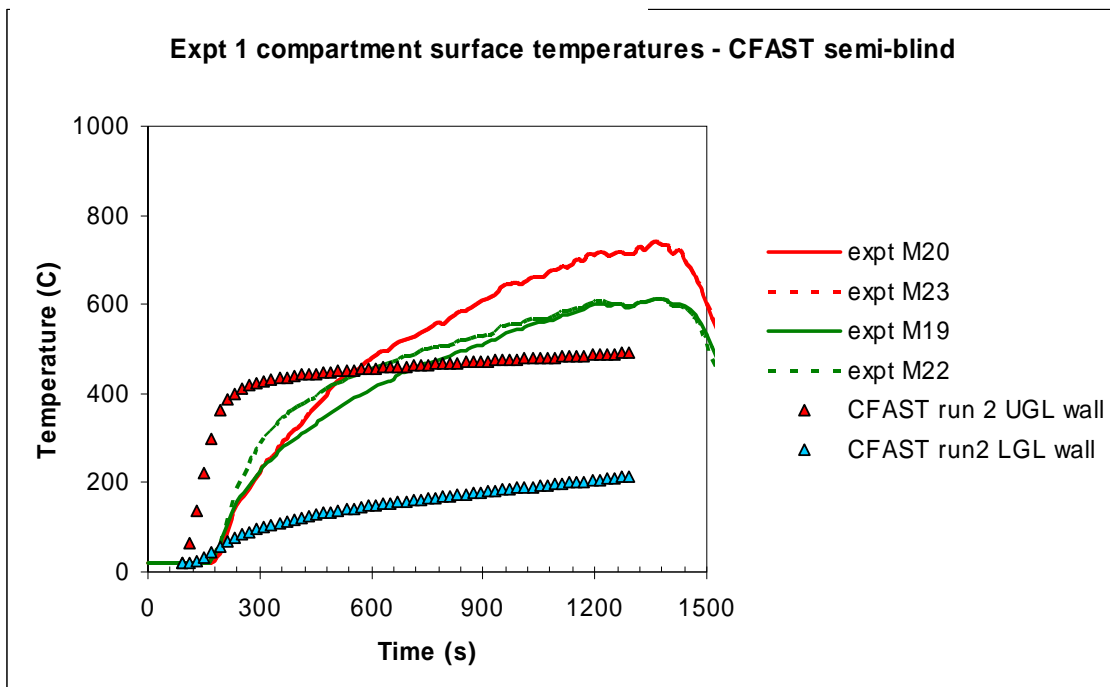


Fig. 5-8 Measured and predicted (open) wall surface temperatures for Test 1 (from Appendix B)

JASMINE Code Results

Appendix B presents details of the JASMINE calculations. These were conducted for the first 18 to 20 minutes of both experiments, after which time convergence problems were encountered. The main observations and findings from the JASMINE calculations are summarized below:

The calculations for Test 1, using the fuel pyrolysis rate derived from the experimental measurements (actually 75% of the measured pyrolysis rate - to account for radiation losses due to soot), were judged encouraging. The main features of the gas temperatures, doorway flows and radiation fluxes were captured quite well. The compartment temperature was arguably calculated to rise too quickly. Fig. 5-9 (from the Appendix B) compares gas temperature and doorway velocity predictions and calculations for Test 1.

While for Test 3 the calculations were generally considered quite reasonable, there was however greater discrepancy with the measured data compared to Test 1. In particular, the direction of the wall vent flow was predicted to be predominantly into the compartment compared to the actual experiment which exhibited a more pronounced two-way flow. Simulations using 75 % of the measured fuel pyrolysis rate generated, on average, results closer to the measurements compared to using the full pyrolysis rate or 50 % of the rate. Recall here that the justification for adjusting the pyrolysis rate is to account, in the overall energy balance, the heat lost from radiating soot particulates (not modeled in the JASMINE calculations), i.e. akin to the radiative fraction in a zone model such as CFAST.

It had been suggested that the level of the imposed exhaust in Test 3 might be the primary reason for the JASMINE calculations indicating less outflow from the wall vent compared to that suggested by the experimental measurements. However, while in a parametric simulation to investigate the effect of reducing the imposed exhaust rate by 50% the wall vent flow was then marginally more bi-directional, the overall effect was to reduce the level of agreement between predicted and measured temperatures and fluxes.

For both experiments the calculated flux densities at WS2 and WS3 were judged overall to be, qualitatively at least, quite reasonable. However, as illustrated in Fig. **5-10** (from Appendix B), the predicted flux density at WS4 (towards the front of the com-

There was no significant influence on the calculated variables when invoking the additional oxygen limitation mechanism on the combustion sub-model. It is perhaps not too surprising that little difference was observed due to the high compartment temperatures, as even with the additional oxygen limitation mechanism combustion still occurs if the local gas temperature is sufficiently high.

The energy 'budget' has been calculated in the JASMINE simulations, and is quite informative. Fig. 5-11 (from Appendix B) shows the energy budget for one of the Test 3 calculations, and illustrates that both heat losses to the solid boundaries and heat convected through the mechanical ventilation duct are significant.

A general note from the JASMINE work is that the presence of soot, and the subsequent radiation absorption and emission, may have an important bearing on the gas temperatures predicted. This in turn influences the radiation fluxes significantly (bearing in mind the T^4 dependency on radiant intensity), which then has a major influence on the conduction into the walls and targets and their temperature rise.

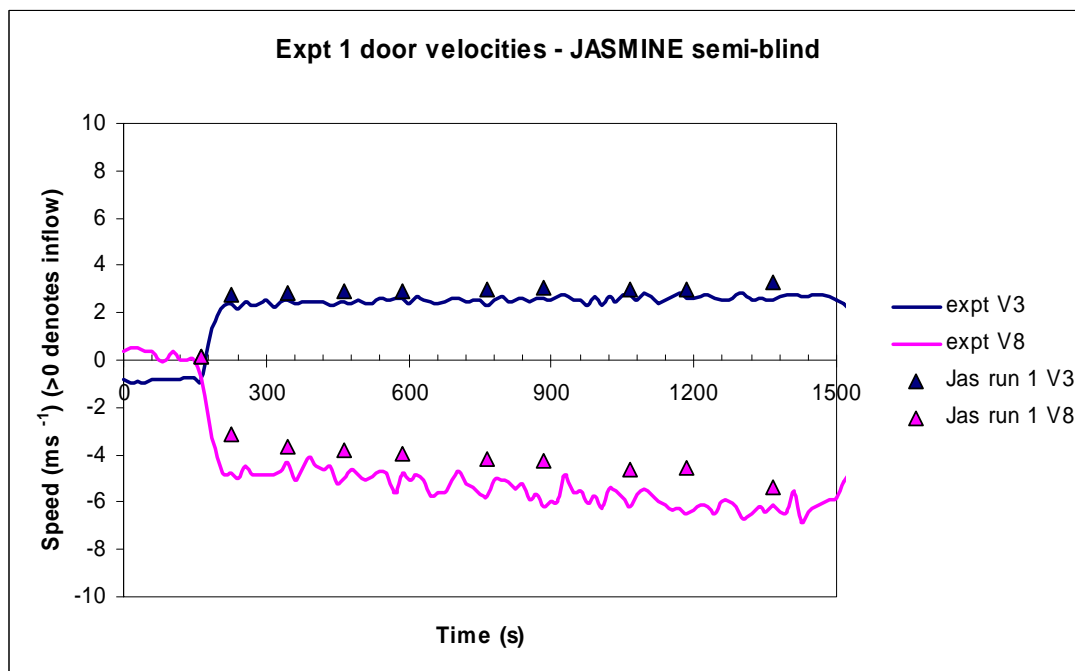
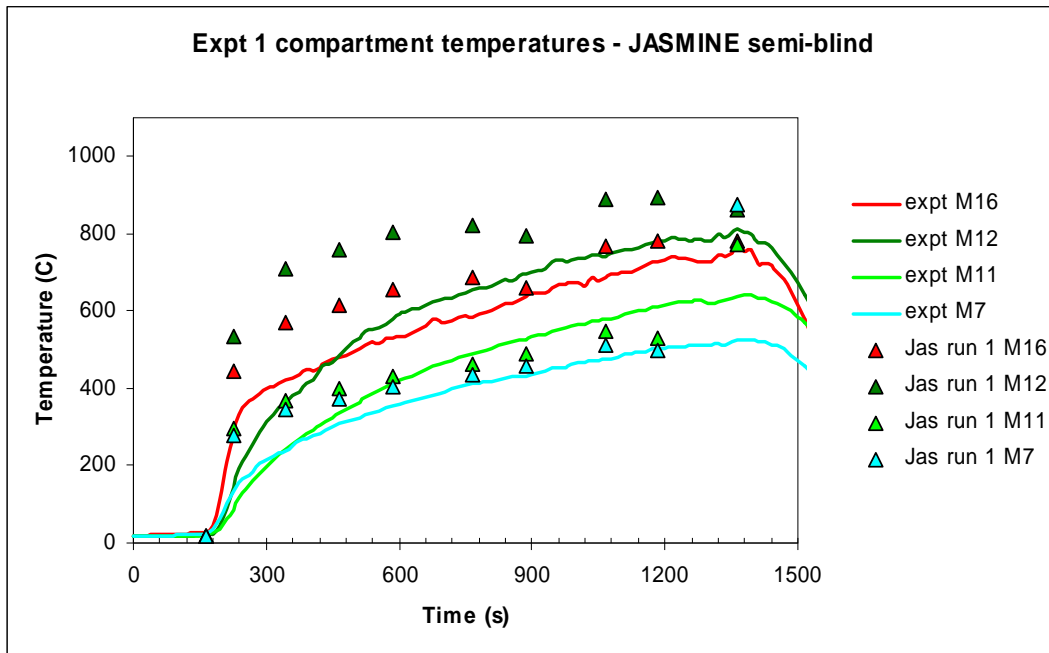


Fig. 5-9 Measured and predicted gas temperatures and door velocities for Test 1 (from Appendix B)

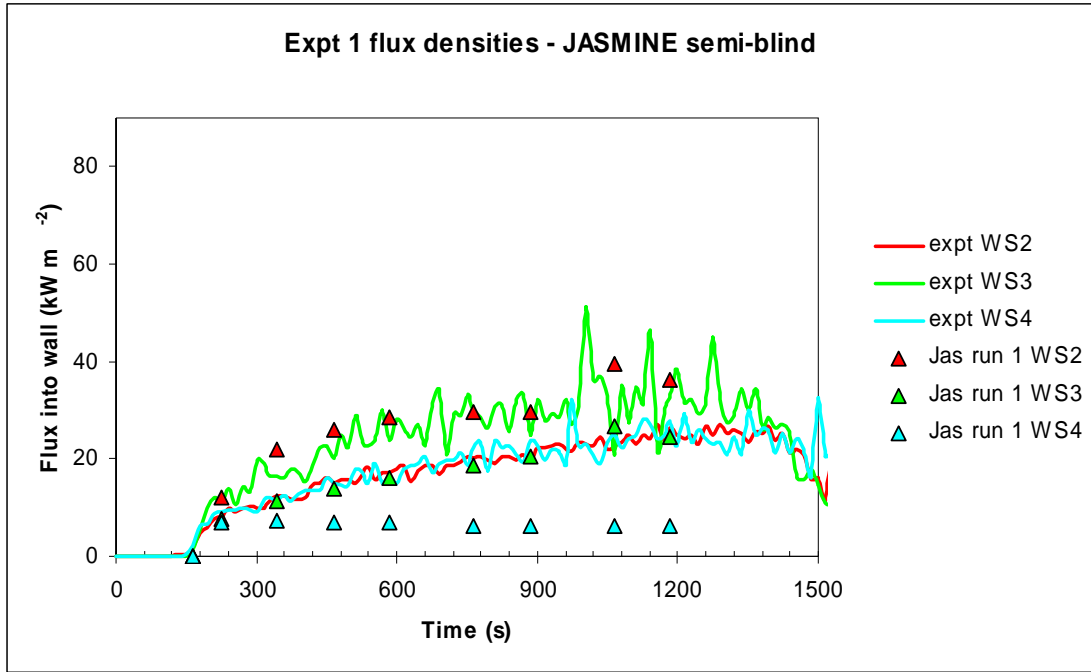


Fig. 5-10 Measured and predicted flux densities for Test 1 (from Appendix B)

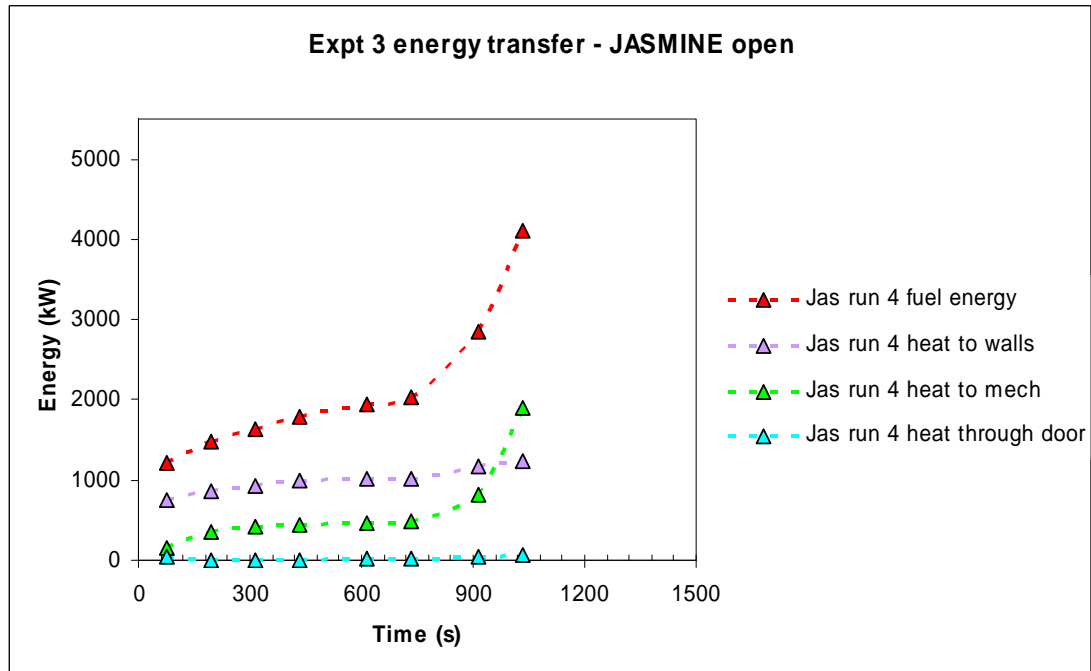


Fig. 5-11 'Energy budget' for a Test 3 simulation (from Appendix B)

5.3 Open Calculations

5.3.1 FATE (Zone Model) Applied by T. Elicson (Fauske & Associates LLC, USA)

The purpose of this benchmark exercise is to perform an integral validation of the FATE™ 2.0 Computer Code fire models for use in nuclear power plants, fuel cycle facilities, and DOE (*Department of Energy*) material handling facilities. Calculations presented below have been performed with FATE Version 2.14 /PLY 04/.

FATE Code Description and Input Assumptions

The FATE™ 2.0 Computer Code /PLY 04/ is used for this analysis. FATE, previously named HADCRT, is the successor code to the HADCRT computer program used in previous ICFMP activities. Specifically, FATE Version 2.14 is used in the following calculations. FATE Version 2.14 contains upgrades to address fire modeling issues. FATE stands for Facility Flow, Aerosol, Thermal, and Explosion Model, for PCs and workstations. FATE 2.0 is used for design, off-normal, and accident analyses of nuclear and chemical facilities. General capabilities of FATE 2.0 include: Fire model, multi-compartment thermodynamics including condensing species, arbitrary topology of flow paths, simulation of aerosol behavior including condensation, re-suspension, one-dimensional heat transfer through multi-layer slab on cylindrical heat sinks, combustion, thermal radiation networks, nuclear fuel and sludge models including chemical reactions. A more detailed description is given in Appendix D.

The fire compartment is simulated with a single region including 14 heat sinks. The wall heat sinks are modeled as “strips” that circumscribe the room perimeter and extend vertically between the indicated elevations. The advantage to this approach is input and computational simplicity, while the limitation is that a single surface temperature is reported for the North, East, South, and West walls at each elevation.

The doorway and the ventilation system are simulated by junctions and allow for buoyancy driven counter current flow. In addition, in flows through the doorway are assumed to be equally distributed between the smoky and lower gas layers, and, for Test 3, air in the lower 1.6 m of the room is assumed to be available for entrainment and consumption in the fire.

Two targets are included in the FATE model. The first target is the concrete material probe with lower corner coordinates of $x = 0.0$ m, $y = 1.9$ m, and $z = 1.7$ m. The probe is modeled with a single vertical rectangular heat sink, heat sink 16, with dimensions 0.3 m \times 0.3 m \times 0.1 m thick. This heat sink is divided into 20 nodes through the thickness to allow one-dimensional conduction through the probe. In addition, the heat sink is included in the radiation heat transfer network; therefore the heat sink surface is subjected to convective and radiative boundary conditions. The second target is the more complex barrel-type waste container. This target is divided azimuthally into four segments. The first three segments cover the cylinder half facing the fire, while the fourth segment is the entire back half side of the barrel facing away from the fire. Each segment height is equal to the height of the barrel. In addition, each of the four segments is represented as a composite heat sink consisting of three layers: an outer metal layer (5 radial nodes), a middle concrete layer (20 radial nodes), and an inner styrene granulate fill layer (20 radial nodes). The tinplate that makes up the inner barrel is defined as a contact resistance between the concrete and styrene. Radial conduction is allowed between the layers, while azimuthal conduction is modeled only in the outer most steel layer. The outer metal surfaces are also included in the radiation heat transfer network.

The given HHR were adjusted based on a 5-point moving average of the raw data and a delay based on the fuel ignition time. The fuel ignition time is taken as the time at which the heat sink temperatures begin to increase (160 s for Test 1 and 15 s for Test 3). FATE input also requires specification of the combustion products yield. The combustion yields used for input are based on real yields for high molecular weight/temperature hydrocarbons for well ventilated flaming fires.

Code Results

Test 1 is characterized by a kerosene fire with a steady state power in the range of 3 to 3.5 MW, peak fan vent flows of 2 m³/sec, a doorway opening of 0.7 m by 3.0 m, and a multi-layer target in close proximity to the fire source. These conditions result in a flame that extends well into the smoky region and significant variation in temperatures across the x-y plane. As with other benchmark tests, the Benchmark Exercise No. 4 demonstrates that the two most influential aspects of the input are the fire power and the room ventilation behavior. To follow the measured ventilation flow rates, which are decreasing at the end of the experiment, the flow area has been adjusted from 0.176 m² to 0.0353 m².

The measured flows were estimated by reducing the reported velocities from doorway velocity probes V3 through V8. A volumetric flow rate was assigned to each measurement by taking the product of the reported velocity and 1/6 of the door area (0.35 m²). The net volumetric flow was then taken as the sum of the individual volumetric flows and is assumed to represent the unidirectional flow rate. Even though the doorway area input to FATE is computed as 100 % of the geometric areas with no reductions taken for entrance and exit losses, the FATE unidirectional flow rate calculation underpredicts the estimated doorway flow rates.

For this particular geometry – a high powered fire in a relatively small and under-ventilated compartment – the measured gas concentration may be a better measure of room conditions rather than the smoky layer height. Reasonable agreement is indicated between the calculated and measured gas concentrations.

The temperature variation inside the fire compartment along the x-y plane is promoted by the room geometry in which the fire essentially blocks free inflow from the door (fire pan width is larger than the narrow doorway width). The FATE smoky layer calculations provide reasonable estimates of the average gas temperatures.

The peak wall temperatures in the back of the room are consistent with the peak gas temperatures, while the side wall temperatures are about 100 K lower. This may be influenced by air circulation which may be diminished toward the back of the room. The FATE wall strip heat sink model presents an average temperature of all four side walls at a particular elevation; therefore it is not surprising that peak wall temperatures are not predicted. The under-prediction of wall temperatures at upper elevations is a result of the overall lower predicted smoky layer gas temperature.

The container surface temperature is reasonably predicted, while the concrete probe temperatures are somewhat under-estimated. The under-estimation of the concrete probe temperature occurs because the probe remains in the lower gas layer in the FATE calculation, while test data indicates the probe is submerged in the smoky layer. Sensitivity calculations for which the probe is submerged in the smoky layer show good agreement with the test data. The significant heat up of the can surface, even though the waste can is located in the lower gas layer, is an indication of the radiative power received from the fire.

To perform a bounding analysis for nuclear power plant applications, the many uncertainties associated with a room fire must be addressed. Uncertainties identified in this benchmark include the fire power, ventilation flows, and air mixing. Perhaps the most straightforward approach to addressing uncertainties to obtain a bounding assessment appropriate for nuclear power plant applications is to increase the fire power. Therefore in a sensitivity calculation the HRR has been increased by 40 %, leading to a better temperature prediction.

The reduction of the door opening cross section leads to an under-ventilated fire. A key assumption used in modeling this case is the length along which oxygen is entrained and consumed in the fire. Finally, following guidance from other fire benchmark exercises, air flowing in through the doorway is assumed to be equally distributed between the smoky and lower gas layers.

The gas concentration is a better measure of conditions in the smoky layer. The measured smoky layer height is based on average of thermocouple readings at 4 separate elevations, with the lowest elevation at 1.5 m. Thus, the reported layer height does not provide indication of smoky layer heights below 1.5 m.

The gas and heat sink temperatures were found to be closely linked to the fire power. For this reason, adjustments were made to the reported fuel burn rate to conform to the times at which test data indicated the plume gas temperatures began to increase and decrease. Overall, reasonable agreement is obtained and no attempt was made to increase the fire power from its nominal value to provide a bounding estimate of the gas temperatures.

Calculation of the concrete probe and waste can temperatures as well as the concrete wall surface temperatures proved to be sensitive to whether or not each heat sink was submerged in the smoky layer.

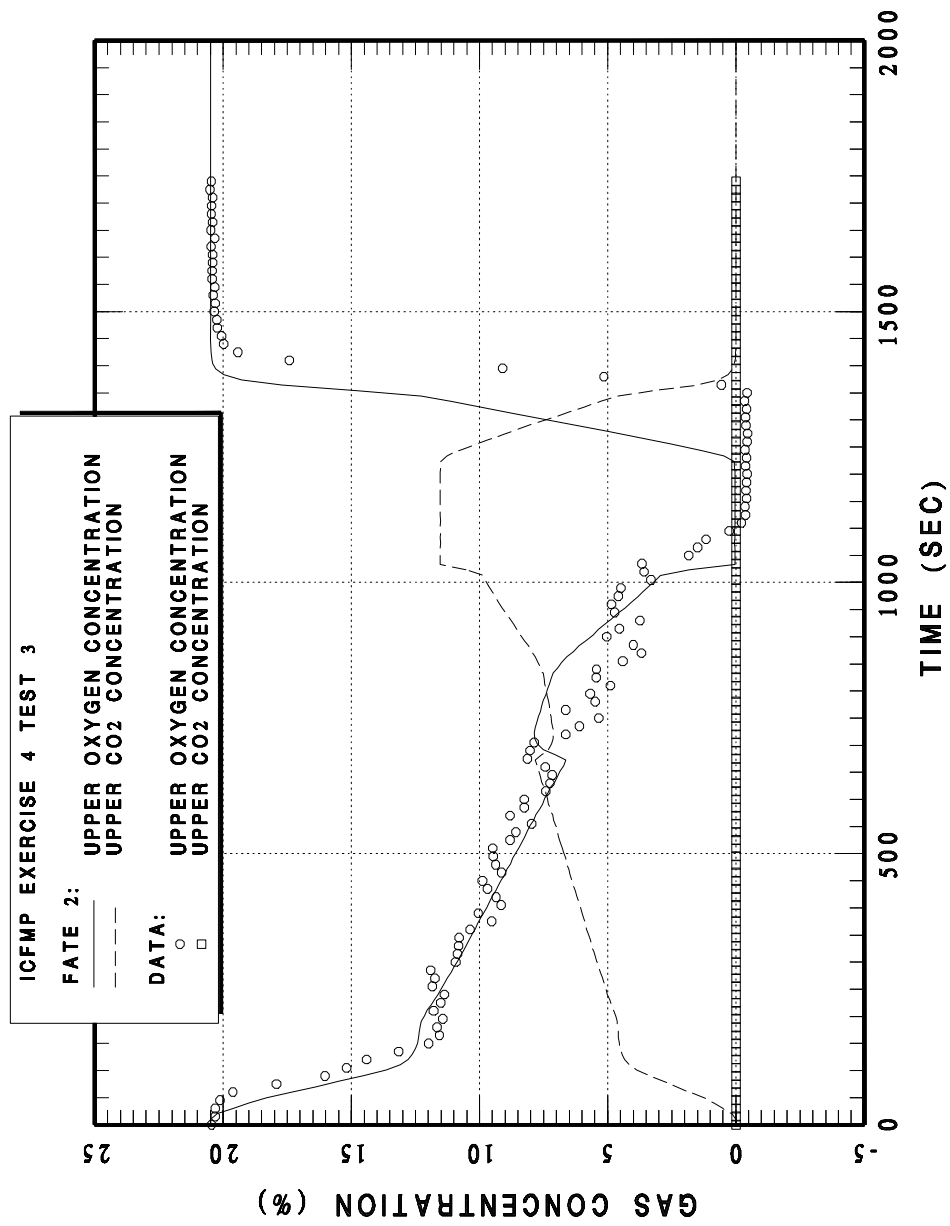


Fig. 5-12 Benchmark Exercise No. 4, Test 3 smoky layer gas concentrations (from Appendix C)

5.3.2 FLAMME-S (Zone Model) Applied by L. Rigollet (IRSN, France)

Tests 1 and 3 have been simulated with the two-zone model code FLAMME-S, Version.2.3.2 /BOU 02/, developed by IRSN. In this context, a remark must be made concerning the fact that the studied cases are outside the validation domain of FLAMME-S, specifically in respect to the two following conditions:

- The ratio of the pool surface area to the floor area of the facility is less than 5 %,
- The ratio of the heat release rate to the volume of the facility is less than 5 kWm^{-3} .

FLAMME-S Code Description and Input Assumptions

The FLAMME-S code is similar to the CFAST code described above. The fuel pyrolysis rate is a pre-defined input, and the burning in the compartment is then modeled to generate heat release and allow species concentrations to be calculated. FLAMME-S is a two-zone model, whereby each compartment is divided into a hot gas upper layer and a cold gas lower layer. In the presence of fire, the sub-model transports heat and mass from the lower to the upper layer making use of an empirical correlation. A notable difference in this context is that FLAMME-S uses the Heskestad correlation for the plume flow, whereas the McCaffrey correlation is utilized in CFAST. Flows through vents and doorways are determined in both codes from correlations derived from the Bernoulli equation. Radiation heat transfer between the fire plume, upper and lower layers, and the compartment boundaries is also included.

The side walls of the fire compartment are constructed from 25 cm of light concrete and 5 cm of insulation. The ceiling is made of a 25 cm concrete layer and a 5 cm insulation layer. For the floor, only 30 cm of concrete are taken into account: the aerated concrete implemented in the experiments in order to protect the mass loss measurement is not modeled. Two material probes, concrete and aerated concrete, are modeled.

In Test 1, the door is completely opened, with a free cross section of 0.7 m x 3 m. In the Test 3, the opening is partly closed, with a free cross section of 0.7 m x 1 m. The fan system, which is not used in the experiments, and the hood above the open front door are not modeled.

The energy released by radiation represents 32 % of the total heat released. A complete combustion reaction is assumed.

Two types of calculations have been performed: In a first step a constant pyrolysis rate has been assumed (Test 1: 65 g/m²s; Test 3: 50 g/m²s) and in a second step the measured rate was used. The LOL value was then reduced from 11.5 % to 0 %.

FLAMME-S Code Results

The layer height calculated by FLAMME-S is lower than that determined from the experimental data. The experimental interface height is determined from thermocouples located at three elevations: 1.5 m, 3.35 m and 5.2 m. Thus, in the experiment, the layer height never decreases under the elevation of the first thermocouple, i.e. 1.5 m. Tournaire and al. /TOU 00/ have shown that the data reduction method is weakly dependant on the number of thermocouples except in the case of three thermocouples where the interface height does not reach the floor.

The gas temperatures calculated for the upper layer are in good agreement with the experimental results of Test 1. As the layer height calculated by the code is lower than the experimental interface, the calculated temperature of the lower layer is colder than the gas temperatures measured.

The oxygen concentrations calculated with the code in the upper layer are lower than those measured in the experiment; however, the comparison is difficult because the sensor GA2-O2 seems to be saturated.

In the experiment, total heat fluxes were measured at one elevation, i.e. 1.7 m. At the upper layer, the FLAMME-S code calculates slightly lower total heat fluxes.

The wall temperatures are not compared, because the FLAMME-S code calculates an average temperature for the first mesh of a wall and thus cannot be compared with a surface temperature measured experimentally.

However, the temperatures of two material probes (concrete and aerated concrete) are compared. Experimentally, the sensors seem to be reversed: M 28 and M 26 for the aerated concrete slab and M 32 and M 30 for the concrete slab. The calculated results are in good agreement with the measurements, if the four sensors mentioned above are indeed reversed.

In the first calculation for Test 3, using the lower oxygen limit (LOL) of 11.5 % rapidly leads to the fire extinguishing by itself, two minutes after the beginning. For the open calculations, even if the experimental pyrolysis rate is imposed in the data file, the code under-estimates the heat release rate: the pyrolysis rate is limited by the code, because the quantity of oxygen involved in the reactive zone is not sufficient for the combustion reaction. Therefore, it should be noted that the comparison of predictions with measurements for all other parameters cannot be expected to be necessarily close since the heat release rate is underestimated. During Test 3, a phenomenon seems to occur which is not modeled by the code. While the oxygen concentration measured in the experiment reached 0 %, the gas temperatures inside the compartment increased up to about 900 °C and a flame was observed at the opening. This experiment presents characteristics similar to those of ghosting flames described by various authors.

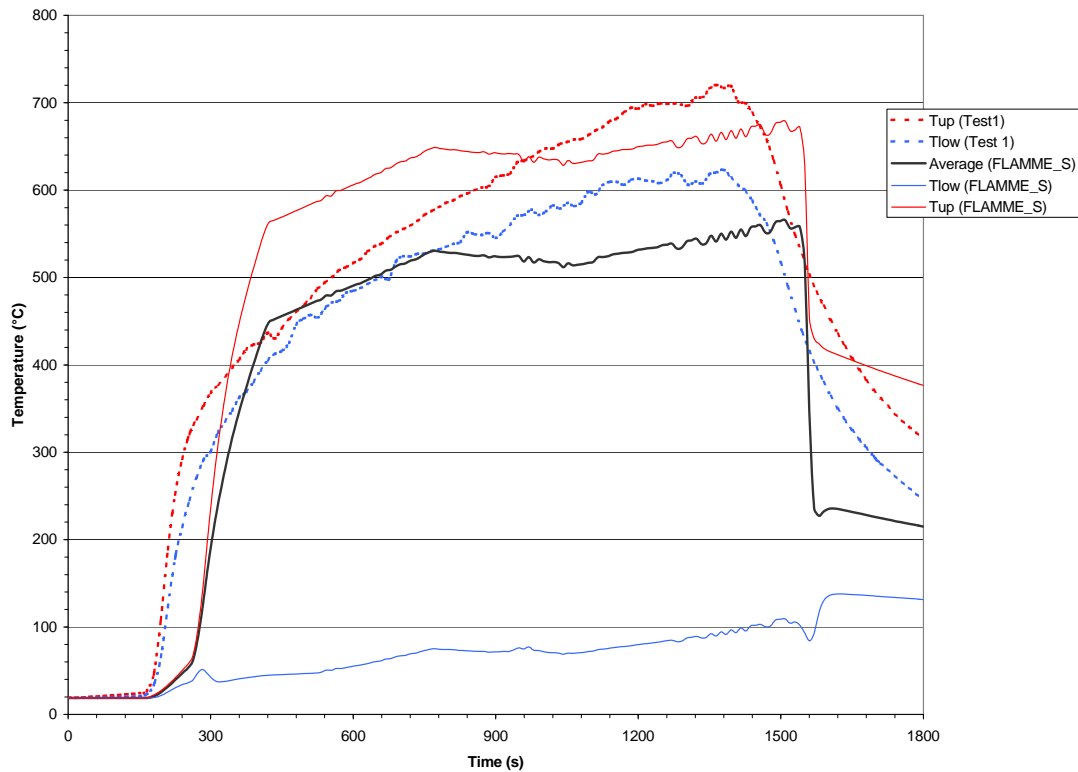


Fig. 5-13 Gas temperature in the compartment - open calculations (from Appendix D)

5.3.3 CFX (CFD Code) Applied by M. Heitsch (GRS, Germany)

Calculations with the CFD code CFX 5.7 have been carried out for Benchmark Exercise No.4 within the frame of the International Collaborative to Evaluate Fire Models for NPP Applications (ICFMP). Version 5 of the CFX family /CFX 04/ represents a completely new code structure compared with previous versions and offers new features.

CFX Code Description and Input Assumptions

CFX /CFX 04/ is a commercial Computational Fluid Dynamics (CFD) multi-purpose code. The latest generation is named version 5. The current release is 5.7. The main features which demonstrate the progress since the previous version 4 are the coupled solver and the ability to handle structured and unstructured meshes. CFX-5 is capable of modeling steady-state and transient flows, laminar and turbulent flows, subsonic, transonic and supersonic flows, heat transfer and thermal radiation, buoyancy, non-Newtonian flows, transport of non-reacting scalar components, multiphase flows, combustion, flows in multiple frames of reference, and particle tracking.

Thanks to the regular geometry of the test arrangement, the computational mesh was decided to be built exclusively with structured cells. The mesh has a total of 115700 cells in the fluid domain of the modeled test volume. Another 2548 cells are in the barrel target (inner and outer part) to describe heat conduction. It reveals that the horizontal resolution chosen may not be fine enough.

The gas mixture of air, fuel (kerosene) and combustion products is modeled by tracking the individual species, which are kerosene, oxygen, nitrogen, carbon-dioxide and steam. Soot is also created according to the Magnusson soot model implemented in CFX. In this model, a number of constants are used, which were not further investigated in this exercise. Nitrogen represents a background fluid, not participating in any reaction. The chemical reaction itself is represented by a single-step mixing controlled reaction within the Eddy Dissipation model. A complete combustion is assumed.

A predefined share of the reaction heat (40 %) is emitted from the surface of the fire pan as radiation flux and distributed by the P1 radiation model in CFX. This radiation model solves an extra transport equation and assumes direction independent radiation transport. It allows heating of the fluid due to radiation from a boundary (here the fuel pan). The radiation is not released from volume cells where the reaction takes place.

Flows through the venting (fan) system “FUCHS” and the hood are specified by flow velocities given in the specification of the tests.

A simplification was made concerning the heat flow into the surrounding walls. These walls are not included in the mesh and hence the heat flow calculated at constant wall temperature. This overestimates the removal of energy from the fluid.

CFX Code Results

The history of the fuel release corresponds exactly to the fuel consumption curve from the experiment. A total amount of 80.7 kg kerosene was added. The temperature distribution is affected by the inflow of cold air through the door and the hottest part of the gas plume is pushed towards the back of the room. The temperatures in the front location show a good correspondence to the measurements up to about 400 s but then change little up to the time when the fire intensity passes its peak. In the simulation this is expressed by a slight reduction of gas temperatures. Then the fire intensity remains constant for a long while and reduces to zero after about 1400 s. The measured temperatures however increase continuously up to the end of fuel combustion. A similar tendency can be observed for temperatures in the back part of the facility. Here, however, measurement and simulation show different trends. During the test the highest temperature was observed at the bottom of the room and decreased towards the ceiling. The simulation predicts the opposite. This was true for all columns of thermocouples.

The measured data for oxygen at GA1 are captured quite well. Only at the beginning and the end of the fire scenario are some differences seen. This may be related to the kerosene release curve, which was specified as an input. The measured CO₂ mole fraction is lower than the values predicted by CFX. This may be due to the fact that the modeled chemical reaction does not include any production of CO and assumes only CO₂ and H₂O.

In the door opening a number of flow sensors recorded the flow speeds in a vertical line. In the upper locations the predictions compare quite well with the measurement, in the lower probe locations however the flow is underestimated.

The barrel inside the fire compartment is built as a cylindrical double vessel container. The inner section was filled by a type of granulate and the outer cylinder by concrete.

In the computer model these two materials have been included but not the vessel walls. The mesh was probably not sufficiently fine to model the temperature rise accurately, and this was over-estimated.

This measured HRR history for Test 3 was input to the code according to the test description. The sudden stopping of kerosene release after about 1100 s can also be identified in the temperature plots and causes some disagreement after that time. The gas with the highest temperatures is pushed towards the back wall. They show a similar good correspondence with the measured data up to the moment the fire is stopped. There might also be some thermal inertia of the thermocouples including continuing radiative heat flux from walls, which causes a slower decrease than predicted by the simulation.

The agreement for oxygen concentration at GA1 is as good as for Test 1.

For the lower velocity probe at the door opening the comparison is very good. At the upper location, however, negative values (inflow) were measured but were not predicted. At the time of about 800 s there is only flow into the test compartment through the door.

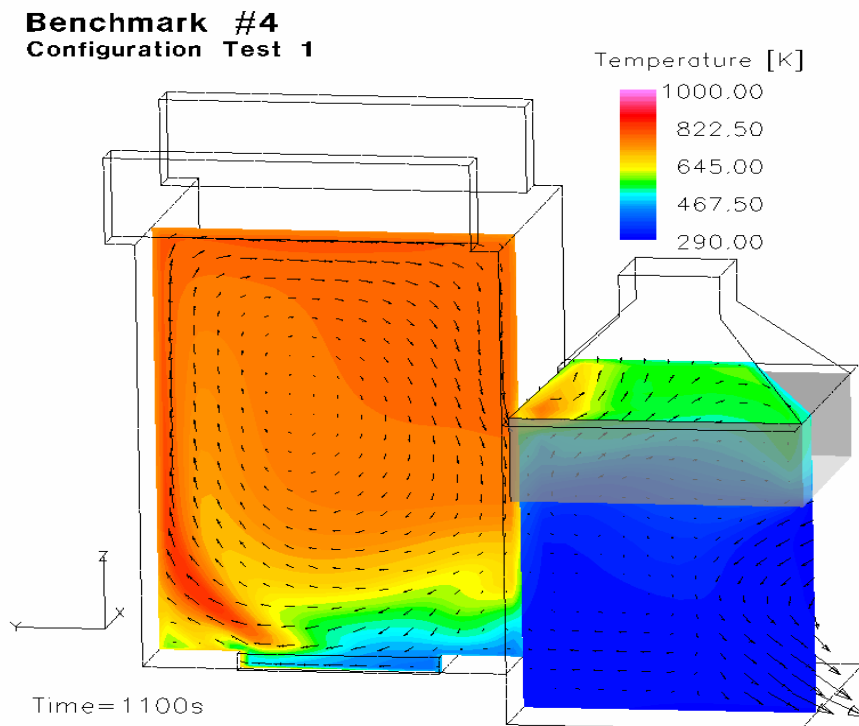


Fig. 5-14 Vertical temperature distribution at a plane $x = 0.95$ m (from Appendix E)

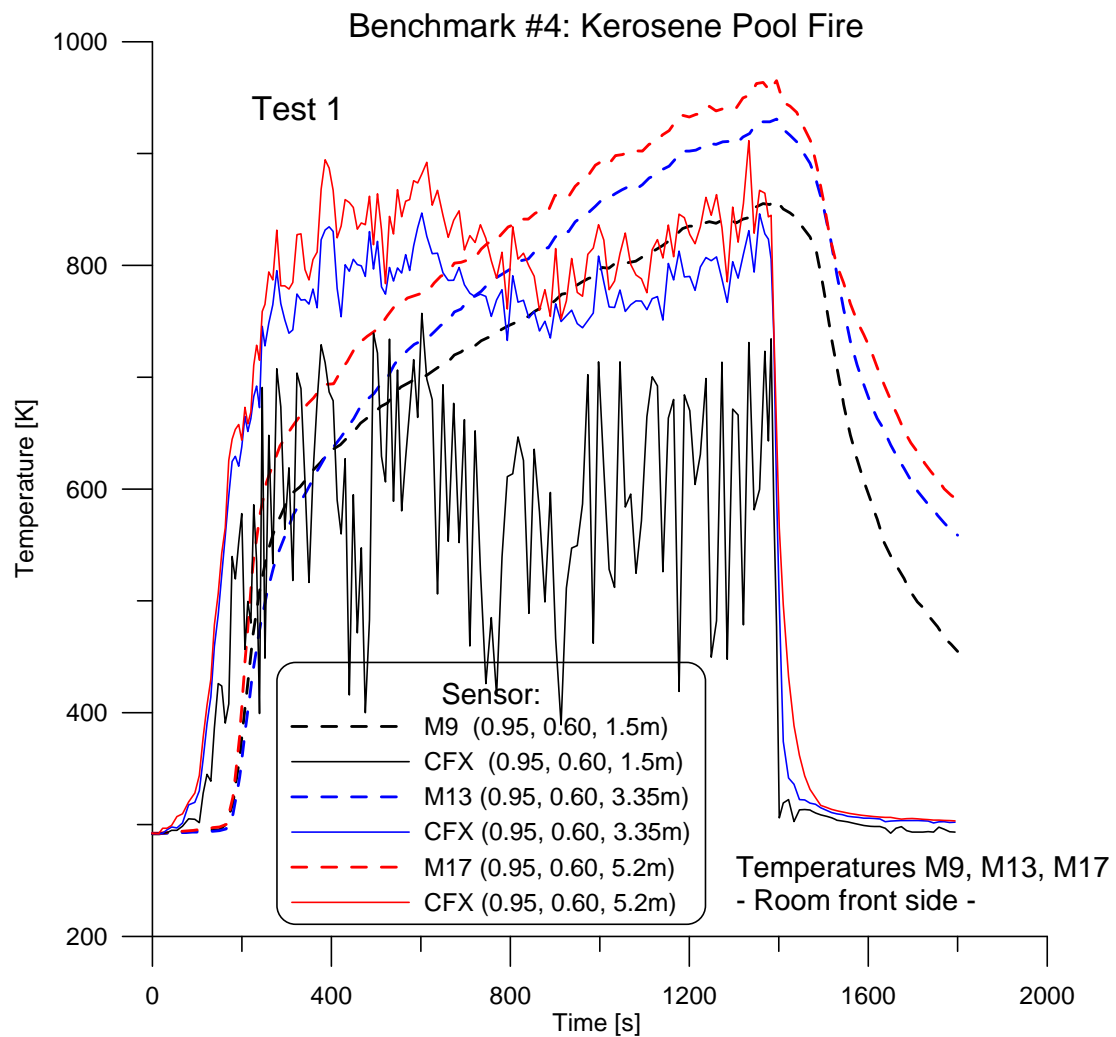


Fig. 5-15 Comparison of selected gas temperatures close to the front of the test facility for Test 1 (from Appendix E)

5.3.4 FDS (CFD Code) Applied by W. Brücher (GRS, Germany)

As an extension to earlier calculations with FDS2 and FDS3 within a project outside the ICFMP, open calculations have now been performed with FDS3 and FDS4 to investigate the influence of different FDS versions and the differences due to the chosen grid.

FDS Code Description and Input Assumptions

The FDS code has already been described in chapter 5.2.1. One major difference between FDS3 and FDS4, with some influence on the results is a different default LOL condition, where the 'no burn' area in under-ventilated conditions is extended to higher temperatures.

FDS Code Results

Actual heat release rates differ from the heat release rate obtained from the prescribed pool mass loss data. Fig. 5-16 shows all heat release rates calculated with different model configurations. Depending on the model configuration not all released fuel is burnt immediately or in some cases it is only partly burnt. The mass release peak in particular is not accompanied by an equivalent strong increase of the heat release due to the under-ventilated conditions in Test 3.

Both calculations with FDS3 use exactly the same set of parameters except for the grid cell size. Temperatures are generally slightly underestimated by the model for most of the time (Fig. 5-17 to Fig. 5-19). The temperature peak appears too early compared to the measurements, which is partly due to the mass loss rate of the benchmark specification. A different (smoothed) interpolation of the questionable weight scale data in former calculations resulted in a better agreement of the temperature development. However, peak temperatures are also underestimated in that case. No obvious increase in the simulation quality of the temperatures is found, although this effect would be expected as a consequence of a better resolution of the flame area. A possible explanation for the slightly worse overall performance with the fine grid may be the missing extension of the fine grid to the whole door area which is crucial for the development of the fire inside. The calculated fine grid gas flow into the compartment is higher than the measured one, resulting in lower gas temperatures inside the compartment. This effect is also found in the calculation for oxygen concentration inside the fire compartment, which is over-estimated.

Due to the modification of the default temperature dependent LOL limit in FDS4, lower heat releases are found in FDS4 compared to FDS3, also including lower gas temperatures and surface heat fluxes. The default LOL definition seems to be a major problem in under-ventilated conditions for both model versions.

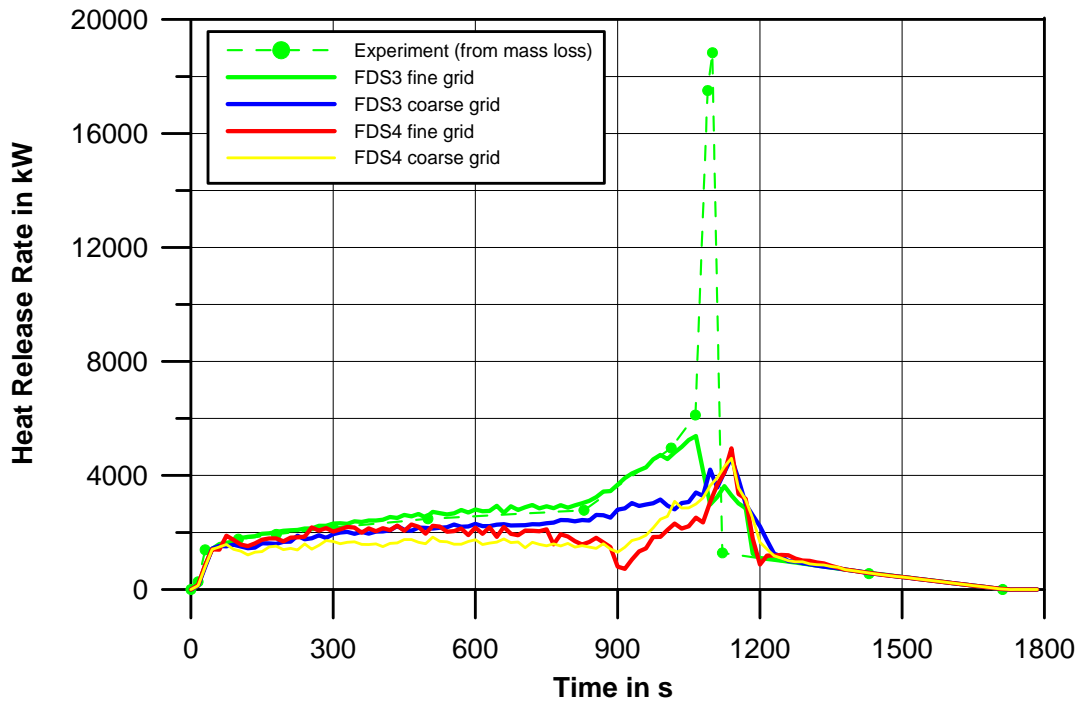


Fig. 5-16 Heat release rates of all FDS3 and FDS 4 calculations for Test 3 (from Appendix G)

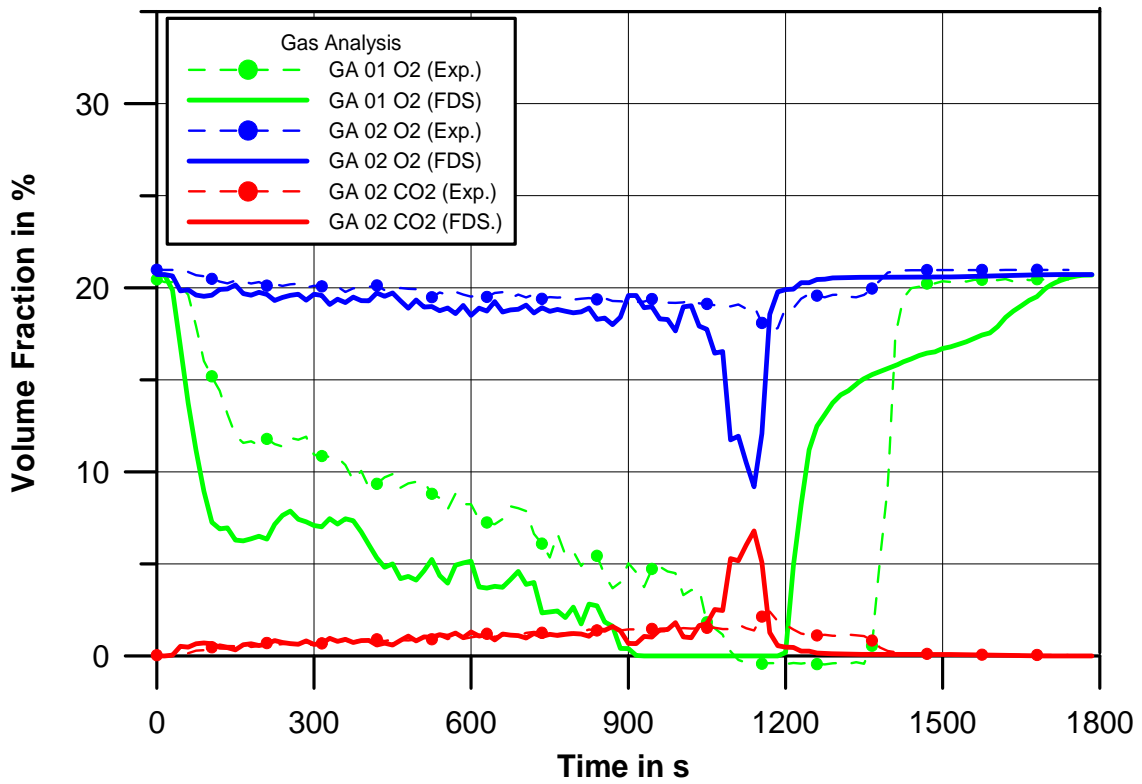
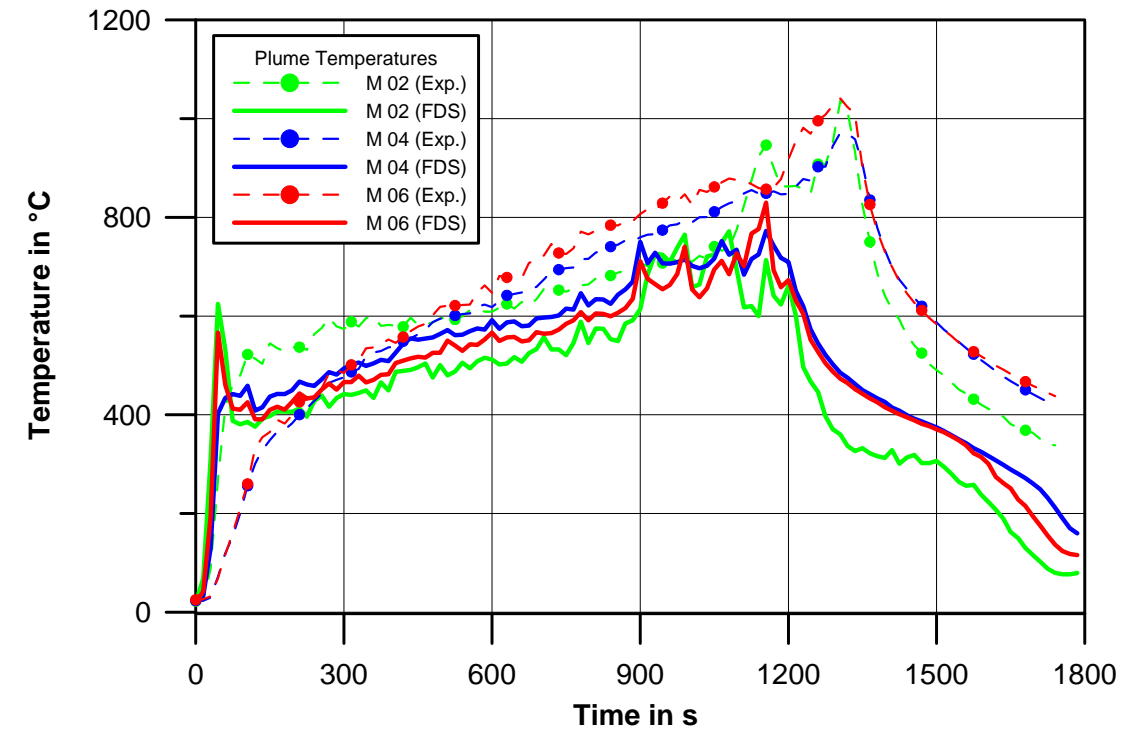


Fig. 5-17 Comparison of FDS results (FDS3 coarse grid; from Appendix G)

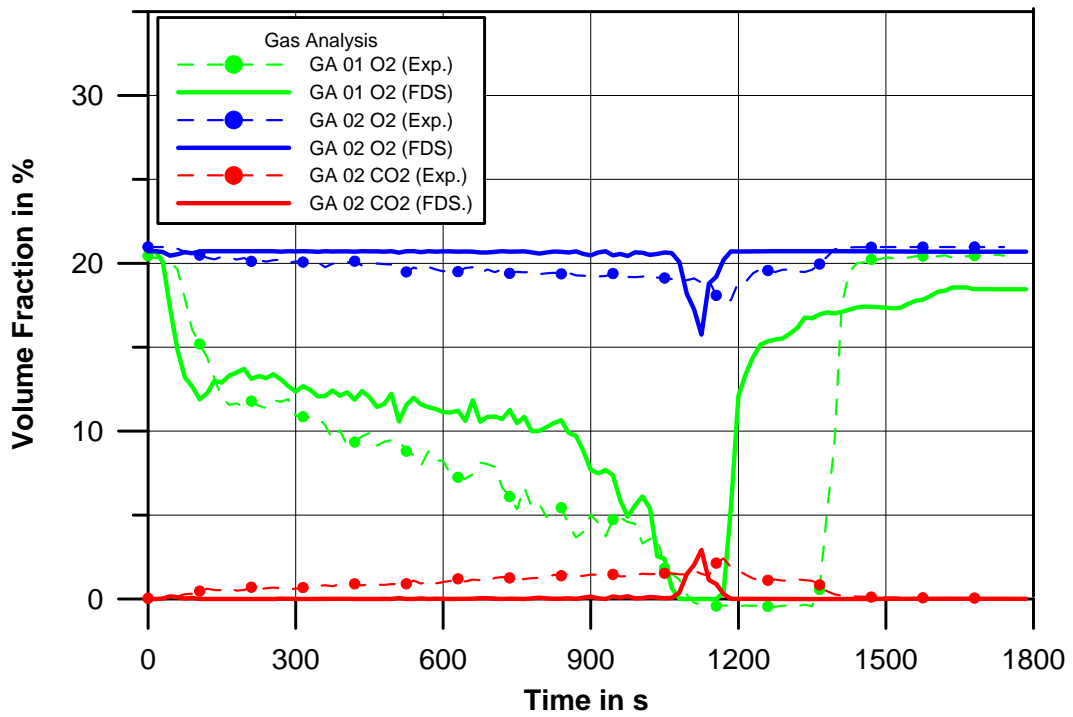
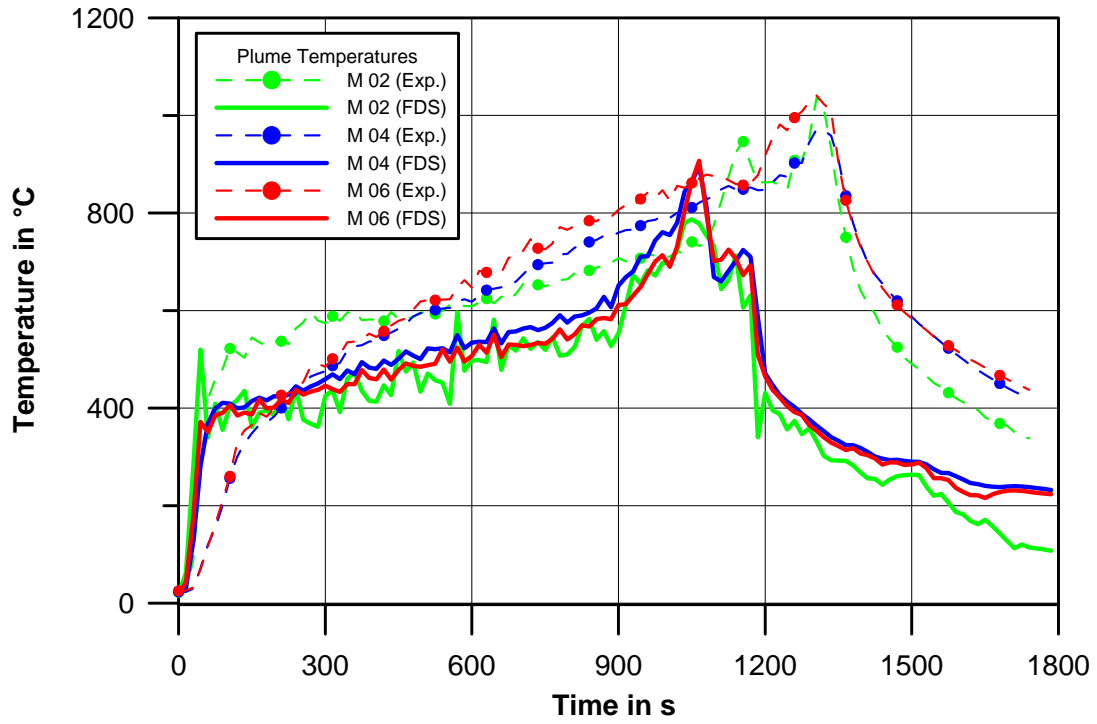


Fig. 5-18 Comparison of FDS results (FDS3 fine grid; from Appendix G)

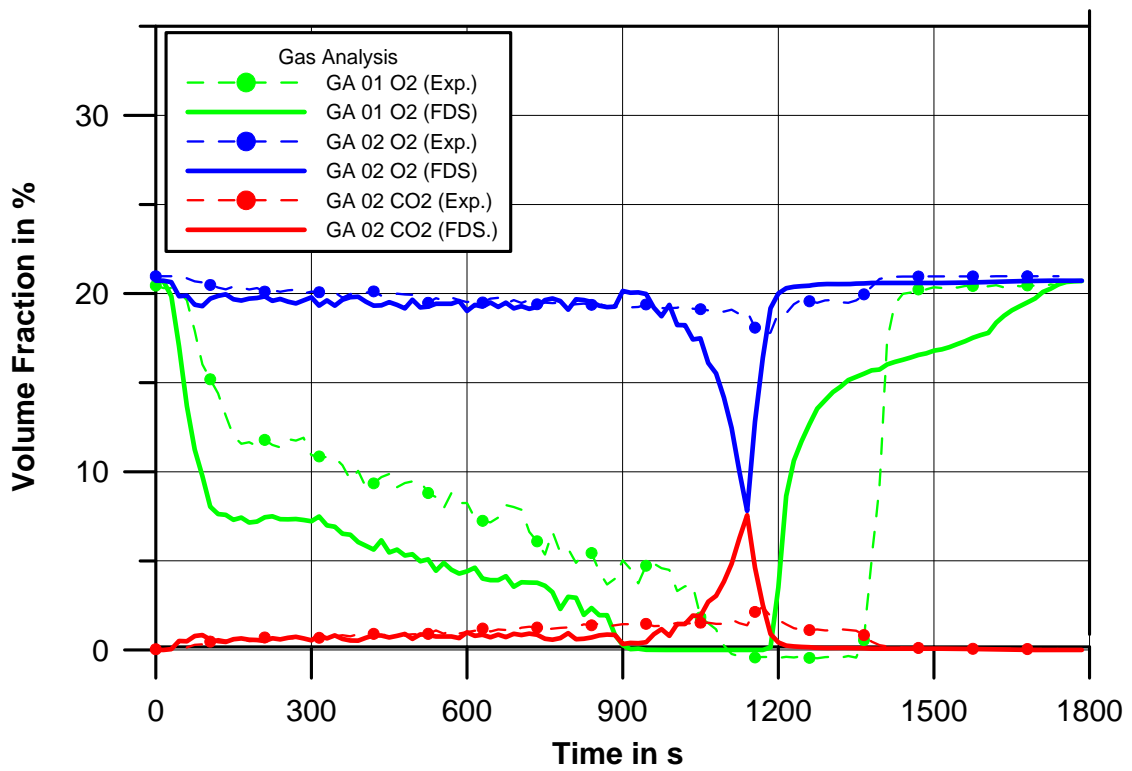
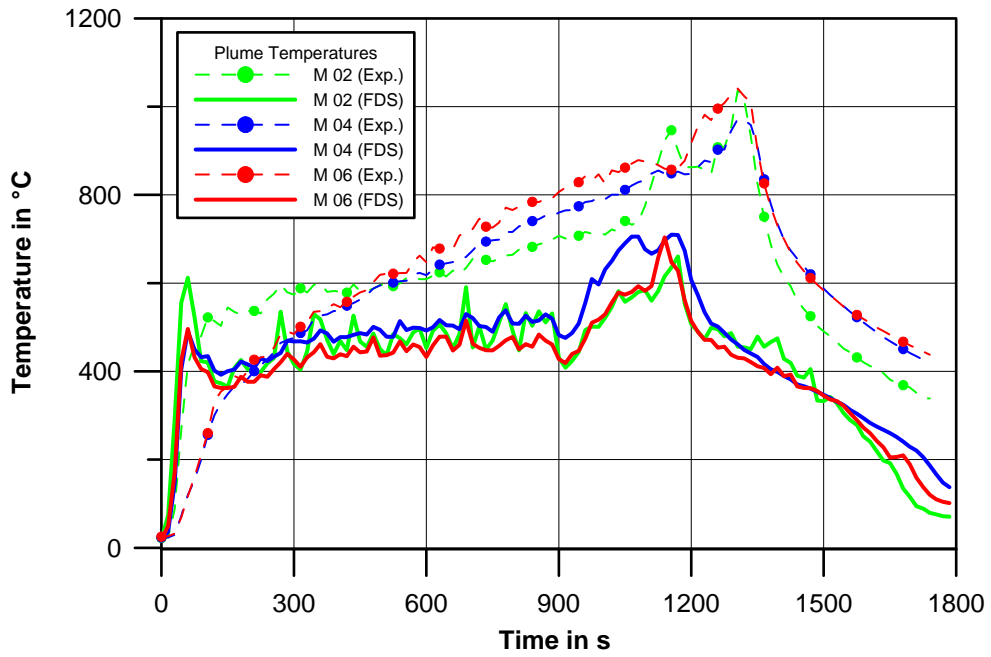


Fig. 5-19 Comparison of FDS results (FDS4 fine grid) (from Appendix G)

5.3.5 COCOSYS (Lumped Parameter Code) Applied by B. Schramm (GRS, Germany)

Both experiments of Benchmark Exercise No. 4 have been simulated with COCOSYS with knowledge of the experimental results. Because of the flame being extinguished due to oxygen depletion in Test 3, the pyrolysis rate has been modified in some parametric calculations.

COCOSYS Code Description and Input Assumptions

The lumped parameter (LP) code COCOSYS /ALL 05/ has been developed and validated for the comprehensive simulation of severe accident progression in light water reactor containments. This code system is to allow the simulation of all relevant phenomena, containment systems and conditions during the course of design basis accidents and severe accidents. In COCOSYS, mechanistic models are used as far as possible for analyzing the physical and chemical processes inside reactor containments. Essential interactions between the individual processes, e.g. feedback from fission product decay heat on thermal hydraulics, are treated in a thorough way. With such a detailed approach, COCOSYS is not restricted only to relevant severe accident phenomena, but will also be able to demonstrate interactions between these phenomena as well as the overall behavior of the containment.

For the simulation of oil and cable fires, pyrolysis and burning models have been implemented in the thermal hydraulic module of COCOSYS. This process is divided into two steps: first the release of pyrolysed species from the oil or cable surface and second the burning processes inside the atmosphere and on the surface of the burning material itself. Two different types of concepts have been implemented in COCOSYS: a very detailed one simulating the combustible materials (oil and cables) with a 1D heat flow model and a simplified concept to handle user specified pyrolysis rates including in some way the feedback from the thermal hydraulic boundary conditions.

In the oil fire model, the material to be burned is represented by a usual structure subdivided into several layers for the calculation of temperature profiles in the material (Fig. 5-20). The surface temperature is calculated by a spline interpolation using all layer temperatures. The heat flux on the surface (e.g. reaction heat, convective heat transfer, radiation) is distributed into the uppermost layer and the second layer according to the volume fraction of the uppermost layer. The released CH_x fractions are

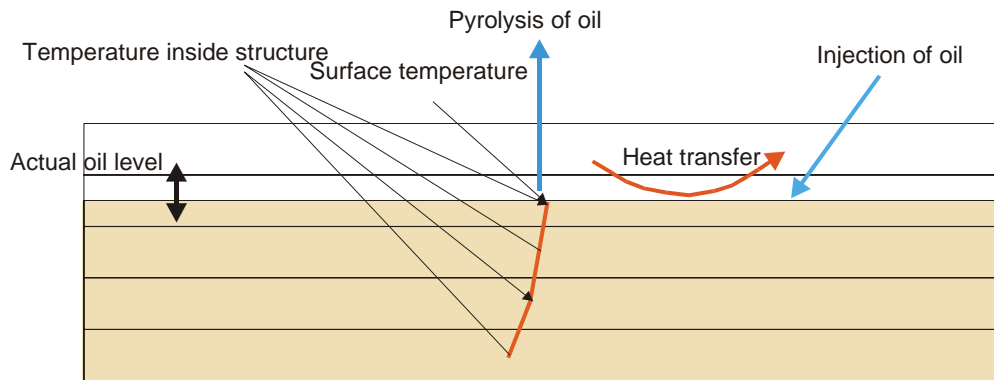


Fig. 5-20 Concept of the pyrolysis model for oil burning

A grid of 102 control volumes with 235 connections in between was used to model the fire compartment. The compartment was divided into 9 vertical levels at the height of 0.0 m, 0.36 m, 0.6 m, 1.1 m, 1.6 m, 2.6 m, 3.6 m and 4.6 m. The difference in the setup between the levels is that the size of the center zone in the fire compartment is increasing with the height. To enable a counter flow through the door opening the fire compartment has to be subdivided so that there are at least be two levels of control volumes at this door elevation. To enable a more detailed flow simulation through the door four levels of control volumes have been used.

COCOSYS Code Results

Especially for Test 3 COCOSYS had some problems in simulating the correct temperature stratification. The plume temperatures as well as most of the other temperatures in the lower part of the fire compartment (level 1) are underestimated by 100 to 200 K but at higher elevations inside the fire compartment the temperatures are over-predicted by 50 - 100 K. After 950 s the temperature in the lowest COCOSYS zone is decreasing rapidly, even though the pyrolysis rate is at its peak. The reason is that all the O_2 in this zone is consumed in the combustion process and not enough air is transported to this control volume. This indicates that the provided pyrolysis rate does not fit to the simulated thermal conditions of COCOSYS. Comparing the temperatures in the material

probes of aerated concrete and concrete it can be observed that the temperature near the surface ($x = 0.02$ m) is under-predicted in the simulation. This can be easily explained with the significant under-prediction of gas temperature in the simulation in this region. The gas composition has been measured at the point GA1 in the fire compartment. In the simulation, the O_2 concentration is lower than in the experiment for the period 0-800 s. From 800 – 1000 s both values show a good agreement. After 1000 s, the O_2 concentration is nearly zero in the experiment, but in the simulation it is increasing again. These discrepancies can be explained by looking at the O_2 concentration over the fuel surface. The flame is extinguished in the lower part of fire compartment above the pan.

Due to the problem of the extinguishing flame, a parametric calculation with a modified pyrolysis rate has been performed. The aim of this calculation was to investigate if better results could be obtained if the pyrolysis rate was reduced in order to prevent the extinguishing of the flame. For the first 900 s the measured fuel weight seems to be realistic, thus the pyrolysis rate was not changed for this period. The measured temperatures show that the combustion process is nearly over after 1300 s. Hence, the pyrolysis rate has to be very small for this period. With the modified pyrolysis rate the temperature stratification is not satisfactorily predicted. At a lower elevation, the temperature is still under-predicted in the simulation and the temperature increase measured during the first 100 - 200 s is over-estimated.

The COCOSYS results of Test 1 are now summarized. The plume temperature increases earlier than in the experiment at the measurement points (M1-M6). In the experiment it took about 180 s until a fast temperature increase was measured, in the simulation this temperature increase is predicted at 100 s, and is less strong. After 200 s the temperature is over-predicted at all measurement points in the plume by 100 - 200 °C (M1-M6). Outside the plume, the characteristic of the results are similar to Test 3. At lower elevations the temperatures are under-estimated and at higher elevations the temperatures are over-estimated with deviations up to 200 K. In the simulation, the mixture of the gas is not simulated correctly. In the calculation, very little hot gas mixes with the cold gas at the lower elevations. It moves due to buoyancy upwards and gathers at the top of the room. It leaves the room via the FUCHS fan system or through the upper part of the door. The gas composition was measured at the point GA1 in the fire compartment. In the experiment, the O_2 concentration was significantly higher than in the simulation. Accordingly, the CO and the CO_2 concentrations predicted in the simu-

lation are too high. An explanation would be that the chemical reaction mechanism is not valid, or, which is more likely, there is a problem with the simulation of the mixing between hot and cold gas layer.

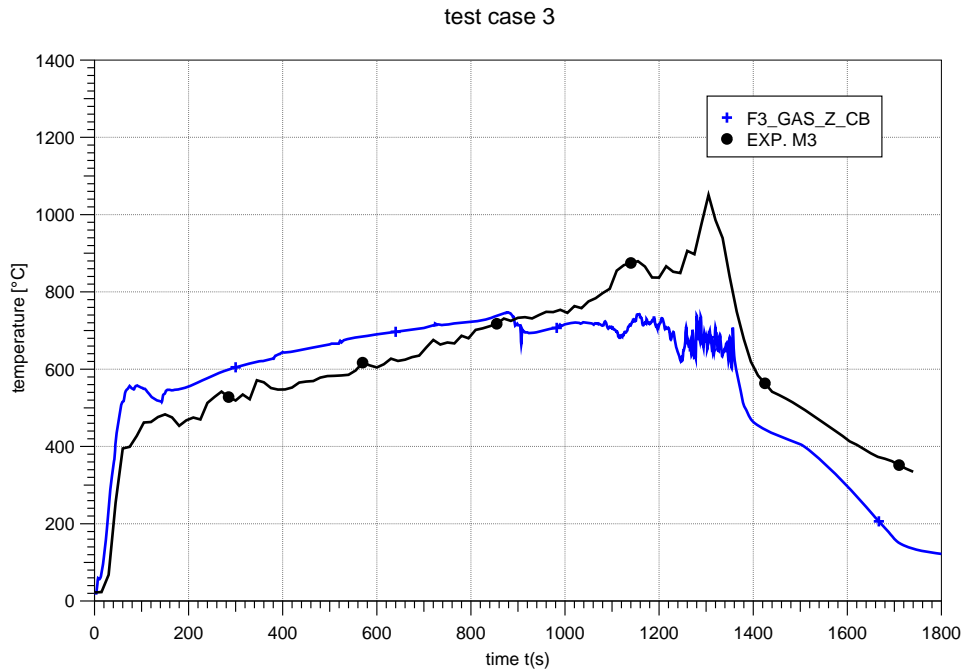


Fig. 5-21 Test 3: Plume temperature at M3 (from Appendix H)

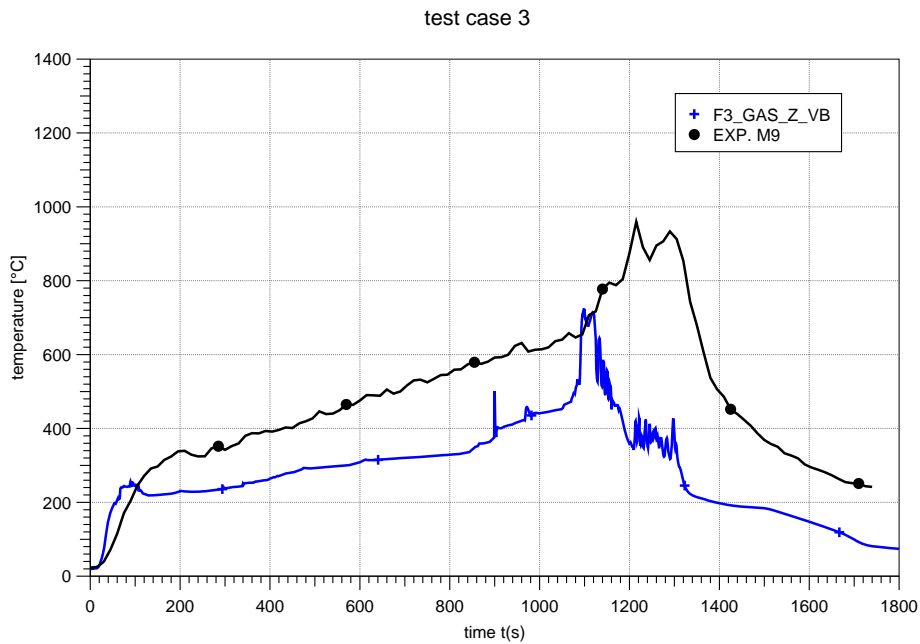


Fig. 5-22 Comparison of measured temperature M9 ($z = 1.5$ m) and COCOSYS results (from Appendix H)

5.3.6 VULCAN (CFD Code) Applied by V.F. Nicolette (SNL, USA)

The CFD code VULCAN has been used for open calculations of Test 3. However, the results have not been optimized to match the available experimental data.

VULCAN Code Description and Input Assumptions

VULCAN is derived from the Kameleon Fire code /HOL 90/. It models the transport and burning of vaporized fuel, as well as the transport of combustion by-products and their thermal impact on targets. Conservation equations are solved for mass, species, momentum, energy (enthalpy), turbulence quantities, and radiation intensity. Convective and radiative heat transfers to targets are included in the code, as well as the subsequent thermal response of the targets. VULCAN contains the following sub-models (algorithms):

- A fuel vaporization sub-model for the estimation of the rate, at which the fuel is transferred from the liquid phase (for liquid fuels) to the vapor phase.
- A k- ϵ turbulence model;
- Eddy Dissipation Concept (EDC) combustion model. Reactions are modeled as either 1-step or 2-step reactions, with irreversible, infinitely fast chemistry (relative to the mixing process);
- A soot generation and transport model;
- Discrete Transfer Method (DTM) of Shah and Lockwood is employed to solve the thermal radiation;
- VULCAN uses an extension of the SIMPLEC method of Patankar and Spalding, 1972, to solve the conservation equations using a control volume formulation. A structured three-dimensional Cartesian grid is used. First- and second-order accurate upwind schemes can be used for the convective terms.

A non-uniform grid of 38 x 55 x 46 (y direction is from the front door to the back of room) control volumes was used for the majority of simulations, and was developed based on previous modeling experience. Additionally, a refined mesh simulation was performed using 74 x 104 x 84 control volumes (essentially dividing the physical length of each control volume side by a factor of 2). This yielded a control volume length scale of order 0.07 – 0.15 m in the x and y directions. The control volumes in the z direction

were somewhat larger in the upper regions of the room, where gradients were expected to be small. The computational domain was taken as the fire compartment plus some reservoir space outside of the fire compartment.

For some simulations, the measured fuel evaporation rate was specified for the code. For other simulations, the fuel evaporation rate was calculated by the code based on the thermal response of the fuel. The chemical reaction was modeled as a two-step reaction with production of intermediate species. In the first step of the chemical reaction, the fuel is assumed to combust to form carbon monoxide and hydrogen. The second step of the reaction converts the intermediate species to water vapor and carbon dioxide.

VULCAN Code Results

A simulation was performed in which the experimentally measured mass loss rate was directly calculated based on the thermal response of the fuel pool (Fig. 5-23).

Oxygen depletion was observed to occur significantly sooner in the simulations than in the experiment. The agreement between simulation and experiment is best discussed when separated into 2 time periods: pre-oxygen depletion, and post-oxygen depletion of the room. Prior to oxygen depletion, very good agreement was obtained for the pool mass loss rate and the majority of heat fluxes to targets. The agreement was not as good for thermocouple temperatures, target thermal response, and doorway velocities. For times that are post-oxygen depletion, the agreement is generally not as good as for the pre-depletion period. This is understandable since the post-oxygen depletion environment is highly dependent upon the locations and amounts of leakage into the compartment. A fine mesh simulation produced essentially the same results as with the coarse mesh, suggesting the coarse mesh results were adequate. The inclusion of buoyancy generated turbulence in the simulations did not change the results substantially, but did improve the prediction of temperature low in the plume and the lower doorway velocity, while resulting in even faster oxygen consumption (relative to the standard $k-\epsilon$ model).

The sources of discrepancies between the predictions and data could not be definitively resolved due to uncertainties in the experiment and documentation. These discrepancies are believed to be primarily due to inputs to the code being significantly different than existed in the experiment. In that context, this experiment is not recom-

mended for code validation purposes, but does provide useful information regarding the potential uncertainties in code predictions when key inputs (e.g., leakage paths) are not accurately specified.

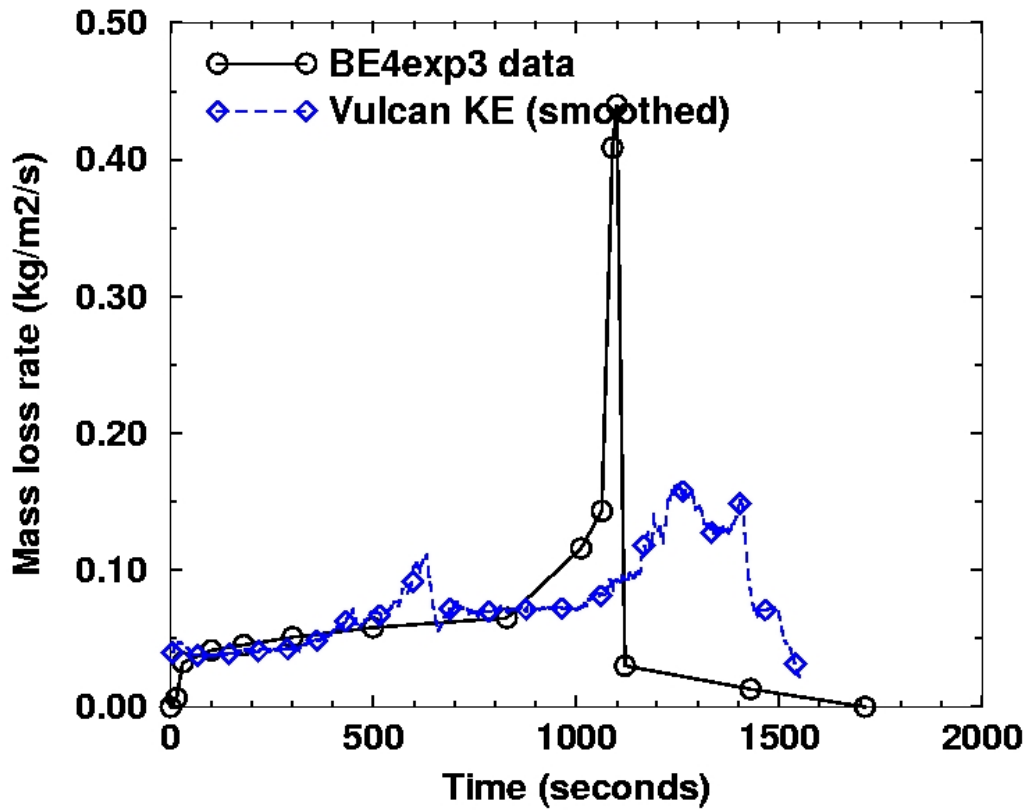


Fig. 5-23 Mass loss rate (smoothed) versus experiment (from Appendix I)

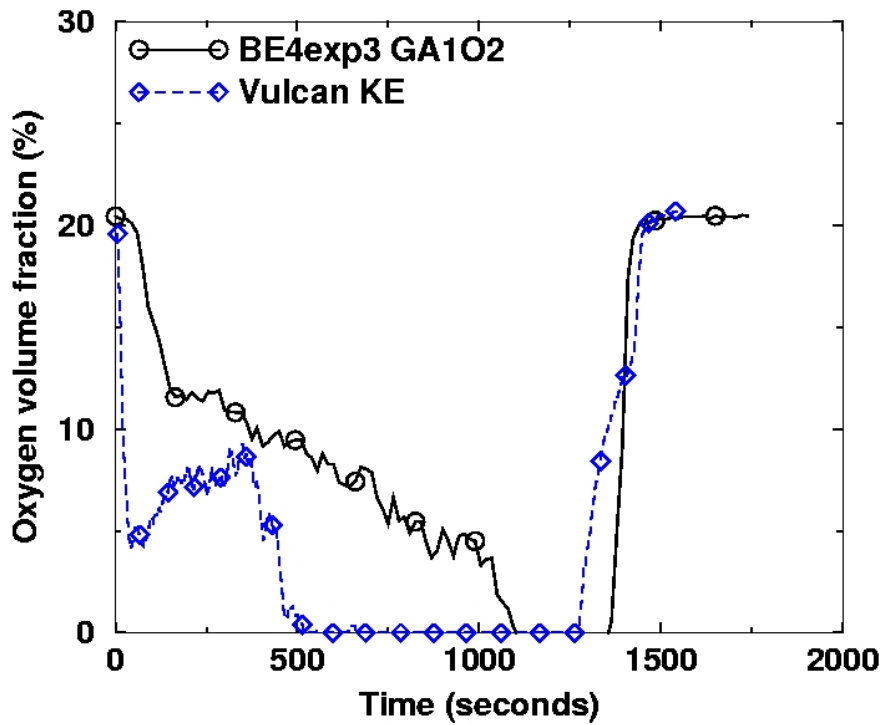
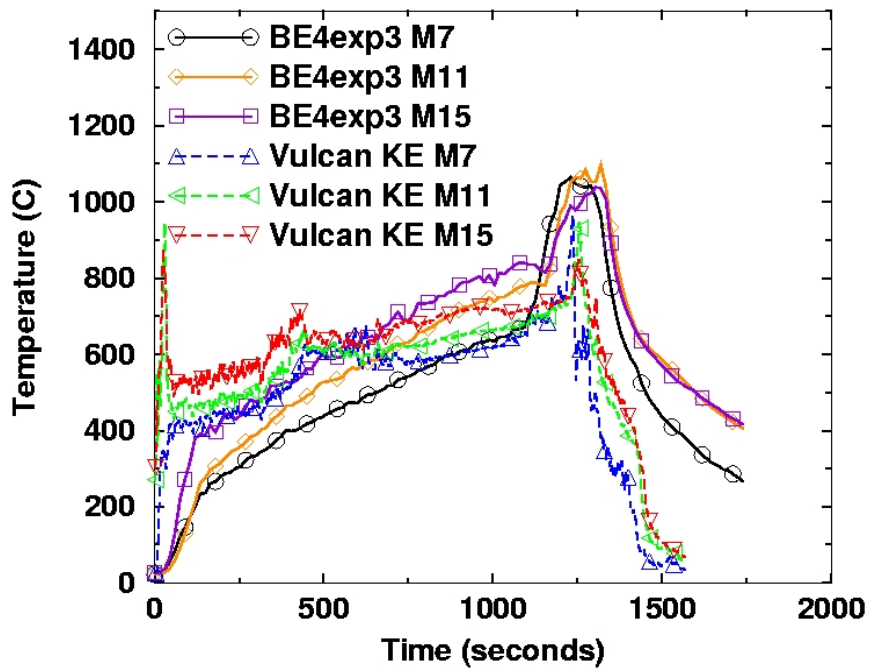


Fig. 5-24 Front room temperatures and oxygen concentration (from Appendix I)

5.3.7 MAGIC (zone code) Applied by B. Gautier (EDF, France)

The zone model MAGIC has been used for open calculations of Tests 1 and 3. Some additional parameter studies concerning the heat release and the effect of light concrete floor have been performed.

MAGIC code description and input assumptions

The calculations presented here were performed with MAGIC V4.1.1b /GAY 06/. The code is used in its standard version using input variables corresponding to a normal risk study approach. MAGIC uses a two-zone model including most of the classic features, like gaseous phase combustion, governed by the properties of emitted products and the air supply attributable to the plume flow, smoke production and transport of unburned products, heat exchange, natural flows and forced ventilation, simulation of targets and sprinkler systems.

The shape of fire compartment has been simplified, and has conserved the total volume. The distances between targets or openings and fuel surface are conserved. The hood in front of the door is not modeled. The ventilation has been simplified to one global exhaust vent at the ceiling. The lower oxygen limit is fixed to 0 % which is the EDF recommended value. The radiation fraction is set to 0.35.

MAGIC code results

MAGIC results appear more realistic in Test 1 (open door) than in Test 3 (semi-closed door). In Test 1 the gas temperature are realistic while target temperature and flux are significantly over-estimated. In Test 3 gas layer temperature is little under-estimated, while the target predictions are in good agreement.

In Test 3, the configuration induces more complex phenomena: the reduction of the opening cross section produces under-ventilated conditions. It seems that the flame was inclined to the door in the experiment. These phenomena are not represented in MAGIC.

Some experimental data appears to be questionable, especially the HRR in Test 3 and the interface height (due to the low number of thermocouples used in the interface height calculation).

More information on the vent system would have allowed it to be modelled and permitted a more realistic "fire risk study" type of approach to the test. Especially in Test 3, the ventilation due to the vent is comparable to the one due to the door (in calculation and probably also in the actual test). It seems that the door flow is under estimated in the calculation, maybe due to the hood effect.

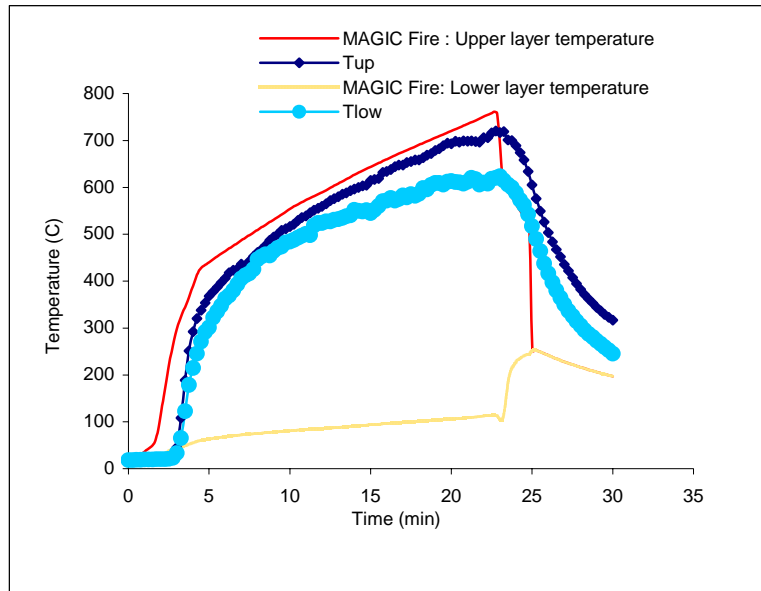


Fig. 5-25 Upper and lower temperature in Test 1 (from Appendix J)

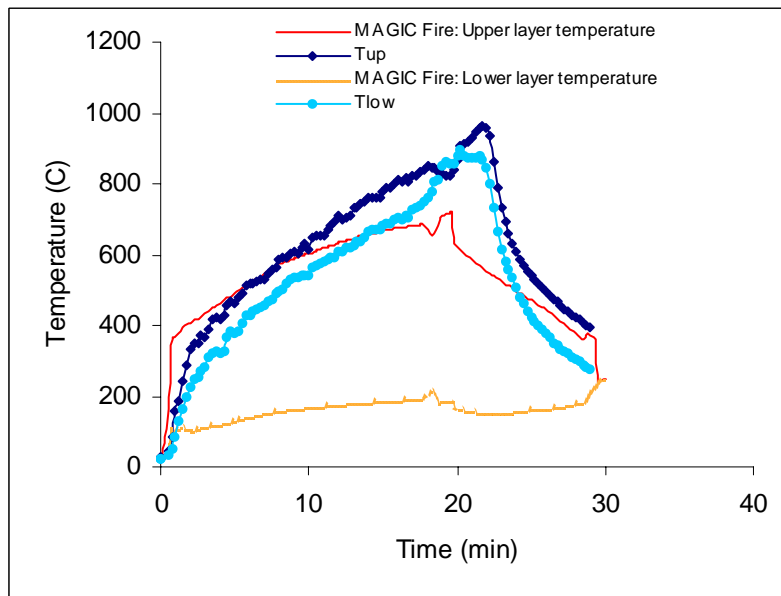


Fig. 5-26 Upper and lower temperature in Test 3 (from Appendix J)

6 Code to Code Comparison

In this chapter the results of the different codes and types of codes are compared to each other. It is clear that the results of simulation tools depend on the quality and capabilities of the models themselves as well as on the experience of the users. Furthermore, it is obvious that this comparison is specific to the Benchmark Exercise considered, with partly oxygen depleted conditions and a relative strong fire.

The objective of this chapter is to look at the overall results of fire simulation tools for:

- characterization of deviations from the experimental results to give some indications on uncertainties, particularly for PSA studies;
- identification of minimum and maximum values of code results;
- characterization of user effects as well as differences between blind and open calculations;
- characterization of potential uncertainties of the experiment itself and the experimental results.

Due to the limited number of participants and calculations it is quite difficult to identify the real causes of deviations of the calculated values from the experimental measurements. Nevertheless, this Benchmark Exercise does give some view on the possible uncertainties of fire simulations.

6.1 Test 1

6.1.1 Plume Temperatures (M1 to M6)

Fig. 6-1 and Fig. 6-2 compare the results for blind and open calculations of the plume temperatures at positions M2 and M6. In comparison to the blind simulations, the results of the semi-blind FDS calculations are much better, having used the pre-defined pyrolysis rate. Larger deviations between semi-blind FDS simulations occur for temperatures closer to the fire surface (like M2). It seems that the user has to be careful to get good results at positions close to the fuel surface. The blind simulations of JASMINE also show an underestimation of the temperatures. This underestimation was not so significant in the semi-blind simulations of JASMINE. The open COCOSYS

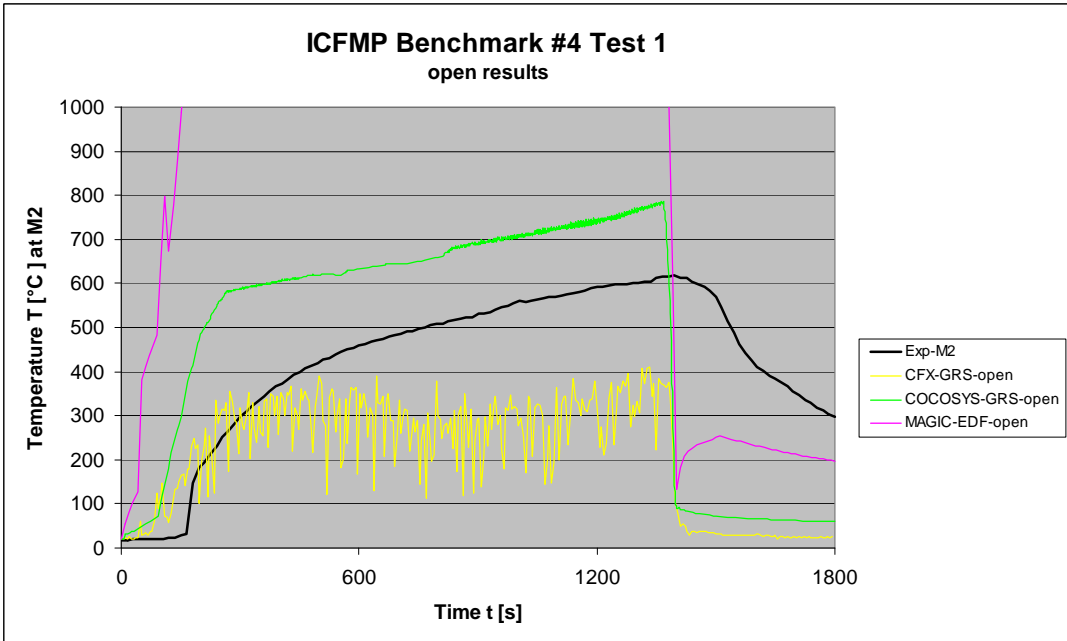
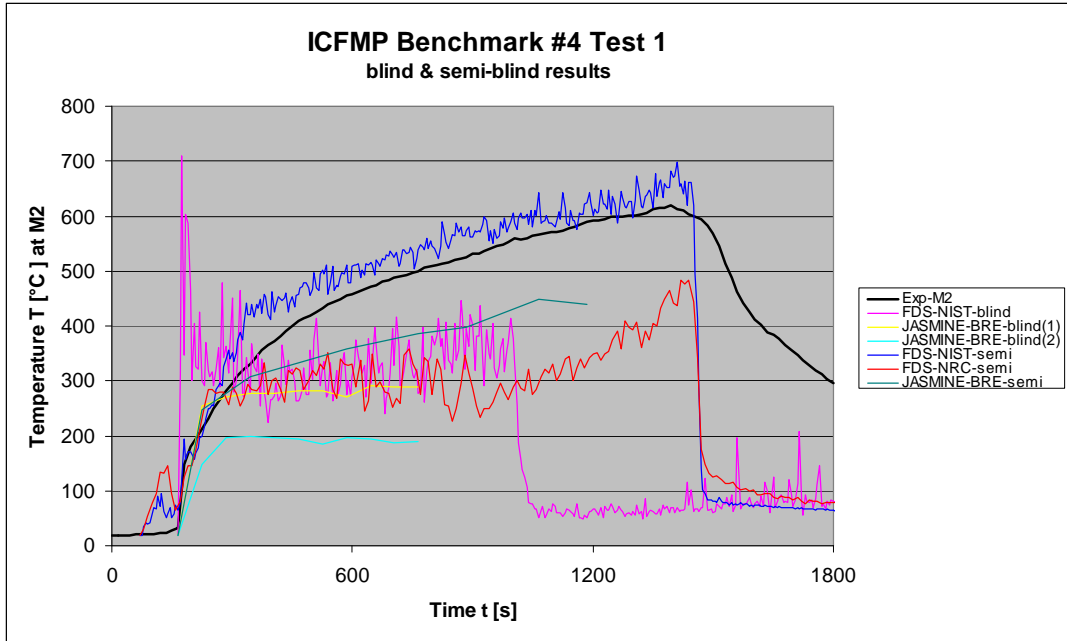


Fig. 6-1 Comparison of plume temperatures M2 (blind & open)

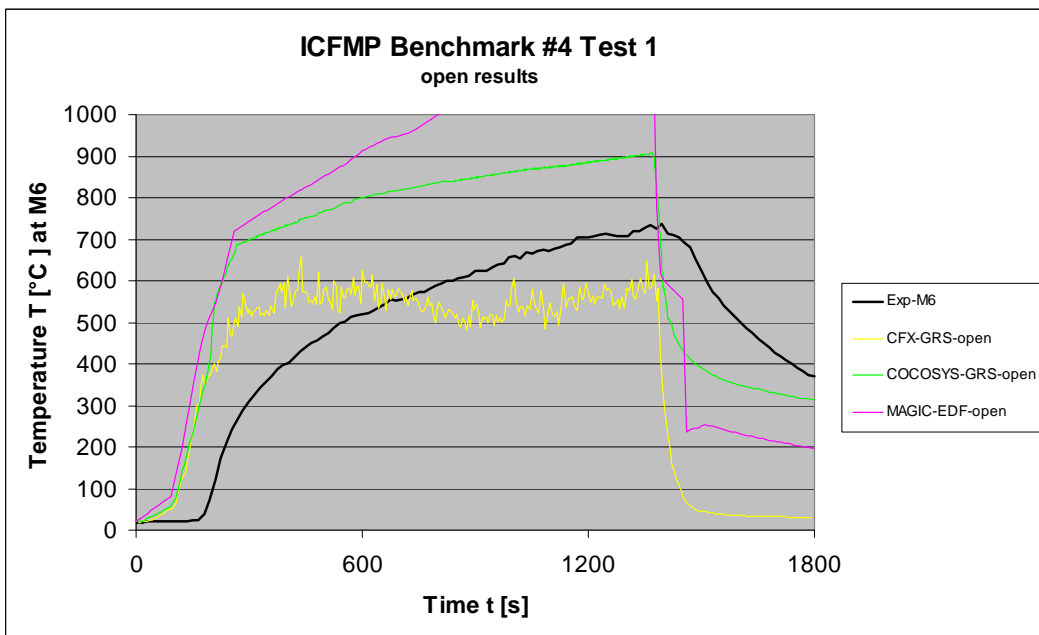
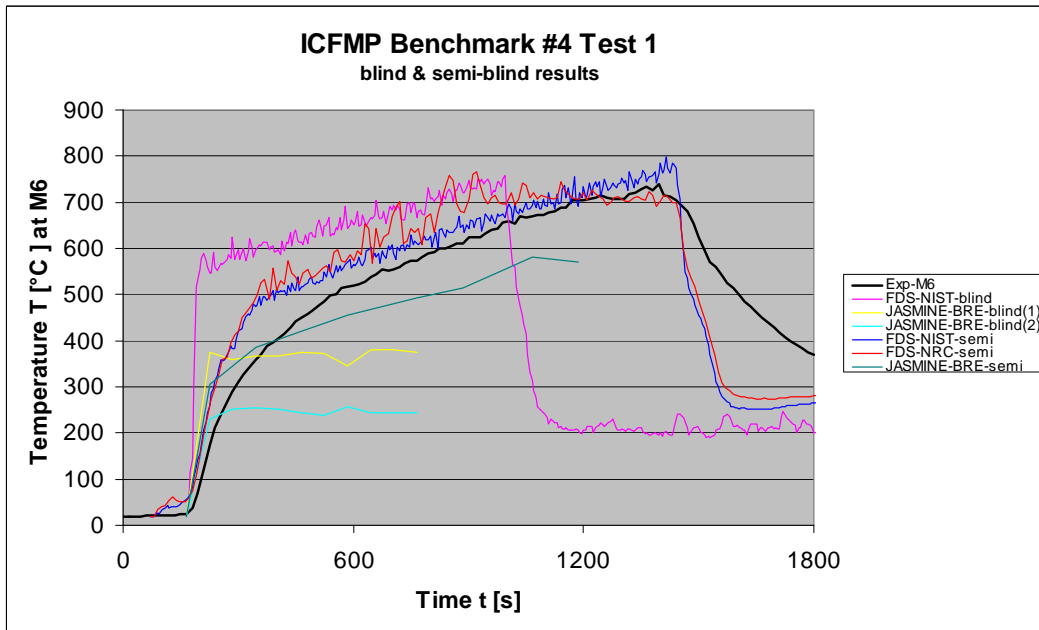


Fig. 6-2 Comparison of plume temperatures M6 (blind & open)

6.1.2 Temperatures inside the Fire Compartment

Fig. 6-3 to Fig. 6-8 present the comparison of the temperatures at the temperature thermocouple tree locations at the front and rear of the fire compartment. The differences between front and back are not very large, indicating that a shift of the fire plume

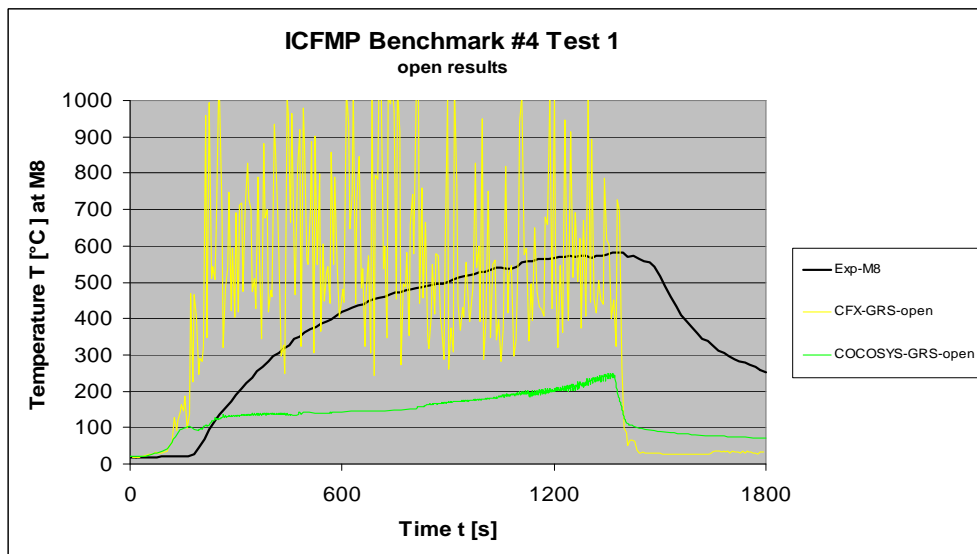
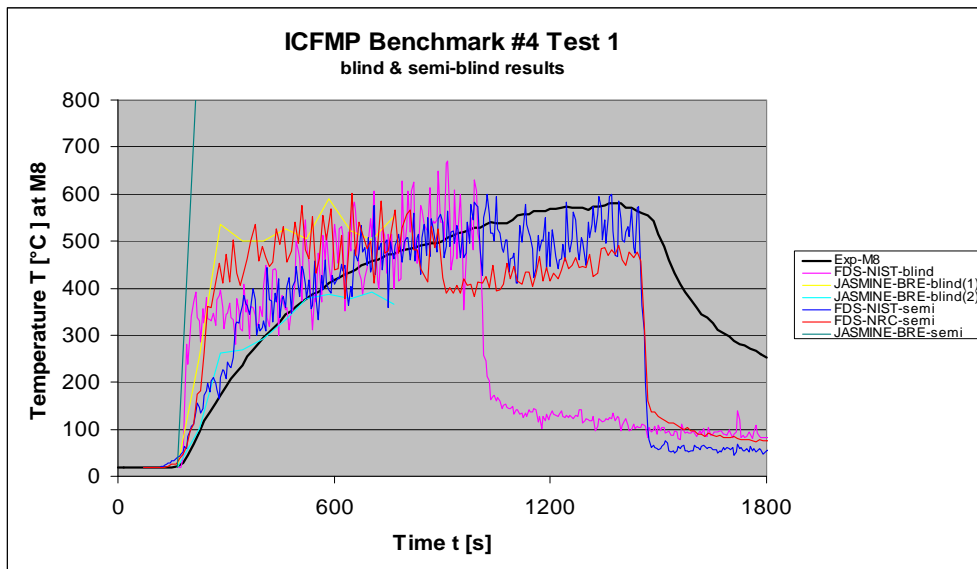


Fig. 6-3 Temperatures on the back side of the compartment (M8, blind & open)

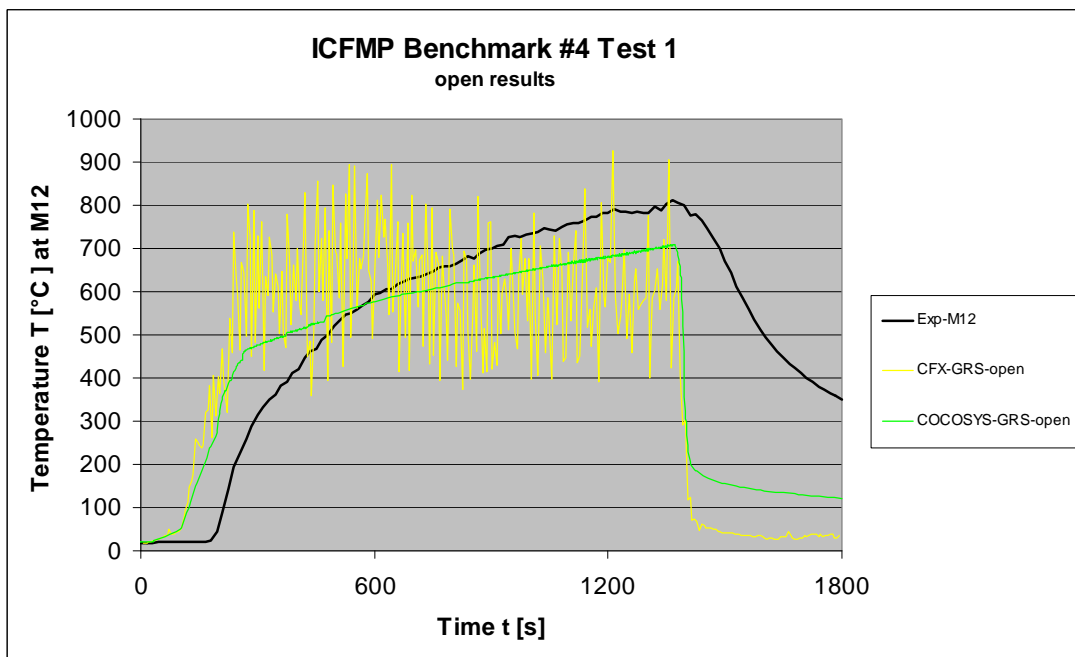
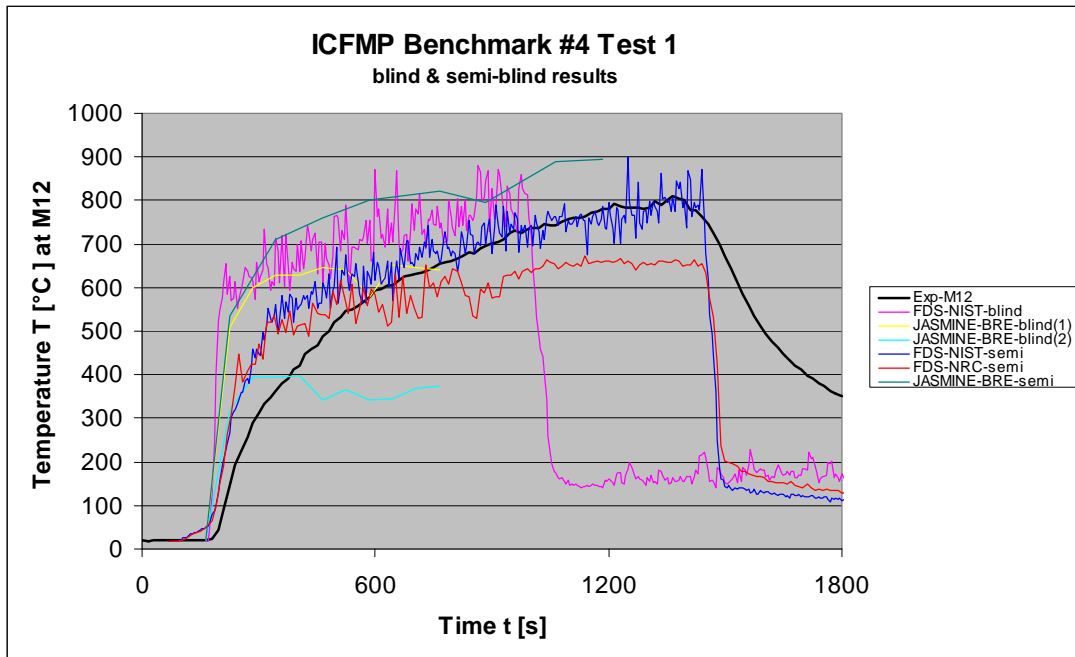


Fig. 6-4 Temperatures on the back side of the compartment (M12, blind & open)

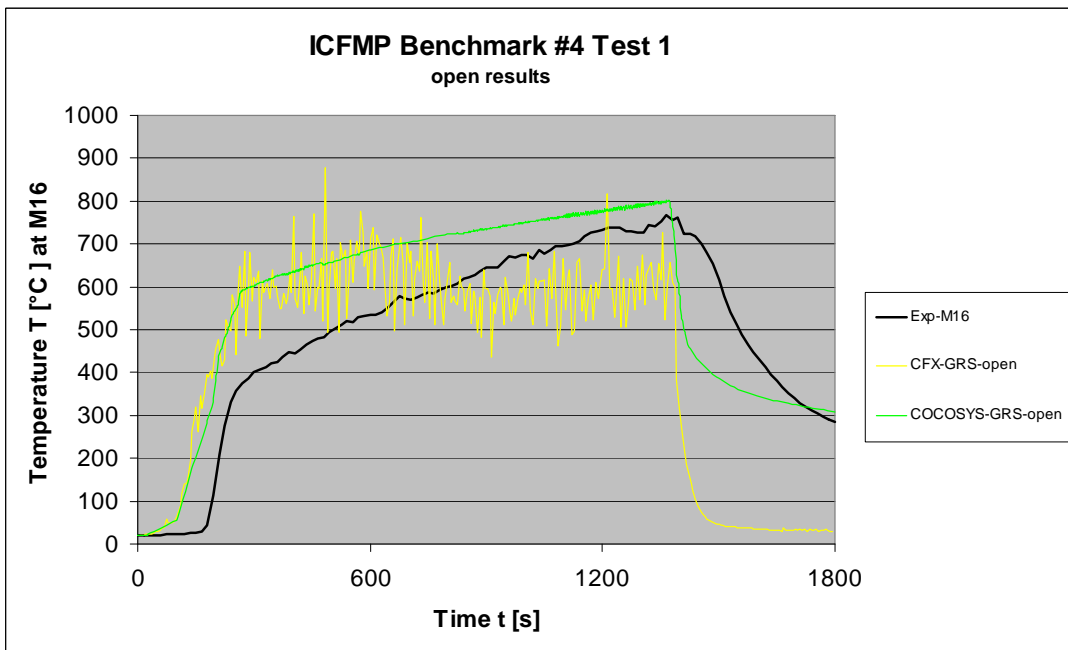
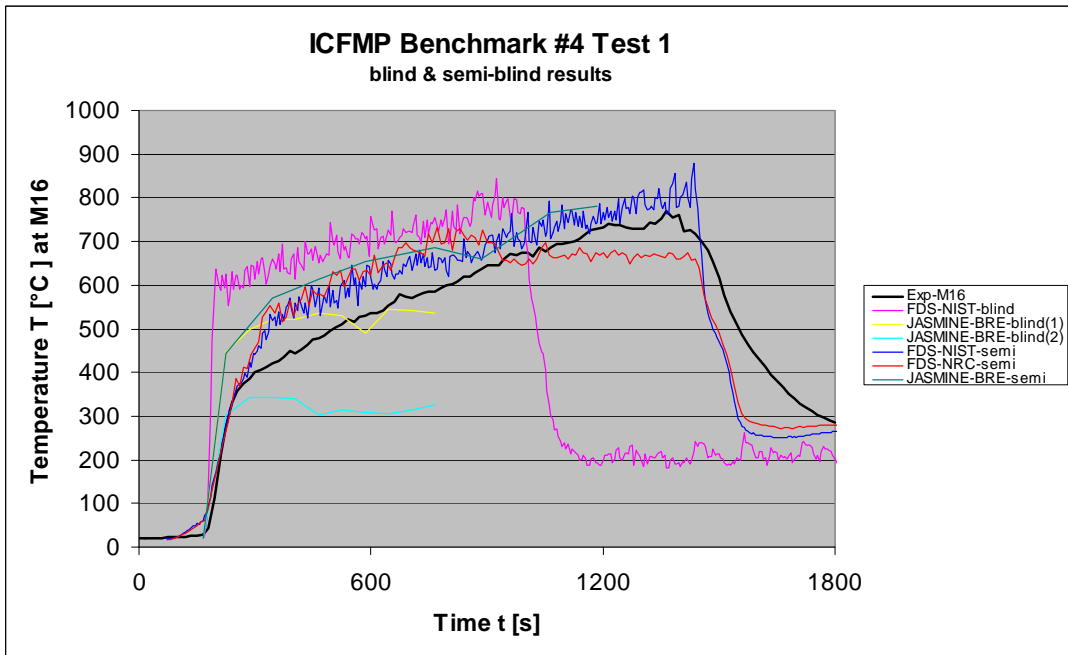


Fig. 6-5 Temperatures on the back side of the compartment (M16, blind & open)

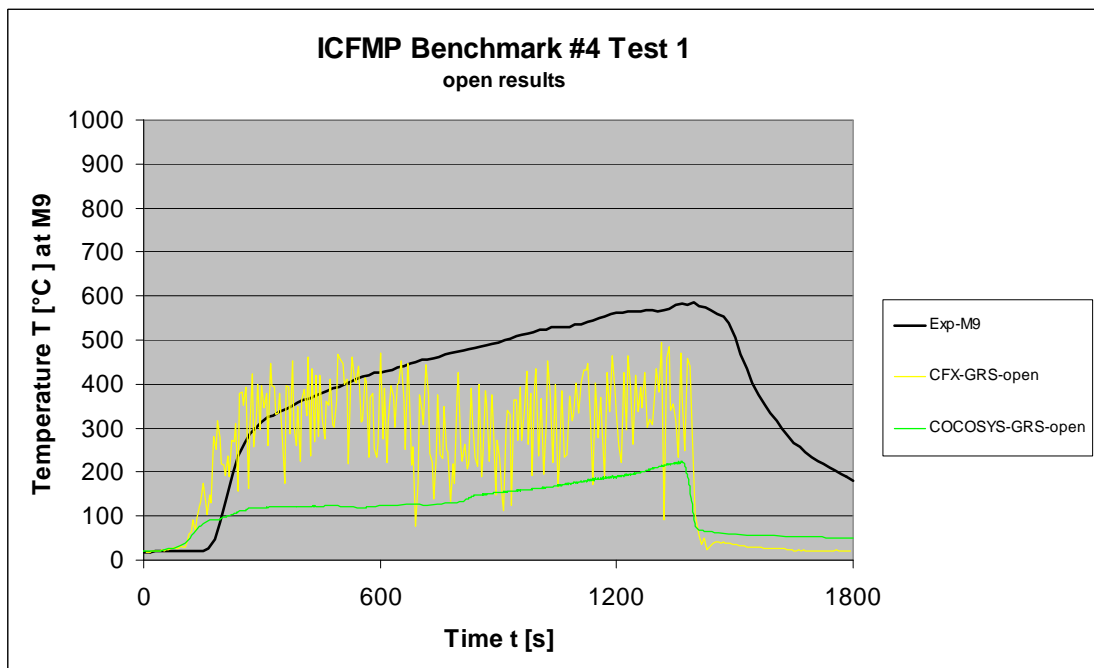
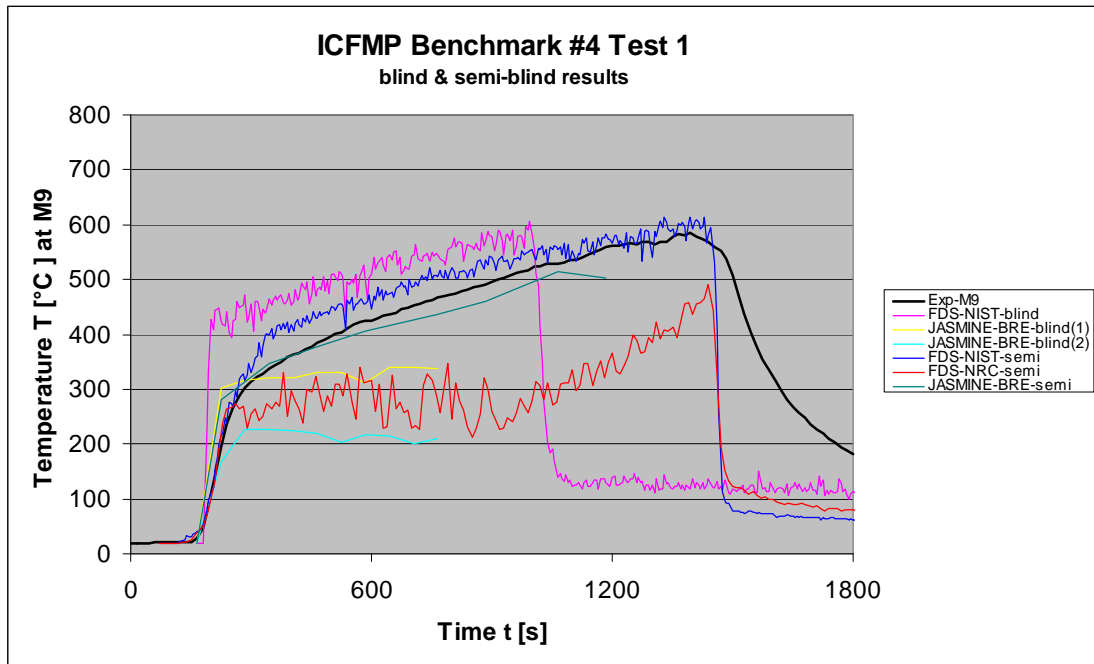


Fig. 6-6 Temperatures on the front side of the compartment (M9, blind & open)

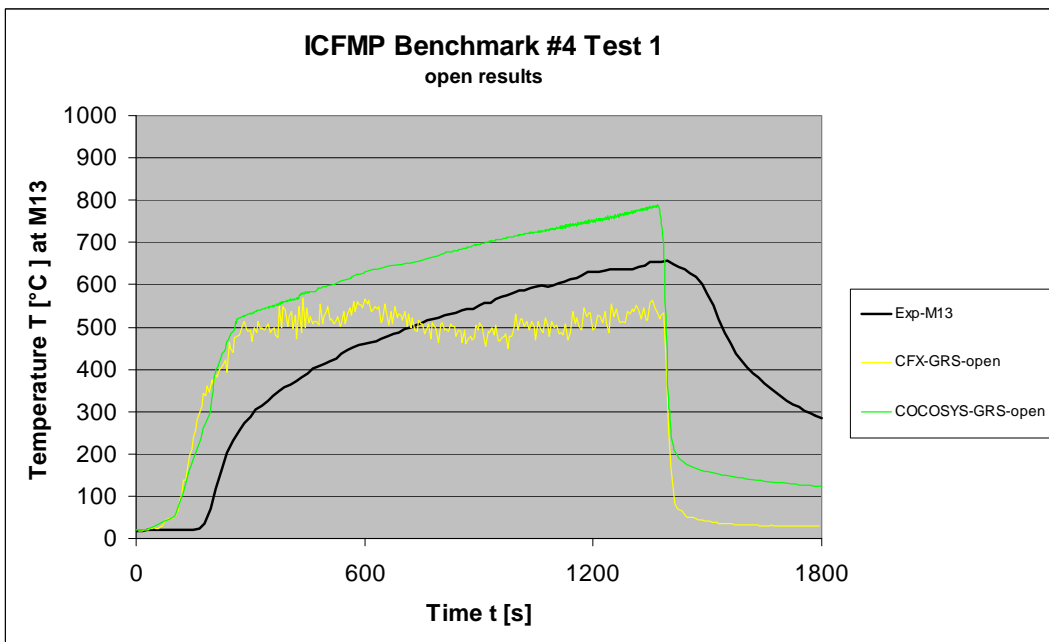
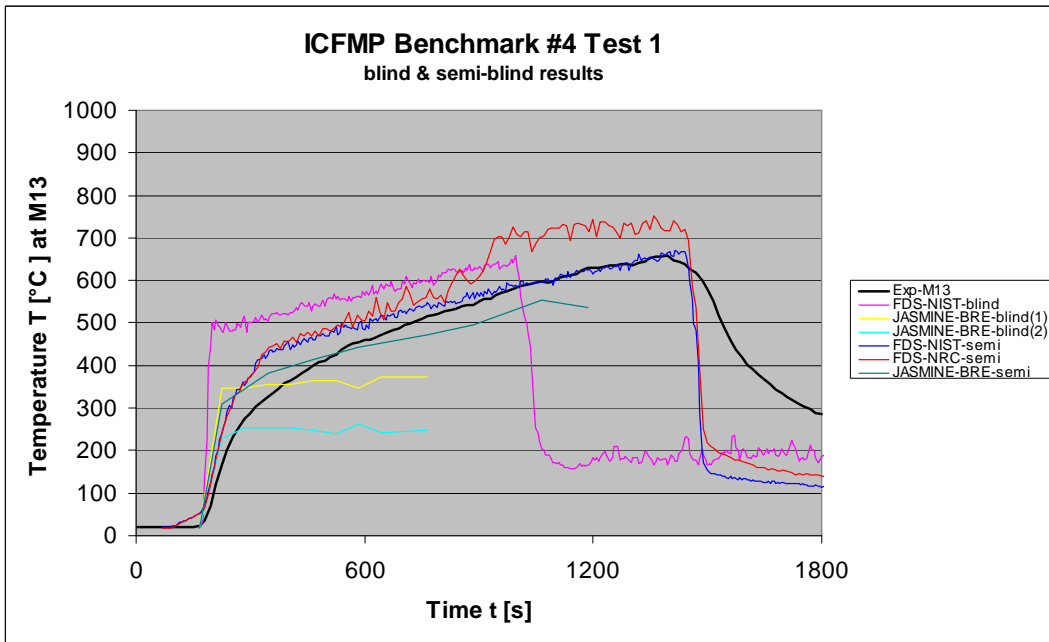


Fig. 6-7 Temperatures on the front side of the compartment (M13, blind & open)

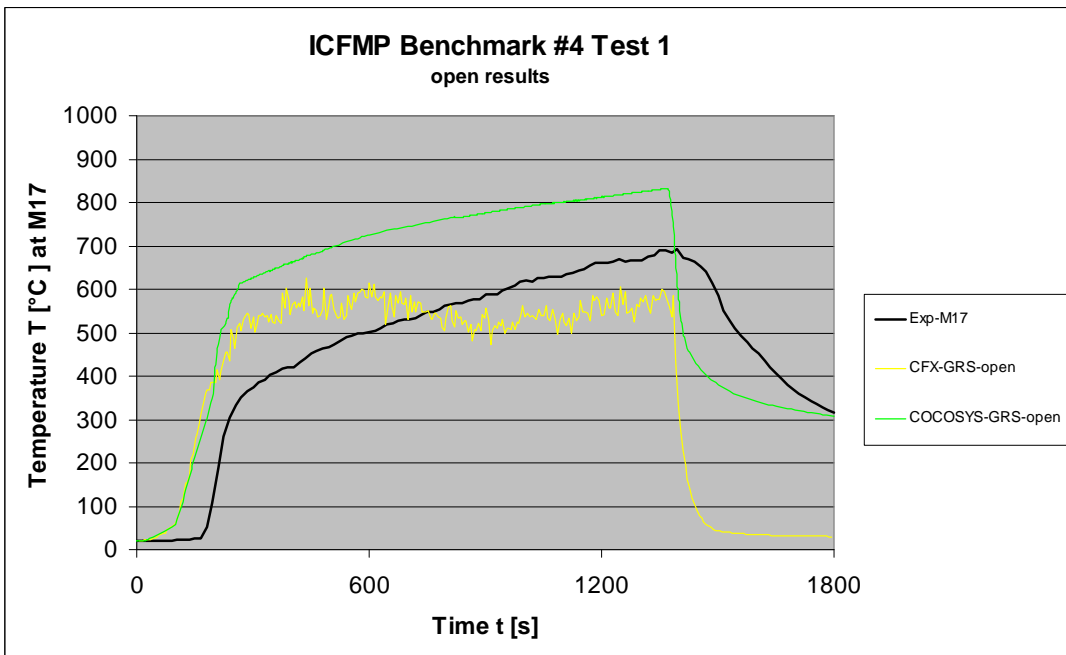
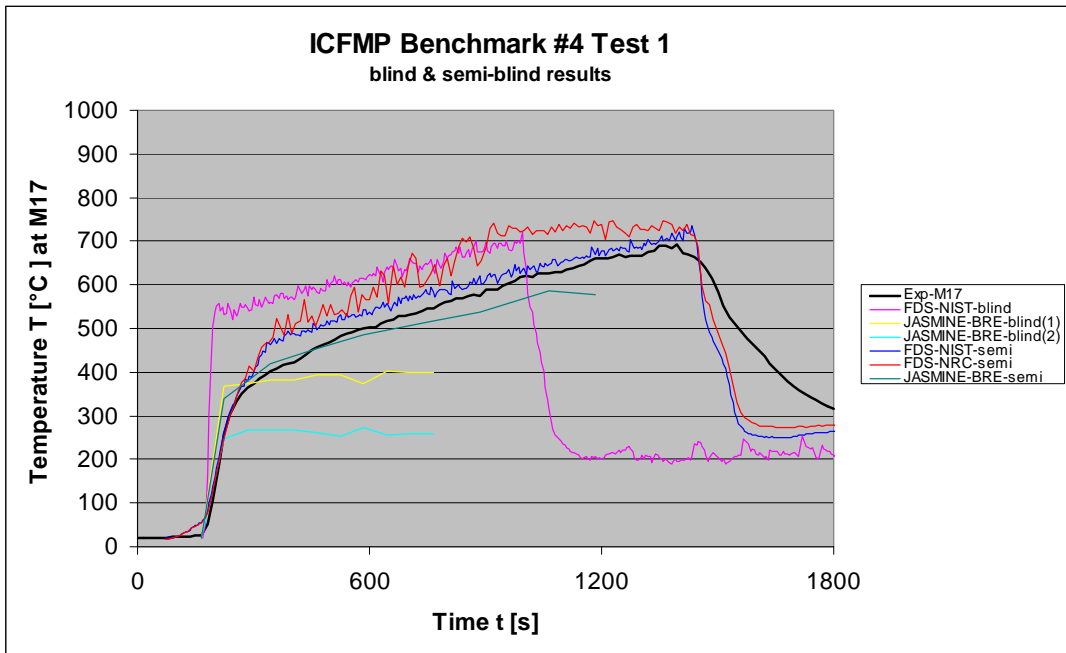


Fig. 6-8 Temperatures on the front side of the compartment (M17, blind & open)

6.1.3 Layer Height and Upper Layer Temperature

Fig. 6-9 and Fig. 6-10 present the hot gas layer height and upper layer temperature. It has to be mentioned in this context, that due to the low number of elevations of measurement positions the calculation of a layer height is not really possible. Therefore, only the general characteristics should be compared. The results of the different codes and code types for the upper layer temperature are reasonably good. The different semi-blind calculations with CFAST show a wide range of about 300 K for the upper layer temperature.

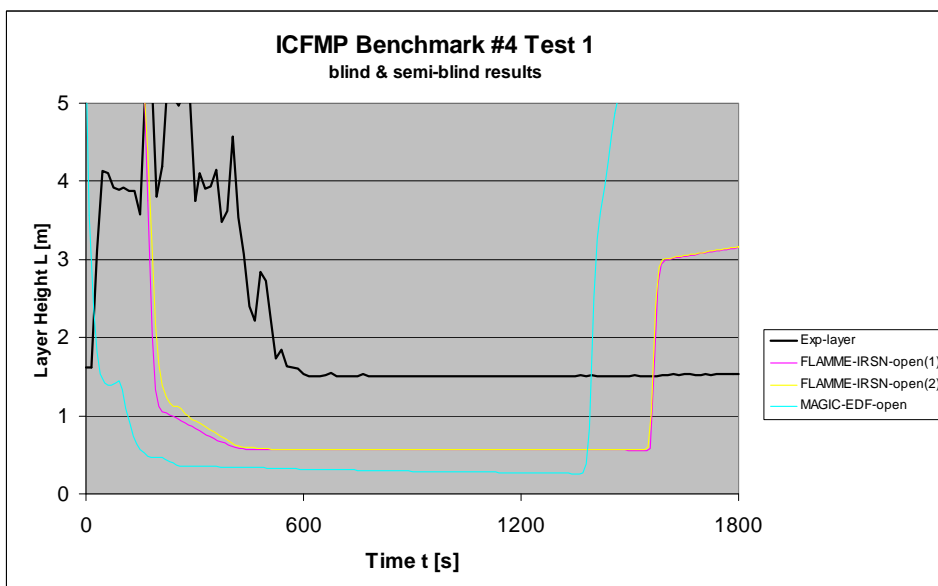
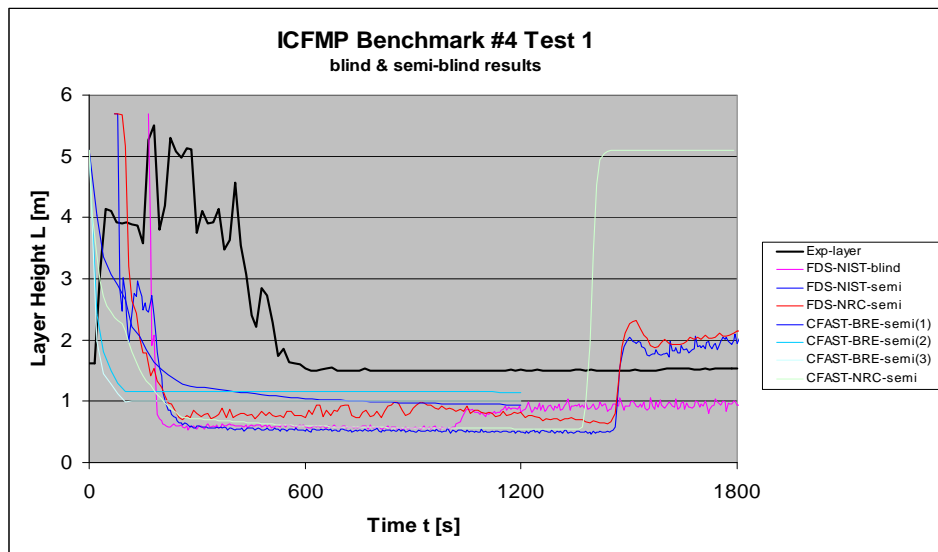


Fig. 6-9 Layer height (blind & open)

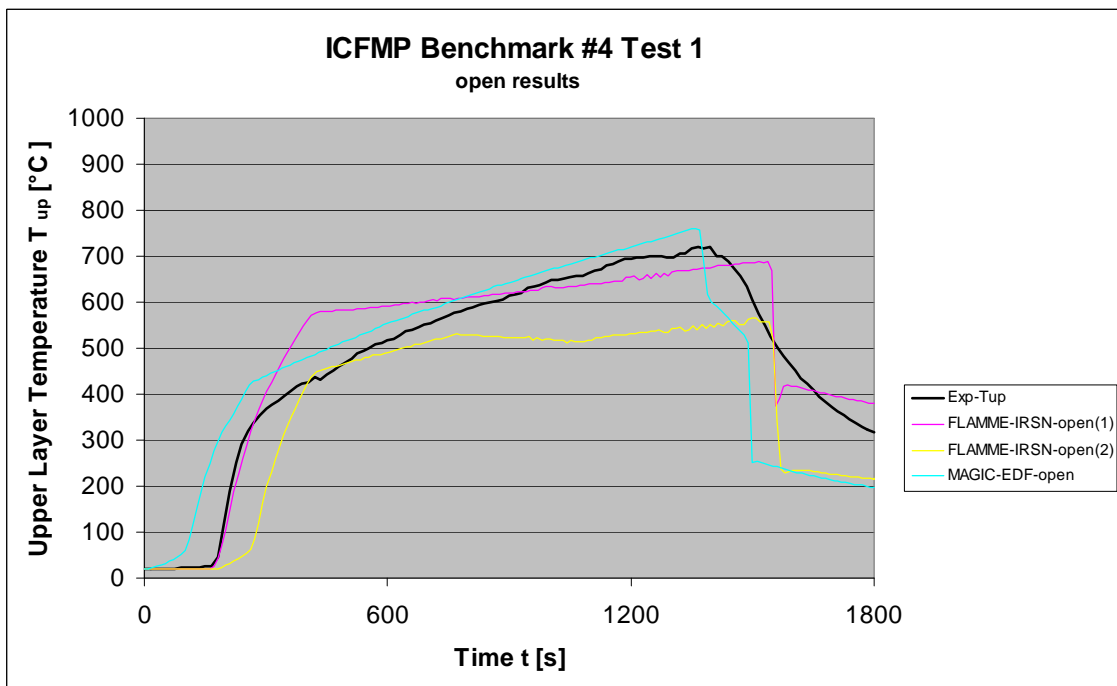
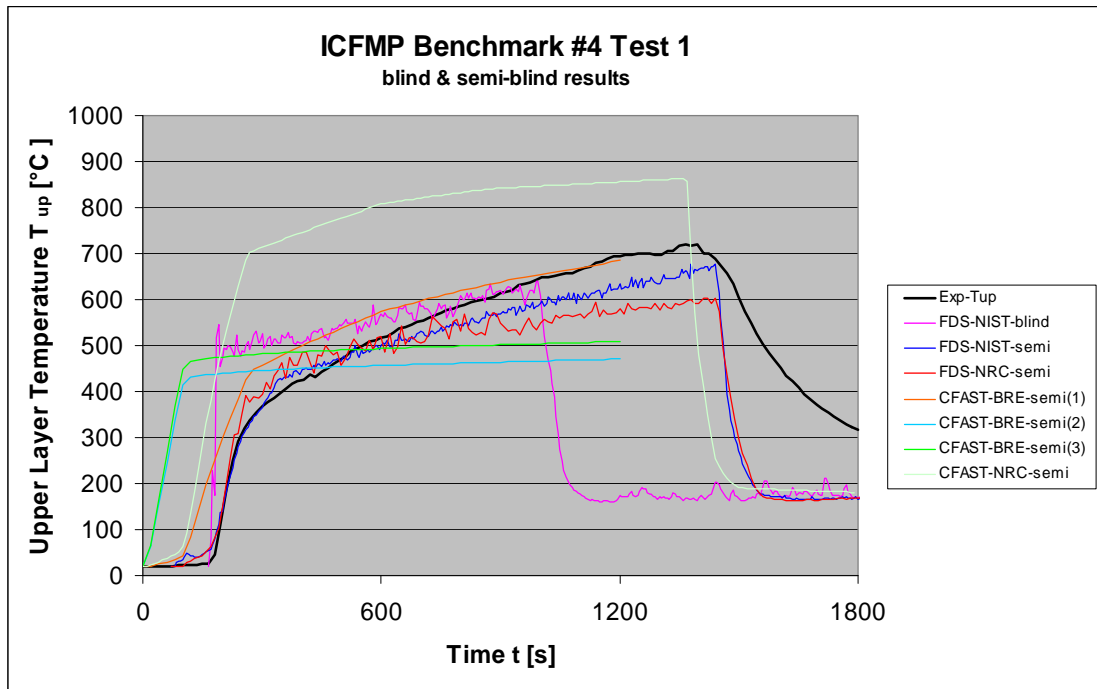


Fig. 6-10 Upper layer temperature (blind & open)

6.1.4 Gas Concentration inside the Fire Compartment

The main difference between Test 1 and Test 3 is the ventilation condition leading to oxygen rich conditions for Test 1. Fig. 6-11 to Fig. 6-14 show the comparison for the gas concentrations of O₂ and CO₂ inside and outside the fire compartment. All codes except CFX underestimate the oxygen concentration inside the fire compartment. Since the experimental values at the measurement position GA1 are quite constant in contradiction to the values at the position GA2, the measurement at GA1 seems to be somewhat questionable. The results of the semi-blind FDS calculation performed by NIST outside the fire compartment are very good. In addition, the measured CO₂ concentration at GA1 does not seem to be reasonable. The value is lower compared to the value at the position GA2.

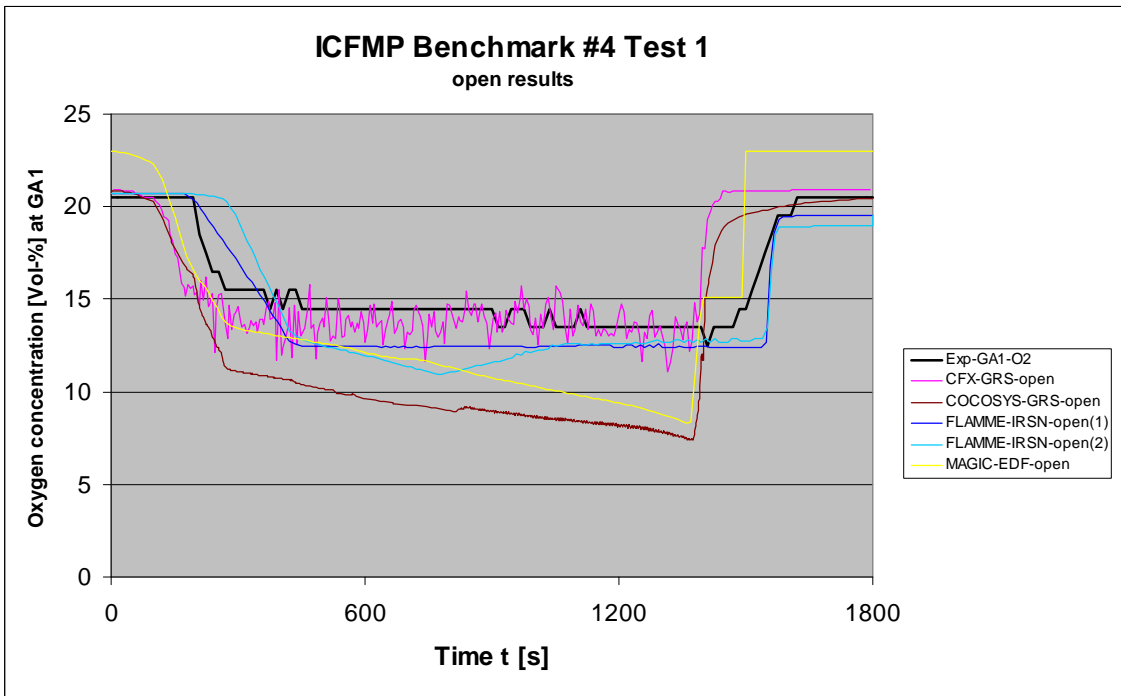
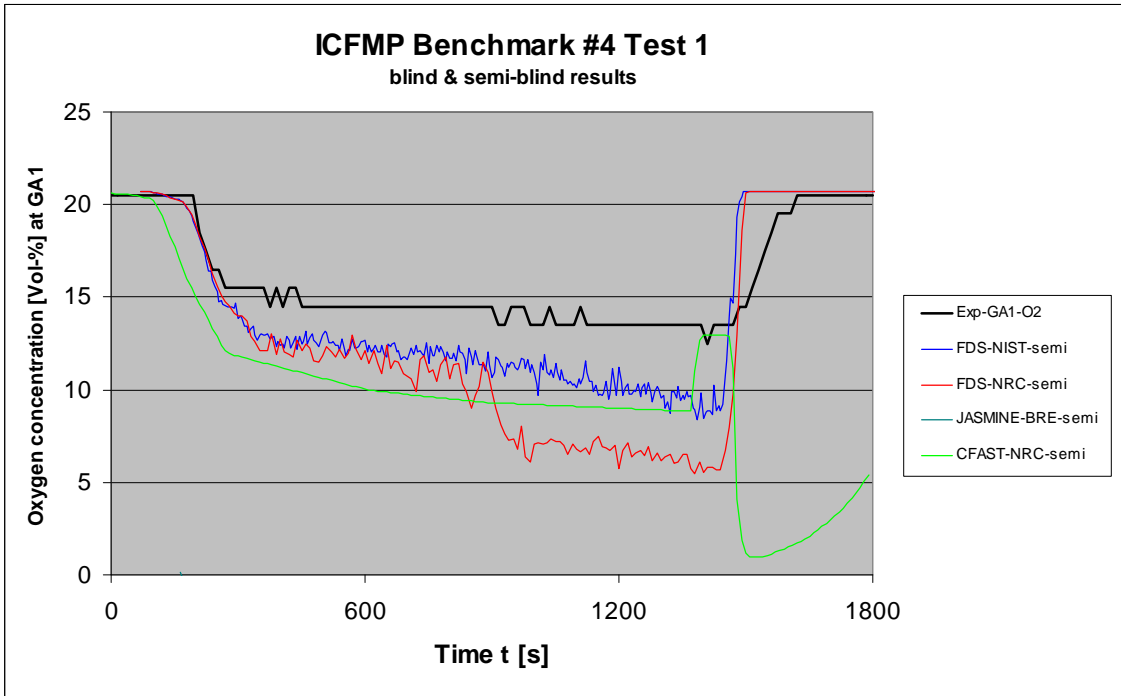


Fig. 6-11 Oxygen concentrations inside the fire compartment (blind & open)

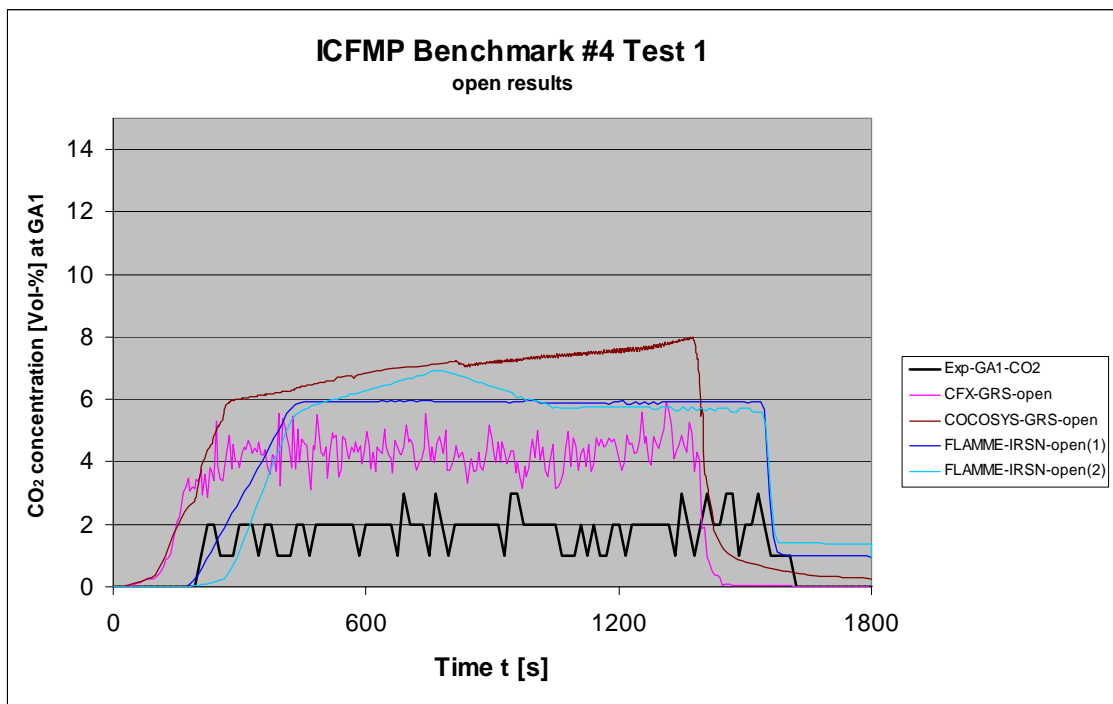
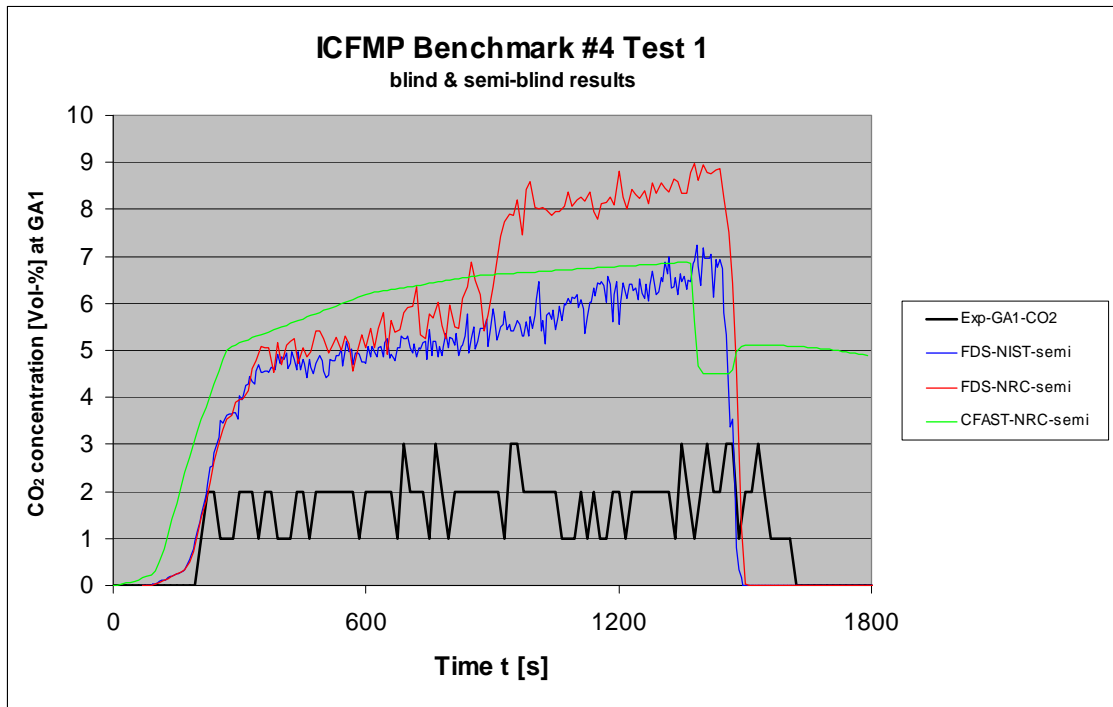


Fig. 6-12 CO₂ concentrations inside the fire compartment

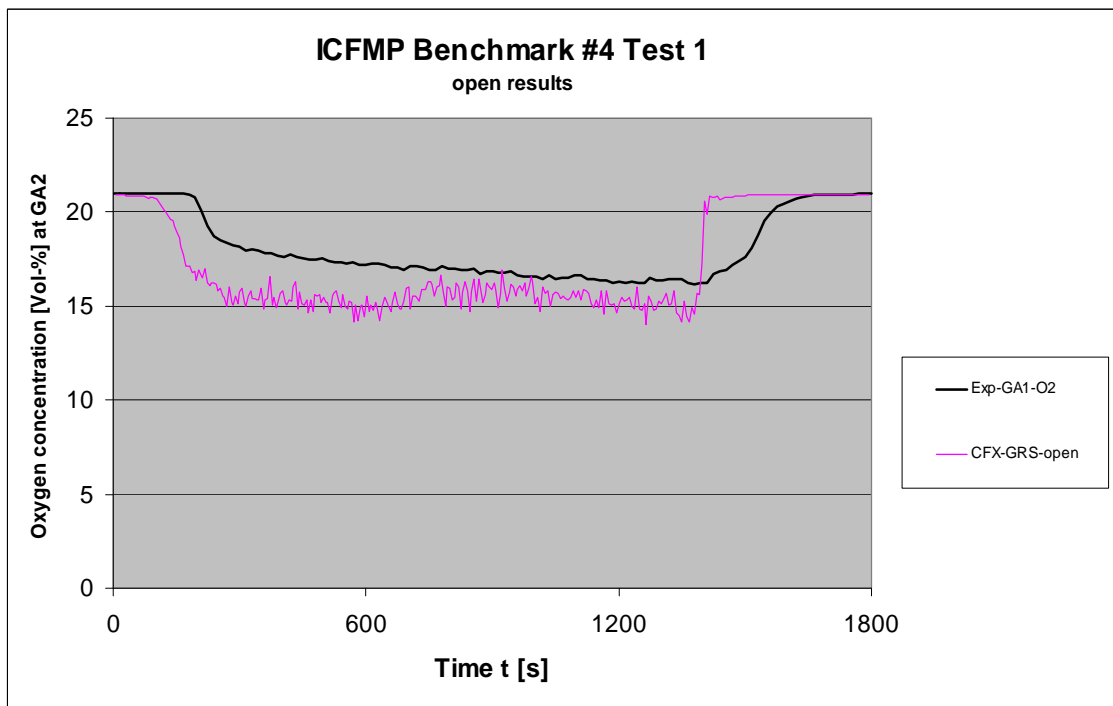
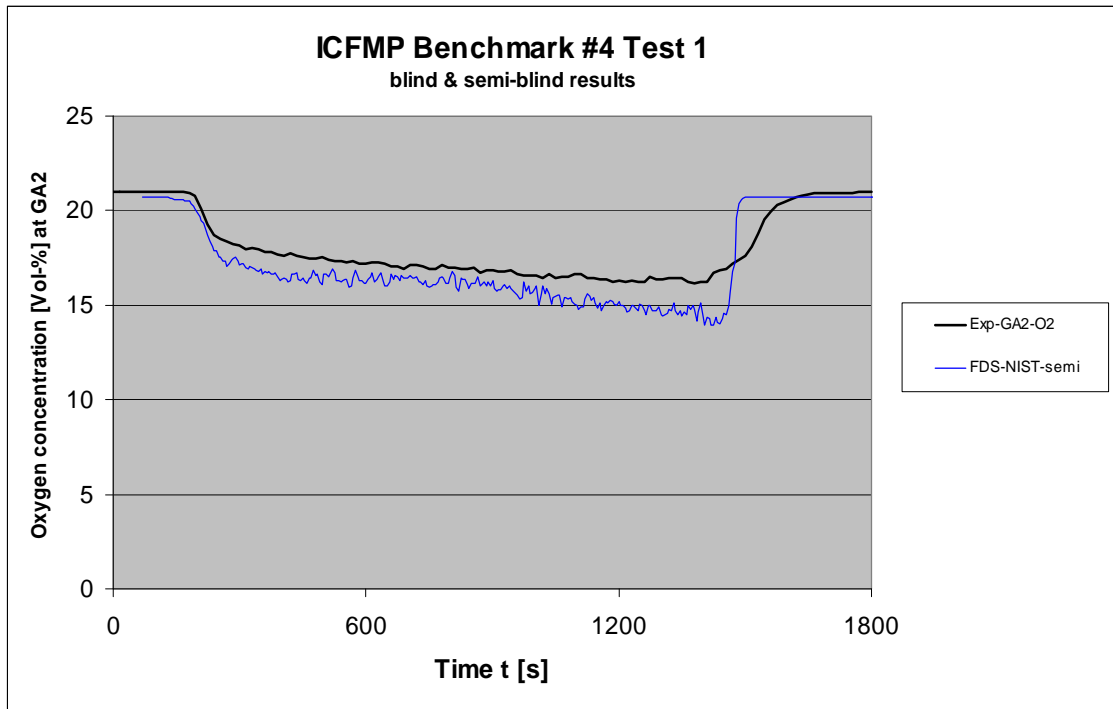


Fig. 6-13 Oxygen concentration outside the fire compartment (blind & open)

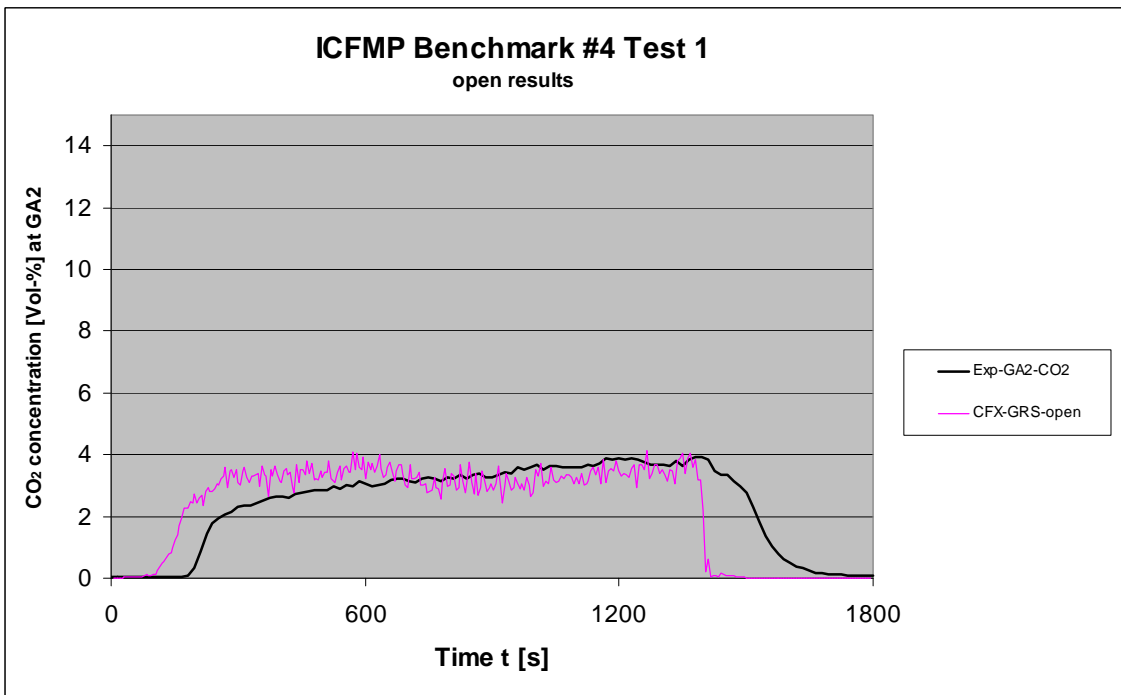
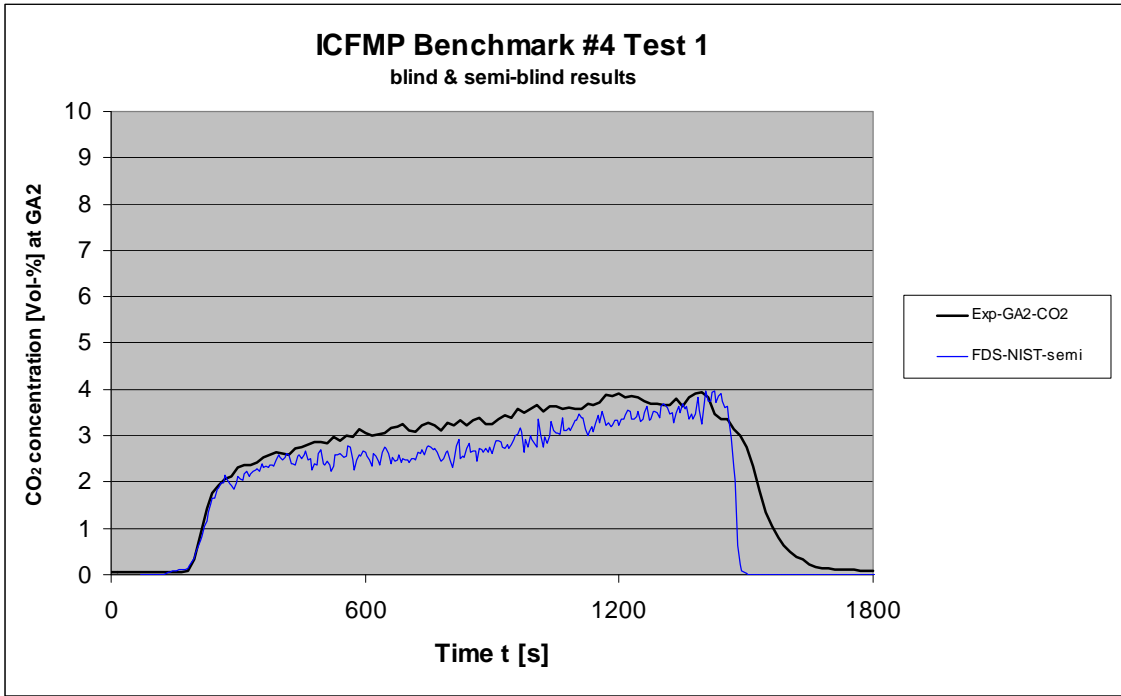


Fig. 6-14 CO₂ concentration outside the fire compartment

6.1.5 Probe Temperatures

The results of the probe temperature measurements have been delivered for the semi-blind and blind calculations only. The simulation results of CFAST performed by NIST show an unstable behaviour for aerated concrete. The calculated surface temperatures for concrete and steel are much too high. Most of the other CFAST calculations overestimate the surface temperatures. The results of the blind JASMINE simulations are too low. FDS overestimates the temperatures at least approx. 100 K in the semi-blind simulations. For the open calculations probe temperature results have been delivered for MAGIC only. The calculated target temperatures are generally higher than measurements.

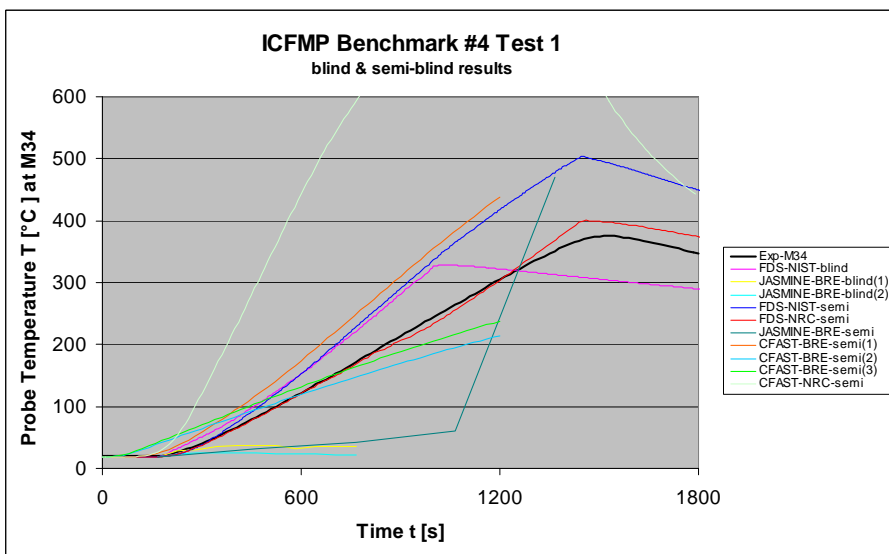
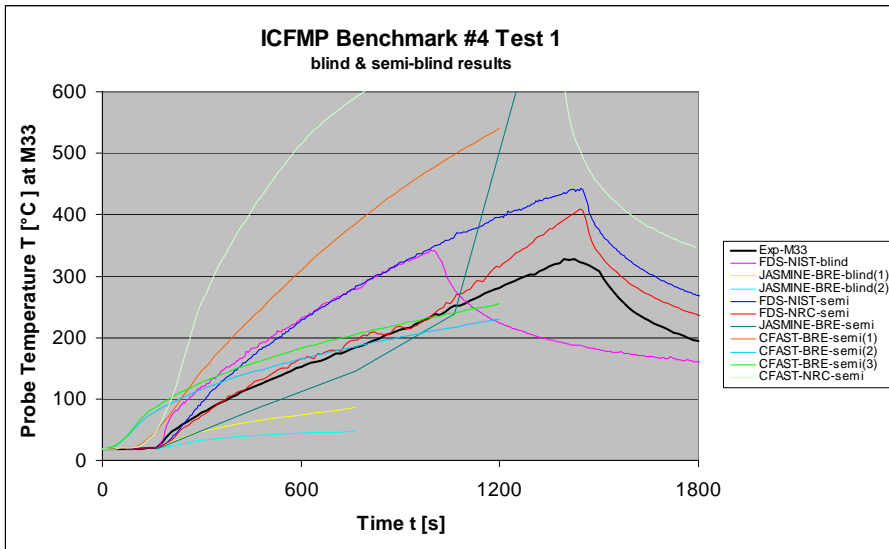
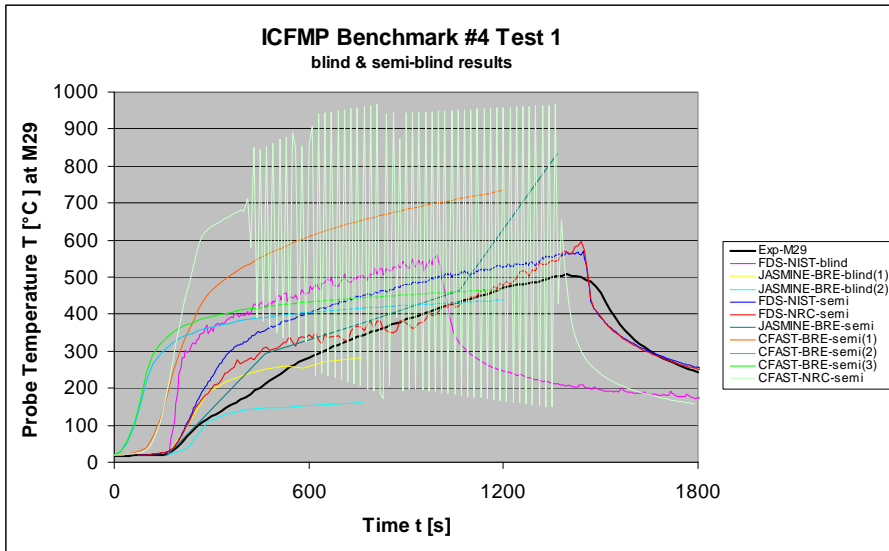


Fig. 6-15 Probe temperatures (blind results)

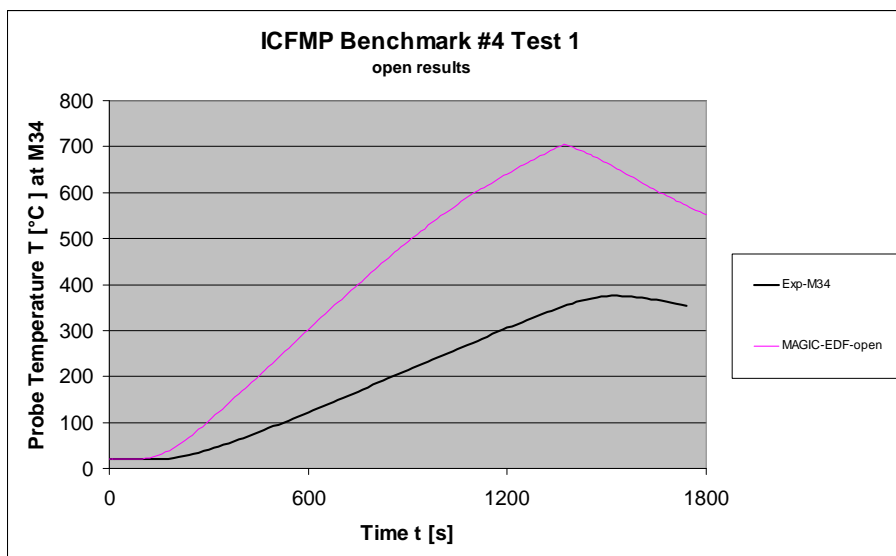
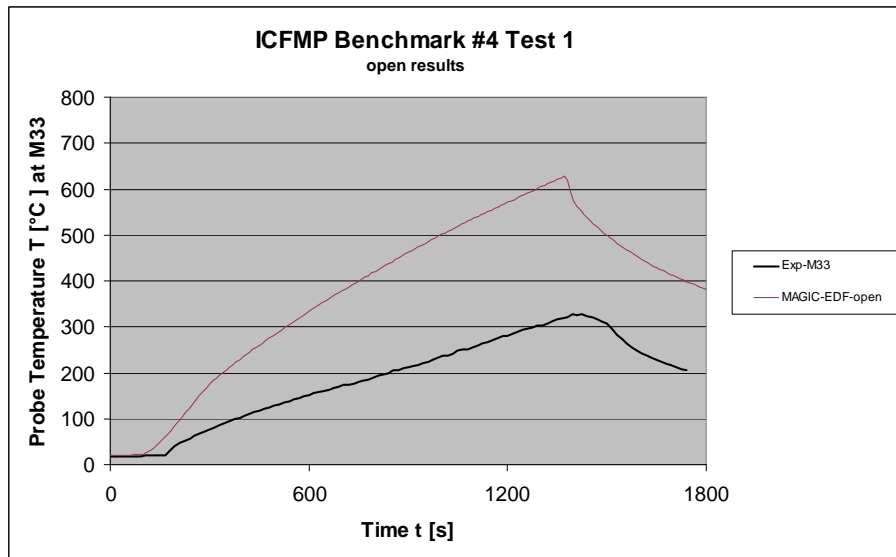
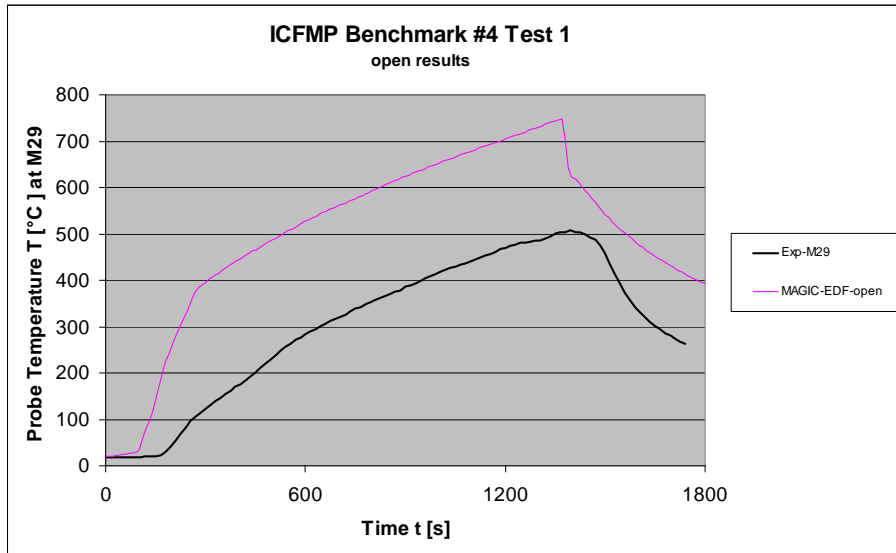


Fig. 6-16 Probe temperatures (open results)

6.2 Test 3

6.2.1 Plume Temperatures (M1 to M6)

Fig. 6-17 and Fig. 6-18 shows the comparison of the plume temperatures M2 and M6 for blind and open calculations. The measured plume temperature in the lower part of fire compartment, such as M1, show a strong temperature increase in the initial phase to values up to 700 °C. At the end of the fire, the temperatures increase again, reaching values of approx. 900 °C. Most of the codes predict temperatures that are much lower than measured toward the end of the experiment. The differences are about 100 to 200 K. In the upper part of the plume, the measured temperature rise is much slower than the calculated ones. Starting with values of approx. 350 °C, values up to 900 °C are reached with a final peak at about 1000 °C. In the blind simulations, the plume temperature increase is underestimated. The results are partly better in the open calculations (e.g. CFX). However, deviations of up to 200 K are possible. It has to be stated that the situation at the end of the fire is more questionable. The simulation strongly depends on the assumptions which have been made for the pyrolysis rate. The peak is simulated approx. 250 s too early. The pyrolysis rate provided to participants could be examined for improvement.

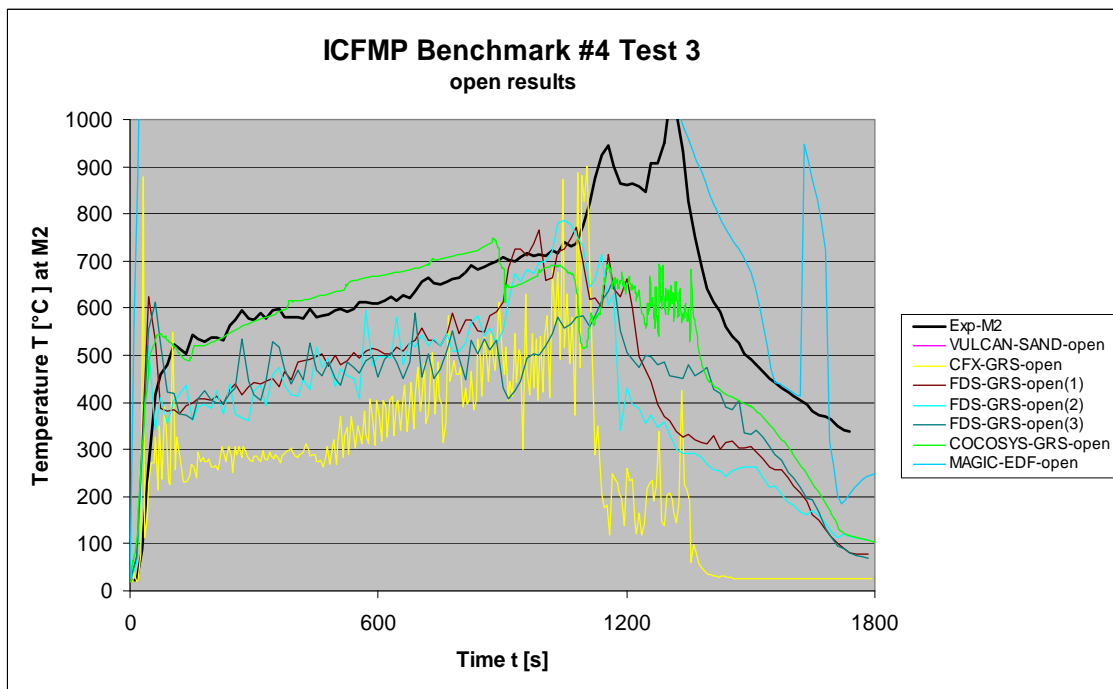
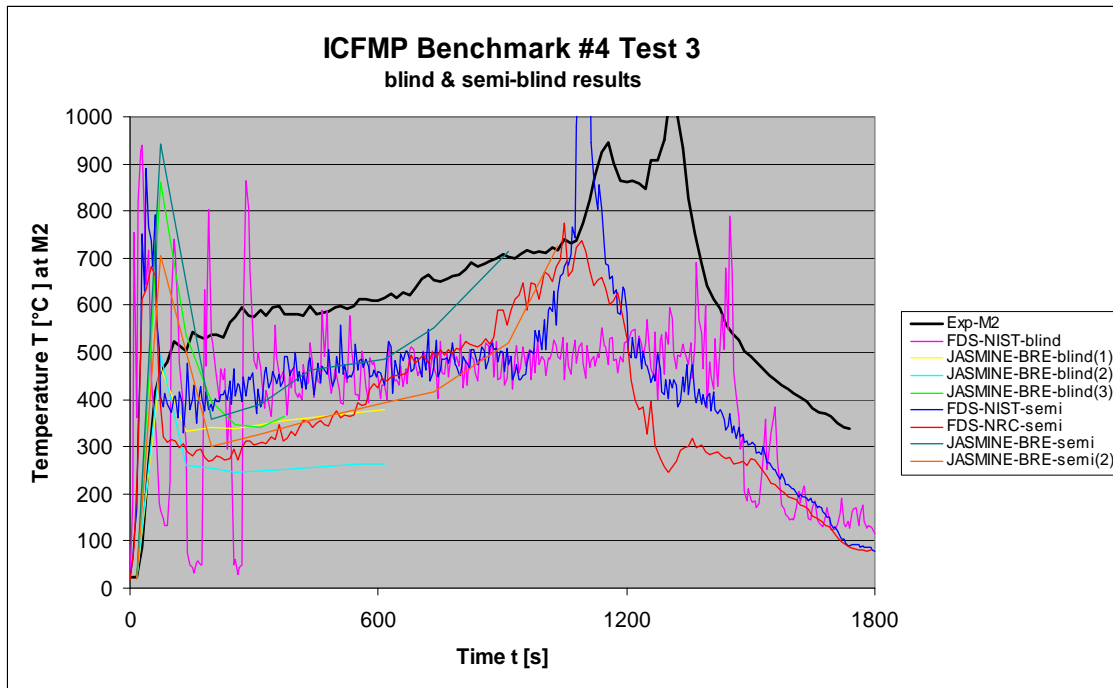


Fig. 6-17 Comparison of plume temperatures M2 (blind & open)

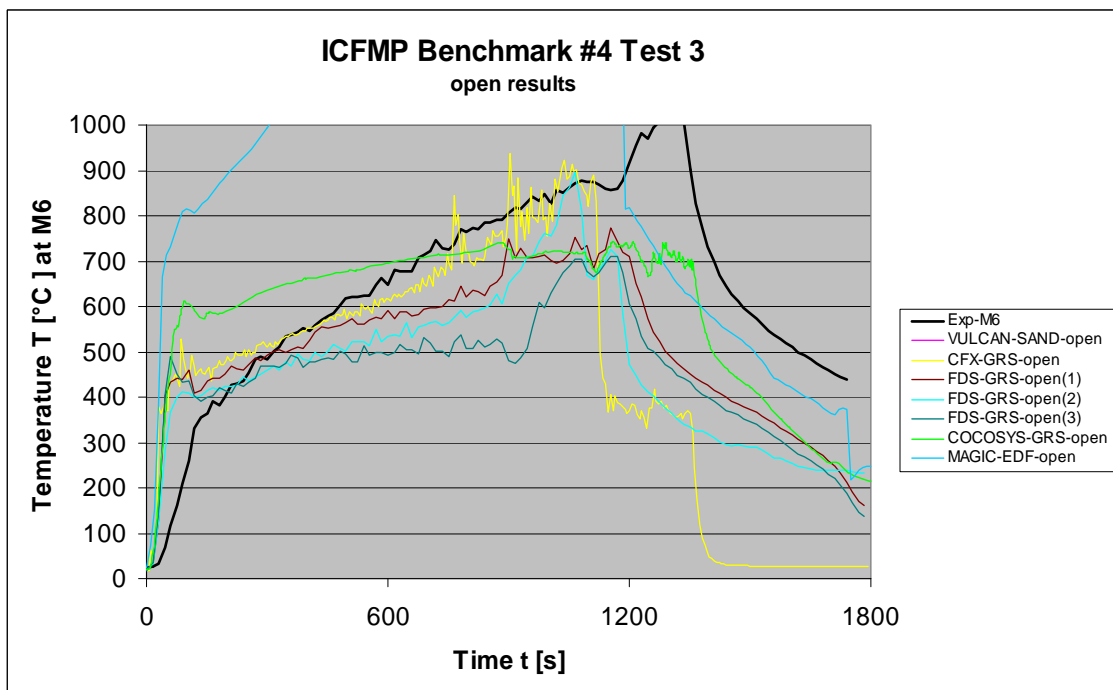
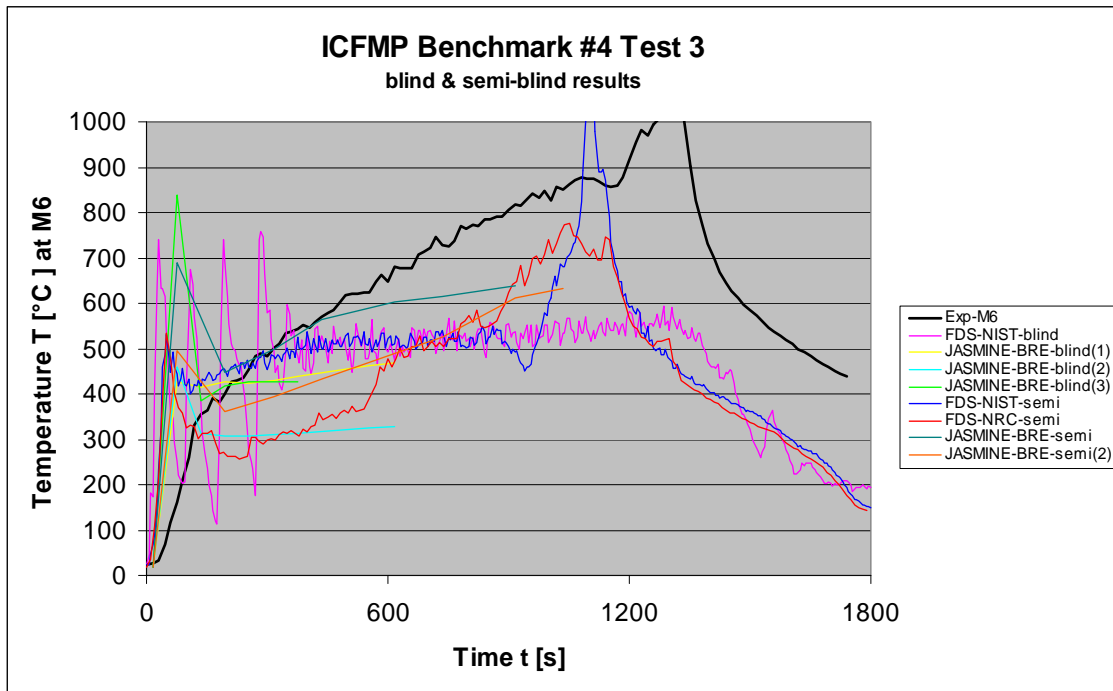


Fig. 6-18 Comparison of plume temperatures M6 (blind & open)

6.2.2 Temperatures inside the Fire Compartment

Fig. 6-19 to Fig. 6-24 present the comparison of blind and open calculations for two temperature trees. These are the measurement positions M8, M12 and M16 at the rear of the fire compartment close to the wall and the positions M9, M13 and M17 at the front. The deviations between the code results are partly quite high with approx. up to 500 K. JASMINE calculates very high temperatures at the rear (position M8), while the results are much better at the front. A possible reason is that a strong shift of the fire plume was calculated in the simulation. Similar to the plume temperatures, the temperature gradient is underestimated by most of the codes. The open CFX calculation shows a somewhat better simulation of the temperature gradient. But, similar to the plume temperature, the measured temperature peak was not calculated. At about 550 s the VULCAN simulation shows a temperature decrease, which was not observed in the experiment. COCOSYS does not solve the momentum balance. Therefore, a plume shift can not be calculated and the results for back and front side are very similar. A temperature peak was also not simulated.

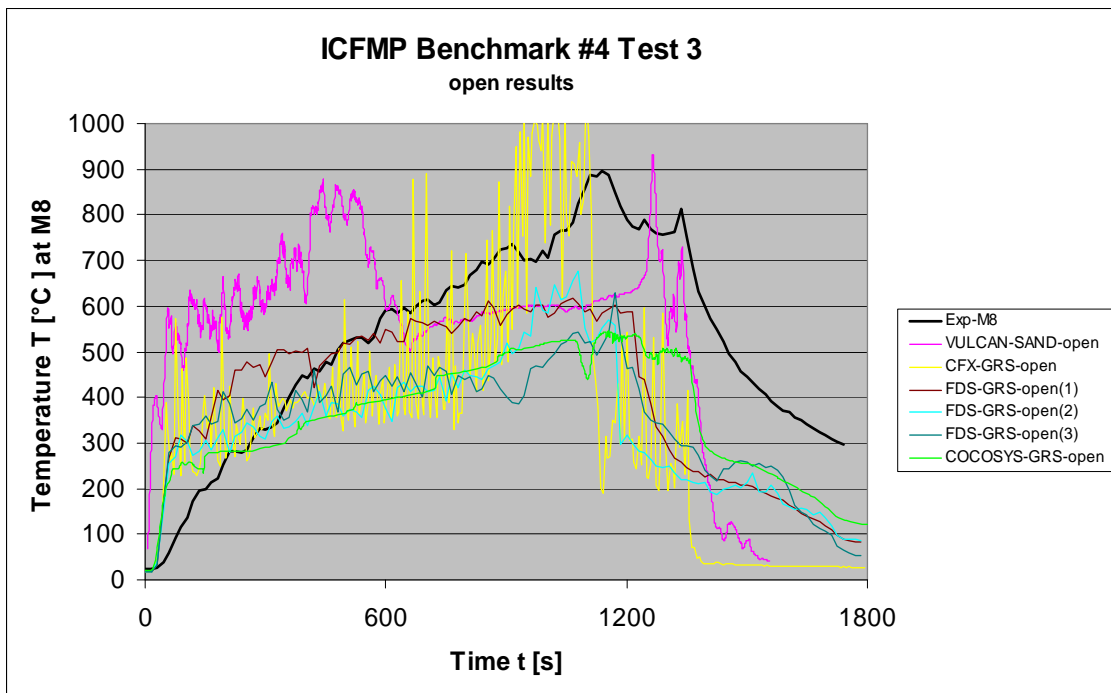
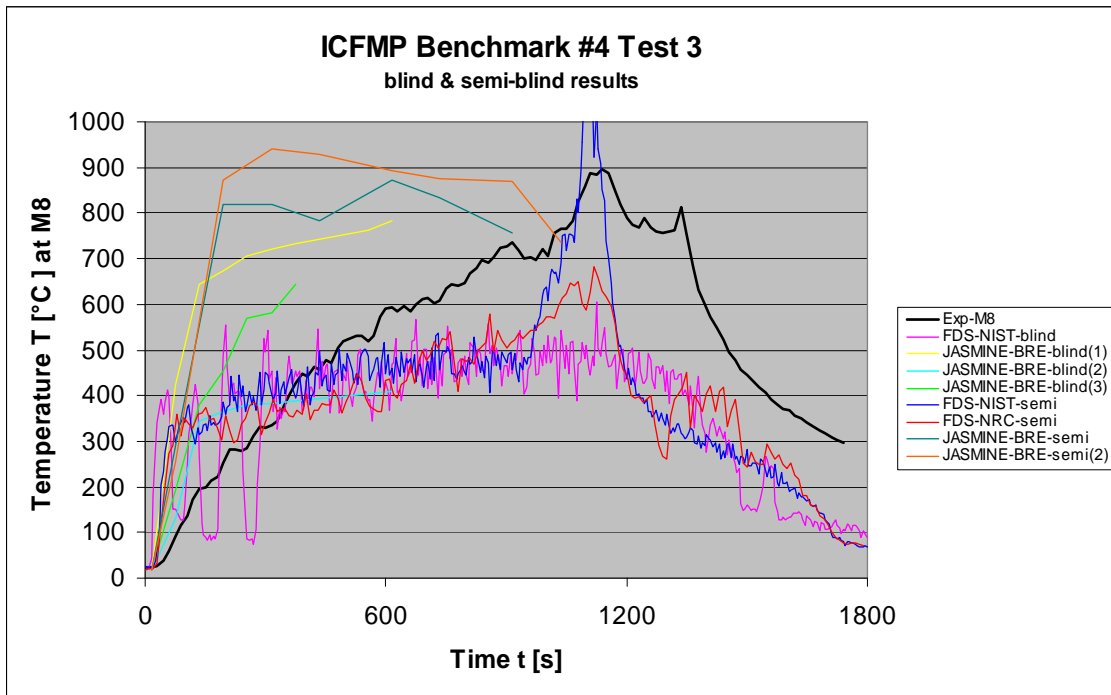


Fig. 6-19 Temperatures on the back of compartment (M8, blind & open)

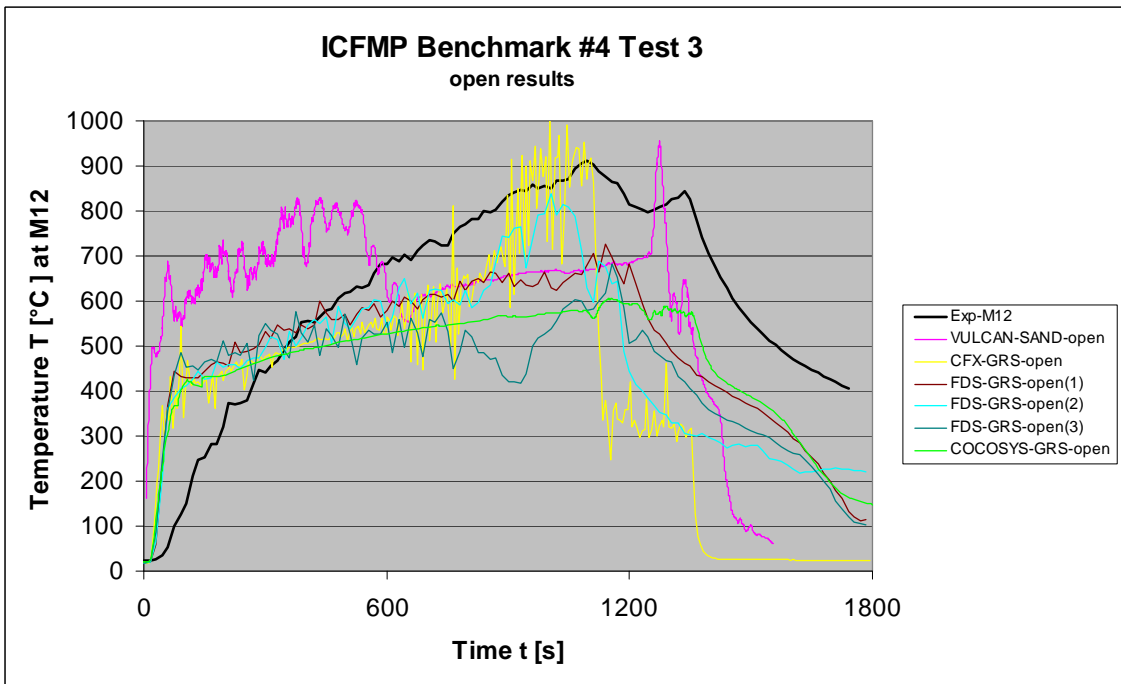
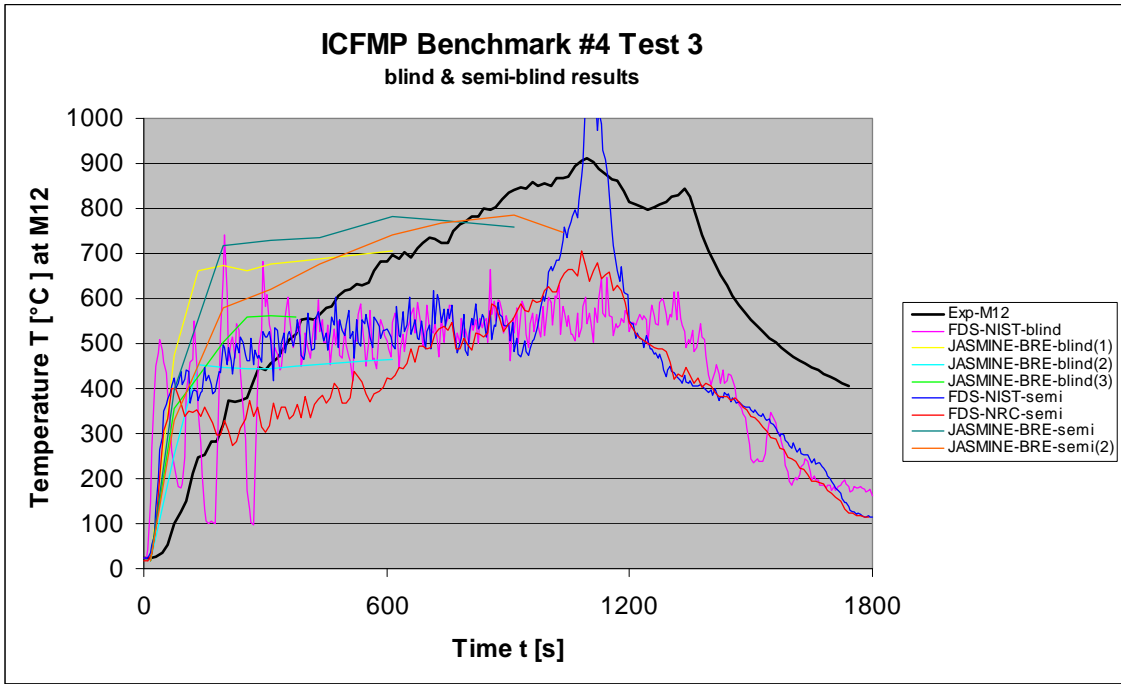


Fig. 6-20 Temperatures on the back of compartment (M12, blind & open)

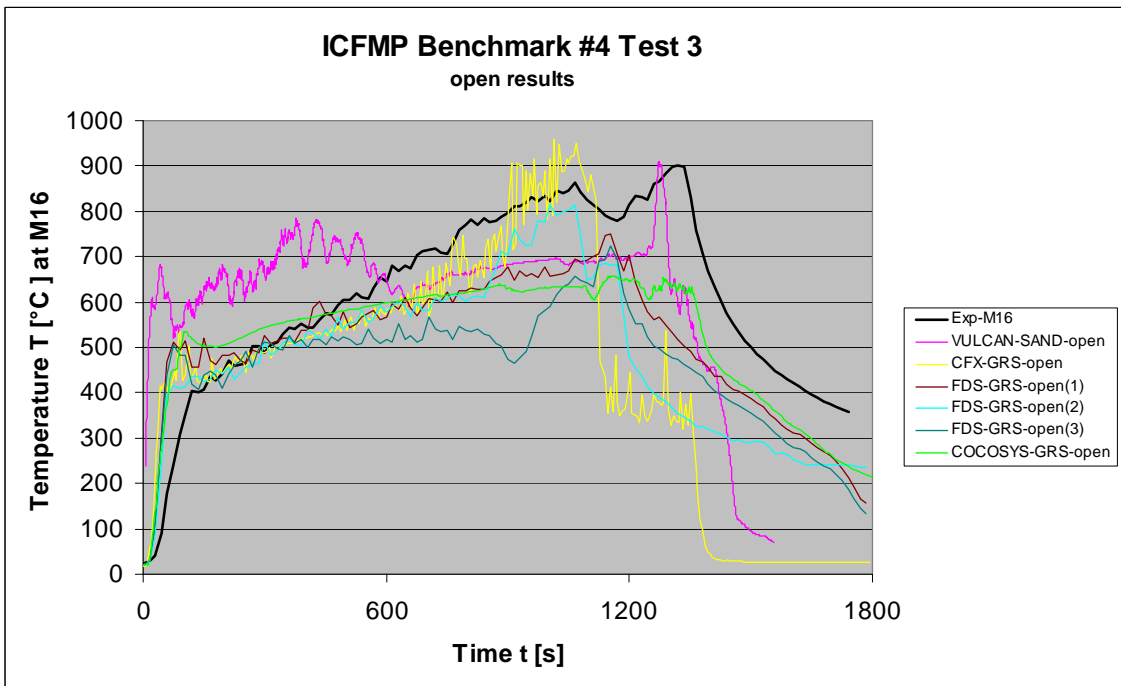
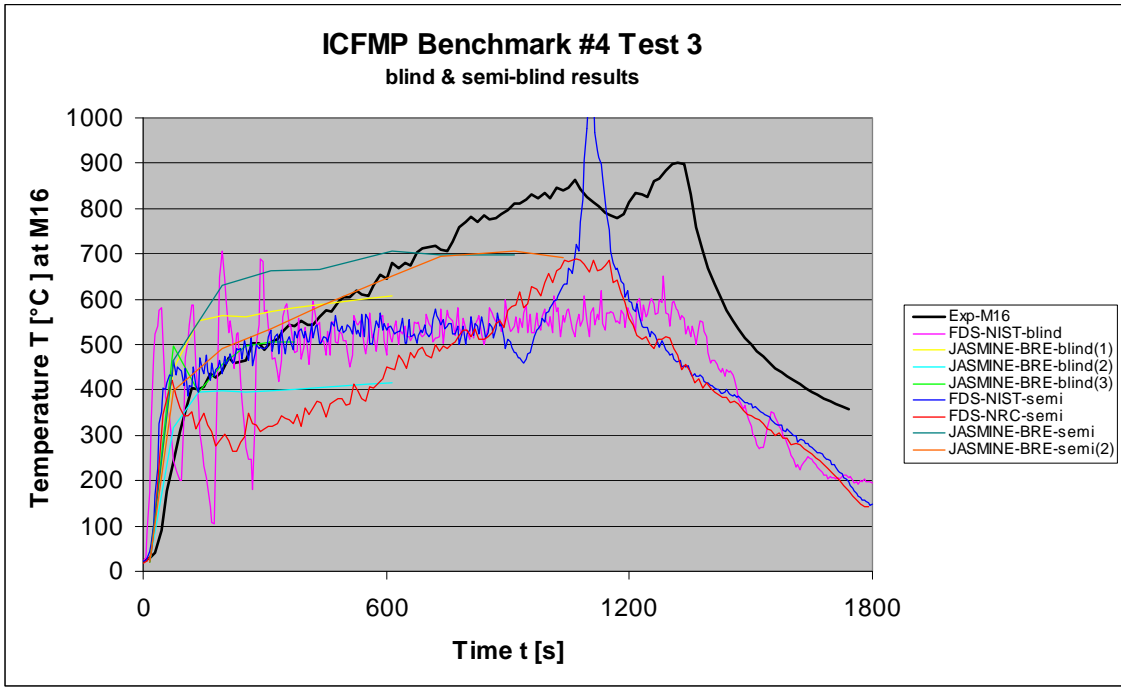


Fig. 6-21 Temperatures on the back of compartment (M16, blind & open)

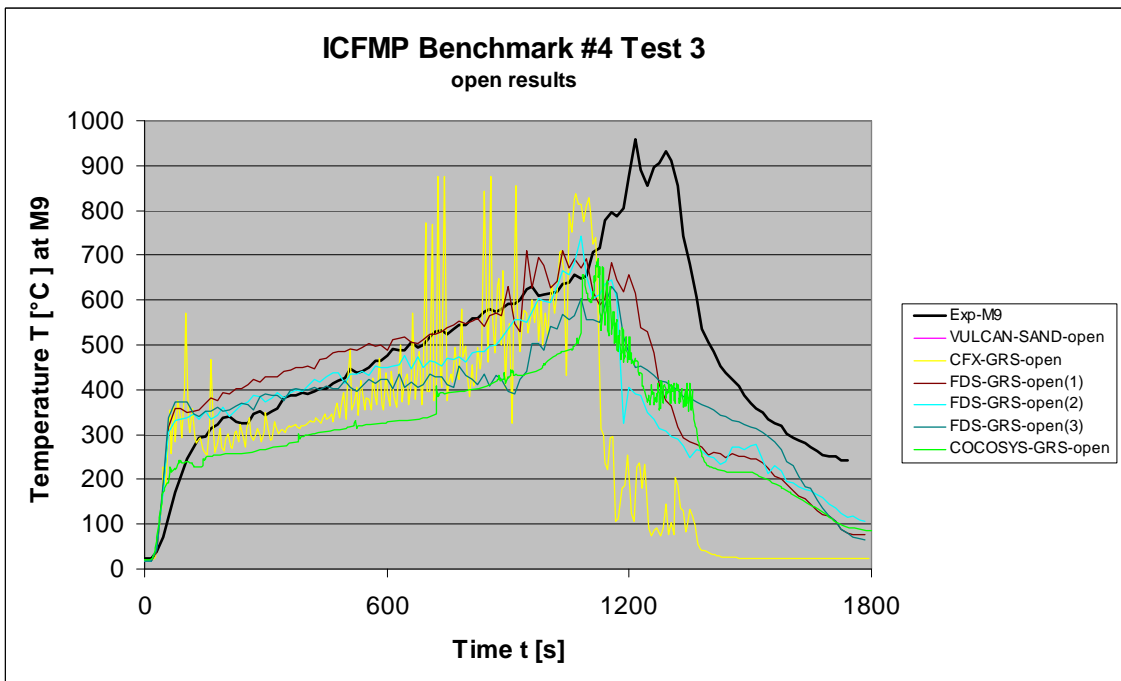
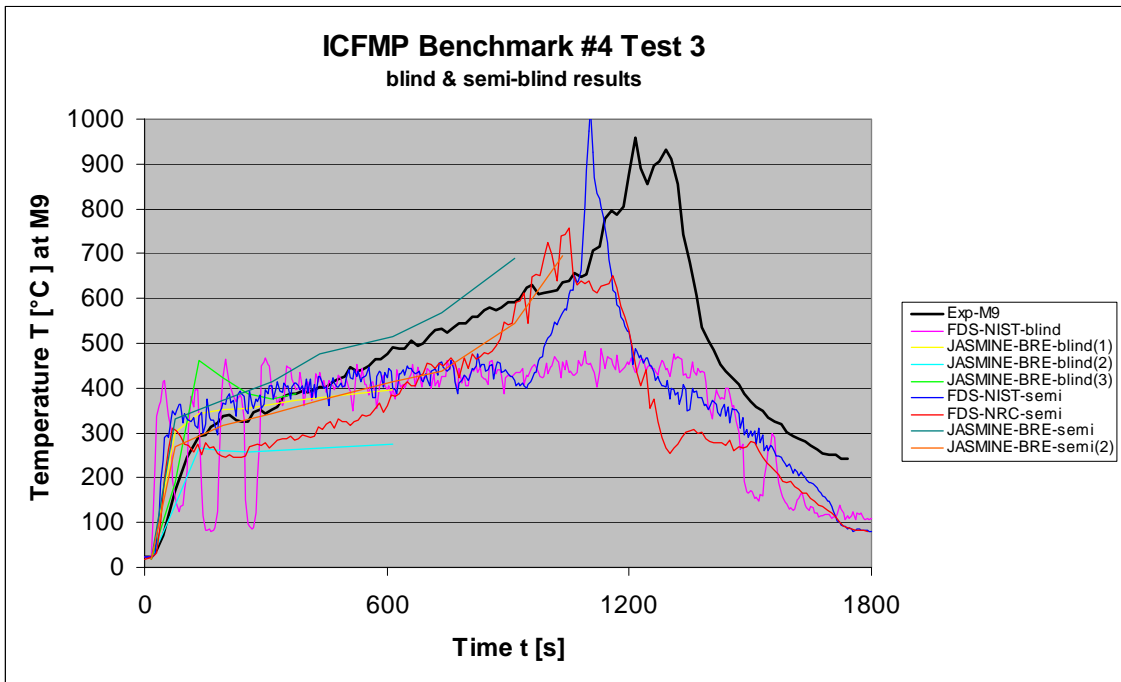


Fig. 6-22 Temperatures on the front side of compartment (M9, blind & open)

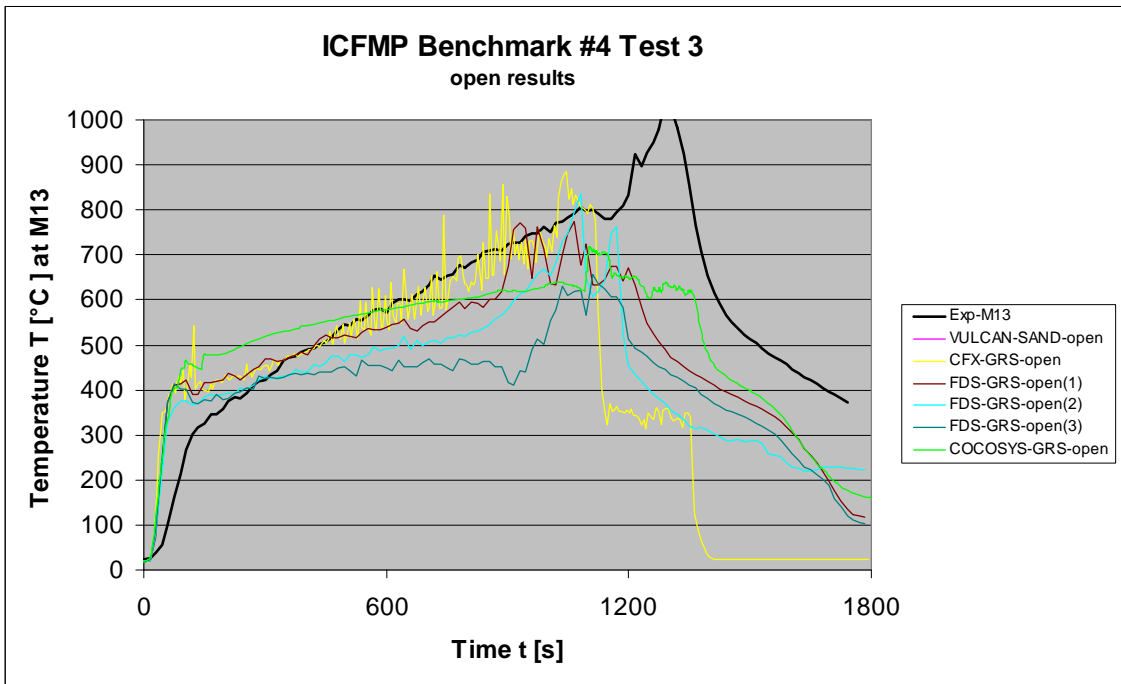
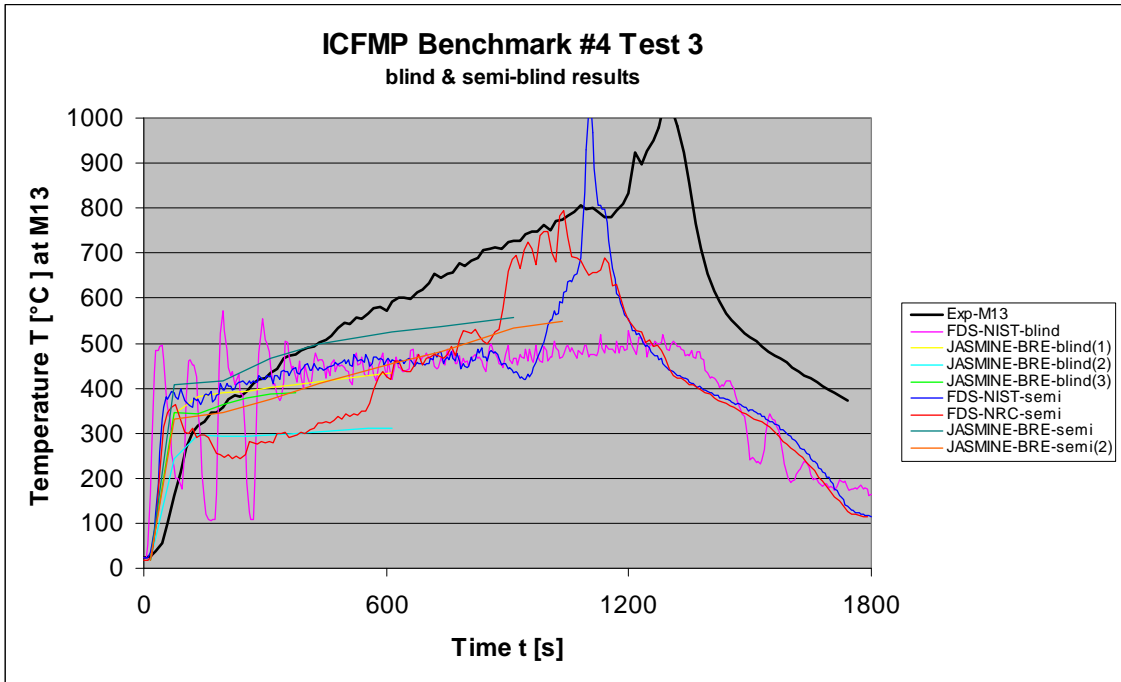


Fig. 6-23 Temperatures on the front of compartment (M13, blind & open)

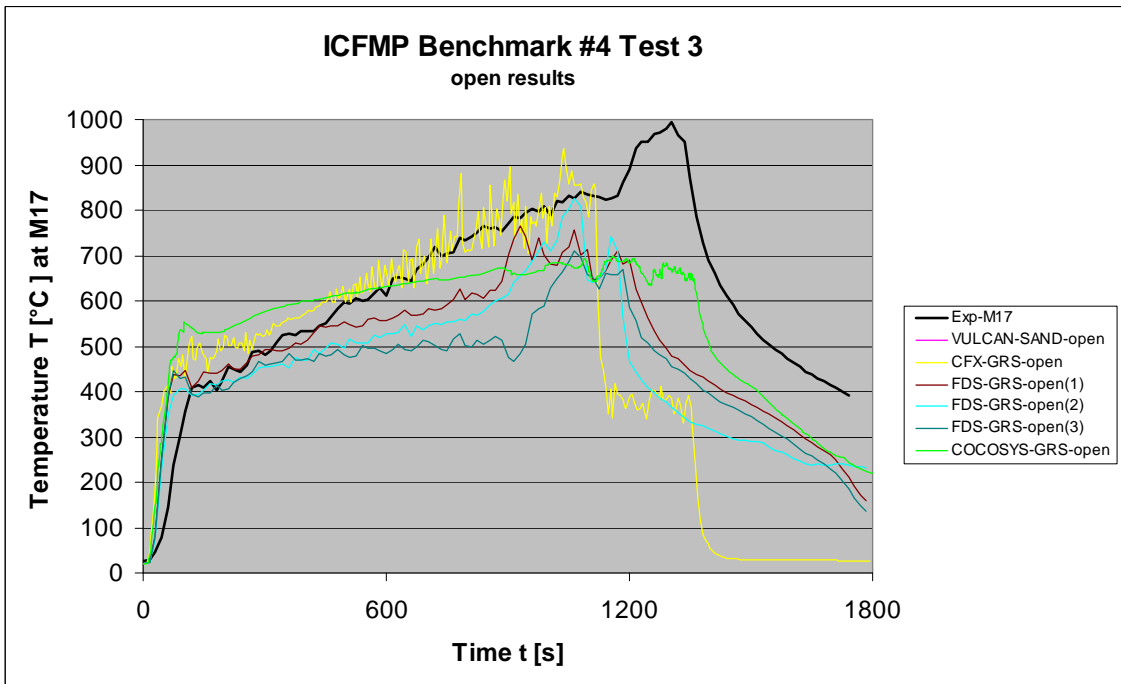
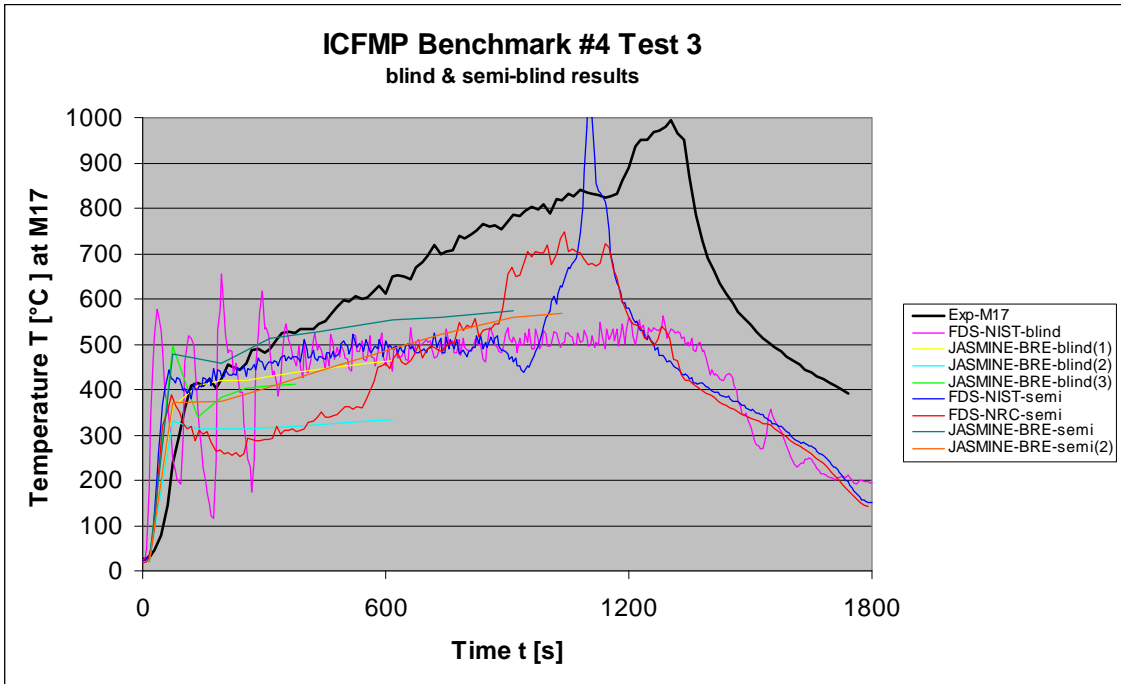


Fig. 6-24 Temperatures on the front of compartment (M17, blind & open)

6.2.3 Layer Height and Upper Layer Temperature

Only three levels of measurements are available inside the fire compartment. Therefore the calculation of the upper layer temperature and the hot gas layer height is questionable. Fig. 6-25 and Fig. 6-26 present the comparison between the results of zone models and experimental results. The calculated layer heights are lower compared to the experiment, in particular close to the floor level. Because the lowest elevation of the measurement is located at 1.5 m, the experimental result cannot be lower.

The semi-blind CFAST calculations performed by different users show a strong deviation of 300 K for the upper layer temperature. Results from open calculations are provided by the code FLAMME-S and MAGIC. The results of MAGIC are quite close to the experimental results. Concerning FLAMME-S it has to be pointed out that this Benchmark Exercise is out of the validated range of this code. The simulated temperatures are too low in comparison to the experimental data.

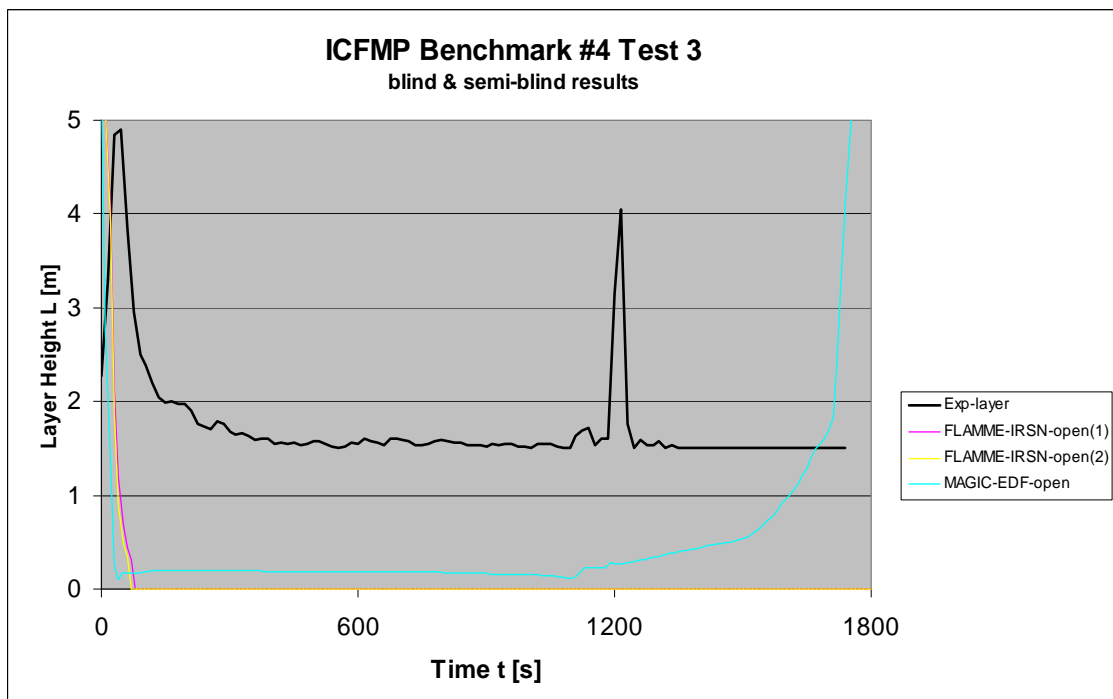
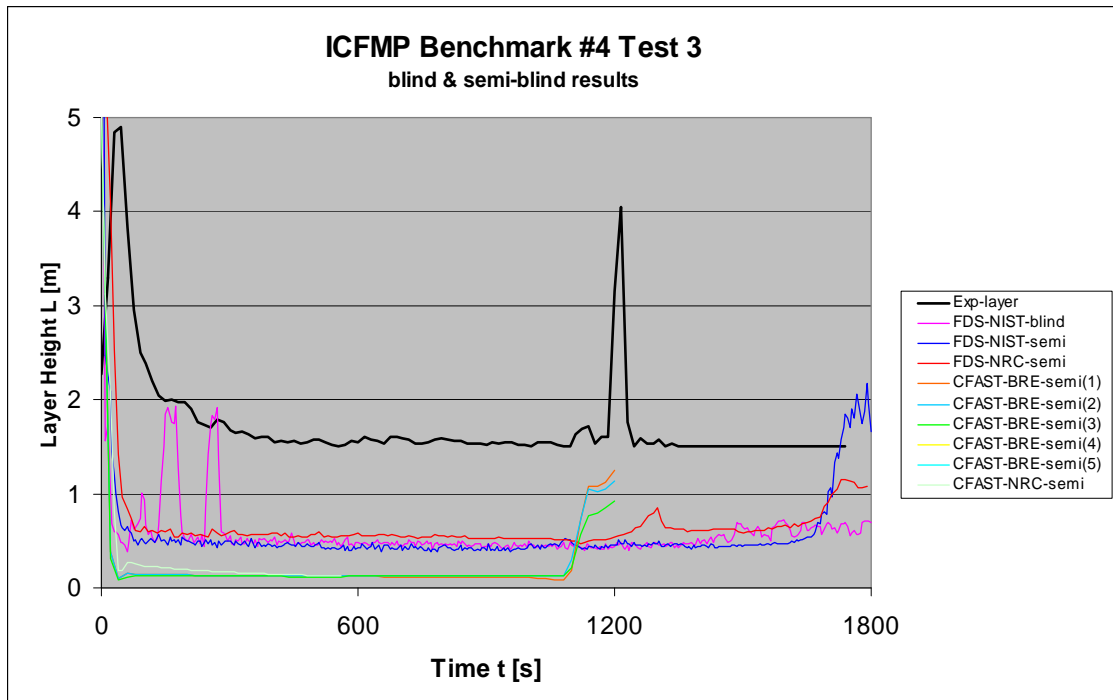


Fig. 6-25 Hot gas layer height (blind & open)

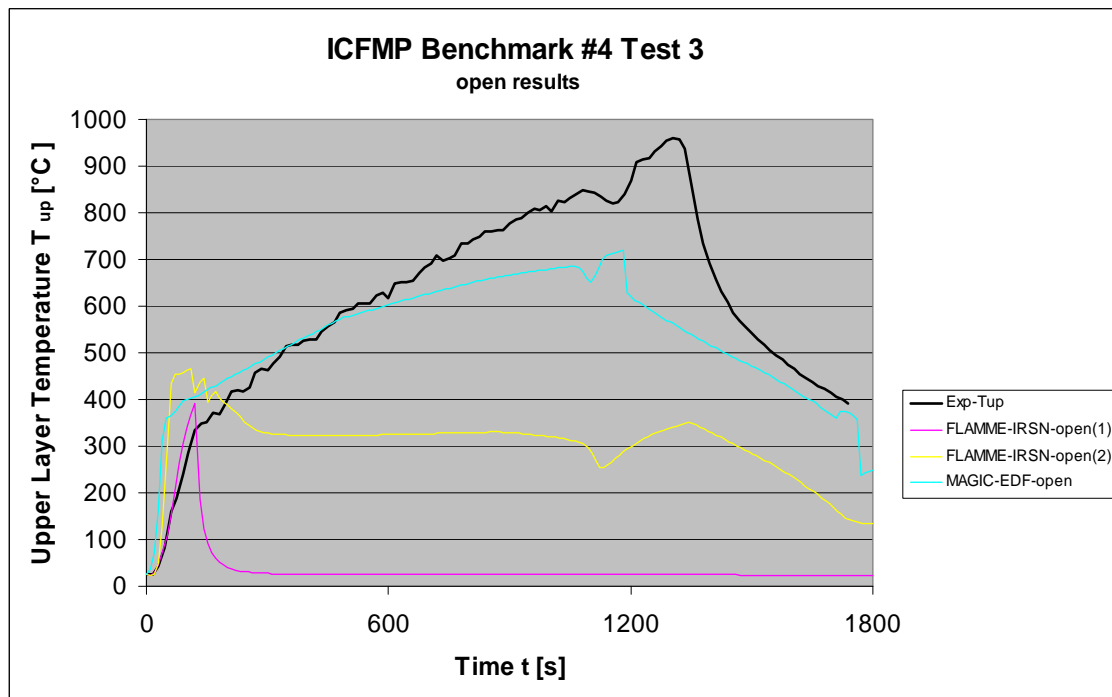
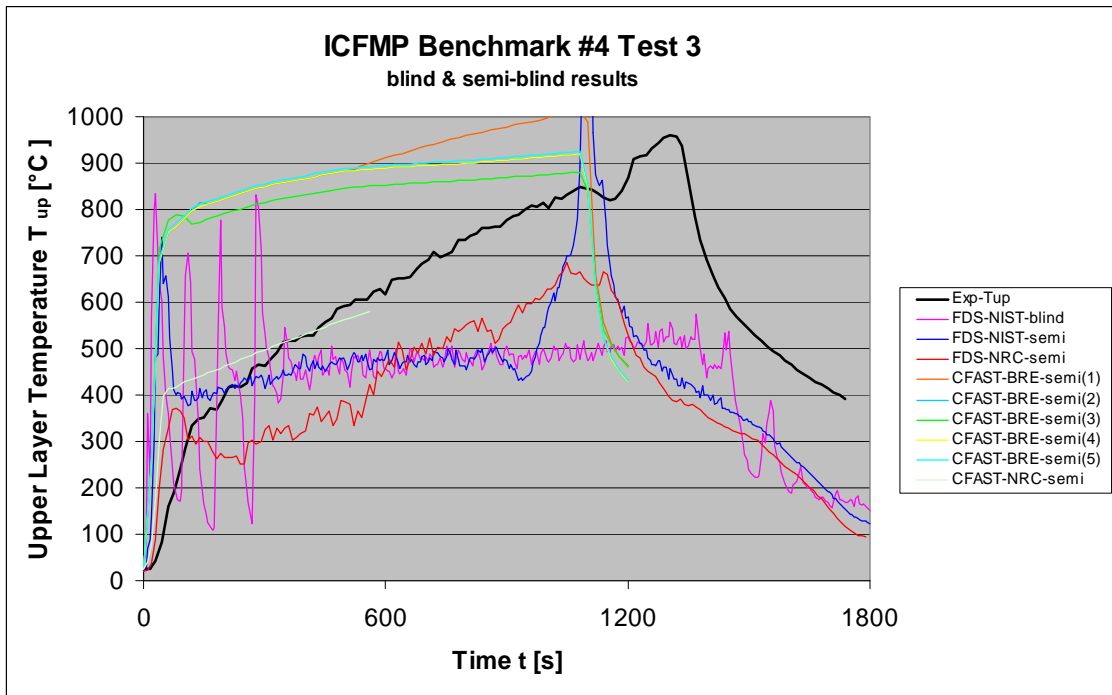


Fig. 6-26 Upper layer temperature (blind & open)

6.2.4 Gas Concentrations inside the Fire Compartment

Fig. 6-27 to Fig. 6-30 provides a comparison of the results for the gas concentrations inside and outside the fire compartment. The elevation of the inside measurement position is 3.2 m above the flame. The blind and semi-blind FDS calculations are in reasonably good agreement with measurement. The oxygen concentration is underestimated by about 2 Vol.-%. The definition of the pyrolysis rate for the semi-blind calculations leads to oxygen concentrations close to 0 Vol.-%. According to the pre-defined peak, the decrease of oxygen arises approx. 100 s too early. The semi-blind CFAST calculation performed by NRC and the open MAGIC calculation show a much too low oxygen concentration, although the calculated upper layer temperature is quite similar to the experimental data. In the open calculations, the deviation range of the results for the oxygen concentration GA1 is quite large at about 7 Vol.-% (without considering the FLAMME-S results). Except for one FDS calculation, the oxygen concentration is underestimated. The behavior of VULCAN is somewhat different compared to the other codes. The complete oxygen depletion already occurs at approx. 500 s. This could explain the different characteristics for the temperature results.

With respect to the CO₂ concentration a similar picture could be drawn. Unfortunately, no experimental data are available for the position GA1. But the variation in the open calculations is even higher compared to the blind calculations. The semi-blind calculation of FDS performed by NIST shows a strong peak in the oxygen and carbon dioxide concentrations (position GA2) at the end of the fire process. This was not been observed in the experiment. Furthermore, the other FDS simulations do not show such a peak. Similar peaks have been calculated in the open phase with CFX and FDS. This shows that the given pyrolysis rate may be somewhat questionable at the end of fire process.

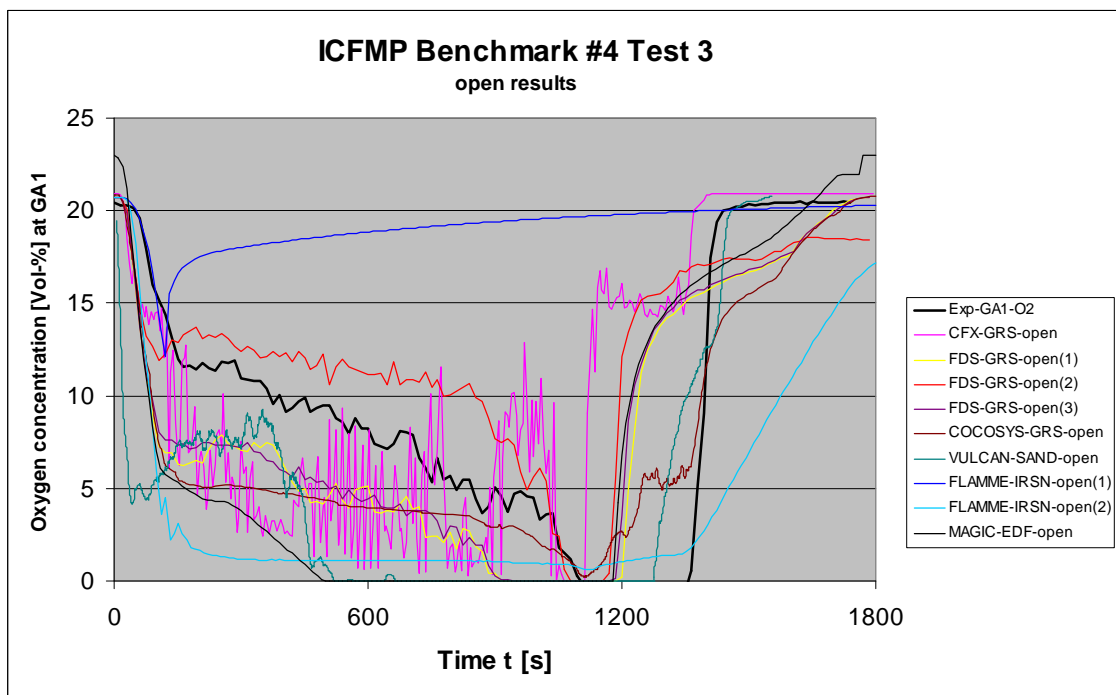
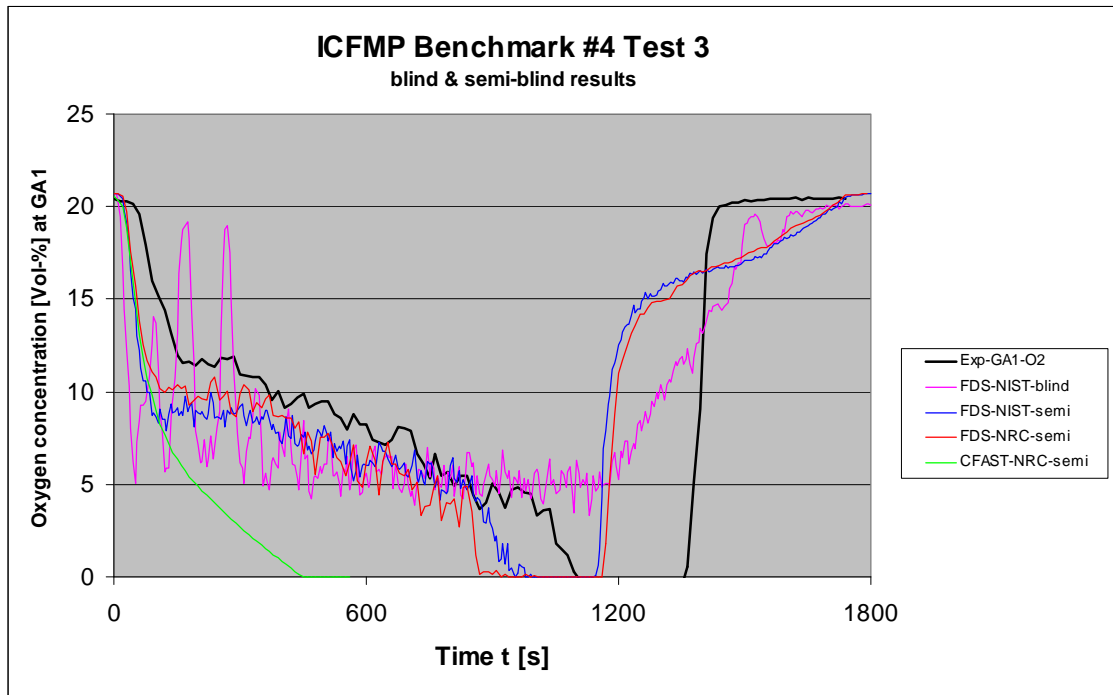


Fig. 6-27 Oxygen concentration inside fire compartment (blind & open)

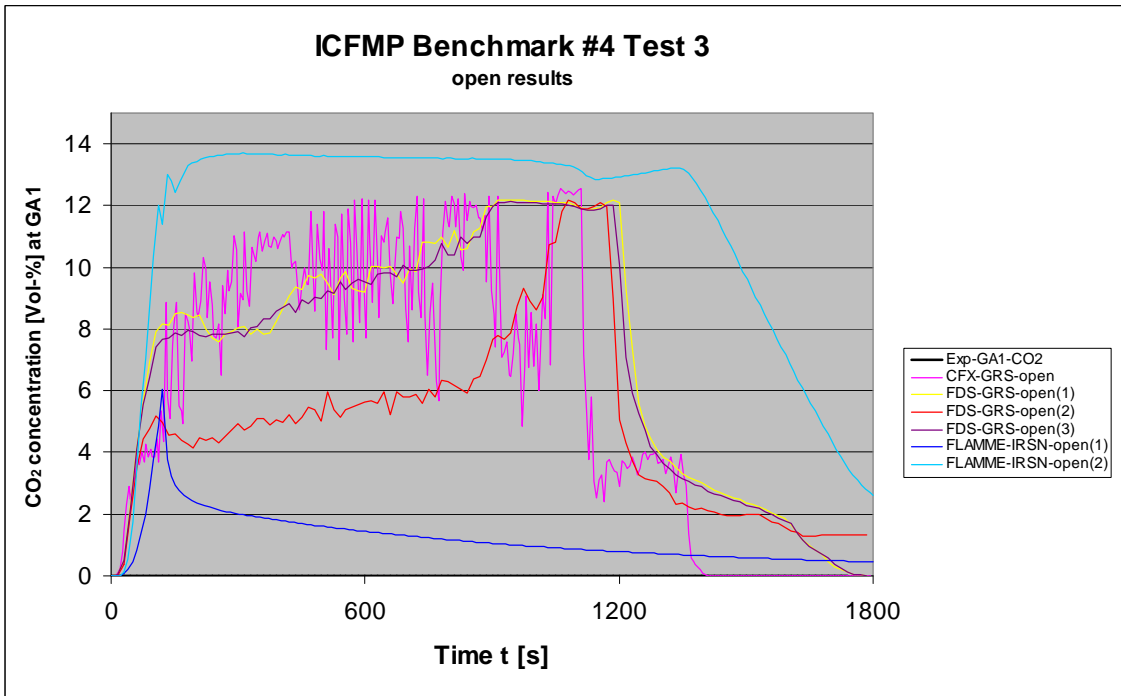
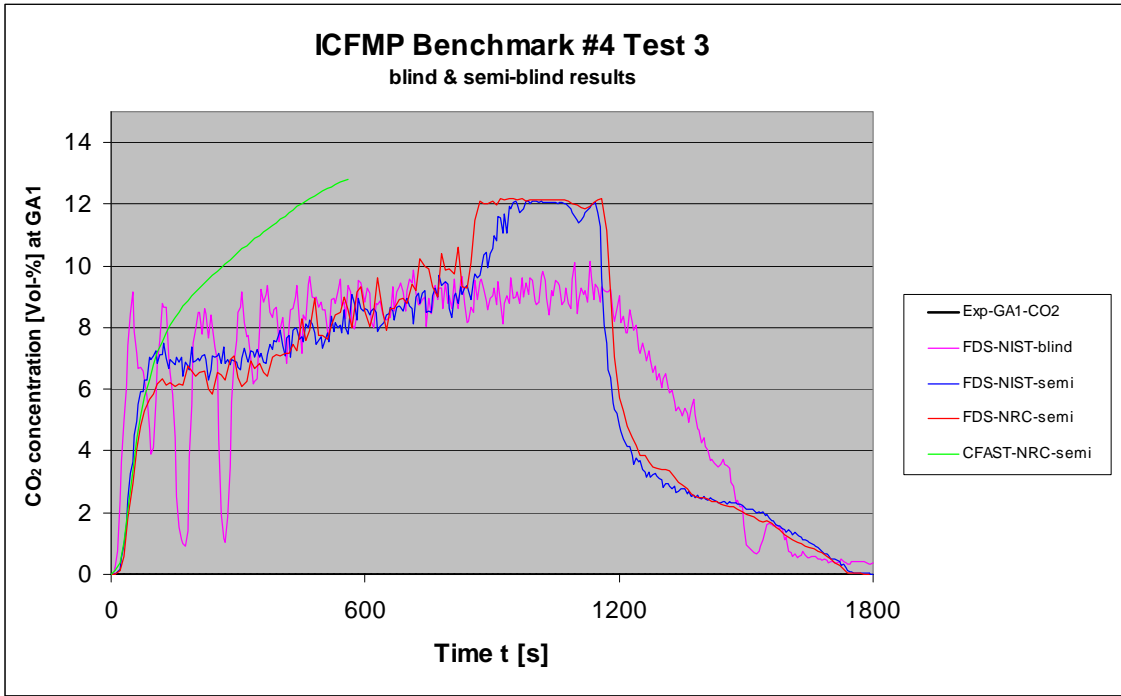


Fig. 6-28 CO₂ concentration inside fire compartment (blind & open)

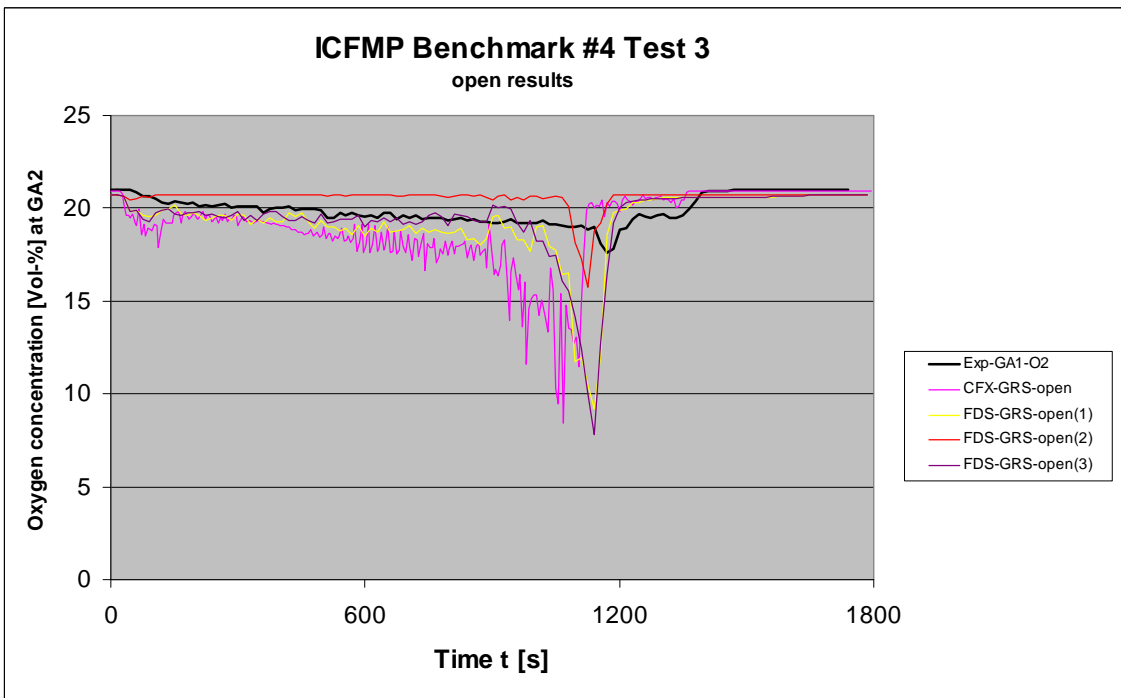
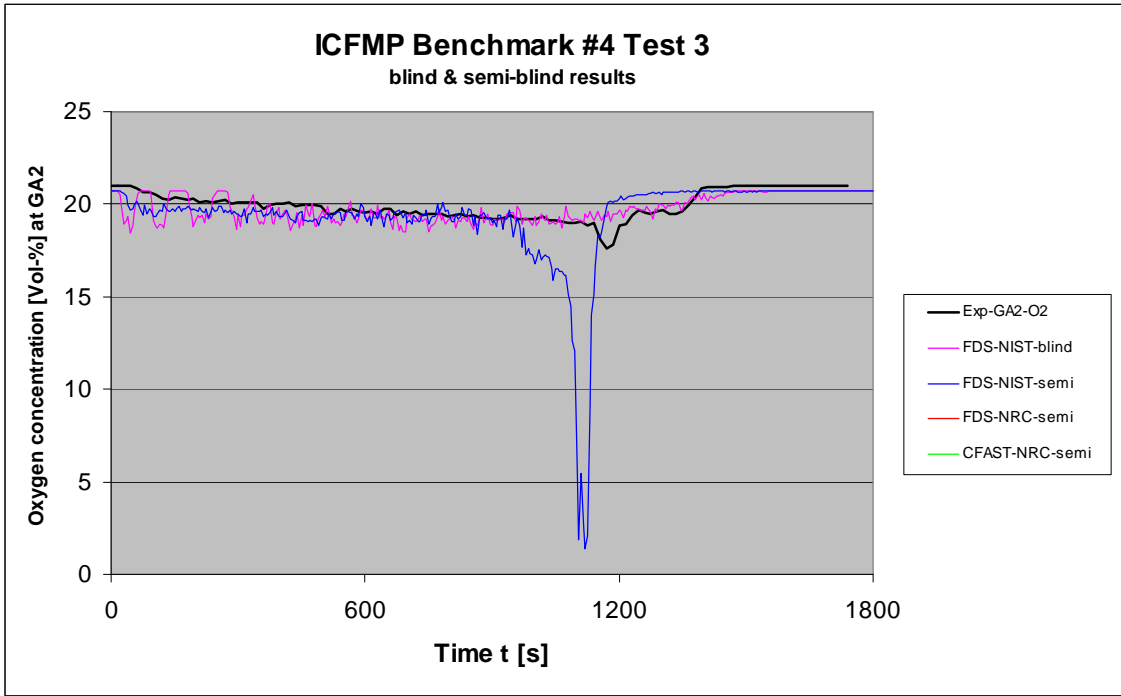


Fig. 6-29 Oxygen concentration outside fire compartment (blind & open)

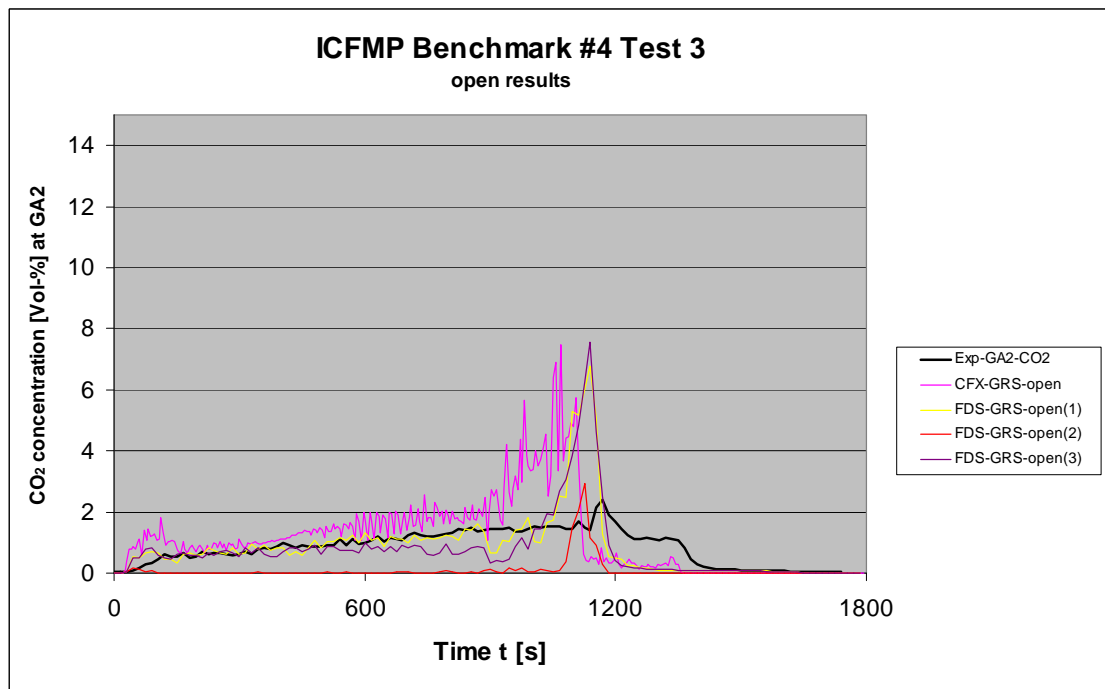
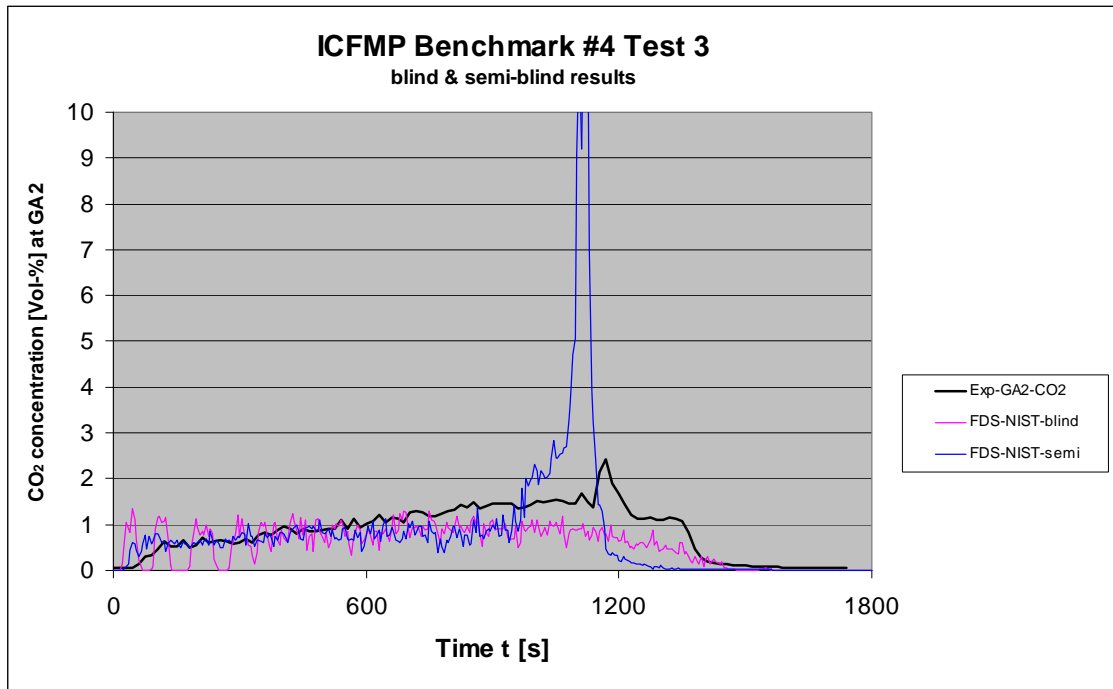


Fig. 6-30 CO₂ concentration outside the fire compartment (blind & open)

6.2.5 Probe Temperatures

One of the main objectives of fire simulation codes for NPP applications is the estimation of thermal loads on different type of targets. On the left wall of the compartment three material probes of different material types, concrete, aerated concrete and steel have been installed. Fig. 6-31 and Fig. 6-32 compare the calculated and experimental temperatures close to the material surface. The results of the blind calculations show a wide range of deviations. The semi-blind CFAST calculation performed by BRE overestimates the temperatures by about 300 K while most of the CFD codes underestimate the temperature by up to 300 K. The strong temperature peak simulated by some CFD codes as a result of the peak in the pyrolysis rate was not observed in the temperature measurements. The results of FDS for the open calculations are comparable to those for the blind simulations. The temperatures are underestimated by approx. 100 K. The results of VULCAN are on the one hand in a very good agreement with the experimental data, except the strong peak for aerated concrete. On the other hand the calculated temperature decrease at the end of the fire process is much too strong, indicating that the thermal heat conduction or heat transfer is not simulated correctly. The results of the open MAGIC calculation are reasonable and better compared to Test 1.

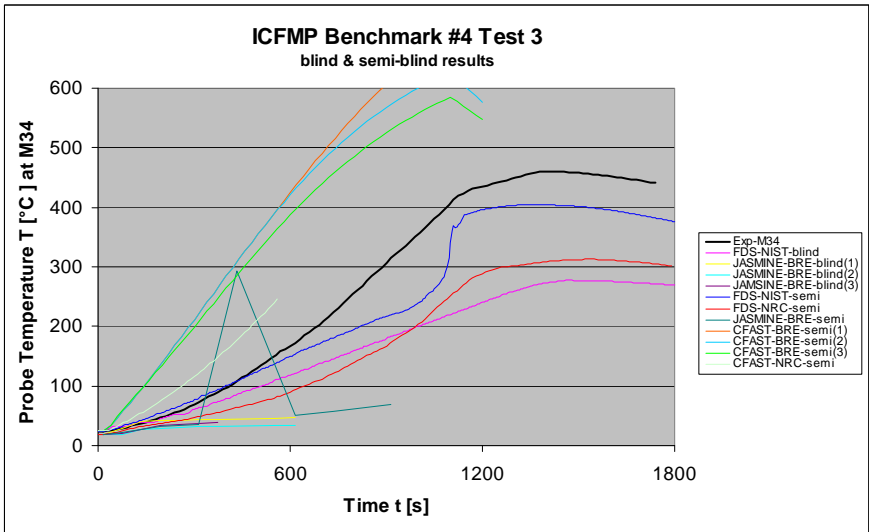
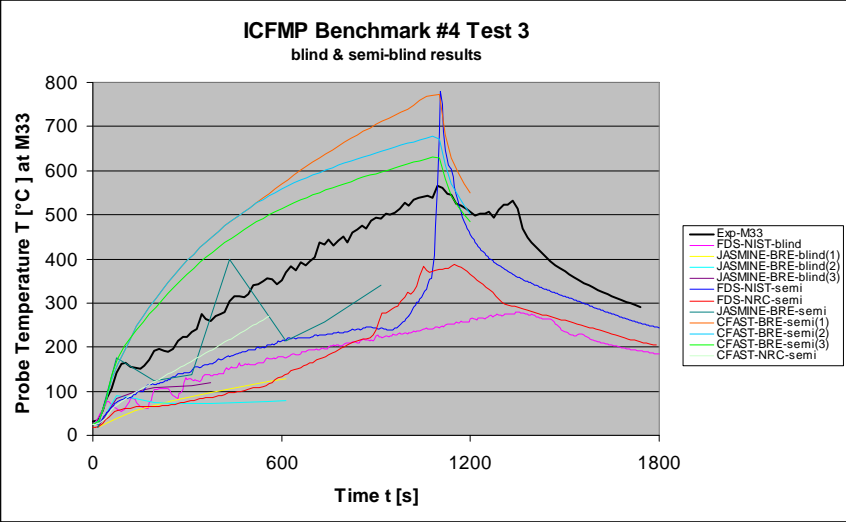
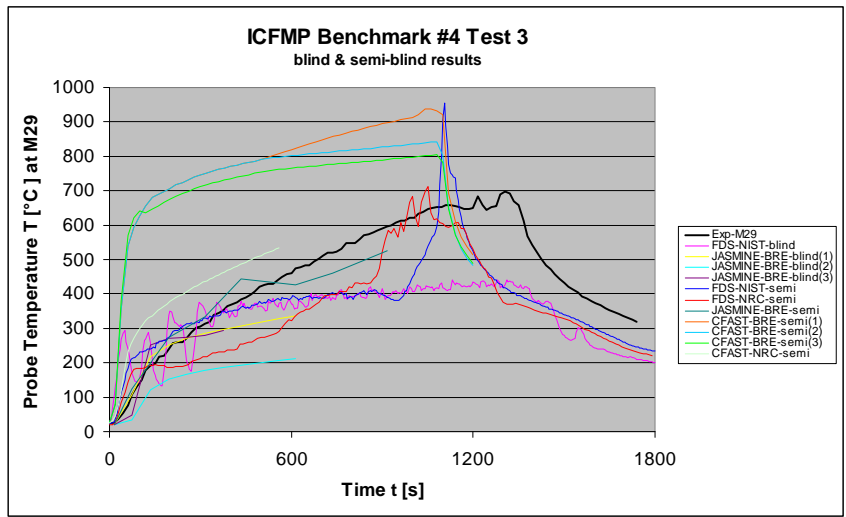


Fig. 6-31 Comparison of the probe surface temperatures (blind simulations)

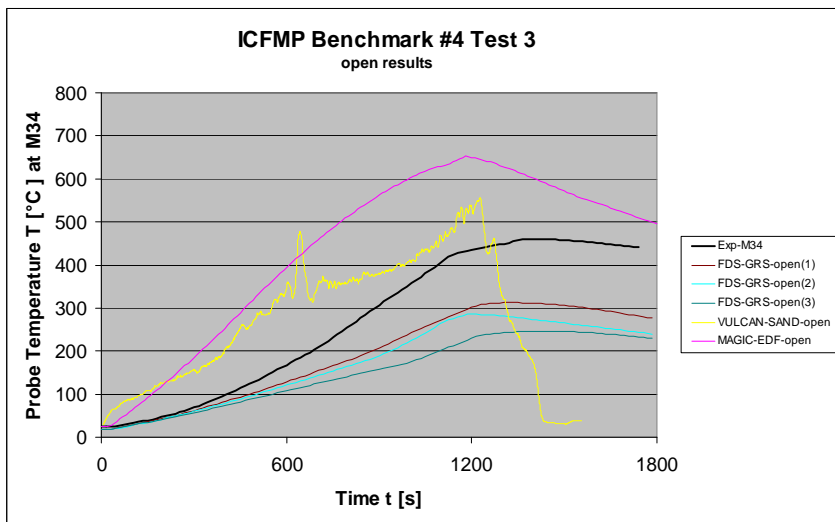
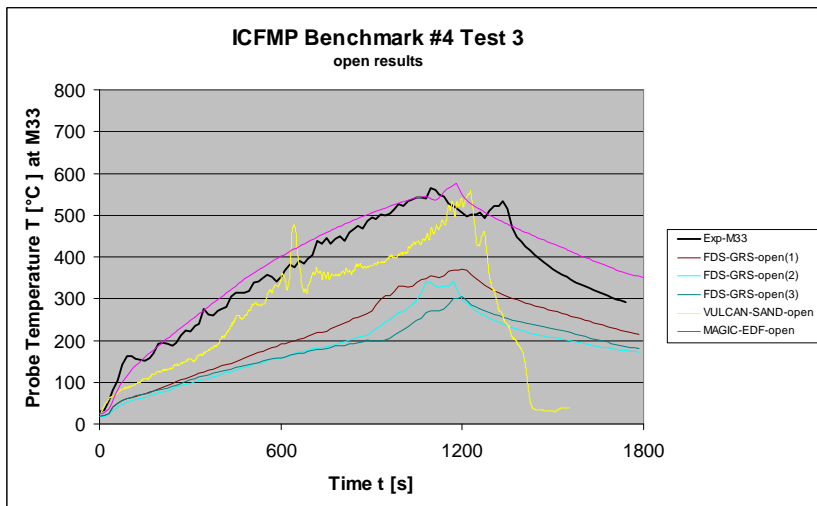
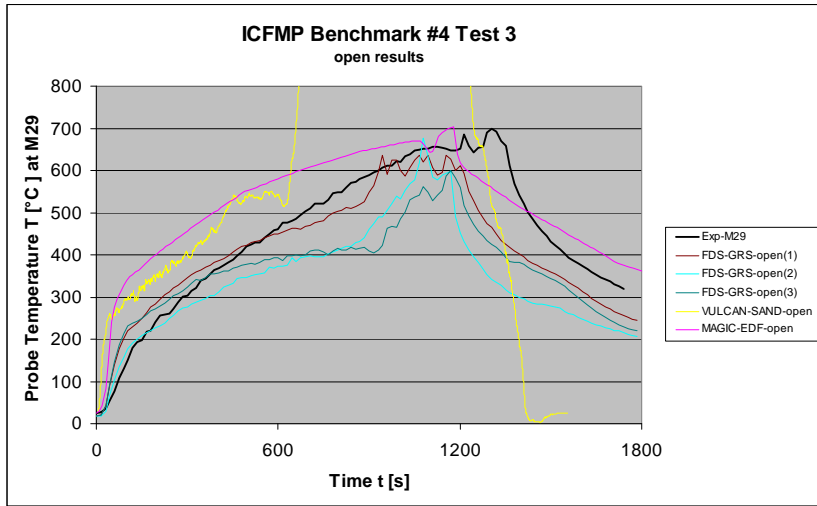


Fig. 6-32 Comparison of the probe surface temperatures (open simulations)

7 General Conclusions and Recommendations

7.1 General Conclusions

This section provides a discussion of the general conclusions derived from Benchmark Exercise No. 4.

Heat Release Rate

The pyrolysis rate and the resulting heat release rate have a great impact on the thermo-fluid conditions inside the fire compartment. The specified (measured) rate for Test 1 seems to be satisfactory, because reasonable temperatures were calculated. The rate for Test 3 is more questionable, because the temperature peak at the end of the experiment is not simulated and the calculated temperature decrease starts too early. On the other hand, due to the under-ventilated conditions, the combustion usually is incomplete and possibly under-estimated.

Blind calculations show that the models to calculate pyrolysis rates are still limited. The results of these calculations show significant deviations from the experimental results.

Gas Temperatures

The overall gas temperatures could be reasonably well simulated by zone models as well as by the more complex CFD codes, although the differences for Test 3 are larger. The CFD codes were able to simulate the drift of the flame to the rear wall due to the fresh air entrainment through the door. However, in comparing the lower temperatures at the measurement locations M8 and M10 at the rear of fire compartment, this effect seems to be over-estimated in the simulations. Particularly for targets close to the fire, these effects may be more important.

Oxygen Concentration

Key parameters for the oxygen concentration inside the fire compartment are the combustion efficiency, the ventilation conditions, and the reaction schemes modeled, particularly for CO and soot production. Here, Test 3 gives some answers for the specification of the LOL value, which should be set to 0 Vol.-%. FDS with only one single transport equation shows some principal limitations in this range.

Wall Temperatures

Wall temperatures are partly influenced by the flame shifting to the back wall. This effect could be simulated, in principle, by CFD codes only. Zone codes assume homogeneous boundary conditions.

Ventilation – Air Entrainment

For zone models the handling of the air entrainment for under-ventilated conditions is important, particularly in Test 3. Here, specific assumptions have been made in some zone model calculations.

Target Simulation

The ability to simulate the targets is restricted in the various codes. Some problems result from the cylindrical shape of the barrel target as well as from the multi-layer material configuration. Radiation has an important influence on the thermal loading, and this has to be partly specified by the user.

7.2 Recommendations

The strong differences between calculations and experiments, in particular for the blind simulations, indicates that models to predict pyrolysis rates are strongly needed. Unfortunately, there is a strong positive feedback from the thermal environment back to fuel surface which then influences the pyrolysis rate. Further local effects, such as edges to the pan, may also have an influence on the pyrolysis rate. The consequences for the estimation of uncertainties should be discussed in more detail. In this context, further blind calculations (for new experiments) will be helpful.

Scenarios with under-ventilated fires are still difficult to simulate. It has to be kept in mind that such scenarios are typical for NPPs, as most of the fire compartments in a NPP can be assumed more or less closed during a fire.

The simulation of targets should be further improved and investigated. This is highly important, because potential failures (e.g. short circuits) may occur much earlier than the ignition of the target itself.

8 Summary

The fuel pool fire Tests 1 and 3, performed in the OSKAR test facility at iBMB of Braunschweig University of Technology at the end of 2003, have been included in the benchmarking and validation exercises of the International Collaborative Fire Model Project (ICFMP) as Exercise No. 4. The objective of the collaborative project is to share the knowledge and resources of various organizations to evaluate and improve the state of the art of fire models for the use in nuclear power plant fire safety assessments, covering deterministic fire hazard analysis (FHA) as well as fire probabilistic safety assessment (PSA) studies.

The main difference between the two experiments carried out is the size of the door area. Both experiments give first indications on the effects of ventilation and fuel controlled fires as well as on the thermal loading on different types of targets. Previous benchmark exercises within the ICFMP had shown that the simulation of these two phenomena should be improved.

During the benchmark procedure, the participants performed different types of calculations. These were totally blind simulations without knowledge of the measurements, semi-blind calculations with knowledge of the pyrolysis rate only, and completely open calculations. It has been demonstrated that the pyrolysis rate has a strong influence on the calculation results. Limited information on the pyrolysis rate affects the results to some extent. This finding was supported from the comparison of the (admittedly few) blind and semi-blind simulations. The range of the results (e. g. JASMINE and FDS) is much larger for the blind simulations compared to the semi-blind ones. This overall result of Benchmark Exercise No. 4 should be somehow considered in the estimation of uncertainty parameters as an input in, for example PSA studies.

The simulation of under-ventilated fires is more difficult for the fire codes. In particular, the high transient behavior at the final phase of Test 3 leads to a wide range of simulation results. Unfortunately, the measured pyrolysis rate is no longer valid in this phase, and so the 'specified' pyrolysis rate may not be very reliable at this time. It should be mentioned, however, that many of the possible fire scenarios in real nuclear power plants will lead to under-ventilated conditions. Therefore, this issue should be further investigated and the models should be further improved.

Some codes have difficulties to simulate more complex targets. Most of the codes are able to simulate the material probes. The range of the results is larger compared to that for the gas temperatures. As this information is significant for estimating failures of safety related equipment, the models should be further developed and improved.

9 References

- /ALL 05/ Allelein, H.-J. et al.:
Weiterentwicklung der Rechenprogramme COCOSYS und ASTEC,
Abschlussbericht, GRS-A-3266, Gesellschaft für Anlagen- und
Reaktorsicherheit, April 2005
- /BOU 02/ Bouton, E.,
Overview of the FLAMME-S code validation matrix, Technical Note
SESHP/GME/IPS/FLS/C40/NT/02.337, 2002
- /CFX 04/ CFX-5.7, User Documentation, ANSYS Inc., USA, 2004
- /COX 87/ Cox, G., and S. Kumar:
Field modelling of fire in forced ventilated enclosures, Combustion Science
and Technology, Vol. 52, pp. 7-23, 1987
- /DEY 02/ Dey M.:
Evaluation of Fire Models for Nuclear Power Plant Applications: Cable Tray
Fires, NISTIR 6872, National Institute of Standard and Technology, USA,
June 2002
- /GAY 06/ L. GAY, B. GAUTIER
"Magic Software Version 4.1.1: Mathematical Model"
HI-82/04/024/B - March 2006
- /HOL 90/ Holen, J., M. Brostrom, and B.F. Magnusson:
Finite Difference Calculation of Pool Fires, 23rd Symposium on Combustion,
Combustion Institute, pp. 1677-1683, 1990
- /JON 04/ Jones, W.W., et al.:
CFAST - Consolidated Model of Fire Growth and Smoke Transport ,
(Version 5): Technical Reference Guide. NIST Special Publication 1030,
October 2004
- /KLE 04/ Klein-Heßling, W.:
Website: <http://techconf.llnl.gov/cgi-fire/topics>

- /MCG 04/ McGrattan, K.B. (ed.):
Fire Dynamics Simulator (Version 4), Technical Reference Guide, NIST
Special Publication 1018, National Institute of Standards and Technology,
Gaithersburg, Maryland, USA, 2004
- /MCG 06/ McGrattan, K.B.:
Evaluation of Fire Models for Nuclear Power Plant Applications: Benchmark
Exercise #3, International Panel Report, NISTIR 7338, to be published
January 2007
- /MIL 04/ Miles, S.:
International Panel Report: Benchmark Exercise # 2 - Pool Fires in Large
Halls. May 2004
- /PLY 04/ Plys, M.G., and J.L. Sung:
FATE™ 2.0: Facility Flow, Aerosol, Thermal, and Explosion Model
(Improved and Combined HANSF and HADCRT Models), FAI/04-71,
SNF-23281, Two Volumes, November 2004
- /RIE 06/ Riese, O., D. Hossler, M. Röwekamp:
Evaluation of Fire Models for Nuclear Power Plant Applications: Flame
Spread in Cable Tray Fires, International Panel Report on Benchmark
Exercise No. 5, Gesellschaft für Anlagen- und Reaktorsicherheit (GRS)
Report Number GRS-214, ISBN-Nr.: 978-3-931995-81-2, in publication,
2006
- /TOU 00/ Tourniaire, B., and L. Audouin:
Sensitivity analysis of a data reduction method estimating the interface
height, the lower and upper temperatures in fire room, Proceedings of the
International Seminar of Fire and Explosion Hazard, 2000

List of Figures

Fig. 2-1	Benchmark Exercise No.1, Part II base case - calculated oxygen concentrations.....	4
Fig. 2-2	Benchmark Exercise No. 1, Part II base case - calculated HGL temperatures	4
Fig. 2-3	3D view of the OSKAR fire compartment.....	9
Fig. 2-4	Top view of the OSKAR fire compartment	10
Fig. 2-5	Side view of the OSKAR fire compartment (in + y direction).....	11
Fig. 2-6	Side view of the OSKAR fire compartment (in + x direction).....	12
Fig. 2-7	Height of the fuel pan side walls and its elevations.....	13
Fig. 2-8	View of the fire compartment through the front door	13
Fig. 2-9	Scheme of the hood above the front door.....	14
Fig. 2-10	View onto the hood installed above the front door	14
Fig. 2-11	View of the three material probes	20
Fig. 2-12	View from top into the open barrel container	20
Fig. 2-13	Measurement positions inside barrel	21
Fig. 2-14	Typical chemical composition of fuel.....	22
Fig. 2-15	Test 1 - Measured velocities (V11 - V13).....	27
Fig. 2-16	Test 3 - Measured velocities (V11 - V13).....	28
Fig. 3-1	Fire development inside the fire compartment - Test 1, view through front door.....	31
Fig. 3-2	Temperature distribution during the fully developed fire phase - Test 1, view through front door	31
Fig. 3-3	Weight loss - Test 1	32
Fig. 3-4	Temperature distribution in measurement level 1 - Test 1	32
Fig. 3-5	Heat flux into material probes - Test 1	33
Fig. 3-6	Measured fuel temperature 3 cm above pan bottom - Test 1	33
Fig. 3-7	Temperature distribution inside the fire - Test 3.....	34
Fig. 3-8	Weight loss - Test 3	35
Fig. 3-9	Oxygen concentration in the fire compartment - Test 3	35
Fig. 3-10	Plume temperatures - Test 3.....	36
Fig. 3-11	Heat flux into the test probe structures - Test 3	36
Fig. 3-12	Temperature distribution inside the barrel during Test 3.....	37
Fig. 3-13	Temperature decrease after Test 3.....	37

Fig. 4-1	Smoothed pyrolysis rate for Test 1	40
Fig. 4-2	Smoothed pyrolysis rate for Test 3	40
Fig. 5-1	Measured and predicted (blind) heat release rates for Tests 1 and 3 (from Appendix A)	46
Fig. 5-2	Measured and predicted (blind) gas temperatures for Test 3 (from Appendix B).....	50
Fig. 5-3	Measured and predicted (blind) wall surface temperatures for Test 3 (from Appendix B)	51
Fig. 5-4	Gas temperature comparisons for Test 3 (from Appendix A).....	54
Fig. 5-5	View of flame sheet output from FDS - Test 1 (from Appendix C)	60
Fig. 5-6	Plume temperature (from Appendix C).....	60
Fig. 5-7	Measured and predicted (open) gas temperatures for Test 1 (from Appendix B).....	64
Fig. 5-8	Measured and predicted (open) wall surface temperatures for Test 1 (from Appendix B)	65
Fig. 5-9	Measured and predicted gas temperatures and door velocities for Test 1 (from Appendix B)	68
Fig. 5-10	Measured and predicted flux densities for Test 1 (from Appendix B).....	69
Fig. 5-11	'Energy budget' for a Test 3 simulation (from Appendix B)	69
Fig. 5-12	Benchmark Exercise No. 4, Test 3 smoky layer gas concentrations (from Appendix C)	74
Fig. 5-13	Gas temperature in the compartment - open calculations (from Appendix D)	77
Fig. 5-14	Vertical temperature distribution at a plane $x = 0.95$ m (from Appendix E).....	80
Fig. 5-15	Comparison of selected gas temperatures close to the front of the test facility for Test 1 (from Appendix E)	81
Fig. 5-16	Heat release rates of all FDS3 and FDS 4 calculations for Test 3 (from Appendix G)	83
Fig. 5-17	Comparison of FDS results (FDS3 coarse grid; from Appendix G).....	84
Fig. 5-18	Comparison of FDS results (FDS3 fine grid; from Appendix G).....	85
Fig. 5-19	Comparison of FDS results (FDS4 fine grid) (from Appendix G)	86
Fig. 5-20	Concept of the pyrolysis model for oil burning	88
Fig. 5-21	Test 3: Plume temperature at M3 (from Appendix H).....	90
Fig. 5-22	Comparison of measured temperature M9 ($z = 1.5$ m) and COCOSYS results (from Appendix H)	90

Fig. 5-23	Mass loss rate (smoothed) versus experiment (from Appendix I)	93
Fig. 5-24	Front room temperatures and oxygen concentration (from Appendix I)....	94
Fig. 5-25	Upper and lower temperature in Test 1 (from Appendix J)	96
Fig. 5-26	Upper and lower temperature in Test 3 (from Appendix J)	96
Fig. 6-1	Comparison of plume temperatures M2 (blind & open).....	98
Fig. 6-2	Comparison of plume temperatures M6 (blind & open).....	99
Fig. 6-3	Temperatures on the back side of the compartment (M8, blind & open)	100
Fig. 6-4	Temperatures on the back side of the compartment (M12, blind & open)	101
Fig. 6-5	Temperatures on the back side of the compartment (M16, blind & open)	102
Fig. 6-6	Temperatures on the front side of the compartment (M9, blind & open).	103
Fig. 6-7	Temperatures on the front side of the compartment (M13, blind & open)	104
Fig. 6-8	Temperatures on the front side of the compartment (M17, blind & open)	105
Fig. 6-9	Layer height (blind & open)	106
Fig. 6-10	Upper layer temperature (blind & open)	107
Fig. 6-11	Oxygen concentrations inside the fire compartment (blind & open).....	109
Fig. 6-12	CO ₂ concentrations inside the fire compartment.....	110
Fig. 6-13	Oxygen concentration outside the fire compartment (blind & open)	111
Fig. 6-14	CO ₂ concentration outside the fire compartment	112
Fig. 6-15	Probe temperatures (blind results)	114
Fig. 6-16	Probe temperatures (open results)	115
Fig. 6-17	Comparison of plume temperatures M2 (blind & open).....	117
Fig. 6-18	Comparison of plume temperatures M6 (blind & open).....	118
Fig. 6-19	Temperatures on the back of compartment (M8, blind & open)	120
Fig. 6-20	Temperatures on the back of compartment (M12, blind & open)	121
Fig. 6-21	Temperatures on the back of compartment (M16, blind & open)	122
Fig. 6-22	Temperatures on the front side of compartment (M9, blind & open).....	123
Fig. 6-23	Temperatures on the front of compartment (M13, blind & open)	124
Fig. 6-24	Temperatures on the front of compartment (M17, blind & open)	125
Fig. 6-25	Hot gas layer height (blind & open).....	127
Fig. 6-26	Upper layer temperature (blind & open)	128
Fig. 6-27	Oxygen concentration inside fire compartment (blind & open).....	130
Fig. 6-28	CO ₂ concentration inside fire compartment (blind & open)	131

Fig. 6-29	Oxygen concentration outside fire compartment (blind & open)	132
Fig. 6-30	CO ₂ concentration outside the fire compartment (blind & open)	133
Fig. 6-31	Comparison of the probe surface temperatures (blind simulations).....	135
Fig. 6-32	Comparison of the probe surface temperatures (open simulations)	136

List of Tables

Table 2-1	Composition of the wall structures	7
Table 2-2	Properties of the fire compartment materials	7
Table 2-3	Properties of the target materials	8
Table 2-4	Location of the material probes	8
Table 2-5	List of measurements performed	16
Table 2-6	Fuel material properties	22
Table 2-7	Smoothed values for the total volume flow and velocity through the FUCHS fan system (measurements V11 and V12) for Test 1	23
Table 2-8	Smoothed values for the total volume flow and velocity through the FUCHS fan system (measurements V11 and V12) for Test 3	24
Table 2-9	Smoothed values for the total volume flow and velocity through the hood (measurement V13) for Test 1	25
Table 2-10	Smoothed table values for the total volume flow and velocity through the hood (measurement V13) for Test 3	26
Table 2-11	Initial and ambient conditions	26
Table 3-1	Test matrix of the iBMB fuel pool fire tests.....	29
Table 5-1	List of fire simulations performed within Benchmark Exercise No. 4.....	43

List of Appendices:

- Appendix A: Benchmark Exercise No. 4 Simulations with FDS
- Appendix B: Benchmark Exercise No. 4 Simulations with JAMINE and CFAST
- Appendix C: Validation of the CFAST and FDS Fire Models with Large Fire Experiments in a Compartment
- Appendix D: FATE™ 2.0 Computer Code Calculations for Benchmark Exercise No. 4
- Appendix E: Benchmark Exercise No. 4: Kerosene Pool Fire Inside A Compartment
- Appendix F: CFX5 Simulations for Benchmark Exercise No. 4
- Appendix G: FDS Simulations for Benchmark Exercise No. 4
- Appendix H: CCOCOSYS Simulations for Benchmark Exercise No. 4
- Appendix I: Vulcan Simulations of ICFMP Benchmark Exercise No. 4, Test 3
- Appendix J: Kerosene pool fire inside a compartment Simulation with MAGIC

Acknowledgments

In addition to the analysts identified in the appendices of this report, who performed the calculations for Benchmark Exercise No. 4, several experts from various organizations contributed to this Benchmark Exercise in many ways. The test series used was co-sponsored by the German Federal Ministry for Economy and Labor (BMWA) within the frame of the project RS 1146, the German Federal Ministry for the Environment, Nature Conservation and Nuclear Safety (BMU) and the German Federal Authority for Radiation Protection (BfS) within the frame of the projects SR 2449 and SR 2491. The tests were performed by Institut für Baustoffe, Massivbau und Brandschutz (iBMB) of Braunschweig University of Technology sub-contracted by GRS.

Dietmar Hossler, Reinhold Dobbernack, Olaf Riese and Hans-Joachim Wolff were the key iBMB staff for the test series. Jonathan Barnett at WPI, USA, Olavi Keski-Rahkonen and Simo Hostikka at VTT, Finland, as well as James Oldham and Doug Brandes at Duke Energy, USA hosted the 7th, 8th and 9th ICFMP meetings, where this Benchmark Exercise was planned and discussed, and also provided peer reviews and technical support. Monideep Dey at NRC/NIST, USA and Marina Röwekamp at GRS, Germany provided project management and technical support to the ICFMP group.

Heinz Peter Berg from BfS, Germany, Monideep Dey, USA, Stewart Miles from BRE, UK, and further members of the institutions participating in the ICFMP project all contributed to this Benchmark Exercise either by providing peer comments, participating in meetings to discuss the test plan and results, or indirectly by sponsoring participants for the project. Benchmark Exercise No. 4 and its corresponding documentation would not have been possible without the help and expertise of all the above.

Appendix A: International Collaborative Project to Evaluate Fire Models for Nuclear Power Plant Applications

Benchmark Exercise No. 4 Simulations with FDS

Presented by

Kevin McGrattan

National Institute for Standards and Technology (NIST)

100 Bureau Drive, Gaithersburg, MD 20899, U.S.A.

Contents

A1	Introduction	1
A2	Input Parameters and Assumptions.....	3
A2.1	Geometry	3
A2.2	Fire	5
A2.3	Radiation	6
A2.4	Ventilation	6
A2.5	Output	6
A3	Comparison of Model Prediction and Measurement	7
A3.1	Heat Release Rate.....	7
A3.2	Gas Temperatures	9
A3.3	Heat Flux and Surface Temperature at the Three Targets	16
A3.4	Gas Species Concentrations.....	21
A3.5	Velocity.....	24
A3.6	Model Sensitivity	27
A4	General Conclusions and Recommendations.....	35
A4.1	General Conclusions.....	35
A4.2	Recommendations	36
A5	References.....	39
	List of Figures	41

A1 Introduction

Benchmark Exercise No. 4 was used to assess the accuracy of the Fire Dynamics Simulator (FDS) in two ways. First, blind calculations were performed to predict the heat release rate of the fire using only its chemical and thermal properties as input. Second, semi-blind calculations were performed in which the measured heat release rate was provided as model input, and predictions were made of the temperatures, heat fluxes and gas composition within the compartment. It is important to emphasize that from the standpoint of validation, the model predictions of heat release rate and transport were assessed separately. Previous Benchmark Exercises have provided data for assessment of transport algorithms only. In Exercise No. 4, the additional challenge of *predicting*, rather than *prescribing*, the HRR has been added.

A2 Input Parameters and Assumptions

In cooperation with the fire protection engineering community, a computational fire model, Fire Dynamics Simulator (FDS), has been developed at the National Institute of Standards and Technology (NIST) in the USA to study fire behaviour and to evaluate the performance of fire protection systems in buildings. The software was released into the public domain in 2000, and since then has been used for a wide variety of analyses by fire protection engineers. A complete description of the model can be found in /MCG 04/. Briefly, FDS is a computational fluid dynamics code that solves the Navier-Stokes equations in low Mach number, or thermally-expandable, form. The transport algorithm is based on large eddy simulation techniques, radiation is modelled using a gray gas approximation and a finite-volume method is used to solve the radiation transport equation. Combustion is modelled using a mixture fraction approach, in which a single transport equation is solved for a scalar variable representing the fraction of gas originating in the fuel stream. In this section, the most important features of the simulations of Benchmark Exercise No. 4 are described.

A2.1 Geometry

The geometry of the compartment was relatively simple. The overall enclosure was rectangular, as were the vents and most of the obstructions. A single, rectilinear grid spanned the interior of the compartment, plus a comparable volume under the hood outside the door. The dimensions of the grid were 36 by 72 by 56, and the cells were exactly 10 cm in size throughout. All objects within the computational domain were approximated to the nearest 10 cm. The decision to use a 10 cm grid was based on the observation that the ratio of the fire's characteristic diameter D^* to the size of the grid cell dx is an indicator of the degree of resolution achieved by the simulation. D^* is given by the expression $(\dot{Q} / \rho_{\infty} c_p T_{\infty} \sqrt{g})^{2/5}$, and was about 1 m for this series of fires. In short, the greater the ratio D^*/dx , the more the fire dynamics are resolved directly, and the more accurate the simulation. Past experience has shown that a ratio of 10 produces favourable results at a moderate computational cost /MCG 03/.

FDS performs a one-dimensional heat transfer calculation into an assumed homogeneous material of given thickness and (temperature-dependent) thermal properties. Solid obstructions within the computational domain must conform to the underlying gas

phase grid, but the assumed thickness of the solid is not tied to the gas phase grid. Thus, the solid phase heat transfer calculation is entirely decoupled from the gas phase except for the transfer of mass and heat at the gas-solid interface.

The compartment walls and ceiling were made of various types of concrete, the thermal properties of which were input directly into the model. It was assumed that the target slabs of concrete, aerated concrete, and steel were only exposed at the front surface, although the internal temperature measurements suggested otherwise.

NIST

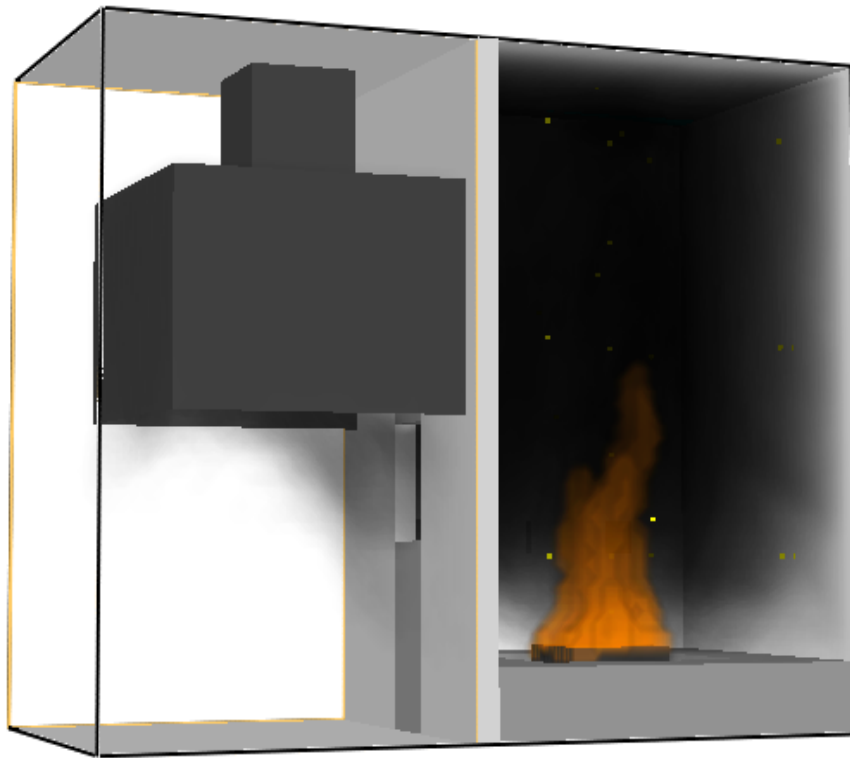


Fig. A1 Simulation of Test 3, showing the fire and smoke in Smokeview

No attempt was made to model the barrel container at the rear of the compartment for two reasons. First, the cylindrical object would have had to be approximated as a series of 10 cm rectangular blocks, and second, the current version of the model cannot accommodate solid objects with multiple layers of different materials. The first limitation could have been overcome, but the second could not have. Even were the model to

predict inner barrel temperatures close to the measurements, there would have been no way to explain why. Often reasonable predictions of solid object temperatures are made with numerical models resulting purely from two errors which off-set each other. More discussion of this is included later.

A2.2 Fire

Some of the properties of the liquid fuel used in the tests were provided. Nominally kerosene, the fuel properties of “dodecane” ($C_{11.64}H_{25.29}$) were input into the model with assumed soot and CO yields of 0.042 and 0.012, respectively. The current version of FDS does not adjust the soot or CO yield as a consequence of reduced compartment ventilation or combustion efficiency. FDS does assume the fuel to evaporate at a rate dictated by the partial pressure of fuel vapors above the pan, but it does not account for convective currents within the liquid fuel itself. The liquid is treated as a solid for the purpose of predicting the temperature profile at and below the fuel surface. The thermal conductivity of the liquid was designated in the test specification to be 0.109 W/m/K, specific heat 2.4 kJ/kg/K, and density 810 kg/m³. These values are typical of liquid hydrocarbons and have not been seen to affect the results of the calculations significantly /HOS 03/. More important was the assumed heat of vaporization and boiling temperature: 256 kJ/kg and 216 °C, respectively.¹

The fire was simulated by including in the simulation a small, hot block that heated up the surface of the pool until the fire was self-sustaining, after which the block literally disappeared from the calculation. FDS predicted the radiative and convective heat flux from the fire to the fuel surface, and the evaporation of the fuel according to the Clausius-Clapeyron equilibrium pressure of the fuel vapors above the pan (details in /MCG 04/). This coupling of the gas and liquid phases is the most challenging problem for any fire model because errors in any of the respective stages are compounded by the feedback loop. Nevertheless, it is of fundamental importance to the study and simulation of fire.

¹ The heat of vaporization and boiling temperature of n-dodecane ($C_{12}H_{26}$) were obtained from the Korea Thermophysical Properties Database (<http://www.thermo.org/kdb>).

A2.3 Radiation

FDS uses a finite volume method to solve the radiation transport equation in the gray gas limit. By default, the radiation from the fire and hot gases is tracked in 100 directions. While this is adequate to predict the radiation heat flux to nearby targets (a few fire diameters away), it is not adequate to predict the flux to distant targets (greater than three diameters, roughly). Because all of the targets were relatively close to the fire, there was no need to modify the default settings of the radiation solver.

A2.4 Ventilation

The ventilation rates for all the compartment fans and hood were input directly into the model. The volume flow time histories were used rather than the velocities because FDS must adjust all vents to conform to the numerical grid. By working with the volume flux, the model can adjust the vent velocity to achieve the desired flow.

A2.5 Output

During the simulation, values of temperature, heat flux and gas species concentrations, *etc.*, were reported as 10 s averages. Linear interpolation was used to approximate values between the 10 cm grid cells. The results were saved in a text file and compared with the measurements. Details about each quantity saved are given in the next section.

A3 Comparison of Model Prediction and Measurement

Blind and semi-blind predictions of Tests 1 and 3 were performed with FDS. The objective of the blind calculations was to predict the heat release rate from the fires. The semi-blind calculations used a *prescribed* heat release rate based on experimental measurement. The blind calculations will only be discussed in the section entitled Heat Release Rate. Following this section, all results will be for the semi-blind calculations.

A3.1 Heat Release Rate

Fig. A2 shows the predicted and measured heat release rates for Tests 1 and 3. For Test 1, the predicted HRR rose very quickly to about 3 MW following ignition, followed by a gradual rise over 15 min as the compartment heated up and the increased thermal radiation from the hot upper layer led to an increased burning rate. The measured HRR did not exhibit the rapid rise, taking several minutes to grow to 3 MW and then gradually increasing at a rate comparable to the prediction. The reason for the discrepancy is that FDS uses a mixture fraction model of combustion. Briefly, the evaporated fuel burns readily with oxygen when mixed to the appropriate ratio, *regardless of temperature*. Thus, FDS did not simulate properly the spreading of the fire across the pan, rather it predicted an almost instantaneous involvement of the entire fuel surface.

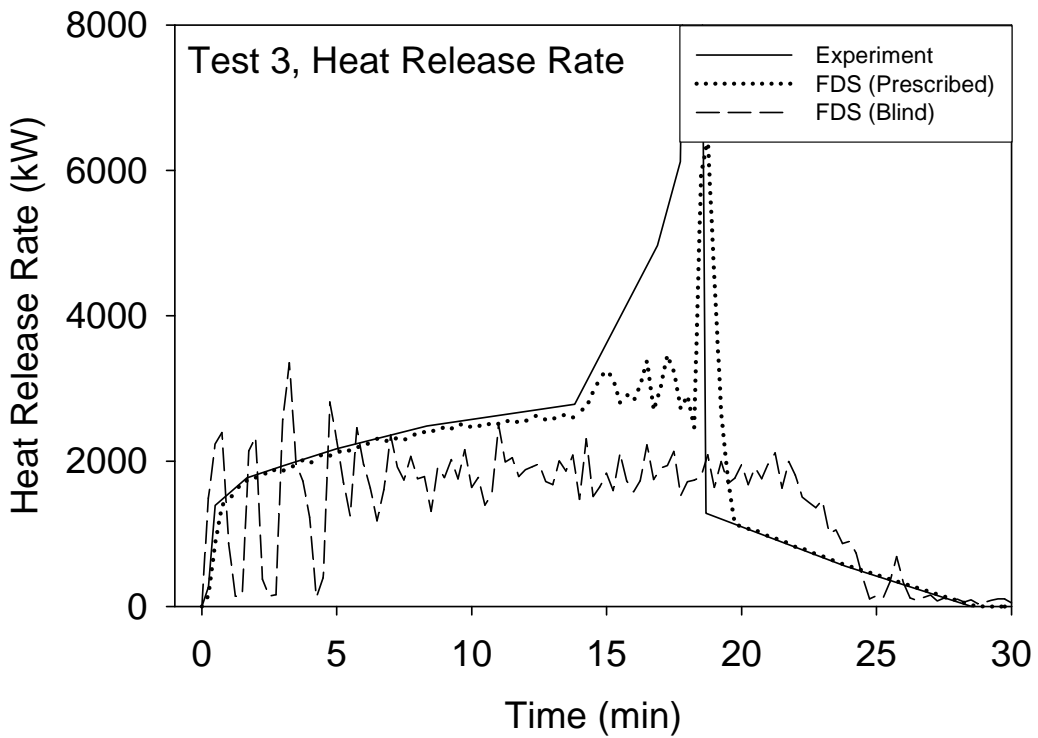
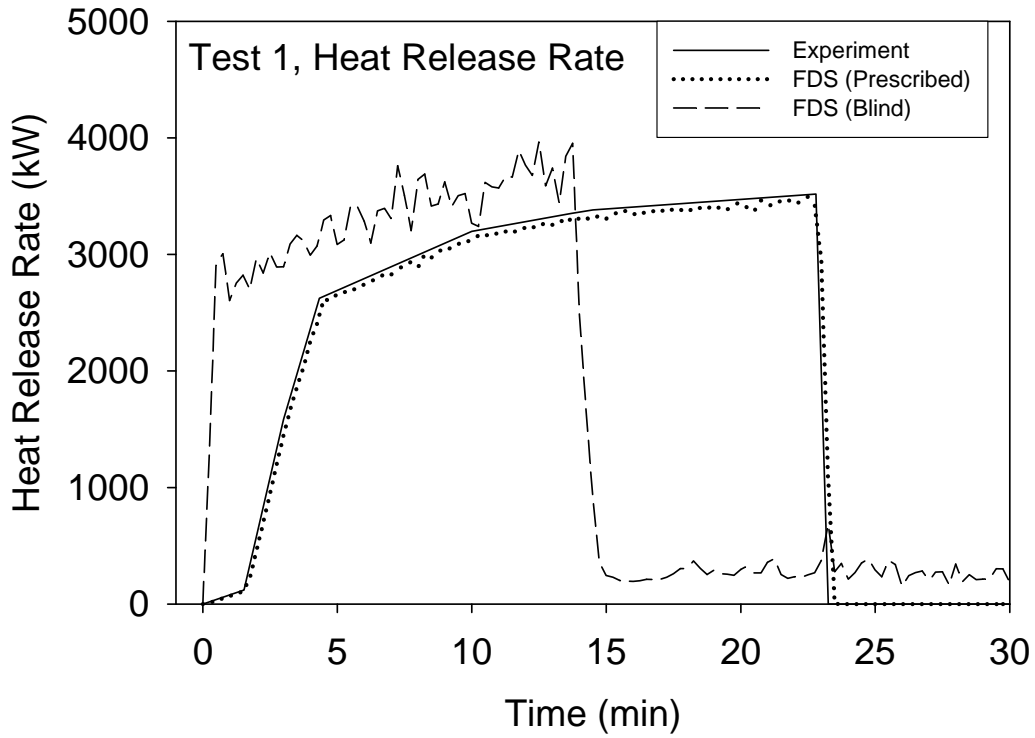


Fig. A2 Measured and predicted (blind) heat release rates for Tests 1 and 3

In Test 3, FDS over-emphasized the effect of the small compartment opening. Initially, it predicted the same rapid growth as it had in Test 1, but then the fire consumed the

available oxygen, and the fire died down, decreasing the burning rate. As air began to re-enter the compartment, the burning rate increased again, and the oscillatory pattern emerged. FDS never predicted the large spike in HRR that was measured at 15 min, most likely because the model was predicting a substantial amount of burning outside the compartment, even though this was not observed in the experiment. Thus in Test 3, there were two problems to contend with – predicting the HRR and modelling combustion in an under-ventilated compartment. Nothing more can be said of the first issue because there were no measurements made with which to assess the accuracy of the heat feedback to the fuel surface, surface temperature, fuel vapour concentration above the pool, *etc.* However, studies of burning liquid pools have been performed with FDS, in which the burning rates have been shown to be sensitive to grid size, fuel properties, radiation assumptions, and edge effects of the pan itself /HOS 03/.

From this point on, the results to be shown are based on simulations performed with a *prescribed*, not a *predicted*, heat release rate.

A3.2 Gas Temperatures

Gas temperatures were measured in the experiments using five vertical thermocouple arrays (or “trees”) distributed throughout the compartment. Fig. A5 and Fig. A8 display the time histories of both measured and predicted compartment gas temperatures². A means of assessing the accuracy of the model is to first consider the accuracy of the prescribed heat release rate. According to an empirical correlation by McCaffrey, Quintiere and Harkleroad /WAL 03/, the rise in the upper layer gas temperature is proportional to the HRR raised to the 2/3 power. The reported uncertainty in the heat release rate measurement for Tests 1 and 3 was 15 %. This uncertainty in the HRR corresponds to a $2/3 \times 15 \% = 10 \%$ uncertainty in the temperature rise. For example, temperatures of approximately 600 °C have an uncertainty of roughly ± 60 °C. In general, the difference between measured and predicted compartment temperatures in Tests 1 and 3 was within the uncertainty bounds established by the *prescribed* HRR, but there were some exceptions, especially in Test 3. In making comparisons between model and experiment, the temperatures were compared from 10 min onwards. Earlier in the

² No attempt was made to “correct” the gas temperature predictions to account for the thermal inertia of the thermocouples used in the experiments.

tests, the measured temperatures exhibited a delay relative to the predictions, probably due to the thermal inertia of the thermocouples.

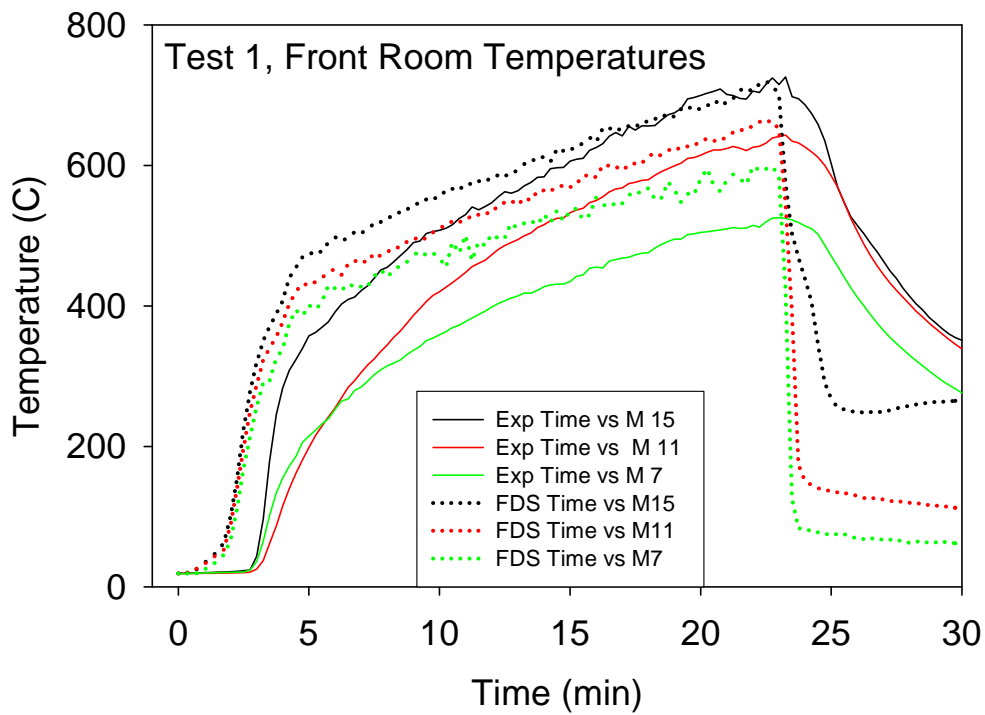
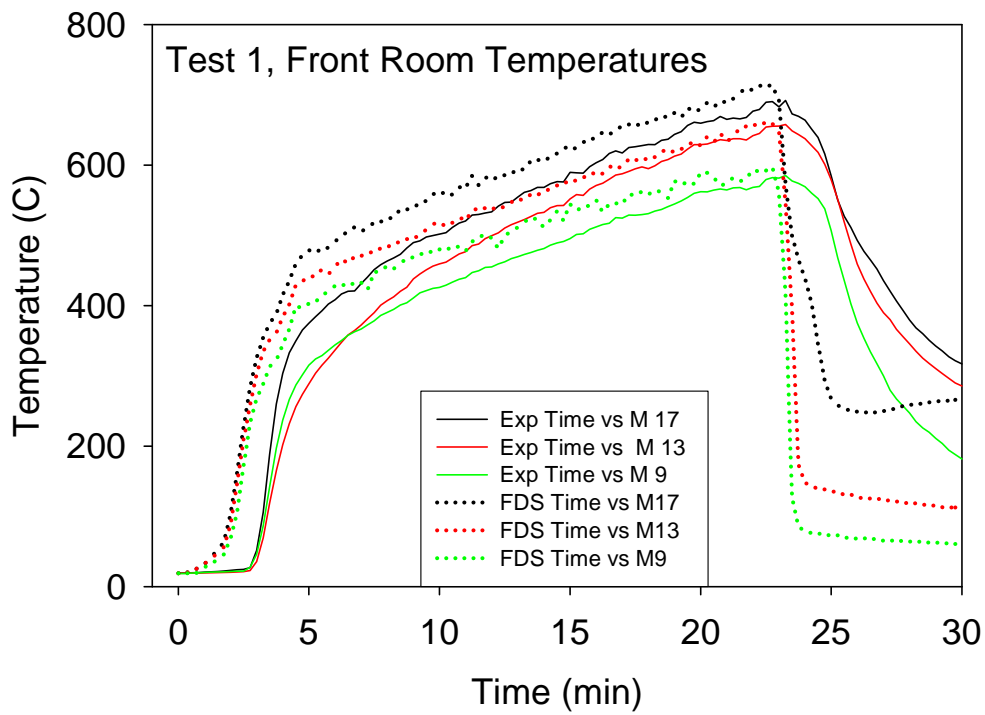


Fig. A3 Gas temperature comparisons for Test 1

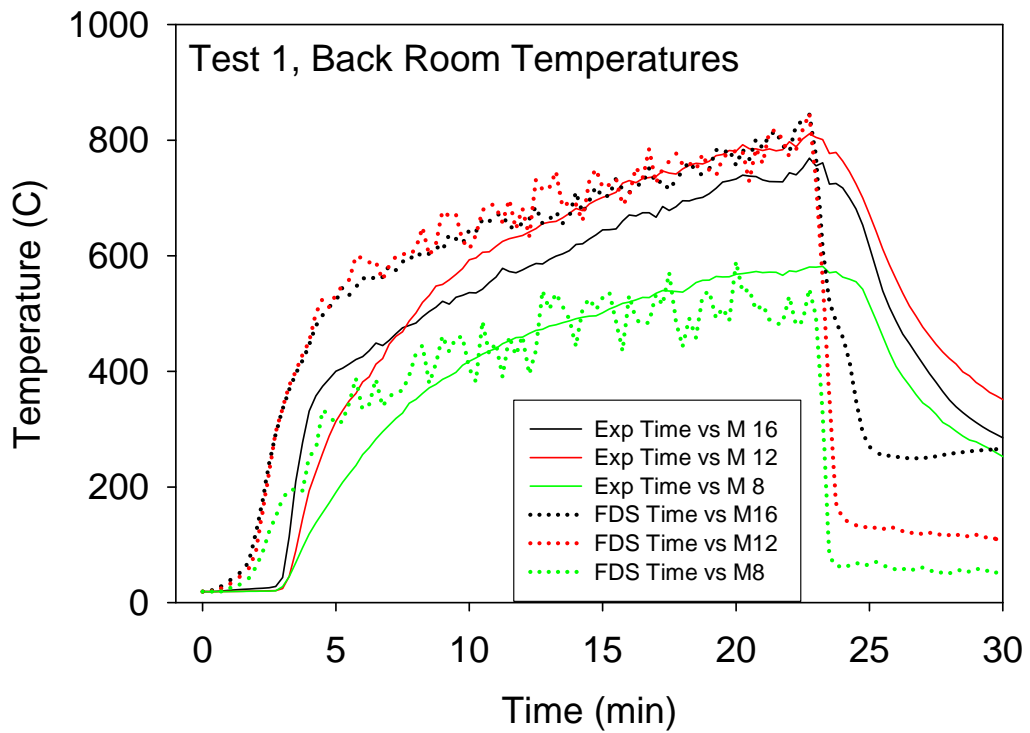
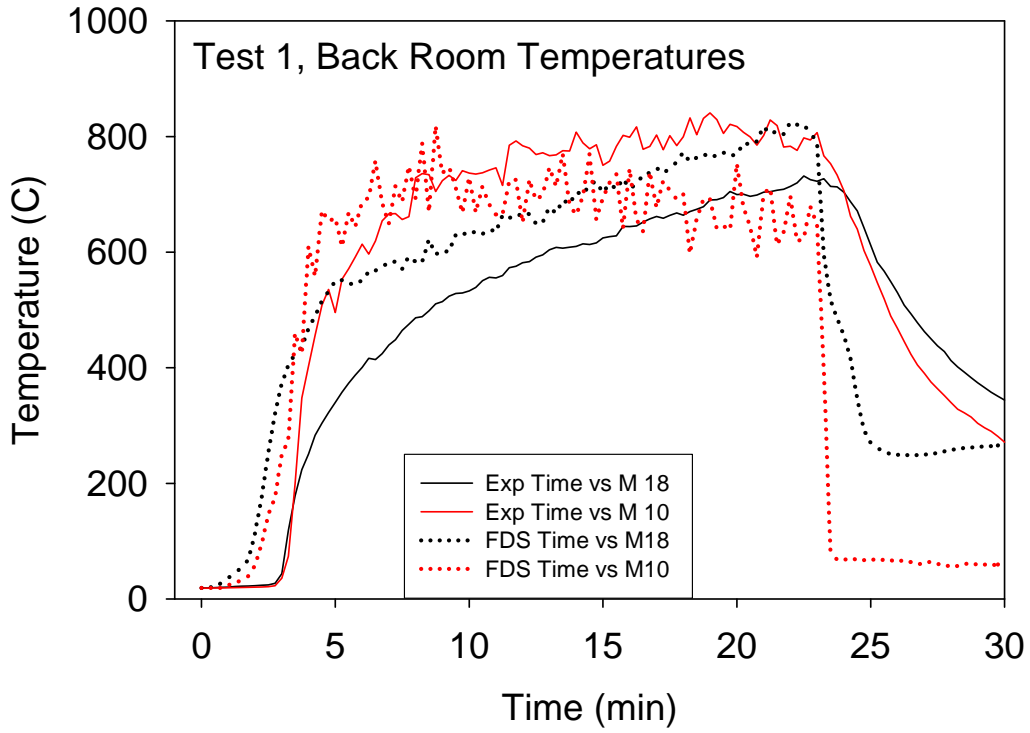


Fig. A4 Gas temperature comparisons for Test 1 (contd.)

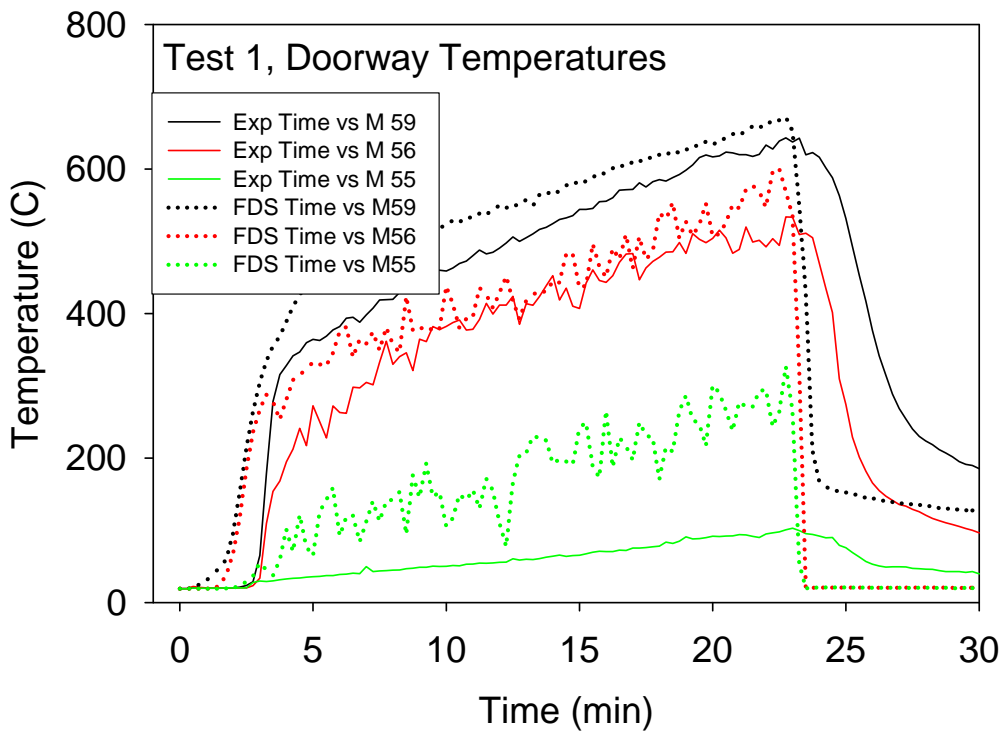
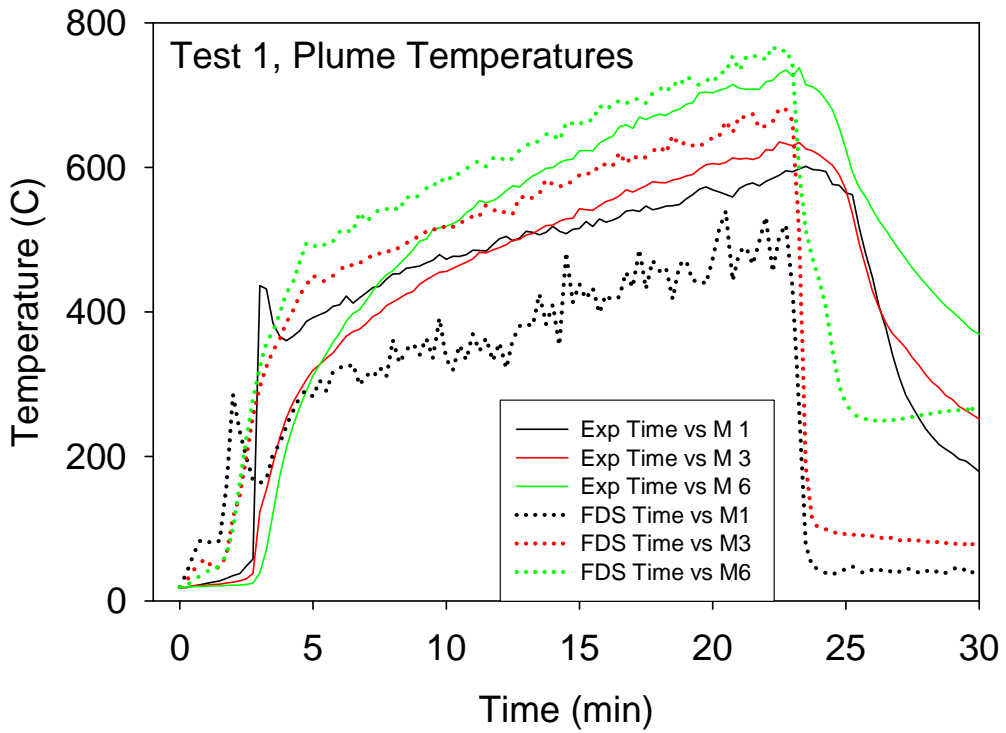


Fig. A5 Gas temperature comparisons for Test 1 (contd.)

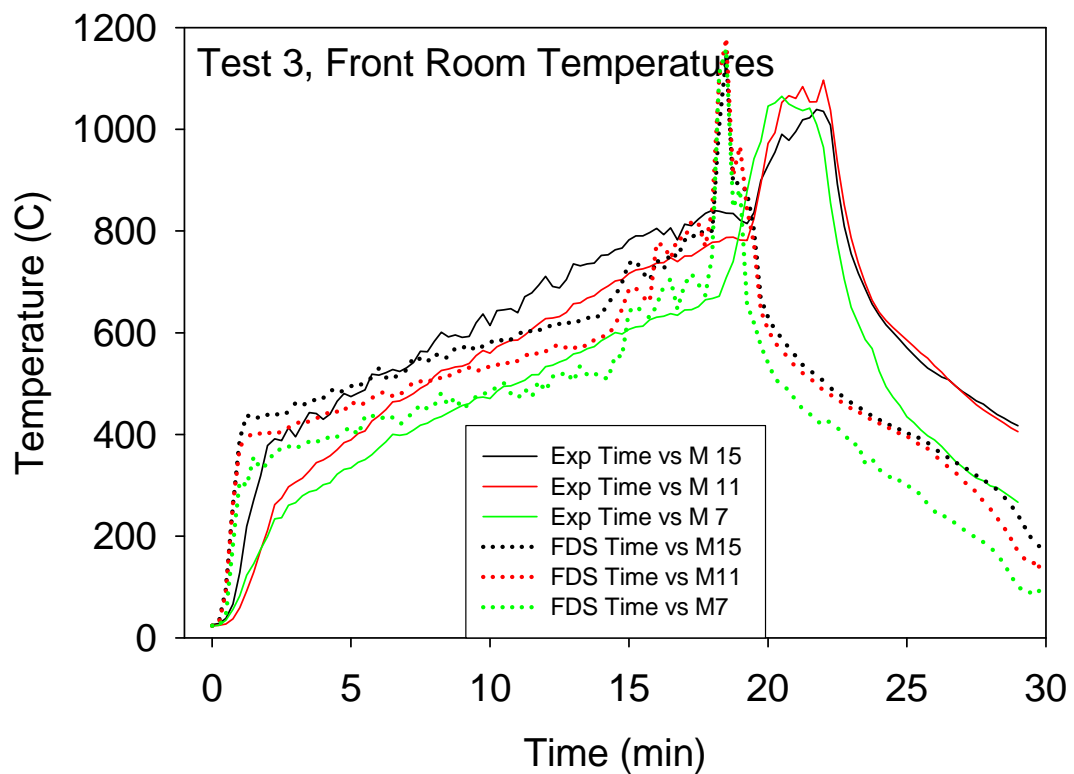
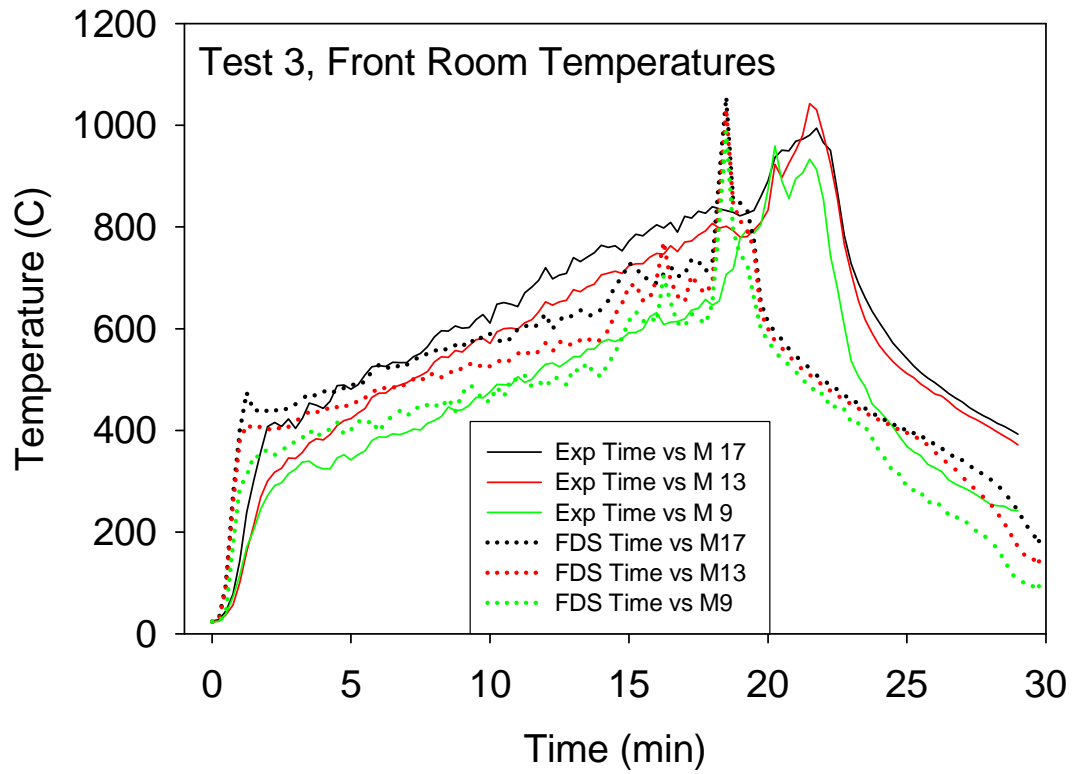


Fig. A6 Gas temperature comparisons for Test 3

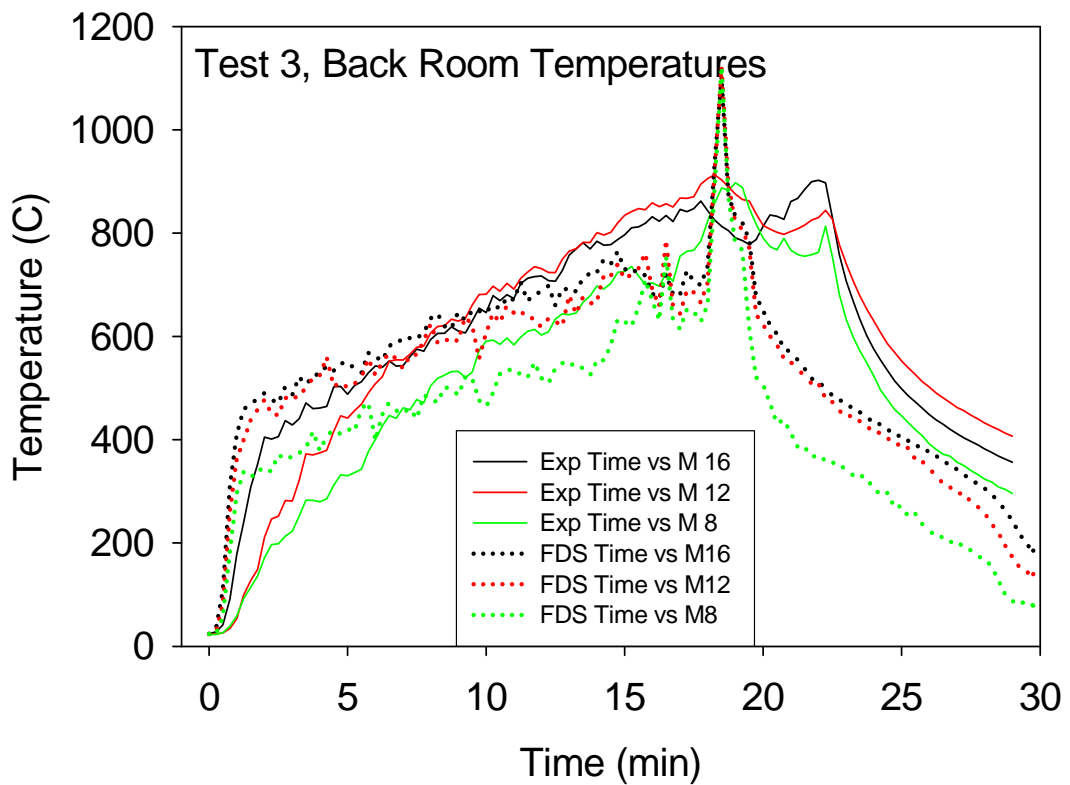
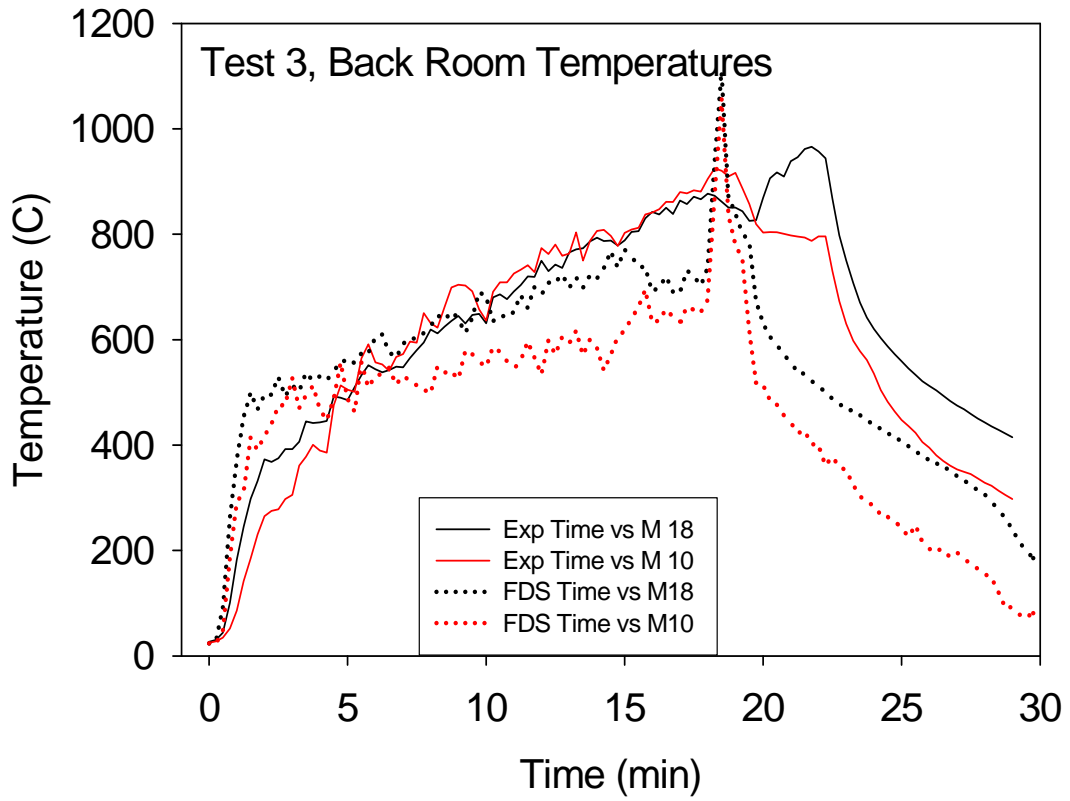


Fig. A7 Gas temperature comparisons for Test 3 (contd.)

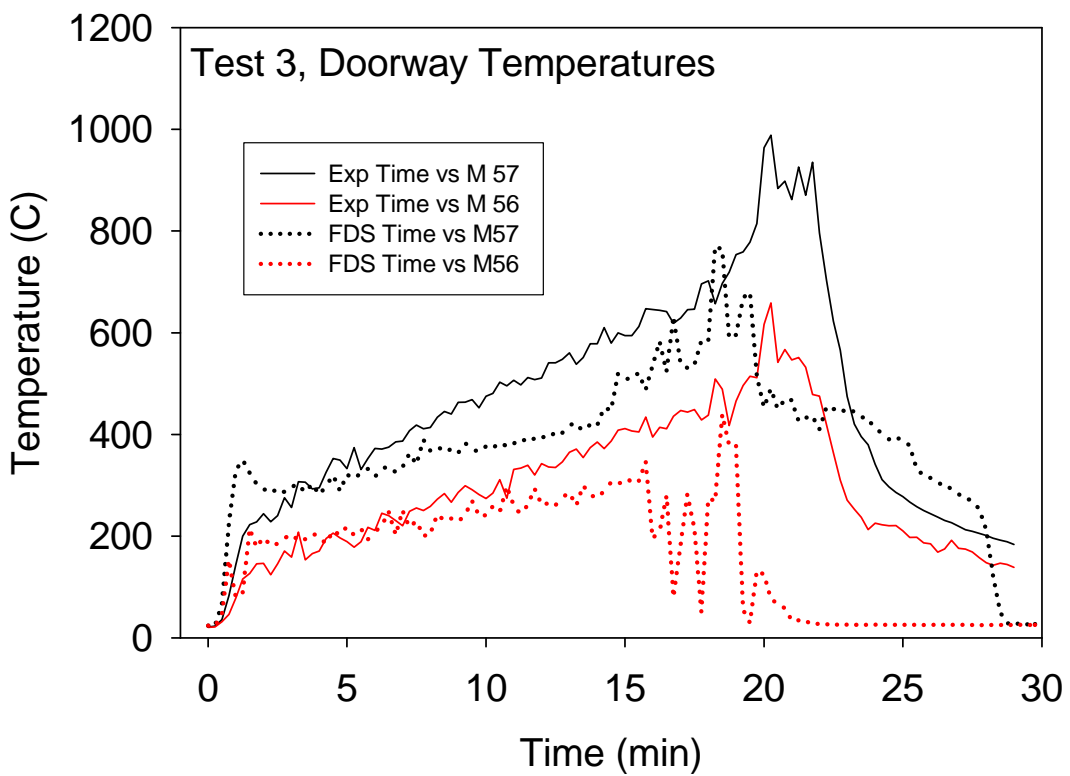
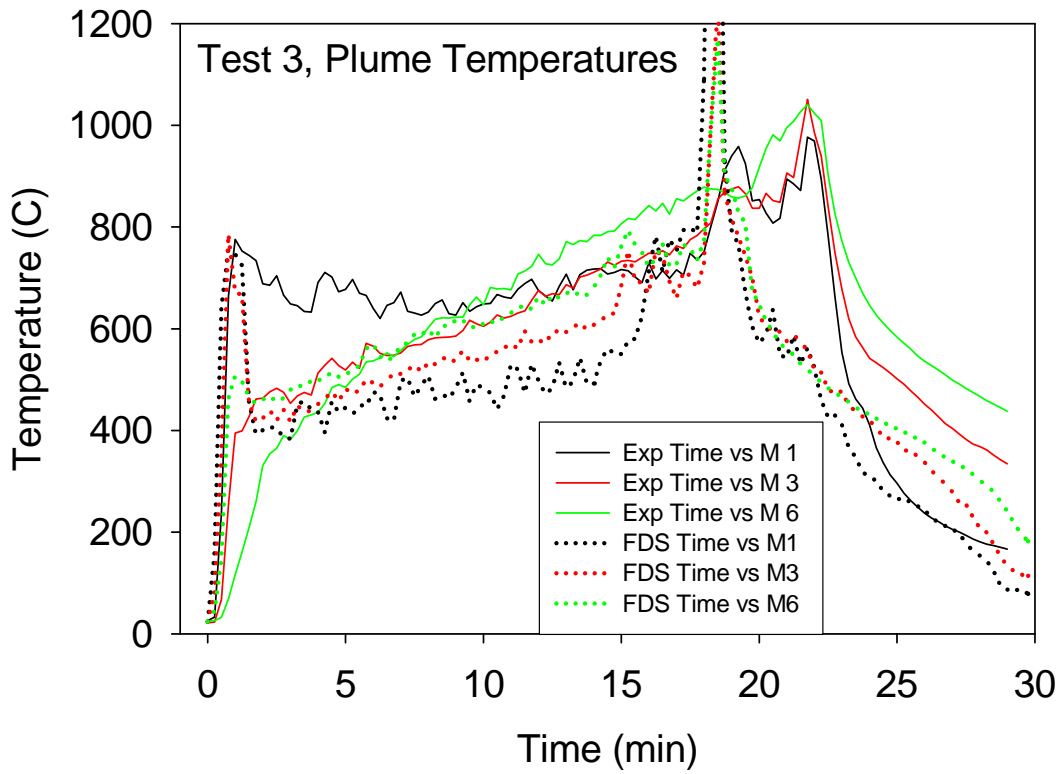


Fig. A8 Gas temperature comparisons for Test 3 (contd.)

A3.3 Heat Flux and Surface Temperature at the Three Targets

Three plates were positioned on the side wall of the compartment, about 1.7 m above the floor. At these three “targets” heat flux gauges were positioned, along with thermocouples on the surface and at various depths inside the slabs. Comparisons between measured and predicted heat fluxes and surface temperatures are shown in Fig. A12. Only the surface temperatures of the steel, concrete, and “gas concrete” are shown. FDS did compute the inner temperatures of the slabs, and the temperatures decreased monotonically with depth since FDS considered the slab to back up to an ambient temperature environment. However, the measured temperatures did not decrease monotonically, either because of a measurement error or the slab might have been heated from behind.

For some of the comparisons, it was possible to assess why a surface temperature was over or under-predicted. For example, in Test 1, the steel temperature is over-predicted, as is the heat flux. The steel target was positioned towards the back of the compartment, and the model predicted that the fire would have leaned towards the target in response to the flow coming in the door. It seems that the effect was not as pronounced in the experiments, possibly due to the presence of the barrel container that was omitted from the FDS simulations.

Overall, it was difficult to provide a single assessment of accuracy in the target temperature prediction based solely on the data shown here. In some situations, the predicted surface temperature was more accurate than the predicted heat flux, suggesting either that the heat flux measurement was inaccurate, or that the model benefited from “two wrongs making a right”; that is, an under or over-prediction in the heat flux was compensated by a comparable error in the surface properties or solid phase heat transfer calculation. Given the considerable uncertainty in any large scale fire experiment, this situation occurs more than one would expect.

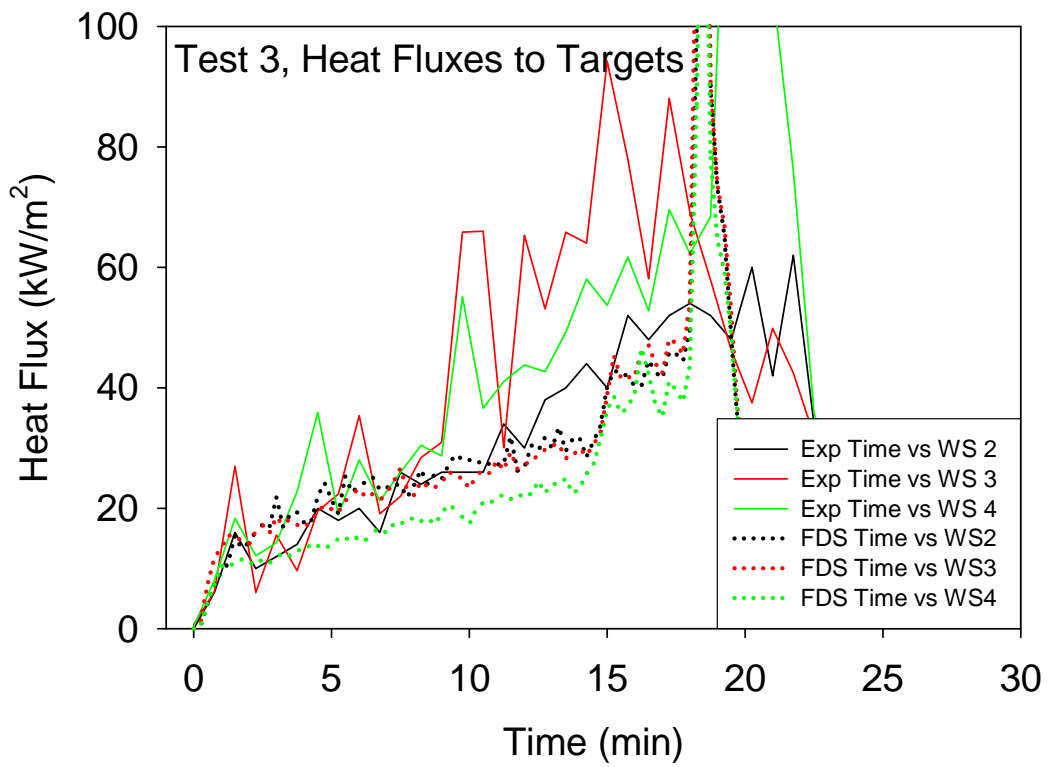
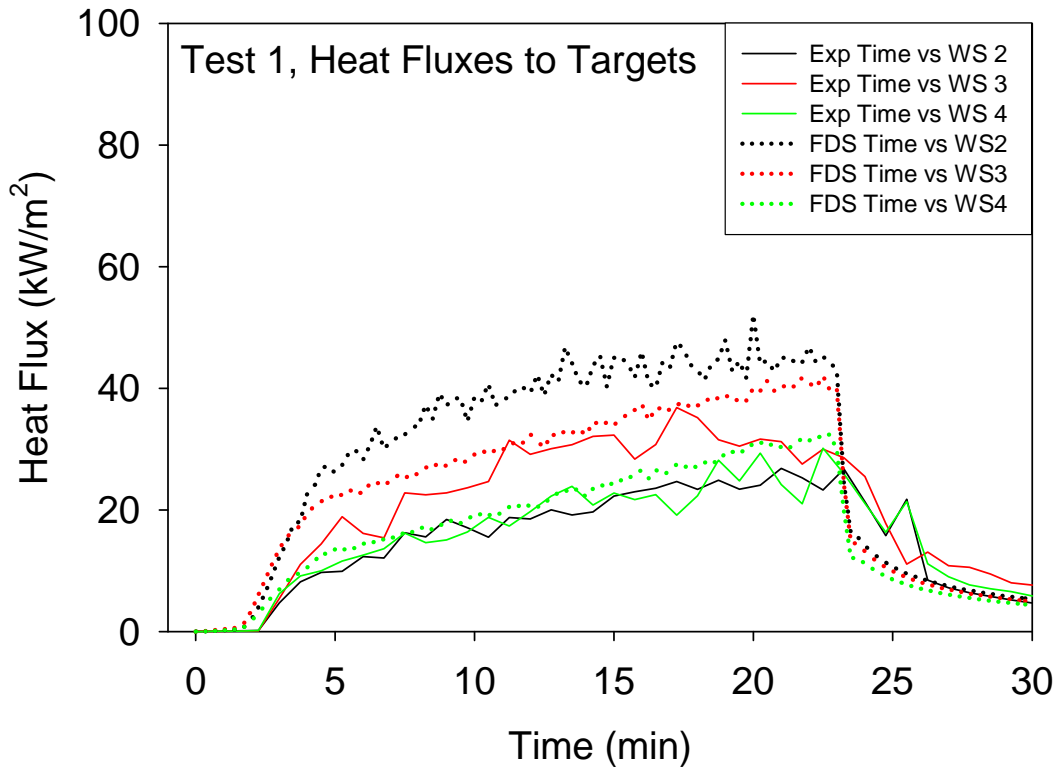


Fig. A9 Heat flux and surface temperature at Targets, Tests 1 and 3

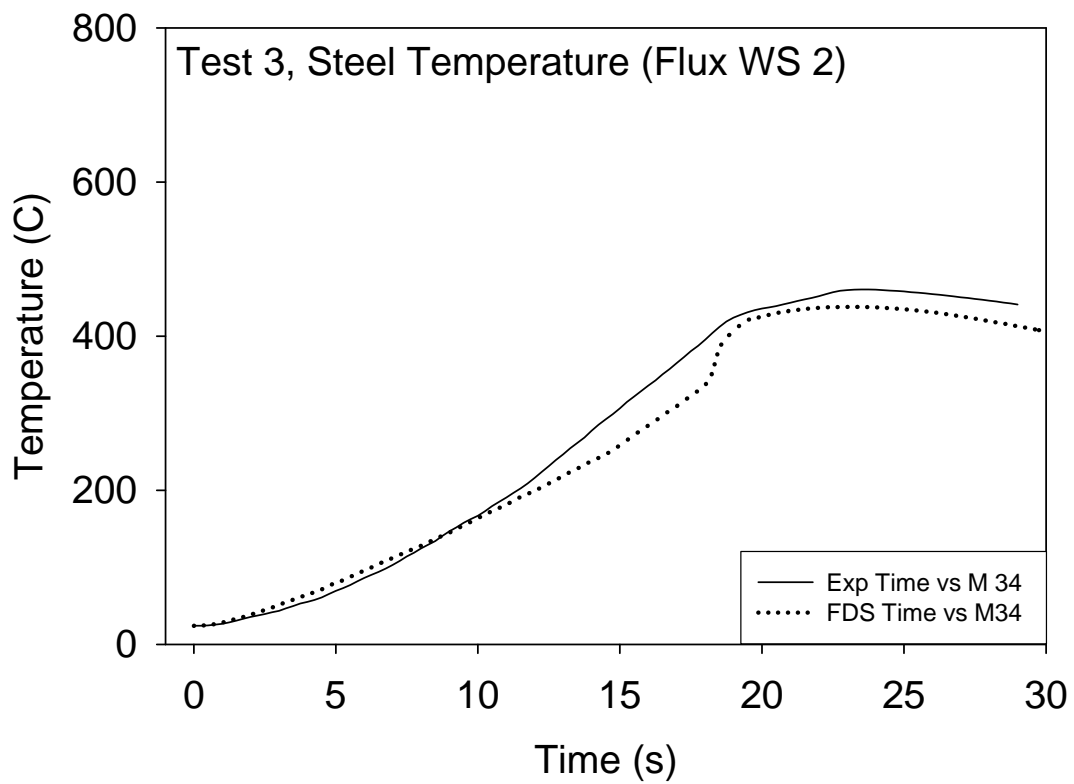
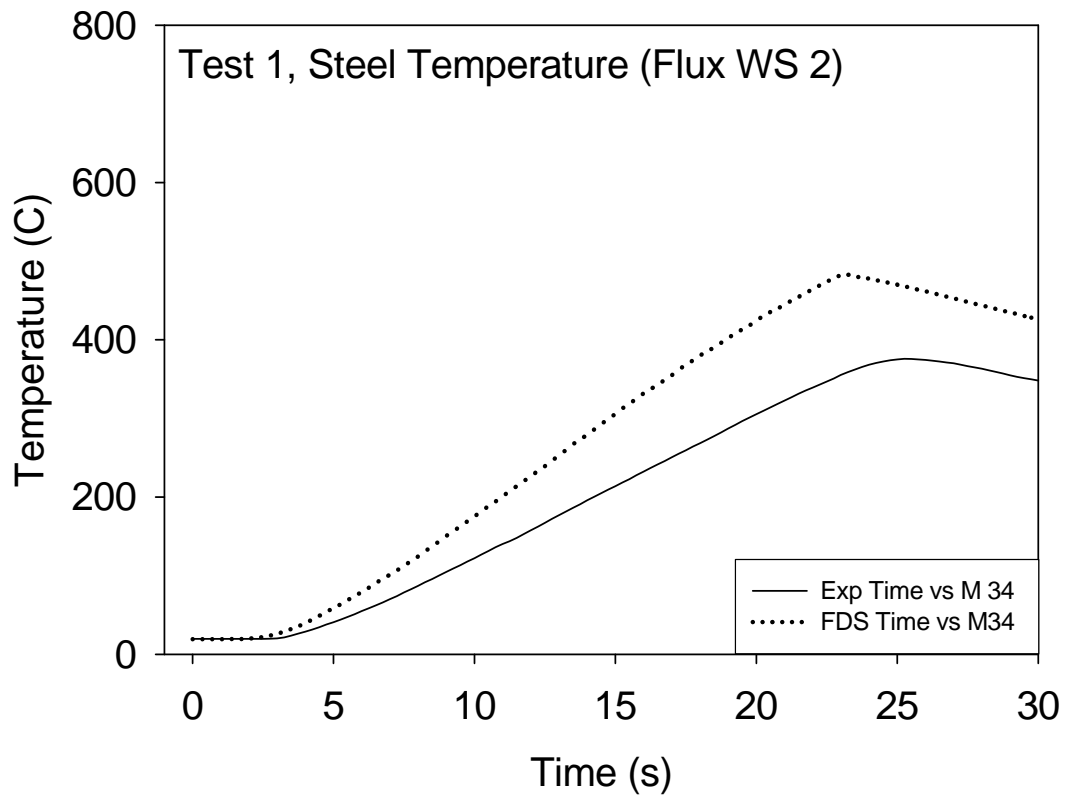


Fig. A10 Heat flux and surface temperature at Targets, Tests 1 and 3 (contd.)

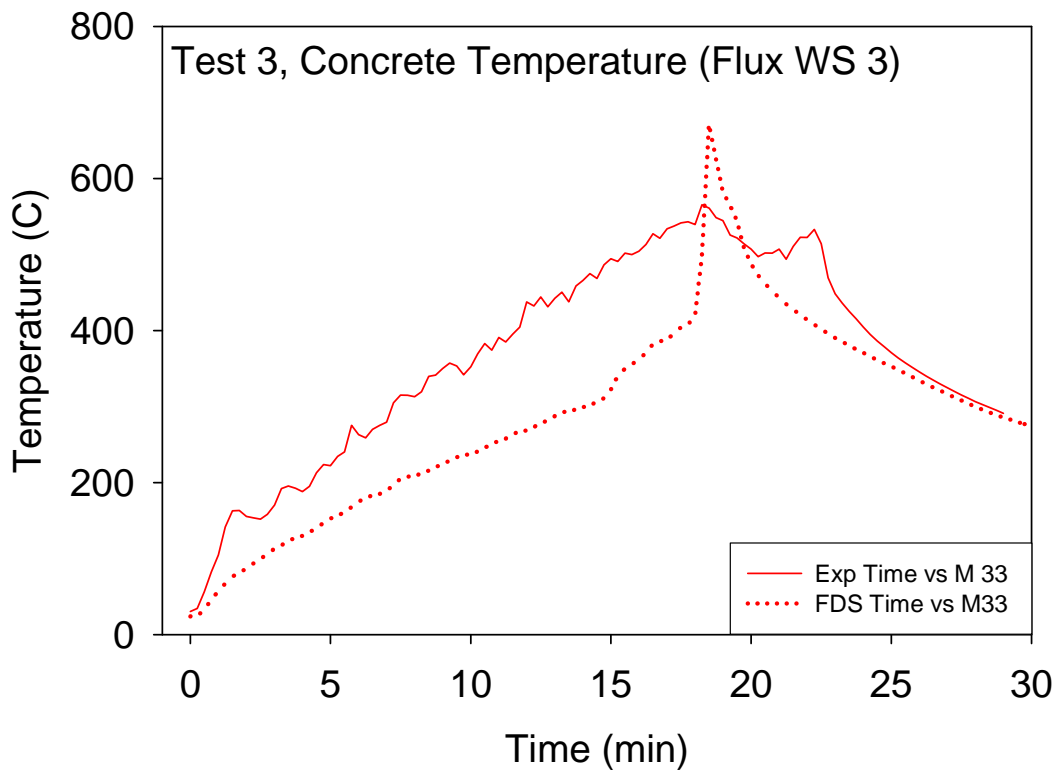
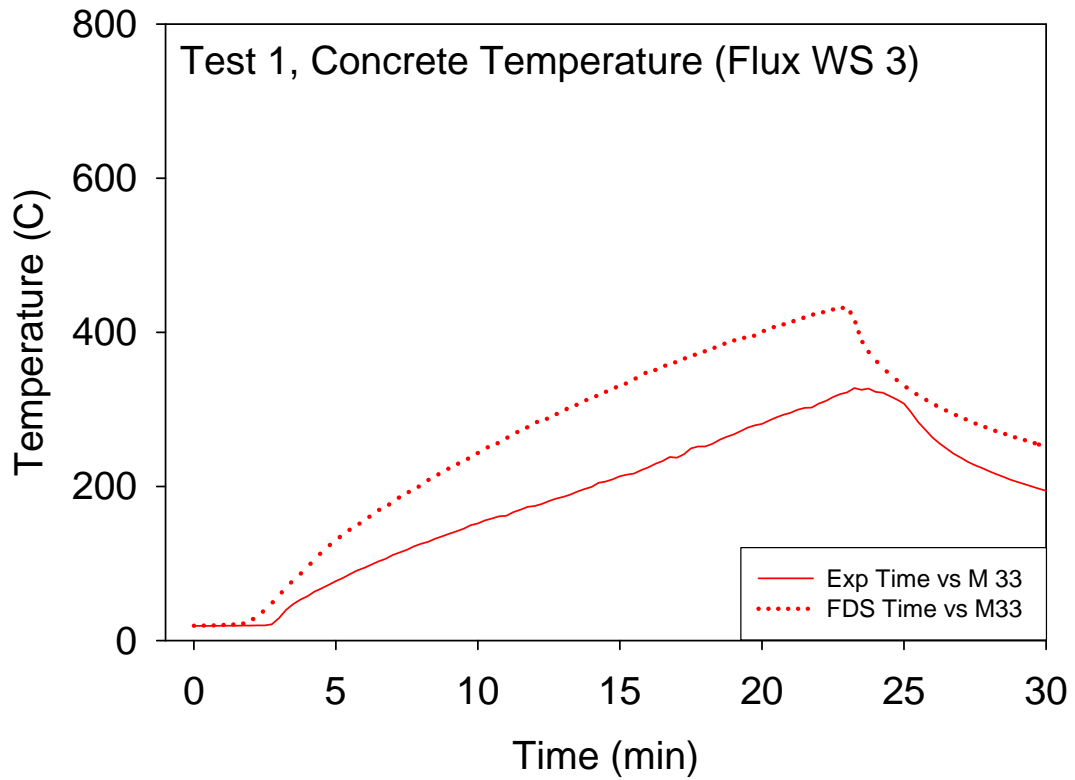


Fig. A11 Heat flux and surface temperature at Targets, Tests 1 and 3 (contd.)

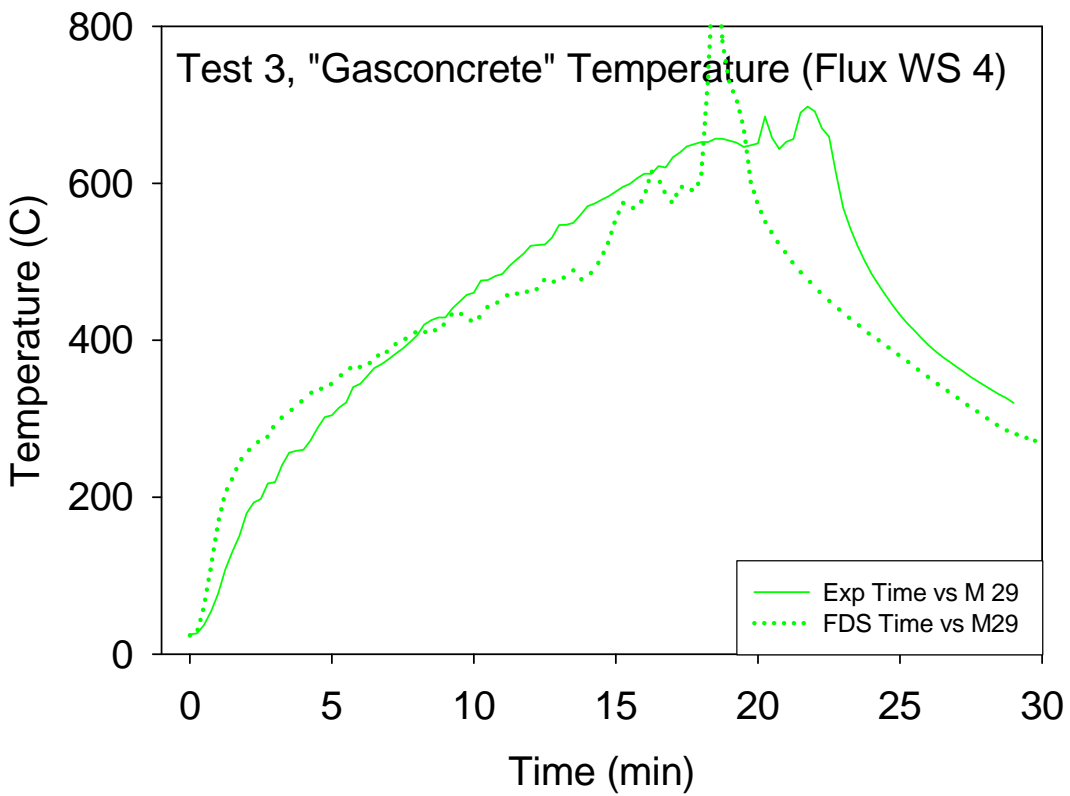
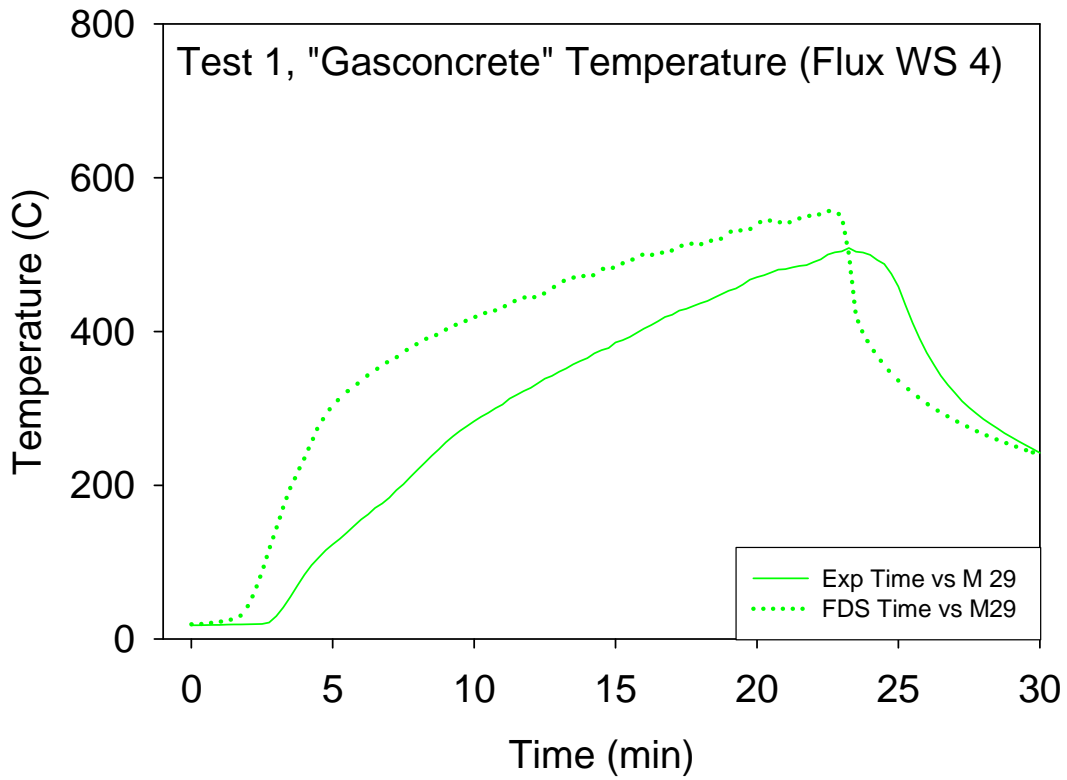


Fig. A12 Heat flux and surface temperature at Targets, Tests 1 and 3 (contd.)

A3.4 Gas Species Concentrations

FDS uses a mixture fraction combustion model, meaning that all gas species within the compartment are assumed to be functions of a single scalar variable. FDS solves only one transport equation for this variable, and reports gas concentrations at any given point at any given time by extracting its value from a pre-computed “look-up table.” For the major species, like carbon dioxide and oxygen, the predictions are essentially an indicator of how well FDS is predicting the bulk transport of combustion products throughout the space. For minor species, like carbon monoxide, FDS at the present time does not account for changes in combustion efficiency, relying only on a fixed yield of CO from the combustion product. In reality, the generation rate of CO changes depending on the ventilation conditions in the compartment.

Fig. A14 presents comparisons of oxygen and carbon dioxide concentration predictions with experiment. There were two measurement locations, one inside and one outside the compartment.

The inside measurement for Test 1 appeared flawed. Outside the agreement was as expected, given that the model transports mass and energy using the same basic numerical scheme. Test 3 was more interesting. Both the measured and predicted oxygen concentrations inside the compartment decreased to zero for about 5 min each, although the time at which this occurred differed by a few minutes. This indicates that the fire consumed all the available oxygen, something that only occurs at high temperature. Otherwise, the fire would probably have self-extinguished.

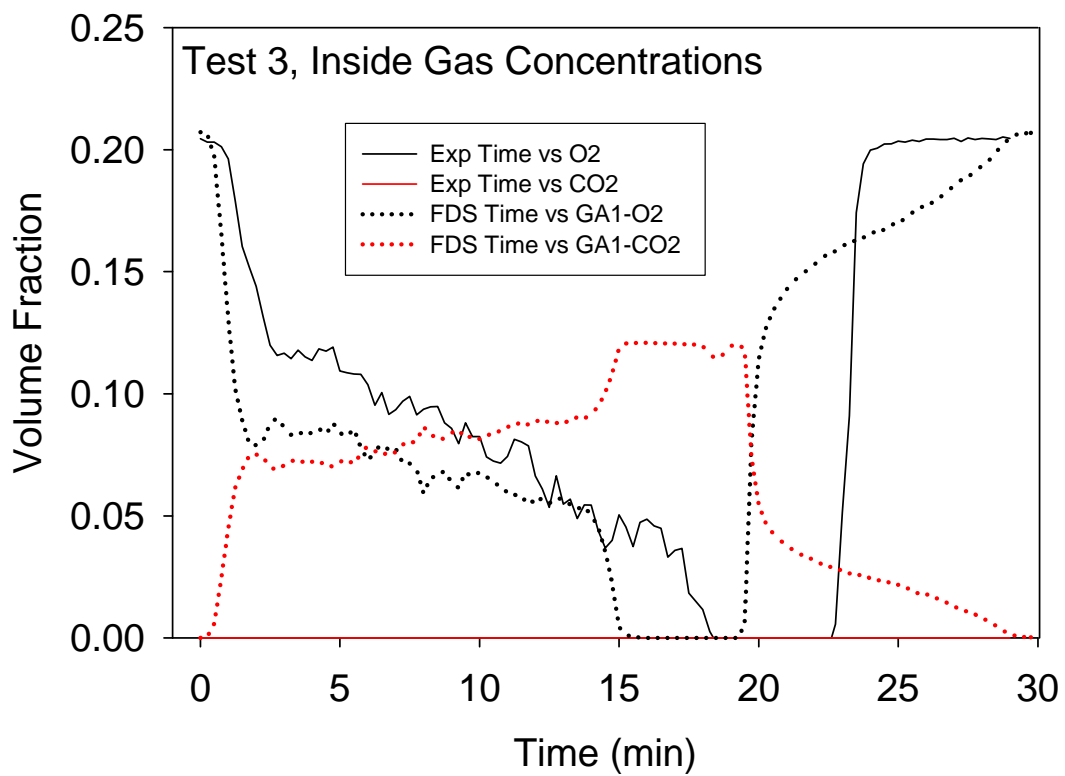
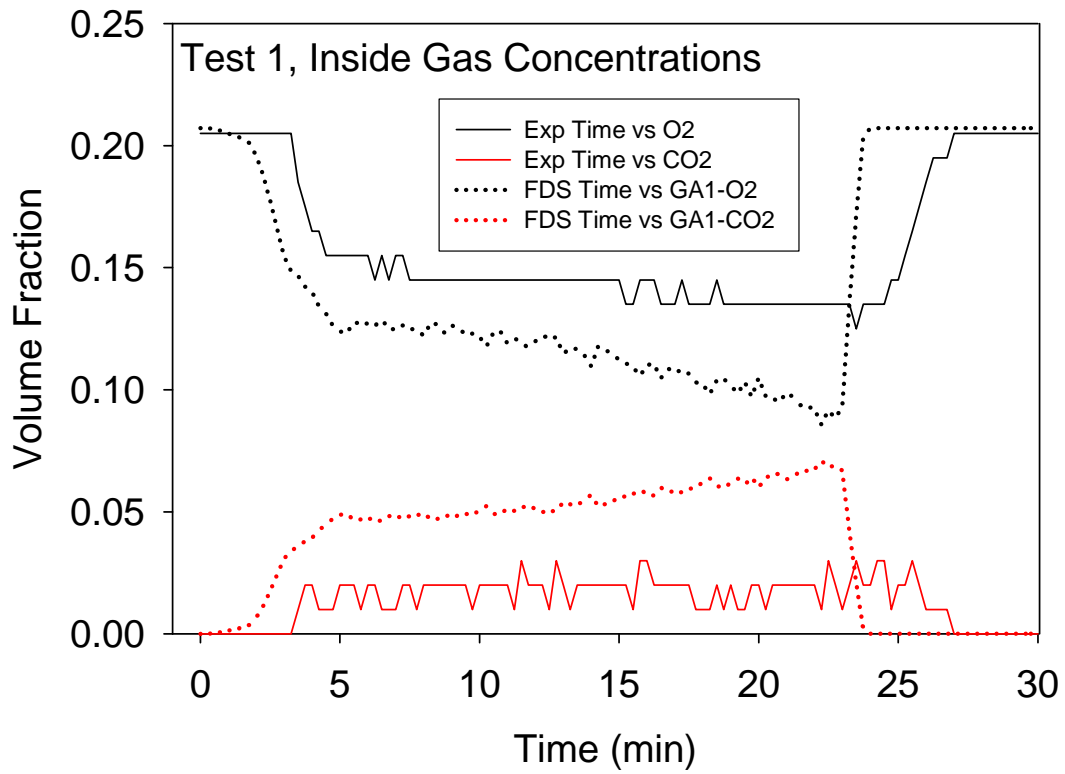


Fig. A13 Oxygen and carbon dioxide concentration, Tests 1 and 3

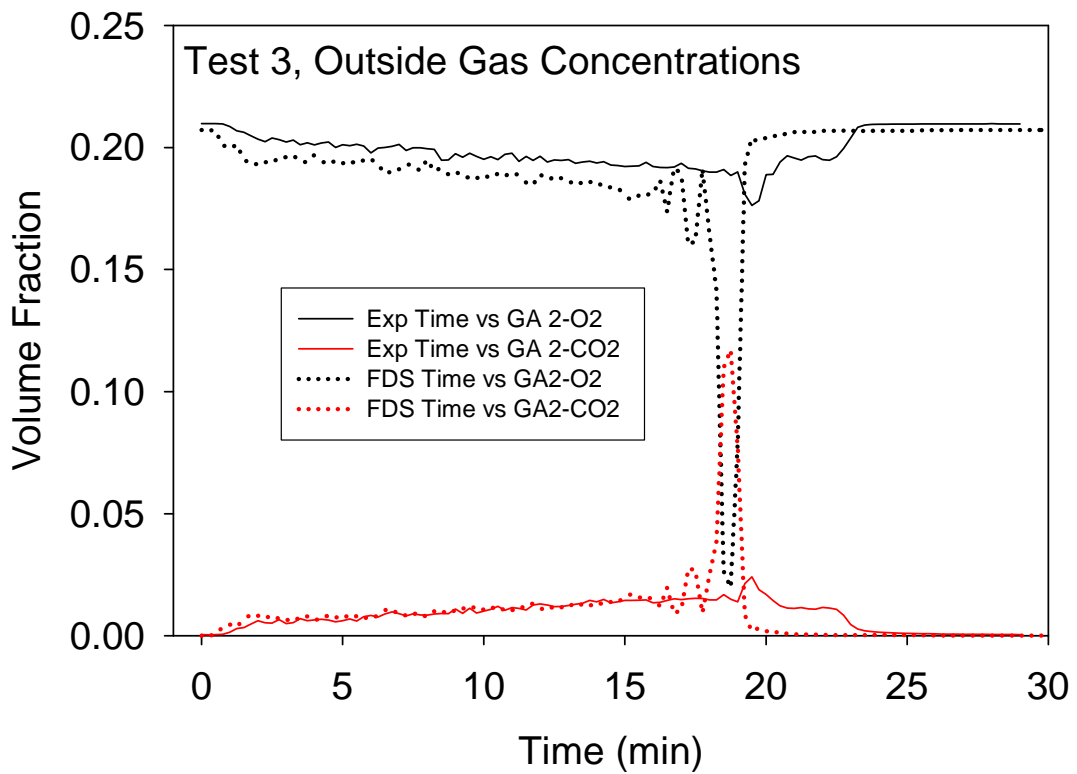
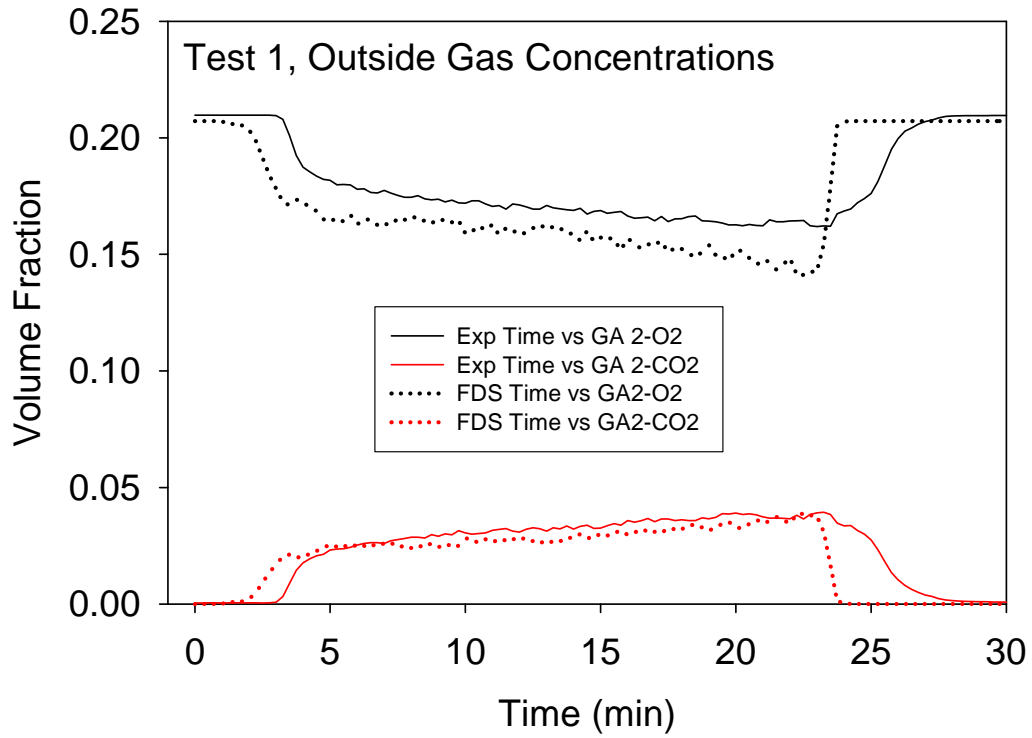


Fig. A14 Oxygen and carbon dioxide concentration, Tests 1 and 3 (contd.)

A3.5 Velocity

Velocity probes were placed in the doorway of the compartment. Comparisons of experimental measurement and model prediction for Test 1 and 3 are shown in Fig. A16. Some of the measurements were noisy, most often resulting from the difficulty in measuring velocities at the interface between incoming and outgoing gases. Discrepancies between model and experiment were most likely caused by model inaccuracy. The model used 10 cm grid cells, fine enough to compute the bulk temperatures and flows within the compartment, but not fine enough to capture the steep gradient in horizontal velocity over the height of the doorway, especially in Test 3 where the door was resolved by just a few cells spanning the vertical dimension.

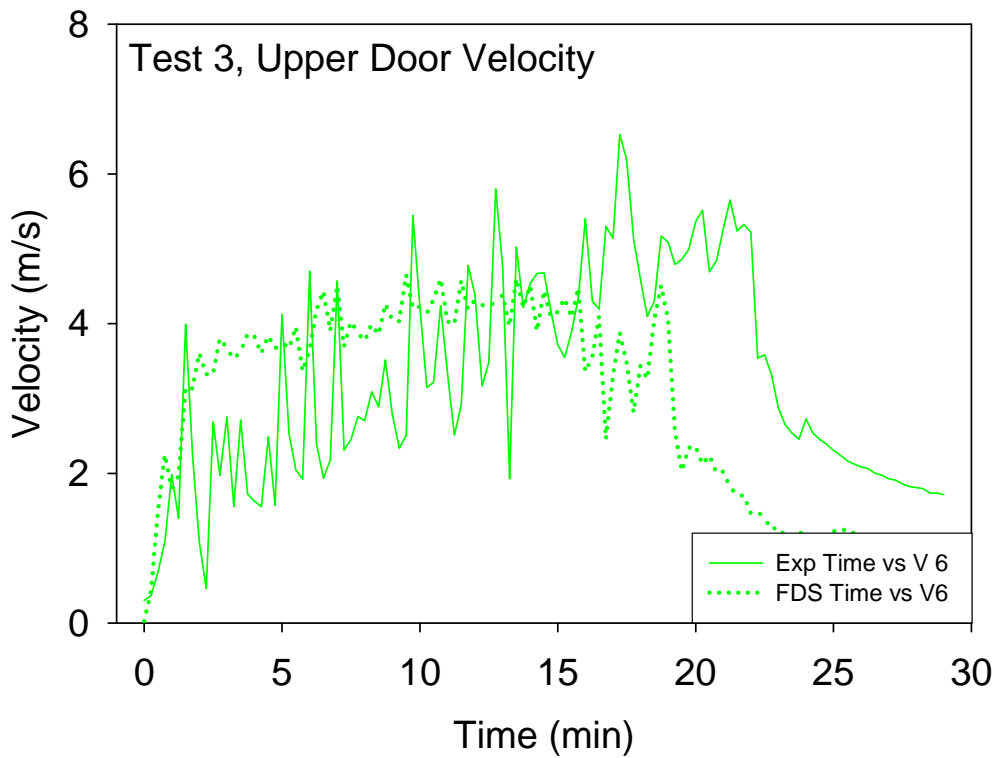
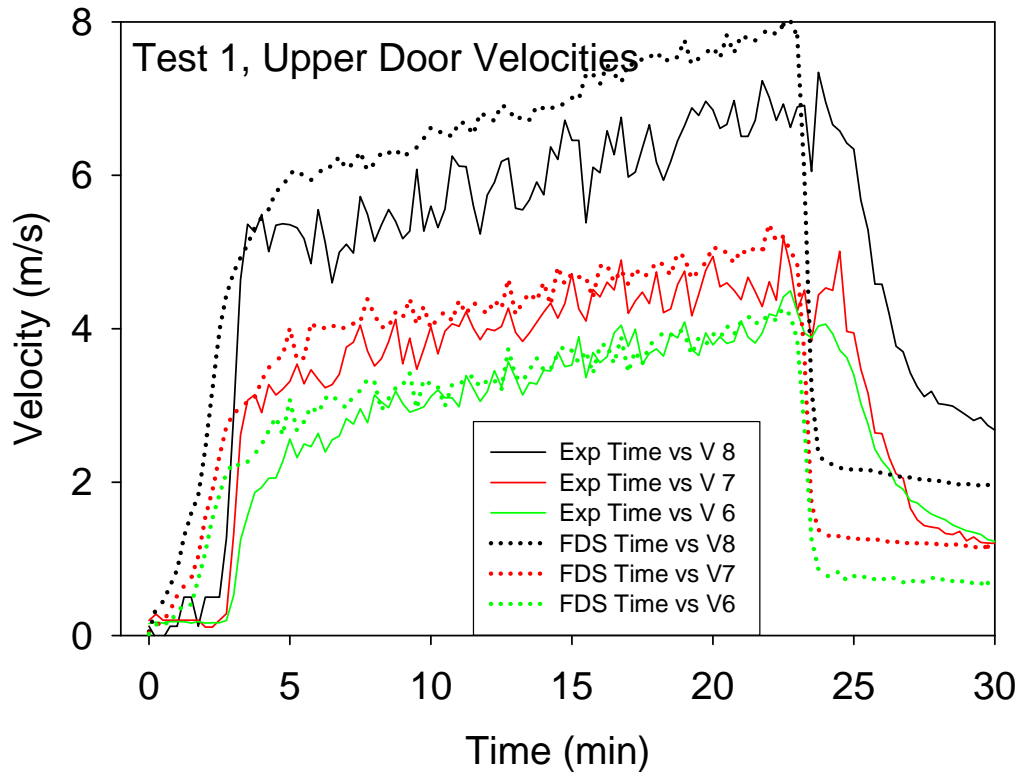


Fig. A15 Velocities in the doorway, Tests 1 and 3

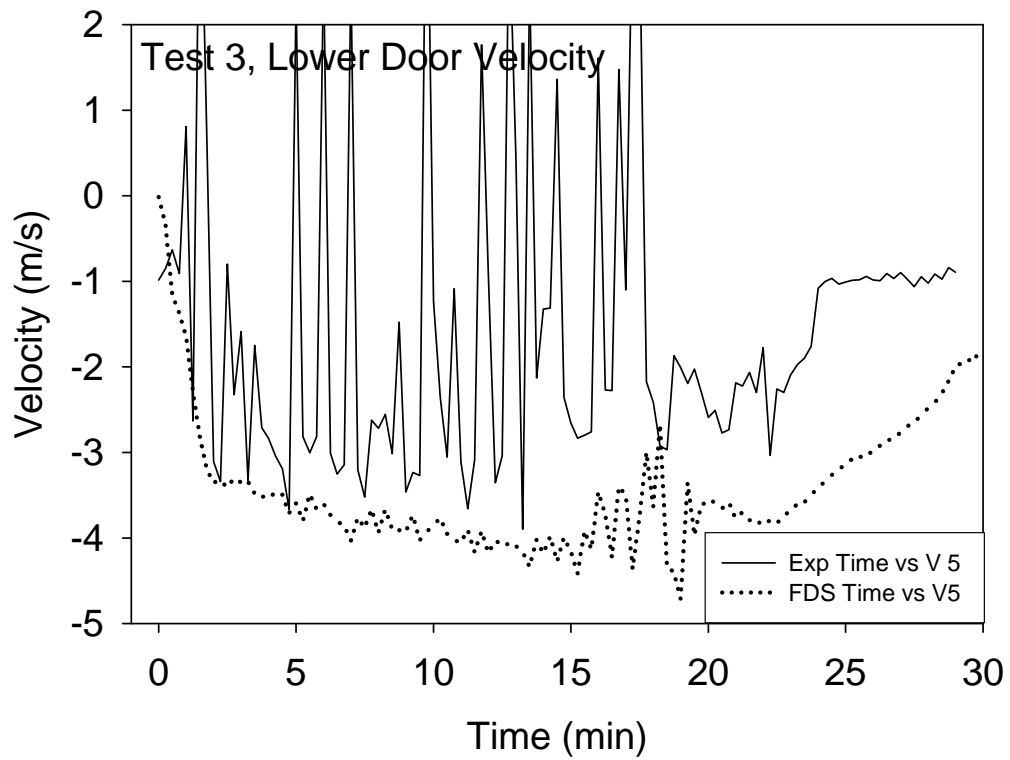
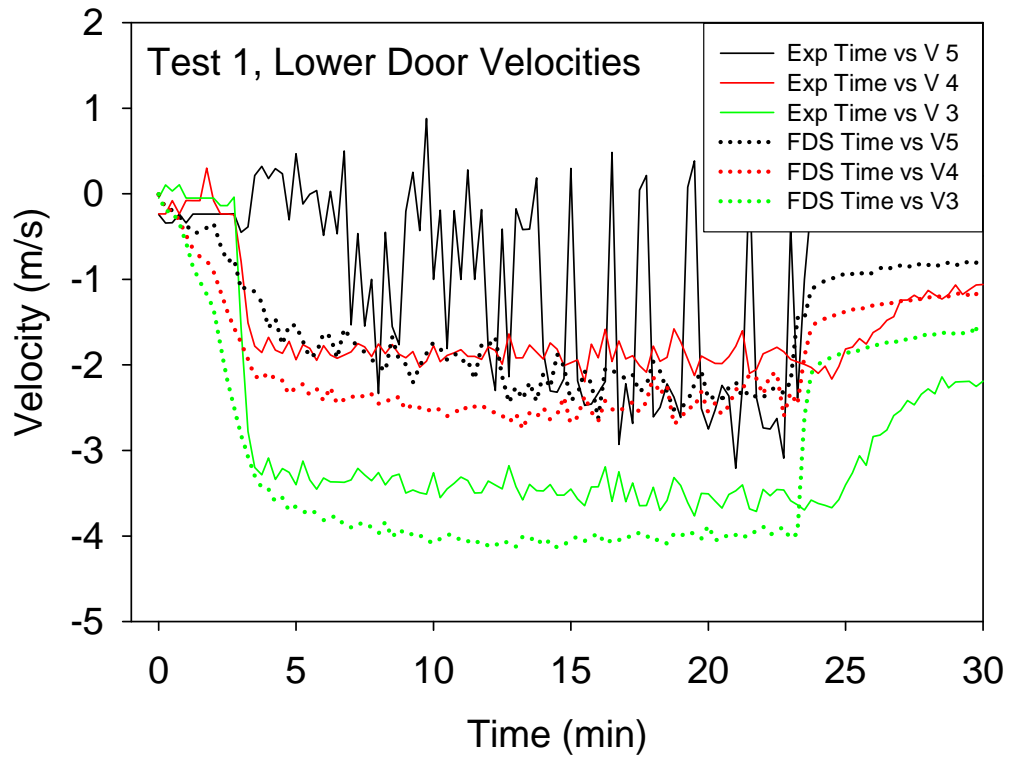


Fig. A16 Velocities in the doorway, Tests 1 and 3 (contd.)

A3.6 Model Sensitivity

There are two types of input parameters: numerical and physical. Physical parameters describe the wall materials, fuel properties, reaction stoichiometry, *etc.* Numerical parameters describe how the calculation is to be performed. The most important numerical parameters are the number of grid cells in each coordinate direction. CFD models solve an approximate form of the conservation equations of mass, momentum and energy. The error associated with the discretization of partial derivatives on a discrete grid is a function of the size of the grid cells and the type of differencing used. FDS uses second-order accurate approximations of both the temporal and spatial derivatives of the Navier-Stokes equations, meaning that the discretization error is proportional to the square of the cell size. In other words reducing the grid cell size by a factor of 2 reduces the discretization error by a factor of 4. However, it also increases the computing time by a factor of 16 (a factor of 2 for the temporal and each spatial dimension). Clearly, there is a point of diminishing returns as one refines the numerical mesh.

Fig. A20 presents predictions of heat flux and target surface temperature using two different sized grids – 10 cm (as was used for all the results shown above) and 20 cm. The 20 cm calculations required about 1/16th the CPU time and 1/8th the computer memory (RAM) as the 10 cm calculations³. In general, there were no significant degradations of the results using the 20 cm grid. Indeed, it appeared that the heat fluxes and surfaces temperatures were predicted more accurately with the coarse grid. This often happens, and it is wrongly suggested that the coarse grid is better than the fine. Actually, there are probably several off-setting errors at work.

³ The fine grid (10 cm) FDS simulations required 3 days to complete on a single 2.4 GHz Intel Pentium processor. The coarse grid (20 cm) simulations required 6 hours.

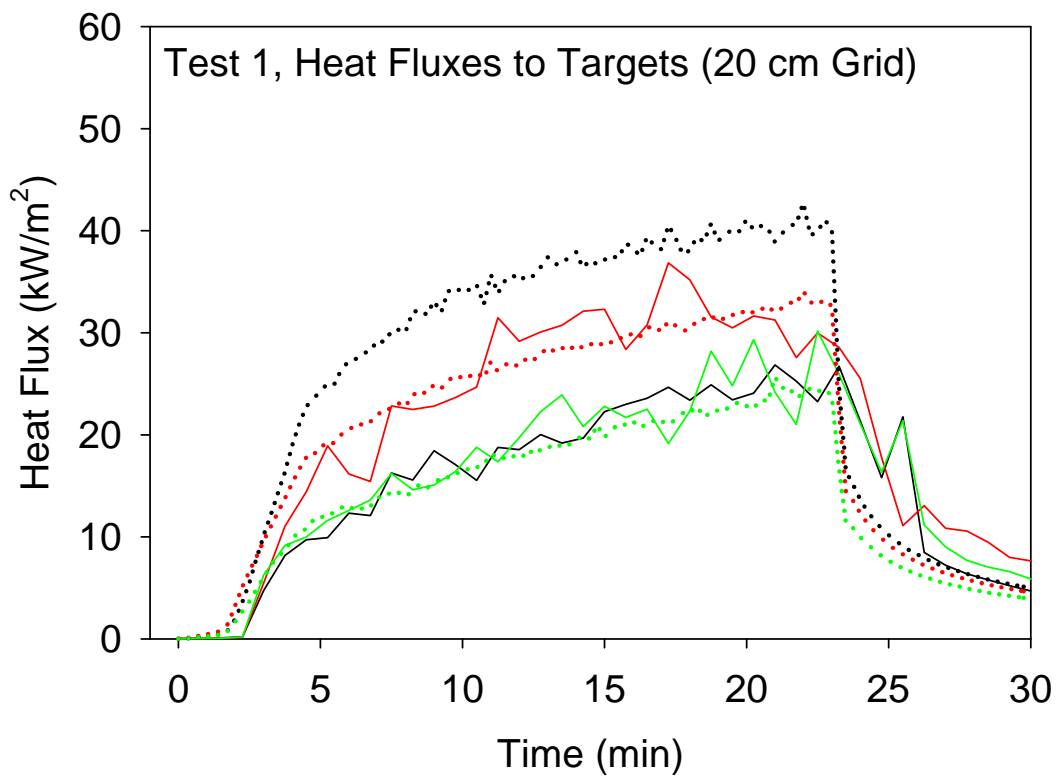
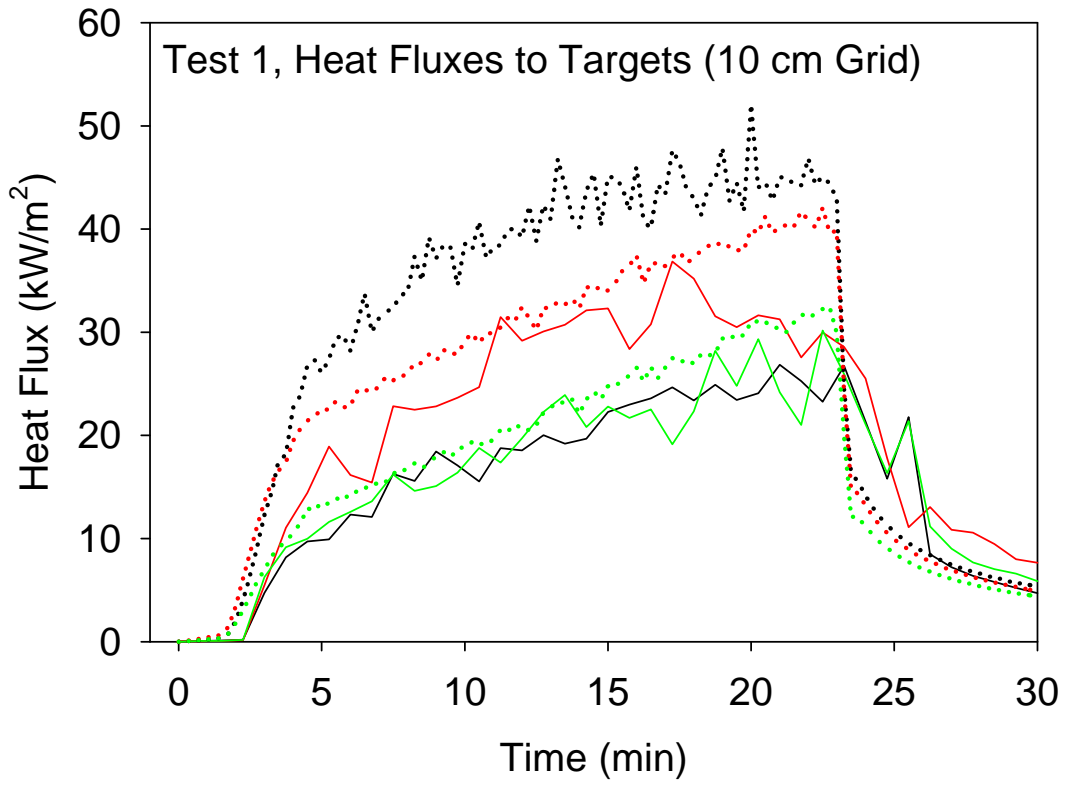


Fig. A17 Fine (upper part) and Coarse (lower part) grid predictions of flux and temperature

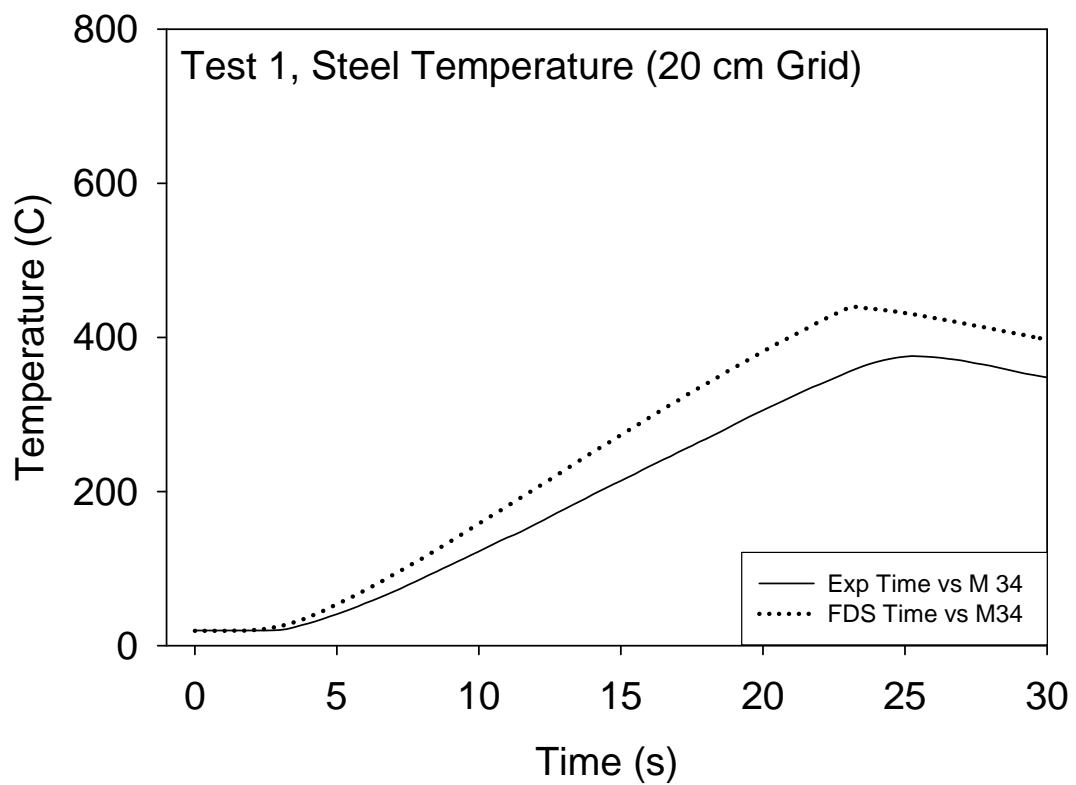
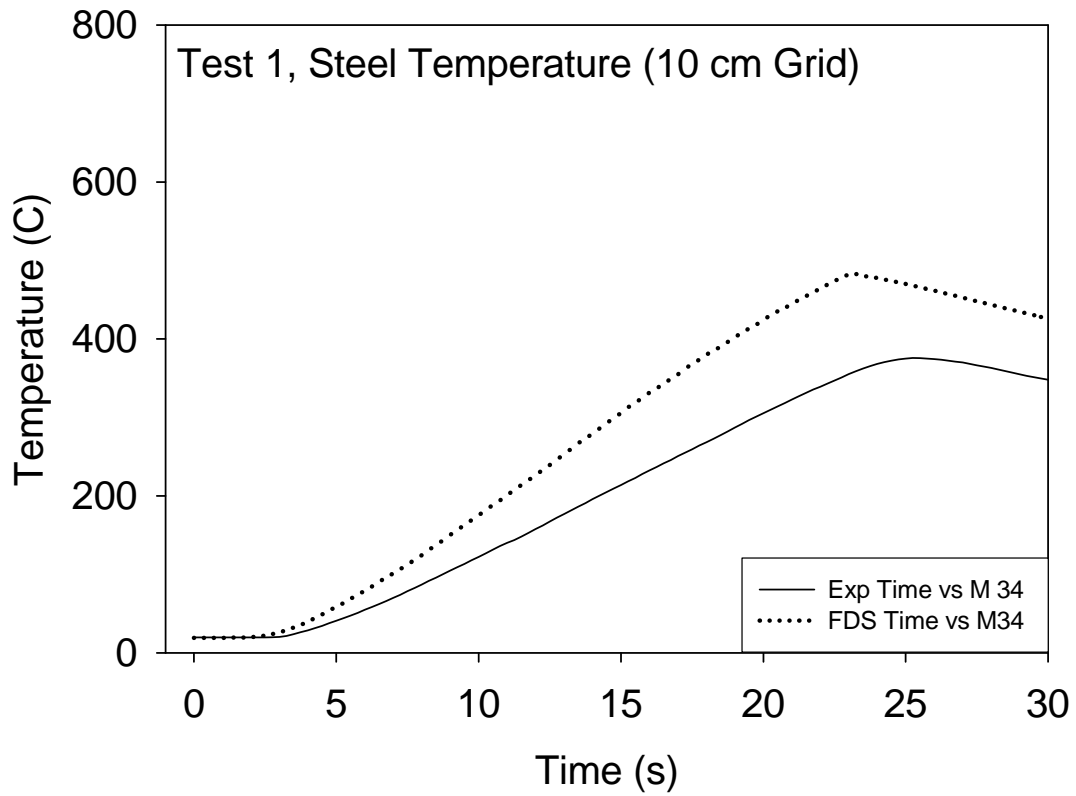


Fig. A18 Fine (upper part) and Coarse (lower part) grid predictions of flux and temperature (contd.)

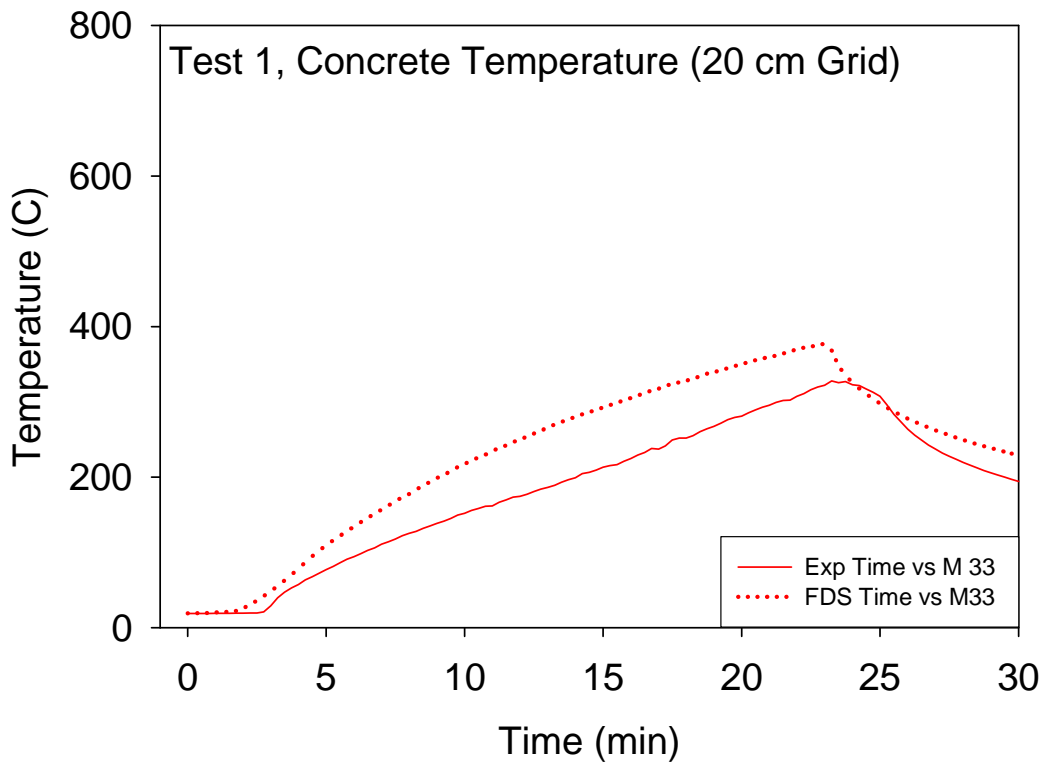
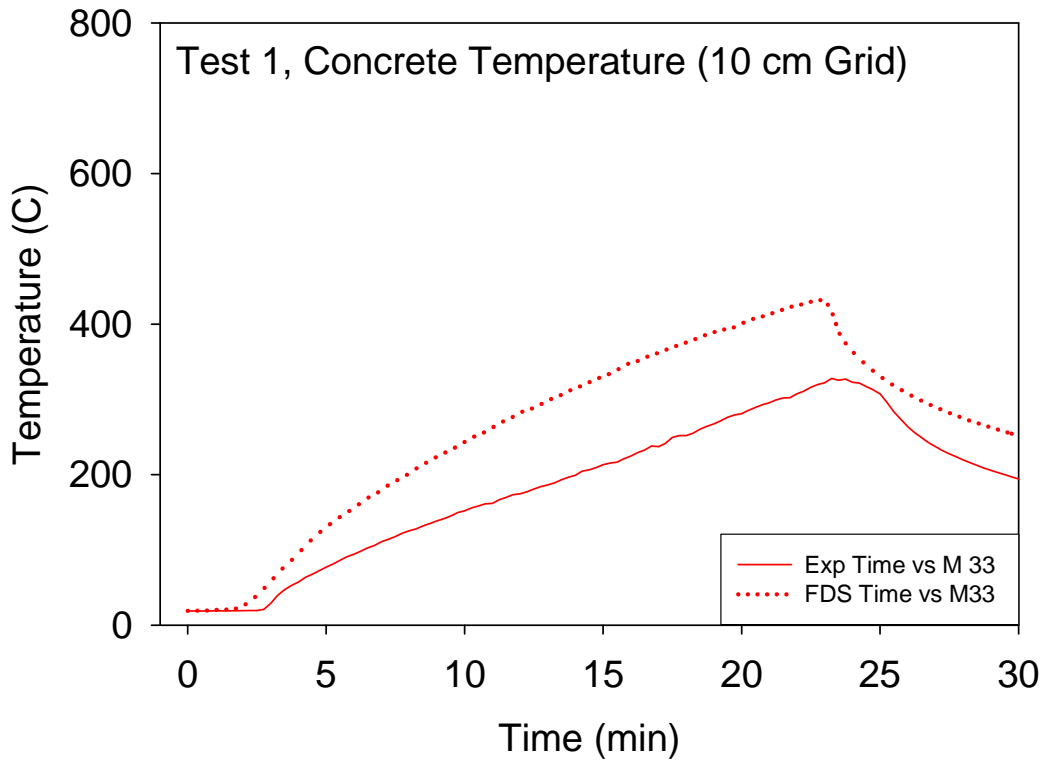


Fig. A19 Fine (upper part) and Coarse (lower part) grid predictions of flux and temperature (contd.)

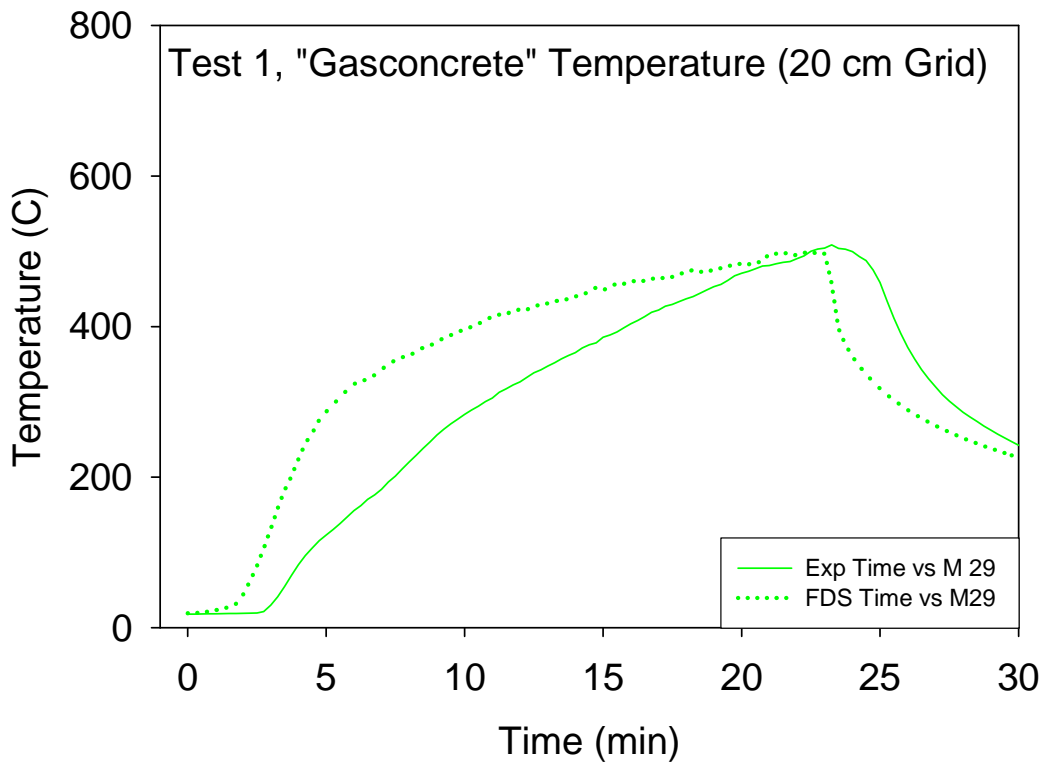
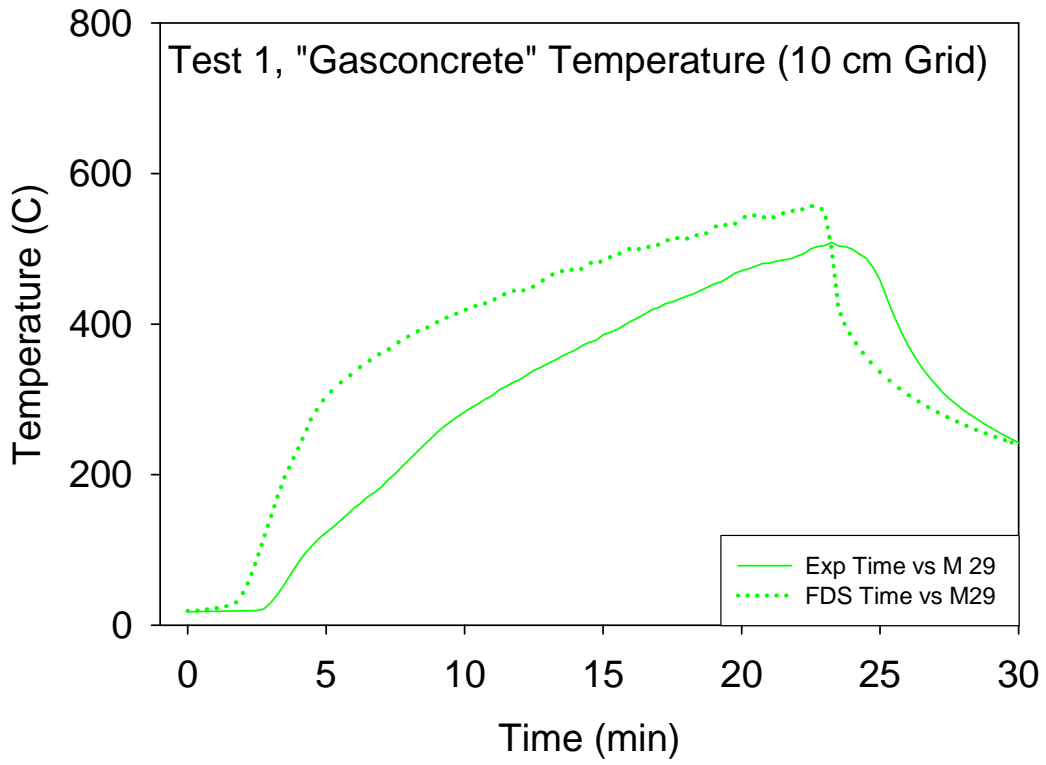


Fig. A20 Fine (upper part) and Coarse (lower part) grid predictions of flux and temperature (contd.)

The coarse grid tends to “smooth out” the temperature and heat flux fields, sometimes resulting in lower predicted values that are closer to the measured values. However, this “smoothing” of the temperature field more often leads to less accurate predictions. For example, consider the plume temperature predictions shown in Fig. A21. The upper layer temperature predictions (M-3 and M-6) were not degraded on the 20 cm grid, but the lower level prediction (M-1) was significantly degraded due to the “smoothing” of high temperatures near the base of the fire.

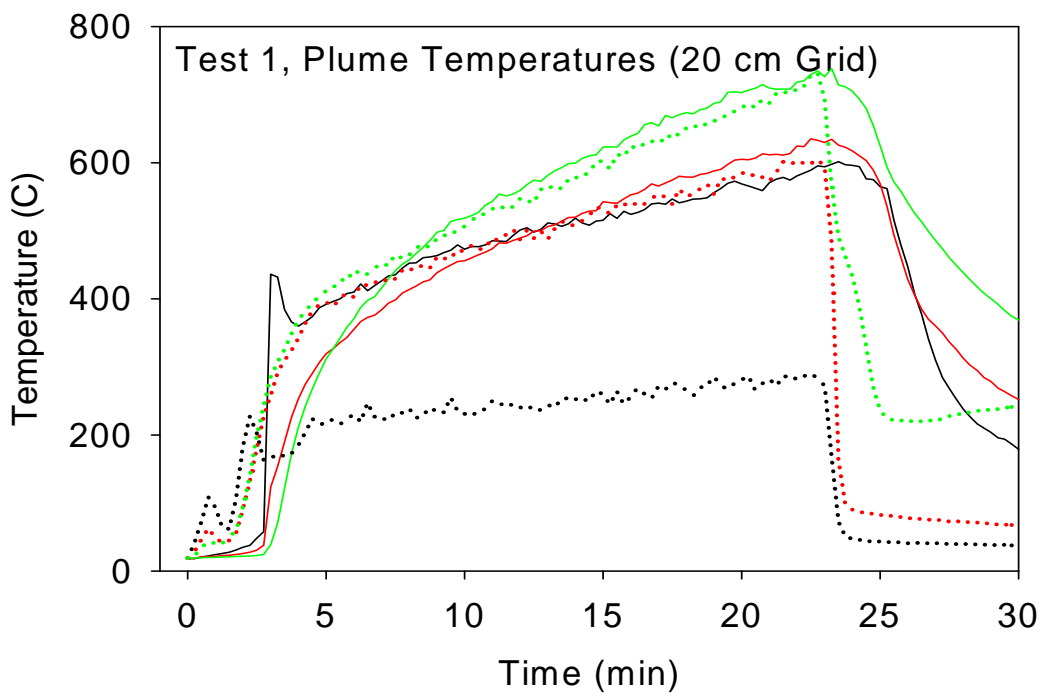
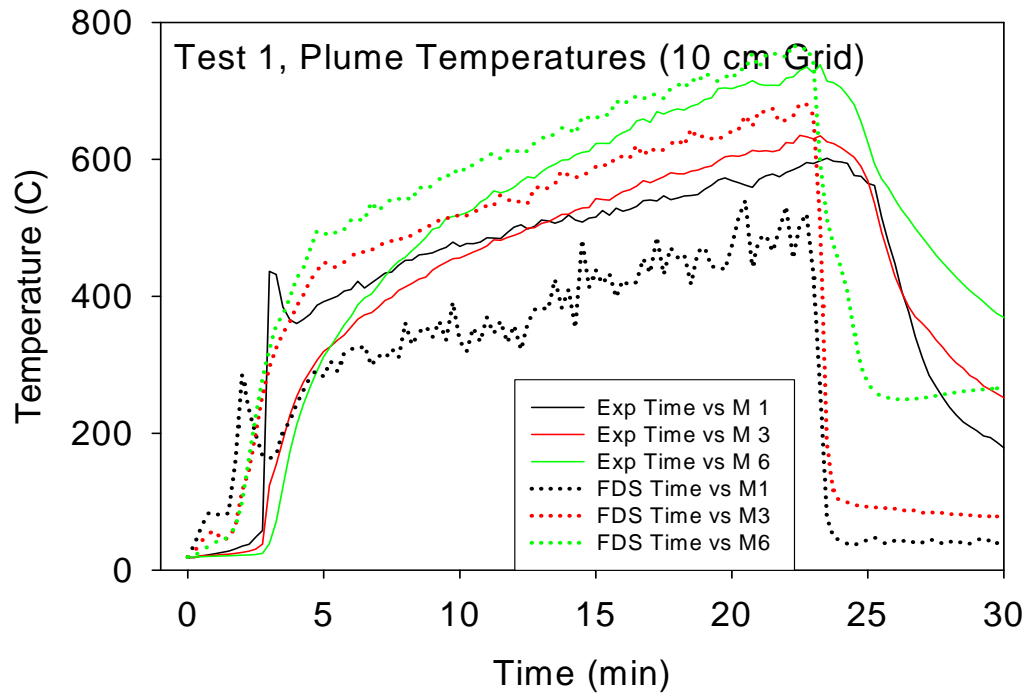


Fig. A21 Fine (upper part) and coarse (lower part) grid predictions of plume temperatures

A4 General Conclusions and Recommendations

Simulations of Benchmark Exercise No. 4 were performed with the NIST Fire Dynamics Simulator (FDS). The exercise had two purposes: (1) to predict the heat release rate of a liquid pool fire within a compartment, and (2) to compute the transport of heat and exhaust gases from this same fire given its measured heat release rate.

The most challenging part of the exercise was predicting the heat release rate. This required the user to supplement the given fuel properties with values drawn from the literature. Because the fuel used was a blend, its properties could not be trusted entirely, especially as these values were culled from different sources.

The simulation of the transport of exhaust products, given the measured burning rates as input, would have been a relatively simple exercise for any engineer with a background in numerical modeling. The geometry (except for the barrel container) was extremely simple, the boundary conditions (*i.e.* ventilation) were well-defined, the solid materials were homogenous with fairly simple properties, and the measurements were well-prescribed. Indeed, of all the Benchmark Exercises conducted thus far, BE #4 would be a good exercise for a fire modeling novice, excluding, of course, the prediction of the burning rate.

A4.1 General Conclusions

The predicted burning rate for Test 1 had the same magnitude as the measured rate, and displayed the same rate of growth over the course of the fire. However, the simulated fire reached its quasi-steady burning rate several minutes earlier than the actual fire, due mainly to the spontaneous ignition of the fuel vapors, an over-simplification of the pyrolysis/combustion model. In Test 3, the predicted burning rate displayed fluctuations that were not observed in the measurements. Plus, the simulation did not predict the rapid growth of the fire near the end of the test.

The difference in steady burning rate between the blind prediction and the measurement was about 10 % in Test 1 and 25 % in Test 3, but important phenomena were not captured in the simulations. Given the uncertainties in the fuel properties, the results of this exercise should be used to assess the qualitative behavior of the model only. More

validation work is needed before the model can be used reliably to predict burning rates of liquid fuels, especially within under-ventilated compartments.

Using the measured HRR, the predicted gas temperatures were within about 15 % of the reported measurements for the simulations of Test 1 and 3. The results for Test 1 were better than Test 3, most likely because the compartment became under-ventilated in Test 3 and the model predicted some burning to have occurred outside the opening even though none was actually observed.

The predicted target surface temperatures were within about 20 % of the measurements. The over or under-prediction of the target temperature at a given point could not always be explained by a comparable error in the heat flux prediction.

There was no detailed solid phase heat transfer model within FDS to predict the thermal response of the cylindrical waste container “target”. All obstructions within the computational domain were assumed to conform to the rectilinear grid, and all solid materials were assumed to be homogenous in composition.

In Test 3, the compartment opening was obstructed and led to under-ventilated conditions within. FDS has a fairly simple “mixed is burnt” combustion model that can only superficially account for under-ventilated conditions. If the local oxygen concentration drops below an empirical cut-off value, combustion is assumed to cease. This led to an under-prediction of the heat release rate in Test 3. Also, FDS predicted burning to have occurred outside the compartment even though the observers did not see it.

A4.2 Recommendations

Two improvements are needed within FDS to better model Benchmark Exercise No. 4. First, the burning rate of a solid or liquid fuel should be predicted more reliably. The blind FDS prediction for Test 1 was encouraging, but it is clear from sensitivity studies that there are numerous parameters, both physical and numerical, that can effect the model’s prediction of burning rate significantly. Such blind predictions should continue to be made, but for the short term, should not be trusted without experimental validation.

Any additional validation work to assess the model's prediction of burning rates of any type of fuel, liquid or otherwise, should focus solely on the fire and the fuel bed. Exhaustive instrumentation of the entire compartment is needed only if there are issues involving smoke and heat transport. At this point in the project, FDS and the other models under consideration have been shown to handle transport well, but there needs to be improvement in the near-field. In addition to the measurement of the burning rate, instrumentation should be installed to measure the heat flux and temperature of the fuel surface, and however difficult it may be, the thermal and chemical environment within the fire itself. Different sized pans should be used to assess size effects, and attempts should be made to minimize boundary and geometrical effects of the apparatus and fuel. For example, solid homogenous slabs or liquid pools ought to be studied before cables, spray fires, spills, etc.

The second, and more important, improvement for CFD models is in the combustion routines. Currently, FDS handles well the dynamics of a well-ventilated fire. However, as compartments go to flashover, the simple "mixed is burnt" combustion rule is no longer true. FDS will have to abandon its single scalar mixture fraction model so that it can transport products of incomplete combustion, like soot, CO, and the fuel itself. This is important because at the very least a fire model should be able to predict where the fuel is burning. In Test 3, FDS mistakenly predicted burning to have taken place partially outside the compartment even though this was not observed.

To look at under-ventilated behavior, a test similar to Test 3 should be re-done with a fixed fuel supply, like a burner. The HRR should be ramped up at discrete increments to see how the models handle the gradual transition from well to under-ventilated conditions. The focus should be on where the fuel is actually burning (inside or outside) and what the overall compartment environment is like. Measurements should be made of the principle carbon-carrying compounds (unburned hydrocarbons, soot, CO₂, and CO) along with oxygen and gas temperature.

A5 References

- /MCG 03/ McGrattan, K., J. Floyd, G. Forney, H. Baum, and S. Hostikka:
Improved Radiation and Combustion Routines for a Large Eddy Simulation
Fire Model. Fire Safety Science - Proceedings of the Seventh International
Symposium, International Association for Fire Safety Science, 2003
- /MCG 04/ McGrattan, K.B. (ed.):
Fire Dynamics Simulator (Version 4), Technical Reference Guide. NIST
Special Publication 1018. National Institute of Standards and Technology,
Gaithersburg, Maryland, USA, 2004
- /HOS 03/ Hostikka, S., K.B. McGrattan and A. Hamins:
Numerical Modeling of Pool Fires Using LES and Finite Volume Method for
Radiation, Fire Safety Science - Proceedings of the Seventh International
Symposium. International Association for Fire Safety Science, 2003
- /QUI 98/ Quintiere, J.G.:
Principles of Fire Behavior. Delmar Publishers, Washington, DC, USA,
1998
- /WAL 03/ Walton, W.D., and P.H. Thomas:
Estimating Temperatures in Compartment Fires. Fire Protection Handbook,
3rd Ed. National Fire Protection Association, Quincy MA, 2003

List of Figures

Fig. A1	Simulation of Test 3, showing the fire and smoke in Smokeview.....	4
Fig. A2	Measured and predicted (blind) heat release rates for Tests 1 and 3.....	8
Fig. A3	Gas temperature comparisons for Test 1.....	10
Fig. A4	Gas temperature comparisons for Test 1 (contd.).....	11
Fig. A5	Gas temperature comparisons for Test 1 (contd.).....	12
Fig. A6	Gas temperature comparisons for Test 3.....	13
Fig. A7	Gas temperature comparisons for Test 3 (contd.).....	14
Fig. A8	Gas temperature comparisons for Test 3 (contd.).....	15
Fig. A9	Heat flux and surface temperature at Targets, Tests 1 and 3.....	17
Fig. A10	Heat flux and surface temperature at Targets, Tests 1 and 3 (contd.).....	18
Fig. A11	Heat flux and surface temperature at Targets, Tests 1 and 3 (contd.).....	19
Fig. A12	Heat flux and surface temperature at Targets, Tests 1 and 3 (contd.).....	20
Fig. A13	Oxygen and carbon dioxide concentration, Tests 1 and 3.....	22
Fig. A14	Oxygen and carbon dioxide concentration, Tests 1 and 3 (contd.).....	23
Fig. A15	Velocities in the doorway, Tests 1 and 3.....	25
Fig. A16	Velocities in the doorway, Tests 1 and 3 (contd.).....	26
Fig. A17	Fine (upper part) and Coarse (lower part) grid predictions of flux and temperature.....	28
Fig. A18	Fine (upper part) and Coarse (lower part) grid predictions of flux and temperature (contd.).....	29
Fig. A19	Fine (upper part) and Coarse (lower part) grid predictions of flux and temperature (contd.).....	30
Fig. A20	Fine (upper part) and Coarse (lower part) grid predictions of flux and temperature (contd.).....	31
Fig. A21	Fine (upper part) and coarse (lower part) grid predictions of plume temperatures.....	33

Appendix B: International Collaborative Project to Evaluate Fire Models for Nuclear Power Plant Applications

Benchmark Exercise No. 4 Simulations with JAMINE and CFAST

Presented by

Stewart Miles

Fire and Security, Building Research Establishment (BRE)

Garston, Watford WD25 9XX, United Kingdom

Contents

B1	Introduction	1
B2	Input Parameters and Assumptions.....	3
B3	Comparison of Code Predictions with Test Results.....	11
B4	General Conclusions and Recommendations.....	71
B5	References.....	75
	List of Figures	79
	List of Tables	83

B1 Introduction

Blind calculations (prior to the dissemination of the experimentally measured fuel mass loss rate) and semi-blind calculations (with knowledge of the above mass loss rate) were conducted for Tests 1 and 3 with Jasmine (CFD model) version 3.2.3. In addition, some calculations (with knowledge of the full set of experimental measurements) were conducted for Test 3. Semi-blind calculations were conducted with CFAST (zone model) version 3.1.6 for Tests 1 and 3.

In all calculations the geometry of the experimental rig was represented as closely as possible to that given in the problem specification /KLE 03/. In the semi-blind calculations the experimentally measured fuel release rates /ICF 03/ were used, and for the limited set of additional open calculations the experimental measurement data /ICF 04a +04b/ was available. Comparisons between calculated results and the experimental measurements have been made and are reported in this annex.

For details of the experiments and the measurements see the main body of this report.

B2 Input Parameters and Assumptions

The calculations were performed using the geometry and input parameters as close as possible to those given in the problem specification. Information on the main modeling choices and assumptions is provided below, with particular emphasis on where the problem specification was deviated from, or engineering judgments of significance made. This is documented separately for the two fire models used.

CFAST

CFAST is a widely used zone model, available from the National Institute of Standards and Technology (NIST), USA. It is the main component of the program suite FAST, which is accessed via a graphical user interface. CFAST is a multi -room zone model, with the capability to model multiple fires and targets.

Fuel pyrolysis rate is a pre-defined input, and the burning in the compartment is then modeled to generate heat release and allow species concentrations to be calculated. For most applications CFAST is used as a conventional two-zone model, whereby each compartment is divided into a hot gas upper layer and a cold lower layer. In the presence of fire, a plume zone/model transports heat and mass from the lower to upper layer making use of an empirical correlation /MCC 83/. Flows through vents and doorways are determined from correlations derived from the Bernoulli equation. Radiation heat transfer between the fire plume, upper & lower layers and the compartment boundaries is included using an algorithm derived from other published work /SIE 81/.

Other features of CFAST relevant to the benchmark exercise include a one-dimensional solid phase heat conduction algorithm employed at compartment walls and targets and a network flow model for mechanical ventilation.

For an in-depth description of CFAST, including its scientific and engineering background, the solved equations and the physical sub-models see the reference /JON 00/ and the later reference accompanying CFAST version 5 /JON 04/. A summary of validation exercises that have been undertaken for the CFAST model is also included in /JON 04/. The panel report /MIL 04/ and accompanying technical annexes for the second benchmark exercise include a number of examples where CFAST calculations have been compared to experimental measurement data for smoke filling inside a large hall.

CFAST version 3.1.6 was used in the work reported here, with the data files edited directly, i.e. the FAST graphical user interface was not employed. Other information relevant to the application of CFAST to this benchmark exercise is given below.

- Main geometry and thermal boundary conditions:
Dimensions of the OSKAR fire compartment and the doorway ventilation openings were modeled as in the problem specification. The thermal properties of the walls, floor and ceiling were included by creating new user defined materials with the required (concrete) properties. Conduction losses to the room walls, ceiling and floor were included, using the one-dimensional heat conduction sub-model.
- Ventilation through the fan system:
This was modeled using a mechanical exhaust vent. A limitation was that a fixed value for the volume flow rate was required, i.e. the time-dependent measured profile was not followed.
- Fire specification:
This was treated as a constrained fire (i.e. oxygen controlled) with an area of 1 m², located at the centre of the compartment at floor level. The fuel was modeled as kerosene, using a heat of combustion of $4.28 \times 10^7 \text{ J kg}^{-1}$. The time-dependent pyrolysis rate was set to that measured experimentally (only semi-blind calculations were performed with CFAST) for the initial calculations, and was then adjusted in subsequent parametric calculations. For Test 1 two calculations were conducted using a fixed fuel pyrolysis rate of 0.039 kg s^{-1} , based upon published engineering information /BAB 02/. This provided a comparison with the blind JASMINE calculations where the same pyrolysis specification was used.

In all calculations a two-layer gas assumption was assumed inside the room, but the 'ceiling jet' option was inactive.

The radiative fraction was set to 0.3 in most calculations (0.6 was also investigated). While in most calculations the lower oxygen limit (LOL) was set to 0 %, it was adjusted to 10 % in some parametric calculations. The choice of radiative fraction and heat of combustion requires careful scientific/engineering judgment. An appropriate choice of the radiative fraction in particular may have a significant bearing on the calculations for upper layer temperature etc. For a discussion of these parameters see panel report of the second benchmark exercise /MIL 04/, where the terms and their meaning are reviewed.

- **Targets:**

A required approximation in CFAST is that targets are treated as rectangular slabs. Furthermore, heat conduction is modeled in one-dimension, i.e. in the direction of the surface normal. The surface temperature of the three material probes was calculated, with the target surface normal directed into the compartment (x direction). The response of the barrel target was not included in the CFAST calculations because CFAST is not capable of modeling cylindrical targets.

JASMINE

JASMINE /COX 87/ solves the Reynolds-Averaged Navier Stokes (RANS) equations of fluid flow on a single-block Cartesian grid. The coupled set of equations for each of the three Cartesian velocity components, enthalpy (heat) and other scalars required by the various sub-models (e.g. fuel mass and mixture fractions for combustion) is approximated as a system of algebraic equations that are solved numerically on a discrete grid. This generates a solution value for each variable at each grid location. JASMINE uses the finite volume method, where the differential equations are first transformed into an integral form and then discretised on the control volumes (or cells) defined by the numerical grid. This solution procedure is coupled with a variant of the SIMPLE pressure-correction scheme /PAT 80/.

In solving the RANS equations, the fluctuating components of the turbulent motion are not solved directly, but instead the effect of turbulence is included by means of a separate sub-model. This saves computational effort, and for many industrial applications, including fire modeling, has been shown to produce reliable solutions provided a suitable turbulence mode is used. JASMINE employs a standard κ - ϵ turbulence model /LAU 74/ with additional buoyancy source terms. An 'effective turbulent viscosity' is calculated at each control volume, which can be considered as an increased viscosity to incorporate the effects of turbulence. Standard wall functions for enthalpy and momentum /LAU 74/ describe the turbulent boundary layer adjacent to solid surfaces. Transient solutions are generated by a first-order, fully-implicit scheme.

The fire combustion process is generally modeled using an eddy break-up assumption /MAG 76a/ in which the fuel pyrolysis rate is specified as a boundary condition. Combustion is then calculated at all control volumes as a function of fuel concentration, oxygen concentration and the local turbulent time-scale (provided by the κ - ϵ model). A simple one-step, infinitely fast chemical reaction is assumed. The eddy break-up model

is appropriate for turbulent diffusion flames characteristic of fire, where the rate of reaction is controlled by the comparatively slow mixing of fuel with oxygen. Complete oxidation of the fuel is assumed when sufficient oxygen is available. The effect of oxygen concentration on the local rate of burning may be incorporated by setting oxygen and temperature limits which define 'burn' and 'no burn' regions. Figure B1 illustrates this concept.

Radiant heat transfer is modeled with either the six-flux model /GOS 73/, which assumes that radiant transfer is normal to the co-ordinate directions or potentially more accurate discrete transfer method /LOC 81/. Local absorption-emission properties are computed using a mixed grey-gas model /TRU 76/, which calculates the local absorption coefficient as a function of temperature and gas species concentrations.

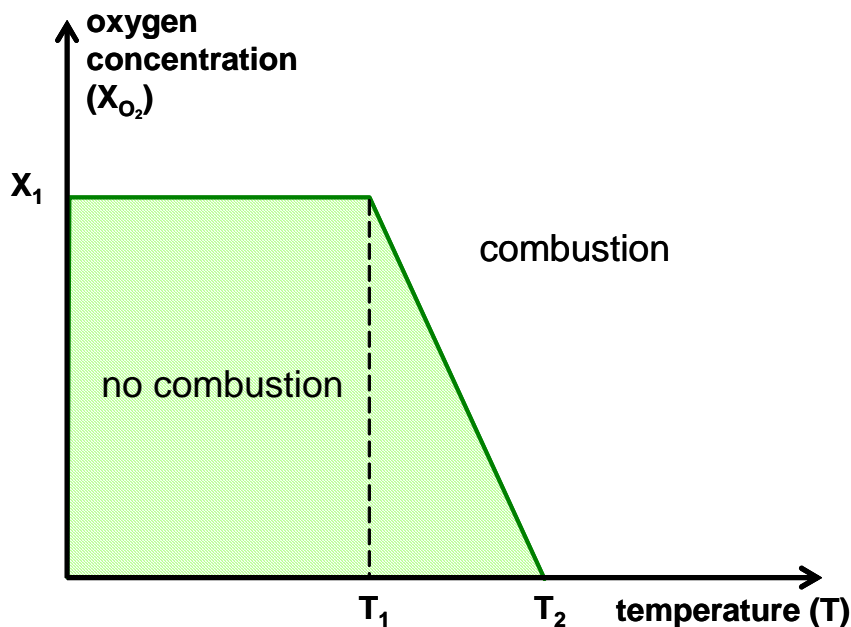


Fig. B1 Oxygen - temperature control on combustion in JASMINE

Thermal conduction into solid boundaries may be included by means of a quasi-steady, semi-infinite, one-dimensional assumption, which is appropriate for many smoke movement applications. Alternatively, the solution of the one-dimensional heat conduction equation into the solid is also available. In both methods, the purpose of the solid-phase conduction calculation is to generate the solid surface temperature, at each control volume adjacent to a solid boundary at each time step, by balancing the convection, radiation and conduction heat fluxes. The surface temperature then provides the (thermal) boundary condition for the next time-step of the CFD solution.

JASMINE has been successfully used to simulate fire and smoke movement in a wide variety of construction projects (e.g. atria, hospitals, sport stadia, warehouses, tunnels, etc.), as well as in other applications such as a nuclear containment cell, transportation vehicles and marine ships. The references /COX 87, MIL 00, MIL 01/ provide some examples of JASMINE validation exercises. The panel report /MIL 04/ and the BRE technical annex (Appendix H) for the second Benchmark Exercise report the comparison of JASMINE calculations and measurement data for the smoke filling of a large hall.

Information relevant to the application of JASMINE to this benchmark exercise is given below.

- Main geometry and thermal boundary conditions:
Dimensions of the compartment, doorway opening and exhaust ventilation duct were modeled exactly as in the problem specification. Only half the compartment was modeled, imposing symmetry at the $x = 1.8$ m plane. The thermal properties of the concrete walls, floor and ceiling were included as specified. Conduction losses to the room walls, ceiling and floor were included, using the one-dimensional heat conduction sub-model available in JASMINE. Radiative and convective fluxes from the radiation/gas fields were calculated at each solid surface cell face at each numerical time step.
- Ventilation through the fan system:
This was modeled as a time-dependent mass sink, set to a value corresponding to the experimentally measured volumetric flow rate. In one open calculation for Test 3 the flow rate was reduced to 50 % of the experimentally measured value.
- Fire specification:
Combustion was included using the eddy break-up sub-model, assuming a kerosene fuel source and a simple one-step chemical reaction to yield CO_2 and H_2O . As in the CFAST calculations the fuel source area was 1 m^2 and the heat of combustion was set to $4.28 \times 10^7 \text{ J kg}^{-1}$.

For the blind calculations a fixed fuel pyrolysis rate was assumed from 60 s after ignition (increasing linearly to this value over the first 60 s). A value of 0.039 kg s^{-1} was chosen, based upon published engineering information /BAB 02/. The sensitivity to reducing this value to 0.0234 kg s^{-1} was investigated. In the semi-blind and

open calculations, the fuel pyrolysis rate was set to the experimentally measured value, or a fraction (0.5 or 0.75) of this value.

Oxygen limitation was not applied in the blind or the semi-blind calculations, i.e. fuel could be combusted wherever oxygen was available. However, in some of the open calculations for Test 3, the effect of oxygen concentration was considered by defining oxygen/temperature limits (see Fig. B1).

A main limitation of the fire modeling adopted is the absence of a soot generation and subsequent radiation process. An attempt to include the effect of soot formation and subsequent radiation emission was, in part at least, incorporated in the reduction in the fuel pyrolysis rate (as done in most of the semi-blind and open calculations). The amount of heat then removed represents that which could be expected to be 'lost' by radiation from the sooty flame region above the fuel source. The remainder of this heat is assumed to be convected into the rest of the compartment or, as a relatively small fraction, by radiation from the plume region due to CO₂ and H₂O. Note also that of the heat convected into the compartment, some of this is subsequently radiated from the smoke gases (due to CO₂ and H₂O). Note that this approach and analysis can be judged only as rather approximate, and that the note made above under CFAST regarding the choice of radiative fraction (here the heat 'lost' by radiation) and heat of combustion applies equally to CFD modeling.

- Targets:

The thermal response of the material probe targets and the heat flow densities (WS2, WS3 & WS4) was included in the JASMINE calculations. Furthermore, the wall surface temperatures at the locations of the plates/thermocouples (M19 etc) were calculated. While the blockage due to the barrel target was included, its thermal response was not modeled and therefore no comparisons were made with the barrel temperature measurements.

- Radiation:

The six-flux radiation model was employed for all blind and semi-blind calculations. This provides a reasonable and efficient treatment for radiation exchange between the hot smoke gases and the compartment boundaries. Its primary limitation with respect to this benchmark exercise is that the radiation intensities are modeled in the Cartesian axial directions, and so important off-axis directional information may be missed. This may have a consequence for the target heating and heat flux density calculations.

The discrete transfer radiation model was used instead of the six-flux model in open calculations for Test 3. This is potentially more accurate as it considers radiative transport in more than just the three Cartesian axis directions. In the benchmark exercise a total of 8 radiation rays were considered at each surface element.

Emission/absorption due to the presence of the primary products of combustion, i.e. CO₂ and H₂O, was included, but not soot (which was not explicitly included in the JASMINE calculations).

- Other settings:
A numerical mesh of approximately 80.000 cells was employed. The numerical time-step was fixed at 2.5 s throughout. For all calculations the κ - ϵ turbulence model with buoyancy modifications was employed.

B3 Comparison of Code Predictions with Test Results

Results are presented in this section primarily as graphs that compare directly calculated quantities against experimental measurements. As in Section B2 above, the CFAST work is presented first followed by that performed with JASMINE.

CFAST

Semi-blind CFAST calculations (runs) were performed for Tests 1 and 3. Table B1 summarizes the main features of each of these calculations.

Table B1 CFAST semi-blind calculation runs

Test	Run No.	Fuel release rate	Flame base height	Radiative fraction	Lower oxygen limit (LOL)	Mechanical vent flow
1	run 1	measured	0	0.6	0 %	2 m ³ s ⁻¹
1	run 2	0.039 kg s ⁻¹	0	0.3	0 %	2 m ³ s ⁻¹
1	run 3	0.039 kg s ⁻¹	0	0.3	0 %	1 m ³ s ⁻¹
3	run 1	measured	0	0.3	0 %	1.5 m ³ s ⁻¹
3	run 2	limited *	0	0.3	0 %	1.5 m ³ s ⁻¹
3	run 3	limited *	0	0.3	0 %	1 m ³ s ⁻¹
3	run 4	limited *	0	0.3	10%	1.5 m ³ s ⁻¹
3	run 5	limited *	0.2 m	0.3	10%	1.5 m ³ s ⁻¹

* measured rate but with upper limit clamped at 0.06 kg s⁻¹

Fig. B2 compares predicted and measured gas temperatures for Test 1, where for the measurements two thermocouple locations are shown for the lower, mid and upper part of the compartment. Fig. B3 compares the predicted layer height for the three CFAST runs. Fig. B4 to Fig. B7 compare predicted and measured oxygen concentration, surface temperatures and flux densities for Test 1.

Fig. B8 to Fig. B13 repeat the above comparisons for Test 3, where for the plot of CFAST layer heights only two of the runs are shown.

The runs included in Table B1 are those for which converged CFAST simulations were achieved. Other parametric combinations were attempted for which a converged solution was not achieved. This is perhaps a reflection on that the physics of the two experiments is quite complex.

The main observations and findings from the CFAST calculations are summarized below:

- For Test 1 the choice of a radiative fraction of 0.6, coupled to the measured fuel pyrolysis rate, resulted in an upper gas layer temperature close to that measured. The layer height predictions, with the layer dropping to approximately 1 m, were perhaps less representative of the actual experiment.

For Test 3 the upper gas layer temperature predictions were less encouraging, with an over-prediction in all parametric calculations undertaken. This was observed, in particular, in the earlier stage of the experiment. It should be noted that radiative fractions higher than 0.3, and up to 0.6, were attempted but that converged solutions were not then obtainable.

- For Test 1 the calculated oxygen concentration appears reasonable. For Test 3 the calculated oxygen concentration, while dropping to zero, does so much more quickly than suggested by the experimental measurement. This is most likely coupled to the fact that too much burning, and associated gas temperature rise, was predicted in the calculation compared to the actual experiment.

For Test 3, where the oxygen concentration dropped to zero, whether the lower oxygen limit was set to 10 % or zero (compare CFAST runs 2 and 4) had very little influence on the calculated values.

- Surface temperatures and incident fluxes for Test 1 were reasonable for the two calculations using a fixed fuel pyrolysis rate of 0.039 kg s^{-1} , but for the calculation using the measured pyrolysis rate they were notably higher than the measured values. Note that this is despite the calculated upper gas temperature being closer to the measurements when using the measured pyrolysis rate.

- Test 3 calculations for wall surface temperature were reasonably close to the experimental measurements for all the parametric runs. Material probe surface temperatures and the heat flux densities were, however, over-predicted compared to measurement in all parametric runs. This may be due, in part at least, to three-dimensional geometry effects that cannot be captured using a zone model such as CFAST.
- Despite the limitation that the flow rate through the mechanical exhaust was fixed in value, and did not vary according to the measurement data, this probably had only a small consequence. However, a more rigorous analysis of the effect of the flow rate imposed at the mechanical extract vent has been performed with JASMINE (see below).

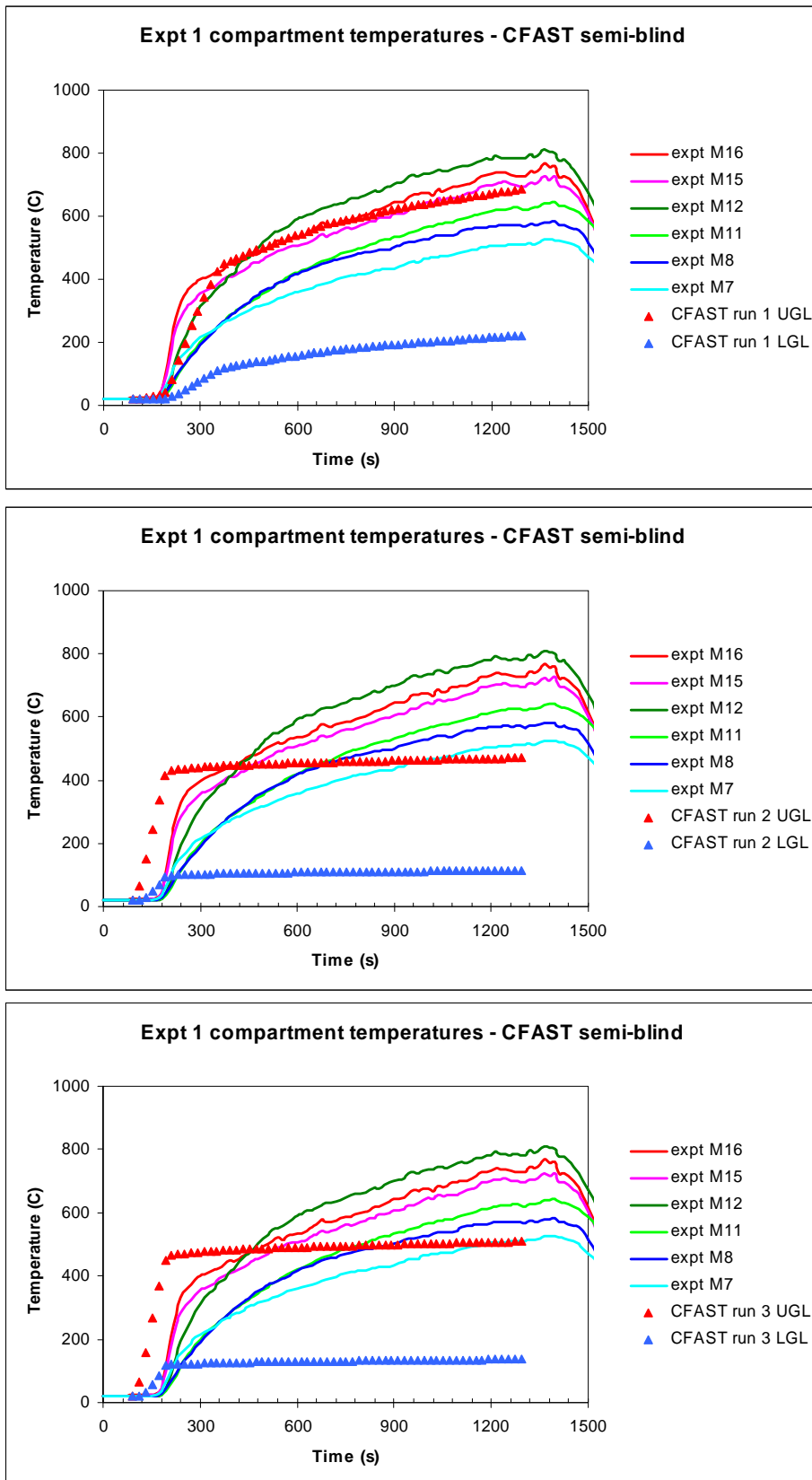


Fig. B2 Measured and CFAST predicted gas layer temperatures for Test 1

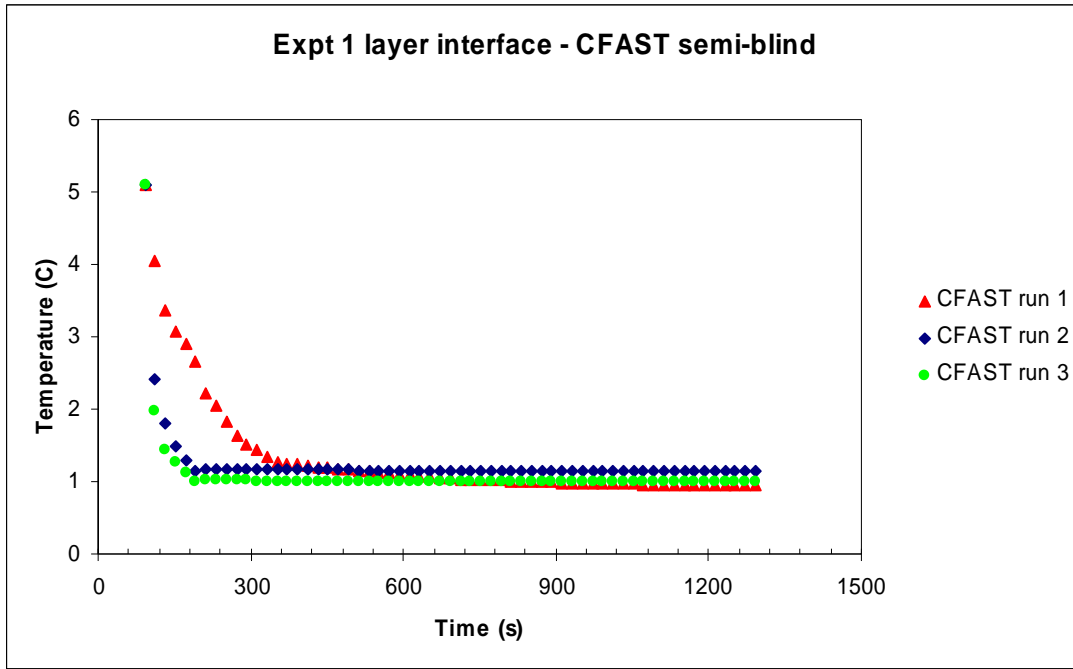


Fig. B3 CFAST predicted hot gas layer height for Test 1

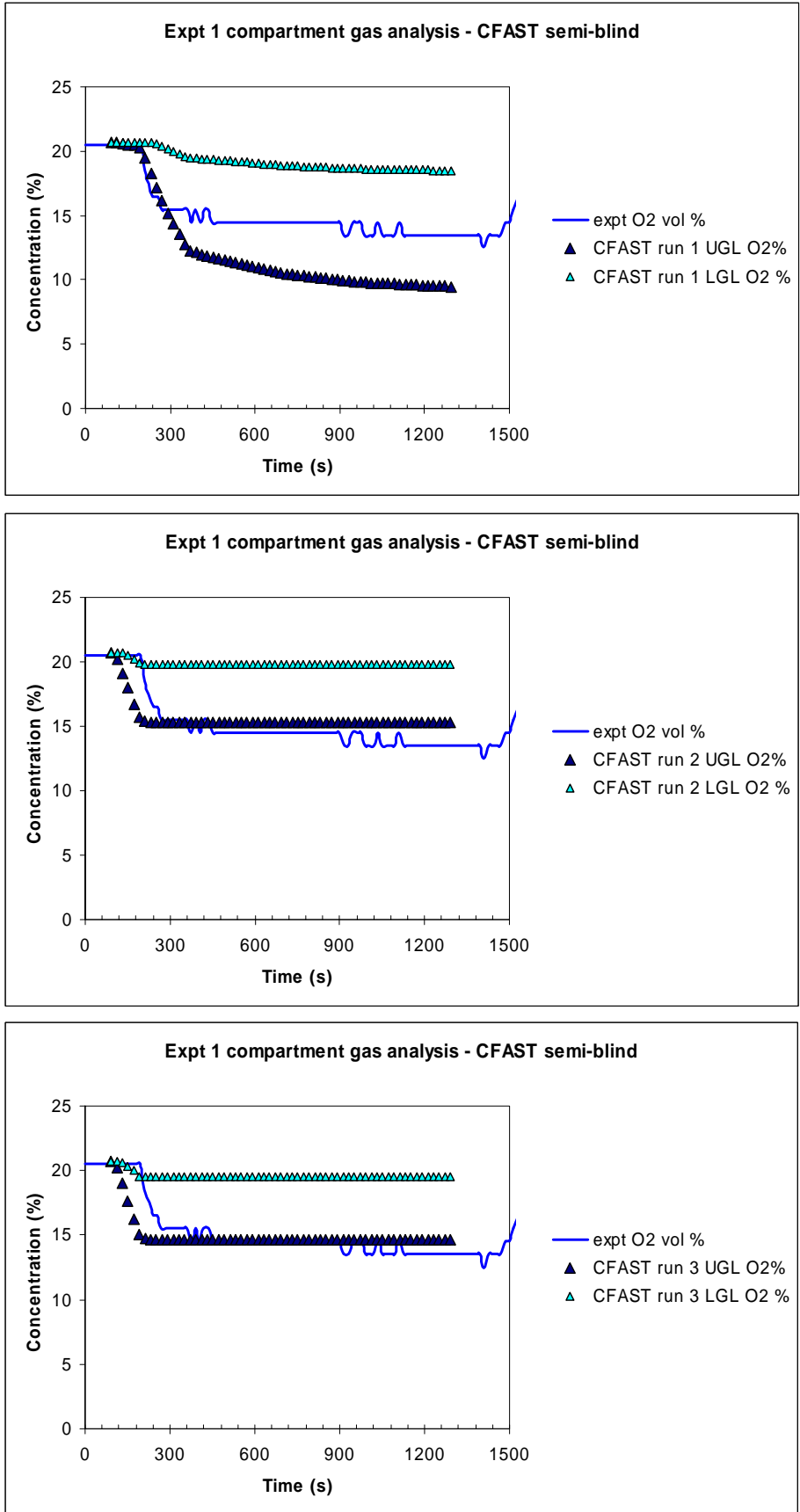


Fig. B4 Measured and CFAST predicted oxygen concentrations for Test 1

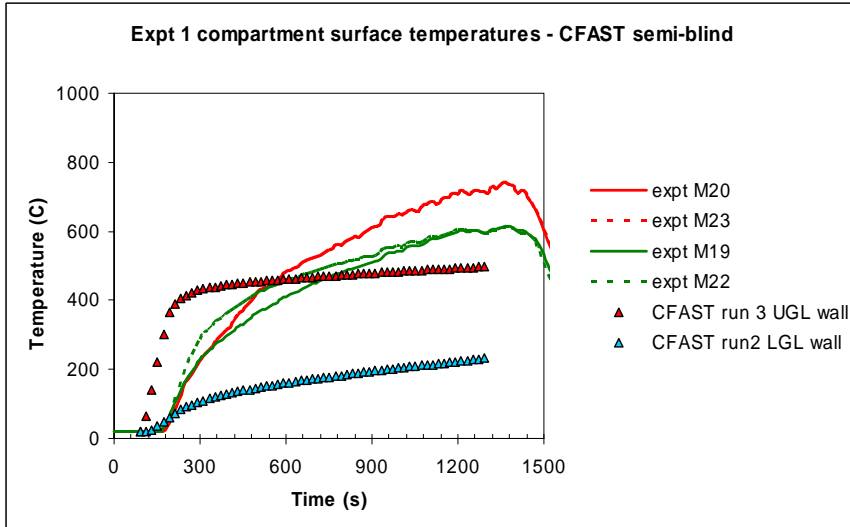
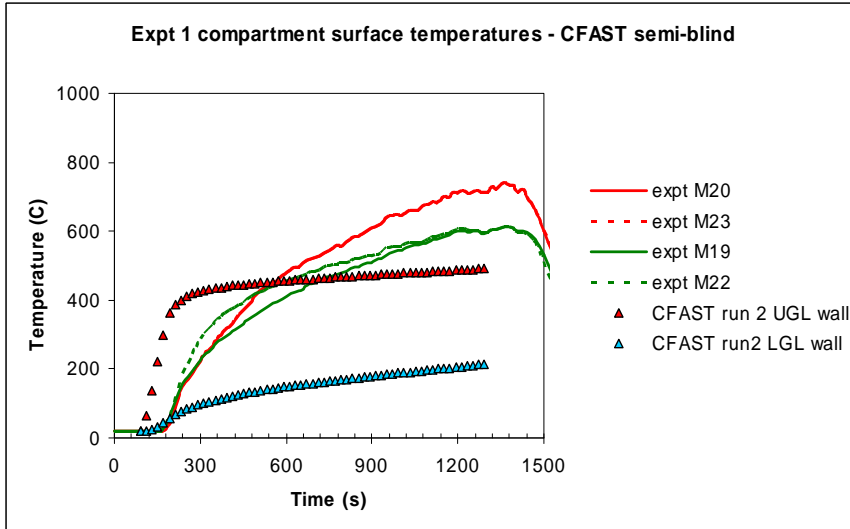
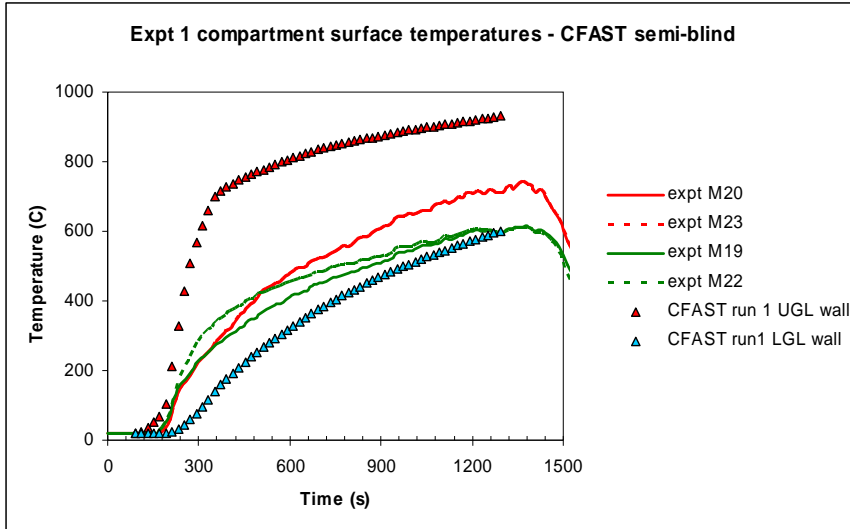


Fig. B5 Measured and CFAST predicted wall surface temperatures for Test 1

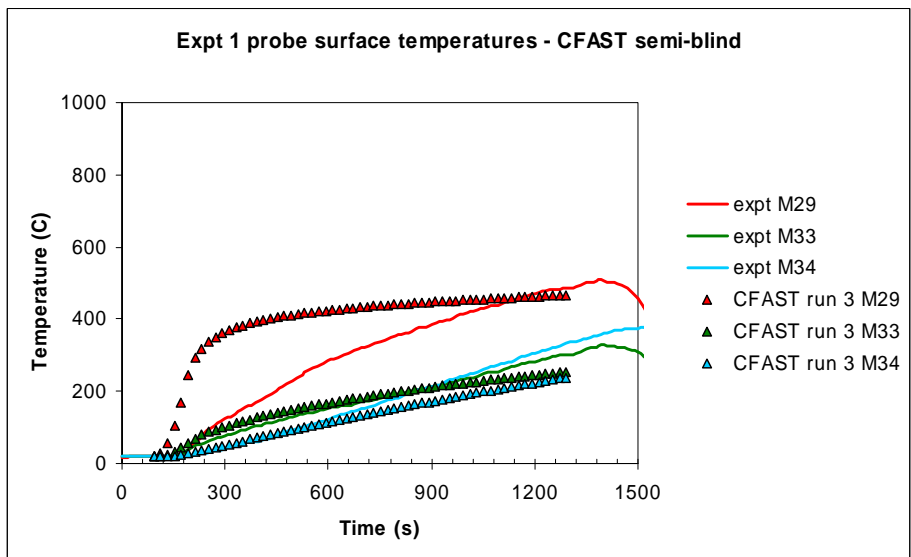
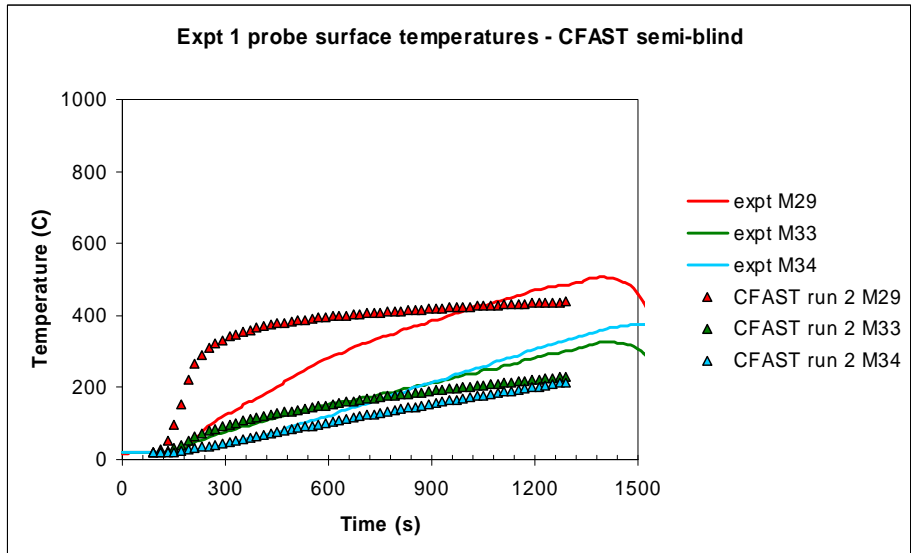
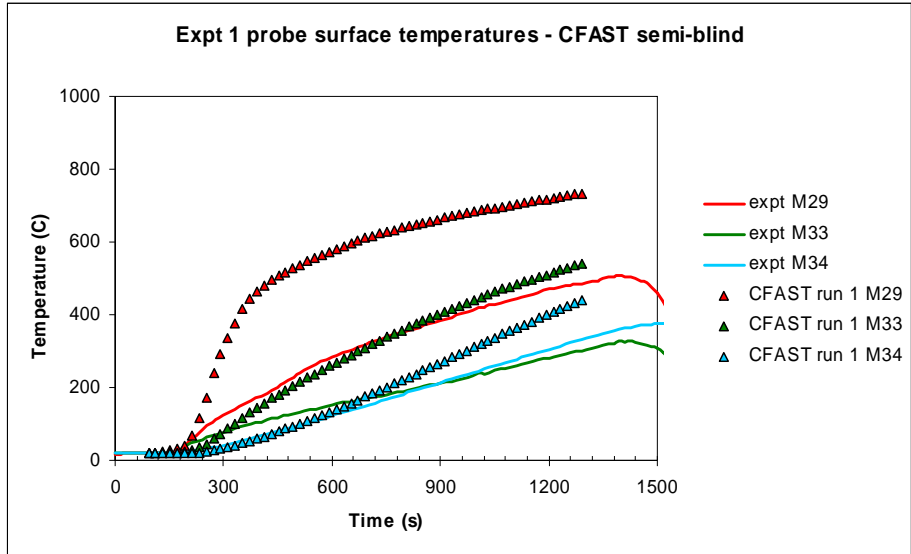


Fig. B6 Measured and CFAST material probe surface temperatures for Test 1

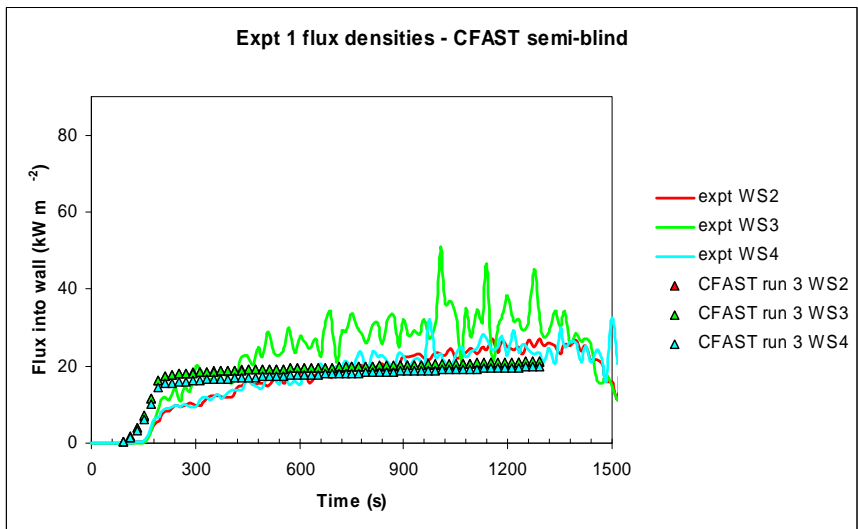
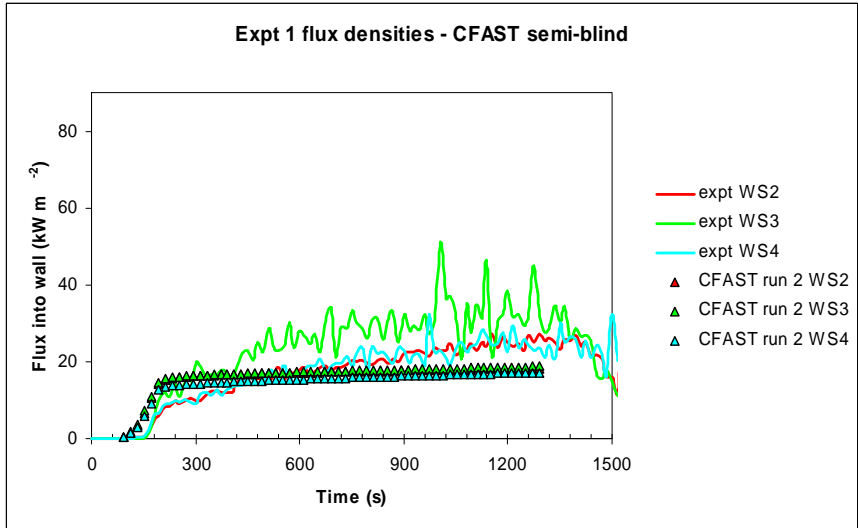
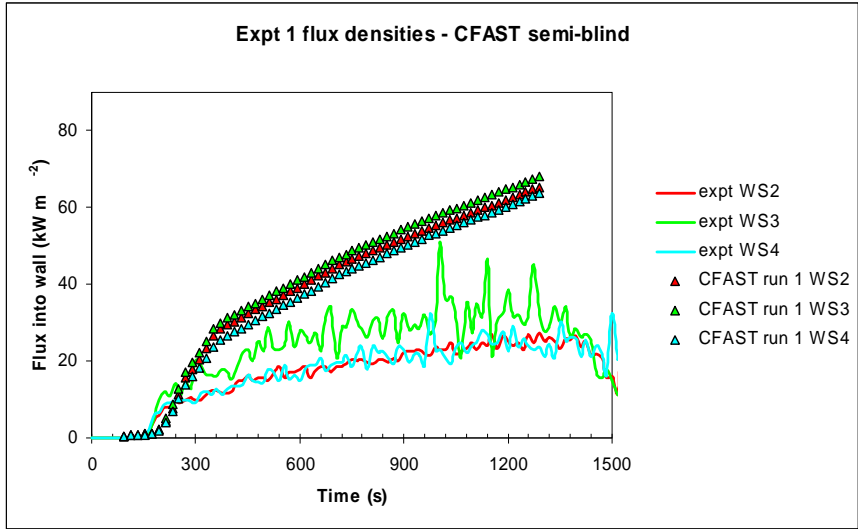


Fig. B7 Measured and CFAST flux densities for Test 1

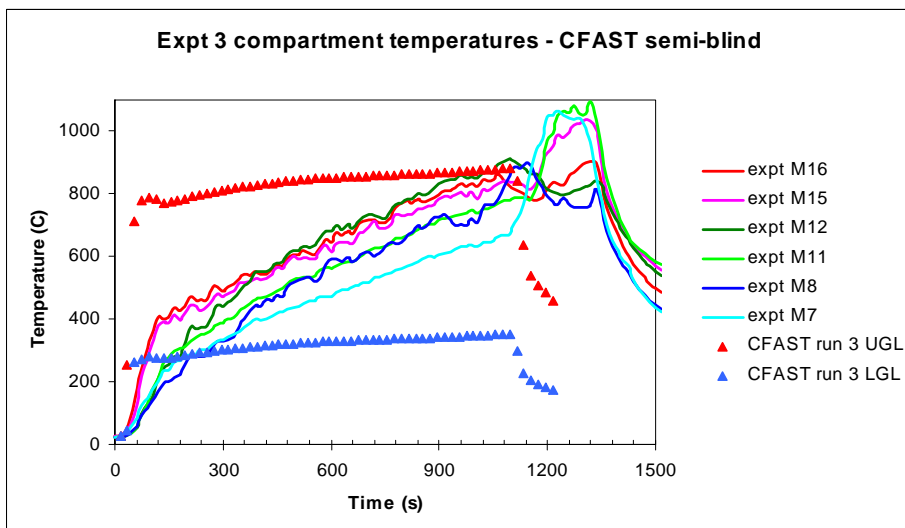
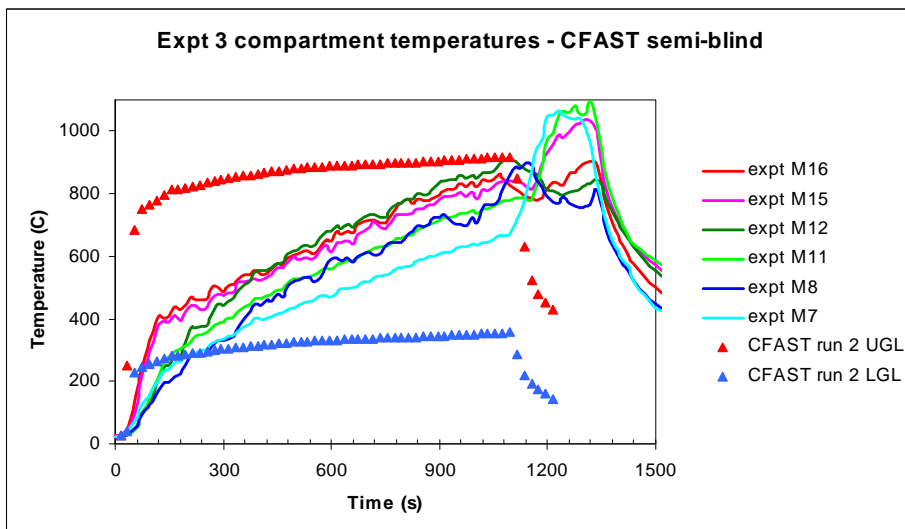
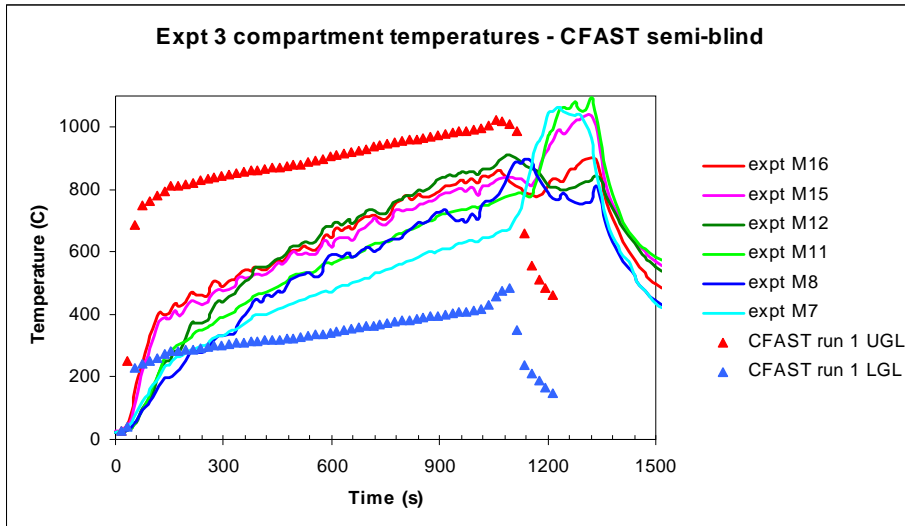


Fig. B8 Measured and CFAST predicted gas layer temperatures for Test 3

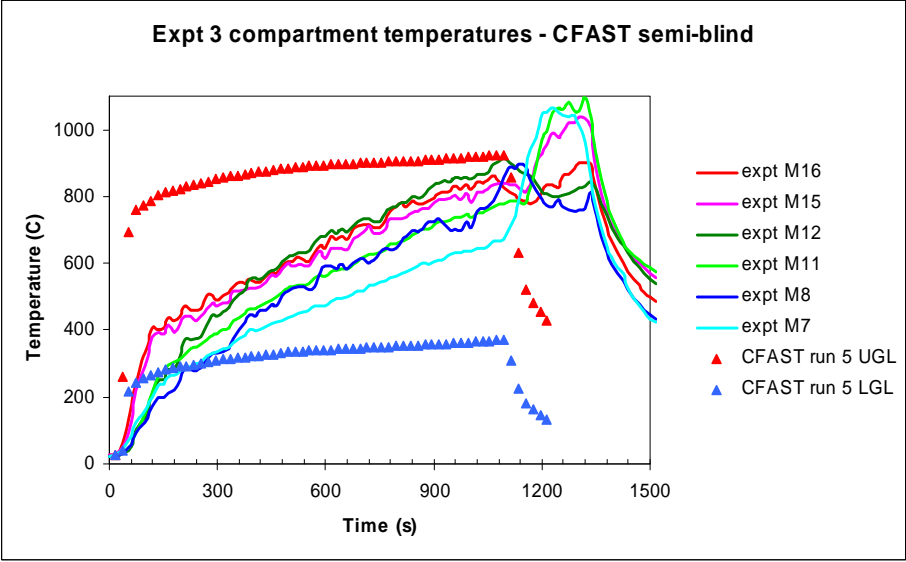
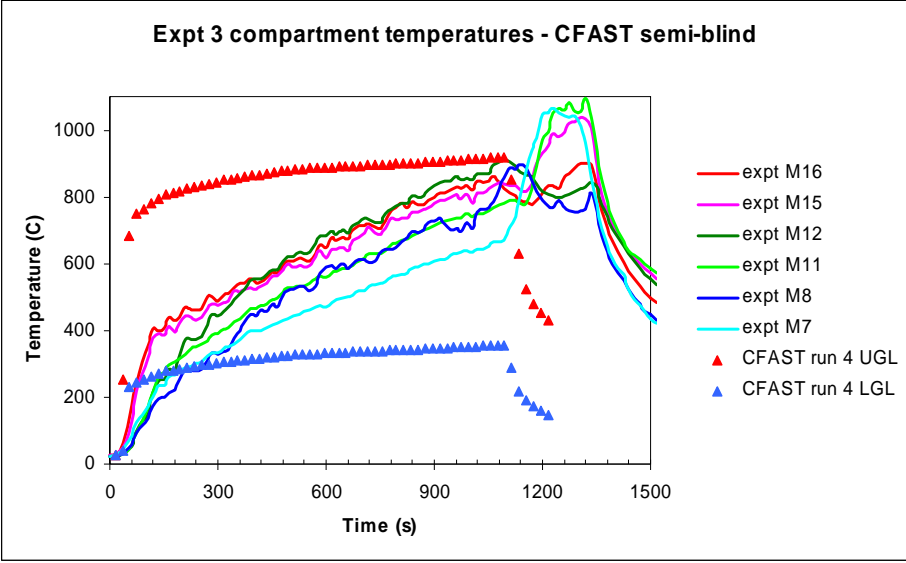


Fig. B8 Measured and CFAST predicted gas layer temperatures for Test 3 (contd.)

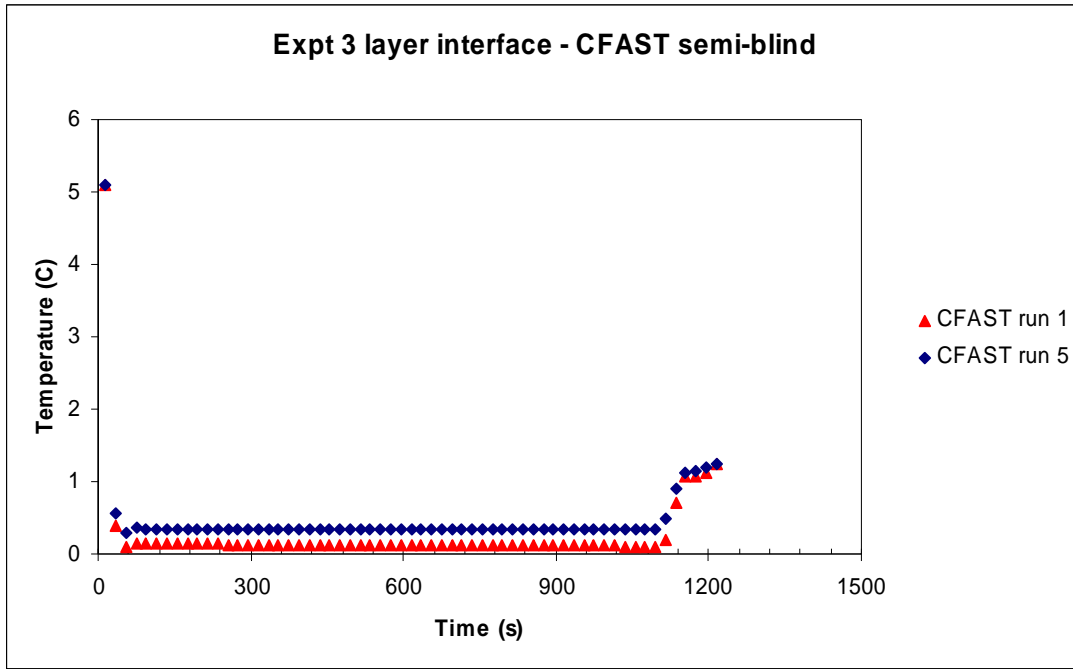


Fig. B9 CFAST predicted hot gas layer height for Test 3

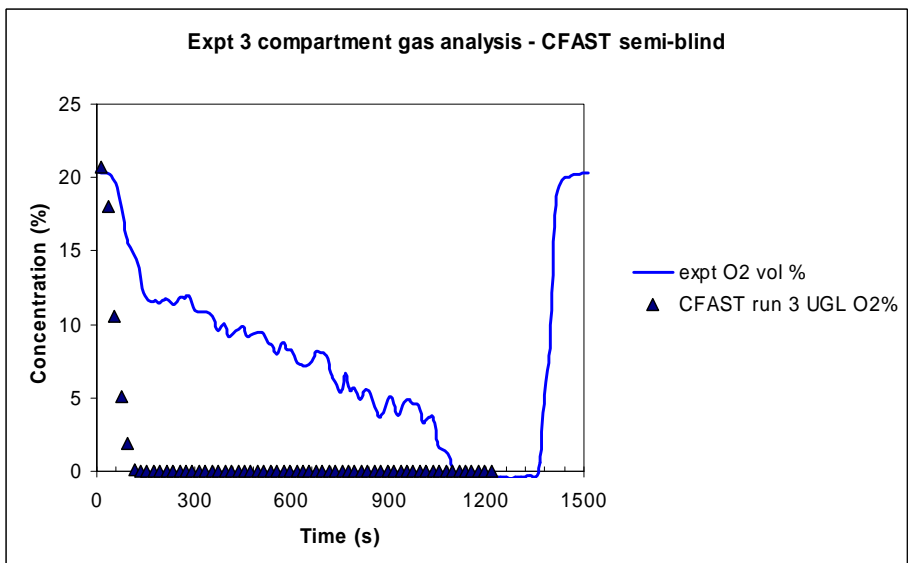
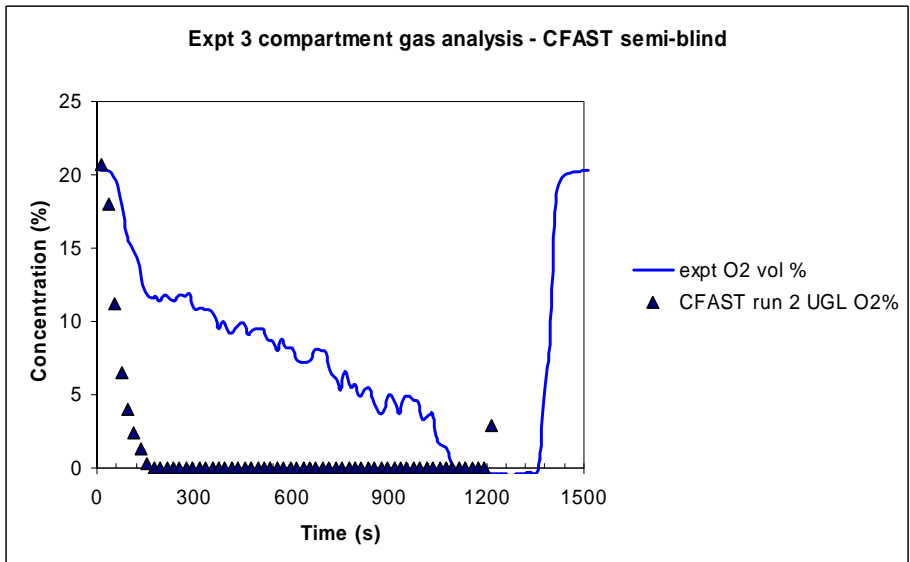
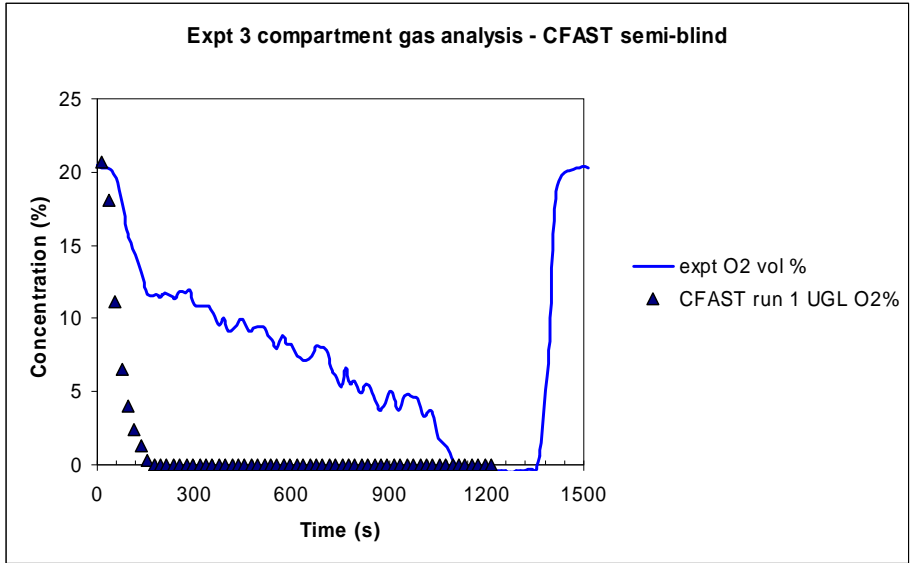


Fig. B10 Measured and CFAST predicted oxygen concentrations for Test 3

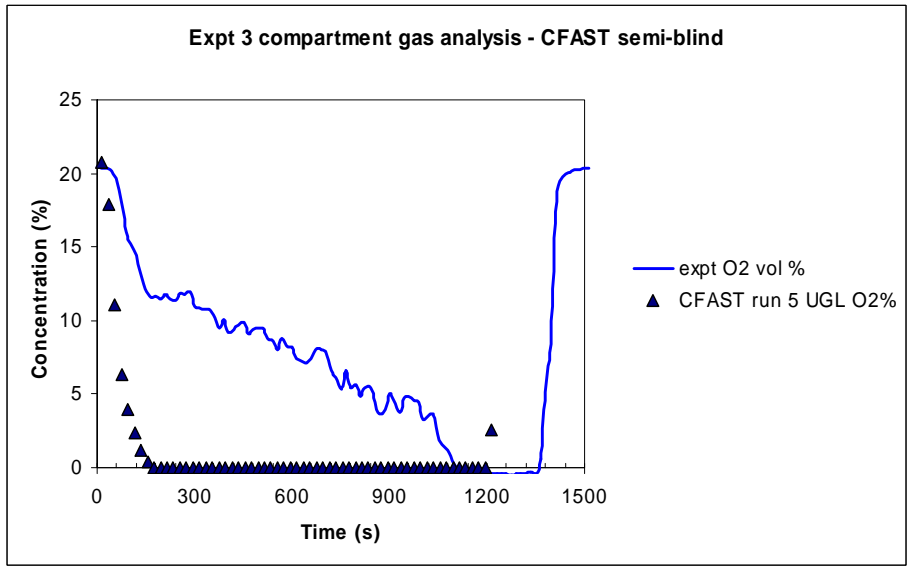
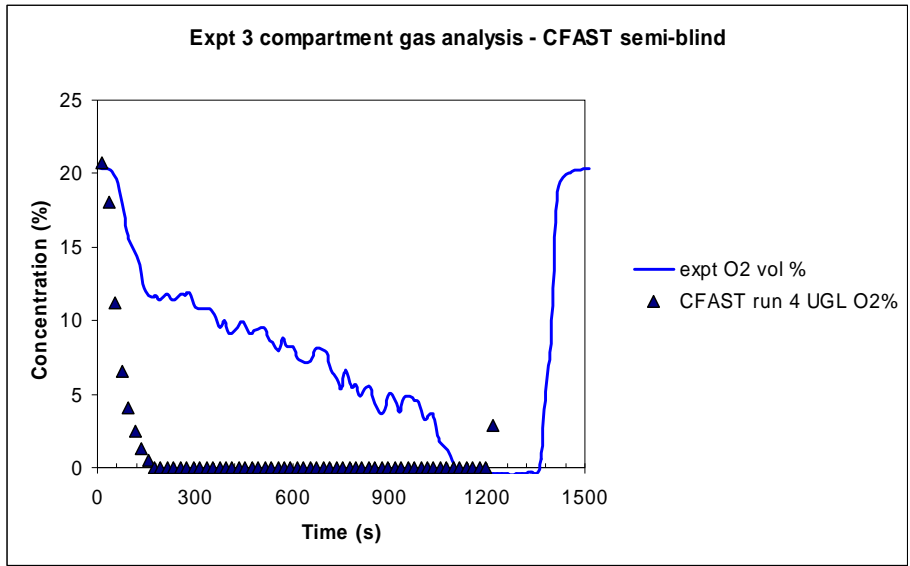


Fig. B10 Measured and CFAST predicted oxygen concentrations for Test 3 (contd.)

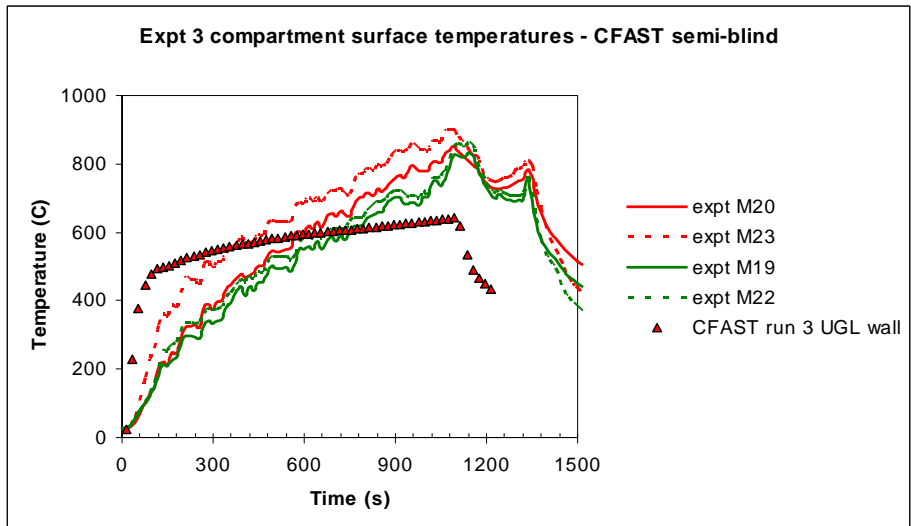
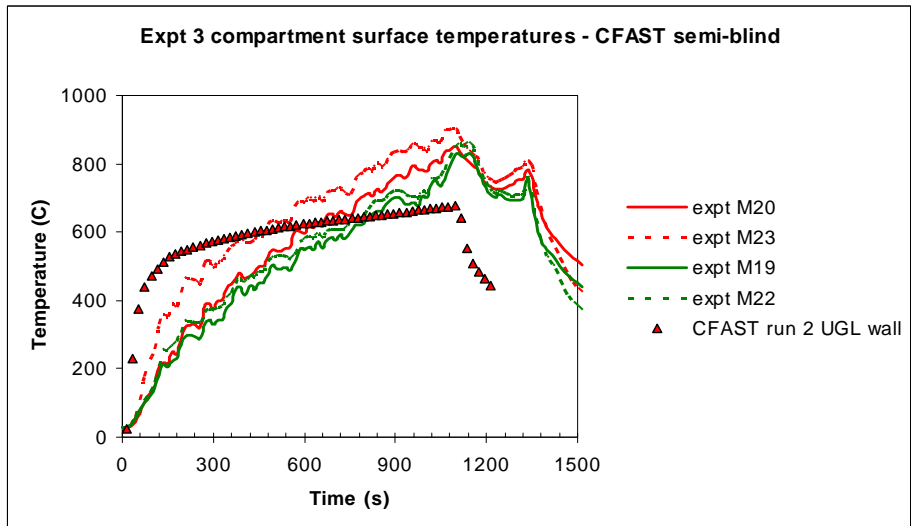
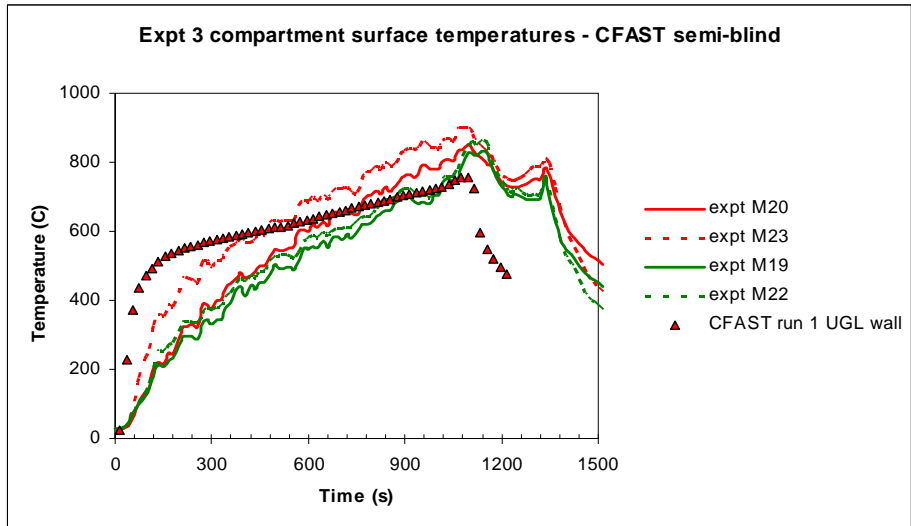


Fig. B11 Measured and CFAST predicted wall surface temperatures for Test 3

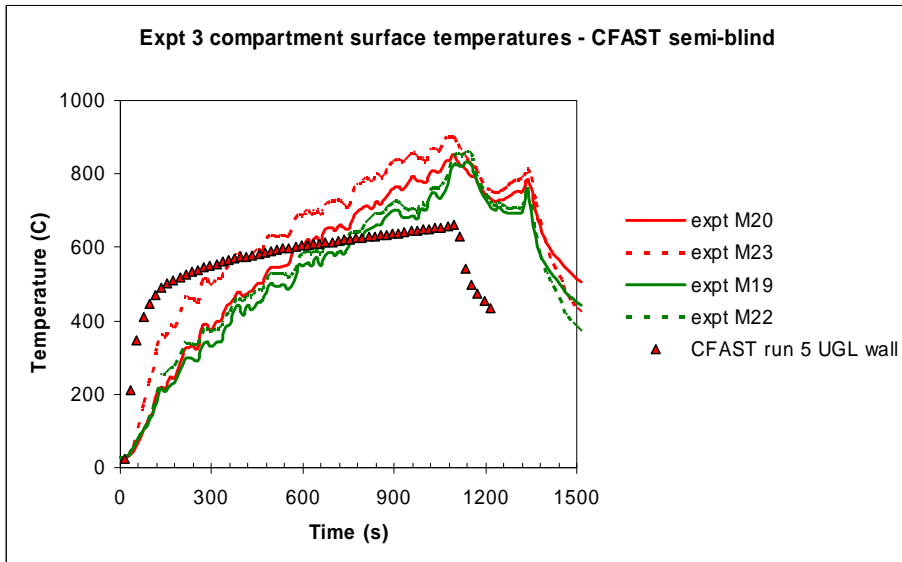
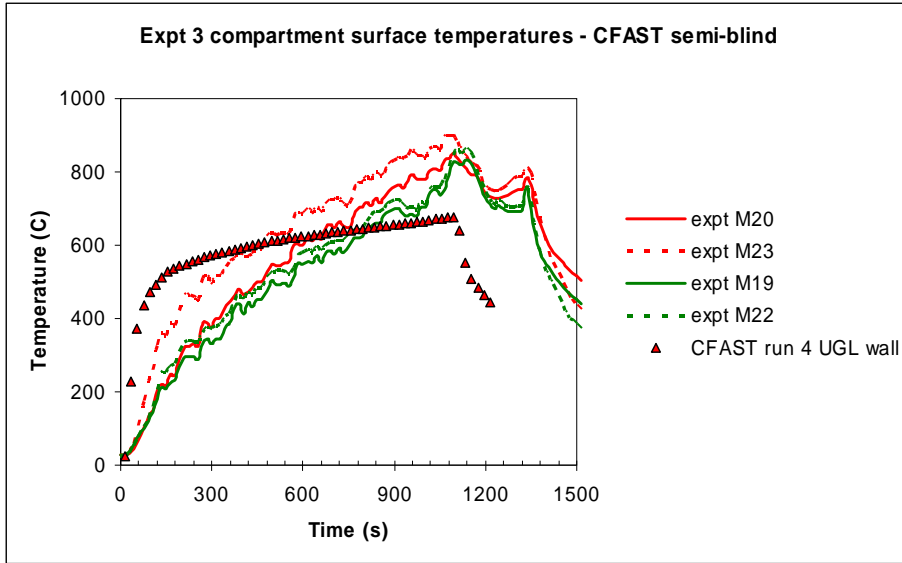


Fig. B11 Measured and CFAST predicted wall surface temperatures for Test 3 (contd.)

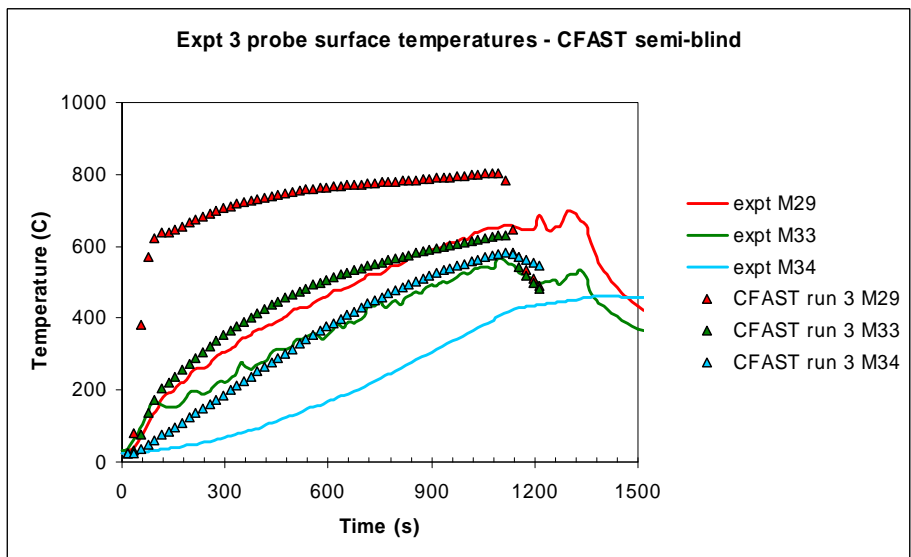
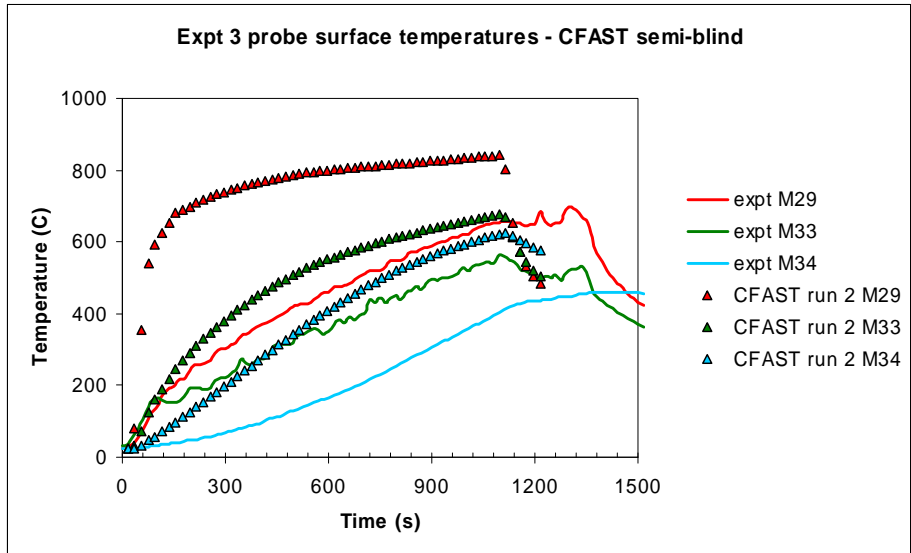
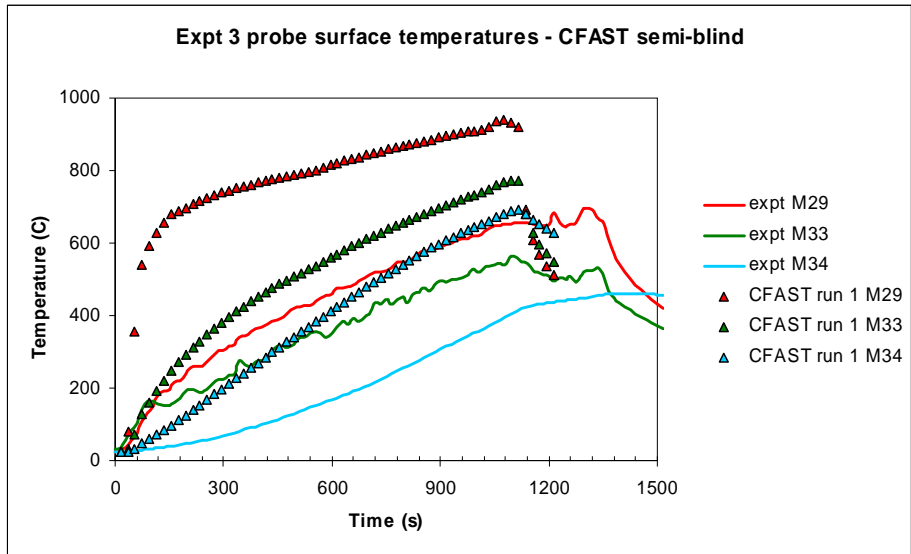


Fig. B12 Measured and CFAST material probe surface temperatures for Test 3

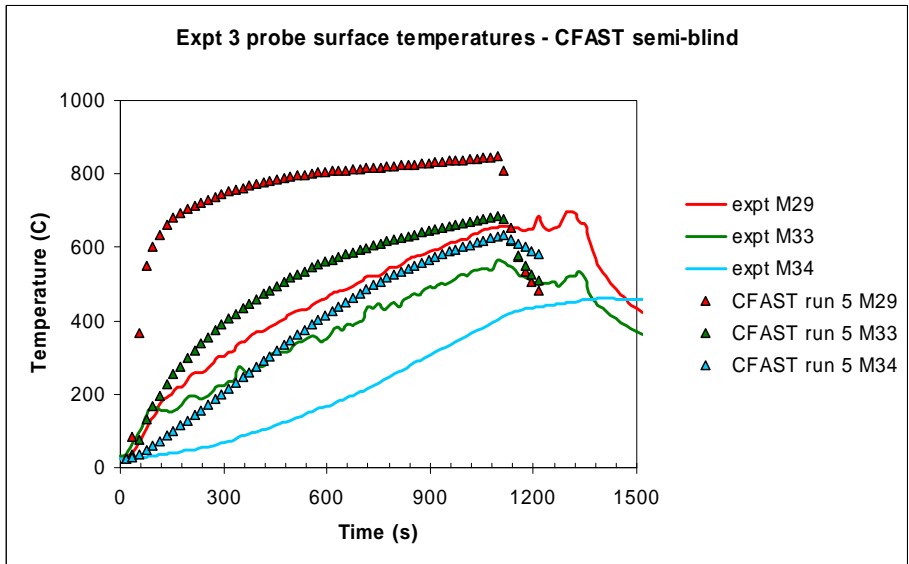
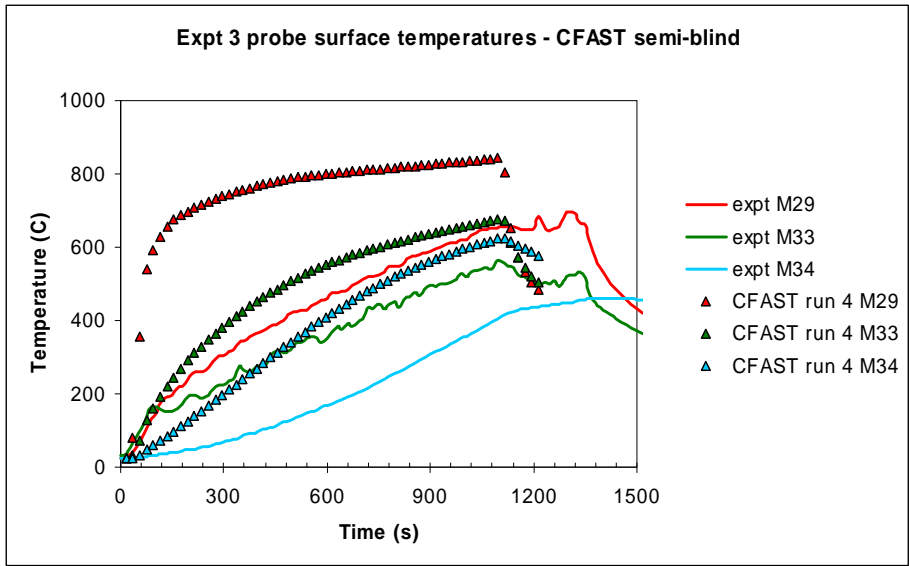


Fig. B12 Measured and CFAST material probe surface temperatures for Test 3 (contd.)

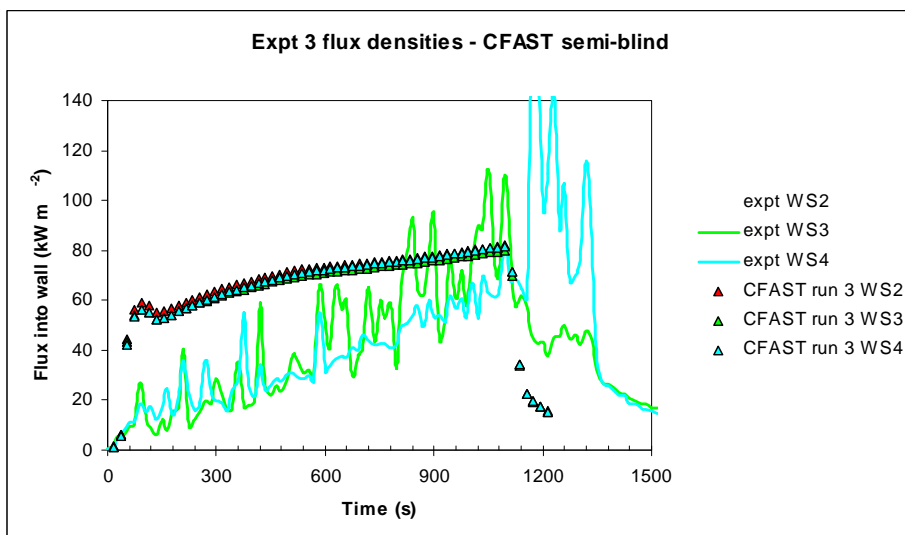
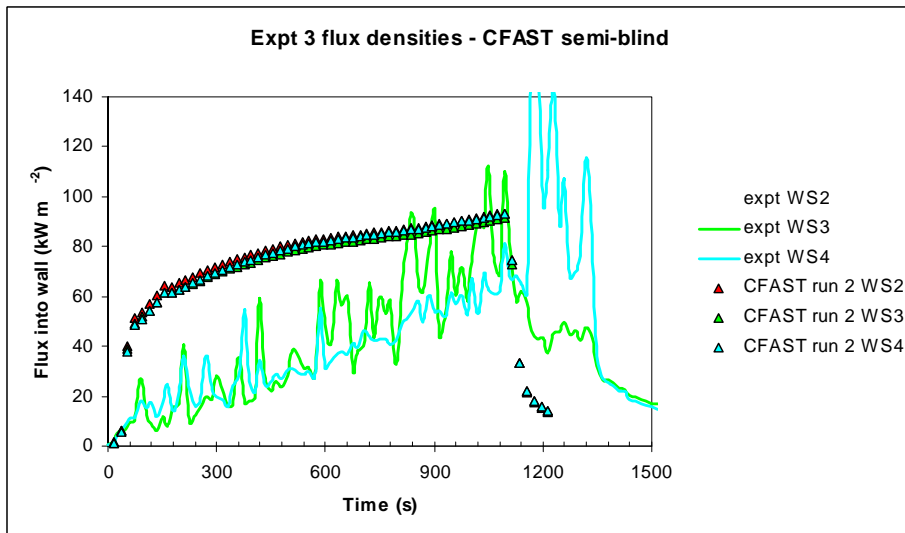
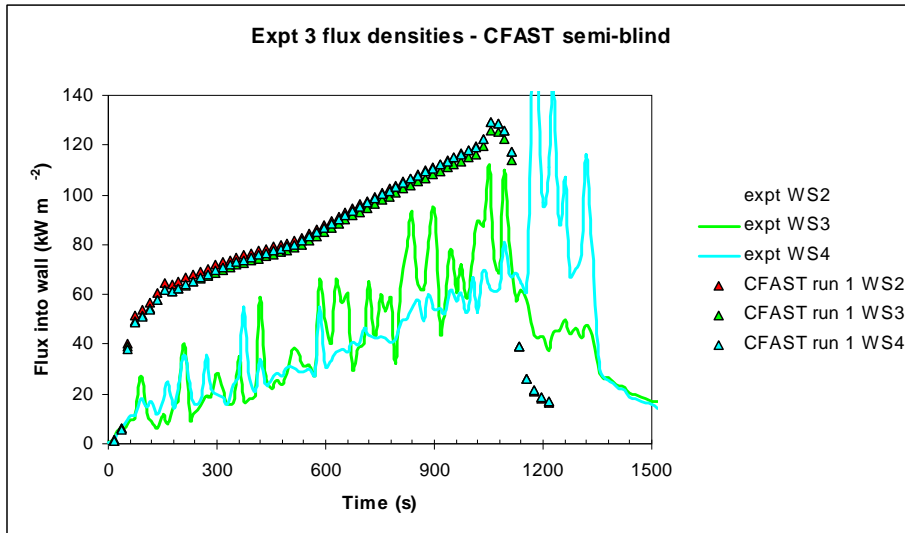


Fig. B13 Measured and CFAST flux densities for Test 3

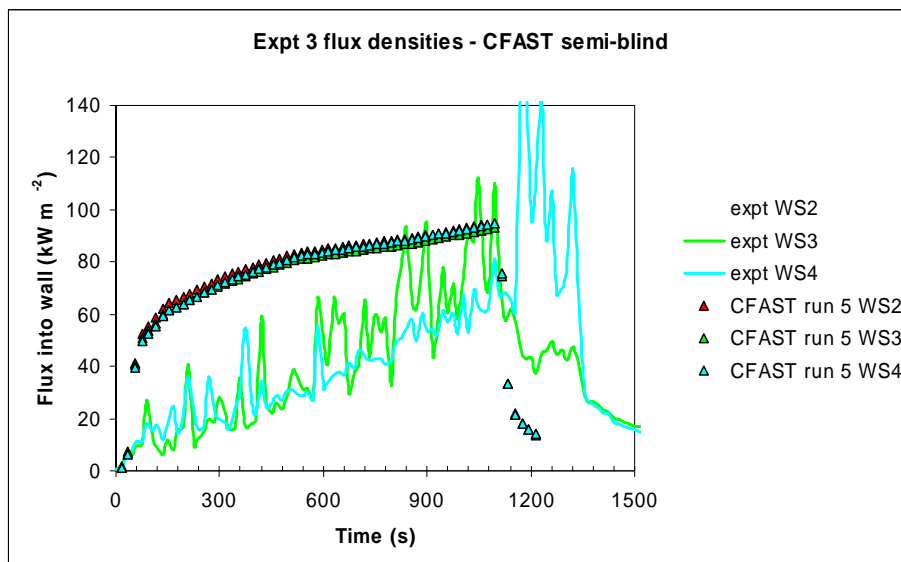
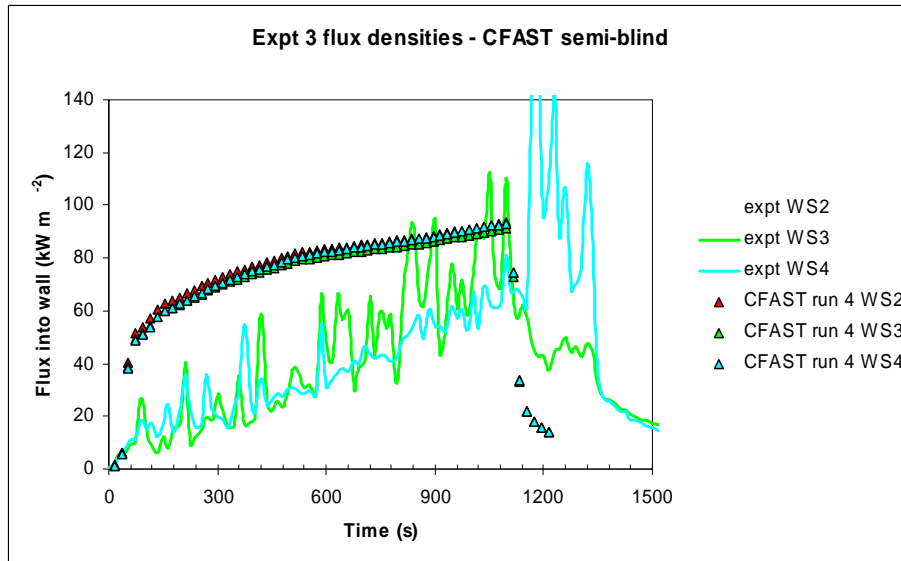


Fig. B13 Measured and CFAST flux densities for Test 3 (contd.)

JASMINE

As noted above in the *input parameters and assumptions* section, a number of parametric calculations (runs) were performed for Tests 1 and 3 in the blind and open stages of the benchmark exercise. Additional open calculations were then conducted for Test 3. Tables B2, B3 and B4 summarize the main features of these calculations.

Table B2 JASMINE blind calculation runs

Test	Run no.	Fuel release rate	Radiation model	Oxygen limit on combustion	Mechanical vent flow
1	run 1	0.039 kg s ⁻¹	six-flux	none	measured
1	run 2	0.0234 kg s ⁻¹	six-flux	none	measured
3	run 1	0.039 kg s ⁻¹	six-flux	none	measured
3	run 2	0.0234 kg s ⁻¹	six-flux	none	measured

Table B3 JASMINE semi-blind calculation runs

Test	Run no.	Fuel release rate	Radiation model	Oxygen limit on combustion	Mechanical vent flow
1	run 1	0.75 x measured	six-flux	none	measured
3	run 1	measured	six-flux	none	measured
3	run 2	0.75 x measured	six-flux	none	measured

Table B4 JASMINE open calculation runs

Experiment	Run no.	Fuel release rate	Radiation model	Oxygen limit on combustion *	Mechanical vent flow
3	run 1	0.75 x measured	discrete transfer	none	measured
3	run 2	0.5 x measured	discrete transfer	X ₁ = 15 %, T ₁ = 300 °C, T ₂ = 600 °C	measured
3	run 3	0.75 x measured	six-flux	X ₁ = 15 %, T ₁ = 300 °C, T ₂ = 600 °C	measured
3	run 4	0.75 x measured	discrete transfer	X ₁ = 15 %, T ₁ = 300 °C, T ₂ = 600 °C	measured
3	run 5	measured	discrete transfer	X ₁ = 15 %, T ₁ = 300 °C, T ₂ = 600 °C	measured

3	run 6 **	0.75 x measured	discrete transfer	$X_1 = 15 \%$, $T_1 = 550 \text{ }^\circ\text{C}$, $T_2 = 600 \text{ }^\circ\text{C}$	measured
3	run 7	0.75 x measured	discrete transfer	$X_1 = 15 \%$, $T_1 = 300 \text{ }^\circ\text{C}$, $T_2 = 600 \text{ }^\circ\text{C}$	0.5 x measured
* see Fig. B2 for explanation of X_1, T_1 and T_2 ** data not presented in this annex					

Fig. B14 illustrates the single-block, Cartesian grid used in the JASMINE calculations, which included approximately 80,000 cells. Note that the grid is relatively uniform, with a minimum cell dimension of 0.05 m in each direction and a maximum cell dimension of 0.3 m (outside the compartment).

Fig. B15 illustrates the development of gas temperatures over the first 18 minutes in the JASMINE semi-blind calculation for Test 1. Note that at 18 minutes the CFD solution had diverged, so the calculated temperatures are no longer valid. Fig. B16 shows the oxygen mass fraction at 1 and 15 minutes for the same simulation. Fig. B17 and Fig. B18 show the same information for semi-blind (run 1) calculation for Test 3.

Fig. B19 - Fig. B22 present various comparisons between measured and predicted values for the blind JASMINE simulations of Test 1. Note that as this part of the benchmark activity was considered to be 'exploratory' in nature, detailed comparisons between measurement and prediction was conducted only for a few key variables. Fig. B23 - Fig. B26 present the comparative plots for the blind simulations of Test 3.

Fig. B27 - Fig. B31 compare predicted and measured gas temperatures (at selected measurement locations), oxygen concentration, surface temperatures, heat flux densities and doorway velocities for Test 1. Fig. B32 - Fig. B37 show the comparisons for Test 3.

The main observations and findings from the JASMINE blind and semi-blind calculations are summarized below:

- The blind calculations for both experiments, when using the higher fuel pyrolysis rate of 0.039 kg s^{-1} , were quite encouraging considering the physics of the problem. A simple engineering estimate of pyrolysis rate was in this case sufficient to capture the main gas phase properties of the experiments. Obviously, the transient effects

due to changes in pyrolysis rate due to the development of conditions inside the enclosure were not captured.

A main discrepancy between the blind calculations and the measurements was in the doorway vent flow in Test 3, where in contrast to the flow being predominantly into the compartment as indicated in the predictions, the measurements suggest a more distinct two-way flow at the wall vent. This discrepancy may be due, in part at least, to the imposed exhaust flow at the mechanical ventilation duct in the JASMINE calculations forcing a significant amount of air into the compartment through the wall vent.

- The semi-blind calculations for Test 1, using the fuel pyrolysis rate derived from the experimental measurements (actually 75 % of the measured pyrolysis rate - to account for radiation losses due to soot), were judged encouraging. The gross features of the gas temperatures, doorway flows and radiation fluxes were captured quite well. Compartment temperature was arguably calculated to rise too quickly. Whereas the calculated flux densities at WS2 and WS3 were quite reasonable, the predicted flux density at WS4 (towards the front of the compartment) was significantly lower than that measured. This could be attributed perhaps to the use of the six-flux radiation model, which misses some of the important angular radiant intensity information.

While for Test 3 the semi-blind calculations were generally considered quite reasonable, there was however greater discrepancy with the measured data compared to Test 1. In particular, the direction of the wall vent flow was predicted to be predominantly into the compartment compared to the actual experiment which exhibited a more pronounced two-way flow. And again, there was a noted under-prediction of the flux density at WS4. Of the two semi-blind simulations, the one using 75 % of the measured fuel pyrolysis rate generated, on average, results closer to the measurements, compared to using the full pyrolysis rate. Recall here that the justification for reducing the pyrolysis rate is to account, in the overall energy balance, the heat lost from radiating soot particulates (not modeled in the JASMINE calculations), i.e. akin to the radiative fraction in CFAST.

A noted feature of the JASMINE calculations when using the measure pyrolysis rate as the fuel source term was the convergence difficulties in both experiments after about 18 minutes. For Test 3 this coincides with the time where there is a sharp increase in the pyrolysis rate derived from the weight measurements, due possibly to

the kerosene boiling off from the fuel tray. This stage of the experiment could be argued to be beyond what can be reasonably expected for a fire model to predict.

Fig. B38 - Fig. B42 summarize the results of open calculations that were then undertaken for Test 3 (arguably the more complex of the two experiments) to investigate a number of issues that had arisen. The main findings from these open calculations were:

- The choice of the radiation model. Calculations were repeated using the discrete transfer radiation model, which includes radiant intensity information from the whole hemisphere surrounding a surface point, e.g. a material probe location, and not just the Cartesian axis directions.

Comparing the predictions from open calculations runs 3 and 4, where the only difference is in the radiation model, it can be seen that there is only a minimal sensitivity to the choice of model for all output variables. On note is the fact that the under-prediction of the flux density at WS4 is maintained even with the discrete transfer radiation model, suggesting that the cause of the discrepancy with measurement lies elsewhere.

- The influence of oxygen concentration on the fuel combustion process. In all blind and semi-blind calculations the effect of oxygen limitation on the combustion process had been ignored, i.e. the local rate of combustion was controlled by the amount of oxygen and fuel available and the local turbulent time-scale. No additional limit was imposed whereby oxygen concentration dropping below some threshold terminated the reaction. In the open stage, calculations were performed with an additional oxygen limiter, as described above in Section B2 (*Input Parameters and Assumptions*) and Fig. B1. Table B4 details the oxygen/temperature limiting parameters investigated. Note that the choice of $X_1, T_1, T_2 = 15\%, 300\text{ }^\circ\text{C}, 600\text{ }^\circ\text{C}$ follows the settings used previously in FDS calculations.

There was no significant influence on the calculated variables when invoking the additional oxygen limitation mechanism, as illustrated by comparing the results for blind runs 1 and 4 (which were otherwise identical). It is perhaps not too surprising that little difference was observed due to the high compartment temperatures, as even with the additional oxygen limitation mechanism combustion still occurs if the local gas temperature is sufficiently high.

- The influence of the imposed exhaust at the mechanical ventilation duct It had been considered possible that the level of the imposed exhaust might be the primary reason for the JASMINE calculations indicating less outflow from the wall vent compared to that suggested by the experimental measurements.

Blind runs 4 and 7 compare directly the effect of reducing the imposed exhaust rate by 50 %. The overall effect, however, was to reduce the level of agreement between predicted and measured temperatures and fluxes. Even the wall vent flow was only marginally more bi-directional.

Mass and energy 'budgets' are shown in Fig. B43 - Fig. B44 respectively for some of the open calculations for Test 3. The energy 'budget' in particular is quite informative and illustrates that both heat losses to the solid boundaries and heat convected through the mechanical ventilation duct are significant.

A general note from the JASMINE work is that the presence of soot, and the subsequent radiation absorption and emission, may have an important bearing on the gas temperatures predicted. This in turn influences the radiation fluxes significantly (bearing in mind the T^4 dependency on radiant intensity), which then has a major influence on the conduction into the walls and targets and their temperature rise.

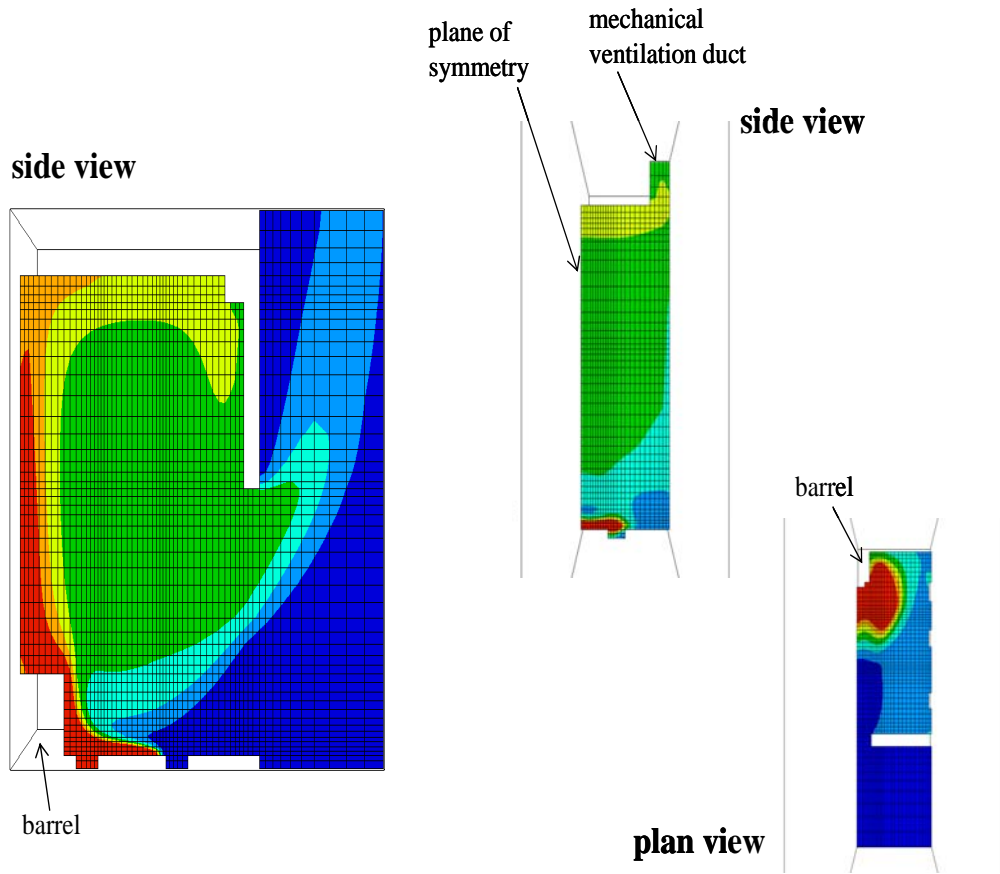


Fig. B14 JASMINE CFD grid

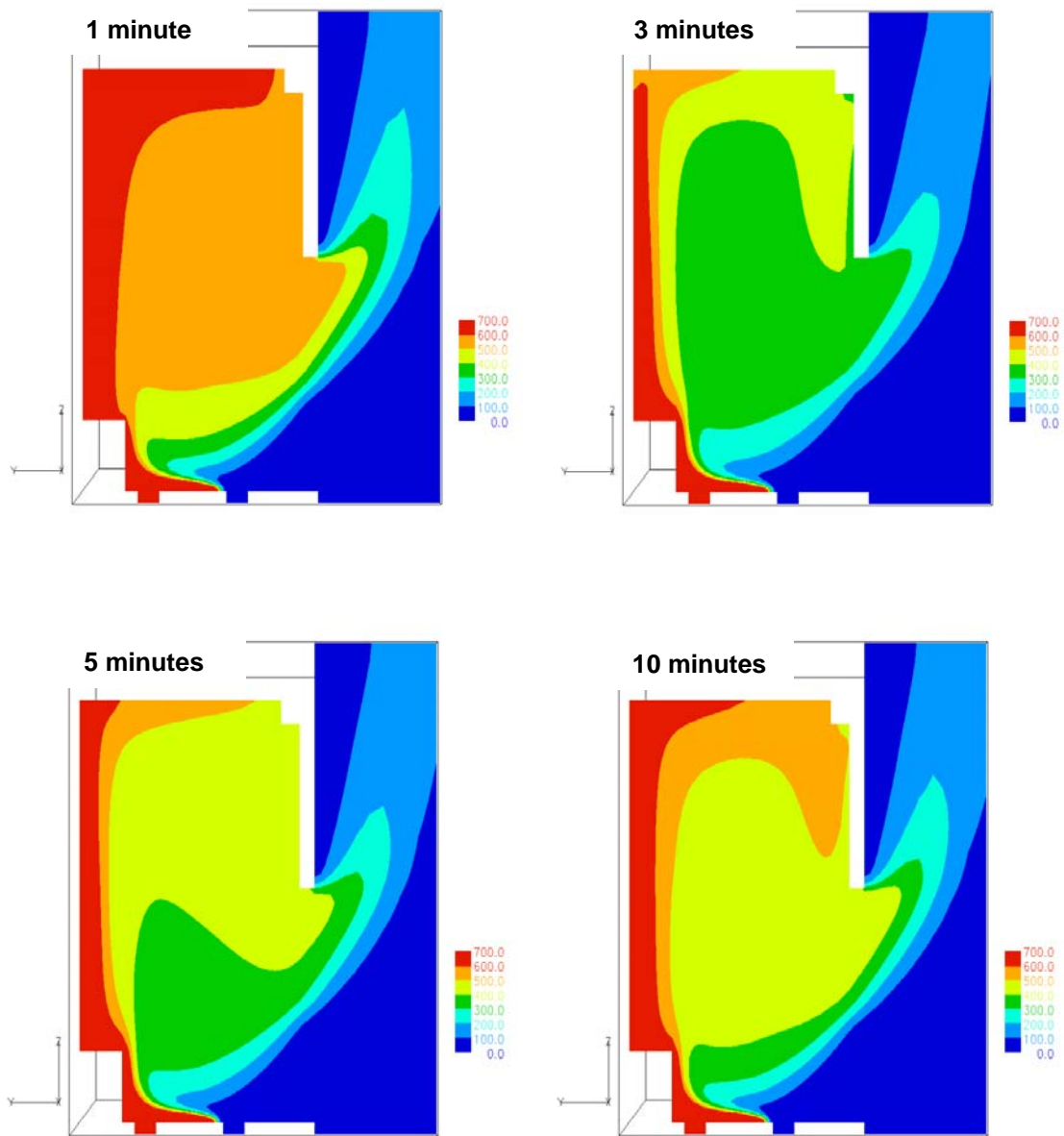


Fig. B15 JASMINE calculated temperatures for Test 1 (semi-blind)

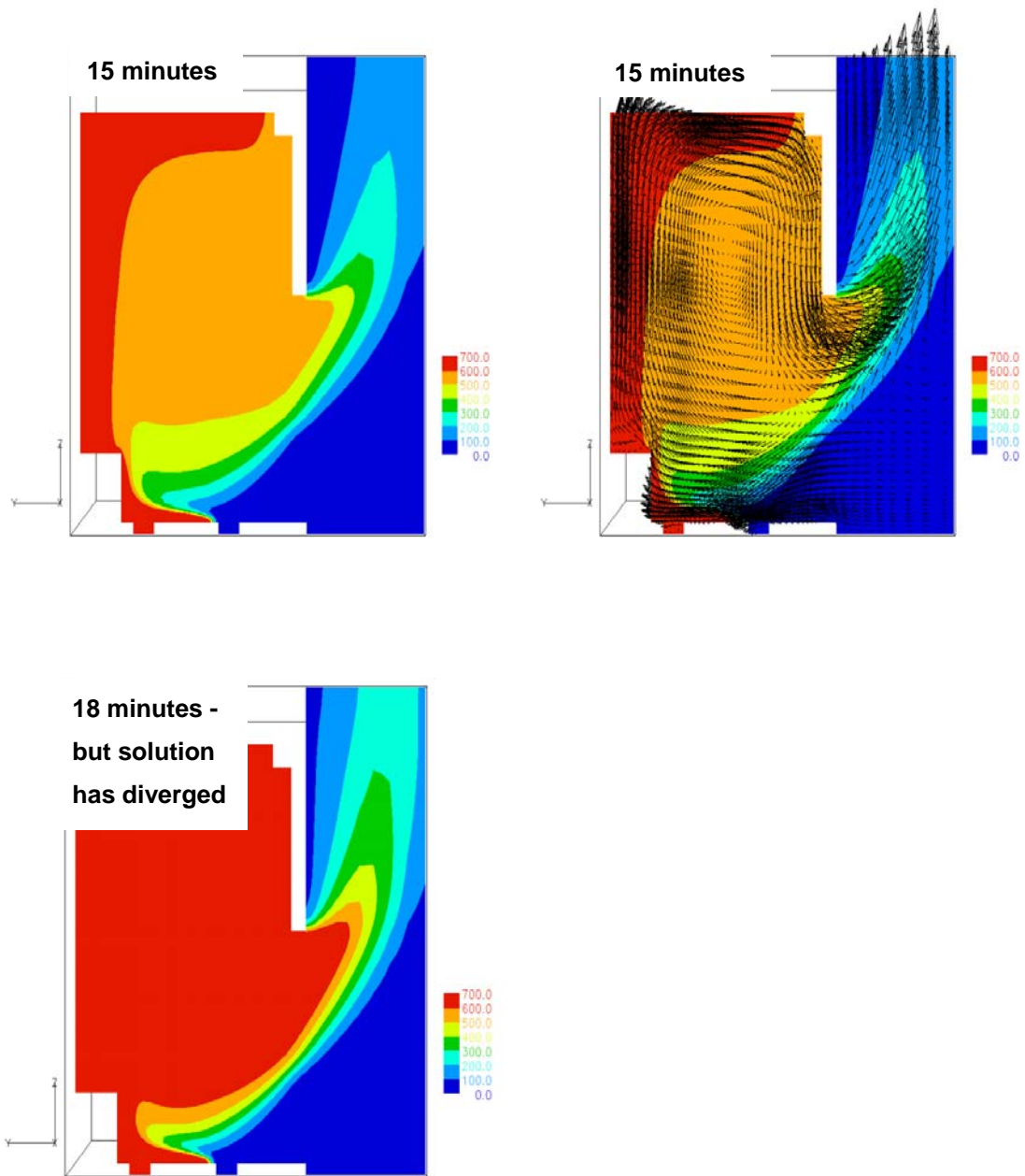


Fig. B15 JASMINE calculated temperatures for Test 1 (semi-blind) (contd.)

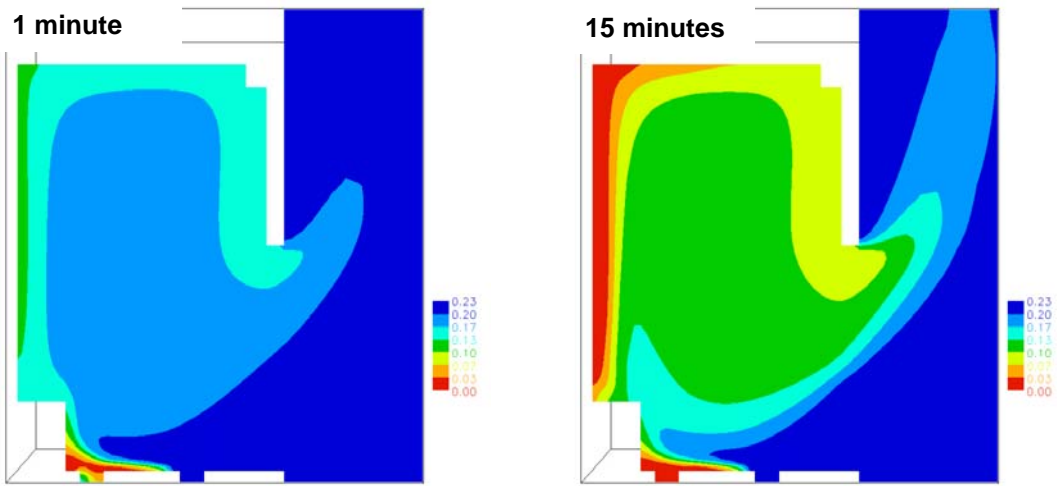


Fig. B16 JASMINE calculated O₂ mass fraction for Test 1 (semi-blind)

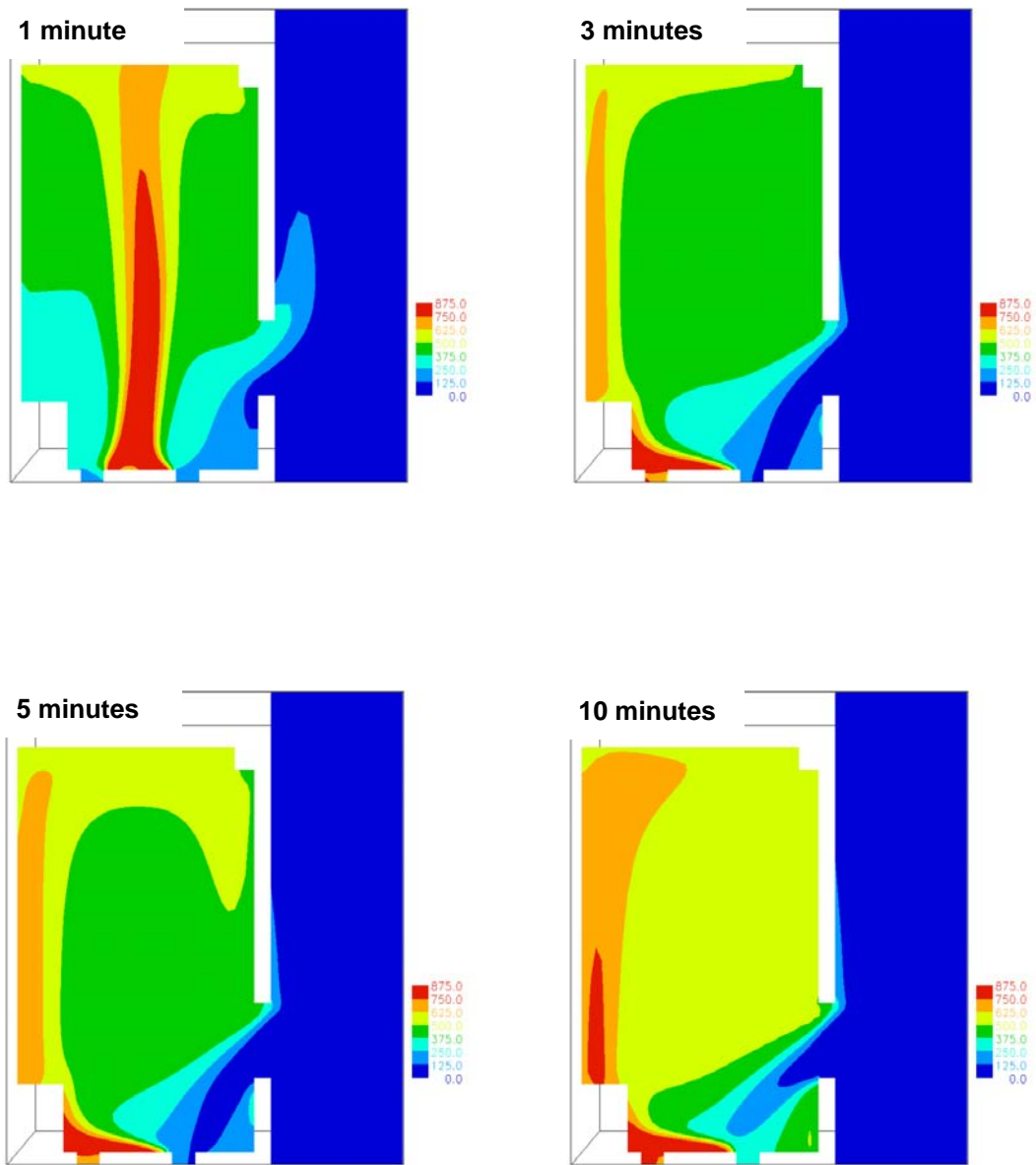


Fig. B17 JASMINE calculated temperatures for Test 3 (semi-blind run 1)

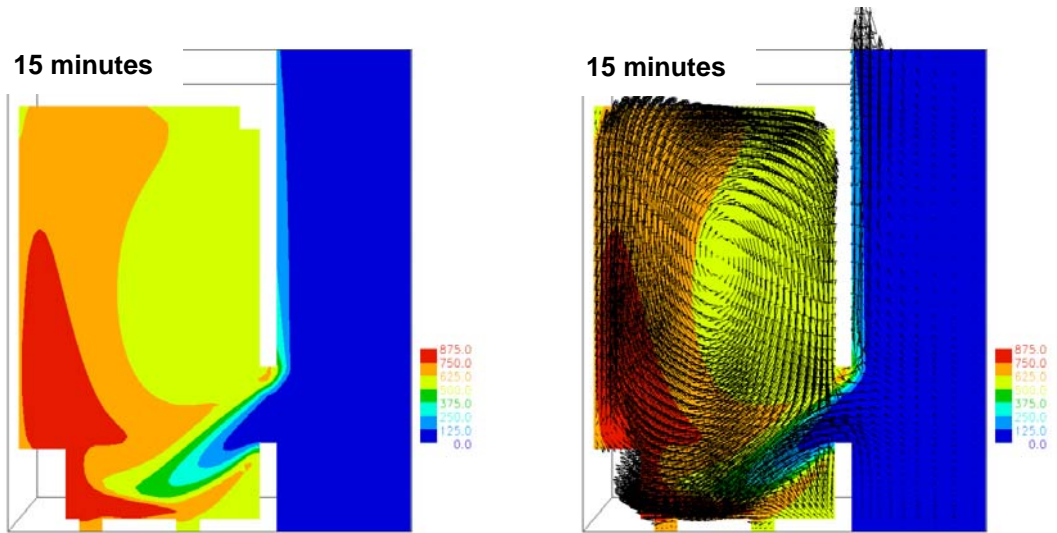


Fig. B17 JASMINE calculated temperatures for Test 3 (semi-blind run 1) (contd.)

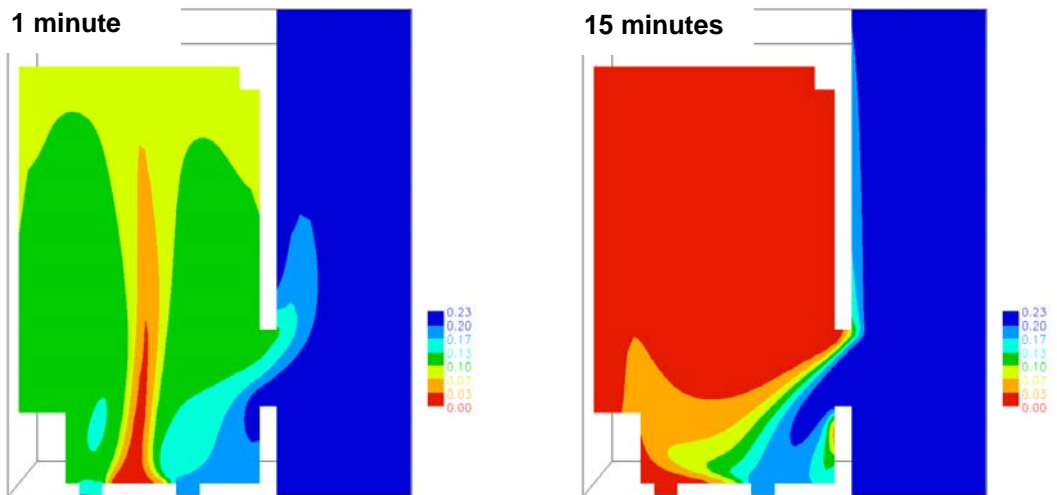


Fig. B18 JASMINE calculated O₂ mass fraction for Test 3 (semi-blind run 1)

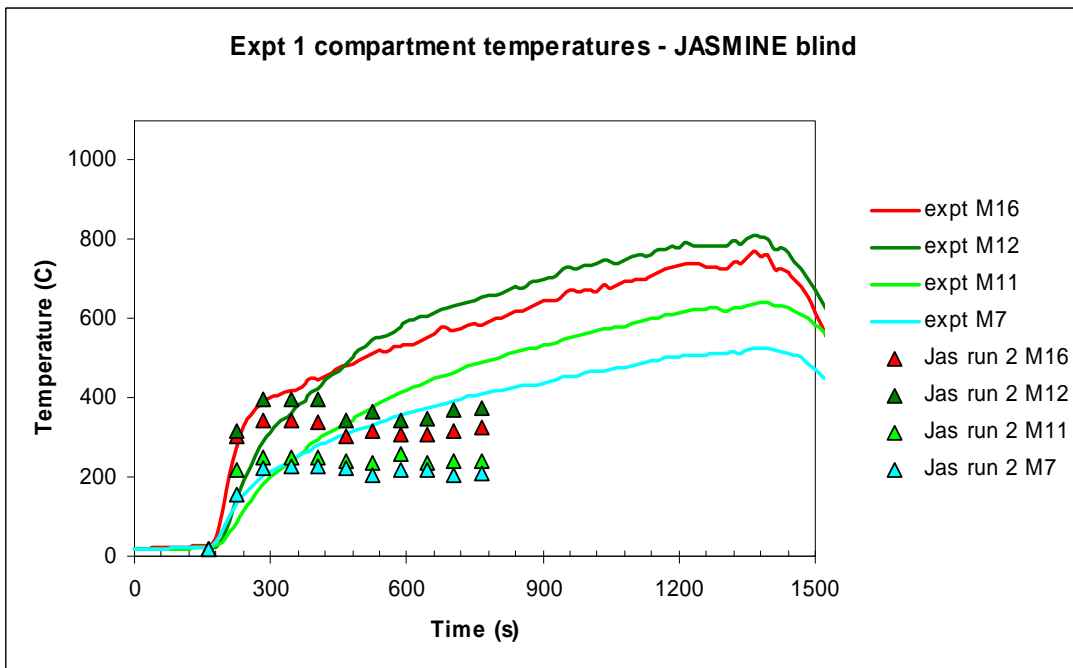
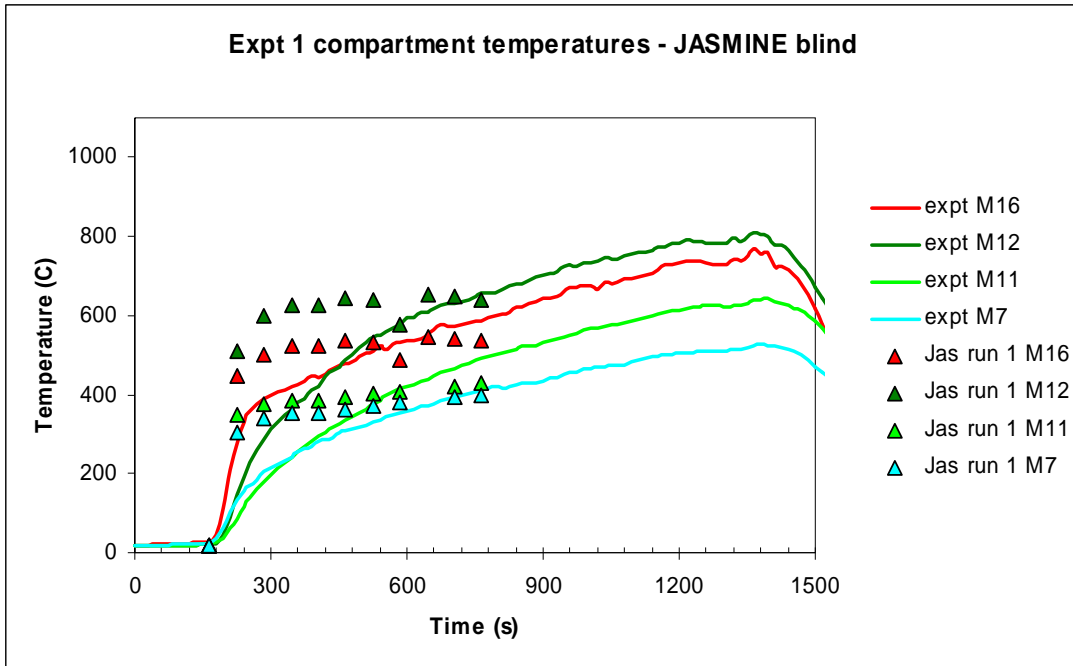


Fig. B19 Measured and JASMINE predicted (blind) gas temperatures for Test 1

Note that Jasmine data gives mass fraction

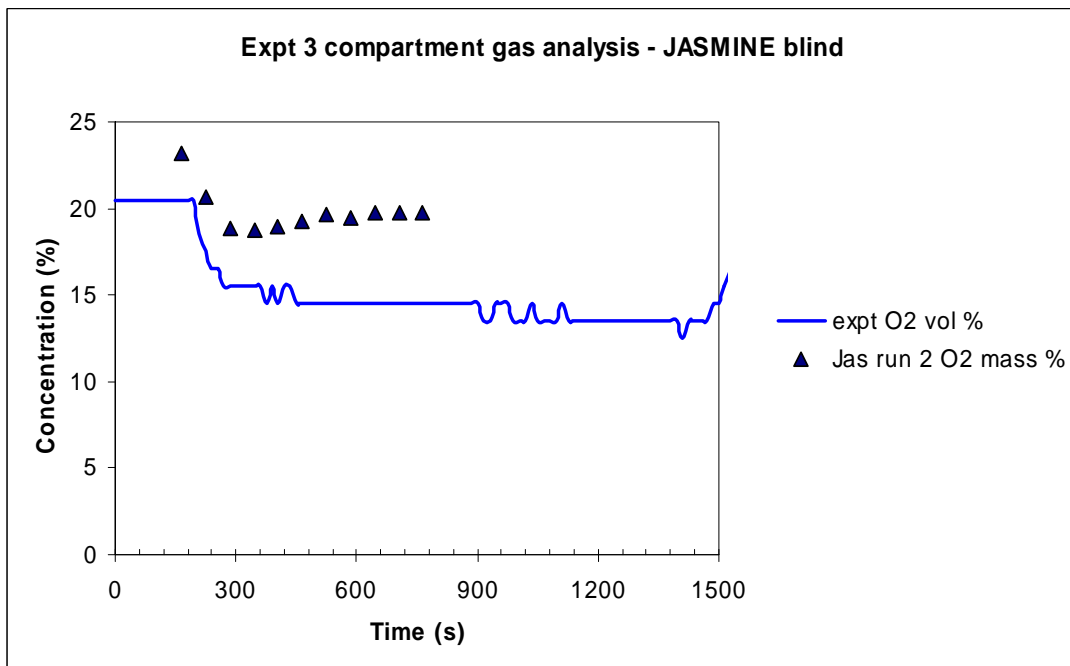
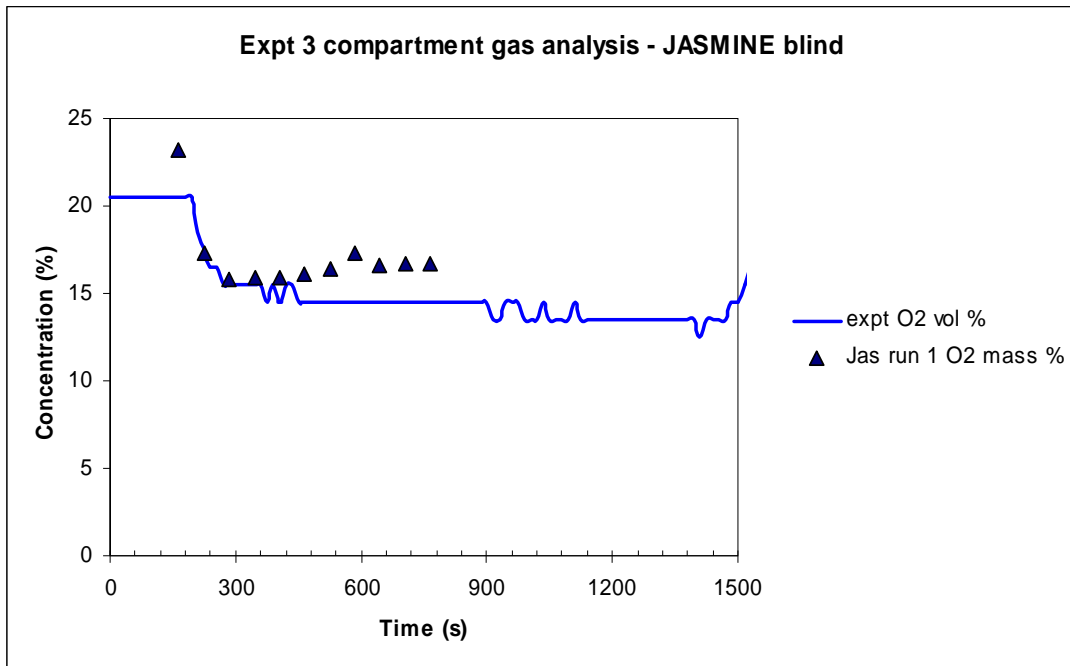


Fig. B20 Measured and JASMINE predicted (blind) oxygen concentration for Test 1

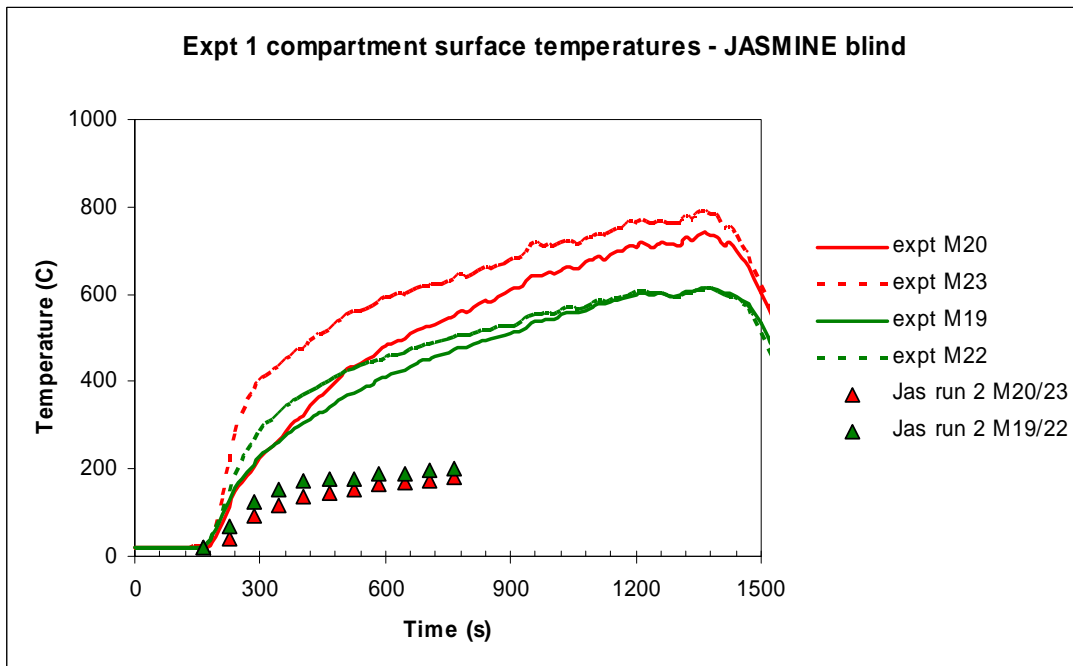
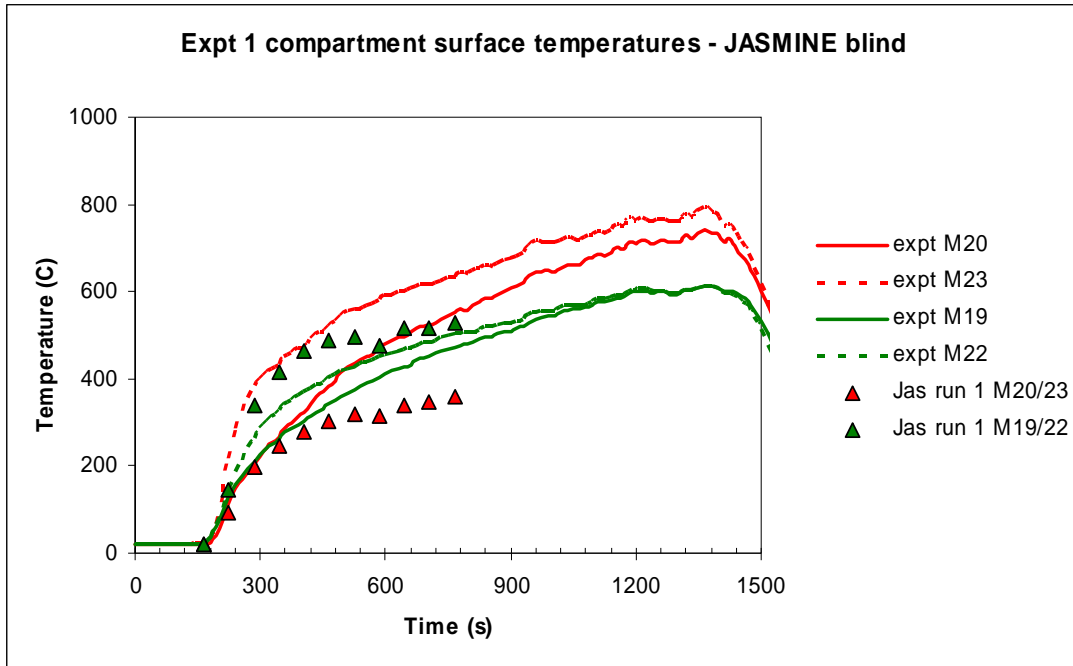


Fig. B21 Measured and JASMINE predicted (blind) wall surface temperatures for Test 1'

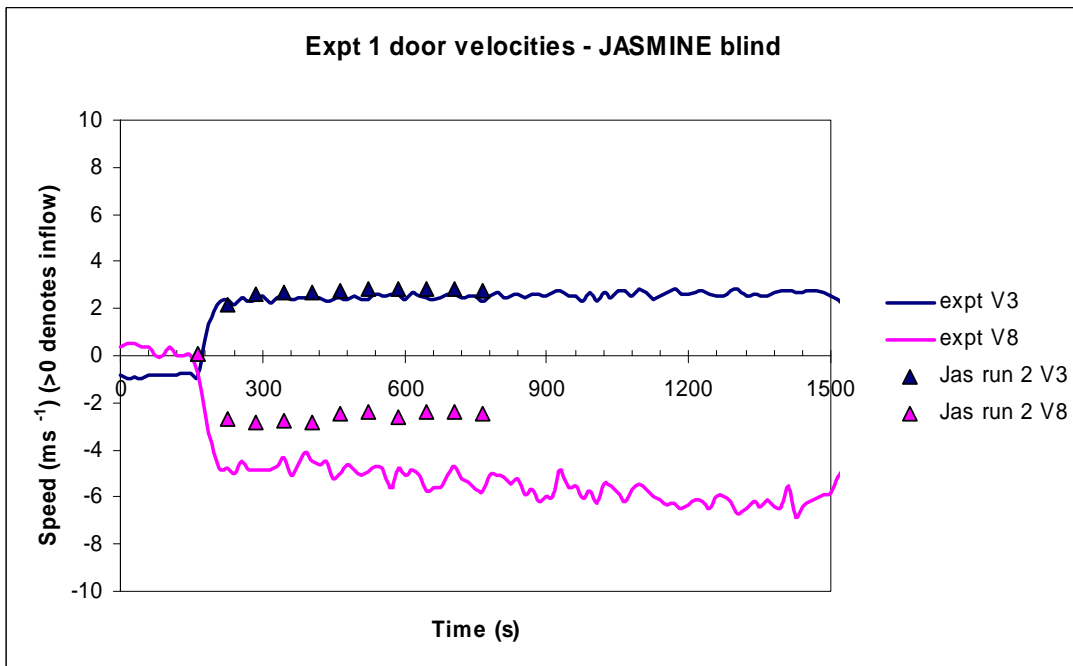
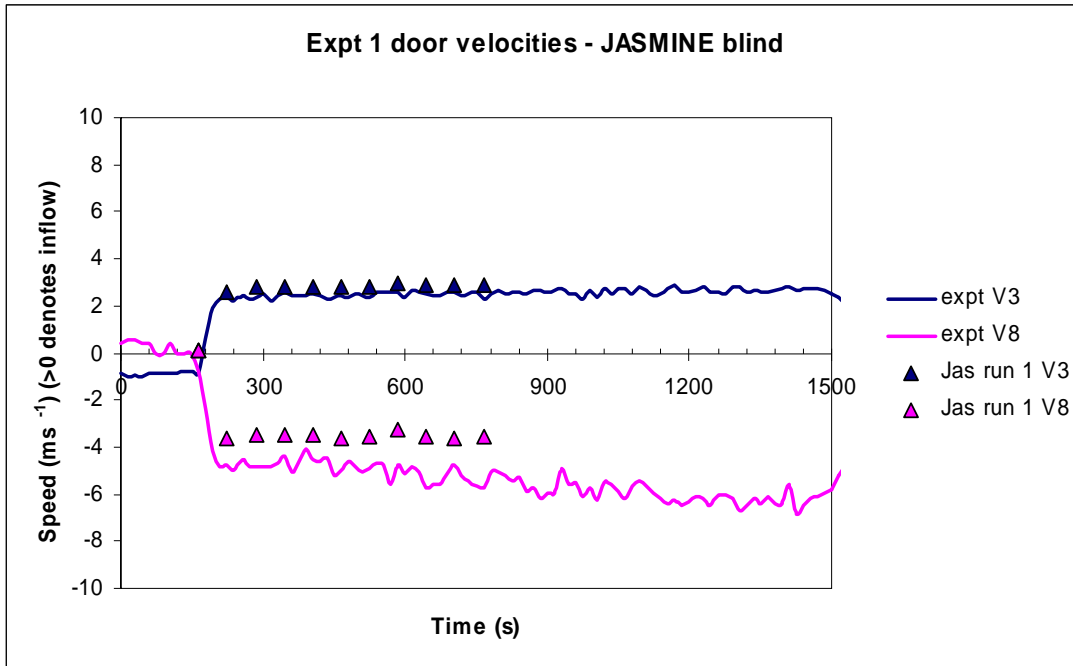


Fig. B22 Measured and JASMINE predicted (blind) door velocities for Test 1

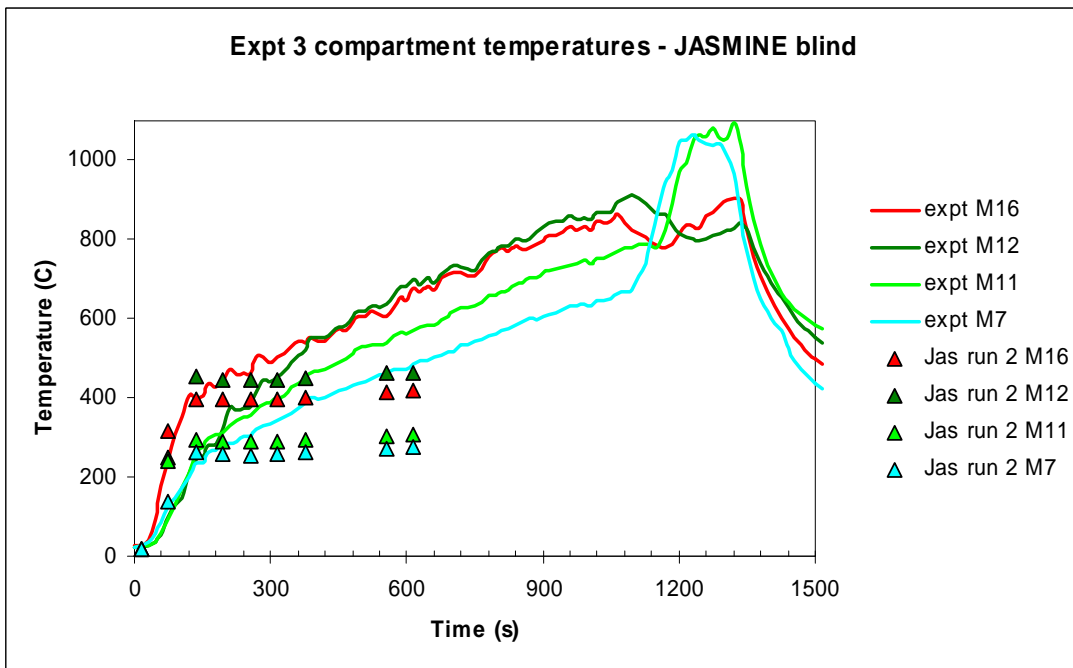
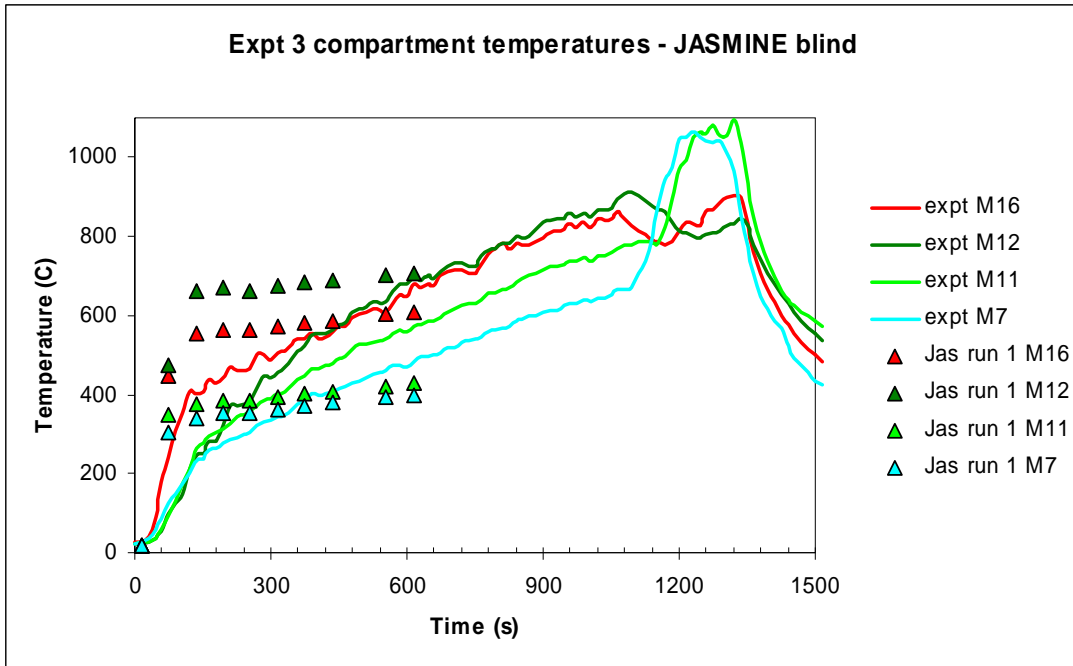


Fig. B23 Measured and JASMINE predicted (blind) gas temperatures for Test 3

Note that Jasmine data gives mass fraction

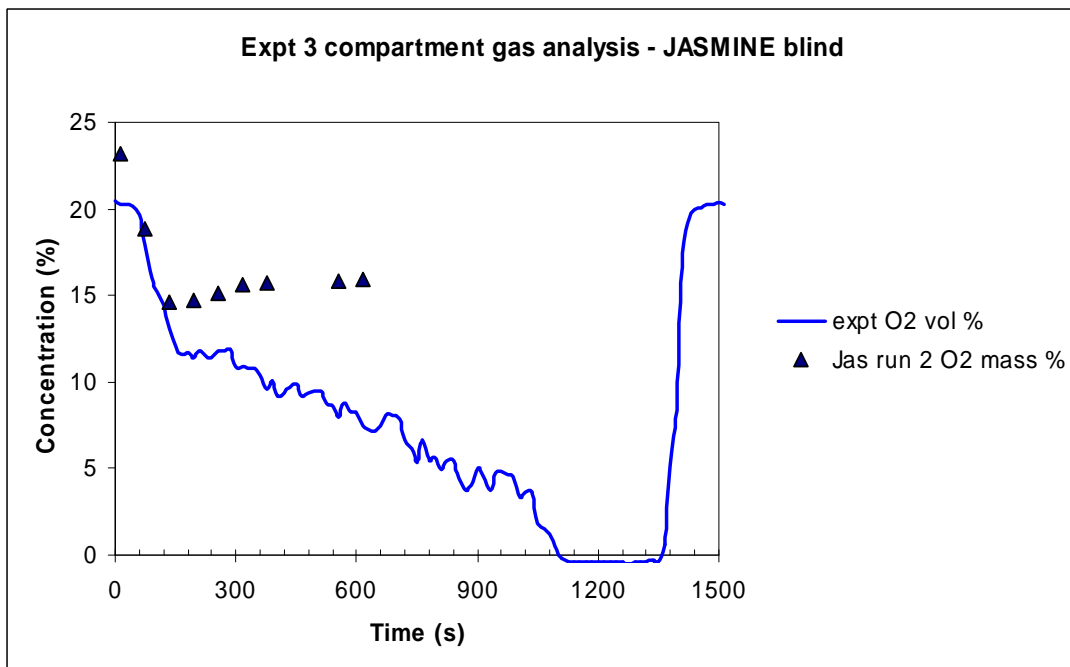
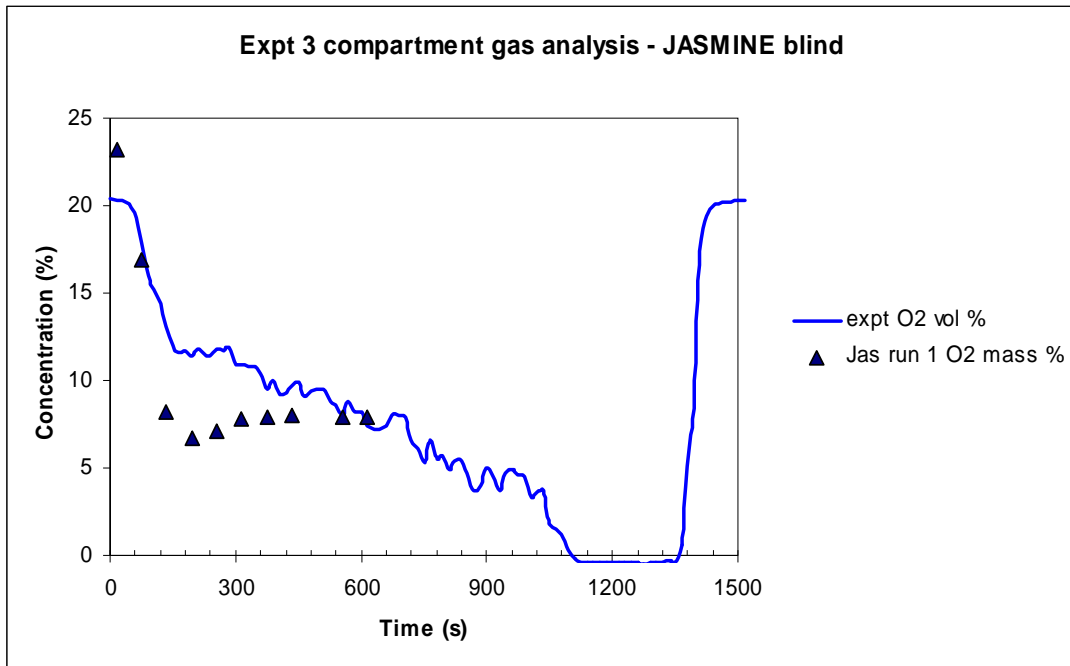


Fig. B24 Measured and JASMINE predicted (blind) oxygen concentration for Test 3

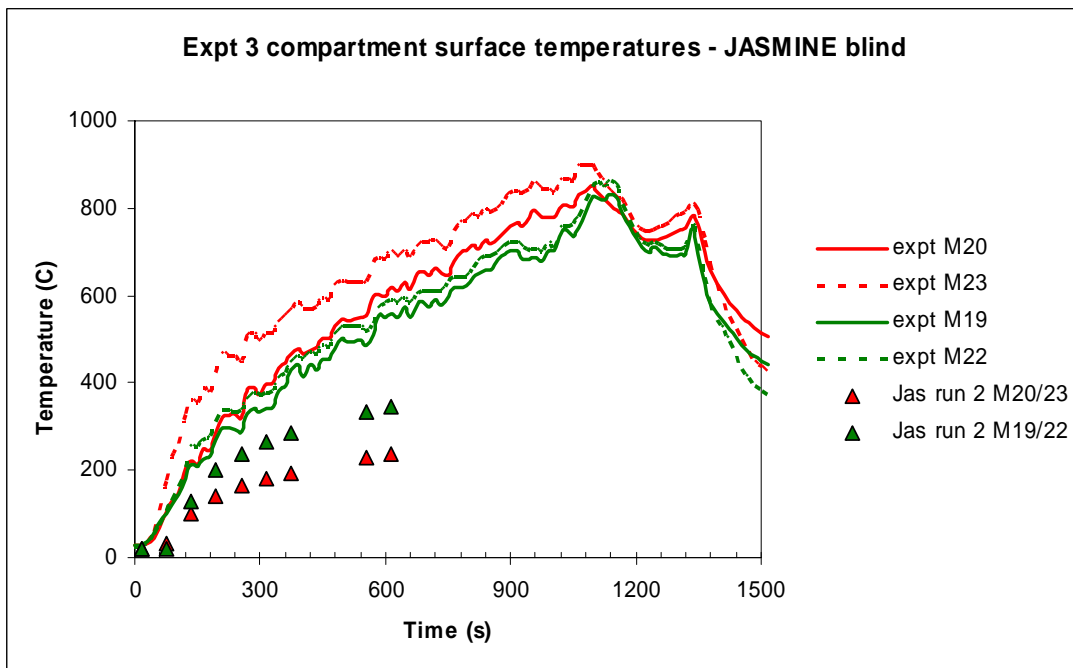
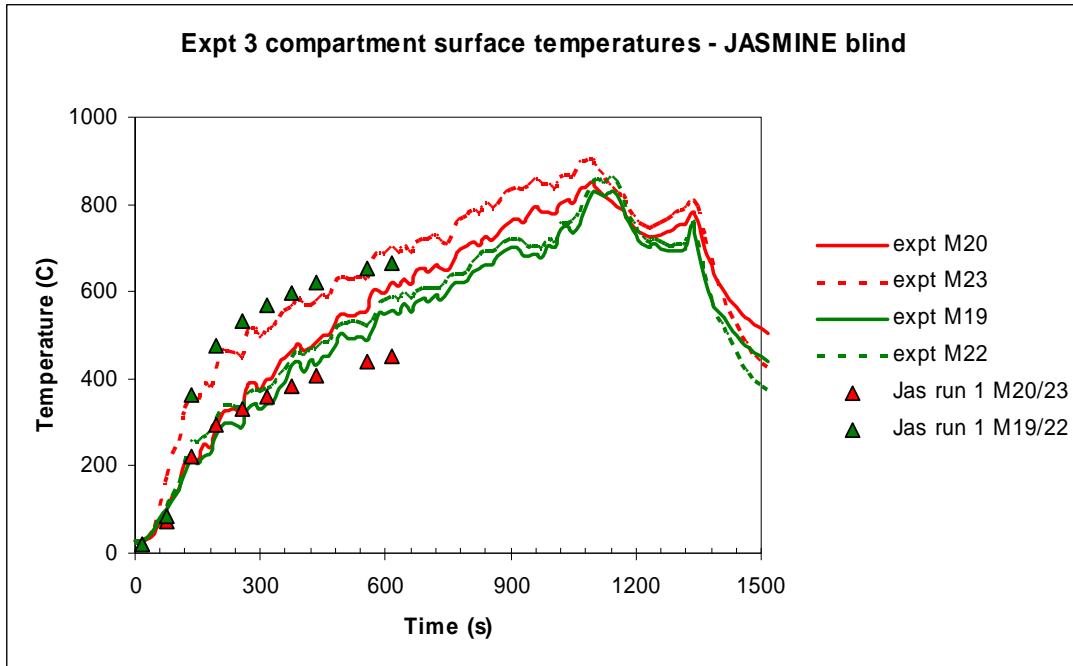


Fig. B25 Measured and JASMINE predicted (blind) wall surface temperatures for Test 3

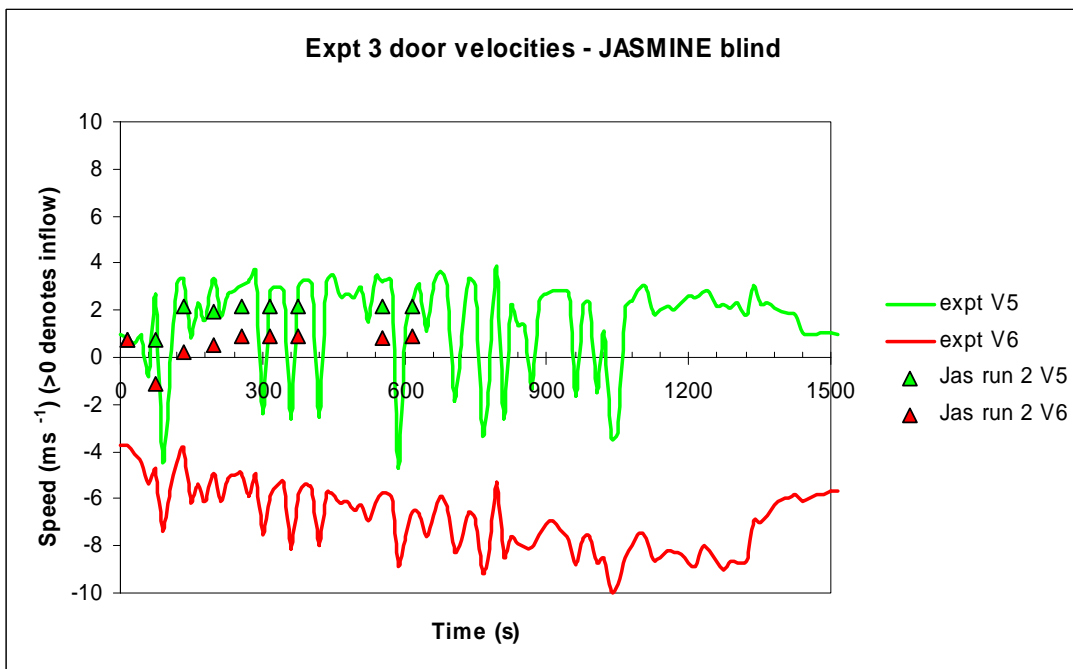
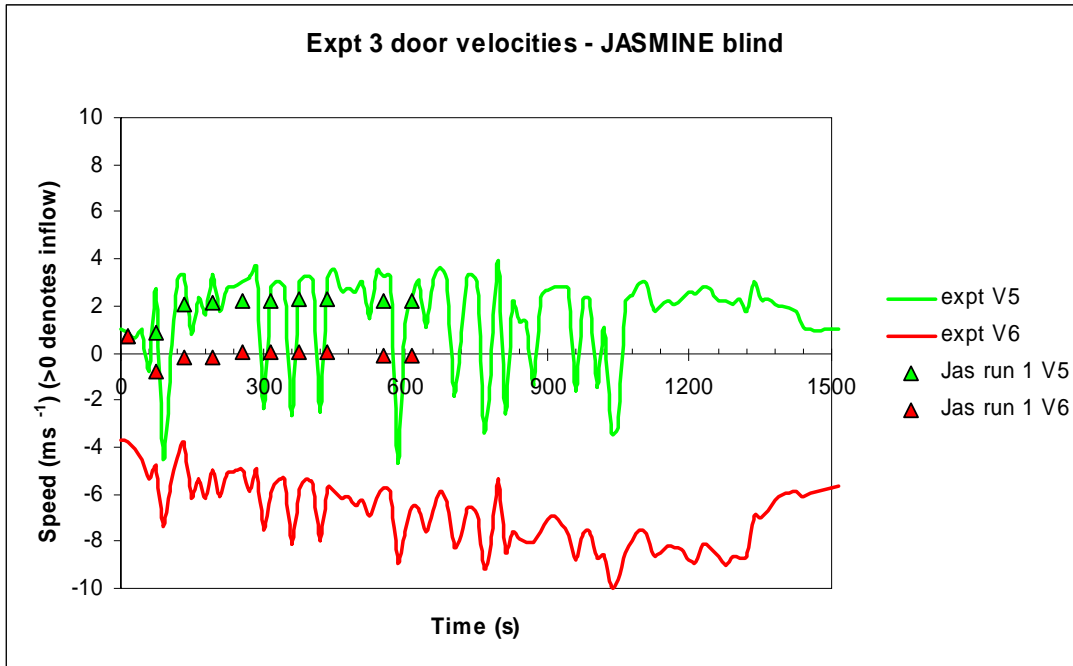


Fig. B26 Measured and JASMINE predicted (blind) door velocities for Test 3

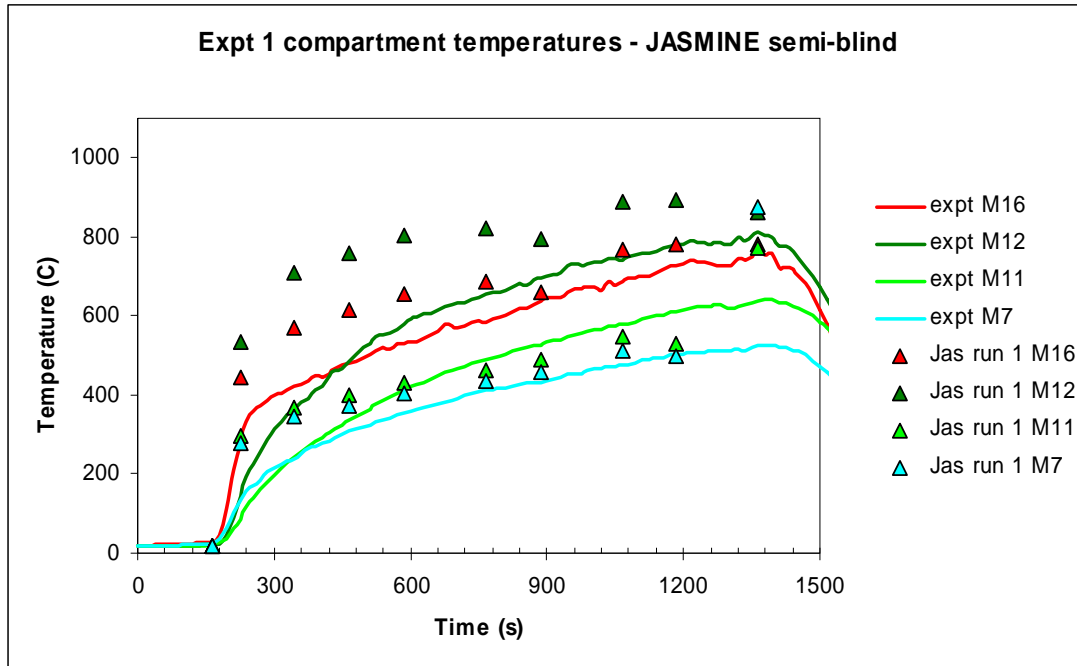


Fig. B27 Measured and JASMINE predicted (semi-blind) gas temperatures for Test 1

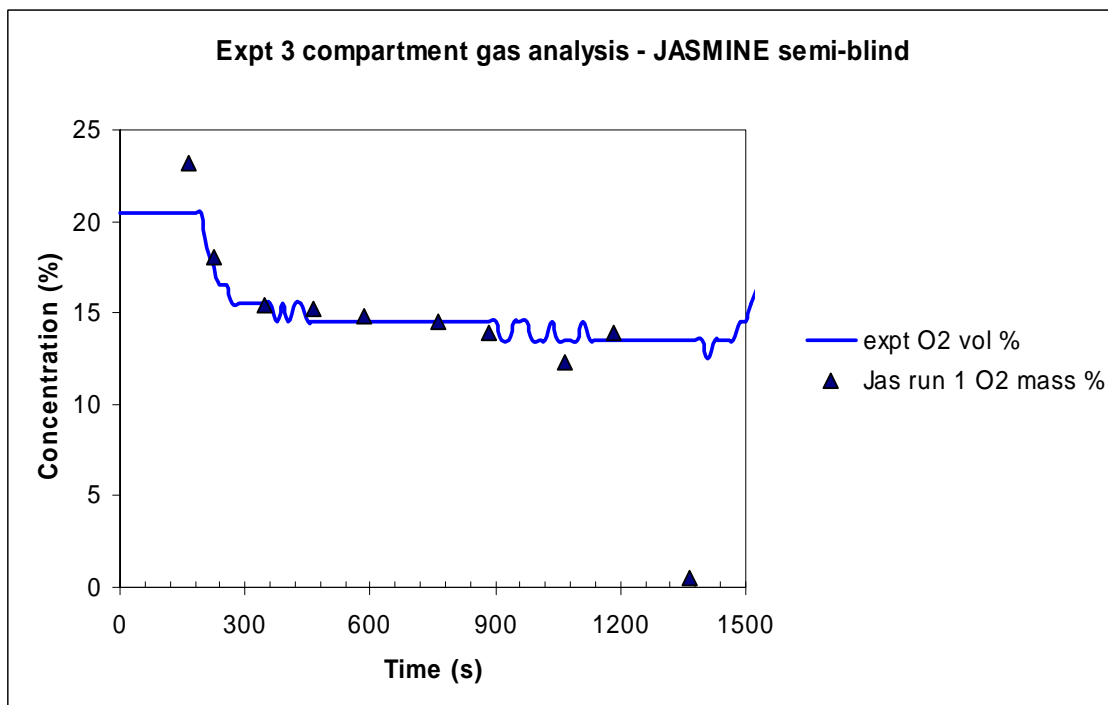


Fig. B28 Measured and JASMINE predicted (semi-blind) oxygen concentration for Test 1

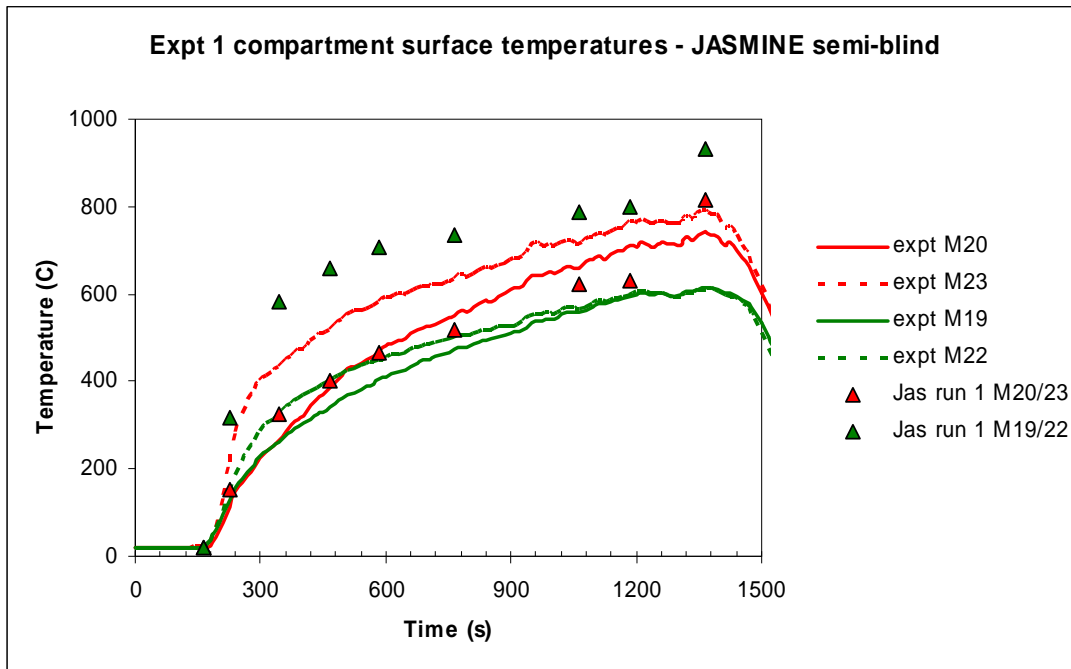


Fig. B29 Measured and JASMINE predicted (semi-blind) wall surface temperatures for Test 1

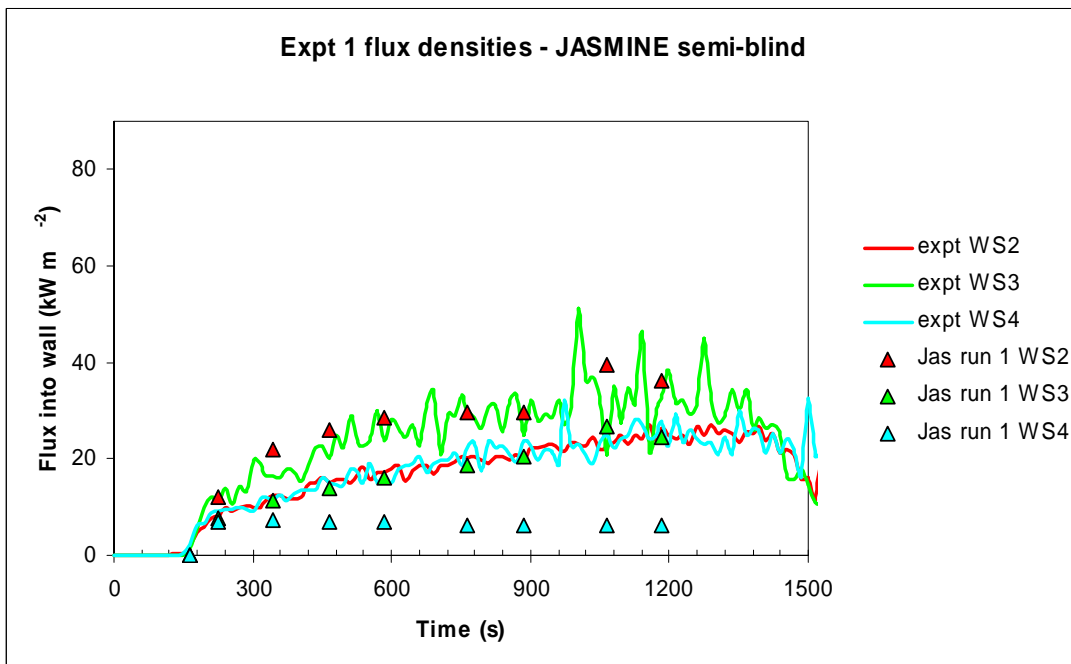


Fig. B30 Measured and JASMINE predicted (semi-blind) flux densities for Test 1

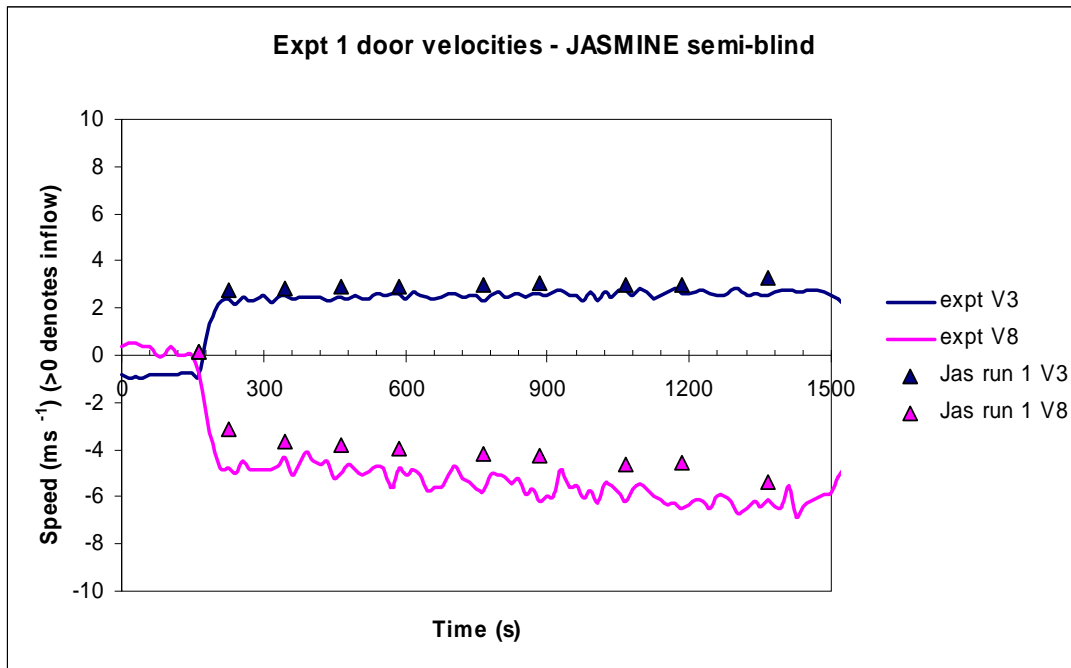


Fig. B31 Measured and JASMINE predicted (semi-blind) door velocities for Test 1

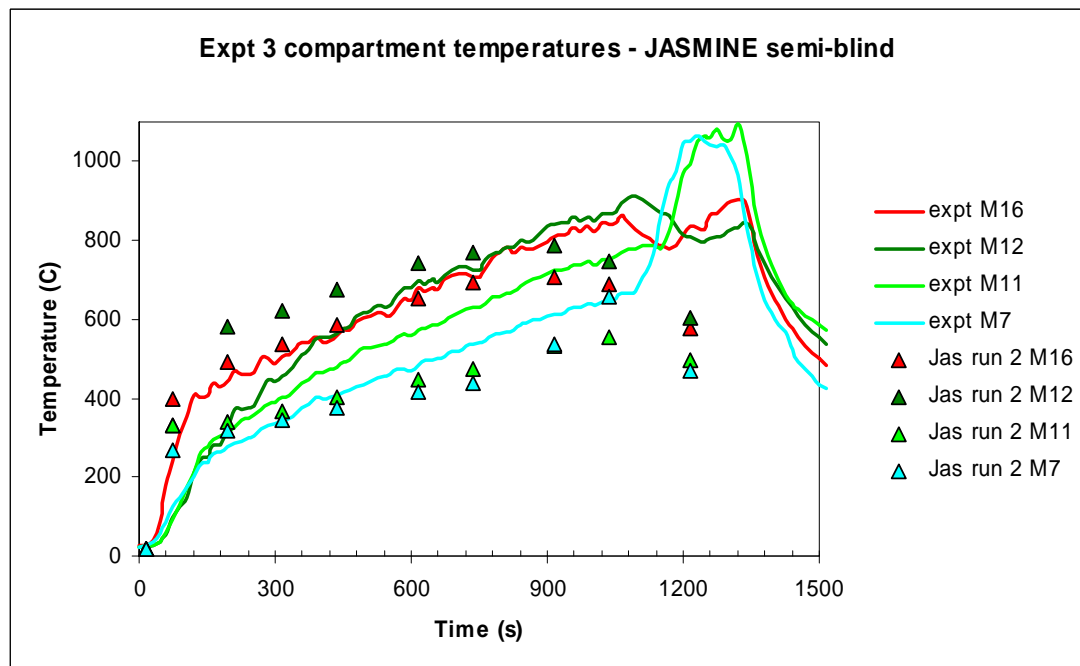
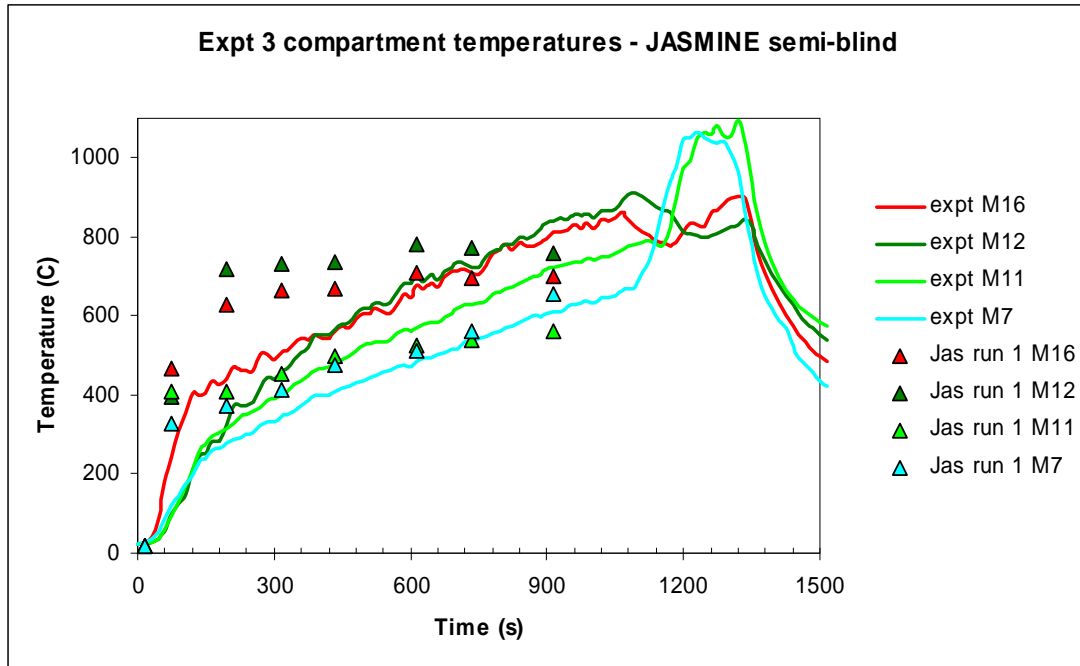


Fig. B32 Measured and JASMINE predicted (semi-blind) gas temperatures for Test 3

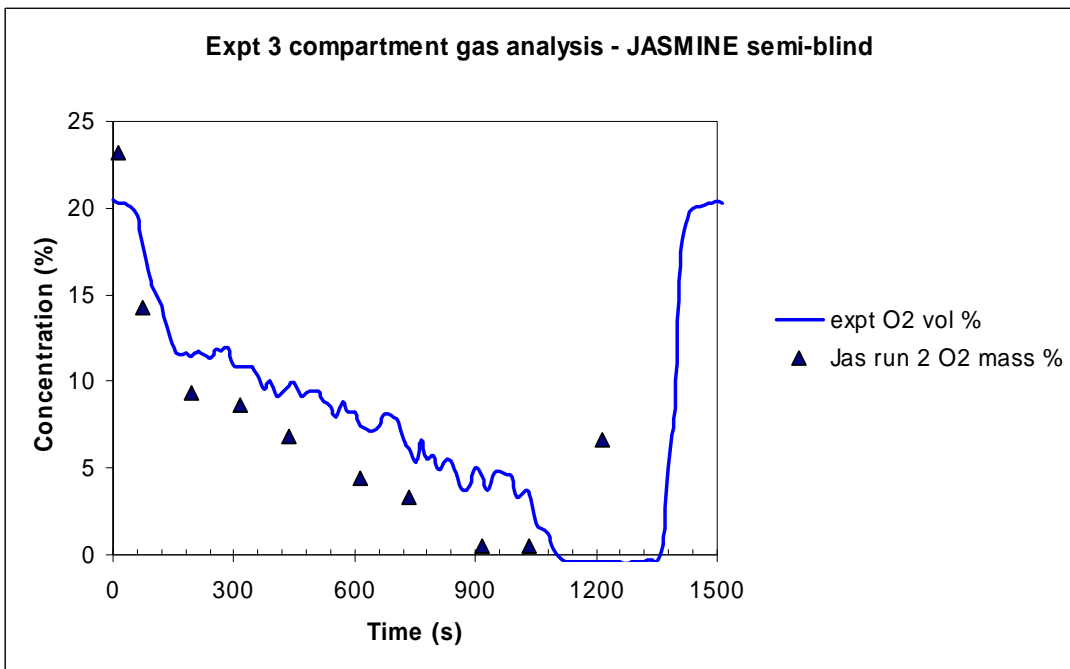
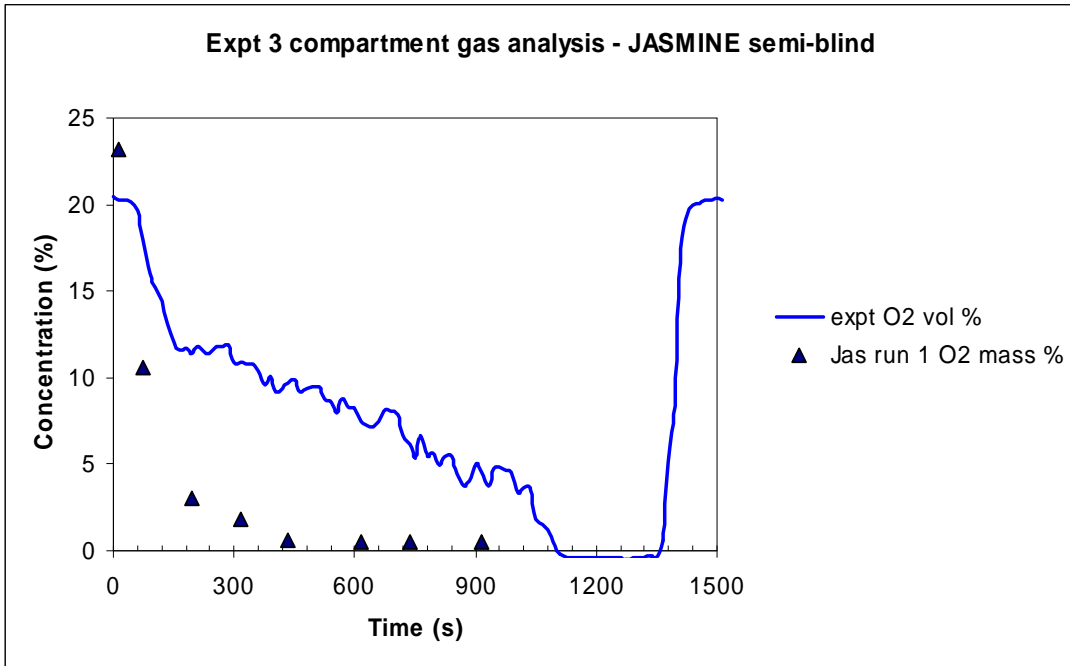


Fig. B33 Measured and JASMINE predicted (semi-blind) oxygen concentration for Test 3

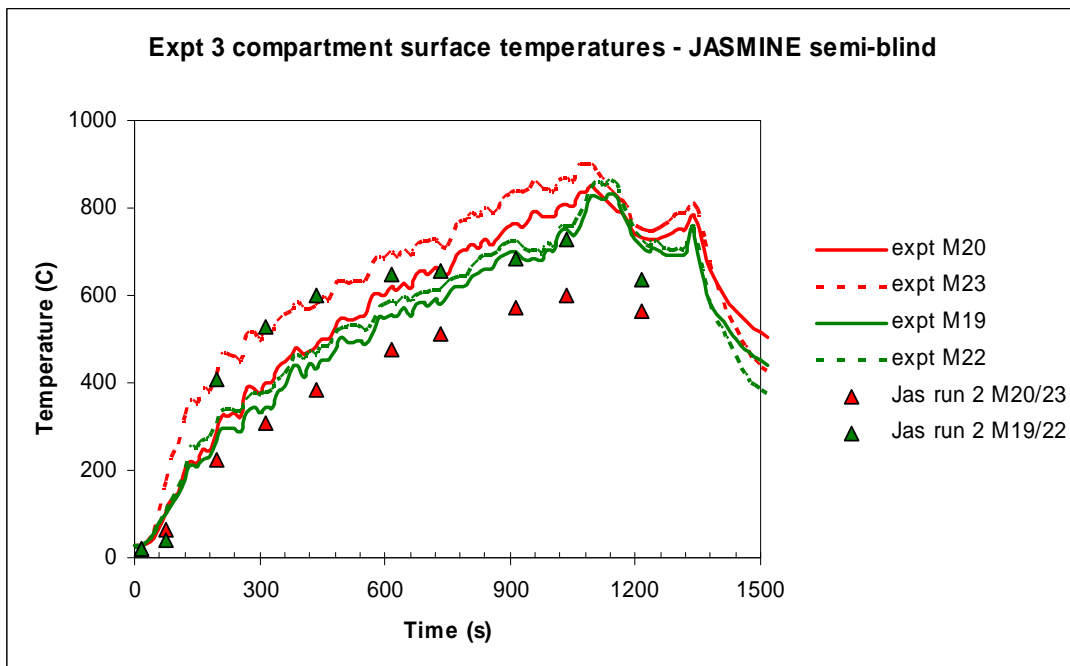
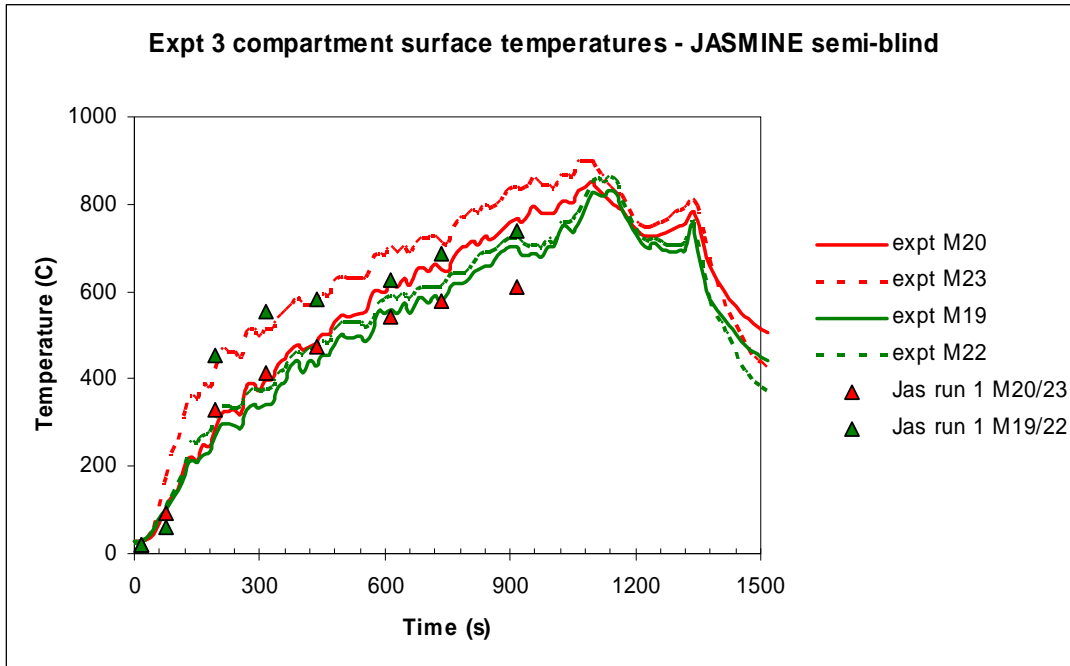


Fig. B34 Measured and JASMINE predicted (semi-blind) wall surface temperatures for Test 3

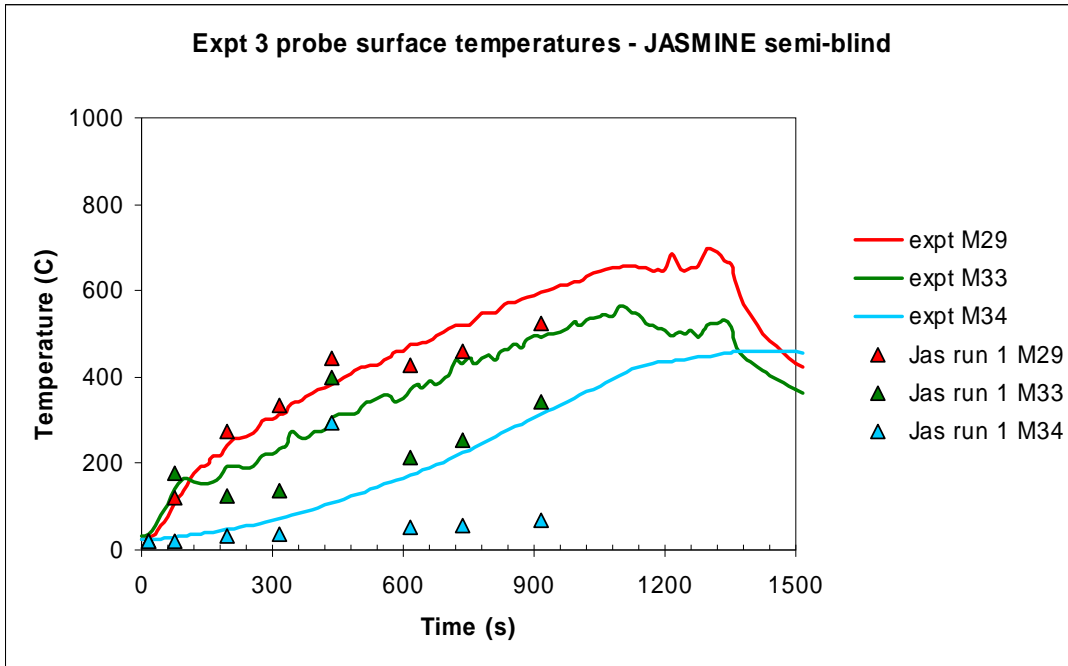


Fig. B35 Measured and JASMINE predicted (semi-blind) wall surface temperatures for Test 3

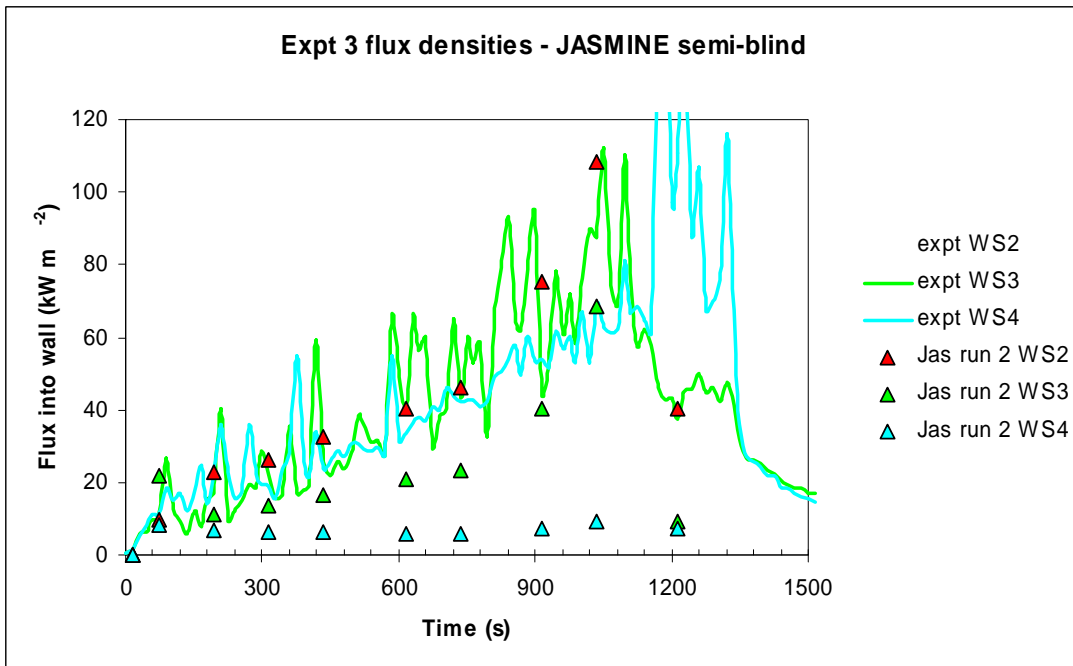
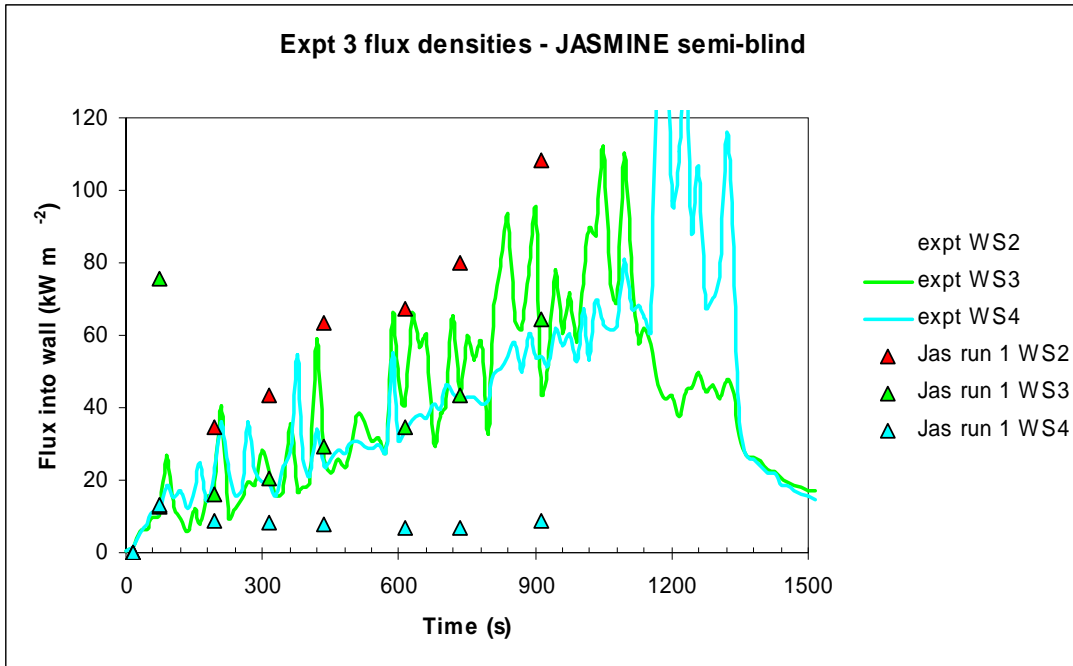


Fig. B36 Measured and JASMINE predicted (semi-blind) flux densities for Test 3

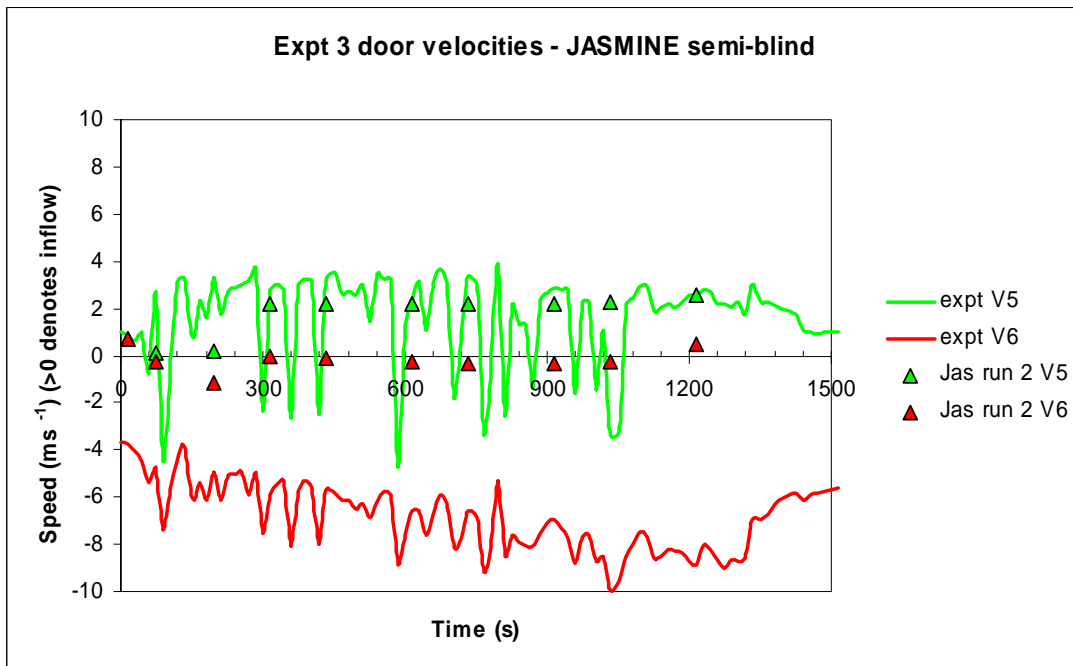
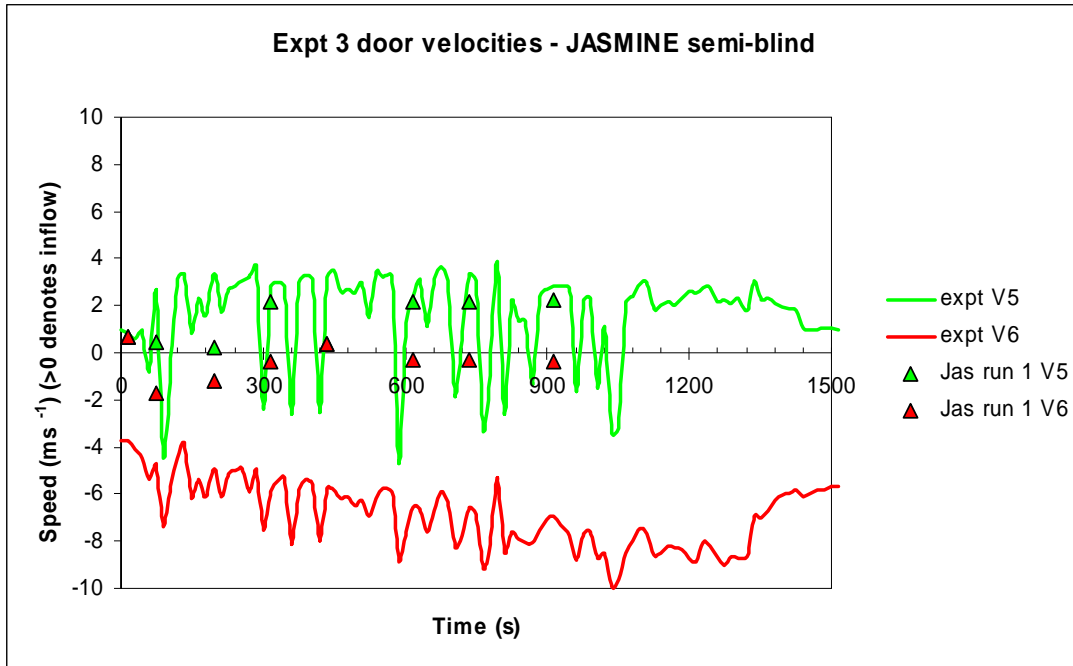


Fig. B37 Measured and JASMINE predicted (semi-blind) door velocities for Test 3

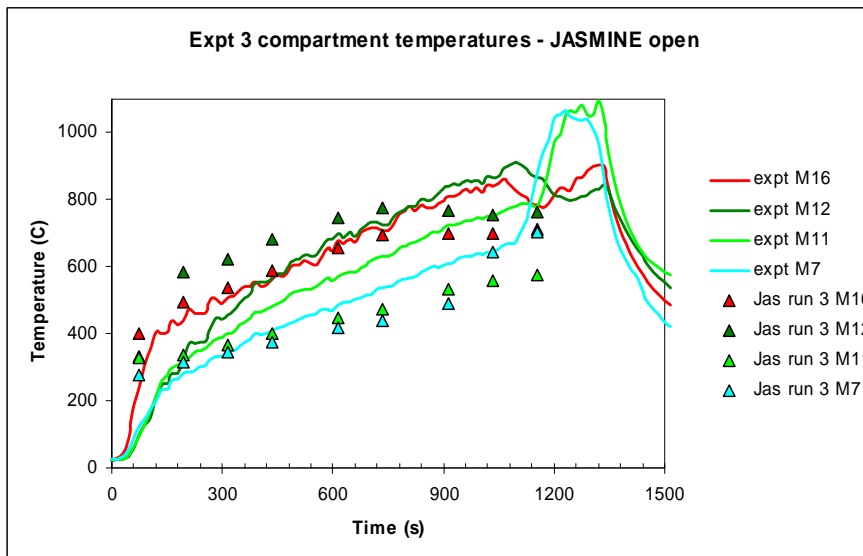
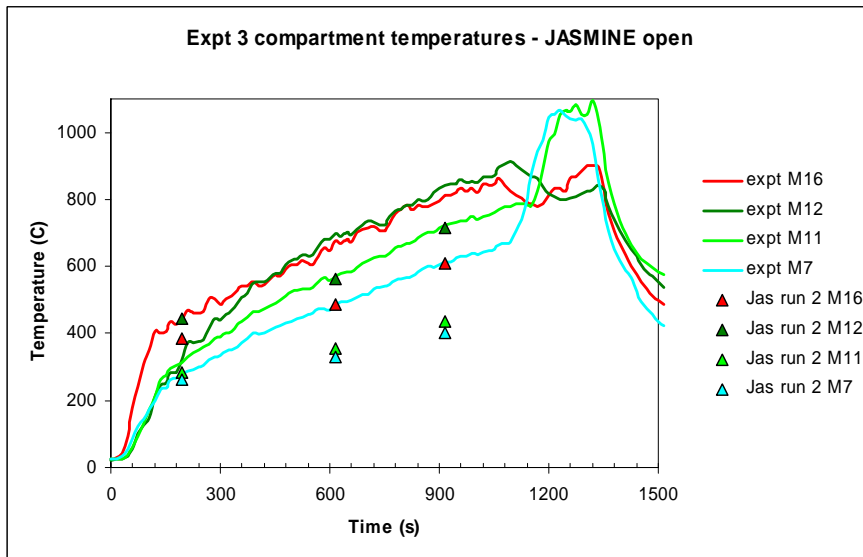
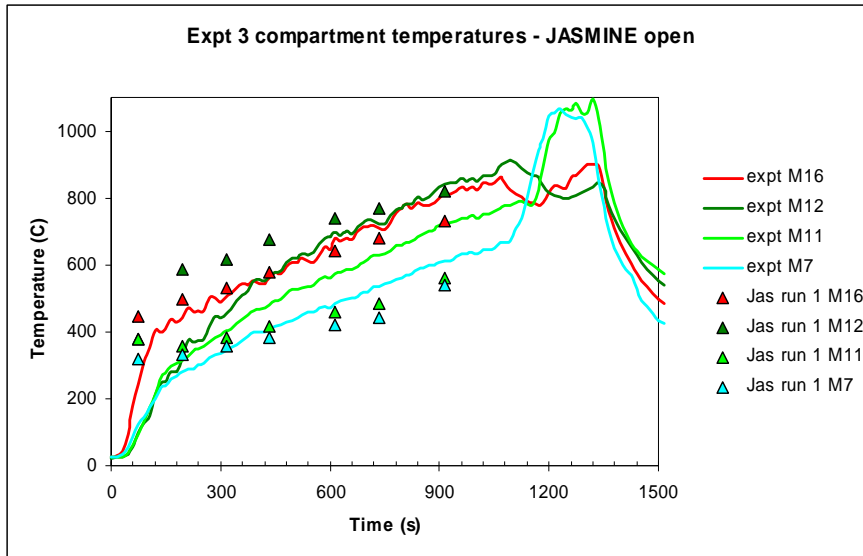


Fig. B38 Measured and JASMINE predicted (open) gas temperatures for Test 3

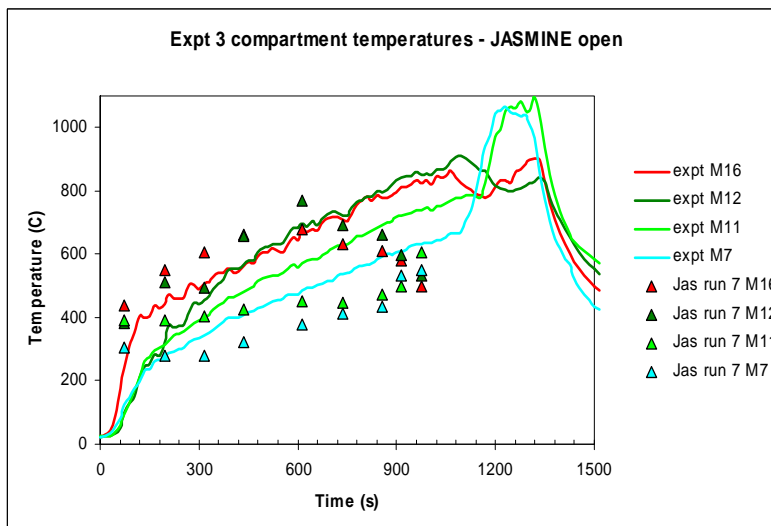
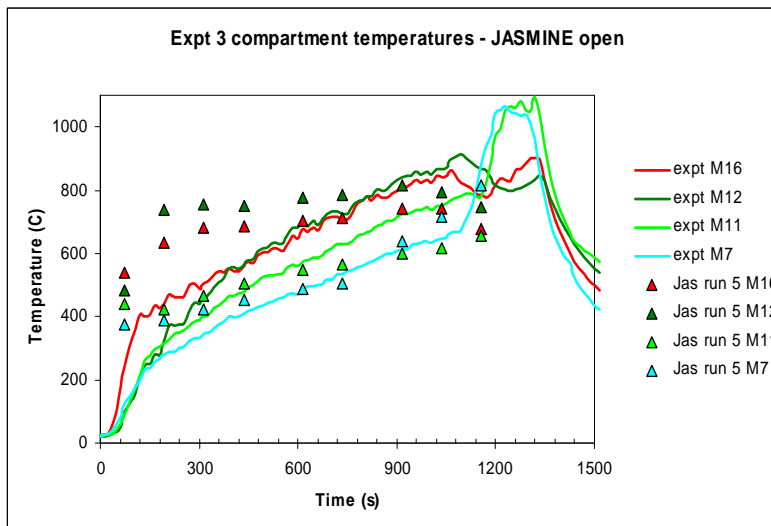
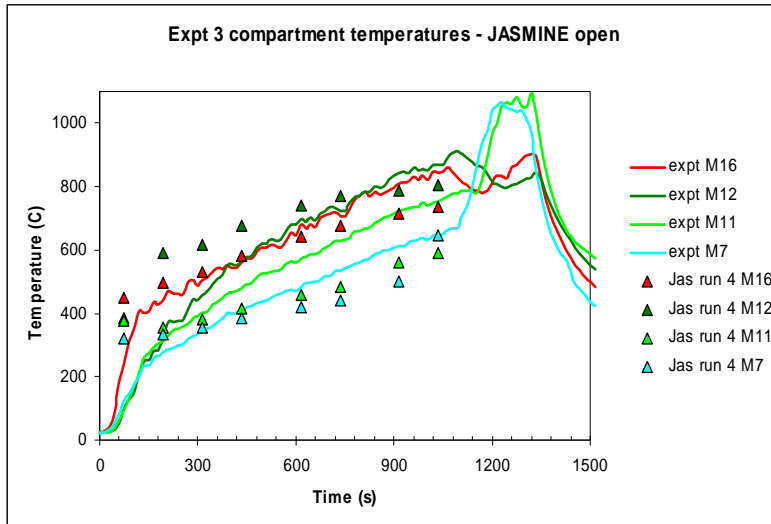


Fig. B38 Measured and JASMINE predicted (open) gas temperatures for Test 3 (contd.)

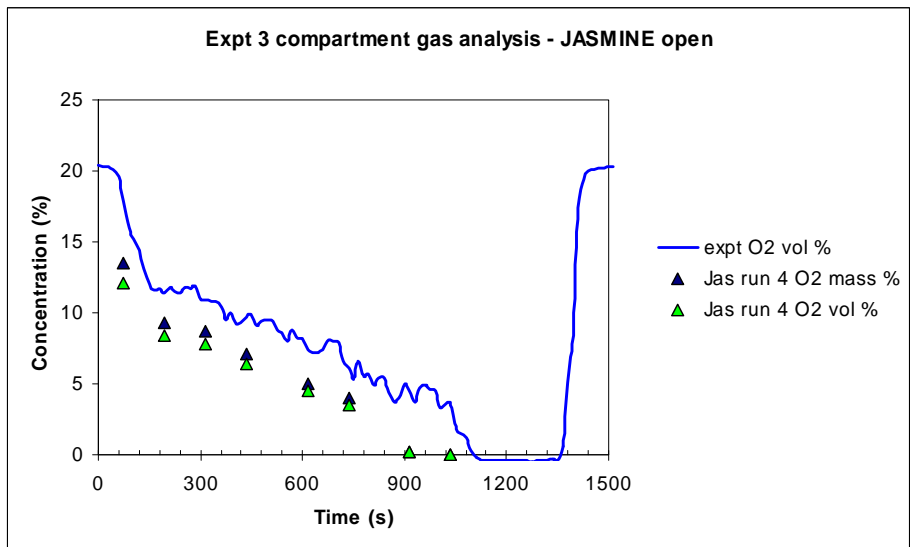
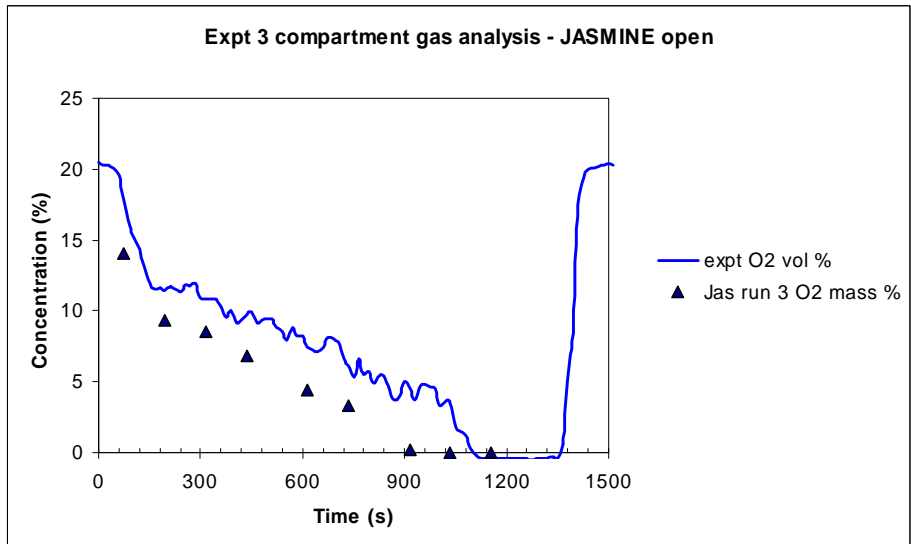
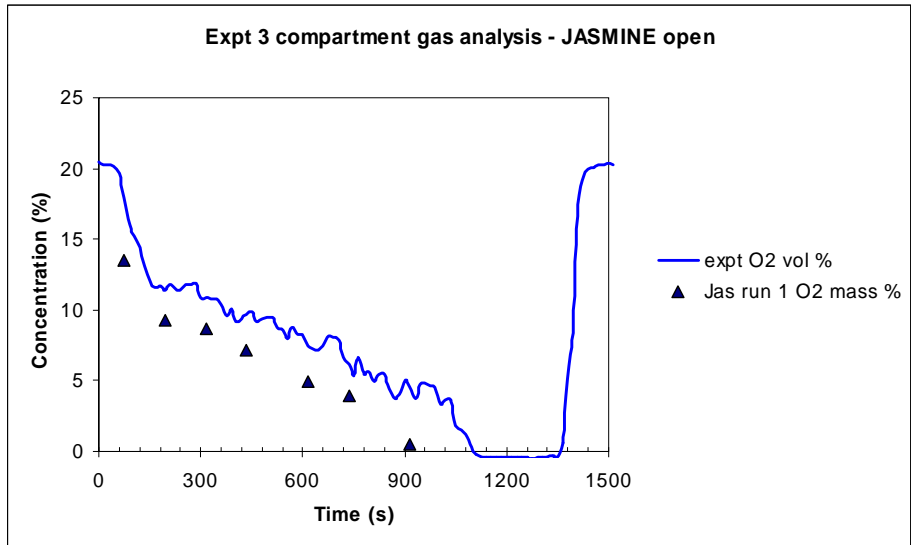


Fig. B39 Measured and JASMINE predicted (open) oxygen concentration for Test 3

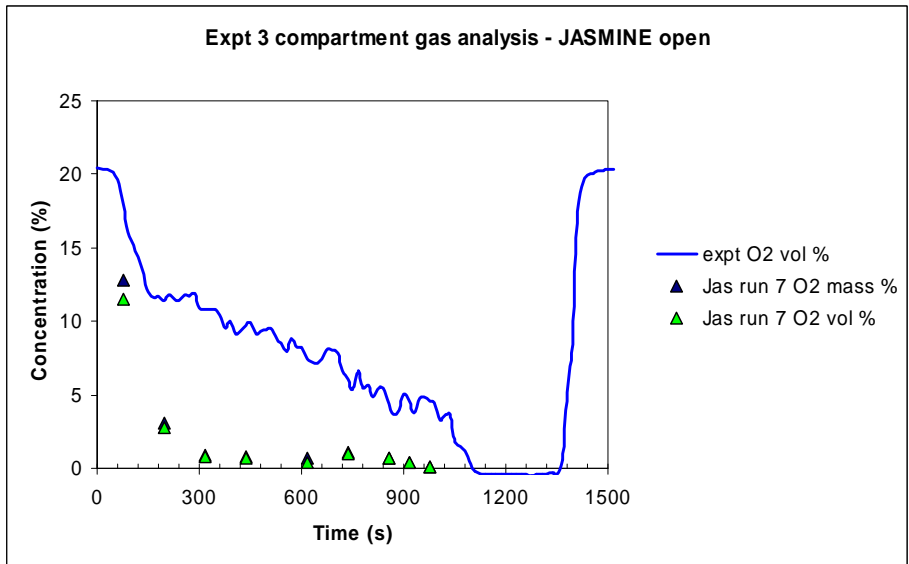
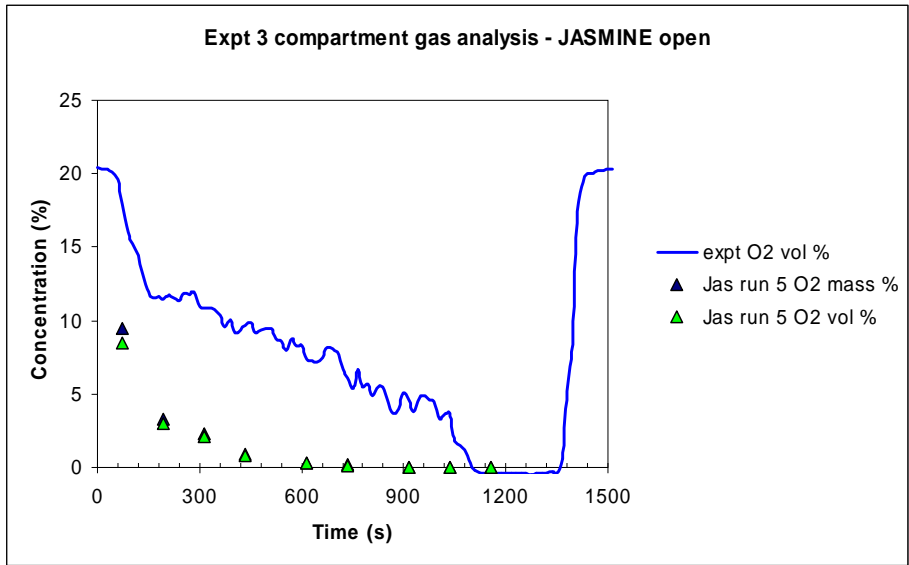


Fig. B39 Measured and JASMINE predicted (open) oxygen concentration for Test 3 (contd.)

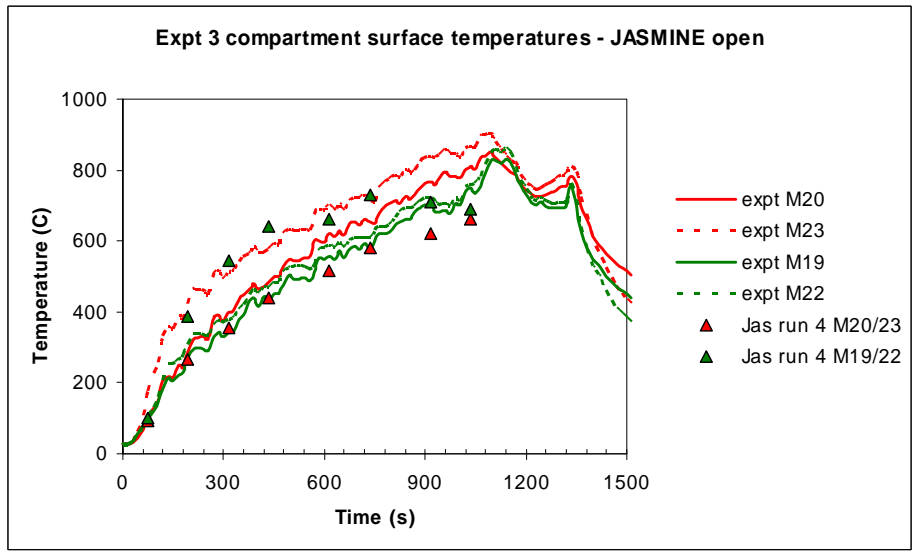
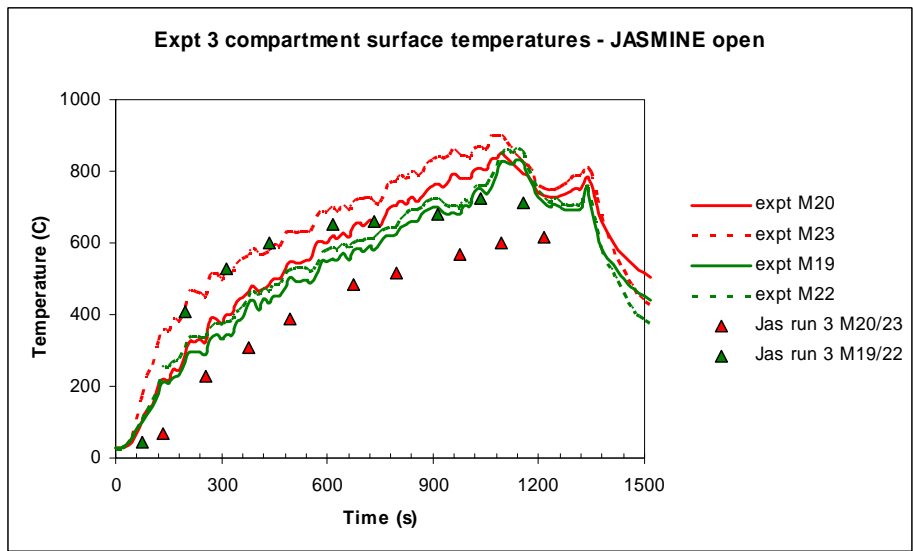
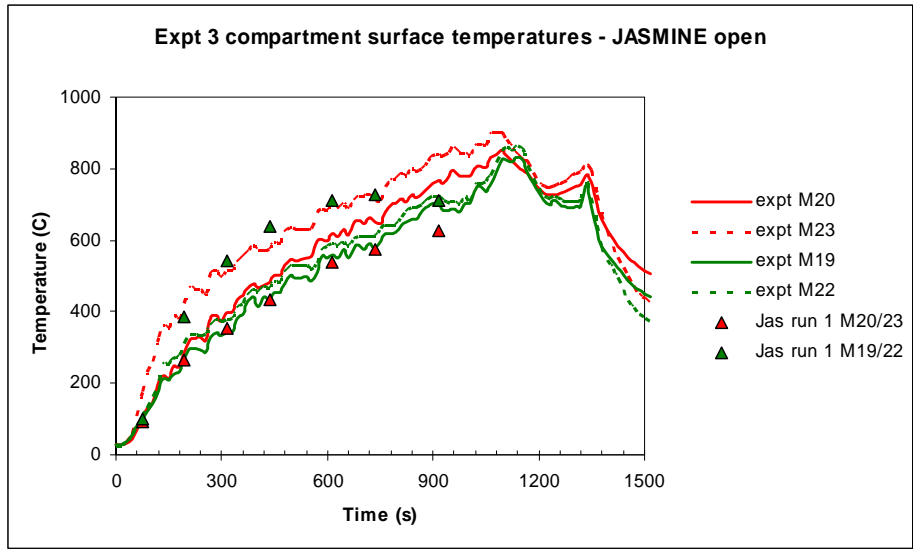


Fig. B40 Measured and JASMINE predicted (open) wall surface temperatures for Test 3

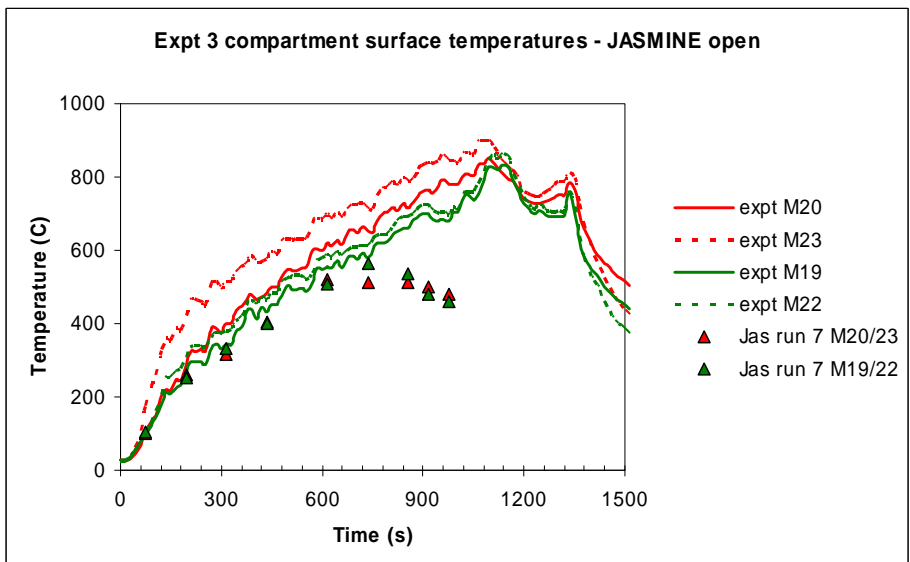
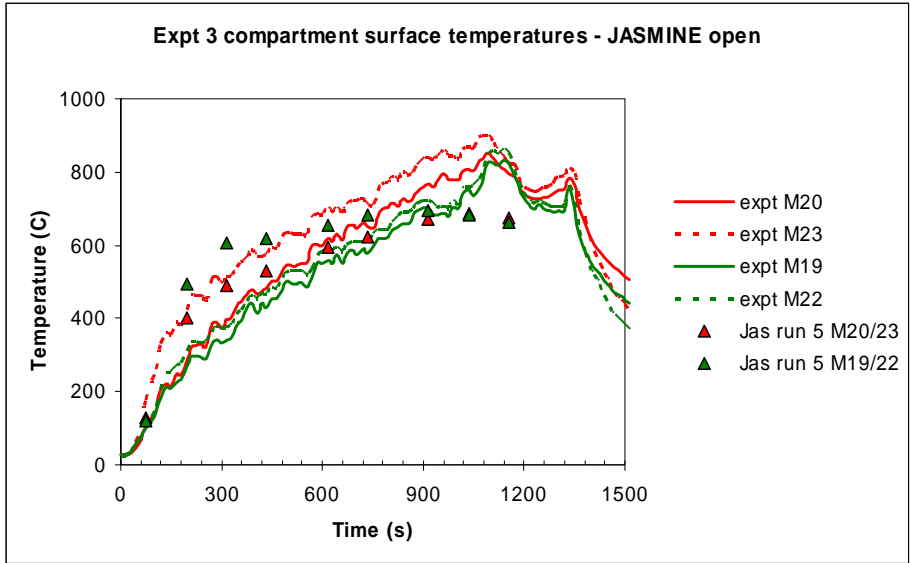


Fig. B40 Measured and JASMINE predicted (open) wall surface temperatures for Test 3 (contd.)

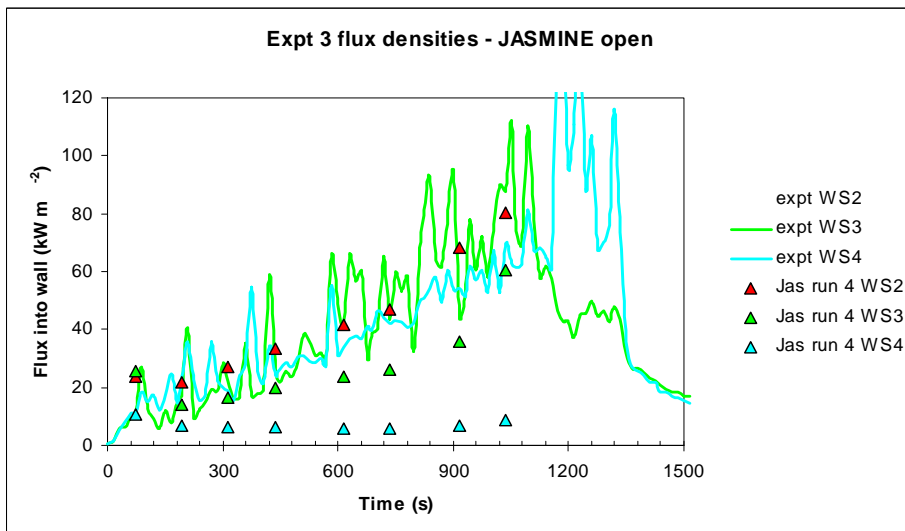
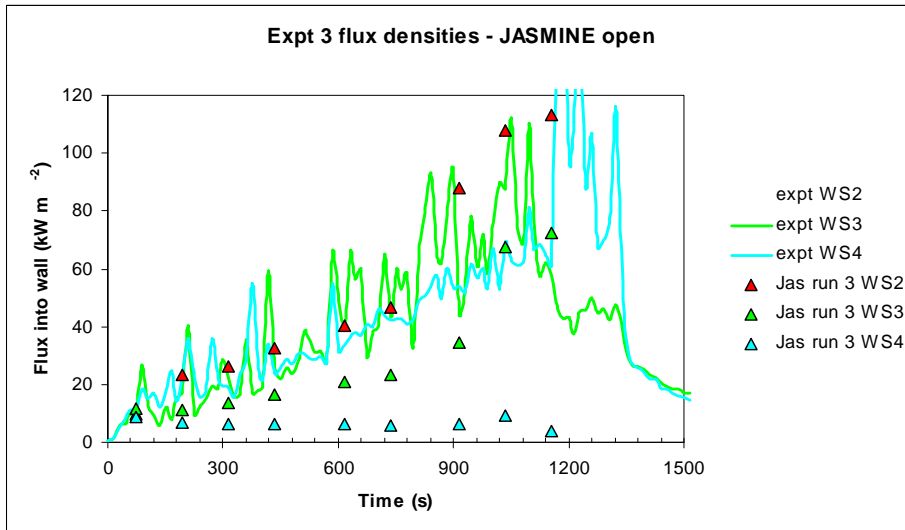
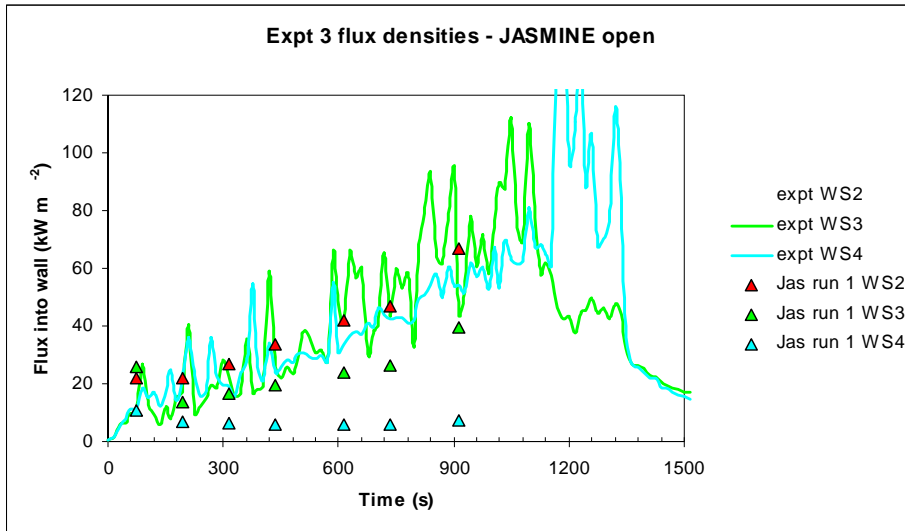


Fig. B41 Measured and JASMINE predicted (open) flux densities for Test 3

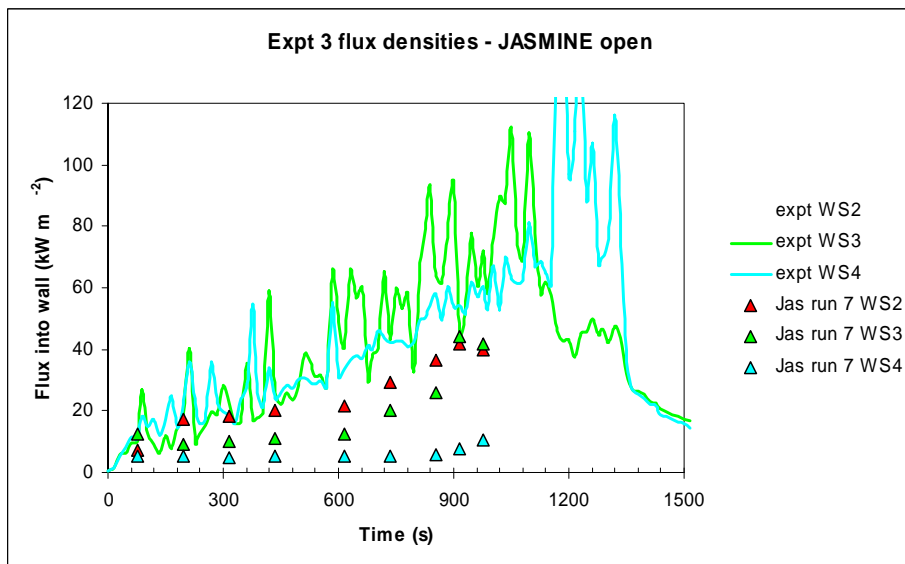
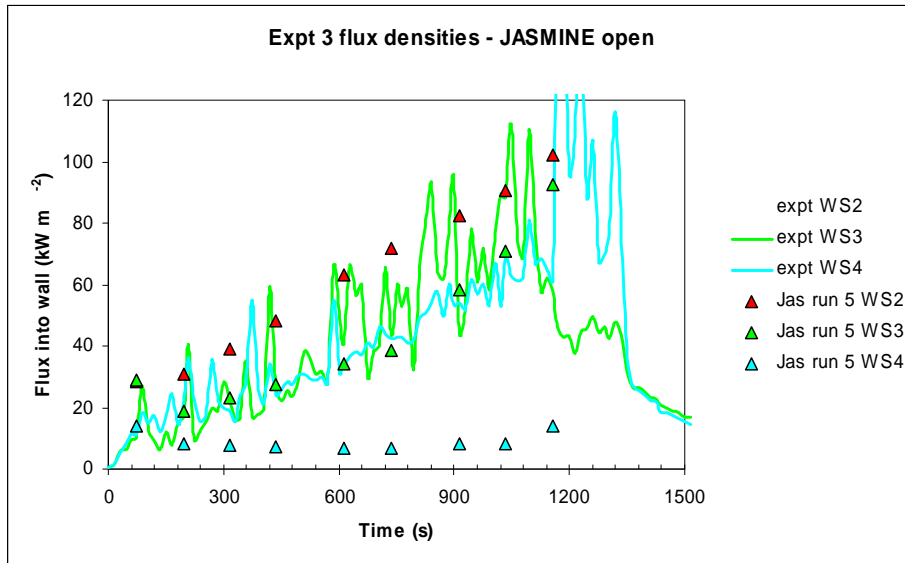


Fig. B41 Measured and JASMINE predicted (open) flux densities for Test 3 (contd.)

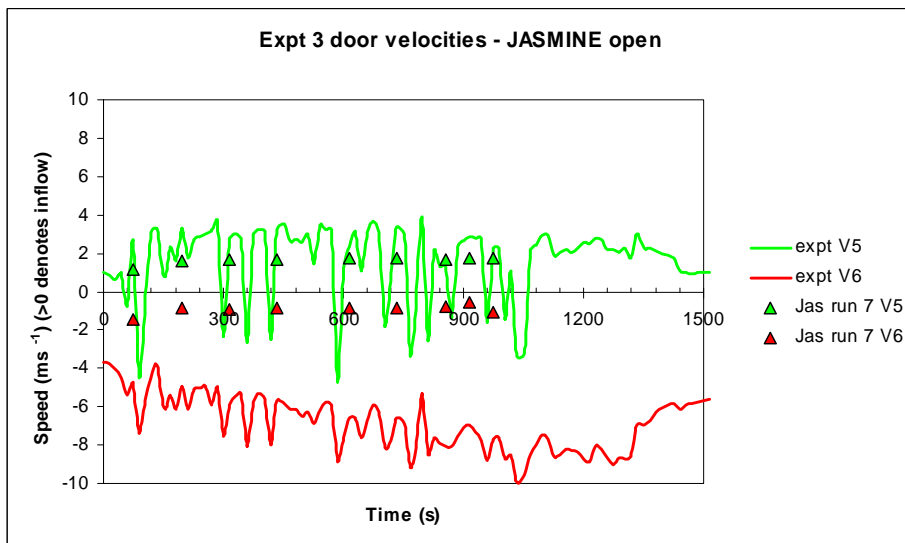
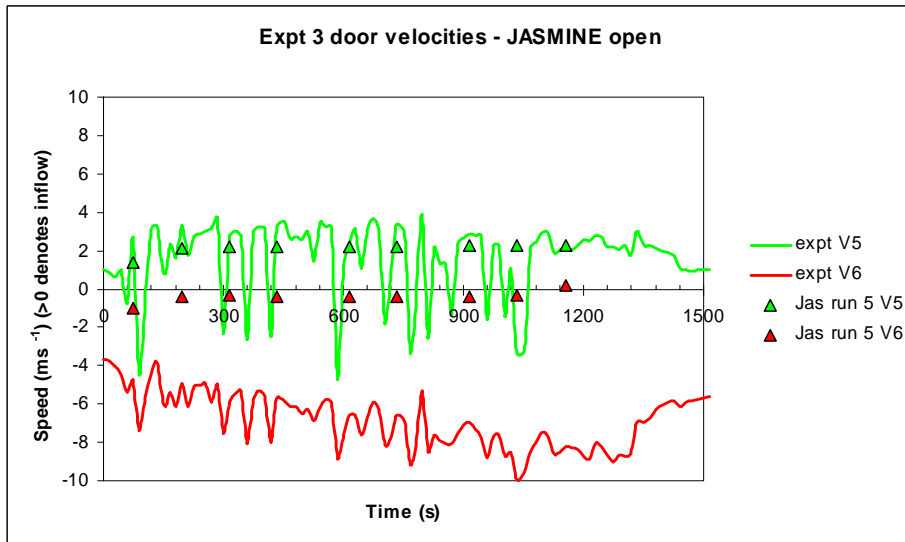
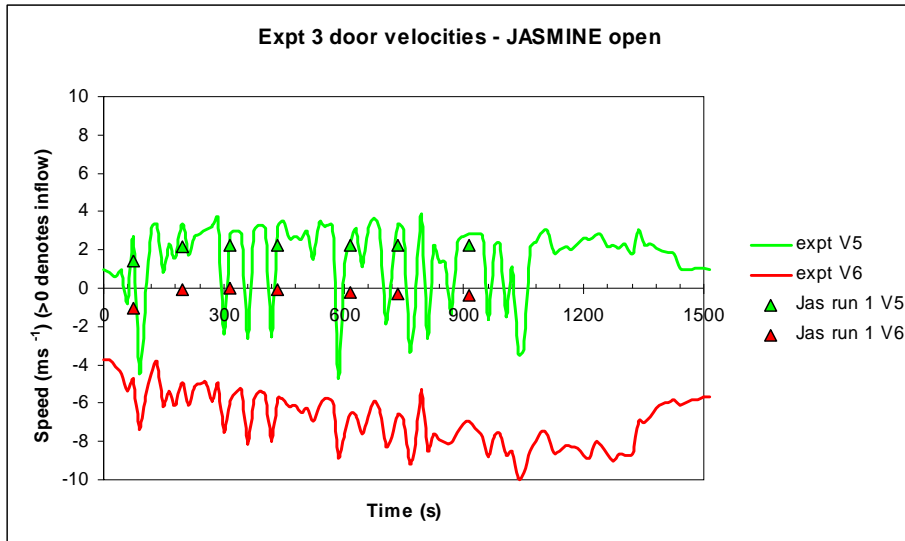


Fig. B42 Measured and JASMINE predicted (open) door velocities for Test 3

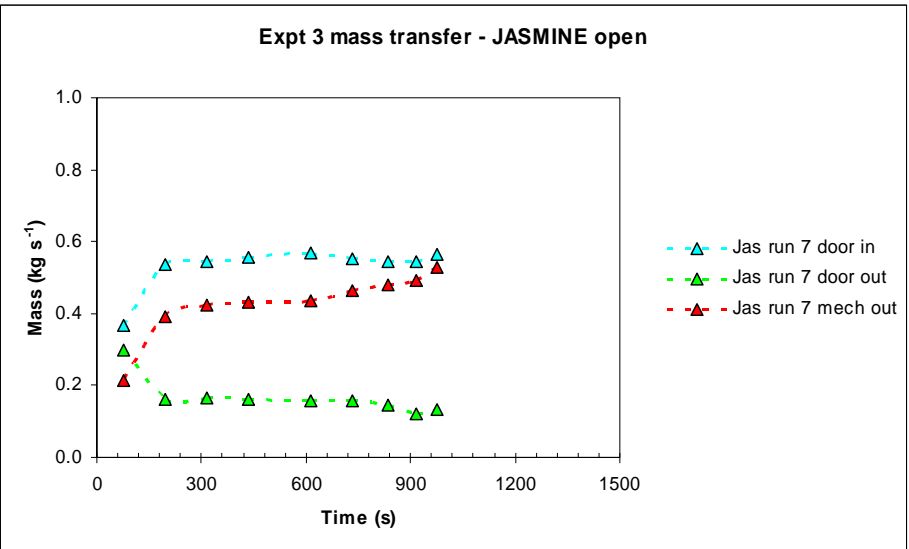
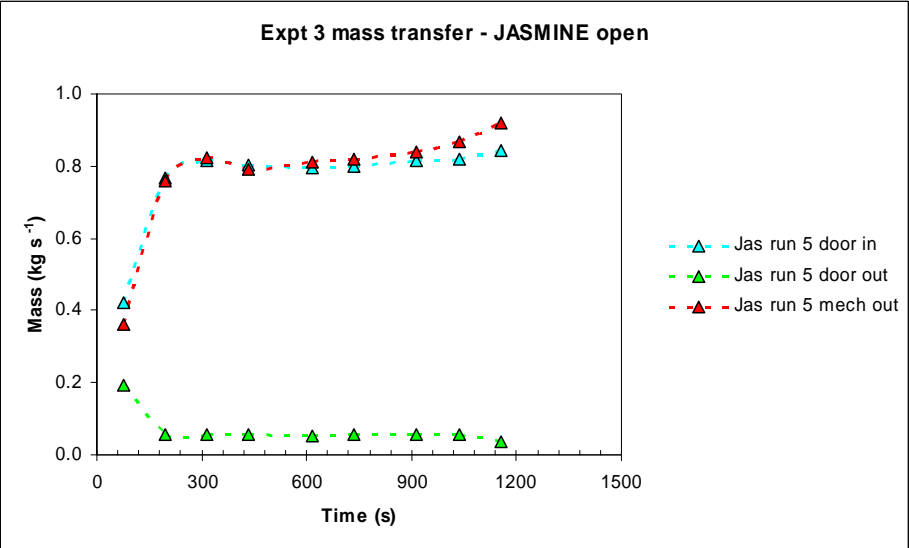
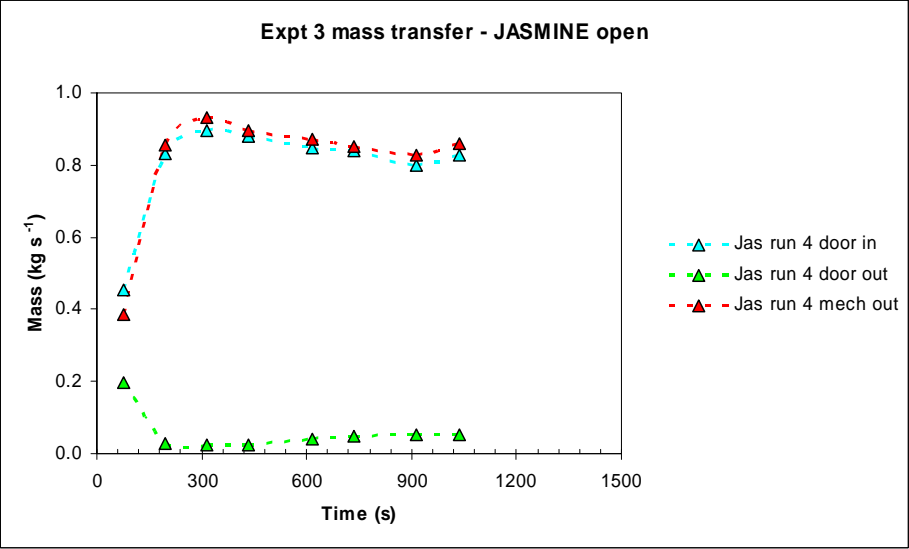


Fig. B43 JASMINE predicted (open) mass flow rates for Test 3

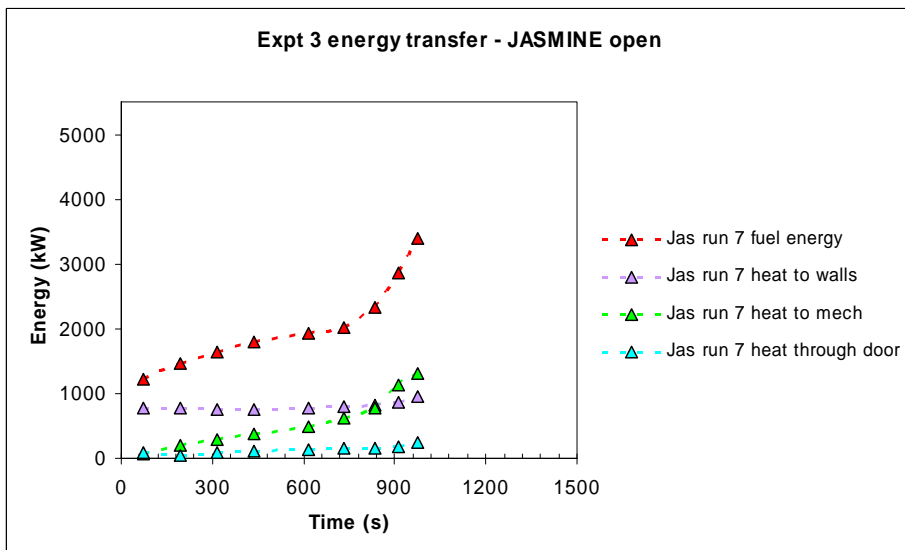
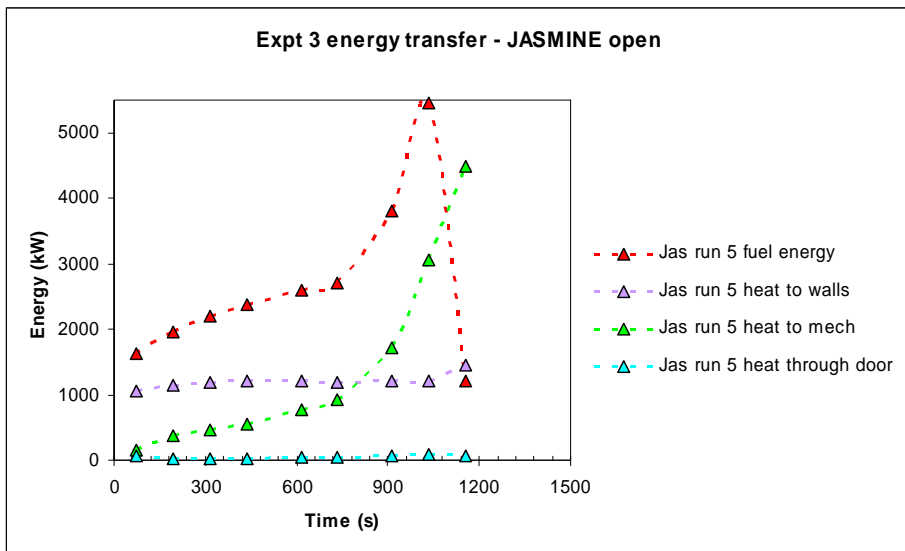
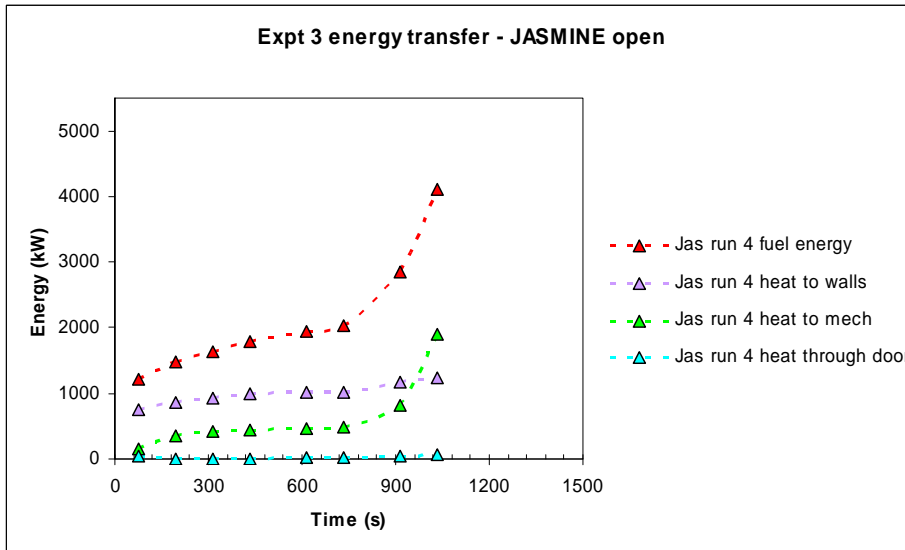


Fig. B44 JASMINE predicted (open) heat losses for Test 3

B4 General Conclusions and Recommendations

The main findings for both the CFAST and JASMINE work were reported in the above section of the annex. The overall conclusions, and some recommendations, are given below:

- Both experiments were challenging to model, with either CFAST or JASMINE. This was due partly to the relatively large size of fire for the size of compartment, generating 'flashed over' conditions. Heat transfer to the compartment boundaries is then an important process. Radiation emission and absorption from CO₂, H₂O and soot particulates is also very important, and is closely coupled to the transfer of energy to the solid boundaries. Test 3 was oxygen controlled adding a further complexity.

For these reasons it is not surprising that convergence was an issue with JASMINE and also, with some combinations of input parameters, CFAST. For CFAST this was the first benchmark exercise that has provided such difficulties for the author.

- A major additional challenge of this benchmark exercise, for the blind calculations at least, was the specification of the fuel pyrolysis rate. Given the importance of radiative feedback and soot formation in determining the pyrolysis rate, the task of calculating this parameter is quite significant. Furthermore, as the fire is inside an enclosure, the effect of radiative feedback from the enclosure boundaries is also important.

Despite the above issues, the blind predictions made with JASMINE were quite encouraging. Using an empirical expression for the fuel pyrolysis rate, it was possible to capture the main gas phase properties of the experiments. Furthermore, for the CFAST semi-blind calculations for Test 1 where the same empirical fuel pyrolysis rate term was employed the results were encouraging. Indeed, although the transient nature of the fire development, due to the pyrolysis rate changing with time, was missed, these CFAST calculations yielded results closer on average to the measured ones than those calculations performed using the measured fuel pyrolysis rate.

- In Test 1 the CFAST calculations, when using the measured fuel pyrolysis rate, yielded gas temperatures comparable to those measured provided the radiative fraction was set to a high value (0.6). For Test 3 the gas temperatures calculated by CFAST were significantly higher than those measured. This may have been due to

setting the radiative fraction to 0.3. However, it was not possible to achieve numerical convergence when using a higher radiative fraction. This suggests that the two layer zone modeling approach may not be suited to scenarios such as Test 3 where there is an oxygen limited, post flashover fire inside an enclosed space.

- The value in reducing the compartment space into an upper and lower gas layer is perhaps questionable for scenarios such as Benchmark Exercise 3 where there is significant mixing inside the space. Nonetheless, CFAST calculated that the layer interface height dropped to floor level in Test 3, and this can be interpreted as a correct behavior. For Test 1, CFAST calculated a layer height of about 1 m, which is a questionable result as in the experiment there was no distinct lower layer.
- JASMINE calculations yielded reasonable gas temperatures, surface temperatures and fluxes provided some account was made for the radiation losses due to soot particulates. Soot was not modeled in the calculations, and so a reduction in the measured fuel pyrolysis rate was required to account for this. A somewhat arbitrary value of a 25 % reduction in pyrolysis rate yielded reasonable results. It is recommended that for CFD models the development of reliable, and computationally expedient, soot formation/combustion models is addressed further. For some promising work undertaken recently in this area see the reference /LAU 05/.

It was noted that the JASMINE calculations could not be conducted after about 18 minutes in both tests due to convergence difficulties. For Test 3 this considered with a sharp rise in fuel pyrolysis rate, which would have been caused by physical processes arguably beyond the capability of current fire models.

- Agreement between predicted and measured flux densities followed, to a greater extent, that observed for gas temperature, e.g. the over-prediction of flux densities for the CFAST calculations for Test 3 follows the over-prediction of compartment gas temperature. A notable discrepancy between predicted and measured flux occurred with JASMINE at measurement location WS4 towards the front of the compartment. While it has been suggested originally that this was due to the use of the six-flux radiation model, later open calculations using the discrete transfer model yielded very similar results.

As remarked in previous benchmark exercises, it is important to stress that the quality of any target response calculation is only as good as the quality of the gas phase and radiation transfer predictions.

- The specification of the exhaust flow rate through the mechanical ventilation (FUCHS) warrants further consideration. For Test 3 the CFD (JASMINE) calculations indicated that the flow of mass and heat through the duct was quite significant, to the extent that the flow at the wall vent was nearly all directed from the outside into the compartment. This resulted in very little outflow of combustion products. However, the measured gas velocity at the wall vent suggests that in the experiment there was a more substantial outflow of combustion gases. An open calculation where the imposed mechanical ventilation exhaust flow was reduced by 50 % yielded a wall vent outflow closer to that measured, but still somewhat lower. Furthermore, the agreement in the other variables such as compartment gas temperatures was then reduced.
- As in Benchmark Exercise 3, the difficulty in specifying time-varying mechanical ventilation in CFAST was noted. However, judging from the results obtained, the significance of using a fixed exhaust rate at the mechanical ventilation duct seems not to have been critical in Benchmark Exercise 4.

B5 References

- /BAB 02/ Babrauskas, V.:
Heat release rates. SFPE Handbook of Fire Protection Engineering, 3rd Edition, pp. 3-1 - 3-27, 2002
- /COX 86/ Cox, G., S. Kumar, and N.C. Markatos:
Some field model validation studies. Fire Safety Science – Proceedings of the First International Symposium, Hemisphere Publishing, pp. 159 -171, 1986
- /COX 87/ Cox, G., and S. Kumar:
Field modelling of fire in forced ventilated enclosures, Combustion Science and Technology, vol. 52, pp. 7-23, 1987
- /GOS 73/ Gosman, A.D., and F.C. Lockwood:
Incorporation of a flux model for radiation into a finite difference procedure for furnace calculations. In Proceedings of the 14th Symposium (International) on Combustion, The Combustion Institute, pp. 661-671, 1973
- /JON 03/ Jones, W.W., et al.:
A Technical Reference for CFAST: An Engineering Tool for Estimating Fire and Smoke Transport. NIST TN 1431, April 2003
- /JON 04/ Jones, W.W., et al.:
CFAST - Consolidated Model of Fire Growth and Smoke Transport (Version 5): Technical Reference Guide, NIST Special Publication 1030, October 2004
- /ICF 04/ International Collaborative Fire Model Project (ICFMP):
Revised pyrolysis rate of kerosene experiments for Benchmark #4,
http://techconf.llnl.gov/cgi-fire/downloader/fire_models_BE4/020-0002.xls,
April 2004
- /ICF 04a/ International Collaborative Fire Model Project (ICFMP):
Test Data for Test 1 - in specified order,
http://techconf.llnl.gov/cgi-fire/downloader/fire_models_BE4/020-0005.xls,
August 2004
- /ICF 04b/ International Collaborative Fire Model Project (ICFMP):
Test Data for Test 3 - in specified order,
http://techconf.llnl.gov/cgi-fire/downloader/fire_models_BE4/020-0006.xls,
August 2004

- /KLE 03/ Klein-Heßling, W., et al.:
Specification of International Benchmarking and Validation Exercise # 4:
Kerosene Pool Fire Inside a Compartment. Rev. 2, October 2003
- /LAU 74/ Launder, B.E., and D.B. Spalding:
The numerical computation of turbulent flows. Computer Methods in Applied Mechanics and Engineering, Vol. 3, pp. 269-289, 1974
- /LAU 05/ Lautenberger, C.W., et al.:
A simplified model for soot formation and oxidation in CFD simulation of non-premixed hydrocarbon flames, Fire Safety Journal, Vol. 40, pp. 141-176, 2005
- /LOC 81/ Lockwood, F.C., and N.G. Shah:
A new radiation solution method for incorporation in general combustion prediction procedures. In Proceedings of the 18th Symposium (International) on Combustion, The Combustion Institute, pp. 1405-1414, 1981
- /MAG 76a/ Magnussen, B.F., and B.H. Hjertager:
On mathematical modelling of turbulent combustion with special emphasis on soot formation and combustion. In Proceedings of the 16th Symposium (International) on Combustion, The Combustion Institute, pp. 719 -729, 1976
- /MAG 76b/ Magnussen, B.F. et, al.
Effects of turbulent structure and local concentrations on soot formation and combustion in C₂H₂ diffusion flames, In Proceedings of the 17th Symposium (International) on Combustion, The Combustion Institute, pp. 1383 -1393, 1976
- /MCC 83/ McCaffrey, B.J.:
Momentum implications for buoyant diffusion flames, Combustion and Flame, Vol. 52, p. 149, 1983
- /MIL 00/ Miles, S.D., S. Kumar, and G. Cox:
Comparisons of 'blind predictions' of a CFD model with experimental data. Fire Safety Science – Proceedings of the Sixth International Symposium, IAFSS, pp. 543-554, 2000
- /MIL 01/ Miles, S.:
The predictive capability of CFD for fully developed fires, Fire and Explosion Hazards - Proceedings Third International Seminar, Windermere, UK, pp. 229-240, 2001

- /MIL 04/ Miles, S.:
International Panel Report: Benchmark Exercise # 2 - Pool Fires in Large Halls. May 2004
- /PAT 80/ Patankar, S.V.:
Numerical heat transfer and fluid flow, Hemisphere Publishing Co., 1980
- /SIE 81/ Siegel, R., and J.R. Howell:
Thermal Radiation Heat Transfer, Hemisphere Publishing Corporation, New York, 2nd ed., 1981
- /TRU 76/ Truelove, J.S.:
Mixed grey gas model for flame radiation, UK Atomic Energy Authority Report AERE HL 76/3448, 1976
- /USN 02/ U.S. Nuclear Regulatory Commission (USNRC):
International Collaborative Project to Evaluate Fire Models for Nuclear Power Plant Applications: Cable Tray Fires, Compiled by M. Dey, NUREG-1758, Washington, DC, June 2002

List of Figures

Fig. B1	Oxygen - temperature control on combustion in JASMINE.....	6
Fig. B2	Measured and CFAST predicted gas layer temperatures for Test 1.....	14
Fig. B3	CFAST predicted hot gas layer height for Test 1.....	15
Fig. B4	Measured and CFAST predicted oxygen concentrations for Test 1.....	16
Fig. B5	Measured and CFAST predicted wall surface temperatures for Test 1....	17
Fig. B6	Measured and CFAST material probe surface temperatures for Test 1...	18
Fig. B7	Measured and CFAST flux densities for Test 1.....	19
Fig. B8	Measured and CFAST predicted gas layer temperatures for Test 3.....	20
Fig. B8	Measured and CFAST predicted gas layer temperatures for Test 3 (contd.).....	21
Fig. B9	CFAST predicted hot gas layer height for Test 3.....	22
Fig. B10	Measured and CFAST predicted oxygen concentrations for Test 3 (contd.).....	24
Fig. B11	Measured and CFAST predicted wall surface temperatures for Test 3....	25
Fig. B11	Measured and CFAST predicted wall surface temperatures for Test 3 (contd.).....	26
Fig. B12	Measured and CFAST material probe surface temperatures for Test 3 (contd.).....	28
Fig. B13	Measured and CFAST flux densities for Test 3.....	29
Fig. B13	Measured and CFAST flux densities for Test 3 (contd.).....	30
Fig. B14	JASMINE CFD grid.....	36
Fig. B15	JASMINE calculated temperatures for Test 1 (semi-blind).....	37
Fig. B15	JASMINE calculated temperatures for Test 1 (semi-blind) (contd.).....	38
Fig. B16	JASMINE calculated O ₂ mass fraction for Test 1 (semi-blind).....	39
Fig. B17	JASMINE calculated temperatures for Test 3 (semi-blind run 1).....	40
Fig. B17	JASMINE calculated temperatures for Test 3 (semi-blind run 1) (contd.).....	41
Fig. B18	JASMINE calculated O ₂ mass fraction for Test 3 (semi-blind run 1).....	41
Fig. B19	Measured and JASMINE predicted (blind) gas temperatures for Test 1...	42
Fig. B20	Measured and JASMINE predicted (blind) oxygen concentration for Test 1.....	43
Fig. B21	Measured and JASMINE predicted (blind) wall surface temperatures for Test 1.....	44
Fig. B22	Measured and JASMINE predicted (blind) door velocities for Test 1.....	45

Fig. B23	Measured and JASMINE predicted (blind) gas temperatures for Test 3...	46
Fig. B24	Measured and JASMINE predicted (blind) oxygen concentration for Test 3	47
Fig. B25	Measured and JASMINE predicted (blind) wall surface temperaures for Test 3	48
Fig. B26	Measured and JASMINE predicted (blind) door velocities for Test 3.....	49
Fig. B27	Measured and JASMINE predicted (semi-blind) gas temperatures for Test 1	50
Fig. B28	Measured and JASMINE predicted (semi-blind) oxygen concentration for Test 1	50
Fig. B29	Measured and JASMINE predicted (semi-blind) wall surface temperaures for Test 1	51
Fig. B30	Measured and JASMINE predicted (semi-blind) flux densities for Test 1	51
Fig. B31	Measured and JASMINE predicted (semi-blind) door velocities for Test 1	52
Fig. B32	Measured and JASMINE predicted (semi-blind) gas temperatures for Test 3	53
Fig. B33	Measured and JASMINE predicted (semi-blind) oxygen concentration for Test 3	54
Fig. B34	Measured and JASMINE predicted (semi-blind) wall surface temperaures for Test 3.....	55
Fig. B35	Measured and JASMINE predicted (semi-blind) wall surface temperaures for Test 3.....	56
Fig. B36	Measured and JASMINE predicted (semi-blind) flux densities for Test 3	57
Fig. B37	Measured and JASMINE predicted (semi-blind) door velocities for Test 3	58
Fig. B38	Measured and JASMINE predicted (open) gas temperatures for Test 3 ..	59
Fig. B38	Measured and JASMINE predicted (open) gas temperatures for Test 3 (contd.)	60
Fig. B39	Measured and JASMINE predicted (open) oxygen concentration for Test 3	61
Fig. B39	Measured and JASMINE predicted (open) oxygen concentration for Test 3 (contd.)	62

Fig. B40	Measured and JASMINE predicted (open) wall surface temperatures for Test 3	63
Fig. B40	Measured and JASMINE predicted (open) wall surface temperatures for Test 3 (contd.).....	64
Fig. B41	Measured and JASMINE predicted (open) flux densities for Test 3.....	65
Fig. B41	Measured and JASMINE predicted (open) flux densities for Test 3 (contd.)	66
Fig. B42	Measured and JASMINE predicted (open) door velocities for Test 3	67
Fig. B43	JASMINE predicted (open) mass flow rates for Test 3	68
Fig. B44	JASMINE predicted (open) heat losses for Test 3	69

List of Tables

Table B1	CFAST semi-blind calculation runs	11
Table B2	JASMINE blind calculation runs	31
Table B3	JASMINE semi-blind calculation runs	31
Table B4	JASMINE open calculation runs.....	31

Appendix C: International Collaborative Project to Evaluate Fire Models for Nuclear Power Plant Applications

Validation of the CFAST and FDS Fire Models with Large Fire Experiments in a Compartment

Presented by

Dr. Monideep K. Dey
United States Nuclear Regulatory Commission (USNRC¹),
Office of Nuclear Regulatory Research
Mail Stop T 10 E 50, Washington, D.C. 20555, U.S.A.

¹ The above analyses were conducted while Dr. Dey served as a Guest Researcher in the Building Fire Research Laboratory, National Institute of Standards and Technology.

Abstract

The analysis presented in this report was conducted for Benchmark Exercise No. 4 in the International Collaborative Fire Model Project (ICFMP). The analysis was conducted with the Consolidated Model for Fire and Smoke Transport (CFAST) Version 3.1.7, a zone model, and Fire Dynamics Simulator (FDS) Version 3.1.5, a computational fluid dynamic model developed by the Building Fire Research Laboratory (BFRL), National Institute of Standards and Technology (NIST). The U.S. Nuclear Regulatory Commission (NRC) is evaluating the CFAST and FDS fire models developed by the National Institute of Standards and Technology for use in NRC's regulatory framework. The objective of the 4th Benchmark Exercise was to examine scenarios in a compartment with intense fire sources. FDS, including its output processor Smokeview, provides a useful tool to examine the phenomena involved in the scenarios, specifically for examining the flow patterns and behavior through the door or ventilation opening. The trends of the results from FDS show that the code contains the physics and is capable of simulating the complex phenomena in the fire scenarios in this exercise. However, CFAST in its current form is unsuitable for simulating these scenarios. Although relatively good general performance is observed for FDS, the heat flux models (for radiation and convection) and target models in FDS require improvement before they can be reliably used for NPP applications. The code also requires improvement to accurately simulate plume behavior and tilting due to varying flow conditions in a compartment.

Executive Summary

The analysis presented in this report was conducted for Benchmark Exercise No. 4 in the International Collaborative Fire Model Project (ICFMP). The analysis was conducted with CFAST Version 3.1.7, a zone model, and FDS Version 3.1.5, a computational fluid dynamic model (CFD) developed by the National Institute of Standards and Technology. The U.S. Nuclear Regulatory Commission (NRC) is evaluating the CFAST and FDS fire models developed by the National Institute of Standards and Technology for use in NRC's regulatory framework. The objective of the 4th Benchmark Exercise was to examine scenarios in a compartment with intense fire sources. The fire scenarios in Benchmark Exercise No. 4 are considered to be the most complex and severe that analysts would model for NPP applications. The scenarios apply to either a very large fire size to compartment volume ratio, or applications involving the calculation of heat fluxes and target response near the fire.

FDS, including Smokeview, provides a useful tool to examine the phenomena involved in the scenarios. The tools were useful in deriving interesting observations regarding the flow pattern and behavior through the door or ventilation opening. The FDS code demonstrated the capability to simulate the severe fire scenarios in Benchmark Exercise No. 4. Temperatures in these scenarios reached 1000 °C, and heat fluxes of up to 100 kW/m² were observed. These ranges represent the most extreme thermal environments one might expect in NPP applications. The accuracy of the model for computing local gas temperature is best.

Several difficulties were encountered with the CFAST code including instabilities in the computation of several parameters. Although the CFAST prediction of global parameters (HGL temperature, interface height) was within 20 %, CFAST predicted unrealistic values for heat flux to the targets and walls, and the corresponding target and wall temperatures.

There were convergence issues in the CFAST simulation of the more severe test. The simulation halted before completion. CFAST is sensitive in cases with a high heat flux. The penetration of the thermal wave in the compartment floor and in less dense materials with low thermal conductivity poses numerical challenges for the CFAST code causing the simulation to halt before the end of the transient. Although the CFAST model could be used to compute global parameters for the less severe scenario in this Benchmark Exercise, its use is limited and not recommended for computing heat fluxes

and target responses due to the limitations noted above. For more severe scenarios, the two zone approximation and inherent weaknesses in the code limit its applications. The CFAST model is unsuitable for these scenarios with intense fire sources.

Although relatively good general performance is observed for FDS, the error of the heat flux predictions by FDS can be large (up to 59 %). There are specific weaknesses in the heat flux models in FDS which make it unreliable for predicting heat fluxes to targets in NPPs.

The FDS code also requires improvement to accurately simulate plume behavior and tilting due to varying flow conditions in a compartment. FDS computations of the plume predict a larger tilt due to flow conditions, whereas, the plumes in the experiments are observed to be stiffer and influenced less by flow conditions. This inaccuracy in FDS limits the reliability of using FDS to evaluate targets near the plume.

A detailed heat transfer model for the barrel target used in the experiments will be fairly complex. The CFAST and FDS fire models are not capable of modeling complex configurations such as the barrel for storing radioactive waste. The cylindrical geometry and multi-material composition poses challenges for modeling. Similar limitations of CFAST and FDS for modeling cable targets were noted in ICFMP Benchmark Exercise No. 1 /DEY 02/.

The large uncertainties in the prediction of heat flux to the targets limit the reliability of using FDS or CFAST for predicting target temperatures. Lack of ability to model targets other than rectangular slabs, e.g. radioactive waste barrels, limit the usefulness of the codes for NPP target analysis.

Although the fluid dynamics of the scenario is simulated well by FDS, the simple extinction model in FDS (LOL) decreases the heat output from the fire in the more severe scenario when in reality combustion is fully sustained. The algorithm in FDS for accounting for the under-ventilation of the fire is too simplistic for complex scenarios as in this Benchmark Exercise.

The CFAST and FDS codes do not have the capability to model multi-layer boundaries; therefore, a single-layer assumption had to be adopted to model the multi-layer boundaries in this Benchmark Exercise. Further, the multi-layer composition of the target barrel could not be modeled, although the modeling of the cylindrical geometry is a

more fundamental limitation. The use of these codes for complex target geometries and composition is very limited.

The CFAST model requires major fundamental improvements if it is to be used for fire scenarios with intense fire sources such as those examined in this Benchmark Exercise. The heat flux models (for radiation and convection) and target models in FDS require improvement before they can be reliably used for NPP applications. The simple algorithms for modeling extinction in FDS should be corrected to maintain the HRRs prescribed by the user to improve the performance and accuracy of the model. The basic extinction phenomena require a more fundamental treatment in FDS to be able to predict under-ventilated conditions. Finally, the ability to simulate multi-layer boundaries and targets needs to be implemented in FDS for NPP applications.

The tests used in this Benchmark Exercise provide fire scenarios with intense fire sources in a compartment. It will be beneficial to conduct tests that provide a range of fire intensities so that one can determine the limits of zone models over which their theoretical formulations remain valid.

Contents

C1	Introduction	1
C1.1	Specification of International Benchmarking Exercise No. 4.....	1
C1.1.1	Room Geometry.....	1
C1.1.2	Natural Ventilation.....	3
C1.1.3	Mechanical Ventilation	4
C1.1.4	Fire	4
C1.1.5	Targets	4
C2	Input Parameters and Assumptions.....	5
C3	Evaluation of Specified Model Predictions.....	9
C3.1	Test 1	10
C3.1.1	Global Compartment Parameters	11
C3.1.2	Local Gas Temperature	12
C3.1.3	Heat Flux to Plate and Block Targets.....	13
C3.1.4	Plate and Block Temperature.....	14
C3.1.5	Heat Flux to Walls	15
C3.1.6	Wall Temperature.....	15
C3.1.7	Conclusion	15
C3.2	Test 3	15
C3.2.1	Global Compartment Parameters	16
C3.2.2	Local Gas Temperature	17
C3.2.3	Heat Flux to Plate and Block Targets.....	18
C3.2.4	Plate and Block Temperature.....	19
C3.2.5	Heat Flux to Walls	19
C3.2.6	Wall Temperature.....	19
C3.2.7	Conclusion	20
C4	General Recommendations and Conclusions.....	21
C4.1	Capabilities.....	21
C4.2	Limitations	21
C4.2.1	General Modeling of Scenario with CFAST.....	21
C4.2.2	Heat Flux Models in CFAST and FDS.....	22
C4.2.3	Plume Model in FDS	23

C4.2.4	Target Models in CFAST and FDS.....	24
C4.2.5	Extinction Models in FDS and CFAST	25
C4.2.6	Modeling of Multi-Layer Boundaries with CFAST and FDS	26
C4.3	User Interface.....	26
C4.4	Benefits of Hand Calculations	27
C4.5	Need for Model Improvements	27
C4.6	Need for Advanced Models	28
C4.7	Need for Additional Test Programs	29
C5	Acknowledgments	31
C6	References	33
	List of Figures	61
	List of Tables	63

C1 Introduction

The validation study of the CFAST and FDS fire computer codes presented here was conducted as part of Benchmark Exercise No. 4 of the International Collaborative Fire Model Project (ICFMP). The USNRC exercised the CFAST and FDS codes, developed by the National Institute of Standards and Technology (NIST), as part of its program to evaluate and validate these computer codes for use in NRC's regulatory framework. A complete specification of the exercise is in the main report. The following provides a summary of the specification of the Benchmark Exercise.

C1.1 Specification of International Benchmarking Exercise No. 4

Experiments with large pool fires in a compartment conducted at iBMB (Institut für Baustoffe, Massivbau und Brandschutz) of Braunschweig University of Technology, Germany were used for this Benchmark Exercise.

C1.1.1 Room Geometry

The experimental room (see Fig. C1) has a floor area of 3.6 m x 3.6 m and a height of 5.7 m. The room is made of concrete and is naturally and mechanically ventilated. The surface materials as well and the thermo-physical properties of those materials are listed in Table C1 and Table C2.

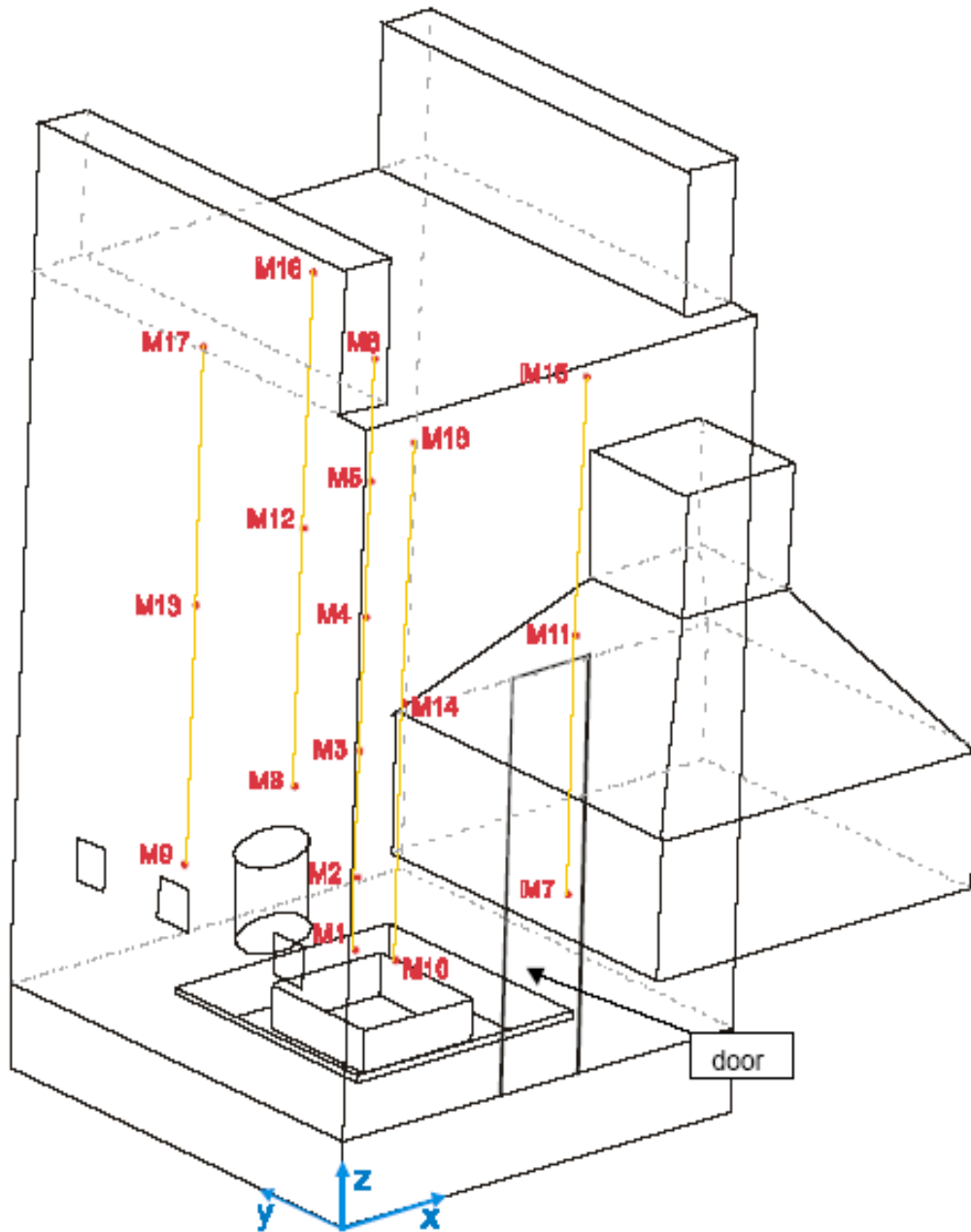


Fig. C1 Compartment for Benchmark Exercise No. 4

Table C1 Wall, floor, and ceiling material

Surface	Material	Thickness [m]
Floor	Concrete	0.3
	Aerated concrete	0.6
Side walls	Light concrete	0.25
	Insulation	0.05
Ceiling	Concrete	0.25
	Insulation	0.05
Side walls channel	Light concrete	0.125
	Insulation	0.06
Ceiling channel	Concrete	0.13
	Insulation	0.07

Table C2 Thermo-physical properties of wall, floor, and ceiling materials

Material	Thermal conductivity [W/m K]	Specific Heat [kJ/kg K]	Density [kJ/m ³]
Concrete	2.10	880	2400
Aerated concrete	0.75	840	1500
Light concrete	0.11	1350	420
Insulation	0.05	1500	100

C1.1.2 Natural Ventilation

In Test 1, an open door (see Fig. C1) is located at the center of the front wall ($x = 1.8$; $y = 0$). The door has an area of $0.7 \text{ m} \times 3.0 \text{ m} = 2.1 \text{ m}^2$. The lower edge of the door is just above the aerated concrete (see section 1.1.4 for further details) at $z = 0.6 \text{ m}$. All other doors are closed.

In Test 3, the door opening was partly closed. The free cross section was reduced to 0.7 m x 1.0 m and opening starts at an elevation of 1.6 m (1 m above the aerated concrete bottom surface).

C1.1.3 Mechanical Ventilation

There are two ventilation ducts with a width of 0.42 m and a height of 1.03 m at the ceiling. The length of both ducts is approximately 3.625 m and leads to the fan system. Although the fan system was not in use, flow velocities were measured.

C1.1.4 Fire

In the center of the floor area, a pan with a size of 4 m² has been installed on a weight scale.

The bottom level of this pan has an elevation of about 0.36 m. The depth is approximately 0.3 m high. The kerosene mass loss is measured with the scale. To protect this measurement aerated concrete has been applied around this pan on the complete floor area up to an elevation of 0.6 m. Also, the inner side of the large pan was covered by 0.05 m thick light concrete plates for protection.

In the center of the large pan, a smaller 1 m² pan has been installed. The bottom of this pan has an elevation of about 0.51 m. The depth is 0.2 m. For stabilization a 0.03 m wide steel plate has been installed around the upper edge of the pan side-wall.

A hood was installed above the front door (see Fig. C1). Using the oxygen consumption method, the energy release can be estimated.

C1.1.5 Targets

Three different types of material probes have been positioned on the right side of the fire compartment ($x = \sim 0$ m). The materials are 'aerated concrete', concrete and steel. The size of these elements is 0.3 m x 0.3 m. The thickness is 0.1 m for the concrete probes and 0.02 m for the steel plate. The properties of the materials are listed in **Table C2**. The location of the center surface is also given in **Table C3**. The sensor M29

represents the aerated concrete material. Sensors M33 and M34 represents the concrete and steel materials, respectively.

Table C3 Target description and location

			Fire Location [m]			
			X	Y	Z	
			1.8	1.8	0.51	
ID	Description	Orientation	Target Location [m]			Distance to
			X	Y	Z	Fire [m]
M29	Gas concrete material	Pointing at fire	0.08	0.065	1.7	2.39
M33	Concrete material	Pointing at fire	0.08	1.9	1.7	2.09
M34	Steel material	Pointing at fire	0.08	2.8	1.7	2.36

C2 Input Parameters and Assumptions

A comprehensive specification of Benchmark Exercise No. 4 was developed such that there would be a minimal amount of unspecified parameters and assumptions for the analysts conducting predictions for the Specified Calculations per ASTM 1355-05 /AST 04/. However, there were still some parameters for which values had to be assumed for conducting the Specified Calculations. These are listed and discussed below:

1. Fire Growth:

An evaluation of the FDS code to simulate fire growth and burning rate of the kerosene in the fuel pan was not attempted in this validation study. Although the capability to simulate burning rate exists in theory in the FDS code, it is acknowledged that such sub-models have inherent limitations that cannot be overcome until further research in this area. This research is summarized later in Section C4.4. Also, the simulation of fire growth will require a solid to liquid heat transfer model in FDS to predict the heat up of the fuel pan. Therefore, the heat release rates (HRRs) measured during the experiments were used for this validation study. The use of prescribed heat release rates neglects the feedback effect between the fire and the compartment conditions. Therefore, the use of prescribed HRRs will include some

uncertainty due to the lack of complete simulation of the fire phenomena in the compartment.

2. Heat Release Rate (HRR):

As indicated above, the HRRs of the fire measured during the experiments were used for this validation study. However, the heat release rate measured during the end of the transient when the fuel level in the pan was low has a large uncertainty associated with it. Oscillations in the heat release rate are noted and may be due to the method used to deduce heat release rates from the derivative of mass loss rate. The value of this parameter, especially during the oscillations and at the peak of the transient, is likely to be the largest source of uncertainty in the predicted results.

3. Lower Oxygen Limit (LOL):

The lower oxygen limit needs to be input to the CFAST code for the simplistic sub-model for predicting the extinction of the fire. There was no value for LOL included in the specifications, allowing judgment from users to define the most appropriate value for the experiments. The specification of this parameter has a large effect on the prediction of extinction and could be a large source of user effects². The FDS code has a similar scheme to extinguish the fire when oxygen levels decrease below a preset value and temperatures remain sufficiently high, however, the user does not need to specify the values. The uncertainty in specifying the LOL may have an impact on the predicted results if the fire growth is under-ventilated during the transients.

4. Target Specification:

A detailed heat transfer model for the barrel used in the experiments will be fairly complex. The CFAST and FDS fire models are not capable of modeling complex configurations such as the barrel for storing radioactive waste. The cylindrical geometry and multi-material composition poses challenges for modeling. No attempt was made at developing a set of assumptions for the target in the CFAST and FDS codes such that predictions of the temperatures in the barrel could be made. Similar limitations of CFAST and FDS for modeling cable targets were noted in ICFMP Benchmark Exercise No. 1 /DEY 02/.

² Test 1 was under-ventilated so the LOL did not impact the simulation. CFAST did not successfully simulate Test 3, as discussed later in Chapter 3. The LOL value chosen would have had an impact on this simulation.

5. Material Properties of Walls and Targets:

The material properties of the walls, ceiling, floor, and targets were specified for the exercise using values available in the literature for these materials. The properties of the specific materials used in the experiments may vary from the generic values reported in the literature. This may be a source of uncertainty in the predicted results.

6. Radiative Fraction:

The radiative fraction of the fuel was not specified. The value (0.35) of the radiative fraction available in the literature /SFP 95/ for n-dodecane was assumed for the analysis. This assumption may have an impact on the predicted results since this parameter determines the convective and radiative heat flow from the plume in both CFAST and FDS fire codes. This parameter was identified as a key parameter effecting fire compartment conditions in ICFMP Benchmark Exercise No. 2 /MIL 04/.

7. Ventilation Flow:

The FUCHS system was simply modeled in CFAST and FDS with prescribed flow rates, without accounting for any feedback effects between the ventilation system and the compartment. Further, the flow through the FUCHS system was assumed to be constant for the CFAST calculations as there is no direct means for providing input for varying ventilation flow rates in the code. The average flow rate was used as input for CFAST. These assumptions will lead to some uncertainty in the predicted results.

8. Grid Size:

A grid size of 10 cm was used for the FDS calculations. It is recognized that CFD calculations are generally sensitive to the grid used. A grid size of 10 cm may be optimal for the type of scenarios simulated; however, this was not confirmed through a grid sensitivity analysis.

9. Multi-layer Boundaries:

The CFAST and FDS codes do not have the capability to model multi-layer boundaries, therefore, a single-layer assumption had to be adopted to model the aerated concrete around the fuel pan and the concrete floor below. It was assumed that the total floor mass consisted of light concrete, with properties in between aerated concrete and concrete, with an equivalent thickness. The layer of insulation covering the walls and ceiling was neglected in the calculations since it could not be directly modeled in CFAST or FDS.

10. Exhaust Hood:

FDS calculations were conducted with and without the exhaust hood above the door of the compartment to determine its effect on the compartment conditions. It was determined that modeling the hood had very little effect on the compartment conditions. Therefore, no attempt was made to account for the exhaust hood as part of a ventilation system in the CFAST calculations.

11. Heat Flux Comparisons:

The comparison of heat flux prediction with measured data poses several challenges. It is important that equivalent measures of heat flux are used in the comparison. The flux gauges in the experiments in Benchmark Exercise No. 4 were cooled and maintained at a constant temperature (10 °C). The CFAST and FDS codes normally output the net heat flux on targets based on the target temperature. It is important that these fluxes be modified to the incident radiative heat flux and the convective heat flux to a block at constant temperature for comparison with measured heat fluxes. Even with the modifications to account for the differences between measured and predicted values, an exact comparison is not possible due to the lack of ability to exactly measure the calculated values from models. Therefore, the comparison of heat fluxes will have some additional uncertainty due to this limitation.

C3 Evaluation of Specified Model Predictions

The following provides a comparison of Specified Calculations per ASTM 1355-05 with CFAST and FDS for the tests conducted for ICFMP Benchmark Exercise No. 4. The results of CFAST, a zone model, and FDS, a CFD code, are presented together to allow a comparison and discussion of the capabilities and limitations of the two types of models. The predictions using CFAST and FDS presented below were made and sent to GRS before the experimental data was released by them. GRS has certified the authenticity of the Specified Calculations. The calculations therefore comply with the requirements for Specified Calculations in ASTM-1355. CFAST Version 3.1.7 and FDS Version 3.1.5 were used for the computations.

The following is a list of the major sub-models implemented in the two fire computer codes for modeling the physical phenomena in the scenarios:

- Combustion chemistry (tracking concentrations of oxygen and combustion products);
- Plume and ceiling jet flow;
- Mass and energy balance;
- Ventilation through doors;
- Forced ventilation;
- Heat transfer to boundaries;
- Heat transfer to targets;
- Thermal response of the target.

The FDS code computes the flows from first principles based on fluid dynamic equations, whereas CFAST utilizes correlations developed from experimental data. The performance of these sub-models is discussed below based on comparison of predicted results with experimental measurements. The theoretical formulation of the two models may be found in /JON 04/ for CFAST and /MCG 04/ for FDS. The theoretical formulations of these codes are presented in these reports according to the format and content required by ASTM-1355, "Evaluating the Predictive Capability of Deterministic Fire Models" /AST 04/. These reports were sponsored by the U.S. Nuclear Regulatory Commission for referencing in its validation studies as that reported herein.

The FDS code simulated Tests 1 and 3 successfully. The CFAST code simulated Test 1 to the end of the specified transient; however, instabilities were noted as discussed below. There were convergence issues in the CFAST simulation of Test 3. The simulation halted at about 14 % to completion. CFAST is sensitive in cases with a high heat flux. The penetration of the thermal wave in the compartment floor and in less dense materials with low thermal conductivity poses numerical challenges for the CFAST code.

The following presents the comparison of predictions by the CFAST and FDS code with experimental data for Test 1 and Test 3 of the series. The discussion is grouped in categories presented below to evaluate the predictive capability of the models according to the general features and sub-models of the codes:

- Global parameters;
- Local gas temperature;
- Heat flux to targets;
- Target temperature;
- Heat flux to walls;
- Wall temperature.

C3.1 Test 1

Fig. C2 to Fig. C20 show the comparison of the trends of the predictions of CFAST and FDS with experimental data, and Table C4 shows the peak values predicted by the models and that measured and the uncertainty of the predictions. The uncertainty value tabulated is: $(\text{model prediction at peak} - \text{measured value at peak}) / (\text{measured value at peak} - \text{initial measured value})$.

A '+' sign in the uncertainty value means that the model prediction was greater than the measured value, and a - sign means that the model prediction was less than measured value.

C3.1.1 Global Compartment Parameters

The HRR measured during the test and prescribed as input to the CFAST and FDS models are shown in Fig. C2. The HRR increases rapidly to 2500 kW in ~ 253 s, and then increases more gradually to 3500 kW before being extinguished at ~ 1368 s due to fuel depletion.

Fig. C3 shows the development of the hot gas layer. Both CFAST and FDS predict the hot gas layer to develop and reach ~ 1 m above the floor in ~ 200 s. The initial development of the HGL shown in Fig. C3 based on measured data seems erratic and may be due to discrepancies in the offset in the initiation of the transient. The measured data shows the HGL interface reaches ~ 1.5 m at ~ 600 s. Table C4 shows the steady state HGL interface height predicted by the codes and measured, and the uncertainties in the CFAST and FDS predictions. Both CFAST and FDS under-predict the steady state HGL interface height by – 19 %.

Fig. C4 shows the hot gas layer (HGL) temperature. Both CFAST and FDS predictions follow the same rate of temperature increase as the experimental data with CFAST over predicting the increase by a larger amount. It should be noted that the discrepancy in the time at which the temperature begins to increase should be ignored since that is caused mainly by the offset between the predictions and measured data. Once reaching the end of the rapid increase at ~ 360 s, the increase in temperature is greater in the experiment than that predicted by both CFAST and FDS. This discrepancy may be due to smaller heat loss in the experiments due to the presence of insulation that was ignored in the code calculations. Table C4 shows the peak values predicted by the models and that measured. The uncertainty in the predictions for CFAST and FDS are + 20 % and – 17 %, respectively.

Fig. C5 shows the O₂-depletion predicted by CFAST and FDS. The O₂ level at GA1-O2, located at 3.8 m above the floor in the HGL (top of door is at 3.0 m), predicted by CFAST and FDS at the end of the transient is 8.9 % and 5.7 %, respectively. The measured O₂ level at the end of the transient is 13.5 %. Since the measured O₂ level does not decrease much after ~ 465 s, there is potentially an error in the measured O₂ level. Therefore, uncertainties of the predictions are not presented here.

C3.1.2 Local Gas Temperature

The local gas temperatures in the plume, ceiling jet, and compartment are only predicted by FDS. FDS outputs are shown in Fig. C6 and Fig. C7. Fig. C6 shows an iso-surface of the mixture fraction (at a value of 0.062) at 238 s which represents the flame sheet created by FDS at that point. Fig. C6 shows that FDS simulates the flame sheet to be significantly pushed toward the rear wall by the flow of ambient air into the compartment through the door. Fig. C7 shows a slice profile (at $x = 1.8$ m) of the gas temperature in the compartment. Fig. C7 again shows that FDS simulates that the plume is pushed significantly toward the rear wall.

Fig. C8 shows the comparison of measured plume temperatures at M2, M4, and M6 with that predicted by FDS. As shown in Fig. C8, FDS predicts peaks in the plume temperature at ~ 50 s. These peaks are explained by the plume development predicted by FDS. Observations of the plume predicted by FDS through Smokeview (the graphical interface for FDS) indicates a steady vertical plume until ~ 50 s when the plume is pushed to the rear wall by flow into the compartment through the door. This causes peaks in the thermocouples, M2, M4, and M6 which are located directly above the fuel pan. The experimental measurements do not indicate this extensive movement of the fire plume. Figure C3-1 in the main text shows a photograph of the fire and plume at steady state conditions in Test 1. The figure shows some degree of plume tilt in the experiment, but not to the extent predicted by FDS. The measured data shows the plume to be fully developed at ~ 105 s after which the plume temperatures increase to ~ 1000 °C without any intermediate peaks. The experimental data shows oscillations in the plume temperature, especially near the fire at M2, indicating oscillation of the fire plume to and from the rear wall. FDS predicts the peaks of the plume temperatures to be ~ 800 °C. As shown in Table C4, the uncertainty in the predicted values are -27% , -16% , and -25% for M2, M4, and M6, respectively.

Fig. C9 shows the local gas temperatures in the compartment at Level 1 for M7, M8, M9, and M10. The measured temperatures show a rapid increase in temperature followed by a more gradual increase until the end of the transient. The temperature measured at M10 is much higher than that measured at M7, M8, and M9. This is due to the tilting of the fire plume toward M10. FDS also shows a rapid increase in temperature followed by large oscillations and unexpected trends. These oscillations may be caused by oscillations in the flow through the door predicted by FDS. The temperature predicted at M8 by FDS is highest since the code predicts the fire plume to be pushed

more toward the rear wall, as discussed above. The experimental data shows some oscillations in the temperature at M10 indicating the movement of the plume in and out of that region. Although the peak values predicted by FDS are similar to that measured for M7, M8, and M9, there is an uncertainty of – 43 % for M10 due to the discrepancy in the degree of plume tilt predicted.

Fig. C10 shows the local gas temperature in the compartment at Level 2 for M11, M12, M13, and M14. The peak values predicted by FDS are similar to those ones measured with an error of - 13 % at M14. The effect of plume tilt is not evident at this level since the plume is maintained (see Figure 3-1 in the main text) mainly in the lower level.

Fig. C11 shows the local gas temperature in the compartment at Level 3 for M15, M16, M17, and M18. The peak values predicted by FDS are similar to those ones measured with an error of – 5 % at M18. Again, the effect of plume tilt is not evident at this level since the plume is maintained in the lower level.

C3.1.3 Heat Flux to Plate and Block Targets

The comparison of heat flux prediction with measured data poses several challenges. It is important that equivalent measures of flux are used in the comparison. The flux gauges in the experiments were cooled and maintained at a constant temperature (10 °C). The CFAST and FDS codes normally output the net heat flux on targets based on the target temperature. These fluxes were modified to the incident radiative heat flux and the convective heat flux to a block at a constant temperature of 10 °C. Even with the modifications to account for the differences between measured and predicted values, an exact comparison is not possible due to the lack of ability to exactly measure the calculated values from models.

Fig. C12 shows a comparison of the total heat flux predicted by CFAST and FDS with measurements at WS4 on the aerated concrete block. As noted earlier, instabilities are noted in the flux predicted by CFAST. The CFAST code is sensitive in cases with high heat flux. The penetration of the thermal wave in less dense materials poses numerical challenges for the CFAST code. Therefore, uncertainties associated with the aerated concrete block are not reported. The uncertainty of FDS for total heat flux at WS4 at ~ 40 kW/m² is + 48 %.

Fig. C13 shows a comparison of the total heat flux predicted by CFAST and FDS with measurements at WS3 on the concrete block. CFAST significantly over-predicts the heat flux with an uncertainty of + 146 %. The FDS prediction is similar to that measured with an uncertainty of + 14 %.

Fig. C14 shows a comparison of the total heat flux predicted by CFAST and FDS with measurements at WS2 on the steel plate. CFAST again significantly over-predicts the heat flux with an uncertainty of + 215 %. The uncertainty in the FDS prediction is + 59 %.

It should be noted that FDS predicts an increase in the heat flux toward the end of the transient, possibly due to the heat flux from the boundaries to the targets. This increase in heat flux toward the end of the transient is not noted in the measurements.

C3.1.4 Plate and Block Temperature

Fig. C15 shows a comparison of the surface temperature of the aerated concrete block predicted by CFAST and FDS with measurement. Oscillations in the CFAST prediction is observed due to oscillations in the heat flux calculation (see Fig. C12) as discussed above. The uncertainty in the FDS prediction is + 19 %.

Fig. C16 shows a comparison of the surface temperature of the concrete block predicted by CFAST and FDS with measurement. CFAST significantly over-predicts the temperature with an uncertainty of + 128 %. The FDS prediction is similar to that measured with an uncertainty in the peak value of + 28 %.

Fig. C17 shows a comparison of the front surface temperature of the steel plate predicted by CFAST and FDS with measurement. CFAST significantly over-predicts the temperature with an uncertainty of + 111 %. The FDS prediction is similar to that measured with an uncertainty of + 7 %.

Fig. C18 shows a comparison of the back surface temperature of the steel plate predicted by FDS with experiment. The FDS prediction is similar to that measured with an uncertainty of + 7 %.

C3.1.5 Heat Flux to Walls

Fig. C19 shows a comparison of the heat flux on the wall predicted by FDS with experiment. FDS under-predicts the heat flux by – 45 %. The experimental values of the heat flux at WS1 and WS3 which are in comparable locations are similar. Although the FDS prediction for heat flux at WS3 was similar to experiment, it under-predicts the flux at WS1.

C3.1.6 Wall Temperature

Fig. C20 shows a comparison of the wall surface temperatures predicted by FDS with experiment. FDS predictions are similar to experimental observations with an uncertainty of – 26 % at M20.

C3.1.7 Conclusion

Several difficulties were encountered with the CFAST code, including instabilities in the computation of several parameters. Although the CFAST prediction of global parameters (HGL temperature, interface height) was within 20 %, CFAST predicted unrealistic values for heat flux to the targets and walls, and the corresponding target and wall temperatures.

FDS predictions were similar to experimental observations for most parameters. Global parameters such as the HGL temperature and interface height were within 20 % of experimental values. The local gas temperatures in the compartment and in the plume predicted by FDS were generally within 15 % and 25 % of experimental observations, respectively. The heat flux to the targets and blocks and corresponding temperatures predicted by FDS deviated by 59 % and 28 % from experimental observation, respectively.

C3.2 Test 3

As discussed above, there were convergence issues in the CFAST simulation of Test 3. The simulation halted at about 14 % to completion. CFAST is sensitive in cases with a high heat flux. The penetration of the thermal wave in the compartment floor and in

less dense materials poses numerical challenges for the CFAST code causing the simulation to halt before the end of the transient. Therefore, only the predictions of FDS are presented here. Figures C21 to C41 show the comparison of the trends of the predictions of CFAST and FDS with experimental data, and Table C5 shows the peak values predicted by the models and that measured and the uncertainty of the predictions.

C3.2.1 Global Compartment Parameters

The HRR measured during the test and prescribed as input to the FDS model is shown in Figure C20. The measured HRR increases rapidly to 1500 kW in ~ 50 s, and then increases more gradually reaching 2700 kW at 850 s. The HRR increases rapidly from this point to 6000 kW at ~ 1050 s before being extinguished. Although the measured HRR was input to the FDS code, the FDS internal calculation of the HRR decreased after the initial rise at ~ 50 s. Although the HRR calculated by FDS started to increase at ~ 200 s, it was less than the measured HRR up to the peak in HRR. This may be due to the internal algorithm in FDS that inadvertently decreases the HRR for under-ventilated conditions.

Fig. C22 shows the development of the hot gas layer. FDS predicts the hot gas layer to develop and reach ~ 0.6 m above the floor in ~ 90 s. The measured data shows the HGL interface starts to level to ~ 1.6 m (bottom of vent) at ~ 95 s. FDS predicts a steady state level is reached more quickly after the initial drop in level compared to experiment. Table C5 shows the steady state HGL interface height predicted by FDS and measured, and the uncertainty in the FDS prediction. FDS under-predicts the steady state HGL interface height by - 24 %.

Fig. C23 shows the hot gas layer (HGL) temperature. FDS under-predicts the HGL temperature because of the discrepancy in the HRR (discussed above). Table C5 shows the peak values predicted by the model and those measured. The uncertainty of the prediction for FDS is - 2 %.

Fig. C24 compares the O₂ depletion predicted by FDS with experiment. The FDS prediction is similar to experimental observation until 840 s at which point FDS predicts a rapid reduction in O₂ level to 0 %, while experimental observation indicates the O₂ level reaches 0 % more gradually at ~ 1095 s. FDS prediction is less than the measured value by ~ 25 % for most of the transient.

C3.2.2 Local Gas Temperature

Fig. C25 shows an isosurface of the mixture fraction (at a value of 0.062), which represents the flame sheet created by FDS, at 45 s. The flame is simulated as being vertical up to this time. Fig. C26 shows an isosurface of the mixture fraction (at a value of 0.062) created by FDS at 130 s. Fig. C26 shows that FDS simulates the flame sheet to be significantly pushed toward the rear wall by the flow of ambient air into the compartment through the door at this time. Fig. C27 shows a slice profile (at $x = 1.8$ m, $t = 101.5$ s) of the gas temperature in the compartment. Fig. C28 shows a slice profile (at $x = 1.8$ m, $t = 102$ s) of the gas temperature in the compartment. Fig. C27 again shows that FDS simulates that the plume is pushed significantly toward the rear wall. However, observations of this temperature slice file in Smokeview shows that FDS simulates the flow through the door to pulsate with a period of ~ 2 s. Fig. C27 shows the flow through the door to be bidirectional, whereas Fig. C28 shows the end of the cycle of the pulsation when the flow is unidirectional through the door flowing out of the compartment. This pulsating behavior was noted during the experiments and mentioned in Chapter 3 of the main report. The pulsating flow through the door provides sufficient oxygen to the fire and prevents it from being under-ventilated.

Fig. C29 shows the comparison of measured plume temperatures at M2, M4, and M6 with that predicted by FDS. As shown in Fig. C29, FDS predicts peaks in the plume temperature at ~ 50 s in Test 3 as in Test 1. These peaks are explained by plume development predicted by FDS. Observations of the plume predicted by FDS through Smokeview (the graphical interface for FDS) indicates a steady vertical plume develop until ~ 50 s (also see Fig. C25) when the plume is pushed to the rear wall by flow into the compartment through the door. This causes peaks in the thermocouples, M2, M4, and M6 which are located directly above the fuel pan. The experimental measurements do not indicate this extensive movement of the fire plume. The measured data shows the plume to be fully developed at ~ 180 s after which the plume temperatures increase to ~ 1000 °C without any intermediate peaks. The experimental data shows oscillations in the fire, especially near the fire at M2. FDS predicts the peaks of the plume temperatures to be ~ 800 °C. As shown in Table C5, the uncertainty in the predicted values are -26% , -17% , and -27% for M2, M4, and M6, respectively.

Fig. C30 shows the local gas temperatures in the compartment at Level 1 for M7, M8, M9, and M10. The measured temperatures show a rapid increase in temperature followed by a more gradual increase until the end of the transient. The temperature meas-

ured at M10 and M8 is higher than that measured at M7 and M9. This is due to the tilting of the fire plume toward the back wall. The plume temperature at M10 is higher than at M8 indicating that the tilt is more toward M10, but not as far as M8. FDS also shows a rapid increase in temperature followed by oscillations and a gradual increase in plume temperature. These oscillations are caused by oscillations in the flow through the door predicted by FDS, as discussed above. The experimental data shows some oscillations in the temperature at M10 indicating the movement of the plume in and out of that region. There are notable peaks in the measured data for M7 and M9 at ~ 1230 s due to the more rapid increase in HRR starting at ~ 800 s and peaking at ~ 1100 s. The uncertainty in the local gas temperatures predicted by FDS at M10 is – 33 %.

Fig. C31 shows the local gas temperature in the compartment at Level 2 for M11, M12, M13, and M14. There are notable peaks in the measured data for M11 and M13 at ~ 1305 s due to the more rapid increase in HRR starting at ~ 800 s and peaking at ~ 1100 s. The peak values predicted by FDS are similar to that measured with an error of – 24 % at M14.

Fig. C32 shows the local gas temperature in the compartment at Level 3 for M15, M16, M17 and M18. There are notable peaks in the measured data for M15, M16, M17, and M18 at ~ 1305 s due to the more rapid increase in HRR starting at ~ 800 s and peaking at ~ 1100 s. The peak values predicted by FDS are similar to that measured with an error of – 27 % at M18.

C3.2.3 Heat Flux to Plate and Block Targets

The comparison of heat flux prediction with measured data poses several challenges. It is important that equivalent measures of flux are used in the comparison. The flux gauges in the experiments were cooled and maintained at a constant temperature (10 °C). The CFAST and FDS codes normally output the net heat flux on targets based on the target temperature. These fluxes were modified to the incident radiative heat flux and the convective heat flux to a block at a constant temperature of 10 °C. Even with the modifications to account for the differences between measured and predicted values, an exact comparison is not possible due to the lack of ability to exactly measure the calculated values from models.

Fig. C33 shows a comparison of the total heat flux predicted by FDS with measurement at WS4 on the aerated concrete block. There is a large increase in heat flux at ~ 1155 s when the HRR reaches its peak at 6000 kW. The uncertainty of the FDS prediction at WS4 at ~ 71 kW/m² is – 53 %.

Fig. C34 shows a comparison of the total heat flux predicted by FDS with measurement at WS3 on the concrete block. The uncertainty in the FDS prediction at 66 kW/m² is - 40 %.

Fig. C35 shows a comparison of the total heat flux predicted by FDS with measurement at WS2 on the steel plate. The uncertainty in the FDS prediction at 46 kW/m² is - 23 %.

C3.2.4 Plate and Block Temperature

Fig. C36 shows a comparison of the surface temperature of the aerated concrete block predicted by FDS with measurement. The uncertainty in the FDS prediction is + 2 %.

Fig. C37 shows a comparison of the surface temperature of the concrete block predicted by FDS with measurement. The uncertainty in the FDS prediction is - 33 %.

Fig. C38 shows a comparison of the front surface temperature of the steel plate predicted by FDS with measurement. The uncertainty in the FDS prediction is - 33 %.

Fig. C39 shows a comparison of the back surface temperature of the steel plate predicted by FDS with experiment. The uncertainty in the FDS prediction is - 34 %.

C3.2.5 Heat Flux to Walls

Fig. C40 shows a comparison of the heat flux on the wall predicted by FDS with experiment. FDS under-predicts the heat flux by – 8 %.

C3.2.6 Wall Temperature

Fig. C41 shows a comparison of the wall surface temperatures predicted by FDS with experiment. FDS predictions are similar to experimental observations with an uncertainty of – 34 % at M20.

C3.2.7 Conclusion

There were convergence issues in the CFAST simulation of Test 3. The simulation halted at about 14 % to completion. CFAST is sensitive in cases with a high heat flux. The penetration of the thermal wave in the compartment floor and in less dense materials poses numerical challenges for the CFAST code causing the simulation to halt before the end of the transient.

FDS predictions were similar to experimental observations for most parameters. Global parameters such as the HGL temperature, interface height, and O₂ concentration were within 32 % of experimental values. The local gas temperatures in the compartment and in the plume predicted by FDS were within 33 % and 27 % of experimental observations, respectively. The heat flux to the targets and blocks and corresponding temperatures predicted by FDS deviated by 53 % and 33 % from experimental observation, respectively. The HRR used by FDS was less than input for the simulation due to algorithms in FDS to account for under-ventilated conditions. If these algorithms are corrected to maintain the prescribed HRR, the FDS predictions should be even closer to experimental measurements.

C4 General Recommendations and Conclusions

The following provides the findings and conclusions of this validation study. The fire scenarios in Benchmark Exercise No. 4 are considered to be the most complex and severe that analysts would model for NPP applications. The scenarios apply to either a very large fire size to compartment volume ratio, or applications involving the calculation of heat fluxes and target response near the fire.

C4.1 Capabilities

FDS

The FDS code demonstrated capability to simulate severe fire scenarios such as in Benchmark Exercise No. 4. Temperatures in these scenarios reached 1000 °C, and heat fluxes up to 100 kW/m² were observed. These ranges represent the most extreme thermal environments one might expect in NPP applications. The accuracy of the model for computing local gas temperature is best. Most phenomena are predicted reasonable well for the scenarios in the Benchmark Exercise.

C4.2 Limitations

C4.2.1 General Modeling of Scenario with CFAST

For Test 1, several difficulties were encountered with the CFAST code including instabilities in the computation of several parameters. Although the CFAST prediction of global parameters (HGL temperature, interface height) was within 20 %, CFAST predicted unrealistic values for heat flux to the targets and walls, and the corresponding target and wall temperatures.

Fig. C12 shows a comparison of the total heat flux predicted by CFAST with measurements at WS4 on the aerated concrete block. Instabilities are noted in the flux predicted by CFAST. The CFAST code is sensitive in cases with high heat flux. Figure C12 shows a comparison of the total heat flux predicted by CFAST with measurements at WS3 on the concrete block. CFAST significantly over-predicts the heat flux with an uncertainty of + 146 %. Fig. C14 shows a comparison of the total heat flux predicted by

CFAST with measurements at WS2 on the steel plate. CFAST again significantly over-predicts the heat flux with an uncertainty of + 215 %.

Fig. C15 shows a comparison of the surface temperature of the aerated concrete block predicted by CFAST with measurement. Oscillations in the CFAST prediction is observed due to oscillations in the heat flux calculation (see Fig. C12) as discussed above. Fig. C16 shows a comparison of the surface temperature of the concrete block predicted by CFAST and measurement. CFAST significantly over-predicts the temperature with an uncertainty of + 128 %. Figure C16 shows a comparison of the front surface temperature of the steel plate predicted by CFAST with measurement. CFAST significantly over-predicts the temperature with an uncertainty of + 111 %.

There were convergence issues in the CFAST simulation of Test 3. The simulation halted at about 14 % to completion. CFAST is sensitive in cases with a high heat flux. The penetration of the thermal wave in the compartment floor and in less dense materials with low thermal conductivity poses numerical challenges for the CFAST code causing the simulation to halt before the end of the transient.

Although the CFAST model could be used to compute global parameters for scenarios like Test 1, its use is limited and not recommended for computing heat fluxes and target responses due to the limitations noted above. For tests more severe than Test 1, the two zone approximation and inherent weaknesses in the code limits its applications. The CFAST model is unsuitable for these scenarios with intense fire sources.

C4.2.2 Heat Flux Models in CFAST and FDS

The limitations of the heat flux models in CFAST were discussed above making the model unsuitable for simulating fire scenarios with intense fire sources.

The following provides a summary of the accuracy of the heat flux predictions by FDS. For Test 1, Fig. C12 shows a comparison of the total heat flux predicted by FDS with measurements at WS4 on the aerated concrete block. The uncertainty of FDS for total heat flux at WS4 at ~ 40 kW/m² is + 48 %. Fig. C13 shows a comparison of the total heat flux predicted by FDS with measurements at WS3 on the concrete block. The FDS prediction is similar to that measured with an uncertainty of + 14 %. Fig. C14 shows a comparison of the total heat flux predicted by FDS with measurements at WS2 on the

steel plate. The uncertainty in the FDS prediction is + 59 %. Fig. C19 shows a comparison of the heat flux on the wall predicted by FDS with experiment. FDS under-predicts the heat flux by – 45 %. The experimental values of the heat flux at WS1 and WS3 which are in comparable locations are similar. Although the FDS prediction for heat flux at WS3 was similar to experiment, it under-predicts the flux at WS1.

For Test 3, Fig. C33 shows a comparison of the total heat flux predicted by FDS with measurement at WS4 on the aerated concrete block. There is a large increase in heat flux at ~ 1155 s when the HRR reaches its peak at 6000 kW. The uncertainty of the FDS prediction at WS4 at ~ 71 kW/m² is – 53 %. Fig. C34 shows a comparison of the total heat flux predicted by FDS with measurement at WS3 on the concrete block. The uncertainty in the FDS prediction at 66 kW/m² is - 40 %. Fig. C35 shows a comparison of the total heat flux predicted by FDS with measurement at WS2 on the steel plate. The uncertainty in the FDS prediction at 46 kW/m² is – 23 %. Fig. C40 shows a comparison of the heat flux on the wall predicted by FDS with experiment. FDS under-predicts the heat flux by – 8 %.

Generally, the error of the heat flux predictions by FDS is large, up to 59 %. There are specific weaknesses in the heat flux models in FDS which make it unreliable for predicting heat fluxes to NPP targets.

C4.2.3 Plume Model in FDS

For Test 1, Fig. C6 shows an isosurface of the mixture fraction (at a value of 0.062) at 238 s which represents the flame sheet created by FDS at that point. Fig. C6 shows that FDS simulates the flame sheet to be significantly pushed toward the rear wall by the flow of ambient air into the compartment through the door. Fig. C7 shows a slice profile (at x = 1.8 m) of the gas temperature in the compartment. Fig. C7 again shows that FDS simulates that the plume is pushed significantly toward the rear wall.

Fig. C8 shows the comparison of measured plume temperatures at M2, M4, and M6 with that predicted by FDS. As shown in Fig. C8, FDS predicts peaks in the plume temperature at ~ 50 s. These peaks are explained by the plume development predicted by FDS. Observations of the plume predicted by FDS through Smokeview (the graphical interface for FDS) indicates a steady vertical plume until ~ 50 s when the plume is pushed to the rear wall by flow into the compartment through the door. This causes

peaks in the thermocouples, M2, M4, and M6 which are located directly above the fuel pan. The experimental measurements do not indicate this extensive movement of the fire plume. Fig. 3-2 of the Panel Report shows a photograph of the fire and plume at steady state conditions in Test 1. The figure shows some degree of plume tilt in the experiment, but not to the extent predicted by FDS. The measured data shows the plume to be fully developed at ~105 s after which the plume temperatures increase to ~ 1000 °C without any intermediate peaks. The experimental data shows oscillations in the plume temperature, especially near the fire at M2, indicating oscillation of the fire plume to and from the rear wall. FDS predicts the peaks of the plume temperatures to be ~ 800 °C. As shown in Table C4, the uncertainty in the predicted values are – 27 %, - 16 %, and – 25 % for M2, M4, and M6, respectively.

Fig. C9 shows the local gas temperatures in the compartment at Level 1 for M7, M8, M9, and M10. The measured temperatures show a rapid increase in temperature followed by a more gradual increase until the end of the transient. The temperature measured at M10 is much higher than that measured at M7, M8, and M9. This is due to the tilting of the fire plume toward M10. FDS also shows a rapid increase in temperature followed by large oscillations and unexpected trends. These oscillations may be caused by oscillations in the flow through the door predicted by FDS. The temperature predicted at M8 by FDS is highest since the code predicts the fire plume to be pushed more toward the rear wall, as discussed above. The experimental data shows some oscillations in the temperature at M10 indicating the movement of the plume in and out of that region. Although the peak values predicted by FDS are similar to that measured for M7, M8, and M9, there is an uncertainty of -43 % for M10 due to the discrepancy in the degree of plume tilt predicted.

Similar observations were made for the results of Test 3 and are discussed in section 3.2.2 in Chapter C3. FDS computations of the plume predict a larger tilt due to flow conditions, whereas, the plumes in the experiments are observed to be stiffer and influenced less by flow conditions. This limits the reliability and accuracy of using FDS to evaluate targets near the plume.

C4.2.4 Target Models in CFAST and FDS

A detailed heat transfer model for the barrel used in the experiments will be fairly complex. The CFAST and FDS fire models are not capable of modeling complex configura-

tions such as the barrel for storing radioactive waste. The cylindrical geometry and multi-material composition poses challenges for modeling. Similar limitations of CFAST and FDS for modeling cable targets were noted in ICFMP Benchmark Exercise No. 1 /DEY 92/.

The limitations and large uncertainties for predicting the temperature of the material probes with CFAST was discussed above. Although the predictions of heat fluxes by FDS have large uncertainties (up to 59 %), the temperature predictions for the material probes for Test 1 are fortuitously better, but larger for Test 3 (-33 %). The large uncertainties in the prediction of heat flux to the targets limit the reliability of using FDS or CFAST for predicting target temperatures. Lack of ability to model targets other than rectangular slabs, e.g. radioactive waste barrels, limit the usefulness of the codes for NPP target analysis.

C4.2.5 Extinction Models in FDS and CFAST

The flow of ambient air through the door in Test 1 provided the fire with full ventilation throughout the transient. The CFAST code was not even capable of modeling Test 3, therefore, it's the limitation of the code for predicting the under-ventilation of the fire in Test 3 is not discussed.

Fig. C27 shows a slice profile (at $x = 1.8$ m, $t = 101.5$ s) of the gas temperature in the compartment. Fig. C28 shows a slice profile (at $x = 1.8$ m, $t = 102$ s) of the gas temperature in the compartment. Observations of this temperature slice file in Smokeview shows that FDS simulates the flow through the door to pulsate with a period of ~ 2 s. Fig. C27 shows the flow through the door to be bidirectional, whereas Fig. C28 shows the end of the cycle of the pulsation when the flow is unidirectional through the door flowing out of the compartment. This pulsating behavior was noted during the experiments and is mentioned in the main report on Benchmark Exercise No. 4. The pulsating flow through the door provides sufficient oxygen to the fire and prevents it from being under-ventilated. Although fluid dynamics of the scenario is simulated well by FDS, the simple extinction model in FDS (LOL) decreases the heat output from the fire when combustion is fully sustained. The discrepancy in the HRR from FDS and measured is shown in Fig. C21. The algorithm in FDS for accounting for the under-ventilation of the fire is too simplistic for complex scenarios as in this Benchmark Exercise.

C4.2.6 Modeling of Multi-Layer Boundaries with CFAST and FDS

The CFAST and FDS codes do not have the capability to model multi-layer boundaries, therefore, a single-layer assumption had to be adopted to model the aerated concrete around the fuel pan and the concrete floor below. The layer of insulation covering the walls and ceiling was neglected in the calculations since it could not be directly modeled in CFAST or FDS. Further, the multi-layer composition of the target barrel could not be modeled, although the modeling of the cylindrical geometry is a more fundamental limitation. The use of these codes for complex target geometries and composition is very limited.

C4.3 User Interface

FDS

The FDS manuals (Technical Reference Guide and User's Guide), in conjunction with the Smokeview graphical interface for reviewing results of the computations, provide a useful interface for the user. The quality of this interface has positively impacted the capability to analyze and interpret the predicted results.

CFAST

Although the Technical Reference Guide for CFAST is detailed, its relationship to the User's Guide, and a useful and comprehensive User's Guide is lacking. Additionally, the graphical user interface (GUI) for CFAST is outdated and does not function in more recent operating platforms such as Windows XP. It would be beneficial to have a comprehensive User's Guide and enhanced GUI to allow more accurate input of data for the simulations and understanding of output parameters such as their units. The GUI and User's Guide for CFAST has now been updated (see /JON 05/) based on the comments derived from this study.

The users of these codes should be knowledgeable of the complexities of the compartment conditions, such as plume movement, to assess and utilize the results of their calculations.

C4.4 Benefits of Hand Calculations

In order to evaluate the benefits of hand calculations, Specified Calculations with FDTs /NRC 04/ were conducted and submitted to GRS. GRS has certified the authenticity of these Specified Calculations. The results of the calculations are compared with experimental data for Test 1 and shown in Table C6 below. The comparisons show that hand calculations could provide a method to quickly calculate global parameters (HGL temperature and interface height), as well as plume temperatures using simple correlations. Some large deviations for heat fluxes (-66 %) and plume temperature at M6 (-66 %) are noted. The heat flux correlations used may not have had a large fire, such as the one in Test 1, included in the development of the correlation. Also, the plume correlation is for erect plumes and not when the fire plume is tilted, as is evident from the uncertainty at M6. Since the range of validity of the correlations is narrow, the results are best suited for a screening calculation where a rough estimate is required, while acknowledging the answers may contain large inaccuracies.

C4.5 Need for Model Improvements

CFAST

The CFAST model requires major fundamental improvements if it is to be used for fire scenarios with intense fire sources such as those examined in this Benchmark Exercise. The computation of thermal propagation through materials with low density and conductivity should be reviewed to determine if this limitation can be solved and eliminated. Further, an examination should be conducted to determine whether the computational limitation for simulating Test 3 is inherent in the code, or whether it can be addressed with improvements to the numerics in the code.

FDS

Although relatively good general performance is noted above, the heat flux models (for radiation and convection) in FDS require improvement before they can be reliably used for NPP applications. The target model also requires improvement to analyze NPP targets. The code should also be improved to accurately simulate plume behavior and tilting due to varying flow conditions in the compartment. For Test 3, the HRR used by FDS was less than input for the simulation due to algorithms in FDS to account for un-

der-ventilated conditions. These algorithms should be corrected to maintain the HRRs prescribed by the user to improve the performance and accuracy of the model. The basic extinction phenomena require a more fundamental treatment in FDS to be able to predict under-ventilated conditions. Finally, the ability to simulate multi-layer boundaries and targets needs to be implemented in FDS for NPP applications.

The prediction of burning rate is an important area of research that is being conducted at NIST. This research was investigated by NIST through exercising FDS for specified calculations for this Benchmark Exercise (see Appendix A). The investigation concluded that the prediction of burning rate was challenging. The analyst was required to supplement the given fuel properties with values from the literature which results in large uncertainties in the simulation. Given the uncertainties, the results should only be used to assess the qualitative behavior of the phenomena. More research and validation work is needed before the model can be used to reliably predict burning rate of liquid fuels, especially in under-ventilated compartments. Validation work should focus on the fire and the fuel bed. FDS requires improvements in the near field. In addition to the measurement of burning rate, measurements are needed to measure the heat flux and temperature at the fuel surface, and the thermal and chemical environment of the fire itself. Boundary and geometrical effects should be minimized by using solid homogeneous slabs or liquid pools.

C4.6 Need for Advanced Models

As discussed above, zone models are limited for simulating the severe thermal environments in the test scenarios of this Benchmark Exercise. CFD codes, such as FDS, inherently include more physics of the phenomena in the compartment that allow them to be less limited and more accurate in simulating parameters of interest for NPP applications of such scenarios.

The computational requirements for CFD codes should be noted. The tests in this Benchmark Exercise required 70 to 160 hours to compute with FDS, whereas, zone models can be executed in less than 10 s.

C4.7 Need for Additional Test Programs

The two test scenarios for Benchmark Exercise No. 4 provide a useful and complete data set for assessing the capabilities of fire models for extreme compartment fire conditions for NPP applications. Other tests were conducted in the series which could also be used for further evaluations. It may be useful to use data from these other tests to evaluate performance of the codes for predicting CO and CO₂ concentrations as these data were not available for Tests 1 and 3.

These tests provide fire scenarios with intense fire sources in a compartment. It will be beneficial to conduct tests that provide a range of fire intensities so that one can determine the limits of zone models over which their theoretical formulations remain valid.

C5 Acknowledgments

The author wishes to acknowledge the efforts of GRS and IBMB for developing the specification of this exercise for the International Collaborative Fire Model Project. It is recognized that development of such a specification and experimental data requires considerable resources from these organizations. Specifically, the efforts of Walter Klein-Hessling and Marina Roewekamp at GRS, and Reinhold Dobbernack and Olaf Riese at iBMB are greatly acknowledged and appreciated. Also, the author thanks the many participants of the International Collaborative Project and this Benchmark Exercise for their comments on the analysis reported herein, and the useful discussions on the complex fire scenarios analyzed in this exercise.

C6 **References**

- /AST 04/ American Society of Testing and Materials:
Evaluating the Predictive Capability of Deterministic Fire Models, ASTM E1355-04, West Conshohocken, PA, 2004
- /DEY 02/ Dey, M., Ed.:
Evaluation of Fire Models for Nuclear Power Plant Applications, U.S. Nuclear Regulatory Commission, NUREG-1758, Washington DC, USA, June 2002
- /JON 04/ Jones, W., Ed.:
CFAST - Consolidated Model of Fire Growth and Smoke Transport (Version 5), National Institute of Standards and Technology, NIST Special Publication 1030, October 2004
- /JON 05/ Jones, W., Ed.: CFAST - Consolidated Model of Fire Growth and Smoke Transport (Version 6) – User's Guide, National Institute of Standards and Technology, NIST Special Publication 1041, December 2005
- /MCG 04/ McGrattan, K., Ed.,:
Fire Dynamics Simulator (Version 4), Technical Reference Guide, National Institute of Standards and Technology, NIST Special Publication 1018, September 2004
- /MIL 04/ Miles, S. Ed.:
Evaluation of Fire Models for Nuclear Power Plant Applications: Pool Fires In Large Halls," Building Research Establishment, BRE Report No. 212214, Watford, UK, May 2004,
- /NRC 04/ U. S. Nuclear Regulatory Commission:
Fire Dynamics Tools (FDTs) Quantitative Fire Hazard Analysis Methods for the U.S. Nuclear Regulatory Commission Fire Protection Inspection Program, NUREG-1805, Washington DC, USA, November 2004

/SFP 95/ Society of Fire Protection Engineers:
The SFPE Handbook of Fire Protection Engineering, 2nd Edition, Bethesda,
Maryland, 1995

Table C4 Summary of Predictions with CFAST and FDS for Test 1 *Specified Predictions*

Parameter	Sensor	Model prediction at peak		Measured value at peak	Initial measured value	Uncertainty	
		CFAST	FDS			CFAST	FDS
Global Parameters							
HGL Interface Ht		0.7 m	0.7 m	1.5 m	5.7 m	- 19 %	- 19 %
HGL Temperature (Average)		857 °C	600 °C	719 °C	19 °C	+ 20 %	-1 7 %
O ₂ Concentration	GA1 O2					NA	NA
Smoke Concentration						NA	NA
CO Concentration						NA	NA
Pressure						NA	NA
Flame Height						NA	NA
Local Gas Temperatures							
Plume Temperature	M 2		768 °C	1036 °C	19 °C		- 27 %
	M 4		824 °C	971 °C	19 °C		- 16 %
	M 6		786 °C	1040 °C	19 °C		- 25 %
Hot Gas Temperature (Point Values)	M 10		464 °C	800 °C	19 °C		- 43 %
	M 14		660 °C	753 °C	19 °C		- 13 %
	M 18		684 °C	722 °C	19 °C		- 5 %
Ceiling Jet Temperature	M 18		684 °C	722 °C	19 °C		- 5 %

Target Heat Flux and Temperature							
Radiative Heat Flux to Cables						NA	NA
Total Heat Flux to Cables						NA	NA
Cable Surface Temperature						NA	NA
Total Heat Flux to Plates/Blocks	WS 2	85 kW/m ²	43 kW/m ²	27 kW/m ²	0	+ 215 %	+ 59 %
	WS 3	86 kW/m ²	40 kW/m ²	35 kW/m ²	0	+ 146 %	+ 14 %
	WS 4	NA	40 kW/m ²	27 kW/m ²	0	NA	+ 48 %
Plates/ Blocks Surface Temperature	M 29	NA	595 °C	504 °C	19 °C	NA	+ 19 %
	M 33	715 °C	409 °C	325 °C	19 °C	+ 128 %	+ 28 %
	M 34	770 °C	400 °C	375 °C	19 °C	+ 111 %	+ 7 %
Wall Flux and Temperature							
Total Heat Flux to Walls	WS 1		16.6 kW/m ²	30 kW/m ²	0	NA	- 45 %
Wall Surface Temperature	M 20		735 °C	589 °C	19 °C		- 26 %

Notes:

+ Model prediction was greater than measured value

- Model prediction was less than measured value

Value tabulated is: (model prediction at peak- measured value at peak)/(measured value at peak - initial measured value)

Table C5 Summary of Predictions with CFAST and FDS for Test 3 *Specified Predictions*

Parameter	Sensor	Model prediction at peak		Measured value at peak	Initial measured value	Uncertainty	
		CFAST	FDS			CFAST	FDS
Global Parameters							
HGL Interface Ht			0.6 m	1.6 m	5.7 m		- 24 %
HGL Temperature (Average)			662 °C	961 °C	19 °C		- 32 %
O ₂ Concentration	GA1 O2						- 25 %
Smoke Concentration							NA
CO Concentration							NA
Pressure							NA
Flame Height							NA
Local Gas Temperature							
Plume Temperature	M 2		774 °C	1036 °C	19 °C		- 26 %
	M 4		811 °C	971 °C	19 °C		- 17 %
	M 6		774 °C	1041 °C	19 °C		- 27 %
Hot Gas Temperature (Point Values)	M 10		628 °C	921 °C	19 °C		- 33 %
	M 14		692 °C	906 °C	19 °C		- 24 %
	M 18		707 °C	966 °C	19 °C		- 27 %
Ceiling Jet Temperature	M 18		715 °C	966 °C	19 °C		- 27 %

C - 37

Target Heat Flux and Temperature							
Cable Surface Temperature							NA
Radiative Heat Flux to Cables							NA
Total Heat Flux to Cables							NA
Total Heat Flux to Plates/Blocks	WS 2		46 kW/m ²	60 kW/m ²	0		- 23 %
	WS 3		66 kW/m ²	110 kW/m ²	0		- 40 %
	WS 4		71 kW/m ²	150 kW/m ²	0		- 53 %
Plates/Blocks Surface Temperature	M 29		712 °C	698 °C	19 °C		+ 2 %
	M 33		387 °C	565 °C	19 °C		- 33 %
	M 34		313 °C	460 °C	19 °C		- 33 %
Wall Heat Flux and Temperature							
Total Heat Flux to Walls	WS 1		92 kW/m ²	100 kW/m ²	0		- 8 %
Wall Surface Temperature	M 20		575 °C	852 °C	19 °C		- 34 %

Notes:

+ Model prediction was greater than measured value

- Model prediction was less than measured value
Value tabulated is: (model prediction at peak - measured value at peak)/(measured value at peak - initial measured value)

Table C6 Summary of Predictions with FDTs - Test 1 *Specified Predictions*

Parameter	Sensor	Model prediction at peak	Measured value at peak	Initial measured value	Uncertainty
Global Parameters					
HGL Interface Ht		0 m @ 60 s	1.5 m	5.7 m	-36 %
HGL Temp. (Average)		719 °C @ 1200 s	719 °C	19 °C	+0 %
Local Gas Temperature					
Plume Temperature	M 2	out of range	1036 °C	19 °C	NA
	M 4	869	971 °C	19 °C	- 11 %
	M 6	347	1040 °C	19 °C	- 66 %
Target Heat Flux					
	WS 3	11.7 kW/m ² solid flame w/o wind	35 kW/m ²	0	- 66 %
		16.7 kW/m ² point source			- 53 %
	at barrel	45.8 kW/m ² solid flame with wind, v=2.5 m/s, angle =48°	no measurement available.		

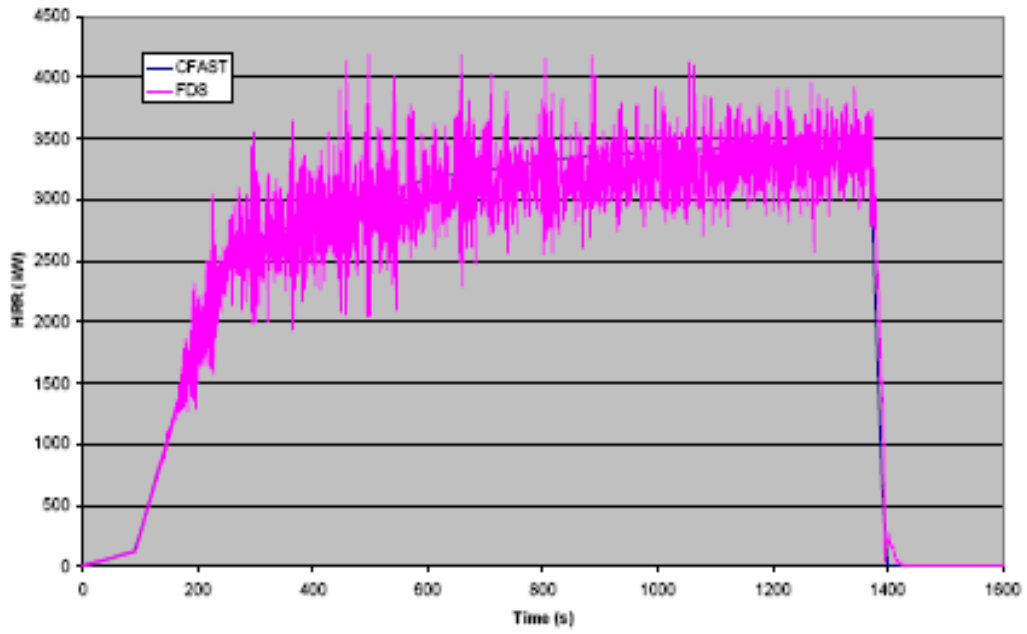


Fig. C2 Heat release rate - Test 1

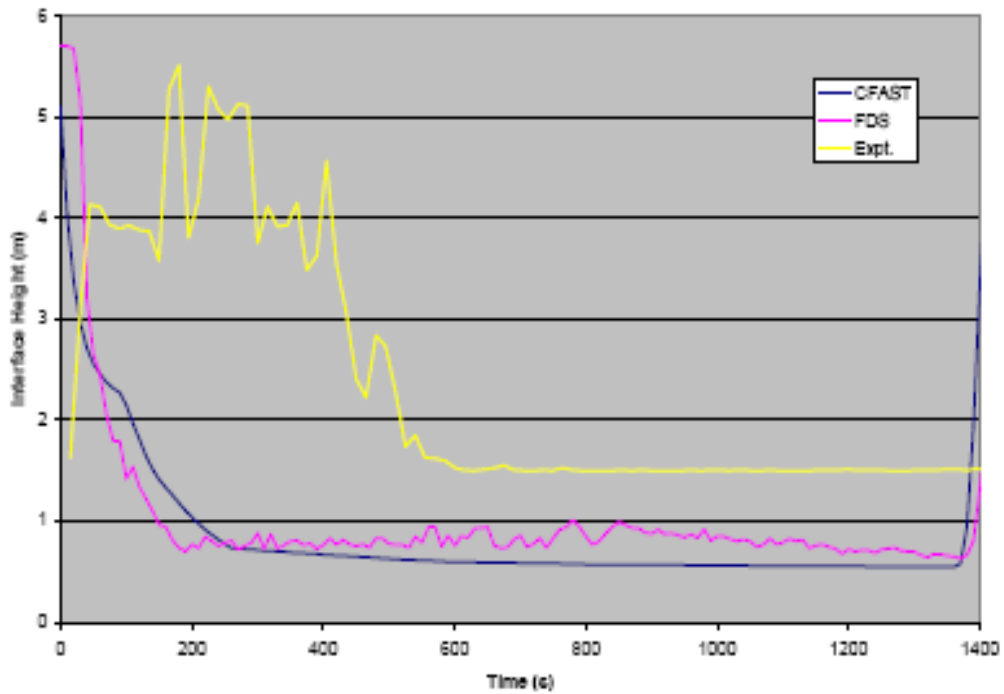


Fig. C3 HGL interface height - Test 1

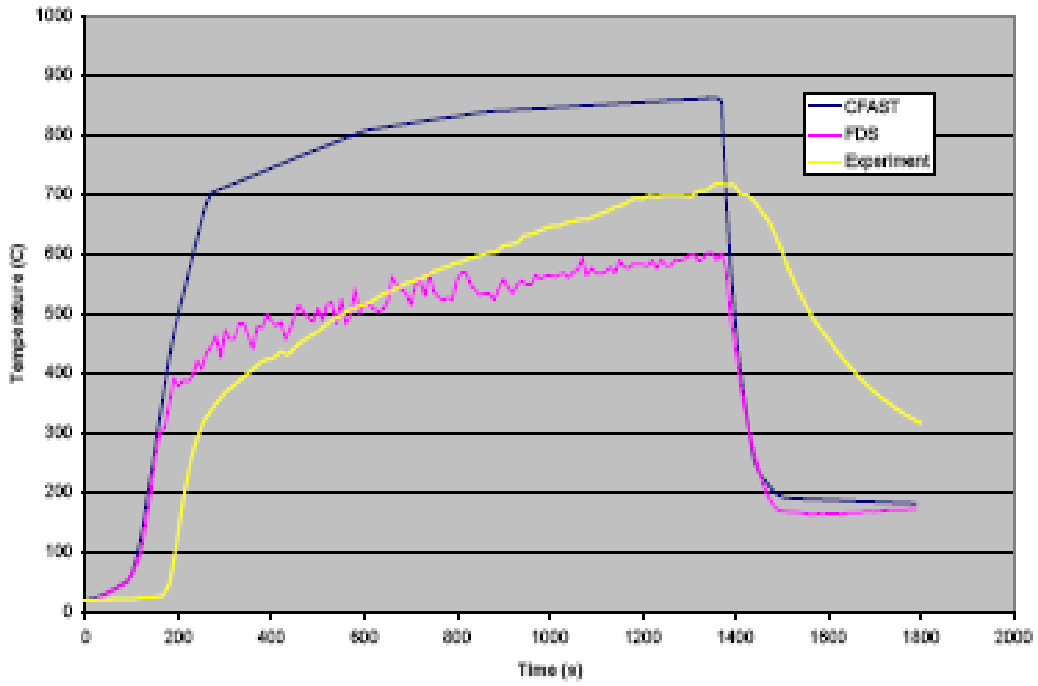


Fig. C4 HGL temperature - Test 1

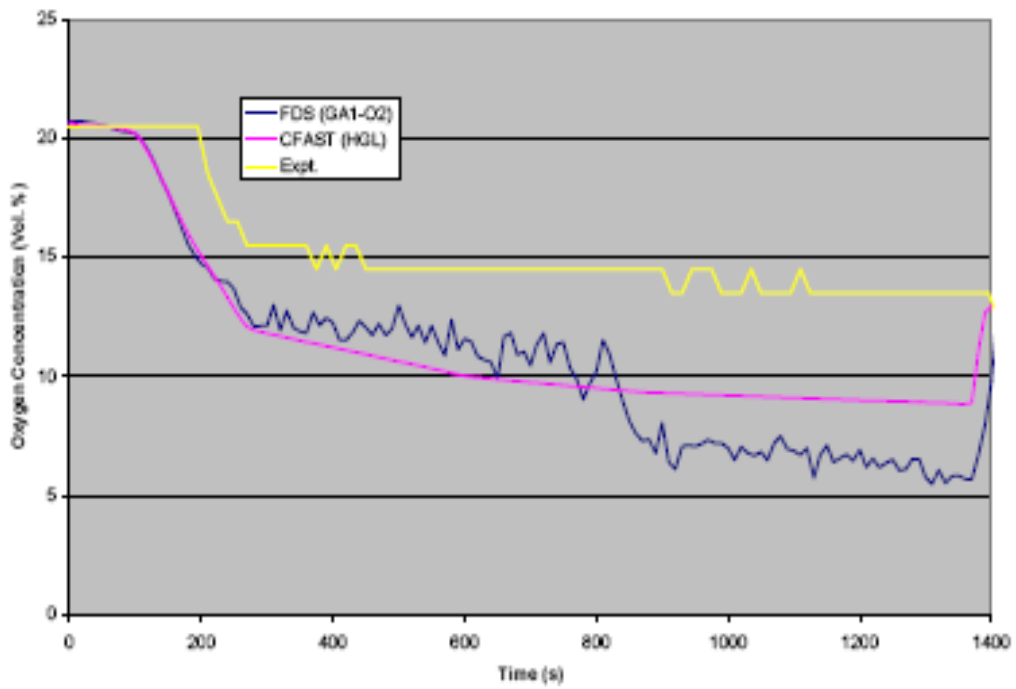


Fig. C5 Oxygen concentration

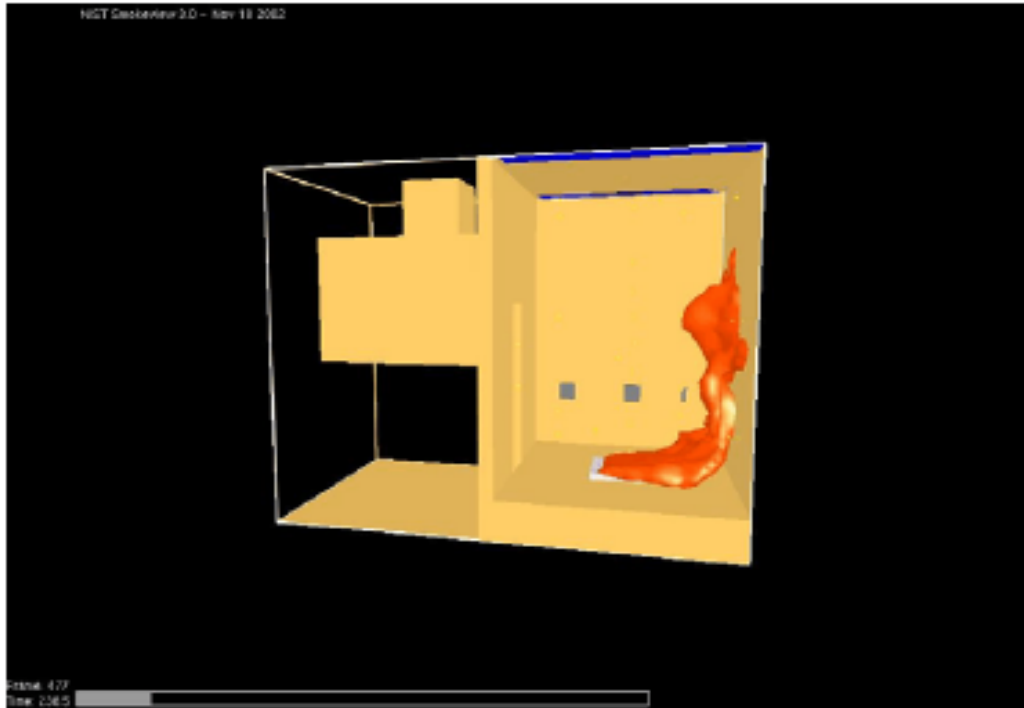


Fig. C6 View of flame sheet output from FDS - Test 1

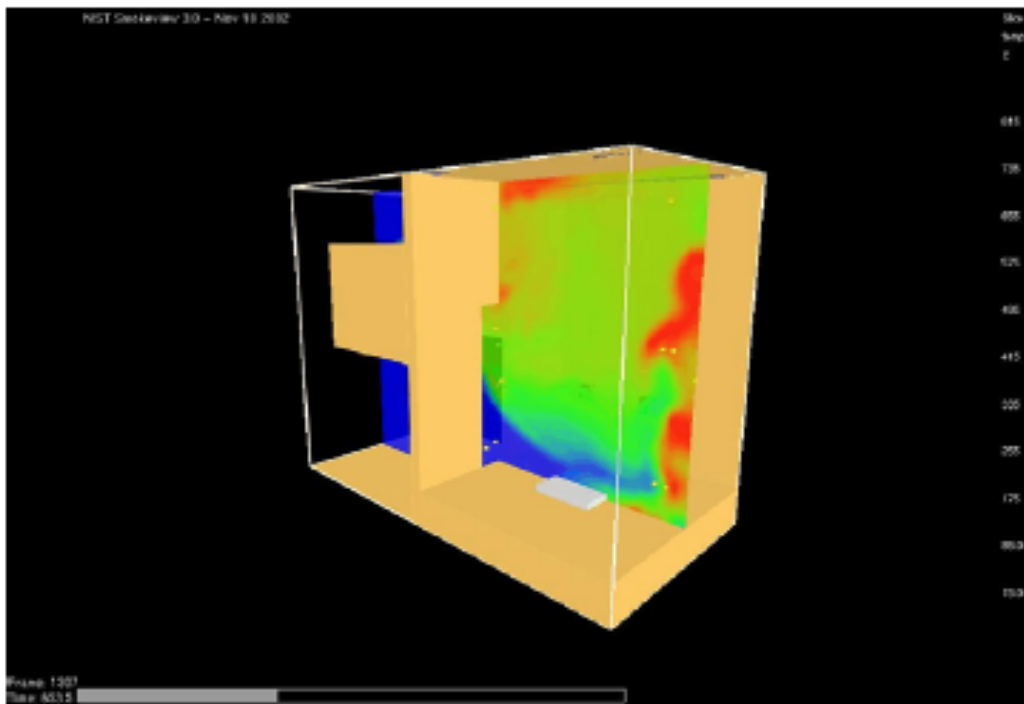


Fig. C7 View of temperature slice (x = 1.8 m) - Test 1

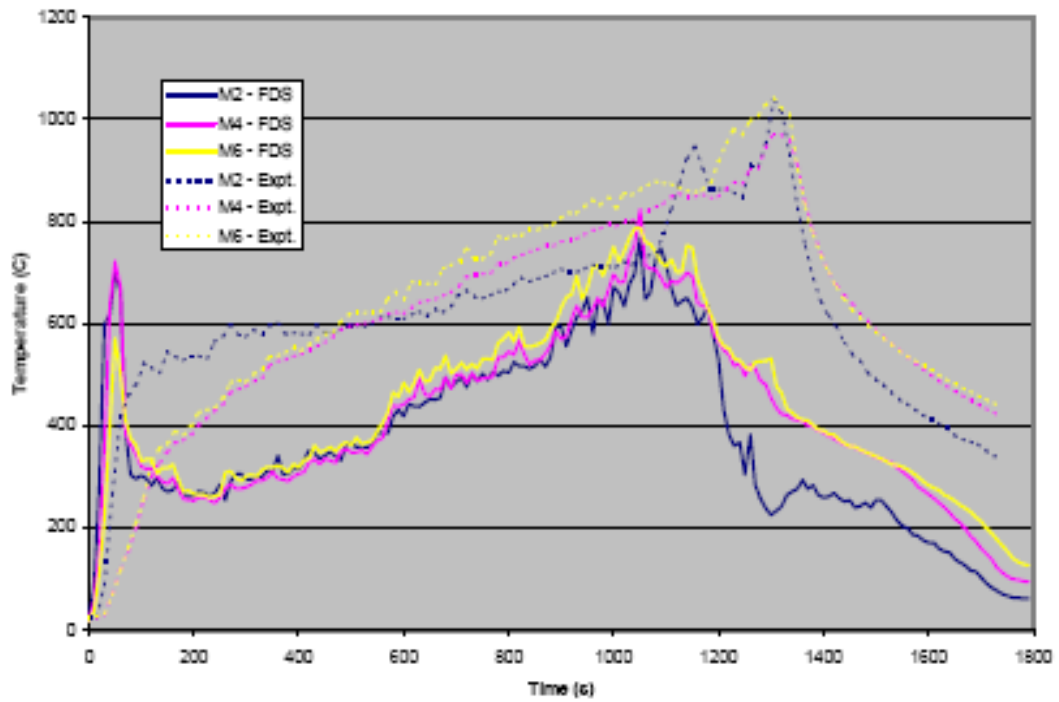


Fig. C8 Plume temperature - Test 1

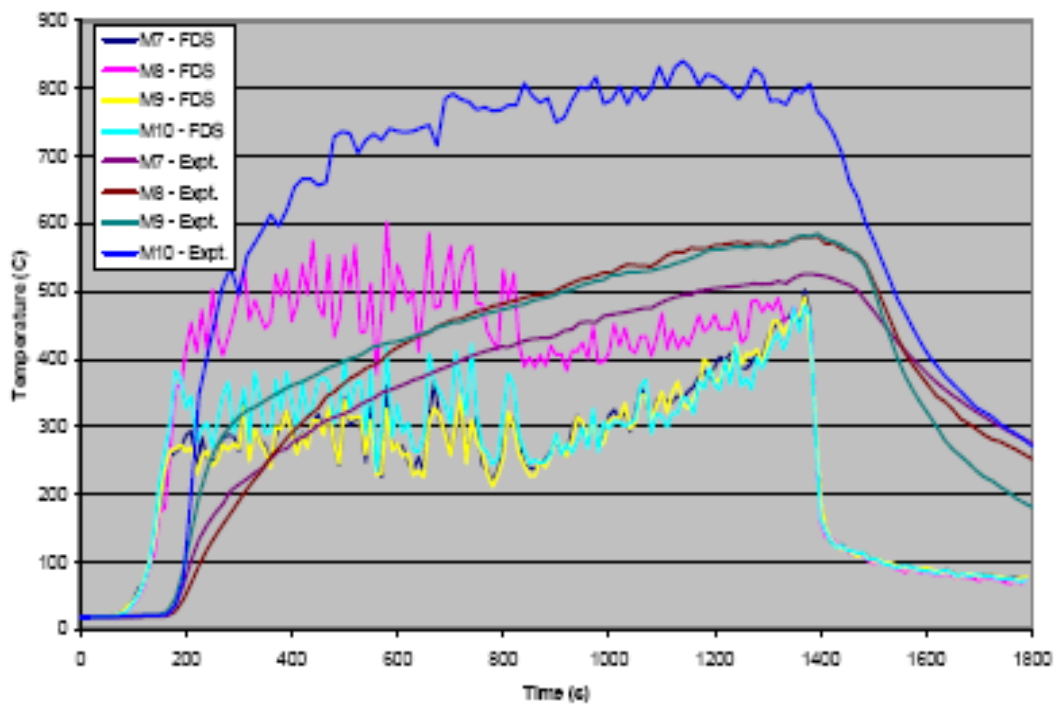


Fig. C9 Level 1 temperatures - Test 1

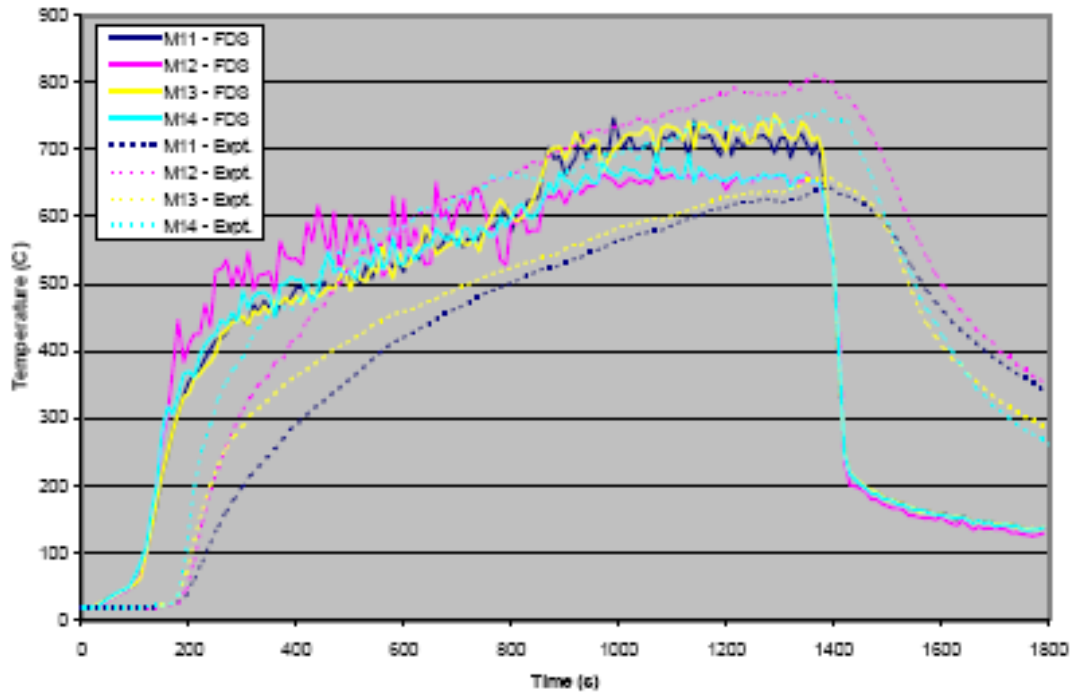


Fig. C10 Level 2 temperatures - Test 1

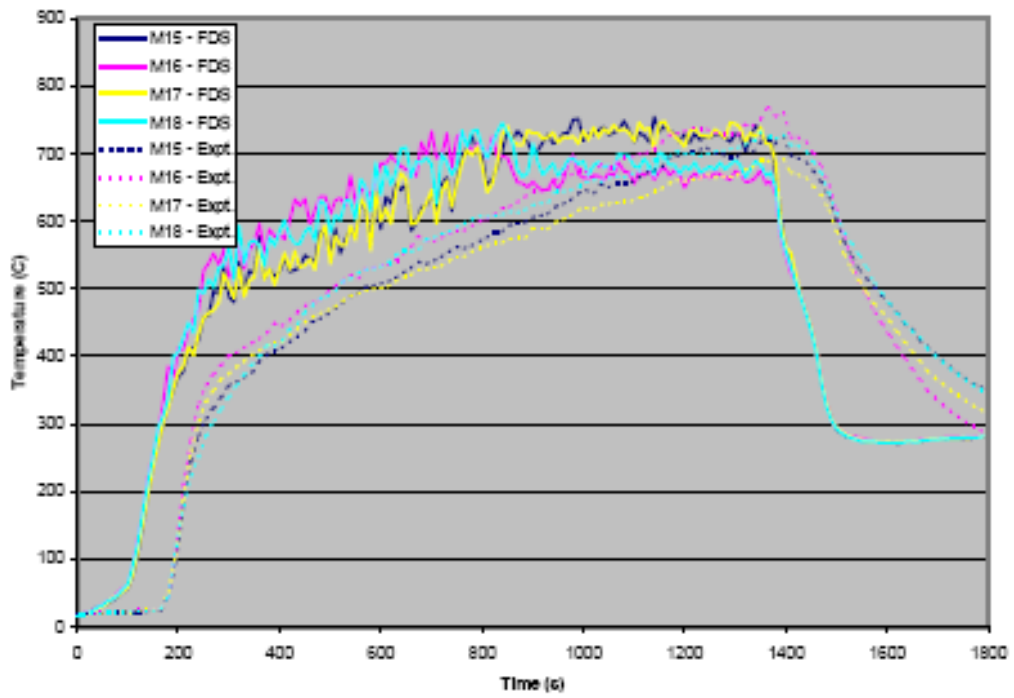


Fig. C11 Level 3 temperatures - Test 1

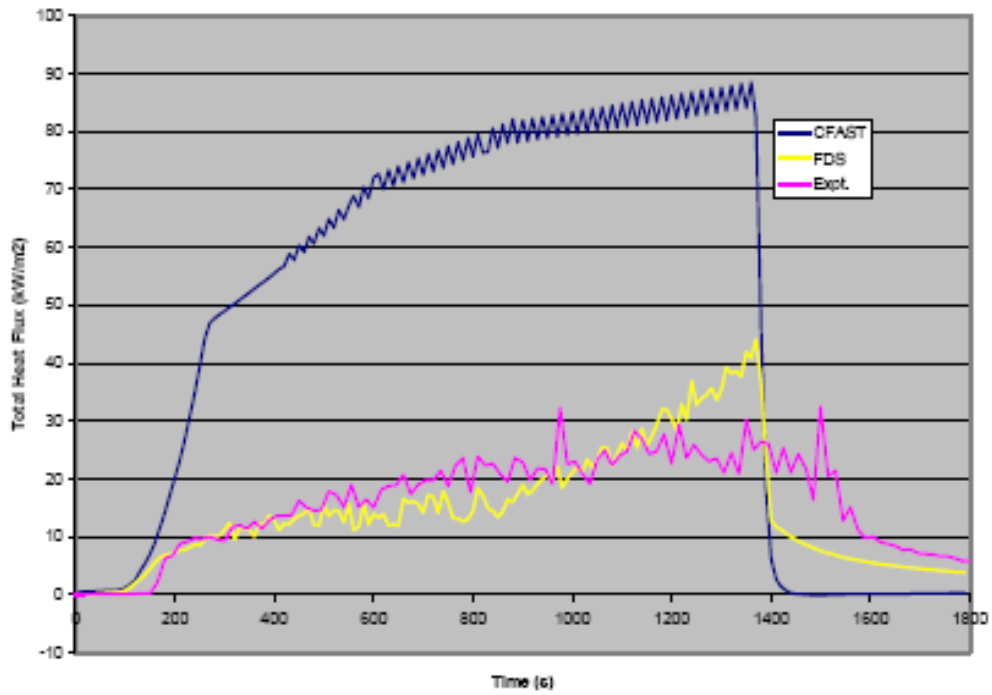


Fig. C12 Heat flux on aerated concrete block (WS4) - Test 1

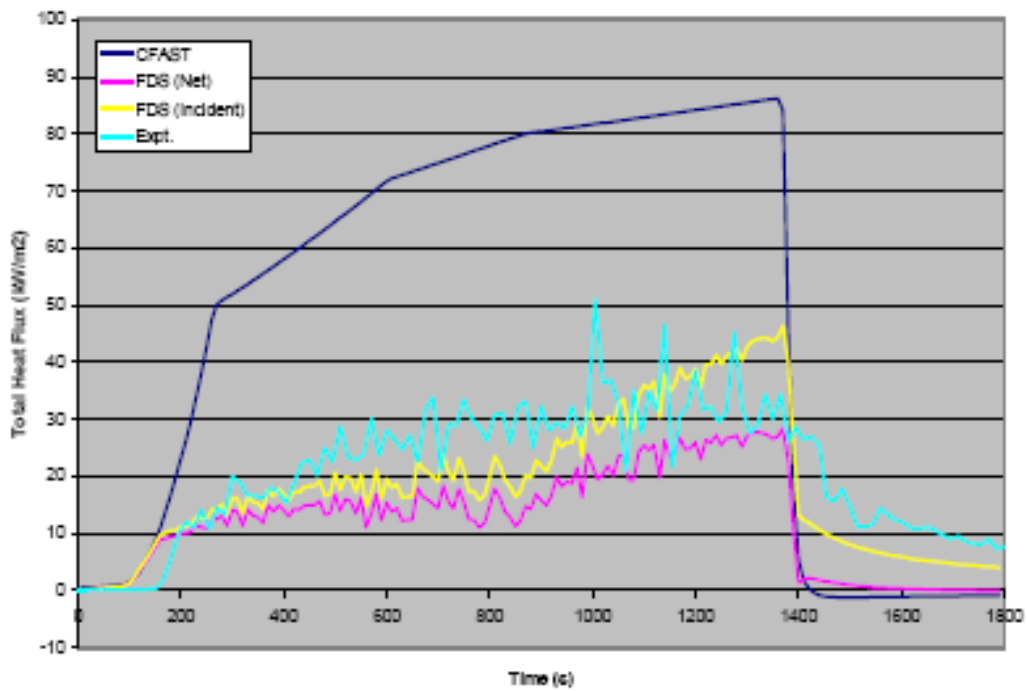


Fig. C13 Heat flux on concrete block (WS3) - Test 1

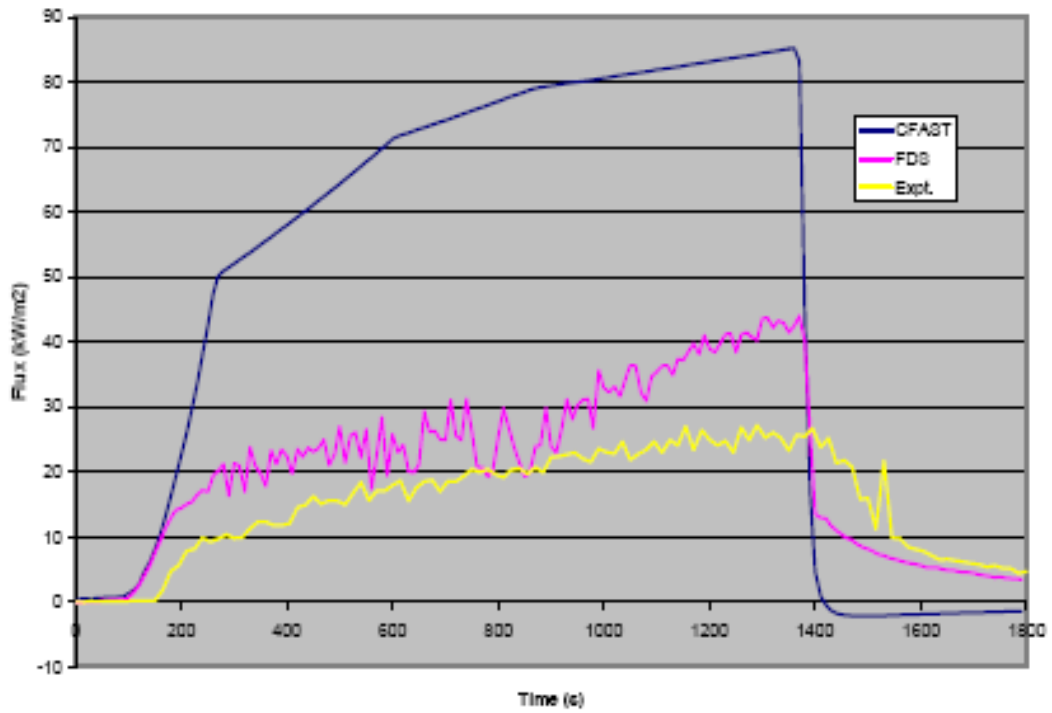


Fig. C14 Heat flux on steel plate (WS2) - Test 1

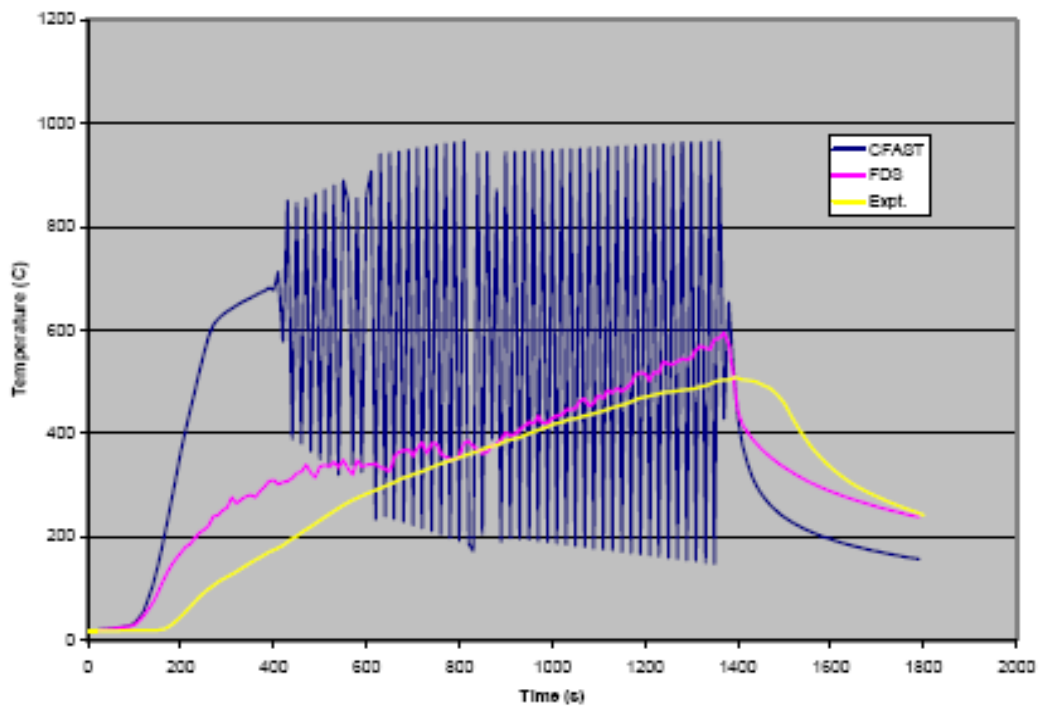


Fig. C15 Aerated concrete block temperature - Test 1

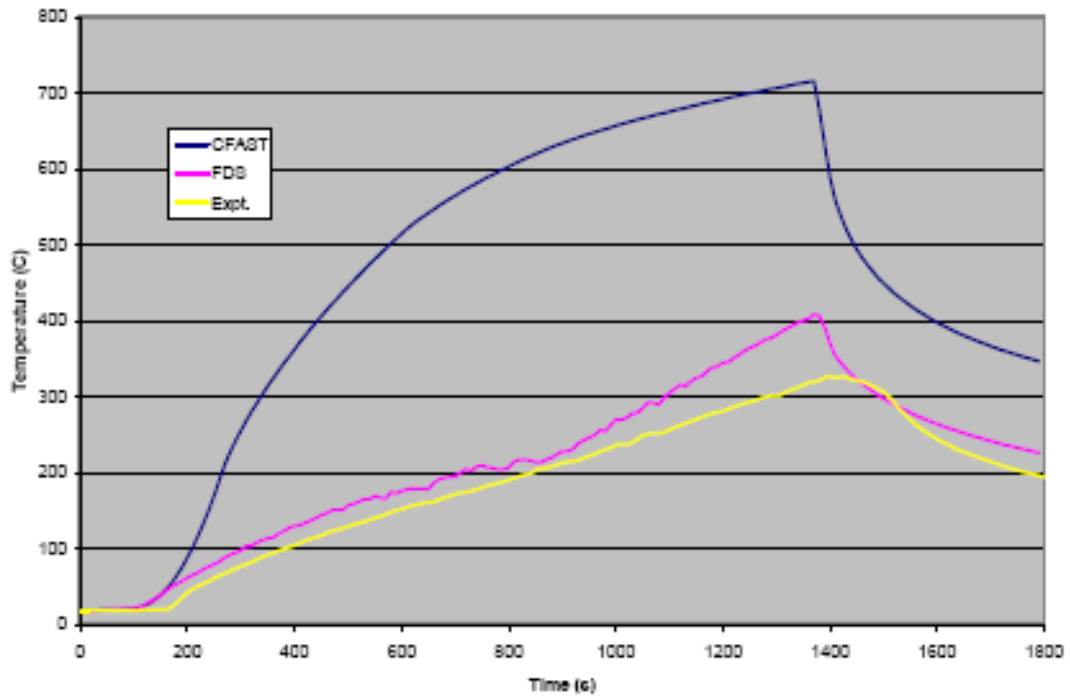


Fig. C16 Concrete block temperature - Test 1

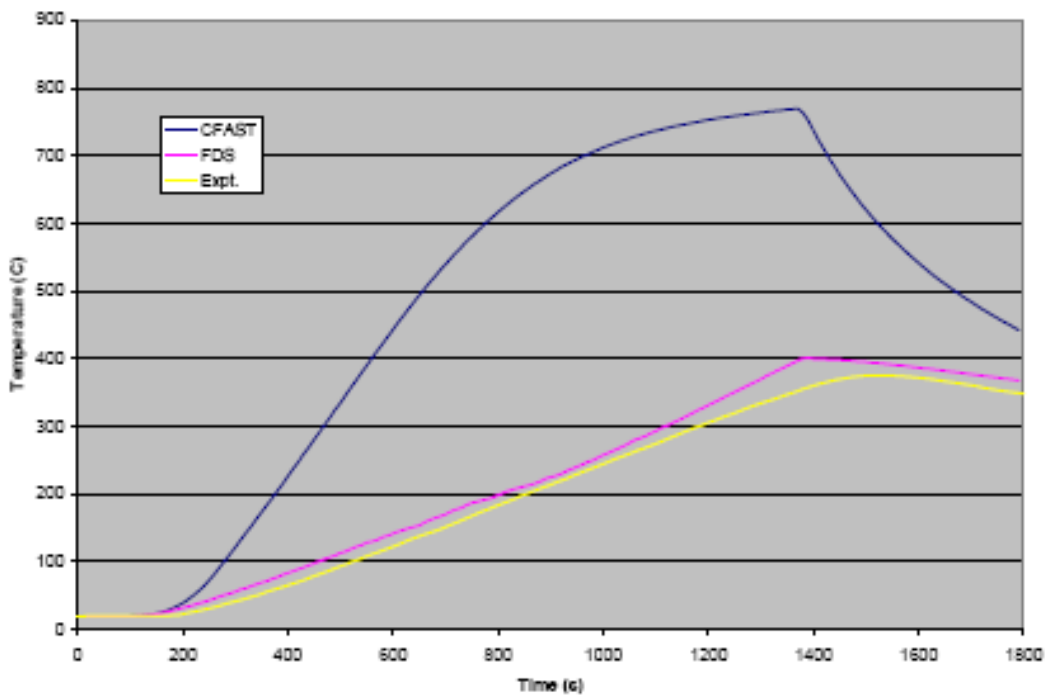


Fig. C17 Steel plate front surface temperature (M34) - Test 1

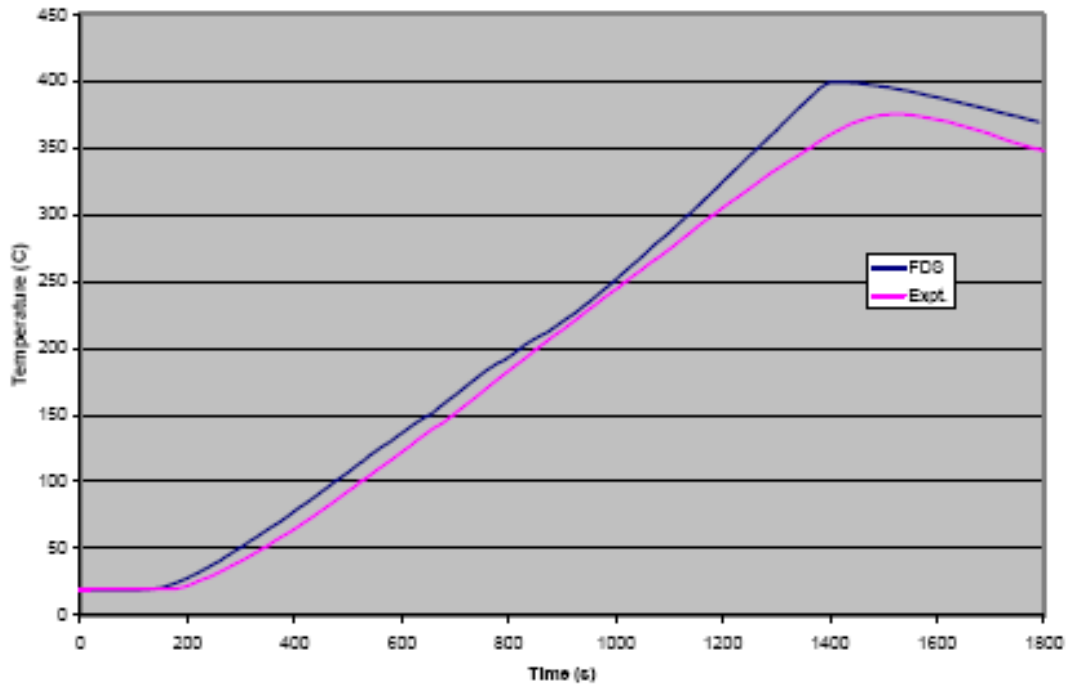


Fig. C18 Steel plate back surface temperature (M35) - Test 1

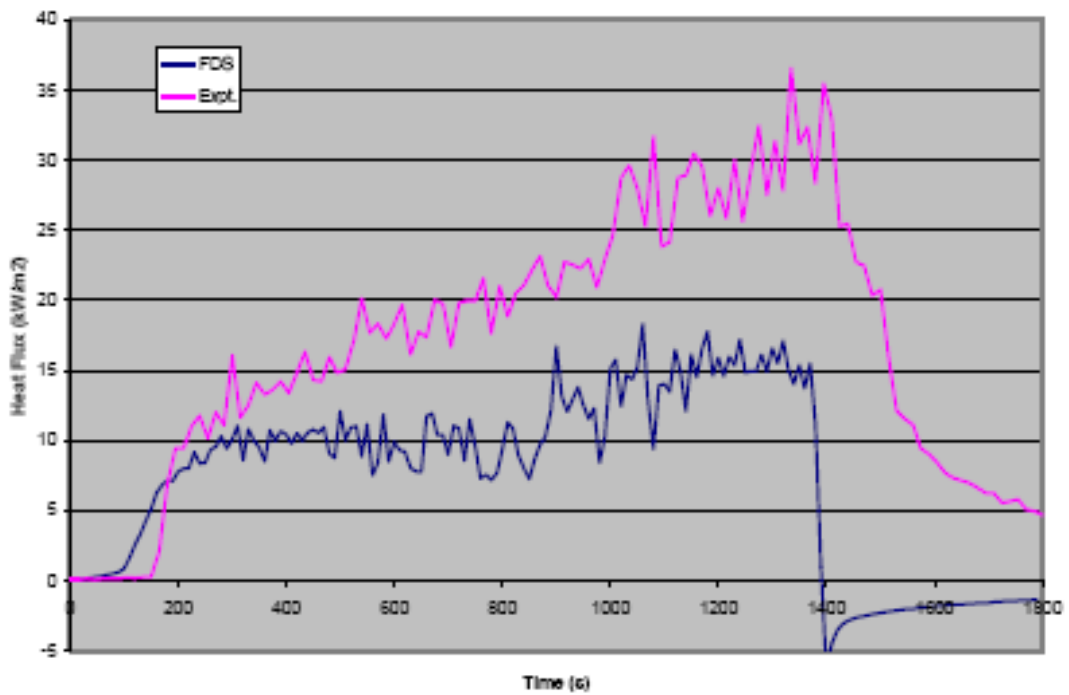


Fig. C19 Heat flux on wall (WS1) - Test 1

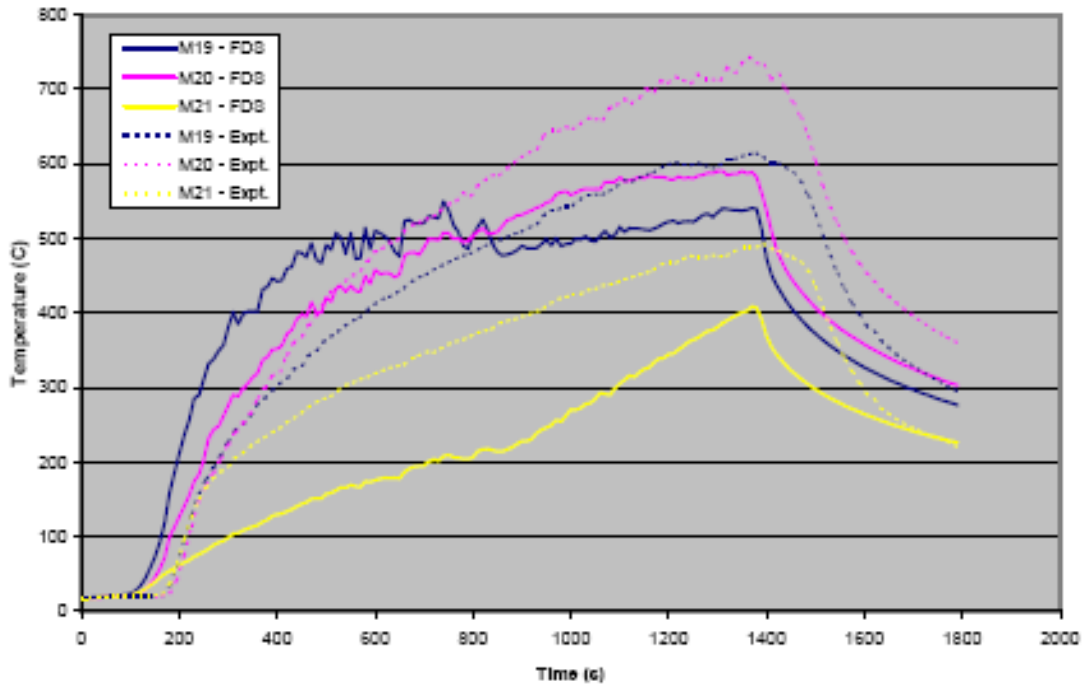


Fig. C20 Wall temperatures - Test 1

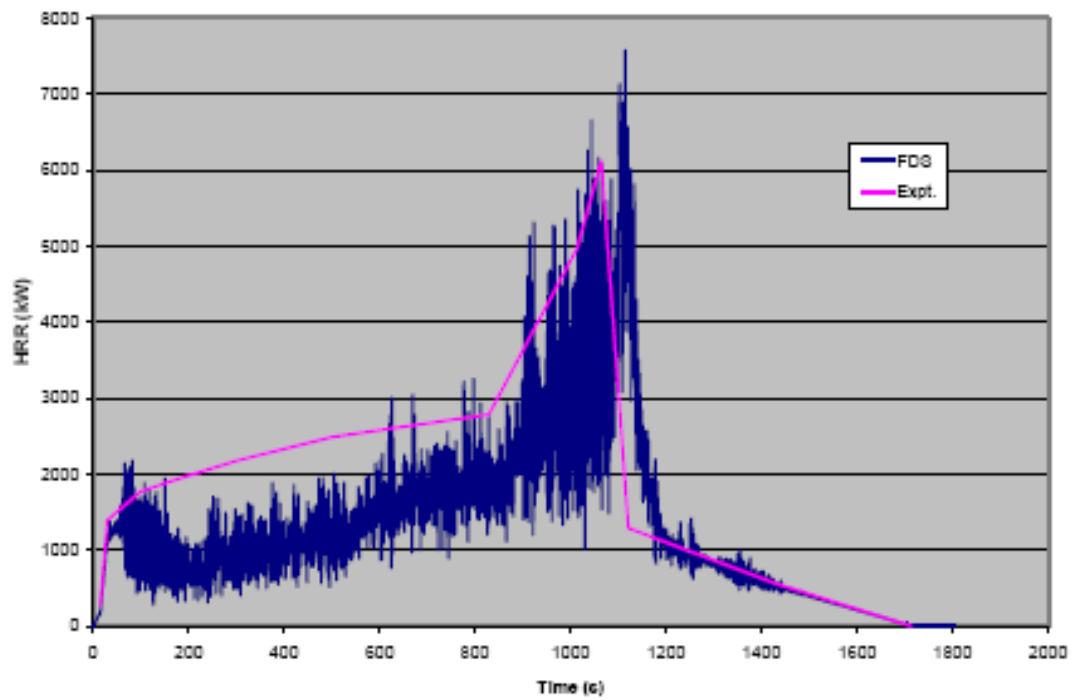


Fig. C21 Heat release rate - Test 3

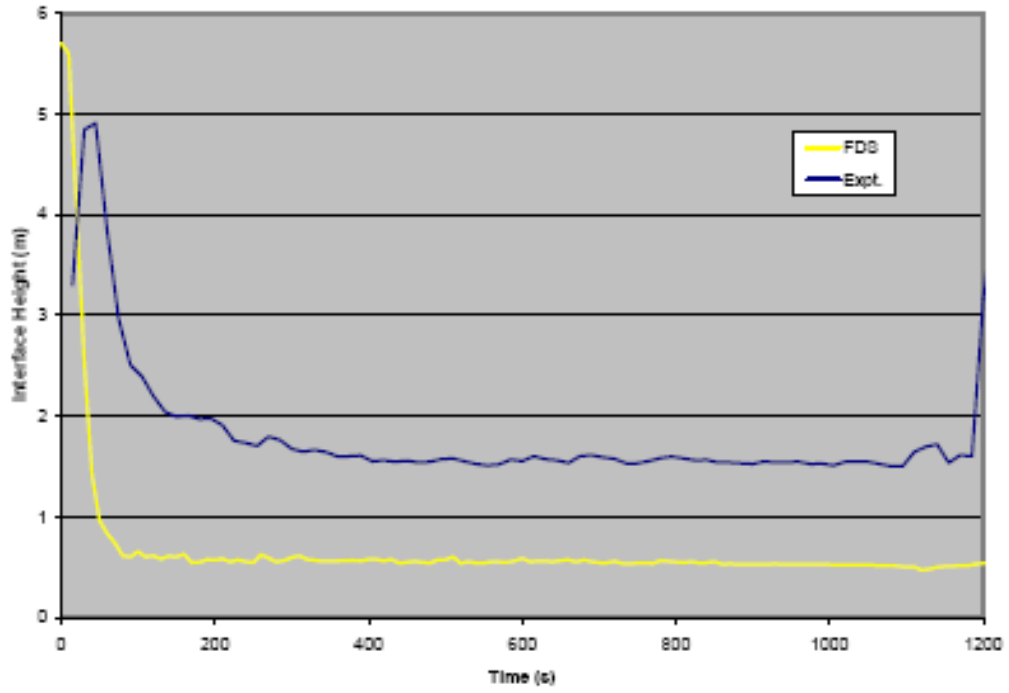


Fig. C22 HGL interface height - Test 3

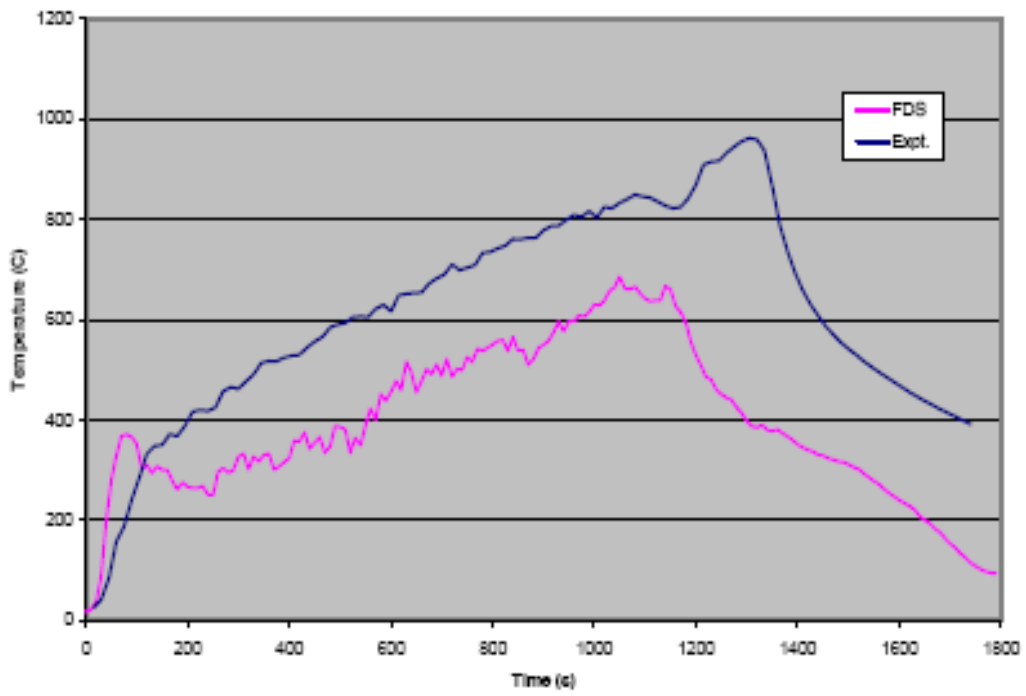


Fig. C23 HGL temperature - Test 3

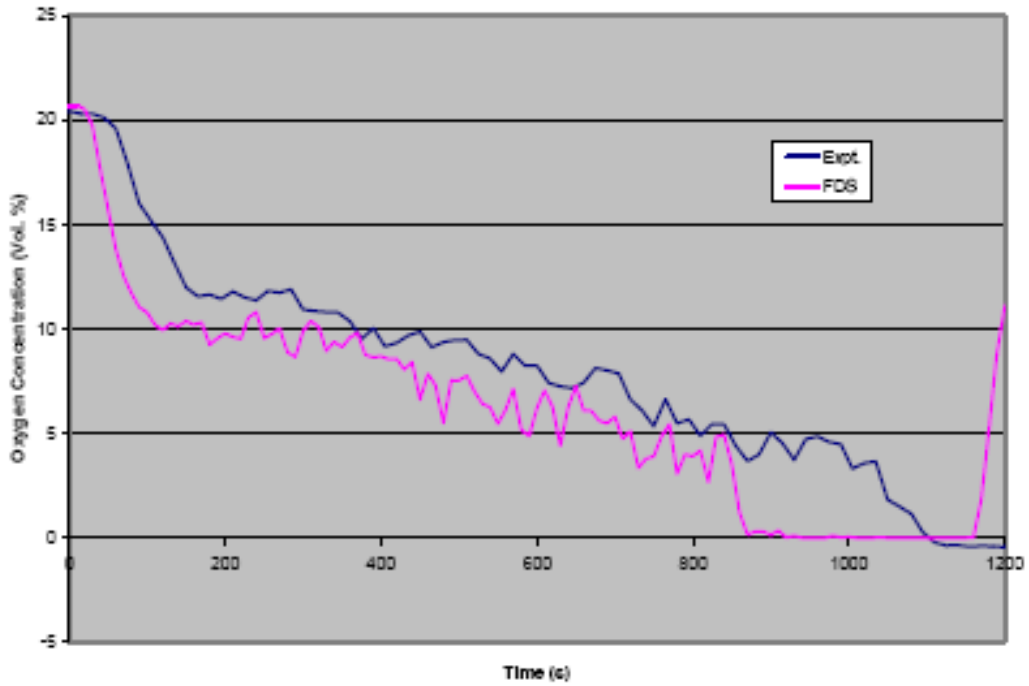


Fig. C24 Oxygen concentration - Test 3

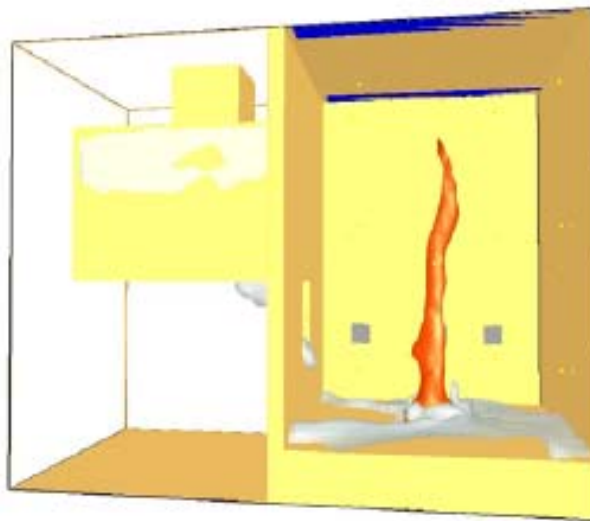
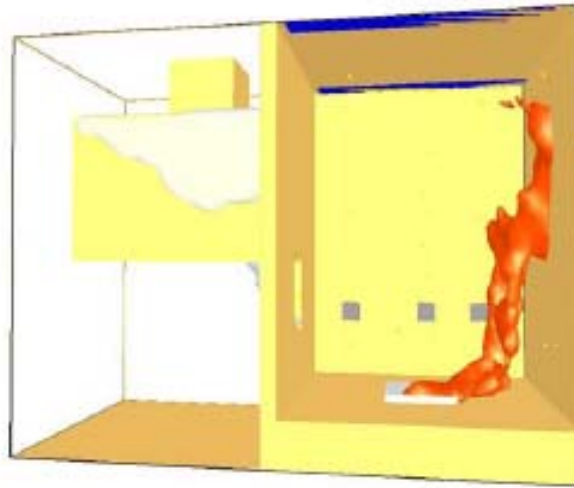


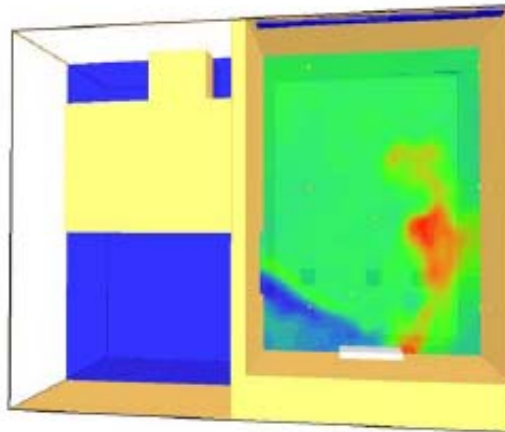
Fig. C25 View of flame sheet output from FDS (45 s) - Test 3



Time: 000
Time: 130.0

Fig. C26 View of flame sheet output from FDS (130 s) - Test 3

002300000001 - Apr 9 2002



Time: 000
Time: 101.5

Fig. C27 View of temperature slice ($x = 2.8$ m, $t = 101.5$ s) - Test 3



Fig. C28 View of temperature slice ($x = 2.8$ m, $t = 102$ s) - Test 3

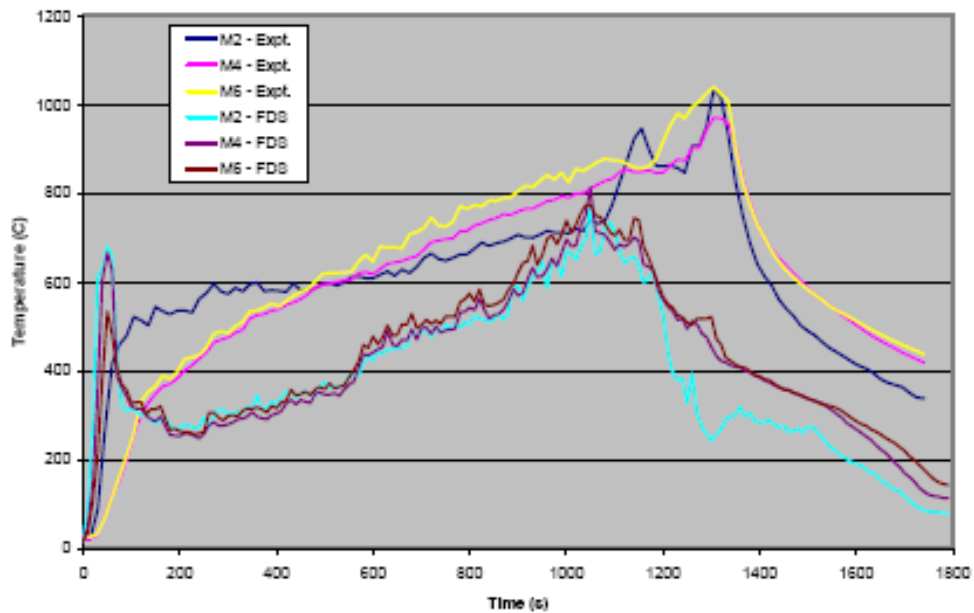


Fig. C29 Plume temperature - Test 3

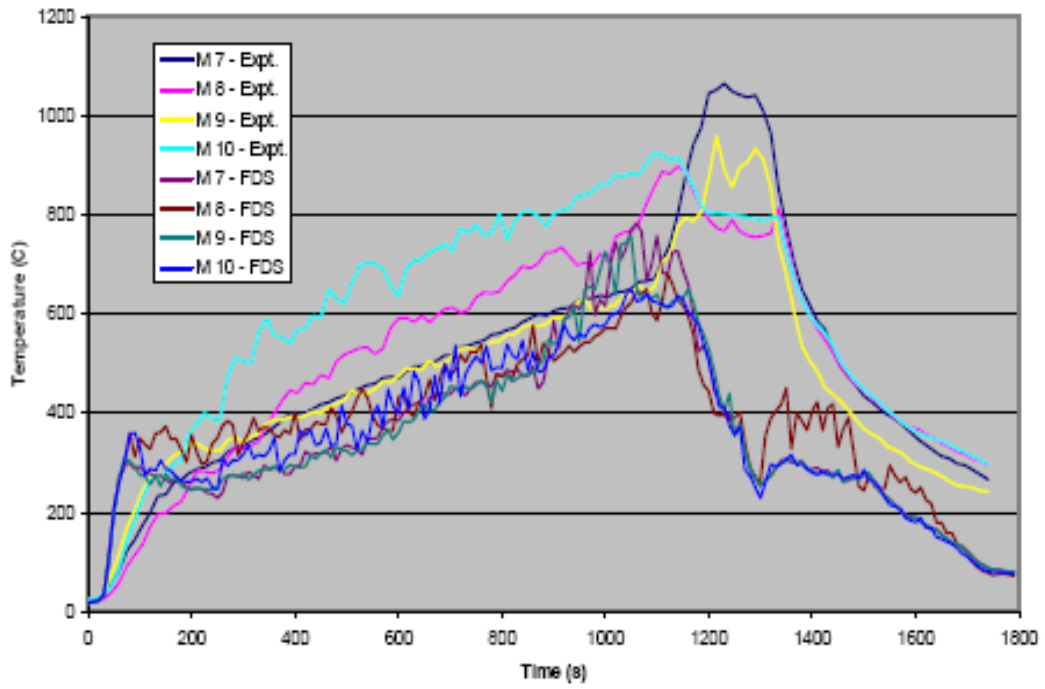


Fig. C30 Level 1 temperature - Test 3

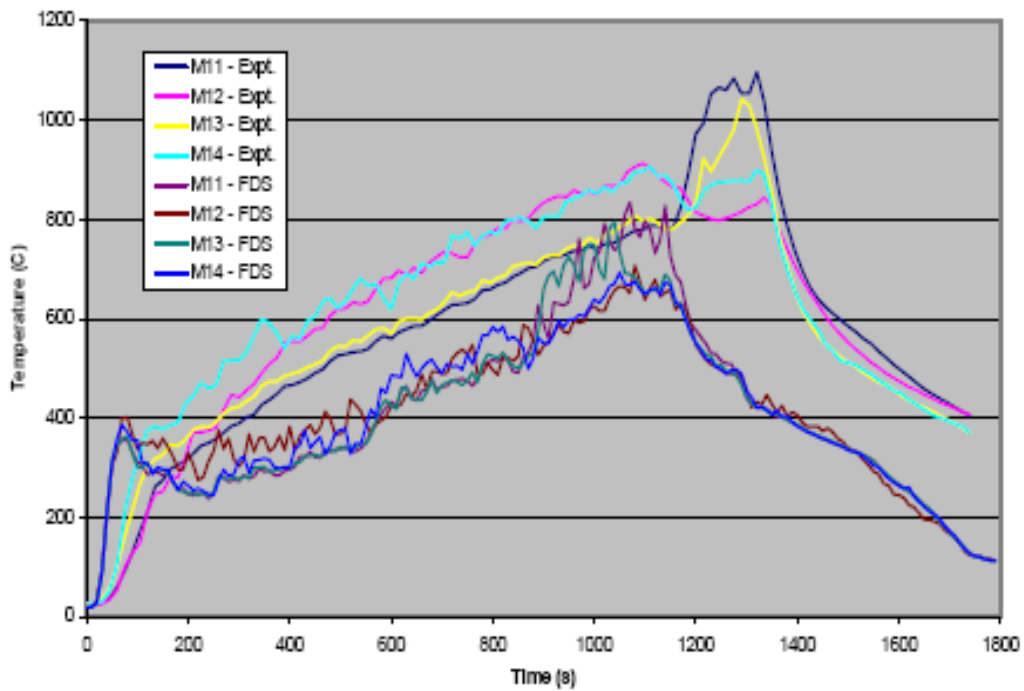


Fig. C31 Level 2 temperature - Test 3

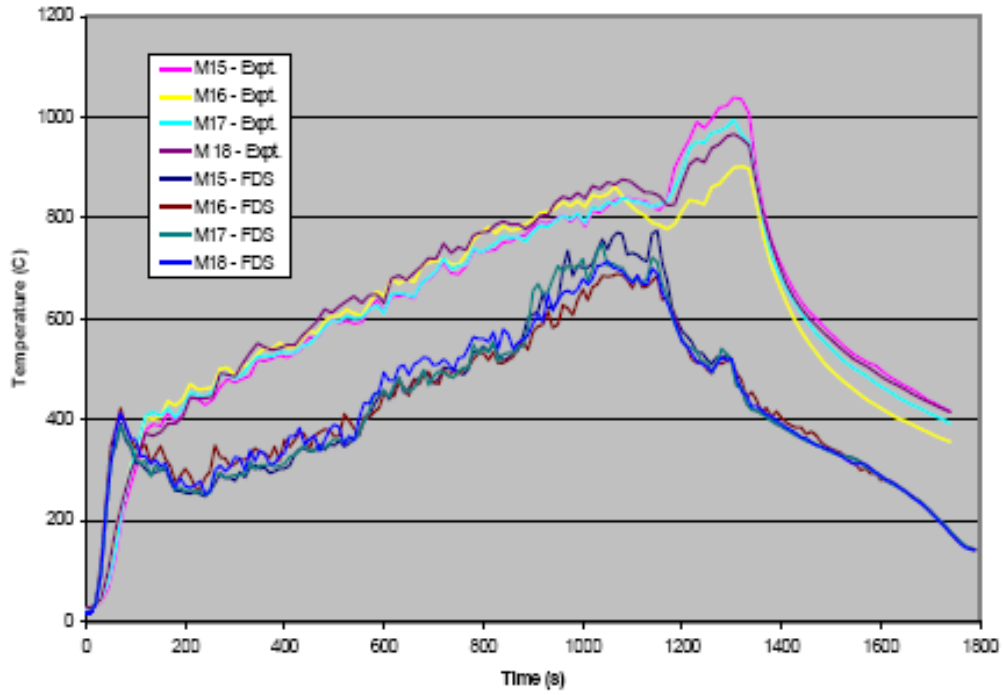


Fig. C32 Level 3 temperature - Test 3

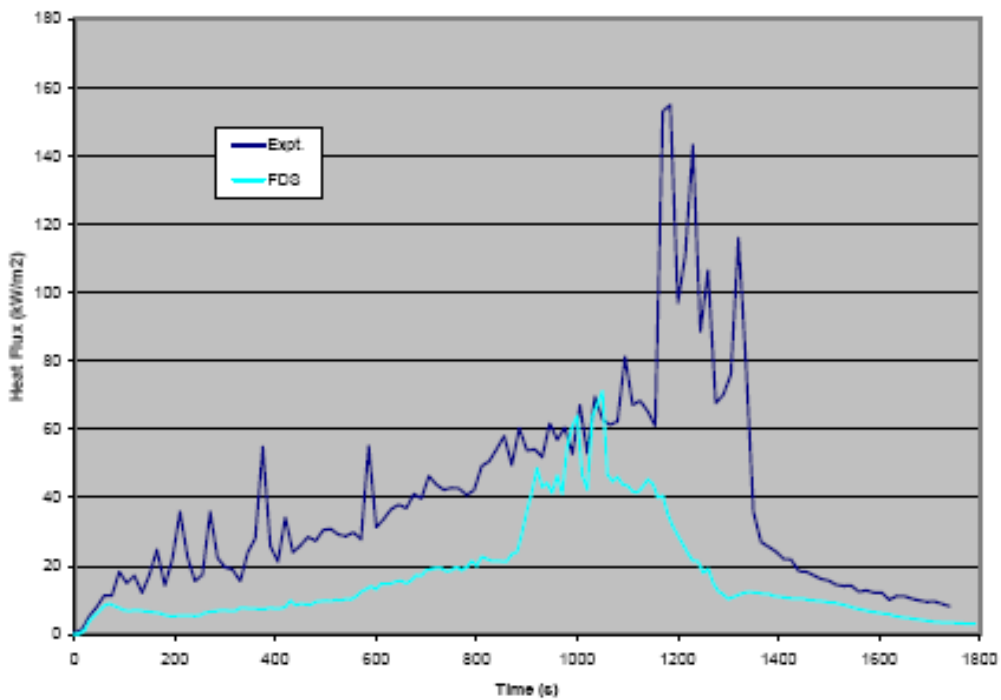


Fig. C33 Heat fflux on aerated concrete block (WS4) - Test 3

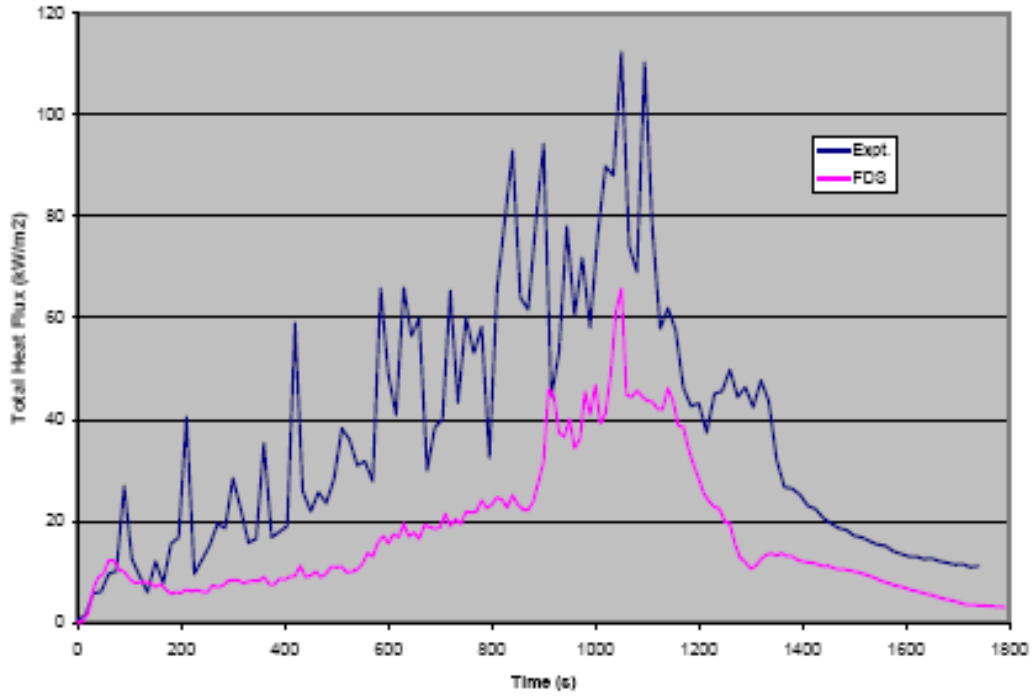


Fig. C34 Heat flux on concrete block (WS3) - Test 3

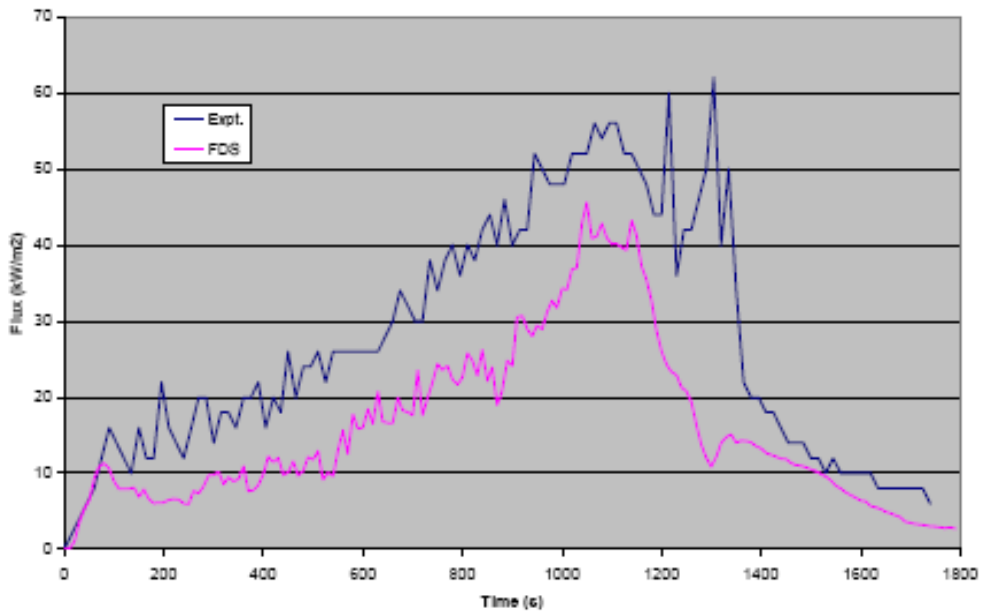


Fig. C35 Heat flux on steel plate (WS2) - Test 3

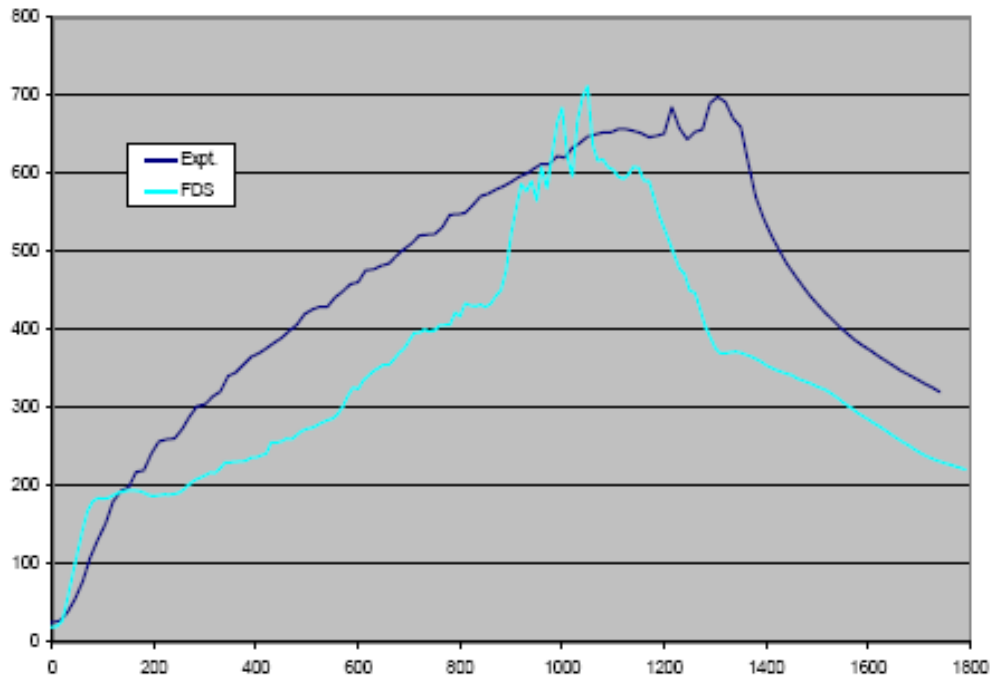


Fig. C36 Aerated concrete block temperature - Test 3

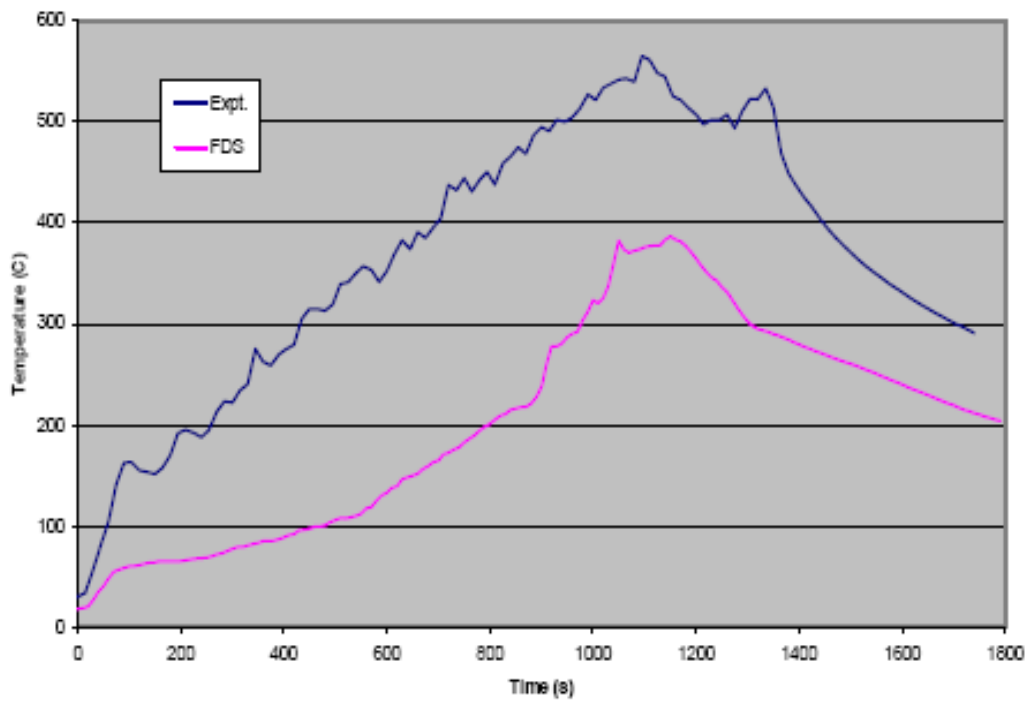


Fig. C37 Concrete block temperature - Test 3

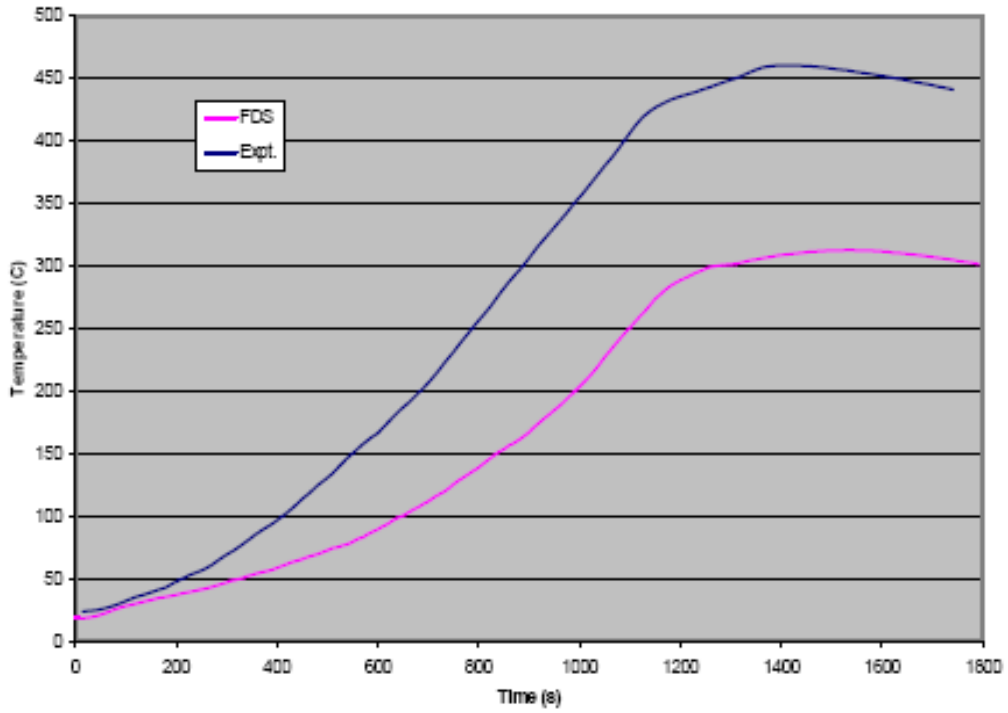


Fig. C38 Steel plate front surface temperature (M34) - Test 3

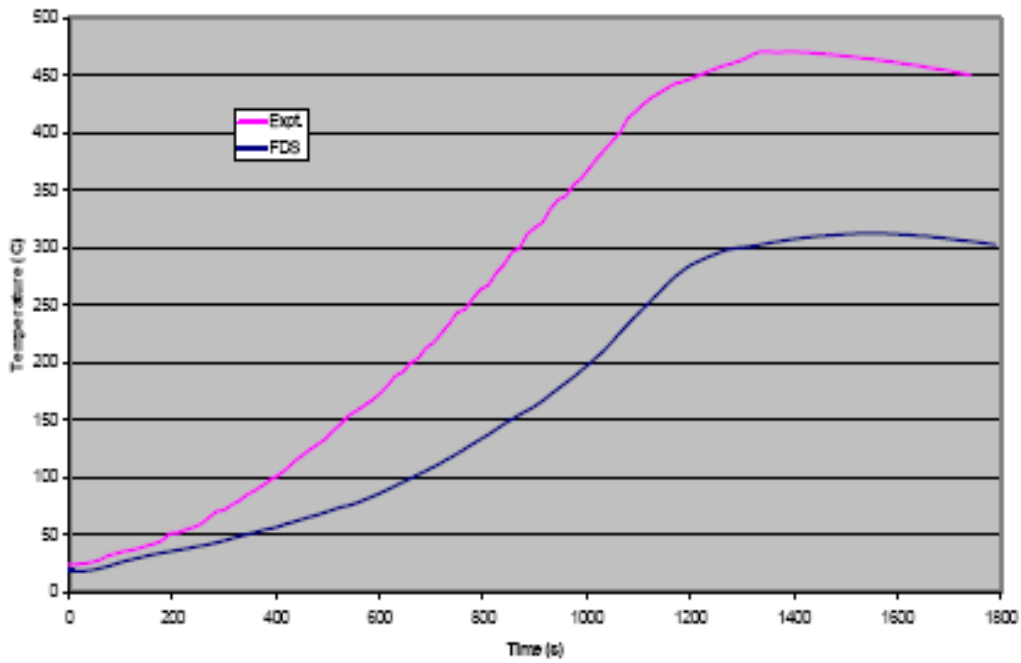


Fig. C39 Steel plate back surface temperature (M35) - Test 3

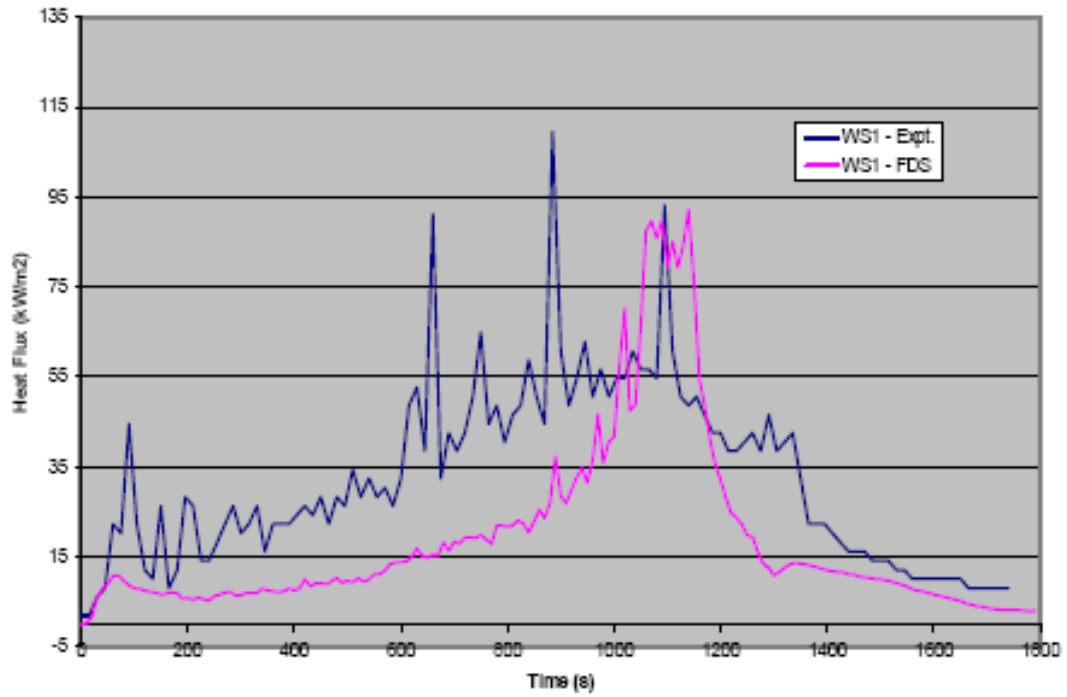


Fig. C40 Heat flux on wall (WS1) - Test 3

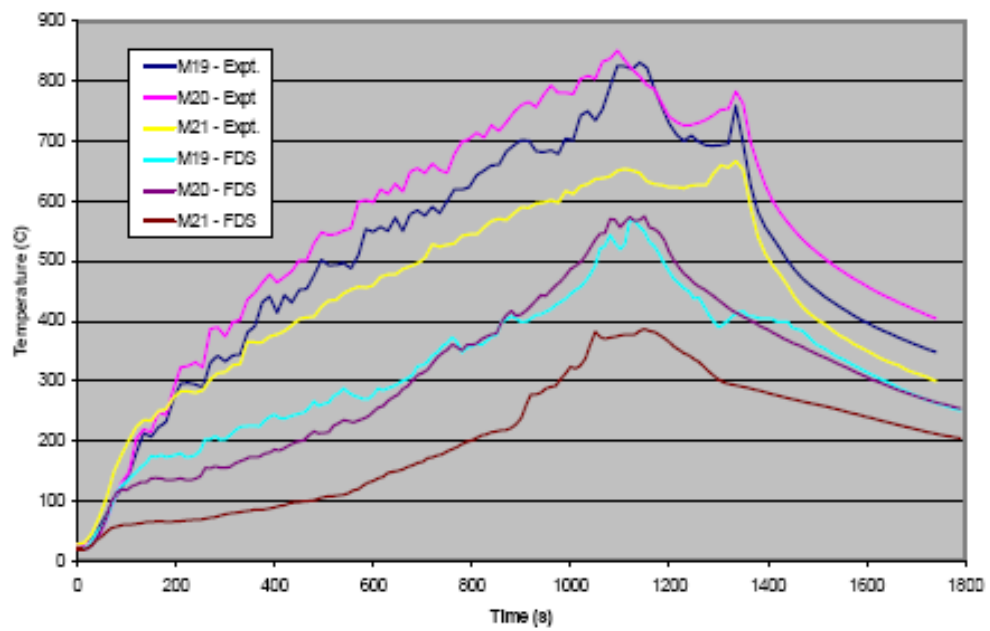


Fig. C41 Wall temperature - Test 3

List of Figures

Fig. C1	Compartment for Benchmark Exercise No. 4.....	2
Fig. C2	Heat release rate - Test 1	40
Fig. C3	HGL interface height - Test 1	40
Fig. C4	HGL temperature - Test 1	41
Fig. C5	Oxygen concentration	41
Fig. C6	View of flame sheet output from FDS - Test 1	42
Fig. C7	View of temperature slice (x = 1.8 m) - Test 1	42
Fig. C8	Plume temperature - Test 1	43
Fig. C9	Level 1 temperatures - Test 1	43
Fig. C10	Level 2 temperatures - Test 1	44
Fig. C11	Level 3 temperatures - Test 1	44
Fig. C12	Heat flux on aerated concrete block (WS4) - Test 1	45
Fig. C13	Heat flux on concrete block (WS3) - Test 1.....	45
Fig. C14	Heat flux on steel plate (WS2) - Test 1	46
Fig. C15	Aerated concrete block temperature - Test 1	46
Fig. C16	Concrete block temperature - Test 1.....	47
Fig. C17	Steel plate front surface temperature (M34) - Test 1	47
Fig. C18	Steel plate back surface temperature (M35) - Test 1	48
Fig. C19	Heat flux on wall (WS1) - Test 1.....	48
Fig. C20	Wall temperatures - Test 1	49
Fig. C21	Heat release rate - Test 3	49
Fig. C22	HGL interface height - Test 3	50
Fig. C23	HGL temperature - Test 3	50
Fig. C24	Oxygen concentration - Test 3	51
Fig. C25	View of flame sheet output from FDS (45 s) - Test 3	51
Fig. C26	View of flame sheet output from FDS (130 s) - Test 3	52
Fig. C27	View of temperature slice (x = 2.8 m, t = 101.5 s) - Test 3.....	52
Fig. C28	View of temperature slice (x = 2.8 m, t = 102 s) - Test 3.....	53
Fig. C29	Plume temperature - Test 3	53
Fig. C30	Level 1 temperature - Test 3	54

Fig. C31	Level 2 temperature - Test 3	54
Fig. C32	Level 3 temperature - Test 3	55
Fig. C33	Heat fflux on aerated concrete block (WS4) - Test 3	55
Fig. C34	Heat flux on concrete block (WS3) - Test 3.....	56
Fig. C35	Heat flux on steel plate (WS2) - Test 3	56
Fig. C36	Aerated concrete block temperature - Test 3.....	57
Fig. C37	Concrete block temperature - Test 3.....	57
Fig. C38	Steel plate front surface temperature (M34) - Test 3	58
Fig. C39	Steel plate back surface temperature (M35) - Test 3	58
Fig. C40	Heat flux on wall (WS1) - Test 3.....	59
Fig. C41	Wall temperature - Test 3.....	59

List of Tables

Table C1	Wall, floor, and ceiling material	3
Table C2	Thermo-physical properties of wall, floor, and ceiling materials.....	3
Table C3	Target description and location	5
Table C4	Summary of Predictions with CFAST and FDS for Test 1 <i>Specified Predictions</i>	35
Table C5	Summary of Predictions with CFAST and FDS for Test 3 <i>Specified Predictions</i>	37
Table C6	Summary of Predictions with FDTs - Test 1 <i>Specified Predictions</i>	39

Appendix D: International Collaborative Project to Evaluate Fire Models for Nuclear Power Plant Applications

FATE™ 2.0 Computer Code Calculations for Benchmark Exercise No. 4

Presented by

Tom Elicson, Sung Jin Lee, Marty Plys

Fauske & Associates, LLC

16W070 West 83rd Street, Burr Ridge, IL 60521, U.S.A.

Contents

D1	Introduction	1
D2	Input Parameters and Assumptions.....	3
D2.1	Room Geometry and Ventilation	3
D2.2	Targets	6
D2.3	Test Matrix and Fire Source	8
D3	Comparison of Code Predictions with Experimental Results.....	13
D3.1	FATE™ 2.0 Computer Code Description	13
D3.2	FATE™ 2.0 Fire Sub-models	14
D3.2.1	Pilot Fire Specification.....	17
D3.2.2	Plume Model	20
D3.2.3	Smoky Layer	22
D3.2.4	Radiation Heat Transfer Network	23
D3.3	FATE Blind Calculations for BE-4	28
D3.4	FATE Open Benchmark Calculations for BE-4	28
D3.4.1	BE-4 Case 1 FATE Open Benchmark Results.....	28
D3.4.2	BE-4 Case 3 FATE Open Benchmark Results.....	54
D4	Conclusions and Recommendations	67
D5	References.....	69
	List of Figures	71
	List of Tables	73

D1 Introduction

The purpose of this benchmark exercise is to perform an integral validation of the FATE™ 2.0 Computer Code fire models for use in nuclear power plants, fuel cycle facilities, and DOE material handling facilities. Calculations presented below have been performed with FATE version 2.14. Additional details of the benchmark exercise are provided in Chapters 1 through 3 of the main report and the test specification report (GRS, 2003).

D2 Input Parameters and Assumptions

D2.1 Room Geometry and Ventilation

FATE input consists of a base model file and a case-specific input file. The base model describes the basic room geometry (heat sinks and radiation network for walls, floors, ceiling), ventilation flow paths, and cable targets. Specific fire power histories and flow path setup is then provided in case-specific input files. One case file is created for each test modeled.

The Benchmark Exercise No. 4 (BE-4) base model is based on a standardized room model successfully developed during the Benchmark Exercise No. 2 (BE-2) effort (NISTIR-6986). The BE-2 effort demonstrated that the rectangular room geometry can be accurately modeled with a single region and 14 heat sinks to represent floor, ceiling, and walls, and a radiation network containing the heat sinks, fire source, and smoky layer. Modeling of specific targets requires additional heat sinks, as discussed subsequently. The BE-2 effort also provides an effective methodology for modeling forced ventilation, natural circulation through open doors, and intrinsic leakage through the use of a maximum of five flow paths. Ventilation in the FATE standardized room model is refined in the current effort.

Table D2-1 summarizes the heat sinks used to define the region boundaries, while Table D2-2 summarizes the flow paths.

The wall heat sinks listed in Table D2-1 are modeled as “strips” that circumscribe the room perimeter and extend vertically between the indicated elevations. The heat sinks are then subdivided in the FATE heat transfer model into 20 slabs for 1-dimensional conduction through the heat sink. The four side walls are modeled as a series of 12 stacked wall strips. The advantage to this approach is input and computational simplicity, while the limitation is that a single surface temperature is reported for the North, East, South, and West walls at each elevation.

As will be discussed, calculational results proved to be sensitive to modeling of intrinsic leakage. The leak centerline elevation, leak area, and leak orientation are all shown to influence the smoky layer elevation and oxygen content of the room. Table D2-2 shows five flow paths, however only three of the five are used in the based case calculations.

Junction 1 represents the open doorway, while the combined fan flow is modeled with a single junction, junction 2, and the leakage is modeled with a single junction, junction 4. In addition, in flows through the doorway are assumed to be equally distributed between the smoky and lower gas layers, and, for Test 3, air in the lower 1.6 m of the room is assumed to be available for entrainment and consumption in the fire. As will be discussed, both of these assumptions are supported by the test data.

Finally, although the gross room volume is $3.6 \times 3.6 \times 5.7 = 74 \text{ m}^3$, this volume is reduced due to the presence of the light concrete bricks stacked up to a height of 0.6 m. Furthermore, it is assumed that the volume beneath the 4 m^2 fire pan does not freely mix with the remainder of the fire room. Thus, the net free volume used in the FATE model discounts the entire volume below the 0.56 m elevation and is calculated as $74 \text{ m}^3 - 3.6 \times 3.6 \times 0.6 = 66 \text{ m}^3$.

Table D2-1 FATE BE-4 base model heat sink summary table

Heat Sink #	Label	Type	Bottom Elevation [m]	Top Elevation [m]	Material	Thickness [m]
1	FLOOR	Upward facing rectangle	0.000E+00	6.000E-01	Aerated Concrete	0.0254
2	WALL-1	Rectangular enclosure strip	0.000E+00	4.750E-01	Light Concrete	0.0254
3	WALL-2	Rectangular enclosure strip	4.750E-01	9.500E-01	Light Concrete	0.0254
4	WALL-3	Rectangular enclosure strip	9.500E-01	1.425E-00	Light Concrete	0.0254
5	WALL-4	Rectangular enclosure strip	1.425E-00	1.900E+00	Light Concrete	0.0254
6	WALL-5	Rectangular enclosure strip	1.900E+00	2.375E+00	Light Concrete	0.0254
7	WALL-6	Rectangular enclosure strip	2.375E+00	2.850E+00	Light Concrete	0.0254
8	WALL-7	Rectangular enclosure strip	2.850E+00	3.325E+00	Light Concrete	0.0254

Heat Sink #	Label	Type	Bottom Elevation [m]	Top Elevation [m]	Material	Thickness [m]
9	WALL-8	Rectangular enclosure strip	3.325E+00	3.800E+00	Light Concrete	0.0254
10	WALL-9	Rectangular enclosure strip	3.800E+00	4.275E+00	Light Concrete	0.0254
11	WALL-10	Rectangular enclosure strip	4.275E+00	4.750E+00	Light Concrete	0.0254
12	WALL-11	Rectangular enclosure strip	4.750E+00	5.225E+00	Light Concrete	0.0254
13	WALL-12	Rectangular enclosure strip	5.225E+00	5.700E+00	Light Concrete	0.0254
14	CEILING	Upward facing rectangle	5.700E+00	6.000E+00	Concrete	0.0254

Table D2-2 FATE BE-4 base model flow path summary

Junction #	Description	Centerline Elevation [m]	Area [m ²]
1	DOOR, Test 1	2.1 (height = 3.0 m)	Area = 2.1 m ² ; K = 0.54
	DOOR, Test 3	2.1 (height = 1.0 m)	Area = 0.70 m ² ; K = 0.54
2	FAN 1	5.49	0.176 m ²
3	FAN 2	N/A	Not used; FAN 1 is sized to deliver combined fan flow
4	MISCELLANEOUS LEAKAGE	1.5	0.05 m ²
5	DOOR GAP LEAK	N/A	Not used

D2.2 Targets

Two targets are included in the FATE model. Both targets are represented by one or more heat sinks and are included in the radiation heat transfer network.

The first target is the concrete material probe with lower corner coordinates of $x = 0.0$ m, $y = 1.9$ m, and $z = 1.7$ m. The probe is modeled with a single vertical rectangular heat sink, heat sink 16, with dimensions 0.3 m x 0.3 m x 0.1 m thick. This heat sink is divided into 20 nodes through the thickness to allow 1-dimensional conduction through the probe. In addition, the heat sink is included in the radiation heat transfer network, therefore the heat sink surface is subjected to convective and radiative boundary conditions. The remaining probes are not included in the current model.

The second target is the more complex barrel-type waste container. As shown in Figure D2-1, this target is divided azimuthally into four segments. The first three segments cover the cylinder half facing the fire, while the fourth segment is the entire back half side of the barrel facing away from the fire. Each segment height is equal to the height of the barrel. In addition, each of the four segments is represented as a composite heat sink consisting of three layers: an outer metal layer (5 radial nodes), a middle concrete layer (20 radial nodes), and an inner styrene granulate fill layer (20 radial nodes). The tinfoil that makes up the inner barrel is defined as a contact resistance between the concrete and styrene. Radial conduction is allowed between the layers, while azimuthal conduction is modeled only in the outer most steel layer. The outer metal surfaces are also included in the radiation heat transfer network.

In all, the targets are represented by 13 heat sinks – one for the probe and 12 for the barrel-type waste container – as summarized in Table D2-3, below.

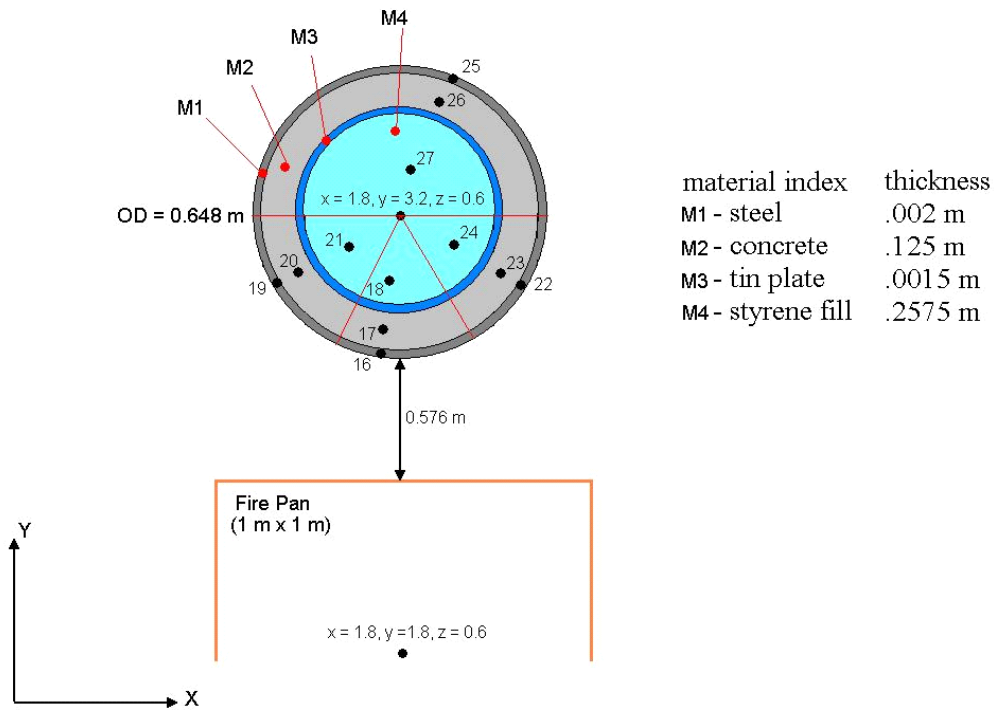


Fig. D2-1 FATE BE-4 nodalization for the barrel-type waste container target

Table D2-3 FATE BE-4 target heat sink summary table

Heat Sink #	Label	Type	Bottom Elevation [m]	Top Elevation [m]	Material	Thick-ness [m]
15	PROBE	Vertical rectangle	1.70E+00	2.00E+00	Concrete	0.100
16	TARGET1	Cylindrical segment	6.00E-01	1.56E+00	Steel	0.002
17	CONC1	Cylindrical segment	6.00E-01	1.56E+00	Concrete	0.125
18	FILL1	Cylindrical segment	6.00E-01	1.56E+00	Granulate	0.2575
19	TARGET2	Cylindrical segment	6.00E-01	1.56E+00	Steel	0.002
20	CONC2	Cylindrical segment	6.00E-01	1.56E+00	Concrete	0.125
21	FILL2	Cylindrical	6.00E-01	1.56E+00	Granulate	0.2575

Heat Sink #	Label	Type	Bottom Elevation [m]	Top Elevation [m]	Material	Thick-ness [m]
		segment				
22	TARGET3	Cylindrical segment	6.00E-01	1.56E+00	Steel	0.002
23	CONC3	Cylindrical segment	6.00E-01	1.56E+00	Concrete	0.125
24	FILL3	Cylindrical segment	6.00E-01	1.56E+00	Granulate	0.2575
25	TARGET4	Cylindrical segment	6.00E-01	1.56E+00	Steel	0.002
26	CONC4	Cylindrical segment	6.00E-01	1.56E+00	Concrete	0.125
27	FILL4	Cylindrical segment	6.00E-01	1.56E+00	Granulate	0.2575

D2.3 Test Matrix and Fire Source

The BE-4 test series consists of two separate tests, Test 1 and Test 3. The distinguishing characteristics between these tests are the fuel burn rate and the doorway opening. Although raw and smoothed fuel burn rates were provided for each of the two tests, the burn rates were adjusted based on a 5-point moving average of the raw data and a delay based on the fuel ignition time. The fuel ignition time is taken as the time at which the heat sink temperatures begin to increase (160 sec for Test 1 and 15 sec for Test 3). Table D2-4 summarizes the differences between the two tests, while Figures D2-2 and D2-3 compare the burn rate table input to FATE against the raw burn rate data.

Table D2-4 Summary of Test 1 and Test 3 distinguishing input

Parameter	Test 1		Test 3	
Doorway area (m ²)	2.1		0.7	
Doorway centerline el. (m)	2.1		2.1	
Doorway total height (m)	3.0		1.0	
Fire burn rate table based on 5-point averaging of burn rate data	Time (s)	Burn rate (kg/s)	Time (s)	Burn rate (kg/s)
	0	0.0000	0	0.0000
	160	0.0000	15	0.0000
	210	0.0380	30	0.0124
	330	0.0570	100	0.0413
	415	0.0700	829	0.0720
	600	0.0720	1013	0.0980
	870	0.0780	1090	0.2100
	1368	0.0822	1099	0.2040
	1380	0.0630	1350	0.0337
	1450	0.0000	1352	0.0000

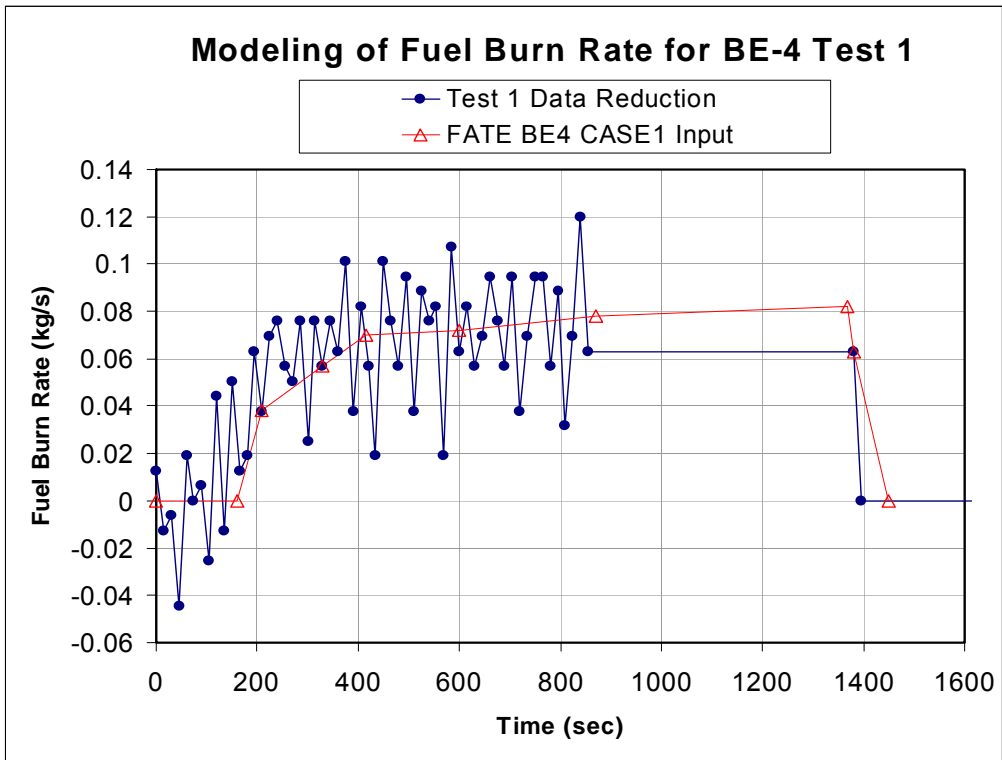


Fig. D2-2 FATE BE-4 Test 1 comparison of fuel burn rate data to FATE input

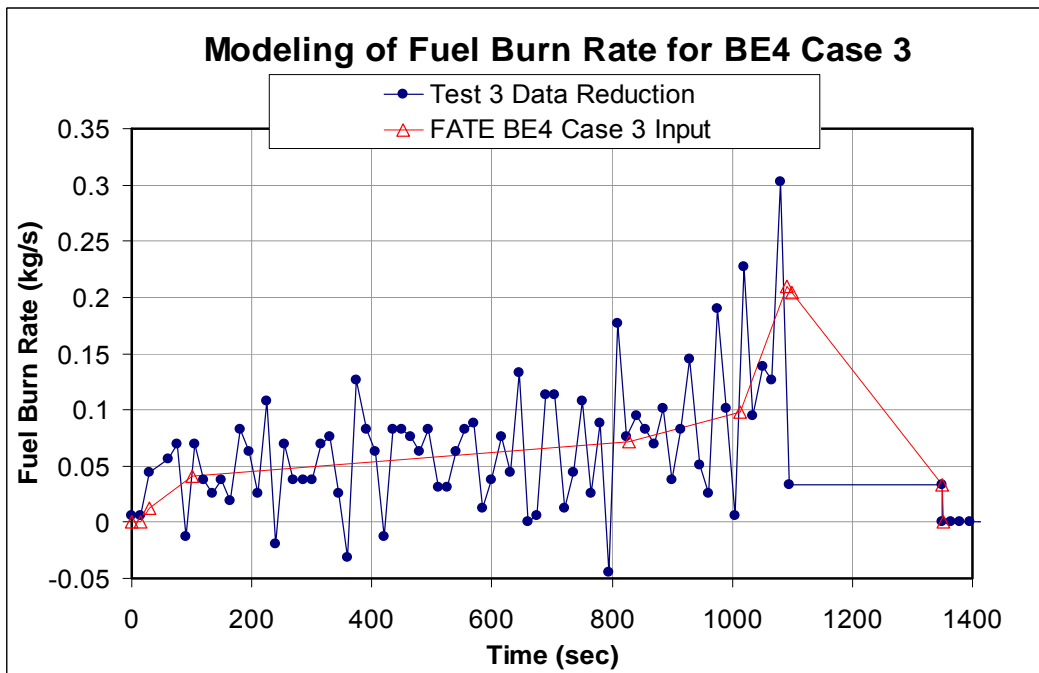
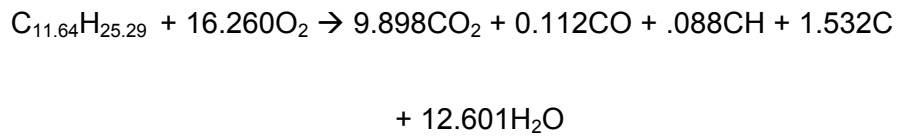


Fig. D2-3 FATE BE-4 Test 3 comparison of fuel burn rate data to FATE input

FATE input also requires specification of the combustion products yield. The combustion yields used for input are based on real yields for high molecular weight/temperature hydrocarbons for well ventilated flaming fires (Tewarson, Tab 1-13.7):

- $Y_{\text{CO}_2} = 2.64$
- $Y_{\text{CO}} = 0.019$
- $Y_{\text{CH}} = 0.007$

When considering the chemical balance, excess carbon is assumed to be released in the form of soot. Thus, the final chemical balance for kerosene combustion becomes,



The yields for soot and water are therefore,

- $Y_{\text{SOOT (carbon)}} = 0.111$
- $Y_{\text{H}_2\text{O}} = 1.375$

D3 Comparison of Code Predictions with Experimental Results

D3.1 FATE™ 2.0 Computer Code Description

The FATE™ 2.0 Computer Code is used for this analysis. FATE, previously named HADCRT, is the successor code to the HADCRT computer program used in previous ICFMP activities. Specifically, FATE version 2.11 is used in the following calculations. FATE version 2.11 contains upgrades to address fire modeling issues.

FATE stands for Facility Flow, Aerosol, Thermal, and Explosion Model, for PCs and workstations [Plys and Lee, 2004]. FATE 2.0 is used for design, off-normal, and accident analyses of nuclear and chemical facilities. FATE 2.0 is the successor to computer codes used extensively for design and safety analyses for U. S. Department of Energy projects at the Hanford site and elsewhere (HADCRT for Tank Farms, Waste Treatment Plant, WESF, PFP; HANSF MCO and HANSF Sludge for Spent Nuclear Fuel and sludge, T Plant).

General capabilities of FATE 2.0 include:

- Fire model:
Define burn rate and yields; Smoky layer model; Propagation of smoke in stratified layers throughout facility; Aerosol transport with smoky layers; Aerosol settling from smoky layer to lower layer and embedded surfaces.
- Multiple-compartment thermodynamics and general species:
Facility rooms have separate pressure, temperature, and composition; Compound property libraries are input; Tracking of condensed, gaseous, and aerosol species.
- Facility nodalization and flow:
Compartments are connected in arbitrary topology by flow paths; Flows are pressure-driven, density-driven counter-current, and diffusional.
- Aerosol behavior:
Aerosol coagulation, sedimentation, transport with flow; Deposition on bends and filters; Deposition by condensation; Aerosol formation by boiling and fog.

- Heat transfer:
Convection of liquids and gases to structures with internal temperature distributions; Linking for 2D and 3D heat transfer; Condensation.
- Flammability and combustion of gases, vapors, and aerosols:
Any input compound may participate; examples include solvent vapors, hydrogen, and U metal or hydride aerosols.
- Entrainment of deposits to form aerosols:
Powder, liquid, and sludge waste may be entrained by combustion or flow.
- Thermal radiation networks:
View factor models and automatic network balancing.
- Event-oriented simulation:
Intervention criteria and actions for scenario evolution.
- Sources and time-dependent conditions:
Prescribe liquid, gas, and aerosol source histories and environmental conditions with time.
- Nuclear fuel and sludge models including chemical reactions.

FATE™ 2.0 is owned and licensed by Fauske and Associates, LLC (FAI) and FATE is a registered trademark of FAI. FATE is created and maintained under the FAI Quality Assurance Program (10CFR50 App. B & ISO 9001 compliant).

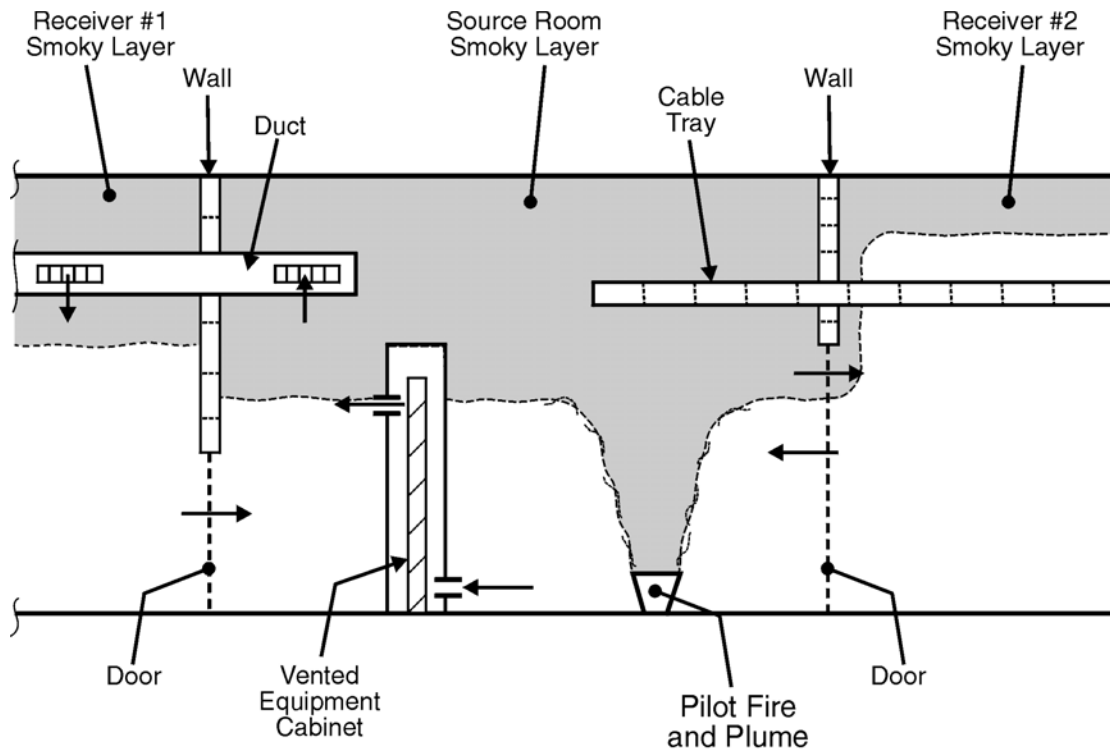
D3.2 FATE™ 2.0 Fire Sub-models

We narrow the vast topic of fire phenomenology to calculating the conditions brought on by liquid pool or solid combustible pilot fires in a multi-compartment facility. Fire analysis involves prediction of local temperatures, pressures and gas compositions for compartments connected by heat sinks such as walls and ceilings, and junctions such as doors and hatches. Combustion product plumes within a fire compartment necessitate that the well-mixed region assumption gives way to the ideal of two distinct layers, one smoky and hot and the other relatively clean and cool. Smoky layer movement and flame height variations require radiation networks with time-dependent properties. Smoke movements also introduce inter-compartmental flow combinations of smoky and non-smoky gas flows; i.e. junctions can contain pure smoke flow, or clean flow or some combination of the two.

Fire modeling is added to the generic features of the code by incorporating four phenomena in the FATE framework:

- Pilot fires specification (burn rates, yields, heat release)
- Plume Model
- Stratified layer composition; i.e., a smoky layer
- Advanced radiation heat transfer with automatic view factor calculation

Figure D3-1 shows a pilot fire and plume in a process facility with a number of compartments that communicate via doors and ventilation ducts, and contain heat sinks such as ceilings, walls and internal equipment. This is the familiar construct of regions, heat sinks and junctions, with the addition of pilot fire and plume in one compartment (region). This figure typifies compartment fire modeling by showing an idealized hot smoky layer above a relatively cold, clean, lower layer. This assumption neglects the true nature of the interface, which at various stages of the fire can be ill-defined or non-existent, and presumes that the smoky layer quickly propagates horizontally along the ceiling. In reality, the smoky plume initially strikes the ceiling and spreads outward until it reaches the confines of compartment walls, at which point the smoky layer proceeds downward. Nevertheless, the two-layer idealization is useful and accurate enough that a number of code and analytical techniques employ it for compartment analysis. Fire test data is often reduced to this ideal.



MP99D450.CDR 3-19-2001

Fig. D3-1 FATE™ 2.0 Fire Model Features

Smoky layer growth then depends on the balance between the fire and plume source and the inter-compartmental flows of both the smoky and lower layers. The fuel burning rate, plume entrainment rate, and fuel properties, namely heat of combustion and product yields, determine the rate at which mass and energy enter the smoky layer. Between the base of the fire and the bottom of the smoky layer, plume entrainment mixes the lower layer gases with the combustion products, thereby increasing total mass flow to the smoky layer, but decreasing the incoming temperature. Inter-compartmental flows, noticeably complicated by the presence of two layers, depend greatly on junction orientation and elevation. As an example, Figure D3-1 shows that the smoky layer must advance below the top of a door before it can proceed to the neighboring compartment. In one junction, inter-compartmental flow can now consist of pure lower layer flow, pure smoky layer flow or a combination of the two. The smoky layer can be thin if the compartment ceiling contains a hatch that allows smoke to escape immediately to a region above, or if an operating ventilation duct is located near the ceiling to draw smoky layer gases from the region. Similarly, flow to the lower layer might stabilize the smoky layer or even cause it to recede.

Additional details of the FATE fire sub models are presented below.

D3.2.1 Pilot Fire Specification

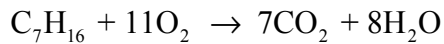
Fire sources are user-defined and must include inputs for the following:

- fuel mass and properties,
- time-dependent burning mass flux,
- fire diameter,
- fire base elevation,
- burn area,
- efficiency, and
- radiation fraction

A fire is presumed to be the reaction of solid or liquid fuel with oxygen to produce carbon dioxide, carbon monoxide, soot, steam and some other carbon containing compound. FATE makes no mechanistic assessments of ignition or burning rate. A fire burns at the user-input rate until all the fuel is consumed or the oxygen concentration falls below a user-defined limit. Up to five separate fires and ten different fuels are allowed. A fire can be placed in any region, but a fire consists of one fuel by definition. Fuel properties are defined on input and need not necessarily correspond to the real properties of any liquid or solid.

Fuel properties are as follows: molecular weight, theoretical heat of combustion, CO₂ yield, CO yield, CH yield, soot yield, steam yield, hydrocarbon name, and an optional heat of formation. Theoretical heat of combustion, Q_T , is the amount of heat released when all the fuel is oxidized completely. This rarely occurs, which is why the theoretical heat of combustion is multiplied by an efficiency, χ_C , to get a chemical heat of combustion value, Q_H . Efficiency varies slightly from test to test, even for the same fuel, but is in the range between 90 and 95%. Theoretical heat of combustion can be determined if the heat of formation is known for the fuel; it is just the sum heat of formation of products (fuel, oxygen) minus the sum heat of formation of reactants (CO₂, CO, CH, soot, steam). The code does this calculation internally if the fuel heat of formation is specified, and in the log file compares this result to the input heat of combustion.

Yields are given in terms of mass product per mass of fuel. If the fuel is completely oxidized, yields are computed by knowing the moles of product per moles fuel and the individual molecular weight of all reactants and products. This is done by writing the balanced chemical reaction with carbon dioxide and steam as the only product, calculating respective moles of product per moles of fuel, and then converting mole ratio to mass ratio. In reality, fuels are not fully oxidized and yields are found from experiment compilations. A heptane pool fire is a good example. The stoichiometric reaction is written:



For carbon dioxide, the yield in terms of mole ratio is 7 to 1, which in terms of mass ratio is $7 \times 44/100$ (heptane molecular weight is 100), or 3.08. The calculation for steam gives a mole ration of 8 to 1 and mass ration of 1.44. Experimental data show that carbon dioxide yield is actually 2.86 g/g, carbon monoxide yield is 0.01 g/g, CH yield is 0.004 g/g, soot yield is 0.037 g/g, and steam yield is 1.36 g/g. Empirical yields of carbon dioxide and water are always somewhat less than stoichiometric yields.

Radiation fraction is specified as a function of time as well. Chemical heat of reaction is comprised of convective and radiation components. Convective power enters the fire plume, while the balance radiates to the compartment walls and the smoky layer. The radiation component is expressed in terms of a heat of combustion (kJ/kg), which is typical in the literature, or as a fraction of the chemical heat of reaction, which is the input for the code. The radiation component of chemical heat of combustion is usually between 15 and 35%.

For an open fire, FATE evaluates a fire source in the following manner:

$$W_b(t) = G_b(t) \times A_f$$

where W_b is the time-dependent burning rate (kg/s), G_b is the input, time-dependent burning mass flux (kg/m²/s) and A_f is the input fire area, which is constant. Here an open fire means that fuel and oxygen are abundant, and that the smoky layer is well above the flame height. The fire source calculations proceeds initially as if the flame were open and then checks for limitations in oxygen. In the general case, burning rate is altered if the smoky layer descends below the top of the flame or envelops the fire entirely. Flame height must be computed to know the location of the smoky layer with

respect to the base of the fire and the top of the flame. If the source oxygen concentration falls below a user-supplied value, burning rate and heat release rate are set to zero.

FATE uses the Heskestad model to calculate flame height, which is needed to determine burning rate and view factors from the flame to compartment heat sinks. Flame heights are correlated by the following dimensionless number:

$$Q^* = \frac{Q}{\rho_{\infty} c_p T_{\infty} D^2 \sqrt{gD}}$$

where Q is the fire power, ρ_{∞} is the ambient air density ($\sim 1.1 \text{ kg/m}^3$), c_p is the constant volume specific heat ($\sim 1000 \text{ J/kg/K}$), T_{∞} is the ambient temperature ($\sim 300 \text{ K}$), g is the acceleration of gravity and D is the flame diameter, which is an input; an effective flame diameter suffices if the fire is not circular. Heskestad's correlation, which is applicable to a large range of liquid pool and solid fires, gives flame height H as follows:

$$\frac{H_f}{D} = 3.7 (Q^*)^{2/5} - 1.02$$

To calculate the concentration of the oxygen source, the code determines where the smoky layer level is with respect to the fire base elevation (H_b , an input) and the elevation at the top of the flame, which is computed from the fire base elevation plus the flame height. A smoky layer cover fraction F_s , that varies between 0.0 and 1.0 is calculated as follows:

- If the smoky layer height is less than the fire base elevation, $F_s = 1.0$
- If the smoky layer height is above the top of the flame, $F_s = 0.0$, and
- Between these extremes, F_s varies linearly: $F_s = [H_f + H_b - S]/H_f$.

Source oxygen concentration is then:

$$x_{O_2} = F_s \times x_{O_{2,s}} + (1 - F_s) \times x_{O_{2,L}}$$

where x is concentration and subscripts s and L stand for the smoky and lower layers, respectively. Source oxygen concentration is a weighted-average based on the smoky layer cover fraction; e.g., if the smoky layer extends halfway down the flame, the source oxygen concentration is a simple average of the smoky and lower layer oxygen concentrations.

D3.2.2 Plume Model

In a compartment fire the plume entrains cool air from the lower layer, heats it in the fire and transports it to the smoky layer. Define the plume as the region in the lower layer between the elevation of the fire and the smoky layer, encompassing both the burning region and the buoyant plume above the flames. Plume height varies over the course of a compartment fire scenario. Early on, plume height is relatively large as the smoky layer is just starting to evolve, but plume height diminishes as the smoky layer advances. While smoky layer thickness depends on the specifics of the fire scenario, this general trend is important to note because entrainment rate is strongly dependent on the plume height. The amount of air entrained into the plume from the lower layer influences the temperature and concentration of combustion products in the smoky layer, and junction flow into or out of both the smoky and lower layers. In principle, entrainment also determines burning rates by supplying air to the fire, but this point is given no regard because burning rate is a user input.

Entrainment into the plume has been repeatedly described by the non-dimensional expression:

$$\frac{W_e}{\rho_\infty D^2 \sqrt{\frac{\Delta T_{ad}}{T_\infty} g D (\chi_C - \chi_R)}} = F\left(\frac{z}{D}\right)$$

which states the dimensionless entrainment rate is a function of the plume height above the base of the fire, z , and D , is the fire diameter for a liquid pool. Dimensionless entrainment rate is defined by W_e , the total entrainment rate in kg/s, ρ_∞ is the ambient (lower layer) gas density, ΔT_{ad} is the adiabatic flame temperature, T_∞ is the ambient (lower layer) temperature, χ_C is the combustion efficiency (~ 0.9), and χ_R is the fire

radiation fraction (~ 0.3). The denominator of the left-hand side is understood to be a mass flow rate by noting that that the term

$$\sqrt{\frac{\Delta T_{\text{ad}}}{T_{\infty}}} g D (\chi_C - \chi_R)$$

is a characteristic entrainment velocity that increases with increasing size and strength as expressed by the adiabatic flame temperature, but decreases as the fractional amount of power radiated away increases.

A complete theoretical understanding of entrainment by fire plumes is not available, but several experimental studies have provided air entrainment rate measurements in the burning region of fire plumes. These studies identify three distinct regimes for entrainment, depending on the ratio of plume height, z to fire pool diameter, D . For FATE, based on an aggregation of the experimental data, we have defined a single correlation spanning all three. The FATE correlation, which is compared to test data in Figure D3-2, has the following functional form:

$$F\left(\frac{z}{D}\right) = 0.1 \left[\left(\frac{z}{D}\right)^6 + 2.85 \times 10^{-4} \left(\frac{z}{D}\right)^{10} \right]^{1/4} ; \quad \text{for } z/D > 0.8$$

Figure D3-2 includes measurements at vertical distances as much as five times the average flame heights, which makes it valid for calculating entrainment rates below and above the flame tops. For vertical distances in the range $0.1 < z/D < 0.8$:

$$F\left(\frac{z}{D}\right) = 0.072 ; \quad 0.1 \leq z/D \leq 0.8$$

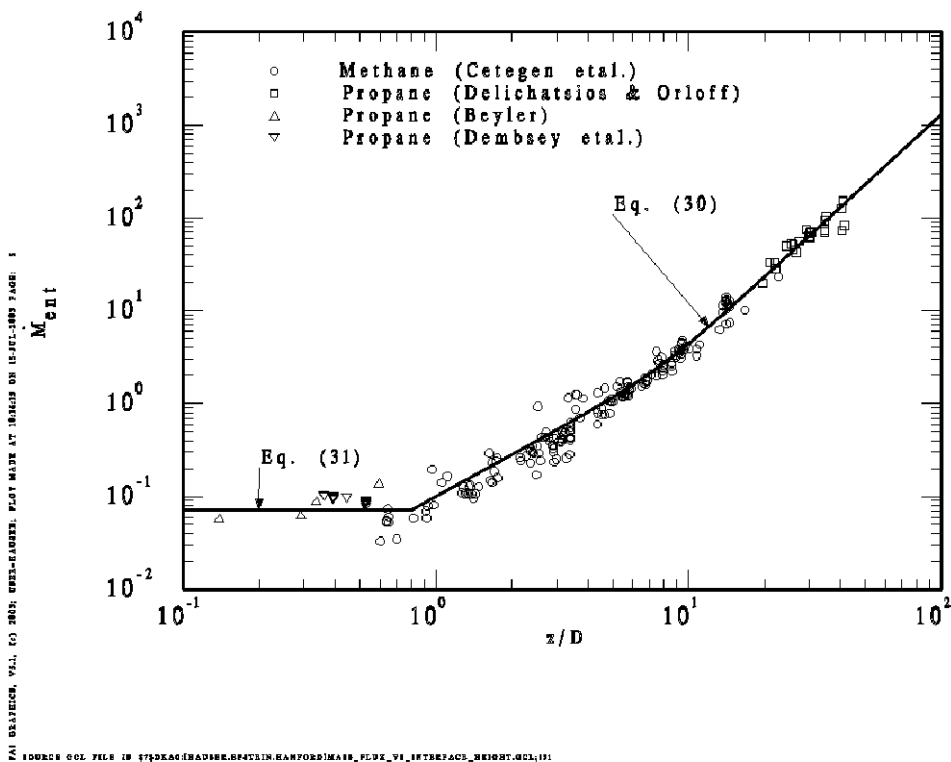


Fig. D3-2 FATE Correlation of experimental data for plume entrainment

D3.2.3 Smoky Layer

To model smoke phenomena, FATE regions are divided into two well-mixed sub-regions, with a hot, smoky layer atop a relatively clean, cool layer referred to here as the lower layer. In terms of the FATE framework, each layer has a unique temperature, pressure, thermal properties, gas composition and aerosol loading. As shown in Figure D3-1, this common idealization simplifies real temperature data to create a distinct, uniform interface, when in reality the temperature data show a transition interval, and instantaneous, local smoky layer thickness is uneven and random. Computer codes or analyses that use this ideal to make quick, straightforward calculations are referred to as zone models. The focus of modeling compartment fires then is to predict smoky layer thickness (interface location) and average temperature, knowing heat release rate and boundary conditions for heat transfer and inter-compartmental flows.

D3.2.4 Radiation Heat Transfer Network

Radiation heat transfer is modeled between surfaces comprising an enclosure, also called a network. Networks may be comprised of heat sink surfaces, a liquid pool surface, gas between surfaces, and a fire source if the fire model is active. Two major components of the radiation network model are calculation of view factors and solution of the network equations.

Radiation heat transfer may be considered in a simple form between heat sink and liquid pool surfaces and the gas region, i.e., no surface-to-surface radiation. This is the optically thick model that assumes all radiation emitted from a surface is absorbed by the gas. The radiation network model is used to override the optically thick model because gas is often not optically thick, and in some situations it may be practically transparent. The current model includes the effect of absorption in the gas, and is able to thereby span the range between transparent and optically thick limits.

Key features of the radiation network model are:

- Radiative exchange among user-defined surfaces and the intervening gas
- Automatic calculation of view factors for common situations, allowing user-input view factors for special situations
- Automatic completion of a view factor matrix using reciprocity and summation laws
- User control over final view factor matrices to consider uncertainty and overcome roundoff, shadow, and approximations
- Provision for expansion of the view factor library

The following logic is used to determine if the network or optically thick models are employed:

1. If a heat sink is not part of a network, then its exchange is only with the region gas as described via the input surface and gas emissivities, the optically thick gas model. This calculation takes place when convection is calculated .
2. If a heat sink is part of a network, its net radiative exchange is calculated and so is the corresponding term for the region gas, which may approach zero in the limit of a transparent gas.

3. Similarly, if a region liquid surface is not part of a network, then its radiation heat transfer is found using the optically thick gas model. If a region liquid surface is part of a network, its net radiative exchange is calculated.
4. Overall control of the radiation models is governed by an active switch specified by input. This allows the network and optically thick models to be toggled, or for radiation to be entirely bypassed.

When a fire is part of the network, its radiative power may either be specified, in which case the power to all other surfaces in the network is apportioned by view factors from the fire. Alternately, the fire temperature may be known (either by specification or calculation), in which case the network solution provides the radiative power from the fire and the power split to each surface in the network.

Note that the fire geometry is assumed to be that of a cylinder of height, H_f , as described in Section 3.2.1. Radiation is then considered from the side of the fire cylinder, but not from the top.

The view factor between two surfaces may be user-specified or automatically calculated from a library of common situations. Calculated view factors are either found by an exact formula or, more commonly, by integration of differential view factor relations. The view factor library employs well-known fundamental relationships and view factor algebra to construct view factors between anticipated surface types, and the model structure is readily expanded to accommodate new situations. Models are listed in Table D3-1 while a handy visual guide to available models appears in Figure D3-1.

The radiant interchange model exploits standard approximations, namely:

1. Gas and surface temperatures are uniform,
2. Gas participation uses a formula for transmittance considering beam length, common gas absorption, and aerosol concentration, and
3. The gas and surfaces obey Kirchoff's law.

If the fire and stratified region models are invoked, the key assumption is that the smoky layer is always optically thick. So, the gray gas considered in the network is the lower layer. The smoky layer acts as a heat sink surface for radiation. Objects are immersed in the smoky layer based upon the fraction of vertical extent within the smoky

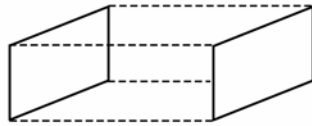
layer. When an object is completely immersed in the smoky layer, its radiative heat transfer is calculated using the optically thick model.

Table D3-1 FATE 2.0 View Factor Summary Table

Model Index	Howell Index ⁽¹⁾	Description
2	C-11	Parallel directly opposed identical rectangles.
3	C-14	Perpendicular rectangles joined by common edge.
4	B-3	Parallel opposed rectangles, arbitrary size and displacement.
5	B-4	Perpendicular rectangles, arbitrary size and displacement.
6	C-18	Rectangular enclosure interior to second such area.
7	n/a	Rectangular enclosure interior to rectangular enclosure end.
11	B-32	Cylinder to rectangle parallel to its axis.
12	B-37	Cylinder to surrounding rectangle in base plane.
13	B-37	Cylinder to rectangle in base plane, non-surrounding.
14	C-77	Cylinder to surrounding annulus in base plane.
15	n/a	Cylinder to exterior cylinder, parallel axes.
16	C-95 C-96 C-97 C-98	Cylinder to concentric cylinder, different heights and elevations. Sub-models are C-95 inner cylinder entirely within outer C-96 inner cylinder extends beyond one end of outer C-97 inner cylinder extends beyond both ends of outer C-98 inner cylinder entirely outside outer (but coaxial).
18	n/a	Cylinder to surrounding non-concentric cylinder.
21	C-40	Opposed identical coaxial circles.
22	C-78	Cylinder interior to self.
23	C-79	Cylinder interior to base.
24	C-87	Cylindrical enclosure to coaxial cylindrical enclosure.
25	C-81	Cylindrical enclosure to enclosure end.
26	n/a	Rectangular enclosure to cylinder: Uses Formula 11, 4 times.
27	B-14	Rectangle to circle, plane of rectangle parallel to plane of circle.
28	B-15	Rectangle to circle, plane of rectangle perpendicular to plane of circle.

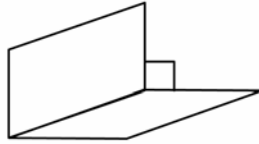
⁽¹⁾ www.me.utexas.edu/~howell/ "A Catalog of Radiation Heat Transfer Configuration Factors," 2nd Edition, by John R. Howell, University of Texas at Austin.

Model 2



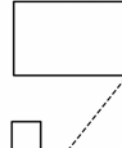
MGP31004-2

Model 3



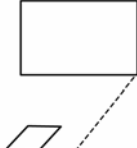
MGP31004-3

Model 4



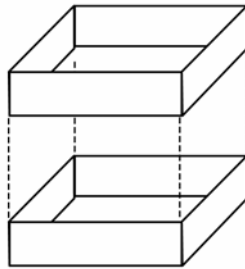
MGP31004-4

Model 5



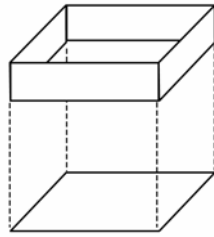
MGP31004-5

Model 6



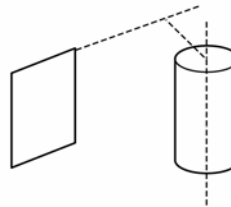
MGP31004-6

Model 7



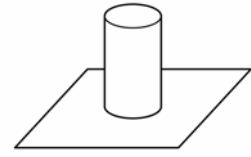
MGP31004-7

Model 11



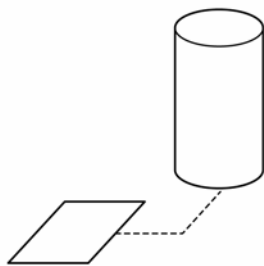
MGP031004-11

Model 12



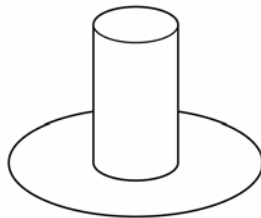
MGP031004-12

Model 13



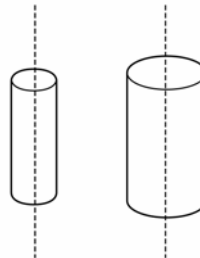
MGP031004-13

Model 14



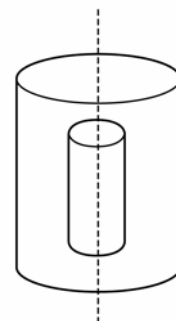
MGP031004-14

Model 15



MGP031004-15

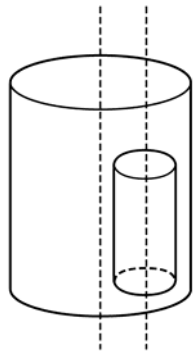
Model 16



MGP031004-16

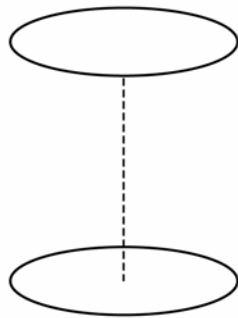
Fig. D3-3 Handy Visual Guide to View Factor Models Available

Model 18



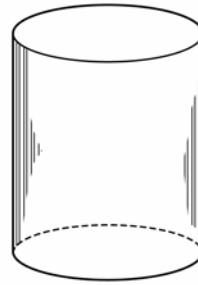
MGP031004-18

Model 21



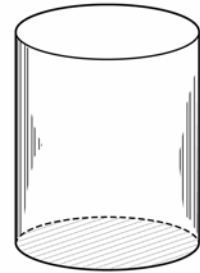
MGP031004-21

Model 22



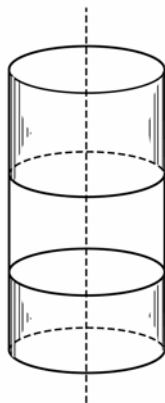
MGP031004-22

Model 23



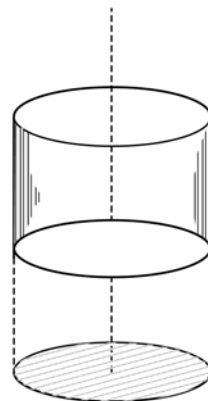
MGP031004-23

Model 24



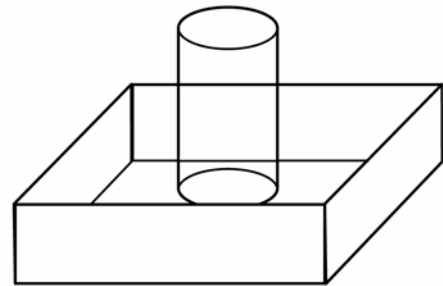
MGP031004-24

Model 25



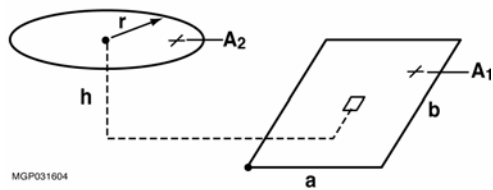
MGP031004-25

Model 26



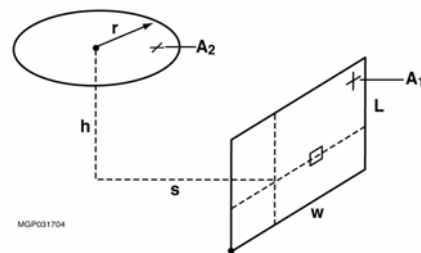
MGP031004-26

Model 27



MGP031604

Model 28



MGP031704

Fig. D3-2 Handy Visual Guide to View Factor Models Available (concluded)

D3.3 FATE Blind Calculations for BE-4

Although the ICFMP offered a period for submission of blind benchmark calculations, no blind calculations were performed with the FATE computer program. All FATE results are provided below as part of the open benchmarking process.

D3.4 FATE Open Benchmark Calculations for BE-4

FATE version 2.14 calculations are presented below for BE-4 Tests 1 and 3. Calculations are performed on a personal computer with a 1.39 GHz AMD Athlon processor and a DOS/Windows XP operating environment. A typical run time for the model described in Section 2 is 120 seconds of CPU time for a 2000 second simulation, or 17 times faster than real time.

D3.4.1 BE-4 Case 1 FATE Open Benchmark Results

Case 1 is characterized by a kerosene fire with a steady state power in the range of 3 to 3.5 MW, peak fan vent flows of 2 m³/sec, a doorway opening of 0.7 m by 3.0 m, and a multi-layer target in close proximity to the fire source. As will be shown, these conditions result in a flame that extends well into the smoky region and significant variation in temperatures across the x-y plane. Thus, this case tests the FATE fire and heat transfer models under conditions of,

1. Extremely high fire power (relative to typical NPP fires)
2. Flame submerged in the smoky layer
3. Varying ventilation and leakage flows

In addition, this test provides insights into the use of a single region with smoky and lower layer sub-regions to model high power fires in small compartments.

FATE calculations for BE-4 Case 1 are presented in Figures D3-4 through D3-24. From these figures, the following key insights are obtained.

As with other benchmark tests, the BE-4 exercise demonstrates that the two most influential aspects of the input are the fire power and the room ventilation behavior. The

agreement shown in the following figures was only obtained after adjustments to the fire power, fan flow rates, and air mixing were performed.

Figure D3-4 compares the measured total fan volumetric flow to the calculated flow. When a constant flow area was used in the FATE model, the ventilation flow after 700 seconds was significantly over predicted. For a constant flow area, as the fire power remains constant or slightly increasing, one would expect that the fan ventilation flow would also remain constant or would increase slightly. Rather, the data showed a significant decrease in the fan flow beginning around 700 seconds. For this reason, the fan ventilation flow was considered to be a boundary condition for the current calculation and the fan vent area was decreased by 10% in steps every 100 seconds from 700 seconds to 1400 seconds. The initial vent area was set at 0.176 m^2 and the final vent area at 1400 seconds was set at 0.0352 m^2 . This variation in the vent area is clearly noticeable in Figure D3-4 by the step decreases in calculated fan vent flow rate. Overall, this simple model for the fan boundary condition achieved reasonable agreement with the test data.

Doorway flows are presented in Figures D3-5 and D3-6. The measured flows were estimated by reducing the reported velocities from doorway velocity probes V3 through V8. A volumetric flow rate was assigned to each measurement by taking the product of the reported velocity and 1/6 of the door area (0.35 m^2). The net volumetric flow was then taken as the sum of the individual volumetric flows and is assumed to represent the unidirectional flow rate. This is based on the assumption that the door flow consists of a counter-current flow which exchanges equal volume amounts through the door and a unidirectional flow. The fire compartment gas density was taken as 0.396 kg/m^3 for purposes of calculating the unidirectional mass flow rate out of the room. Since the net, or unidirectional flow is out of the room (Figure D3-5), the counter-current flow is taken as the sum of the inflows which were reported on probes V3, V4, and V5 (Figure D3-6). Probe V5 indicated intermittent inflow and outflow, however only the inflows were used for the counter-current flow estimation. The air density was taken as 1.2 kg/m^3 . Even though the doorway area input to FATE is computed as 100% of the geometric areas with no reductions taken for entrance and exit losses, the FATE unidirectional flow rate calculation under predicts the estimated doorway flow rates. The counter-current flows show better agreement.

Figures D3-7 and D3-8 present the smoky layer height and the smoky layer gas concentrations. For this particular geometry – a high powered fire in a relatively small and

under ventilated compartment – the measured gas concentration may be a better measure of room conditions rather than the smoky layer height. Reasonable agreement is indicated between the calculated and measured gas concentrations. Exact agreement is not expected since the measurement is performed at a single location ($x = 0.10$ m, $y = 1.90$ m, $z = 3.80$ m) and the FATE calculation represents an average value for the entire smoky layer. This agreement was obtained by modeling the door inflows (due to either uni-directional or counter-current flows) to be distributed equally between the smoky and lower layer. A mechanistic mixing model is an area for consideration for future code development.

Figure D3-7 also presents the calculated flame height. As shown, the flame height extends well into the smoky region. Thus, uncertainties related to air mixing and oxygen consumption are of increased significance for this particular fire geometry.

Figures D3-9 through D3-11 present the measured and calculated room gas temperatures. A key insight from these figures is that there is a substantial variation in the temperature along the x-y plane. For example, at the 1.5 m elevation (Figure D3-9), the maximum temperature variation is approximately 300 C. At the 3.5 and 5.2 m elevations (Figure D3-10), the temperature variations are 150 C and 100 C, respectively. As the elevation increases, the temperature variation decreases. At the upper elevations (Figure D3-11) the lowest temperatures are reported near the front of the room (i.e., between the doorway and the fire) while the highest temperatures are reported near the back of the room.

This temperature variation along the x-y plane is promoted by the room geometry in which the fire essentially blocks free inflow from the door (fire pan width is larger than the narrow doorway width). As shown in the figures, while the FATE smoky layer calculations provide reasonable estimates of the average gas temperatures, a two or three region model may be more appropriate to account for the x-y plane temperature variations. Because the lowest thermocouples were located at the 1.5 m elevation and were submerged in the smoky layer, there is no appropriate comparison for the FATE lower layer gas temperature indicated in the figures.

Figures D3-12 and D3-13 compare calculated and measured wall surface temperatures. As shown in Figure D3-12 (wall temperature at lower elevations), the peak wall temperatures in the back of the room are consistent with the peak gas temperatures presented in Figure D3-9, while the side wall temperatures are about 100 C lower. This

may be influenced by air circulation which may be diminished toward the back of the room. The FATE wall strip heat sink model presents an average temperature of all four side walls at a particular elevation, therefore it is not surprising that peak wall temperatures are not predicted. Furthermore, the FATE wall presented in Figure D3-12 is located between the 1.4 m and 1.9 m elevations, which are in the FATE lower layer. A key to accurately predicting heat sink temperatures is proper modeling of the heat sink location relative to the smoky layer. Also, because of the significant temperature variation in the x-y plane, a multi node compartment may be appropriate.

The under prediction of wall temperatures at upper elevations, presented in Figure D3-13 is a result of the overall lower predicted smoky layer gas temperature (Figure D3-10). This will be addressed subsequently.

Figures D3-14 through D3-17 present measured and calculated target temperatures. The concrete probe temperature (Figure D3-14) is somewhat under predicted, however in the FATE calculation, the probe remains in the lower gas layer, while test data indicates the probe is submerged in the smoky layer. Figure D3-15 shows reasonable agreement between FATE calculations and measured waste container surface temperature. The slight under prediction may be a result of the overall lower prediction in gas temperatures. The FATE model of the waste container includes three heat sinks at different azimuthal locations to represent the half of the can facing the fire. The solid line in the plot represents the center heat sink most directly facing the fire, while the dotted and dashed lines represent the side portions of the waste can not directly facing the fire. The significant heat up of the can surface, even though the waste can is located in the lower gas layer, is an indication of the radiative power received from the fire.

Figures D3-16 and D3-17 compare the concrete fill temperatures. These are subject to some uncertainty regarding contact resistance between the metal can and the concrete. Since the can outer surface temperature is under predicted, it is no surprise that the concrete temperatures are also under predicted. However, the proper heat conduction behavior through the concrete is exhibited by the FATE code.

To perform a bounding analysis for nuclear power plant applications, the many uncertainties associated with a room fire must be addressed. Uncertainties identified in this benchmark include the fire power, ventilation flows, and air mixing. Perhaps the most straightforward approach to addressing uncertainties to obtain a bounding assessment

appropriate for nuclear power plant applications is to increase the fire power. Thus, a sensitivity calculation has been performed which increases the nominal fire power by 40% (i.e., increases the nominal fuel burn rate by 40%). Sensitivity results are presented in Figures D3-18 through D3-24.

First, in Figure D3-18, the increased fuel burn rate is compared to the nominal curve used in the base case calculations and the fuel burn data. As shown, the 40% increase represents an upper bound to the data, so a 40% power increase is not unreasonable for a sensitivity calculation.

Figure D3-19 demonstrates that the use of a realistic upper bound to the fuel burn rate results in a bounding prediction of gas temperatures. This, in turn, results in reasonable upper bound estimates of all wall and target heat sink temperatures, as shown in Figures D3-20 through D3-24.

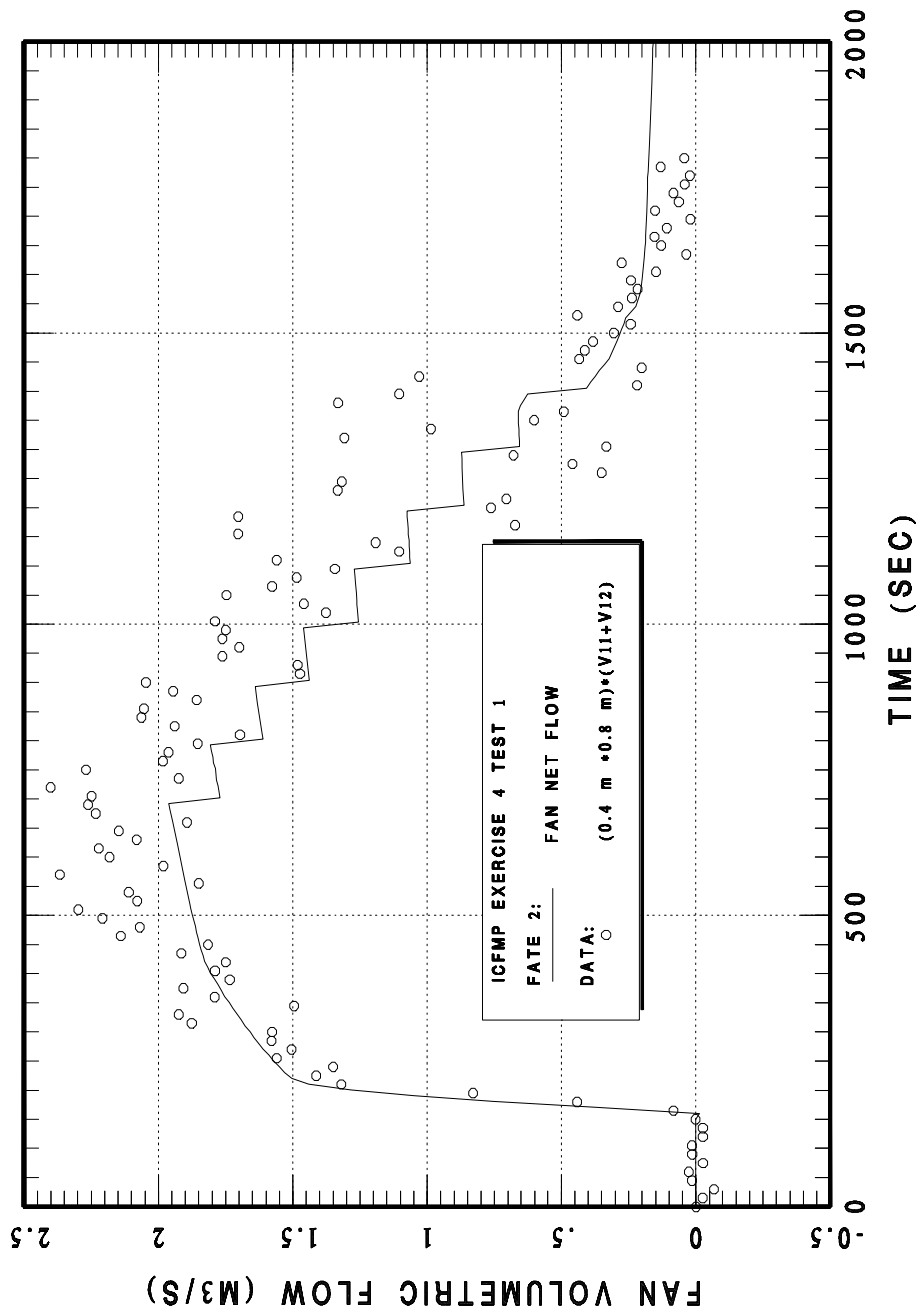


Fig. D3-4 BE4 Case 1 Vent Fan Volumetric Flow Rate Modeled as a Boundary Condition

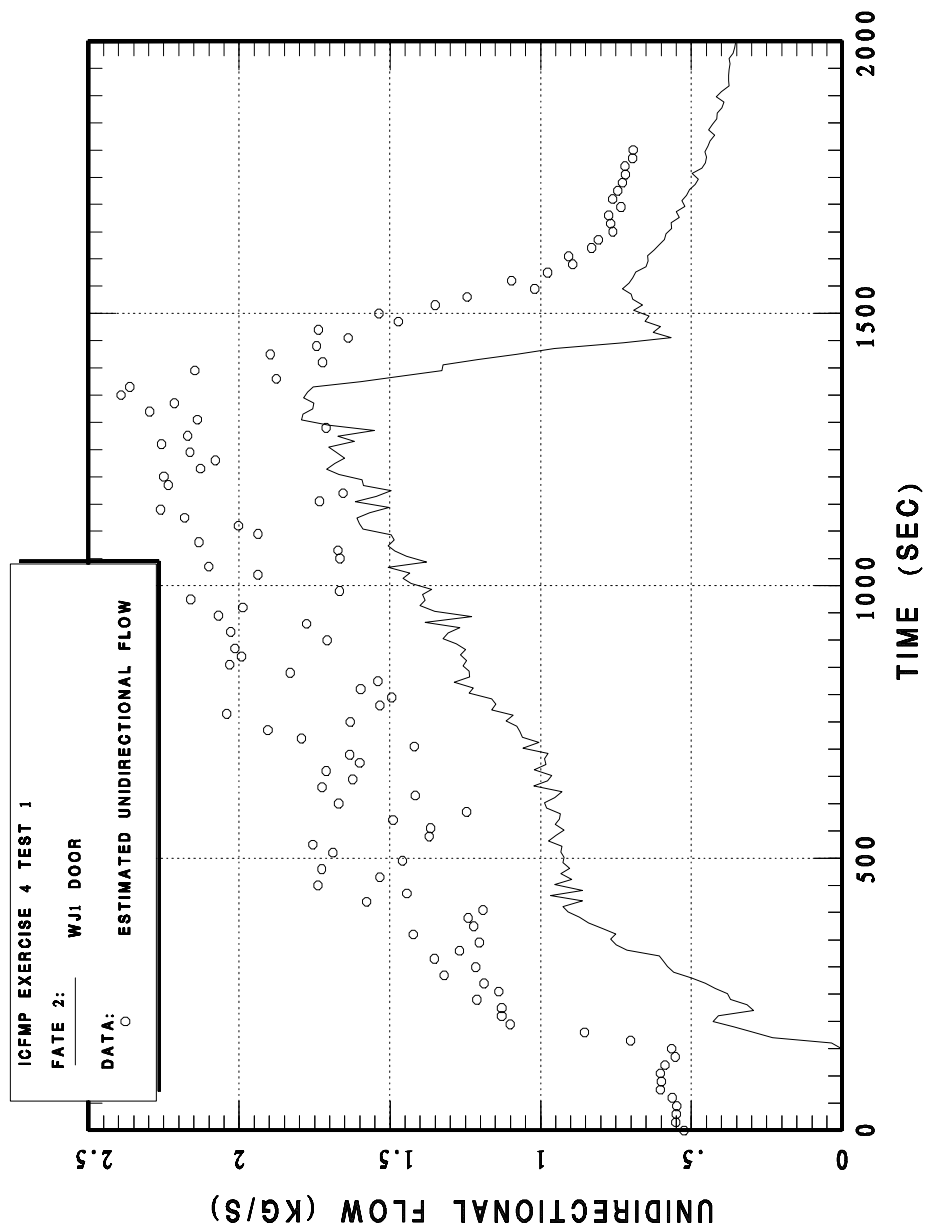


Fig. D3-5 BE4 Case 1 doorway unidirectional volumetric flow rate (positive flows are out of fire compartment)

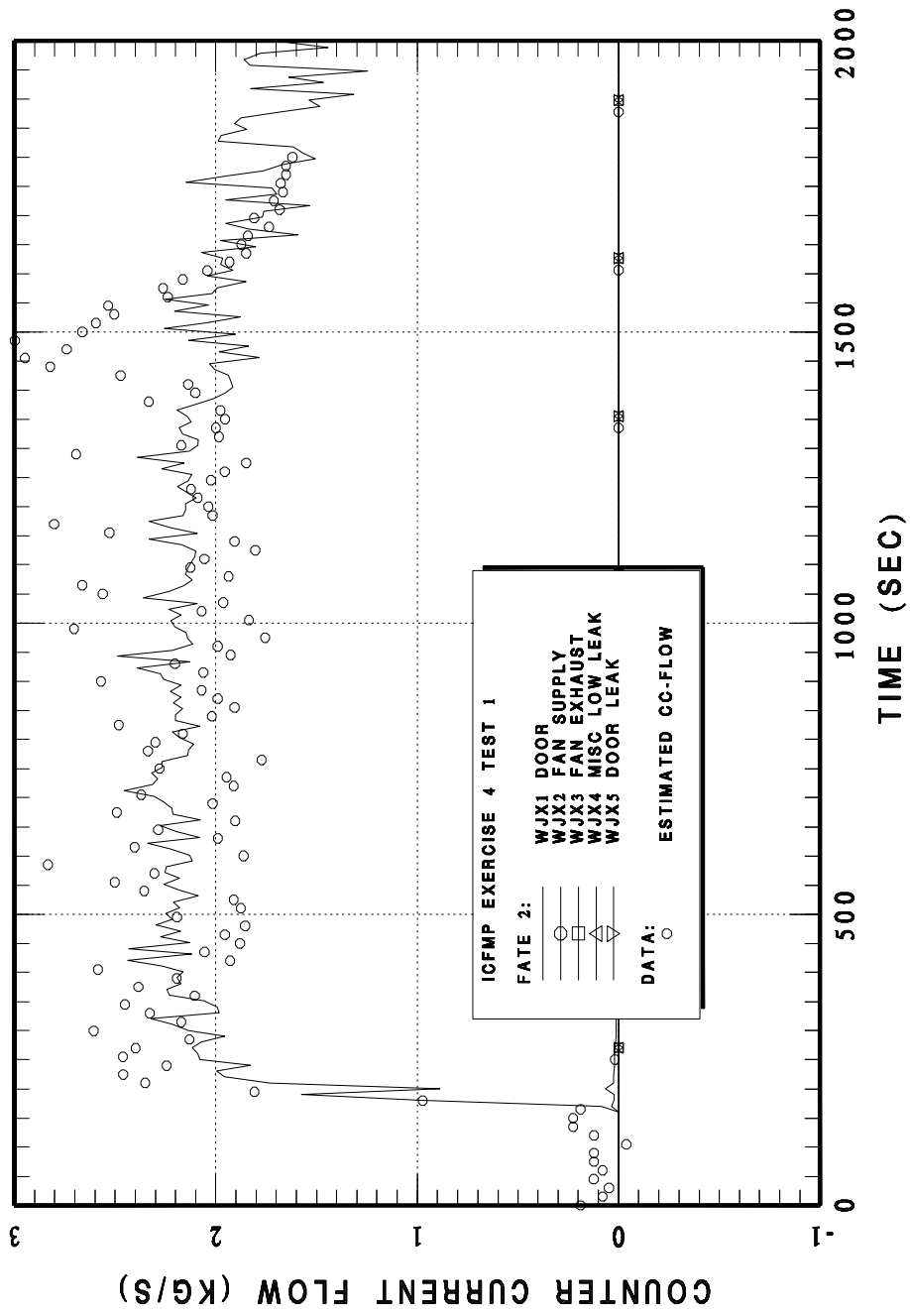


Fig. D3-6 BE4 Case 1 doorway counter-current flow rate

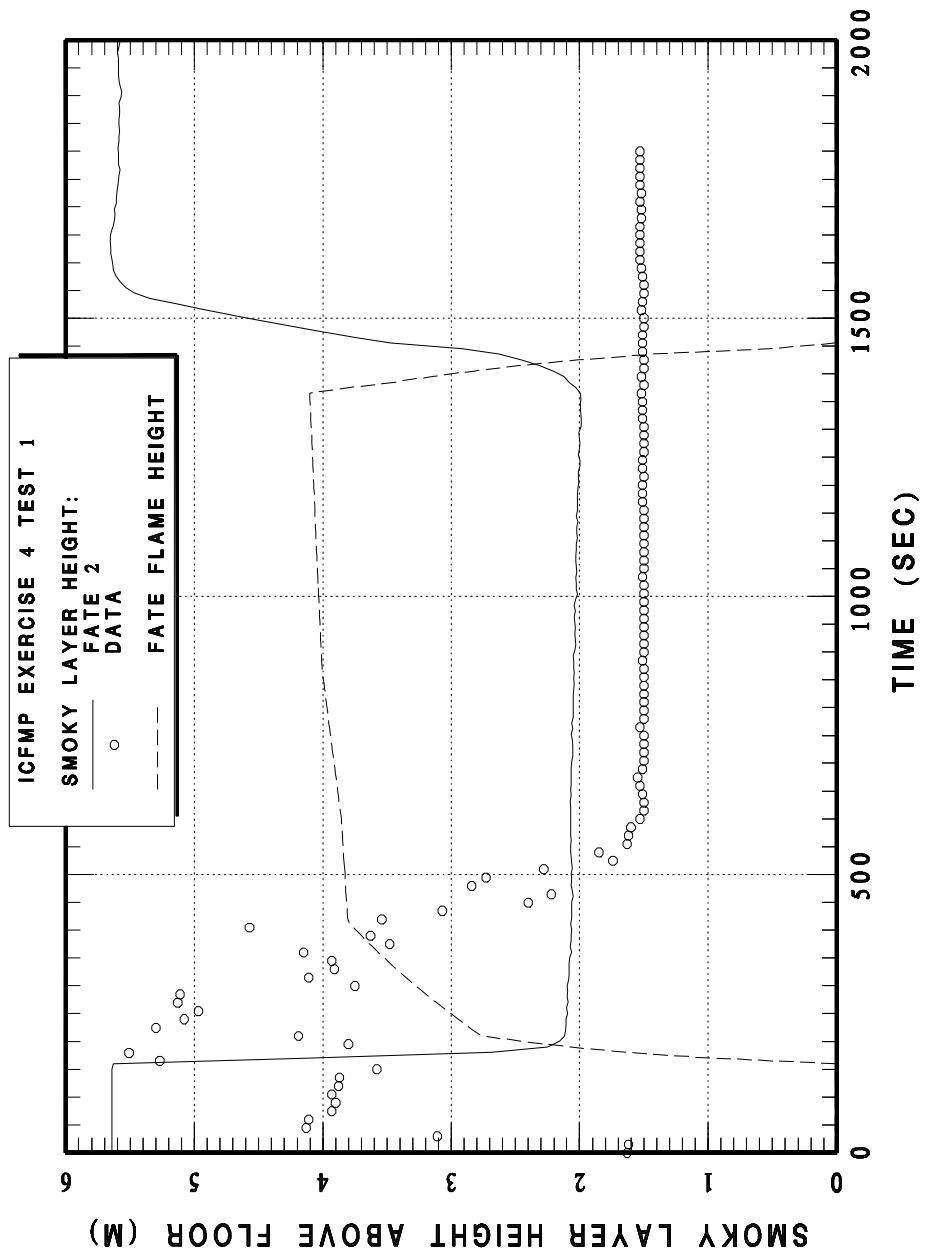


Fig. D3-7 BE4 Case 1 smoky layer and flame height

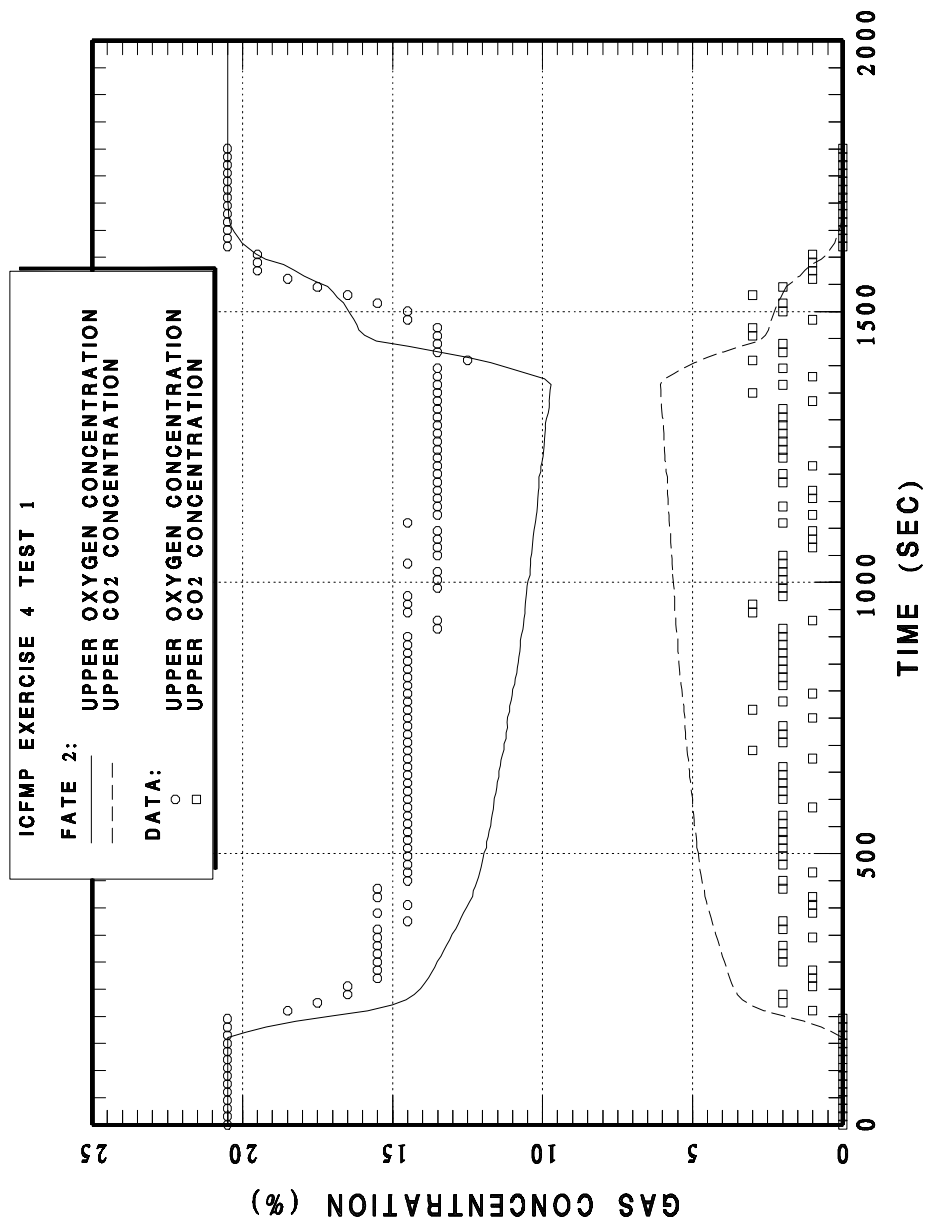


Fig. D3-8 BE4 Case 1 smoky layer gas concentrations (test data measured at coordinate $x = 0.10 \text{ m}$, $y = 1.90 \text{ m}$, $z = 3.80 \text{ m}$)

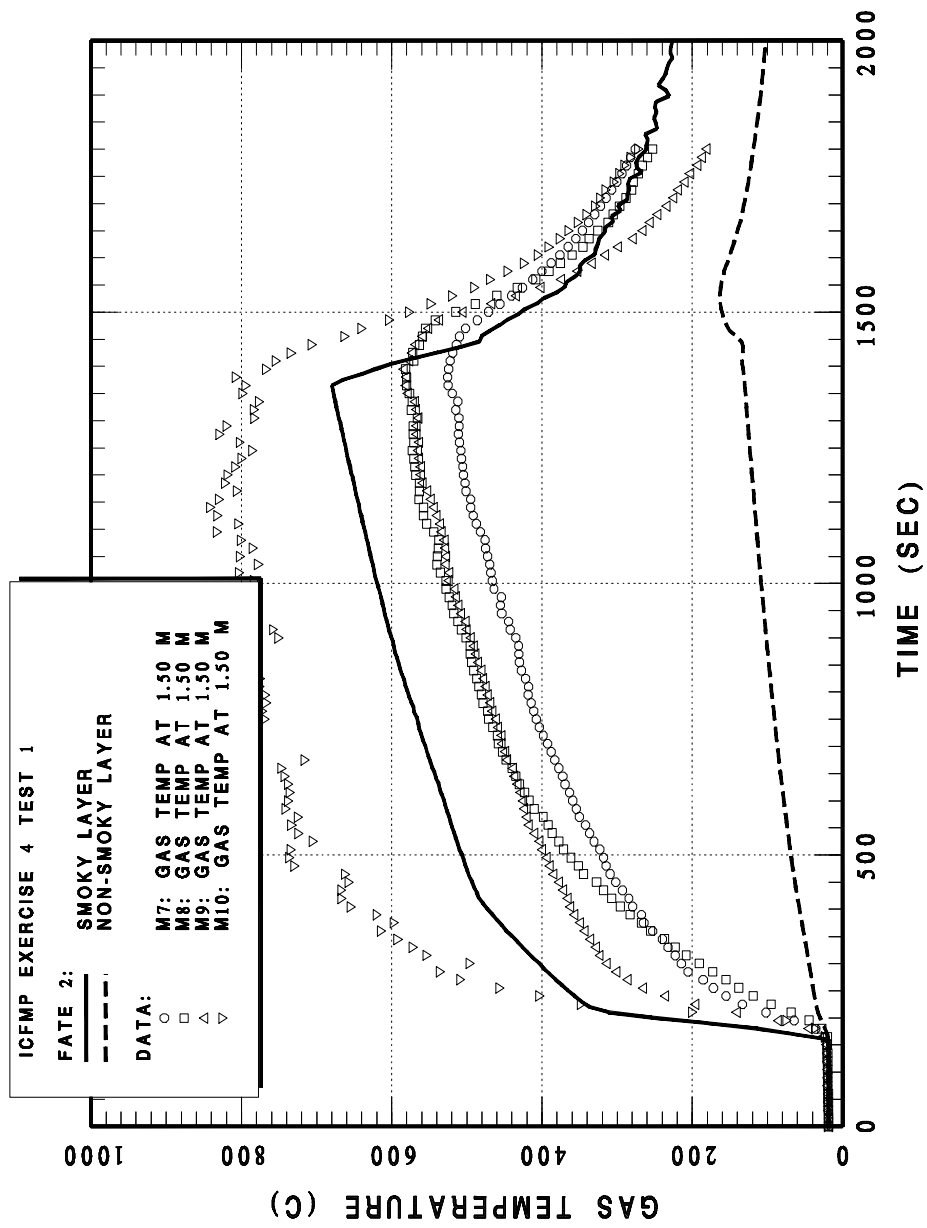


Fig. D3-9 BE4 Case 1 gas temperatures at 1.5 m

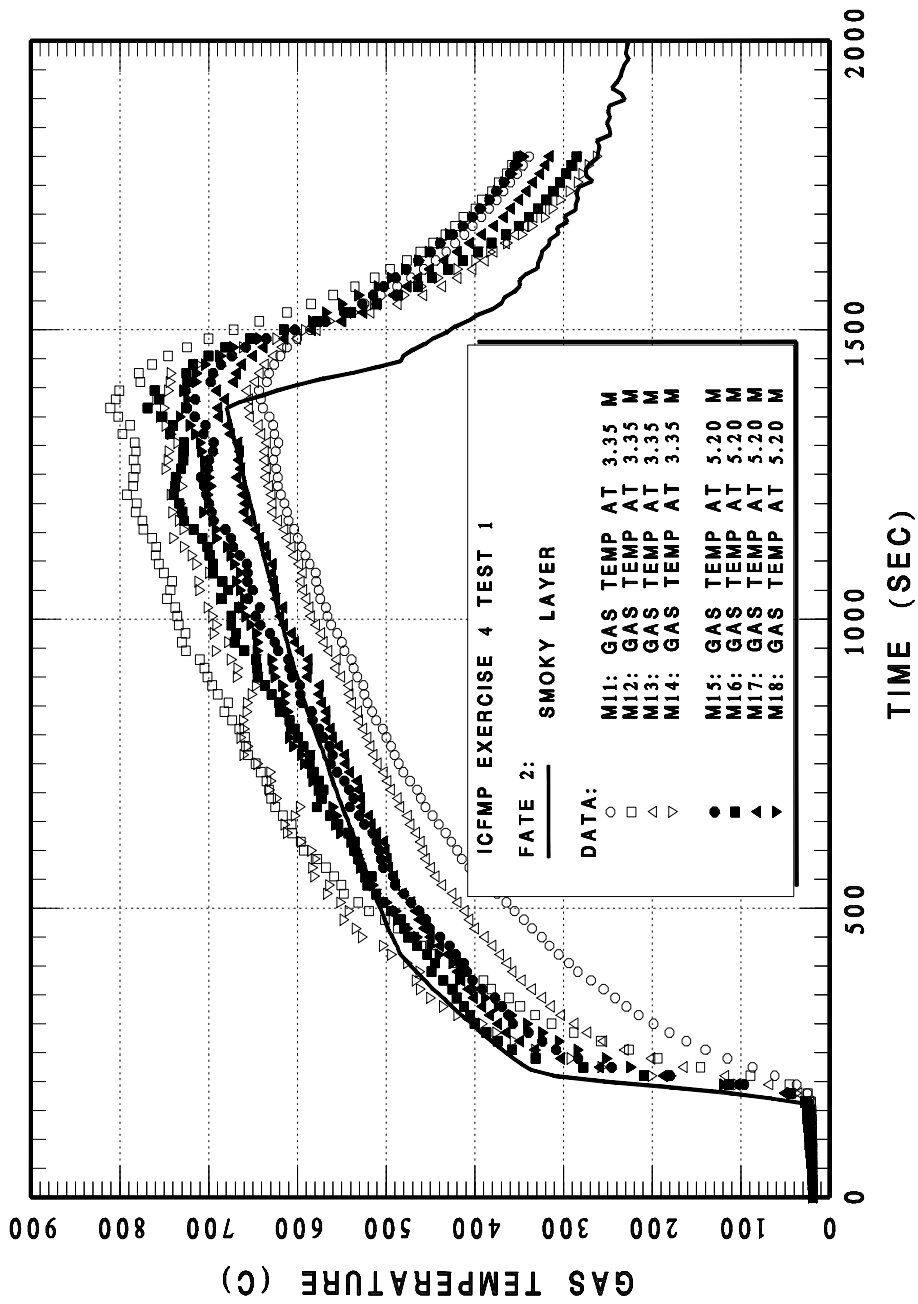


Fig. D3-10 BE4 Case 1 gas temperatures at 3.35 m and 5.20 m

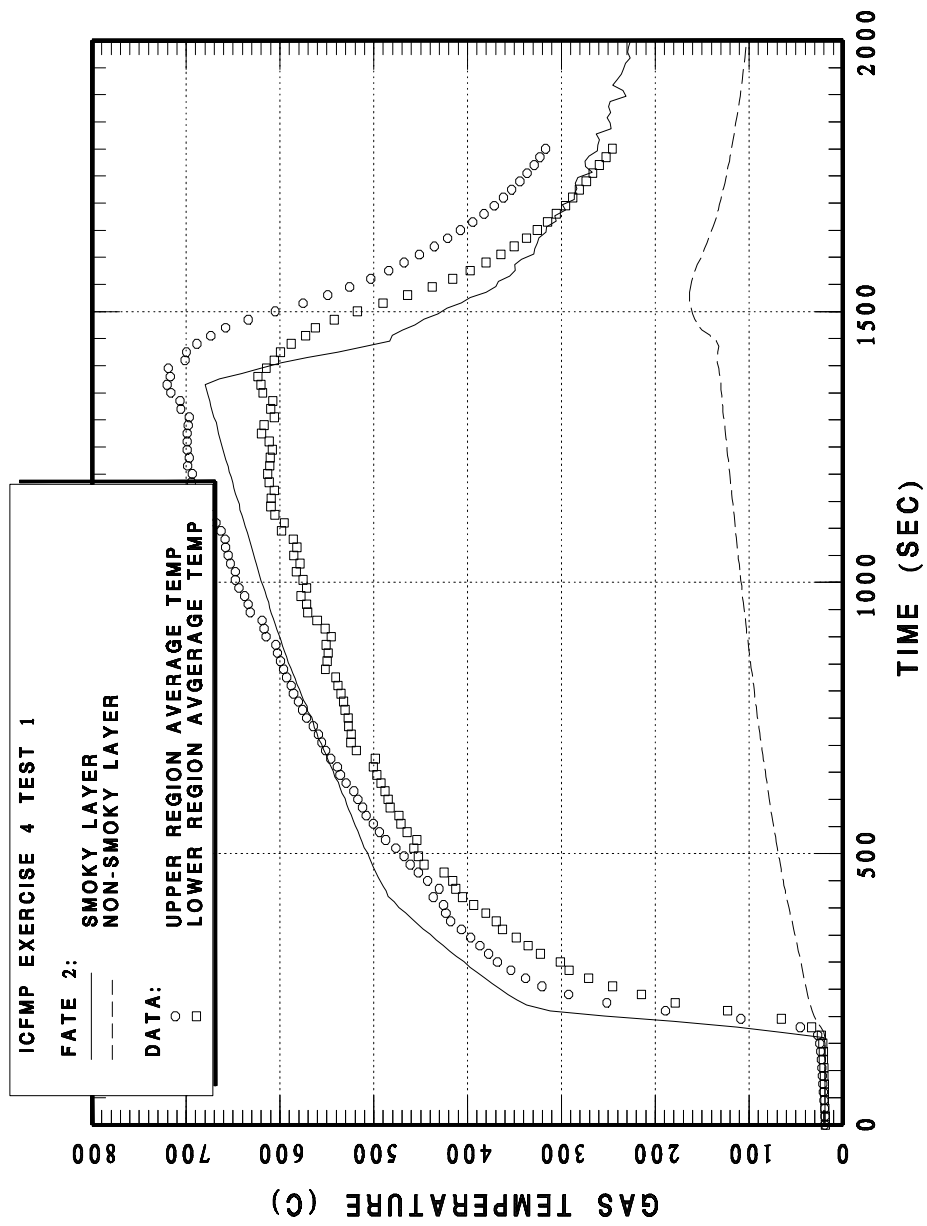


Fig. D3-11 BE4 Case 1 average gas temperatures

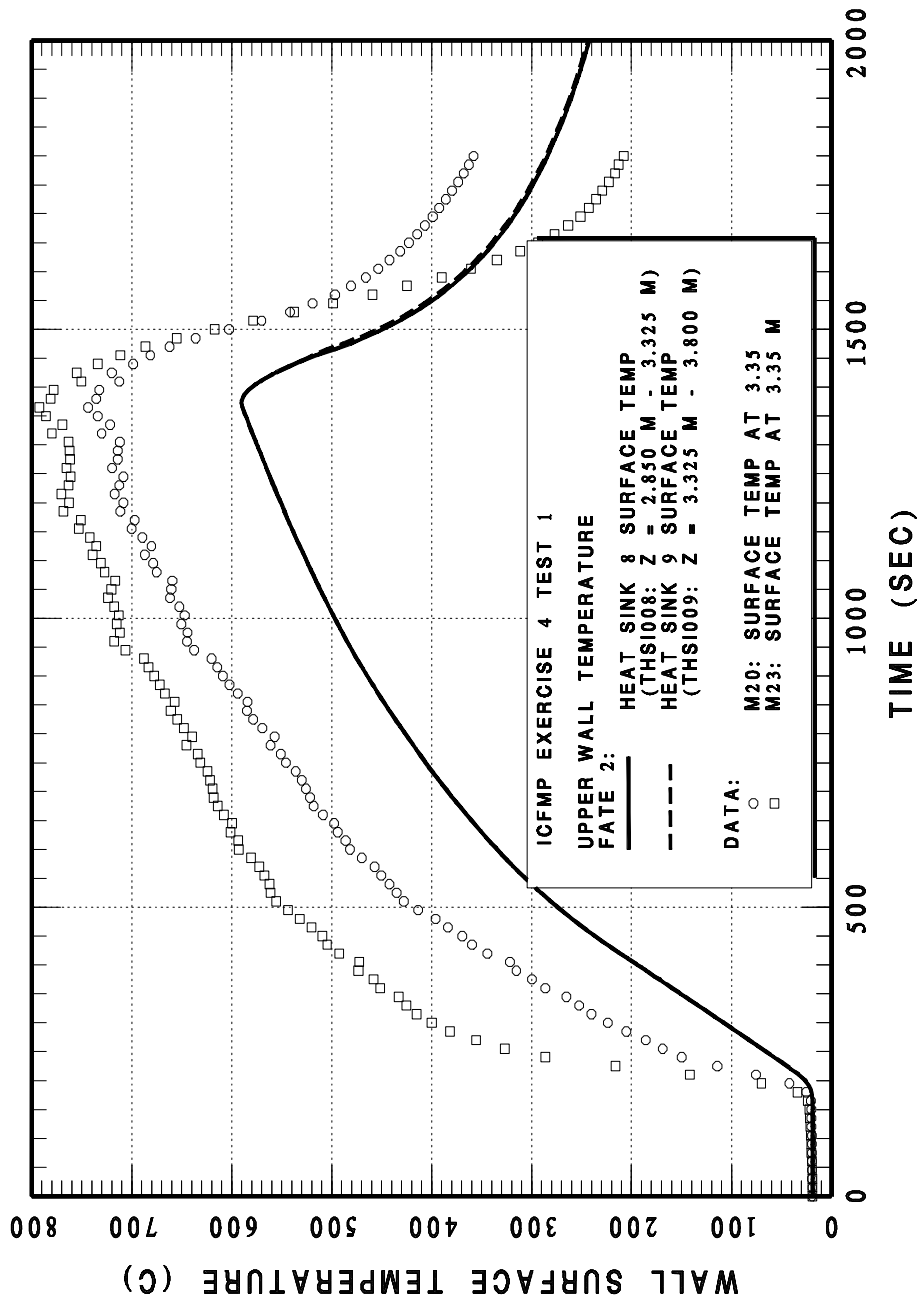


Fig. D3-13 BE4 Case 1 wall surface temperature at upper elevations.

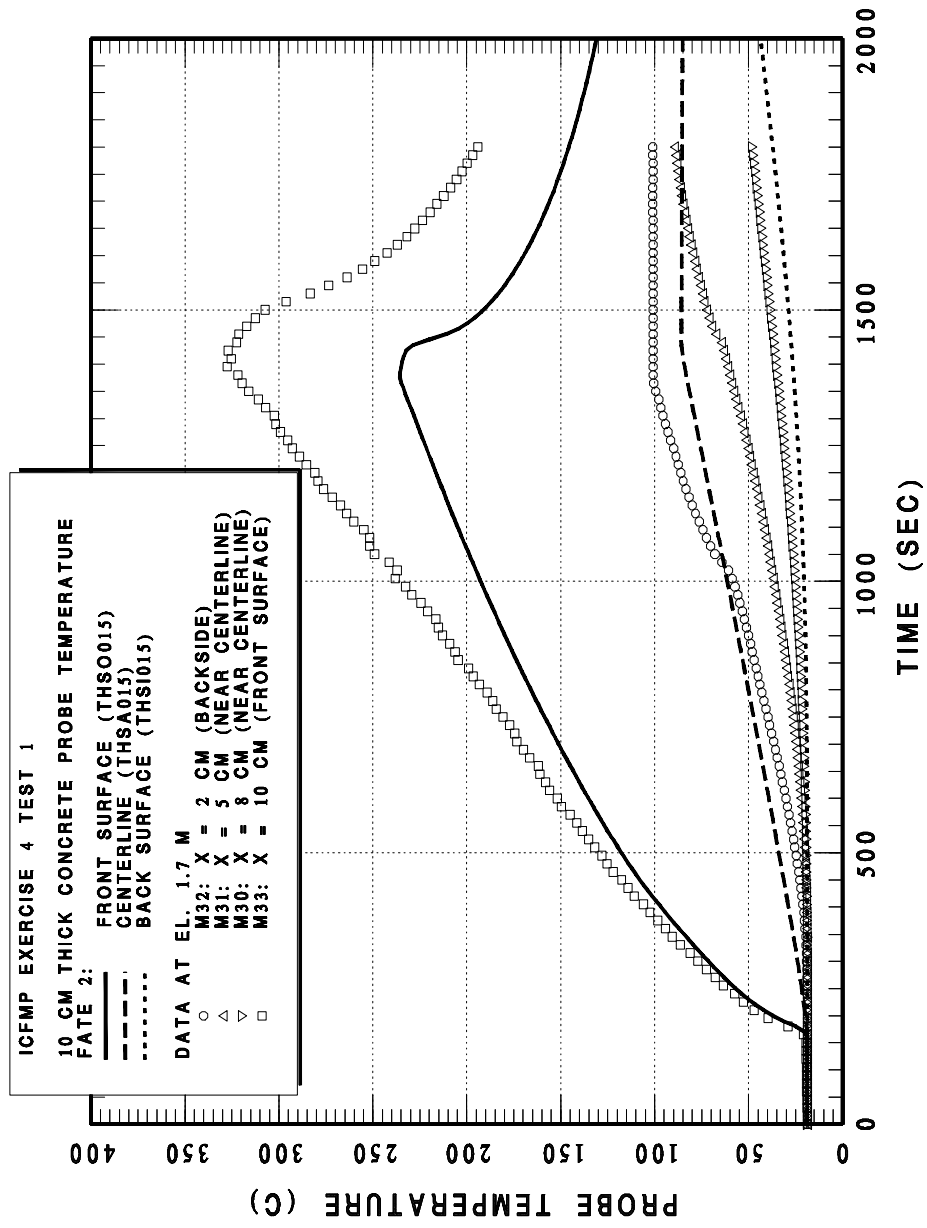


Fig. D3-14 BE4 Case 1 concrete probe temperatures

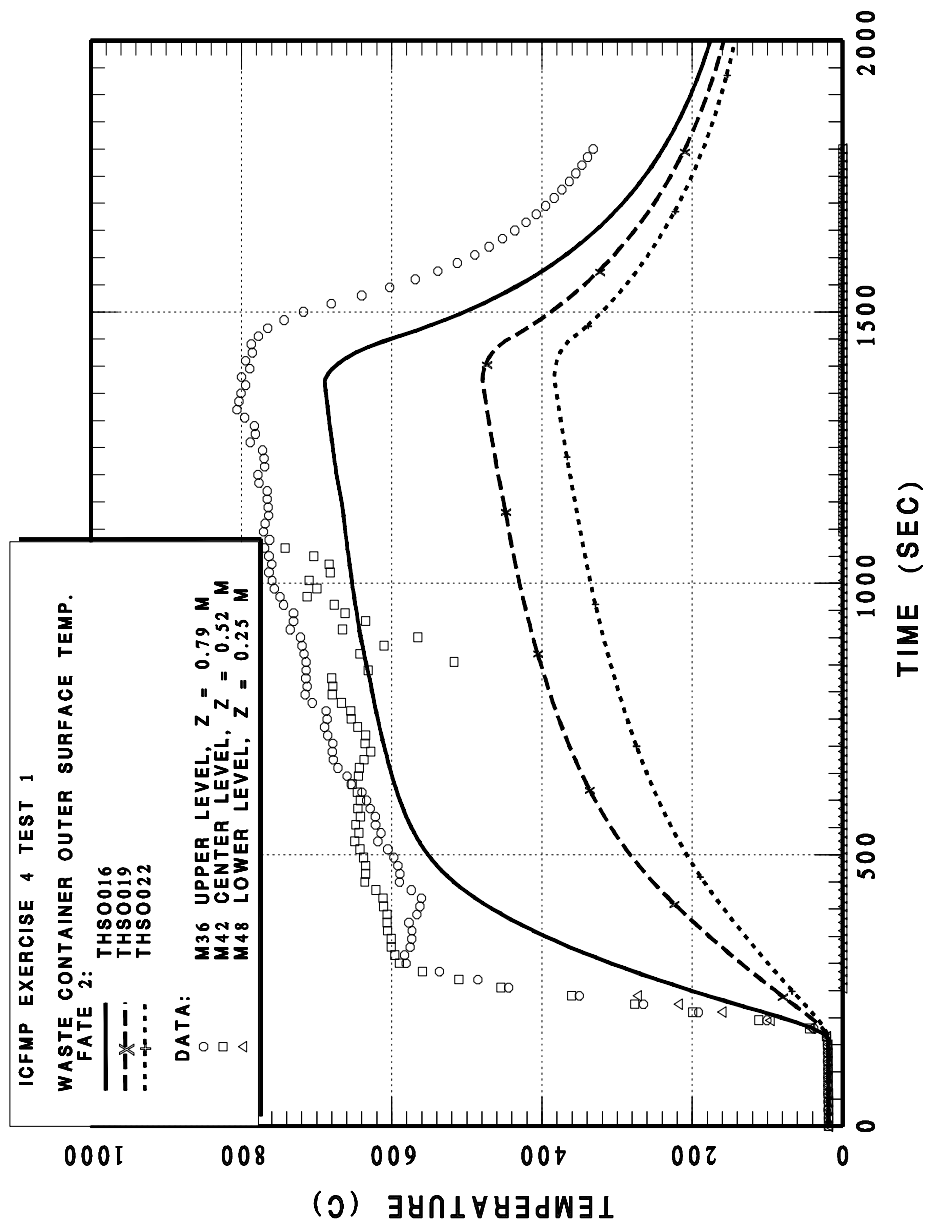


Fig. D3-15 BE4 Case 1 waste container metal surface temperature

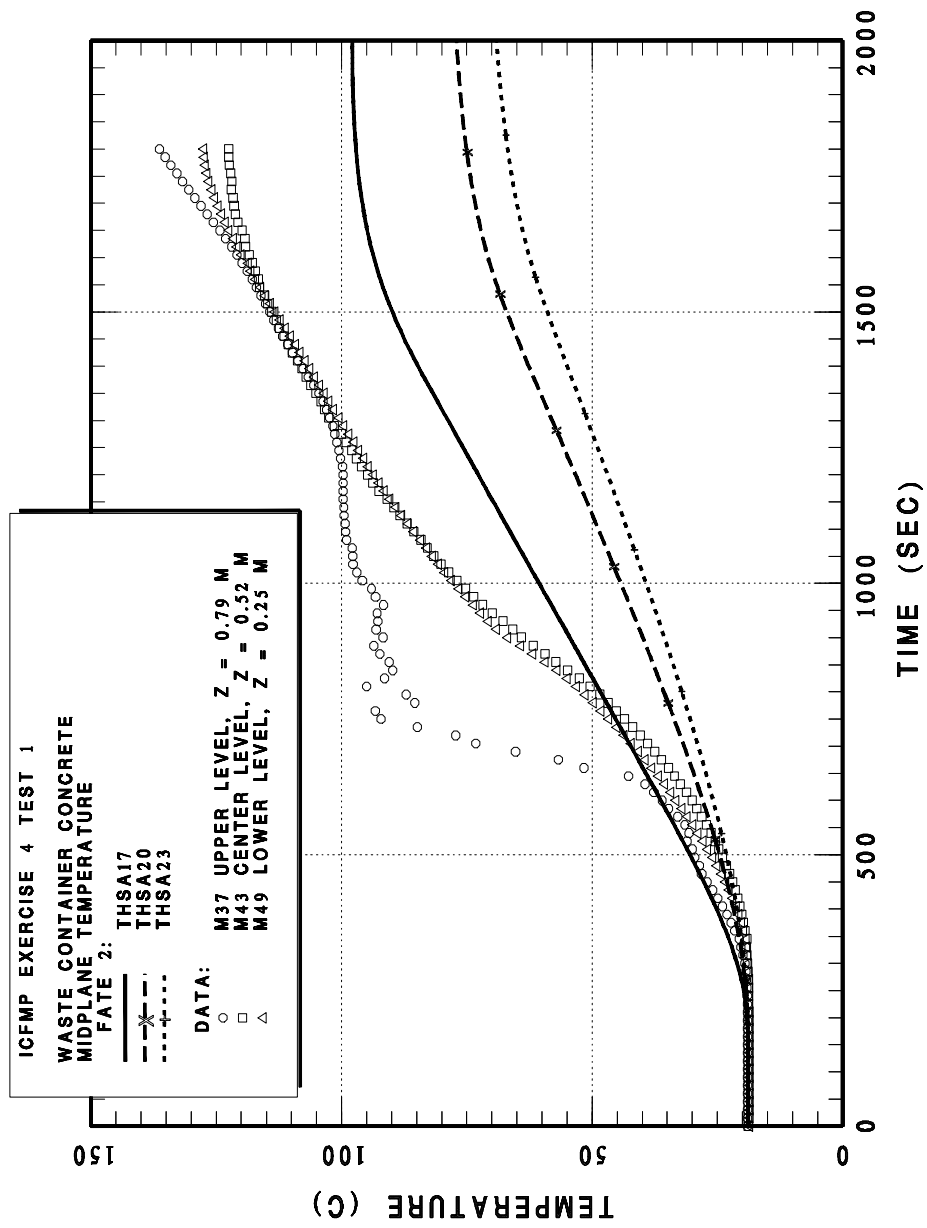


Fig. D3-16 BE4 Case 1 waste container concrete midplane temperature

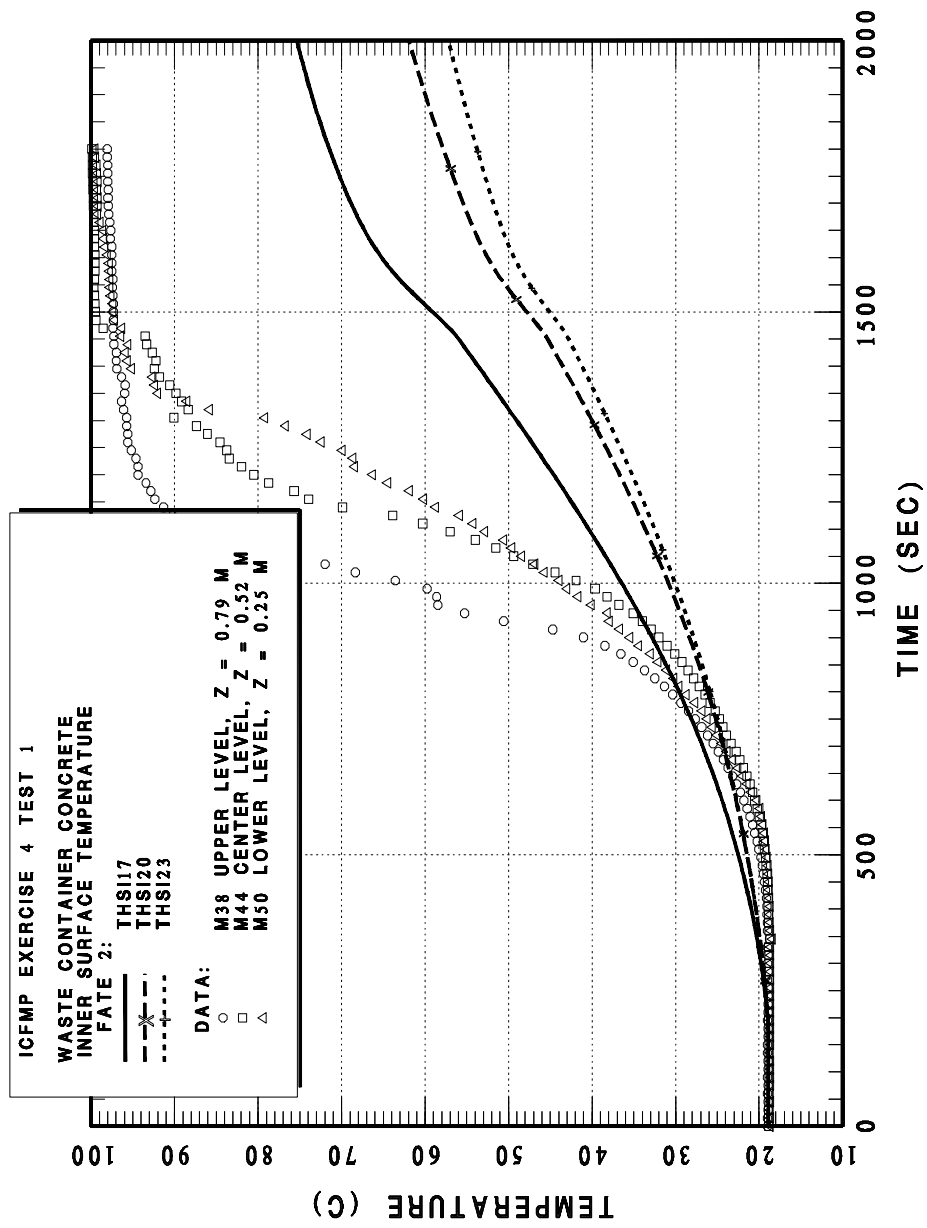


Fig. D3-17 BE4 Case 1 waste container concrete inner surface temperature

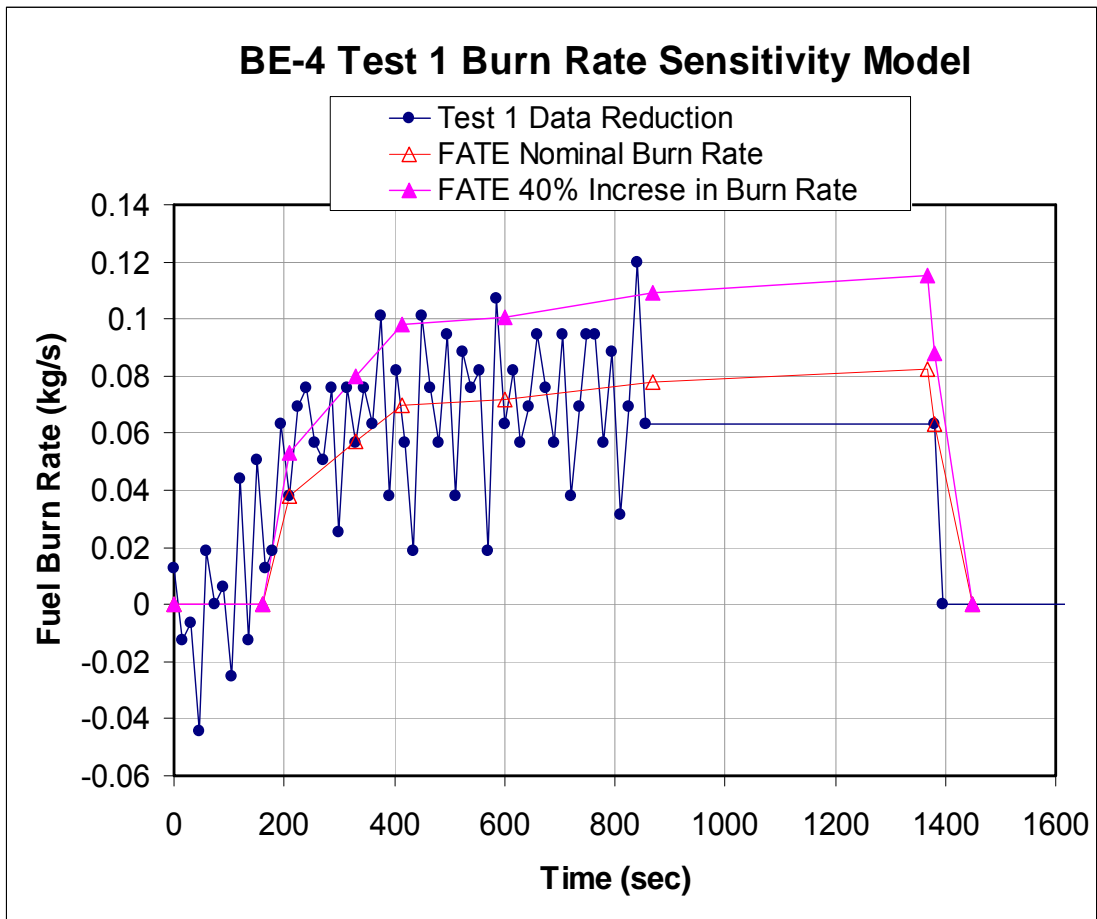


Fig. D3-18 BE4 Case 1 40% Power Increase Sensitivity: Burn Rate

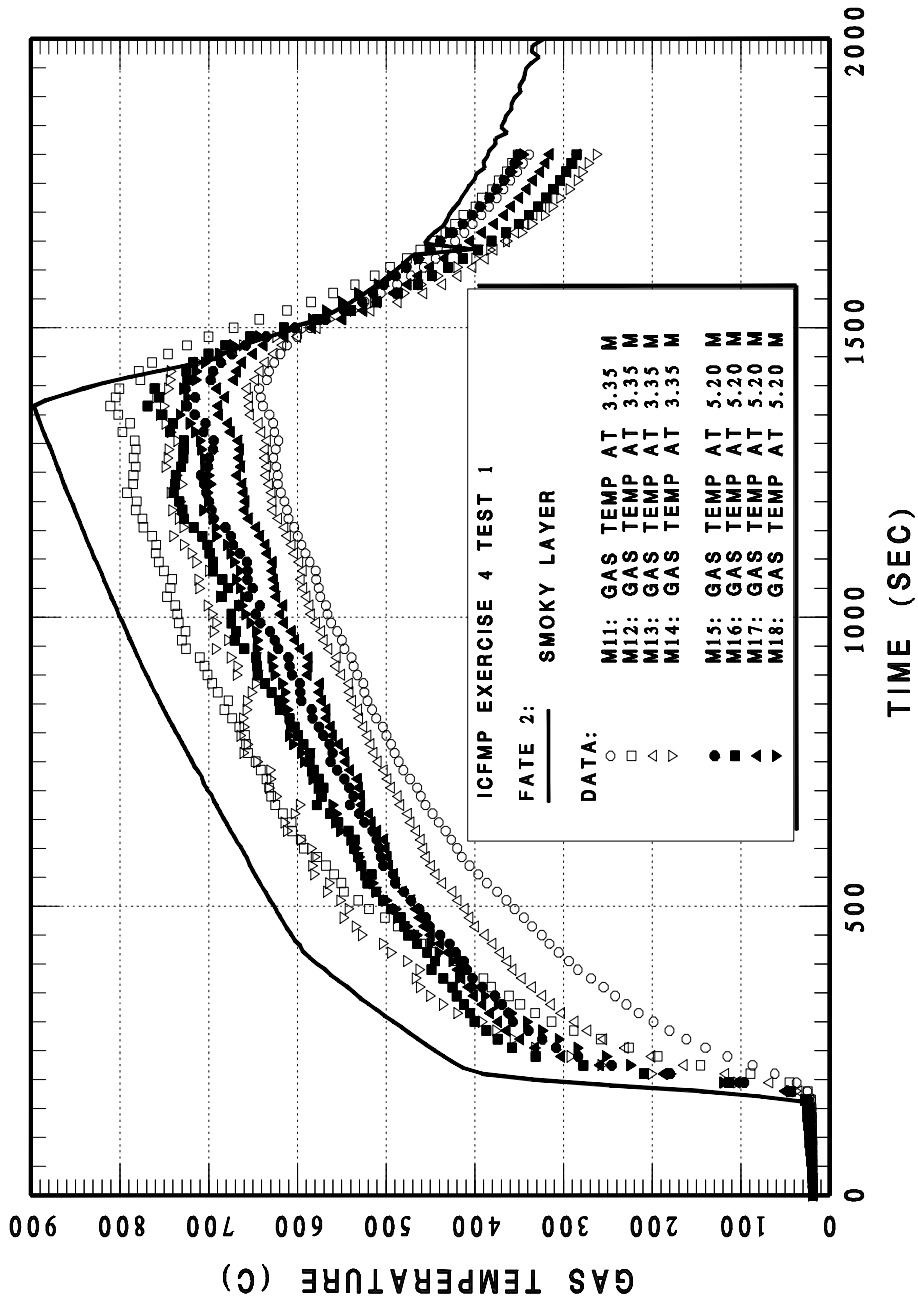


Fig. D3-19 BE4 Case 1 40% Power Increase Sensitivity: upper gas temperature

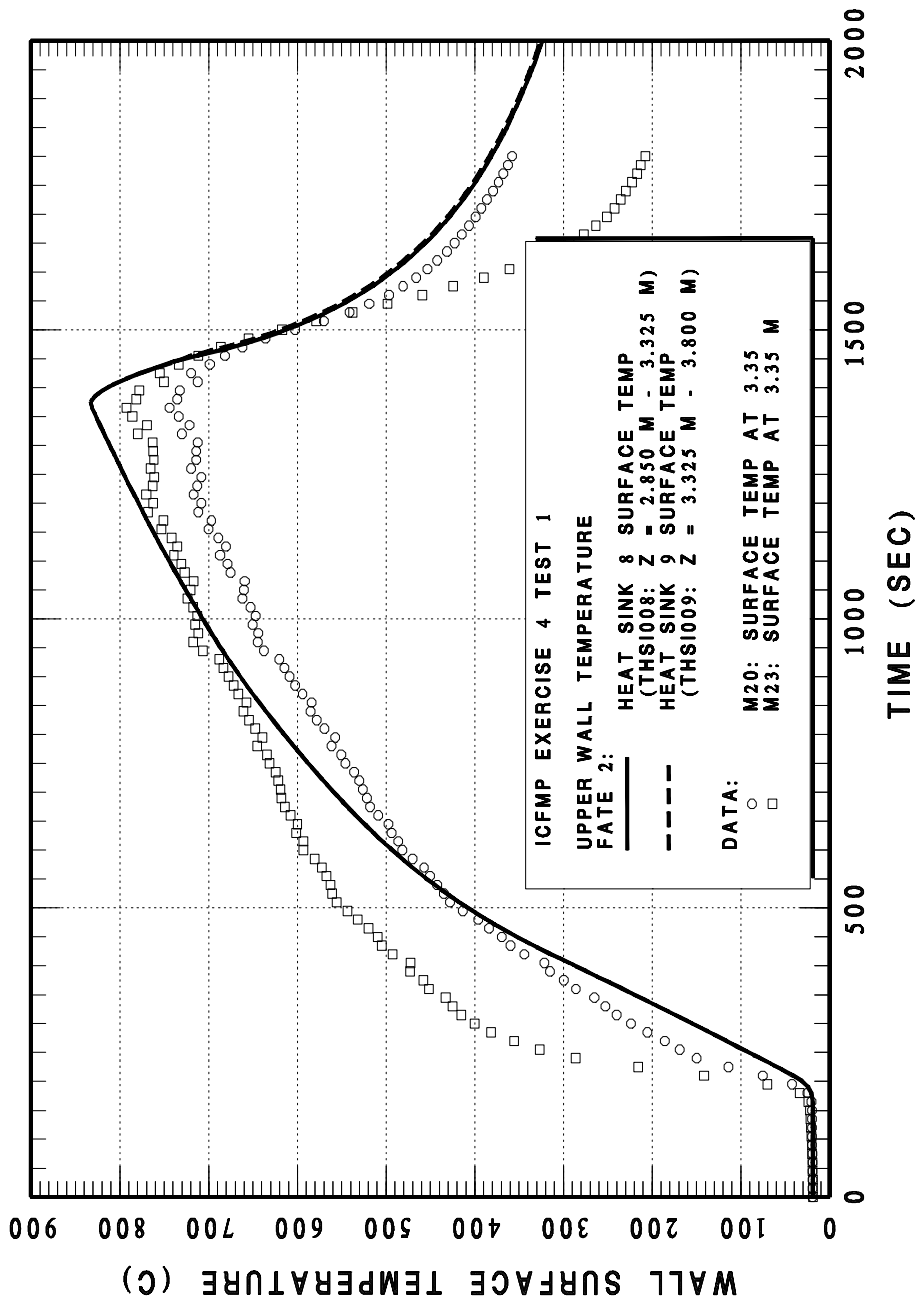


Fig. D3-20 BE4 Case 1 40% Power Increase Sensitivity: upper wall temperature

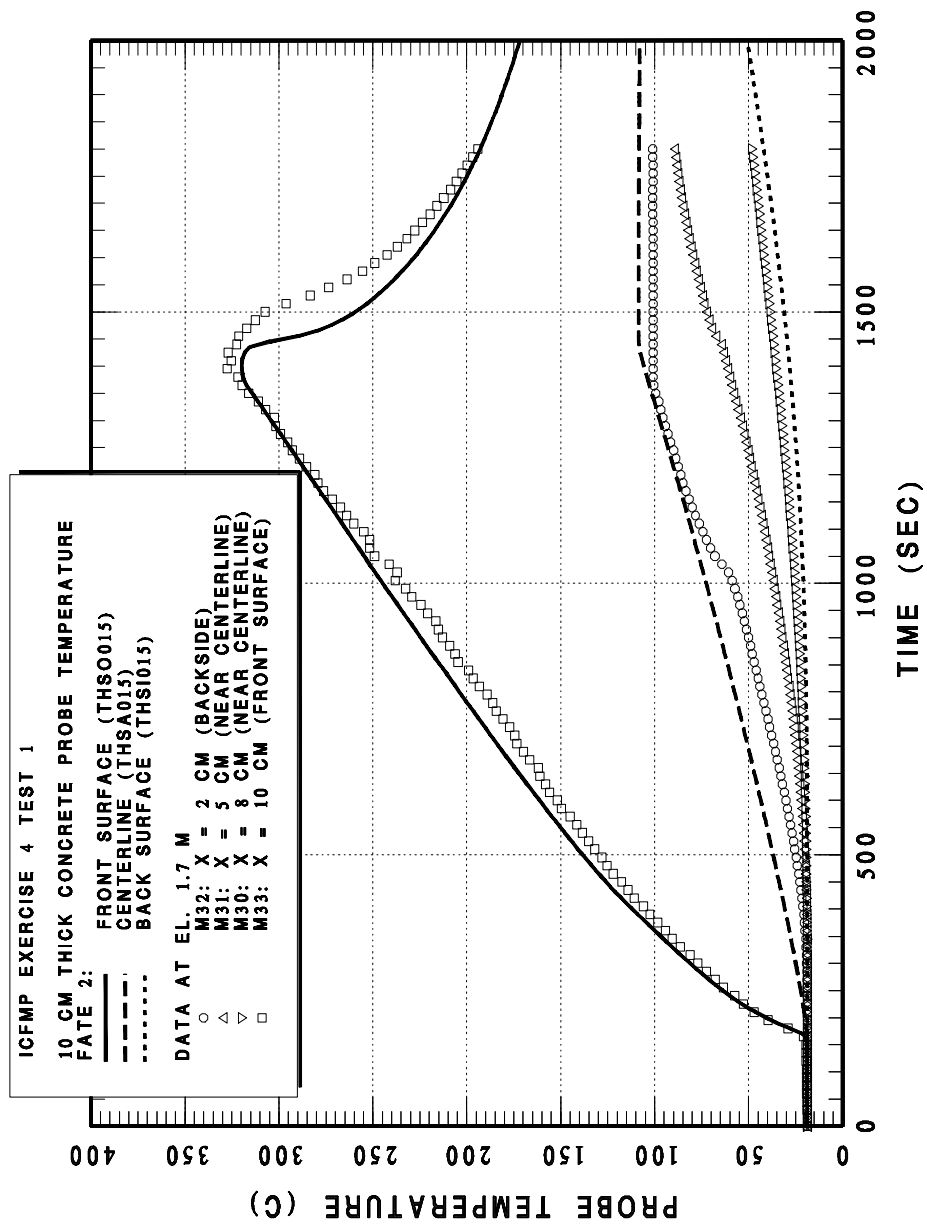


Fig. D3-21 BE4 Case 1 40% Power Increase Sensitivity: probe temperature

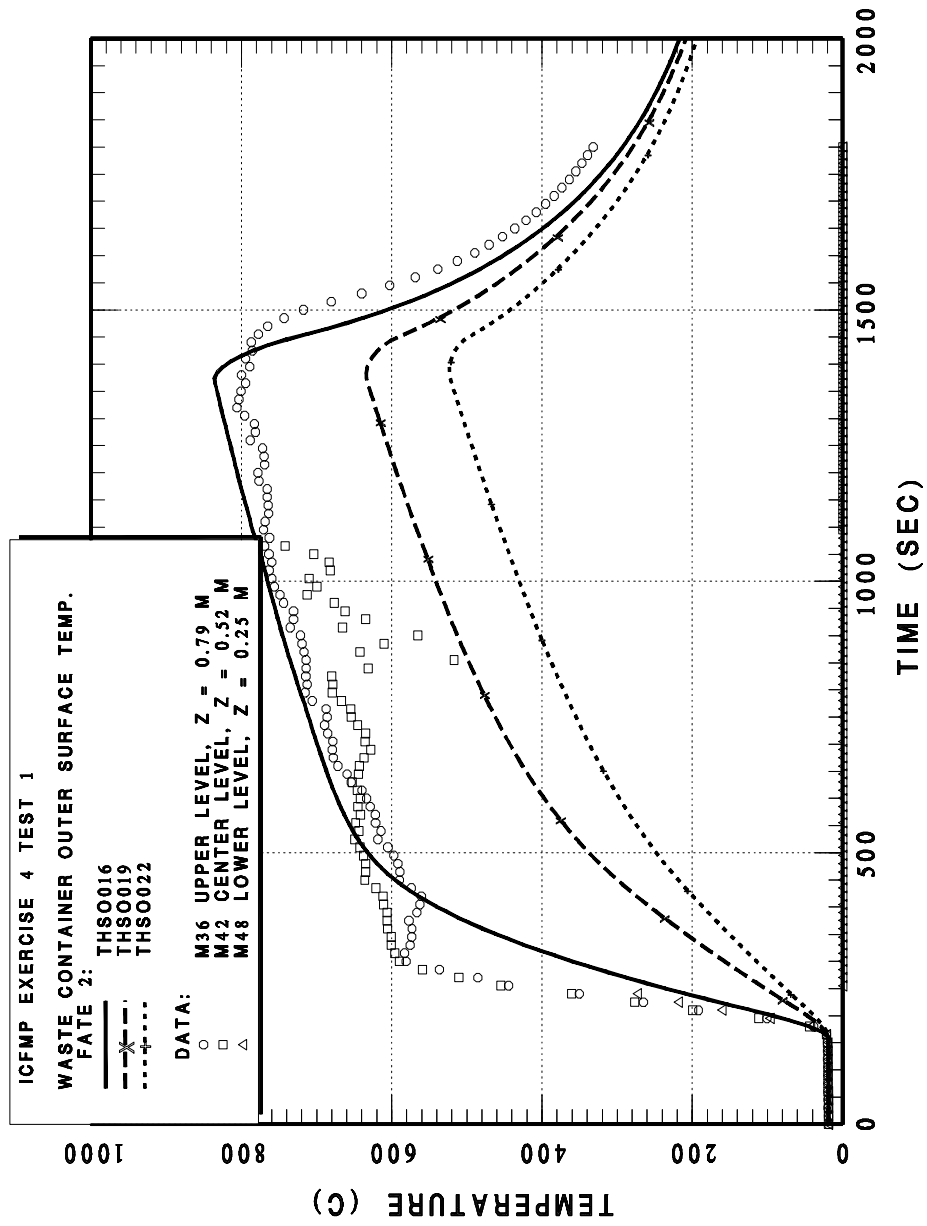


Fig. D3-22 BE4 Case 1 40% Power Increase Sensitivity: waste can surface temperature

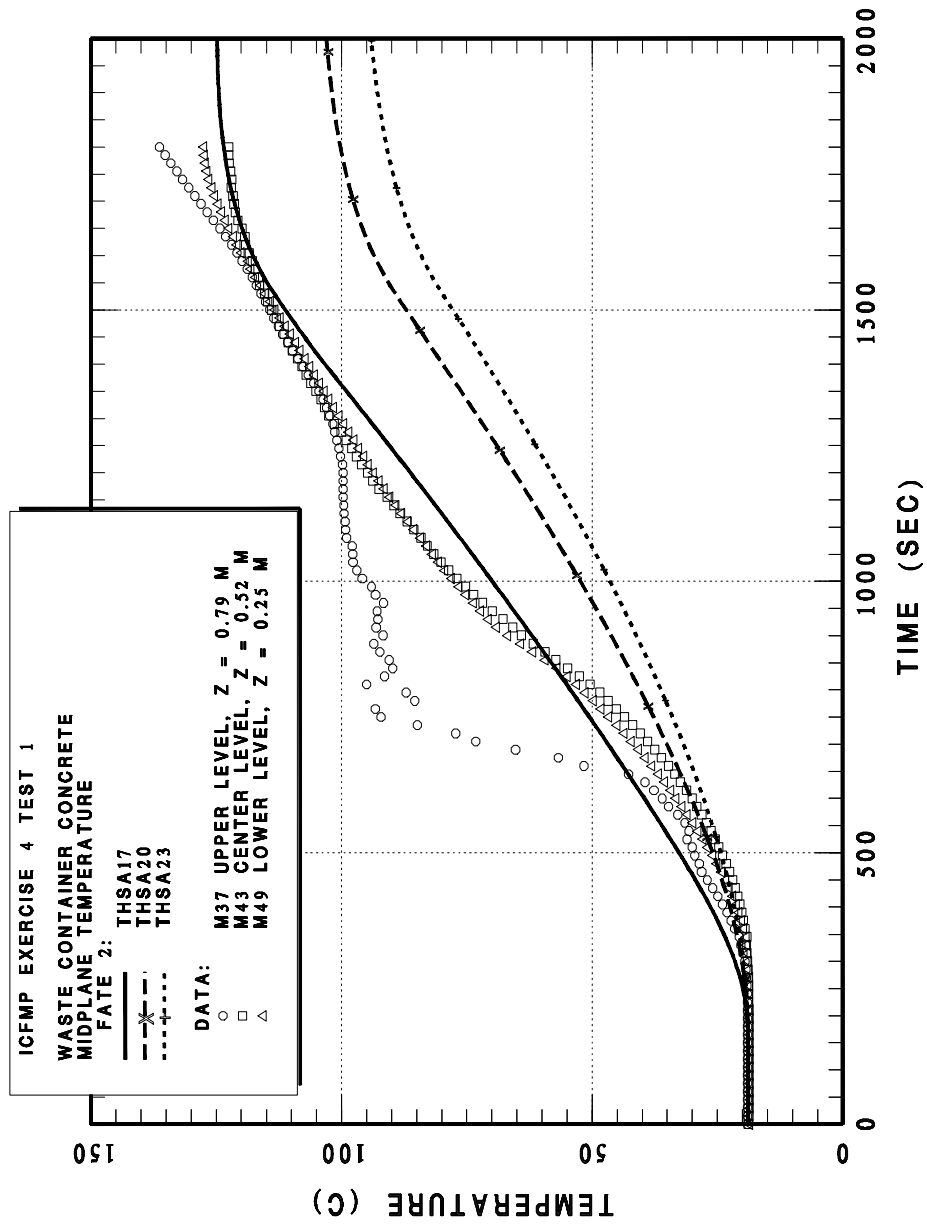


Fig. D3-23 BE4 Case 1 40% Power Increase Sensitivity: waste can concrete mid-plane temperature

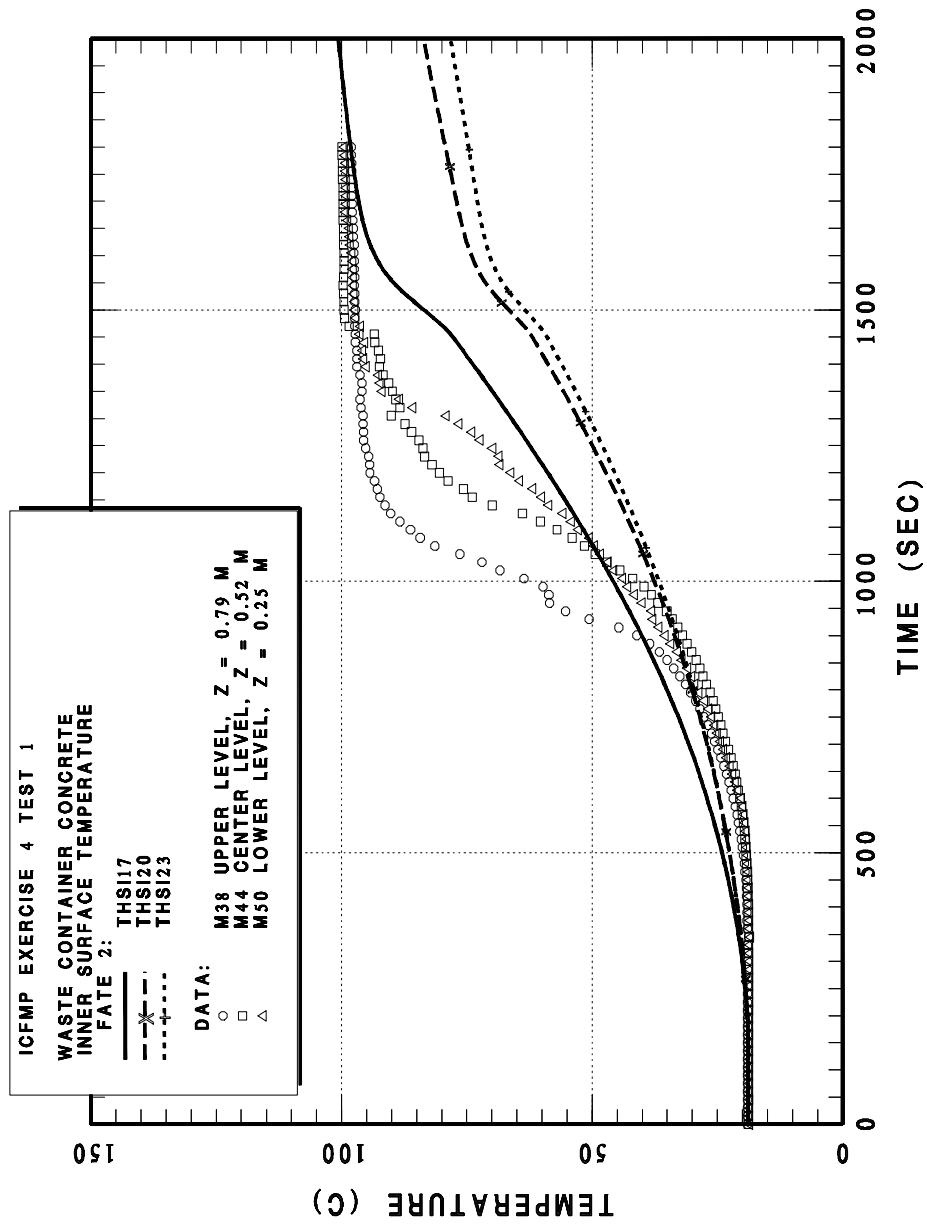


Fig. D3-24 BE4 Case 1 40% Power Increase Sensitivity: waste can concrete inner surface temperature

D3.4.2 BE-4 Case 3 FATE Open Benchmark Results

Case 3 is characterized by a kerosene fire with an equilibrium power in the range of 3 to 3.5 MW with a peak power near the end of the burn of 8 MW. In addition, the doorway opening has been reduced to 0.7 m x 1.0 m. The net result, as will be shown, is an under ventilated fire. Thus, this case tests the FATE fire and heat transfer models under conditions of extremely high fire power (relative to typical NPP fires) with poor ventilation.

A key assumption used in modeling this case is the length along which oxygen is entrained and consumed in the fire. As with the previous case, the flame height is predicted to be well into the smoky layer and well above the top of the doorway. In addition, as will be shown, nearly all oxygen in the upper and lower regions is consumed. To prevent the fire from extinguishing due to oxygen starvation, air flowing in through the door must therefore be entrained and consumed in the fire. To model this turbulent mixing of fresh air and fuel, the FATE model parameter for air entrainment height is set equal to the bottom of the reduced doorway opening at the 1.6 m elevation. In FATE, this implies that once the calculated smoky layer descends to 1.6 m, air will be consumed in the fire directly from the smoky layer. Prior to this point, air is consumed only from the lower gas layer. Finally, following guidance from other fire benchmarks, air flowing in through the doorway is assumed to be equally distributed between the smoky and lower gas layers.

Key insights are obtained regarding oxygen consumption in the smoky and lower gas layers for the under ventilated conditions. FATE calculations for BE-4 Case 3 are presented in Figures D3-25 through D3-35.

Figures D3-25 and D3-26 present the smoky layer height and smoky layer gas concentrations. Once again, the gas concentration is a better measure of conditions in the smoky layer. The measured smoky layer height is based on an average of thermocouple readings at 4 separate elevations, with the lowest elevation at 1.5 m. Thus, the reported layer height does not provide indication of smoky layer heights below 1.5 m. Furthermore, the FATE calculation is controlled by the specification of the height of air entrainment into the fire (1.6 m). The only insight to be gained is that the smoky layer quickly descends and fills nearly the entire room. The FATE calculation of oxygen concentration closely follows the test data, with both the data and calculation indicating

zero oxygen around 1100 seconds, returning to normal oxygen concentrations following fire termination.

Once again, the gas and heat sink temperatures were found to be closely linked to the fire power. For this reason, adjustments were made to the reported fuel burn rate (see Figure D2-3) to conform to the times at which test data indicated the plume gas temperatures began to increase and decrease. Figures D3-27 through D3-29 present the measured and calculated gas temperatures. Because the room is essentially completely filled with smoke, the lower layer gas temperature calculation has no corresponding test measurement. Overall, reasonable agreement is obtained and no attempt was made to increase the fire power from its nominal value to provide a bounding estimate of the gas temperatures.

Calculation of the concrete probe and waste can temperatures (Figures D3-30 through D3-33) as well as the concrete wall surface temperatures (Figures D3-34 and D3-35) proved to be sensitive to whether or not each heat sink was submerged in the smoky layer. This suggests that further analysis of the heat sink-smoky layer energy balance calculations is warranted.

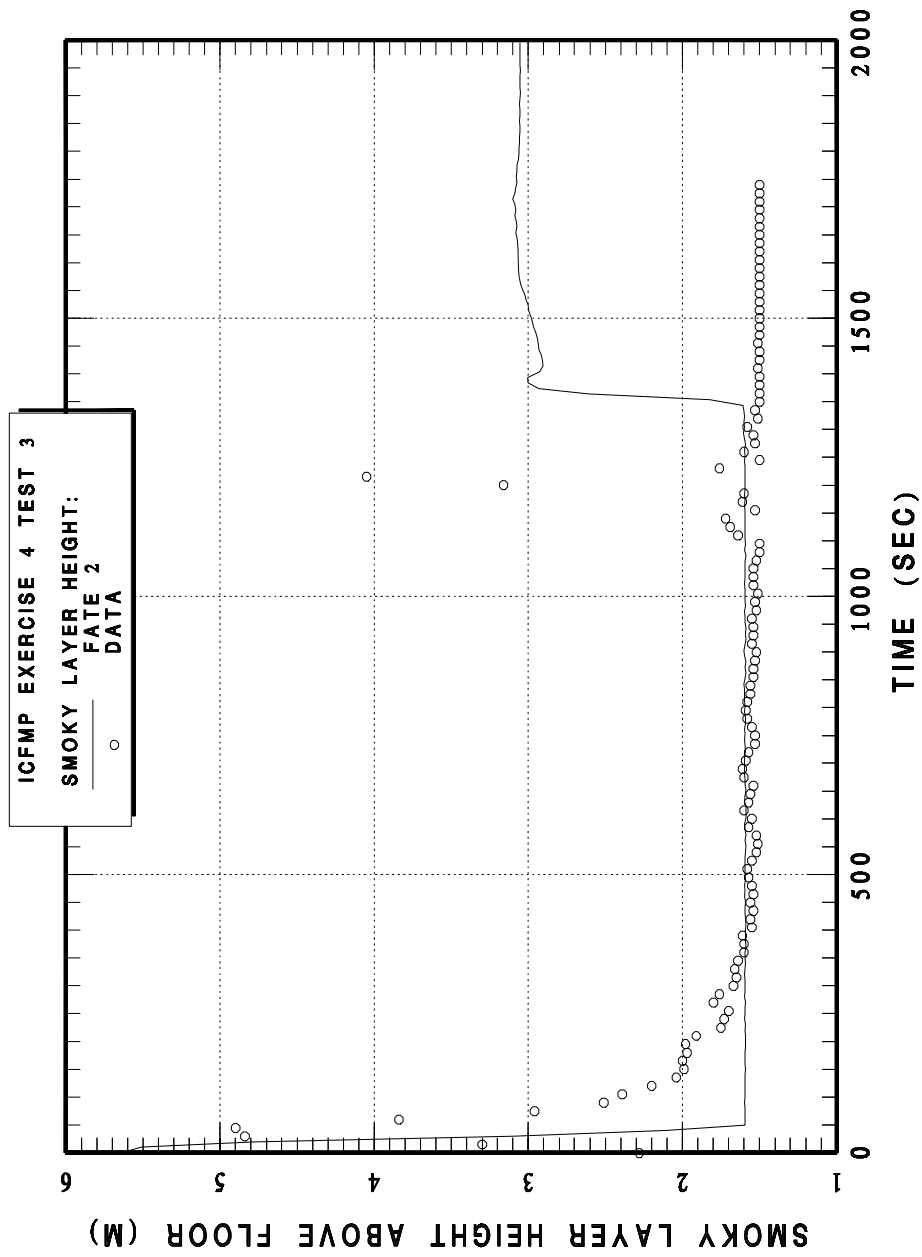


Fig. D3-25 BE4 Case 3 Smoky layer height

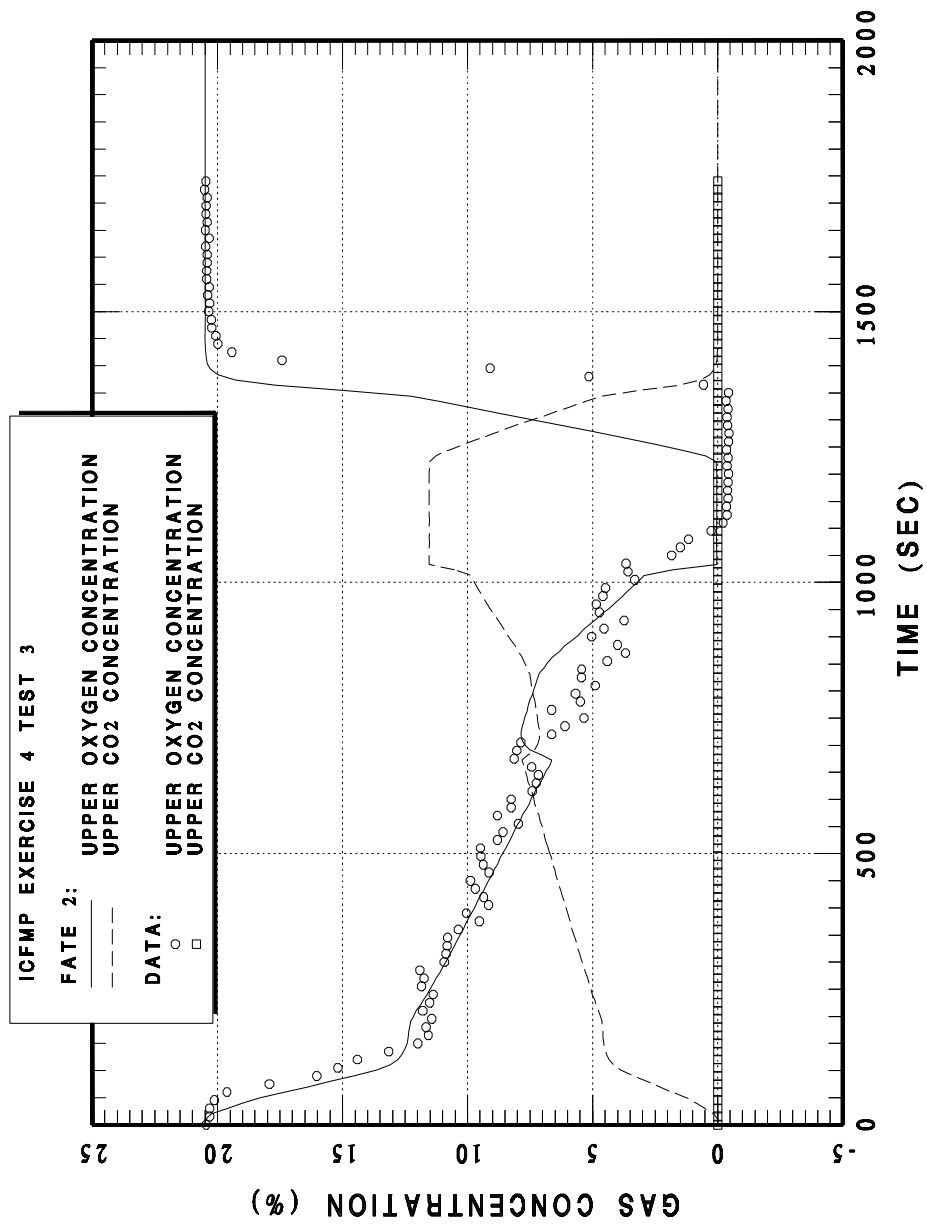


Fig. D3-26 BE4 Case 3 smoky layer gas concentrations

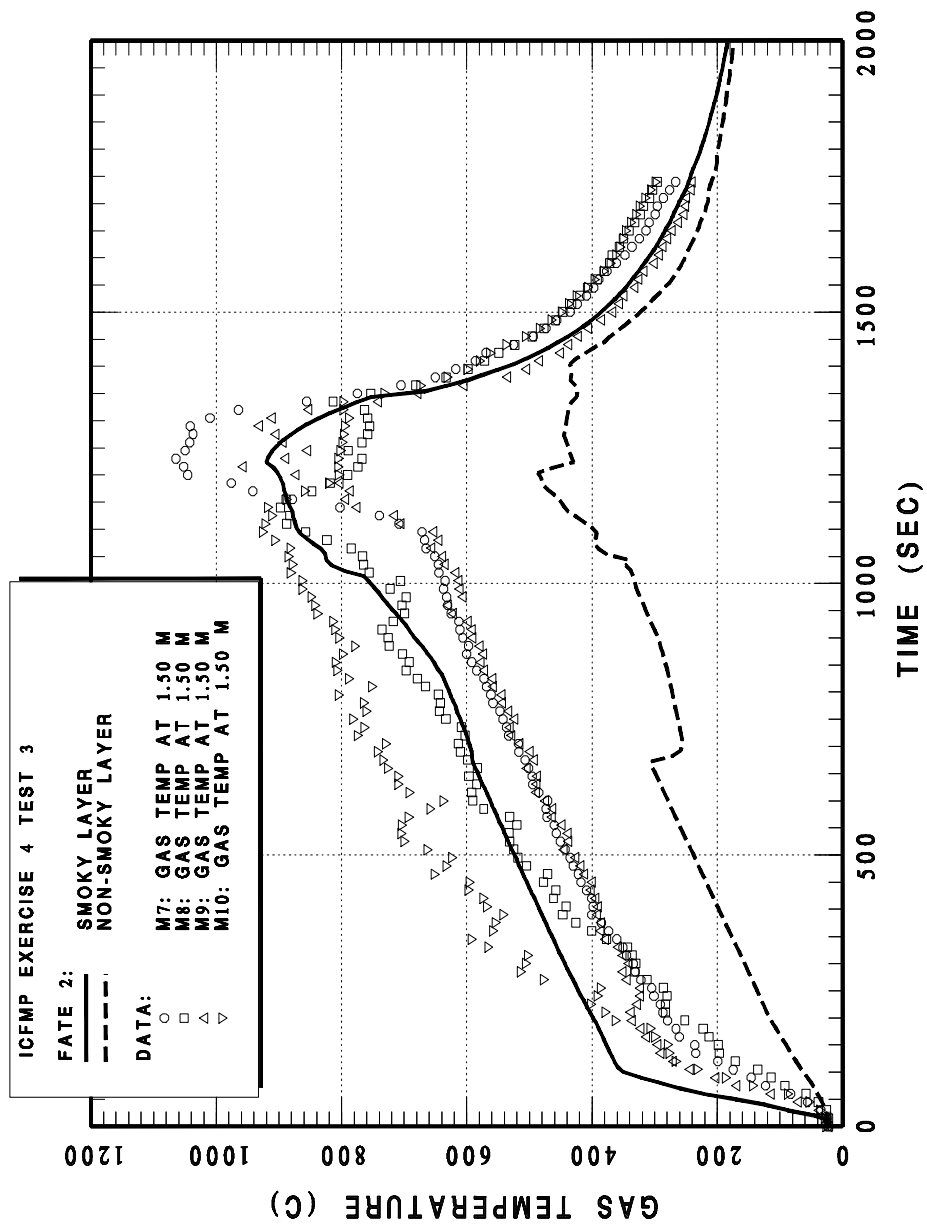


Fig. D3-27 BE4 Case 3 gas temperature at 1.5 m

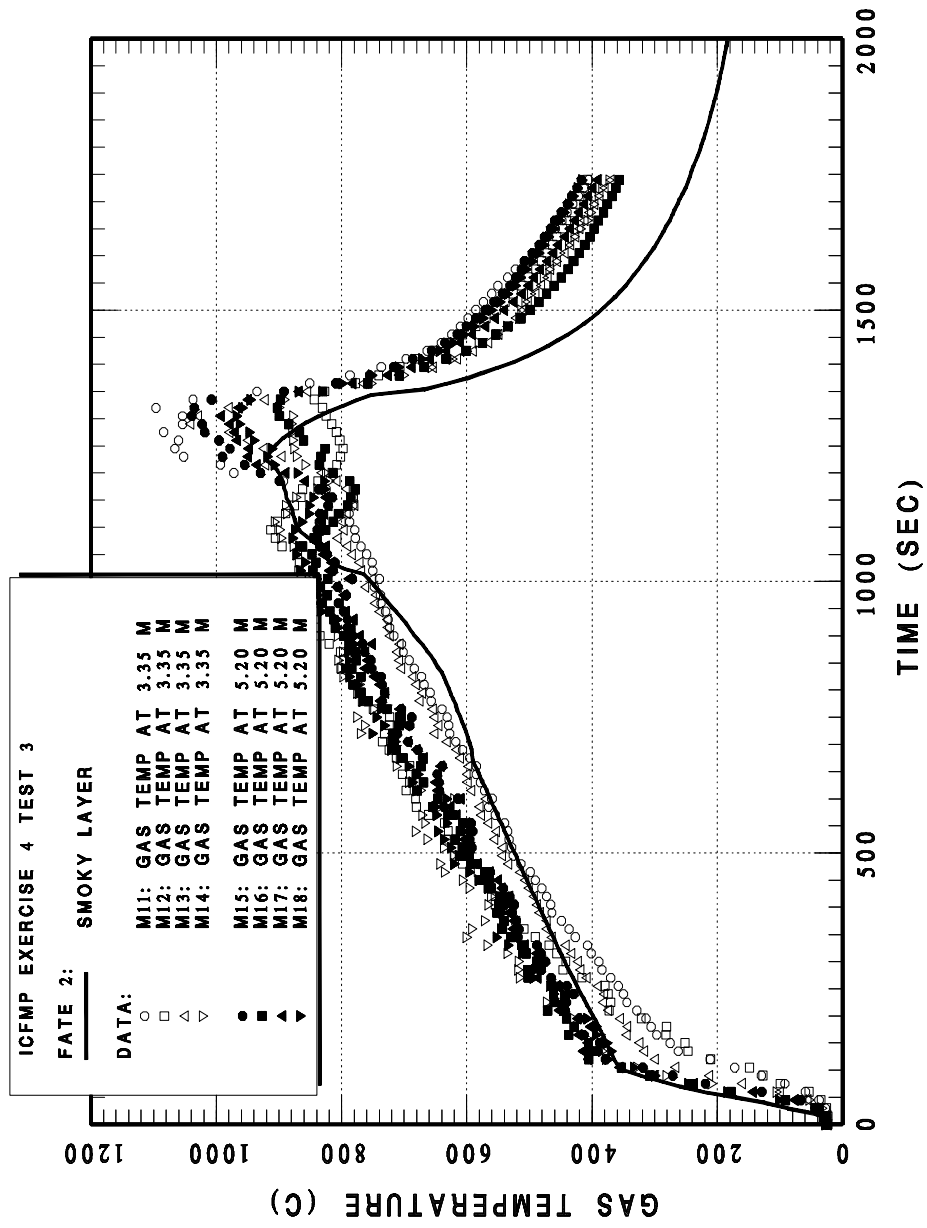


Fig. D3-28 BE4 Case 3 gas temperatures at 3.35 m and 5.2 m

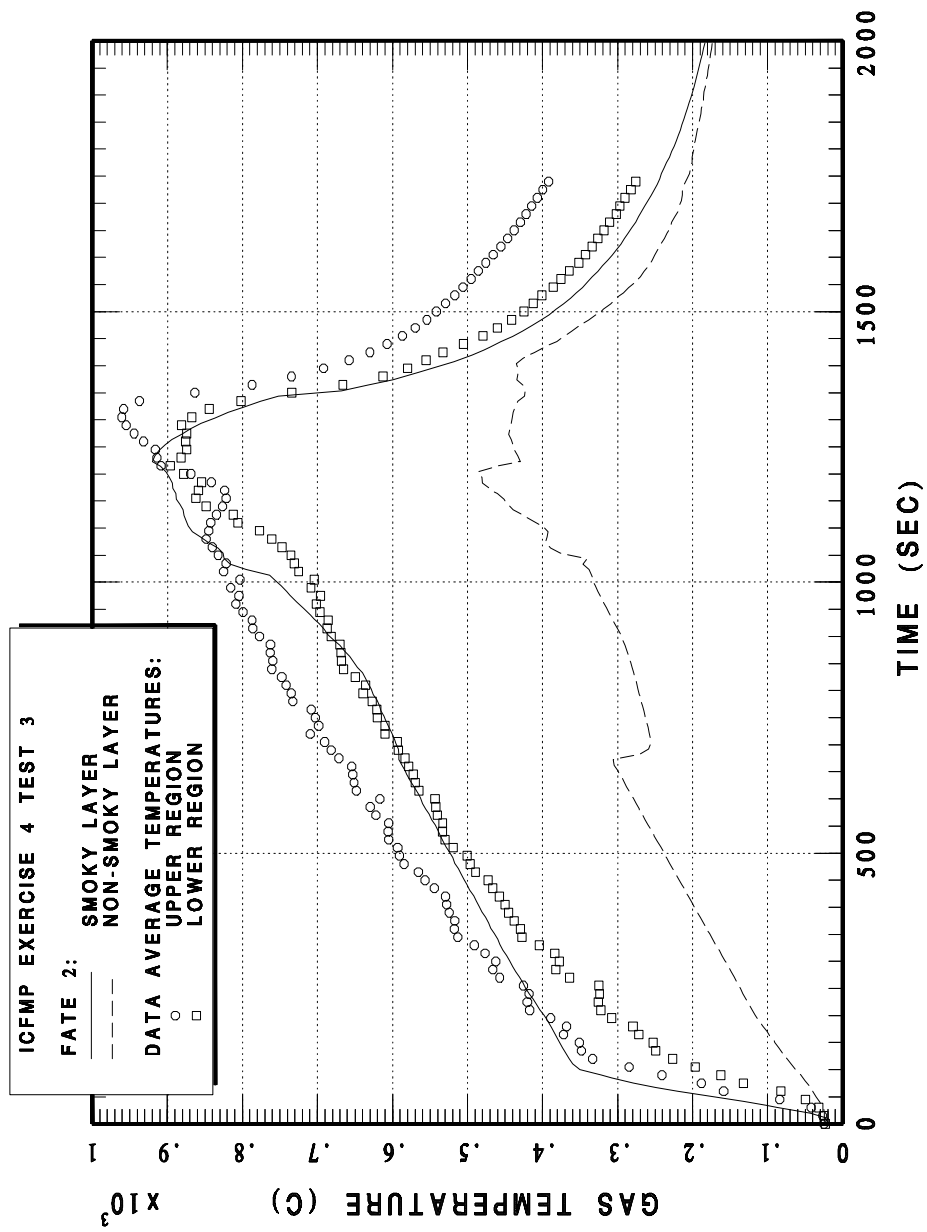


Fig. D3-29 BE4 Case 3 average gas temperatures

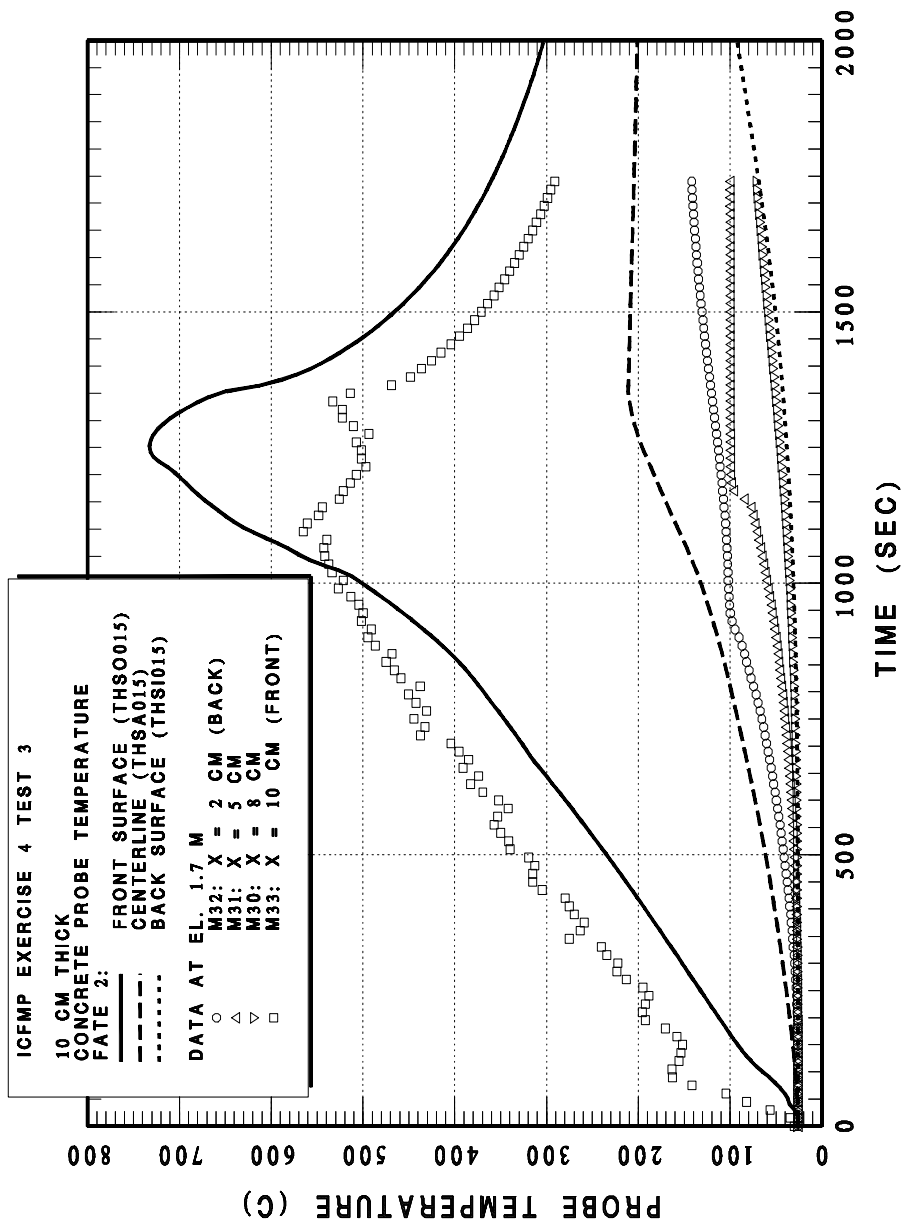


Fig. D3-30 BE4 Case 3 concrete probe temperatures

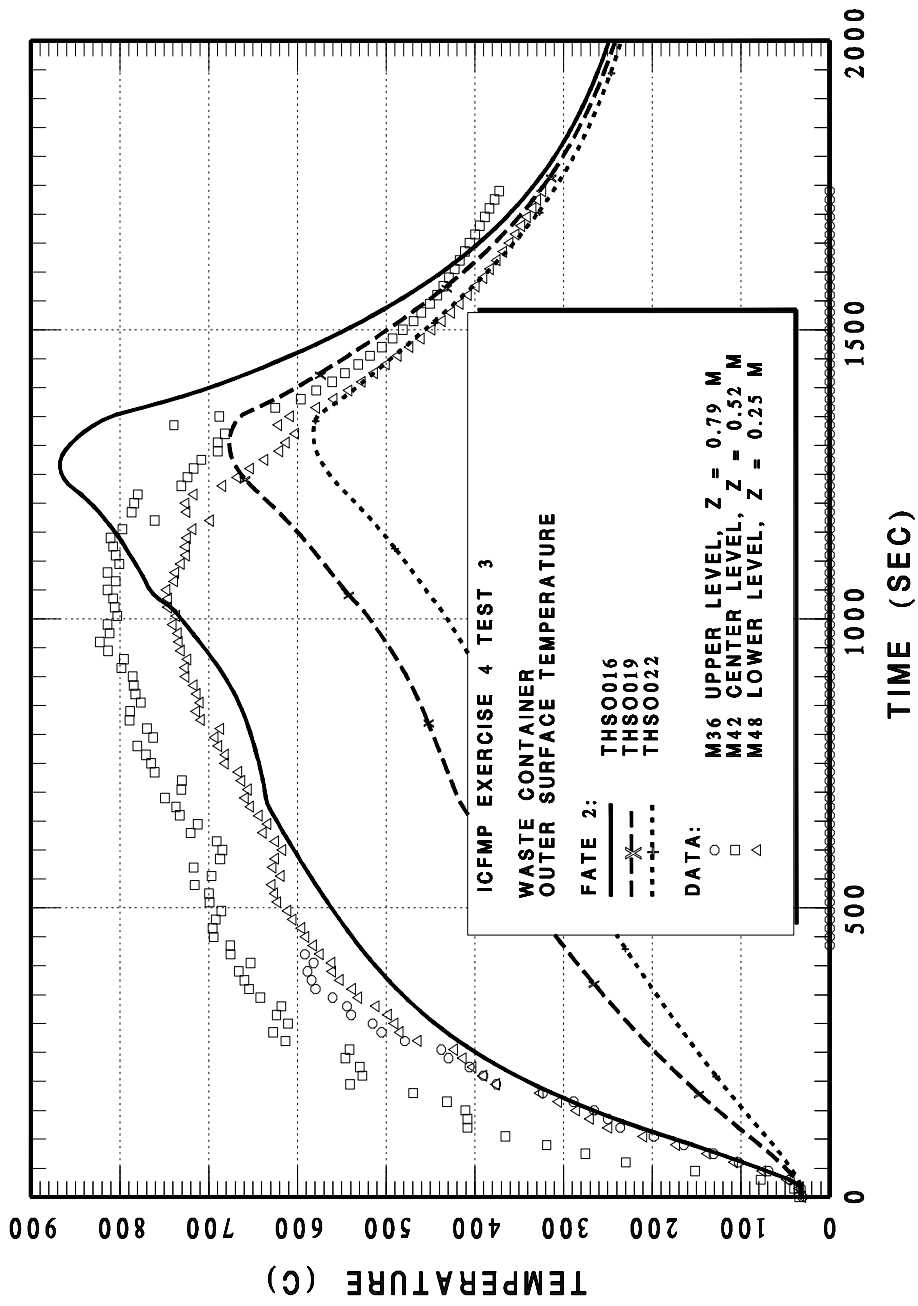


Fig. D3-31 BE4 Case 3 waste can surface temperatures

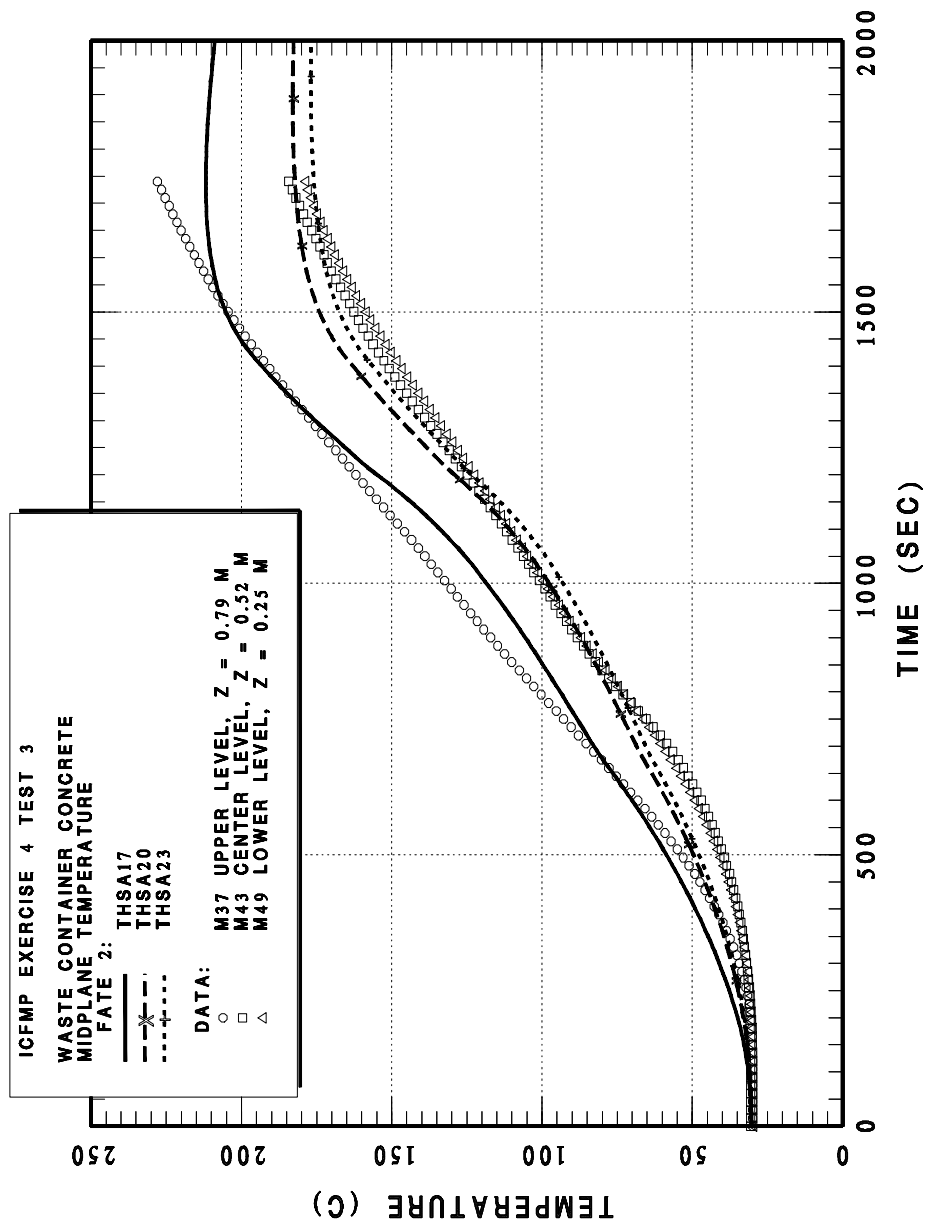


Fig. D3-32 BE4 Case 3 waste concrete midplane temperatures

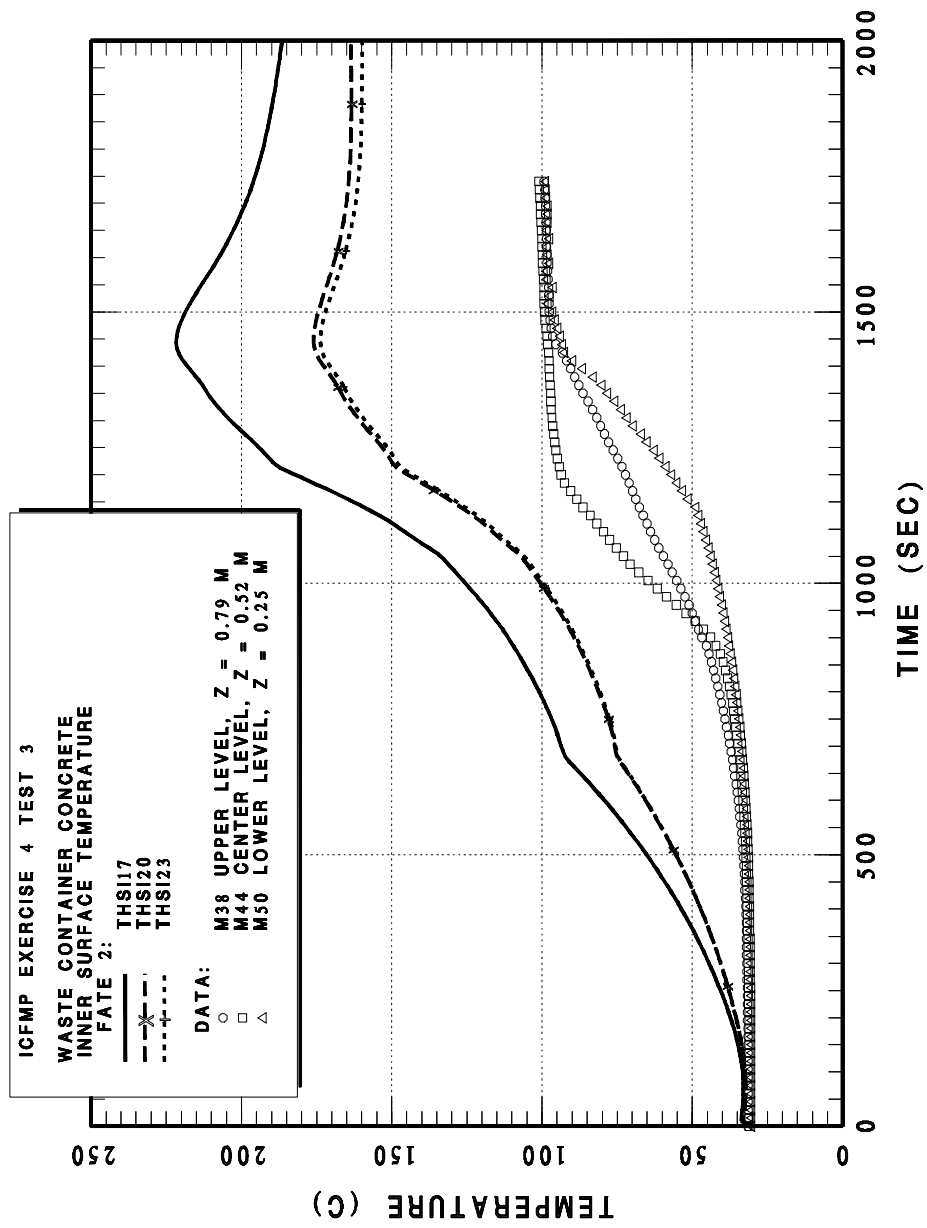


Fig. D3-33 BE4 Case 3 waste can concrete inner surface temperature

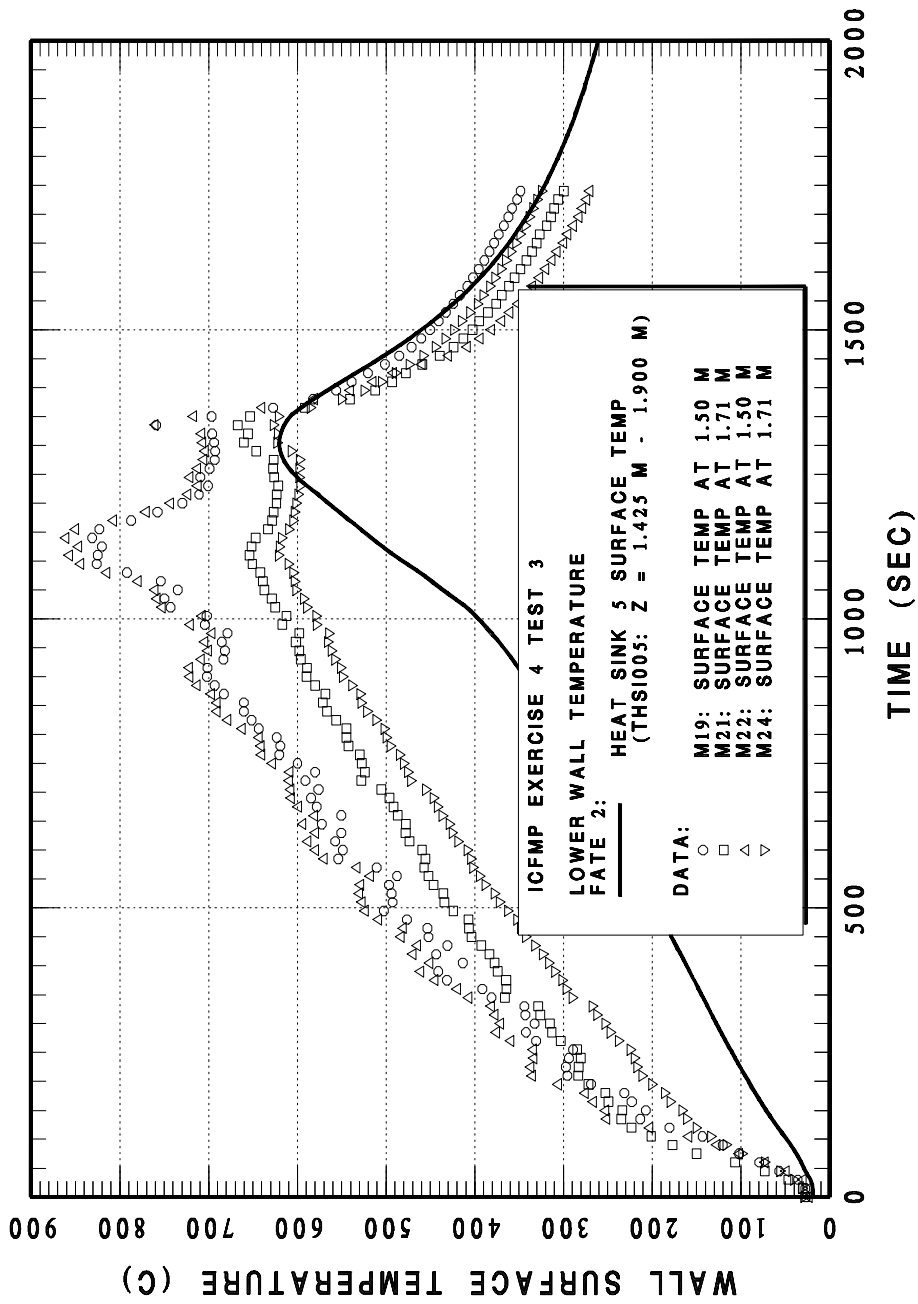


Fig. D3-34 BE4 Case 3 lower wall surface temperature

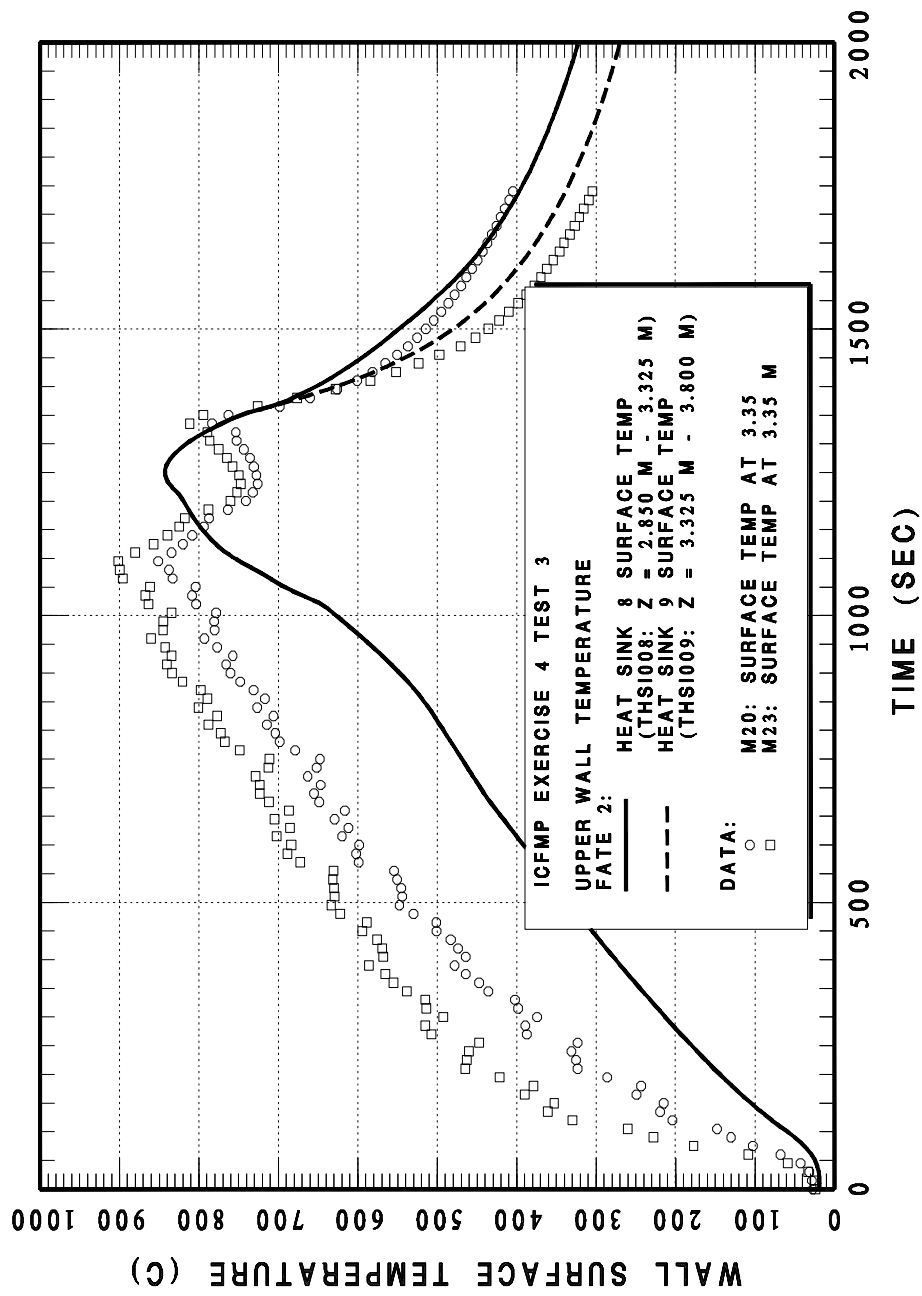


Fig. D3-35 BE4 Case 3 upper wall surface temperature

D4 Conclusions and Recommendations

Open benchmark results based on the FATE computer program have been presented for Benchmark Exercise 4 Cases 1 and 3. Key conclusions from this benchmark effort are:

1. Calculations are most sensitive to assumptions regarding fire power, ventilation flows, and air mixing. Considering all uncertainties, using a reasonable upper bound estimate of the fire power or fuel burn rate can produce upper bound estimates of target temperatures. This approach can be considered in nuclear power plant fire analyses.
2. Certain fire room geometries, such as that considered here, may require modeling with multiple regions rather than a single region to obtain fine details of the room response. However, the single region model used here is shown to be appropriate if the goal of fire analysis is prediction of critical target response. The combination of a single region model, with smoky layer and lower layer sub regions, and an upper bound on fire power yielded bounding estimates of the target temperatures.
3. Smoky layer behavior, in terms of layer height and gas concentration, proved sensitive to assumptions regarding mixing of air inflows between the smoky and lower layers as well as assumptions regarding oxygen consumption in the fire for an under ventilated fire. Furthermore, results proved to be sensitive to the smoky layer behavior.
4. This integral code benchmark show that the FATE code calculations follow the trends of the test data and can produce bounding estimates of target temperatures. Thus, this benchmark provides validation for applicability of the FATE fire sub-models and the standard one-region room model to conditions of high powered fires in under ventilated rooms.

The preceding results and conclusions suggest the following areas for future FATE code development:

1. Mechanistic mixing of air inflows between the smoky and lower layers.
2. Mechanistic treatment of oxygen consumption for under ventilated fires.

D5 References

- /KLE 03/ Klein-Heßling, W., M. Röwekamp, R. Dobbernack, O. Riese:
“Specification of International Benchmarking and Validation Exercise # 4:
Kerosene Pool Fire Inside a Compartment,” Revision 2, October, 2003,
Website: <http://techconf.llnl.gov/cgi-fire/topics>
- /DEY 03/ Dey, M., A. Hamins, S. Miles:
International Collaborative Project to Evaluate Fire Models for Nuclear
Power Plant Applications: Summary of 5th Meeting, NISTIR-6986, Septem-
ber, 2003
- /PLY 04/ Plys, M.G., and S. J. Lee:
FATETM 2.0: Facility Flow, Aerosol, Thermal, and Explosion Model (Im-
proved and Combined HANSF and HADCRT Models), FAI/04-71, SNF-
23281, Two Volumes, November 2004

List of Figures

Fig. D2-1	FATE BE-4 nodalization for the barrel-type waste container target	7
Fig. D2-2	FATE BE-4 Test 1 comparison of fuel burn rate data to FATE input	10
Fig. D2-3	FATE BE-4 Test 3 comparison of fuel burn rate data to FATE input	10
Fig. D3-1	FATE™ 2.0 Fire Model Features	16
Fig. D3-2	FATE Correlation of experimental data for plume entrainment	22
Fig. D3-3	Handy Visual Guide to View Factor Models Available	26
Fig. D3-2	Handy Visual Guide to View Factor Models Available (concluded).....	27
Fig. D3-4	BE4 Case 1 Vent Fan Volumetric Flow Rate Modeled as a Boundary Condition	33
Fig. D3-5	BE4 Case 1 doorway unidirectional volumetric flow rate (positive flows are out of fire compartment)	34
Fig. D3-6	BE4 Case 1 doorway counter-current flow rate.....	35
Fig. D3-7	BE4 Case 1 smoky layer and flame height	36
Fig. D3-8	BE4 Case 1 smoky layer gas concentrations (test data measured at coordinate $x = 0.10\text{ m}$, $y = 1.90\text{ m}$, $z = 3.80\text{ m}$).....	37
Fig. D3-9	BE4 Case 1 gas temperatures at 1.5 m	38
Fig. D3-10	BE4 Case 1 gas temperatures at 3.35 m and 5.20 m	39
Fig. D3-11	BE4 Case 1 average gas temperatures	40
Fig. D3-12	BE4 Case 1 wall surface temperature at lower elevations	41
Fig. D3-13	BE4 Case 1 wall surface temperature at upper elevations.	42
Fig. D3-14	BE4 Case 1 concrete probe temperatures	43
Fig. D3-15	BE4 Case 1 waste container metal surface temperature	44
Fig. D3-16	BE4 Case 1 waste container concrete midplane temperature	45
Fig. D3-17	BE4 Case 1 waste container concrete inner surface temperature	46
Fig. D3-18	BE4 Case 1 40% Power Increase Sensitivity: Burn Rate.....	47
Fig. D3-19	BE4 Case 1 40% Power Increase Sensitivity: upper gas temperature	48
Fig. D3-20	BE4 Case 1 40% Power Increase Sensitivity: upper wall temperature	49
Fig. D3-21	BE4 Case 1 40% Power Increase Sensitivity: probe temperature	50
Fig. D3-22	BE4 Case 1 40% Power Increase Sensitivity: waste can surface temperature	51
Fig. D3-23	BE4 Case 1 40% Power Increase Sensitivity: waste can concrete midplane temperature	52
Fig. D3-24	BE4 Case 1 40% Power Increase Sensitivity: waste can concrete inner surface temperature	53

Fig. D3-25	BE4 Case 3 Smoky layer height.....	56
Fig. D3-26	BE4 Case 3 smoky layer gas concentrations.....	57
Fig. D3-27	BE4 Case 3 gas temperature at 1.5 m.....	58
Fig. D3-28	BE4 Case 3 gas temperatures at 3.35 m and 5.2 m.....	59
Fig. D3-29	BE4 Case 3 average gas temperatures.....	60
Fig. D3-30	BE4 Case 3 concrete probe temperatures.....	61
Fig. D3-31	BE4 Case 3 waste can surface temperatures.....	62
Fig. D3-32	BE4 Case 3 waste concrete midplane temperatures.....	63
Fig. D3-33	BE4 Case 3 waste can concrete inner surface temperature.....	64
Fig. D3-34	BE4 Case 3 lower wall surface temperature.....	65
Fig. D3-35	BE4 Case 3 upper wall surface temperature.....	66

List of Tables

Table D2-1 FATE BE-4 base model heat sink summary table.....	4
Table D2-2 FATE BE-4 base model flow path summary	5
Table D2-3 FATE BE-4 target heat sink summary table	7
Table D2-4 Summary of Test 1 and Test 3 distinguishing input	9
Table D3-1 FATE 2.0 View Factor Summary Table.....	25

Appendix E: International Collaborative Project to Evaluate Fire Models for Nuclear Power Plant Applications

Benchmark Exercise No. 4 Kerosene Pool Fire Inside A Compartment

Presented by

Laurence Rigollet

Institute de Radioprotection et de Sûreté Nucléaire (IRSN)

Direction de la Prévention des Accidents Majeurs (DPAM)

Service d'études et de modélisation de l'incendie, du corium et du confinement (SEMIC)

Cadarache bât 702 BP 3, 13115 St Paul les Durance, France

Résumé

Ce rapport présente les résultats de simulations numériques réalisés avec le code FLAMME-S pour des scénarios de feux de kérosène dans un local. Ce travail a été réalisé dans le cadre d'un projet international visant à évaluer les modèles incendie appliqués à des feux dans des installations nucléaires.

Mots-clés: feux de kérosène, modélisation

Abstract

This report presents the results of numerical simulations achieved with the FLAMME-S code on kerosene pool fires inside a compartment. This work has been performed in the frame of an international collaborative project to evaluate fire models for nuclear power plant applications.

Key-words: kerosene fire, simulations

Contents

	Résumé	III
E1	Introduction	1
E2	Input Parameters and Assumptions.....	3
E2.1	Characteristics of the Facility	3
E2.2	Characteristics of the Fire Source	4
E3	Comparison of Code Predictions and Experimental Results	7
E3.1	Test 1	7
E3.1.1	Comparison with Experimental Results.....	7
E3.1.2	Other Calculated Results	14
E3.2	Test 3	16
E4	Conclusions.....	23
E5	References.....	25
	List of Figures	27

E1 Introduction

The Benchmark Exercise No. 4 is set up to evaluate the capabilities of codes to model relevant phenomena with kerosene fires in a compartment. The results of calculations are compared to two experiments performed at the iBMB of Braunschweig University of Technology.

The two experiments studied, called Test 1 and Test 3, implement a 1 m² pool of kerosene in the OSKAR facility, with a volume of 74 m³. In the first experiment, a door is completely open, with a free cross section of 0.7 m x 3 m. In the second one, the door is partly closed and reduced to 0.7 m x 1 m.

The purpose of this document is to present the results of the numerical simulations achieved with a two-zone models code FLAMME-S Version 2.3.2, developed by IRSN.

Before presenting the results, a remark must be made concerning the fact that the studied cases are outside the validation domain of FLAMME-S. The two following conditions of application of the code are not proved in these cases 0:

- The ratio of the pool surface to the area of the floor of the facility is less than 5 %.
- The ratio of the heat release rate to the volume of the facility is less than 5 kW m⁻³.

Indeed, the two configurations can be described as a large fire in a small enclosure. And, the assumptions used in a two-zone models code are not valid in these cases: for example the plume model, radiation model, or point source is not applicable for these scenarios.

E2 Input Parameters and Assumptions

Most of input data are given in the specifications 0. Assumptions and input data which are not identified in the Benchmark Exercise specifications are presented in this section.

E2.1 Characteristics of the Facility

The OSKAR facility of iBMB is simulated by a compartment with 3.6 m depth, 3.6 m width and 5.7 m height.

Characteristics of the Walls

The side walls are constructed from 25 cm of light concrete, on the side of the fire compartment, and 5 cm of insulation. The ceiling is made of a 25 cm layer of concrete and a 5 cm layer of insulation. For the floor, only 30 cm of concrete are taken into account: the aerated concrete implemented in the experiments in order to protect the mass loss measurement is not modeled. The properties of the compartment materials are given in 0.

Two material probes, concrete and aerated concrete, are modeled. The size of these elements is 0.3 m x 0.3 m, with a thickness of 0.1 m. The slabs are meshed in order to compare the results of the code with the different temperatures measured inside the material probes.

Heat Transfer

The emissivity of all surfaces is assumed to be 0.95.

The convective heat transfer is $10 \text{ W m}^{-2} \text{ K}^{-1}$ to the inside and $6 \text{ m}^{-2} \text{ K}^{-1}$ to the outside environment.

Ventilation

In Test 1, the door is completely opened, with a free cross section of 0.7 m x 3 m. In Test 3, the opening is partly closed, with a free cross section of 0.7 m x 1 m. The fan system, which is not used in the experiments, is not modeled. The hood above the

open front door which is used to estimate experimentally the heat release rate is also not modeled. Thus, only natural ventilation through the door is considered in simulations with FLAMME-S.

E2.2 Characteristics of the Fire Source

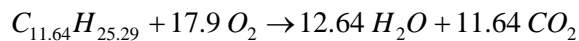
Geometry of the Pool

The fire source is a 1 m² pool of kerosene located at the center of the room. For the simulations, the bottom of the pan is set to be on the floor instead at 0.51 m above the floor in the experiments to simplify the calculations.

Kerosene Properties

Most of the kerosene properties are given in the specifications 0. The energy released by radiation represents 32 % of the total heat released 0.

A complete reaction of combustion is assumed:



This reaction corresponds to an efficiency coefficient of combustion equal to 1.

Pyrolysis Rate

In a first step, semi-blind calculations are achieved with a constant pyrolysis rate of kerosene. For the semi-blind calculations of Test 1, the pyrolysis rate is assumed to be equal to 65 g m⁻² s⁻¹, a value measured in large scale fires 0. For Test 3, calculations are realized with a lower value of 50 g m⁻² s⁻¹. This value is close to the one measured during the steady state. For these simulations, fire self-extinguishing may occur when the oxygen concentration reaches 11.5 %.

In a second step, open calculations are achieved with the pyrolysis rate measured during the experiments. In these cases, the lower oxygen concentration is fixed at 0 %, because the decrease of oxygen is taken into account with the variation of the experimental pyrolysis rate.

The pyrolysis rates used as input data for calculations are shown in the figures Fig. E1 and Fig. E2.

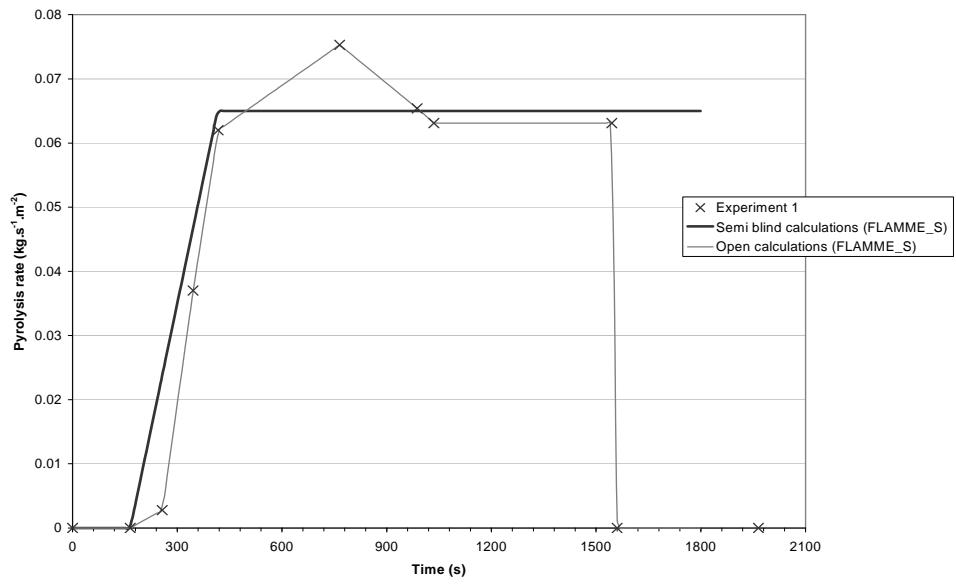


Fig. E1 Pyrolysis rate of Test 1

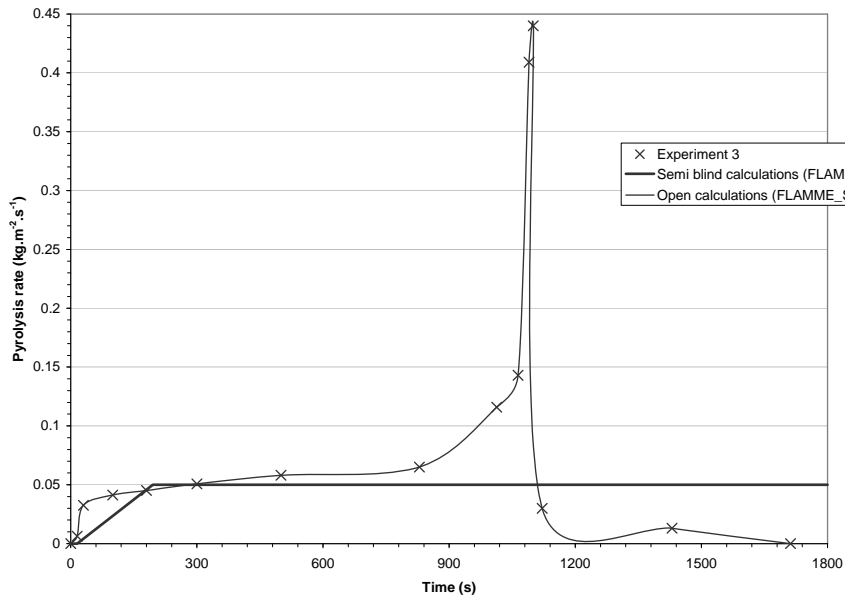


Fig. E2 Pyrolysis rate of Test 3

E3 Comparison of Code Predictions and Experimental Results

In this part, the values calculated by FLAMME-S code are compared with experimental results. Two types of calculations are realized: semi-blind, i.e. with an estimated pyrolysis rate, and open, i.e. with the experimental pyrolysis rate as input data.

E3.1 Test 1

Test 1 is a 1 m² pool fire of kerosene in a room with an open door with a free cross section of 2.1 m².

E3.1.1 Comparison with Experimental Results

Heat Release Rate

Fig. E3 shows the evolution of the heat release rate of the fire for the two types of calculations. In semi-blind calculations, the extinction of the fire occurs when the oxygen concentration in the upper layer reaches 11.5 %. With this assumption, the calculated duration of the fire corresponds to the one observed experimentally.

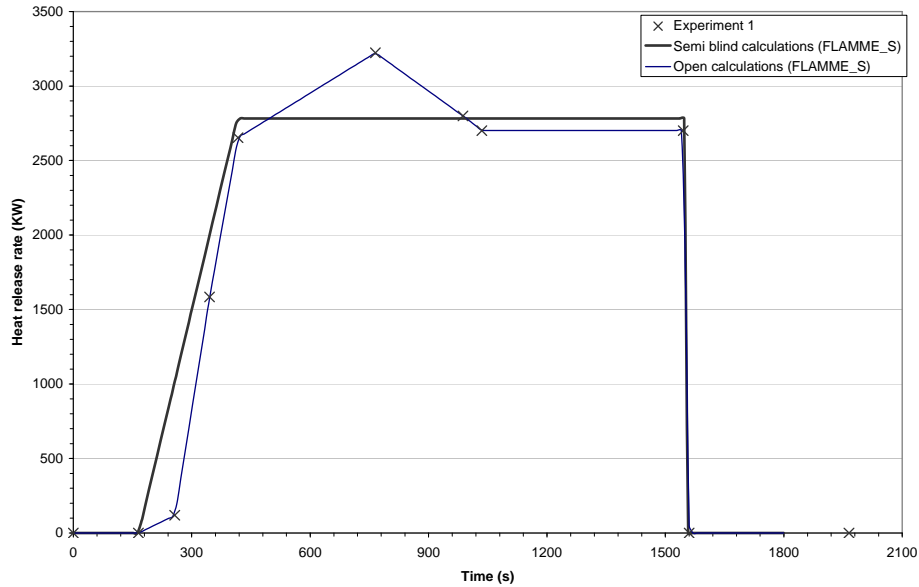


Fig. E3 Heat release rate of Test 1

Interface Layer

As shown in Fig. E4, the layer height calculated by FLAMME-S is lower than the interface determined from the experimental data.

The experimental interface height is determined with thermocouples located at three elevations: 1.5 m, 3.35 m and 5.2 m. So, in the experiment, the layer height never decreases under the elevation of the first thermocouple, i.e. 1.5 m. Tourniaire et al. have shown that the data reduction method is weakly dependant on the number of thermocouples, except, with three thermocouples, the interface height does not reach the floor 0.

For semi-blind and open calculations, the location of the upper layer rapidly moved from the ceiling down to approximately 0.5 m above the floor (see Fig. E4).

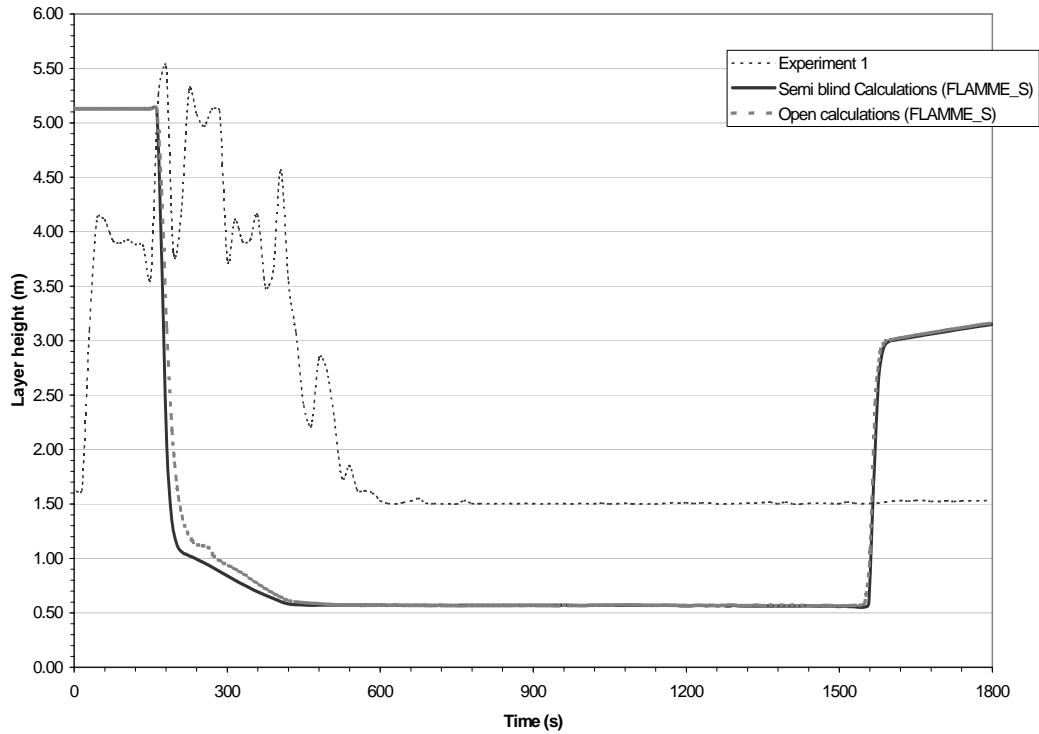


Fig. E4 Layer height of Test 1

Gas Temperature

The gas temperatures calculated of the upper layer are in good agreement with the experimental results. As the layer height calculated by the code is reasonably lower than the experimental interface, the temperature of the lower layer is colder than the gas temperatures measured (see Fig. E5 and Fig. E6). The experimentally measured lower layer thickness and temperature are higher than the corresponding results calculated by the code.

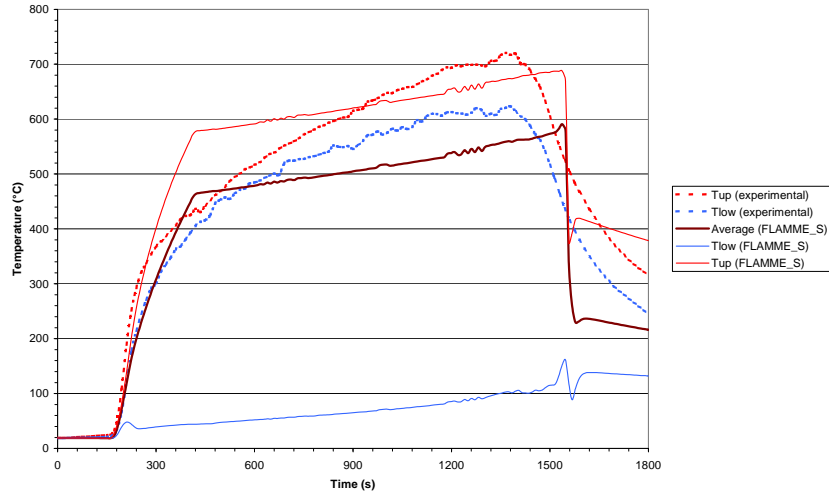


Fig. E5 Gas temperature in the compartment - semi-blind calculations

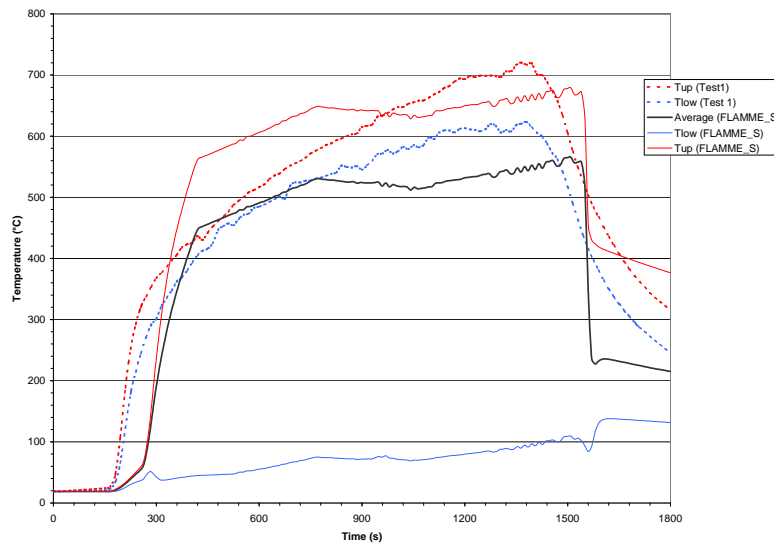


Fig. E6 Gas temperature in the compartment - Open calculations

Oxygen Concentration

The oxygen concentrations calculated with the code in the upper layer are lower than those measured, but the comparison is difficult because the sensor GA2-O2 seems to have saturated (see Fig. E7).

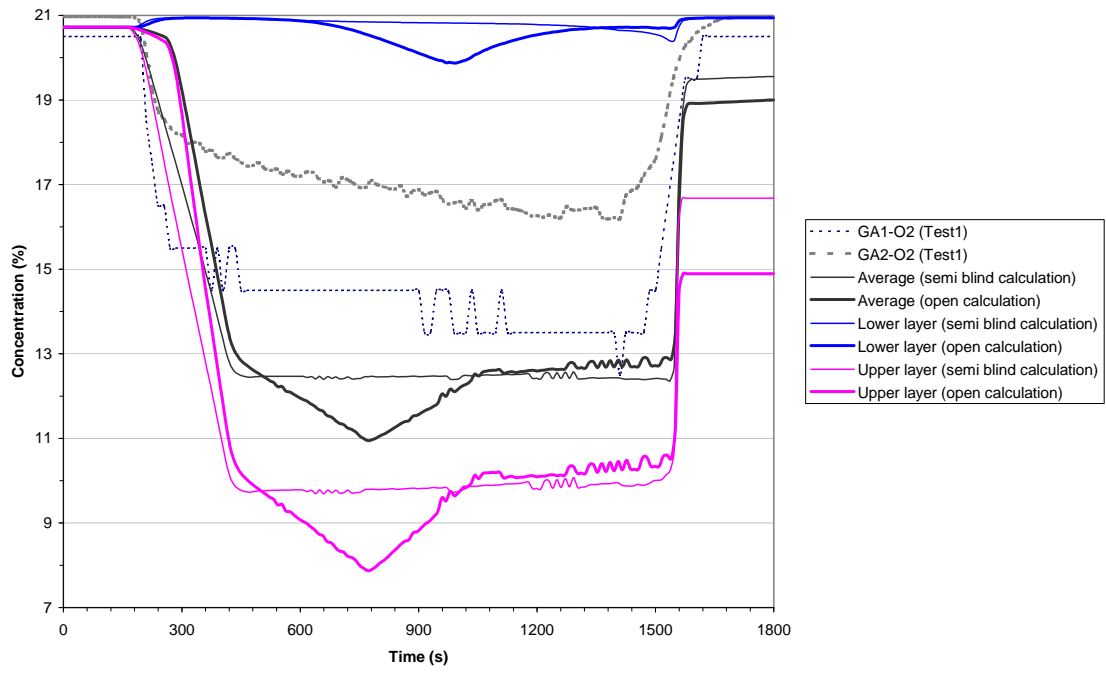


Fig. E7 Oxygen concentrations

Heat Fluxes of the Walls

Experimentally, the total heat fluxes are measured at one elevation, i.e 1.7 m. At the upper layer, the code calculates slightly lower total heat fluxes (see Fig. E8).

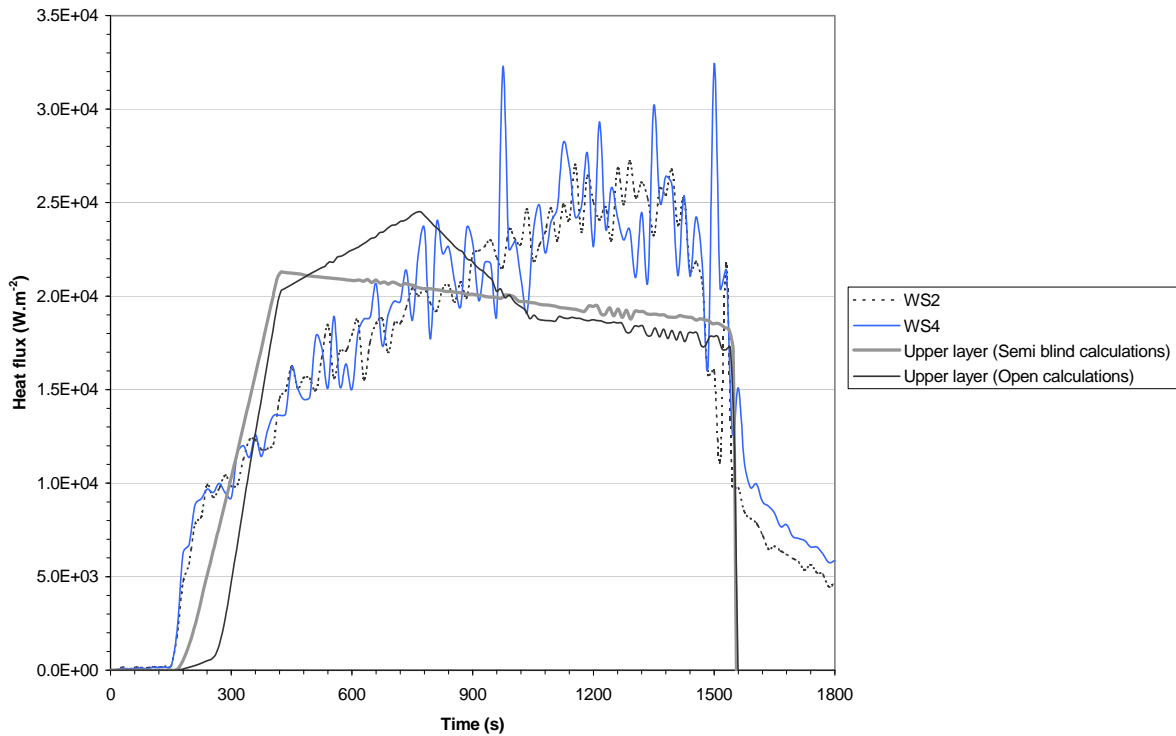


Fig. E8 Heat fluxes of Test 1

Wall Temperatures

The wall temperatures are not compared because the FLAMME-S code calculates an average temperature for the first mesh of a wall and it can not be compared with a surface temperature measured experimentally.

However, the temperatures of the two material probes are compared (see Fig. E9 and Fig. E10). In the experiment, sensors seem to be reversed M 28 and M 26 for the aerated concrete slab and M 32 and M 30 for the concrete slab. The calculated results are in good agreement with measurements if the four sensors mentioned above are really reversed.

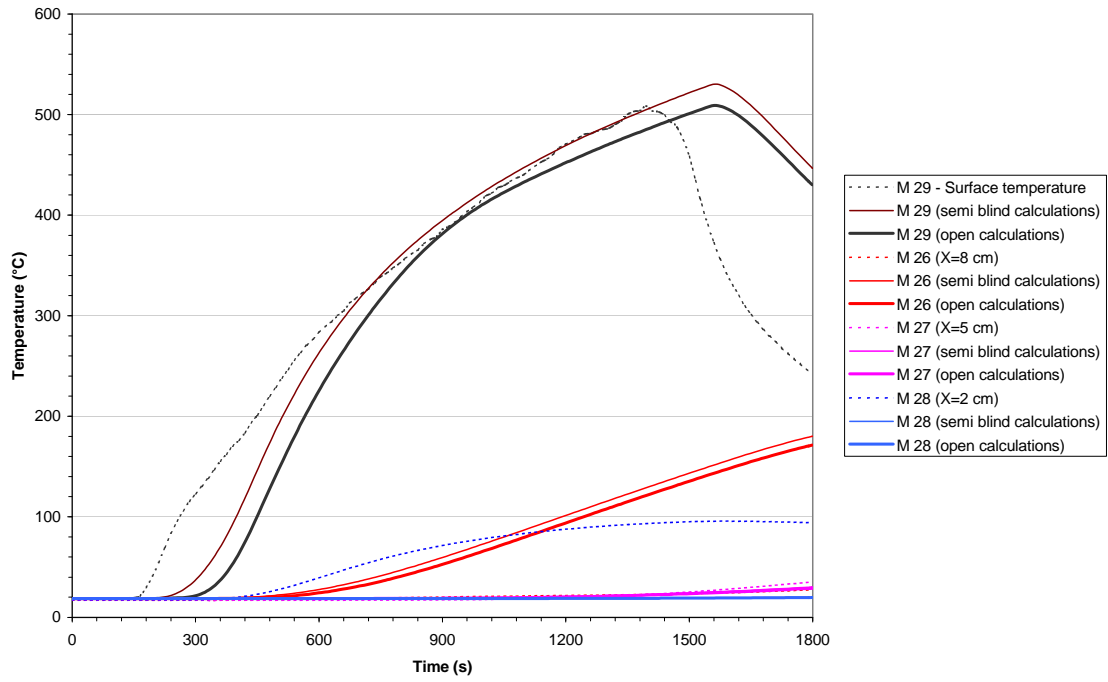


Fig. E9 Temperatures of the aerated concrete slab

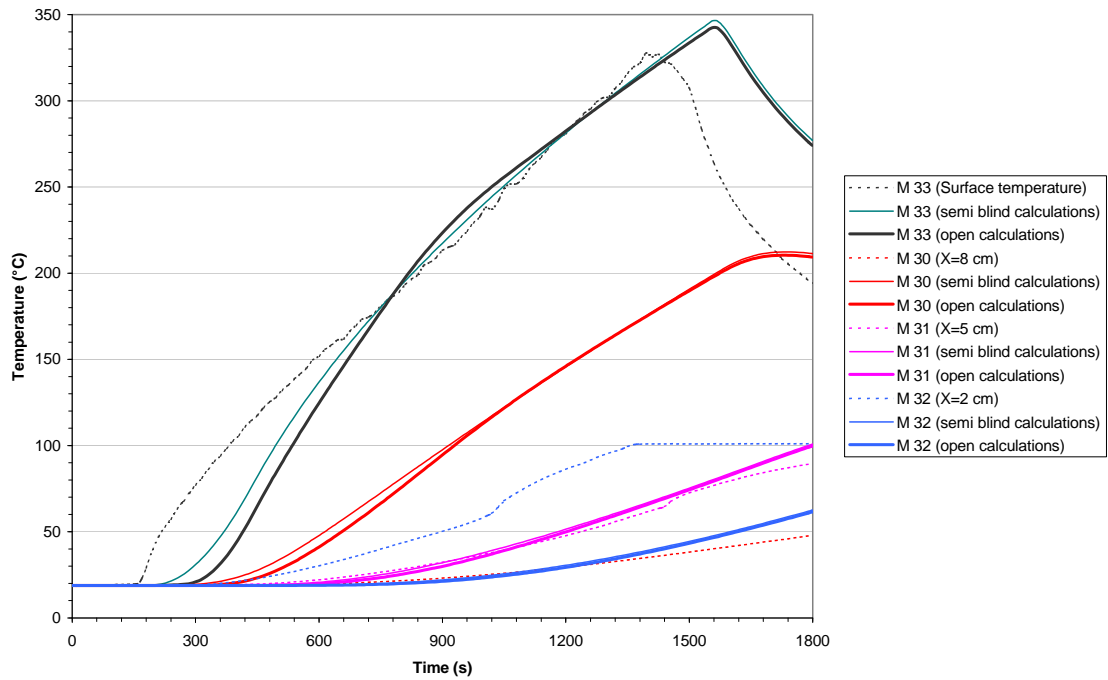


Fig. E10 Temperatures of the concrete slab

E3.1.2 Other Calculated Results

Other calculated results are presented, however they are not compared to experimental results, because these parameters are not measured.

Heat Losses into the Walls of the Fire Compartment

Fig. E11 and Fig. E12 show the total heat losses into the walls of the fire compartment. These losses represent approximately 70 % of the heat released by the fire.

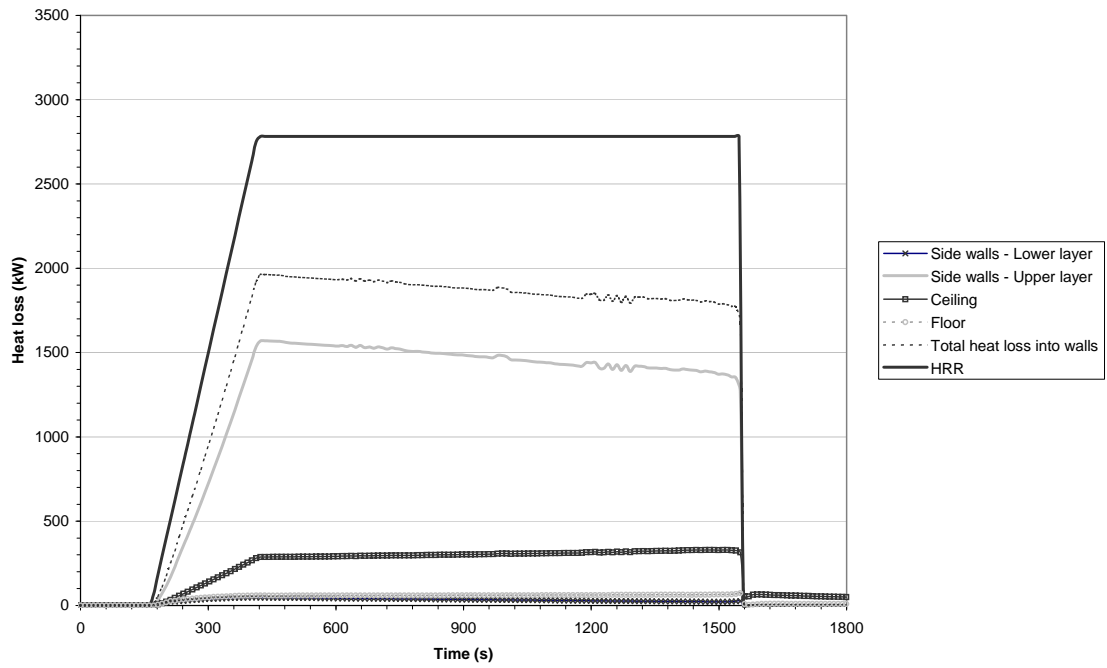


Fig. E11 Heat loss into the walls of the fire compartment – semi-blind calculations

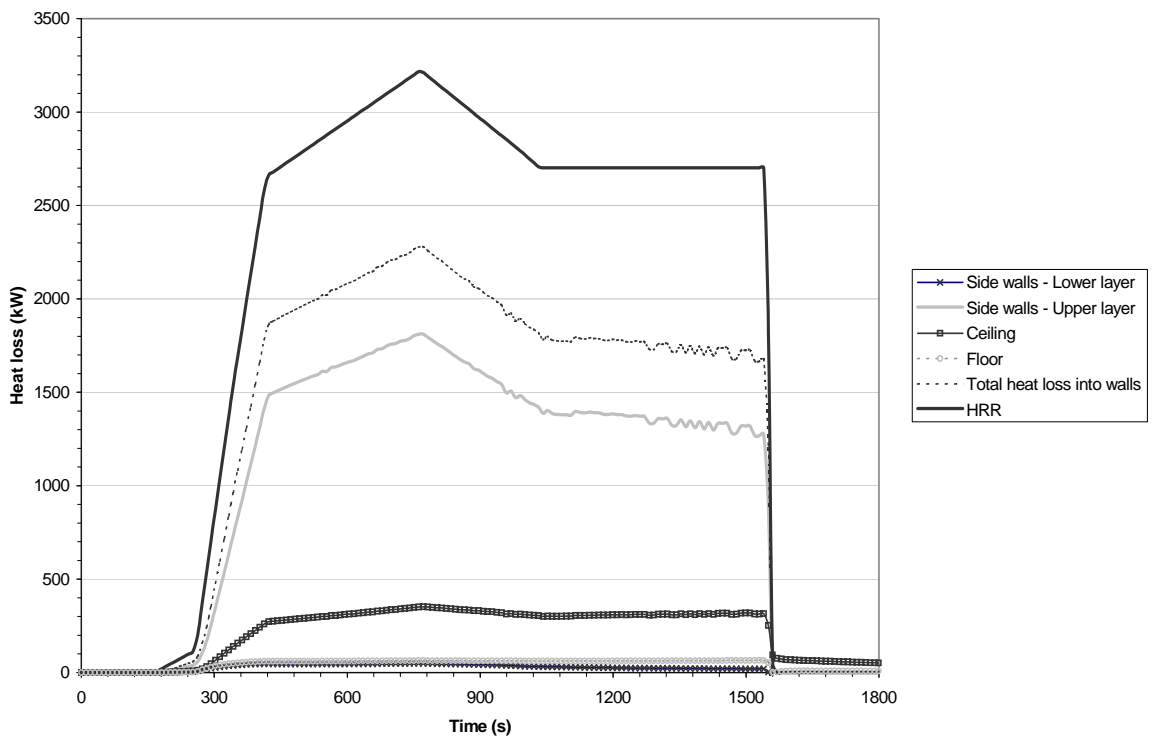


Fig. E12 Heat loss into the walls of the fire compartment – open calculations

Mass Flow Rates through the Door

The evolutions of mass flow rates through the door are generally similar for the two kinds of calculations. The results show one difficulty with the use of the code: there are a lot of numerical variations due to low pressure difference through the door during the stationary phase of the fire.

For the two cases, the mass flow rate through the front door from the fire compartment, i.e. GOUT, is around 1.8 kg s^{-1} at the beginning of the fire, and increases at the end of the fire.

Neutral Plain

For the two cases, the neutral plain at the door is around 1.3 m.

E3.2 Test 3

The experimental conditions of the Test 3 are similar to those of Test 1 but with a smaller opening, with a free cross section of 0.7 m^2 .

Heat release rate

For the semi-blind calculations, the concentration limit of oxygen (imposed in the data file on a value of 11.5 %) leads rapidly to an extinction of the fire, two minutes after the beginning of the fire.

For the open calculations, even if the experimental pyrolysis rate is imposed in the data file, the code under-estimates the heat release rate: the pyrolysis rate is limited by the code because the quantity of oxygen involved in the reactive zone is not enough for the combustion reaction (see Fig. E17).

So for all others parameters, the comparison of code/measurements will be not satisfactory since the heat release rate is under-estimated.

The results of the code concerning the heat release rate seem to show that, during the Test 3, a phenomenon occurred that it is not modeled by the code. Experimentally, the oxygen concentration measured reached 0 %, the gas temperatures inside the com-

partment increase up to about 900 °C (see Fig. E16) and a flame was observed at the opening. This experiment presents characteristics similar to those of the ghosting flame described by different authors. For example, Audouin *et al.* observe a flame that migrates from the original fuel surface towards the opening 0. A two-zone model code is not able to model this phenomenon: in the code, the unburned gases cannot move from the fire zone to an opening. Interesting results of the code are the comparison of the pyrolysis mass (input data), with the burned and unburned masses of fuel calculated by the code (see Fig. E14). These results show that all the pyrolysis fuel burns during the first three minutes, but later, under ventilated conditions in the compartment (due to the smaller opening) leads to only a proportion of vaporized gases burning inside the facility.

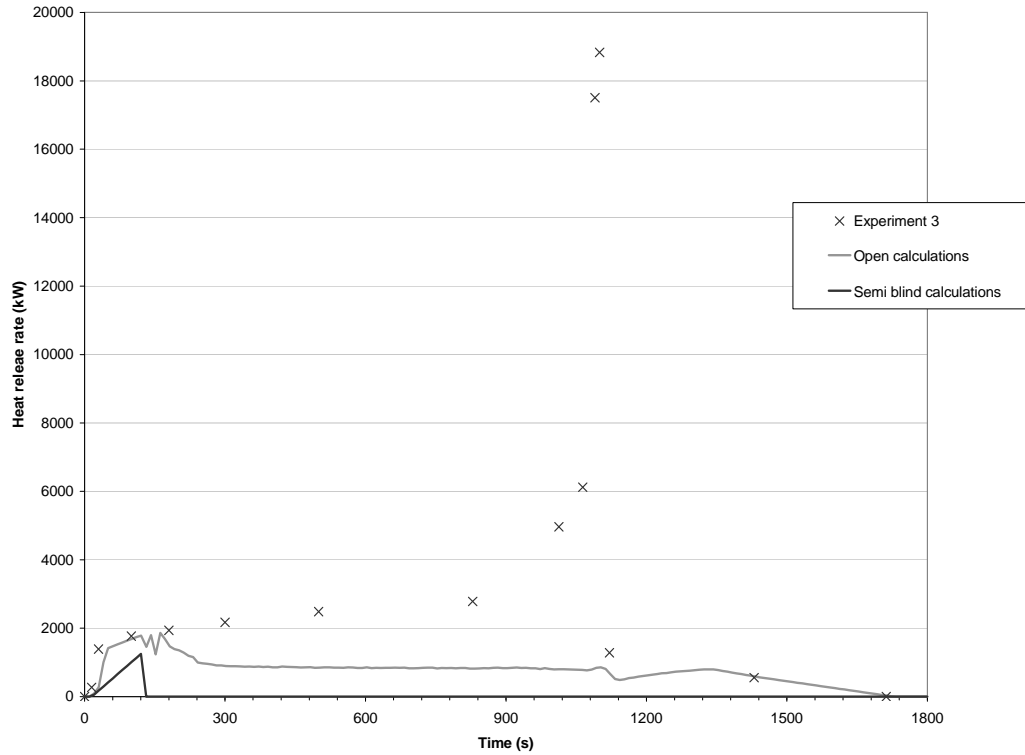


Fig. E13 Heat release rate of Test 3

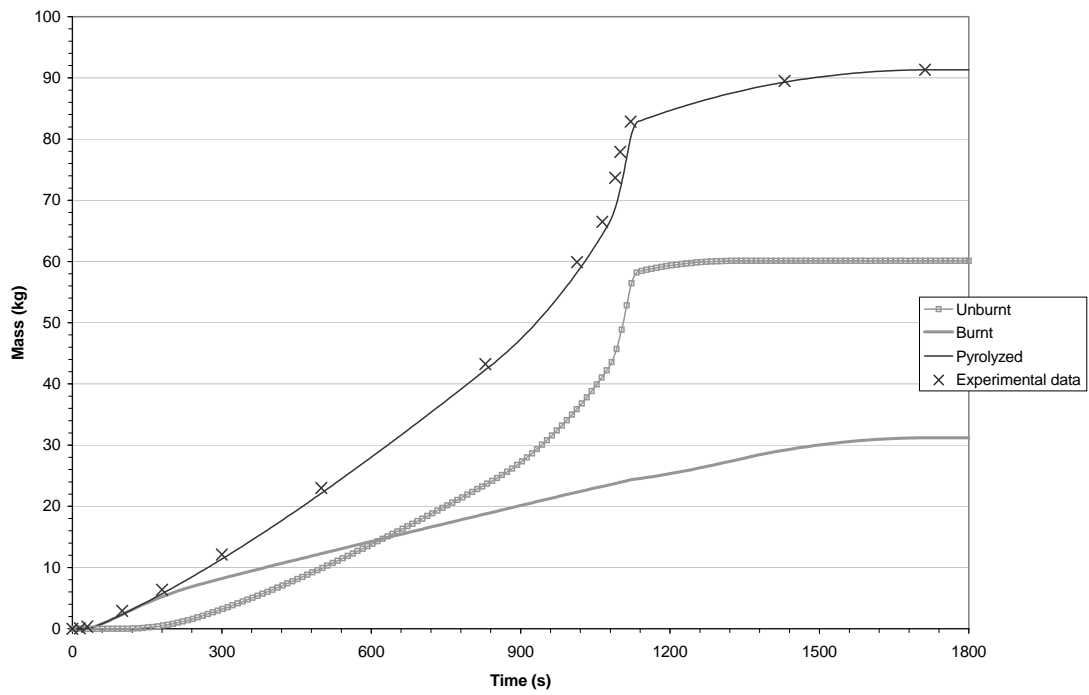


Fig. E14 Quantities of burned and unburned fuel

Interface Layer

The calculated location of the upper layer rapidly moved from the ceiling down to the floor, for the semi-blind and the open calculations. In the code, when the interface reaches the floor, there is only one gas zone. Experimentally, the height of the layer never reaches a level below the elevation of the first thermocouple, i.e. 1.5 m (see chapter E3.1).

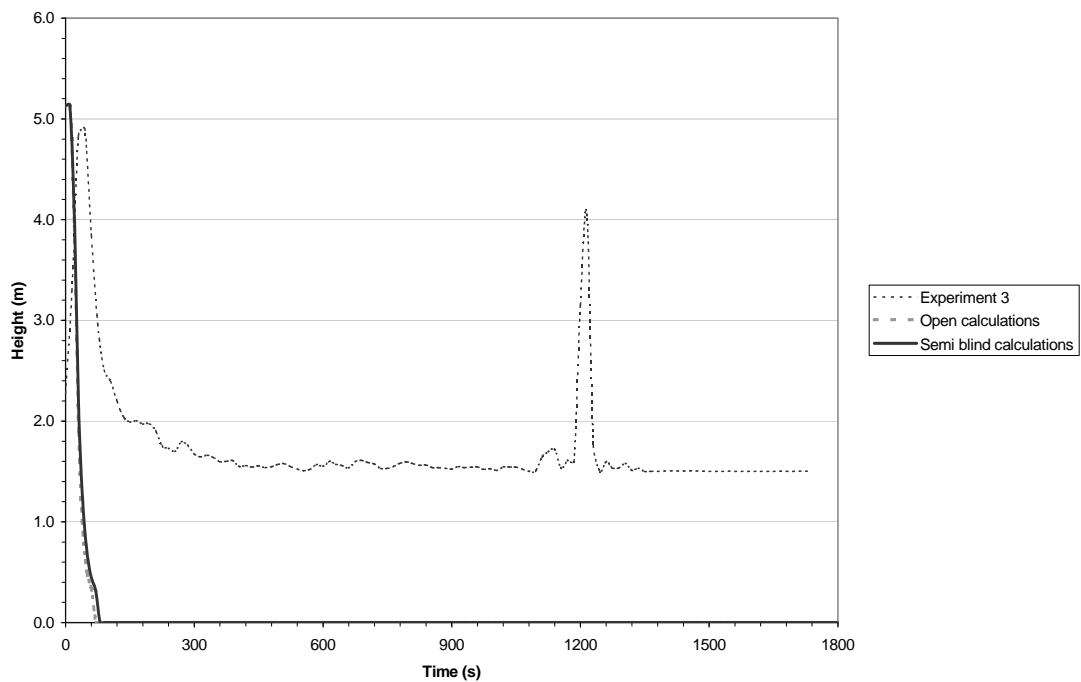


Fig. E15 Layer height of Test 3

As it is mentioned above, the code under-estimates the heat release rate so the calculated average temperature is cooler than the measured gas temperatures (see Fig. E16) and the heat fluxes are lower than those measured (see Fig. E18).

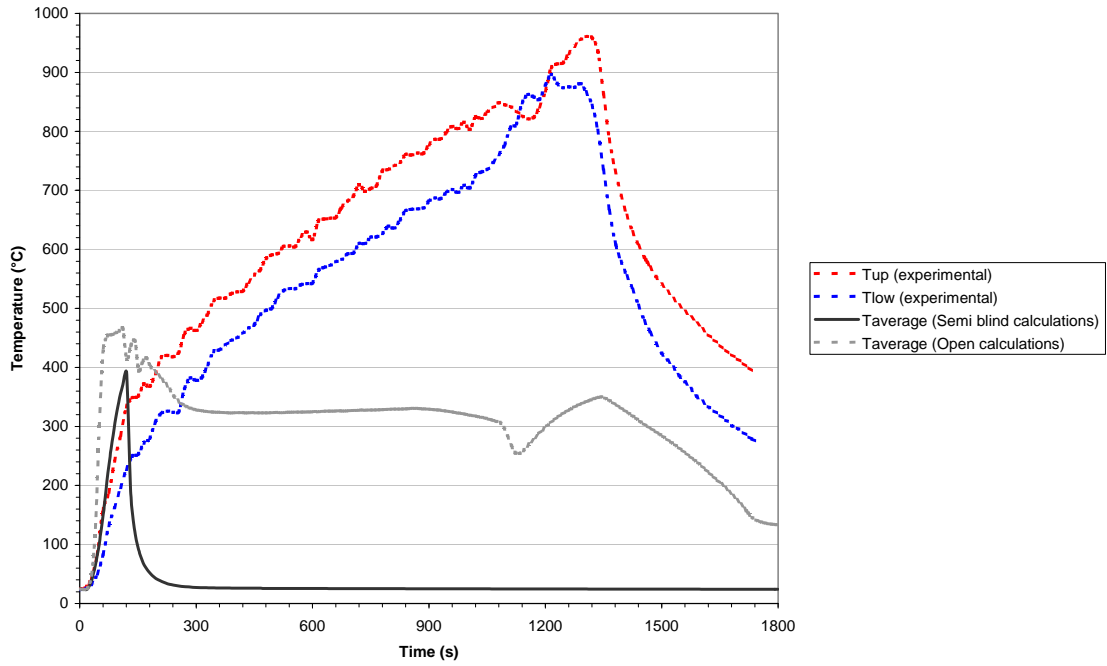


Fig. E16 Gas temperature in the fire compartment

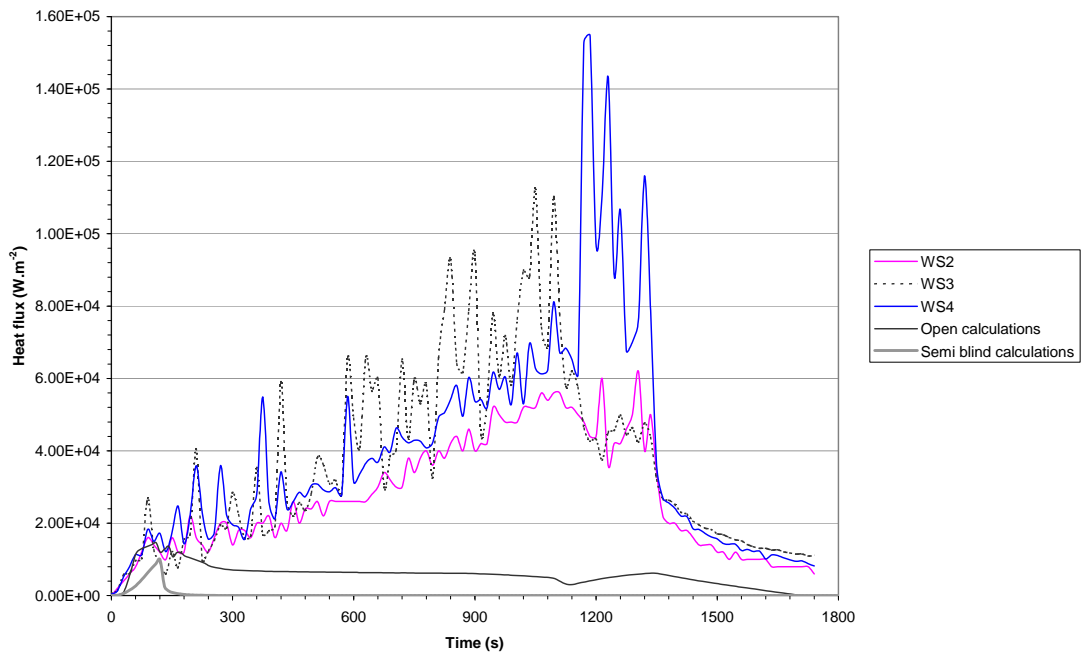


Fig. E17 Heat fluxes of Test 3

Mass Flow Rates through the Door

The development of mass flow rates through the door is presented in Fig. E18. However, these results are not correct, because all others parameters are under-estimated.

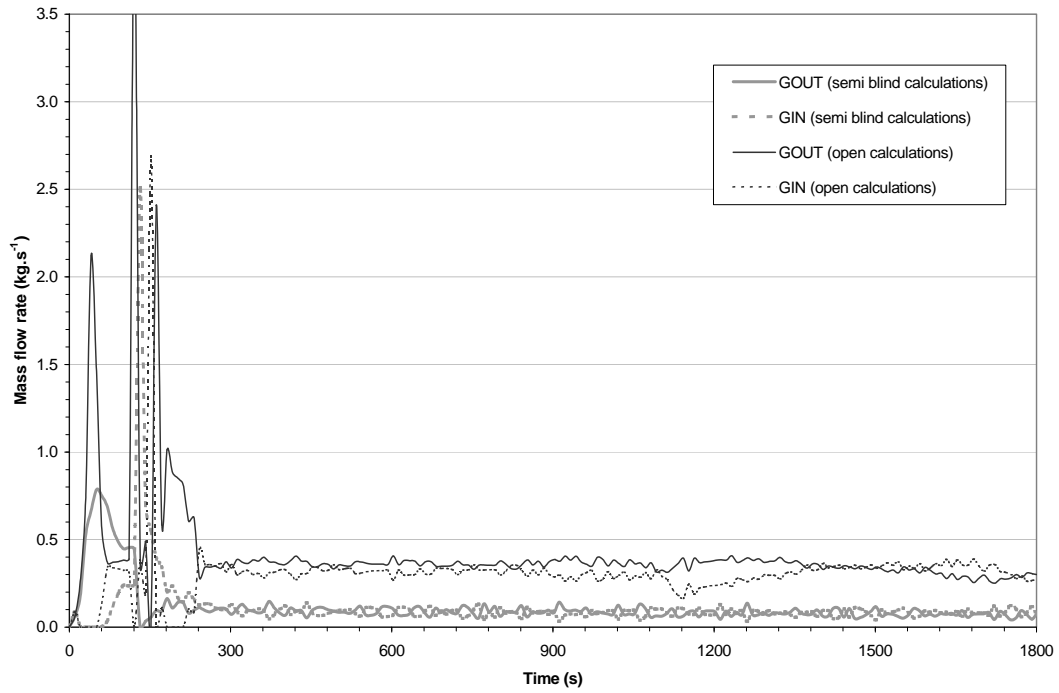


Fig. E18 Mass flow rates through the door of Test 3

E4 Conclusions

The two-zone model FLAMME-S has been applied to perform calculations for the Benchmark Exercise No. 4 to simulate kerosene pool fires inside a compartment. The results calculated are compared to experimental measurements of two experiments, implementing a 1 m² liquid fuel pool of kerosene in a compartment with natural ventilation through an opening.

In the first experiment, the opening is a door with a free cross section of 2.1 m². A more adapted instrumentation would be necessary, in particular in the gas zone, to compare the experimental results to code simulations. Nevertheless, for this case, the FLAMME-S results show a good overall agreement with the measured data.

In the second experiment simulated, the opening is smaller, with a free cross section of 0.7 m². For this case, the FLAMME-S results cannot be compared to the experimental data because the phenomenon observed experimentally, when the fire stabilizes at the opening, is not modeled by the two-zone code, FLAMME-S.

These two scenarios studied are outside the validation domain of FLAMME-S 0. However, the comparison of the code results to the experimental ones show that the calculated results are in good agreement with the experimental data according the size of the opening.

E5 References

- /KLE 03/ Klein-Heßling W., M. Röwekamp, R. Dobbernack, O. Riese:
Specification of International Benchmarking and Validation Exercise #4:
Kerosene Pool Fire Inside A Compartment, GRS, June 2003
- /BOU 02/ Bouton, E.:
Overview of the FLAMME-S code validation matrix, Technical Note
SESHP/GME/IPS/FLS/C40/NT/02.337, 2002
- /TEW 95/ Tewarson, A.:
Generation of heat and chemical compounds in fires, The SFPE Handbook
of Fire Protection Engineering, 1995
- /TOU 00/ Tourniaire, B., and L. Audouin:
Sensitivity analysis of a data reduction method estimating the interface
height, the lower and upper temperatures in fire room, Proceedings of the
International Seminar of Fire and Explosion Hazard, 2000
- /AUD 99/ Audouin, L., J.M. Such, J.C. Malet, and C. Casselman:
A real scenario for a ghosting flame, Proceedings of the fifth international
symposium, pp. 1261-1272, 1999

List of Figures

Fig. E1	Pyrolysis rate of Test 1	5
Fig. E2	Pyrolysis rate of Test 3.....	5
Fig. E3	Heat release rate of Test 1	8
Fig. E4	Layer height of Test 1	9
Fig. E5	Gas temperature in the compartment - semi-blind calculations	10
Fig. E6	Gas temperature in the compartment - Open calculations.....	10
Fig. E7	Oxygen concentrations	11
Fig. E8	Heat fluxes of Test 1	12
Fig. E9	Temperatures of the aerated concrete slab	13
Fig. E10	Temperatures of the concrete slab	13
Fig. E11	Heat loss into the walls of the fire compartment – semi-blind calculations	15
Fig. E12	Heat loss into the walls of the fire compartment – open calculations.....	15
Fig. E13	Heat release rate of Test 3.....	18
Fig. E14	Quantities of burned and unburned fuel.....	18
Fig. E15	Layer height of Test 3	19
Fig. E16	Gas temperature in the fire compartment	20
Fig. E17	Heat fluxes of Test 3	20
Fig. E18	Mass flow rates through the door of Test 3.....	21

**Appendix F: International Collaborative Project to Evaluate Fire
Models for Nuclear Power Plant Applications**

CFX5 Simulations for Benchmark Exercise No. 4

Presented by

Matthias Heitsch

Gesellschaft für Anlagen- und Reaktorsicherheit (GRS) mbH,
50667 Köln, Germany

Contents

F1	Introduction	1
F2	Computer Model of the Test Facility	3
F3	Physical Description of the Tests by CFX	5
F4	Test Results and Comparison.....	7
F4.1	Test 1	7
F4.2	Test 3	9
F5	Conclusions.....	11
F6	Acknowledgement	13
F7	References	13
F8	Figures	15
	List of Figures	43

F1 Introduction

This report describes the calculations carried out for Benchmark Exercise #4 with the code CFX 5.7 /CFX 04/ within the frame of the International Collaborative Project for the Evaluation of Fire Models (ICFMP). The code version 5 of the CFX family represents a completely new code structure compared with previous versions and offers new features. An assessment of CFX 5 in blind mode for benchmark #4 failed because of lack of time to test relevant new test options. Post-test analysis comparisons against test data have now been made. The following chapters present the results obtained for tests 1 and Test 3 and draw comparisons to experimental data.

F2 Computer Model of the Test Facility

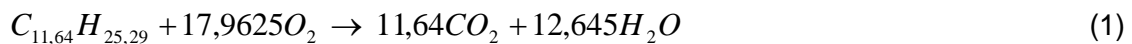
The OSKAR test facility includes the fan system Fuchs and a hood outside the test room to collect the gas stream through the door opening. Fig. F1 shows the computer model developed for CFX. The fire tray is shown in red. The barrel tray has a blue color. The venting openings from the hood and to the fan system are shown in cyan. The outer boundary of the computational domain to the environment, lateral from the hood, has a light yellow color.

Thanks to the regular geometry of the test arrangement, the computational mesh was decided to be built exclusively with completely structured cells. This usually improves the convergence of the simulation compared with unstructured or mixed meshes. A cut through the mesh is displayed in Fig. F2. The mesh is quite uniform and less dense underneath the hood outside of the test room. The mesh has a total of 115700 cells in the fluid domain of the modeled test volume. Another 2548 cells are in the barrel target (inner and outer part) to describe heat conduction. Later in the text, when the simulation results are compared with the measured temperature increase in the solid barrel, it reveals that the horizontal resolution chosen is probably not yet fine enough.

Both tests analyzed differ only in the size of the door opening. The two variants used are shown in Fig. F3. The smaller opening at Test 3 provides less fresh air supply to the fire.

F3 Physical Description of the Tests by CFX

The gas mixture of air and the fuel kerosene is modeled by the individual species, which are kerosene, oxygen, nitrogen, carbon-dioxide and steam. Soot is also created according to the Magnusson soot model implemented in CFX. In this model a number of constants are used, which were not further investigated in the given context. Nitrogen represents a background fluid, not participating in any reaction. The chemical reaction itself is represented by a single-step mixing controlled reaction within the Eddy Dissipation model. The reaction modeled reads



A predefined share of the reaction heat (40%) is emitted from the surface of the fire pan as radiation flux and distributed by the P1 radiation model in CFX. This radiation model solves an extra transport equation and assumes direction independent radiation transport. It allows heating of the fluid due to radiation from a boundary (here the fuel pan). The fuel flow from the fire pan is prescribed according to the measured fuel consumption. The chemical reaction happens according to the mixing intensity in the fluid domain and the local availability of fuel and oxygen. Flows through the venting system "Fuchs" and the hood are specified by flow velocities given in the specification of the tests.

A simplification was made concerning the heat flow into the surrounding walls. These walls are not included in the mesh and hence the heat flow calculated at constant wall temperature. This over-estimates the removal of energy from the fluid. Alternatively, a one-dimensional heat conduction model as a boundary condition without including the walls in the mesh is available, but was not applied.

F4 Test Results and Comparison

Tests 1 and 3 differ in the release history of kerosene and the size of the opening to the environment.

F4.1 Test 1

The fuel release rate from the fire pan is shown in Fig. F4. This history corresponds exactly to the fuel consumption curve from the experiment. A total amount of 80.7 kg kerosene was calculated. A typical temperature distribution in a vertical plane is shown in Fig. F5. This plane includes the locations chosen for time histories in the front and back of the test room in Fig. F6 and Fig. F7. The temperature distribution is affected by the inflow of cold air through the door and the hottest part of the gas plume is pushed towards the back of the room. For the temperature histories in Fig. F6 and Fig. F7 three vertical locations were selected. The temperatures in the front location show a good correspondence to the measurements up to about 400 s and then stagnate up to the time when the fire intensity passes its peak. In the simulation this is expressed by a slight reduction of gas temperatures. Then the fire intensity remains constant for a longer while and reduces to zero after about 1400 s. The measured temperatures however increase continuously up to the end of fuel combustion. It seems that radiative heat flow to the thermocouples may have caused this behaviour. CFX provides pure gas temperatures, which do not include any radiative contribution. A similar tendency can be observed for temperatures in the back part of the facility (Fig. F7). Here, however measurement and simulation show different trends. During the test the highest temperature was observed at the bottom of the room and decreasing towards the ceiling. The simulation predicts the opposite. Fig. F8 provides a planar distribution of temperature together with a linear profile including the same locations as from Fig. F7. Fig. F8 shows a stratification of temperature, which is strongly distorted to the right side of the figure. The probe locations according to Fig. F7 are located in a region with temperature increase from bottom to ceiling. The predicted temperature of CFX varies with time and sometimes decreases with increasing height. The code calculates a fluctuation of the fire plume with time.

Selected temperatures in a vertical line directly above the fire pan are depicted in Fig. F9. Similar to the temperatures in the front location of the room, the calculated values increase faster than the measured ones, but do not show a continuous increase

throughout the transient. Instead, they have almost constant values for a longer time. This is typical for all locations of probes in relation to the simulation. Fig. F10 displays the temperature profile for the same locations as in Fig. F9 at 1100 s. The maximum temperature exists directly above the fire tray and then remains almost constant with increasing height.

The oxygen history at probe GA1 is compared to simulated values in Fig. F11 (location of GA1 shown in Fig. F12). The measured data are captured quite well. Only at the beginning and the end of the fire scenario some differences can be seen. This may be related to the kerosene release curve, which was specified as input. An illustration of the oxygen distribution influenced by the gas exchange through the door opening can be seen in Fig. F12. Lowest mole fractions are found above the fire tray in a plume pushed to the back of the room. Most other locations of the plane in Fig. F12 have relatively uniform oxygen mole fractions. The CO₂ generation as a product of the kerosene combustion behaves opposite to the oxygen consumption. This can be seen by a comparison of Fig. F12 and Fig. F14. The quantitative comparison of the CO₂ measurement with simulation data in the vicinity is depicted in Fig. F13. The measured CO₂ mole fraction is lower than the values predicted by CFX. This may be due to the fact that the modelled chemical reaction does not include any production of CO and contributes all directly to CO₂. A global circulation pattern forms in the combustion room, which considerably homogenizes the species concentrations.

In the door opening a number of flow sensors recorded the flow speeds in a vertical line. Fig. F15 compares predictions to measurements. In the upper locations the predictions compare quite well with the measurement, in the lower probe locations however the flow is under-estimated. It is possible, that some of the lower sensors were not working correctly. A more illustrative representation of the stratified flow through the door can be seen in Fig. F16. The vertical velocity profile, which was added to Fig. F16, shows that the flow is directed inwards in the lower section of the door and outwards in the upper part. A zero velocity region is approximately in the middle of the door. Mass flows through the hood area outside of the room together with the flow out of the fan system (Fuchs) are drawn in Fig. F17. From the specification of the experiment flow velocities through the respective openings were used as input to the code. These values are also shown in Fig. F17. Mass flows out of the computational model are negative.

The next two figures show the temperature growth in the selected locations of the barrel target. This barrel is built as a double vessel container. The inner section was filled by some sort of granulate and the outer cylinder by concrete. In the computer model only these two materials have been included but not the vessel walls. Also the mesh was probably not sufficiently fine to model the correct temperature built-up. A coarser mesh inside the solid body results in less heat-up because of averaging over a larger volume. Fig. F18 and Fig. F19 show the calculated temperature histories at some locations in the inner and outer part of the barrel.

F4.2 Test 3

The modelled kerosene release curve is shown in Fig. F20. This history was submitted to the code according to the test description. The imposed sudden termination of kerosene release after about 1100 s can also be identified in the temperature plots and causes some disagreement after that time (see Fig. F21 or Fig. F23). The gas temperature history along a vertical line in the front of the test facility is depicted in Fig. F21. An isosurface of temperature including the profile line of Fig. F21 is illustrated in Fig. F22. This figure reveals the impact of the inflow through the door on the temperature distribution. The gas with the highest temperatures is pushed towards the back wall. Gas temperatures in the back are shown in Fig. F23. They show a similar good correspondence with measured data up to the moment the fire is stopped. There might also be some thermal inertia of the thermocouples including continuing radiative heat flux from walls, which causes a slower decrease than predicted by the simulation. The temperature distribution directly above the fire tray is shown in Fig. F24. The measurement indicates a relatively uniform temperature. The simulation however calculates a quite low temperature in the lowest elevation and indicates a stronger stratification. This is related to the calculated strong distortion of hot gases towards the back wall. A typical temperature pattern is also shown in Fig. F25. The inflow of cold air decreases the lower temperature.

Due to the combustion the oxygen concentration in the atmosphere is reduced. The corresponding history at several locations close to sensor location GA1 is depicted in Fig. F26. For this test the correspondence to measured data is as good as for Test 1. A more comprehensive distribution is presented in the isosurface of Fig. F27. The corresponding CO₂ contents in the test facility at the same time can be seen in Fig. F28.

The flow through the door opening can be characterized by the available velocity probes. A comparison between measurement and calculation is illustrated in Fig. F29. For the lower velocity probe the comparison is very good. At the upper location however negative values (inflow) were measured but the predictions were positive. Fig. F30 confirms this situation. At the time shown (800 s) there is only flow into the test compartment through the door. This is also illustrated in Fig. F31. This top view from inside the test compartment shows the flow pattern directed inwards. At other times the flow direction changes. The flow out of the fan system (Fuchs) however supports inflow through the door. Fig. F32 shows the flow speeds for both ventilation systems (blue lines) together with the calculated mass flows by CFX (black lines).

In Fig. F34 and Fig. F34 the temperature increase at selected locations in the barrel container is summarized. The barrel container with its inner and outer cylinder was modelled with some simplifications. The steel shells were not included in the mesh. Therefore the heat-up in the simulation may progress slightly faster. This becomes obvious in Fig. F33. In the inner section filled with granulate there is almost no temperature built-up as depicted in Fig. F34. At the beginning of the experiment the temperature was not uniform. The simulation however started from an equal distribution throughout the barrel. Therefore simulated temperatures are shifted by a certain amount.

F5 Conclusions

Both experiments simulated by CFX-5.7 show satisfactory or good agreement to measured data. The mesh used is completely structured. This involves difficulties if the length scales to be represented differ strongly. Following this consideration, the three material probes were not included and corresponding temperature predictions are not provided. This could be improved if locally unstructured cells are used to model tiny objects in combination with a structured main mesh.

The simulations were carried out without taking into account the thermal reaction of the surrounding walls. Heat releases are modelled using the wall function of the turbulence model but the walls do not heat up. This was chosen in order to save computing time but involves too much heat leaving the domain. Now a separate heat conduction model acting as variable boundary condition is available to provide a more realistic wall behaviour.

Further improvement of predictions might be achieved if the radiative share from the flame would be released where the reaction really takes place. In the given model of the test facility the flame radiation is emitted from the fire pan, which does not match reality for the floor radiation in particular.

F6 Acknowledgement

The presented work was funded by the German Federal Ministry for the Environment, Nature Conservation and Nuclear Safety (BMU), which is gratefully acknowledged.

F7 References

/CFX 04/ ANSYS Inc.:
CFX-5.7, User Documentation, ANSYS Inc, USA, 2004

F8 Figures

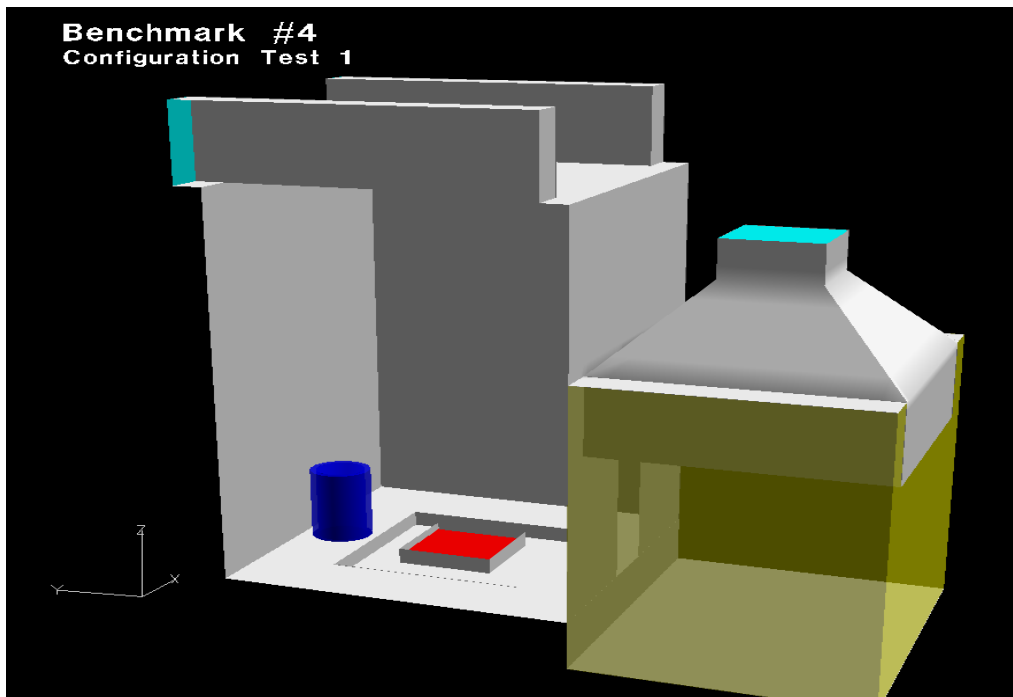


Fig. F1 Cut through the CFX model of the test facility OSKAR

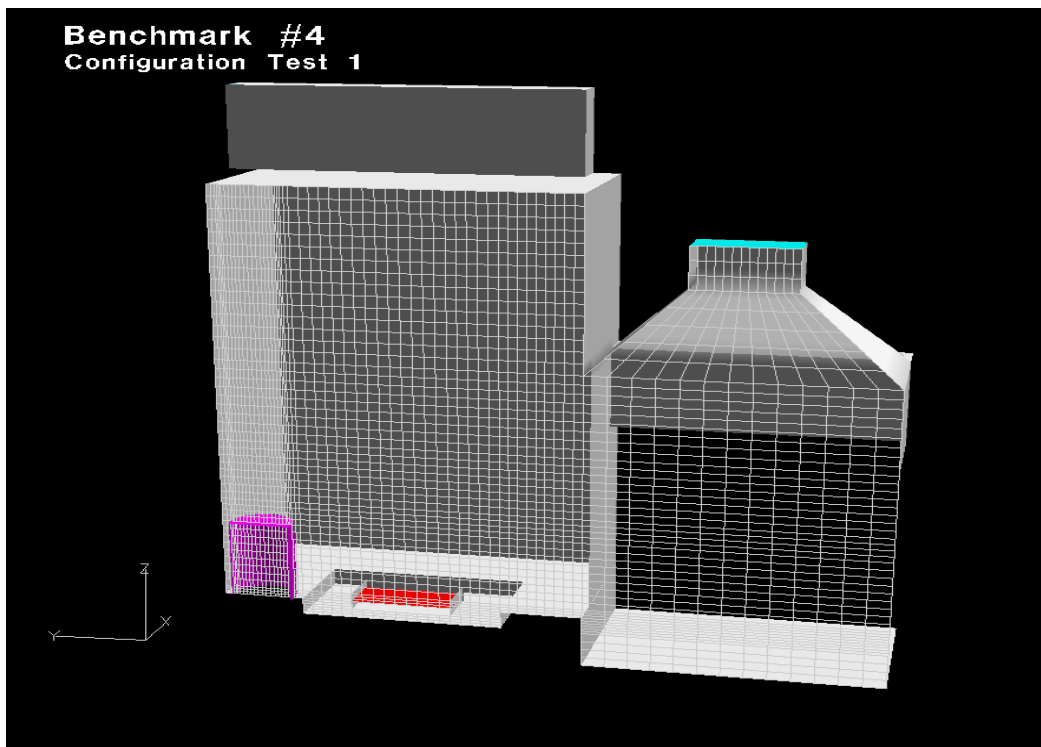


Fig. F2 Mesh distribution in a vertical plane

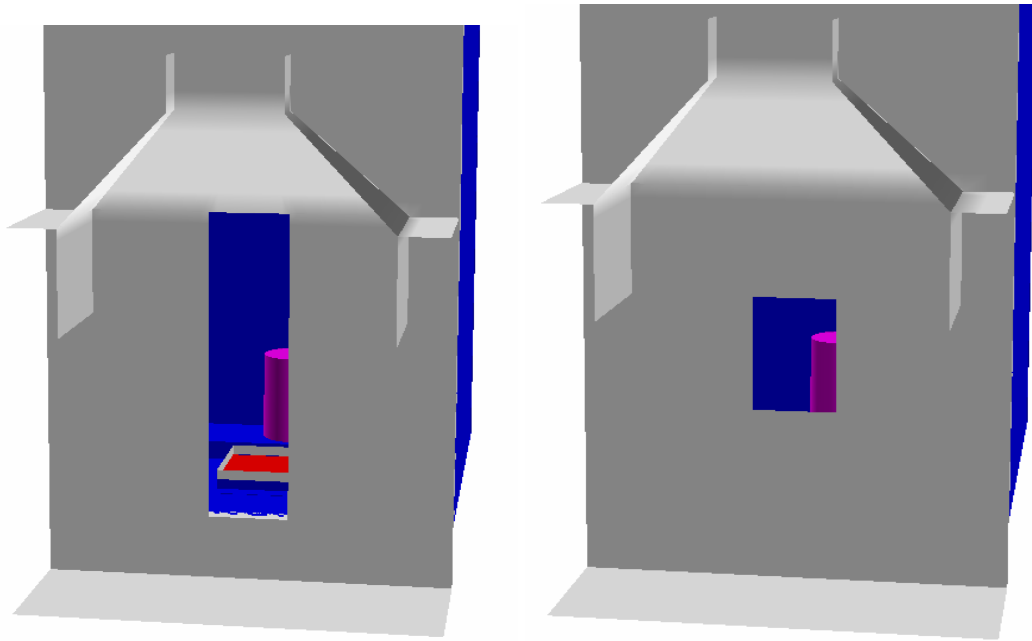


Fig. F3 View of the vent openings for Test 1 (left) and Test 3 (right)

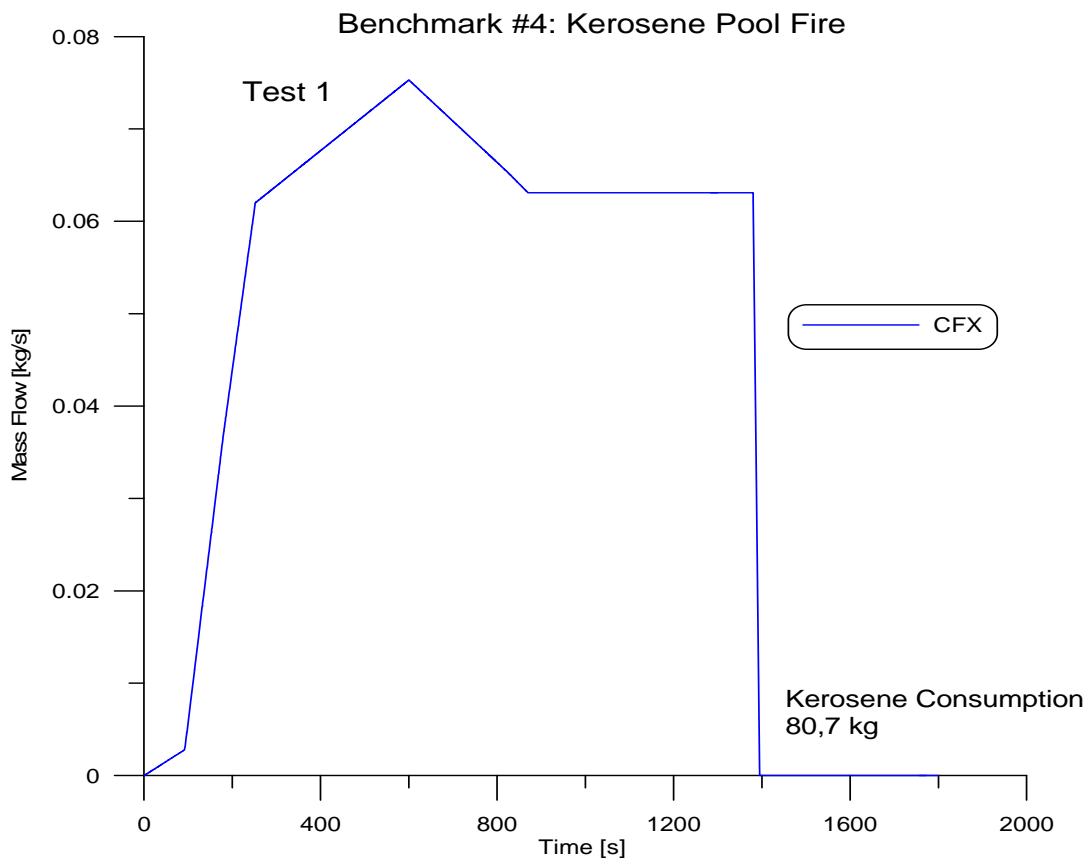


Fig. F4 Released and burned kerosene mass history for Test 1

Benchmark #4
Configuration Test 1

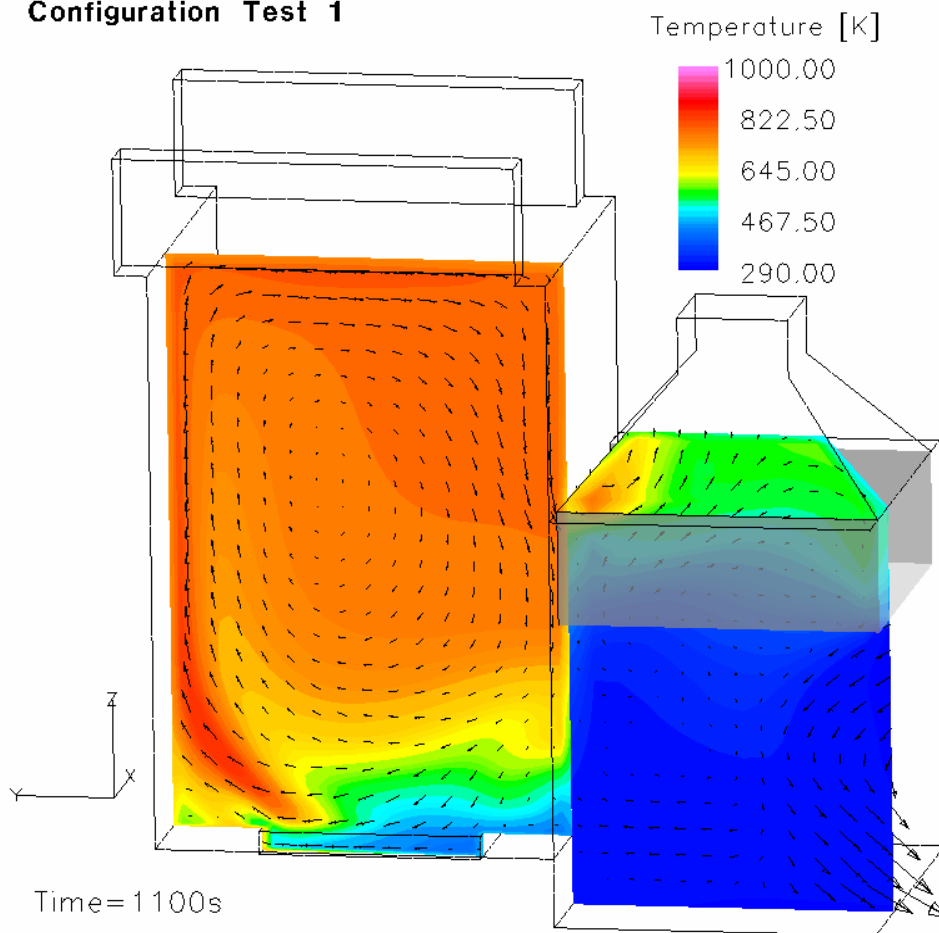


Fig. F5 Vertical temperature distribution at a plane $x=0.95$ m

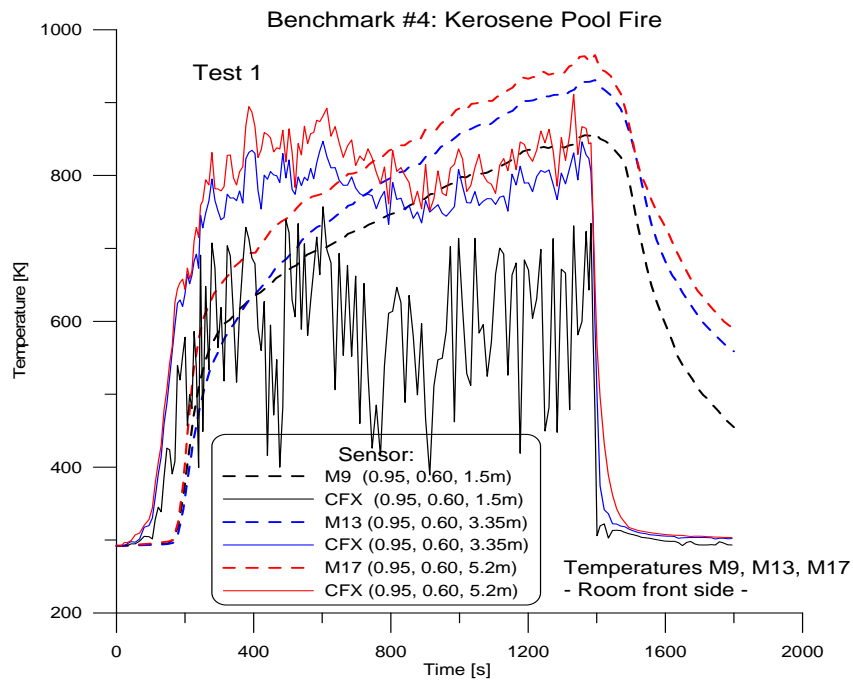


Fig. F6 Comparison of selected gas temperatures close to the front of the test facility (Test 1)

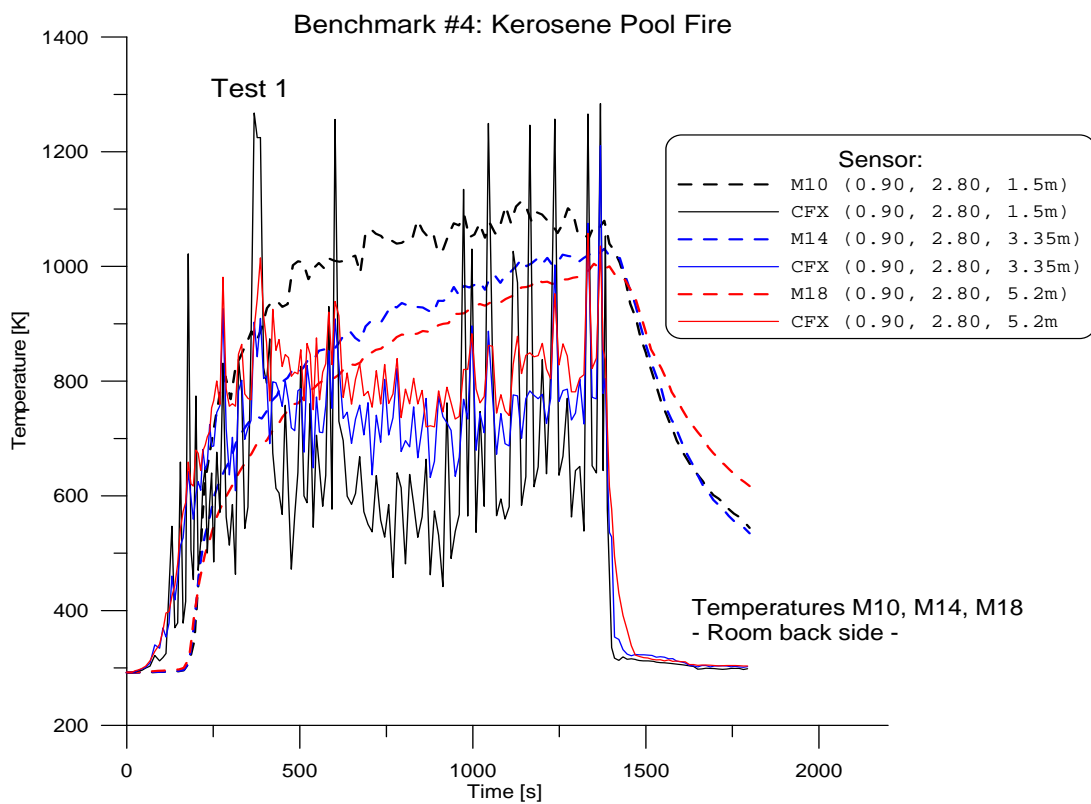


Fig. F7 Comparison of selected gas temperatures in the back of the test facility (Test 1)

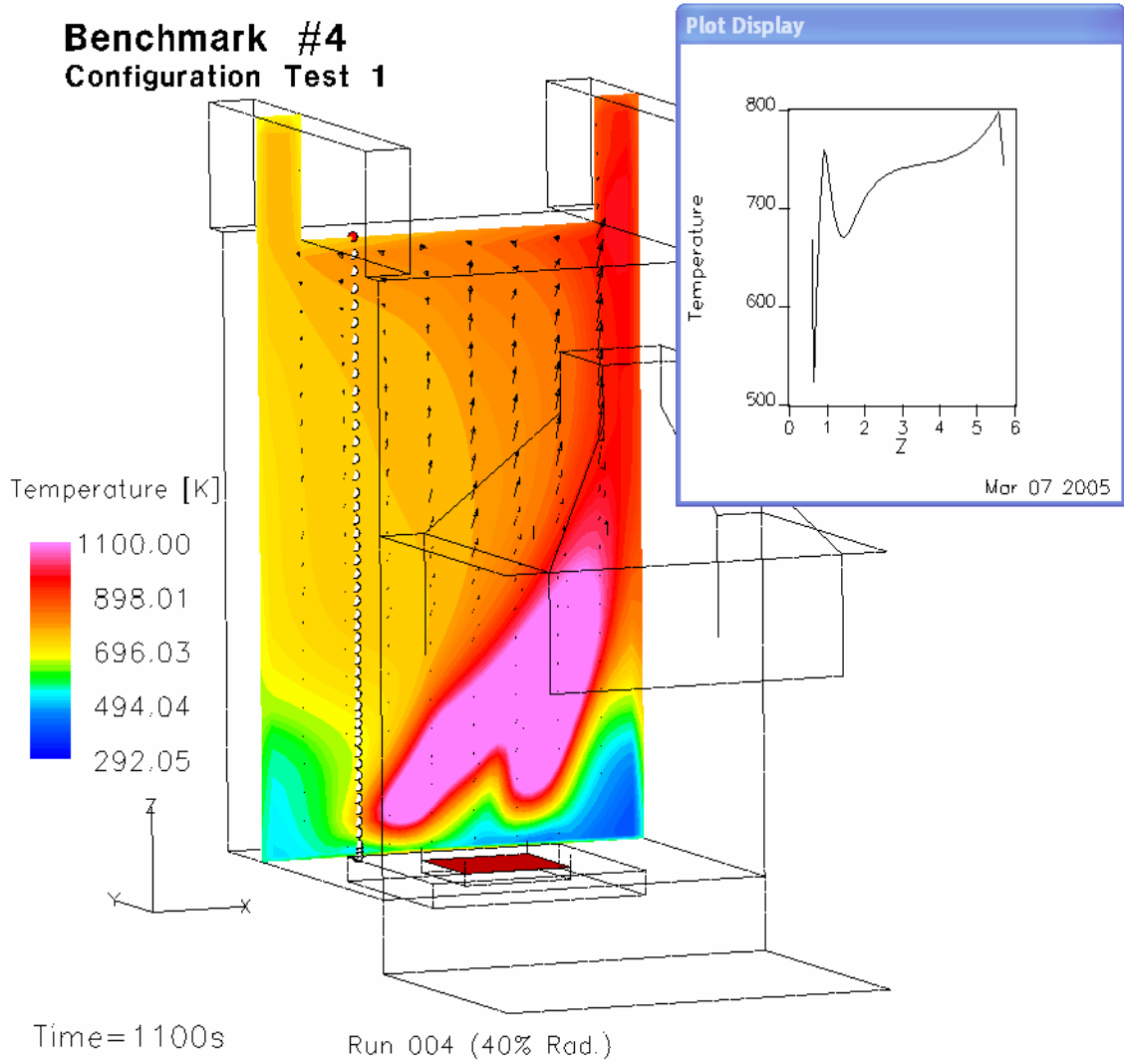


Fig. F8 Illustration of the vertical temperature distribution in the back of the facility (Test 1)

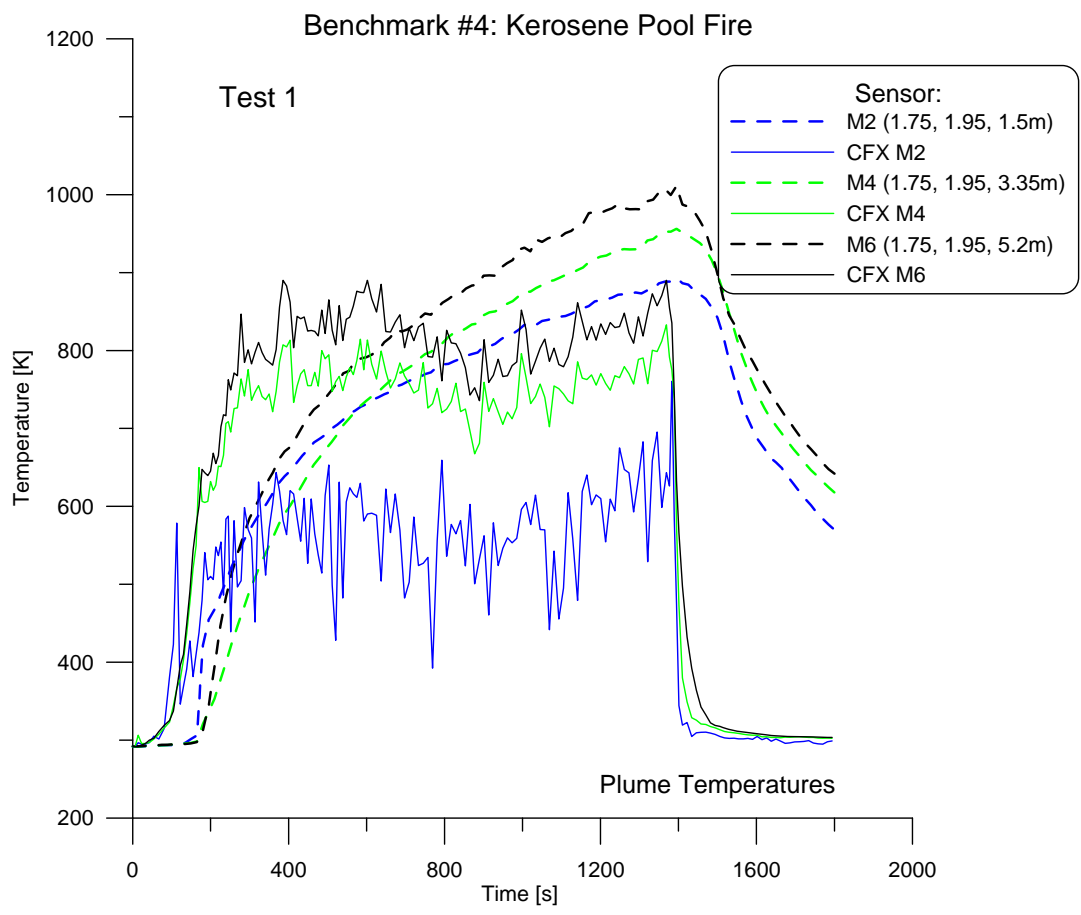


Fig. F9 Comparison of selected gas temperatures above the fire pan

Benchmark #4
Configuration Test 1

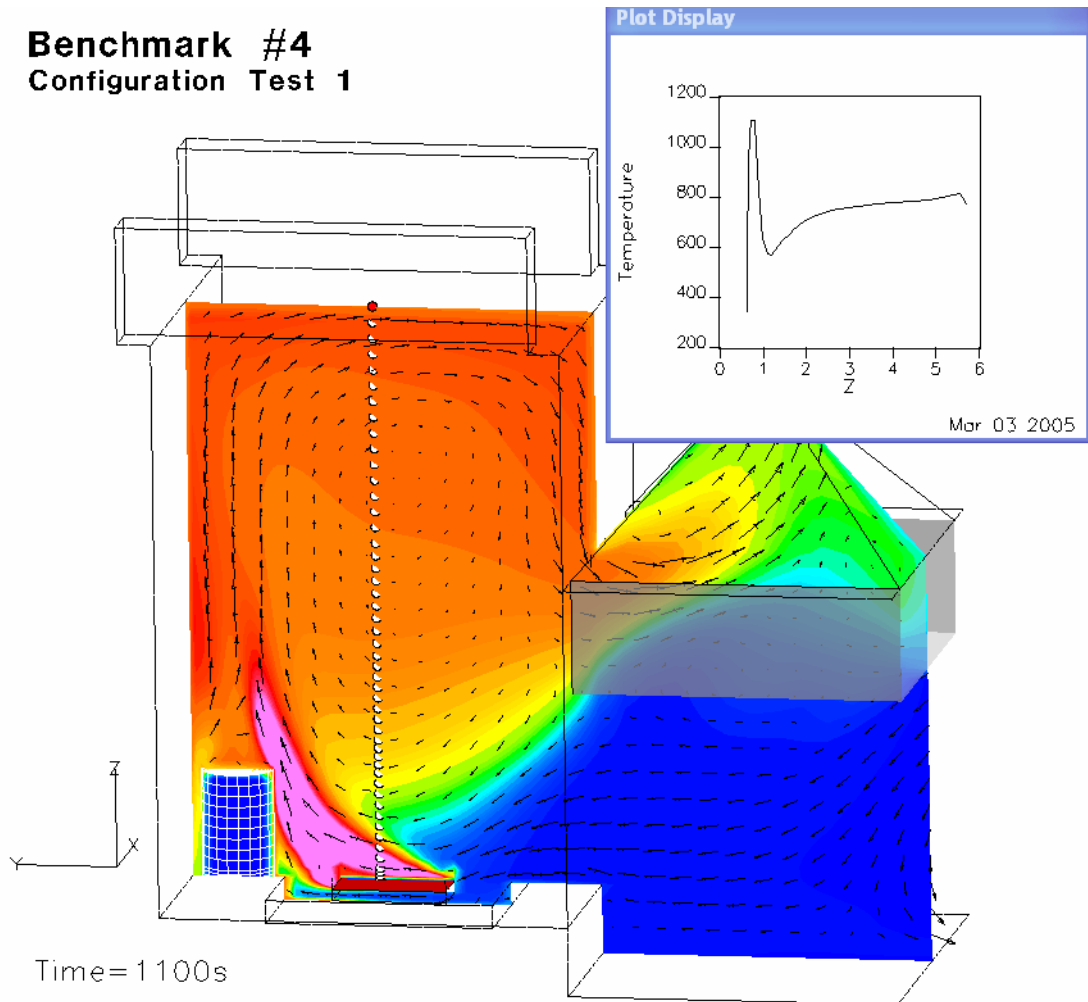


Fig. F10 Vertical temperature distribution at a plane $x=1.75$ m

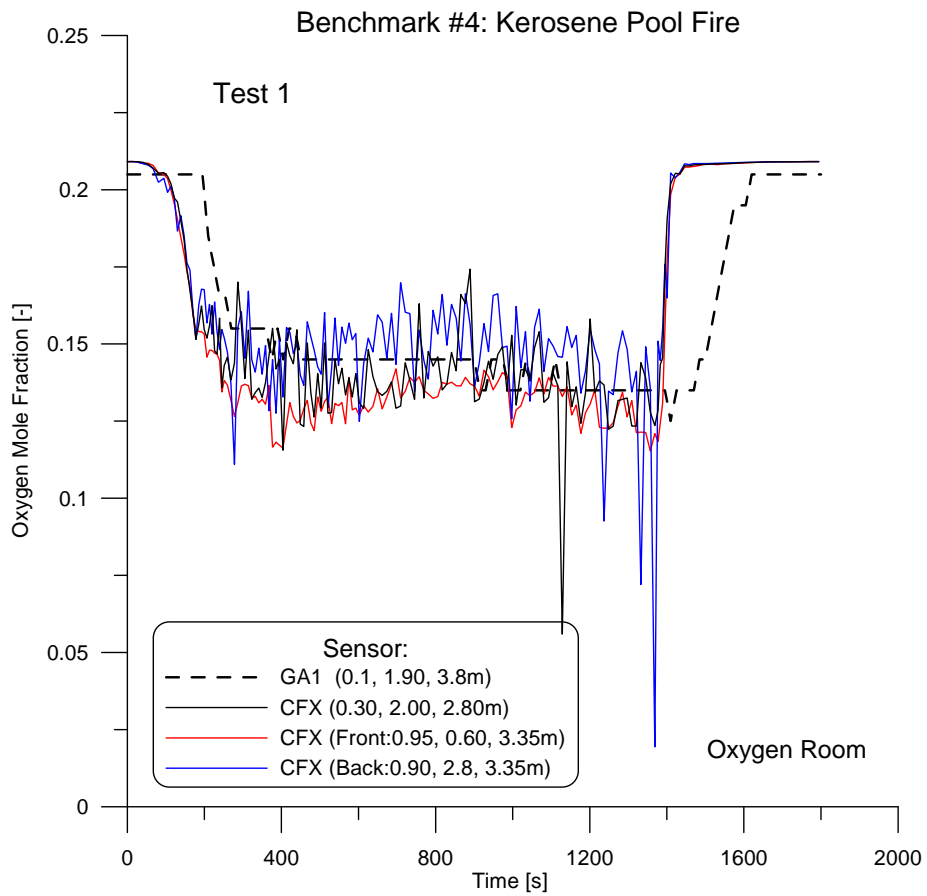


Fig. F11 Oxygen history for Test 1

Benchmark #4
Configuration Test 1

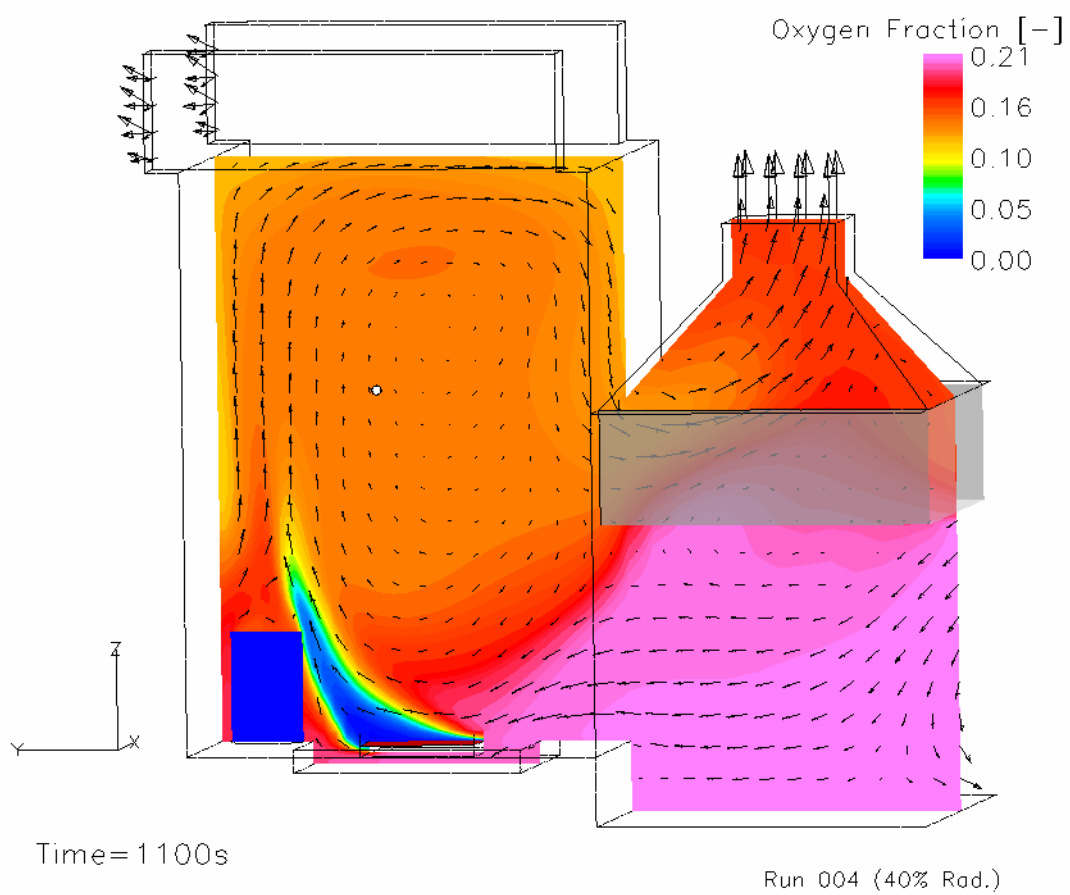


Fig. F12 Oxygen distribution in the test facility in a vertical plane ($x=1.8$ m)

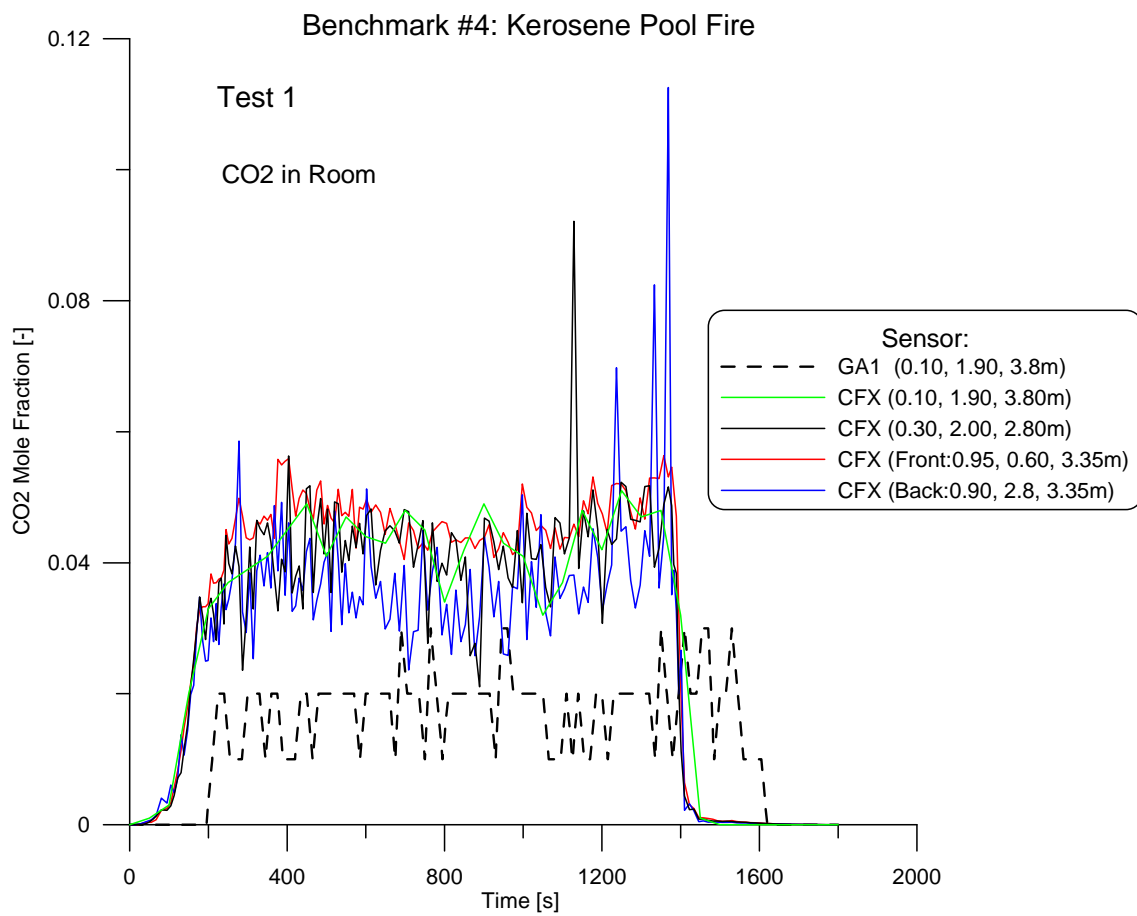


Fig. F13 Measured CO2 concentration in comparison with simulated values (Test 1)

Benchmark #4
Configuration Test 1

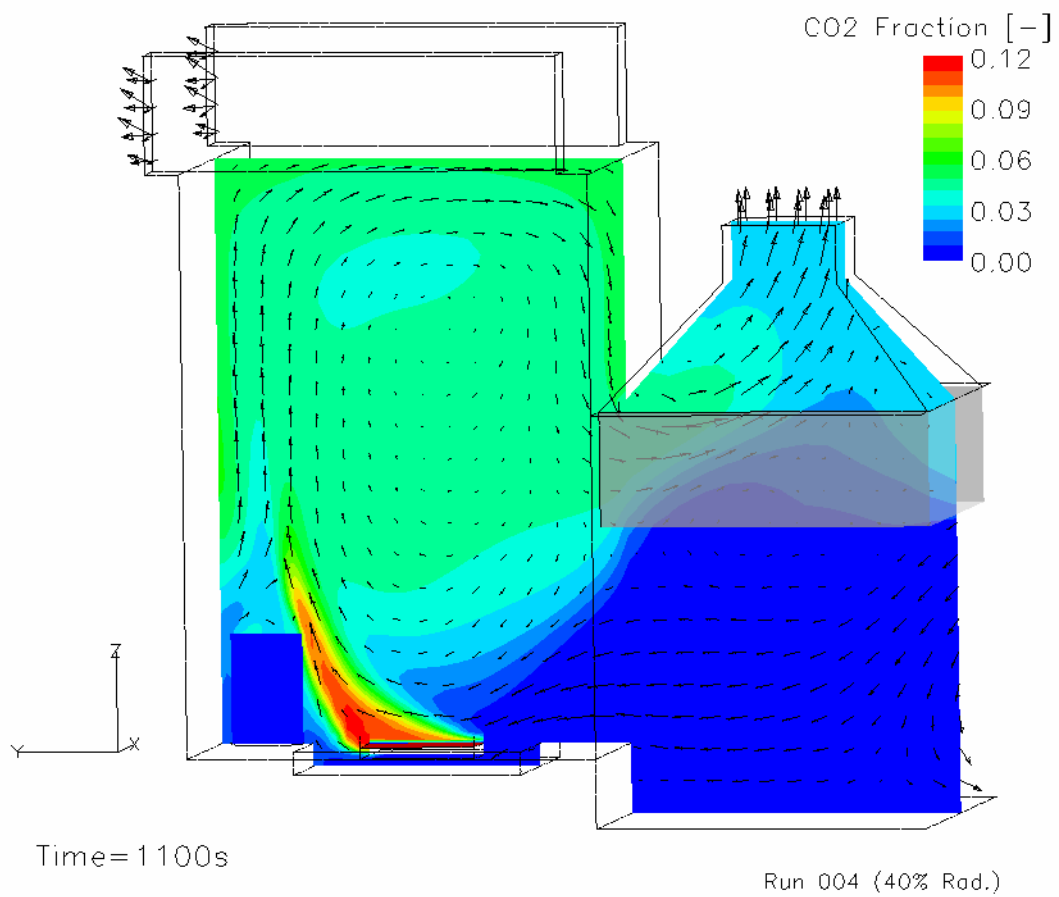


Fig. F14 CO₂ distribution in the test facility in a vertical plane (x=1.8 m)

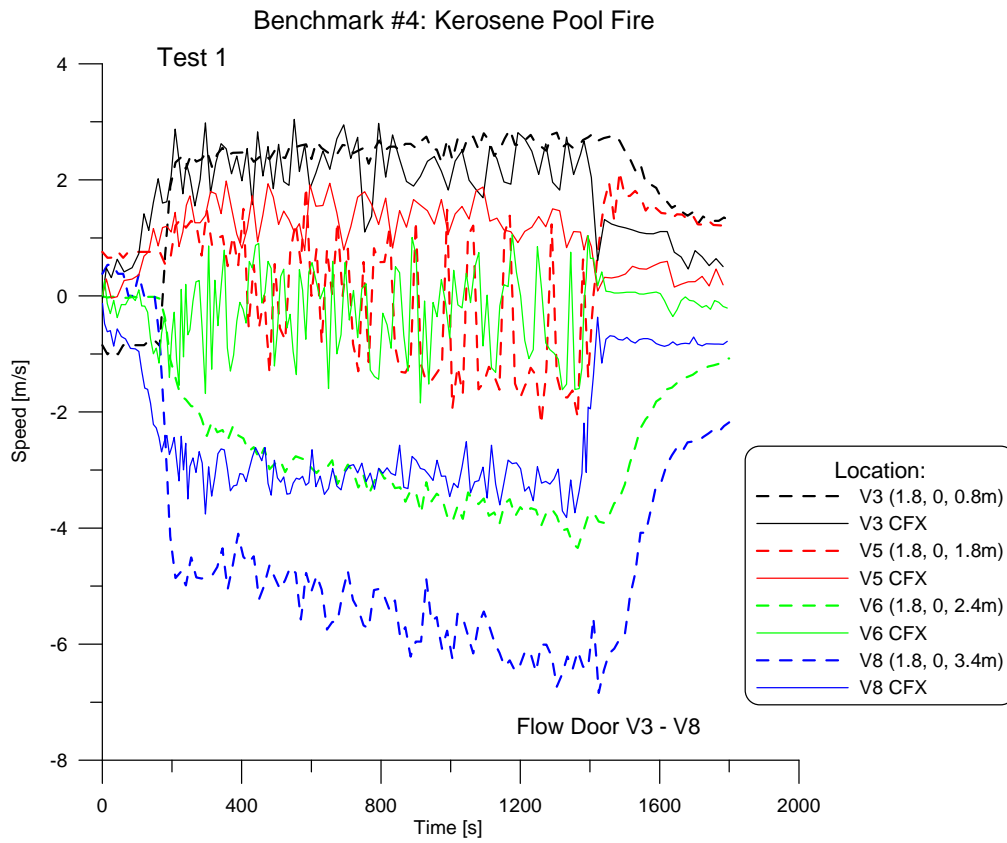


Fig. F15 Flow speed distribution in the door opening for Test 1

Benchmark #4
Configuration Test 1

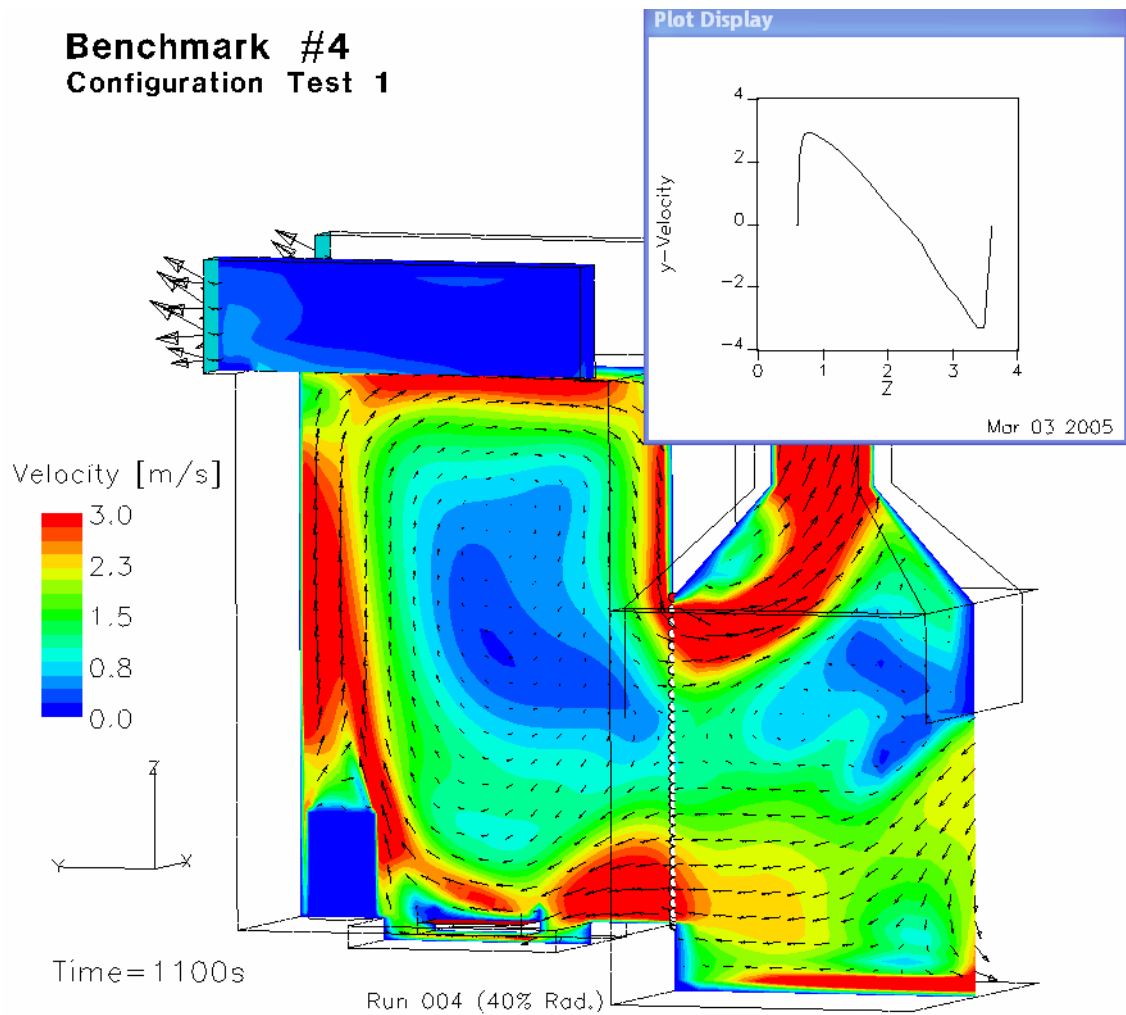


Fig. F16 Flow distribution through the door opening (Test 1)

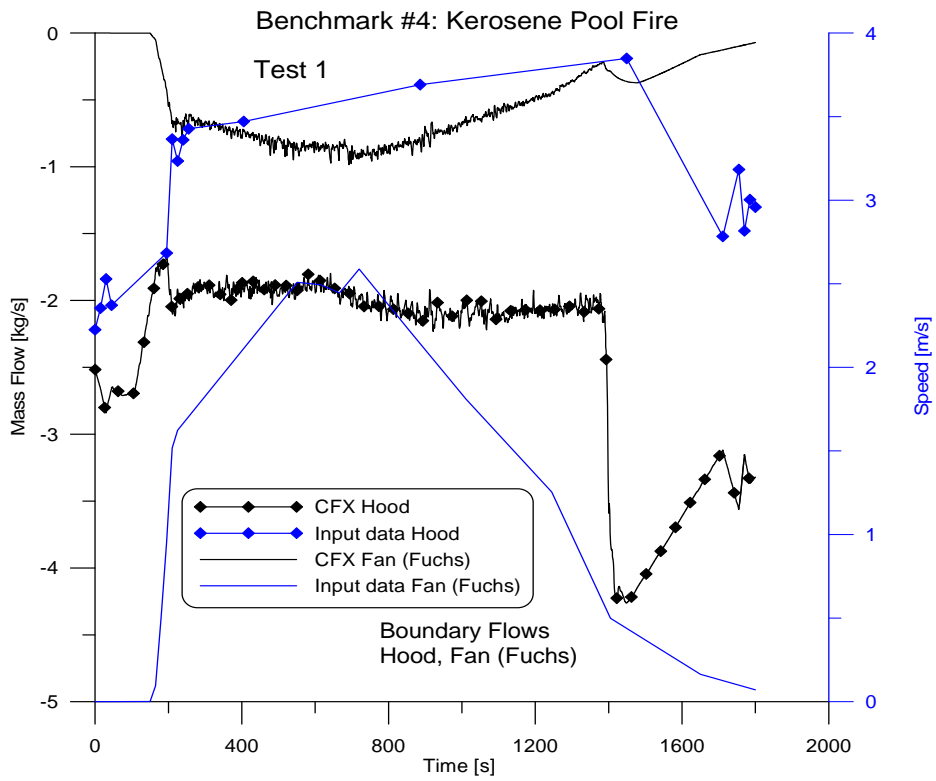


Fig. F17 Calculated mass flows through hood and ventilation system (Test 1)

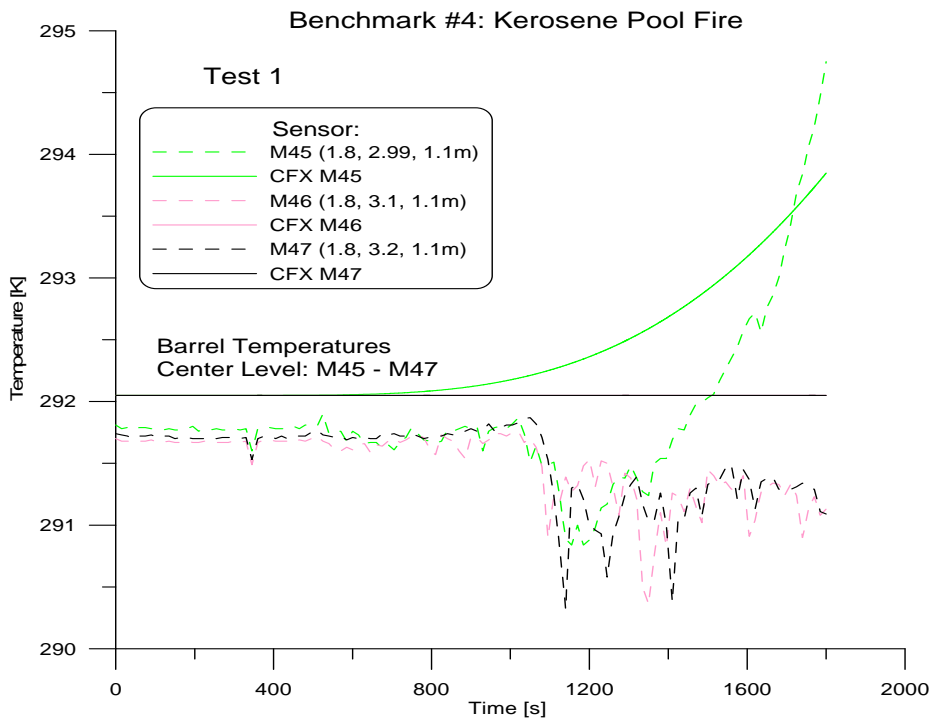


Fig. F18 Selected temperatures in the barrel target (M45 to M47, Test 1)

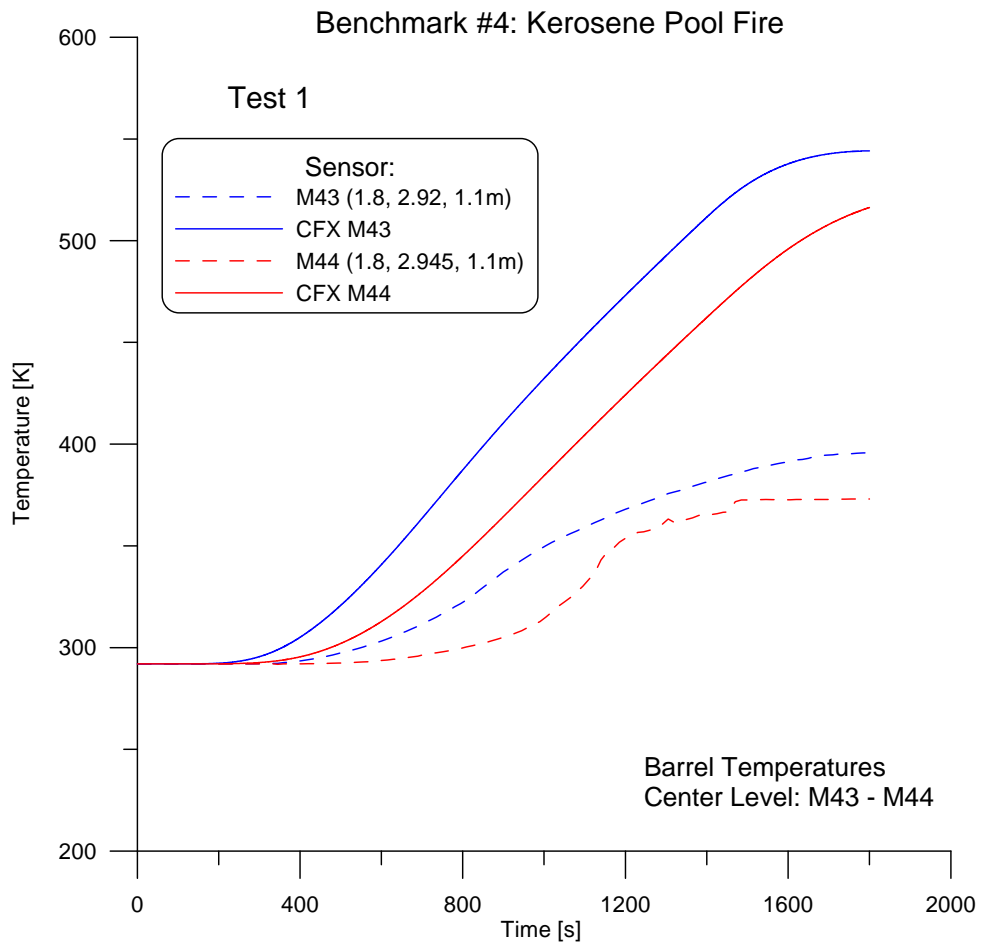


Fig. F19 Selected temperatures in the barrel target (M43 to M44, Test 1)

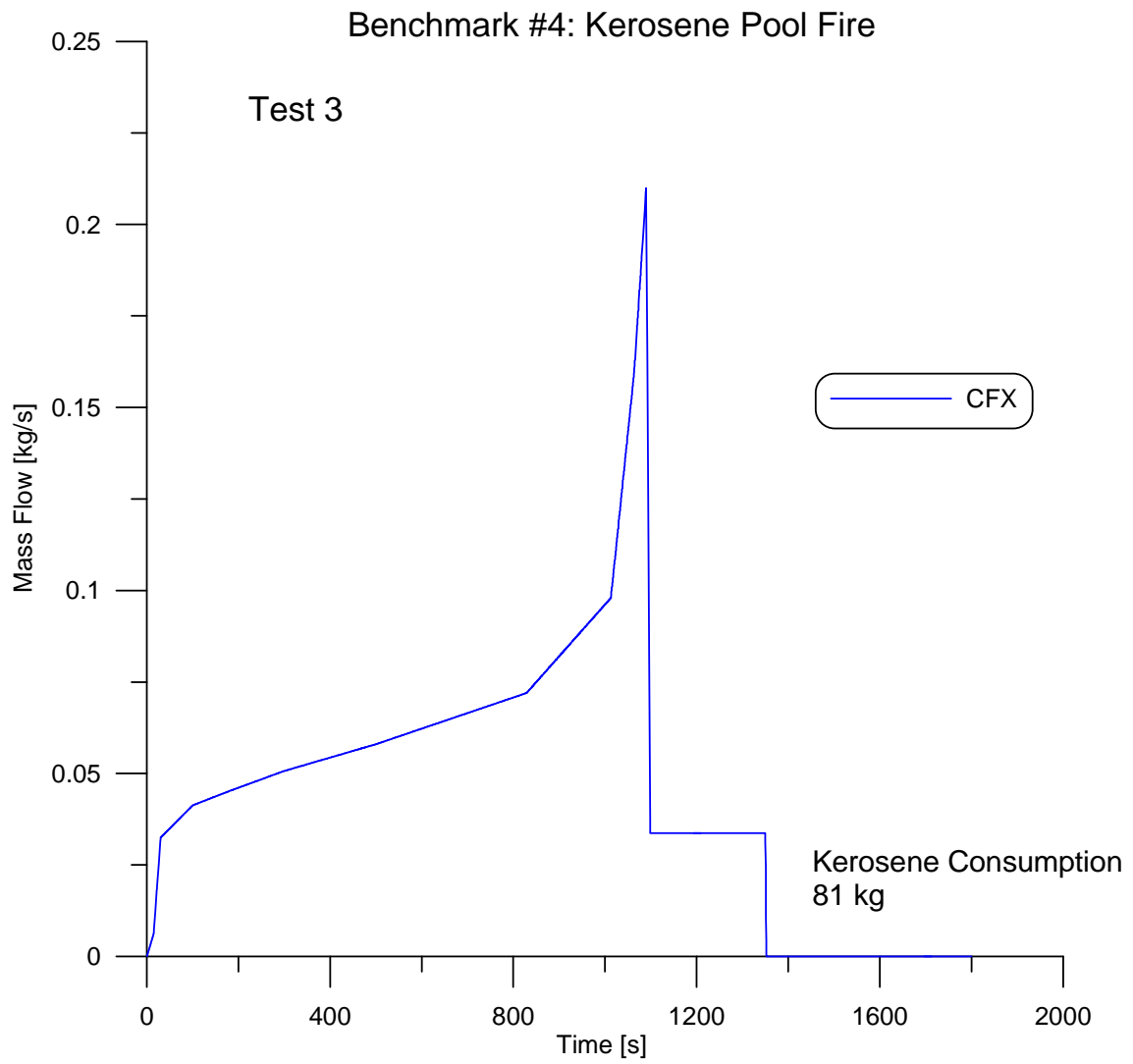


Fig. F20 Released and burned kerosene mass history for Test 3

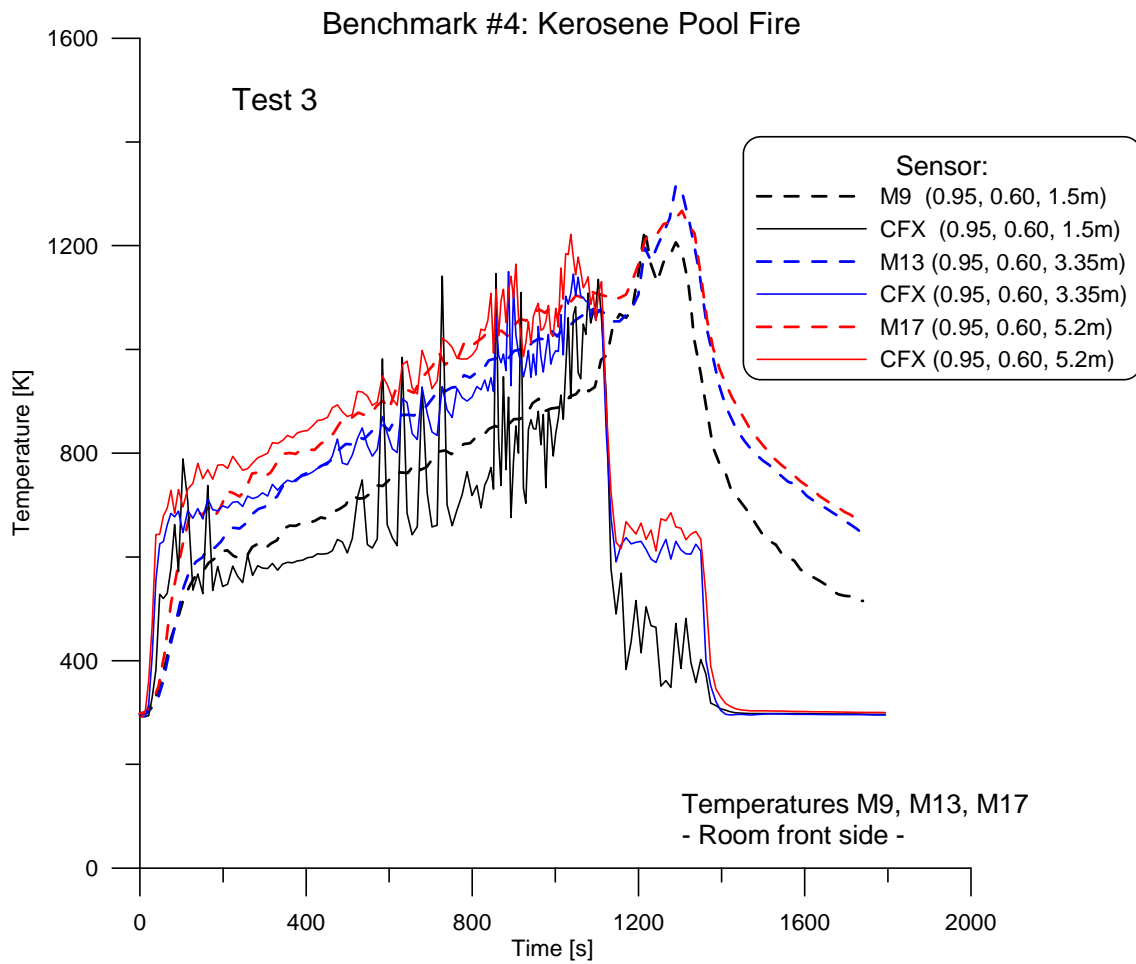


Fig. F21 Comparison of selected gas temperatures close to the front of the test facility (Test 3)

Benchmark #4
Configuration Test 3

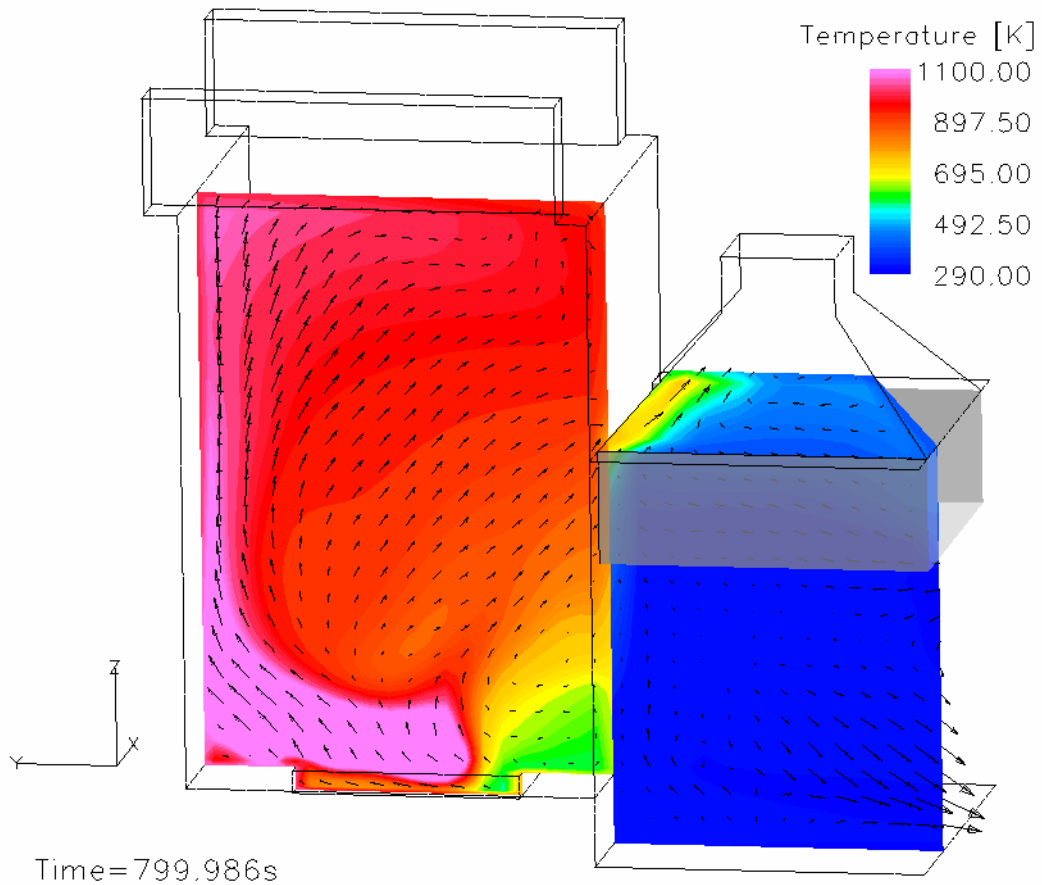


Fig. F22 Temperature distribution in OSKAR in a vertical plane ($x=0.95$ m)

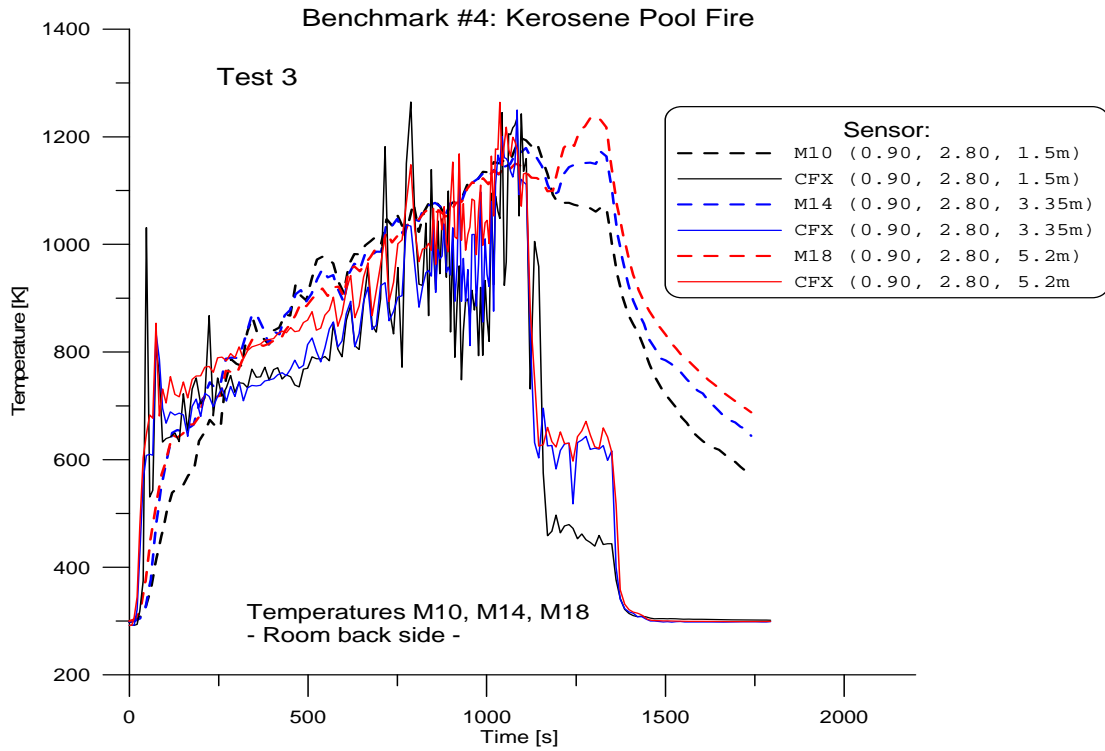


Fig. F23 Comparison of selected gas temperatures in the back of the test facility (Test 3)

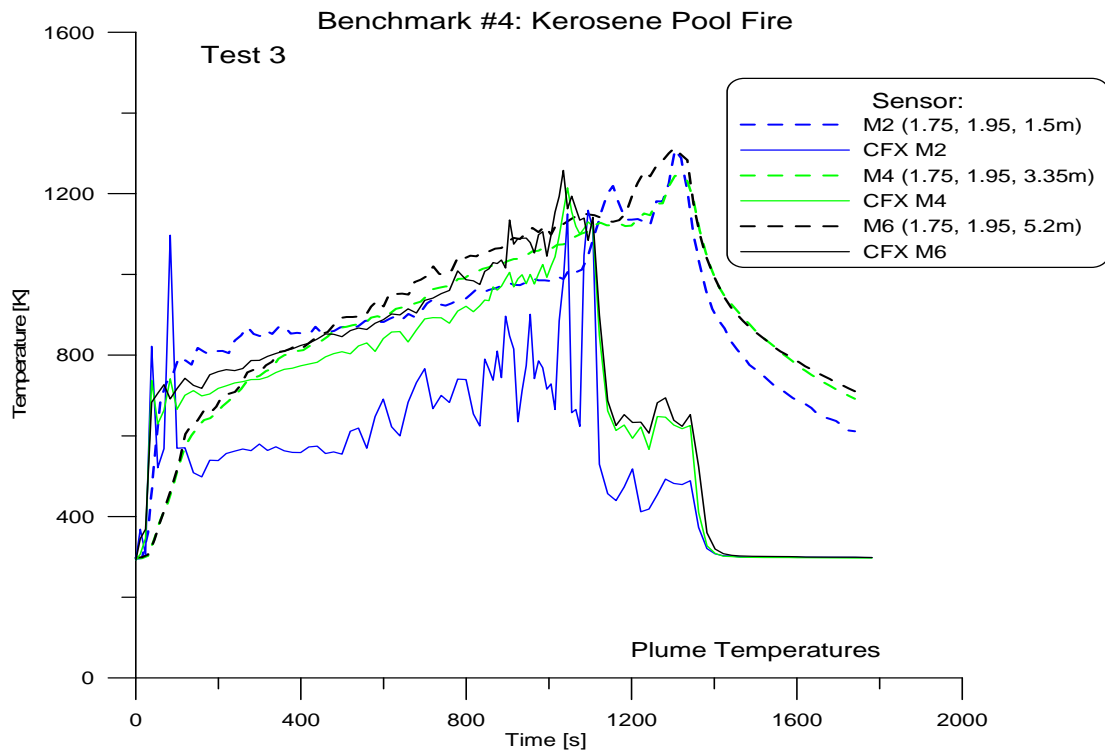


Fig. F24 Comparison of selected gas temperatures above the fire pan (Test 3)

Benchmark #4
Configuration Test 3

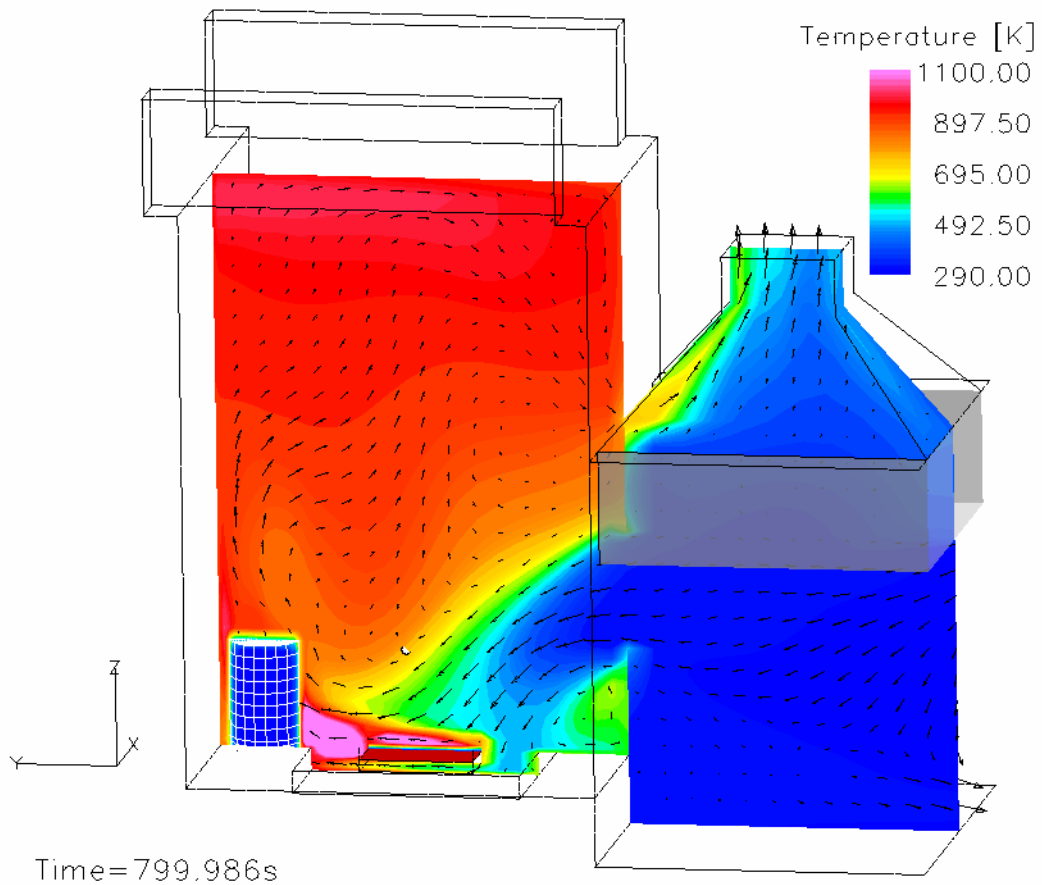


Fig. F25 Temperature distribution in OSKAR in a vertical plane ($x=1.75$ m)

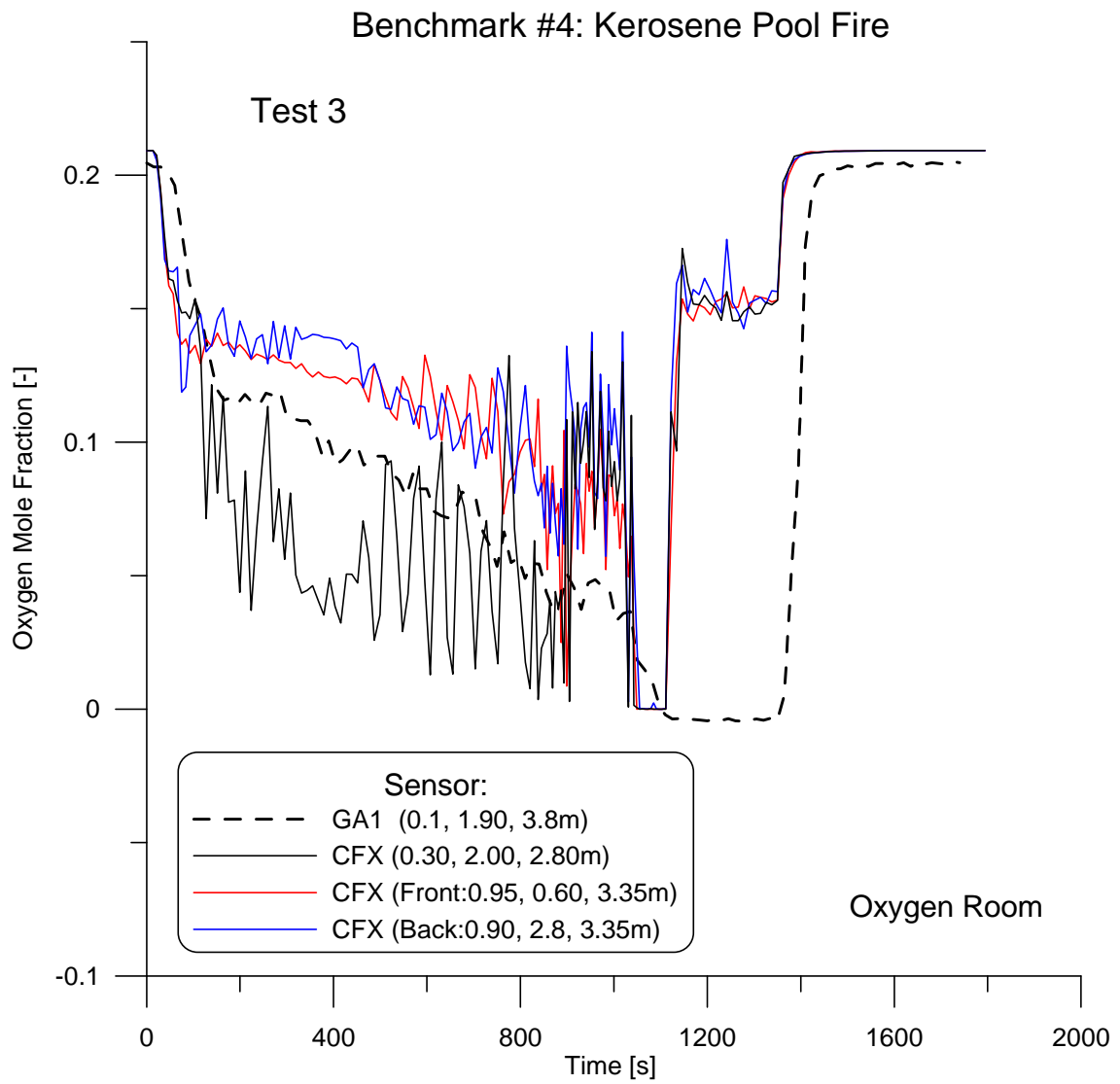


Fig. F26 Oxygen history during Test 3

Benchmark #4
Configuration Test 3

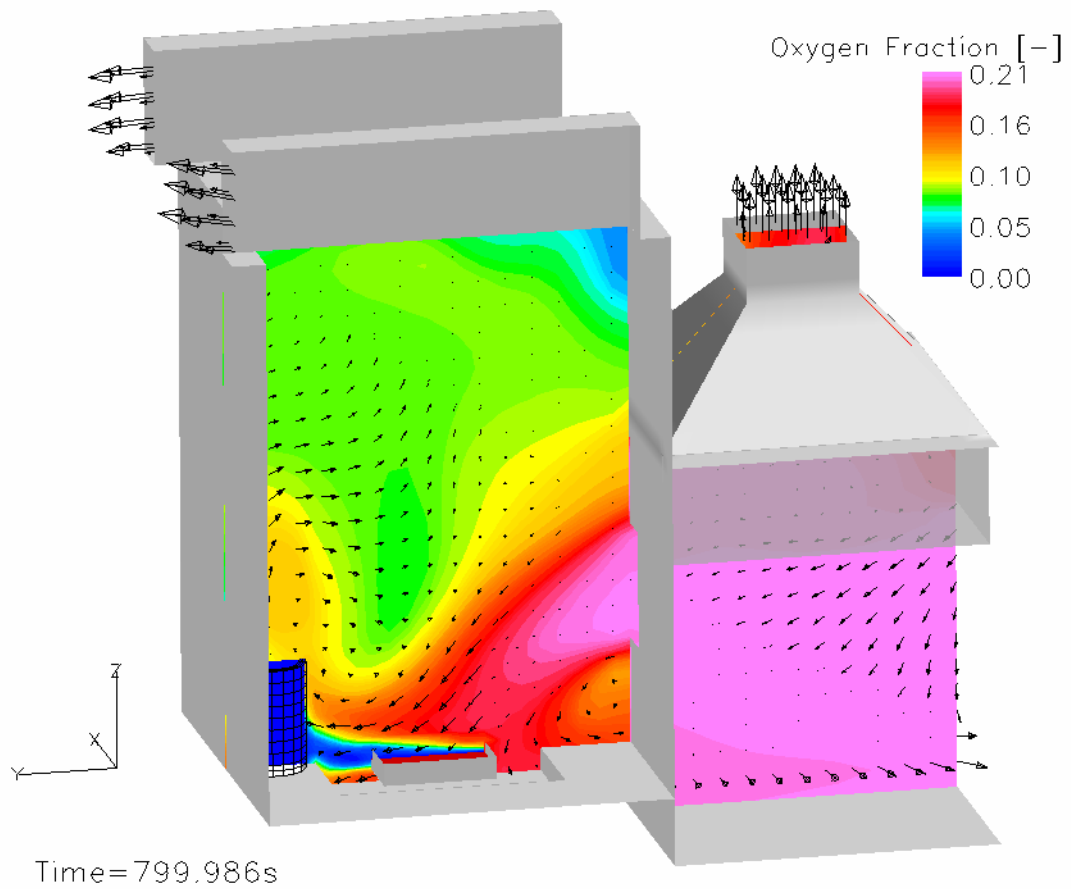


Fig. F27 Oxygen distribution in a vertical center plane (Test 3)

Benchmark #4
Configuration Test 3

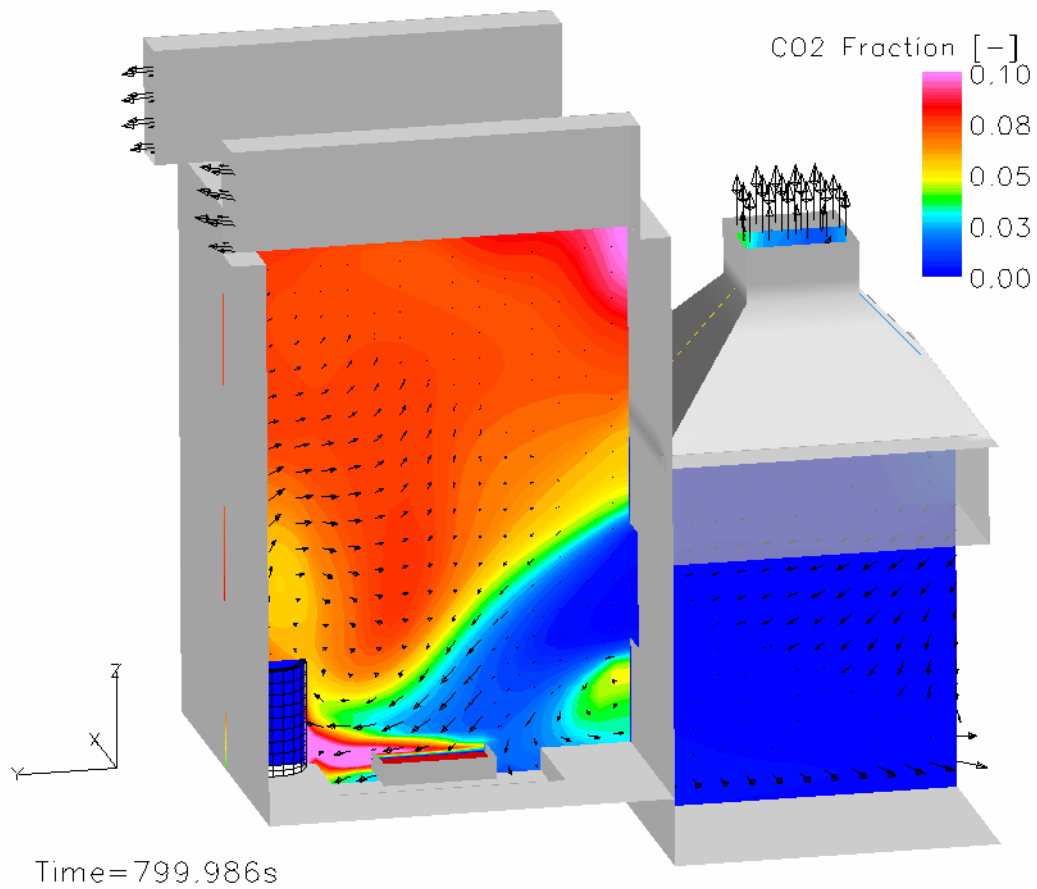


Fig. F28 CO₂ distribution in a vertical center plane (Test 3)

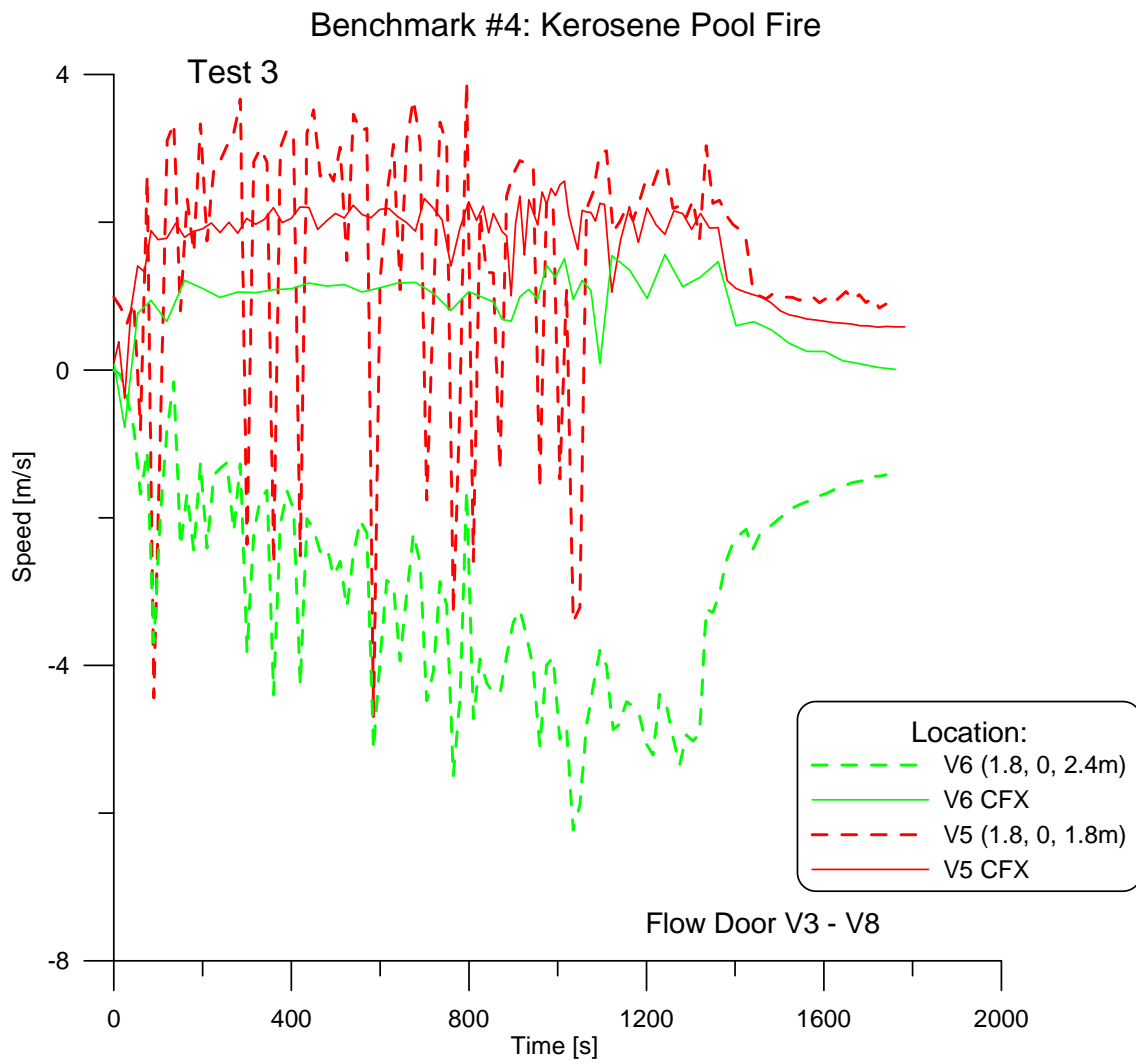


Fig. F29 Flow measurements in the door opening (Test 3)

Benchmark #4
Test 3

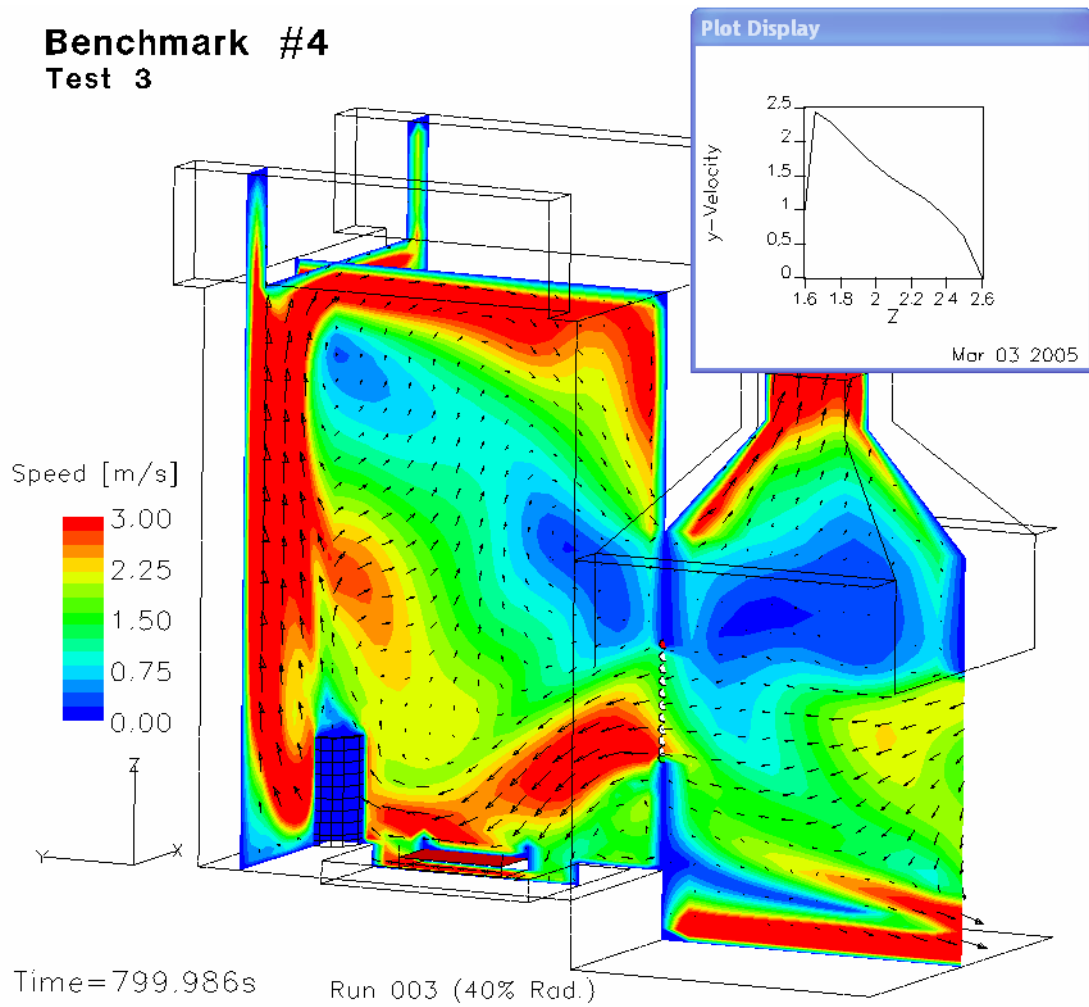


Fig. F30 Typical flow distribution in a vertical plane through the door (at $x=1.8$ m, Test 3)

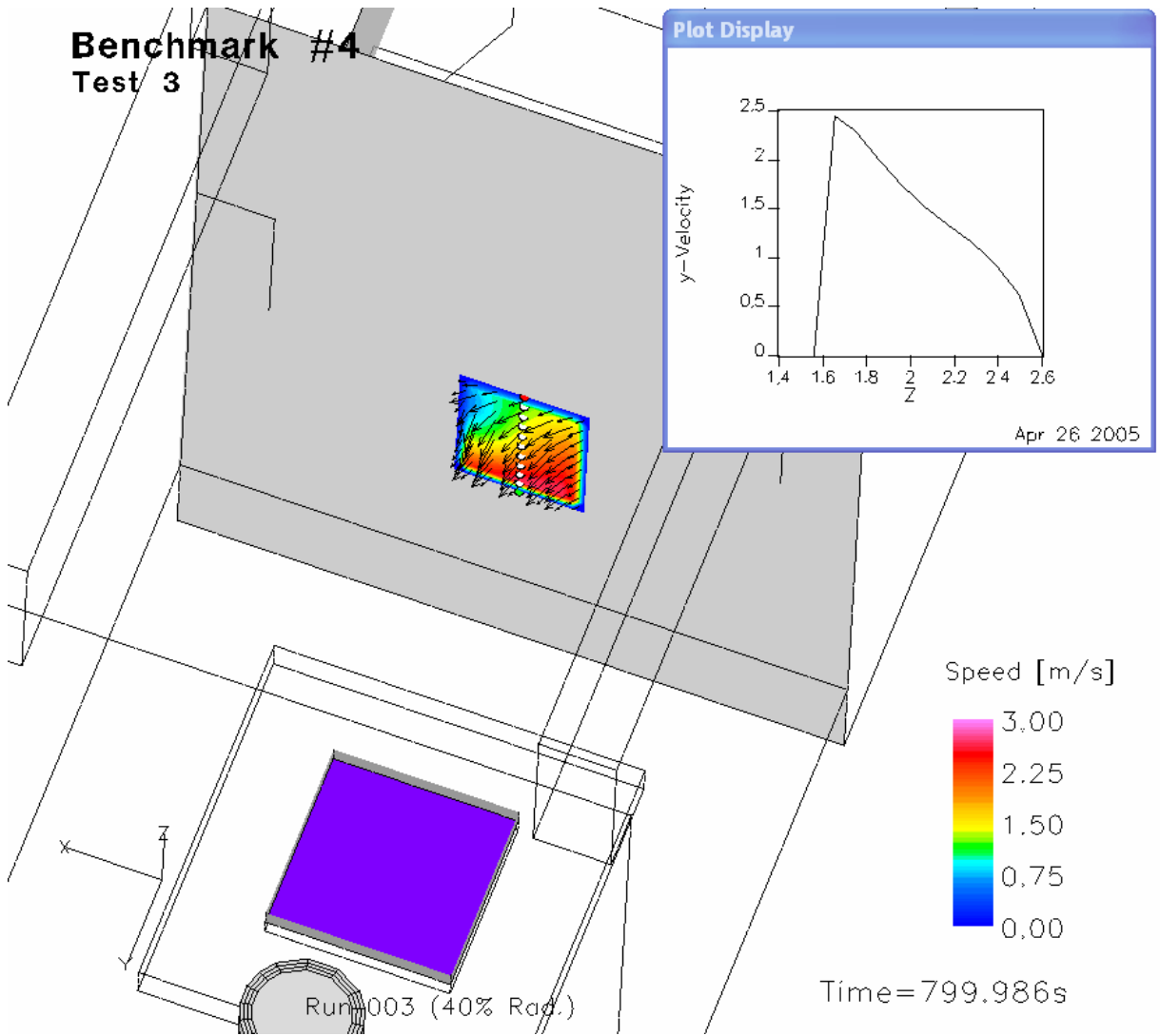


Fig. F31 Flow pattern through the door opening at 800 s (Test 3)

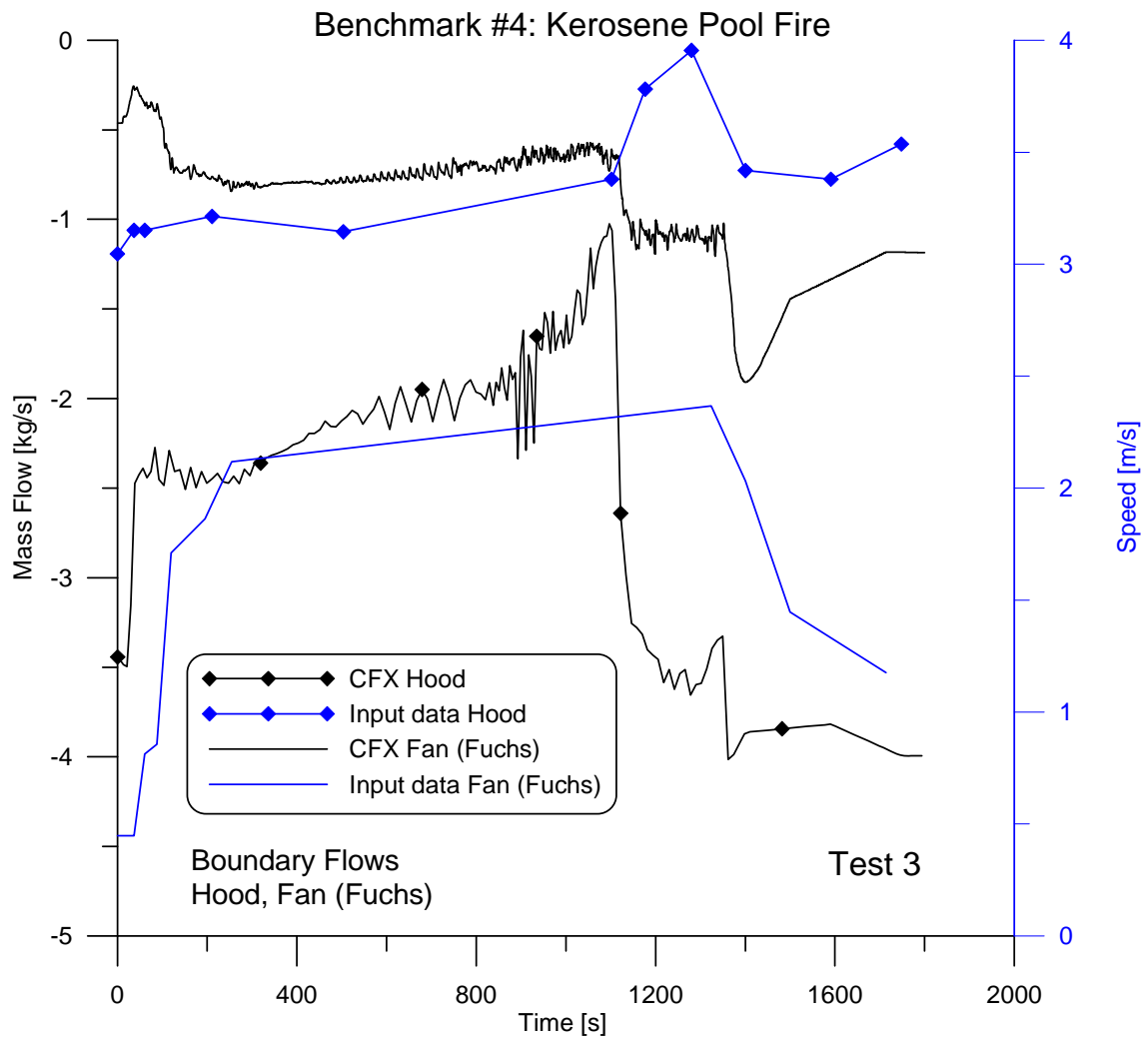


Fig. F32 Calculated mass flows through hood and ventilation system (Test 3)

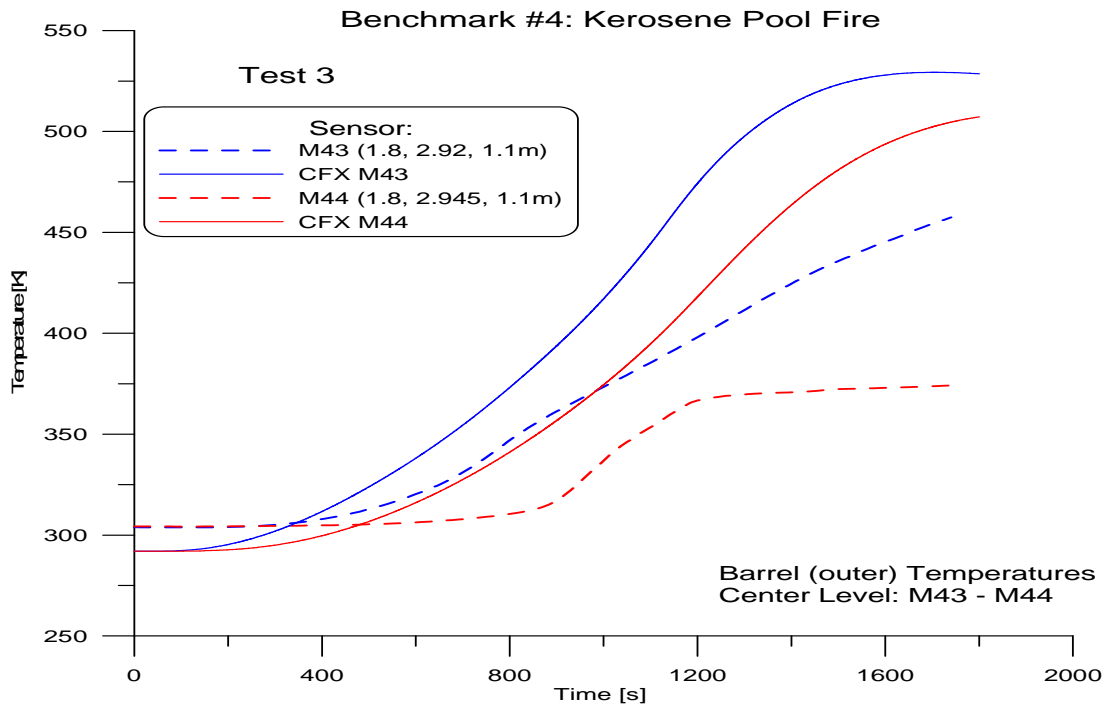


Fig. F33 Temperature build-up in the outer section (concrete) of the barrel target (Test 3)

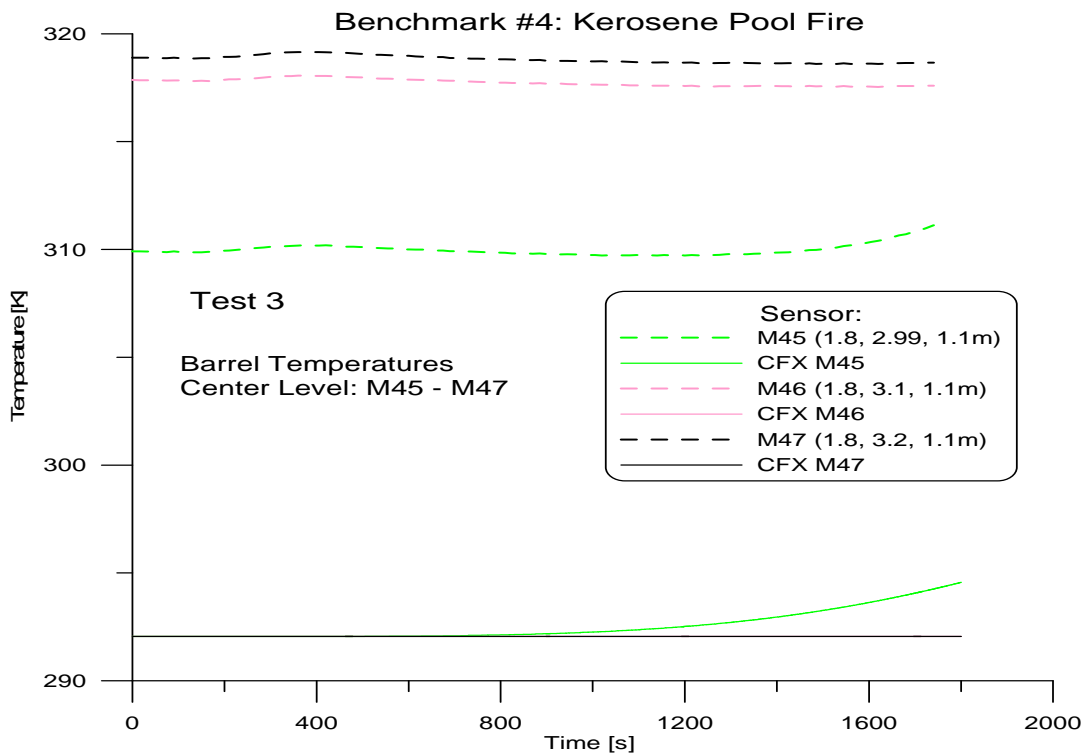


Fig. F34 Temperature build-up in the inner section (styrene granulate) of the barrel target (Test 3)

List of Figures

Fig. F1	Cut through the CFX model of the test facility OSKAR	15
Fig. F2	Mesh distribution in a vertical plane	15
Fig. F3	View of the vent openings for Test 1 (left) and Test 3 (right)	16
Fig. F4	Released and burned kerosene mass history for Test 1	16
Fig. F5	Vertical temperature distribution at a plane $x=0.95$ m	17
Fig. F6	Comparison of selected gas temperatures close to the front of the test facility (Test 1)	18
Fig. F7	Comparison of selected gas temperatures in the back of the test facility (Test 1)	18
Fig. F8	Illustration of the vertical temperature distribution in the back of the facility (Test 1)	19
Fig. F9	Comparison of selected gas temperatures above the fire pan	20
Fig. F10	Vertical temperature distribution at a plane $x=1.75$ m	21
Fig. F11	Oxygen history for Test 1	22
Fig. F12	Oxygen distribution in the test facility in a vertical plane ($x=1.8$ m)	23
Fig. F13	Measured CO ₂ concentration in comparison with simulated values (Test 1)	24
Fig. F14	CO ₂ distribution in the test facility in a vertical plane ($x=1.8$ m)	25
Fig. F15	Flow speed distribution in the door opening for Test 1	26
Fig. F16	Flow distribution through the door opening (Test 1)	27
Fig. F17	Calculated mass flows through hood and ventilation system (Test 1)	28
Fig. F18	Selected temperatures in the barrel target (M45 to M47, Test 1)	28
Fig. F19	Selected temperatures in the barrel target (M43 to M44, Test 1)	29
Fig. F20	Released and burned kerosene mass history for Test 3	30
Fig. F21	Comparison of selected gas temperatures close to the front of the test facility (Test 3)	31
Fig. F22	Temperature distribution in OSKAR in a vertical plane ($x=0.95$ m)	32
Fig. F23	Comparison of selected gas temperatures in the back of the test facility (Test 3)	33
Fig. F24	Comparison of selected gas temperatures above the fire pan (Test 3)	33
Fig. F25	Temperature distribution in OSKAR in a vertical plane ($x=1.75$ m)	34
Fig. F26	Oxygen history during Test 3	35
Fig. F27	Oxygen distribution in a vertical center plane (Test 3)	36
Fig. F28	CO ₂ distribution in a vertical center plane (Test 3)	37

Fig. F29	Flow measurements in the door opening (Test 3).....	38
Fig. F30	Typical flow distribution in a vertical plane through the door (at x=1.8 m, Test 3)	39
Fig. F31	Flow pattern through the door opening at 800 s (Test 3)	40
Fig. F32	Calculated mass flows through hood and ventilation system (Test 3)	41
Fig. F33	Temperature build-up in the outer section (concrete) of the barrel target (Test 3).....	42
Fig. F34	Temperature build-up in the inner section (styrene granulate) of the barrel target (Test 3)	42

**Appendix G: International Collaborative Project to Evaluate Fire
Models for Nuclear Power Plant Applications**

FDS Simulations for Benchmark Exercise No. 4

Presented by

Wenzel Brücher

Gesellschaft für Anlagen- und Reaktorsicherheit (GRS) mbH,
50667 Köln, Germany

Contents

G1	Introduction	1
G2	Model Parameters	3
G3	Comparison with Measurements	5
G3.1	Heat Release	5
G3.2	FDS3: Variation of Model Resolution	5
G3.3	FDS4 Calculations	10
G4	Conclusions.....	15
G5	References	17
	List of Figures	19

G1 Introduction

FDS (Fire Dynamics Simulator) was applied to Test 3 of Benchmark Exercise No. 4 in order to compare the performance of different versions of FDS, and to compare the influence of the model user on results. FDS versions 2 and 3 had been applied to this benchmark at GRS in the framework of a former project which was not part of the ICFMP. Those simulations were performed at a stage when only parts of the information on the test parameters were available. Hence, those simulations were not suitable for a comparison within the ICFMP project.

This report is about some additional calculations with FDS based on the official benchmark specification of experiment 4, Test 3. Due to the late start this work (spring 2005) these are all open calculations. Model calculations concentrated on the application of FDS3 (coarse grid and nested fine grid) to compare results with former calculations. In addition, similar calculations were made with FDS4 (coarse grid and nested fine grid). Reports and presentations on similar FDS simulations performed by NIST and NRC were not studied before, or during the work in order to test the influence of the model user on results.

G2 Model Parameters

Two mesh resolutions were used within FDS: 20 cm (coarse grid) and 10 cm (fine grid). In case of fine grid simulations this grid resolution has only been applied in the lower two thirds of the compartment using the multiple mesh option of FDS whereas all other areas were resolved with 20 cm resolution only (see Fig G2.1). The coarse grid consists of 20x36x36 cells. The fine grid area containing 24x36x40 cells was intended to cover the fire and its surrounding. Compared to a full area application of the fine resolution this approach only increases the CPU demand by a factor of approx. 3.5 compared to an increase by a factor of 16, otherwise.

Depending on the resolution, some objects and openings were slightly shifted in order to align with the grid, especially in the coarse grid case. Sloping or cylindrical objects were approximated as "stair steps".

All objects were defined as homogeneous material. The mock-up waste drum was defined as an artificial material obtained from linear mixture of contained material properties because of all limitation discussed in the corresponding benchmark report of NIST. FDS calculates only one-dimensional heat conduction inside all these objects.

Boundary conditions in the outer area were open. Hood and compartment fan ventilation were prescribed as velocities at the outer model boundaries according to the benchmark specification.

The pool fire was included using the dodecane $C_{12}H_{26}$ definition of the FDS2 database instead of $C_{11.64}H_{25.29}$ as given in the specification. Later FDS databases use $C_{14}H_{30}$ for kerosene. Standard FDS values for soot yield (0.042) and CO yield (0.012) were applied. Fuel evaporation rates were prescribed as given in the experimental documentation. All other model parameters were applied in default configuration. A short description of FDS model physics is found in the NIST report on Benchmark Exercise No. 4 calculations (Appendix A).

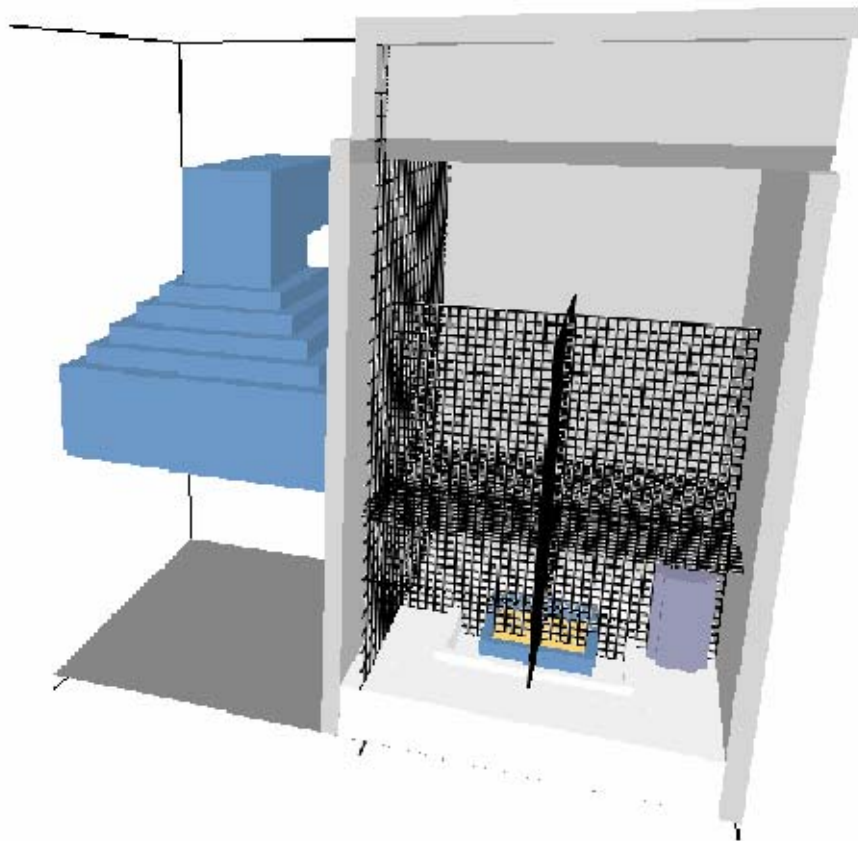


Fig. G2-1 Model geometry in FDS with fine grid area inside the compartment

All measured quantities at given locations were saved in 10 s intervals. Within the FDS4 calculations the “thermocouple” model option was logged in addition to the gas temperature values. With this option the model simulates an additional heating of a virtual thermocouple due to thermal radiation in order to make numerical values and observations more comparable. All figures in the following section use the gas temperature as a standard for comparison. The use of thermocouple option data for analysis is indicated.

G3 Comparison with Measurements

G3.1 Heat Release

Actual heat release rates differ from the heat release rate obtained from the prescribed pool mass loss data. Fig G3-1 shows all heat release rates calculated with different model configurations. Only the model version and the way of resolving the experimental geometry have been changed, respectively.

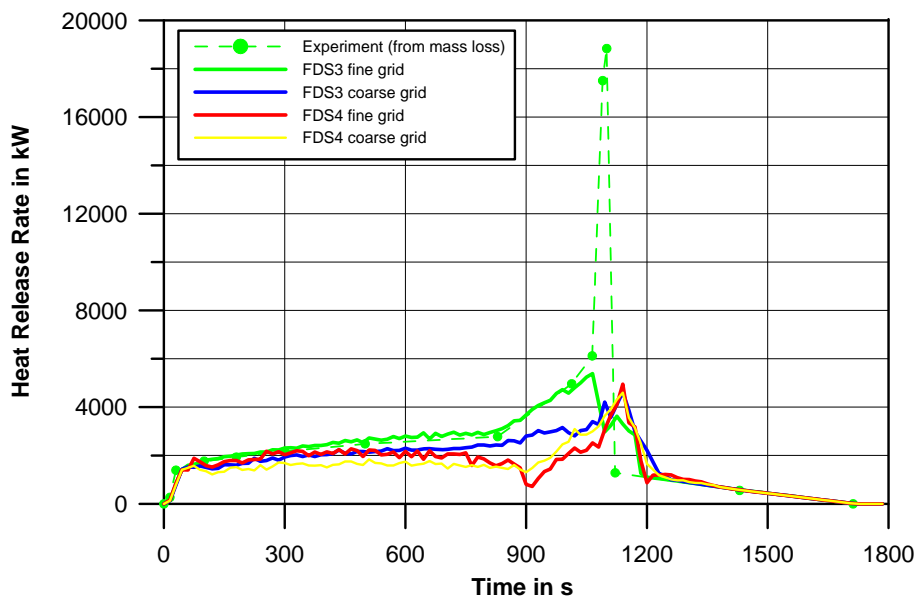


Fig. G3-1 Heat release rates of all FDS3 and FDS 4 calculations (Test 3)

Depending on the model configuration not all released fuel is burnt immediately or in some cases it is only partly burnt. Especially the mass release peak does not follow by the sharp rise of heat release due to the under-ventilated conditions in Test 3. A discussion of the differences between all calculations is found in the following sections.

G3.2 FDS3: Variation of Model Resolution

Both calculations with FDS3 use exactly the same set of parameters except for the grid resolution. Fig G3-2 compares simulated and measured gas temperatures in different areas (front room, plume and back room area). Temperatures are generally slightly under-estimated by the model for most of the experiment. The temperature peak ap-

pears too early compared to measurement which is partly due to the mass loss rate of the benchmark specification. A different (smoothed) interpolation of the questionable weight scale data in former calculations resulted in a better agreement of the temperature evolution. However, peak temperatures were also under-estimated in that case.

Lowest deviations are found in the front room area whereas larger differences occur in the back room area where the mock-up drum is located. Compared to the coarse grid results, the fine grid calculation shows a better agreement with peak temperatures but a worse performance with respect to average temperatures. No obvious increase in the quality of simulating temperature is observed, although this effect would be expected as a consequence of a better resolution of the flame area.

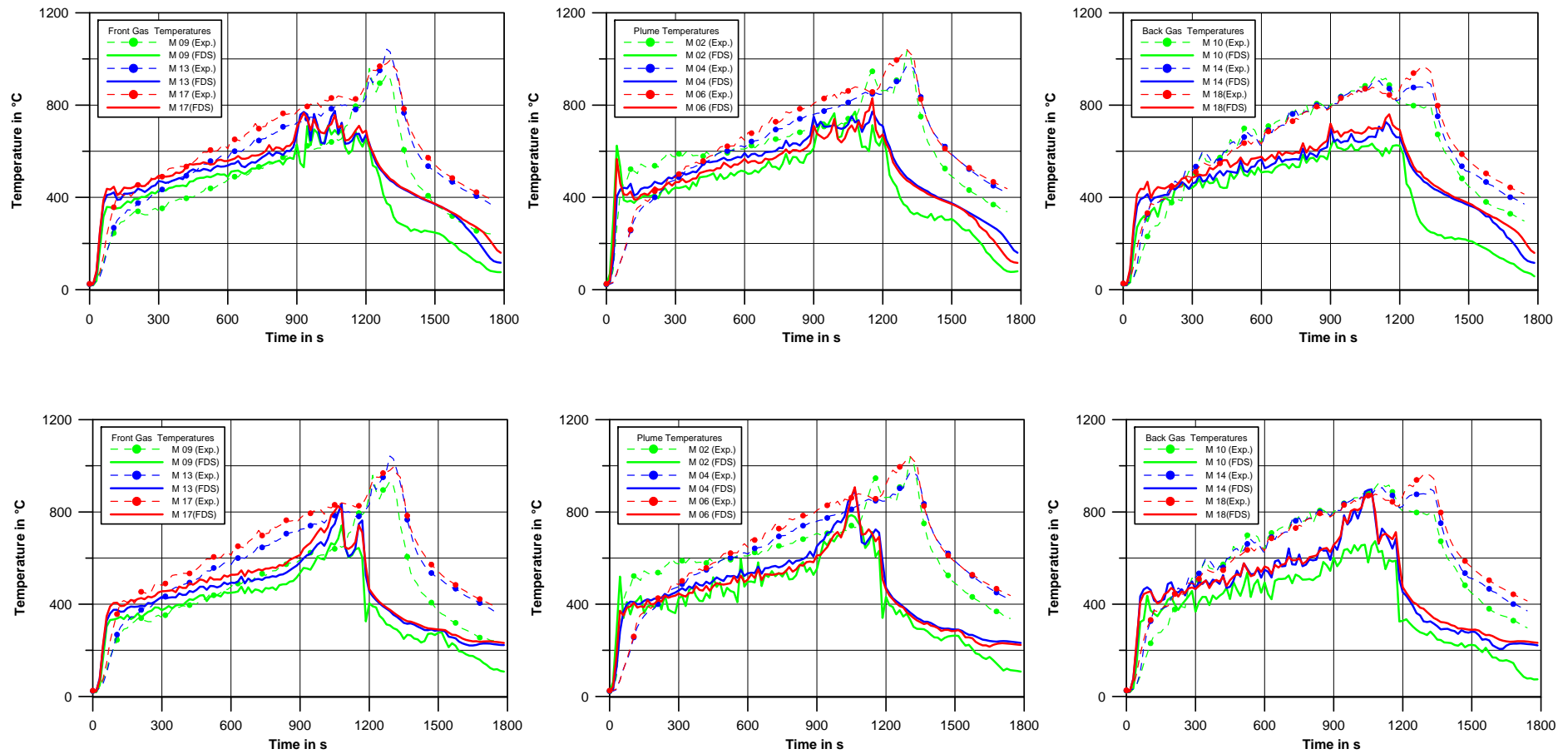


Fig. G3-2 Gas temperatures for Test 3 calculated with FDS3 (top: coarse grid, bottom: nested fine grid)

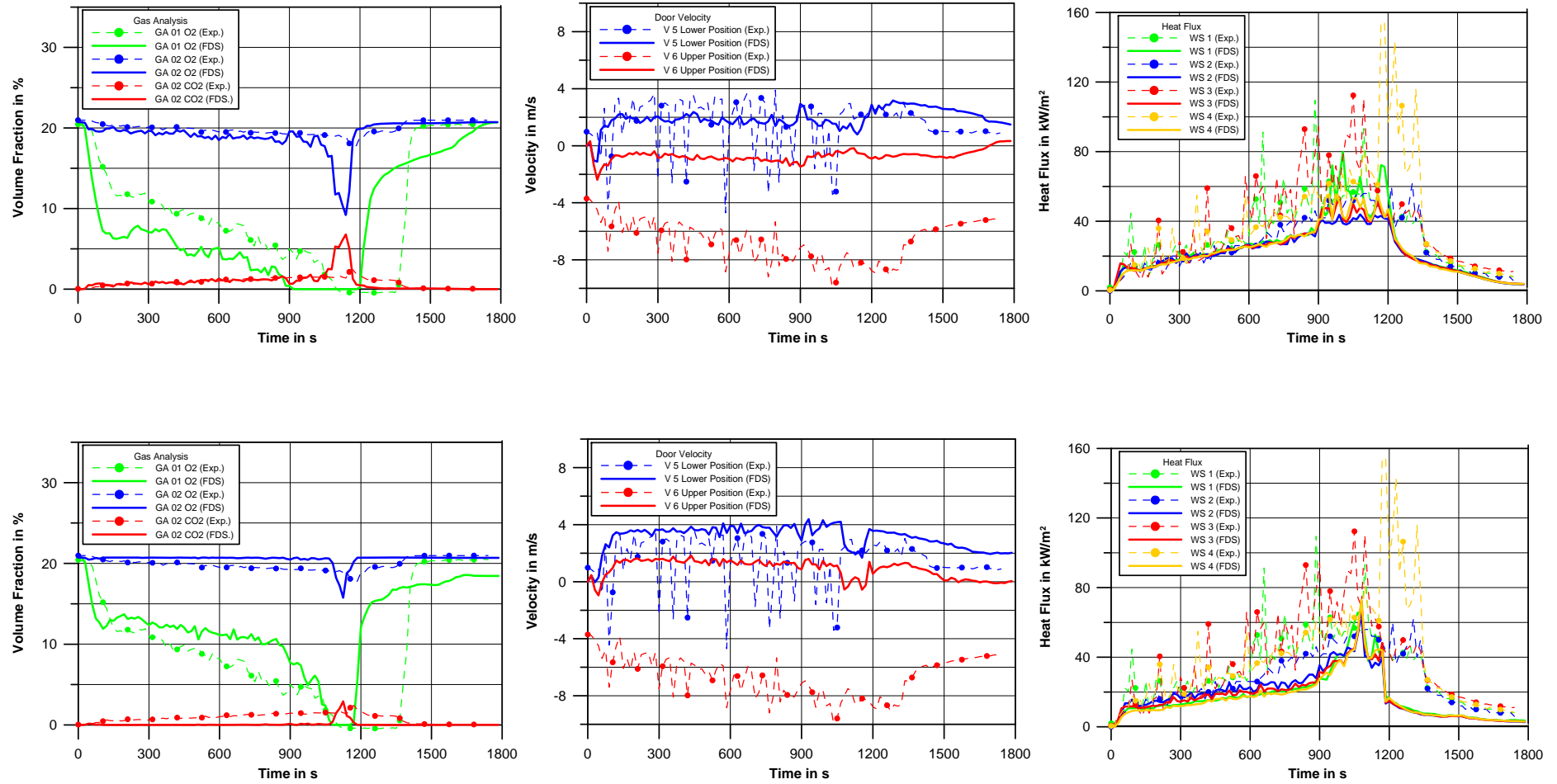


Fig. G3-3 Gas concentrations, door velocities and heat fluxes for Test 3 calculated with FDS3 (top: coarse grid, bottom: nested fine grid)

Gas flow into the compartment through the lower part of the compartment opening is simulated quite satisfactorily, whereas the FDS3 outflow out of the upper part is much lower than measured (Fig. G3-3). The latter deviation may be mainly attributed to the low resolution of the real sharp flow profile in the opening, because at least in the case of the coarse grid the simulation of the concentrations outside the compartment shows a reasonable prediction of gas exchange between the compartment and the outside.

A possible explanation for the slightly worse overall performance of the fine grid simulation may be the lack of extending the fine grid to the whole door area which is crucial for the evolution of the fire inside. Calculated fine grid gas flow into the compartment is higher than measured resulting in lower gas temperatures inside. This effect is also found in the evolution of oxygen concentration inside the compartment which is higher than observed. Due to the application of the default FDS3 definition of a temperature-dependent lower oxygen limit (LOL) this higher fresh air flow allows a slightly higher heat release rate. However, the net effect on gas temperatures and surface heat fluxes results in higher values than coarse grid values only during the peak period of fuel mass release rate.

Surface temperatures of target materials show a similar tendency as gas temperatures and surface heat fluxes (see Fig. G3-4). Best agreement is found in the front room area (aerated concrete) and coarse grid results compare better to observed temperatures than fine grid results. Temperatures inside the mock-up waste drum show the inadequacy of the chosen simplified representation as homogeneous material for this kind of application.

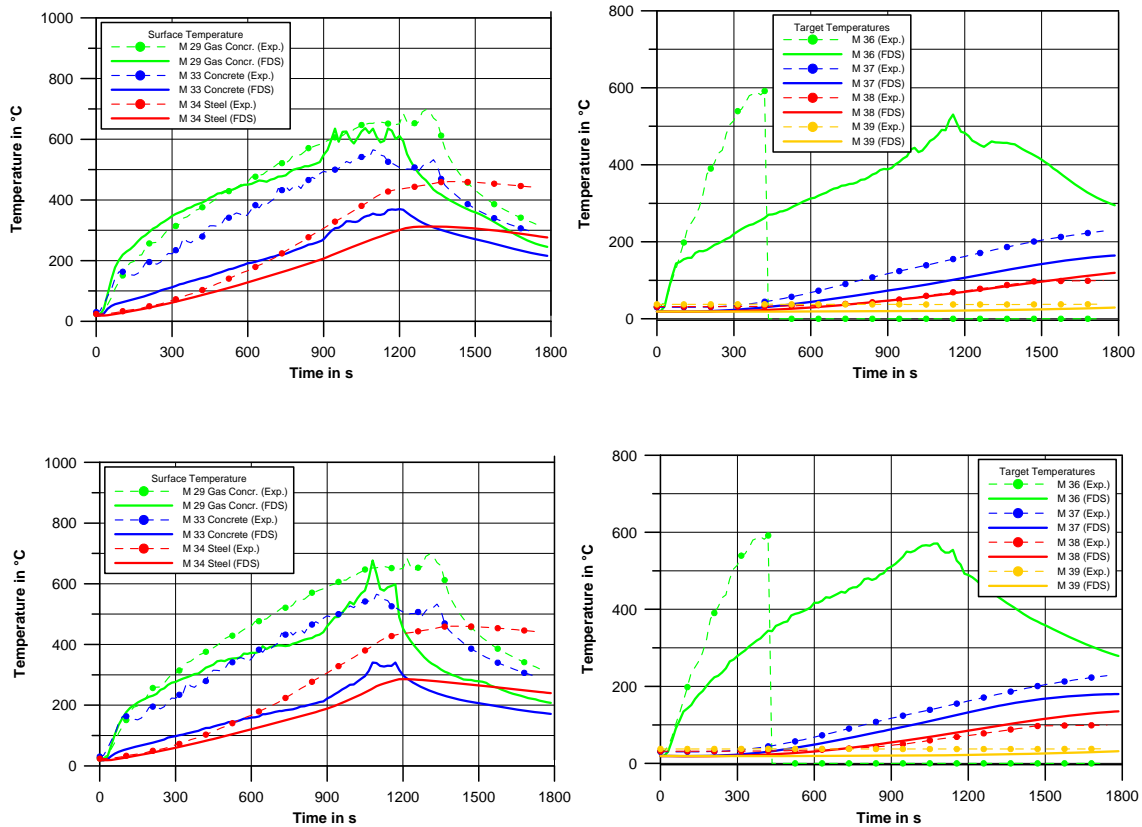


Fig. G3-4 Target and waste drum temperatures calculated with FDS3 (top: coarse grid, bottom: nested fine grid)

G3.3 FDS4 Calculations

Based on the model documentation of FDS3 and FDS4 only minor differences between fine grid calculations with both models would be expected. No changes in model parameters including chemical reaction and material properties were made. However the use of the default lower oxygen limit (LOL) definition results in a difference which becomes obvious only after careful reading of the technical documentation /MCG 02/, /MCG 05/. Fig. G3-5 shows the different definitions of the respective default definition of the LOL. In FDS4 the “no burn” area in under-ventilated conditions is extended to higher temperatures compared to the FDS3 definition.

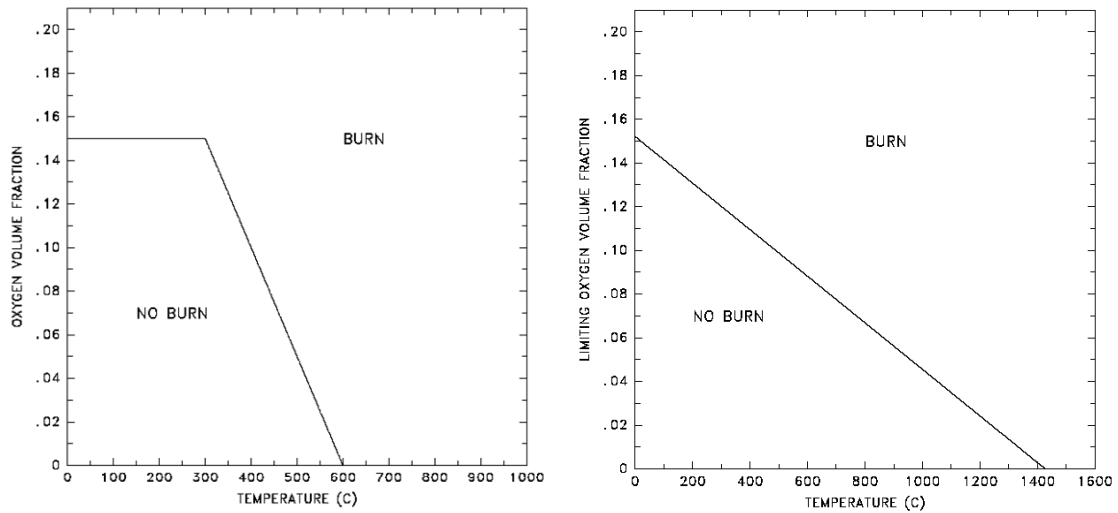


Fig. G3-5 Default LOL conditions in FDS3 (left /MCG 02/) and FDS4 (right /MCG 05/)

As a consequence, lower heat release rates are found in the FDS4 compared to FDS3, including lower gas temperatures and surface heat fluxes (Fig. G3-6). No attempt was made to compare both models with similar LOL definitions. Anyhow, the default LOL definition seems to be a major problem in under-ventilated conditions for both model versions.

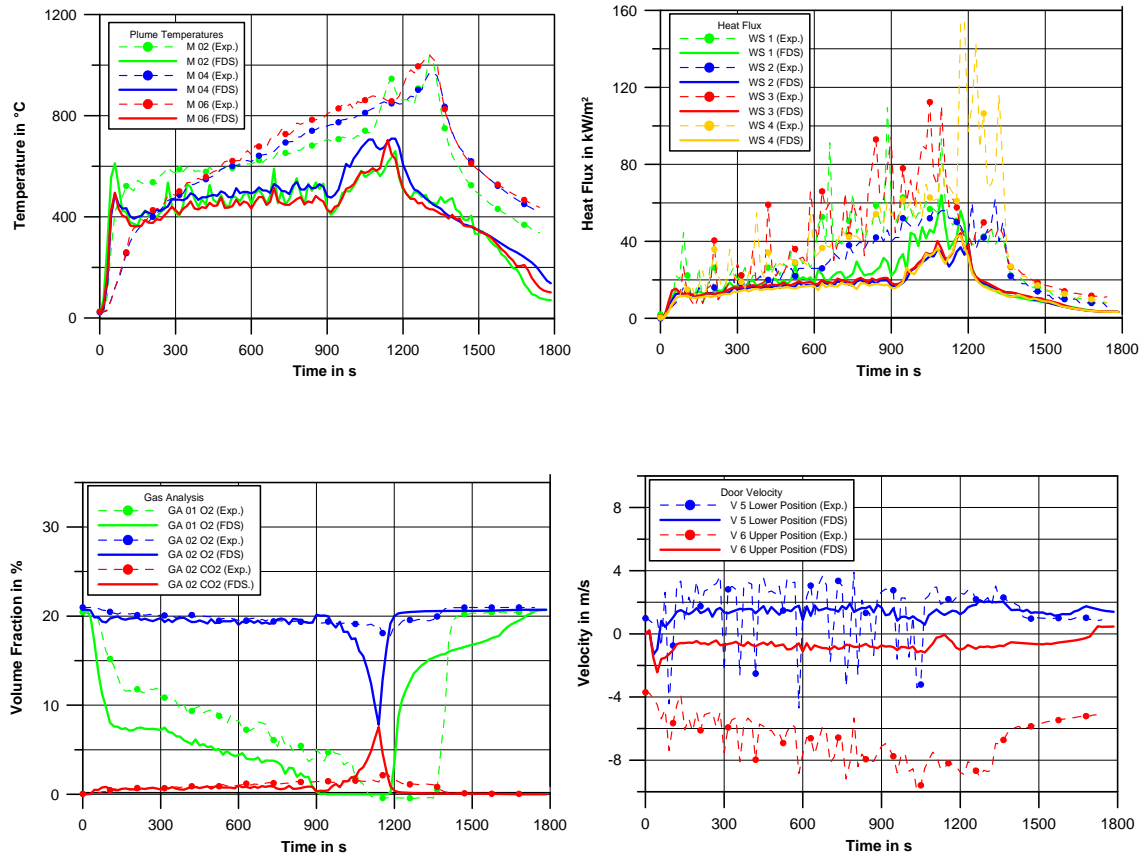


Fig. G3-6 Plume temperatures, heat fluxes, gas concentrations and door velocities calculated with FDS4 (nested fine grid)

Concerning the influence of grid resolution Fig G3-1 shows less influence of this parameter on heat release rates in case of the FDS4 calculations in which is opposite to the FDS3 results. Similar tendencies are found with respect to gas temperatures and surface heat fluxes.

Another question raised in discussions on the benchmark measurements was the influence of the lack of thermocouple shielding against radiation. The suspicion arose that measured gas temperature values might be flawed by intense radiation from the flame surface. The comparison of FDS4 gas temperatures and FDS4 virtual unshielded thermocouple temperatures in Fig. G3-7 shows nearly no difference. Hence, the lack of shielding seems to be of minor importance in this experiment.

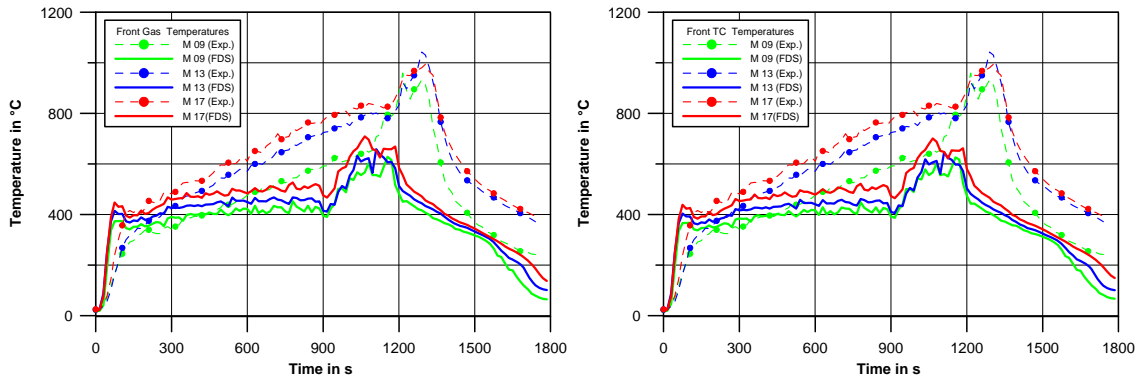


Fig. G3-7 Front gas temperatures (left) and unshielded thermocouple temperatures (right) calculated with FDS4 (nested fine grid)

G4 Conclusions

The calculations performed with FDS3 and FDS4 do not allow a complete general assessment of both models. Taking the above analysis of calculations into account as well as results obtained by other ICFMP members it is obvious that the choice of model parameters and of the model grid (which is more than simply resolution) may strongly affect the quality of results. Hence, the experience of the user as well as a sufficient amount of time for a conscientious and optimized configuration of the model setup is essential.

With the chosen model setup, FDS is able to represent many features of the test 3 fire scenario satisfactorily. Parts of the analyzed deviations between model calculations and measurements may be caused by the questionable mass release rate data of the benchmark specification. Former attempts with FDS3 to predict the burn rate via the built-in evaporation model were even worse. Consequently, further work is needed to improve this sub-model of FDS.

One major problem of both FDS versions seems to be the treatment of under-ventilated conditions via a lower oxygen limit for combustion. Lower limits might have resulted in a better correlation with observations. Analyzed differences between results of both models can mainly be attributed to the differences in default LOL definitions.

The chosen way to increase the model resolution in the flame area did not give better agreement with measurements than the coarse grid simulation, as was expected. Hence, the FDS feature of multiple meshes which allows a fine mesh structure in “hot” areas with minimized CPU needs is rather sensitive to the actual choice of mesh configuration. In case of sufficient computer power an overall fine resolution should be preferred.

The lack of shielding of thermocouples against radiation seems to have no impact with respect to the comparison of gas temperatures between calculations and measurements.

G5 References

/MCG 02/ McGrattan, K.B. et al.:
Fire Dynamics Simulator (Version 3) – Technical Reference Guide
NISTIR 6783, 2002 Ed., National Institute of Standards and Technology,
November 2002

/MCG 05/ McGrattan, K.B. (Ed.):
Fire Dynamics Simulator (Version 4) – Technical Reference Guide
NIST Special Publication 1018, National Institute of Standards and
Technology, February 2005

List of Figures

Fig. G3-1	Heat release rates of all FDS3 and FDS 4 calculations (Test 3).....	5
Fig. G3-2	Gas temperatures for Test 3 calculated with FDS3 (top: coarse grid, bottom: nested fine grid)	7
Fig. G3-3	Gas concentrations, door velocities and heat fluxes for Test 3 calculated with FDS3 (top: coarse grid, bottom: nested fine grid).....	8
Fig. G3-4	Target and waste drum temperatures calculated with FDS3 (top: coarse grid, bottom: nested fine grid).....	10
Fig. G3-5	Default LOL conditions in FDS3 (left /MCG 02/) and FDS4 (right /MCG 05/)	11
Fig. G3-6	Plume temperatures, heat fluxes, gas concentrations and door velocities calculated with FDS4 (nested fine grid).....	12
Fig. G3-7	Front gas temperatures (left) and unshielded thermocouple temperatures (right) calculated with FDS4 (nested fine grid)	13

**Appendix H: International Collaborative Project to Evaluate Fire
Models for Nuclear Power Plant Applications**

**CCOCOSYS Simulations for Benchmark
Exercise No. 4**

Presented by

Walter Klein-Heßling, Berthold Schramm
Gesellschaft für Anlagen- und Reaktorsicherheit (GRS) mbH,
50667 Köln, Germany

Contents

List of Figures	III
H1 Discretization of the Fire Compartment in COCOSYS	1
H1.1 Grid for Test 1	1
H1.2 Grid for Test 3	1
H2 Modeling Ventilation And Combustion	3
H3 Simulation of Benchmark Exercise No. 4 Test 3	7
H3.1 Comparison of simulation and experimental results.....	7
H3.1.1 Plume temperature.....	7
H3.1.2 Temperature in the combustion room outside the plume	8
H3.1.3 Temperature in structures and material probes	9
H3.1.4 Velocity.....	9
H3.1.5 Gas composition	10
H4 Simulation of Test 3 with a Modified Pyrolysis Rate	31
H5 Simulation of Test 1	43
H5.1 Geometry and pyrolysis rate	43
H5.2 Comparison between experiment and simulation	43
H5.2.1 Gas temperature	43
H5.3 Flow field	44
H5.4 Gas composition	45
H5.5 Surface temperatures.....	45
H6 Summary	61
H7 References	63

H1 Discretization of the Fire Compartment in COCOSYS

H1.1 Grid for Test 1

A grid of 102 zones with 235 atmospheric junctions was used to model the fire compartment (Fig. H1-1, Fig. H1-2). The compartment was divided into 9 vertical levels at the following elevations: 0 m, 0.36 m, 0.6 m, 1.1 m, 1.6 m, 2.6 m, 3.6 m and 4.6 m in order to prevent artificial flow circulations /KLE 00/. Every level is modeled by COCOSYS zones in the same way. The room where the combustion occurs is subdivided into 13 zones (Fig. H1-2). At lower levels, some zones are missing due to the geometry, e.g. in the area of the target.

One zone is in the center above the fuel pan with the oil. Two rings of zones (4 zones each) surround the center zone. It is expected that in the center zone the flame and the hot plume occur. Further from the center the temperature will decrease. To predict this temperature decrease two rings of zones were used. Due to topological reasons four additional zones were needed to model the area above and around the target.

The second room with the hood and the connection between the two rooms is modeled by one zone each. Only the part of this room, which is under the hood, is included as a zone in the model. The difference in the setup between the levels is that the size of center zone in the combustion room is growing with the height (Fig. H1-2). The reason for this modification was to improve the modeling of the hot gas plume. To enable a counter flow the connection between the two rooms has to be modeled at least by two zones. To enable a better velocity field the junction was subdivided into 4 zones.

H1.2 Grid for Test 3

The geometry and the grid used for Test 3 are very similar to that in Test 1. The only difference is that the connection between the two rooms is reduced to 1 m². To enable a counter flow with a reasonable velocity field again 4 vertical levels in the connection were defined (Fig. H1-1). The discretization of a given level was the same as in the simulation of Test 1. Thus, the total number of vertical levels was increased to 11. The total number of zones for the simulation was 129 und the number of junctions 314.

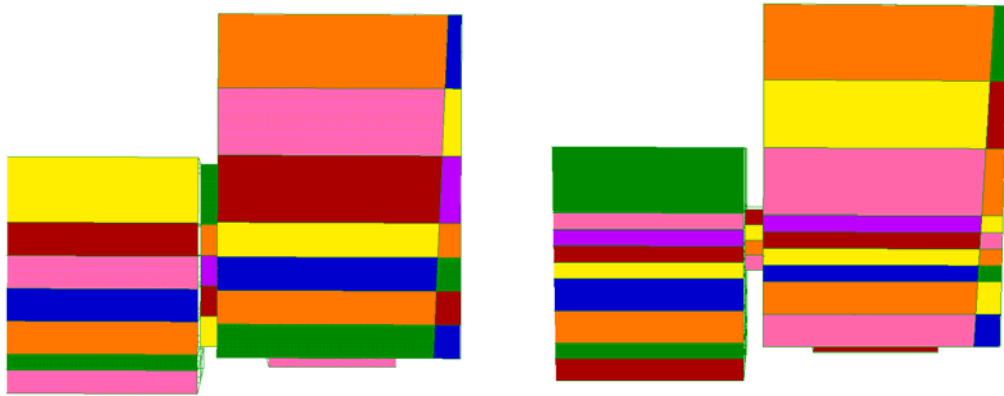


Fig. H1-1 Discretization of the fire compartment in COCOSYS - side view;
left: Test 1; right: Test 3

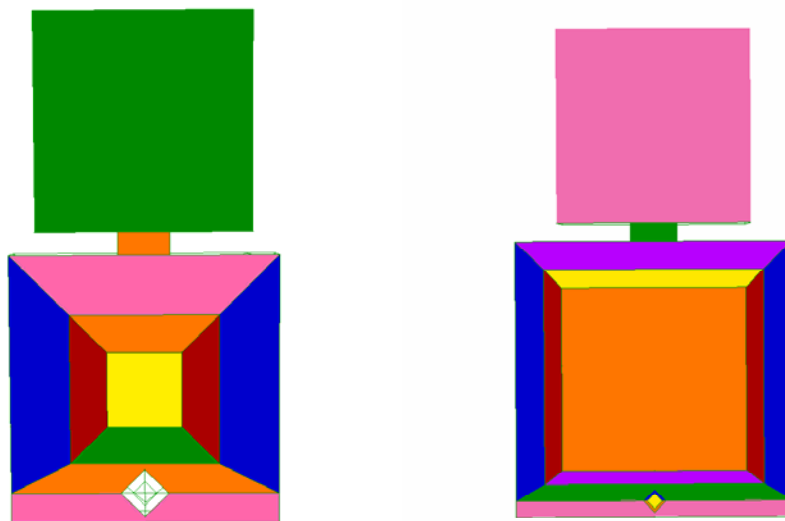


Fig. H1-2 Discretization of the fire compartment in COCOSYS - view from the bottom
(left) and from the top (right)

H2 Modeling Ventilation and Combustion

The ventilation was simulated using the fan module of COCOSYS /KLE 00/. For the FUCHS ventilation system installed at the ceiling of the fire compartment above the fire in the exhaust channel, it is assumed, that the mass flow through each channel is equal. The volume flow rates for the fan systems are chosen as measured in the experiment.

The model in COCOSYS to predict the pyrolysis rate is not yet fully completed. Therefore, the pyrolysis for the simulation was not calculated, but the values were achieved from the change of the measured weight of the pan filled with fuel. The derivative of the measured weight is very sensitive to measurement errors. Therefore, the derived values for the pyrolysis rate have to be smoothed. The disadvantage of this method is that the rate is decoupled from the conditions simulated in the area above the pan with the fuel.

Usually the pyrolysis rate depends strongly on the temperature of the gas above the fuel surface. Decreasing the temperature should decrease the pyrolysis rate, too. Giving the measured pyrolysis rates as input parameter to the calculation leads to a decoupling from the simulated state. This could produce some unphysical behavior of the system if the pyrolysis rate does not fit to the gas state above the fuel (see chapter H3.1.1).

One additional problem was that in Test 3 the weight of the fuel was not measured correctly at least during the time period between 1100 s and 1430 s. Temporarily the weight of unburnt fuel increases again, which does not represent the physical phenomena correctly. Thus for this period the pyrolysis rate depending on the weight loss of the unburnt liquid fuel has to be interpolated using the total weight loss for a relative long period. For Test 1, data for the pyrolysis rate was not available after approx. 850 s.

The combustion process of gaseous fuel is modeled by a two-step reaction including the gaseous species fuel ($C_{11.64}H_{25.29}$), CO , CO_2 and H_2O /ALL 05/. This simple mechanism is often sufficient, but under oxygen rich conditions neglecting the soot production and its interaction with radiation may lead to some errors.

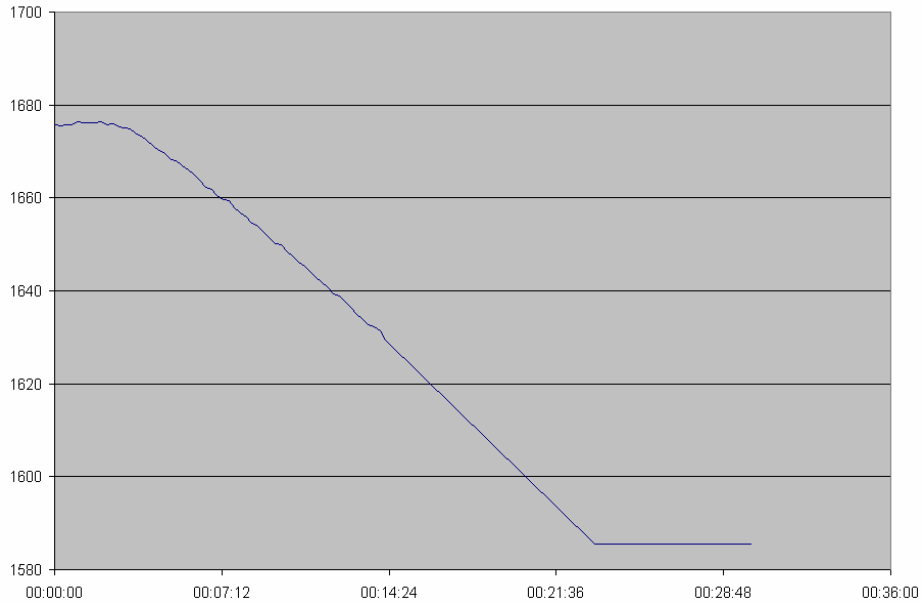


Fig. H2-1 Test 1: Measured and extrapolated weight of the pan filled with fuel

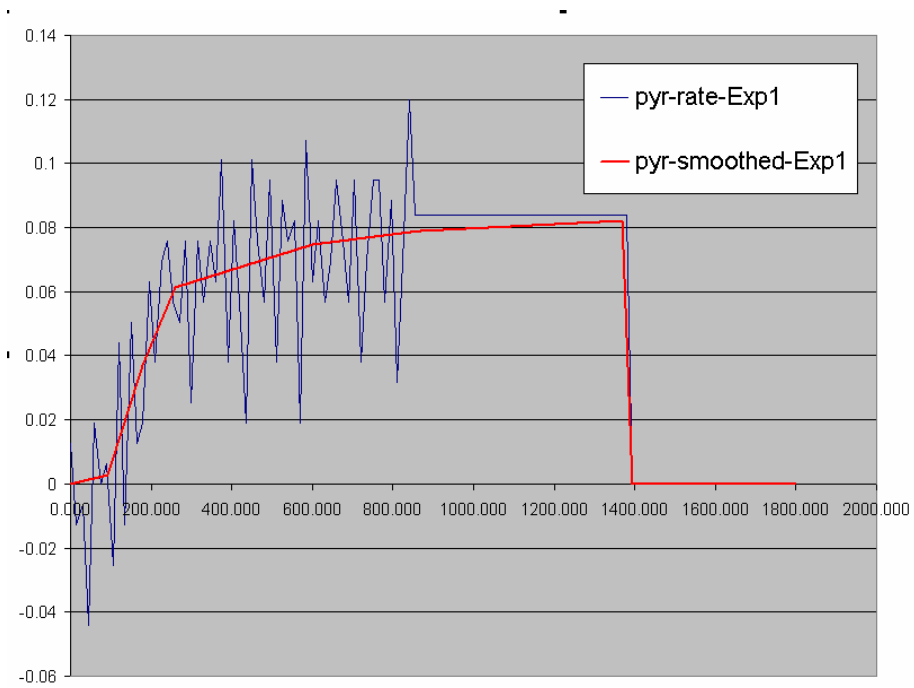


Fig. H2-2 Test 1: Original and smoothed pyrolysis rate

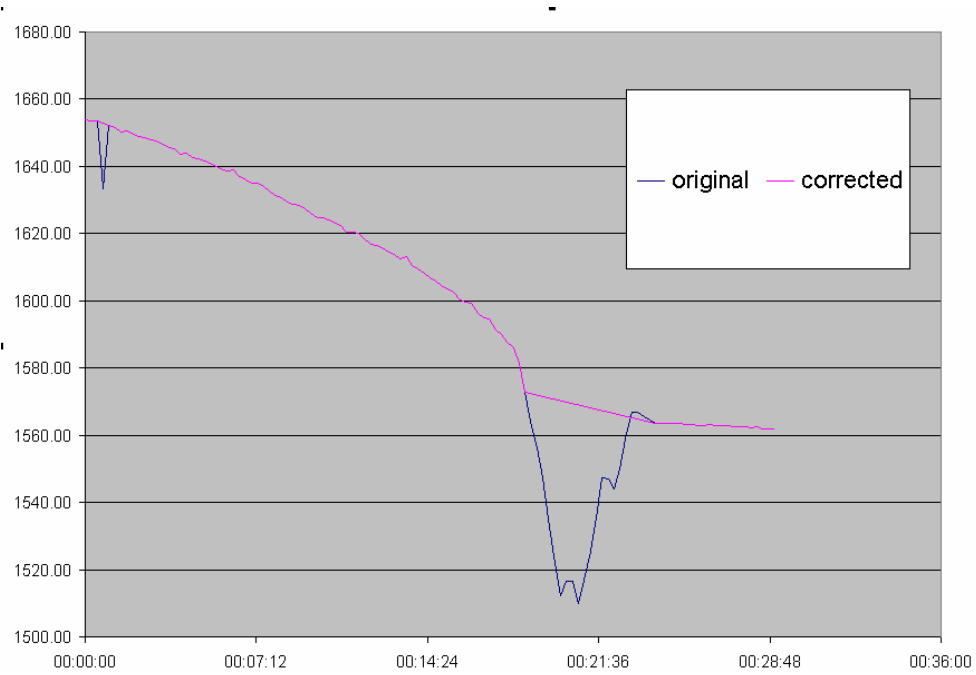


Fig. H2-3 Test 3: Measured weight of the pan filled with fuel

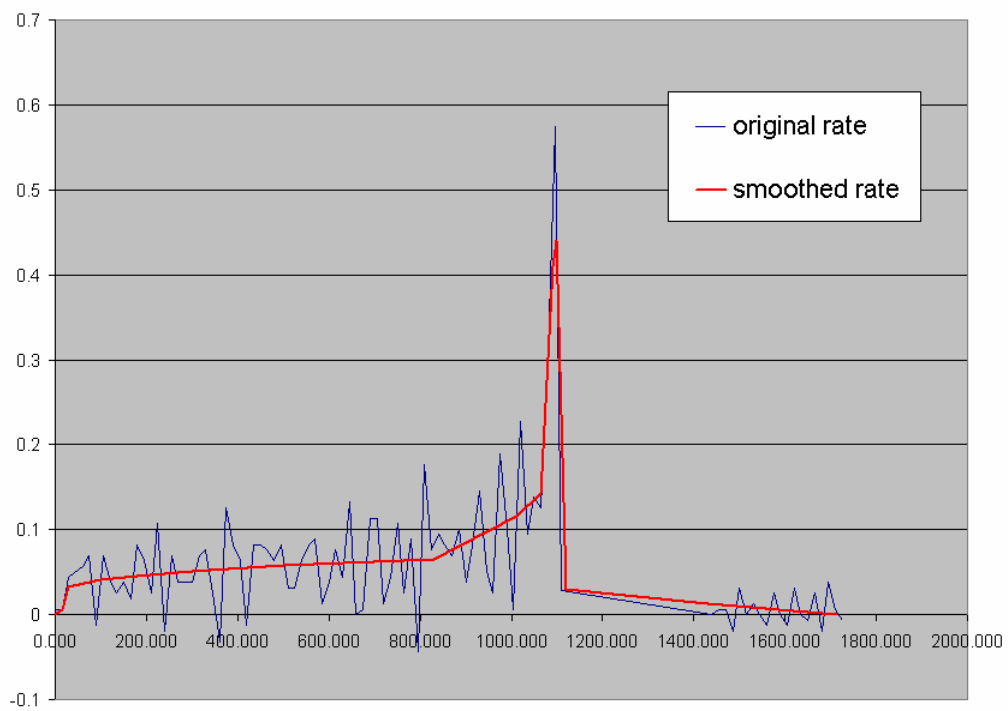


Fig. H2-4 Test 3: Original and smoothed pyrolysis rate

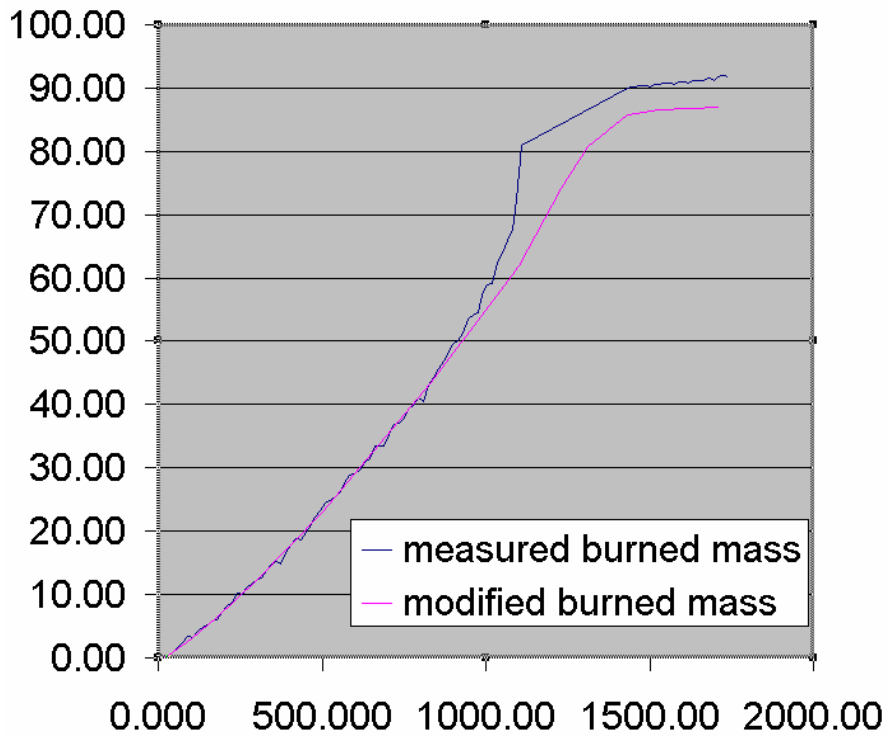


Fig. H2-5 Test 3: Measured burned fuel mass and burned fuel with the modified pyrolysis rate

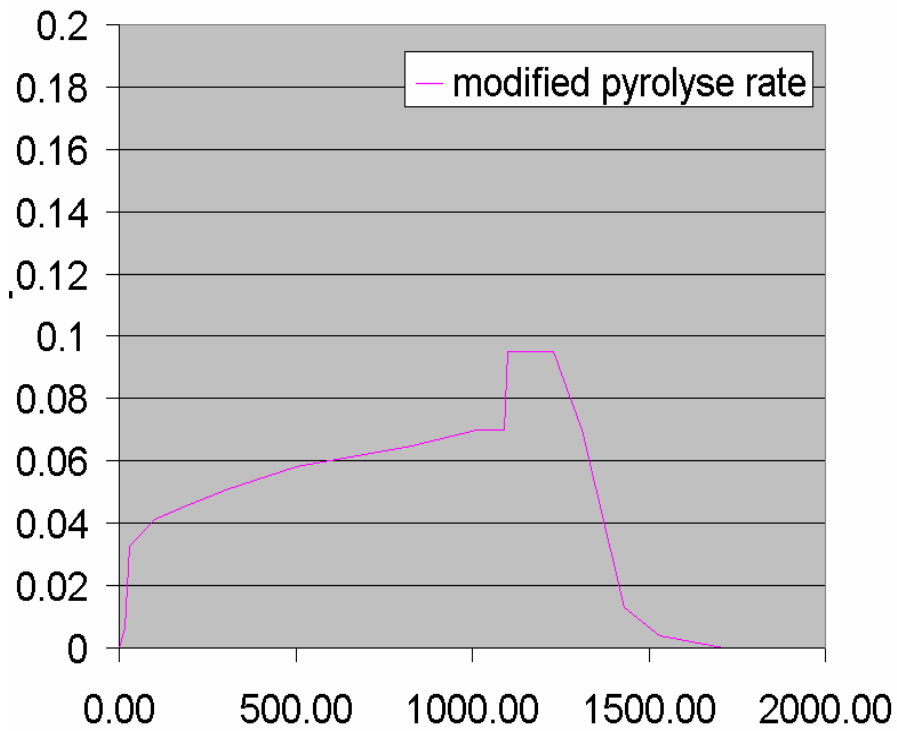


Fig. H2-6 Test 3: Modified pyrolysis rate

H3 Simulation of Benchmark Exercise No. 4 Test 3

As mentioned in Section H1, the pyrolysis rate is set by the user to the value measured in the experiment. After 1100 s, problems with measurement of the weight occurred and no reasonable data are available. For this period a linear interpolation is implemented to achieve a reasonable pyrolysis rate. This may lead to some additional errors. The pyrolysis rate set as boundary condition for this simulation was set according to Fig. H2-4.

H3.1 Comparison of simulation and experimental results

H3.1.1 Plume temperature

In the lower part of the plume, the temperature of the gas is under-predicted for the first 400 s (M1, Fig. H3-1). However, in the higher parts of the plume in the centre the temperature is increasing more rapidly than in the experiment. After 100 s, for the highest measurement point in the centre (M6) the temperature is about 300 °C, but in the simulation nearly 600 °C is predicted (M6, Fig. H3-6). From 400 s to 800 s the temperature in the lower part of the plume is predicted well (M1), but in the higher regions the temperature is over-predicted by 50 - 100 °C. After 950 s the temperature in the lowest COCOSYS zone decreases rapidly, even the pyrolysis rate reaches its maximum. The reason is that all O₂ in this zone is exhausted in the combustion process and not enough air is transported to this zone.

The same phenomena can be found in the next higher COCOSYS zone where measurement point M1 is located (M1, Fig. H3-1). Thus, the temperature in the simulation decreases and starts oscillating in the entire plume during this period, instead of reaching a maximum. As soon as the flame self-extinguishes the system does not behave physically and terminates. With decreasing temperature and radiation, the pyrolysis rate should decrease, too; however depending only on the measured data it stays on the high level. In addition, with the change in the heat release the flow field also changes. To investigate the effect of the error in the pyrolysis rate another simulation was performed with a lower pyrolysis rate and no flame extinguishment (see Section H4).

After 1300 s, both the simulated as well as the experimental temperatures decrease rapidly. The temperature in the simulation is too low for the middle and the upper part of the plume. Due to the large differences earlier in the gas state it does not make sense to spend too much time comparing both values. Nevertheless, it seems that the rate of the temperature decline is similar in experiment and in the simulation.

H3.1.2 Temperature in the combustion room outside the plume

In the discussion of the gas temperatures outside the hot plume (M7-M18), the attention is drawn to the first 900 s. Later, the extinction of the gas in the simulation will cause the major difference between calculation and experiment.

Except the first measurement point, the temperature for all measurement points is over-predicted for the first 100 to 200 s (see Fig. H3-1 to Fig. H3-18).

In the simulation, the fast growth in the temperature stops after 100 s; however in the experiment, the growth is weaker. At some measuring points (M7, M8, M10), a steep temperature increase cannot be found at all at the beginning of the experiment (Fig. H3-2).

From 200 to 900 s, good agreement between experiment and simulation can be found for measurement point M7 (Fig. H3-7). For the other measuring points (M8, M9, M10) outside the hot plume at this low level ($z = 1.5$ m) the temperatures are much lower (100 – 200 °C) in the simulation (Fig. H3-8 to Fig. H3-10). The good agreement for point M7 can be explained by the position of the hot plume. In the experiment, the plume is not vertical, but is inclined towards the wall on the opposite side of the connection between the two rooms. In the COCOSYS simulation, no equations for the momentum are solved. Thus, the plume is vertical in the center of the room. Therefore, the point M7 is closer to the plume in the simulation than in the experiment. Thus, in general, the temperature in the lower part of the compartment is under-predicted by 100 – 200 °C. However, for the measurement point M7 two errors eliminate each other.

The predicted temperatures in the middle of the room (M11-M14; $z = 3.35$ m) show a reasonable agreement with the experimental data (Fig. H3-11 to Fig. H3-14). Only the temperature for point M12 is under-estimated. This may be explained by the different positions of the plume, too.

In the upper part of the combustion room, the temperature increase during the first 100 to 200 s is over-predicted by several hundred degrees. Later, the temperature growth is slower in the simulation than in the experiment, and after 600 to 900 s the measured and the predicted temperatures are at the same level (Fig. H3-15 to Fig. H3-18). After 900 s the combustion process is not very well predicted in the zones close to the fuel pan, which leads to an under-estimation of the heat release in the simulation as well as to a lower temperature in all other parts of the compartment.

H3.1.3 Temperature in structures and material probes

Comparing the temperatures in the material probes made of gasconcrete and concrete it can be observed that the temperature near the surface ($x = 0.02$ m) is under-predicted in the simulation. This can be easily explained by the significant under-prediction of the gas temperature in the simulation in this area.

H3.1.4 Velocity

COCOSYS /KLE 00/ representing a lumped parameter code is not able to predict local velocities. COCOSYS can only calculate the mass flow between two zones, which gives an average velocity of the gas flowing between the two zones. If this velocity is compared to a measured velocity, several problems occur.

In general, the velocity at a measurement point inside a zone is a superposition of the mass flows of the connections to all neighbouring zones in COCOSYS. The velocity often strongly depends on the local position, for example there can be curls, in pipes a velocity profile will appear, etc. In addition, turbulences will lead to an oscillation in the measured values. Even if all mass flows to the other zones are calculated correctly, the predicted velocities at the zone junctions might not be the same as the measured velocity at a point in the middle of a COCOSYS zone.

The comparison between both values will give a satisfactory agreement only in case that the flow field is homogenous in zone and the direction corresponds to a COCOSYS junction. The comparison of the mass flows at zone junctions and the experimental data can only give a hint, if the predicted mass flows between the zones are reasonable.

In addition to these problems, the measured velocities sometimes do not seem to be realistic. Thus, only a brief comparison of the measured and the predicted velocities will be given.

At the measuring points V1 and V2 in the plume large oscillations occur in the experiment (Fig. H3-24, Fig. H3-25). As mentioned before, a quantitative comparison with the experiment is difficult. But at least the velocities are in the same order of magnitude. For the measurement point V5 at the door between the two rooms the experimental data show again an oscillating velocity profile. The simulation predicts a mass flow, which is consistent to the experimental data.

For the second measurement point V6 at the door large deviations between the experiment and the simulation results appear. In the simulation nearly no gas flows through this junction, but in the experiment velocities of over 5 m/s can be observed at the measurement point. This might be an indication that the simulated flow field does not match. On the other hand, it is not clear if the experimental data are correct, because even at $t = 0$ s a velocity of approx. 4 m/s is detected. This seems to be large, even if the mass flow through the two fan system, which is not zero at $t = 0$ s, is considered.

H3.1.5 Gas composition

The gas composition has been measured at the point GA1 in the combustion room. In the simulation the O_2 concentration is lower than in the experiment for the period between 0 and 800 s (Fig. H3-22). From 800 to 1000 s both values show a good agreement. After 1000 s the O_2 concentration is nearly zero in the experiment, but in the simulation it increases again. These discrepancies can be explained by looking at the O_2 concentration above the fuel surface (Fig. H3-23).

In the simulation, the O_2 concentration decreases rapidly after 900 s. From 1000 to 1300 s it is zero in the zone above the fuel surface. The flame is extinguished in the lower region. Thus, the temperature decreases, and it seems that due to less light gases moving upwards the flow field is changed in a way that even less fresh air is transported to the fuel surface. This could explain, why the temperature is lower for this period than it was at $t = 900$ s.

As discussed earlier (Section H1) the pyrolysis rate is derived using experimental data, which is not valid for this time. The extrapolated pyrolysis rate has many uncertainties. Here the pyrolysis rate is still increasing even when the flame is extinguished in the lower region and the temperature is lower. The pyrolysis rate has a very strong influence on the results. Therefore, a second simulation was performed using a lower pyrolysis rate for this period (see Section H4).

The measurement for CO and CO₂ are invalid. Thus, no comparison is possible with the experimental data.

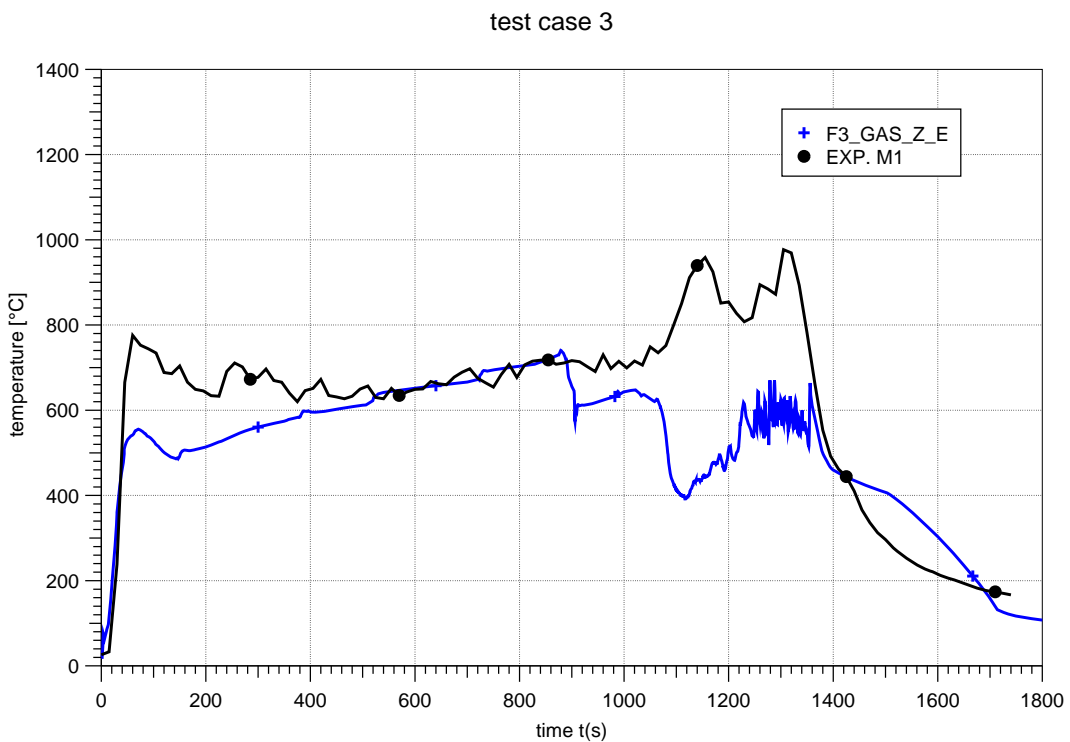


Fig. H3-1 Test 3: Plume temperature at M1

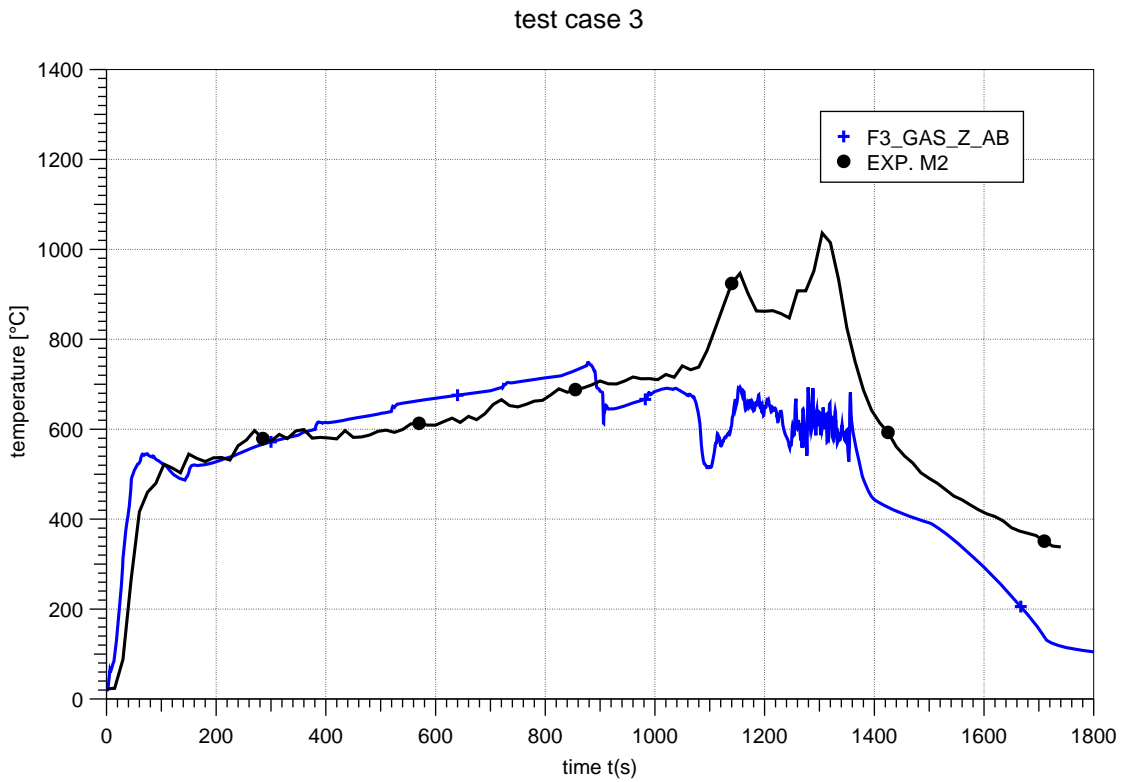


Fig. H3-2 Test 3: Plume temperature at M2

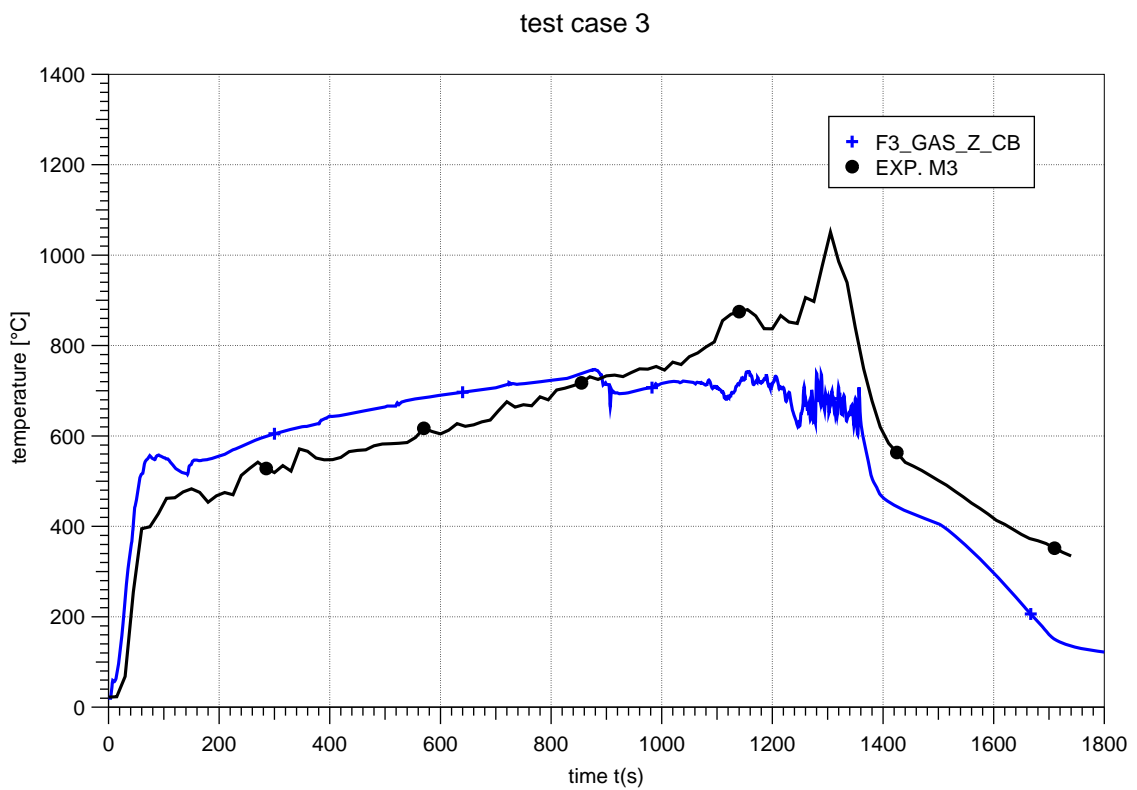


Fig. H3-3 Test 3: Plume temperature at M3

test case 3

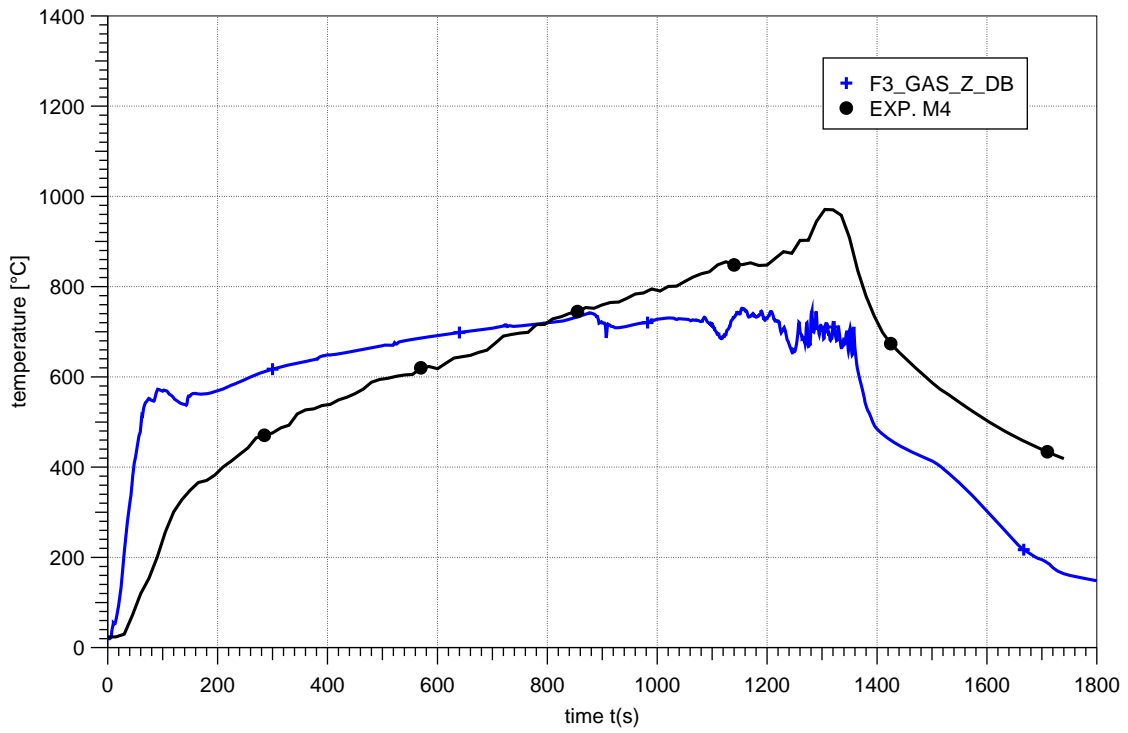


Fig. H3-4 Test 3: Plume temperature at M4

test case 3

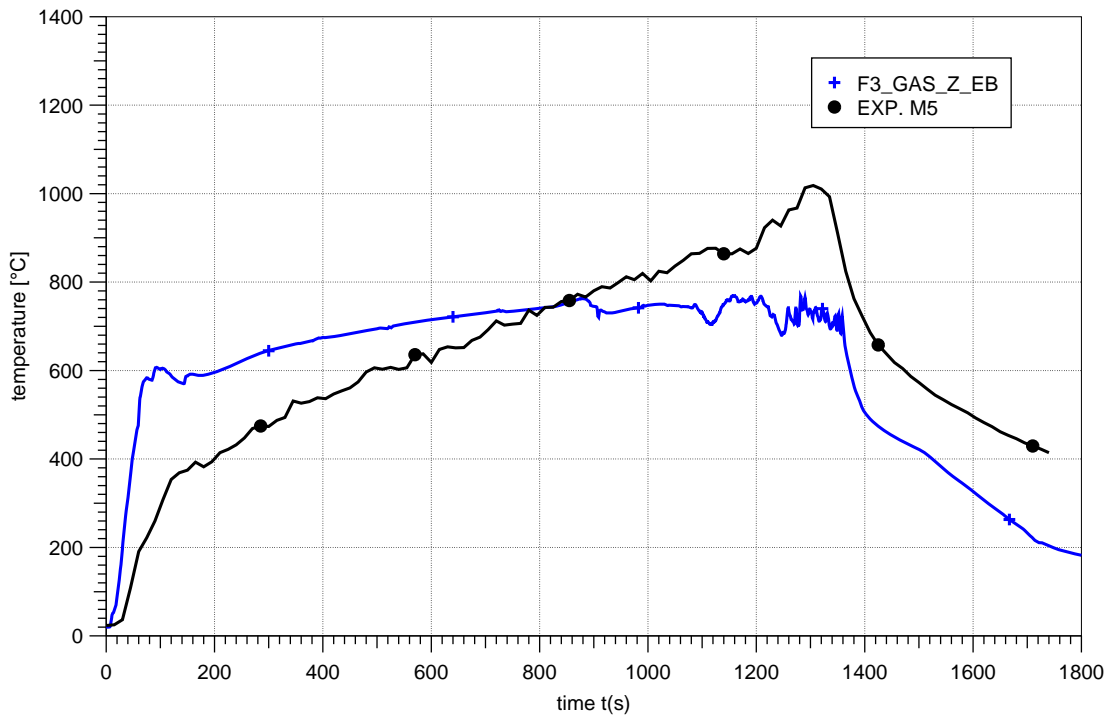


Fig. H3-5 Test 3: Plume temperature at M5

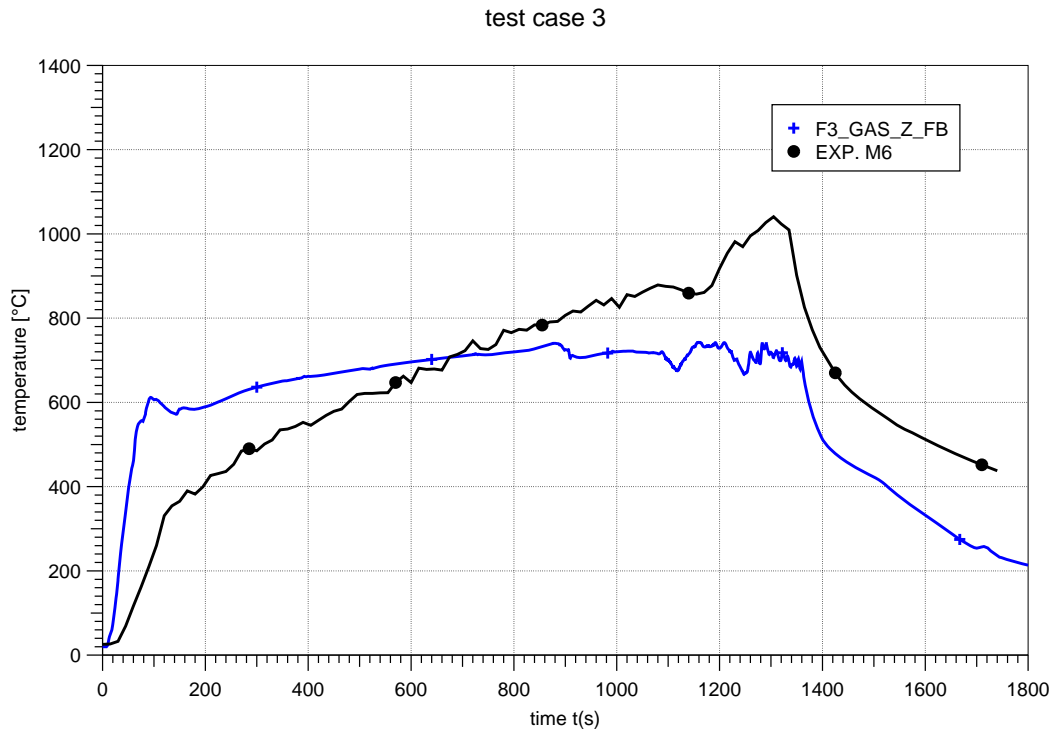


Fig. H3-6 Test 3: Plume temperature at M6

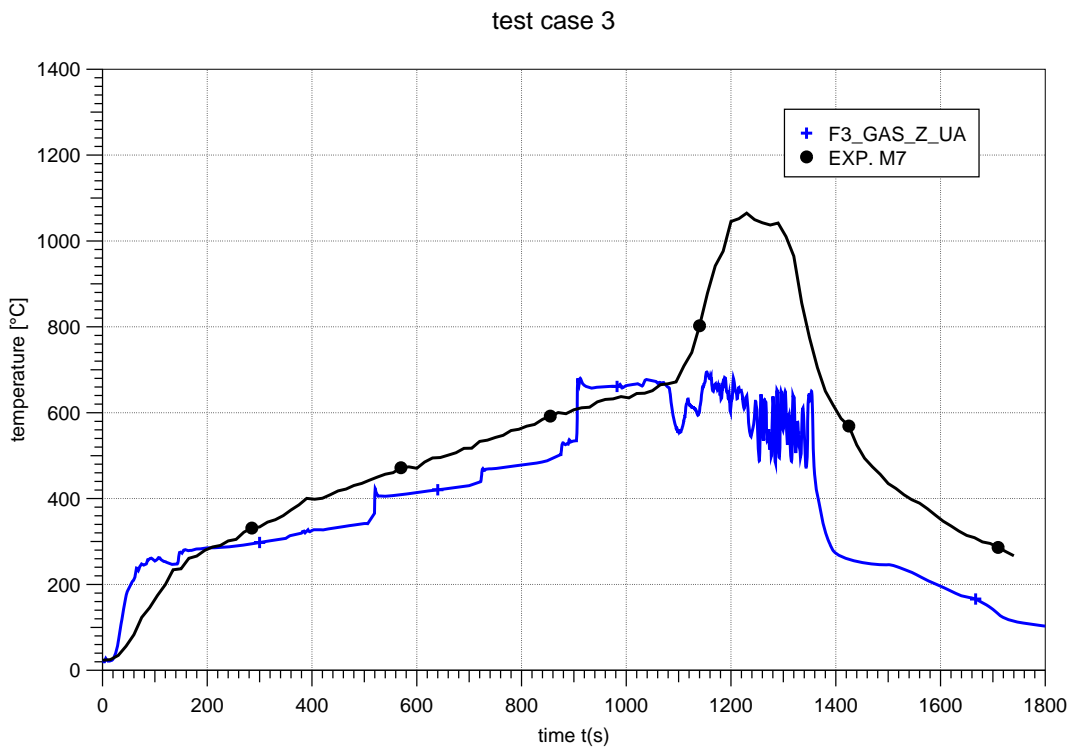


Fig. H3-7 Test 3: Temperature inside fire compartment (level 1, at M7)

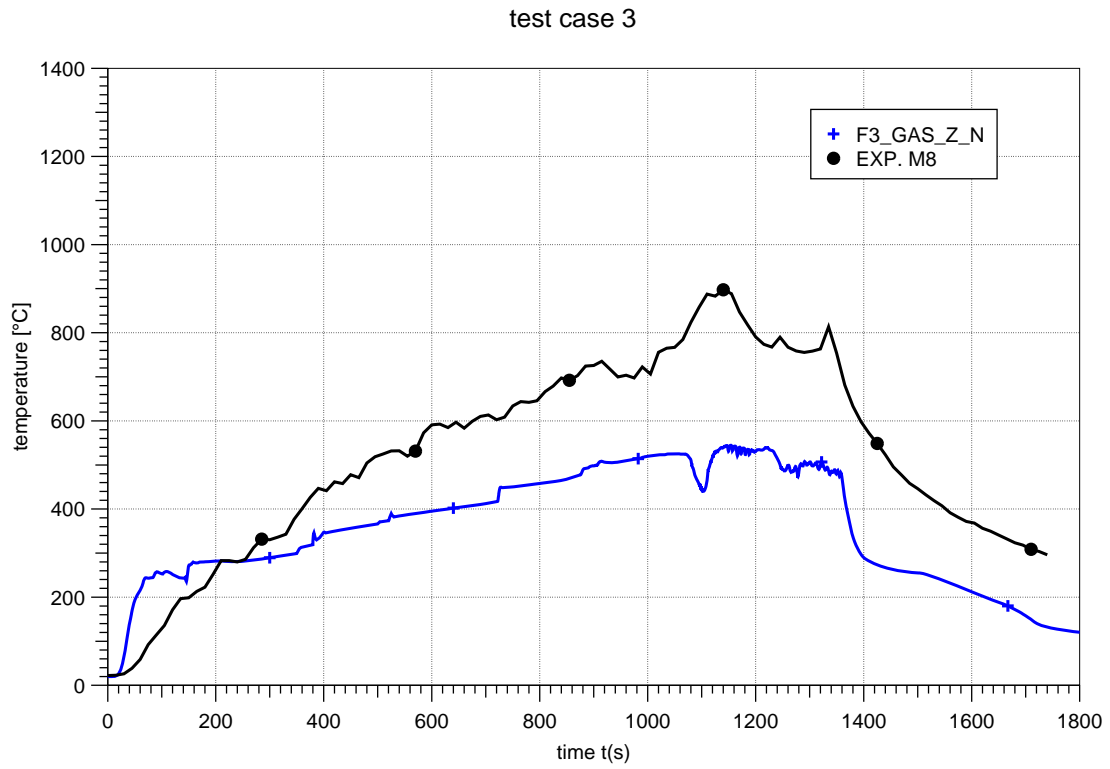


Fig. H3-8 Test 3: Temperature inside fire compartment (level 1, at M8)

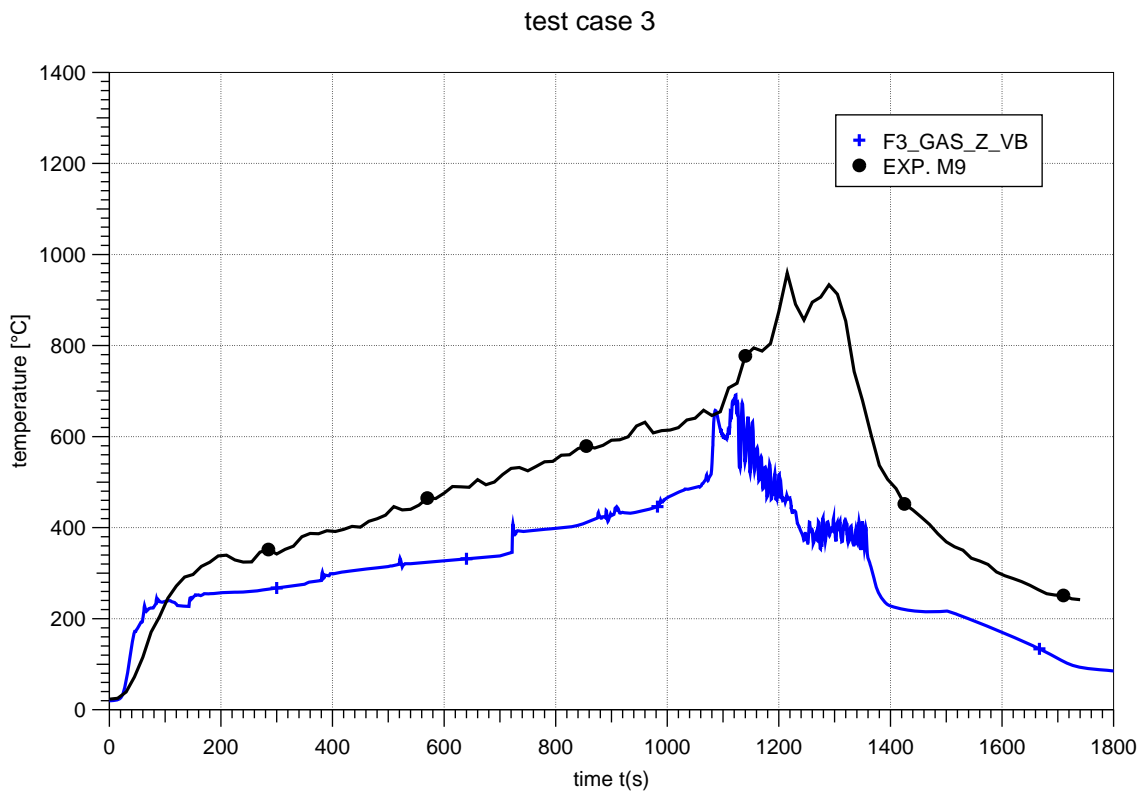


Fig. H3-9 Test 3: Temperature inside fire compartment (level 1, at M9)

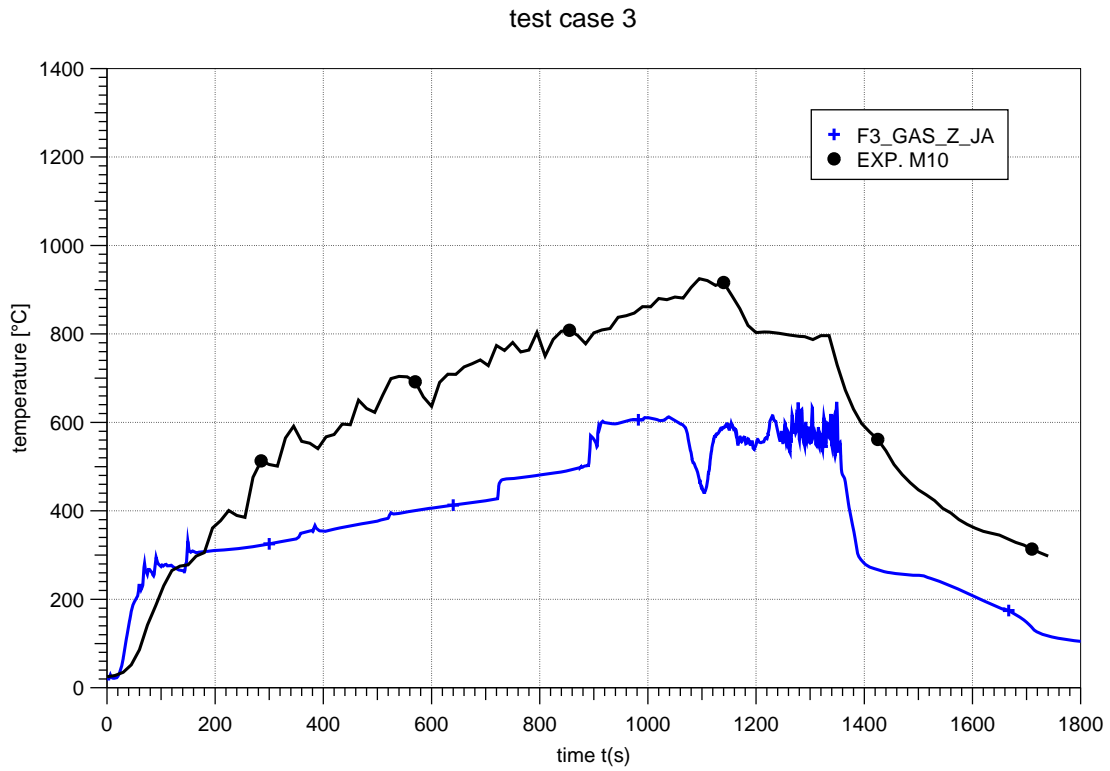


Fig. H3-10 Test 3: Temperature inside fire compartment (level 1, at M10)

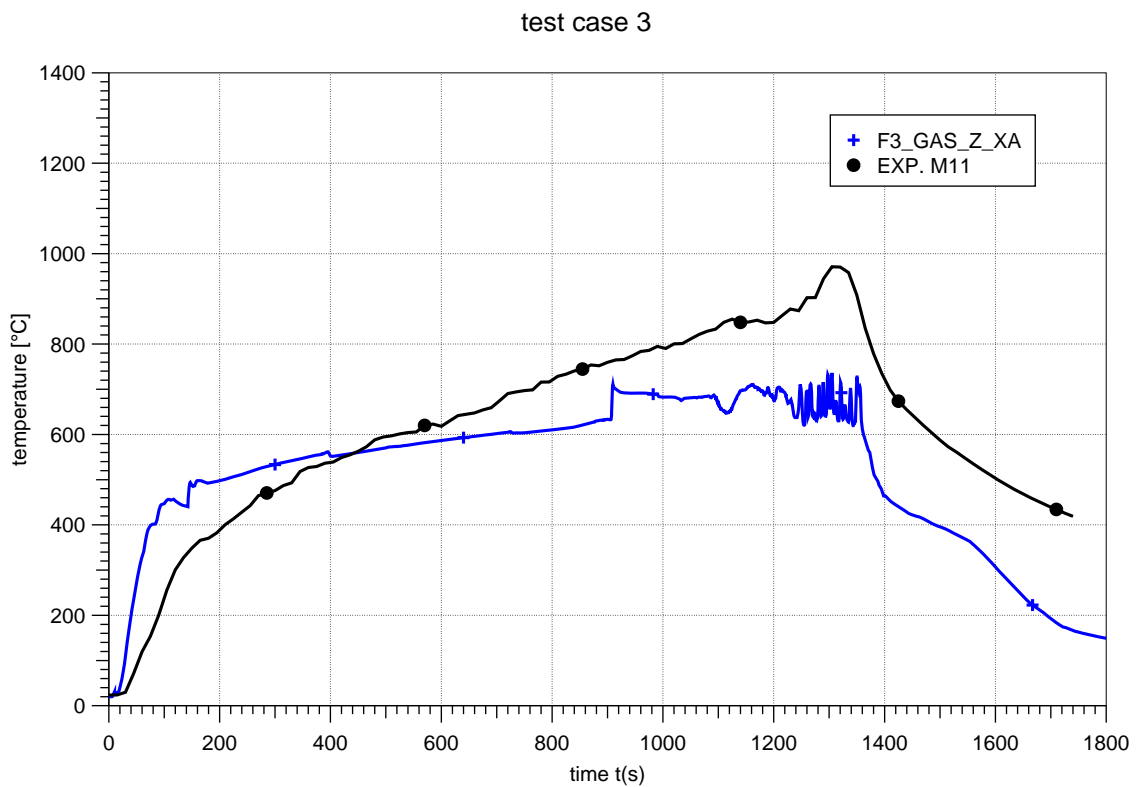


Fig. H3-11 Test 3: Temperature inside fire compartment (level 2, at M11)

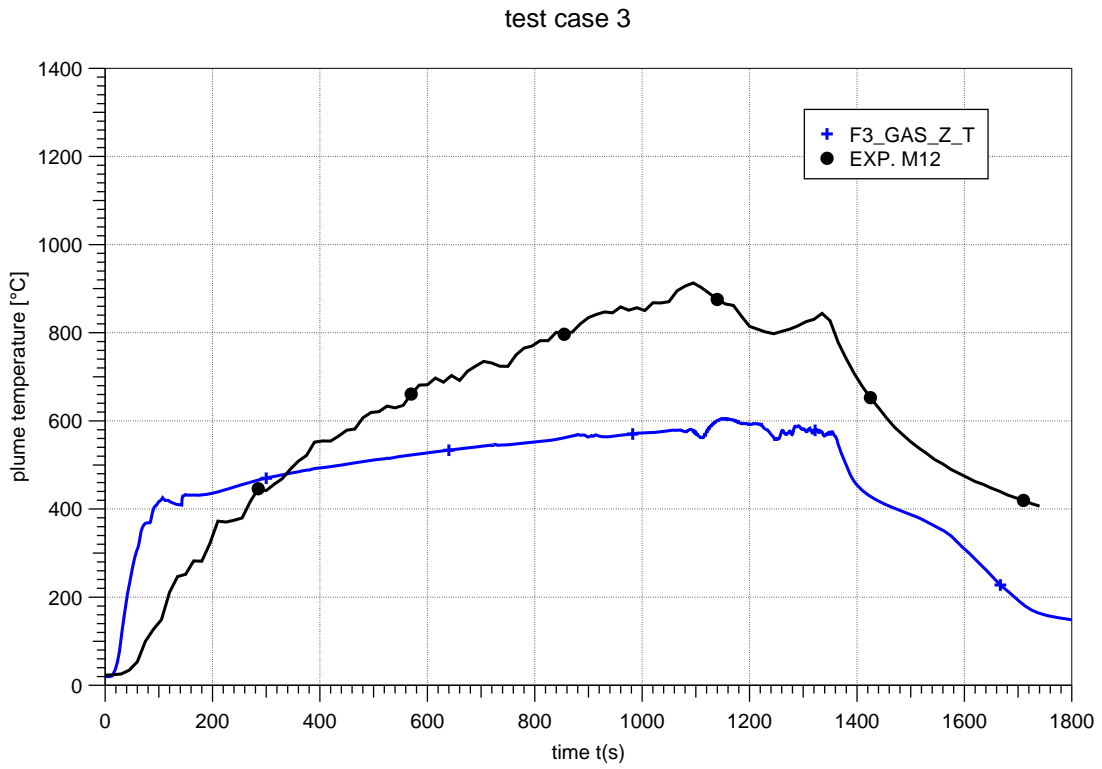


Fig. H3-12 Test 3: Temperature inside fire compartment (level 2, at M12)

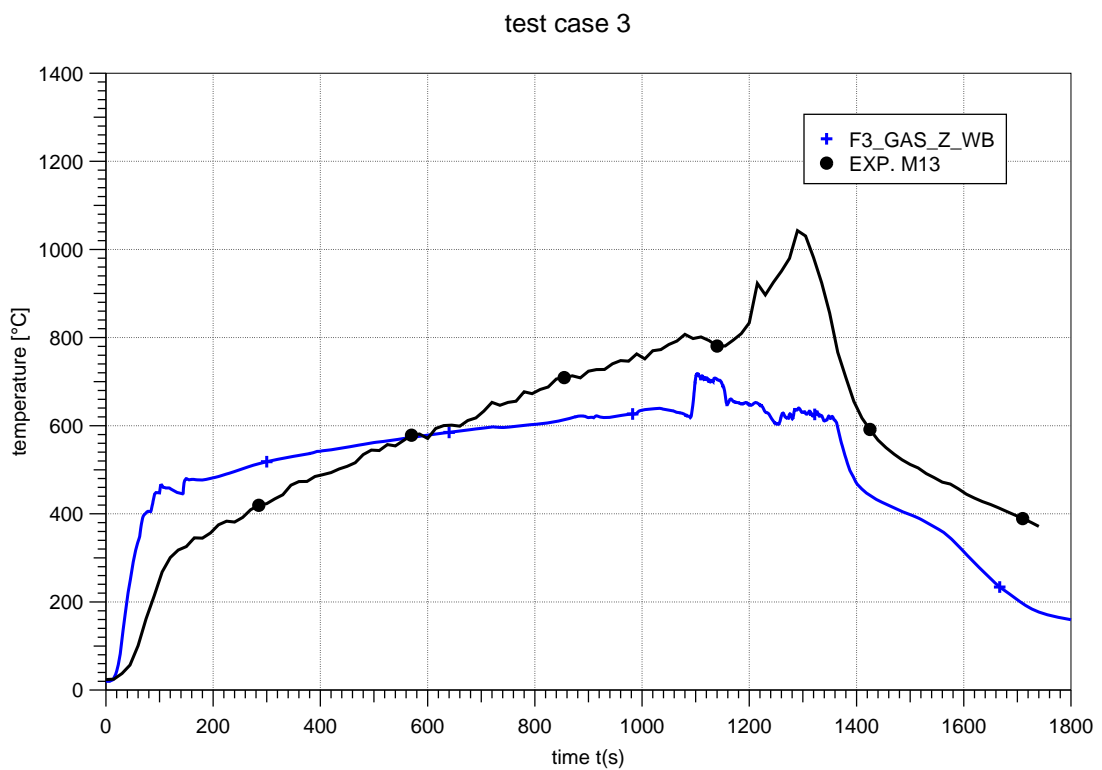


Fig. H3-13 Test 3: Temperature inside fire compartment (level 2, at M13)

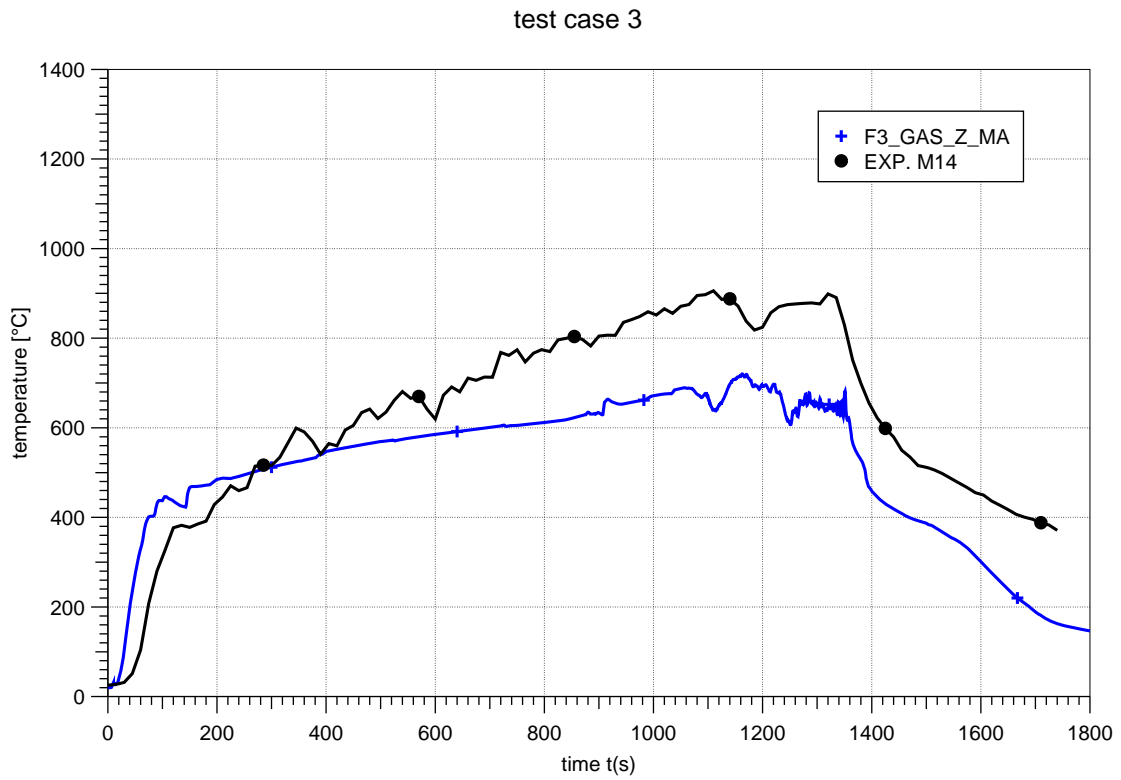


Fig. H3-14 Test 3: Temperature inside fire compartment (level 2, at M14)

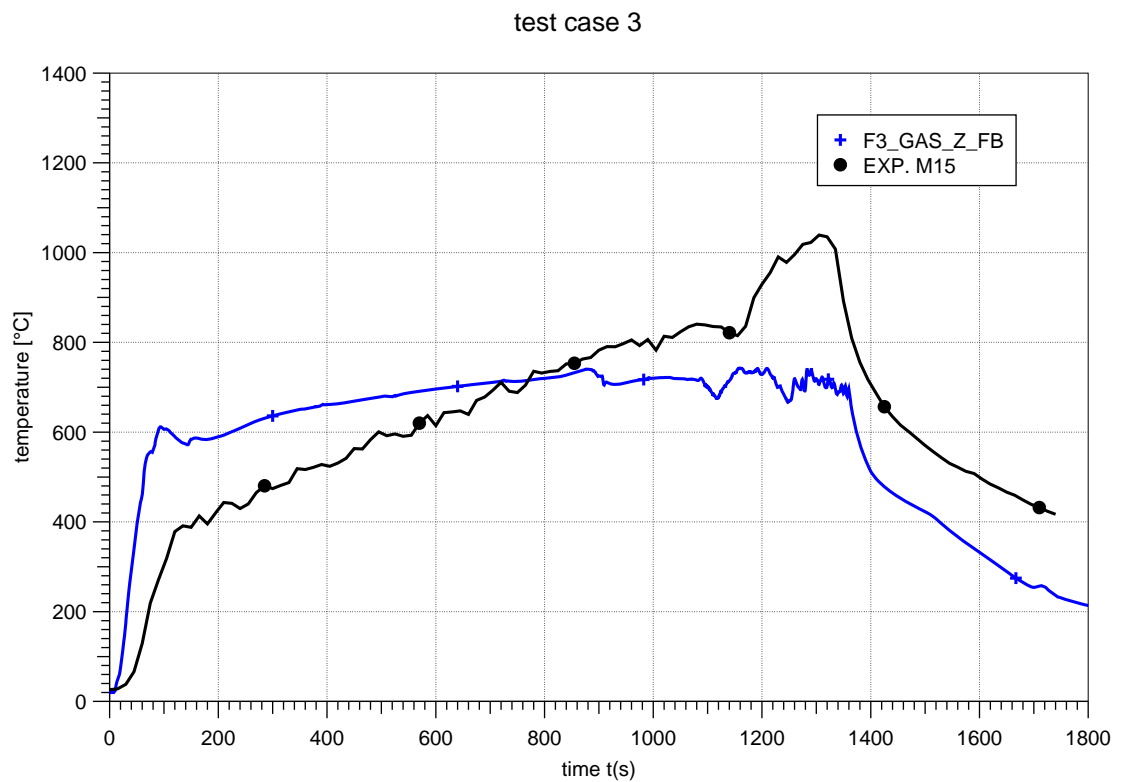


Fig. H3-15 Test 3: Temperature inside fire compartment (level 3, at M15)

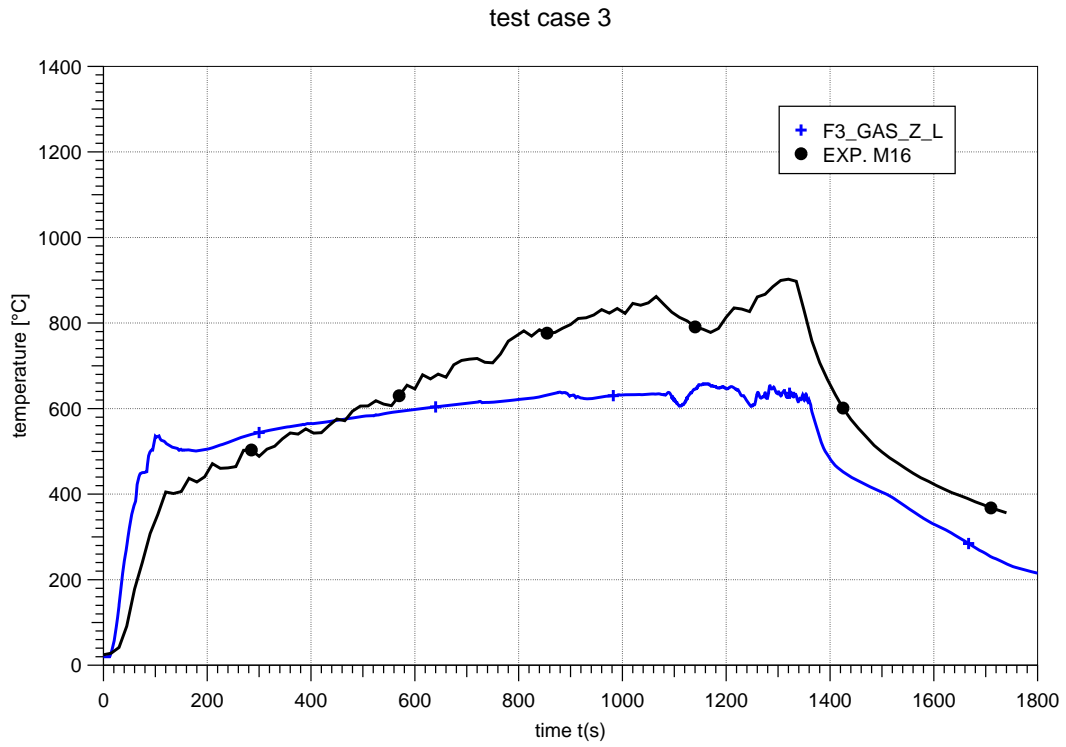


Fig. H3-16 Test 3: Temperature inside fire compartment (level 3, at M16)

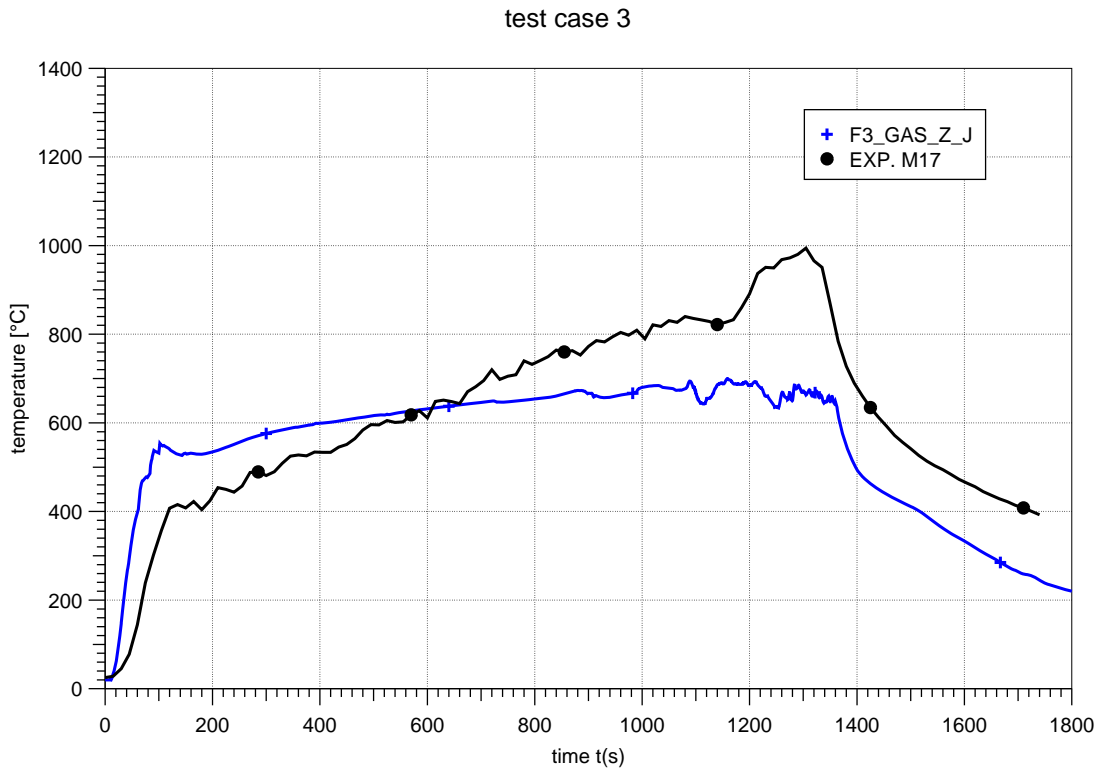


Fig. H3-17 Test 3: Temperature inside fire compartment (level 3, at M17)

test case 3

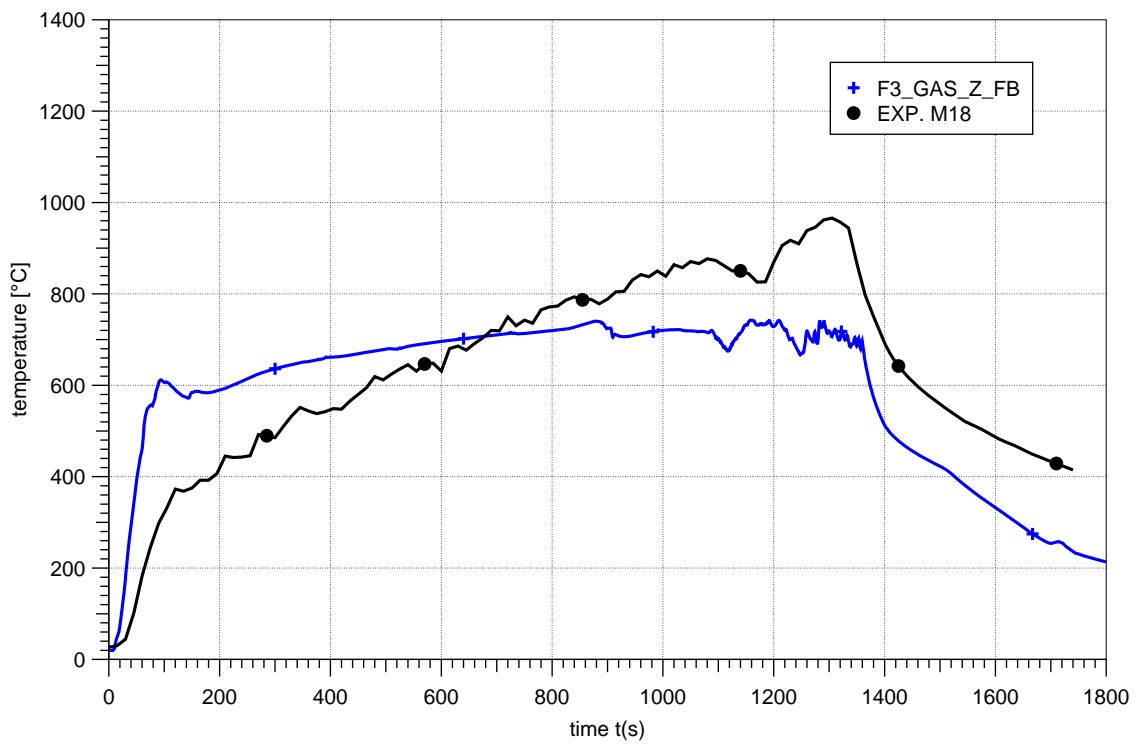


Fig. H3-18 Test 3: Temperature inside fire compartment (level 3, at M18)

test case 3

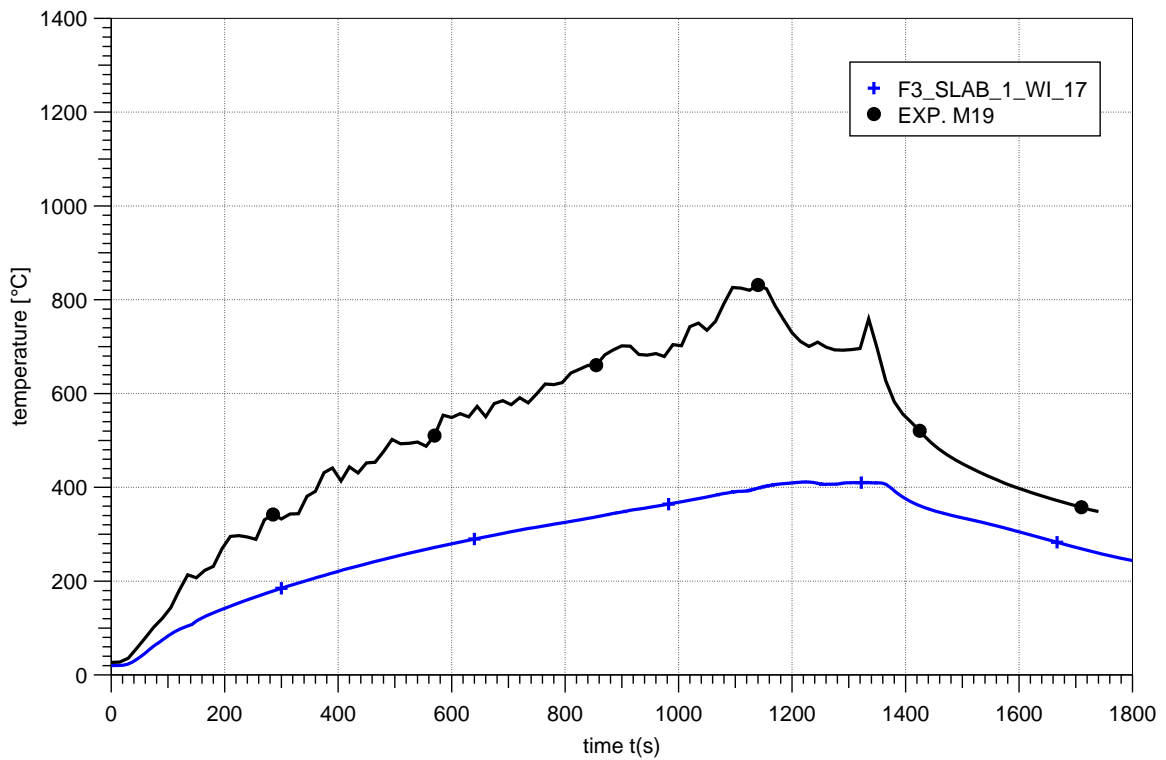


Fig.H 3-19 Test 3: Surface temperature (M19)

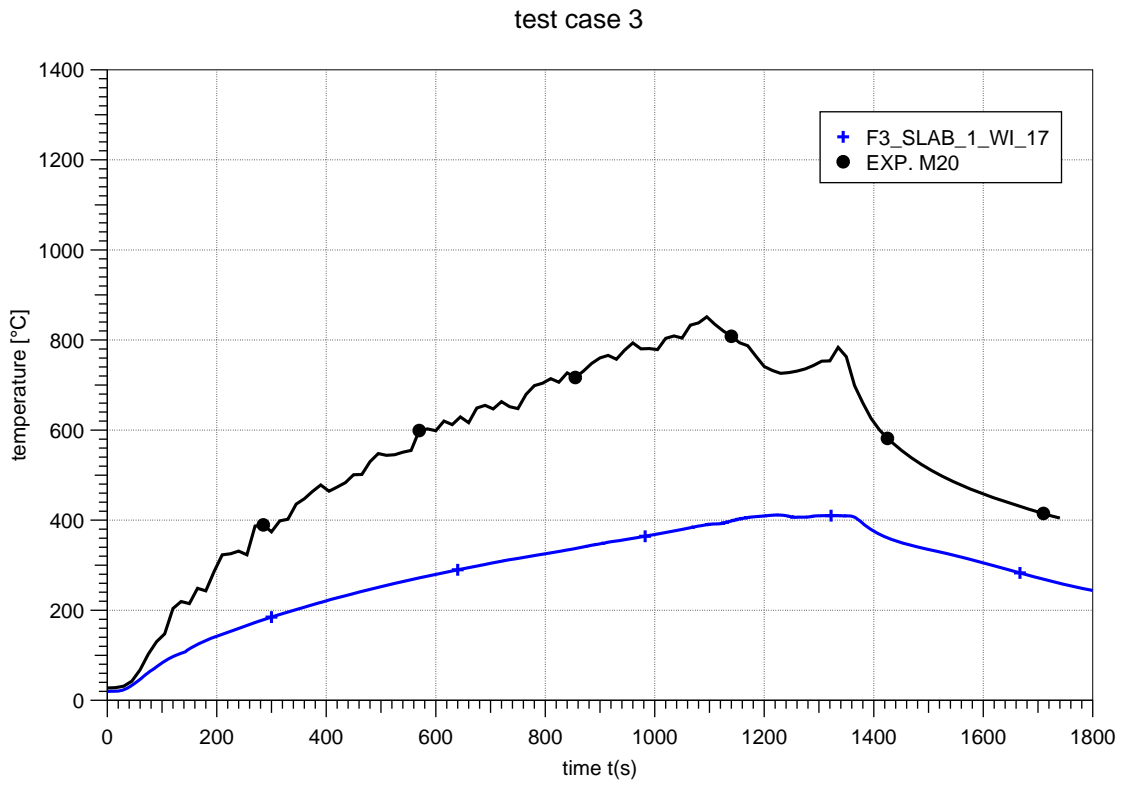


Fig. H3-20 Test 3: Surface temperature (M20)

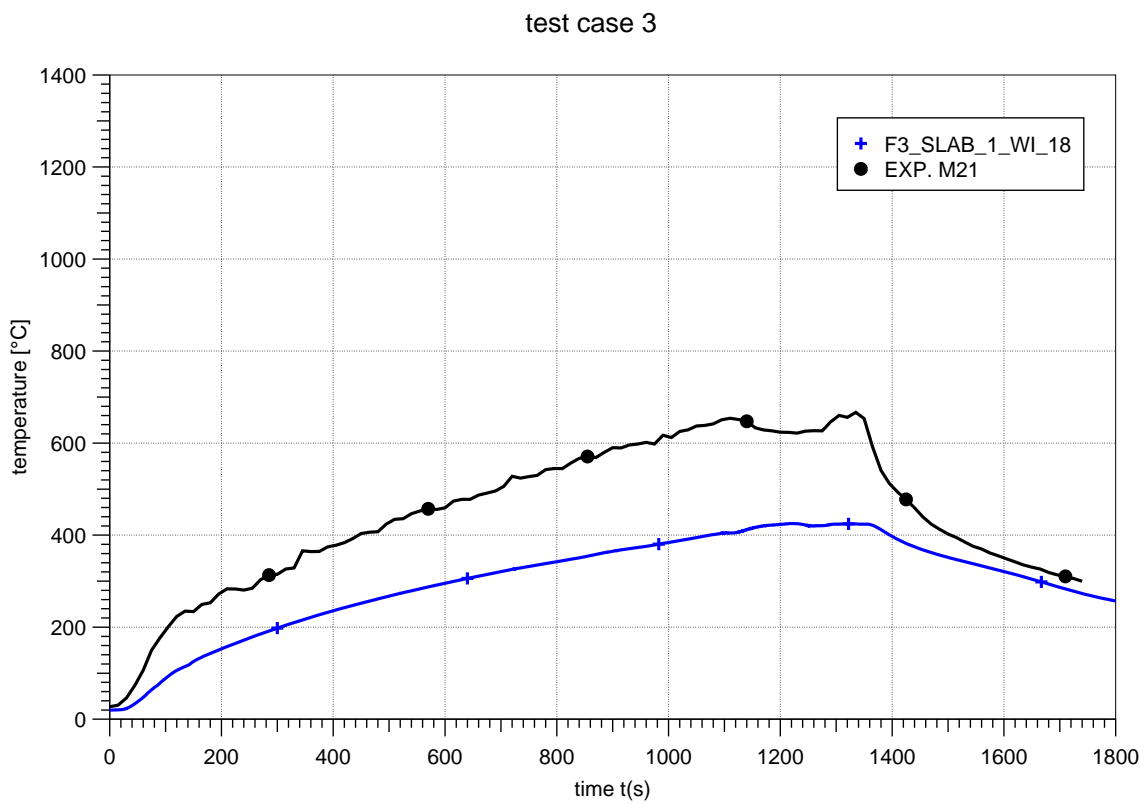


Fig. H3-21 Test 3: Surface temperature (M21)

test case 3

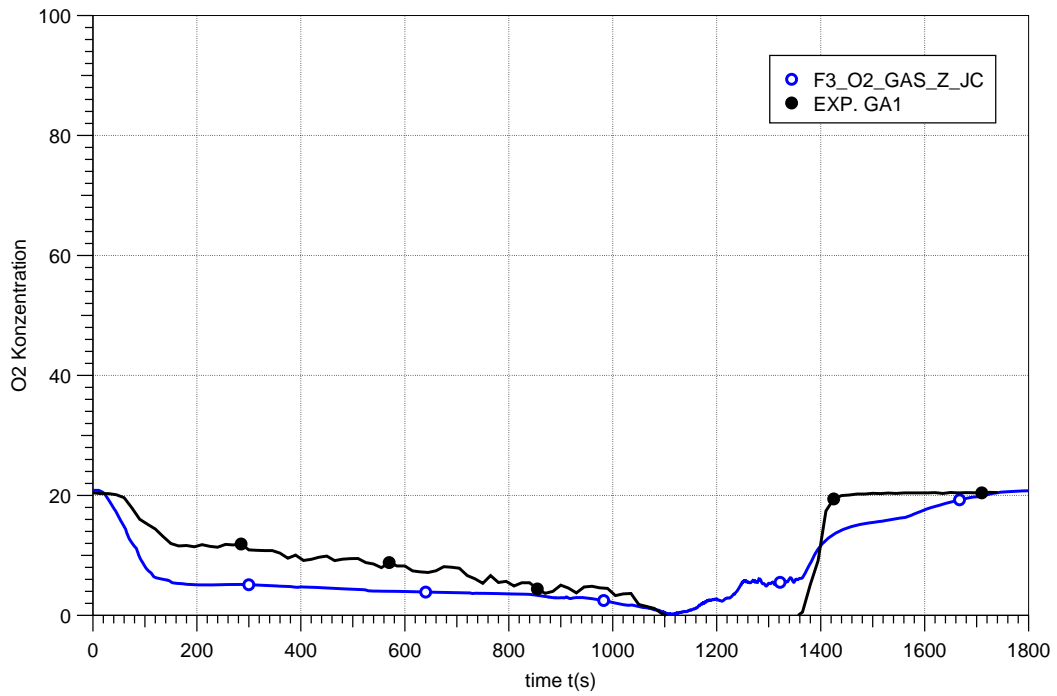


Fig. H3-22 Test 3: O₂ concentrations at the measurement point GA1

test case 3

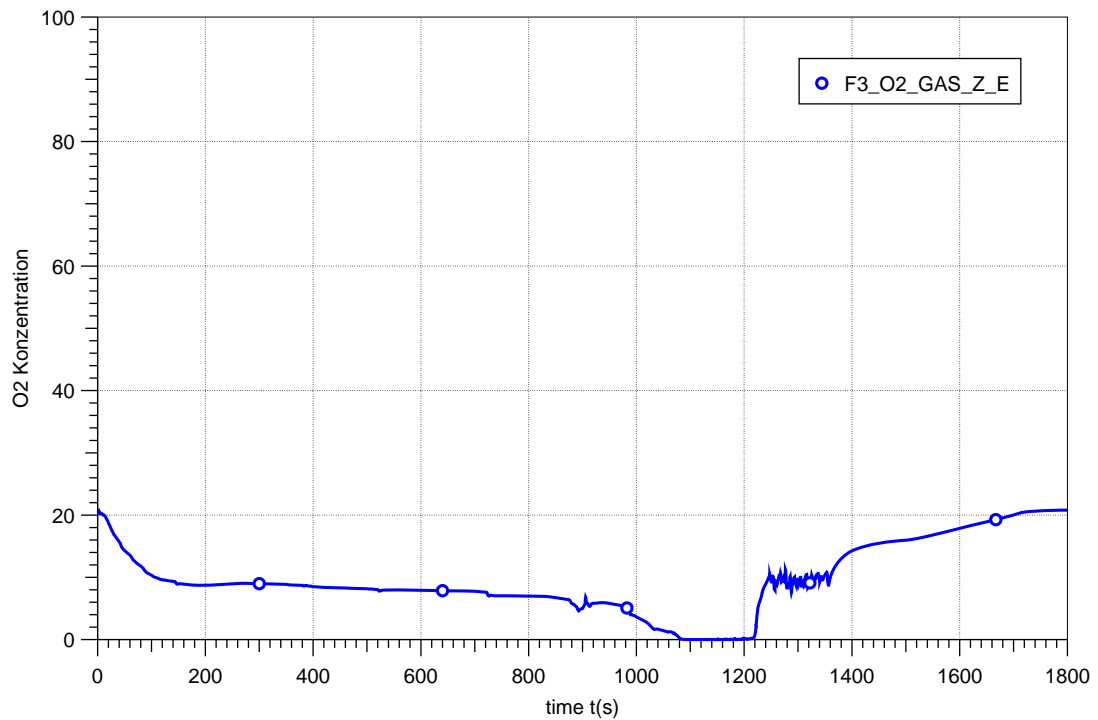


Fig. H3-23 Test 3: O₂ concentrations in the COCOSYS zone above the fuel surface

test case 3

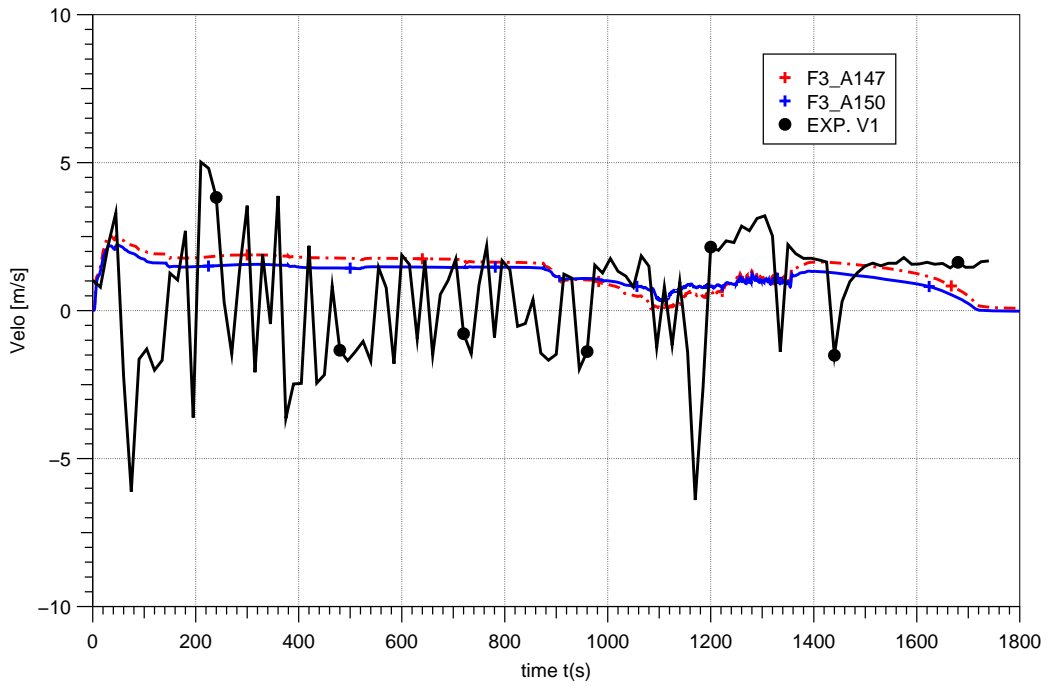


Fig. H3-24 Test3: Plume velocity at position V1

test case 3

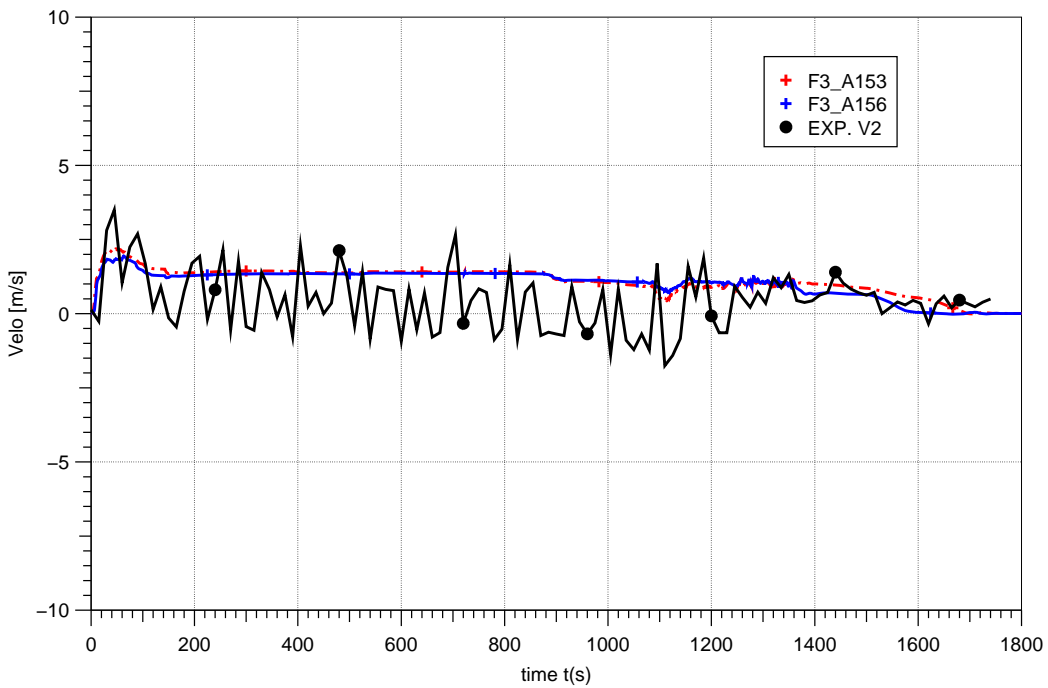


Fig. H3-25 Test3: Plume velocity at position V2

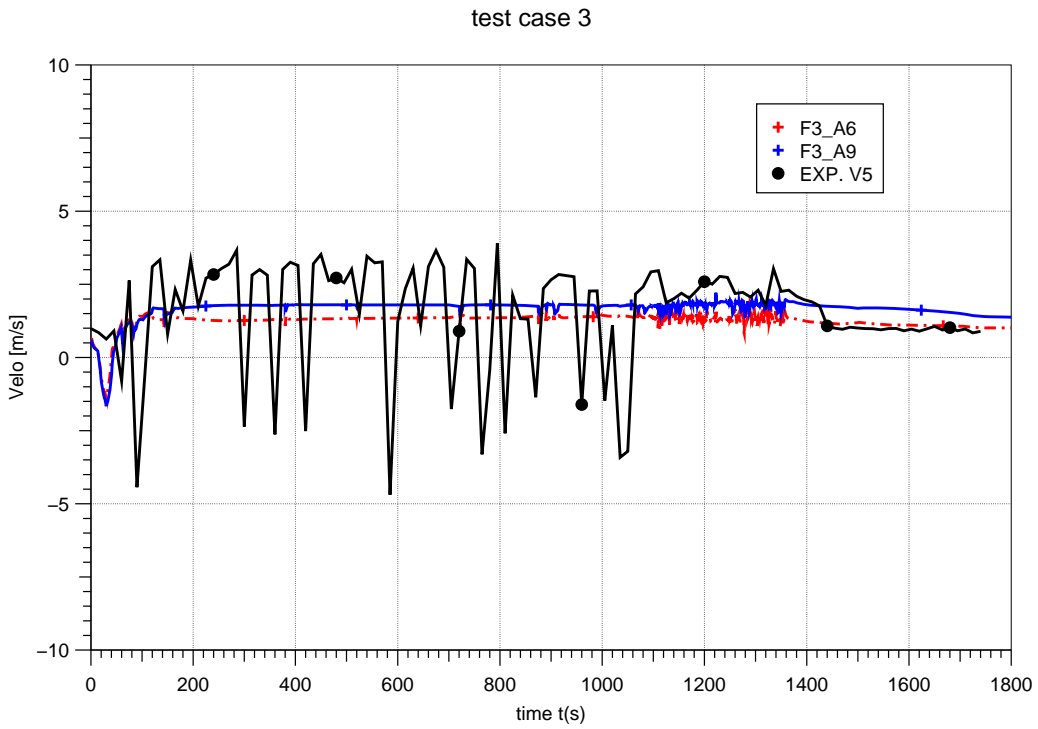


Fig. H3-26 Test3: Velocity at door position V5

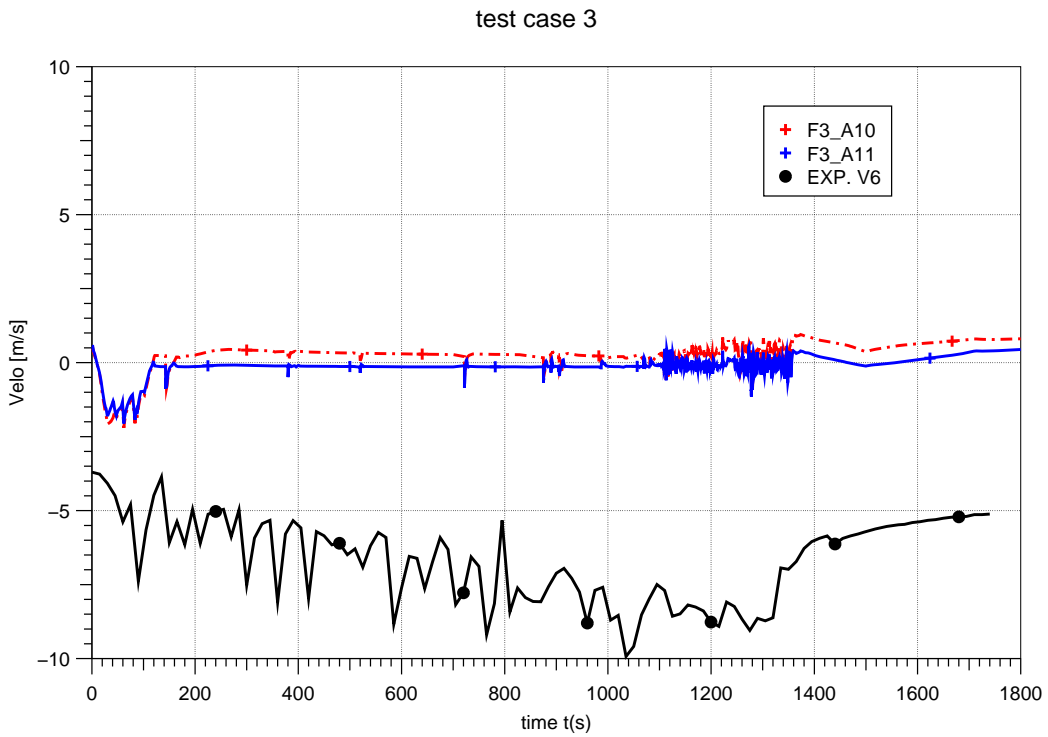


Fig. H3-27 Test3: Velocity at door position V6

test case 3

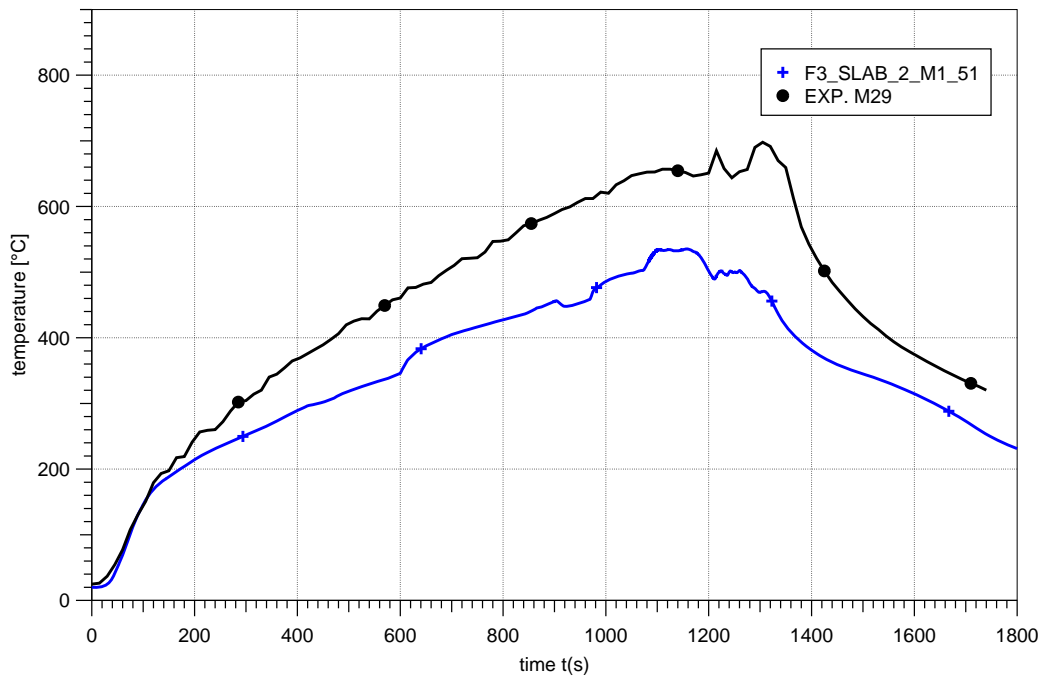


Fig. H3-28 Test 3: Temperature inside aerated concrete probe (M29, 0.02 m)

test case 3

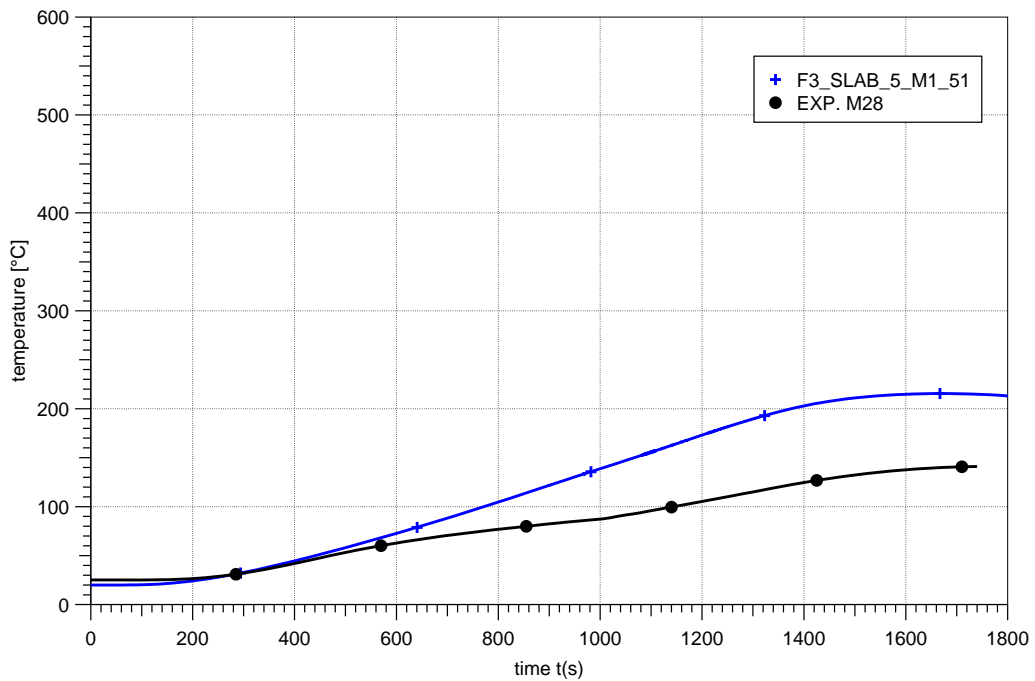


Fig. H3-29 Test 3: Temperature inside aerated concrete probe (M28, 0.05 m)

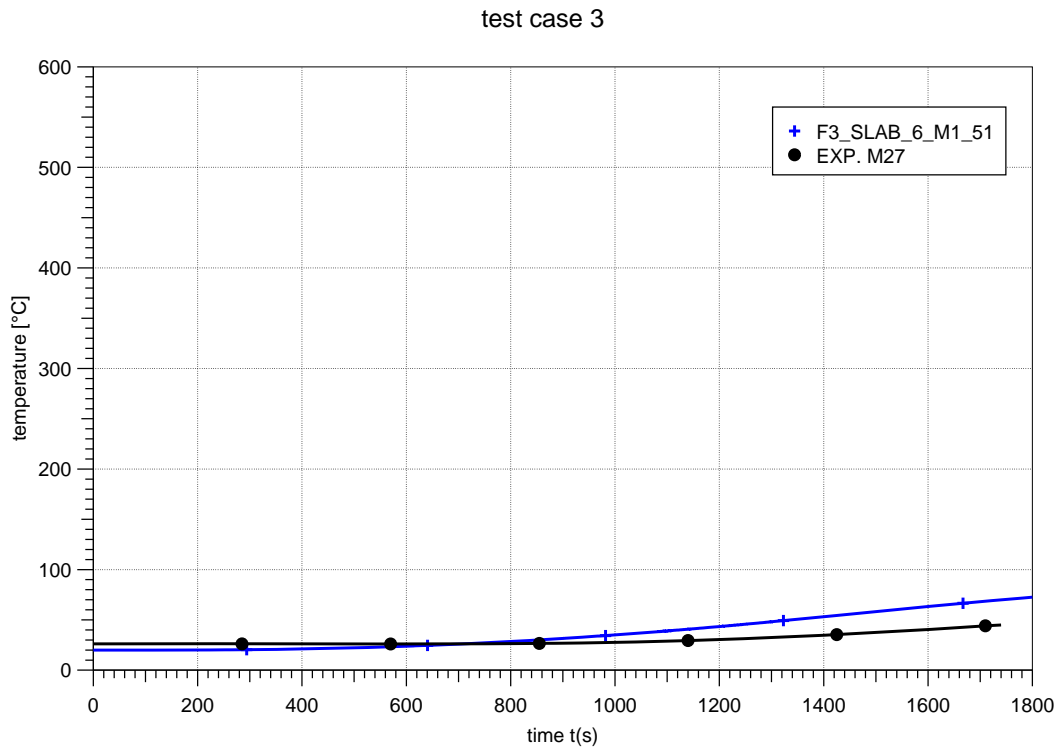


Fig. H3-30 Test 3: Temperature inside aerated concrete probe (M27, 0.08 m)

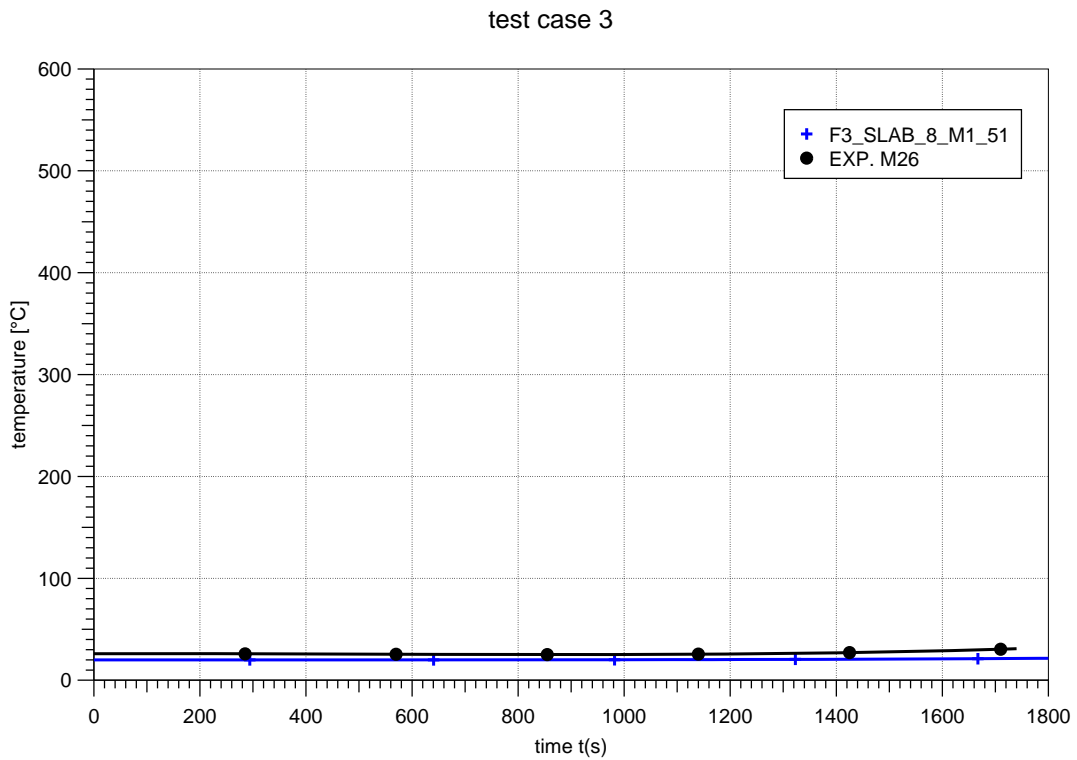


Fig. H3-31 Test 3: Temperature inside aerated concrete probe (M26, 0.10 m)

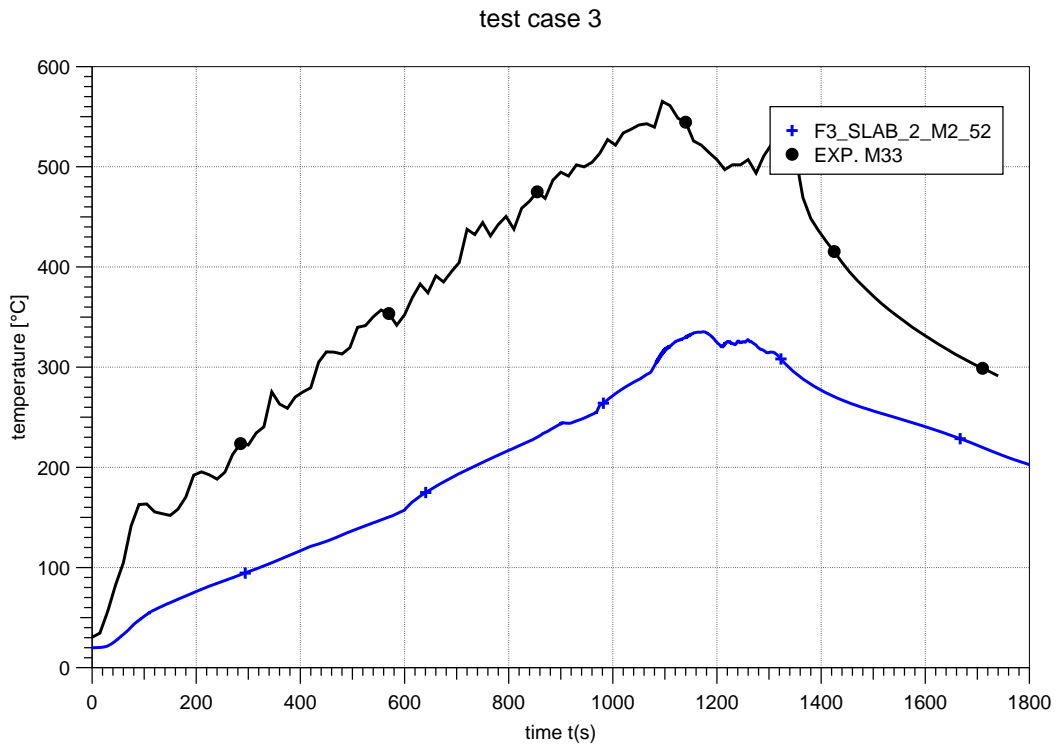


Fig. H3-32 Test 3: Temperature inside concrete probe (M33, 0.02 m)

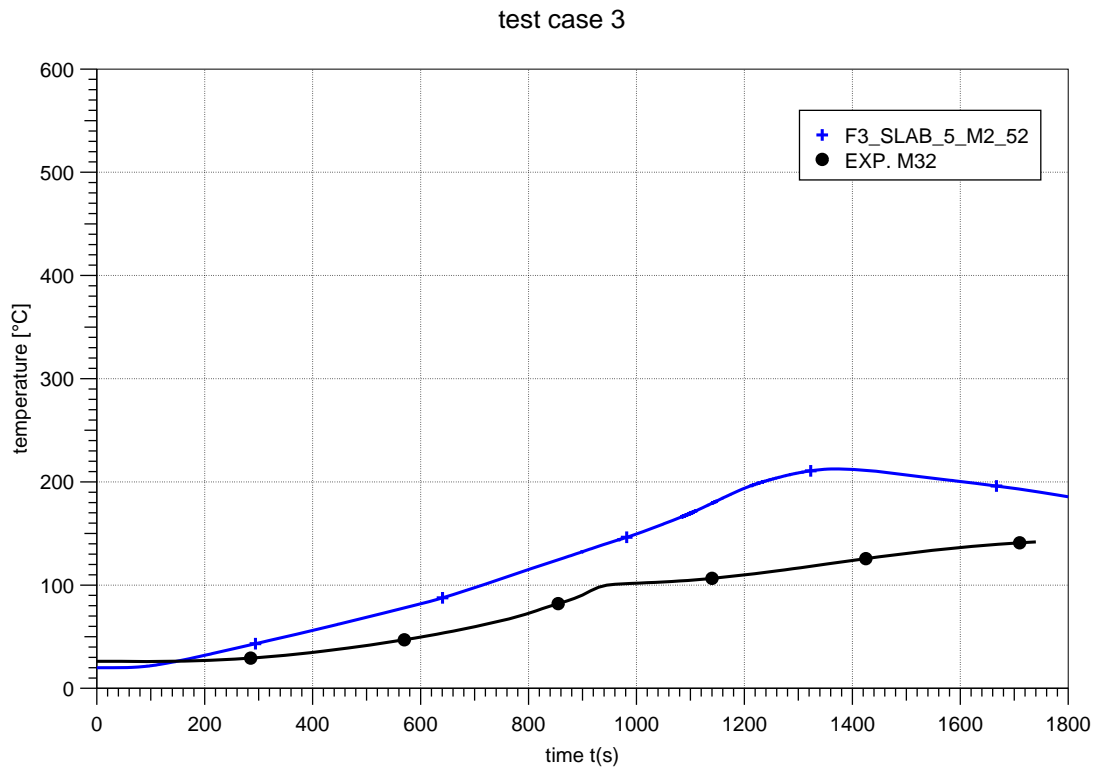


Fig. H3-33 Test 3: Temperature inside concrete probe (M32, 0.05 m)

test case 3

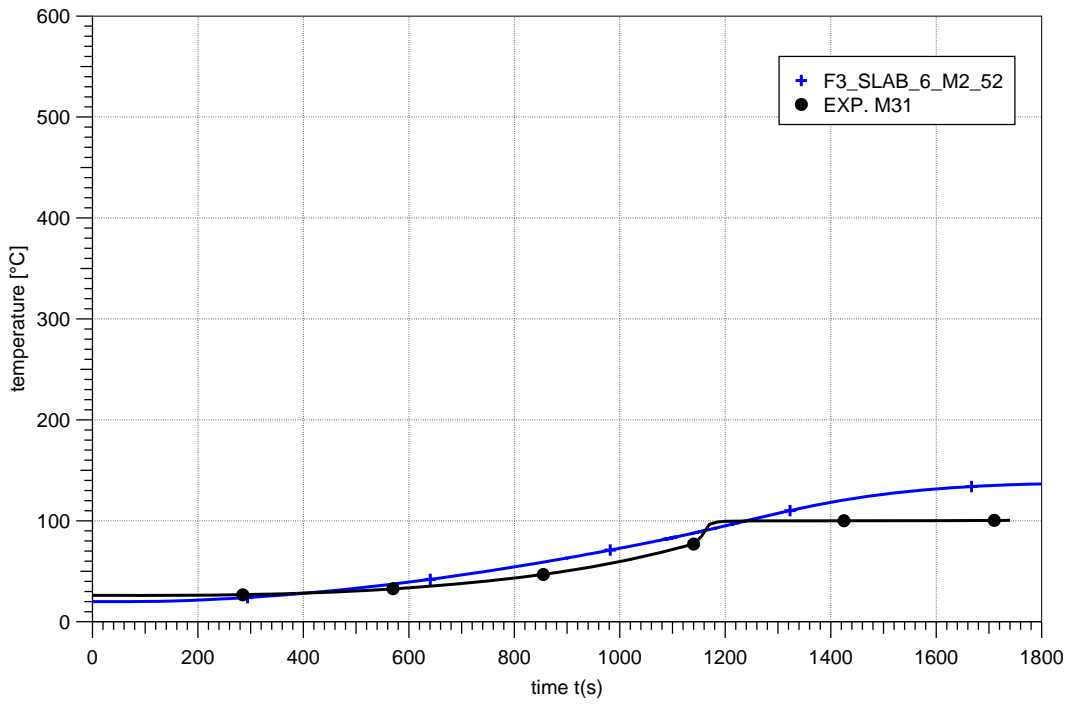


Fig. H3-34 Test 3: Temperature inside concrete probe (M31, 0.08 m)

test case 3

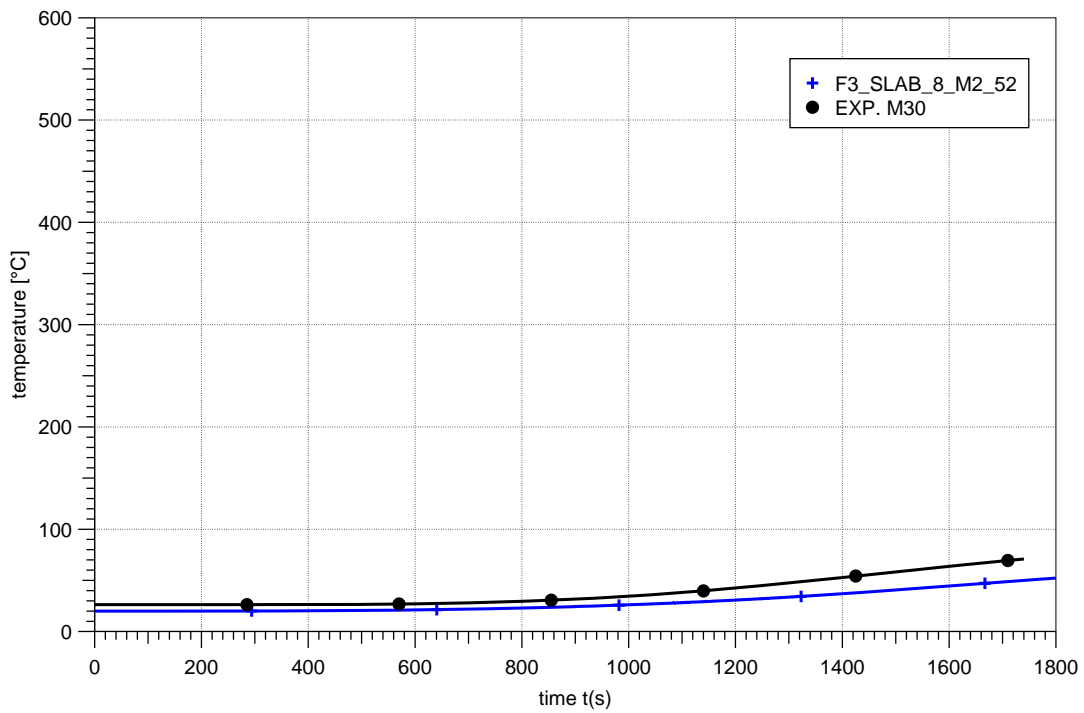


Fig. H3-35 Test 3: Temperature inside concrete probe (M30, 0.10 m)

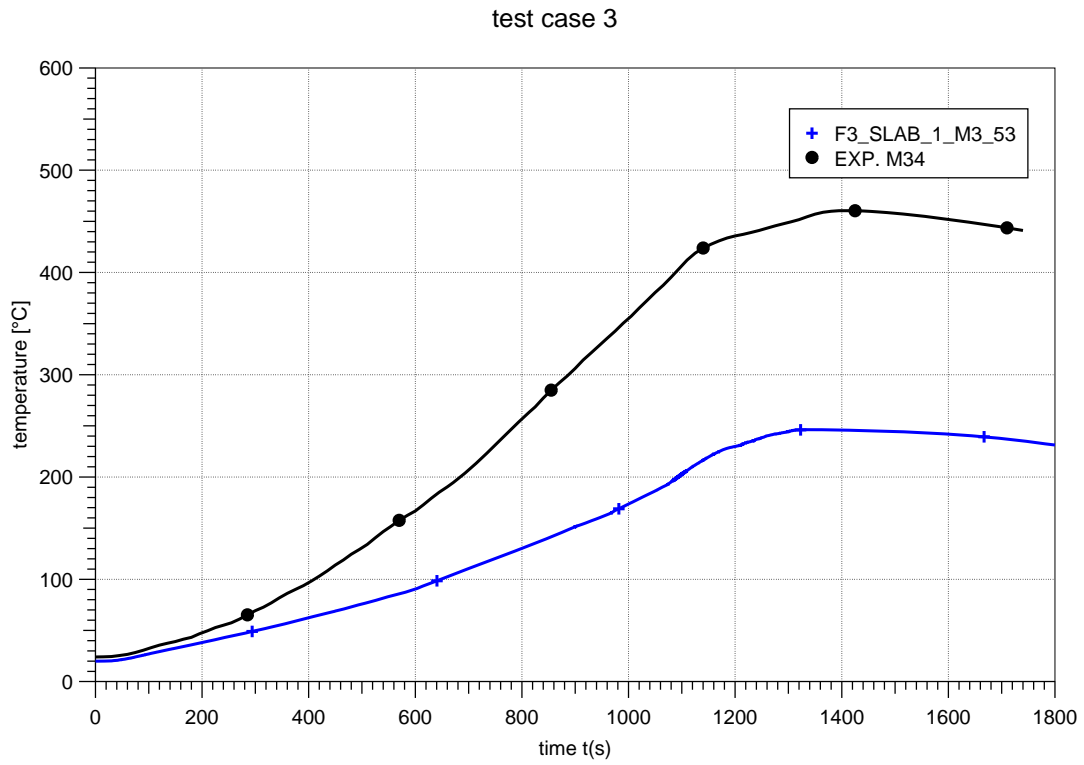


Fig. H3-36 Test 3: Temperature inside steel probe (M34, $x = 0.0$ m)

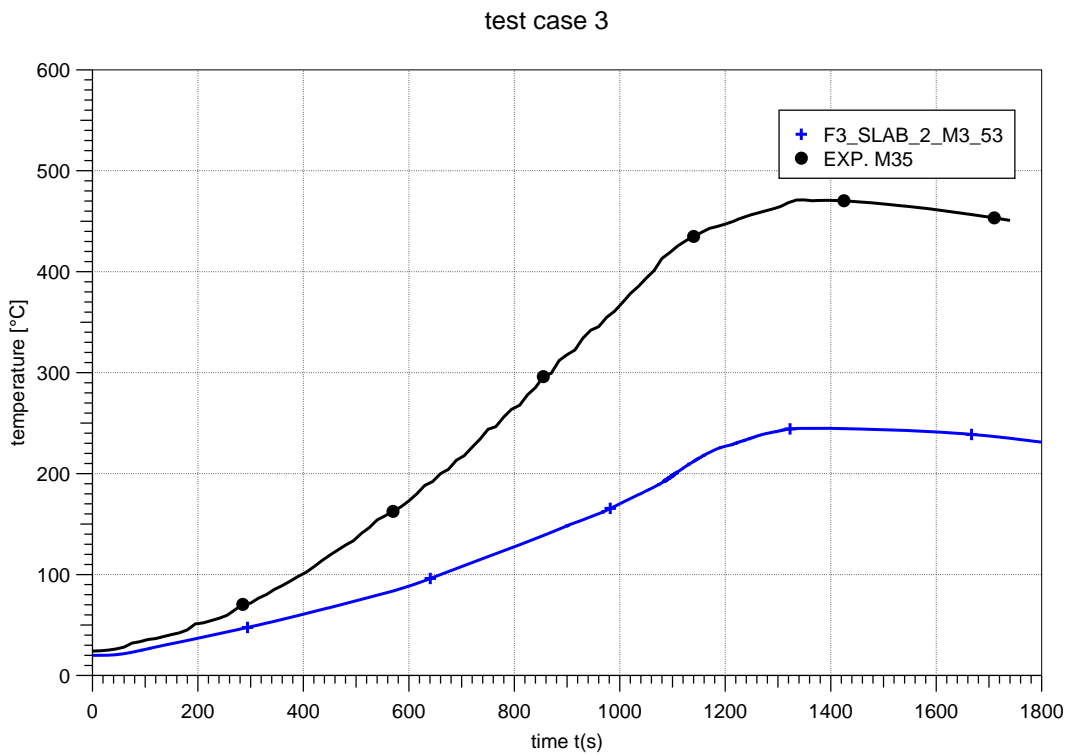


Fig. H3-37 Test 3: Temperature inside steel probe (M35, $x = 0.02$ m)

H4 Simulation of Test 3 with a Modified Pyrolysis Rate

The simulation of Test 3 points out that the pyrolysis rate is a very sensitive parameter in the calculation. Due to the high pyrolysis rate more O_2 is burned in the lowest zone than new fresh air is transported to this zone after 900 s. The flame extinguishes and even less O_2 reaches this zone due to the modified flow field. The aim of this calculation is to investigate, if better results can be received, if the pyrolysis rate is reduced in order to prevent the extinction of the flame.

For the first 900 s the measured fuel weight seems to be realistic, thus the pyrolysis rate does not need to be changed for this period. The measured temperatures show that the combustion process is nearly finished after 1300 s. Hence, the pyrolysis rate has to be very low during this period. With these boundary conditions it was not possible to find a realistic pyrolysis rate, which does not extinguish the flame and which integrally leads to the total mass burned in the experiment. The total mass of the burned fuel is an item, which can be measured with a small error, even if problems with the adjustment of weight occur during the experiment. Thus, it is problematic not to use the measured value in the simulation. Therefore, this calculation is not used as a result of Benchmark Exercise No. 4. Nevertheless, the simulation may provide a better understanding of the problems in the simulation in Section H3.

In addition to an error in the simulation of the mass flow between the zones leading to an under-estimation of the O_2 concentration in the lower zones, there might be also a problem with the chemical mechanism. For oxygen rich conditions, the assumption that all fuel is oxidized to CO and later, if possible, to CO_2 is not sufficient. In fact, a lot of soot is produced. The soot production will influence the oxygen removed during the combustion in a zone. In addition, the heat release will be different and soot can absorb radiation. All this will affect the temperature and due to buoyancy the gas velocity as well.

The nodalization is the same as it was in first simulation (see Section H3). The boundary conditions are the same for the first 900 s. Therefore, in the discussion only the later phase will be taken into account.

With the reduced pyrolysis rate, no flame extinguishing occurs in the zones near the fuel surface. Thus, the temperature of this simulation is higher than in that with the original pyrolysis rate. It could not be expected to predict the exact amplitude and

shape of the temperature profile for the time period from 1100 s to 1300 s. The predicted temperature is too low, which is reasonable considering the smaller pyrolysis rate.

With the modified pyrolysis rate the temperature stratification is not satisfactorily predicted. At a lower elevation, the temperature is still under-predicted in the simulation and the temperature increase for the first 100 to 200 s is over-estimated.

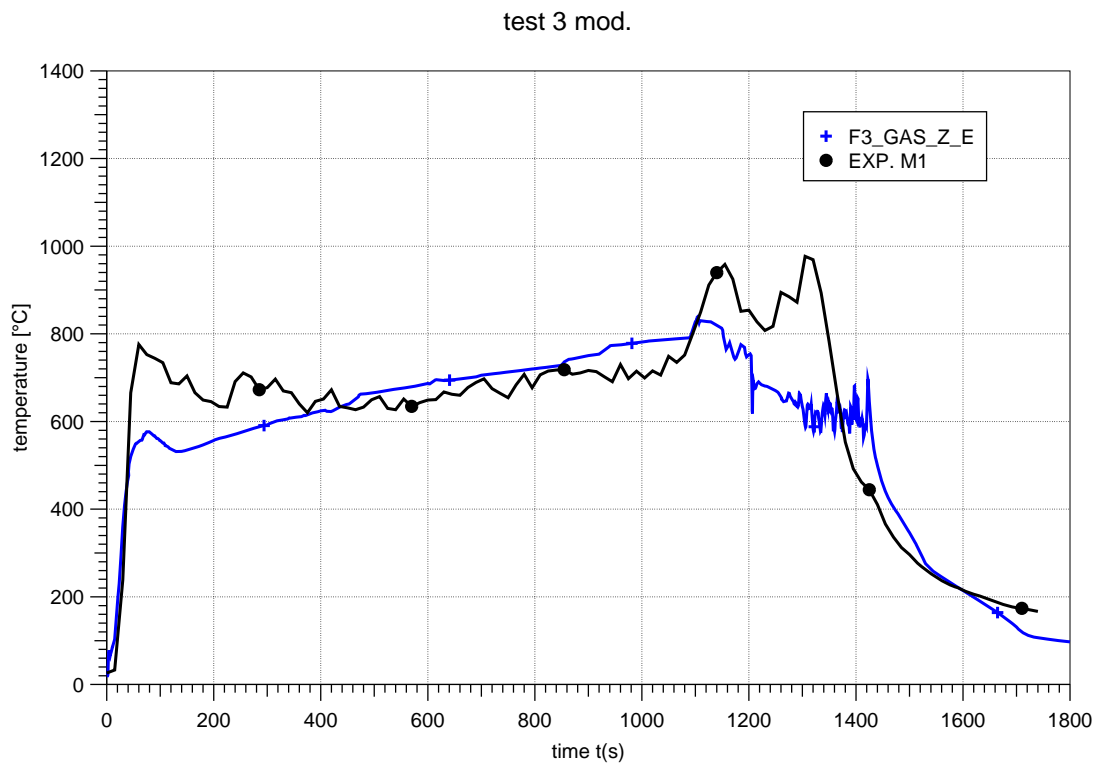


Fig. 4-1 Test 3 mod: Plume temperature at M1

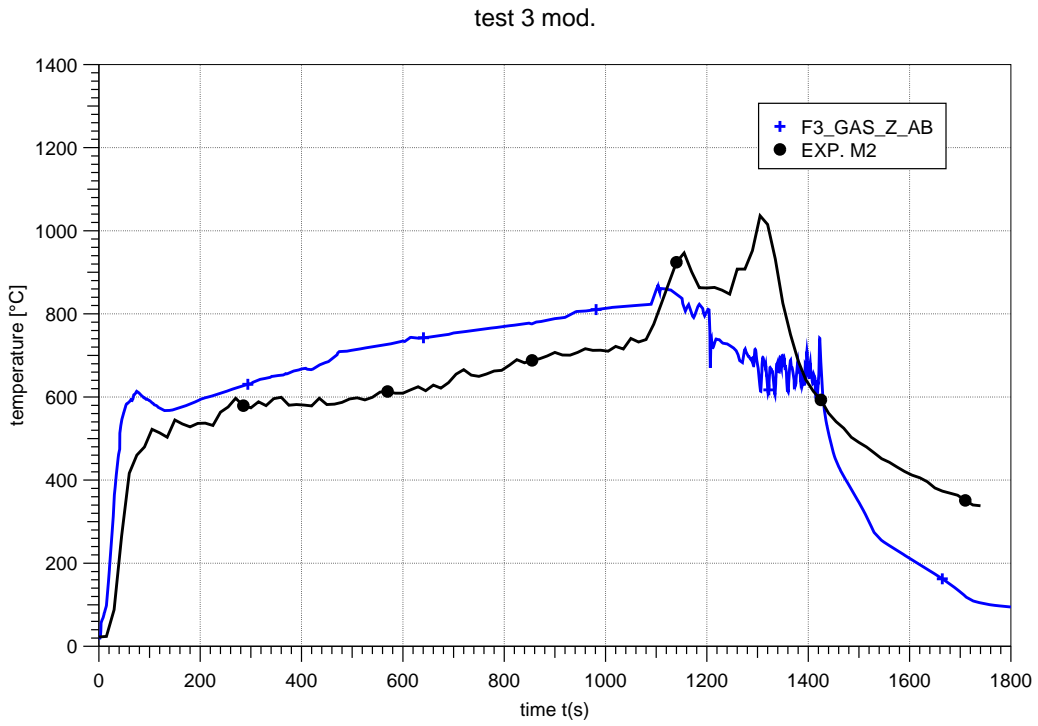


Fig. H4-2 Test 3 mod: Plume temperature at M2

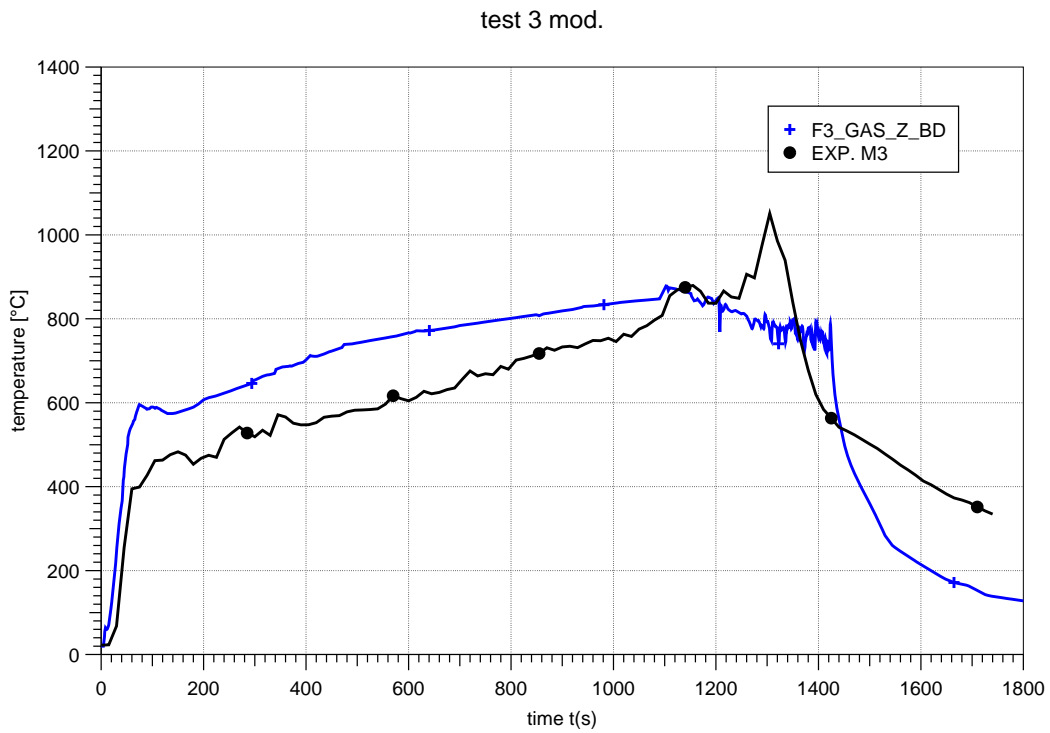


Fig. 4-3 Test 3 mod: Plume temperature at M3

test 3 mod.

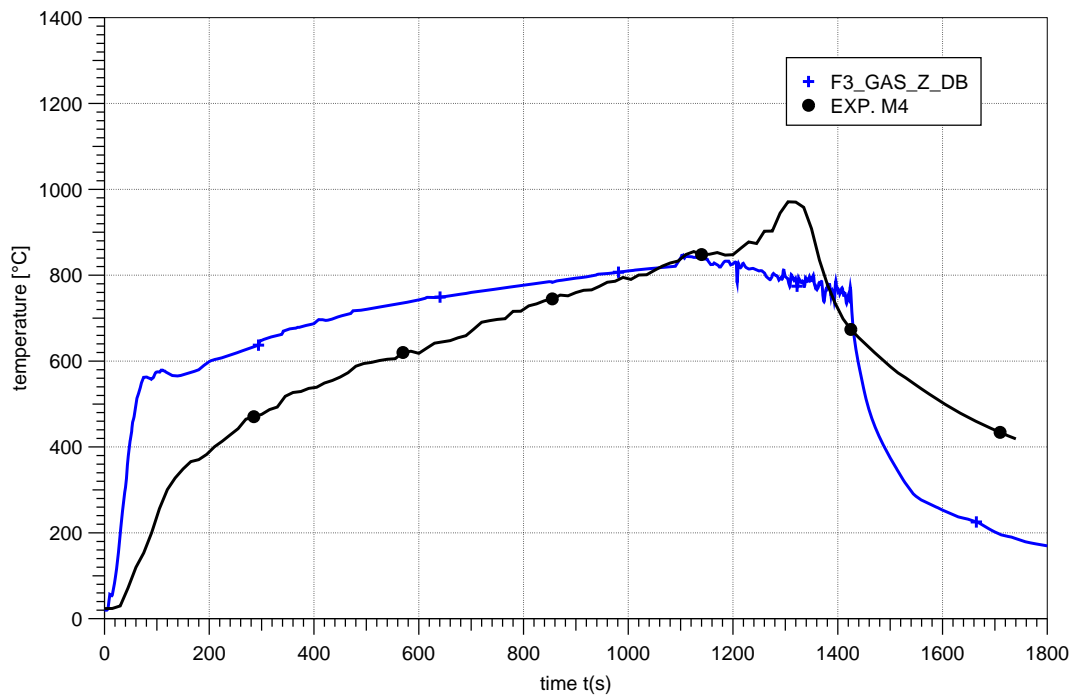


Fig. 4-4 Test 3 mod: Plume temperature at M4

test 3 mod.

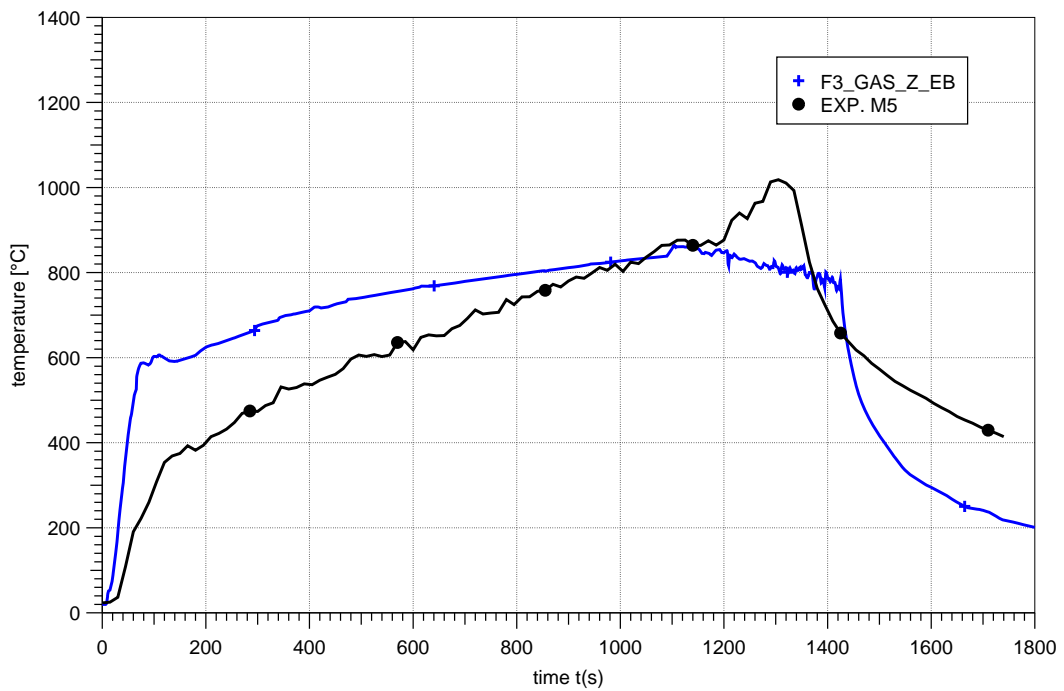


Fig. 4-5 Test 3 mod: Plume temperature at M5

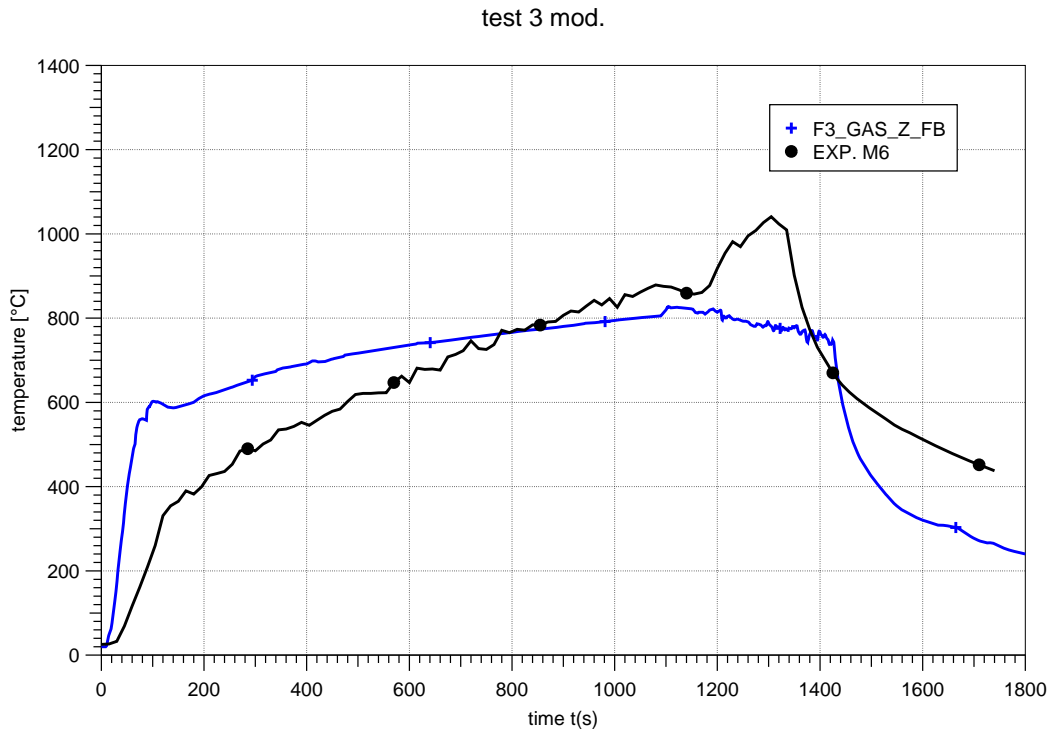


Fig. H4-6 Test 3 mod: Plume temperature at M6

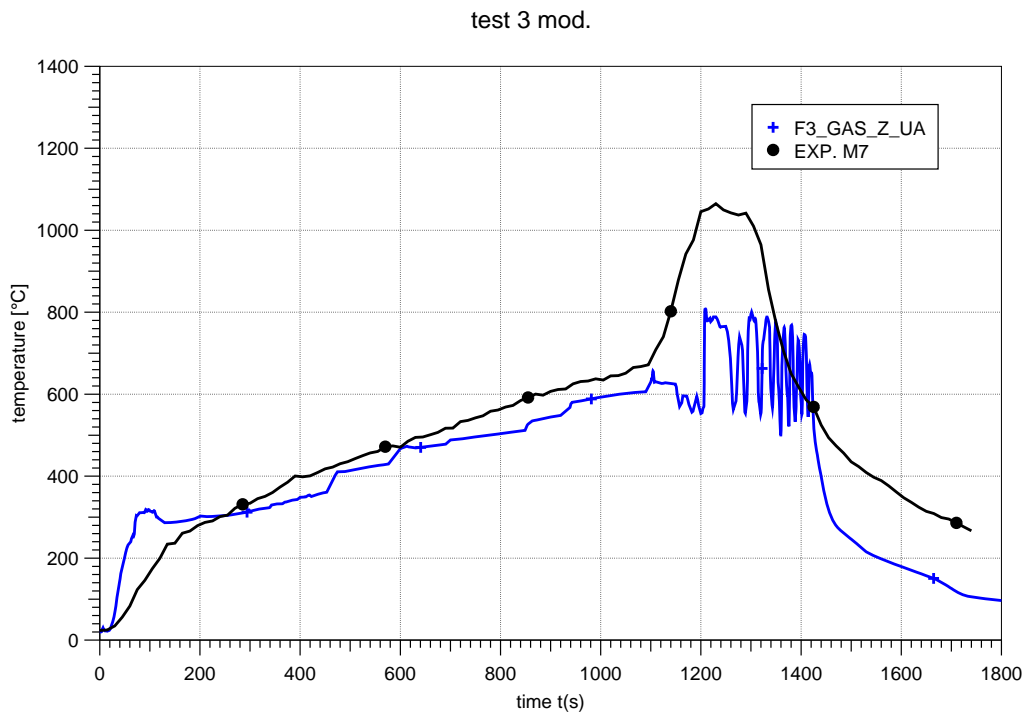


Fig. H4-7 Test 3 mod: Temperature inside fire compartment (level 1, at M7)

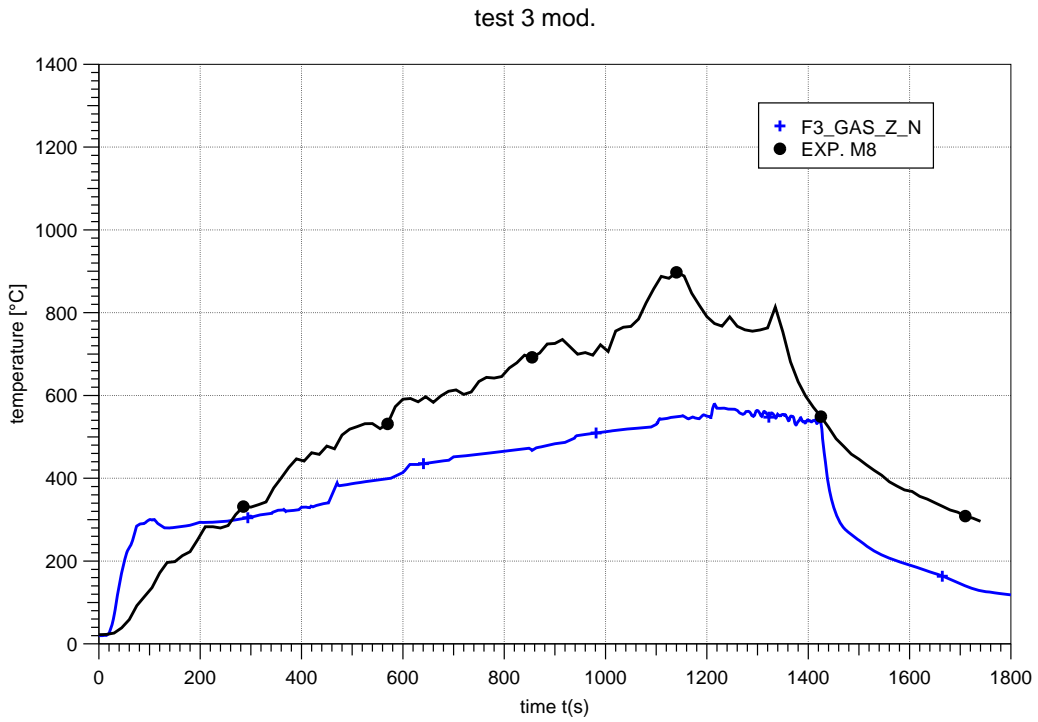


Fig. H4-8 Test 3 mod: Temperature inside fire compartment (level 1, at M8)

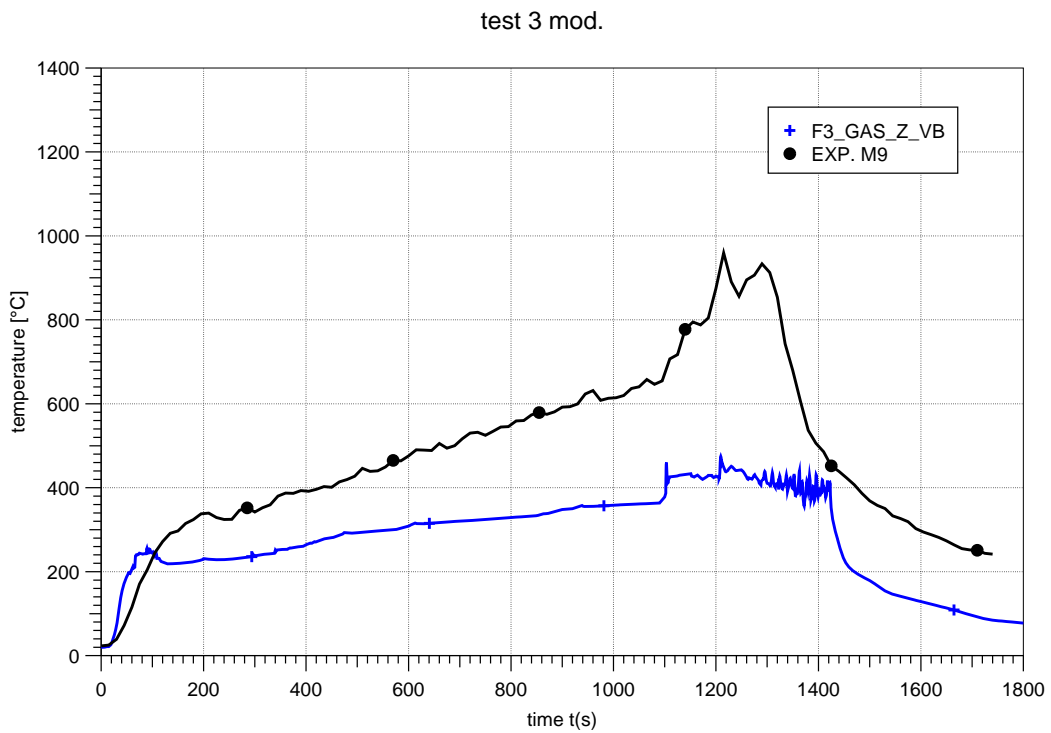


Fig. H4-9 Test 3 mod: Temperature inside fire compartment (level 1, at M9)

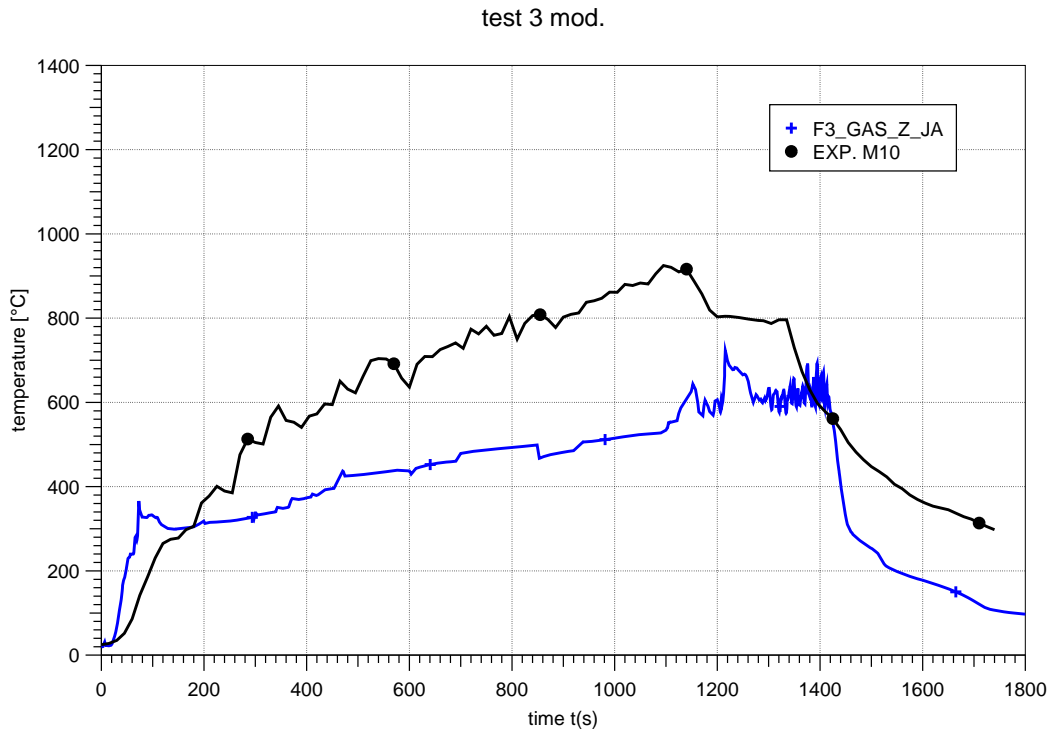


Fig. H4-10 Test 3 mod: Temperature inside fire compartment (level 1, at M10)

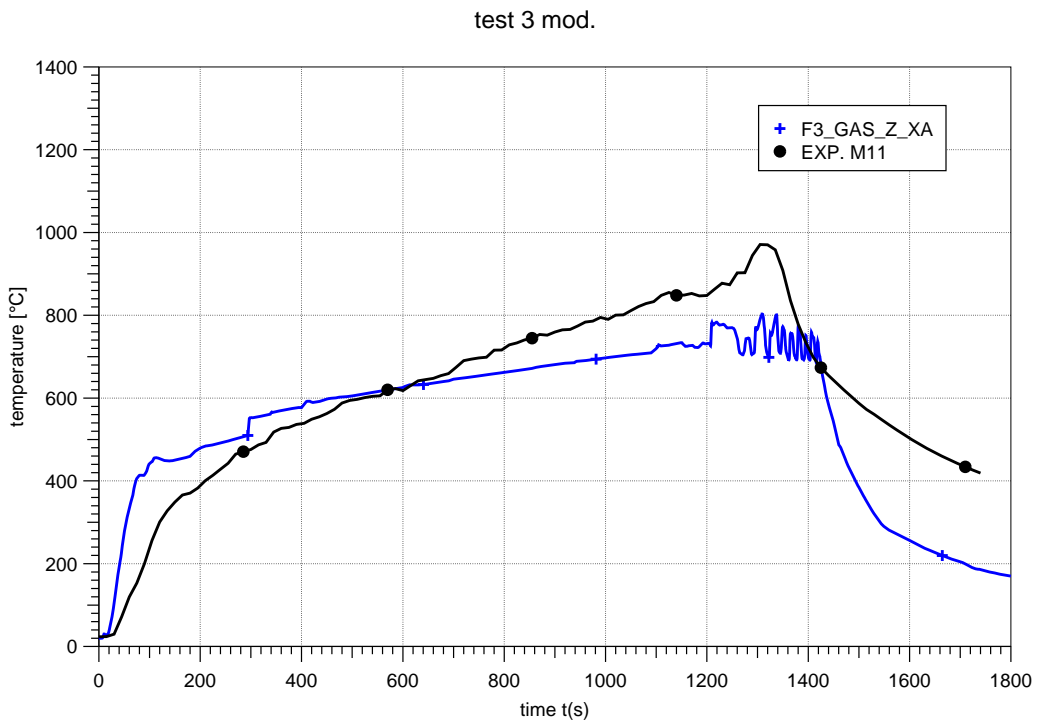


Fig. H4-11 Test 3 mod: Temperature inside fire compartment (level 2, at M11)

test 3 mod.

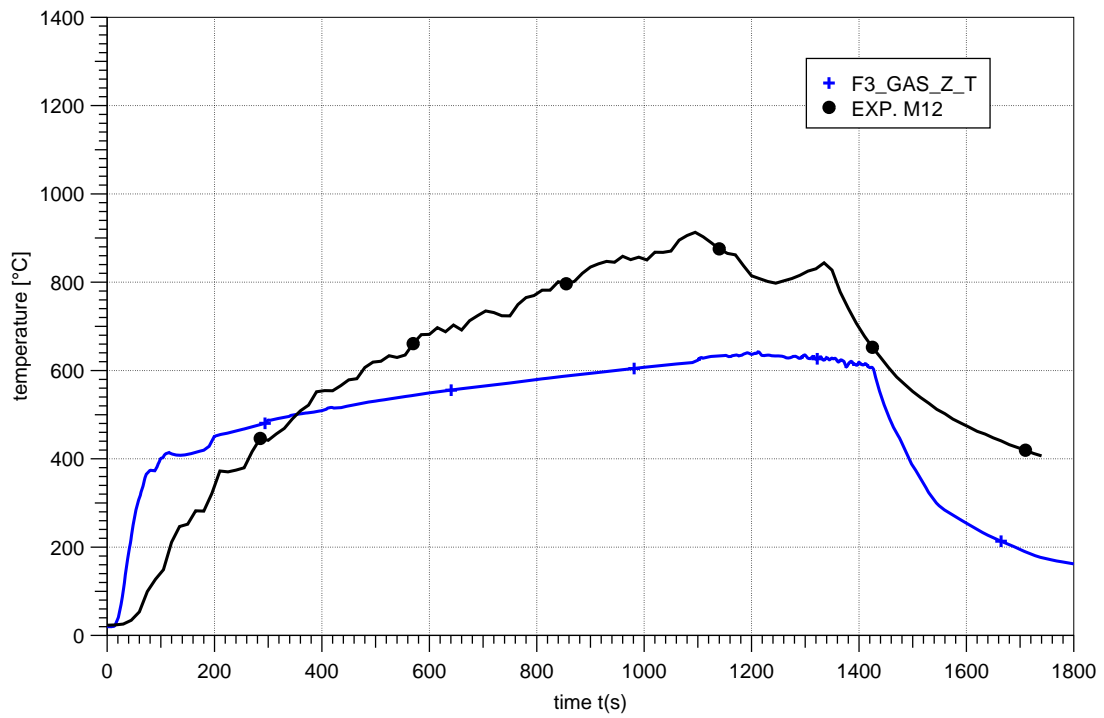


Fig. H4-12 Test 3 mod: Temperature inside fire compartment (level 2, at M12)

test case 3

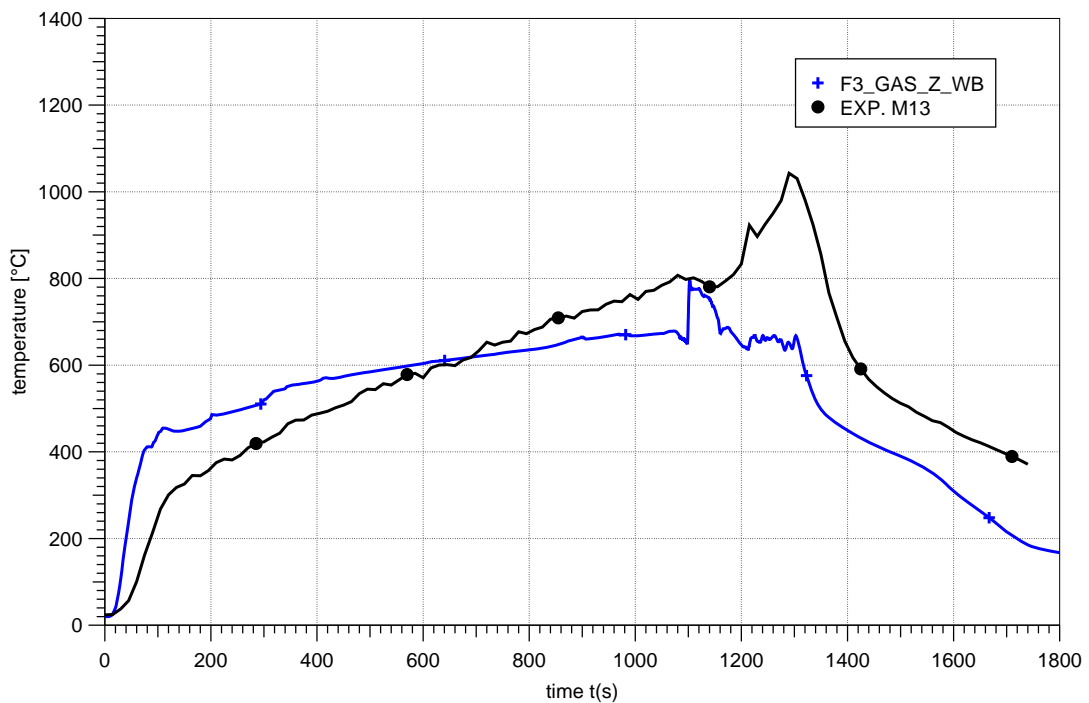


Fig. H4-13 Test 3 mod: Temperature inside fire compartment (level 2, at M13)

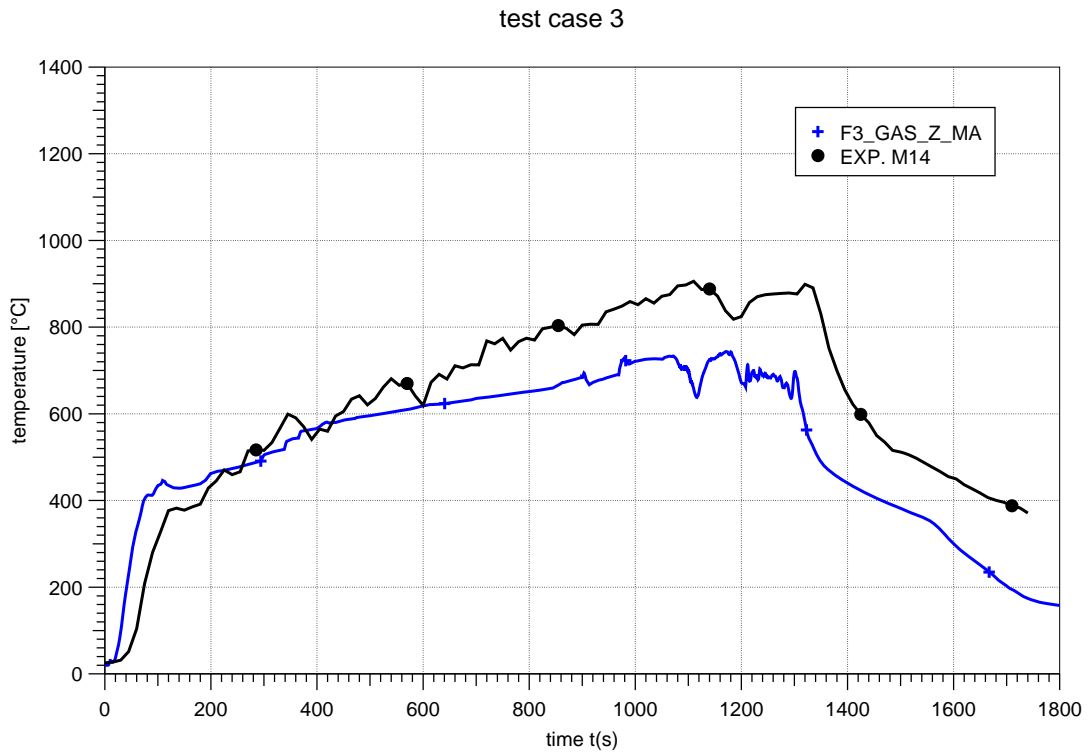


Fig. H4-14 Test 3 mod: Temperature inside fire compartment (level 2, at M14)

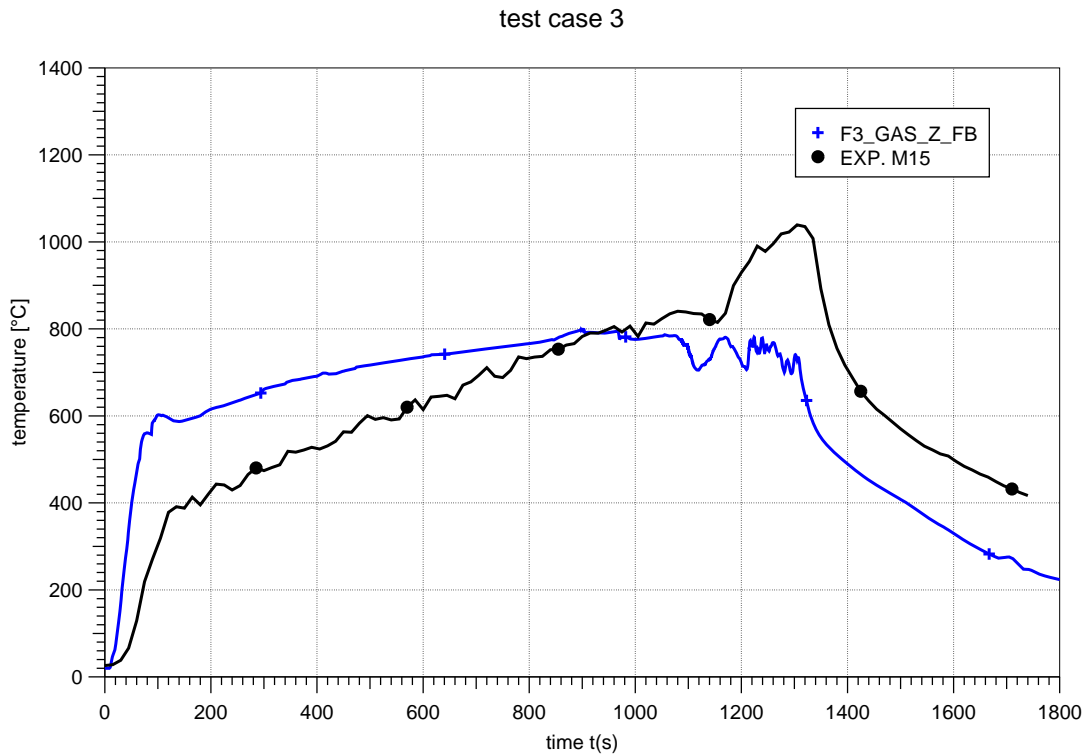


Fig. H4-15 Test 3 mod: Temperature inside fire compartment (level 3, at M15)

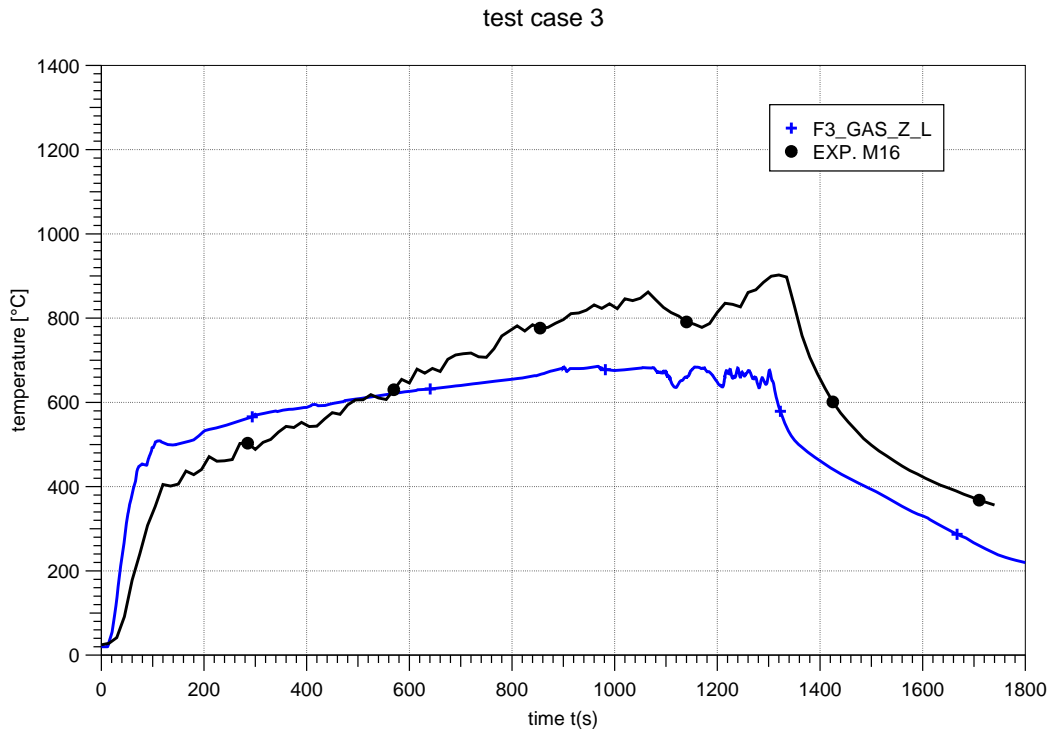


Fig. H4-16 Test 3 mod: Temperature inside fire compartment (level 3, at M16)

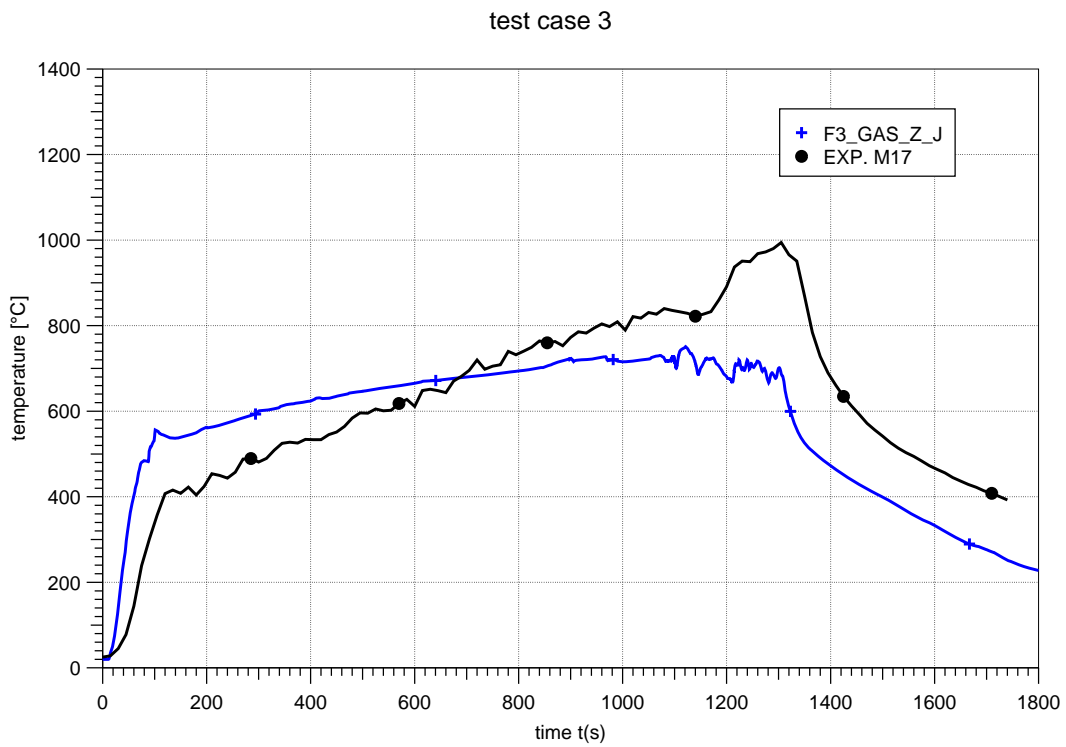


Fig. H4-17 Test 3 mod: Temperature inside fire compartment (level 3, at M17)

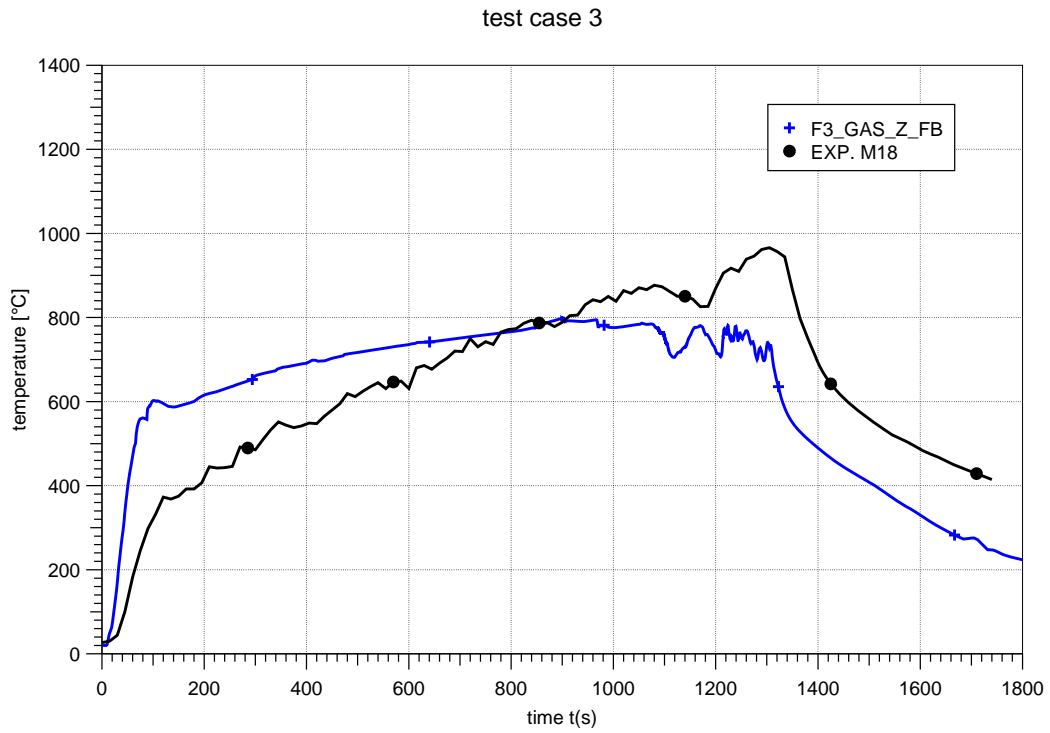


Fig. H4-18 Test 3 mod: Temperature inside fire compartment (level 3, at M18)

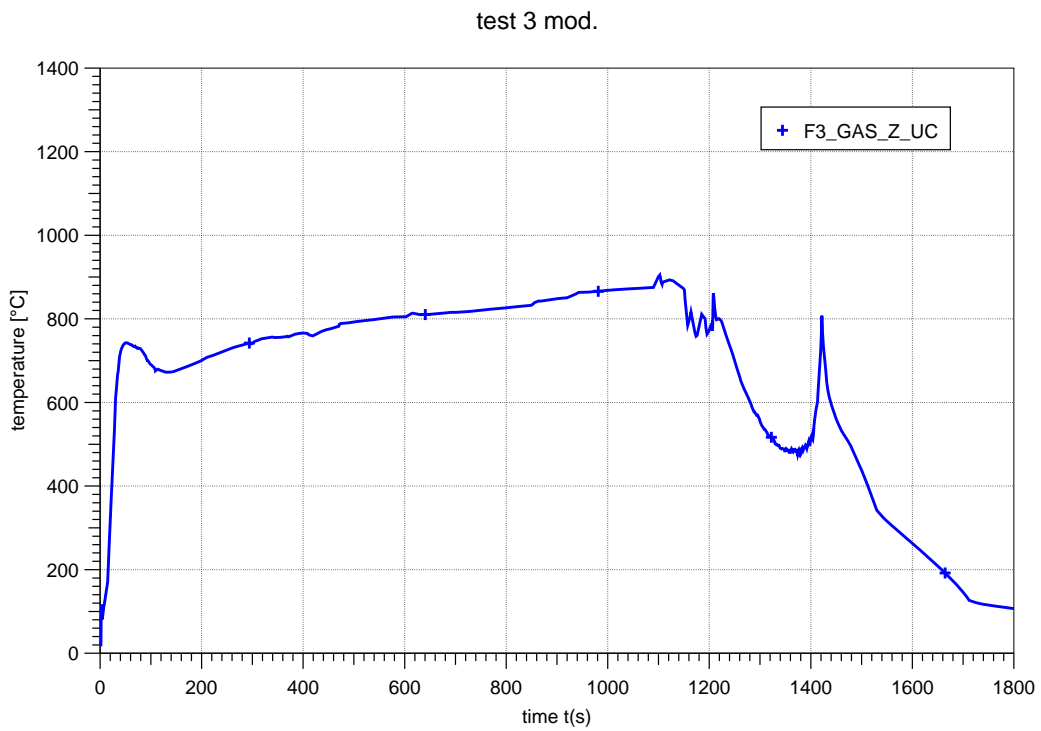


Fig. H4-19 Test 3 mod: O₂ concentrations in the COCOSYS zone above the fuel surface

test 3 mod.

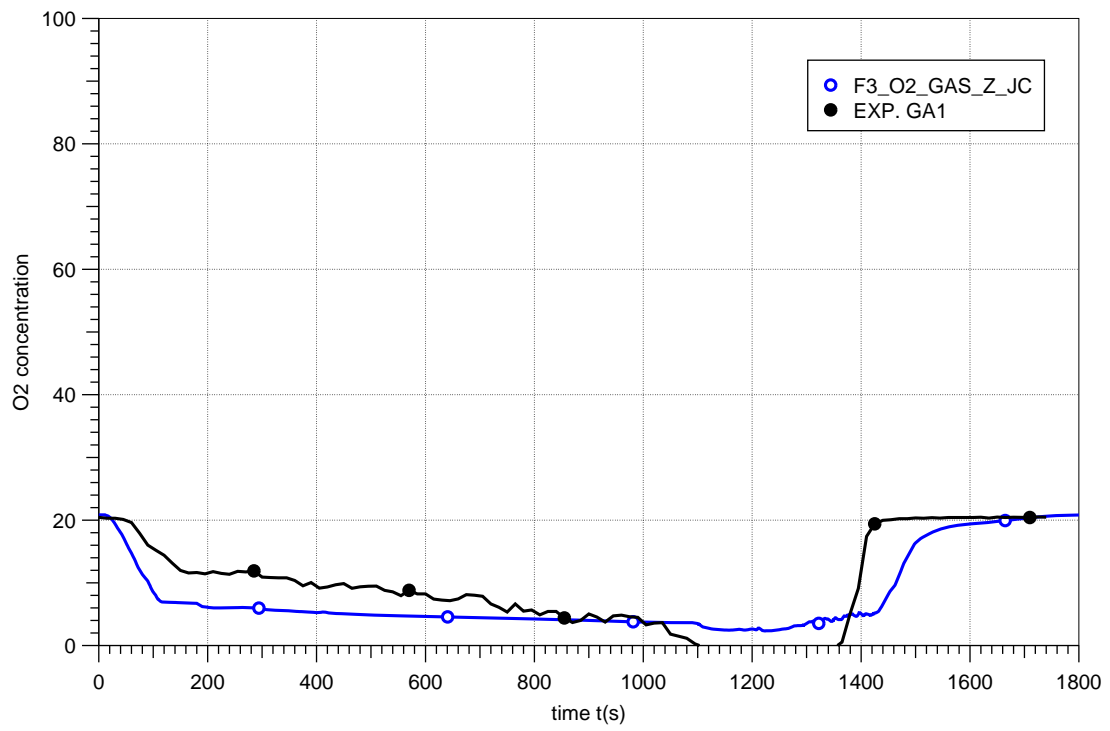


Fig. H4-20 Test 3 mod: O₂ concentrations at GA1

H5 Simulation of Test 1

H5.1 Geometry and pyrolysis rate

Using the same models as described in the previous chapters, the first experiment of Benchmark Exercise No. 4 was simulated by COCOSYS. The door in the first experiment is opened completely; it has a height of 3 m (0.6 - 3.6 m). This is the only change in the geometry. Other differences are the mass flows through the fans. Because of these changes, a different pyrolysis rate is determined by the measured fuel weight.

After approx. 850 s the weight measurement was defect and the pyrolysis rate has to be extrapolated (Fig. H2-2). This will cause additional uncertainties to the simulation, because the results are very sensitive to the pyrolysis rate as shown in Sections H3 and H4.

H5.2 Comparison between experiment and simulation

H5.2.1 Gas temperature

The plume temperature increases earlier as in the experiment at the measurement points (M1-M6, see Fig. H5-1). In the experiment it took about 180 s until a more rapid temperature increase was measured, while in the simulation this temperature increase is simulated at 100 s, predicting a less rapid increase.

After 200 s the temperature is over-predicted at all measurement points in the plume by 100 - 200 °C (M1-M6, Fig. H5-1 to Fig. H5-6). After 1350 s there is a rapid temperature decrease in the simulation, but in the simulation the temperature is growing until 1400 s and later the temperature decreases more slowly. An explanation for this is the pyrolysis rate assumed. The values were extrapolated. In Test 3 the pyrolysis rate did not become zero immediately, there were several hundreds of seconds with a small rate, maybe in Test 1 something similar happened. It is possible to change the assumed pyrolysis rate to overcome this problem, but due to the limited time and the large uncertainties in the value this change was not performed.

The temperature outside the hot plume is under-estimated at a low elevation (Fig. H5-7 to Fig. H5-10). For all measurement points M7-M10 ($z = 1.5$ m) the predicted temperature is several hundred degrees lower than in the experiment. At the measurement points at the level $z = 3.35$ m (M11-14) the temperature is more or less similar to that measured (Fig. H5-11 to Fig. H5-14). In this context, a second problem becomes obvious. In the experiment, the hot plume is not vertical. It is tilted to the wall at the opposite side of the door due to the flow field. In COCOSYS no equations for the velocity field are solved, thus this effect cannot be seen. This is the reason why the temperatures for points M11 and M13 are over-predicted. In the simulation, these points are close to the hot plume, but in the experiment, the distance to the plume is larger. On the top of the compartment the temperatures are over-predicted by 100 - 200 °C (Fig. H5-15 to Fig. H5-18).

In the simulation, the mixture of the gas is not simulated correctly. In the calculation, none of the hot gas mixes with the cold gas at the lower elevations. It moves due to buoyancy effects upwards and gathers at the top of the room. It leaves the room via the FUCHS fan system or through the upper part of the door.

H5.3 Flow field

As discussed before, it is problematic to compare the velocities at some points in the experiment with the velocities calculated from the mass flow between two zones. Nevertheless, if these velocities are compared for the two points V1 and V2 in the plume the velocities fit quite well (Fig. H5-24, Fig. H5-25).

The velocities measured at the door between the two rooms show a qualitative good agreement, too (Fig. H5-26 to Fig. H5-30). In both cases, hot gases flow out of the combustion room and gas flows into the room at the bottom of the connection. The velocities are in the same order, only for the point V6 the calculated velocity is half of that measured in the experiment. However, for V6 even at the beginning ($t = 0$ s) a gas velocity of nearly - 4 m/s can be found. It is therefore not clear if there is an error in the experimental data for this measuring point.

H5.4 Gas composition

The gas composition was measured at the point GA1 in the combustion room. In the experiment, the O₂ concentration was significantly higher than in the simulation (Fig. H5-22). Accordingly, the CO and the CO₂ concentrations predicted in the simulation are too high. An explanation could be that the chemical reaction mechanism is not valid, or, which is more likely, that there is a problem with the simulation of the mixing between burned and not burned gas.

H5.5 Surface temperatures

As there is a problem with the prediction of the temperature, particularly in the lower part of the combustion room, it could not be expected to find an agreement with the measured wall and material probe temperatures. According to the much lower gas temperatures, the surface temperatures are significantly under-estimated, also (Fig. H5-19 to Fig. H5-21).

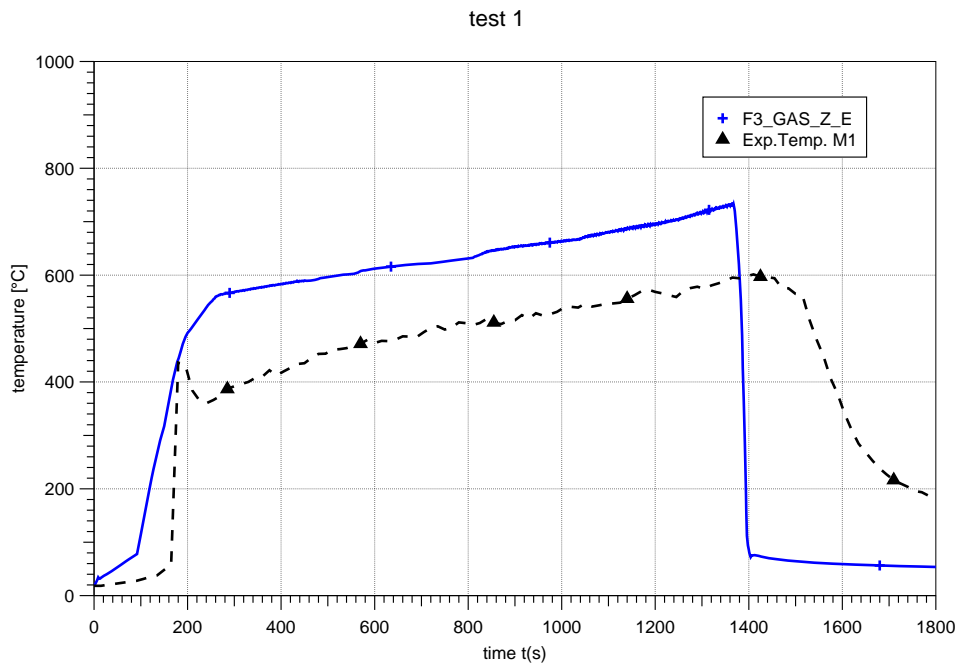


Fig. H5-1 Test 1: Plume temperature at M1

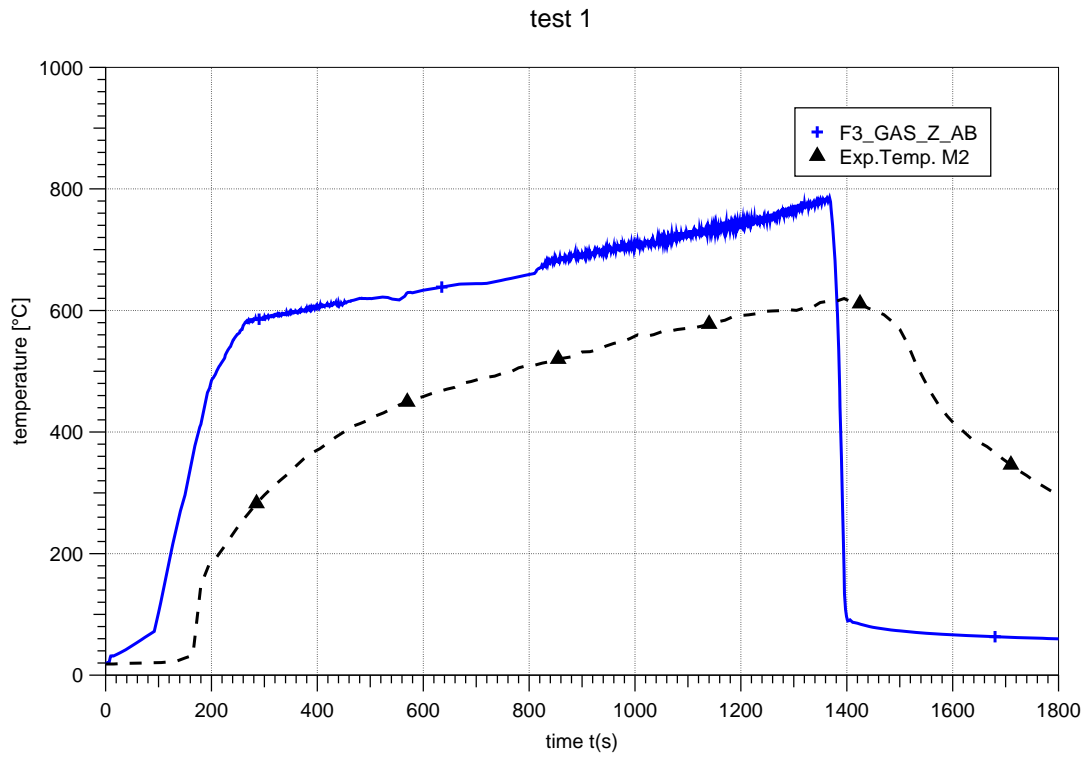


Fig. H5-2 Test 1: Plume temperature at M2

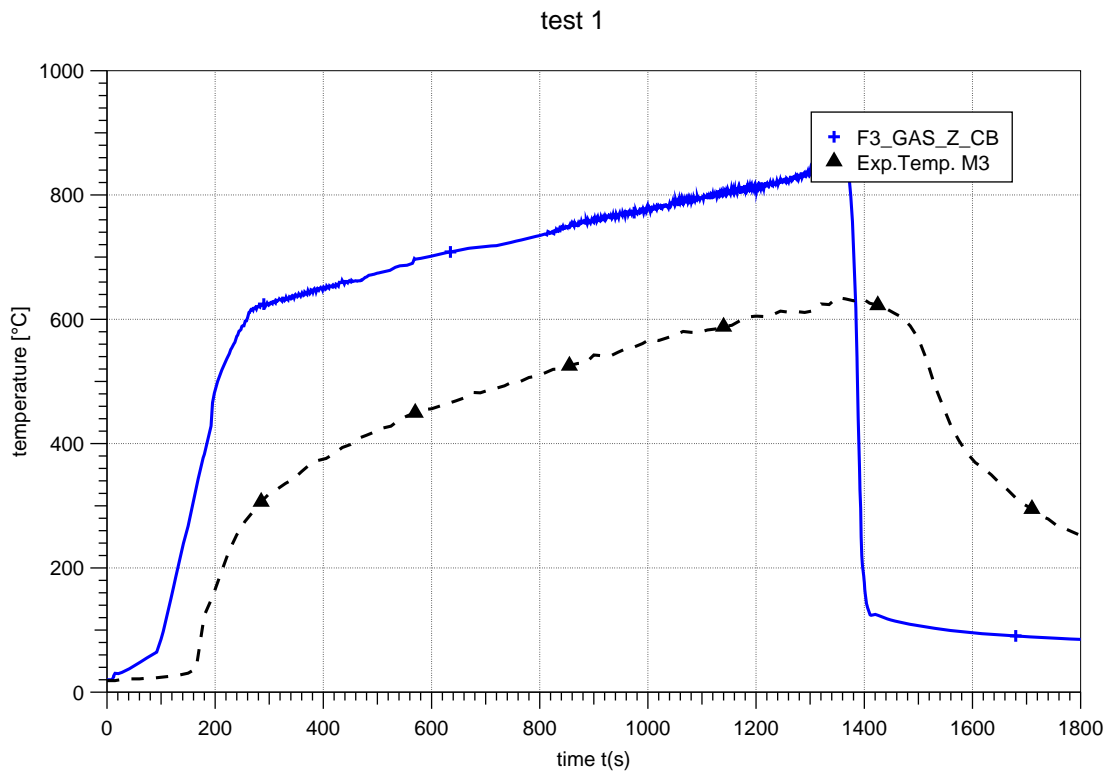


Fig. H5-3 Test 1: Plume temperature at M3

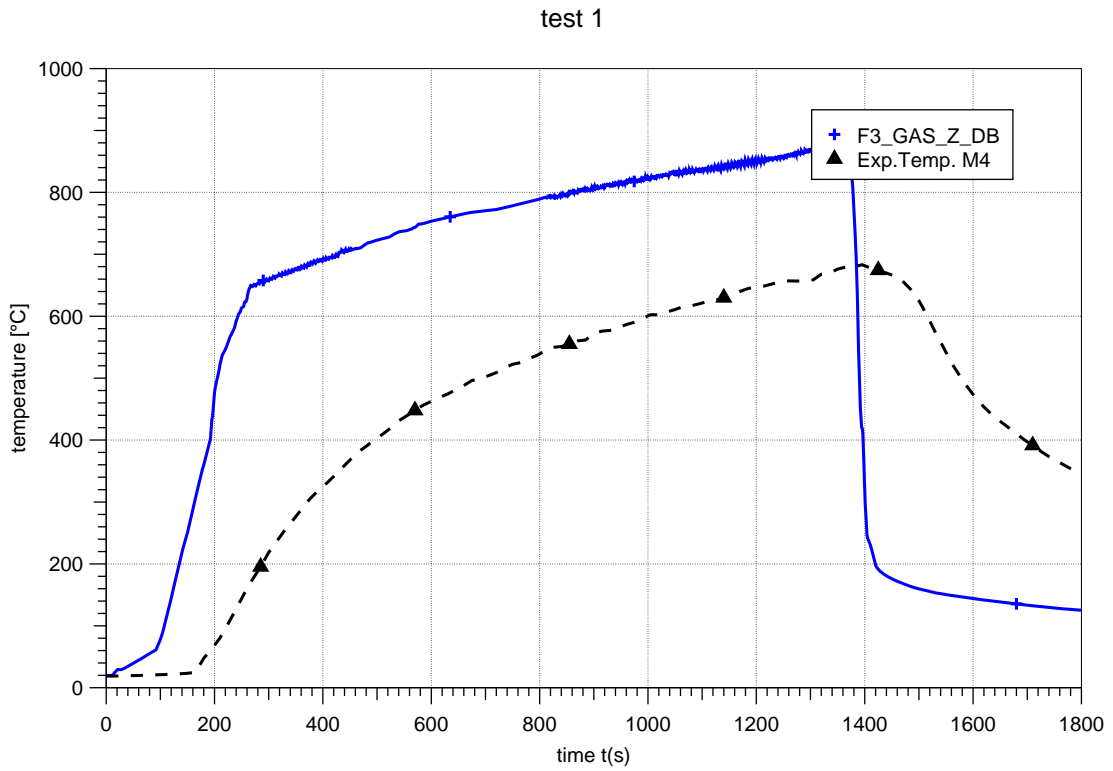


Fig. H5-4 Test 1: Plume temperature at M4

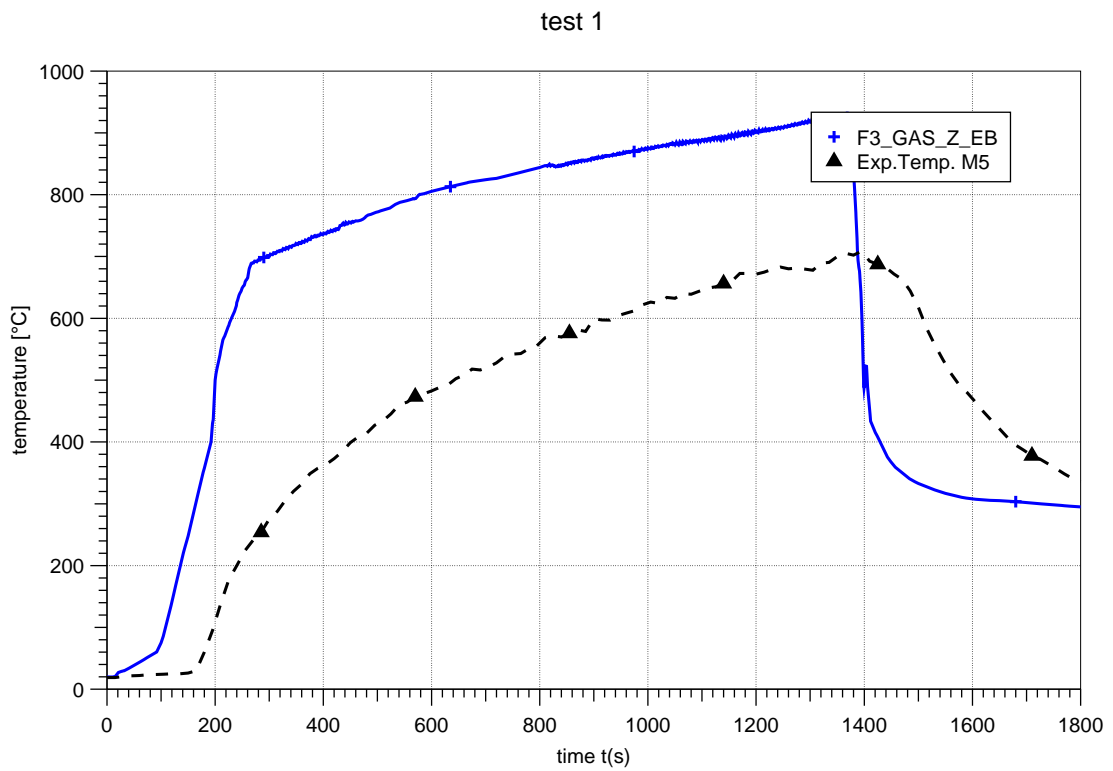


Fig. H5-5 Test 1: Plume temperature at M5

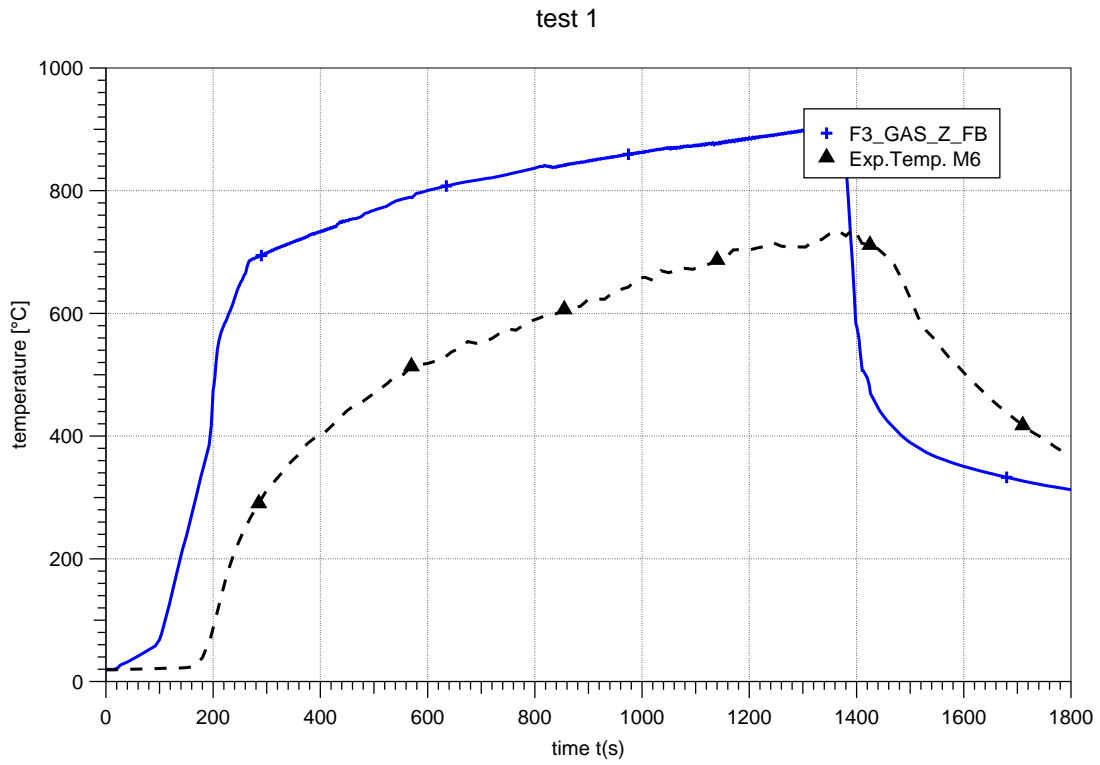


Fig. H5-6 Test 1: Plume temperature at M6

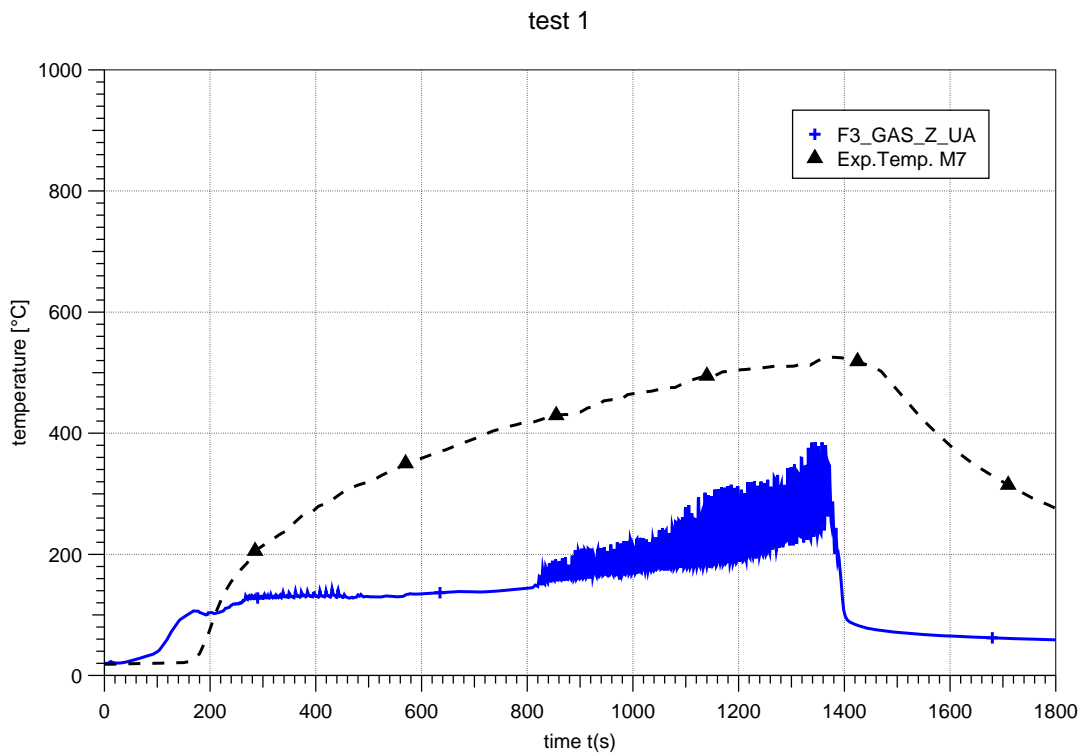


Fig. H5-7 Test 1: Temperature inside fire compartment (level 1, at M7)

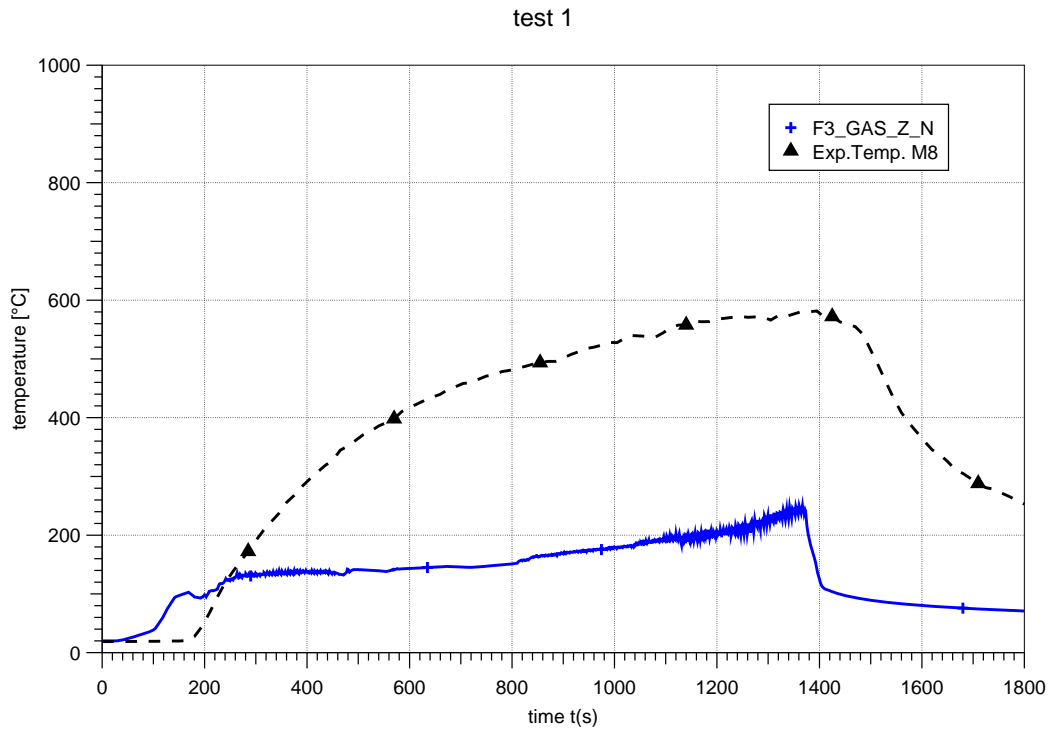


Fig. H5-8 Test 1: Temperature inside fire compartment (level 1, at M8)

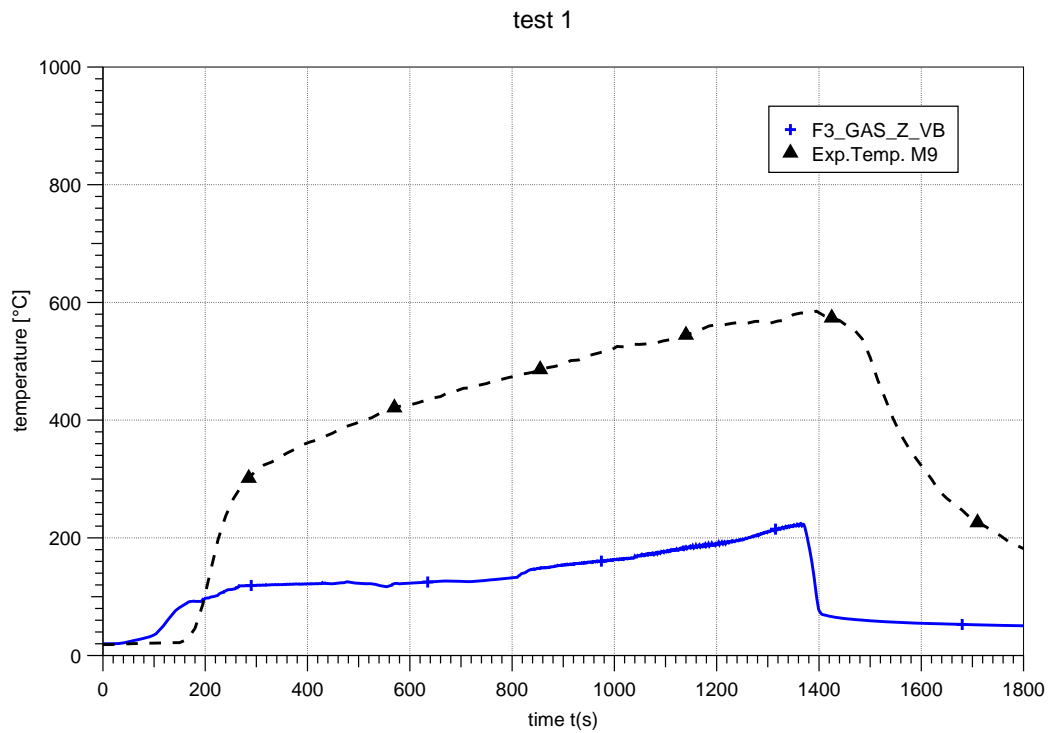


Fig. H5-9 Test 1: Temperature inside fire compartment (level 1, at M9)

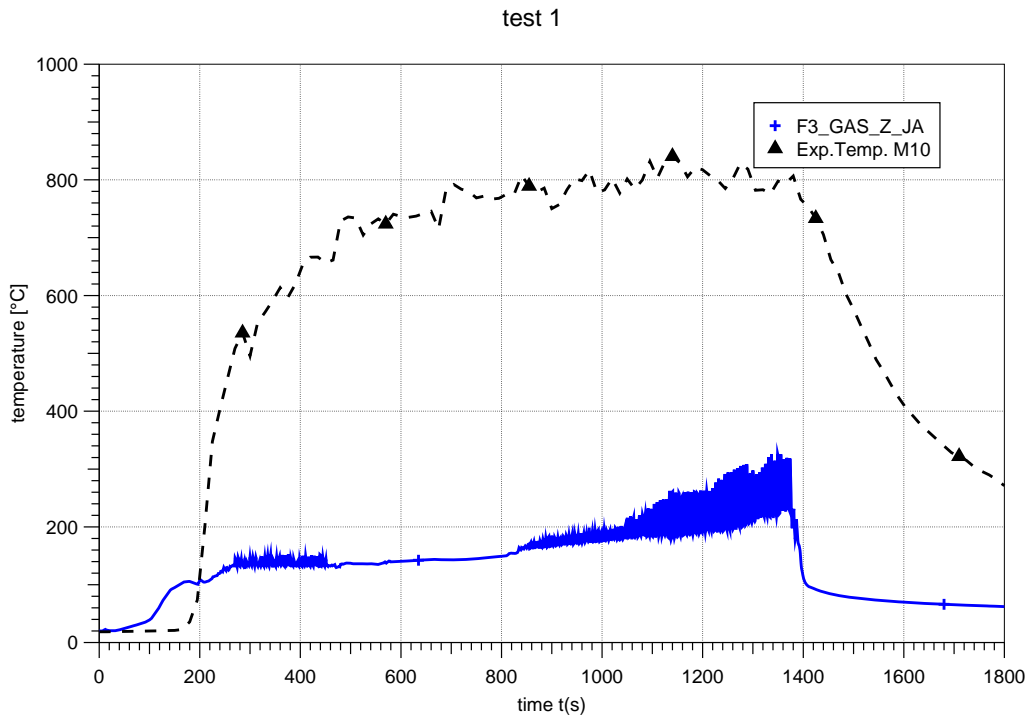


Fig. H5-10 Test 1: Temperature inside fire compartment (level 1, at M10)

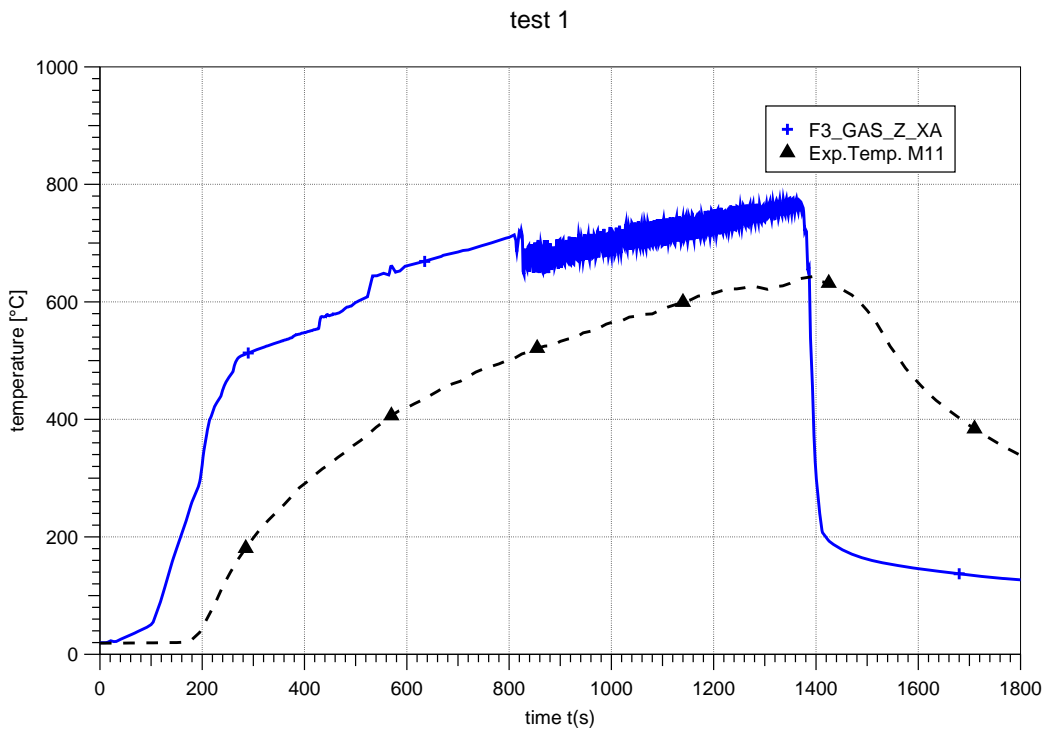


Fig. H5-11 Test 1: Temperature inside fire compartment (level 2, at M11)

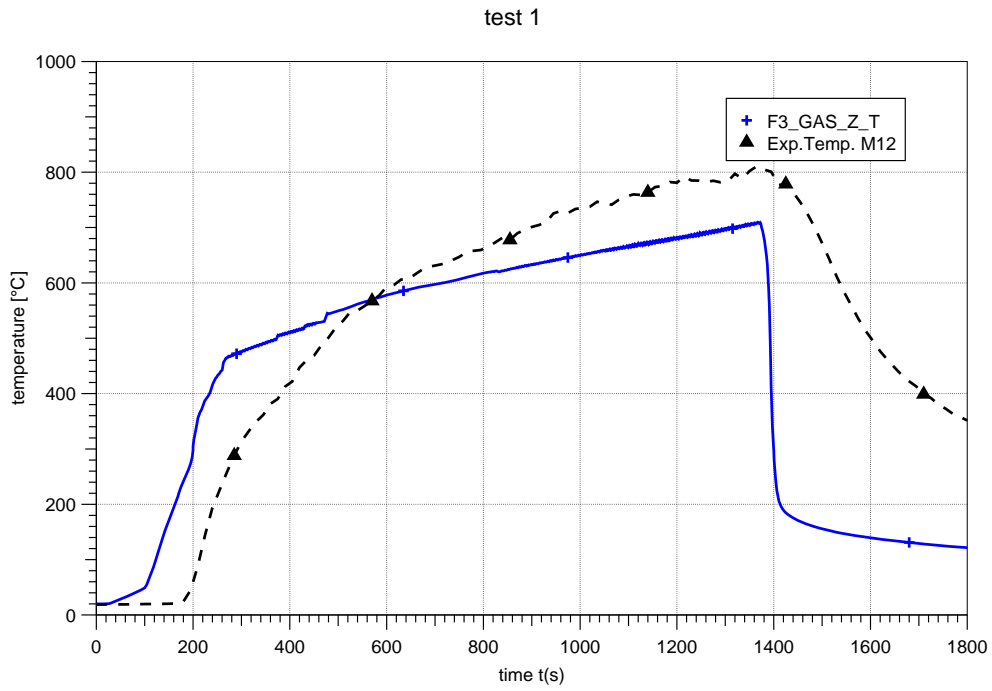


Fig. H5-12 Test 1: Temperature inside fire compartment (level 2, at M12)

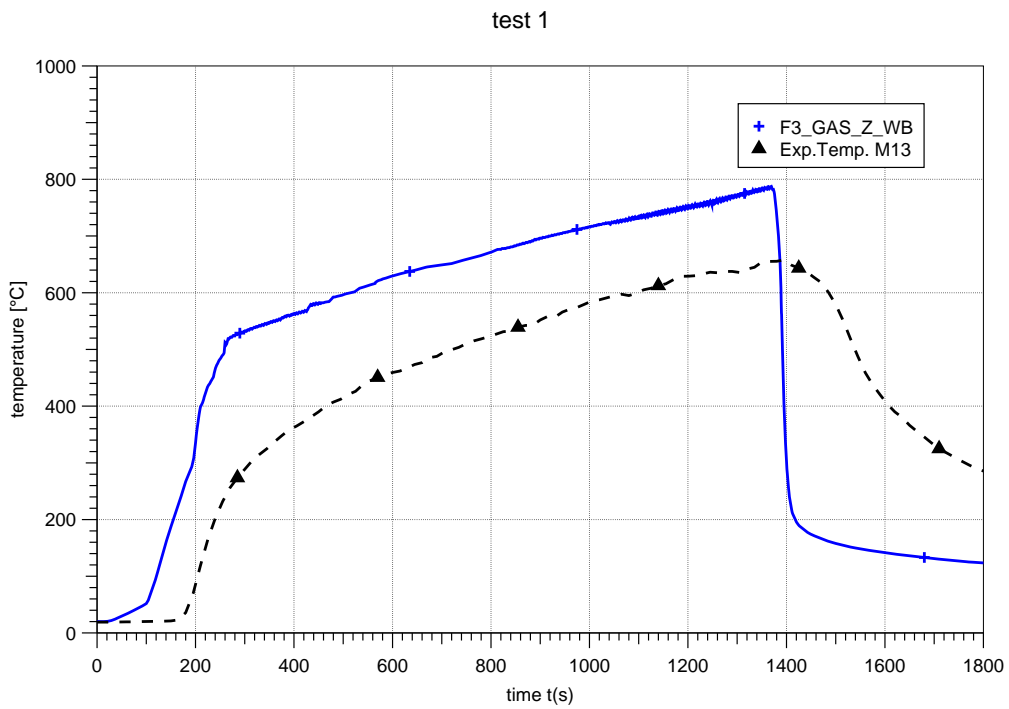


Fig. H5-13 Test 1: Temperature inside fire compartment (level 2, at M13)

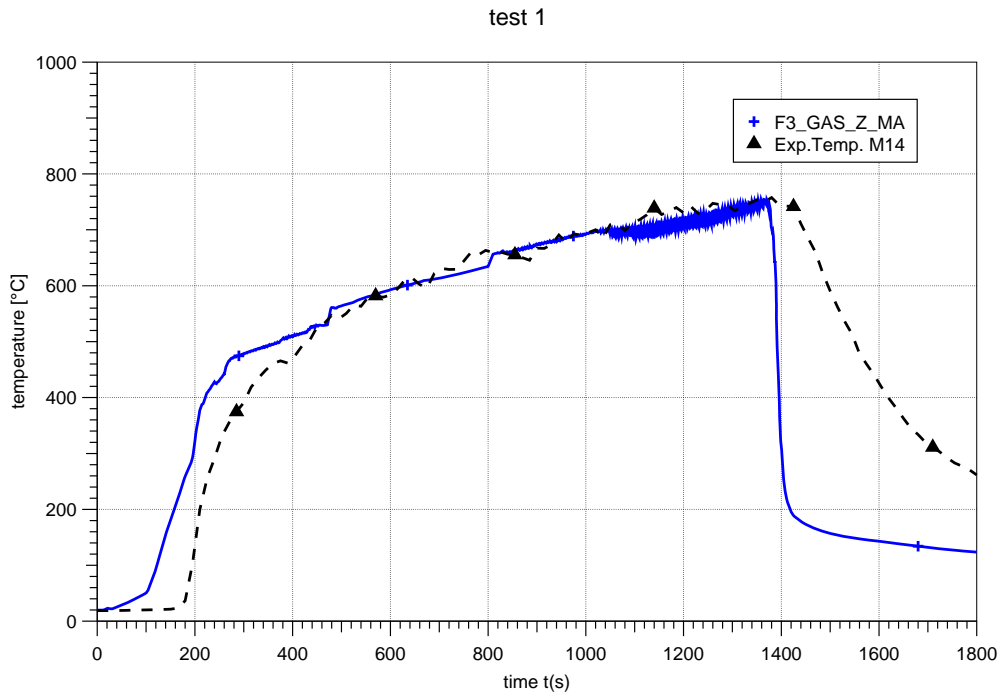


Fig. H5-14 Test 1: Temperature inside fire compartment (level 2, at M14)

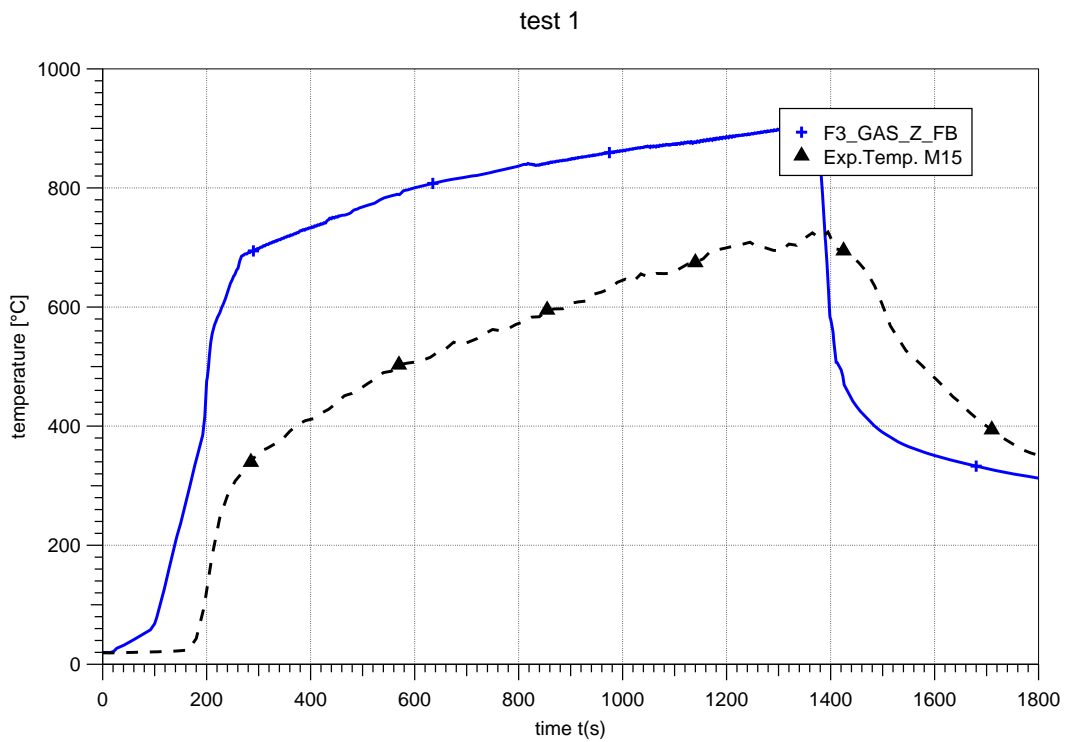


Fig. H5-15 Test 1: Temperature inside fire compartment (level 3, at M15)

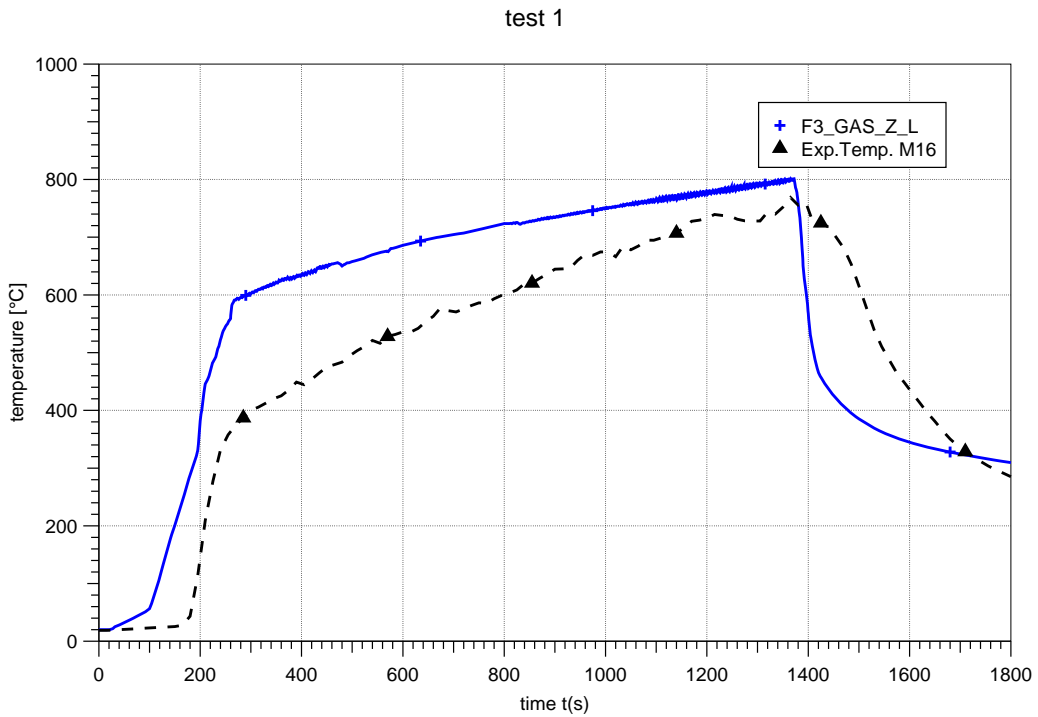


Fig. H5-16 Test 1: Temperature inside fire compartment (level 3, at M16)

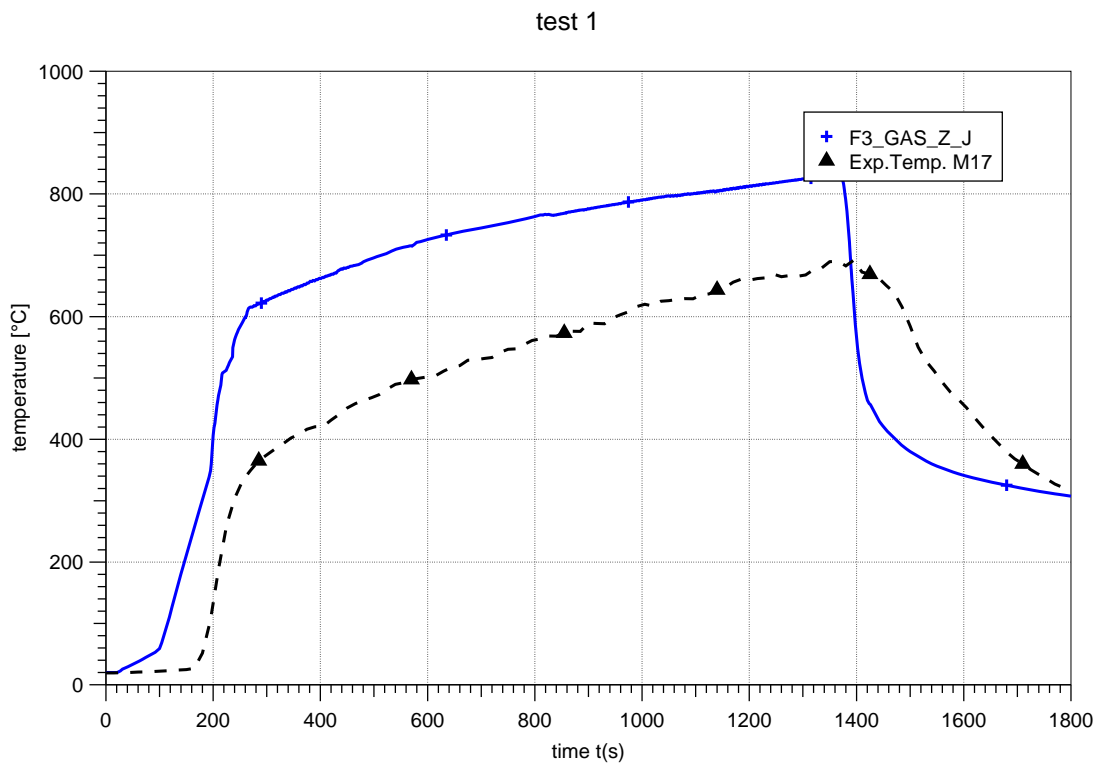


Fig. H5-17 Test 1: Temperature inside fire compartment (level 3, at M17)

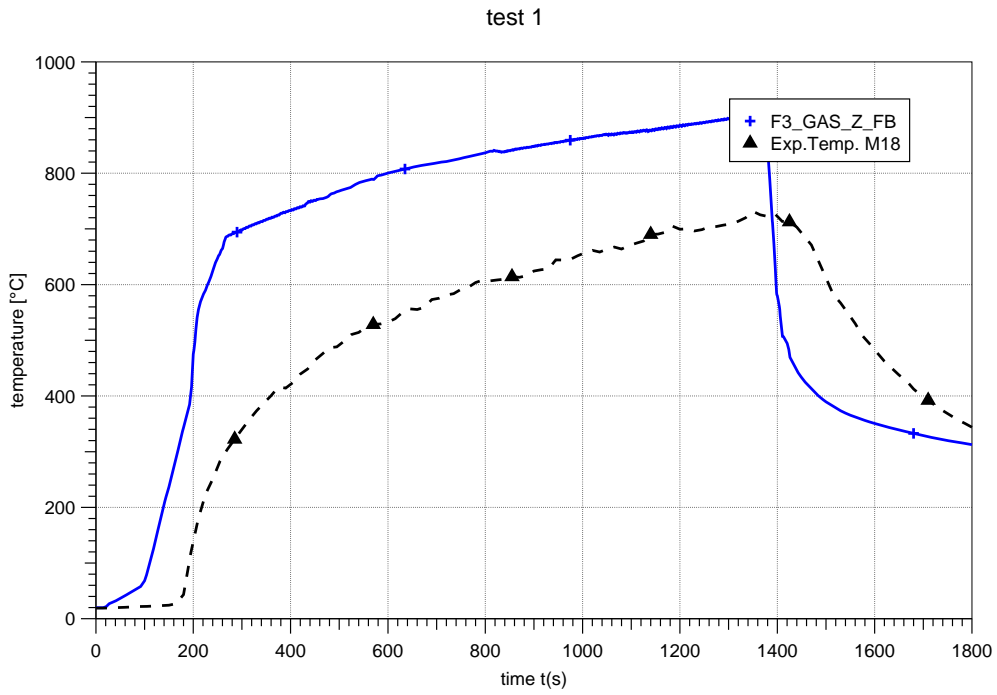


Fig. H5-18 Test 1: Temperature inside fire compartment (level 3, at M18)

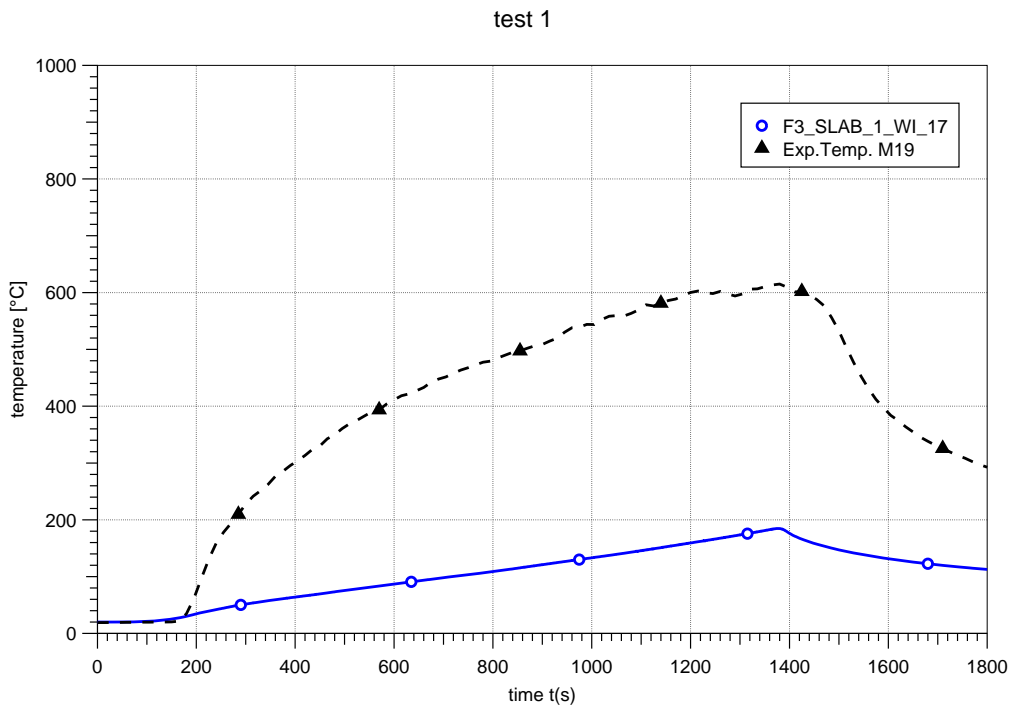


Fig. H5-19 Test 1: Surface temperature at M19

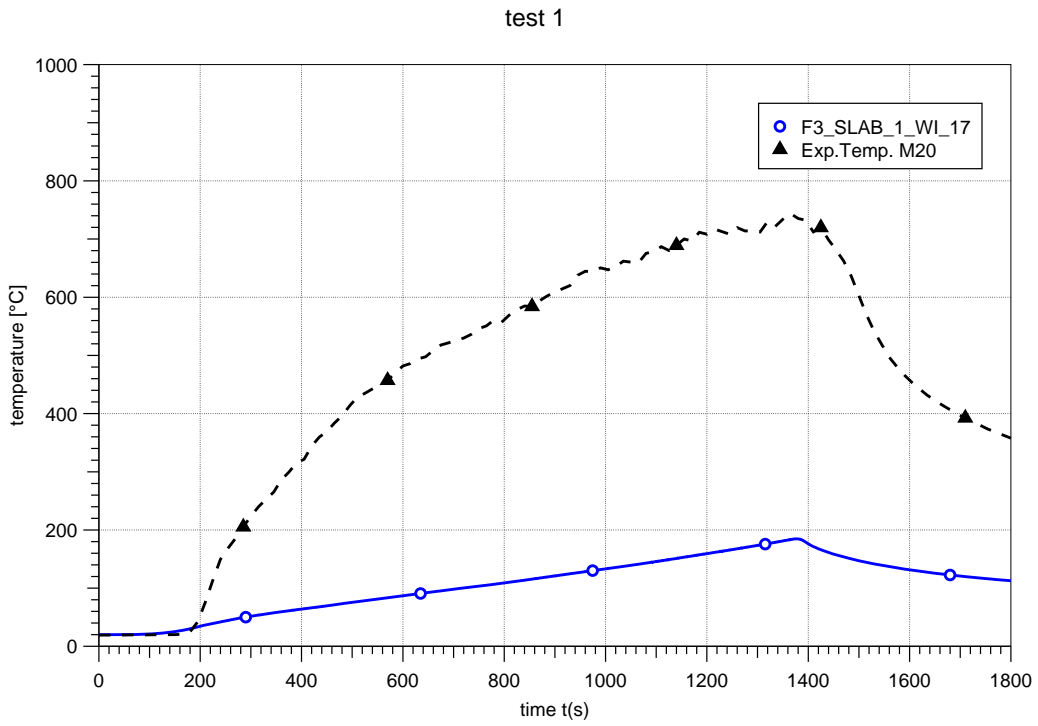


Fig. H5-20 Test 1: Surface temperature at M20

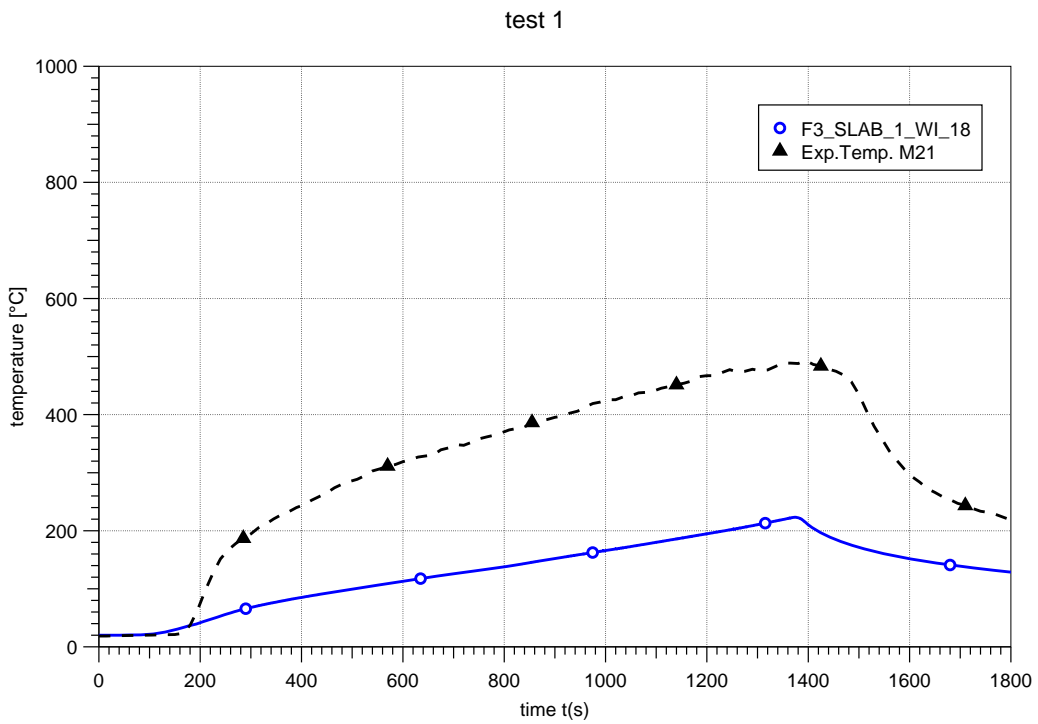


Fig. H5-21 Test 1: Surface temperature at M21

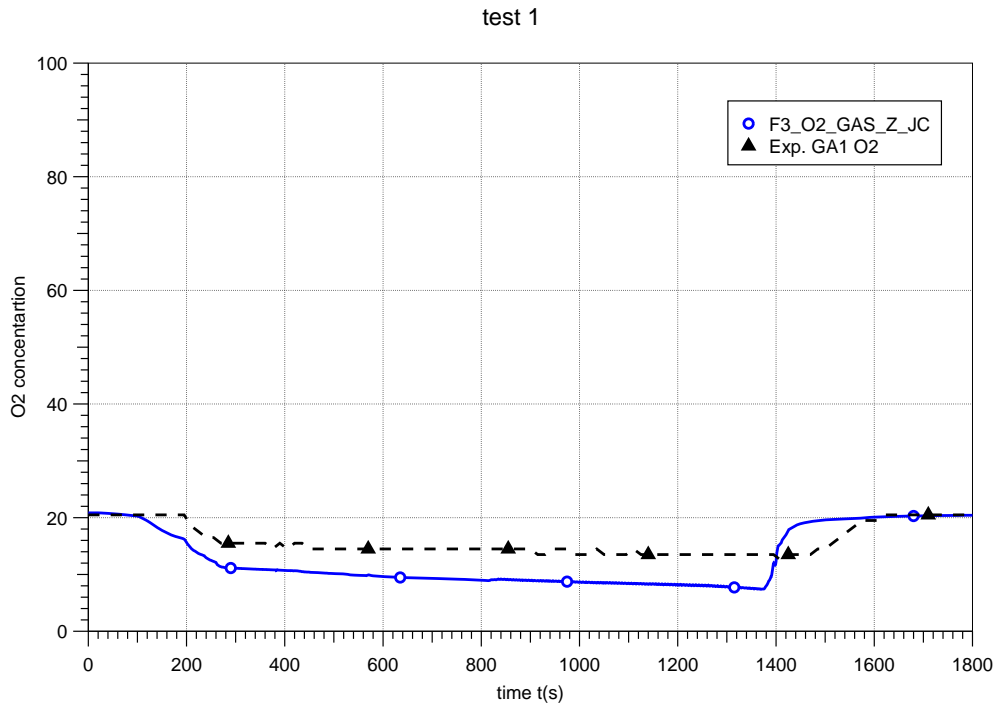


Fig. H5-22 Test 1: O₂ concentrations at the measurement point GA1

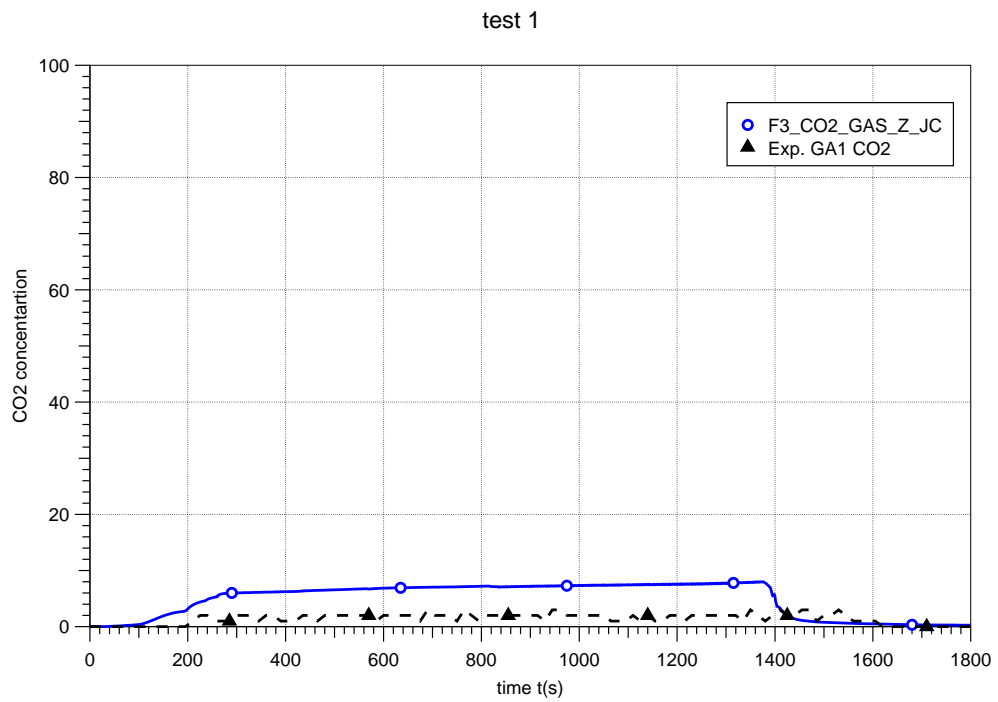


Fig. H5-23 Test 1: CO₂ concentrations at the measurement point GA1

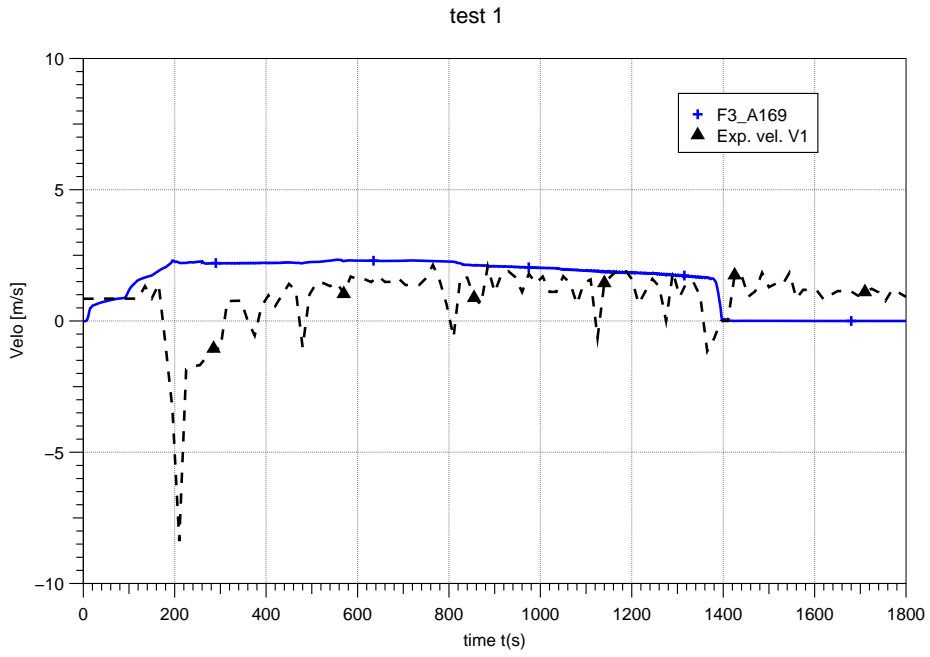


Fig. H5-24 Test 1: Plume velocity at V1

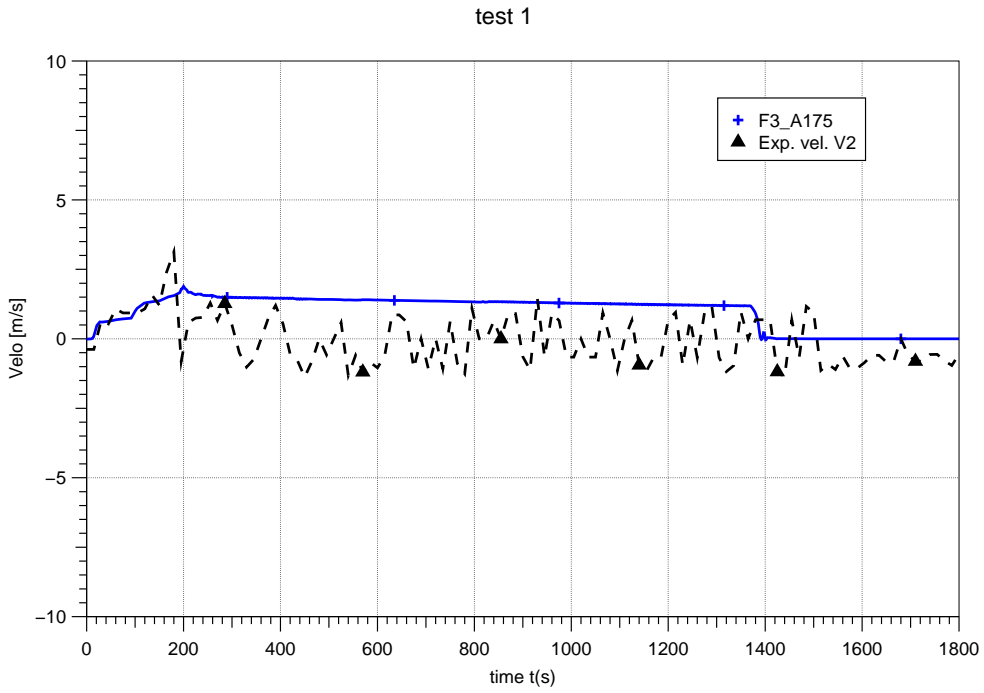


Fig. H5-25 Test 1: Plume velocity at V2

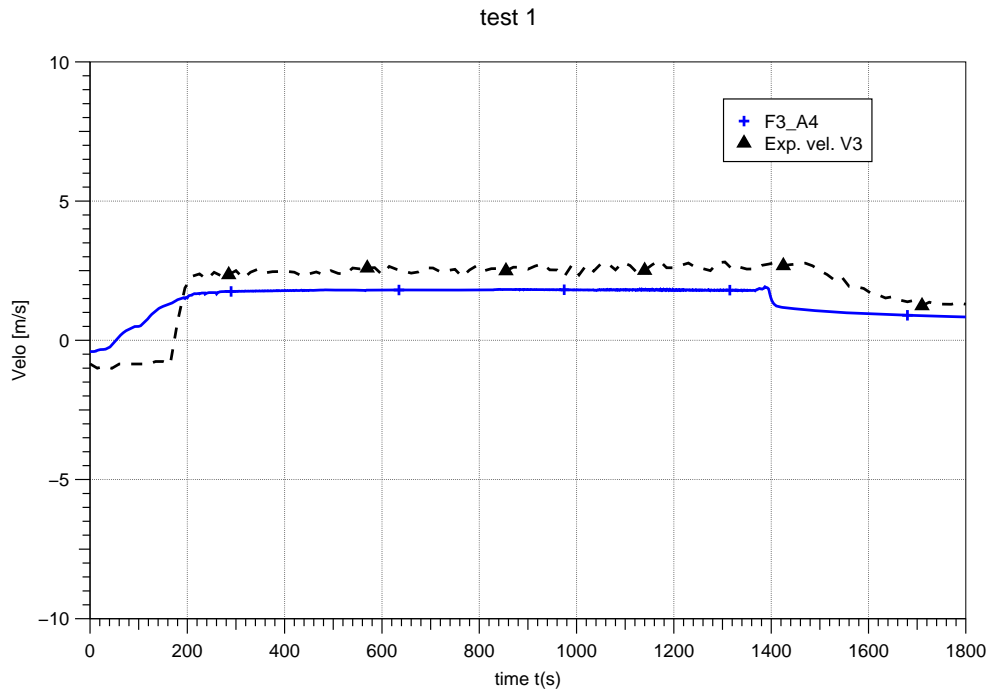


Fig. H5-26 Test 1: Velocity at door position V3

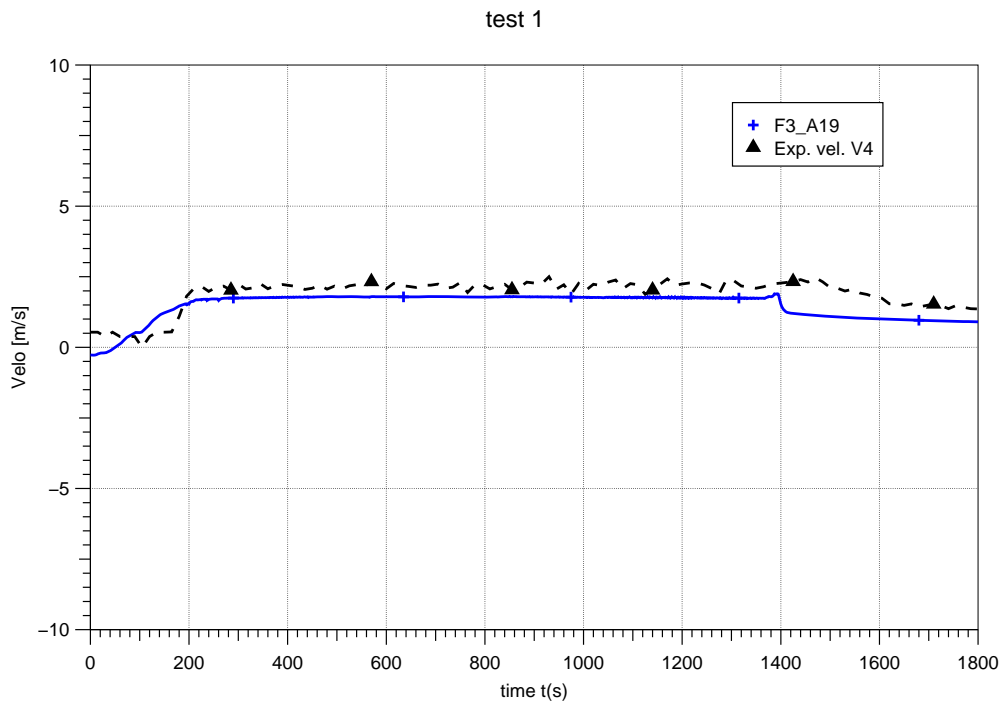


Fig. H5-27 Test 1: Velocity at door position V4

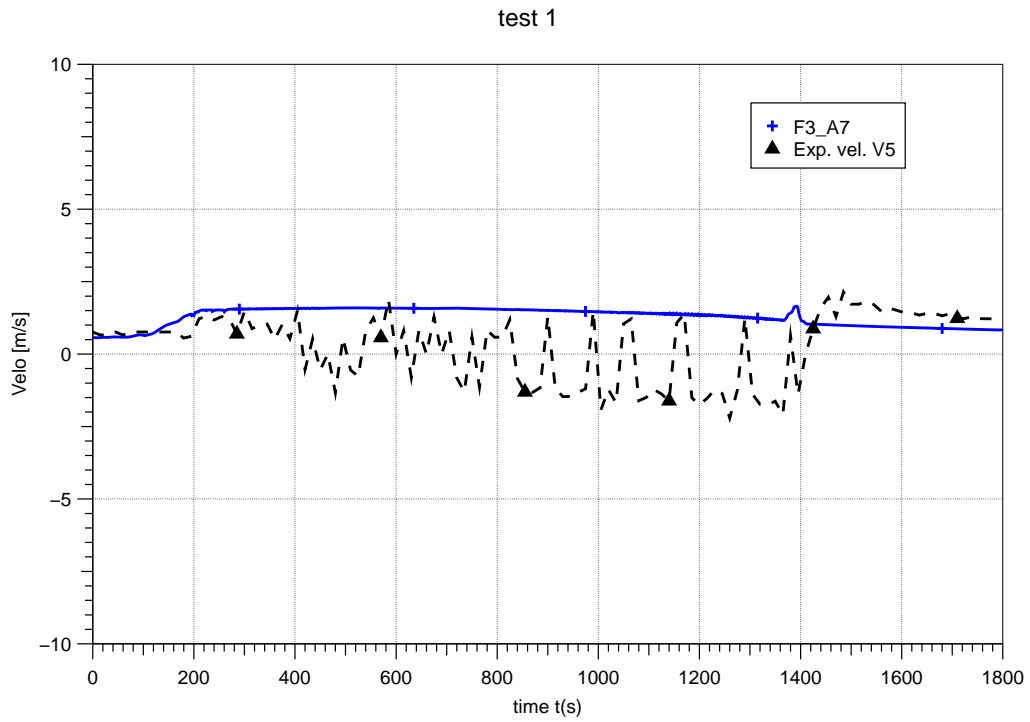


Fig. H5-28 Test 1: Velocity at door position V5

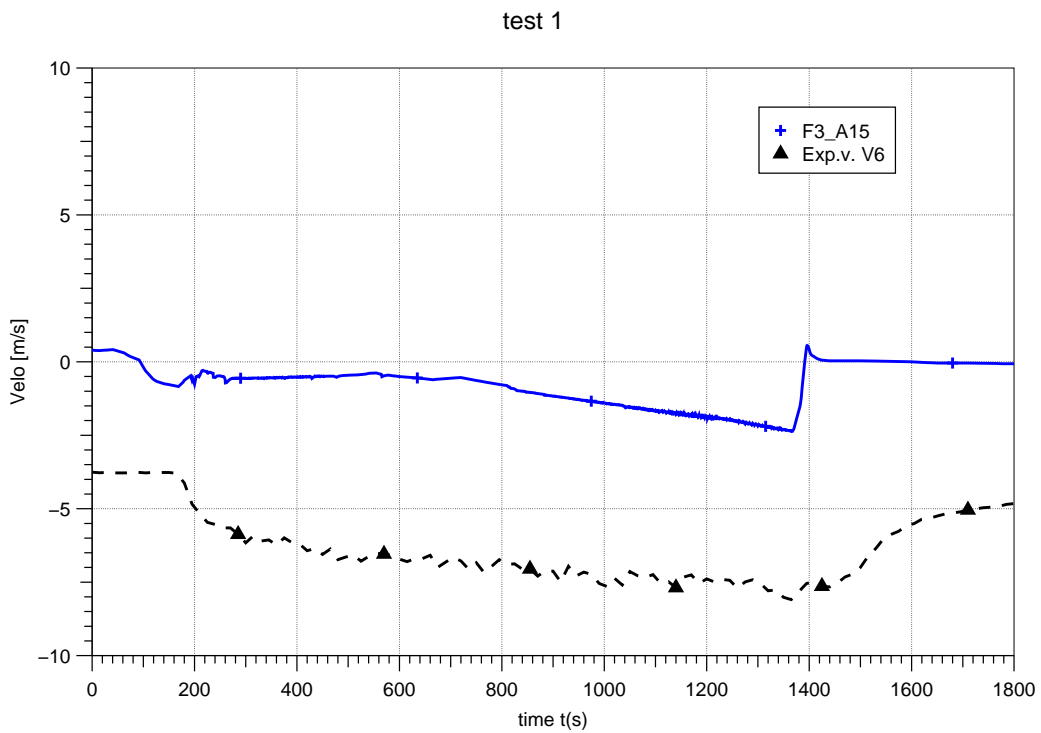


Fig. H5-29 Test 1: Velocity at door position V6

test 1

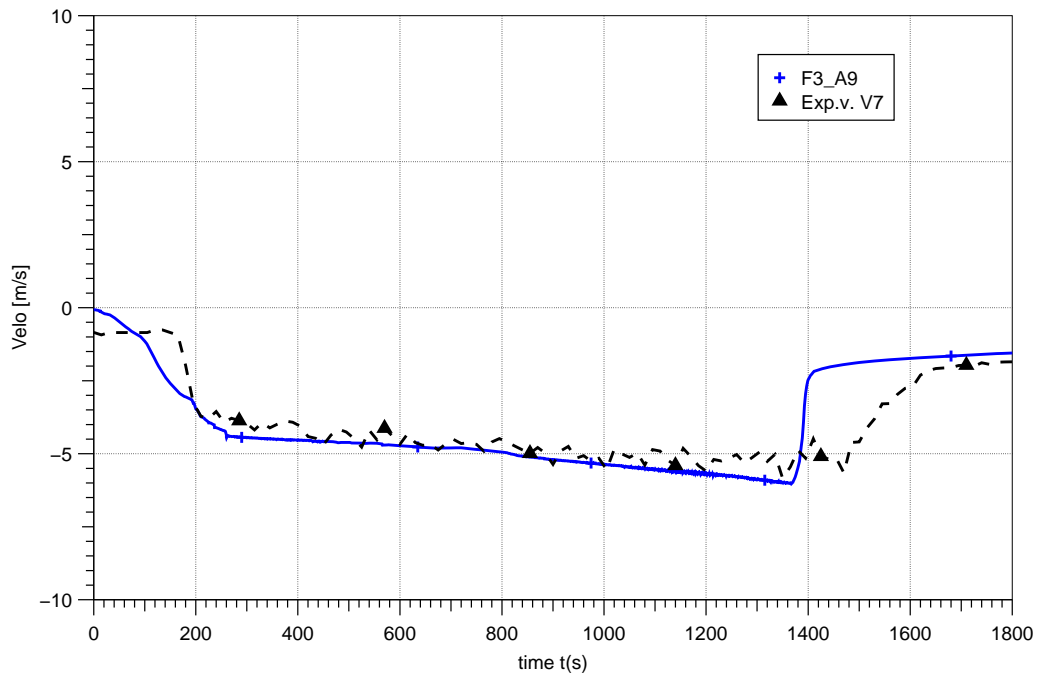


Fig. H5-30 Test 1: Velocity at door position V7

H6 Summary

Two COCOSYS calculations simulating Test 1 and test 3 of Benchmark exercise No. 4 have been performed. In both cases the stratification was over-predicted. The temperatures in the fire compartment were significantly under-estimated outside the hot plume at the lower elevations. At higher elevations, the temperatures were over-estimated, but the agreement was better. Increasing the COCOSYS zones at the plume in the center of the compartment with increasing level did not improve the results of simulation significantly.

The investigations show that the pyrolysis rate is a very sensitive parameter. In the simulations for both Test 1 and Test 3 this was one weak point, because the experimental data were insufficient, due to measurement errors. This emphasizes that a reliable modeling of the pyrolysis rate is needed not using experimental data. Due to the large deviations in the gas temperatures, no specific comparison of heat fluxes into the walls and material probes was possible.

H7 References

/KLH 00/ Klein-Heßling, W., et al.:
COCOSYS V1.2 User's Manual, GRS-P-3, Gesellschaft für Anlagen- und
Reaktorsicherheit (GRS) mbH, July 2000

/ALL 05/ Allelein, H.-J., et al.:
Weiterentwicklung der Rechenprogramme COCOSYS und ASTEC,
Abschlussbericht, GRS-A-3266, Gesellschaft für Anlagen- und
Reaktorsicherheit, April 2005

List of Figures

Fig. H1-1	Discretization of the fire compartment in COCOSYS - side view; left: Test 1; right: Test 3	2
Fig. H1-2	Discretization of the fire compartment in COCOSYS - view from the bottom (left) and from the top (right).....	2
Fig. H2-1	Test 1: Measured and extrapolated weight of the pan filled with fuel.....	4
Fig. H2-2	Test 1: Original and smoothed pyrolysis rate	4
Fig. H2-3	Test 3: Measured weight of the pan filled with fuel	5
Fig. H2-4	Test 3: Original and smoothed pyrolysis rate	5
Fig. H2-5	Test 3: Measured burned fuel mass and burned fuel with the modified pyrolysis rate	6
Fig. H2-6	Test 3: Modified pyrolysis rate	6
Fig. H3-1	Test 3: Plume temperature at M1	11
Fig. H3-2	Test 3: Plume temperature at M2.....	12
Fig. H3-3	Test 3: Plume temperature at M3.....	12
Fig. H3-4	Test 3: Plume temperature at M4.....	13
Fig. H3-5	Test 3: Plume temperature at M5.....	13
Fig. H3-6	Test 3: Plume temperature at M6.....	14
Fig. H3-7	Test 3: Temperature inside fire compartment (level 1, at M7).....	14
Fig. H3-8	Test 3: Temperature inside fire compartment (level 1, at M8).....	15
Fig. H3-9	Test 3: Temperature inside fire compartment (level 1, at M9).....	15
Fig. H3-10	Test 3: Temperature inside fire compartment (level 1, at M10).....	16
Fig. H3-11	Test 3: Temperature inside fire compartment (level 2, at M11).....	16
Fig. H3-12	Test 3: Temperature inside fire compartment (level 2, at M12).....	17
Fig. H3-13	Test 3: Temperature inside fire compartment (level 2, at M13).....	17
Fig. H3-14	Test 3: Temperature inside fire compartment (level 2, at M14).....	18
Fig. H3-15	Test 3: Temperature inside fire compartment (level 3, at M15).....	18
Fig. H3-16	Test 3: Temperature inside fire compartment (level 3, at M16).....	19
Fig. H3-17	Test 3: Temperature inside fire compartment (level 3, at M17).....	19
Fig. H3-18	Test 3: Temperature inside fire compartment (level 3, at M18).....	20
Fig. H3-19	Test 3: Surface temperature (M19)	20
Fig. H3-20	Test 3: Surface temperature (M20)	21
Fig. H3-21	Test 3: Surface temperature (M21)	21
Fig. H3-22	Test 3: O ₂ concentrations at the measurement point GA1	22

Fig. H3-23	Test 3: O ₂ concentrations in the COCOSYS zone above the fuel surface	22
Fig. H3-24	Test3: Plume velocity at position V1	23
Fig. H3-25	Test3: Plume velocity at position V2	23
Fig. H3-26	Test3: Velocity at door position V5.....	24
Fig. H3-27	Test3: Velocity at door position V6.....	24
Fig. H3-28	Test 3: Temperature inside aerated concrete probe (M29, 0.02 m).....	25
Fig. H3-29	Test 3: Temperature inside aerated concrete probe (M28, 0.05 m).....	25
Fig. H3-30	Test 3: Temperature inside aerated concrete probe (M27, 0.08 m).....	26
Fig. H3-31	Test 3: Temperature inside aerated concrete probe (M26, 0.10 m).....	26
Fig. H3-32	Test 3: Temperature inside concrete probe (M33, 0.02 m)	27
Fig. H3-33	Test 3: Temperature inside concrete probe (M32, 0.05 m)	27
Fig. H3-34	Test 3: Temperature inside concrete probe (M31, 0.08 m)	28
Fig. H3-35	Test 3: Temperature inside concrete probe (M30, 0.10 m)	28
Fig. H3-36	Test 3: Temperature inside steel probe (M34, x = 0. 0 m)	29
Fig. H3-37	Test 3: Temperature inside steel probe (M35, x = 0. 02 m)	29
Fig. H4-1	Test 3 mod: Plume temperature at M1	32
Fig. H4-2	Test 3 mod: Plume temperature at M2.....	33
Fig. H4-3	Test 3 mod: Plume temperature at M3.....	33
Fig. H4-4	Test 3 mod: Plume temperature at M4.....	34
Fig. H4-5	Test 3 mod: Plume temperature at M5.....	34
Fig. H4-6	Test 3 mod: Plume temperature at M6.....	35
Fig. H4-7	Test 3 mod: Temperature inside fire compartment (level 1, at M7).....	35
Fig. H4-8	Test 3 mod: Temperature inside fire compartment (level 1, at M8).....	36
Fig. H4-9	Test 3 mod: Temperature inside fire compartment (level 1, at M9).....	36
Fig. H4-10	Test 3 mod: Temperature inside fire compartment (level 1, at M10).....	37
Fig. H4-11	Test 3 mod: Temperature inside fire compartment (level 2, at M11).....	37
Fig. H4-12	Test 3 mod: Temperature inside fire compartment (level 2, at M12).....	38
Fig. H4-13	Test 3 mod: Temperature inside fire compartment (level 2, at M13).....	38
Fig. H4-14	Test 3 mod: Temperature inside fire compartment (level 2, at M14).....	39
Fig. H4-15	Test 3 mod: Temperature inside fire compartment (level 3, at M15).....	39
Fig. H4-16	Test 3 mod: Temperature inside fire compartment (level 3, at M16).....	40
Fig. H4-17	Test 3 mod: Temperature inside fire compartment (level 3, at M17).....	40
Fig. H4-18	Test 3 mod: Temperature inside fire compartment (level 3, at M18).....	41
Fig. H4-19	Test 3 mod: O ₂ concentrations in the COCOSYS zone above the fuel surface	41

Fig. H4-20	Test 3 mod: O ₂ concentrations at GA1.....	42
Fig. H5-1	Test 1: Plume temperature at M1.....	45
Fig. H5-2	Test 1: Plume temperature at M2.....	46
Fig. H5-3	Test 1: Plume temperature at M3.....	46
Fig. H5-4	Test 1: Plume temperature at M4.....	47
Fig. H5-5	Test 1: Plume temperature at M5.....	47
Fig. H5-6	Test 1: Plume temperature at M6.....	48
Fig. H5-7	Test 1: Temperature inside fire compartment (level 1, at M7).....	48
Fig. H5-8	Test 1: Temperature inside fire compartment (level 1, at M8).....	49
Fig. H5-9	Test 1: Temperature inside fire compartment (level 1, at M9).....	49
Fig. H5-10	Test 1: Temperature inside fire compartment (level 1, at M10).....	50
Fig. H5-11	Test 1: Temperature inside fire compartment (level 2, at M11).....	50
Fig. H5-12	Test 1: Temperature inside fire compartment (level 2, at M12).....	51
Fig. H5-13	Test 1: Temperature inside fire compartment (level 2, at M13).....	51
Fig. H5-14	Test 1: Temperature inside fire compartment (level 2, at M14).....	52
Fig. H5-15	Test 1: Temperature inside fire compartment (level 3, at M15).....	52
Fig. H5-16	Test 1: Temperature inside fire compartment (level 3, at M16).....	53
Fig. H5-17	Test 1: Temperature inside fire compartment (level 3, at M17).....	53
Fig. H5-18	Test 1: Temperature inside fire compartment (level 3, at M18).....	54
Fig. H5-19	Test 1: Surface temperature at M19	54
Fig. H5-20	Test 1: Surface temperature at M20	55
Fig. H5-21	Test 1: Surface temperature at M21	55
Fig. H5-22	Test 1: O ₂ concentrations at the measurement point GA1	56
Fig. H5-23	Test 1: CO ₂ concentrations at the measurement point GA1	56
Fig. H5-24	Test 1: Plume velocity at V1	57
Fig. H5-25	Test 1: Plume velocity at V2.....	57
Fig. H5-26	Test 1: Velocity at door position V3.....	58
Fig. H5-27	Test 1: Velocity at door position V4.....	58
Fig. H5-28	Test 1: Velocity at door position V5.....	59
Fig. H5-29	Test 1: Velocity at door position V6.....	59
Fig. H5-30	Test 1: Velocity at door position V7.....	60

**Appendix I: International Collaborative Project to Evaluate Fire
Models for Nuclear Power Plant Applications**

**Vulcan Simulations of ICFMP Benchmark Exercise
No. 4, Test 3**

Presented by

V.-F. Nicolette

Fire Science and Technology Dept. 1532

Sandia National Laboratories (SNL),

Albuquerque, NM, U.S.A.

Contents

I1	Introduction	1
I2	Fire Code.....	3
I3	The ICFMP Process.....	5
I4	Fire Code Inputs and Assumptions.....	7
I5	Comments on Experimental Data.....	11
I6	Results	13
I6.1	Simulation with mass loss rate prediction	13
I6.1.1	Mass loss rate and oxygen fraction.....	13
I6.1.2	Doorway velocities	15
I6.1.3	Thermocouple temperatures	15
I6.1.4	Target heat fluxes and temperatures	16
I6.2	Refined mesh results	17
I6.3	Simulation with specified mass loss rate.....	19
I6.3.1	Oxygen concentration	19
I6.3.2	Doorway velocities	19
I6.3.3	Thermocouple temperatures	19
I6.3.4	Target heat fluxes and temperatures	20
I6.4	Simulation with BVG Turbulence Model, Specified Mass Loss Rate	21
I6.4.1	Oxygen concentration	21
I6.4.2	Doorway velocities	22
I6.4.3	Thermocouple temperatures	22
I6.4.4	Target heat fluxes and temperatures	23
I7	Discussion	25
I8	Conclusions.....	27
I9	References.....	29
I10	Acknowledgments	31
I11	Figures	33
	List of Figures	49
	List of Tables	51

I1 Introduction

As part of the International Collaborative Fire Modeling Project (ICFMP), a series of large-scale experiments were conducted to simulate single compartment fires in nuclear power plants (NPPs). The main purpose of the series of experiments was to provide data for an international benchmarking exercise to validate and assess fire codes over a range of conditions relevant to NPP fires. The fire size and location, type of fuel, natural and forced ventilation, were varied to provide data sets for code assessment and validation. Organizations from Germany, France, UK, and USA participated in the benchmarking exercise. This report documents the results of simulations of one of these experiments (Benchmark Exercise No. 4, Test 3) performed with the Sandia National Laboratories Vulcan fire code.

12 Fire Code

The Sandia Vulcan fire code /TIE 96/ was used for the simulation of ICFMP Benchmark Exercise No. 4, Test 3. Vulcan is derived from the Kameleon Fire code /HOL 90/ and models the transport and burning of vaporized fuel, as well as the transport of combustion by-products and their thermal impact on targets. Conservation equations are solved for mass, species, momentum, energy (enthalpy), turbulence quantities, and radiation intensity. Convective and radiative heat transfer to targets is included in the code, as well as the subsequent thermal response of the targets.

Vulcan contains the following sub-models (algorithms):

- A fuel vaporization sub-model for the estimation of the rate at which fuel is transferred to the vapor phase from the liquid phase (for liquid fuels). This model uses the code-calculated incident heat flux to the fuel to determine the vaporization rate.
- A k - ϵ turbulence model /JON 72/ to mix the vaporized fuel with air and combustion products as a function of the local turbulence levels. A buoyant vorticity generation (BVG) variant of the k - ϵ turbulence model is also available /NIC 05/, and was used in one of the simulations.
- A combustion model to determine the amount of fuel that is combusted. The Eddy Dissipation Concept (EDC) combustion model /MAG 81/ is used. The EDC is a general concept for describing the interaction between the turbulence and the chemistry in flames. The combustion process is assumed to occur in the turbulent fine structures (vortex tubes), which are modeled as perfectly stirred reactors. Reactions are modeled as either 1-step or 2-step reactions, with irreversible, infinitely fast chemistry (relative to the mixing process). Local extinction is calculated based on comparison of the mixing and chemical time scales.
- A soot generation and transport model. Soot is treated as a trace species in the problem, and a transport equation is solved to determine its local variation with time. Soot production and combustion are modeled according to the work of Magnusson and Hjertager /MAG 77/, which is based on the work of Tesner, et al. /TES 71/, utilizing a two-step formation process. The first step treats the formation of radical nuclei, and the second step treats the formation of soot particles from the radical nuclei. The combustion (oxidation) of soot is also modeled.

- Thermal radiation heat transfer. The Discrete Transfer Method (DTM) of Shah and Lockwood /SHA 79/ is employed to solve the thermal radiation. Combustion products modeled include soot, CO₂ and H₂O. The soot and combustion gases are treated as a gray gas with an effective absorption and emission coefficient based on the local concentrations and temperature. The DTM is a ray tracing technique.
- Convective heat transfer and wall shear stresses are modeled using the wall function approach /LAU 74/.
- Object thermal response. A one dimensional conduction calculation is used to determine object thermal response (temperature) as a function of the incident radiative and convective heat fluxes.
- A liquid fuel spread model is included in the code, based on lubrication theory.
- Decomposition and combustion of solid materials is modeled.

Vulcan uses an extension of the SIMPLEC method of Patankar and Spalding, 1972 /PAT 72/, to solve the conservation equations using a control volume formulation. A structured three-dimensional Cartesian grid is used. First- and second-order accurate upwind schemes can be used for the convective terms. A temporally-filtered Navier-Stokes method (quasi-LES method) is also available in the code /TIE 05/, but was not used for any of the simulations in this report.

I3 The ICFMP Process

The approach taken in the ICFMP was to ask the participants to perform a 'blind' calculation in which the ventilation flow rates were specified (but not the pool mass loss rate). A second round of simulations was conducted (semi-blind) in which the mass loss rate was also specified, but the other experimental results were not yet released. Finally, a round of 'open' simulations was conducted in which all of the experimental results were made available.

Sandia was invited to join the ICFMP at a late stage of the program. Consequently, the Vulcan simulations discussed in this report were conducted after the release of the experimental results, so they are best assessed against the 'open' round results of the other participants. However, no attempt was made in the present simulations to adjust any of the parameters to obtain a better solution. The results shown are what were obtained using 'best estimates' for the inputs based on the author's experience in applying Vulcan to a number of problems, and based on assumptions that had to be made where the experimental details were not clearly specified. Adjusting parameters may have improved the agreement, but that was not the intention of this work.

14 Fire Code Inputs and Assumptions

The problem specification is given in the Panel report itself (Test 3 of Benchmark Exercise No. 4). The problem consists of a 1 m² hydrocarbon pool fire in a compartment that is naturally ventilated via a doorway and 2 exhaust ducts in the ceiling. The compartment measures 3.6 m wide by 3.6 m long by 5.7 m high. An exhaust hood was located outside the room doorway. A wire frame model of the fire room itself is shown in Fig. I1. The geometry used in the simulation, including the hood, is shown with the walls removed for clarity in Fig. I2.

A non-uniform grid of 38 x 55 x 46 (y direction is from the front door to the back of room) control volumes was used for the majority of simulations (Fig. I3), and was developed based on previous modeling experience. Additionally, a refined mesh simulation was performed using 74 x 104 x 84 control volumes (essentially dividing the physical length of each control volume side by a factor of 2). This yielded a control volume length scale of order 0.07 – 0.15 m in the x and y directions. The control volumes in the z direction were somewhat larger in the upper regions of the room, where gradients were expected to be small.

The computational domain was taken as the fire room plus some reservoir space outside of the fire room. Some of the simulations included modeling of the hood located outside the door of the fire room. The computational domain spanned the following dimensions:

$$0 < x < 3.6 \text{ m}$$

$$-4.3 < y < 3.6 \text{ m}$$

$$0 < z < 6.735 \text{ m}$$

Note that $y=0$ corresponds to the doorway, and $y=3.6$ m corresponds to the back wall of the fire room. Roughly 4 m of reservoir space outside of the fire room was included in the computational domain.

The $k-\epsilon$ turbulence model implementation requires a maximum turbulence length scale. This was set to the room dimension in x and y, or 3.6 m.

The fuel composition was specified as $C_{11.64}H_{25.29}$ per the experimental description. Based on the composition, the boiling temperature and heat of gasification were assumed to be approximately halfway between that of n-dodecane and n-undecane. These were taken from the SFPE Fire Protection Handbook /SFP 88/. The values used as inputs were:

$$T_{\text{boil}} = 480 \text{ K (207 C)}$$

$$\Delta h_{\text{fg}} = 300,000 \text{ J/kg}$$

For some simulations, the measured fuel evaporation rate was specified for the code. For other simulations, the fuel evaporation rate was calculated by the code based on the thermal response of the fuel.

The chemical reaction was modeled as a 2-step reaction with production of intermediate species. In the first step of the chemical reaction, the fuel is assumed to combust to form carbon monoxide and hydrogen. The second step of the reaction converts the intermediate species to water vapor and carbon dioxide.

A chemical time scale of 7×10^{-5} s was specified for the reaction. The heat of combustion was taken to be $\Delta H_c = -4.28 \times 10^7$ J/kg of fuel consumed. The fuel was assumed to be ignited at time equal to zero.

The velocity of the ventilation flow through the ceiling ducts was specified for the code. For the simulations that included modeling of the external hood, the experimentally measured velocity of the flow through the hood was specified for the code.

The thermal radiation was calculated using 24 rays per wall point (4 x 6 rays), with rays focused on targets of interest. Thermal radiation was updated every time step of the simulation.

The temperature of the surroundings (reservoir) was assumed to be 291.6 K. The initial temperatures were as given in the experiment report.

Virtual thermocouples were included in the simulation. These enable estimates to be made of the reading a thermocouple would yield in the predicted environment. The properties assumed for the virtual thermocouples were: length = 1 cm; bead diameter

=3 mm; density = 5000 kg/m³; specific heat = 500 J/kgK; thermal conductivity = 1 W/mK; and an absorption coefficient = 0.9.

The numerical time step used was roughly 0.01 s, and a maximum Courant number of 1.0 was used for the simulations. The SIMPLEC algorithm was used, with a tri-diagonal matrix solver for solution of the transport equations. The pressure correction equation was solved using a Stone solver. The maximum number of iterations on the energy and species equations was 5. The maximum number of iterations on the pressure correction equation was 500. The maximum number of iterations on the other equations was set to 5. The linear solver convergence criterion was set to 1×10^{-4} . A second order upwind scheme was used (weighted 90% to 2nd order with 10% to first order). Picard looping was not used.

The run times were around 4 - 6 days on a single processor Linux workstation, with the exception of the refined mesh simulation. The table below lists the simulations that were performed.

Table 1 VULCAN simulations

List of simulations performed with Vulcan	Fuel mass loss rate	Turbulence model	Grid
Calculated m \dot{m} (coarse)	calculated	k- ϵ	coarse
Calculated m \dot{m} (fine)	calculated	k- ϵ	fine
Specified m \dot{m}	specified	k- ϵ	coarse
BVG	specified	BVG	coarse

15 **Comments on Experimental Data**

Before proceeding with the results of the code, it is appropriate to comment on the experimental data and problem description. Fire codes have many different inputs/parameters that can be adjusted. When specifying a problem for code validation, it is generally accepted that the less uncertainty associated with the inputs, boundary conditions, and assumptions a user must make to model the problem, the better one can ascertain the ability of the code to predict the experiment. The ICFMP deviated from this philosophy, since they had a desire to also get a sense for the differences in results one could expect when the inputs, boundary conditions, and assumptions are not well-defined (as would be the situation when modeling a real NPP). This approach, while understandable, does not lead to a true test of a code's capability. When the inputs, boundary conditions, and assumptions that need to be applied are not well-quantified, a user must make assumptions for particular inputs and boundary conditions. The different assumptions a modeler can make can lead to a variety of answers. These degrees of freedom make it impossible to make a meaningful comparison between codes (or even between code and experiment), as the modelers are essentially specifying '*different*' problem statements based on their particular set of assumptions.

Information given regarding the fan and hood ventilation ducts was a bit unclear. An assumption was made (in these simulations) that the specified velocity for the fan system was actually too high by a factor of 2, if one simulates both of the exhaust outlets. This assumption was made to correct what appears to be an inconsistency between the specified volumetric flow rate and specified velocity through the ventilation ducts. The experimentalists later concurred that this assumption was in fact correct. It should be noted that discussions with several ICFMP participants were necessary to clarify the experimental setup and pertinent choices for some code inputs.

Other important features were also not well-characterized. The location of leakage (relative to the location of the oxygen sensor) is very important for prediction of oxygen levels and flame location in an under-ventilated fire, and this input was not specified. It was assumed for all of the present simulations that the leakage location was near the floor in both side walls of the compartment.

Heat transfer to the back side of each of the 3 targets was similarly poorly characterized, as were the target surface properties. Liquid fuel heat of vaporization

was not well known. *All of these contribute in adding uncertainty as to exactly what problem inputs should be specified in order to model the experiment.* However, as noted above, this philosophy was partly intentional on the part of the ICFMP, and should be understood in the context of the goals of the ICFMP.

I6 Results

As shown in the previous table, four simulations were performed. One simulation specified only the ventilation flows through the ducts and hood (the mass loss rate from the fuel pool was calculated by the code). A refined mesh simulation of this case was also performed to explore grid resolution effects. Another simulation specified the mass loss rate of the fuel pool in addition to the ventilation flows through the ducts and hood. Finally, a simulation with specified pool mass loss rate and specified ventilation was performed using a buoyant vorticity generation model (BVG) modification to the standard k- ϵ turbulence model.

I6.1 Simulation with mass loss rate prediction

A simulation was performed in which the experimentally measured mass loss rate was directly calculated based on the thermal response of the fuel pool. The experimentally measured ventilation duct and hood flows were specified as input data to the calculations. However, the specified velocities for the ventilation ducts were divided by a factor of two, as there appeared to be some discrepancy (see above discussion) between the reported volumetric flow rates and duct velocities. This same ventilation rate was specified for all of the simulations presented in this report.

I6.1.1 Mass loss rate and oxygen fraction

The predicted mass loss rate is compared to the data in Fig. I4. The simulation results are highly transient, and make it difficult to make a direct comparison. In order to facilitate direct comparisons to the data, the results are time-smoothed using a 10 second interval for computing a 'running-average'. This smoothing technique is used for the majority of results that are presented in order to facilitate direct comparisons to the data. The smoothed mass loss rate results are shown in Fig. I5. The predicted mass loss rate tracks the experimental data quite well for the first 500 seconds. The prediction begins to depart from the data about 500 seconds after ignition, returns to the data at about 650 seconds, and then departs from the data again at 850 seconds. After this time, there is a large difference in the prediction and experimentally observed results. However, for the first 900 seconds of the transient, the predicted and experimental mass loss rates are in good agreement, indicating that reasonable CFD

prediction of mass loss rate in under-ventilated fires is achievable. This result is especially encouraging considering the uncertainty in the fuel properties, since it was a mixture of different components.

To assist in understanding the behavior of the mass loss rate prediction, it is instructive to consider the local oxygen prediction shown in Fig. I6. The local oxygen (measurement location GA1) was measured at a single location 3.8 m above the floor (and located near the wall with the 3 targets). The predicted local oxygen fraction (note: at the single measurement location) drops to zero around 550 seconds after ignition, as compared to 1100 seconds in the data. Based on the behavior of the mass loss rate and local oxygen predictions, it can be inferred that ventilation-limited burning begins around a time of 620 seconds in the simulation, compared to a time of 1100 seconds in the data.

It is inconsistent that the experimental results indicate that substantial oxygen returns to the compartment at 1400 seconds, but the mass loss rate remains at a very low rate over the last 300 seconds of the experiment (from 1400 to 1700 seconds). The very sharp spike in the experimental mass loss rate would appear to result from more than just the heat up of the compartment with time. It could also be attributed somewhat to greater exposure of the fuel pan as the fuel level drops, and the effects of a multi-component fuel with different properties for each component. However, neither of these phenomena should produce such a large (seemingly non-physical) increase in mass loss rate as observed in the experiment. While Vulcan does account for the effect of room heat up, it does not account for either of these other two phenomena, which could be the reason that the sharp spike in mass loss rate is not reproduced in the simulation results, although the credibility of the experimentally observed spike appears questionable.

Regarding the predicted versus experimental oxygen fractions, one possible reason for the observed discrepancy is that the numerical simulation assumes that all the walls are perfectly leak-proof (with the exception of the leakage area suggested in the experiment report). Increased leakage area above that specified would explain this discrepancy. It should also be noted that the oxygen measurement was a point measurement. The specified leakage was assumed (in the numerical simulation) to be at floor level. If the actual leakage were located near the measurement point, it could easily explain this discrepancy, even without assuming an increased leakage area beyond that specified. However, based on the overall behavior of the mass loss rate,

the location of the leakage does not appear to be a big factor. Another possibility is that the velocity specification assumed for the ventilation ducts was incorrect (see discussion above regarding this). Other possible reasons for the discrepancy could be that the flow through the doorway is under-resolved, or that the combustion model is over-predicting the burning rate (given the mass loss rate). Based on the author's experience with Vulcan, neither of these last two possibilities would yield a discrepancy as large as observed in the present case. Therefore, the reason for the discrepancy is believed to be due to an underestimate of the amount of leakage into the compartment, or an incorrect specification of the ventilation duct velocity.

I6.1.2 Doorway velocities

The doorway velocities are shown in Fig. 17. Predicted velocities in the lower doorway (~ 1 m/s) are about half of the measured values (~ 2 m/s) before oxygen depletion occurs, and then are in good agreement with the data during the post-depletion period. These lower velocities would contribute to the predicted early depletion of oxygen, and may explain the large differences observed in oxygen concentration. The predicted velocities in the upper doorway (0 - 2 m/s out of the room) significantly under-predict the data (5 - 10 m out of the room). This could result from the under resolution of the doorway (i.e., the mesh is too coarse), but the fine mesh results suggest otherwise.

I6.1.3 Thermocouple temperatures

The measured thermocouple temperatures were compared to the predicted thermocouple temperatures obtained via the virtual thermocouple model. For fires of this type (under-ventilated), the presence of hot combustion products throughout the fire room tends to equilibrate the temperature field, such that large differences between thermocouple temperatures and actual gas temperatures would not be expected (apart from the initial lag in the measurements). This was indeed the case when the numerical predictions for gas temperatures were compared to the predictions for thermocouple temperatures (i.e., there was very little difference, other than some lag in the predicted virtual thermocouple results relative to the predicted gas temperatures). Therefore, only virtual thermocouple temperatures (and not gas temperatures) are presented in this report.

The temperature comparisons can be considered for two periods of time: pre-oxygen depletion and post-oxygen depletion. For the post-oxygen depletion period, the predictions all under-predict the data. The temperatures directly above the fuel pool (i.e., the plume temperatures) are shown in Fig. I8 at 3 elevations. The predicted temperature at M1 (low above the pool, at $z = 1$ m) under predicts the data initially (by about 300 C), and then is in good agreement with the data near the point of oxygen depletion. This under-prediction is typical low in the plume, and results from an under-prediction of the turbulence. This is somewhat a consequence of using a standard $k-\epsilon$ model (although it is readily observed in LES models, as well), since they are based only on shear-generated turbulence, whereas buoyancy-generated turbulence is also important near the base of a pool fire. Beyond the point of oxygen depletion, the predicted temperature shows the same trends as the data, but is lower by about 200 C. The predicted temperatures directly above the fuel pool at M3 (elevation of 2.4 m above the pool) are in very good agreement with the measured thermocouple data up to the point of oxygen depletion. Beyond that point, the predictions are lower by about 100 K. The predicted temperatures at M6 (5.2 m above the pool) are slightly higher than the data initially (by 50-100 C), and then under predict the data after oxygen depletion occurs.

The temperatures in the front of the room are shown in Fig. I9. For the pre-depletion period, the correct trends are reproduced (the virtual thermocouple model at higher elevations predicts higher temperatures). However, all of the predicted temperatures are greater than the measured values (within 200 C). A similar result is observed for the temperatures in the back of the room, as seen in Fig. I10. However, here the predictions exceed the measurements by a greater amount (as much as 400 C). This could result from the predicted flame being tilted more toward the back of the room than occurred in the experiment.

I6.1.4 Target heat fluxes and temperatures

One of the target heat flux gauges was mounted on a sidewall. As shown in Fig. I11, the measured heat flux to the gauge during the pre-depletion period is reproduced very

well (within 5 kW/m²) by the simulation¹. Following depletion of the oxygen, the agreement between experiment and simulation is not as good (as expected, given the different burning conditions). Similarly, as shown in Fig. I12, the heat fluxes to the 3 targets slabs are also very well reproduced during the pre-depletion period (within 10 kW/m²), with considerable disagreement with the data following depletion. The surface temperatures of the target slabs are shown in Fig. I13, and the predictions are within 100 C before oxygen depletion occurs. Discrepancies can be attributed to a lack of knowledge of the surface properties of the material targets, back side heating effects, and perhaps temperature-dependent thermal properties of the materials. The influence of the temperature 'probe' on the target (not included in the code) may also be significant near the target surface, affecting the thermal response.

One of the target heat flux gauges was mounted on a sidewall. As shown in Fig. I11, the measured heat flux to the gauge during the pre-depletion period is reproduced very well (within 5 kW/m²) by the simulation². Following depletion of the oxygen, the agreement between experiment and simulation is not as good (as expected, given the different burning conditions). Similarly, as shown in Fig. I12, the heat fluxes to the 3 targets slabs are also very well reproduced during the pre-depletion period (within 10 kW/m²), with considerable disagreement with the data following depletion. The surface temperatures of the target slabs are shown in Fig. I13, and the predictions are within 100 C before oxygen depletion occurs. Discrepancies can be attributed to a lack of knowledge of the surface properties of the material targets, back side heating effects, and perhaps temperature-dependent thermal properties of the materials. The influence of the temperature 'probe' on the target (not included in the code) may also be significant near the target surface, affecting the thermal response.

I6.2 Refined mesh results

In order to assess the effect of grid resolution on the results, a simulation was performed with a fine mesh for the case with calculated mass loss rate from the pool.

¹ The heat flux results from the simulation were computed using a running average over a 10 second time period, in order to smooth out shorter frequency temporal variations.

² The heat flux results from the simulation were computed using a running average over a 10 second time period, in order to smooth out shorter frequency temporal variations.

The simulation was carried out for about 1000 s. Fig. I14 shows the calculated mass loss rate versus the experimental data. There is an initial discrepancy between simulation and experiment, as a result of the fact that Vulcan injects fuel initially in order to get the combustion process started above a pool. The mass loss rate results quickly approach the experimental data following the initial ignition process, and follow the data reasonably closely until about 800 seconds, when the experimentally determined mass loss rate begins to increase significantly. The fine mesh results are quite close to the coarse mesh results for mass loss rate.

The oxygen percentage in the fire room at the single measurement location is shown in Fig. I15 for the fine mesh and for the experiment. The oxygen depletion for the fine mesh simulation occurs at about the same rate as for the coarse mesh (see Fig. I6).

A comparison of the doorway velocities (not shown) between the coarse and fine mesh results are in good agreement. This diminishes the likelihood that the doorway velocities were under-resolved in the coarse grid simulation.

The plume temperatures for the fine mesh simulation are shown in Fig. I16, and are compared directly to the coarse mesh results. The results are basically the same as for the coarse mesh simulations, although there is some deviation initially in the results for M1 (the lowest thermocouple in the plume).

The heat fluxes to the 3 targets for the fine mesh simulation are compared directly to the coarse mesh results in Fig. I17. The results are in very good agreement with each other for the duration of the simulations. The fine mesh results are also in good agreement with the experimental data (shown in Fig. I12) for times before oxygen depletion occurred. Fig. I18 presents the thermal response of the surface of the 3 targets for the fine mesh simulation. Once again, the results are in good agreement with the coarse mesh result.

Since heat fluxes and surface temperatures are generally regarded as the metrics of primary interest for fire simulations, the results of the fine mesh simulation suggest that the coarse mesh solutions are of adequate resolution for this problem. Therefore the remaining simulations were performed with the coarse mesh.

I6.3 Simulation with specified mass loss rate

A simulation was performed in which the experimentally measured mass loss rate was specified as input to the calculations. The experimentally measured ventilation duct and hood flows were also specified as input data to the calculations.

I6.3.1 Oxygen concentration

The oxygen concentration within the fire room at the measurement location is shown in Fig. I19. The simulation predicts oxygen burnout in the room considerably earlier (at ~750-850 s) than measured (at ~1100 s). Consequently, the simulation predicts the room will begin to refill with oxygen at an earlier time (at ~1225 s) than in the experiment (at ~1325 s).

I6.3.2 Doorway velocities

The doorway velocities are shown in Fig. I20. The experimentally measured velocities in the lower doorway indicate that the flow is alternately in and then out through the lower doorway. The predicted velocities for the lower doorway indicate that the flow is primarily into the room through the lower doorway, but the average value of the prediction is consistent with the measurements. The predicted upper doorway velocities are directed primarily out of the room, in agreement with the data, but the average values are substantially lower than the measured values.

I6.3.3 Thermocouple temperatures

The temperatures directly above the fuel pool are shown in Fig. I21 at 3 elevations. The predicted temperature at M1 (low above the pool, at $z = 1$ m) under predicts the data initially (by about 200 C), and then is in good agreement with the data at later times (prior to total oxygen depletion in the room). Note that due to the earlier depletion of oxygen in the simulations, all of the simulation results are expected to drop off earlier than the measurements, and this is indeed the case. The predicted temperatures directly above the fuel pool at M3 (elevation of 2.4 m above the pool) are in very good agreement with the measured thermocouple data. The predicted temperatures at M6

(5.2 m above the pool) over predict the data initially (by about 150 C), and then under predict the data (by about 100 C) before total oxygen depletion occurs.

It is interesting to note the trends in the temperature decay as total oxygen depletion occurs. The temperature decay appears to be predicted quite well by the code, but occurs earlier in time (per the previous discussion). The temperature lower in the compartment (M1) decays the most rapidly, with temperatures at the higher elevations (M3 and M6) decaying more slowly.

16.3.4 Target heat fluxes and temperatures

The heat flux results are presented in Fig. I22 for four locations. For the aerated concrete (WS4), concrete (WS3), and surface mounted heat flux gauge, the predictions show very good agreement with the data until the time when oxygen depletion occurs. Since oxygen depletion occurs sooner in the simulation, the predicted heat fluxes also decrease sooner than the measured values (as expected).

The heat flux results for the steel probe do not show as good agreement as the results for the other targets. The predicted values are roughly 25 kW/m² higher than the data. The reason for this could be that the predicted flame shape is stretched toward the back of the room to a greater degree than in the experiment.

The target surface temperature results are presented in Fig. I23. The aerated concrete surface temperature predictions over predict the data by about 100 C for times less than the predicted oxygen depletion time. This is surprising in view of the relatively good agreement in heat fluxes. The Vulcan code assumes that surfaces are gray, i.e., that they absorb and emit thermal radiation with an absorptivity that is equal to the emissivity. If the absorptivity of the aerated concrete is less than the emissivity, this could explain the difference in the target temperature results. The concrete target surface temperature predictions are in good agreement with the data up to the time of total oxygen depletion (as expected in view of the good agreement of the heat fluxes). The steel target surface temperature predictions are in good agreement with the data up to a time of approximately 500 s, after which the predictions are lower than the data. The good agreement is fortuitous in view of the differences in heat flux for the steel target, and could result from heating of the back side of the steel plate in the experiments.

Overall, during the pre-oxygen depletion period, the results of the simulation conducted with a specified mass loss rate are not significantly different than the results for the case with a calculated mass loss rate. This is expected since the experimental fuel mass loss rate is reasonably reproduced by the fuel mass loss rate model in Vulcan during the pre-depletion period.

16.4 Simulation with BVG Turbulence Model, Specified Mass Loss Rate

Standard $k-\epsilon$ models include only shear-generated turbulence mechanisms. This results in an under-prediction of the turbulence in pool fires, since much of the turbulence in pool fires is generated from buoyancy (as opposed to shear). In order to assess the impact of including buoyancy-generated turbulence on the results, a simulation was performed in which the BVG turbulence model variation of the standard $k-\epsilon$ model was used. The experimentally measured mass loss rate was specified as input to the calculations, as were the experimentally measured ventilation duct and hood flows. Note that use of the BVG turbulence model in Vulcan for fire simulations is a standard procedure for certain types of fires, and the decision to use the BVG model as part of the suite of simulations was made before observing the results of the standard $k-\epsilon$ model.

16.4.1 Oxygen concentration

The oxygen concentration within the fire room at the measurement location is shown in Fig. I24. The simulation predicts oxygen burnout in the room considerably earlier (~400 s) than measured (~1100 s). This is also considerably earlier than predicted using the standard $k-\epsilon$ model (~750-800 s). The BVG model consumes oxygen faster than the standard model due to its prediction of higher turbulence levels (and hence, more mixing and more combustion) as a result of the inclusion of buoyancy generated turbulence. The reasons for the discrepancy with the data are believed to be as discussed previously. The simulation predicts the room will begin to refill with oxygen at approximately 1225 s, versus ~1325 s in the experiment.

I6.4.2 Doorway velocities

The doorway velocities are shown in Fig. I25. The experimentally measured velocities in the lower doorway indicate that the flow is alternately in and then out through the lower doorway. The predicted velocities for the lower doorway indicate that the flow is primarily into the room through the lower doorway. The BVG lower doorway velocities are slightly higher on average (~ 2 m/s) than for the standard k- ϵ model (~ 1 m/s) over the first 600 seconds, and in better agreement with the data. The BVG model could produce higher inflow through the doorway as a result of higher combustion levels from enhanced turbulence (and hence fresh air pulled into the room more strongly). The good/reasonable agreement with measured lower doorway velocities would indicate that sufficient oxygen is pulled into the room through the doorway, so the reason for the under-prediction of oxygen concentration lies elsewhere (perhaps in the leakage). The predicted upper doorway velocities are directed primarily out of the room, in agreement with the data, but the average values are substantially lower than the measured values (and are about the same as for the standard k- ϵ model results).

I6.4.3 Thermocouple temperatures

The temperatures directly above the fuel pool are shown in Fig. I26 at 3 elevations. The predicted temperatures at all three locations are in good agreement with the data initially (the first ~800 seconds). Note that due to the earlier depletion of oxygen in the simulations, all of the simulation results are expected to drop off earlier than the measurements, and this is indeed the case. The BVG model predicts enhanced turbulence levels low in the plume (as a result of buoyant production) relative to the standard k- ϵ model, and results in more combustion and higher temperatures low in the plume. This results in better agreement between simulation and experimental results low in the plume (location M1).

The temperatures in the front of the room are shown in Fig. I27. The correct trends are reproduced and the predicted temperatures are in good agreement with the measured values, similar to the standard k- ϵ model results. Similar comments apply to the results for the temperatures in the back of the room, shown in Fig. I28.

I6.4.4 Target heat fluxes and temperatures

The heat flux results are presented in Fig. I29 for four locations. For the steel (WS1), concrete (WS3), and surface mounted heat flux gauge, the predictions show very good agreement with the data until the time when oxygen depletion occurs. Since oxygen depletion occurs sooner in the simulation, the predicted heat fluxes also decrease sooner than the measured values (as expected).

The heat flux results for the aerated concrete probe do not show as good agreement as the results for the other targets. The predicted values are roughly 20 kW/m² higher than the data. The reason for this could be that the predicted flame shape is not tilted toward the back of the room as much as in the experiment. The enhanced turbulence of the BVG model increases the turbulent viscosity, which does not allow the flame shape to be as readily tilted backward by the incoming fresh air flow.

The target surface temperature results are presented in Fig. I30. The agreement with data is about the same for the BVG results as for the standard k-ε model results.

During the pre-oxygen depletion period, most of the BVG results are similar to the results for the simulation with the standard k-ε model. There are 3 exceptions to this statement: 1) the oxygen depletion occurs faster with the BVG model, 2) the temperatures low in the plume are better predicted, and 3) the lower doorway velocity is more accurately predicted. All of these are attributable to the inclusion of buoyancy generated turbulence by the BVG model.

I7 Discussion

The results presented were obtained without any 'tuning' of parameters, using only a single 'best estimate' of the inputs. In this sense, they are indicative of the level of agreement that can be expected in typical applications where there are no experimental data available. This approach is consistent with the ICFMP philosophy.

The agreement between simulation and experiment is best discussed in terms of 2 time periods: pre-oxygen depletion and post-oxygen depletion. For the pre-oxygen depletion period, the fire behaves essentially as an open pool fire in a cross-wind (due to the doorway inflow effect). For this period of time, the code predictions are generally in good to reasonable agreement with the data. Following oxygen-depletion of the fire room, the fire becomes ventilation limited. The agreement between code and experiment during this period (the post-oxygen depletion period) is generally not as good. The lack of agreement is not believed to be due to the inability of the code to simulate this environment, but more due to the lack of specificity of the airflow pathways. In the post-oxygen depletion period, the fire begins to burn wherever it finds available oxygen. For this experiment, available oxygen would be found at the doorway and at any leakage paths into the fire room. Since these pathways were difficult to characterize as to location and size, good agreement would not be expected for this time period. For the post-oxygen depletion period, the predicted temperatures are lower than those measured. This suggests (as with the oxygen depletion occurring too soon in the simulations) that leakage into the compartment was under-estimated in the simulations.

The sources of discrepancies in the results are difficult to identify, and in this regard the results of this exercise are not very satisfying. Without a rigorously controlled and documented experiment, it is impossible to separate out modeling uncertainty from measurement uncertainty. One cannot ascertain whether the source of discrepancy is something incorrect in the code, or if the discrepancy arises because the problem being modeled differs from what existed in the experiment. Several possibilities can be put forth, but it is impossible to pin down the source of a discrepancy in such cases. For example, the inability to rigorously determine leakage into the compartment, and the location of that leakage, makes it impossible to determine if premature oxygen depletion in the simulations occurs as a result of too fast burning by the combustion

model, or as a result of incorrect boundary conditions for the inflow³. Similarly, the source of the discrepancy in the thermal response of the surface of the targets can not be ascertained unless the surface properties and temperature dependency of the thermal properties are well-characterized. Use of a multi-component fuel in the experiments resulted in additional ambiguity in the problem specification. With such important inputs to the code not well characterized, this particular experiment does not serve as a good validation exercise for a specific code.

The early oxygen depletion in the simulation results is believed to be indicative that some input from the experiment is not being specified properly in the code (as opposed to there being something wrong with the code itself). Since Vulcan conserves mass, species, energy, and momentum, early oxygen depletion in the simulation results is indicative that a leakage pathway was not correctly specified, or that the assumed ventilation rate was incorrect. As mentioned above, the ventilation rate discrepancy appearing in the experimental description was eventually clarified by the experimentalists, and should not be the reason for the early oxygen depletion observed in the simulations.

Having made the above statements, it is also acknowledged that one of the goals of the ICFMP was to examine the level of predictive capability for situations where a user does not accurately know all of the input details (such as leakage pathways, surface thermal properties, etc.). In this sense, the experiments provided results with the desired level of accuracy for the purposes of the ICFMP.

³ For most NPP fire applications, the amount of leakage into a room will be very difficult to rigorously ascertain (as a result of pipe chases, penetrations, seals, etc.). If the simulation results are indeed strongly sensitive to the amount of leakage, this has strong implications for the confidence one can place in the results of simulations for oxygen-limited fires (since rigorous specification of the leakage is difficult for most real NPP fire applications). Further study would be needed to determine the sensitivity of the code results to the leakage specification.

18 Conclusions

The Vulcan fire code was used to simulate Benchmark Exercise No. 4, Test 3 of the ICFMP. Best estimates were used for the inputs. Oxygen depletion was observed to occur significantly sooner in the simulations than in the experiment. The agreement between simulation and experiment is best discussed when separated into 2 time periods: pre-oxygen depletion, and post-oxygen depletion of the room. Prior to oxygen depletion, very good agreement was obtained for pool mass loss rate and the majority of heat fluxes to targets. The agreement was not as good for thermocouple temperatures, target thermal response, and doorway velocities. For times that are post-oxygen depletion, the agreement is generally not as good as for the pre-depletion period. This is understandable since the post-oxygen depletion environment is highly dependent upon the locations and amounts of leakage into the compartment. A fine mesh simulation produced essentially the same results as with the coarse mesh, suggesting the coarse mesh results were adequate. The inclusion of buoyancy generated turbulence in the simulations did not change the results substantially, but did improve the prediction of temperature low in the plume and the lower doorway velocity, while resulting in even faster oxygen consumption (relative to the standard $k-\epsilon$ model).

The sources of discrepancies between the predictions and data could not be definitively resolved due to uncertainties in the experiment and documentation. These discrepancies are believed to be primarily due to inputs to the code being significantly different than existed in the experiment. In that context this experiment is not recommended for code validation purposes, but does provide useful information regarding the potential uncertainties in code predictions when key inputs (e.g., leakage paths) are not accurately specified.

I9 References

- /HOL 90/ Holen, J., M. Brostrom, and B.F. Magnusson:
Finite Difference Calculation of Pool Fires, 23rd Symposium on Combustion,
Combustion Institute, pp. 1677-1683; 1990
- /JON 72/ Jones, W.P., and B.E. Launder:
The Prediction of Laminarization with a Two-Equation Model of Turbulence,
International Journal of Heat and Mass Transfer, vol. 15: 301-314; 1972
- /LAU 74/ /MAG , B.E., and D.B. Spalding:
The Numerical Computation of Turbulent Flows, Computer Methods in
Applied Mechanics and Engineering, vol. 3, pp. 269-289; 1974.
- /LEC 72/ Leckner, B.:
Spectral and Total Emissivity of Water Vapor and Carbon Dioxide,
Combustion and Flame, vol. 19, pp. 33-48; 1972
- /MAG 77/ Magnusson, B.F., and B.H. Hjertager:
On Mathematical Modeling of Turbulent Combustion with Special Emphasis
on Soot Formation and Combustion, 16th Symposium on Combustion, The
Combustion Institute, pp. 719-729; 1977
- /MAG 81/ Magnusson, B.F.:
On the Structure of Turbulence and a Generalized Eddy Dissipation
Concept for Chemical Reactions in Turbulent Flow, 9th AIAA Sc. Meeting,
St. Louis; 1981.
- /NIC 05/ Nicolette, V.F., S.R. Tieszen, A.R. Black, S.P. Domino, and T.J. O'Hern:
A Turbulence Model for Buoyant Flows Based on Vorticity Generation,
SAND2005-6273, Sandia National Laboratories report; October 2005
- /PAT 72/ Patankar, S.V., and D.B. Spalding:
International Journal of Heat and Mass Transfer, Vol. 15, p. 1787; 1972
- /SHA 79/ Shah, N.G.:
The computation of radiation heat transfer, Ph.D. thesis, University of
London, Faculty of Engineering; 1979

- /SFP 88/ Society of Fire Protection Engineering (SFPE):
SFPE Fire Protection Engineering Handbook, first edition, Society of Fire Protection Engineers, Quincy, MA; 1988
- /TES 71/ Tesner, P.A., T.D. Snegiriova, and V.G. Knorre:
Kinetics of dispersed carbon formation," Combustion and Flame, vol. 17, pp. 253-260; 1971
- /TIE 96/ Tieszen, S.R., V.F. Nicolette, V.F., L.A. Gritzko, J.K. Holen, D. Murray, and J.L. Moya:
Vertical Structures in Pool Fires: Observation, Speculation, and Simulation," Sandia National Laboratories report SAND96-2607, November 1996.
- /TIE 05/ Tieszen, S.R., Domino, S.P., Black, A.R.:
Validation of a Simple Turbulence Model Suitable for Closure of Temporally-Filtered Navier-Stokes Equations using a Helium Plume, Sandia National Laboratories report SAND2005-3210, June 2005.

I10 Acknowledgments

This work was funded by the U.S. Nuclear Regulatory Commission.

Helpful discussions in understanding the experimental setup and appropriate modeling parameters were conducted with W. Klein-Heßling (GRS), O. Riese (iBMB), K. McGrattan (NIST), and J. Sutherland (SNL). Helpful comments were provided by A. Brown (SNL) and N. Siu (USNRC) who served as reviewers of this report.

Sandia is a multi-program laboratory operated by Sandia Corporation, a Lockheed Martin Company, for the United States Department of Energy's National Nuclear Security Administration under Contract DE-AC04-94AL85000.

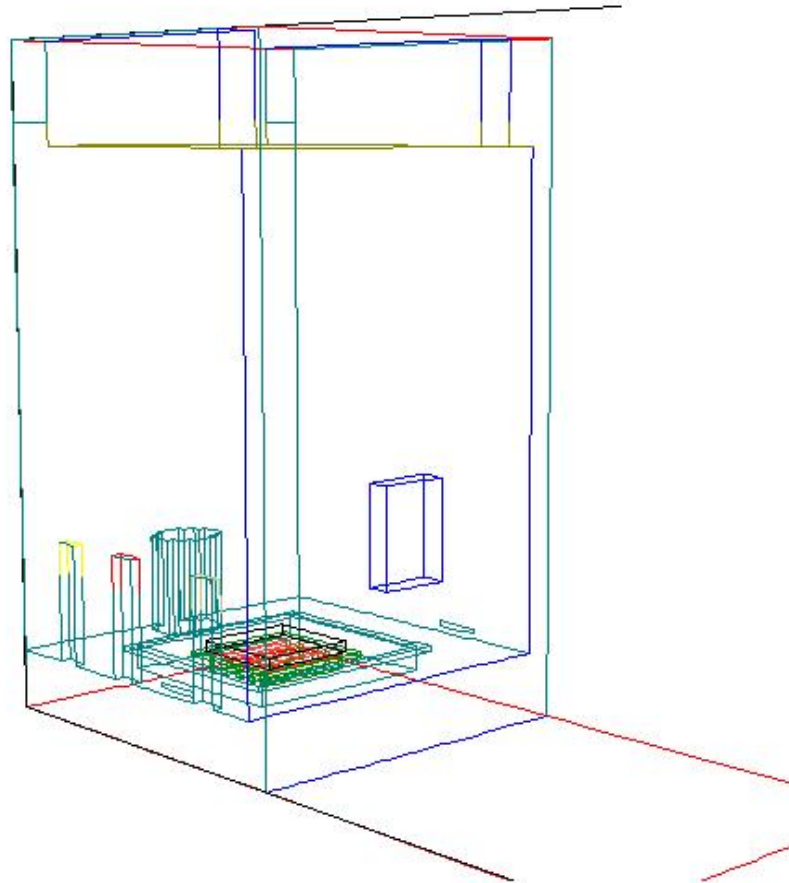


Fig. I 1 Wire frame sketch of fire room, showing pan of fuel on floor, barrel-type container against back wall, sidewall targets, doorway/window part-way up the front wall, and two ventilation duct outlets near ceiling (back wall). Hood is not shown for clarity.

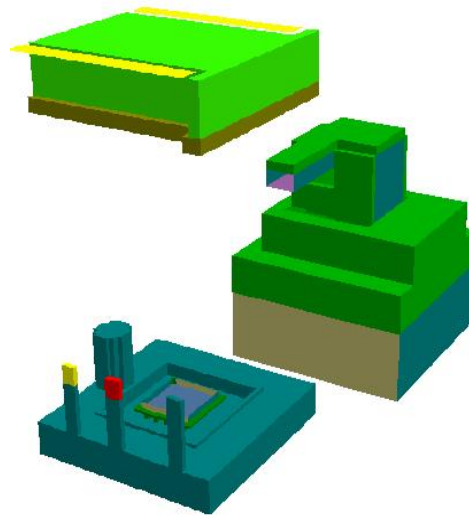


Fig. I 2 Geometry model (walls removed), including hood (object on the right). Cylindrical barrel is at back of room, opposite the doorway. Tops of ventilation channels in ceiling are denoted by yellow panels in ceiling of uppermost object.

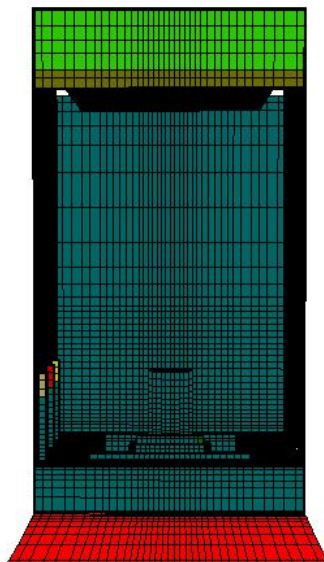


Fig. I 3 Non-uniform coarse grid used for fire room (front wall removed for clarity); view is looking toward the back wall. Note: x-axis is from left to right; y-axis is into the page; z-axis is from bottom to top of page.

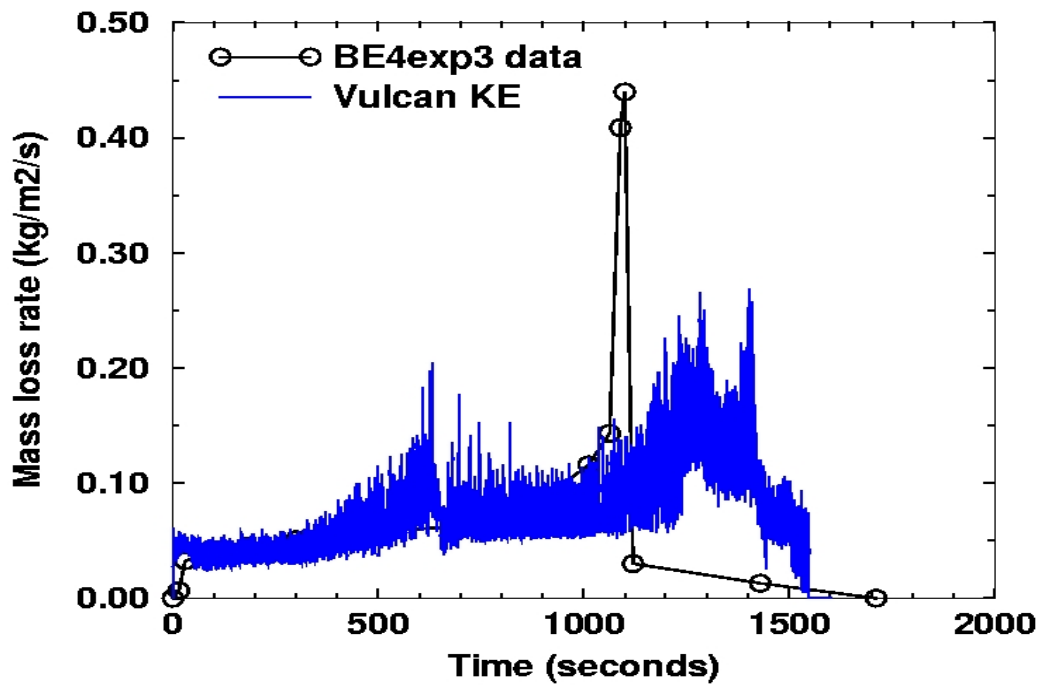


Fig. I 3 Mass loss rate (calculated) vs. experiment. "Vulcan KE" designates the results of the simulation using Vulcan with the standard k- turbulence model.

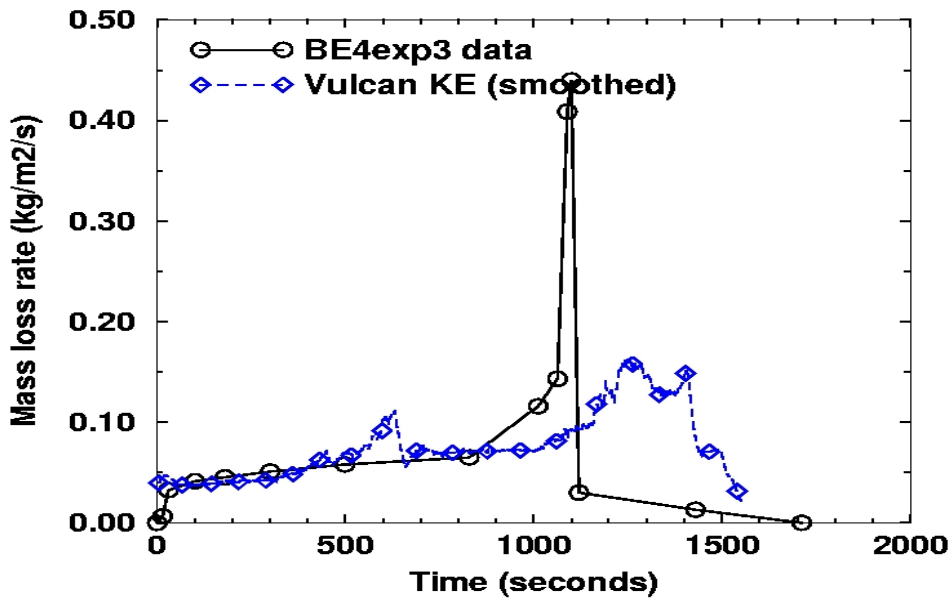


Fig. I 4 Mass loss rate (smoothed) vs. experiment. "Vulcan KE" designates the results of the simulation using Vulcan with the standard k- turbulence model.

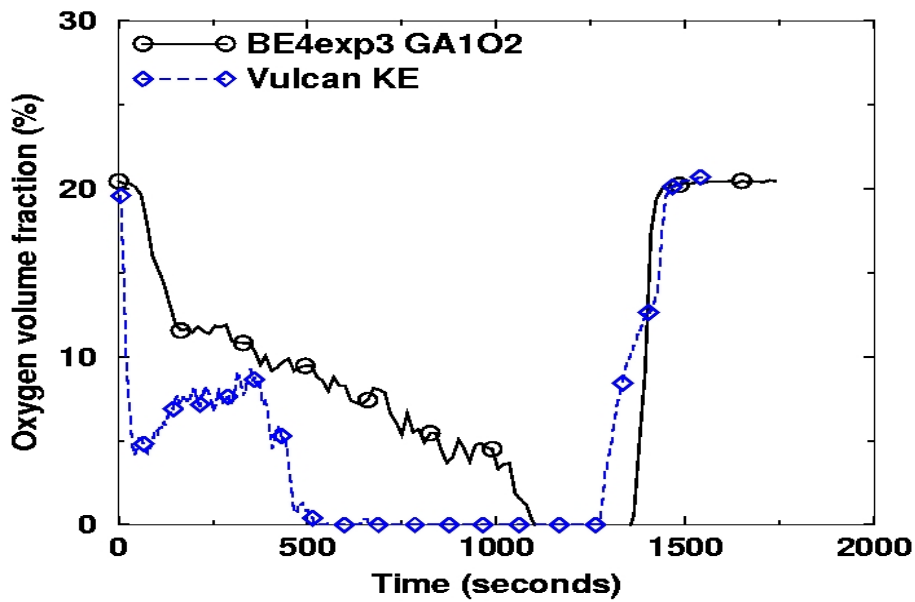


Fig. I 5 Oxygen percentage in fire room vs. experiment for simulation with calculated mass loss rate. "Vulcan KE" designates the results of the simulation using Vulcan with the standard k-ε turbulence model.

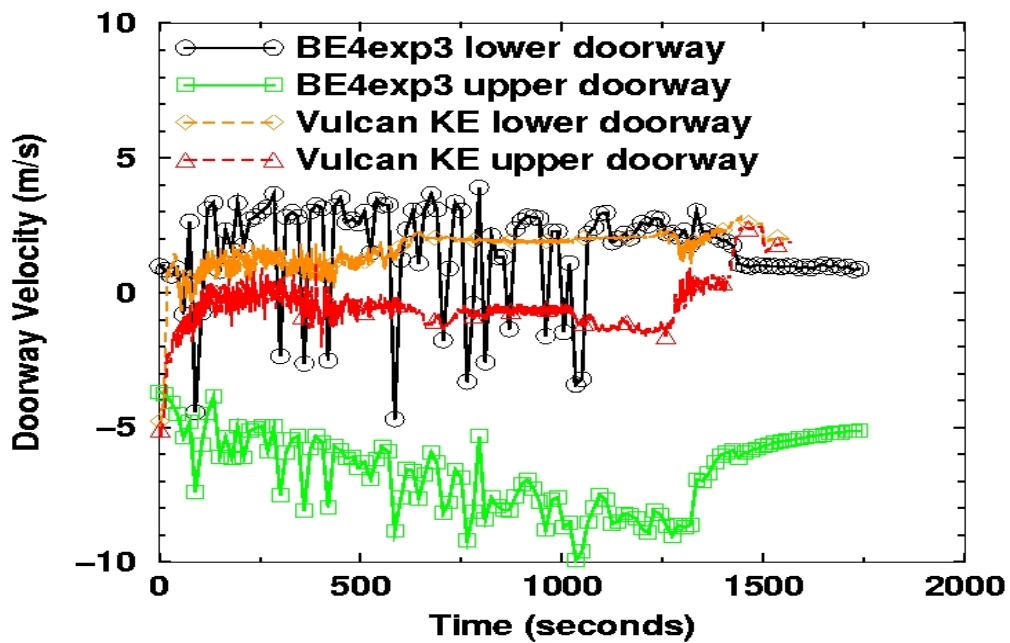


Fig. I 6 Doorway velocities vs. experiment for simulation with calculated mass loss rate. "Vulcan KE" designates the results of the simulation using Vulcan with the standard k-ε turbulence model.

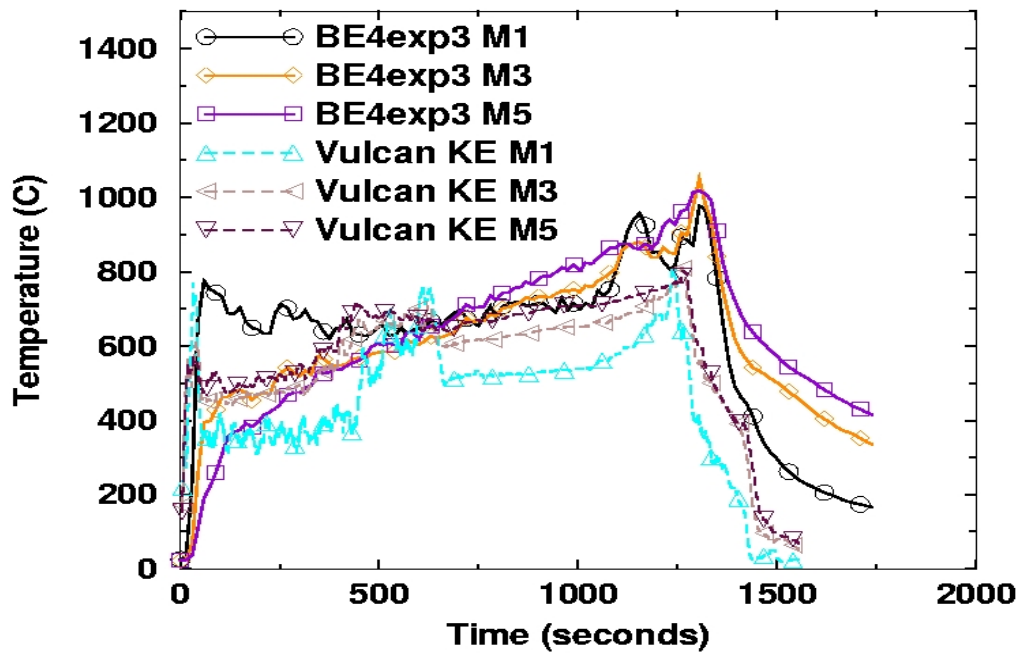


Fig. I 7 Plume temperatures vs. experiment for simulation with calculated mass loss rate. "Vulcan KE" designates the results of the simulation using Vulcan with the standard k- turbulence model.

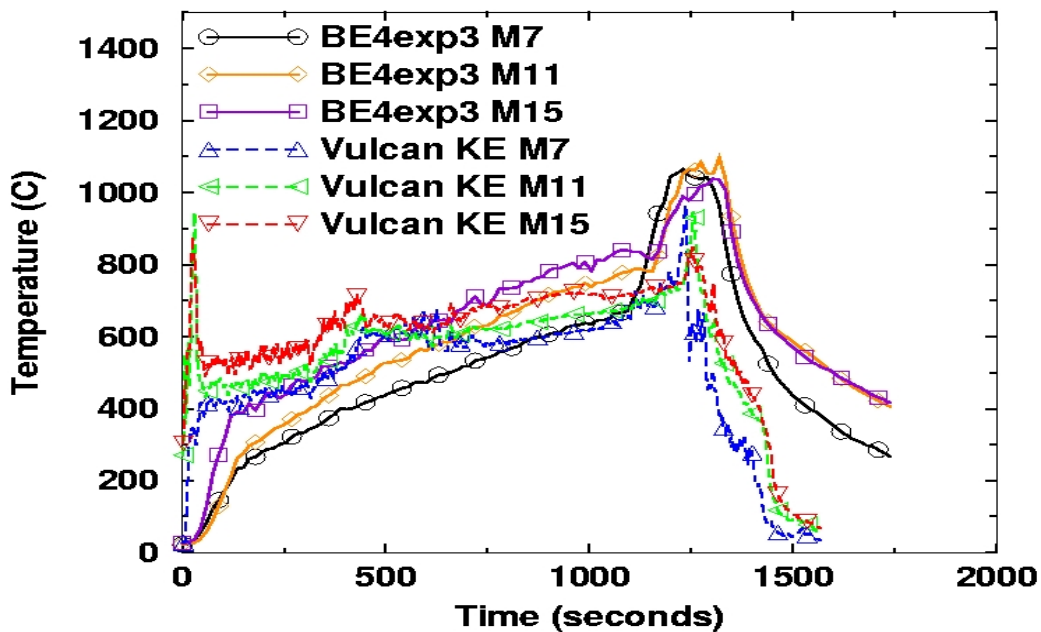


Fig. I 8 Front room temperatures vs. experiment for simulation with calculated mass loss rate. "Vulcan KE" designates the results of the simulation using Vulcan with the standard k- turbulence model.

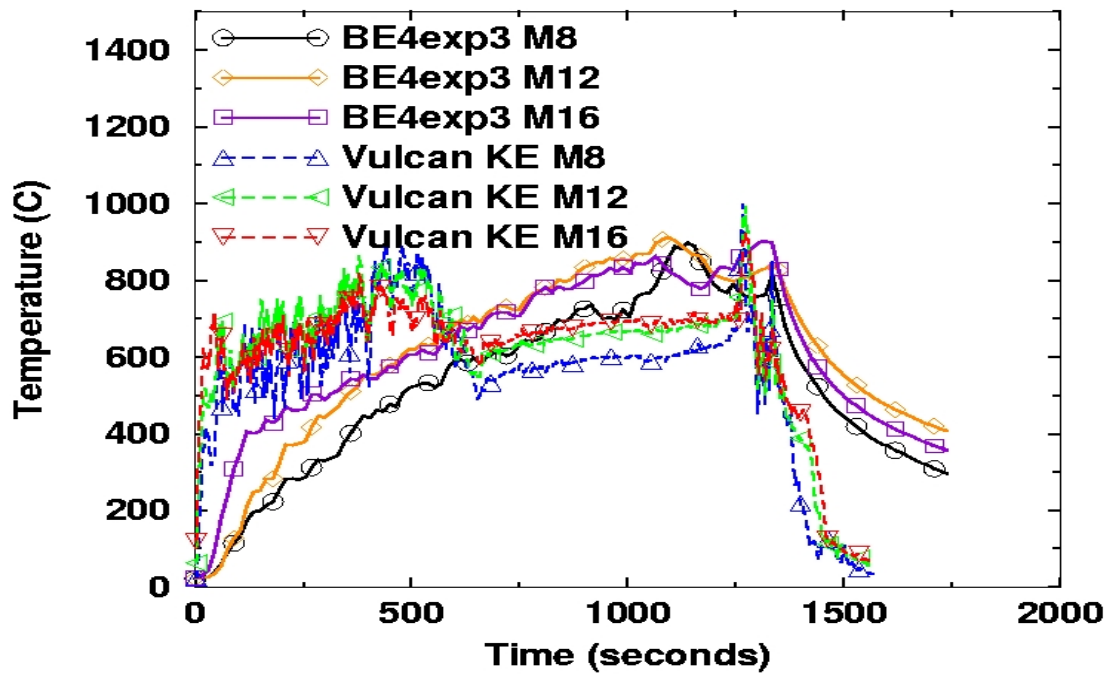


Fig. I 9 Back room temperatures vs. experiment for simulation with calculated mass loss rate. "Vulcan KE" designates the results of the simulation using Vulcan with the standard k- turbulence model.

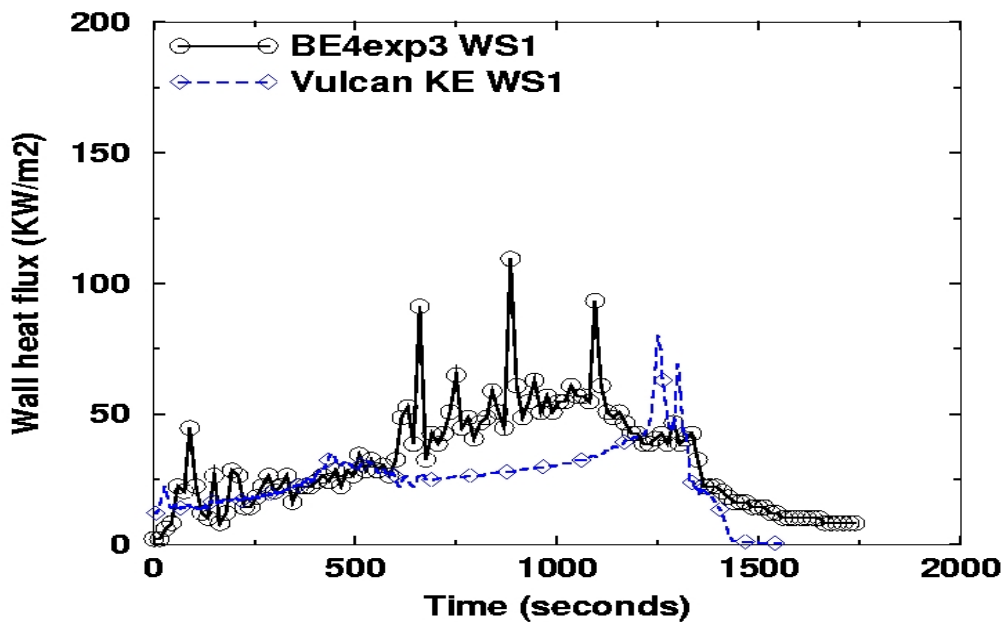


Fig. I 10 Heat flux to gauge embedded in sidewall vs. experiment for simulation with calculated mass loss rate. "Vulcan KE" designates the results of the simulation using Vulcan with the standard k- turbulence model.

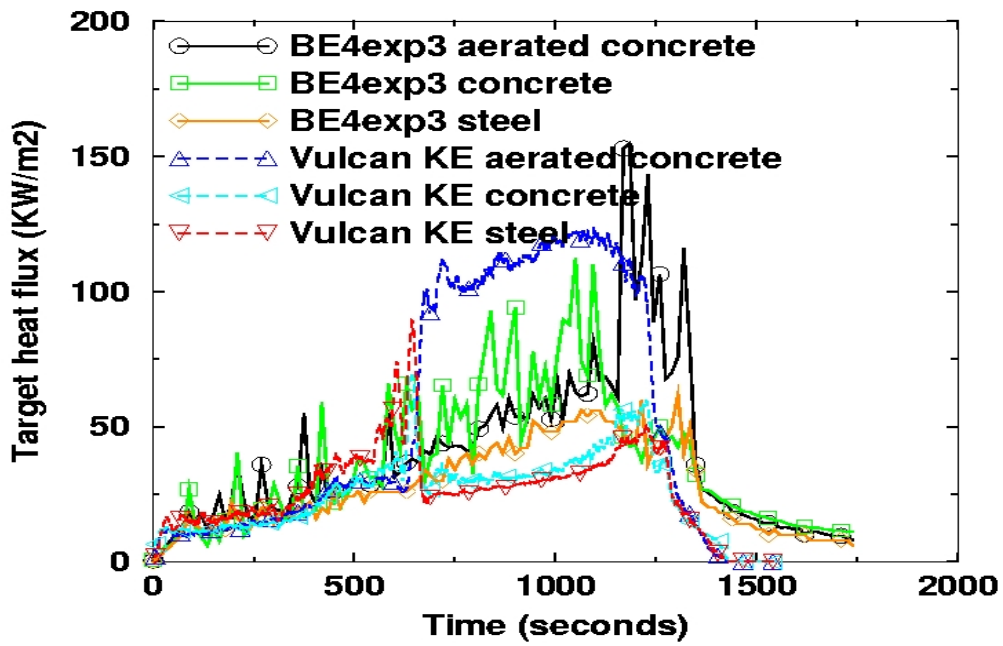


Fig. I 11 Heat flux to targets vs. experiment for simulation with calculated mass loss rate. "Vulcan KE" designates the results of the simulation using Vulcan with the standard k- turbulence model.

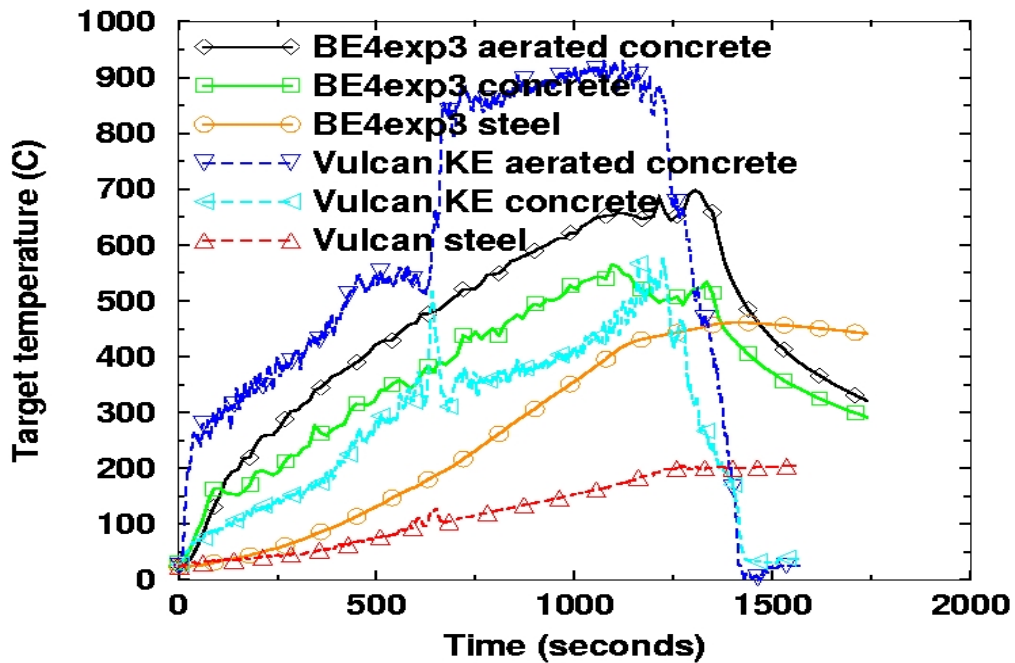


Fig. I 12 Surface temperatures of targets vs. experiment for simulation with calculated mass loss rate. "Vulcan KE" designates the results of the simulation using Vulcan with the standard k- turbulence model.

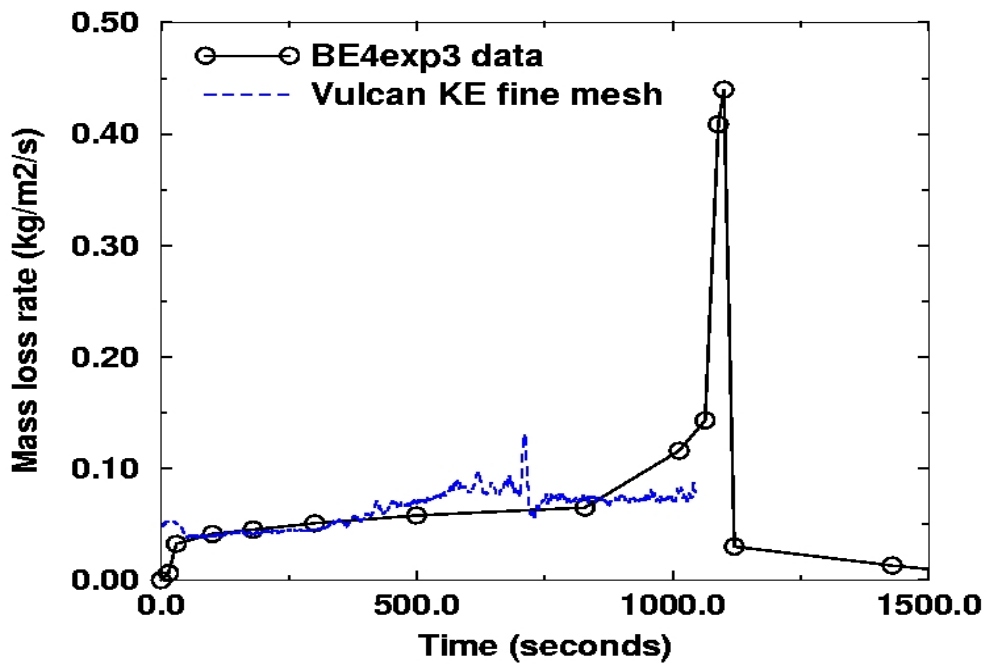


Fig. I 13 Fine mesh mass loss rate (smoothed) vs. experiment for simulation with calculated mass loss rate. "Vulcan KE" designates the results of the simulation using Vulcan with the standard k-ε turbulence model.

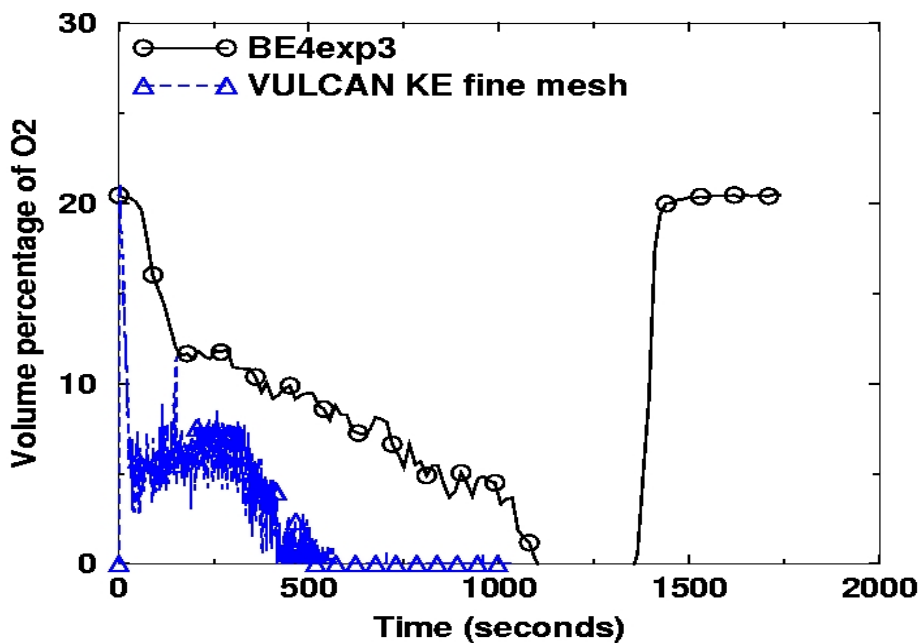


Fig. I 15 Fine mesh oxygen percentage in fire room vs. experiment for simulation with calculated mass loss rate. "Vulcan KE" designates the results of the simulation using Vulcan with the standard k-ε turbulence model.

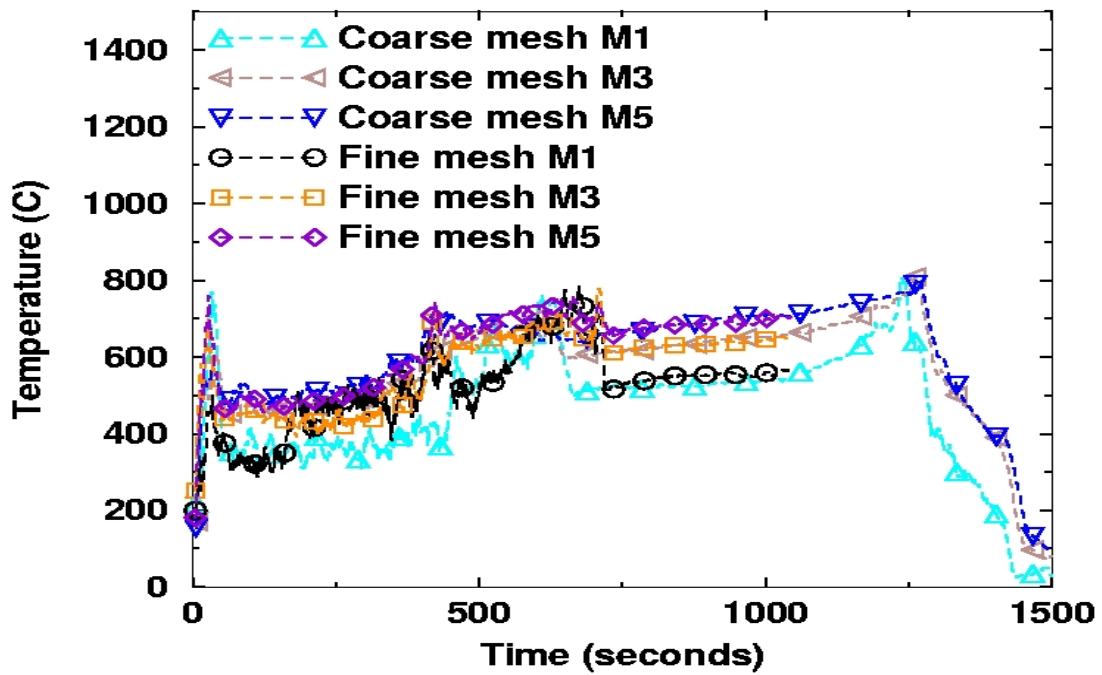


Fig. I 16 Fine mesh plume temperatures vs. coarse mesh results for simulation with calculated mass loss rate.

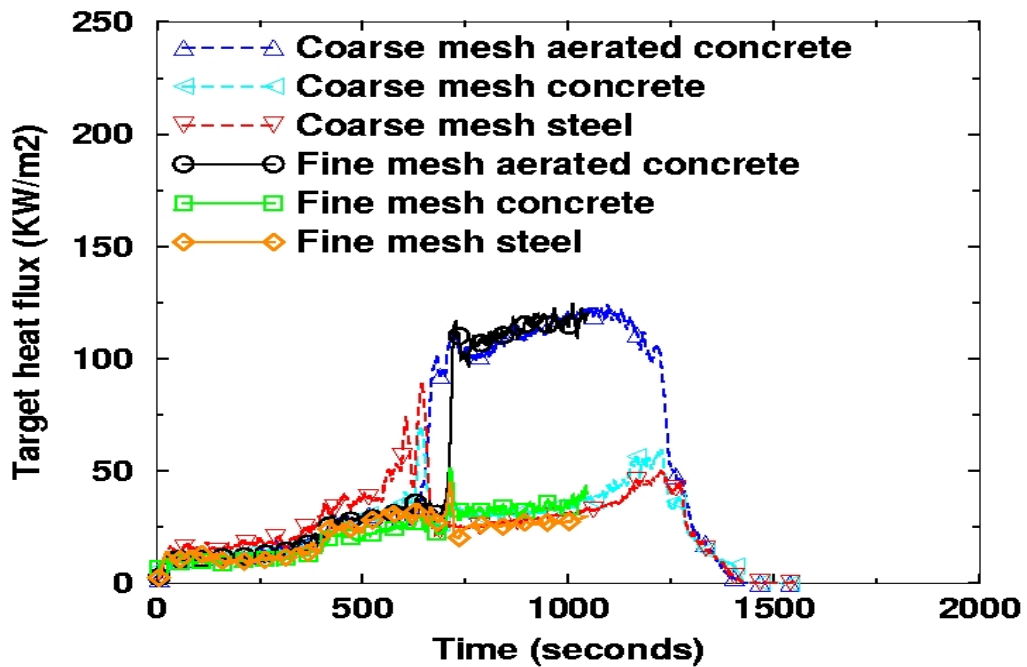


Fig. I 17 Fine mesh heat flux to targets vs. coarse mesh results for simulation with calculated mass loss rate.

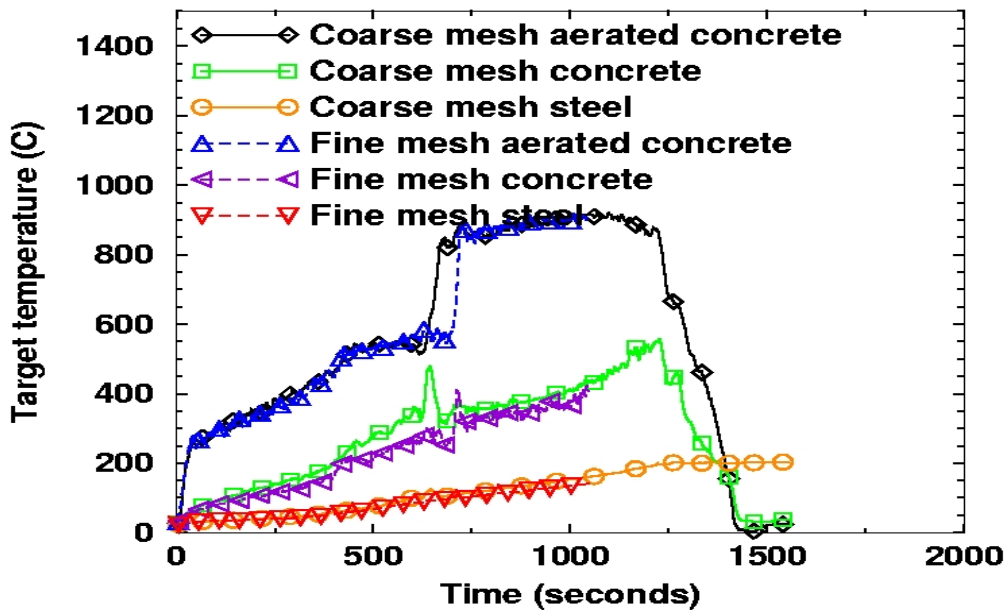


Fig. I 18 Fine mesh surface temperatures of targets vs. coarse mesh results for simulation with calculated mass loss rate.

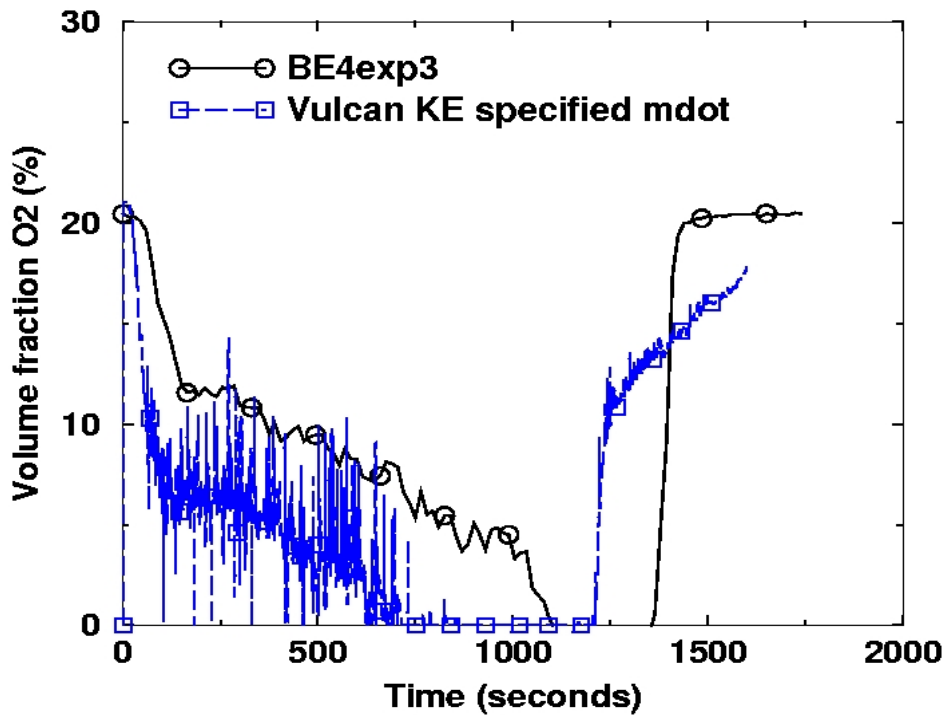


Fig. I 19 Oxygen percentage in fire room vs. experiment for simulation with specified mass loss rate. "Vulcan KE" designates the results of the simulation using Vulcan with the standard k-ε turbulence model.

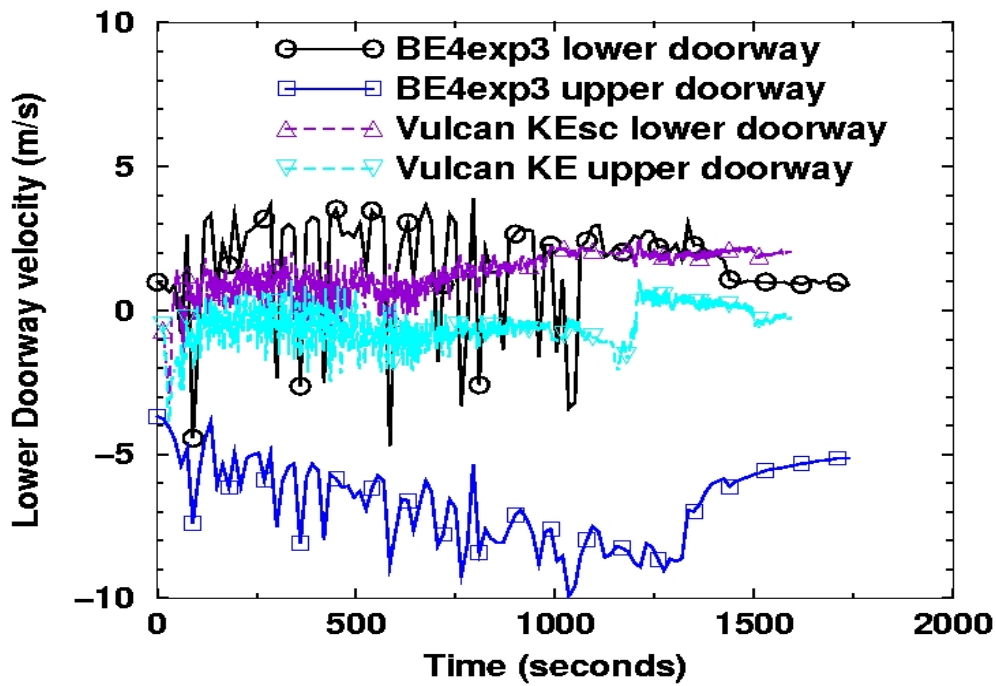


Fig. I 20 Doorway velocities vs. experiment for simulation with specified mass loss rate. "Vulcan KE" designates the results of the simulation using Vulcan with the standard k- turbulence model.

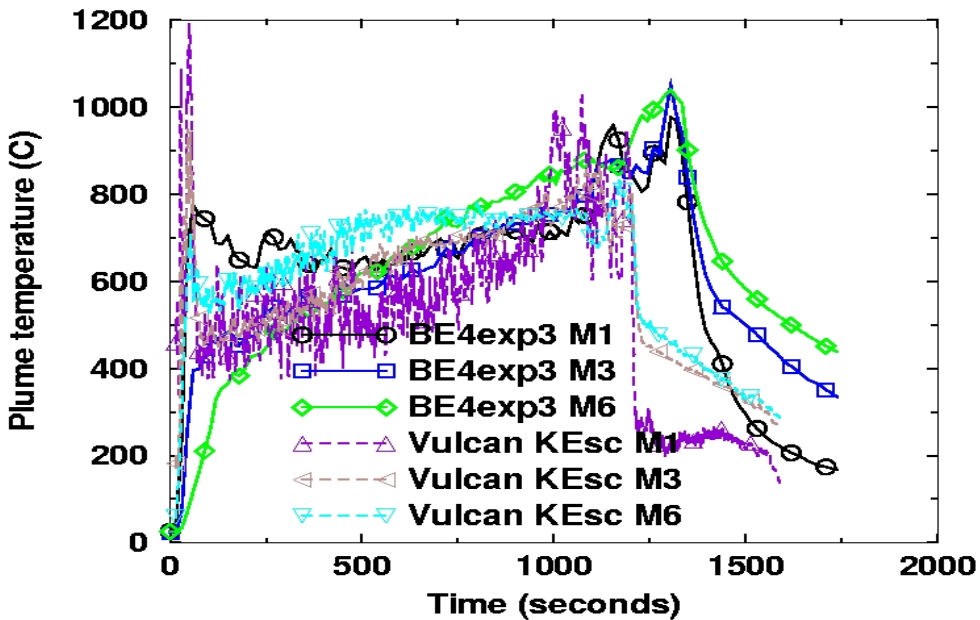


Fig. I 21 Plume temperatures vs. experiment for simulation with specified mass loss rate. "Vulcan KE" designates the results of the simulation using Vulcan with the standard k- turbulence model.

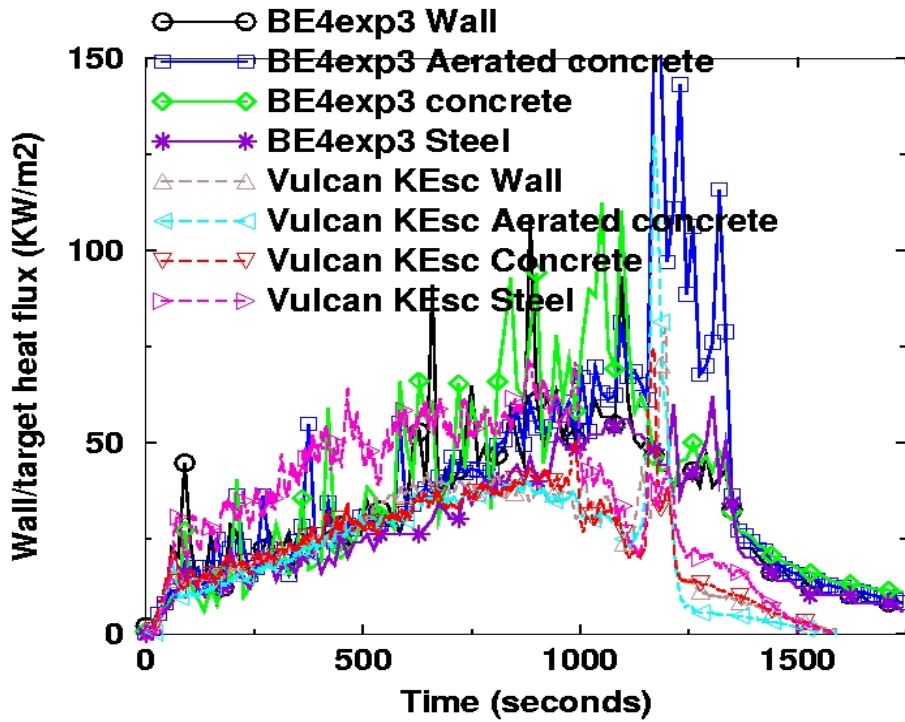


Fig. I 22 Heat flux to targets vs. experiment for simulation with specified mass loss rate. "Vulcan KE" designates the results of the simulation using Vulcan with the standard k- turbulence model.

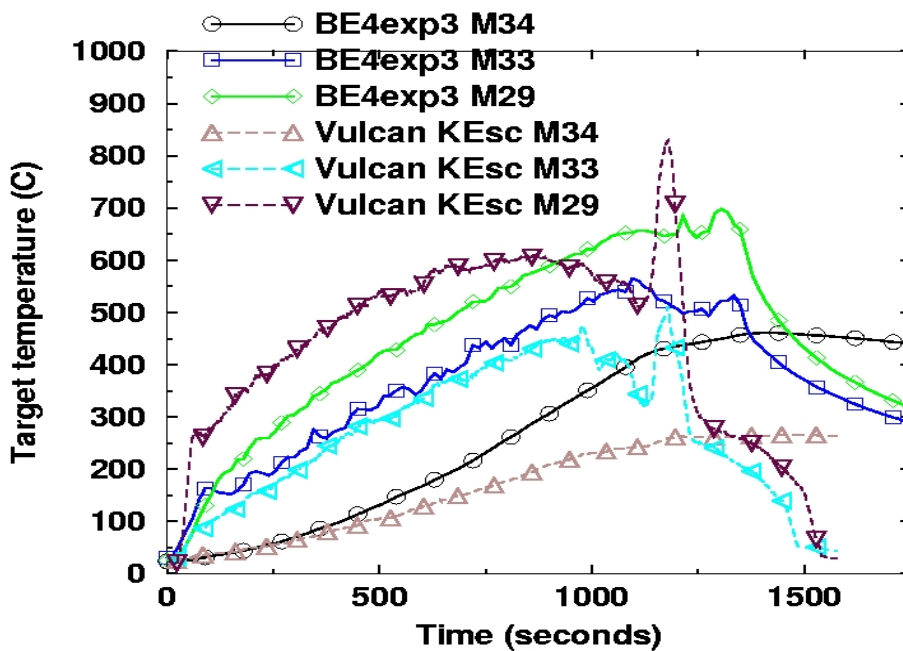


Fig. I 23 Surface temperatures of targets vs. experiment for simulation with specified mass loss rate. "Vulcan KE" designates the results of the simulation using Vulcan with the standard k- turbulence model.

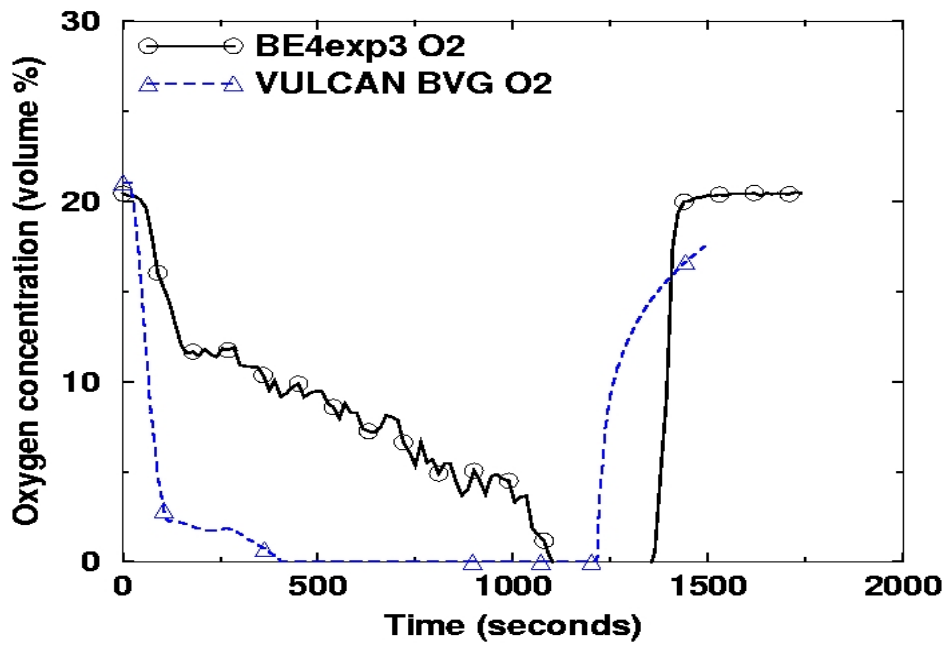


Fig. I 24 BVG simulation: Oxygen percentage in fire room vs. experiment for simulation with specified mass loss rate.

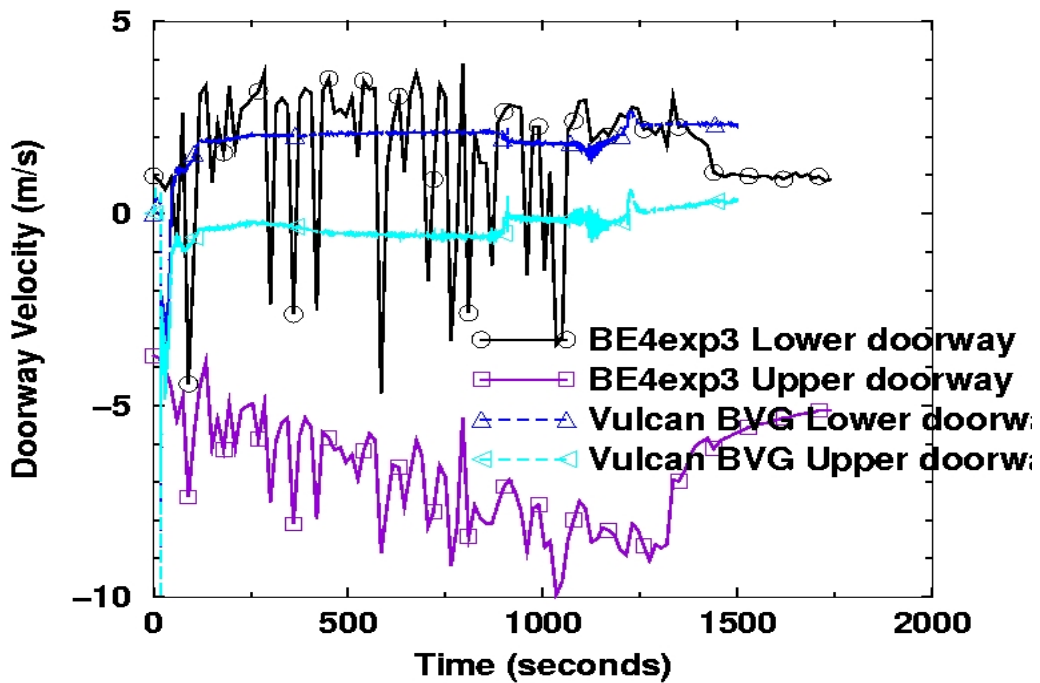


Fig. I 25 BVG simulation: Doorway velocities vs. experiment for simulation with specified mass loss rate.

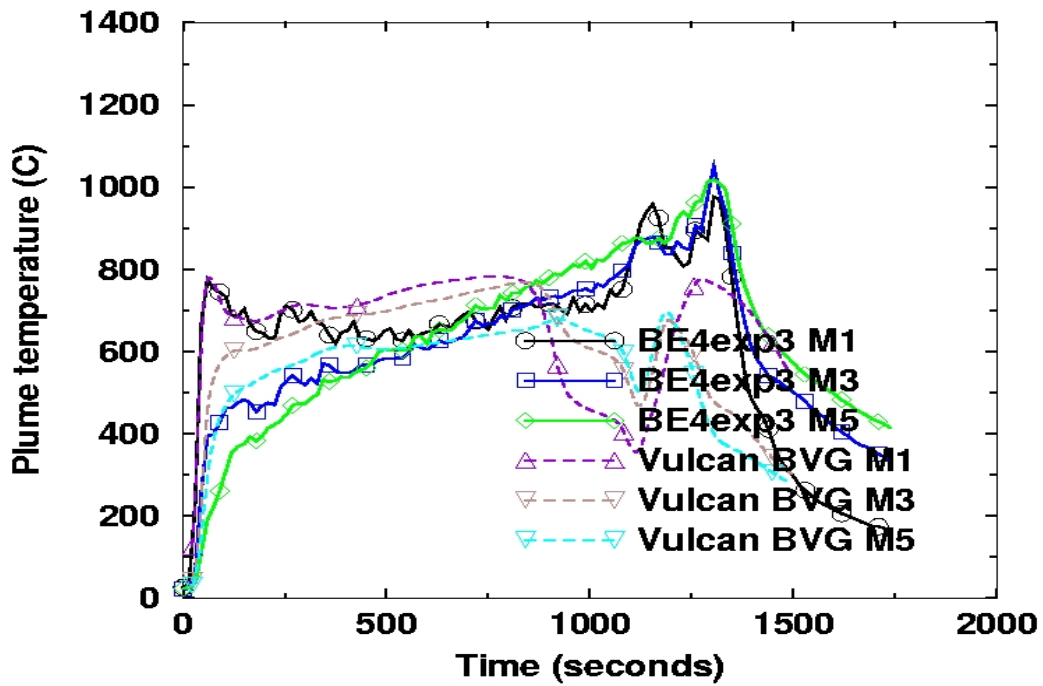


Fig. I 26 BVG simulation: Plume temperatures vs. experiment for simulation with specified mass loss rate.

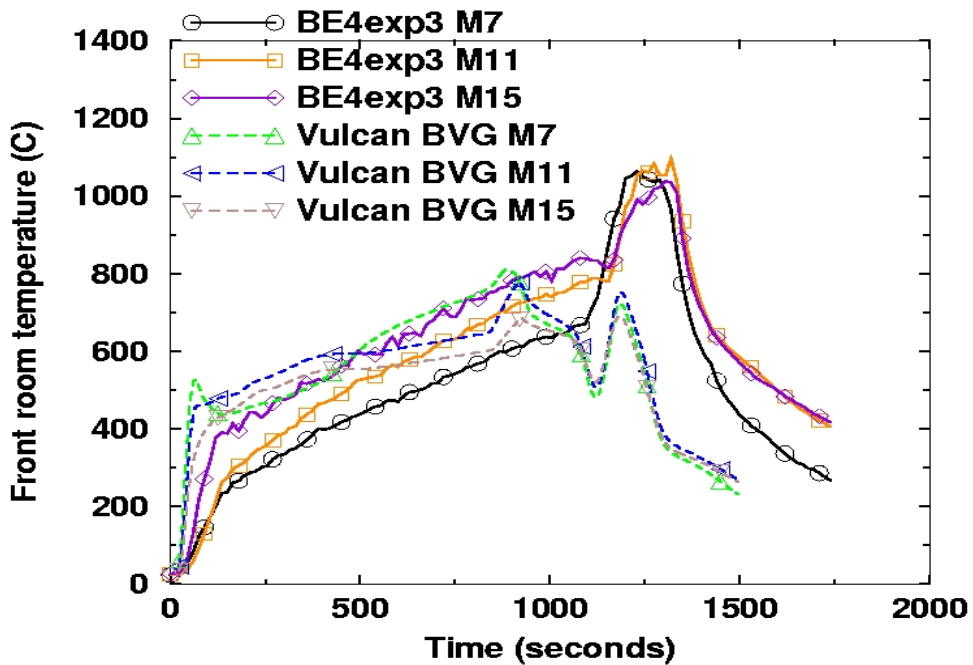


Fig. I 27 BVG simulation: Front room temperatures vs. experiment for simulation with specified mass loss rate.

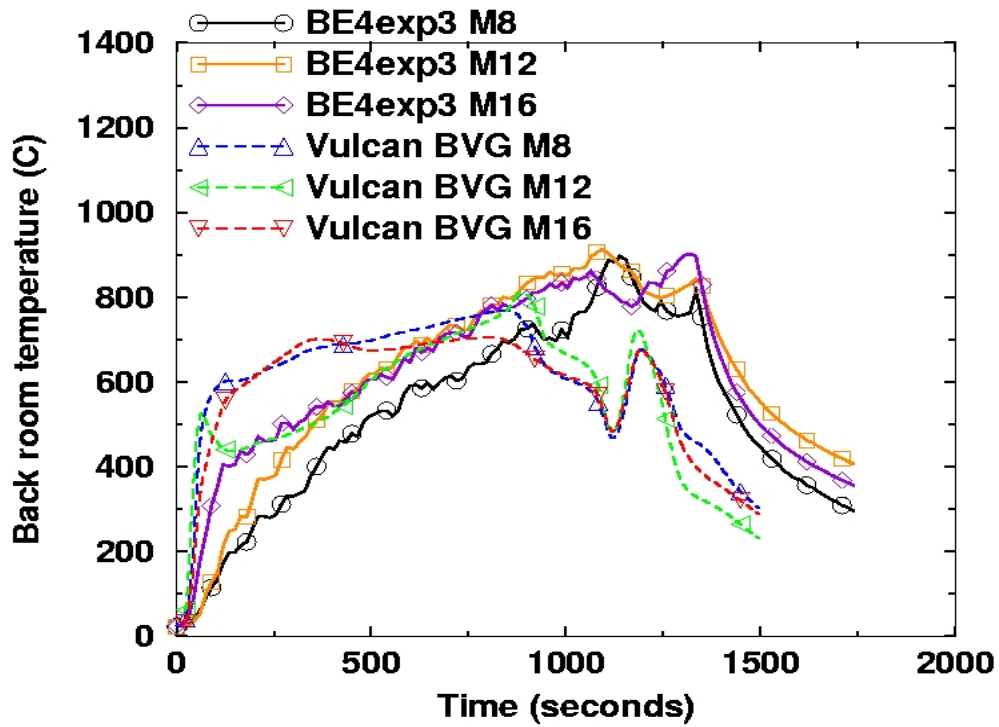


Fig. I 28 BVG simulation: Back room temperatures vs. experiment for simulation with specified mass loss rate.

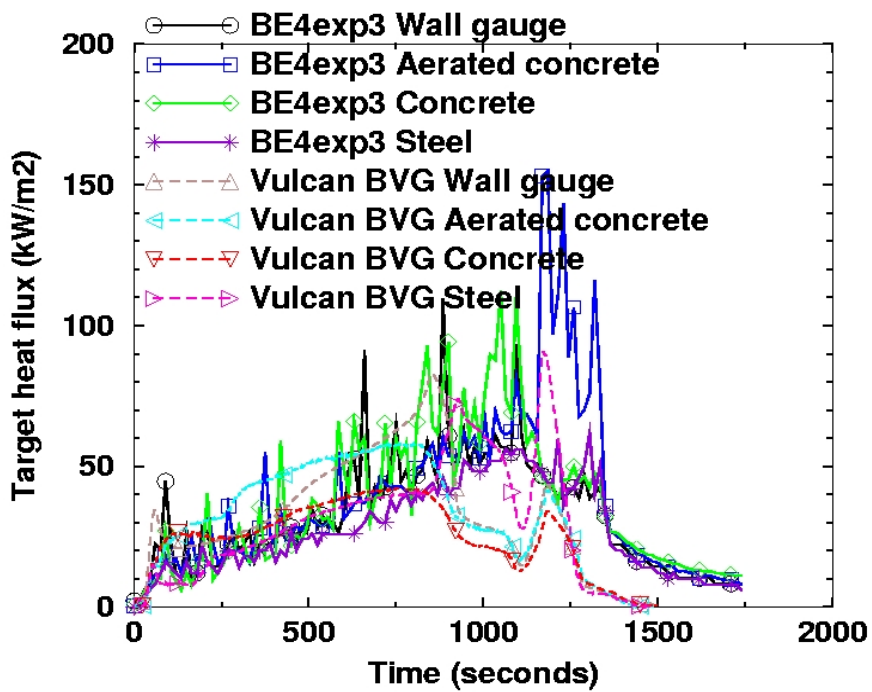


Fig. I 29 BVG simulation: Heat flux to targets vs. experiment for simulation with specified mass loss rate.

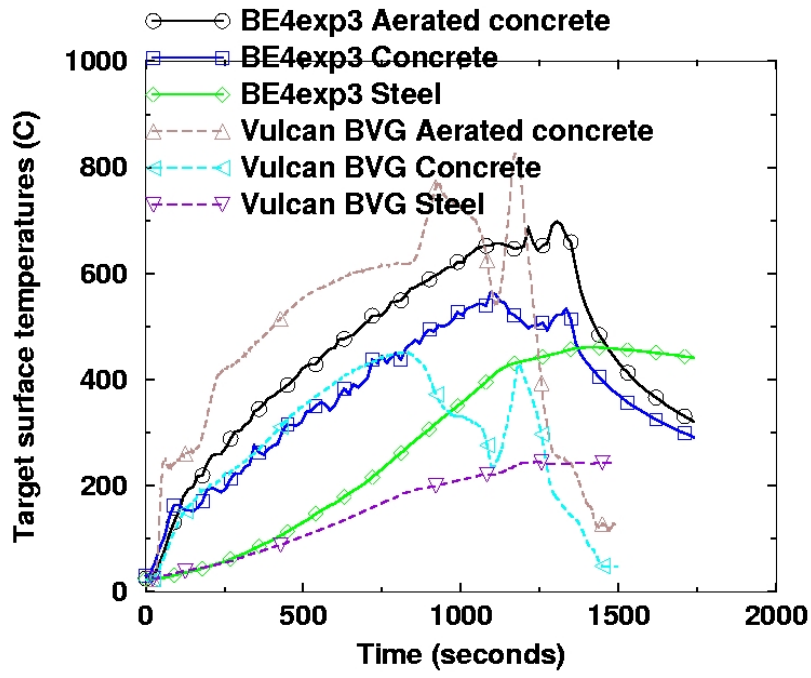


Fig. I 30 BVG simulation: Surface temperatures of targets vs. experiment for simulation with specified mass loss rate.

List of Figures

Fig. I 1	Wire frame sketch of fire room, showing pan of fuel on floor, barrel-type container against back wall, sidewall targets, doorway/window part-way up the front wall, and two ventilation duct outlets near ceiling (back wall). Hood is not shown for clarity.	33
Fig. I 2	Geometry model (walls removed), including hood (object on the right). Cylindrical barrel is at back of room, opposite the doorway. Tops of ventilation channels in ceiling are denoted by yellow panels in ceiling of uppermost object.	34
Fig. I 3	Non-uniform coarse grid used for fire room (front wall removed for clarity); view is looking toward the back wall. Note: x-axis is from left to right; y-axis is into the page; z-axis is from bottom to top of page.	34
Fig. I 3	Mass loss rate (calculated) vs. experiment. "Vulcan KE" designates the results of the simulation using Vulcan with the standard k- turbulence model.	35
Fig. I 4	Mass loss rate (smoothed) vs. experiment. "Vulcan KE" designates the results of the simulation using Vulcan with the standard k- turbulence model.	35
Fig. I 5	Oxygen percentage in fire room vs. experiment for simulation with calculated mass loss rate. "Vulcan KE" designates the results of the simulation using Vulcan with the standard k-ε turbulence model.	36
Fig. I 6	Doorway velocities vs. experiment for simulation with calculated mass loss rate. "Vulcan KE" designates the results of the simulation using Vulcan with the standard k- turbulence model.	36
Fig. I 7	Plume temperatures vs. experiment for simulation with calculated mass loss rate. "Vulcan KE" designates the results of the simulation using Vulcan with the standard k- turbulence model.	37
Fig. I 8	Front room temperatures vs. experiment for simulation with calculated mass loss rate. "Vulcan KE" designates the results of the simulation using Vulcan with the standard k- turbulence model.	37
Fig. I 9	Back room temperatures vs. experiment for simulation with calculated mass loss rate. "Vulcan KE" designates the results of the simulation using Vulcan with the standard k- turbulence model.	38

Fig. I 10	Heat flux to gauge embedded in sidewall vs. experiment for simulation with calculated mass loss rate. "Vulcan KE" designates the results of the simulation using Vulcan with the standard k-ε turbulence model.....	38
Fig. I 11	Heat flux to targets vs. experiment for simulation with calculated mass loss rate. "Vulcan KE" designates the results of the simulation using Vulcan with the standard k-ε turbulence model.....	39
Fig. I 12	Surface temperatures of targets vs. experiment for simulation with calculated mass loss rate. "Vulcan KE" designates the results of the simulation using Vulcan with the standard k-ε turbulence model.....	39
Fig. I 13	Fine mesh mass loss rate (smoothed) vs. experiment for simulation with calculated mass loss rate. "Vulcan KE" designates the results of the simulation using Vulcan with the standard k-ε turbulence model.....	40
Fig. I 15	Fine mesh oxygen percentage in fire room vs. experiment for simulation with calculated mass loss rate. "Vulcan KE" designates the results of the simulation using Vulcan with the standard k-ε turbulence model.	40
Fig. I 16	Fine mesh plume temperatures vs. coarse mesh results for simulation with calculated mass loss rate.	41
Fig. I 17	Fine mesh heat flux to targets vs. coarse mesh results for simulation with calculated mass loss rate.	41
Fig. I 18	Fine mesh surface temperatures of targets vs. coarse mesh results for simulation with calculated mass loss rate.	42
Fig. I 19	Oxygen percentage in fire room vs. experiment for simulation with specified mass loss rate. "Vulcan KE" designates the results of the simulation using Vulcan with the standard k-ε turbulence model.....	42
Fig. I 20	Doorway velocities vs. experiment for simulation with specified mass loss rate. "Vulcan KE" designates the results of the simulation using Vulcan with the standard k-ε turbulence model.....	43
Fig. I 21	Plume temperatures vs. experiment for simulation with specified mass loss rate. "Vulcan KE" designates the results of the simulation using Vulcan with the standard k-ε turbulence model.....	43
Fig. I 22	Heat flux to targets vs. experiment for simulation with specified mass loss rate. "Vulcan KE" designates the results of the simulation using Vulcan with the standard k-ε turbulence model.....	44

Fig. I 23	Surface temperatures of targets vs. experiment for simulation with specified mass loss rate. "Vulcan KE" designates the results of the simulation using Vulcan with the standard k- turbulence model.....	44
Fig. I 24	BVG simulation: Oxygen percentage in fire room vs. experiment for simulation with specified mass loss rate.	45
Fig. I 25	BVG simulation: Doorway velocities vs. experiment for simulation with specified mass loss rate.	45
Fig. I 26	BVG simulation: Plume temperatures vs. experiment for simulation with specified mass loss rate.	46
Fig. I 27	BVG simulation: Front room temperatures vs. experiment for simulation with specified mass loss rate.	46
Fig. I 28	BVG simulation: Back room temperatures vs. experiment for simulation with specified mass loss rate.	47
Fig. I 29	BVG simulation: Heat flux to targets vs. experiment for simulation with specified mass loss rate.	47
Fig. I 30	BVG simulation: Surface temperatures of targets vs. experiment for simulation with specified mass loss rate.	48

List of Tables

Table 1	VULCAN simulations.....	9
----------------	-------------------------	---

Appendix J: International Collaborative Project to Evaluate Fire Models for Nuclear Power Plant Applications

Benchmark Exercise No. 4 Simulation with MAGIG

Presented by

B. Gautier, EDF France

C. Mollard, AUSY France

EDF R&D

6 quai Watier, 78401 Chatou cedex

Contents

J1	Introduction	1
J2	Input Parameters and Assumptions.....	3
J2.1	Geometry	3
J2.2	Ventilation	4
J2.3	Combustible	4
J2.4	Wall Temperature.....	5
J3	Comparison of Code Predictions with Experimental Results.....	7
J3.1	Heat release rate.....	7
J3.2	Layer height	8
J3.3	Layer average temperatures	10
J3.4	Wall surface temperature	12
J3.5	Heat flow to the walls	12
J3.6	Steel target, Concrete target and Light concrete target	14
J3.6.1	Temperature on targets.....	14
J3.6.2	Flux on targets	17
J3.7	Flame and Plume temperatures.....	20
J3.8	Oxygen concentration	21
J4	Parametric Study.....	23
J4.1	Heat release rate.....	23
J4.2	Effect of light concrete floor.....	24
J5	Conclusions and Remarks	25
J6	General Conclusions and Recommendations.....	27
J7	References.....	29
	List of Figures	31

J1 Introduction

The calculations presented here are done with MAGIC V4.1.1b /GAY 06/. The code is used in its standard version using input variables corresponding to a normal risk study approach.

MAGIC uses a two-zone model including most of the classic features:

- Mass loss rate scenario of the fuel on fire
- Gaseous phase combustion, governed by the properties of emitted products and the air supply attributable to the plume flow
- Smoke production and unburned products
- The fire plume over each source in various configurations
- Heat exchange by convection and radiation between the flame, air, hot gas layer, walls, and environment
- Natural flows through the openings
- Forced or natural ventilation
- Thermal behavior and reaction of critical elements
- Thermal behavior and combustion of electric cables
- Water spray from sprinklers

The results of the numerical simulations are compared with two experiments performed at the IBMB Laboratory.

Two tests, called Test 1 and Test 3, are proposed to the participants (**Fig. J1**). Both are based on a fire compartment with a floor size of 3.6m×3.6m and a height of 5.7m. A 1 m² pool of kerosene is located in the middle of the floor. In the first experiment, the door is completely open with a free cross section of 0.7×3 m. In the second one, the opening is partly closed and the free cross section is reduced to 0.7×1 m.

Nota: the calculations for Test1 are the same than the one performed with Magic in the NRC NUREG 1824 report (V&V report /SAL 06/).

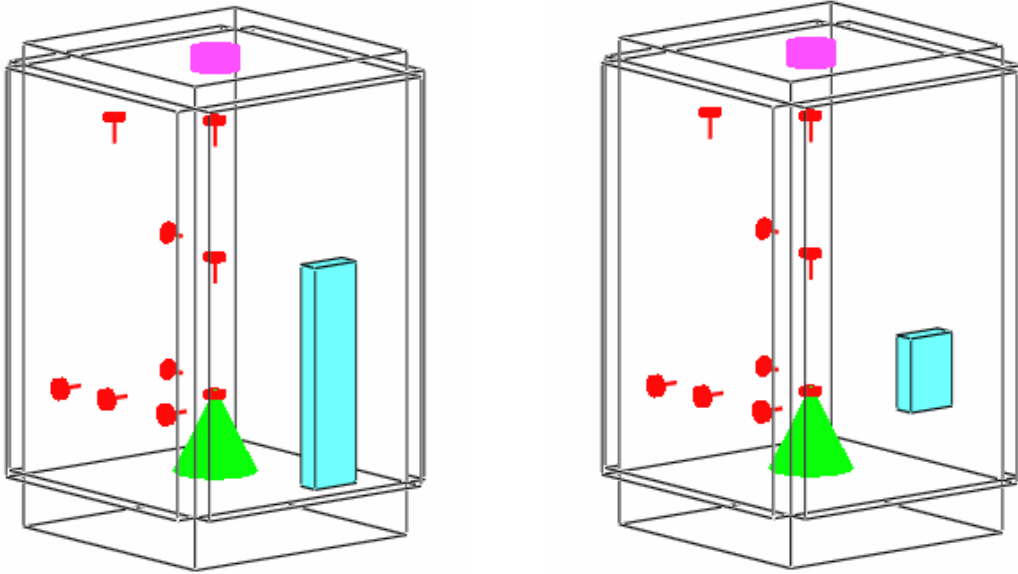


Fig. J1 The proposed cases 1 and 3 (as represented in MAGIC)

J2 Input Parameters and Assumptions

Most of input data is given in the benchmark BE#4 specifications /KLE 03/.

Specific assumptions and input parameters are reported in the following sections.

J2.1 Geometry

Simplifications have been made, based on typical assumptions for fire risk study in NPP /KAS 02/ and similar to those proposed together with F. Joglar Billoch in NUREG 1824 /SAL 06/. As shown in **Fig. J2**, the compartment geometry is fairly simple, consisting in a parallelepiped with 3.6 m deep, 3.6 m wide and 5.53 m high.

The air volume above the ceiling is respected.

The floor is constructed from 0.3 m of concrete and the aerated concrete is simulated as a uniform 0.43 m layer in order to conserve the volume. The different layers of the walls are fully represented as Magic allows the description of multi-layer walls.

The distances between targets or openings and fuel surface are conserved.

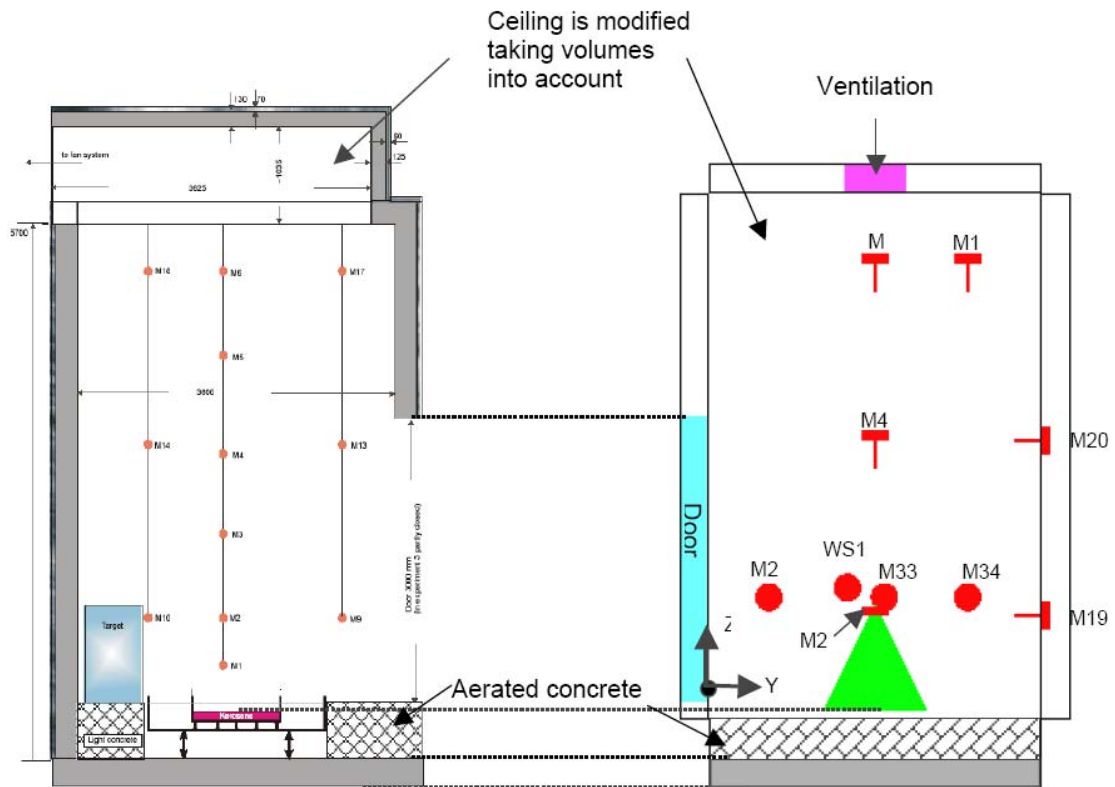


Fig. J2 Side view of OSKAR compartment - comparison to MAGIC representation

J2.2 Ventilation

The hood above the front door is not modelled. A simplification for the ventilation is made, only one global exhaust vent is considered. It is located at the middle of the ceiling and modelled as a 0.67 m diameter cylinder. As far as the vent is an exhaust and the ceiling has been simplified, this simplification has no significant effect on results.

J2.3 Combustible

The fuel is modelled as a circular fire with a 1.12 m diameter and a combustion heat of 42800 J/g. It is located at the center of the compartment and at 0.1 m of the floor. Calculations are achieved with the pyrolysis rate measured during the experiments, based on the smoothed data provided by iBMB (**Fig. J3**). The lower oxygen limit is fixed to 0 % which is the EDF recommended value. The radiation part is set to 0.35 (typical value for kerosene).

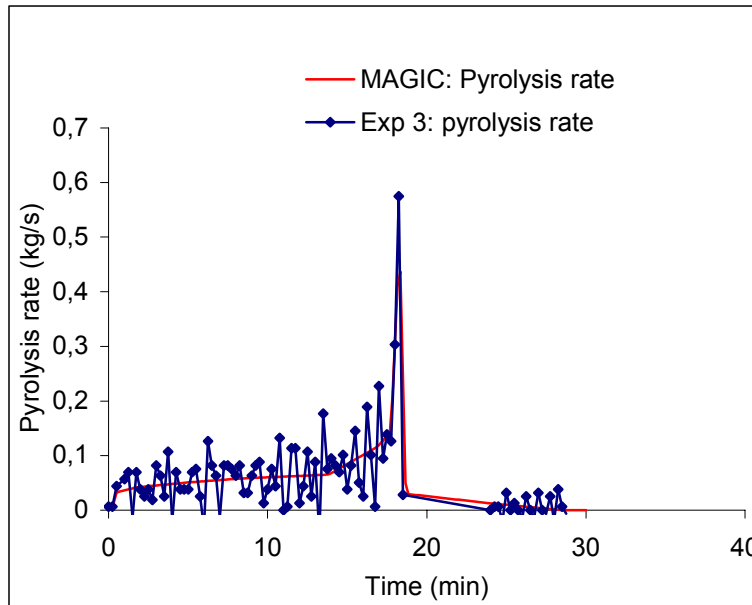
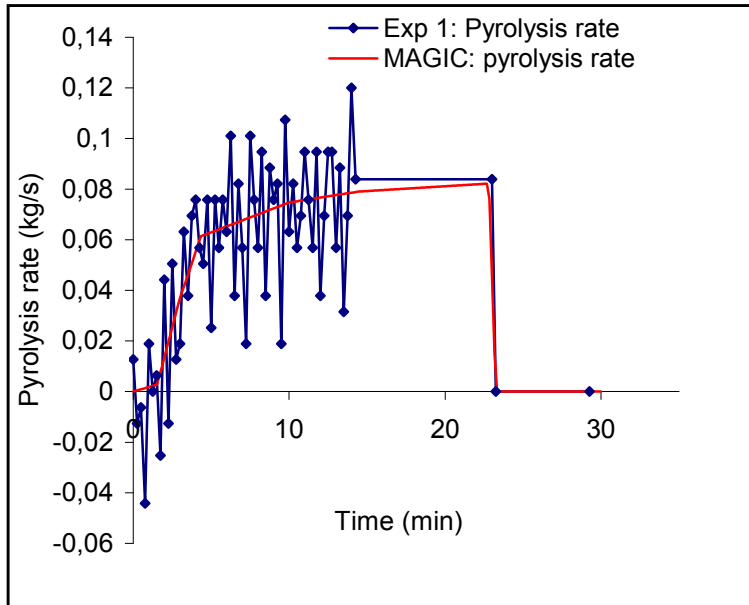


Fig. J3 Pyrolysis rate: Test 1 and Test 3

J2.4 Wall Temperature

Wall temperatures are measured with targets located on walls (M19 and M20).

J3 Comparison of Code Predictions with Experimental Results

In this part, the values calculated by MAGIC are compared to experimental results. The targets have the same depth and composition as the wall.

J3.1 Heat release rate

Heat release rate in Test 1 is in good agreement with the experimental results.

In Test 3, there is a significant difference during the HRR peak. The experiment data is not a measurement but the product of measured pyrolysis rate and heat of combustion. Therefore it cannot be considered as valid in this confined test. Unburned gas appears in the simulation, due to oxygen depletion. In Test 1 there is no strong oxygen depletion so the comparison can be made (see **Fig. J4**).

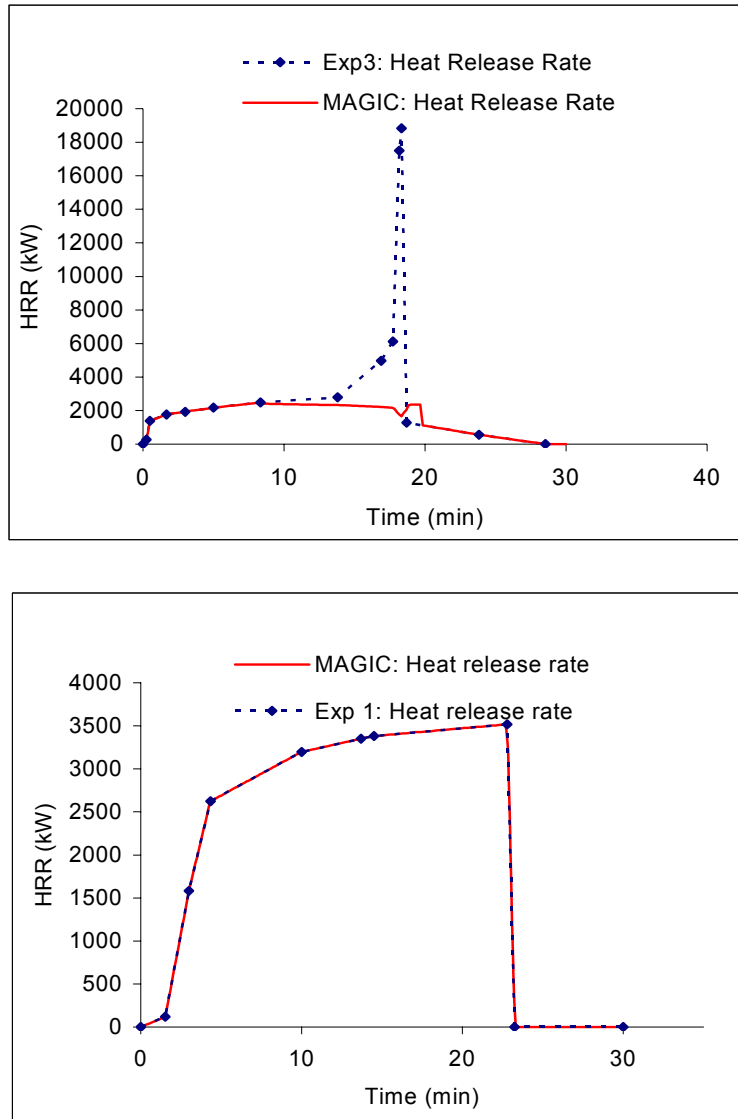


Fig. J4 Heat release rate: Test 1 and Test 3

J3.2 Layer height

There is a significant difference in the smoke layer height between calculations and experiment. The experimental layer height is measured with thermocouples at different levels, with the lowest elevation at 1.5 m. The Tests 1 and 3 don't provide values of smoke layer heights below 1.5 m which cannot be considered as valid, neither the lower layer temperature. In MAGIC calculations, the upper layer begins at the level of the ceiling and rapidly decreases to roughly 0.5 m.

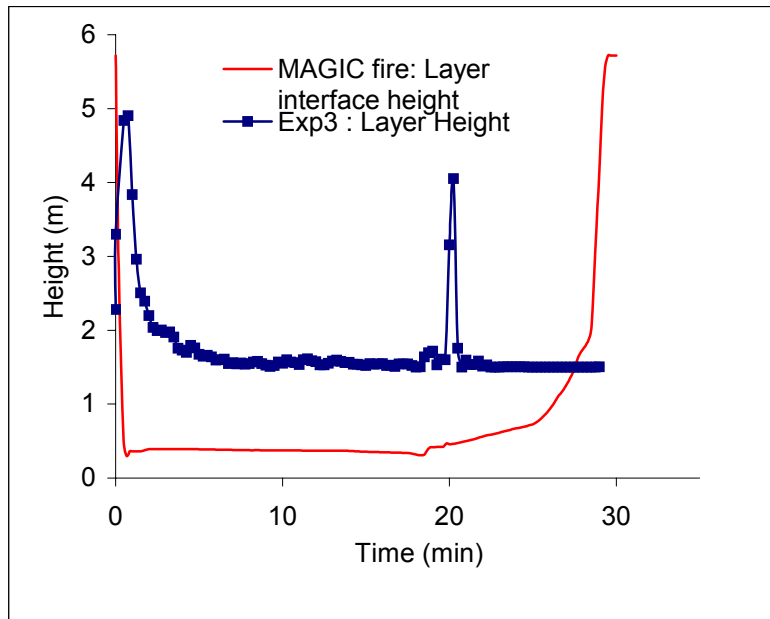
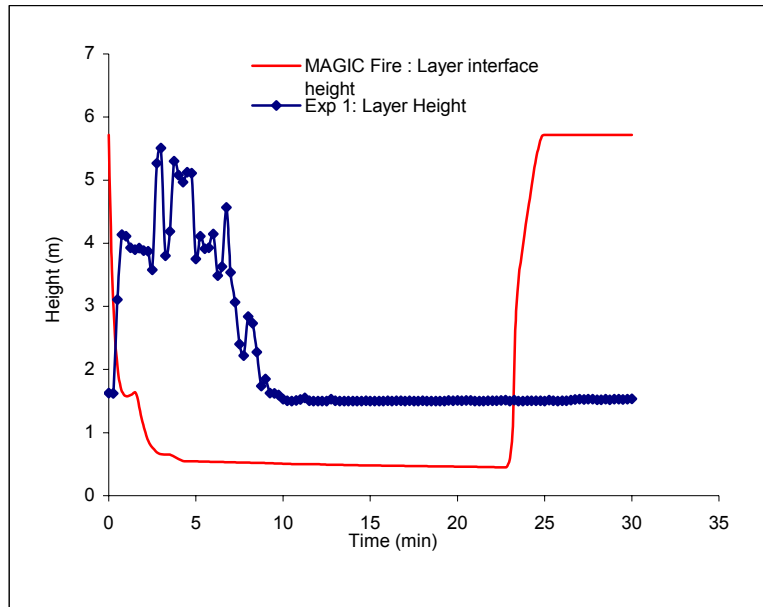


Fig. J5 Layer height: Test 1 and Test 3

At the end of the test, Magic predicts logically that the layer height should get back to the ceiling, due to persisting outflow at the vent. The experimental value is questioning.

J3.3 Layer average temperatures

For the Test 1, the upper layer temperature is almost similar to the experience while it is under the experimental data in the Test 3.

For the reasons seen previously for the layer height calculation, the experimental lower layer temperature, which appears colder than calculated data, should not be considered as valid.

In Test 1, upper layer temperature is similar for calculated and measured results.

In Test 3, upper layer temperature is higher in the experiment than in the calculation, which indicates that the combustion efficiency has been higher in the experiment, even if the HRR peak is not confirmed.

It seems that unburned gas was produced in the test, as predicted, even if no measurement has been made to confirm. Nevertheless it seems that more oxygen was available than calculated, maybe due to a higher mass flow at the door. Again this cannot be confirmed by some measurement. The effect of the hood on the outside door pressure could be a factor.

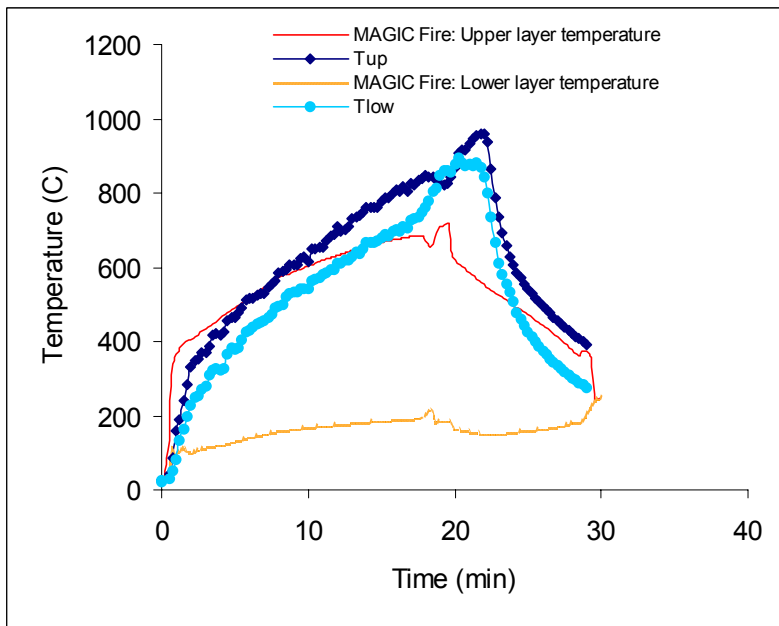
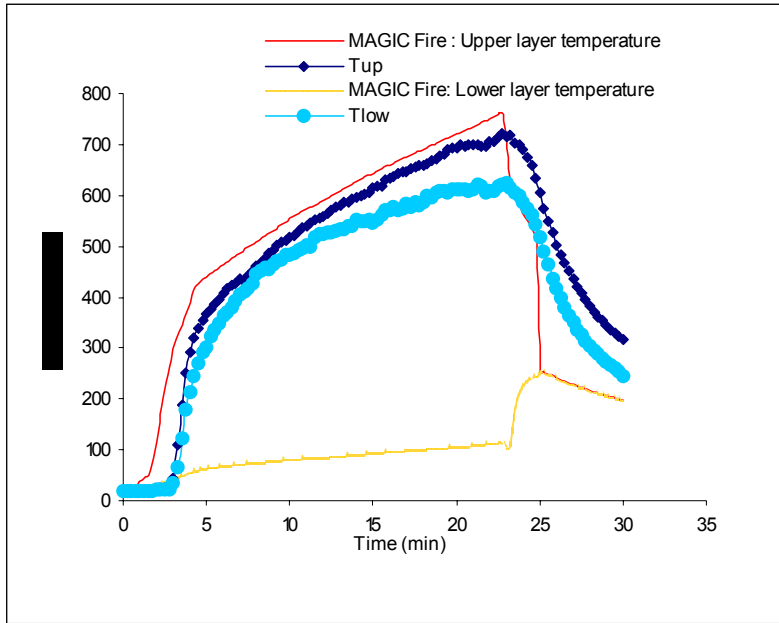


Fig. J6 Upper and lower temperature: Test 1 and Test 3

J3.4 Wall surface temperature

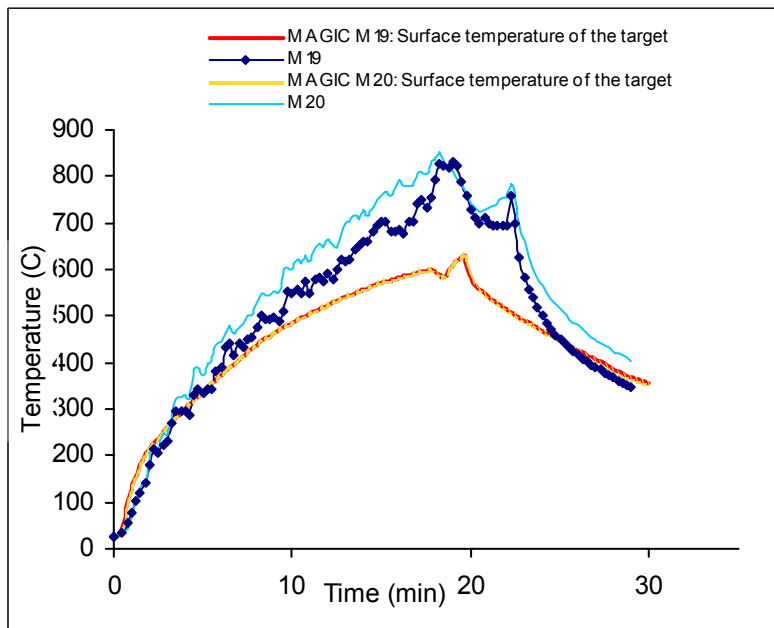
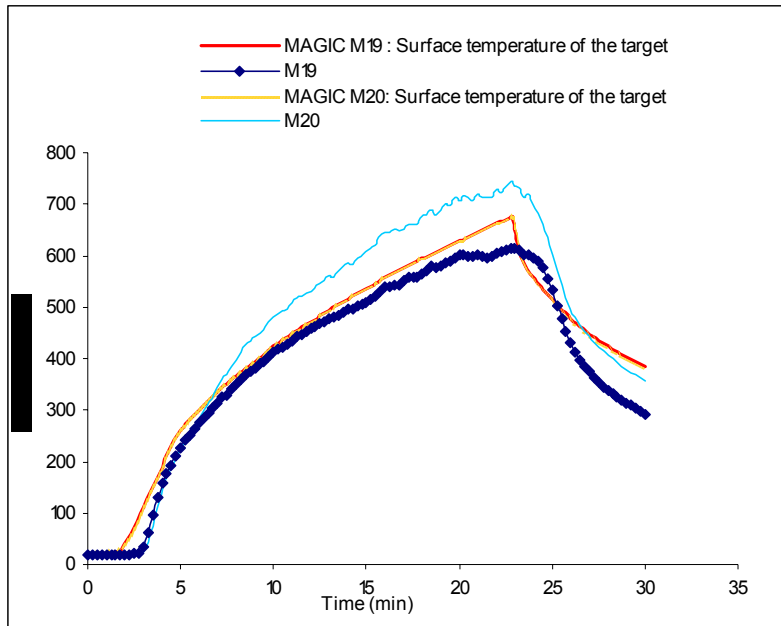


Fig. J7 Wall surface temperature: Test 1 and Test 3

J3.5 Heat flow to the walls

The calculations for heat flux to the wall are quite high in Test 1.

In Test 3, the flux is similar to the measurement. Knowing that the layer temperature is under-estimated, it indicates that MAGIC over predicts those fluxes here.

An important information missing is the soot concentration or the extinction coefficient in the upper layer. Benchmark No. 3 has shown that confined conditions could affect the soot production rate.

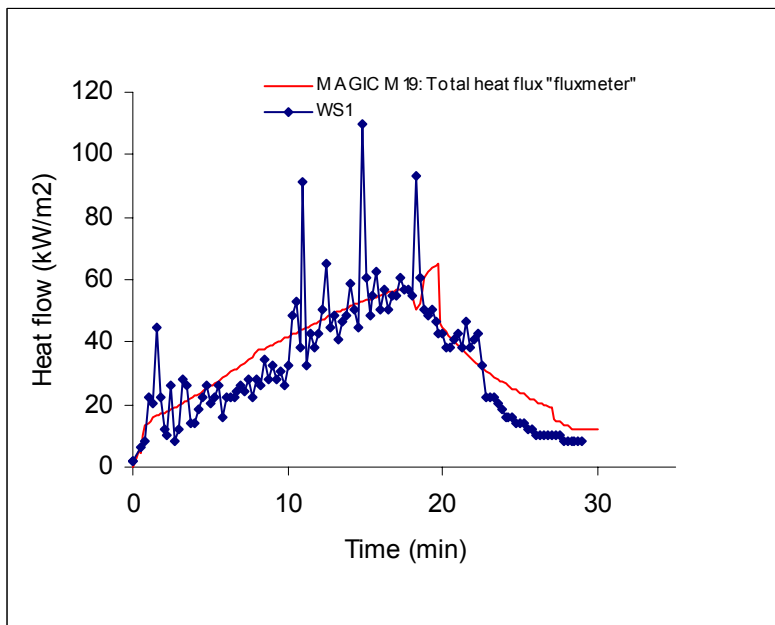
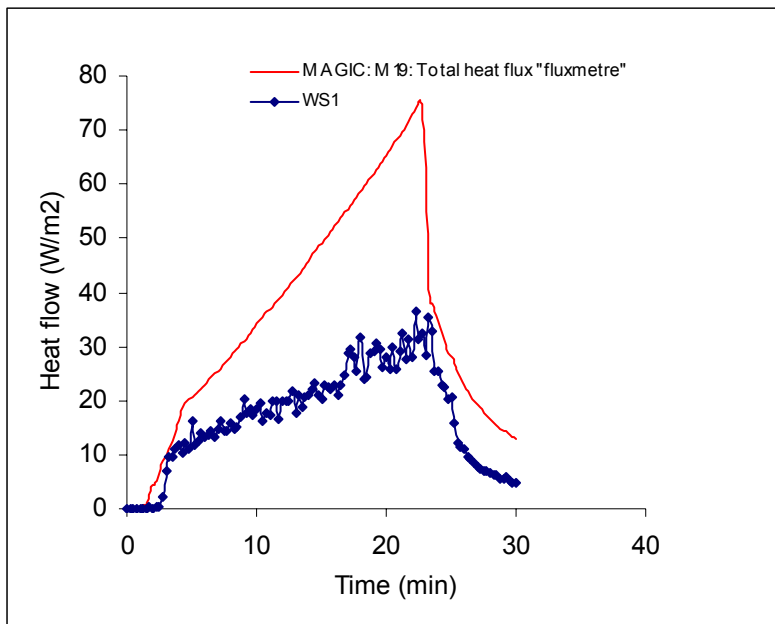


Fig. J8 Heat flow to the walls: Test 1 and Test 3

J3.6 Steel target, Concrete target and Light concrete target

J3.6.1 Temperature on targets

Calculated target temperatures are generally higher than measurements. For some targets in Test 3, calculation results are similar to measurement.

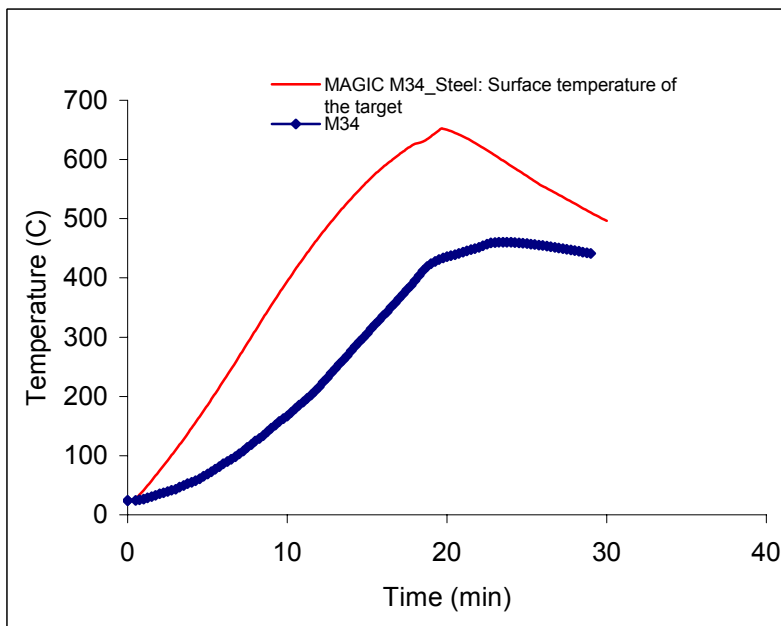
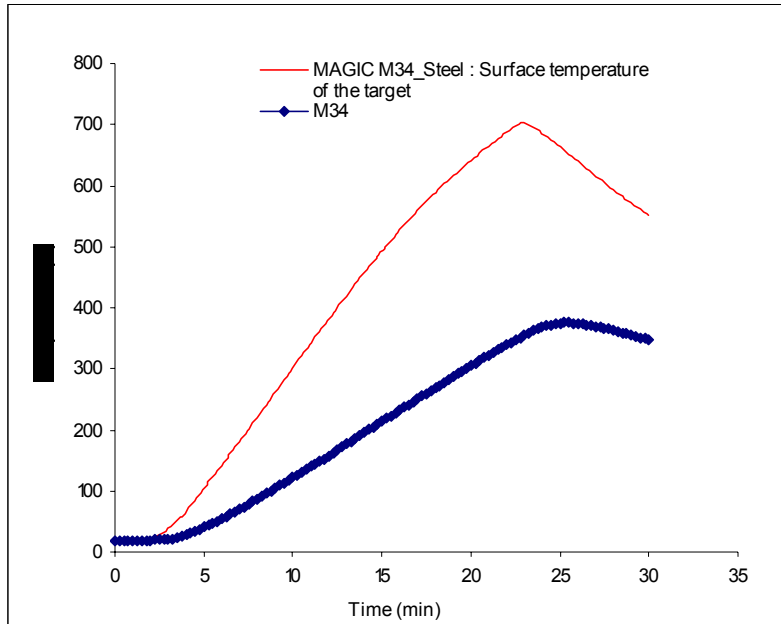


Fig. J9 Steel target temperature: Test 1 and Test 3

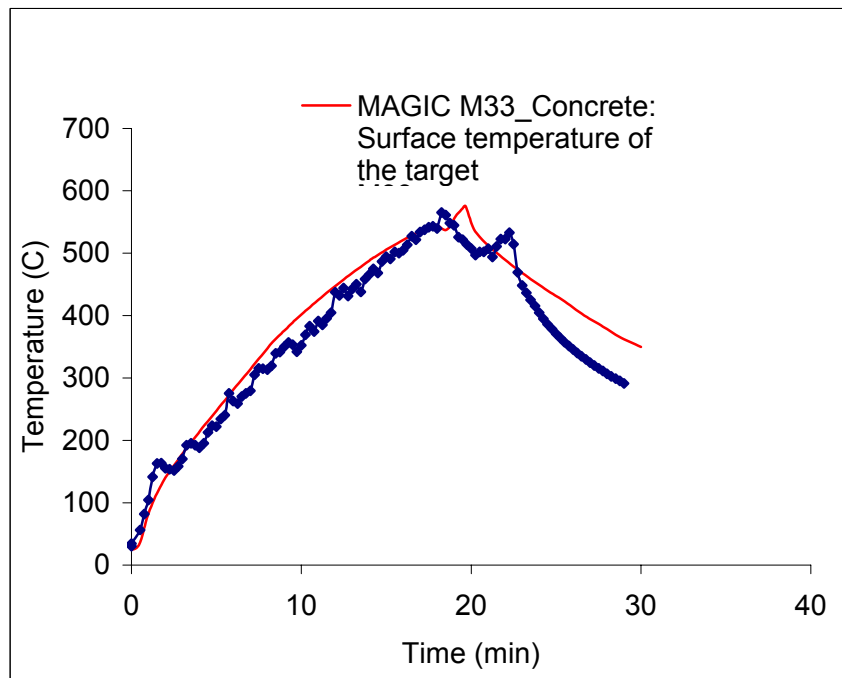
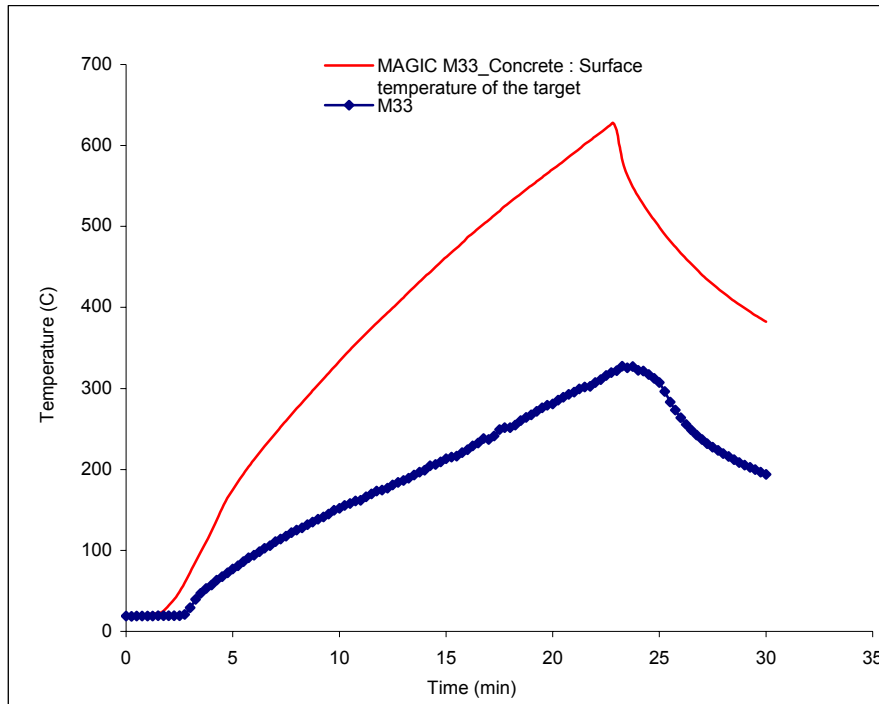


Fig. J10 Concrete target temperature: Test 1 and Test 3

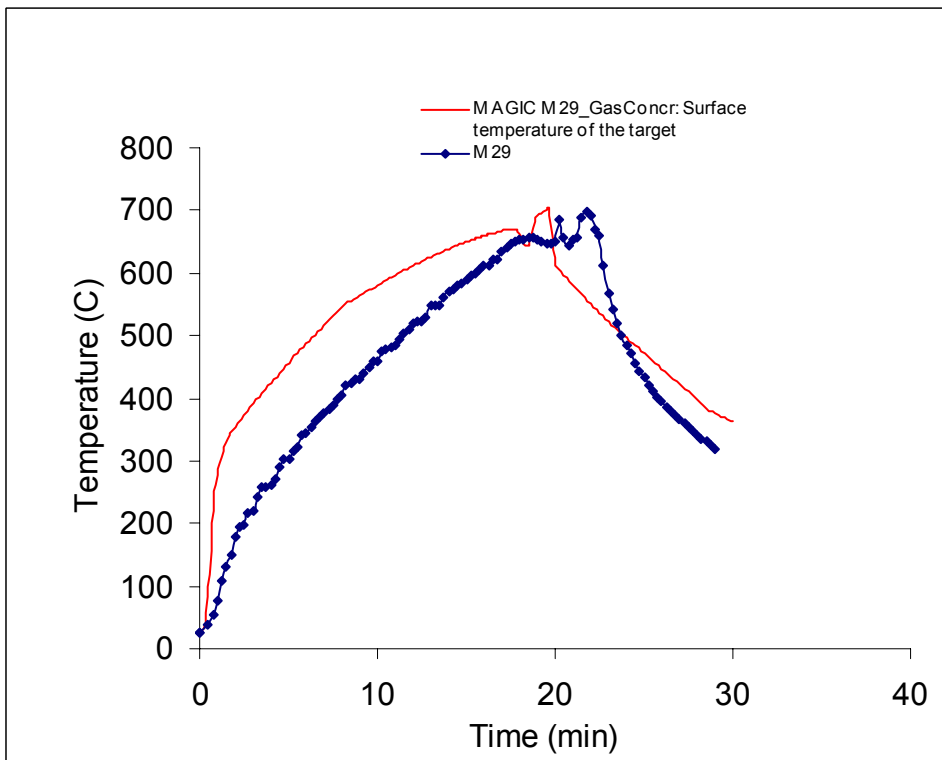
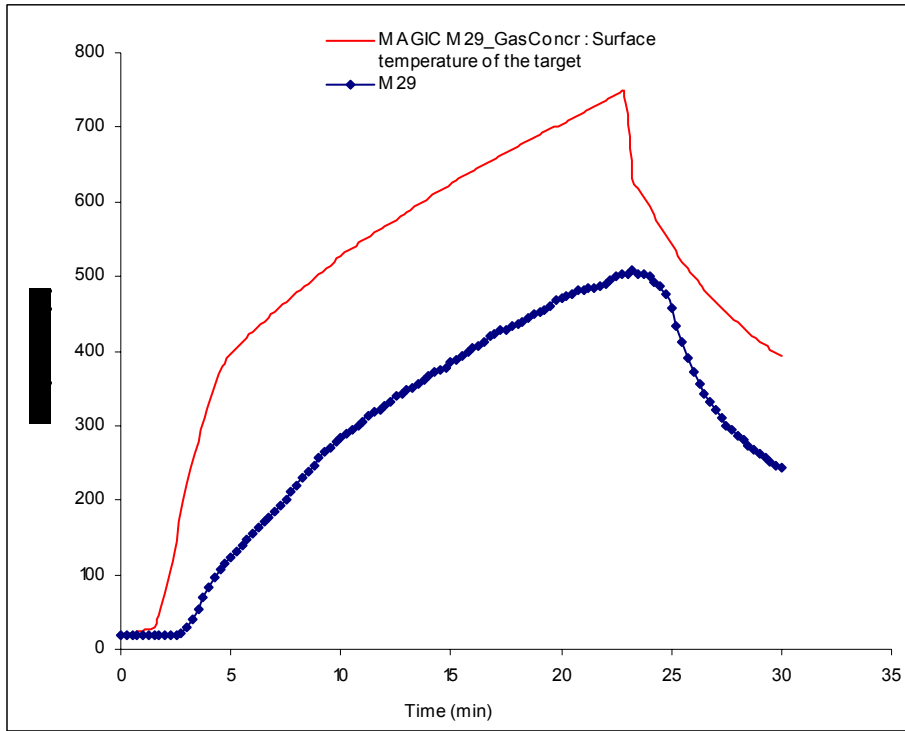


Fig. J11 Light Concrete target temperature: Test 1 and Test 3

J3.6.2 Flux on targets

Flux can be correct in Test 3 but they are significantly higher than measurement in Test 1.

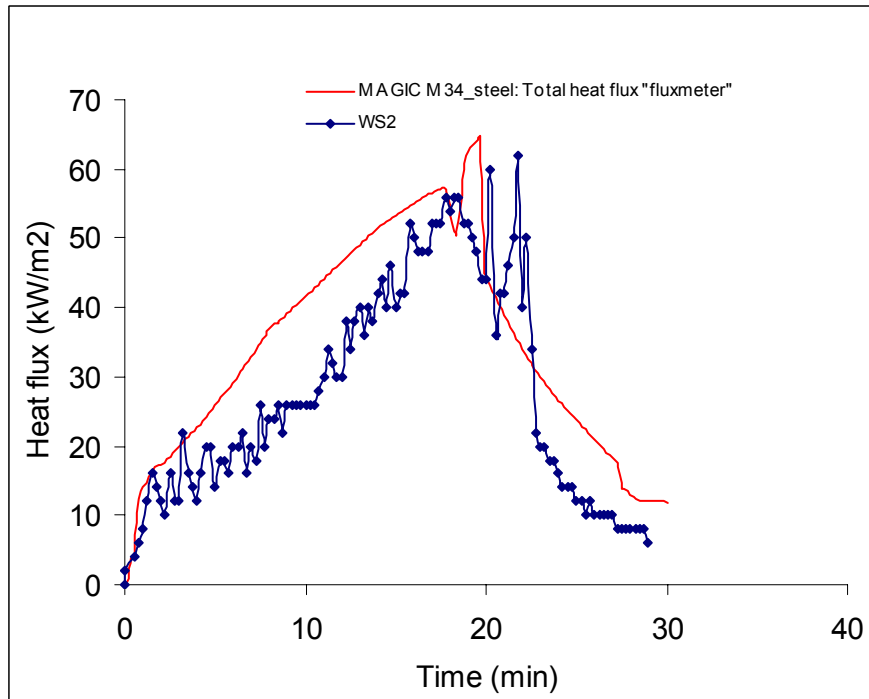
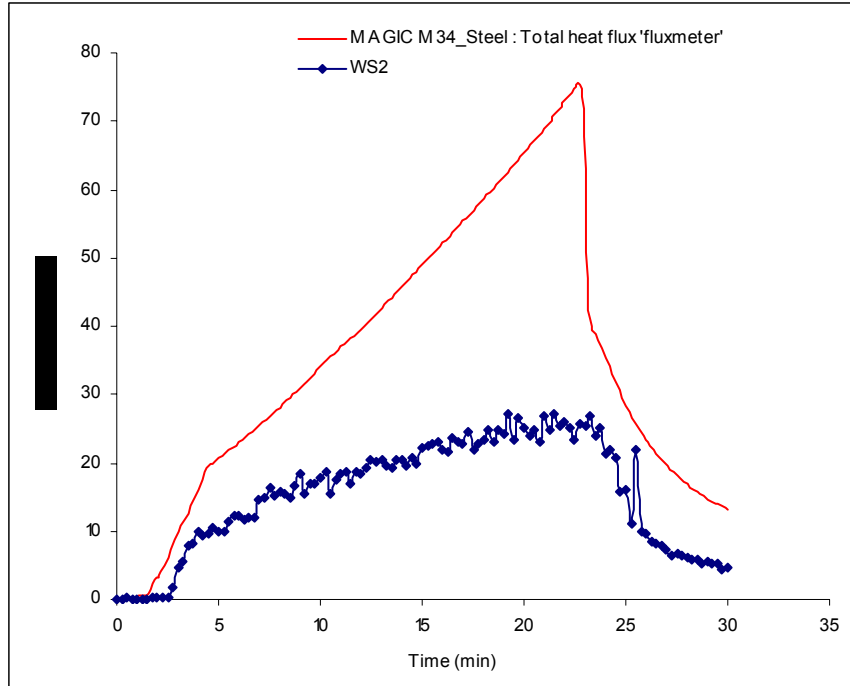


Fig. J12 Total flux to Steel target : Test 1 and Test 3

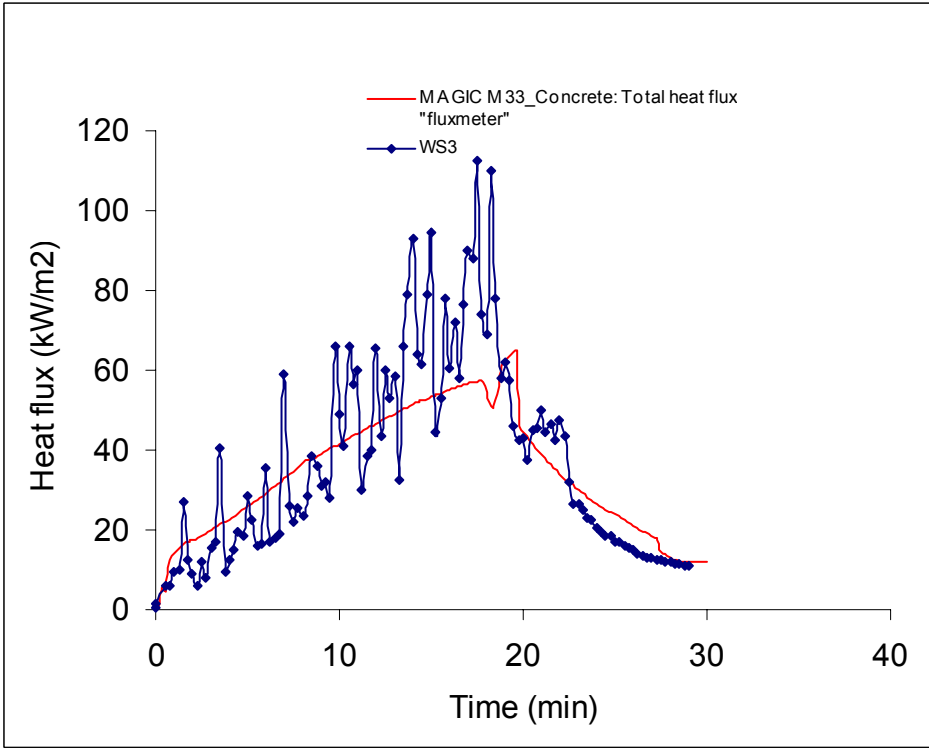
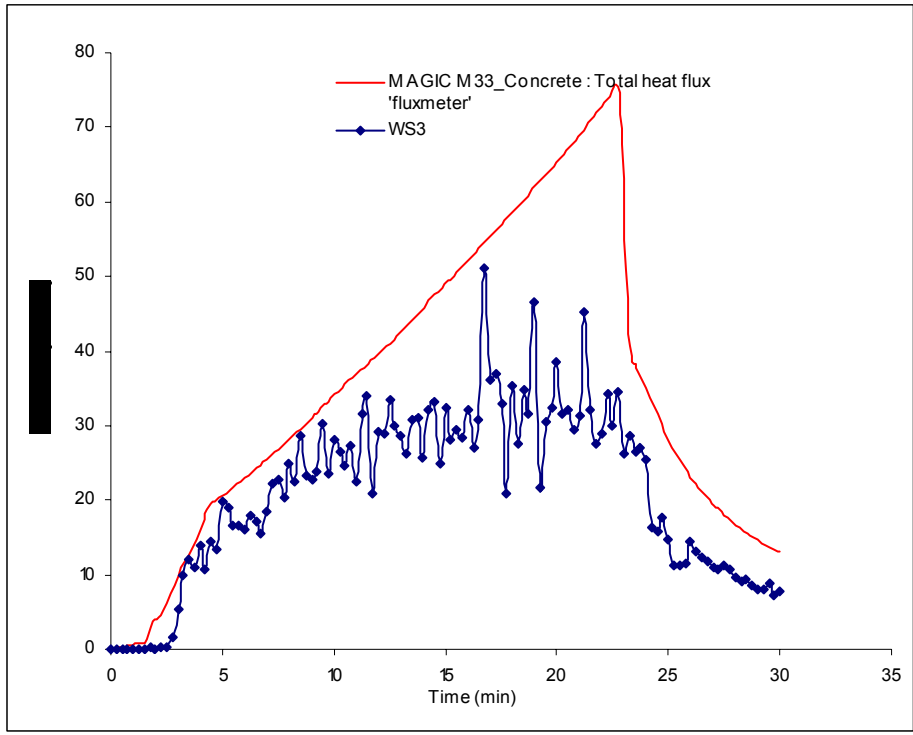


Fig. J13 Total flux to Concrete target: Test 1 and Test 3

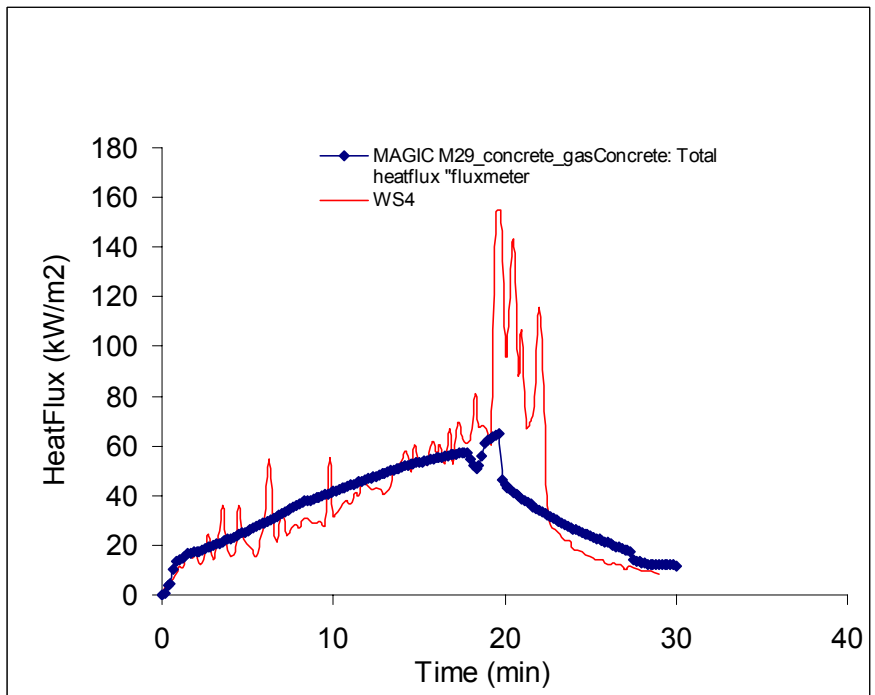
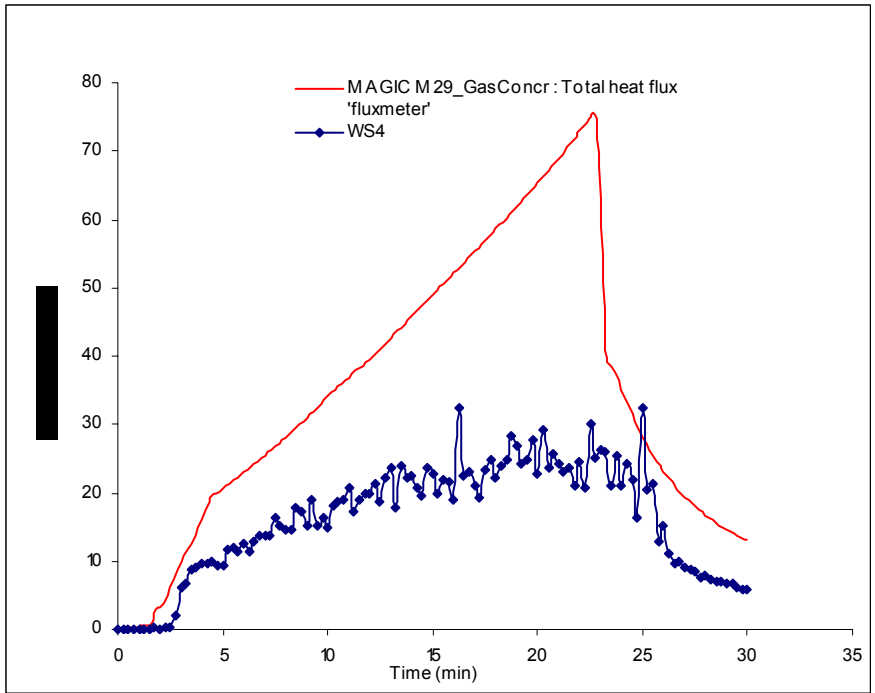


Fig. J14 Total flux to Light Concrete target: Test 1 and Test 3

J3.7 Flame and Plume temperatures

Magic temperature in the flame appears excessively high in the flame zone (M2 and M4 appear in the flame zone in the calculation, M6 is between flame and plume). Values superior to 2000 °C cannot be considered as realistic. On the contrary, experimental value seems to be somehow low.

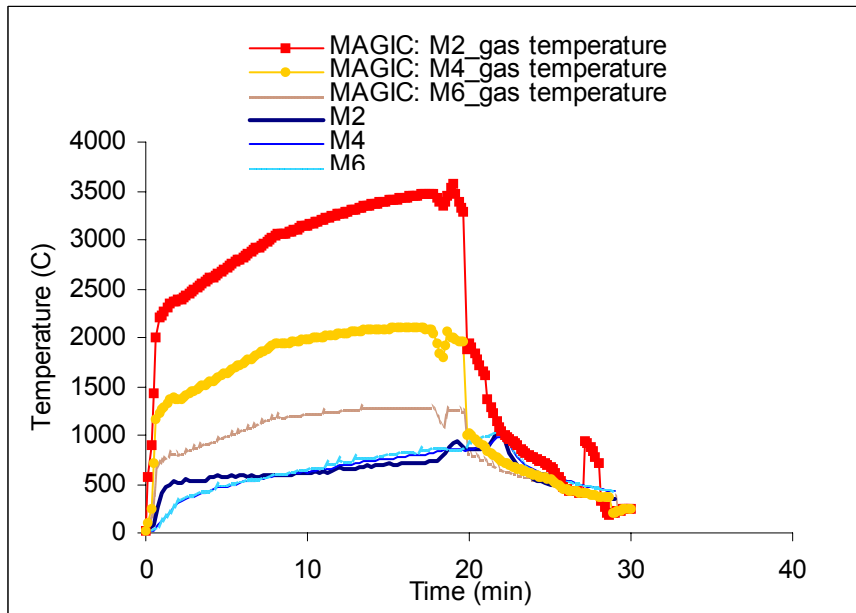
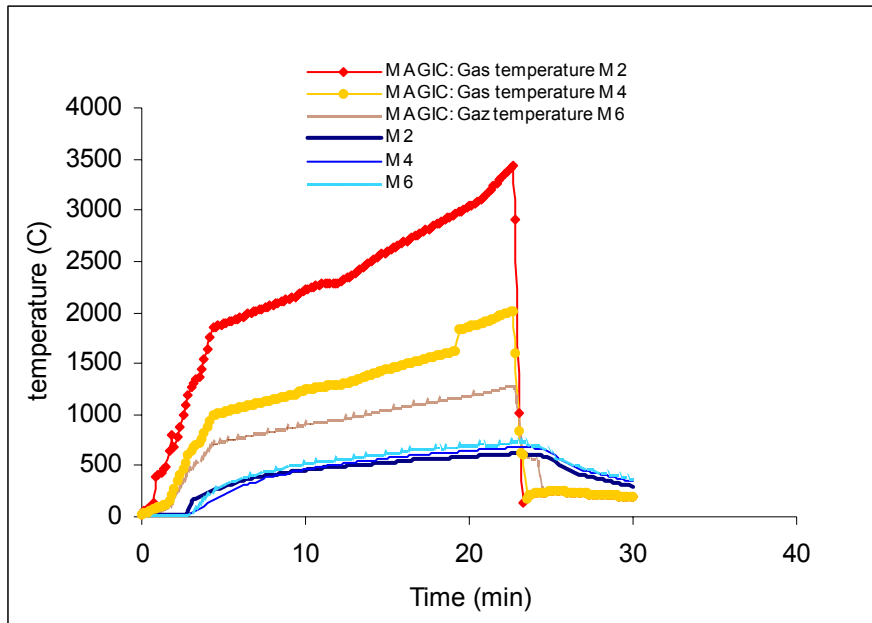


Fig. J15 Plume temperature: Test 1 and Test 3

J3.8 Oxygen concentration

The oxygen concentration predicted by MAGIC seems lower than the experimental results. In fact, the direct comparison is not really possible because the results given by sensor GA1-O2 indicate a local rather than an average layer value.

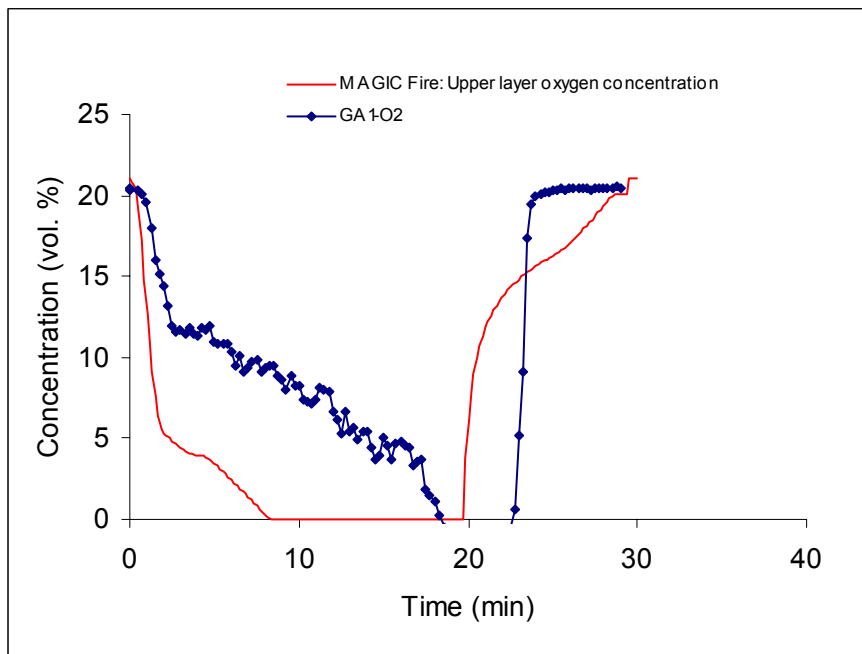
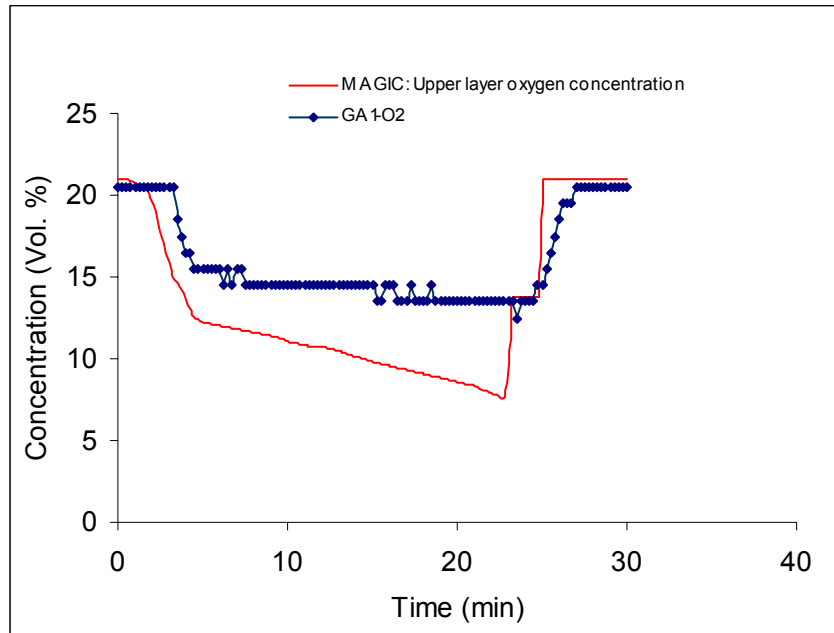


Fig. J16 Oxygen concentration: Test 1 and Test 3

J4 Parametric Study

J4.1 Heat release rate

A general assumption for fire risk studies is to use Babrauskas coefficients for HRR steady stage and a dynamic stage following a αt^2 law. Here for a kerosene fire /BAB 02/:

$$\Delta H_c = 43.2 \text{ MJ.kg}^{-1}; \dot{m}''_{\infty} = 0.039 \text{ kg.m}^{-2}.\text{s}^{-1}; k\beta = 3.5 \text{ m}^{-1}$$

Comparison to the HRR observed in the experiment shows that the real mass loss rate is far higher than the Babrauskas law prediction. Concerning fire risk study implications, this fact is mitigated by the fact that the Benchmark No. 4 room materials are thermally resistant, which is not the case in general for NPP.

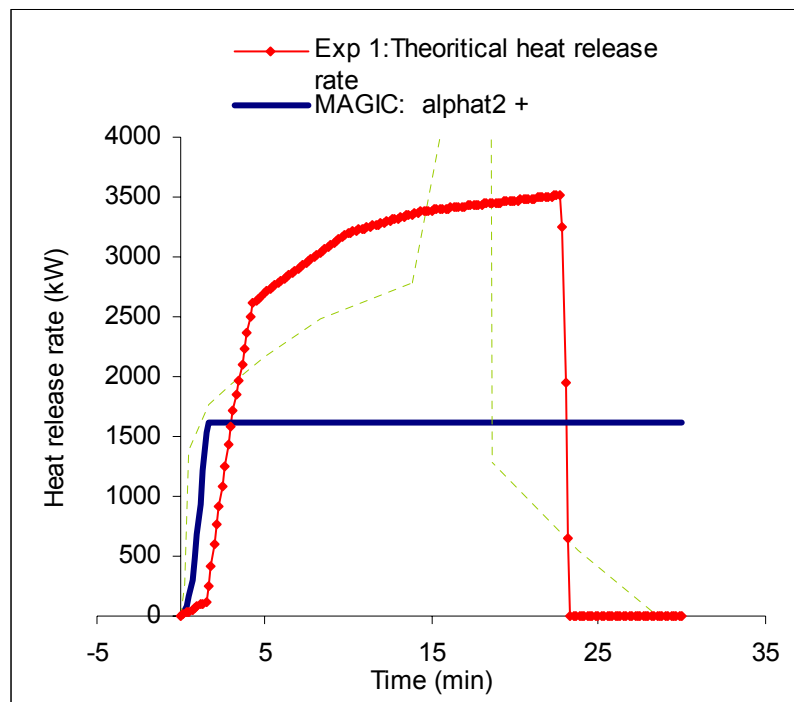


Fig. J17 Heat release rate: Test 1

J4.2 Effect of light concrete floor

The effect of taking into account or not the aerated concrete floor is evaluated in **Fig. J18**. A difference of about 80 °C is obtained on the upper layer temperature, which demonstrates the importance of the building materials on gas temperature levels.

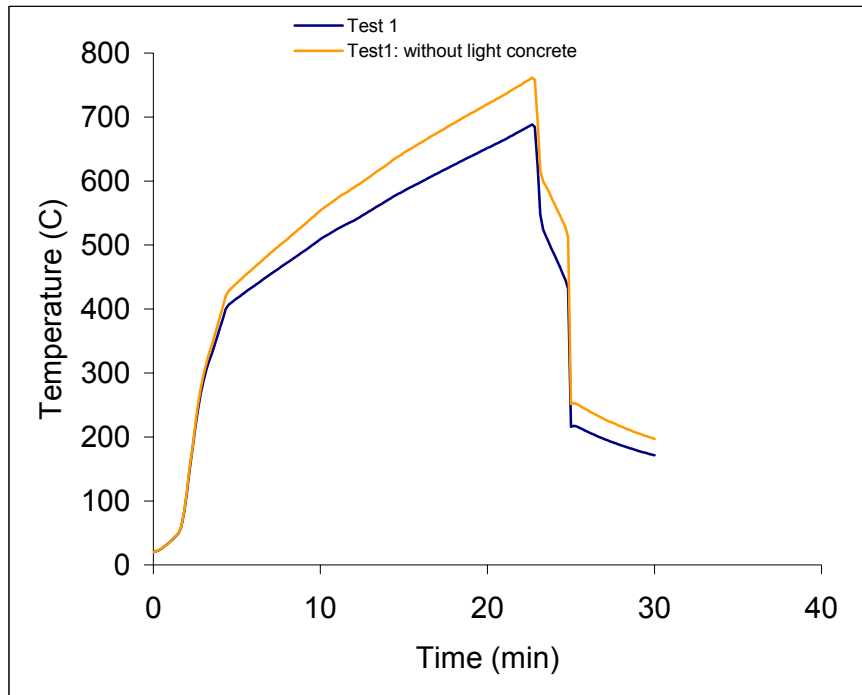


Fig. J18 Hot gas layer temperature: Test 1

J5 Conclusions and Remarks

MAGIC results appear more relevant in Test 1 (open door) than in Test 3 (semi-closed door). In Tests 1 gas temperature are realistic while target temperature and flux can be significantly over-estimated. In Test 3 gas layer temperature is little under-estimated, while condition on targets are in good prediction.

Indeed, in Test 3, the configuration induces more complex phenomena: the reduction of the opening cross section involves under-ventilated conditions. It seems that the flame was inclined to the door in the experiment. These phenomena are not represented in MAGIC.

Some experimental data appears to be questionable especially HRR in Test 3 and interface height. Some measurement like soot concentration or mass flow rate through the door are missing for a better understanding of the phenomena.

Information on the vent system would have permitted a more "fire risk study" approach of the test, by modelling also this system. Especially in Test 3, the ventilation due to the vent is comparable to the one due to the door (in calculation and probably in the test). It seems that the door circulation is under estimated by the calculation, maybe due to the hood effect.

J6 General Conclusions and Recommendations

We try to answer here - briefly - to the outline recommendation topics for conclusion.

What are the capabilities and strengths of the fire model for these specific scenarios?

Most of the results obtained by EDF are acceptable. When they differ sensibly with experimental data they are generally conservative.

What are the weaknesses and limitations of the fire model for the specific scenarios?

Predictions are less reliable in Test 3 where strong confinement and door interactions are strong.

Can the model be used with sufficient confidence for engineering analysis of this type of problem?

Yes as far as typical observed values are gas or target temperatures, flux on surface, and higher values considered as conservative.

Are there any specific elements of the model that need improvement for simulating the types of scenarios in this exercise?

Possibly on soot production and door/flame interaction but experimental data is missing to confirm that fact.

Is there a need for a more advanced model (e. g. CFD compared to zone) for predicting specific aspects of this scenario?

Best estimation of the flame zone location should be obtained from CFD calculation

Could more simple models (e.g. hand calculations) be adequate for some aspects?

Probably, depending on the observed results

Discuss any limitations of the two-zone approximation used in zone models in modeling the phenomena in the scenarios of the benchmark exercise

Done in the previous chapters.

What additional type of validation is necessary to determine the accuracy (uncertainty) of the model predictions for these specific scenarios?

See §J5

Identify the necessary knowledge required for the proper use of the model for these scenarios by engineers? Provide information that will be useful to other users that would prevent major errors in their use of the code for this specific problem?

See §J4: appropriate data for mass loss scenario is necessary here.

J7 References

- /GAY 06/ Gay L., Gautier B.,
 "Magic Software Version 4.1.1: Mathematical Model"
 HI-82/04/024/B - March 2006
- /SAL 06/ Salley, M. H. et al.
 "Verification and validation of selected fire models for nuclear power plant
 applications"
 NUREG-1824 / EPRI 1011999 January 2006
- /KLE 03/ Klein-Heßling, W. Röwekamp, M. Dobbernack R., Riese O.,
 "Specification of International Benchmarking and Validation Exercise #4:
 Kerosene pool fire inside a compartment"
 GRS, June 2003
- /KAS 02/ Kassawara, R. et al.,
 "Fire Modeling Guide for Nuclear Power Plant Applications"
 Final Report, August 2002 EPRI 1002981
- /BAB 02/ Babrauskas, V. ,
 "SFPE Handbook of Fire Protection Engineering".
 §3.1 Heat Release Rates 3d Edition 2002

List of Figures

Fig. J1	The proposed cases 1 and 3 (as represented in MAGIC).....	2
Fig. J2	Side view of OSKAR compartment - comparison to MAGIC representation	4
Fig. J3	Pyrolysis rate: Test 1 and Test 3.....	5
Fig. J4	Heat release rate: Test 1 and Test 3.....	8
Fig. J5	Layer height: Test 1 and Test 3	9
Fig. J6	Upper and lower temperature: Test 1 and Test 3.....	11
Fig. J7	Wall surface temperature: Test 1 and Test 3	12
Fig. J8	Heat flow to the walls: Test 1 and Test 3	13
Fig. J9	Steel target temperature: Test 1 and Test 3.....	14
Fig. J10	Concrete target temperature: Test 1 and Test 3	15
Fig. J11	Light Concrete target temperature: Test 1 and Test 3	16
Fig. J12	Total flux to Steel target : Test 1 and Test 3	17
Fig. J13	Total flux to Concrete target: Test 1 and Test 3.....	18
Fig. J14	Total flux to Light Concrete target: Test 1 and Test 3	19
Fig. J15	Plume temperature: Test 1 and Test 3.....	20
Fig. J16	Oxygen concentration: Test 1 and Test 3	21
Fig. J17	Heat release rate: Test 1.....	23
Fig. J18	Hot gas layer temperature: Test 1.....	24